

# **2019-2023**

# **China National Report on IUGG**

For

The 28th IUGG General Assembly

Berlin, Germany, July 11-20, 2023

Prepared by Chinese National Committee for  
International Union of Geodesy and Geophysics (CNC-IUGG)

July 6 2023

# **China National Report of IUGG/IACS (2019-2023)**

## **Content**

1. List of Committee members of CNC-IACS .....	2
2. Brief report for Important Conferences on Cryospheric Sciences .....	4
2.1 International Workshop on Cryospheric Changes in a Warming Climate....	4
2.2 The 2022 China Society of Cryospheric Science Council conference.....	7
3. Progresses on the Cryospheric Science in China .....	9
3.1 Glacier.....	9
3.2 Permafrost.....	16
3.3 Snow, Remote Sensing and Data.....	24
3.4 Cryospheric Hydrology.....	27
3.5 Cryosphere and Sustainable Development.....	33
3.6 Cryospheric Archives .....	42
3.7 Women Scientists Division.....	47

**China National Committee of IUGG/IACS  
(CNC-IACS)**

**June 28th, 2023**



## **1. List of Committee members of CNC-IACS**

**Honorary Chair:** Qin Dahe

**Chair:** Ding Yongjian

**Vice-Chair:**

Yao Tandong   Lai Yuanming   Zhang Renhe   Ma Wei   Yang Huigen   Luo Yong  
Kang Shichang   Xiao Cunde   Dong Wenjie

**Secretary General:** Kang Shichang

**Vice-Secretary General:** Li Chuanjin (Executive), Li Guoyu (Executive)

**Executive secretary:**

Mu Yanhu   Wang Shijin   Xie Aihong   Wang Shengxia

**Committee (in alphabetical order):**

Bian Lingen   Che Tao   Chen Rensheng   Chen Yaning   Chen Zhenlin  
Cheng Xiao   Ding Minghu   Ding Yongjian   Du Debin   Fang Chuanglin  
Fang Yiping   Dong Wenjie   He Daming   Gao Jing   Geng Lei   Hou Shugui  
Hu Yongyun   Jin Huijun   Kang Shichang   Lai Zhongping   Li Chuanjin  
Li Guoyu   Li Rongxing   Li Xichen   Li Xin   Li Yueqing   Li Yuansheng  
Li Zhen   Li Zhijun   Li Zhongqin   Liu Shiyin   Luo Yong   Lv Haishen   Ma Wei  
Ma Yaoming   Niu Fujun   Pan Baotian   Pang Hongxi   Qin Dahe   Ren Jiawen  
Shi Guitao   Shi Jiancheng   Sun Liguang   Sun Bo   Tian Feng   Tian Lide

Wang Chenghai Wang Genxu Wang Ninglian Wang Xin Wei Wenshou  
Wu Bingyi Wu Qingbai Xiao Cunde Xie Zhouqing Xu Baiqing Xu Shiming  
Yang Huigen Yang Jianping Yang Qinghua Yao Tandong Yi Shuhua  
Zhang Haisheng Zhang Qiang Zhang Renhe Zhang Shiqiang Zhang Tingjun  
Zhang Yili Zhang Xiaolei Zhang Jinzhao Zhao Jinping Zhao Lin  
Zhao Xinquan Zhou Shangzhe Zhu Liping

## **2. Brief report for Important Conferences on Cryospheric Sciences**

### **2.1 International Workshop on Cryospheric Changes in a Warming Climate**

In the context of global warming, the cryosphere is undergoing significant changes, which substantially impacts global and regional natural ecosystems as well as social and economic sustainable development. The social, economic and environmental problems caused by the cryosphere changes have attracted more attention from the scientific community, governments and public.

The International Workshop on “Cryospheric Changes in a Warming Climate: Filling the Gap between Observations and Decision-making” was successfully held in Lijiang, Yunnan Province, during October 26th-27th, 2019. The conference was co-organized by the State Key Laboratory of Cryosphere Sciences, Lijiang Municipal People's Government and Yulong Snow Mountain Glacier and Environment Observation and Research Station of the Chinese Academy of Sciences. More than 120 experts and scholars from the Northwest Institute of Eco-Environment and Resources, Chinese Academy of Sciences, the University of Alaska, the Menikov Institute of Permafrost Research of the Siberian Branch of the Russian Academy of Sciences and other universities and research institutes attended the meeting.

The conference featured three sub-forums: (1) Arctic cryosphere change and sustainable development, focusing on reviewing the latest progress of environmental and engineering research in the Arctic cryosphere in 2019 among China, United States, and Russia, and discussed specific work plans for 2020. (2) Changes, impacts and adaptation of the third polar cryosphere, discussing the research progress on the changes, impacts and adaptation of the third polar cryosphere. (3) Cryospheric services and functional evaluation in China, probing into the sustainable development of ecology, agriculture, economy and society in the western cryosphere of China.



**Fig. 1** Attendees were listening keynote speeches

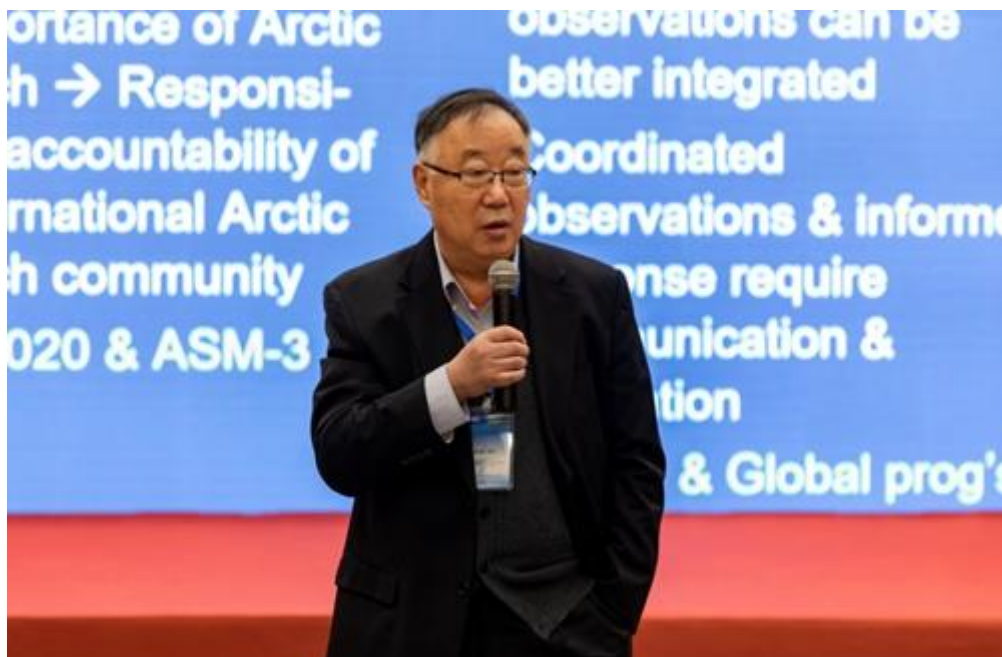


**Fig. 2** Prof. Qin Dahe representing a report

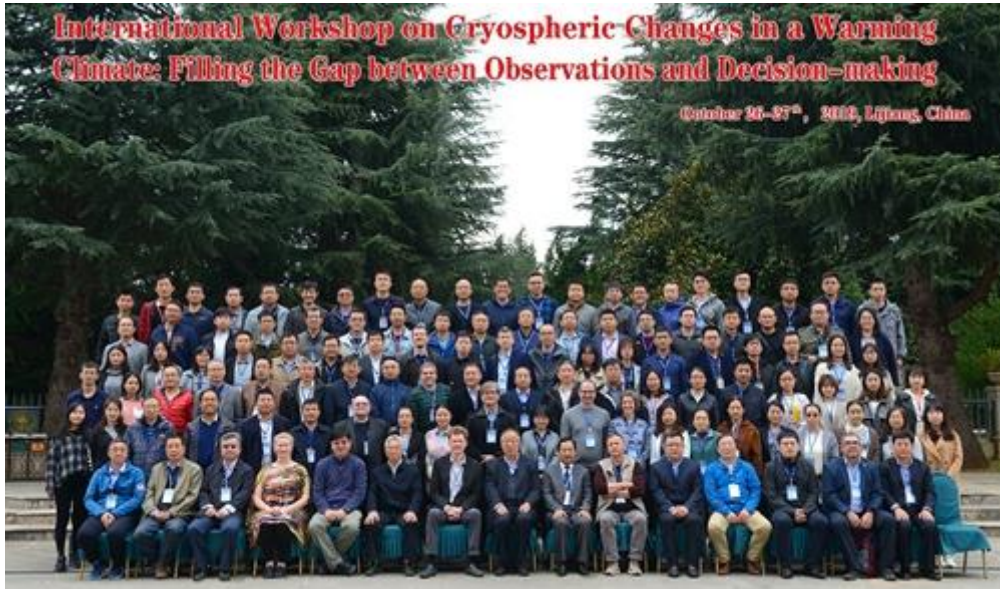


**Fig. 3** Group photo for most of the attendees

## 2.2 The 2022 China Society of Cryospheric Science Council conference

The 2022 China Society of Cryospheric Science Council conference was successfully held in Lingshui, Hainan, China, from March 25 to 26, 2023. The conference was hosted by the China Society of Cryospheric Science. The co-organizers include the State Key Laboratory of Cryospheric Science and State Key Laboratory of Frozen Soil Engineering, Northwest Institute of Eco-Environment and Resources, Chinese Academy of Sciences. The purposes of this conference were to further promote the development of cryospheric science in China, explore new direction for the development of cryospheric science, and make the scientific research of cryospheric science better serve the social economy and promote regional sustainable development. On March 25, Professor Dahe Qin (Member of the Chinese Academy of Sciences) first introduced the China Society of Cryospheric Science and the current status and development directions of cryospheric science. On behalf of the International Geographical Union (IGU), Guoyou Zhang presented the “2022 IGU Highest Honor Award” to Dahe Qin. “Shi Yafeng Cyrosphere and Environment Foundation” and “2022 Outstanding Scientist Award and Young Scientist Award” were also presented during the conference. Afterward, the experts had in-depth discussions about the development strategy of cryospheric science, and 18 professional committees introduced the annual work progress and achievements, hot topics, and key scientific issues and future works in detail.



**Fig. 4** the scene of the meeting





**Fig. 5** Guoyou Zhang presented the “2022 IGU Highest Honor Award” to Dahe Qin.



**Fig. 6** Group photo for most of the attendees

### **3. Progresses on the Cryospheric Science in China**

#### **3.1 Glacier (by Wang Ninglian, Li Zhongqin)**

China is the largest middle latitude country with highest glacier surface around the world besides Antarctica and Greenland. The investigations of glacier distribution and predicting their changes are thus very important, from evaluate the status of water resources and maintaining the national defense infrastructure in western China. Furthermore, such studies contribute to the development of Chinese cryospheric research, and also to the planetary change study. The Glacier Division aims to integrate the academic resources of glaciology in China, build a new platform for the global cooperation and exchange of cryosphere science in China, and strive to promote the development of cryosphere science. During the past five years, we have made remarkable progress in glacier investigation by providing scientific and technological support for snow safety at the Beijing 2022 Winter Olympics, constructing the "Mountain Glacier Mass Balance and Dynamics Monitoring Simulation Platform", and making scientific progress and achievement in local services.

#### **1. Conduct the Second Tibetan Plateau Scientific Expedition and the Third Xinjiang Scientific Expedition**

The Second Tibetan Plateau Scientific Expedition and the Pan Three Pole Special Glacier Survey was launched. On May 4, 2022, 13 members of the "Peak Mission" Everest Scientific Research of the Second Tibetan Plateau Scientific Expedition successfully climbed to the top of Mount Qomolangma to set up the world's highest Automatic Weather Station at 8830 m a.s.l. We used high-precision radar to measure the ice and snow thickness on the peak for the first time, and collected ice, snow, and atmospheric samples, from the scientific expedition to Mount Qomolangma. This is the first time that China's Mount Everest scientific research has exceeded an altitude of over 8000 m a.s.l., which is of epoch-making significance in the history of scientific research on the Tibetan Plateau. After the completion of the meteorological station installation, 8 meteorological gradient observation stations was established in the



Everest area from an altitude of 5200 a.s.l. to 8830 a.s.l. for achieving complete meteorological gradient information of Everest. This will provide valuable first-hand scientific data for perceiving climate and environmental variations in the Everest region. Concurrently, the Third Xinjiang Scientific Expedition Program has been launched, mainly focusing on the practical needs of green development and sustainability in Xinjiang. At watershed scales, problem-oriented and contemporary high-tech amenities, the project emphasizes on conducting comprehensive scientific investigations throughout the Xinjiang Uygur Autonomous Region, for an in-depth understanding of the resources and environment in Xinjiang region together with intensive scientifically estimation of the carrying capacity of regional resources and environment. Moreover novel and systematic plans were proposed to eradicate driving forces for achieving high-quality development. Relying on the Tianshan Glaciological Station, a total of 6 glacier wide projects have been approved by the Third Xinjiang Scientific Expedition Program.

## **2. Conduct research on key technologies of Event Snow Support to provide scientific and technological support for the snow safety of the Beijing 2022 Winter Olympics**

We have undertaken the National Key R&D Program of China "Research and Application Demonstration of Key Technologies for Event Snow Support". Through nearly six years of research, we have provided a wide range of technical support and service for the snow-related projects of the Beijing 2022 Winter Olympics in ski resorts, snow storage, snow quality assurance, and track maintenance. Among them, the developed discriminative model of track snow quality grade has been applied in the evaluation of track snow quality risk grade for the 2021 "Meet Beijing" test event, and a series of snow quality analysis reports have been released. In the National Alpine Skiing Centre in Yanqing, Beijing, the experiment of making an ice snow track was carried out, and the key technologies of different water injection techniques and compaction methods were achieved. In November 2021, a "one game, one strategy"

snow storage and maintenance plan for each competition snow field was submitted to the Olympic Organizing Committee. During the Winter Olympics, it will provide technical support and service guarantee for the Big Air Shougang, the National Jump Center, Genting Snow Park and other Olympic venues. At present, this achievement is undergoing system integration to form an integrated solution for snow protection with Chinese characteristics. During the "Post Winter Olympics" period, it will help achieve the goal of "driving 300 million people to participate in ice and snow sports" and provide technological support for China's ice and snow industry's strategy of "expanding south, west, and east". The achievement of "snow protection for Winter Olympics events" was selected as a highlight of scientific and technological innovation by the Chinese Academy of Sciences in 2021.

### **3. Construct a "Mountain Glacier Mass Balance and Dynamics Monitoring Simulation Platform"**

The construction of massive apparatus is done with a focus on the two "Cryosphere Simulator" and "Mountain Glacier Mass Balance and Dynamics Monitoring Simulation Platform" projects of the field station of the Chinese Academy of Sciences: a) Building a reference glacier monitoring network using ultra-long-range terrestrial laser scanning. Up to now, four glacier monitoring towers (including Urumqi Glacier No.1 monitoring tower, Keqicar Glacier monitoring tower in western Tianshan Mountains, Glacier No.29 in Zhazigou of Qilian Mountains, and one glacier in the Altai Mountain) have been carried out, and b) TGS glacier simulation platform construction. The TGS Glacier Simulation Main Platform's interior décor and the configuration of a few instruments and pieces of equipment are currently complete, and the platform's data processing, research simulation, and display capabilities will be implemented one at a time. c) "Cryosphere simulator" construction. After completion of laboratory setup, it will be easier to precisely simulate wide-scale regional glacier mass balance, long-term dynamics, and high-precision future prediction along with snow-ice water melting and contribution towards arid regions of northwest China.

### **4. Numerous significant scientific advances have been accomplished**

- **The latest achievements systematically explain the imbalance of Asian water tower**

The Second Tibetan Plateau Scientific Expedition published the latest research results in "Nature Reviews: Earth and Environment", systematically elaborating on the issue of the imbalance of Asian water tower (Yao et al., 2022). This achievement found that the main characteristic of the imbalance of Asian water tower is that solid water (e.g. ice and snow) is rapidly melting and liquid water is showing an increasing trend; From a spatial perspective, the increase in liquid water is mainly in the northern endorheic basin, while the liquid water in some watersheds in the southern exorheic basins shows a decreasing trend. The rapid warming of the Third Pole climate has changed the proportion of solid water such as glaciers and liquid water such as lakes and rivers. At present, the water supply in the southern exorheic basins of the Asian Water Tower is decreasing, but the water demand in the downstream area of the southern endorheic basin has sharply increased. So the contradiction between water supply and demand will become increasingly serious.

- **Underestimation of mass loss from lake-terminating glaciers in the greater Himalaya**

The Second Tibetan Plateau Scientific Expedition published the latest research results on the underestimated mass loss from lake-terminating glaciers in the greater Himalaya in Nature Geoscience (Zhang et al., 2023). The research results that proglacial lakes have increased 47% by number,  $33 \pm 2\%$  by area and  $42 \pm 14\%$  by volume from 2000 to 2020. The expansion of glacial lakes has resulted in  $2.7 \pm 0.8$  Gt of subaqueous mass loss between 2000 and 2020. A preliminary estimate of the global underwater ice loss caused by ice lake contact with glaciers was also made, with a loss of approximately 210 billion tons, accounting for 12%. This study provides a framework for quantifying underwater ice mass loss, reduces the uncertainty of estimating total ice mass loss, and provides important scientific basis for more accurate simulation of past and future glacier mass balance, assessment of glacier and ice lake disasters and changes in water resources.

- **Glacier retreat accelerates global chemical weathering**

The Second Tibetan Plateau Scientific Expedition published conclusive evidence on Nature Communications that glacier retreat accelerates global chemical weathering (Li et al., 2022). With the support of the Second Tibetan Plateau Scientific Expedition Project, this study completed the sampling and data collection of glacier meltwater chemistry from 43 glaciers in Tibetan Plateau and its surroundings. Combined with the monitoring results of meltwater chemistry from glaciers in other regions around the world, we formed a hydro-chemical dataset of 5465 meltwater runoff samples worldwide. Using cation erosion rate as a proxy indicator for chemical weathering rate, contemporary cation denudation rates beneath glaciers are ~3 times higher than two decades ago, up to 10 times higher than ice sheet catchments, up to 50 times higher than whole ice sheet means and ~4 times higher than major non-glacial riverine means. Glacial cation denudation rates are positively correlated with air temperature, suggesting glacial chemical weathering yields are likely to increase in future. Our findings highlight that chemical weathering beneath glaciers is more intense than many other terrestrial systems and may become increasingly important for regional biogeochemical cycles.

- **The risk of glacial lake outburst flood in the Third Pole will increase in the future**

Increasing climate uncertainties and unpredicted changes at the Earth's Third Pole is collectively accelerating the rapid loss of ice, which resulted in formation and expansion of glacial lakes, becoming a severe threat to flash floods downstream. Researchers have published a paper in Nature Climate Change to reveal the increasing risk of glacial lake outburst floods from future Third Pole deglaciation (Zheng et al., 2021). The results demonstrate maximum glacial lake outburst flood (GLOF) risk is concentrated in the eastern Himalayas as compared with its adjacent regions, which is projected to be increased in coming decades. Additionally, GLOF risk be increased dramatically in the near future by developing new and rapid spatial expansion of

existing lakes together with alarming frontal glacier recession. With apparent increases in GLOF risk already anticipated by the mid-twenty-first century in some regions, the results highlight the urgent need for forward-looking, collaborative, long-term approaches to mitigate future impacts and enhance sustainable development across the Third Pole.

## **5. Remarkable results have been achieved in local services**

- Assist Jimunai County in the Altai Prefecture of Xinjiang Uygur Autonomous Region in industrial poverty alleviation: By analyzing and evaluating the future variation of water resources in Jimunai County, and obtain the conclusion that “one side of water and soil cannot nurture one side of people”. Only through water diversion can the fundamental problem of water shortage in Jimunai County be solved. And help to strive for 100 million cubic meters of water diversion rights. Participate in the construction project of Jimunai County's introduction of the “Ten Thousand Camels Garden” Industrial Park, and help Jimunai County to alleviate poverty and revitalize the countryside.

- Applying artificial snowfall to reduce glacier melt and further help the sustainable development of regional ecotourism: Dagu Glacier is located at the eastern edge of the Tibetan Plateau. Since Dagu Glacier is an important tourism resource in Heishui County, its rapid retreat has seriously restricted the sustainable development of local glacier tourism, so it is particularly urgent to use artificial measures to retard the glacier melting. Since 2020, researchers at Tianshan Glaciological Station have conducted glacier "blanket" protection experiments on the Dagu Glacier using the method of covering insulation materials. Based on previous experiments, a new type of nano material will be laid on the surface of glaciers. After summer, it is preliminarily estimated that the new nanomaterials can effectively reduce glacier ablation by about 80%, which is comparatively better than the geotextile implemented in 2020. This effort plays an important role in continuously serving the region's geo-environmental protection and sustainable development.

## **References:**

1. Li X., Wang N., Ding Y. et al. Globally elevated chemical weathering rates beneath glaciers. *Nat Commun* 13, 407 (2022).
2. Yao T., Bolch T., Chen D. et al. The imbalance of the Asian water tower. *Nat Rev Earth Environ* 3, 618–632 (2022).
3. Zhang G., Bolch T., Yao T. et al. Underestimated mass loss from lake-terminating glaciers in the greater Himalaya. *Nat. Geosci.* 16, 333–338 (2023).
4. Zheng G., Allen SK., Bao A. et al. Increasing risk of glacial lake outburst floods from future Third Pole deglaciation. *Nat. Clim. Chang.* 11, 411–417 (2021).

### **3.2 Permafrost (by Wu Qingbai, Zhao Lin)**

#### **1. Academic exchanges in permafrost research are gradually normalizing**

- The International Permafrost Association has been forced to cancel the 12<sup>th</sup> International Conference of permafrost in China due to the COVID-19 pandemic. The canceled 12<sup>th</sup> International Conference on Frozen Soil Engineering is scheduled to be held in Lanzhou in September 2024.
- In order to extensive academic exchanges on frozen soil and cold region engineering, the State Key laboratory of Frozen soil Engineering proposed the initiative of National Conference on Frozen Soil Environment and Cold Region Engineering, and the first National Conference was held in Lanzhou. The second conference was held in Nanchang in 2021, and the third conference was held in Nanjing in 2023. The fourth conference will be held in Lanzhou in 2024.
- Under the guidance of the Chinese Society of Rock Mechanics and Engineering, the Polar Geotechnical Engineering Professional Committee was set up, and the founding meeting of the professional committee was held in Harbin in 2023, and a high-end forum was held on polar geotechnical engineering issues.

#### **2. Progress on permafrost research**

- **Permafrost in the Cretaceous supergreenhouse**

Earth's climate during the last 4.6 billion years has changed repeatedly between cold and warm (greenhouse) conditions. The hottest conditions (supergreenhouse) are widely assumed to have lacked an active cryosphere. Here we show that during the archetypal supergreenhouse Cretaceous Earth, an active cryosphere with permafrost existed in Chinese plateau deserts (astrochronological age ca. 132.49–132.17 Ma), and that a modern analog for these plateau cryospheric conditions is the aeolian–permafrost system we report from the Qionghuailake area, Xinjiang Uygur Autonomous Region, China. Significantly, Cretaceous plateau permafrost was coeval with largely marine cryospheric indicators in the Arctic and Australia, indicating a strong coupling

of the ocean–atmosphere system. The Cretaceous permafrost contained a rich microbiome at subtropical palaeolatitude and 3–4 km palaeoaltitude, analogous to recent permafrost in the western Himalayas. The mindset of persistent ice-free greenhouse conditions during the Cretaceous has stifled consideration of permafrost thaw as a contributor of C and nutrients to the palaeo-oceans and palaeo-atmosphere.

- **Permafrost thawing puts the frozen carbon at risk over the Tibetan Plateau**

Soil organic carbon (SOC) stored in permafrost across the high-latitude/altitude Northern Hemisphere represents an important potential carbon source under future warming. Here, we provide a comprehensive investigation of the spatiotemporal dynamics of SOC over the high-altitude Tibetan Plateau (TP), which has previously received less attention as compared with the circum-Arctic region. The permafrost region covers ~42% of the entire TP and contains ~37.21 Pg perennially frozen SOC at the baseline period (2006–2015). With continuous global and regional warming, the active layer is projected to further deepen, resulting in  $\sim 1.86 \pm 0.49$  Pg and  $\sim 3.80 \pm 0.76$  Pg permafrost carbon thawing by 2100 under moderate and high representative concentration pathways (RCP4.5 and RCP8.5), respectively. This could largely offset the regional carbon sink and even potentially turn the region into a net carbon source. Our findings also highlight the importance of deep permafrost thawing which is generally ignored in current Earth system models.

- **Characteristics of methane emissions from alpine thermokarst lakes on the Tibetan Plateau**

Understanding methane (CH<sub>4</sub>) emission from thermokarst lakes is crucial for predicting the impacts of abrupt thaw on the permafrost carbon-climate feedback. However, observational evidence, especially from high-altitude permafrost regions, is still scarce. Here, by combining field surveys, radio- and stable-carbon isotopic analyses, and metagenomic sequencing. We presents an analysis of multiple characteristics of



CH<sub>4</sub> emissions from 120 thermokarst lakes in 30 clusters along an 1100 km transect on the Tibetan Plateau. We find that thermokarst lakes have high CH<sub>4</sub> emissions during the ice-free period ( $13.4 \pm 1.5$  mmol m<sup>-2</sup> d<sup>-1</sup>; mean  $\pm$  standard error) across this alpine permafrost region. Ebullition constitutes 84% of CH<sub>4</sub> emissions, which are fueled primarily by recent carbon decomposition through the hydrogenotrophic pathway. The relative abundances of methanogenic genes correspond to the observed CH<sub>4</sub> fluxes. Overall, multiple parameters obtained in this study provide benchmarks for better predicting the strength of permafrost carbon-climate feedback in high-altitude permafrost regions.

- **Divergent changes in particulate and mineral-associated organic carbon upon permafrost thaw**

Permafrost thaw can stimulate microbial decomposition and induce soil carbon (C) loss, potentially trigger a positive C-climate feedback mechanism. However, earlier observations have concentrated on bulk soil C dynamics upon permafrost thaw, with limited evidence involving soil C fractions. Here, we explore the distinct performance fractions, including particulate and mineral-associated organic C (POC and MAOC) as well as iron-bound organic C (OC-Fe), respond to permafrost thaw using systematic measurements derived from one permafrost thaw sequence and five additional thermokarst-impacted sites of the Tibetan Plateau. We find that topsoil POC content substantially decreases, while MAOC content remains stable and OC-Fe accumulates due to the enriched Fe oxides after permafrost thaw. Moreover, the proportion of MAOC and OC-Fe increase along the thaw sequence and at most of the thermokarst-impacted sites. The fairly enriched stable soil C fractions would alleviate microbial decomposition and deteriorate its response to climate warming over long-term thermokarst progress.

- **The first synthesis dataset of permafrost thermal state for the Qinghai–Tibet (Xizang) Plateau, China**

A comprehensive dataset has been first released, which consisting of long-term meteorological, ground temperature, soil moisture, and soil temperature data was

compiled after quality control from an integrated, distributed, and multiscale observation network in the permafrost regions of Qinghai-Tibet Plateau. The dataset includes six automatic meteorological stations, 12 active layers and 84 boreholes in the Qinghai-Tibet Plateau permafrost region, with observations of meteorology (temperature, precipitation, wind speed, specific humidity, etc.), multi-layer soil temperature and moisture, active layer thickness and permafrost temperature. The dataset is helpful for scientists with multiple study fields (i.e., climate, cryospheric, ecology and hydrology, meteorology science), which will significantly promote the verification, development, and improvement of hydrological models, land surface process models, and climate models on the Qinghai-Tibet Plateau. Since its release in 2021, the dataset has been viewed more than 10,000 times and downloaded more than 2,000 times for contemporary research purposes.

- **Characteristic, changes and impacts of permafrost on Qinghai-Tibet Plateau**

A systematic summary of the latest research progress on the characteristics of the current state permafrost on the Qinghai-Tibet Plateau (QTP), including the active layer thickness, the spatial distribution of permafrost, permafrost temperature and thickness, as well as the ground ice and soil carbon storage in the permafrost region. The permafrost thickness varies greatly among topography, with the maximum value in mountainous areas, which could be deeper than 200 m, while the minimum value in the flat areas and mountain valleys, which could be less than 60 m. The mean active layer thickness of the permafrost on the QTP is 2.3 m, with 80% of the permafrost regions ranging from 0.8 m to 3.5 m. From 2004 to 2018, the increasing rate of the soil temperature at the bottom of the active layer was  $0.486^{\circ}\text{C}/10\text{ a}$ .

The ground ice volume of the permafrost is estimated up to  $1.27 \times 10^4\text{ km}^3$  (liquid water equivalent). The soil organic carbon in the upper 2 m of the permafrost region is about 17 Pg; there is a large uncertainty in this estimation however due to the great heterogeneities in the soil column. Although the permafrost ecosystem is a carbon sink

at present, it may shift to a carbon source due to the loss of soil organic carbon along with permafrost degradation. Most of the permafrost on the QTP belongs to the unstable permafrost, meaning that permafrost over QTP is very sensitive to climate warming. Permafrost degradation greatly affects regional hydrology, ecology, and even the global climate system.

- **Establishment of the permafrost model and deformation inversion method for permafrost change on the Qinghai-Tibet Plateau**

A moving-grid permafrost numerical model considering phase change, ground ice, geothermal flux and thawing settlement was developed and used to simulate the long-term dynamic changes and spatial and temporal distribution of thawing settlement in the permafrost regions on the Qinghai-Tibet Plateau, and to predict the future change trends and possible thawing risks. Meanwhile, a ground deformation detection method for active layer thickness change and ground ice melting was developed, and its accuracy in the permafrost regions on the Qinghai-Tibet Plateau was improved by the SBAS-InSAR process algorithm, and the amount of ground ice loss in the permafrost was estimated based on the relationship between the long-term deformation trend and ground ice melting rate.

- **Permafrost thawing and water resources**

Recent studies have identified long-term surface subsidence, which can serve as an indicator of ground ice melting and provide a proxy to an approximation of cryospheric meltwater budget. By correlating subsidence measurements with ground ice richness from drilling cores, the rate of active layer thickening, and the increase in liquid water at the bottom of the active layer, it has become evident that the long-term ground subsidence directly represents the melting of ground ice.

The Differential Interferometric Synthetic Aperture Radar (D-InSAR) technique and the derived multitemporal InSAR (MT-InSAR) exhibit great potential in detecting terrain deformation on the order of millimeters to centimeters over large permafrost

areas. Through the application of InSAR monitoring, it becomes possible to estimate the volume of ground ice meltwater based on ground deformation at the regional and watershed scales. Results reveal that ground ice meltwater contributes around 10% increase in lake volume within the endorheic basins and contributes approximately 2% (1.3% for the source region of the Yellow River and 2.8% for the source region of the Yangtze River) to river runoff in the upstream regions of these two major rivers in China.

### **3. Great programs during 2019-2023**

- **“Survey on Latitudinal Permafrost and Frost hazards along the infrastructures in Northeast China”, Science & Technology Fundamental Resources Investigation Program (Grant No. 2022FY100705)**

The latitudinal permafrost in Northeast China is the largest reservoir of soil organic carbon and an important ecological barrier in North China, as well as a hub area for the transportation and Oil & gas pipeline projects along the China-Mongolia-Russia Economic Corridor. As a result of permafrost degradation, significant changes are occurring in the water cycle, forest and wetland ecosystems, and carbon cycling processes in permafrost regions. Moreover, freeze-thaw related geohazards also frequently occurred widely along the infrastructure routes.

This research project aims to collect, compile, investigate, and observe basic data on permafrost characteristics, frozen soil engineering damage, and environmental factors in Northeast China. Kamalan River Basin on the east slope of the Greater Khingan and the Genhe River Basin on the west slope is as the typical survey areas to carry out the field survey on the permafrost characteristics and the distribution of frost damage along the existing infrastructures in Northeast China. A comprehensive permafrost observation network is carried out in-situ observations of permafrost ground temperature, active layer hydrothermal and meteorological elements. Then, all data are used to compile the spatial distribution map of the main characteristic parameters of the permafrost in Northeast China, as well as the distribution map of engineering frost damage and stability. A basic database including permafrost characteristics, engineering frost damage and environmental factors in Northeast China is constructed. Eventually,

the current situation and development pattern of permafrost and engineering frost damage in Northeast China will be assessed, and the evolvement process of permafrost and engineering stability under climate change will be predicted. It provides important scientific and technological support for national and regional ecological environment protection, green silk-road construction along the China-Mongolia-Russia Economic Corridor, water resources protection with regional economic and social development.

- **The National Key R&D Program supported by the Ministry of Science and Technology, “Arctic terrestrial environmental change and their effects” 2020YFA0608500**

This project intends to conduct interdisciplinary research around the core theme of "clarifying the temporal and spatial changes of Arctic terrestrial environmental factors, the processes of energy and water exchange between the land and atmospheric systems and their climate feedback, as well as the release, migration and transformation of terrestrial environmental pollutants and their ecological impacts, and quantitatively assessing of the beneficial and harmful effects of Arctic terrestrial environmental change", aiming to solve the following key scientific problems: (1) What is the process and mechanism of terrestrial environmental response to rapid warming in different regions of the Arctic? (2) What is the impact of Arctic terrestrial environmental change on the energy-water exchange process in the land-atmosphere system and its feedback to climate? (3) What is the mechanism of occurrence, source, migration and transformation of typical pollutants in the Arctic terrestrial environment? (4) How can the service function and disaster risk of Arctic terrestrial environmental change be assessed quantitatively and comprehensively? The project attempts to carry out monitoring and simulation research on key factors of the Arctic terrestrial environment, to establish a comprehensive Arctic terrestrial environment data platform based on multi-source data such as in-situ observations, remote sensing and reanalysis of existing glaciers, permafrost, snow and vegetation in the Arctic, and to develop parameterisation schemes for Arctic glaciers, permafrost, snow and vegetation; To elucidate the process

mechanism of deposition, release and migration of pollutants in the Arctic terrestrial environment; to quantitatively assess the beneficial and detrimental effects of changes in the Arctic terrestrial environment. Through cross-cutting research in natural and human sciences, we propose adaptation strategies for Arctic sustainable development.

### **3.3 Snow, Remote Sensing and Data (By Li Xin and Che Tao)**

- **Ground-based Snowpack Observation**

Based on field practices in snowpack observation, ground-based snowpack observation standards were established. The snowpack observations from meteorological stations in China were compiled, and the representativeness of stations was evaluated. Two complete snow season surveys on snowpack were conducted at points, lines, and surfaces. Annual work reports and investigation reports for typical snow cover areas in China were written. Based on quality checks on all observations, data description documents and metadata were compiled, resulting in the creation of 7 datasets. The datasets and standards were reviewed by experts and have been published and shared by the National Cryosphere Desert Data Center (<http://www.ncdc.ac.cn/portal/>).

- **Long-term Snow Products**

Using station observations, high-resolution remote sensing data, and reanalysis data, the characteristics, properties and deficiencies of existing major snow products were comprehensively evaluated in northern Xinjiang, the Qinghai-Tibet Plateau, and the Inner Mongolia-Northeast China snow (Hao et al. 2019; Liu et al. 2020), resulting in a snow product evaluation report. Daily cloud-free snow cover products with a resolution of 5 km from 1980 to 2020 and daily cloud-free snow cover products with a resolution of 500 m from 2000 to 2020 were developed with accuracies of 90% and 94%, respectively (Hao et al. 2021). The total data volume of the cloud-free snow cover products was 13.7 TB. A daily snow water equivalent product with a resolution of 25 km from 1980 to 2020 was developed with an accuracy of 10 mm and a data volume of 100 GB (Yang et al. 2019a; Yang et al. 2019b). A daily and 8-day cloud-free snow albedo product with a resolution of 1 km from 2000 to 2020 was developed with an accuracy of 0.11 and a data volume of 500 GB. Expert reviews of accuracy indicators were completed. All datasets were accompanied by accuracy verification reports and data description manuals and have been published and shared by the National Cryosphere Desert Data Center.

## ● Thematic Maps and Database

Based on the water and thermal properties and stability of snow cover, the snow cover types in China were classified, and a distribution map of snow cover types was produced (Li et al. 2022). Based on ground-based observations, remote sensing data, and the results of snow cover type classification, a series of Chinese snow cover type maps were compiled. In addition, a series of thematic maps including the water-thermal effect of snow cover in typical agricultural areas of Northeast China, the snow-melt flood hazards on the north and south slopes of the middle section of the Tian Shan Mountains in Xinjiang, the snow disasters over pastoral areas of Qinghai-Tibet Plateau, and the snow water resources in typical watersheds in northwest China were completed. A database of Chinese snow cover characteristics and distribution survey was constructed, including database queries, statistics, analysis, and other related functions. The data including observations and products were standard and stored, and the remote access and remote operation of the database were enabled. Additionally, the "Demand Analysis Report of the Chinese Snow Cover Characteristics Survey Database" was compiled. The thematic maps and database were reviewed by experts and have been published and shared by the National Cryosphere Desert Data Center.

## References:

1. Hao X, Huang G, Che T, et al. The NIEER AVHRR snow cover extent product over China – a long-term daily snow record for regional climate research. *Earth System Science Data*, 2021, 13(10): 4711-4726. <https://doi.org/10.5194/essd-13-4711-2021>.
2. Hao X, Luo S, Che T, et al. Accuracy assessment of four cloud-free snow cover products over the Qinghai-Tibetan Plateau. *International Journal of Digital Earth*, 2019, 12(4): 375-393. <https://doi.org/10.1080/17538947.2017.1421721>.
3. Li H, Zhong X, Zheng L, et al. Classification of Snow Cover Persistence across China. *Water*, 2022, 14: 933. <https://doi.org/10.3390/w14060933>.
4. Liu C, Li Z, Zhang P, et al. An Assessment and Error Analysis of MOD10A1 Snow



- Product Using Landsat and Ground Observations Over China During 2000–2016. *IEEE Journal of Selected Topics in Applied Earth Observations and Remote Sensing*, 2020, 13: 1467-1478. <https://doi.org/10.1109/JSTARS.2020.2983550>.
5. Yang J, Jiang L, Dai L, et al. The Consistency of SSM/I vs. SSMIS and the Influence on Snow Cover Detection and Snow Depth Estimation over China. *Remote Sensing*, 2019a, 11(16): 1879. <https://doi.org/10.3390/rs11161879>.
  6. Yang J, Jiang L, Wu S, et al. Development of a Snow Depth Estimation Algorithm over China for the FY-3D/MWRI. *Remote Sensing*, 2019b, 11(8): 977. <https://doi.org/10.3390/rs11080977>.

### **3.4 Cryospheric Hydrology (by Chen Rensheng, Zhang Shiqiang)**

#### **1. Hydrological basis and discipline system of Cryohydrology**

Cryohydrology is a new interdisciplinary branch of Cryosphere and Hydrology science, which aims to deepen the understanding of the theoretical and cognitive levels of its mechanisms and processes, accurately quantify the hydrological functions of the basin, and promote understanding of the ecological and environmental impacts of the cryosphere (Ding et al., 2020).

Initially, Cryohydrology was referred to as hydrology involving low temperatures, for example, the hydrological study of snow, ice, frozen ground, and cold water. This discipline broadened with the development of cryospheric science and now involves hydrological processes of various cryosphere elements systematically coupled with river basin hydrological processes. However, limited studies have introduced the characteristics and discipline connotations of Cryohydrology from a perspective of cryospheric science (Ding et al., 2020).

Here, we reviewed the evolution of the connotations of Cryohydrology and analyzed its hydrological basis and discipline system. Three major conclusions were drawn: (1) Cryohydrology was developed based on traditional hydrology for a single element of the cryosphere and focuses on the hydrological functions of the cryosphere and its impact on the water cycle and water supply to other spheres; (2) The hydrological basis of Cryohydrology can be summarized as water conservation, runoff recharge, and hydrological regulation. In detail, the water conservation function is primarily expressed as “source of freshwater” and “cold and wet islands”, the runoff recharge function is concerned with water supply, and the regulation function is effective at intra and inter-annual scales; (3) The core research issues of Cryohydrology are research methods, hydrological processes, watershed functions and regional impact. The important characteristics of Cryohydrology are frequent water phase transitions and high variability across spatial and temporal scales (Ding et al., 2020).

#### **2. Impact of cryospheric changes on runoff in the main cold basins in China**

Based on the long-term observation in several alpine watersheds and previous research on Cryohydrology, a cryospheric basin hydrology model was created to simulate and project the past and future runoff in the main cold basins in China (Chen et al., 2019). As a result, the impact of cryospheric changes on runoff in these cold basins was analyzed. The main conclusions are shown as follows (Chen et al., 2019; Ding & Xiao, 2019):

1) The tipping point of glacier runoff has or will appeared in the near future in most of cold basins in China. The time of occurrence depends on the glacier size in these basins.

2) Degradation of frozen ground (including permafrost and seasonally frozen ground) has increased and decreased the river discharge in winter and summer respectively in most of the cold basins. In addition, it has shortened the annual runoff hydrograph. However, these effects have not appeared in the basins with permafrost coverage greater than 40%.

3) Due to increasing snowfall above the snowline, the snowmelt has increased in the past 50 years and would also increase in the next 80 years in most alpine cold basins in China. However, the rapid warming has caused an earlier onset of spring that induces earlier snowmelt and associated peak streamflow, especially in the mountainous basins where the snowmelt occupies the majority of river runoff.

4) Increased winter runoff, earlier snowmelt flood and increased glacier runoff (with large glaciers) are the main present impacts of the cryosphere to river runoff in cold basins in China.

5) Although the cryospheric runoff would decrease largely in the near future, the future runoff would increase weakly due to increasing precipitation in the most of the western river basins in China. However, the runoff distribution would vary largely on month, year and decade scales. The available stable water resources would depend on the limited temperature rise to 2 °C in western especially in the arid Northwest China.

### **3. Water supply function of Cryosphere in China**

With global warming and rapid shrinkage of the cryosphere, the decreasing cryosphere water resources (CWR) supply function would weaken its service and then affect local economic development and implement of United Nations Sustainable Development Goals (SDGs) in the world, but how does the CWR supply affect its service and their variations in the past and future are still not clear at present. Therefore, the past dynamics (1960-2020), current situation (2010s) and projected changes (2020-2100) of CWR in China were assessed by calculating the meltwater from glacier, snow cover and the ground ice of permafrost under Representative Concentration Pathways scenarios (RCP2.6, RCP4.5, and RCP8.5) (Li et al., 2022).

The annual CWR in China is about  $3107 \times 10^8 \text{ m}^3$  in the 2010s, with glacier runoff, snowmelt, and ground ice meltwater accounting for 24.1%, 72.7% and 3.2%, respectively. The annual average glacier runoff and snowmelt is about  $615 \times 10^8 \text{ m}^3$  and  $2370 \times 10^8 \text{ m}^3$  from 1961 to 2017 in China (Li et al., 2022; Yang et al., 2022). Although the total volume of ground ice in the permafrost regions is twice of the glacier in China, its annual meltwater is only  $175 \times 10^8 \text{ m}^3$  at present.

The CWR accounts for large amounts ratio in Western and Northeast basins especially in the arid Northwest China, where the CWR ratio varies from about 20% to 85%.

From 1960 to 2017, the CWR has weakly increased. Whereas in the future, the quantity of CWR was projected to decline by 14%-18% over the next 80 years Under SSP1-RCP2.6. While under SSP5-RCP8.5, CWR would be reduced by 40% by 2100. The study of CWR is of great significance for water security, sustainable development and risk avoidance in the arid endorheic region (Li et al., 2022).

#### **4. Water resources service of Cryosphere in China**

The global warming has been accelerating the cryospheric ablation in the recent years. Therefore, it should know about the future changes of cryospheric water and its effects to the social and economic development under Paris Agreement, but the corresponding knowledge is very limited. In the past five years, the theoretical research

was conducted including the concept, catalog, contact framework with the United Nations Sustainable Development Goals (SDGs) and its specific implementation path, as well as the synergy and tradeoff theory to meet the SDGs and the national needs of the Belt and Road Initiative (Li et al., 2022).

The cryospheric water including the glacier runoff, snowmelt and ground ice melt water was estimated from 1961 to 2017 by using the CBHM model in about 45 inland river basins, the arid region of Northwest China where the cryospheric water accounting for about 20%~85% of the basin water resources. Under CMIP5 RCPs scenarios, the cryospheric melt water and river runoff were also projected up to the year 2100 in these river basins. Based on these cryospheric data and the GDP, population, water supply and the total surface water resources data in each county in the Northwest China, the cryospheric water service was evaluated from 1961 to 2017 and projected up to 2100 under SSP1-2.6, SSP2-4.5, SSP3-8.5 and SSP5-8.5 scenarios. The cryospheric water and its service were also estimated by using the similar methods from 1961 to 2017 and projected up to 2100 in each city in China. After that, the cryospheric water service was divided into four classes named significant enhancement area, relatively stable region, rapid decline area and potential loss area during 2030s, 2050s and 2090s in China, respectively.

Under SSP1-RCP2.6, the cryospheric water resources service potential would reach the peak in 2100, while under SSP5-RCP8.5, it would gradually decline from 2050 (Li et al., 2022).

## **5. Key technologies in forecasting of snowmelt flood disaster in arid areas, Northwest China**

Under the global warming, the extreme warming process, heavy snowfall and Rain-On-Snow event occur more frequently, resulting in more frequent snowmelt floods, and the rain, snow and ice mixed floods. Therefore, the projection, prediction, forecasting and early warning of the flood disasters are urgently needed in the arid regions of Northwest China.

According to the present research progress on key technologies of snowmelt flood disaster forecasting, the mechanism of flood disasters has been revealed in the past four years. In addition, the monitoring and early warning device of snowmelt flood disasters are developed, and the three-dimensional monitoring system has been constructed in the arid regions. Based on the in situ, remote observation and involved research results, a hydrological model has been developed to accurately simulate the rain, snow and ice mixed floods. As a result, an Intelligent Decision Support System (IDSS) has been constructed to demonstrate the flood submerged areas, evaluate the risk of the flood disasters and give the best solutions in the arid regions of Northwest China (Chen et al., 2021).

Using the IDSS, several snowmelt floods have been forecasted with very high accuracy in the past two years in the source Irtysh river valley, Northwest China.

## **References**

1. Ding Y, Zhang S, Chen R, et al. 2020. Hydrological basis and discipline system of Cryohydrology: from a perspective of Cryospheric Science. *Frontiers in Earth Science*, 8:574707. Doi: 10.3389/feart.2020.574707
2. Chen R, Zhang S, Liu J, Zhao Q, 2019. Impact of cryospheric changes on runoff in the main cold basins in China. Beijing: Science Press.
3. Ding Y, Xiao C, 2019. Cryosphere changes and its effects. Beijing: Science Press.
4. Li K, Chen R, Liu G, Yang Y, 2022. Cryosphere water resources supply function and service in China. *Advances in Climate Change Research*, 13(3): 408-420. doi: 10.1016/j.accre.2022.03.004
5. Yang Y, Chen R, Liu G, et al. 2022. Trends and variability in snowmelt in China under climate change. *Hydrology and Earth System Sciences*, 26, 305-329. doi: 10.5194/hess-26-305-2022
6. Chen R, Shen Y, Mao W, et al. 2021. Progress and issues on key technologies in forecasting of snowmelt flood disaster in arid areas, Northwest China. *Advances in Earth Science*, 36(3): 233-244.

### 3.5 Cryosphere and Sustainable Development (by Fang Yiping, Yang Jianping)

#### 1. Mismatch between the Population and Meltwater Changes Creates Opportunities and Risks for Global Glacier-fed Basins

• The results show the important role played by GWR in the 36 glacier-fed basins, especially in the Indus, Ganges, Tarim, Junggar, Syr Darya and Amu Darya of Asia, Rapel, Mapocho and Santa of South America and Yukon of North America (Fig.7). The total area of the 36 important glacier-fed basins (IGFBs) is  $1.3 \times 10^7 \text{ km}^2$ , accounting for 9.7% of the world's total land area in which all 109,447 glaciers cover a total area of  $114,711 \text{ km}^2$ . Approximately 1159.6 million people were living in these 36 IGFBs in 2015, of which approximately 87.3% were in Asia. Moreover, nearly 12.6% and 39.0% were living under highly or extremely highly water-stressed conditions, with a water availability per capita of less than  $500 \text{ m}^3 \text{ a}^{-1}$  and an average of more than 40% and 80% of the available supply withdrawn year-round, respectively. The vast majority of HWSP live in Asia.

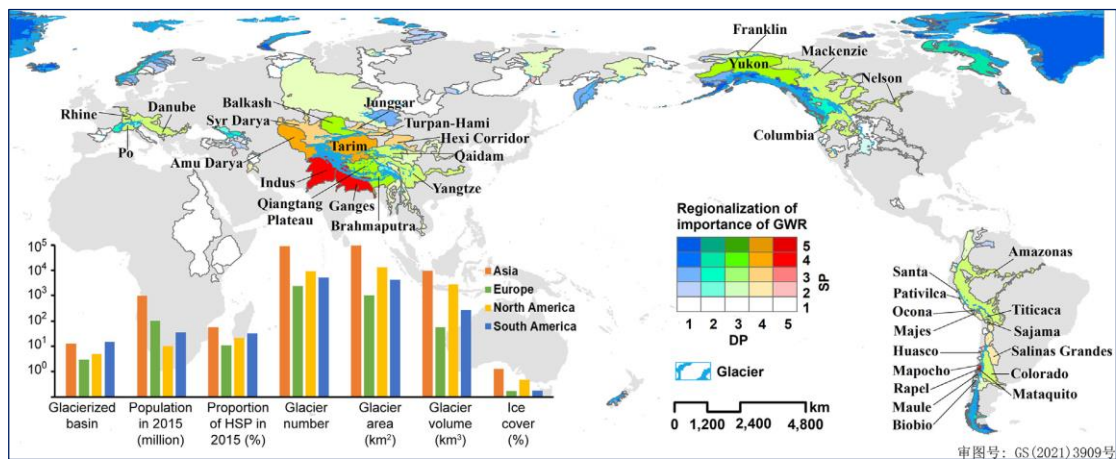


**Fig. 7.** Regionalization of the importance of the world's glacier water resources (GWR) in terms of their meltwater supplying potential (SP) and downstream human dependence (demanding potential, DP) in 2015 at the basin scale. The SP and DP are classified into extremely low (1), low (2), medium (3), high (4) and extremely high (5) categories based on normalized supply and demand indicators. The labels indicate 36 important glacier-fed basins (IGFBs) without low SP and DP values. The inset shows the basic information of IGFBs at the continental scale, including the glacierized basin number, population and proportion of the highly water-stressed population (HWSP) in 2015,

glacier number, area and volume, and ice coverage.

- Although the SPGMs in the Indus, Ganges, Yangtze, Mekong, Rhine, Titicaca and Amazon basins have been increasing significantly before the “peak water” years, the opportunities associated with the increases of the SPGMs only meet the basic needs of part of the population due to the large population growth at the same time. However, in the other basins, the opportunities offered by the increase of the SPGM can not only seasonally meet the basic water needs for the increasing populations, but also relieve the water pressure for those populations under highly water-stressed conditions. Most of the investigated basins would see the peak meltwater earlier than the projected peak population, not only creating a risk in terms of not meeting the basic water demands for the increased population but also imposing water pressure on the existing population. This is especially true for the Indus, Ganges, Amu Darya and Syr Darya.



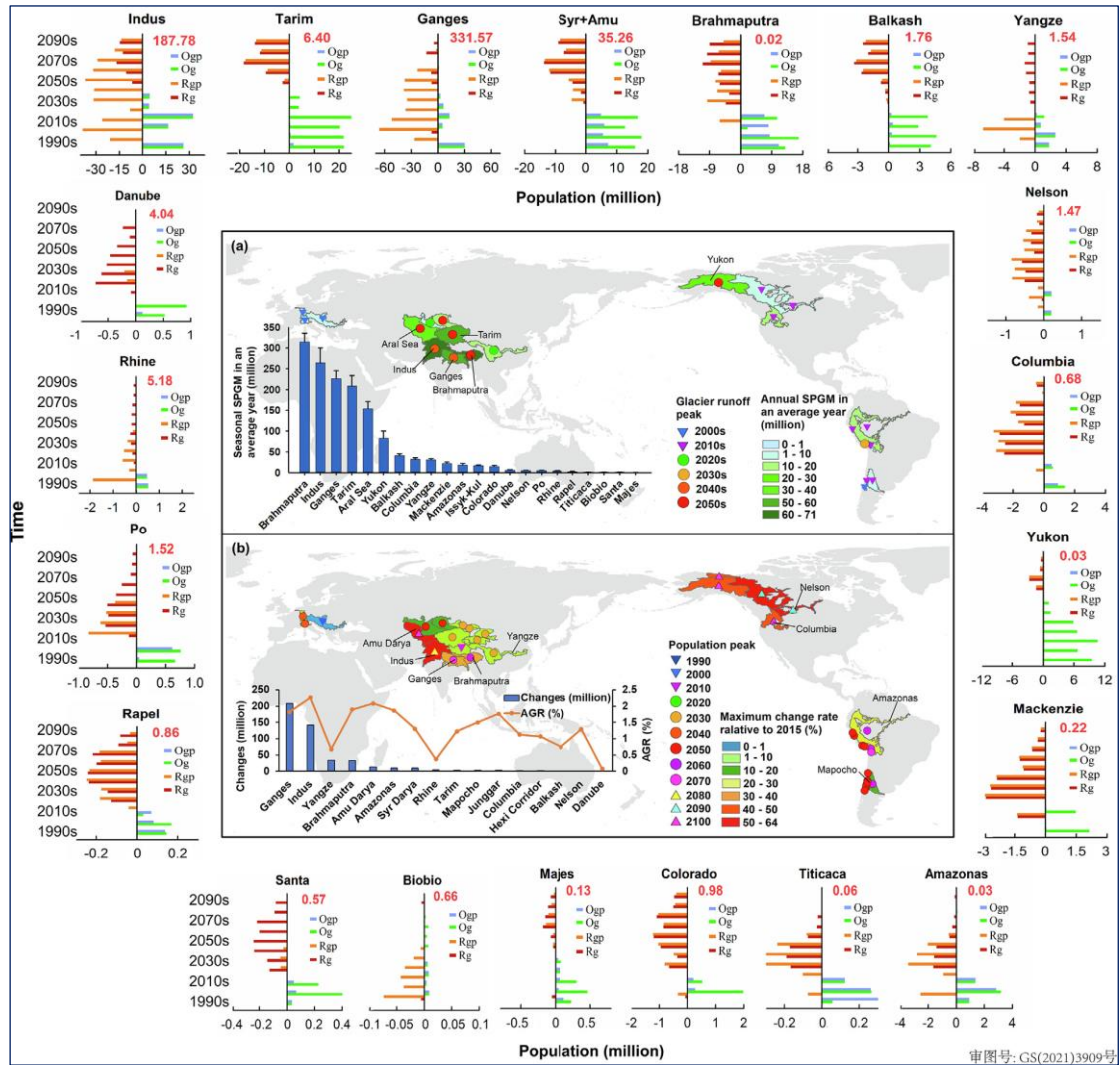


**Fig. 8.** Changes in the service potential of glacial meltwater (SPGM) and population as well as their associated opportunities and risks in the world's IGFBs during historical (1980-2015) and future periods (2020-2100) under the mid-range Representative Concentration Pathway and Shared Socioeconomic Pathways, i.e., RCP4.5 and SSP2. (a) Annual and seasonal SPGM (insert, 4 months, from June to September in the Northern Hemisphere and from December to the next March in the Southern Hemisphere) in an average year during 1980 and 2015 and the annual glacier runoff peaks in 22 IGFBs. The labels show the 6 IGFBs with an annual SPGM of more than 20 million. (b) Population dynamics and their annual growth rates (AGR) during 1980 and 2015 (insert), along with future population peaks and their maximum change rates relative to 2015 in all 36 IGFBs. The labels indicate the 9 IGFBs with the biggest population change rates in the population peak year compared to 2015. Surrounding figures show seasonal opportunities and risks associated with only changes in the SPGM (POgi and PRgi) and jointly affected by changes in the SPGM and population dynamics (POgpi and PRgpi) from the 1990s to the 2090s (with the 1980s as the first baseline period) in 21 IGFBs. The red labels show the HWSP with a water availability per capita of fewer

than  $500 \text{ m}^3 \text{ a}^{-1}$  in 2015.

- The result show that both opportunities and risks are greatest in the Indus River basin, which provides a good example of typical consequences caused by mismatching between the meltwater and population changes. The increase in glacial meltwater can seasonally satisfy the basic needs of an additional 83.7 million people from the 1990s to the 2040s, but 129.1 million would be exposed to severe water scarcity due to the decrease in glacial meltwater and the population increase after the 2040s. After the peak population, the risk of water shortage would decline gradually.

- When the SPGM initially increases, the utilization of GWR can improve regional human well-being. Meanwhile, great attention should also be paid to effective adaptation once the SPGM continually declines after the population peak has been reached. Especially, there are urgent needs for transboundary cooperation under a co-design and win-win strategy. This study also implies that the transformation towards the sustainable pathway (SSP1) before 2030 can significantly reduce the risk of a water shortage caused by rapid population growth in the IGFAs of South and Central Asia, as well as South America (Fig. 8).

(Source: Bo Su, Cunde Xiao, Deliang Chen, Xue Ying, Yi Huang, Rong Guo, Hongyu Zhao, Aifang Chen, Yanjun Che. Mismatch between the population and meltwater changes creates opportunities and risks for global glacier-fed basins. *Science Bulletin*, 2022(67):9-12.)

## **2. Cascading costs of snow cover reduction trend in northern hemisphere**

- The average snow radiative forcing (SRF) was  $-1.49 (\pm 0.13) \text{ Wm}^{-2}$ , which indicates an equivalent increase of  $116.69 (\pm 10.30)$  gigaton carbon (GtC) in the atmosphere since the pre-industrial period. The average increase rate for SRF due to the trend of snow cover reduction in NH during 1988-2015 was  $0.1141 (\pm 0.0227) \text{ Wm}^{-2}/10\text{a}$ . Subsequently, the average equivalent carbon of climate regulation service (CRS) of NH lowland snow during 1988-2015 reduced at a rate of  $-8.95 (\pm 1.78) \text{ GtC}/10\text{a}$ , which accelerated to  $-28.38 (\pm 14.06) \text{ GtC}/10\text{a}$  during 2008-2015. The areas of high

latitudes and altitudes have high CRS because of the relatively long snow cover duration. However, a significant decrease of CRS can be observed in most other areas, especially in those of low latitudes and altitudes.

- Nearly half of the EEC would occur in sectors related to “trade and service”. The cost rate in sectors of “mining and quarrying” and “basic and fabricated metals” would reach 60% and 54%. The trade and service sectors would be 33%. The cascading cost of climate change pertinent to NH snow cover reduction trend in the “trade and service” sectors would be 37.0 trillion euros, 56.9% of the global EEC. The EECs of “manufacturing” and “petroleum, chemical and non-metallic mineral products” sectors are 6.5 and 5.1 trillion euros, respectively. The cost rates of “wood and paper,” “electricity, gas, and water,” as well as “basic metals and fabricated metal” sectors would reach 79%, 70%, and 66%, respectively (Fig. 9). The results highlight that the world economy could fall in the circumstance that a remarkable proportion of the global total output would be constrained as a cascading cost to neutralize the impacts of the NH snow cover reduction.

- Each nation would bear different cascading costs pertinent to the trend of snow cover reduction in NH, subject to the responsibility-sharing mechanisms. Fig. 10a shows the national EECs under the emission-based scenario. China would experience the most prominent national EEC followed by the USA and Japan. Western European nations, South Korea, and India would also incur massive costs when reducing direct CO<sub>2</sub> emissions. Fig. 10b shows the regional disparity with a view of the national cost rates. It indicates that the impacts of global actions are relatively high in the large developing nations (e.g., China and India) and Eastern European nations, while relatively small in the developed nations in North America and Western Europe. The ramification would be significantly different in the GDP emission-based scenario (Fig.10c). In this circumstance, the cascading cost in China would be 4.1 trillion euros, which is less than half of the cost in the emission-based scenario. Developed nations (e.g., the USA, Western European nations, and Japan) would then bear massive cascading costs to neutralize the impacts of the declining trend of NH snow cover. Meanwhile, the USA would incur a 12.9 trillion euros of cascading cost, at the top of the world, followed by France, the United Kingdom, and Germany. Fig. 10d illustrates the national cost rates under the GDP-emission-based responsibility-sharing mechanism. Western and Northern European nations would be confronted with high

relative impacts. In contrast, the cost rates are lower in South Africa, Greece, India, and Russia.

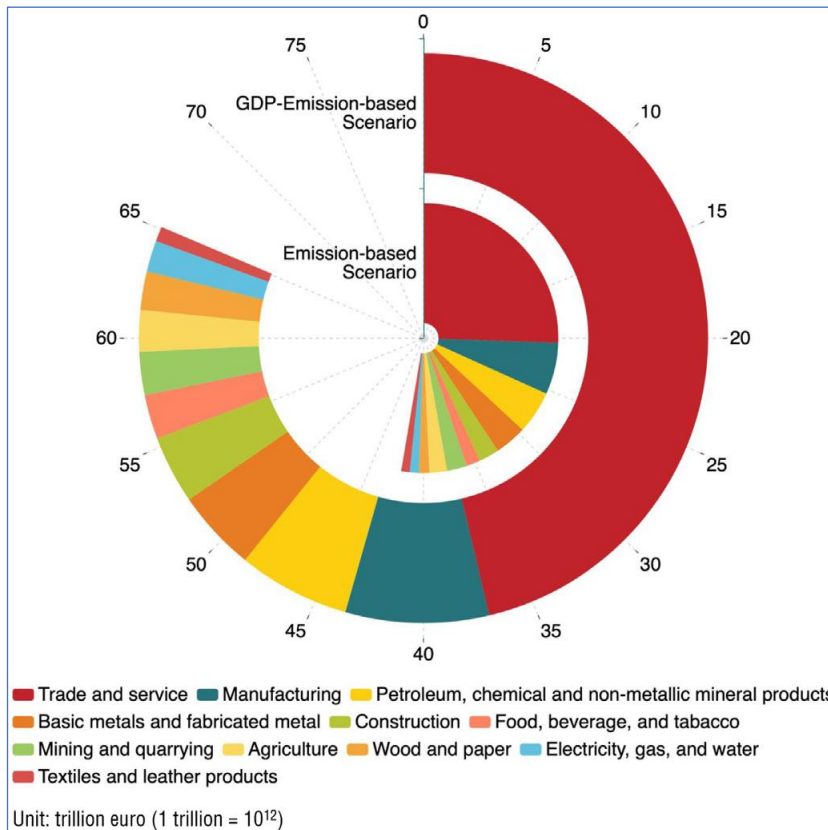


**Fig. 9.** Equivalent economic costs (EECs) and the sectoral structures in two responsibility sharing scenarios. The emission-based scenario represents that the virtual carbon burden is shared based on each sector's CO<sub>2</sub> emission amount. In contrast, the GDP-emission based mechanism indicates that nations with larger GDP take more responsibility, then each nation's share is assigned to sectors based on their CO<sub>2</sub> emissions. The results are calculated based on the global economic situation and carbon intensity in 2015.

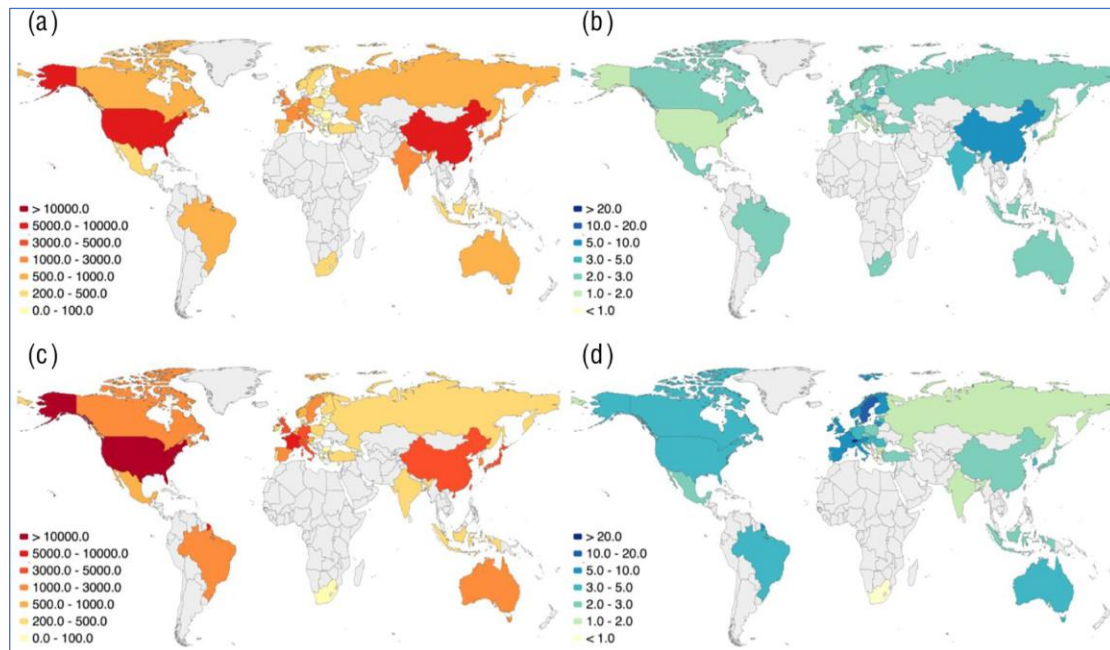


**Fig. 10.** The equivalent economic costs (EECs) of nations (a, trillion euros) and the proportions of the EECs in the total outputs of nations (b, %) in the emission-based scenario. The EECs of nations (c, trillion euros) and the proportions of the EECs in the total outputs of nations (d, %) in the GDP-emission-based scenario. Darker colors indicate larger EEC (a, c) or higher proportions of the EECs in the national total outputs (b, d).

(Source: Shiwei Liu, Jianchuan Qi, Sai Liang, Xiaoming Wang, Xuejiao Wu, Cunde Xiao. Cascading costs of snow cover reduction trend in northern hemisphere. *Science of the Total Environment*, 2022,806, 150970.)

### 3. Global Snow- and Ice-Related Disaster Risk

- SIRD's formation requires not only cryosphere hazards as incentive conditions, but also the objects that are subject to disasters such as people, property, resources, and infrastructure. Generally, a SIRD is the result of combined effects of the cryosphere hazard, the disaster's formative environment, and the vulnerability of the economic and social system. SIRDs include ice/snow avalanches, glacial surges, glacial-snow flood/debris flows, melting snow floods, freeze-thawing, ice jam/floods, iceberg sea ice, coastal freeze-thaw erosion, snowstorms, blowing snow, freezing rain and snow, hail, frost freezing, and other disasters according to their trigger factors (Fig. 8). The disaster's formative environments include natural factors such as climate, topography, geological activity, ecological vegetation, elevation, river distribution, and social factors such as population, economy, and infrastructure. For cryosphere events in the same intensity, the higher the sensitivity of the disaster's formative environment, the

greater the probability of disaster and the greater the losses. In addition, the size of the damage depends on the exposure and vulnerability of the disaster-bearing bodies. The greater the vulnerability, the greater the risk of the SIRD. Sometimes, the SIRD size is determined by the scale of the hazard, and sometimes by the degree of exposure or vulnerability as well as the disaster's formative environment (Fig. 11).

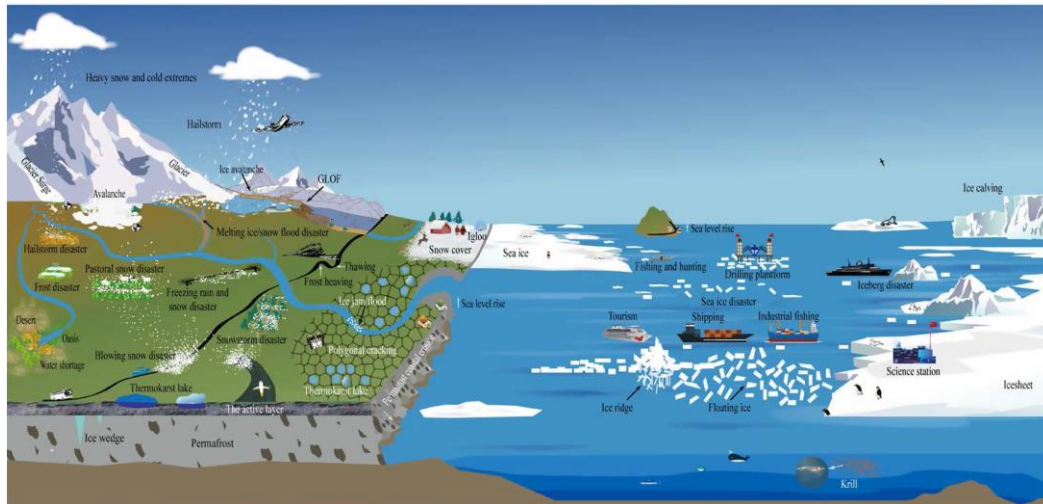


**Fig. 11.** Schematic diagrams of SIRDs

- On land, SIRDs mainly occur in the high mountainous areas of middle-low latitude and the permafrost regions of high latitude. The recorded frost events show a decreasing trend but the hail hazard distributions are greatly heterogenous. Overall, the frequency of rain-on-snow events is projected to increase on land in the future. In the ocean, SIRDs are mainly distributed in the Arctic coastal areas and global low-lying islands or areas, with great potential risk. Among them, coastal freeze-thaw, icebergs, and sea-level rise and its impacts are likely or expected to continue increasing in the next few decades (Fig. 12).



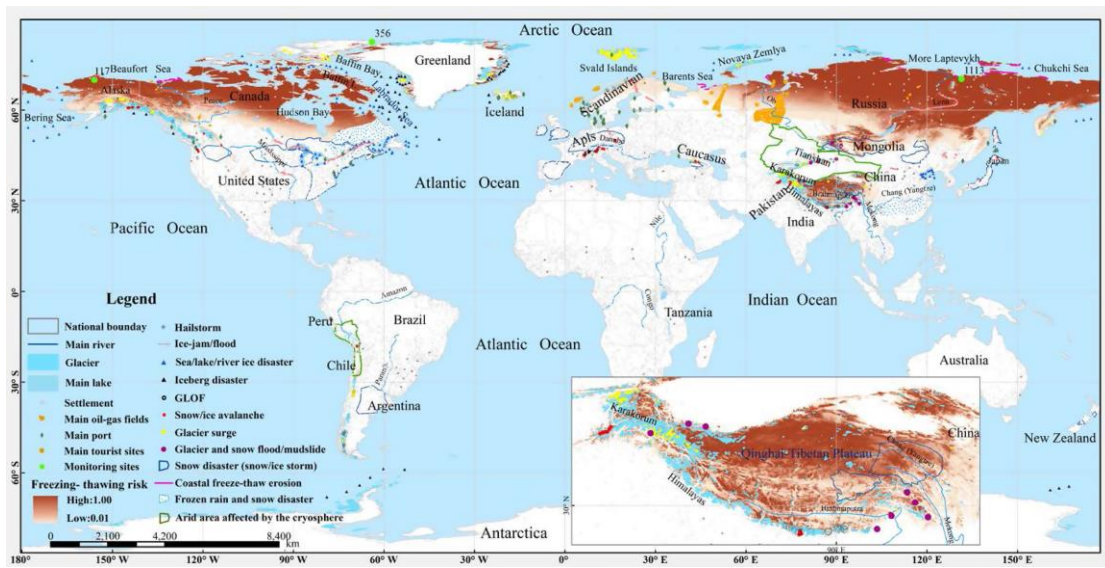


**Fig. 12.** Observed and recorded SIRD sites or ranges in the world

(Source: Wang Shijin, Yang Yuande, Che Yanjun. Global snow- and ice-related disaster risk: A review. *Nat. Hazards Rev.*, 2022, 23(4): 03122002)

### **3.6 Cryospheric Archives (by Kang Shichang, Jin Huijun, and Zhang Yulan)**

- **Glacier surface snow and ice**

The concentrations and transport pathways of microplastics have been comprehensively analyzed from the surface snow and ice of glaciers on the Tibetan Plateau (Wang et al., 2022; Zhang et al., 2021). Migration and transformation of mercury on a watershed scale in the Himalayas has been revealed, with discussions of the potential impact on the ecological environment in the alpine glacier melt region (Sun et al., 2022). Chemical weathering rates of global glaciers and ice sheets have been investigated, indicating the spatiotemporal variation patterns and impact mechanisms of glacier weathering rates (Li et al., 2022). The dataset release of the genome and gene catalog of the largest glacier microbiome in the Tibetan Plateau helps to deepen our understanding of the structure and function of the microbiome in Tibetan glaciers (Liu et al., 2022b).

- **Ice cores**

The new technology of  $^{39}\text{Ar}$  radioactive dating of the ice core has established an accurate dating scale for thousands of years for the Qiangtang glacier ice core (Ritterbusch et al., 2022). Characteristics of  $\text{NO}_3^-$  and  $\text{NH}_4^+$  changes have been reconstructed from the Tibetan Segangri ice core over the past thousand years (Zou et al., 2022). Ice core records have also revealed the significant impact of atmospheric circulation, specially the Arctic air mass and the North Atlantic oscillation, on ice core records in the Northern Tibetan Plateau (Du et al., 2022). The temperature records of ice cores in the western and southeastern Tibetan Plateau have also been clarified, providing insights into glacier changes (Zhao et al., 2021). Furthermore, the Guliya ice core records of microorganisms and bacteriophages from nearly 15000 years ago have contributed to the sampling procedures for microorganisms and viruses in glacier ice, providing a scientific basis for understanding the virus communities and functions in ancient glacier environments (Zhong et al., 2021).



- **Tree rings**

Tree ring records revealed the historical changes in temperature and precipitation in different regions of the Tibetan Plateau and the response of radial growth of Qilian juniper to different types of drought in the northeastern Tibetan Plateau (Xu et al., 2022). The oxygen isotope records of tree rings indicated that the Asian monsoon precipitation increased during the 4.2 kaBP period, indicating the extreme hydrological events in the upper reaches of the Yangtze River over the past 700 years (Yang et al., 2021). Variations of mercury from tree rings in permafrost regions of Northeast China were investigated, emphasizing the possible geographical impact on mercury records in tree rings and improving understanding of forest mercury cycling in permafrost regions (Kang et al., 2022).

- **Lake sediment cores**

The lake sediment cores illustrated the seasonal deviation of Holocene temperature variations in the Tibetan Plateau and clarified the influence of the Westerlies on Holocene climate change in the central transitional zone of the plateau (Zhang et al., 2022). Using lake core isotopes ( $\delta^{18}\text{O}$ ), it also revealed the characteristics of Holocene hydrological climate changes in the Tibetan Plateau (Wu et al., 2022). The spatial distribution of the pollen community on the Tibetan Plateau has been reconstructed for the past 15000 years, reflecting the large-scale vegetation gradient on the plateau (Li et al., 2021).

- **Permafrost**

The distribution characteristics and formation mechanism of heavy metal pollutants such as mercury and microbial communities in permafrost soil have been characterized, indicating the impact of global warming on the cycle of mercury and Persistent organic pollutant in the Tibetan Plateau (Liu et al., 2022a). It revealed the distribution of microbial communities in seasonally frozen soil layers of the plateau and

their driving environmental factors (Wang et al., 2023). The spatial variability of typical soil trace elements in different regions was elucidated, and their migration and transformation characteristics and influencing factors were discussed (Cao et al., 2022). The changing trend of natural gas hydrates in the permafrost of the Tibetan Plateau has been revealed under the background of global warming and its impact on carbon emissions (Lu et al., 2022).

### References:

1. Cao, W., Sheng, Y., Wu, J.C., Peng, E.X., Gao, R.X., Zhou, M.Y. (2022) Spatial variability and source analysis of typical soil trace elements at permafrost section along national highway 214 in the eastern Qinghai-Tibet Plateau. *Environmental Geochemistry and Health*.
2. Du, W.T., Kang, S.C., Chen, J.Z., Sun, W.J., Qin, X., Sun, W.X., Zhang, Y.L. (2022) Arctic air mass triggered the extreme temperature events recorded in the Laohugou ice core from the northeastern Tibetan Plateau. *Atmospheric Research* 265.
3. Kang, H.H., Liu, X.H., Guo, J.M., Zhang, Q.L., Wang, Y.B., Huang, J., Xu, G.B., Wu, G.J., Ge, W.S., Kang, S.C. (2022) Long-term mercury variations in tree rings of the permafrost forest, northeastern China. *Science China-Earth Sciences* 65, 1328-1338.
4. Li, X.Y., Wang, N.L., Ding, Y.J., Hawkings, J.R., Yde, J.C., Raiswell, R., Liu, J.T., Zhang, S.Q., Kang, S.C., Wang, R.J., Liu, Q., Liu, S.Y., Bol, R., You, X.N., Li, G.Y. (2022) Globally elevated chemical weathering rates beneath glaciers. *Nature Communications* 13.
5. Li, Z., Wang, Y.B., Herzsuh, U., Cao, X.Y., Ni, J., Zhao, Y. (2021) Pollen-based mapping of Holocene vegetation on the Qinghai-Tibetan Plateau in response to climate change. *Palaeogeography Palaeoclimatology Palaeoecology* 573.
6. Liu, Y.L., Wang, J.F., Guo, J.M., Wang, L.Y., Wu, Q.B. (2022a) Vertical distribution characteristics of soil mercury and its formation mechanism in

- permafrost regions: A case study of the Qinghai-Tibetan Plateau. *Journal of Environmental Sciences* 113, 311-321.
7. Liu, Y.Q., Ji, M.K., Yu, T., Zaugg, J.L., Anesio, A.M., Zhang, Z.H., Hu, S.N., Hugenholtz, P., Liu, K.S., Liu, P.F., Chen, Y.Y., Luo, Y.F., Yao, T.D. (2022b) A genome and gene catalog of glacier microbiomes. *Nature Biotechnology* 40, 1341-+.
  8. Lu, Z., Wu, C., Wu, N., Lu, H., Wang, T., Xiao, R., Liu, H., Wu, X. (2022) Change trend of natural gas hydrates in permafrost on the Qinghai-Tibet Plateau (1960-2050) under the background of global warming and their impacts on carbon emissions. *China Geology* 5, 475-509.
  9. Ritterbusch, F., Tian, L., Gu, J.Q., Jiang, W., Lu, Z.T., Shao, L., Tang, M.X., Yang, G.M., Zhang, M.J., Zhao, L. (2022) A Tibetan ice core covering the past 1,300 years radiometrically dated with Ar-39. *Proceedings of the National Academy of Sciences of the United States of America* 119.
  10. Sun, X., Zhang, Q., Zhang, G., Li, M., Li, S., Guo, J., Dong, H., Zhou, Y., Kang, S., Wang, X., Shi, J. (2022) Melting Himalayas and mercury export: Results of continuous observations from the Rongbuk Glacier on Mt. Everest and future insights. *Water Research* 218.
  11. Wang, X.J., Yu, Z.Q., Shen, G.F., Cheng, H.F., Tao, S. (2023) Distribution of microbial communities in seasonally frozen soil layers on the Tibetan Plateau and the driving environmental factors. *Environmental Science and Pollution Research* 30, 1919-1937.
  12. Wang, Z., Zhang, Y., Kang, S., Yang, L., Luo, X., Chen, P., Guo, J., Hu, Z., Yang, C., Yang, Z., Gao, T. (2022) Long-range transport of atmospheric microplastics deposited onto glacier in southeast Tibetan Plateau. *Environmental Pollution* 306, 119415.
  13. Wu, D., Ma, X.Y., Yuan, Z.J., Hillman, A.L., Zhang, J.W., Chen, J.H., Zhou, A.F. (2022) Holocene hydroclimatic variations on the Tibetan Plateau: An isotopic perspective. *Earth-Science Reviews* 233.

14. Xu, H., Wang, J., Peng, X., Ren, Z. (2022) Responses of radial growth of *Juniperus przewalskii* to different droughts over the northeastern Tibetan Plateau, China. *Chinese Journal of Applied Ecology* 33, 2097-2104.
15. Yang, B., Qin, C., Brauning, A., Osborn, T.J., Trouet, V., Ljungqvist, F.C., Esper, J., Schneider, L., Griessinger, J., Buntgen, U., Rossi, S., Dong, G.H., Yan, M., Ning, L., Wang, J.L., Wang, X.F., Wang, S.M., Luterbacher, J., Cook, E.R., Stenseth, N.C. (2021) Long-term decrease in Asian monsoon rainfall and abrupt climate change events over the past 6,700 years. *Proceedings of the National Academy of Sciences of the United States of America* 118.
16. Zhang, C.J., Zhang, W.Y., Cheng, D.S., Yang, N., Hou, X.Y., Li, H.W., Zhang, X.J., Ayyamperumal, R. (2022) Hydrochemical characteristics and paleoclimate changes recorded from Sugan Lake on the northern boundary of Tibetan Plateau since mid-Holocene. *Catena* 217.
17. Zhang, Y., Gao, T., Kang, S., Allen, S., Luo, X., Allen, D. (2021) Microplastics in glaciers of the Tibetan Plateau: Evidence for the long-range transport of microplastics. *Science of The Total Environment* 758, 143634.
18. Zhao, H.B., Yao, T.D., Xu, B.Q. (2021) High-elevation climate changes recorded in Tibetan ice cores and their impact on glacier behavior. *Palaeogeography Palaeoclimatology Palaeoecology* 576.
19. Zhong, Z.P., Tian, F.N., Roux, S., Gazitua, M.C., Solonenko, N.E., Li, Y.F., Davis, M.E., Van Etten, J.L., Mosley-Thompson, E., Rich, V.I., Sullivan, M.B., Thompson, L.G. (2021) Glacier ice archives nearly 15,000-year-old microbes and phages. *Microbiome* 9.
20. Zou, X., Hou, S.G., Wu, S.Y., Pang, H.X., Liu, K., Zhang, W.B., Yu, J.H., Song, J., Huang, R.H., Liu, Y.P. (2022) Ice-core based assessment of nitrogen deposition in the central Tibetan Plateau over the last millennium. *Science of the Total Environment* 814.

### **3.7 Women Scientists Division (by Zang Shuying, Wang Puyu)**

The Women Scientists Division aims to play a role as a bridge and link between women scientists in the research field of cryospheric science, promote the growth and development of women scientists, exchanges and cooperation with domestic and foreign women scientists groups, enhance their role and status in scientific and technological innovation and social development, and establish a home for women scientists in the cryosphere science field. The Women Scientists Division was initiated by the Council meeting of the Chinese Society of Cryosphere Science in 2019. By drawing up the constitution of the working committee, establishing the organizational structure and recruiting members, the Women Scientists Division has been formed. Although it was established for a short time, remarkable progresses have been made during the past years in the following aspects:

#### **1. Establishment of the Division**

- **The first working meeting was held**

On January 13, 2022, the Women Scientists Division held the first meeting of the first Working Committee of Women scientists. Professor Kang Shichang, Vice President of Northwest Institute of Ecology, Environment and Resources, Chinese Academy of Sciences, and Professor Xiao Cunde, Secretary-General of the Society of Cryosphere Sciences, delivered speeches respectively, expressing congratulations on the establishment of the working committee and the convening of the first working conference. Director Zang Shuying introduced the preparatory process of the Working Committee for Women Scientists, and the members introduced themselves respectively, and had a heated discussion on the committee's charter and the next work plan. Researcher Kang Shichang and Professor Xiao Cunde fully affirmed the work of the Working Committee of Women Scientists, and put forward opinions and suggestions for the next step, hoping to strengthen the diversity of members, especially the work exchange in the fields of cryosphere science and humanities, and jointly promote the vigorous development of cryosphere science.

- **Establish the committee working groups and exchange groups**

In order to effectively promote the work of the committee, transmit information related to cryosphere science, and promote the exchange of female cryosphere workers, wechat groups of "Committee of Cryosphere Women Scientists" and "Cryosphere Women Scientists Exchange Group" have been established respectively. The "Committee of Women Scientists of the Cryosphere" is composed of 30 members, and the relevant work notices of the women scientific work committee are issued within the group, and all kinds of activities are carried out together. The "Cryosphere Women Scientists Exchange Group" has more than 100 women scientists working in the field of cryospheric sciences. On this platform, information about academic exchanges and journal conferences related to cryosphere science is shared and released, which promotes the growth and development of female scientists.

## **2. Various special activities were organized**

- **Academic Salon**

- Online held the “ice and snow, East-west linkage” cryosphere female scientists first academic salon. There are two academic reports, “changes of ecological environment and water resources in the middle and upper reaches of the Yellow River”, and “Effects of wildfires on boreal forest ecosystems and permafrost environments”, respectively.

- Online held the “A new era of pursuing dreams, women exhibit their unique style” cryosphere female scientists academic salon. The main contents of the two academic reports were about “Climate change, cryosphere change and regional sustainable development”, and “Progress of permafrost environment work of China-Russia pipeline in northern Greater Khingan Mountains”, respectively.

- **Hosted the fifth National Youth Academic Forum on Geotechnical Mechanics and Engineering in Cold Areas**

- As one of the organizers, the Women Scientists Division participated in the preparation of the conference, and convened the offline special report venue of the

“Cold Area Engineering and Environment Forum for Women Scientists” and the online special report venue of the “Cold Area Environment”.

### **3. A number of important scientific advances have been made**

Women Scientists Division members actively participate in domestic and foreign academic conferences and make academic reports; Won various awards, such as the first prize of provincial Science and Technology Progress Award; Approved various projects, such as the key technology research and development and application project of the Ministry of Science and Technology, the Third Xinjiang Scientific Expedition Program, and the Provincial Outstanding Youth Fund; Serve local work, such as providing data and reference for provincial frozen soil mapping, engineering survey alignment, investigation and design scheme determination, design, etc.

For example, research progress of permafrost in northeast China was achieved. Utilizing the 8-day Aqua/MODIS land surface temperature (LST) products in 2003–2020, the southern limits of a sub-Arctic boreal mountain permafrost in the Amur River Basin bordering China, Russia, and Mongolia was extracted. Response of SOC mineralization and the soil bacterial community to two microtopographic features (hummocks and hollows) under two different incubation temperatures were investigated. Warming decreased soil bacterial  $\alpha$ -diversity and significantly separated soil bacterial community structure. Soil labile substrates were the main factor affecting the SOC mineralization between the different microfeatures in the permafrost wetland. Effects of temperature, moisture, and their interactions on carbon emissions in the permafrost peatlands were investigated. In addition, the Third Xinjiang Scientific Expedition Program has been launched and was undertaken by members, mainly focusing on the practical needs of green development and sustainability in Xinjiang, especially about the cryospheric sciences.

# **2019-2023 China National Report on Geodesy**

**For**

**The 28th IUGG General Assembly**

**Berlin, Germany, July 11-20, 2023**



**Prepared by Chinese National Committee for  
International Association of Geodesy (CNC-IAG)**

**June 25 2023**



# Preface

This report presents the progress of research and development on geodesy in China during the time period from January 2019 to June 2023. It is to be submitted, on behalf of the Chinese National Committee for International Association of Geodesy (CNC-IAG), to the IAG General Assembly at the 28th IUGG General Assembly to be held in Berlin, Germany, July 11-20, 2023.

It is hoped that this national report would be of help for Chinese scientists in exchanging the results and ideas in the research, development and application of geodesy with scientists all over the world.

Colleagues listed below made their contribution for this national report (sorted alphabetically by last name):

Lifeng Bao, Yachuan Bao, Jinzhong Bei, Bin Chen, Peng Chen, Qiuji Chen, Ruizhi Chen, Shi Chen, Xiaodong Chen, Zhaohui Chen, Yingyan Cheng, Yonghai Chu, Xiaoming Cui, Xiaolei Dai, Yamin Dang, Mingli Deng, Zhongliang Deng, Wei Feng, Haiqiang Fu, Haiyang Fu, Yanguang Fu, Zhouzheng Gao, Shengfeng Gu, Chunxi Guo, Jinyun Guo, Xiang Guo, Xinwei Guo, Zehua Guo, Houzeng Han, Jiancheng Han, Changyong He, Lin He, Qianqian He, Pengyu Hou, Andong Hu, Jun Hu, Minzhang Hu, Tong Hua, Lu Huang, Xingliang Huo, Haonan Jia, Lulu Jia, Yongjun Jia, Guangwei Jiang, Haitao Jiang, Tao Jiang, Taoyong Jin, Baogui Ke, Xiang Lei, Ang Li, Bijun Li, Bofeng Li, Dehai Li, Hang Li, Honglei Li, Min Li, Pan Li, Qianqian Li, Qiong Li, Shuang Li, Tao Li, Tuan Li, Wang Li, Xin Li, Xingxing Li, Yongbo Li, Zishen Li, Wei Liang, Jianchi Liao, Ang Liu, Chun Liu, Lin Liu, Qi Liu, Sulan Liu, Teng Liu, Xiaogang Liu, Yanxiong Liu, Ziwei Liu, Yidong Lou, Feng Lu, Hongyan Lu, Zhicai Luo, Jie Lv, Xiaoji Niu, Ming Ou, Yuanjin Pan, Zongpeng Pan, Ling Pei, Fukai Peng, Xianping Qin, Xia Ren, Xiaodong Ren, Yingying Ren, Yunzhong Shen, Chuang Shi, Wen Shi, Yong Su, Fuping Sun, Heping Sun, Zhongmiao Sun, Chengpan Tang, Xiaoyun Wan, Cheng Wang, Hu Wang, Jian Wang, Lei Wang, Leyang Wang, Liang Wang, Linhai Wang, Ningbo Wang, Wei Wang, Yunjia Wang, Zhengtao Wang, Weisong Wen, Lin Wu, Yihao Wu, Yunlong Wu, Longwei Xiang, Yun Xiao, Guodong Xu, Jianqiao Xu, Qiaozhuang Xu, Tianhe Xu, Weimin Xu, Xinyu Xu, Shuqiang Xue, Cheng Yang, Fan Yang, Heng Yang, Jinling Yang, Lianjun Yang, Qiang Yang, Yuanxi Yang, Yibin Yao, Shuang Yi, Wei You, Baoguo Yu, Fangwen Yu, Wenxian Yu, Yunbin Yuan, Jiuping Zha, Baocheng Zhang, Bei Zhang, Chuanyin Zhang, Hongjuan Zhang,

Miaomiao Zhang, Qiang Zhang, Quan Zhang, Xiaohong Zhang, Dongsheng Zhao, Qiuyue Zheng, Bo Zhong, Jiahao Zhong, Yulong Zhong, Hao Zhou, Jiangcun Zhou, Feng Zhu, Jianjun Zhu, Xinhui Zhu, Yiqing Zhu, Jancang Zhuang, Xiancai Zou.

Prof. Yamin Dang  
President of CNC-IAG

# Contents

Development of Comprehensive PNT and Resilient PNT .....	<i>Xia Ren, Yuanxi Yang</i> (1)
Maintenance of mm-level Geodetic Reference Framework.....	<i>Yamin Dang, Hu Wang, Fuping Sun, et al.</i> (12)
Research progress in Earth Gravity.....	<i>Heping Sun, Minzhang Hu, Ziwei Liu, et al.</i> (28)
Development Status of Chinese Gravimetry Satellite.....	<i>Yun Xiao, Yuanxi Yan, Zhicai Luo, et al.</i> (54)
Progress in Earth Gravity Model and Vertical Datum.....	<i>Tao Jiang, Yonghai Chu, Xinyu Xu, et al.</i> (67)
Temporal Gravity Field Modelling by Satellite Gravimetry .....	<i>Zhicai Luo, Qiujie Chen, Bo Zhong, et al.</i> (96)
Progress and Achievements of Wide-area Real-time Precise Positioning.....	.....
.....	<i>Xiaohong Zhang, Yidong Lou, Xingxing Li, et al.</i> (109)
Development Status and Trend of Indoor Positioning and Navigation Technology .....	.....
.....	<i>Baoguo Yu, Lu Huang, Yachuan Bao, et al.</i> (123)
Undifferenced and Uncombined GNSS Data Processing Activities .....	.....
.....	<i>Baocheng Zhang, Pengyu Hou, Teng Liu, et al.</i> (136)
Progress and Achievements of Multi-sensor Fusion Navigation .....	.....
.....	<i>Xingxing Li, Xiaohong Zhang, Xiaoji Niu, et al.</i> (143)
Progress of Geodesy related Ionosphere .....	<i>Zishen Li, Ningbo Wang, Liang Wang, et al.</i> (161)
2020 Qomolangma Height Survey.....	<i>Yamin Dang, Tao Jiang, Chunxi Guo, et al.</i> (181)
Recent Advance in Geodetic Data Processing .....	<i>Jianjun Zhu, Leyang Wang, Jun Hu, et al.</i> (188)
Scientific Computation Platform for Geophysical Geodesy .....	<i>Chuanyin Zhang, Tao Jiang, Wei Wang, et al.</i> (200)
Seafloor Geodetic Positioning and Subsea Navigation Application .....	.....
.....	<i>Shuqiang Xue, Tianhe Xu, Yanxiong Liu, et al.</i> (209)
Progress on Hydrogeodesy.....	<i>Wei Feng, Shuang Yi, Bo Zhong, et al.</i> (216)

# Development of Comprehensive PNT and Resilient PNT

Xia Ren<sup>1,2</sup>, Yuanxi Yang<sup>1,2</sup>

<sup>1</sup> State Key Laboratory of Geo-Information Engineering, Xian, China

<sup>2</sup> Xi'an Research Institute of Surveying and Mapping, Xian, China

Any single positioning, navigation and timing (PNT) technology has its vulnerability and limits, even powerful Global Navigation Satellite System (GNSS) is no exception. To provide continuous and reliable PNT information to users, the theory and technique of comprehensive PNT information system and resilient PNT application system have attracted great attention from Chinese scholars. We try to summarize the progress and development of the synthetic PNT system, including the proposal, the modification and the improvement of the comprehensive PNT, as well as the follow-up resilient PNT. The frame of China's comprehensive PNT system consisted of comprehensive PNT infrastructure and comprehensive PNT application system is initially described; the achievements on some main PNT technologies are introduced; the conceptual models of resilient PNT are given; besides, existing researches on resilient function models and stochastic models are summarized according to different user scenarios.

## 1 Introduction

Satellite navigation system have advantages in high precision, global coverage and real-time service, making it the most widely used positioning, navigation and timing (PNT) technology in the world. However, Global Navigation Satellite System (GNSS) signals are vulnerable with low landing power and poor penetrating, that cannot serve non-exposed spaces or easy to be interfered. With the explosion of the weaknesses of GNSS, it is realized that only relying on GNSS or any single PNT technology may bring potential risks, and a new PNT system needs to be built to guarantee the safety of core PNT users (Yang et al., 2023). Published in Nov. 2022, "China's BeiDou Navigation Satellite System in the New Era" by the State Council Information Office of the People's Republic of China says that a more extensive, more integrated, and more intelligent comprehensive spatiotemporal system with BDS as the core is going to be created in the coming years (State Council Information Office of the People's Republic of China, 2022).

In 2016, the concept of comprehensive PNT system was proposed, namely a PNT information source frame covering from deep space to deep sea providing seamless PNT information for users in any environments (Yang, 2016). Correspondingly, in 2017 and 2019, the thinking of micro-PNT terminal system and resilient PNT application system were proposed for the resilient application of multiple PNT information (Yang and Li, 2017; Yang, 2018). Since then, the key technologies on the construction of comprehensive PNT information sources and study on resilient PNT methods and algorithms became a research highlight in China. With deeper study, intelligent PNT concept was proposed as a more advanced PNT application mode catering to the requirement of intelligent society (Yang et al., 2021, Liu et al., 2022). Then, a secure PNT system is formed with comprehensive PNT information sources, resilient PNT application mode and intelligent PNT service mode (Yang et al., 2023).

In the following sections, the frame of Comprehensive PNT system consisted of

comprehensive PNT infrastructures and comprehensive PNT application system is presented; then, the significant achievements are introduced on the aspects of navigation satellite constellation at Lagrange points, BeiDou global navigation system (BDS-3), Low Earth Orbit Satellite (LEO) Augmentation System, and various ground-based PNT systems; besides, the resilient PNT concept and its key elements are described, and the study progress on resilient methods and algorithms in underwater scenario, indoor scenario and urban scenario are presented.

## 2 Comprehensive PNT system

The concept of Comprehensive PNT system described a PNT information source system without distinguishing the comprehensive PNT infrastructure and the comprehensive application system at the initial description (Yang, 2016; Yang and Li, 2017). By a series discussion, it is realized that the comprehensive PNT system should be divided into comprehensive PNT infrastructure system and comprehensive PNT application system (as shown in Figure 1.) (Yang et al., 2023). Comprehensive PNT infrastructure system contains all the large artificial PNT information sources covering from deep space to deep sea, and the comprehensive PNT application system is various PNT terminal sensors receiving artificial and natural PNT signals or self-sensing the state of motion of the carriers.

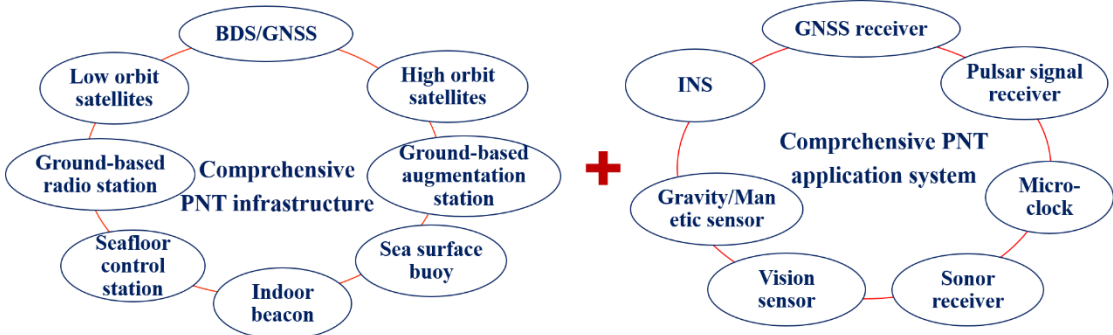


Figure 1. Comprehensive PNT system

As an important part of national comprehensive PNT system, the comprehensive PNT infrastructure system is a seamless PNT main information source frame which should be designed and constructed based on different PNT information sources. In the exposed space from deep space to the ground, the artificial PNT information source frame includes navigation satellite constellation at Lagrange points connecting the PNT service from ground to deep space; the existing or improved BeiDou navigation satellites at high and medium earth orbits, serving for the exposed ground users, ships and low orbit vehicles; the low orbit navigation satellite constellation, augmenting the BeiDou navigation system; the ground-based radio stations such as the ground-based radio navigation stations “Changhe”, ground-based augmentation stations of BDS/GNSS and mobile base stations, augmenting or compensating satellite navigation systems. In non-exposure spaces, beacons such as WiFi, infrared and radio frequency and Ultra Wide Band are also important PNT information sources. In under water environments, sea surface buoys and seafloor beacons are all main PNT infrastructures providing PNT information

and transmitting time-space datum.

Also, the integrated PNT sensors like INS and micro clock, as well as the natural PNT information sources like matching information (magnetism, gravity and image) and pulsar signals, could be applied as compensation methods in many scenarios. Besides, scene-based augmentation systems (SceneBAS) for comprehensive PNT should also be included in the comprehensive PNT application system, for example, the geo-graphic scene in three dimension could be important PNT augmentation information (Zhang et al., 2023).

### Navigation satellite at Lagrange points

The navigation satellite constellation at Lagrange points of Sun-Earth and Earth-Moon system is still under demonstration. A feasible thinking on navigation satellite at Lagrange points is making it not only the navigation method for cislunar spaces, but also navigation relay station from the surface of the earth to deep space. The navigation signal should follow the same structure as BeiDou/GNSS signals to realize the compatibility and interoperability with BeiDou/GNSS. Besides, the satellites should carry upward and downward antennas directing to the deep space and the earth respectively. The upward antenna is to broadcast navigation signal for deep space users, and the downward antenna is to receiving the signal of GNSS to realize the transferring of the space and time datum (Yang et al., 2023).

### Satellite navigation technology

BDS-3 was accomplished in June 2020, and officially opened service in July 2022. Series of creative designs are used such as the hybrid constellation, the whole constellation inter-satellite links, and Asymmetric Constant Envelope Binary Offset Carrier (ACE-BoC) signal modulation mode (Yang et al., 2020a, 2022; Xie and Kang, 2021). These creative designs strongly support not only the PNT performance but also six featured services namely Regional Short Message Communication Service (RSMCS), Precise Point Positioning Service via B2b signal (PPP-B2b), Global Short Message Communication Service (GSMCS), International Search & Rescue Service (MEOSAR) and Satellite Based Augmentation Service (SBAS).

The performance of BDS-3 is evaluated and assessed by academies and organizations (Yang et al., 2022; Guo et al., 2019; Cai et al., 2021). The international GNSS monitoring and assessment (iGMAS) evaluated the performances of BDS-3 signal and the basic PNT service in 2022, and the results showed that each item could fill the requirement of design index (as shown in Table 1). The SBAS service could broadcast GPS/BDS single- and dual-frequency augmentation information through BDS GEO satellites achieving APV-I and the CAT-I precision. The PPP-B2b performance for real-time positioning is about 0.1-0.2 m which is at the same level of PPP with IGS real-time products, and the convergence time is about 20-30 min (Yang et al., 2021, 2022; Yu et al., 2022; Song et al., 2021).

Table 1. performance of BDS-3 signal and system service

Signal accuracy	SISRE (m)		Orbit (m)		Clock (ns)		BDGIM (m)	
	B1I/B3I		IGSO	MEO	IGSO	MEO	day	night
	1.13		1.81	1.24	2.13	1.78	0.89	0.59
	Positioning (m)						Timing (ns)	
	B1I	B3I	B1C	B2a				

System performance	H	V	H	V	H	V	H	V		PDOP availability
	3.50	5.45	4.66	7.04	2.99	4.22	4.06	7.28	13.01	100%

On the aspect of further development, demonstrations are made on the inter-satellite links and the IGSOs to improve the service performance (Yang et al., 2020a, 2023). A space-based autonomous time keeping method was proposed using Hydrogen maser as the reference clock, and the predicted clock bias is 0.1 ns in 1 h (Yang Y F et al., 2021). IGSOs are suggested to increase the inclination angle to support PNT service in polar region, and involve in RSMCS, BDSBAS and PPP-B2b to overcome “South Wall” effect (Yang et al., 2020a).

### **Low Earth Orbit Satellite (LEO) augmentation system**

Low earth orbit (LEO) satellite augmented space-based PNT is a research highlight in recent years and progresses have been made on both technology development and LEO constellation construction. With stronger received signal power and better special geometry, LEO constellation becomes a key component of comprehensive PNT system (Ma et al., 2019). China now has many commercial LEO navigation augmentation constellation projects, such as “Hongyan” constellation, “Hongyun” constellation, and “Centispace” (Meng et al., 2018). In Oct. 2022, the Beijing Future Navigation Technology Co., Ltd launched the S5 and S6 satellites of “Centispace” for the demonstration of the LEO navigation augmentation system ([http://www.beidou.gov.cn/yw/xwzx/202210/t20221026\\_24755.html](http://www.beidou.gov.cn/yw/xwzx/202210/t20221026_24755.html)). The whole constellation is planned to be hundreds of satellites and will help to realize rapid kinematic positioning and navigation at centimeter level. The system is designed to be highly compatible with BDS and users may directly use it through software update.

The related key technologies on LEO augmentation system have been researched, such as constellation design, broadcast ephemeris design, the combined orbit determination of LEO and GNSS satellites and rapid PPP augmented with LEO etc. (Ma et al., 2020; Hou et al., 2019; Zhang et al., 2020, Meng et al., 2021). A confirmed conclusion is that the PPP accuracy and convergence time could be significantly improved by LEO constellation (Ge et al., 2018; Li et al., 2019, Meng et al., 2018).

### **Ground-based augmentation system**

As an important support of BDS, the Network ground stations of ground-based augmentation system have been built across China, with the guidance of the government and efforts from Central Enterprise and related departments (State Council Information Office of the People’s Republic of China, 2022). Until 2020, over 25000 stations were built or under construction with over 10,000,000 high precision receivers, chips and cards (Jiang and Wang, 2021). Also, a series of National Standards were published on the technologies of station construction, communication network, data processing center, broadcasting interface etc. The system could provide real-time meter-level, decimeter-level, centimeter-level, and post processing millimeter-level positioning augmentation service, which has been applied in many fields such as transportation and electric power industry (Zhao et al., 2021; Jia, 2020).

### **Land-based radio navigation system**

Land-based radio navigation system at very-low frequency is planned to be updated with the re-awareness of its advantages on better anti-inference. Chinese “Changhe 2” system is still on operation with 6 navigation stations, 3 monitoring stations and 1 control center. The system can serve the South China Sea, East China Sea and North China Sea. More navigation stations is going to be built to expand the coverage of the system, and improve the service accuracy, continuity and integrity through the improvement of signal structure etc. (Hu, 2018; Zhen, 2018).

### **Ground-based communication base stations**

Recently, ground-based communication base stations are engaged in PNT service. With more than 4.8 million communication base stations and 500 thousand 5G stations, China has the largest 5G network and user group in the world. The positioning pattern integrated with 5G and BDS is developed rapidly and the largest high-precision positioning system based on it is published by China Mobile in Oct. 2020. The system is able to provide sub-meter, centimeter, and millimeter level positioning service through 5G network which has good application prospect in areas like vehicle management, autonomous driving and vehicle-road cooperation (Yin et al., 2020).

### **Seafloor and underwater beacon positioning system**

The start of Chinese seafloor PNT infrastructure construction is relatively late and facing many difficulties not only in device development but also the positioning theory and methods. With the support of “Maritime Power Policy”, some progresses have been made in both device development and seafloor geodetic network establishment. Following the criteria of long-term working ability, and better pressure-resistant, anti-corrosive, anti-dragging and anti-flow, the seafloor geodetic station shelter in deep sea is developed with an overflow structure and a stable foundation bed; the shallow-sea shelter is developed with an overflow-type anti-dragging structure and a penetrating design (Sun et al., 2019; Yang et al., 2020b). The seafloor geodetic network is realized by extending and densifying the basic configuration with one master station located in the center of a square, and four auxiliary stations distributed on the four vertexes of the square. Successfully verified the performance of geodetic station devices in shallow sea, long-term seafloor geodetic stations were initially established in the deep-sea area of 3000 m in 2019. The internal positioning accuracy of the seafloor station is turned out to be better than 0.05 m, and the navigation accuracy within the geodetic network coverage of 10 km with acoustic/INS/gravity is better than 10 m (Yang et al., 2020b).

## **3 Resilient PNT technology**

With so many PNT information sources provided by comprehensive PNT infrastructure and nature PNT information, the coming problem for PNT users is how to use multiple information optimally according to the scenario and requirements of the users. Resilient PNT concept was then proposed to provide a PNT application pattern with full use of available information in comprehensive PNT to generate continuous, robust and reliable PNT results



(Yang, 2018). Following up, the connotation and characteristic of resilient PNT is discussed (Ming et al., 2023; Bian et al., 2021).

On the aspect of sensor integration, the PNT terminal should resiliently integrate available PNT sensors based on the optimal, available, compatible and interoperable principles; on the aspect of model building, resilient algorithms should be applied to adjust and optimize the basic functional model and stochastic model making them more suitable for the scenario (Yang, 2018).

Resilient model modification should take both functional model and stochastic model into account (Yang, 2018). The common expression of resilient observation model at time  $t_k$  can be given as (Yang, 2018)

$$L_i(t_k) = A_i \hat{X}(t_k) + F_i(\Delta_{t_{k-m}, t_{k-m}}) + e_i$$

where,  $\hat{X}(t_k)$  is the estimating parameter vector at time  $t_k$ ,  $L_i$  is the observation measured by sensor  $i$ ,  $A_i$  and  $e_i$  are the corresponding design matrix and observation random error vector, and  $F_i(\Delta_{t_{k-m}, t_{k-m}})$  is the modification function related with observation error series  $\Delta_{t_{k-m}, t_{k-m}}$  from time  $t_{k-m}$  to  $t_k$ . If extended Kalman filtering (EKF) algorithm is used, resilient dynamic function model is also needed, whose common expression at time  $t_k$  can be given as (Yang, 2018)

$$\bar{X}(t_k) = \Phi_{k,k-1} \hat{X}(t_{k-1}) + G_i(\Delta_{\bar{X}_{t_{k-m}, t_{k-m}}}) + W_i$$

where  $\bar{X}(t_k)$  is the prediction parameter vector at  $t_k$ ,  $G_i(\Delta_{\bar{X}_{t_{k-m}, t_{k-m}}})$  is the modification function related with dynamic model error series  $\Delta_{t_{k-m}, t_{k-m}}$  from time  $t_{k-m}$  to  $t_k$ ,  $W_i$  is the processing noise matrix.

Resilient stochastic model is to adjust the stochastic model of observation information and dynamic information according to their uncertainty in parameter estimation. Existing variance component estimation, robust estimation and adaptive estimation are typical resilient stochastic models (Yang et al., 2001ab, 2004ab, 2005), and the common expression for EKF can be used as:

$$\hat{X}_k = \left( \bar{P}_{\bar{X}_k} + A_1^T \bar{P}_1 A_1 + \cdots + A_r^T \bar{P}_r A_r \right)^{-1} \left( \bar{P}_{\bar{X}_k} \bar{X}_k + A_1^T \bar{P}_1 L_1 + \cdots + A_r^T \bar{P}_r L_r \right)$$

where  $\bar{P}_{\bar{X}_k}$  and  $\bar{P}_j$  are the adjusted weight matrix of predicted vector and observation vector  $L_i$ .

Absolutely, resilient PNT is the development trend of PNT application, and relevant researches have already started based on different application scenarios.

## **Resilient PNT application in urban scenarios**

In urban area, GNSS signals are easy to be sheltered by buildings and interfered by other signals. The cellular net and ground-based navigation stations can be the backup of GNSS, and ground-based GNSS augmentation system, pseudo-satellites and magnetic/image matching can be the compensation. In urban environment, multipath and non-line-of-sight (NLOS) signals are one of the main errors affecting the final PNT results. To increase the signal reception classification and control the effect of NLOS and multipath on final results, some machine learning methods are applied. With advanced study on the sample observations, a gradient boosting decision tree (GBDT)-based method and adaptive neuro-fuzzy inference system are applied in multipath/NLOS signal classification in specific areas (Sun et al., 2019, 2020). Without a priori information, K-means++, Gaussian mixed model (GMM) and fuzzy C-means (FCM) clustering methods are employed to separate LOS, multipath and NLOS signals (Zhu et al., 2021). Based on the predicted multipath value, adaptive filtering is applied to adjust the weight of the multipath signals (Sun et al., 2022). On the aspect of multi-source data fusion, a GNSS/INS-integrated system is formed enabling to calibrate INS autonomously based on a robust motion mode self-recognition technique (Mu et al., 2019a); a GNSS/INS/Odometer-integrated system is formed enabling the real-time calibration and compensation of odometer error based on environment information (Mu et al., 2019b, 2021).

## **Resilient PNT application in indoor/underground scenario**

Indoor and underground PNT system are mainly relay on radio frequency positioning technologies such as WiFi, Bluetooth, UWB and compensated with autonomous positioning methods such as INS, pseudo-satellites, cellular and magnetic matching. Deep learning and machine learning methods such as convolutional neural network are applied in 5G positioning models (Xiong et al., 2022) to achieve better accuracy. Robust estimation and robust Bayesian estimation are used to control the effect of observation outliers, and covariance component estimation is applied to adjust the contribution of different observations (Zhang et al., 2022a, b). Although GNSS can barely serve non-exposed spaces, the 5G/GNSS positioning mode and the integration of 5G and GNSS are also studied to realize the seamless positioning from outdoor to indoor (Shi et al., 2019; Yin et al., 2020; Hong et al., 2020).

## **4 Summary**

Comprehensive PNT is to provide seamless and redundant information, and resilient PNT is to use the information to provide optimal multi-source PNT application strategies. For users in complex environment with secure PNT requirement, the collaborative utilization of comprehensive PNT system and resilient PNT system are of great significance for the continuous, robust and reliable PNT services. China scholars pay highly attention to comprehensive PNT infrastructure design and resilient PNT application research, progresses and achievements have been made on the construction of comprehensive infrastructures, as well as the theoretical and experimental study of resilient PNT methods.

(1) Comprehensive PNT infrastructure is the prerequisite for resilient PNT applications, and resilient PNT provides important support for comprehensive PNT. Without comprehensive

PNT, resilient PNT is impossible to realize; without resilient PNT, comprehensive PNT is nothing but individual PNT information.

(2) Comprehensive PNT system is consisted of comprehensive PNT infrastructure and comprehensive PNT system. There is no doubt that BDS has been and will always be the core of China's comprehensive PNT system.

(3) The development schedule of comprehensive PNT system in different area is unbalanced, with advancing in satellite-based PNT technology, and relatively falling behind in that of deep space and deep sea.

(4) Resilient PNT includes resilient integration of multiple PNT sensors, resilient function models and resilient stochastic models. Initiated by Chinese scholars, the resilient PNT system design and resilient model establishment have become research focuses in PNT field. Although some achievements are made, the realization and application of a relatively complete resilient PNT system is still on the way.

## Bibliography

- Bian H W, Xu J N, He H Y et al (2021) The concept of resilience of national comprehensive PNT system (in Chinese). *Geomatics and Information Science of Wuhan University*, 46:1265-1272
- Cai H L, Meng Y N, Geng C J (2021) BDS-e performance assessment: PNT, SBAS, PPP, SMC and SAR (in Chinese). *Acta Geodaetica et Cartographica Sinica* 50: 427-435
- Chen G X, Liu Y, Liu Y X et al (2019) Adjustment of transceiver lever arm offset and sound speed bias for GNSS-Acoustic positioning. *Remote Sensing* 11: 1606
- Deng Y F (2019) Application research of railway GBAS based on BeiDou satellite. *Railway signaling & communication engineering* 16: 37-41
- Ge H B, Li B F, Ge M R et al (2018) Initial assessment of precise point positioning with LEO enhanced global navigation satellite systems (LeGNSS). *Remote Sensing* 10: 984
- Guo S R, Cai H L, Meng Y N (2019) BDS-3 RNSS technical Characteristics and service performance. *Acta Geodactica et Cartographica Sinica* 48: 810-821
- Hong X M, Xu X T, Peng A et al (2021) Key technologies and system architecture evolution of fusion positioning based on 5G mobile communication systems (in Chinese). *Xiamen Univ Nat Sci* 60: 571-585
- Hu A P (2018) Research on the development of land-based ultra-long-range radio navigation (in Chinese). *Navigation Positioning & Timing* 5: 1-6
- Hou Z, Yi X, Zhang Y et al (2019) Satellite-ground link planning for LEO satellite navigation augmentation networks. *IEEE Access* 7: 98715-98724
- Jia Y (2020) Development and Application Overview of GBAS in Civil Aviation. *Modern Navigation* 11: 272-276
- Jiang K, Jiao W H, Hao X L et al (2023) Scientific experiments and achievements of XPNAV-1 (in Chinese). *Acta Aeronautica et Astronautica Sinica*. *Acta Aeronautica et Astronautica Sinica* 44: 97-106
- Jiang L J, Wang T S (2021) Present and development thinking of BDS ground-based augmentation system (in Chinese). *Satellite Application* 11:8-12
- Li X X, Ma F J, Li X et al (2019) LEO constellation-augmented multi-GNSS for rapid PPP convergence. *Journal of Geodesy* 93: 749-764

- Liu J N, Luo Y R, Guo C et al (2022) PNT intelligence and intelligent PNT (in Chinese). *Acta Geodaetica et Cartographica Sinica*, 51: 811-828
- Liu Q, Wang Y, Liu Y et al (2019) Automatic radio environment measurement system for QTT site (in Chinese). *Sci Sin-Phys Mech Astron* 49: 099512
- Ma F, Zhang X, Li X et al (2020) Hybrid constellation design using a genetic algorithm for a LEO-based navigation augmentation system. *GPS solutions* 24: 1-14
- Meng L, Chen J, Wang J, et al (2021) Broadcast ephemerides for LEO augmentation satellites based on nonsingular elements. *GPS Solutions* 25: 129
- Meng Y S, Bian L, Wang Y et al (2018) Global navigation augmentation system based on Hongyan satellite constellation. *Space International* 10: 20-27
- Ming F, Yang Y X, Zeng A M et al (2023) The conceptual connotation, characteristics and discrimination of resilient PNT. *Bulletin of surveying and mapping* 4: 79-86
- Mu M X, Zhao L (2019a) A GNSS/INS-integrated system for an arbitrarily mounted land vehicle navigation device. *GPS solutions* 23:112-13
- Mu M X, Zhao L (2019b) Improved decentralized GNSS/SINS/odometer fusion system for land vehicle navigation applications. *Meas. Sci. Technol* 34: 035117-13
- Mu M X, Zhao L (2021) A Data Fusion Algorithm of GNSS/INS/ Odometer Integrated System In Consideration of Total Odometer Errors. 2021 The 21st International Conference on Control, Automation and Systems (ICCAS 2021) Ramada Plaza Hotel, Jeju, Korea, Oct. 12~15, 2021:1093-1098
- Qi K, Qu G Q, Xue S Q et al (2019) Analytical optimization on GNSS buoy array for underwater positioning, *Acta Oceanologica Sinica* 38: 137–143
- Shi C, Gu S F, Jing G F et al (2019) Fog positioning and its applications (in Chinese). *GNSS World of China* 44: 1-9
- Shuai P, Liu Q, Huang L et al (2019) Pulsar navigation test satellite XPNAV-1 and its observation results (in Chinese). *Journal of Chinese Inertial Technology* 27: 281-287
- Song W W, Zhao X K, Lou Y D et al (2023) Performance Evaluation of BDS-3 PPP-B2b Service (in Chinese). *Geomatics and Information Science of Wuhan University* 48: 408-415
- State Council Information Office of the People's Republic of China (2022) China's BeiDou Navigation Satellite System in the New Era [2022-11-04]. <http://www.scio.gov.cn/zfbps/32832/Document/1732795/1732795.html>
- Sun D J, Zheng C E, Zhang J C (2019) Development and prospect for underwater acoustic positioning and navigation technology (in Chinese). *Bull Chin Acad Sci* 34: 331–338
- Sun R, Hsu L T, Xue D B (2019) GPS signal reception classification using adaptive Neuro-Fuzzy inference system. *Journal of Navigation* 72: 685-701
- Sun R, Wang G Y, Cheng Q (2020) Improving GPS code phase positioning accuracy in urban environments using machine learning. *IEEE Internet of Thing Journal* 8: 7065-7078
- Sun R, Zhang Z, Cheng Q (2022) Pseudorange error prediction for adaptive tightly coupled GNSS/IMU navigation in urban areas. *GPS solutions* 26, 1-13
- Wang J T, Xu T H, Liu Y F et al (2021a) Kalman filter based acoustic positioning of deep seafloor datum point with two-step systematic error estimation. *Applied Ocean Research* 114: 102817
- Wang J T, Xu T H, Liu Y F et al (2023) Augmented Underwater Acoustic Navigation with Systematic Error Modeling Based on Seafloor Datum Network. *Marine Geodesy* 46: 129-148
- Wang J T, Xu T H, Zhang B S et al (2021b) Underwater acoustic positioning based on the robust zero-difference Kalman filter.

- Journal of Marine Science and Technology 26: 734-749
- Wang W, Meng F C, Kan B X (2022) Multi-source autonomous navigation system technology under national comprehensive PNT system (in Chinese). *Navigation and Control* 21: 10
- Xie J, Kang C B (2021) Engineering Innovation and the Development of the BDS-3 Navigation Constellation (in Chinese). *Engineering* 7: 558-563
- Xiong X Y, He D, He Z J et al (2022) Wireless Localization Method Based on Convolutional Neural Network Using 5G Cellular Networks. *Journal of Data Acquisition and Processing* 37: 1228-1245
- Yang Y F, Yang Y X, Chen J P et al Pseudo-stable constellation bias error of BDS-3 and its high-precision prediction. *Acta Geodaetica et Cartographica Sinica* 50: 1728-1737
- Yang Y X (2016) Concept of comprehensive PNT and related key technologies. *Acta Geodaetica et Cartographica Sinica* 45: 505-510
- Yang Y X (2017) Resilient PNT concept frame. *Acta Geodaetica et Cartographica Sinica*,2018,47: 893-898
- Yang Y X, Cui X Q, Gao W G (2004a) Adaptive Integrated Navigation for Multi-sensor Adjustment Outputs. *The Journal of Navigation* 57: 287-295
- Yang Y X, Ding Q, Gao W G (2022) Principle and performance of BDSBAS and PPP-B2b of BDS-3. *Satell Navig* 3: 1-9
- Yang Y X, Gao W G (2004b) Integrated Navigation by Using Variance component estimates of Multi-sensor measurements and Adaptive Weights of Dynamic Model information (in Chinese). *Acta Geodaetica et Cartographica Sinica* 33: 22-26
- Yang Y X, He H B, Xu G C (2001a) Adaptively Robust Filtering for Kinematic Geodetic Positioning. *Journal of Geodesy* 75:109-116
- Yang Y X, He H B, Xu T H (2001b) Adaptive Robust Filtering for Kinematic GPS Positioning (in Chinese). *Acta Geodaetica et Cartographica Sinica* 30: 293-298
- Yang Y X, Mao Y, Sun B J (2020a) Basic performance and future developments of BeiDou global navigation satellite system. *Satell Navig* 1: 1-8
- Yang Y X, Li X Y (2017) Micro-PNT and comprehensive PNT. *Acta Geodaetica et Cartographica Sinica* 46(10):1249-1254
- Yang Y X, Liu L, Li J L et al (2021d) Featured services and performance of BDS-3. *Chin Sci Bull*, 66: 2135-2143
- Yang Y X, Liu Y X, Sun D J et al (2020b) Seafloor geodetic network establishment and key technologies. *Science China Earth Science* 50: -DOI:10.1360/SSTe-2019-0242
- Yang Y X, Qin X P (2021) Resilient observation models for seafloor geodetic positioning, *Journal of Geodesy* 95: 79
- Yang Y X, Xu T H, Song L J (2005) Robust Estimation of Variance Components with Application in Global Positioning System Network Adjustment. *Journal of Surveying Engineering* 131:107-112
- Yin L, Ma Y Z, Li G W et al (2020) Research Progress of Communication-Positioning Integrated Technology. *Navigation Positioning & Timing* 7: 64-76
- Yu d Y, Jin J H, Liu Y et al (2022) Marine precise positioning experimental analysis based on BeiDou-3 PPP-B2b signal (in Chinese). *Hydrographic Surveying and Charting* 42: 51-55, 64
- Zhang H C, Yu B G, Bi J Z et al (2023) A survey of scene-based augmentation systems for comprehensive PNT. *Geomatics and Information Science of Wuhan University* 48: 491-505
- Zhang W, Yang Y X, Zeng A M et al (2022a) A GNSS/5G integrated three-dimensional positioning scheme based on D2D communication. *Remote Sensing*, 14: 1517
- Zhang W, Yang Y X, Zeng A M et al (2022b) Robust BDS/5G integrated positioning based on resilient observation model.

Advances in Space Research 71: 4006-4017

Zhang X H, Ma F J (2019) Review of the development of LEO navigation-augmented GNSS (in Chinese). *Acta Geodaetica et Cartographica Sinica* 48:1073-1087

Zhang Y, Li Z, Li R et al (2020) Orbital design of LEO navigation constellations and assessment of their augmentation to BDS. *Advances in Space Research* 66: 1911-1923

Zhao W, Wang Q, Shang K Y (2021) Electric Power Industry Precise Time-Space Service Network Based on BD Navigation System (in Chinese). *ELECTRIC POWER ICT* 29: 75-82

Zhen W, Ding C (2019) Development status and trend of land-based radio navigation system (in Chinese). *GNSS world of China* 44: 10-15

Zhou Q Y, WEI Z Q, LEI Y H et al (2023) X-ray telescope for pulsar deep space reference and its development vision (in Chinese). *Acta Aeronautica et Astronautica Sinica* 44: 526608

Zhou Q Y, Wei Z Q, Yan L L et al (2021) Space/ground based pulsar timescale for comprehensive PNT system. *Acta Phys* 70: 471-483

Zhu B, Yang C, Liu Y. 2021. Analysis and comparison of three unsupervised learning clustering methods for GNSS multipath signals (in Chinese). *Acta Geodaet Cartograph Sin*, 50: 1762-1771

# Maintenance of mm-level Geodetic Reference Framework

Yamin Dang <sup>1</sup>, Hu Wang <sup>1</sup>, Fuping Sun <sup>2</sup>, Yingyan Cheng <sup>1</sup>, Guangwei Jiang <sup>3</sup>, Xinhui Zhu <sup>2</sup>, Qiang Yang <sup>1</sup>, Yingying Ren <sup>1</sup>

<sup>1</sup> Chinese Academy of Surveying and Mapping, Beijing, China

<sup>2</sup> Institute of Geospatial Information, Information Engineering University, Zhengzhou, China

<sup>3</sup> College of Geology Engineering and Geomatics, Chang'an University, Xi'an, China

## 1 Introduction

The high-precision regional reference frame is the basis of the air-space-earth geodetic observation system and the national major infrastructure. A long-term and stable high-precision Earth reference framework is not only of great significance for national economic development and national defense construction, but also plays a significant role in fields such as Earth science research, disaster reduction and prevention. A high-precision maintenance method is the key to maintain the accuracy and stability of the terrestrial reference frame. Up to Date, the coordinate precisions of ITRF reference stations have already reached to mm level, even submillimeters, at reference epoch, but the coordinate maintenance precision of these stations are still at cm level due to non-linear movements related with geophysical phenomena.

Extensive observation collection, unified and rigorous data processing, and accurate construction of the station motion model are the three essential elements for the accuracy and reliability of the Global Navigation Satellite System (GNSS) velocity field. Based on the GNSS observation data from continuous observation data of the Crustal Movement Observation Network of China (CMONOC) and IGS stations over the past thirty years, more Chinese geodesy scientists devoted more efforts to themMaintenance of mm-level geodetic reference framework. The main contributions of this work included the followings.

- The Research Progress on the Method of Maintenance of Regional Reference Frame based on GNSS.
- The Dynamic maintenance of mm-level terrestrial reference frame
- The Reprocessing and Reanalysis of Two-Decade GNSS Observation in Continental China
- The Refinement of Provincial Plate and Establishment of Horizontal Relative Motion Velocity Field Model in Chinese Mainland
- The Distribution characteristics of crustal Deformation in Chinese Mainland and its relationship with strong earthquakes
- The progress of CGCS2000 frame maintenance in millimeter level accuracy
- The Preliminary Realization and Evaluation of CTRF2020

## 2 Methods of Maintenance of Regional Reference Frame based on GNSS

The high-precision regional reference frame is the basis of the air-space-earth geodetic observation system and the national major infrastructure. Due to frequent regional tectonics activities in China, continuous elastic changes in the surface morphology, multiple nonlinear signals superimposed on the base station, and internal relative movements between plates,

various factors make it difficult to maintain the regional reference frame. GNSS technology has the advantages of high precision, all-weather, real-time, etc., so it is necessary to carry out the maintenance of regional reference frame based on GNSS technology.

From 2014 to 2022, China successively carried out the Modern Surveying and Mapping Datum Construction and Maintenance Project and the National Satellite Navigation and Positioning Datum Station Network Adjustment Project, and conducted regular monitoring and analysis of China's geodetic datum and updating of local coordinate frame, achieving millimeter level monitoring of the national coordinate frame. At the same time, it also monitors and maintains the reference station network in multiple provinces and cities across the country, providing important guarantees for railway construction, water conservancy and hydropower projects, mineral resource development, earthquake prevention and disaster reduction, and ecological environment governance. At present, many provinces and cities of China have basically completed the upgrading and transformation of provincial reference stations, and the scale of the national reference station network has reached a super large scale of 3000 stations, of which about 2400 support BDS services, accounting for about 89% of the total number in the country. Related studies have shown that BDS-3 is equivalent to GPS in building high-precision reference frame. By using IGS station stability indicators as constraints and jointly maintaining coordinate frames with multiple GNSS, the maximum deviation of three-dimensional coordinates of stable points is better than 2mm, and the RMS is better than 1mm. Using long-term data from national large-scale GNSS reference stations to maintain regional frame in China will be an important means of frame maintenance and monitoring. In response to the complex terrain and mountainous areas in China, a rapid monitoring algorithm for the GNSS network solution of mountainous frame points with additional ground point tropospheric delay information correction is proposed, and a GNSS based regional reference frame maintenance software is developed to achieve high-precision dynamic monitoring and maintenance of regional reference frames in complex mountainous environments.

The research on the maintenance methods of regional reference frame based on GNSS has partly promoted the role of GNSS technology in dynamic monitoring and maintenance of regional reference frame and datum services, improved the theory and methods of regional reference frame maintenance, and provided technical support for the maintenance and use of regional reference frame. Relevant methods and technologies have played an important role in multiple national and provincial projects.

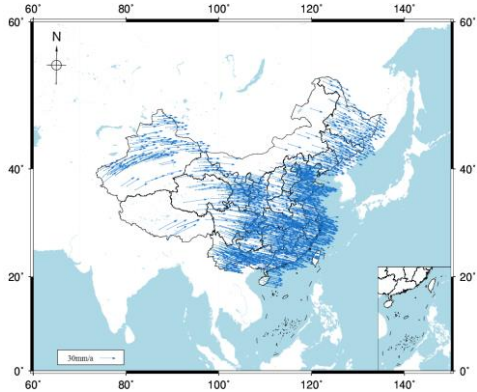


Figure 1. ITRF2014 Horizontal Velocity Field of GNSS Reference Station in Chinese Mainland



### 3 Dynamic maintenance of mm-level terrestrial reference frame

A long-term and stable high-precision Earth reference framework is not only of great significance for national economic development and national defense construction, but also plays a significant role in fields such as Earth science research, disaster reduction and prevention. A high-precision maintenance method is the key to maintain the accuracy and stability of the terrestrial reference frame.

At present, the accuracy of the measured velocity field of the terrestrial reference frame can reach within 1 mm/a, which can accurately and linearly maintain the reference frame, ensuring its millimeter level accuracy on a long-term scale. However, under the influence of nonlinear motion of the reference station and geocentric motion, the maintenance method based solely on linear velocity makes the accuracy of the reference frame only at the centimeter level on a seasonal scale, which cannot meet the needs of millimeter level Earth change monitoring and research. Therefore, considering the linear motion, nonlinear motion and geocentric motion of the reference station, the comprehensive maintenance of the reference frame is the development trend of the dynamic maintenance technology of the millimeter-level terrestrial reference frames (Sun et al., 2022).

Linear maintenance refers to the maintenance of a reference frame based on the linear (or long-term) changes in the position of the reference station. Linear maintenance relies on the linear speed of the reference station. There are two sources of linear velocity at reference stations, namely crustal motion models and measured velocity fields. Zhu et al (2014) proposed to use SLR data to establish a globally unified reference datum for vertical crustal movement; Zhu et al (2009, 2010) established a current plate motion model by using the results of space geodesy and ITRF velocity field. Compared with the methods of geology and geophysics, the accuracy has been greatly improved.

The nonlinear maintenance of the terrestrial reference frame can be divided into two categories. One is the modeling of nonlinear changes based on geophysical influence mechanisms. The main factors causing nonlinear motion of the reference station include environmental loads, thermal expansion effects, tidal deformation, and post-earthquake deformation (Zhu et al., 2020). Sun et al (2012) confirmed that there is a strong positive correlation between temperature changes and station annual displacement changes through correlation analysis.

And the other of nonlinear change modeling is based on coordinate time series. The methods for modeling nonlinear changes in coordinates include harmonic models, SSA, ARIMA models, and global statistical correction models. Dai et al (2021) proposed a nonlinear motion modeling method that combines wavelet multi-scale decomposition and singular spectrum analysis, and demonstrated that its modeling accuracy can be improved by about 26% compared to the SSA method. Jia et al (2023) extracted the time-varying amplitude of the annual term in the GNSS vertical coordinate time series, and conducted a thorough analysis of the time-varying characteristics of the annual term amplitude at global stations. It was found that the average consistency of the weekly amplitude changes between environmental loads, thermal expansion displacement, and GNSS vertical coordinates was around 60%. Moreover, after both corrections, 68% and 76% of the stations showed a decrease in the amplitude fluctuations of the annual term amplitude (as shown in Figure 1), indicating that environmental loads and

thermal expansion effects are important reasons for the amplitude changes of the annual term.

In addition to the above aspects, the dynamic maintenance of the millimeter level terrestrial reference frame still needs to consider the following issues: firstly, further improve the spatial observation data processing technology, weaken the impact of system errors, and obtain more accurate reference station coordinates, which is the foundation for improving the dynamic maintenance accuracy of the terrestrial reference frame; Secondly, the accuracy of nonlinear motion modeling of reference stations based on geophysical influence mechanisms and coordinate time series needs to be further improved; Thirdly, we need to further improve the implementation accuracy and stability of the epoch reference frame.

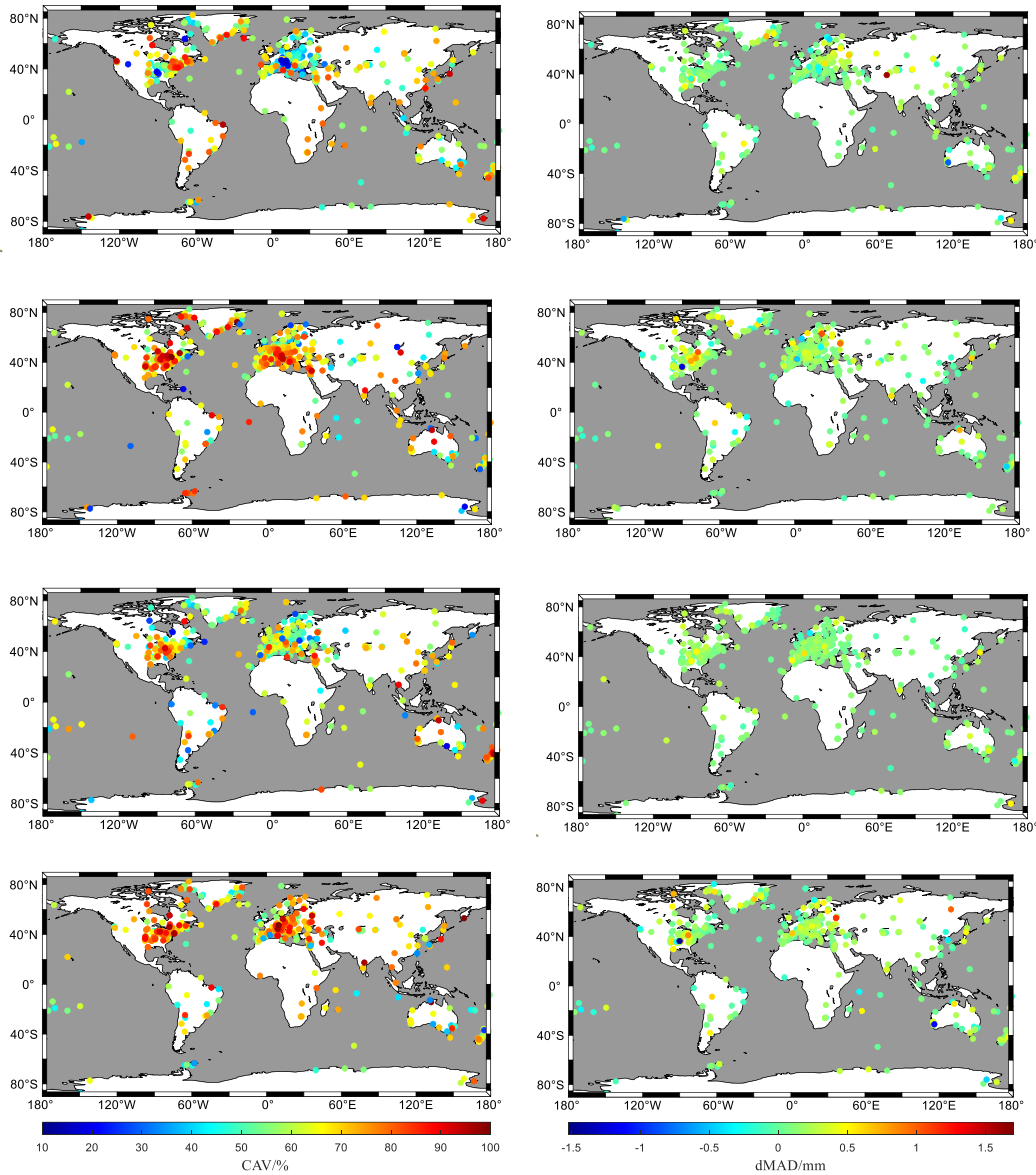


Figure 2. Spatial distribution of CAV (consistency of amplitude variation) of the annual signals between the environmental loading and coordinate time series (left) and the change of MAD (mean absolute deviation) (right). From top to bottom are ATML, CWSL, NTOL and total environmental loading

## 4 Reprocessing and Reanalysis of Two-Decade GNSS Observation in Continental China

Extensive observation collection, unified and rigorous data processing, and accurate construction of the station motion model are the three essential elements for the accuracy and reliability of the Global Navigation Satellite System (GNSS) velocity field. GNSS data reprocessing not only can weaken the influence of untrue nonlinear site signals caused by imperfect models but also can eliminate the displacement offset caused by frame transformation, solution strategy, and model change. Based on the new repro3 criteria of the International GNSS Service (IGS), we process rigorously GNSS observations of continental China from the period 2000 to 2020 to refine GNSS station secular velocities and analyze the present-day crustal deformation in continental China. The main contributions of this work included the followings. Firstly, the repro3 algorithm and model are used to uniformly and rigorously process the two-decade GNSS historical observations to obtain more reliable GNSS coordinate time series with mm-level precision. Combined with the historical records of major earthquakes in continental China, we build a GNSS time series model considering nonlinear factors (velocity, offset, period, co-seismic/post-seismic deformation) to extract GNSS horizontal velocity field whose root mean square (RMS) mean is 0.1 mm/a.

To ensure the accuracy and consistency of the GNSS coordinate solutions, we use the updated convention and processing settings of repro3 to reprocess the two-decade GNSS observations of continental China in an entirely consistent way. The offsets caused by receiver fault, antenna replacement, earthquake, and other factors can be detected using station logs, while the offsets caused by frame transformation, solution strategy, and model change need to be eliminated by data reprocessing. The basic input GNSS sites of this research are shown in Figure 2. The CMONOC comprises 260 continuous operation reference stations (daily observation) and more than 2000 regional stations (irregular observation). It has preliminarily realized the dynamic monitoring of the primary and secondary tectonic blocks, main active fault zones, and key seismic risk areas in continental China. These GNSS stations have laid a foundation for describing the detailed characteristics of crustal movement in continental China. In addition, IGS stations around China and other continuous observation stations are collected.

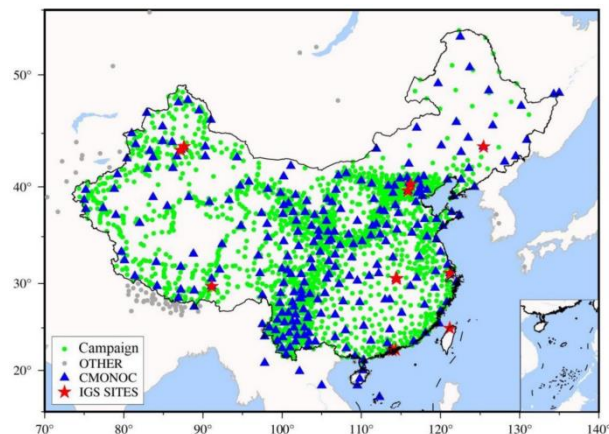


Figure 3. GNSS sites in continental China

A GNSS coordinate time series usually contains the secular trend (linear velocity),

seasonal variation (annual and semi-annual signals), offsets caused by non-seismic factors (equipment replacement, antenna height measurement error, phase center modeling error, or other human and software errors) or seismic factors (co-seismic deformation), post-seismic deformation, and other unmodeled errors. For these errors, an Integrated Time Series Method (ITSM) concerning the effect of seismic deformation was proposed to model the station's nonlinear motion accurately. Distinguished with existing studies, all parameters including seismic relaxation time can be simultaneously estimated by ITSM, which improves the accuracy and reliability of GNSS station velocity significantly. After analysis of the time series for all sites, we can obtain the ITRF2014 GNSS horizontal velocity field of continental China. As shown in Figure 4, there is a clockwise rotation movement from southwest to southeast in continental China, especially in the western region. The velocity field in the eastern region points from northwest to southeast.

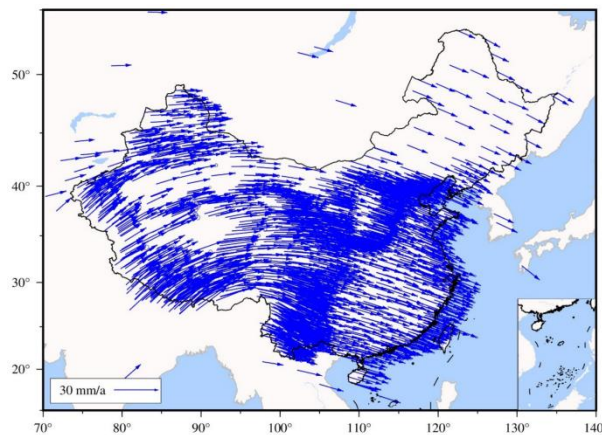


Figure 4. GNSS horizontal velocity field of ITRF2014 in continental China

In general, the emergence and development of GNSS technology in the 1990s significantly promoted the research of tectonic movement and deformation monitoring into a new stage. With over 30 years of research, horizontal tectonic movement and main deformation characteristics in continental China have been clear, and the tectonic deformation in most areas has been accurately quantified. In the future, it is necessary to intensify the continuous GNSS observation further to obtain the three-dimensional tectonic movement information and its evolution characteristics with time. At the same time, it is necessary to strengthen the integration of GNSS and different geodetic technologies, and interdisciplinary research.

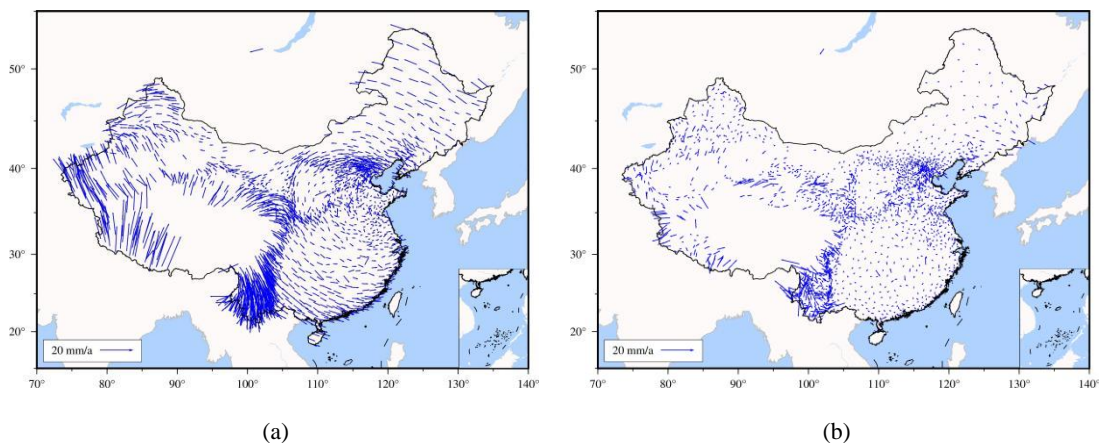
## 5 Refinement of Provincial Plate and Establishment of Horizontal Relative Motion Velocity Field Model in Chinese Mainland

Provincial CORS system is an important part of modern city digitization, informatization and intellectualization, which is easy to obtain the spatiotemporal information of various objects and their related dynamic changes. In order to further realize the modernization and autonomy of the regional framework benchmark, improve the comprehensive service level and emergency support capacity of the modern surveying benchmark, upgrade the accuracy of the regional velocity field and accurately depict its own local motion characteristics in the mainland of China, the velocity field is derived from continuous observation data of the Crustal Movement

Observation Network of China (CMONOC).

Both high precise coordinate and velocity of these CMONOC stations have been calculated with GAMIT/GLOBK software. In addition, the Euler vector of the whole Chinese continent and two-stage plates in the China mainland are reanalyzed based on the above velocity field. On the basis of the Euler vectors of the abovementioned, i. e. the whole Chinese continent, two-stage plates, provincial plates, sub-blocks in some provinces' interior, as well as that of Eurasia plate derived from NNR-NUVEL1A plate motion model, the contribution of the average movement of each block to the horizontal velocity field could be available and then the residual velocity fields in Mainland China are further analyzed and compared.

The results show that the NNR-NUVEL1A model only deducts the partial movement trend of the velocity field in Mainland China. In contrast, the overall movement model of Mainland China plate can better reflect the overall movement trend. The movement model of two-stage plates and provincial plates in Chinese mainland, both of whose inner and outer average precision is less than  $2 \text{ mm.a}^{-1}$  and  $3 \text{ mm.a}^{-1}$ , respectively, can both depict the local movement characteristics of Mainland China more precisely, and the only difference between them is that the former is easier to understand in the sense of physics while the latter is simpler in using. However, both of them is not perfect for researching the relative motion of some regions such as Xinjiang, Tibetan Plateau, Sichuan, Yunnan where exist complex crustal movement. Hence, through cluster analysis with K-Means++ on horizontal velocity field in these complex areas, these provincial blocks are further decomposed into some sub-blocks quickly and accurately. Our results are in accordance with those of present-day blocks of second order. Consideration to the impact of complex geological structure, topography and geomorphology in these provinces and the physical significance in respect to each corresponding provincial plate, we also give the Euler vectors of these sub-blocks in some provinces' interior. The result can be concluded that not only the average error and mean square error are less than  $2 \text{ mm.a}^{-1}$  in Mainland China but also the precision of horizontal velocity fields can reach  $2 \text{ mm.a}^{-1}$  in some complex regions, that is Xinjiang, Tibet, Sichuan, Yunnan. Obviously, the scheme of the sub-block demarcation in some provinces' interior by the method of K-Means++ is effective and feasible in terms of high precision and convenience.





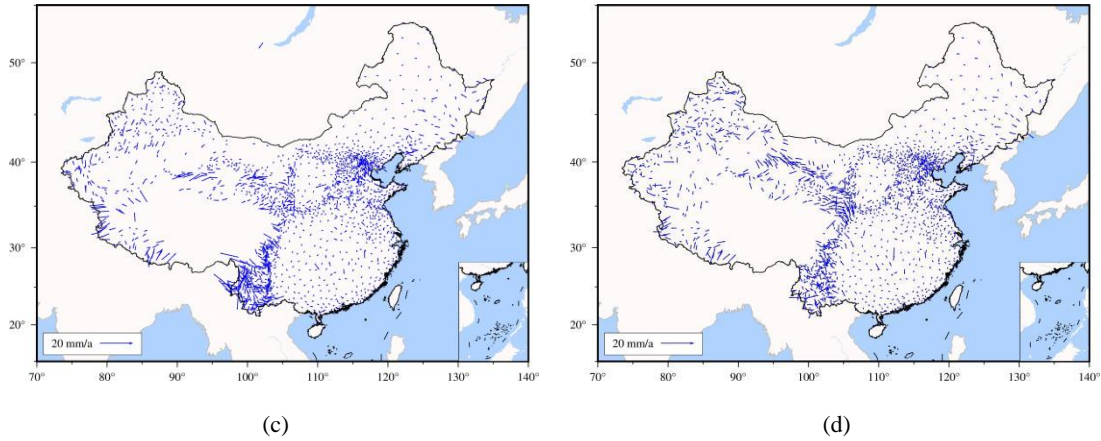


Figure 5. The horizontal relative velocity field of Chinese Mainland: (a) relative to Chinese mainland ; (b) relative to the secondary block; (c) relative to provincial blocks; (d) relative to sub blocks within the province

## 6 Distribution characteristics of crustal Deformation in Chinese Mainland and its relationship with strong earthquakes

GNSS velocity field can directly reflect the characteristics of crustal movement in the study area under a certain reference frame, and its spatial distribution characteristics will vary with the change of datum. While the crustal strain field is not limited by datum, and it can reflect the dynamic mechanism of crustal deformation. This section estimates the GNSS horizontal crustal strain rate field in continental China using the GNSS horizontal velocity field of more than 2000 sites from the above solution to analyze the characteristics of the current crustal strain rate field in continental China. And we obtained the horizontal grid velocity field ( $1^\circ \times 1^\circ$ ) of continental China, as shown in Figure 6. The red arrow is raw velocity, and the blue arrow is interpolation velocity.

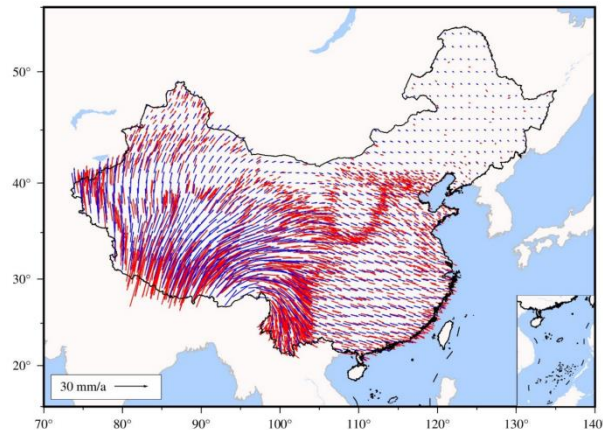


Figure 6. The horizontal grid velocity field ( $1^\circ \times 1^\circ$ ) of continental China (The red arrow is the known velocity, and the blue arrow is the grid velocity).

The principal strain rate field of continental China can be estimated using the horizontal grid velocity field . The overall pattern of tectonic deformation in continental China in the past two decades is shown in Figure 7. The principal strain rate in West China is much higher than that in East China. Among them, the principal strain rate in the west is large, and the strain

distribution is complex, indicating that the crustal deformation in this area is intense and the geological tectonic movement is more complex. The high-strain areas in continental China are mainly located in the Qinghai Tibet Plateau and Tianshan Mountains. The principal compressive strain rates of the Himalayas and Tianshan orogenic belts are perpendicular to the orogenic belt trend, and the other principal strain rate is much lower than the principal compressive strain rate, revealing the northward pushing of the Indian plate. In contrast, the total amount of principal strain rates in the east is small. The principal strain rates of several active blocks in the east are less than 5 nstrain/year, and the principal strain rate field has no significant regional distribution characteristics.

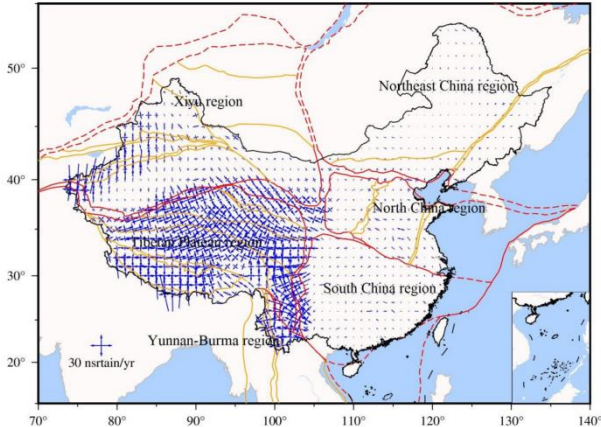


Figure 7. The principal strain rate field in continental China (The red and yellow lines are block boundaries).

Figure 8 shows the relationship between a strong earthquake and the second strain invariant field in the Chinese mainland. Similarly, we find that there is a strong correlation between the distribution of strong earthquakes and the second strain invariant field, that is, most strong earthquakes are concentrated in yellow and red areas where the second strain invariant is greater than 20 nstrain/year. It can be seen that the second strain rate invariance of the Tianshan, Qinghai, Tibet Plateau, and Sichuan-Yunnan regions is large, and the second strain rate invariance changes greatly. The range of the second strain rate in Sichuan Yunnan, Qinghai Tibet Plateau, and Tianshan region are 5~40, 10~60, and 10~45 nstrain/year respectively. In fact, strong earthquakes occur widely in the Qinghai, Tibet Plateau, Sichuan Yunnan, and Tianshan regions, while there are relatively few strong earthquake activities in other regions. From this, we can infer that the occurrence of strong earthquakes is closely related to the magnitude and change rate of the second strain rate invariant field.

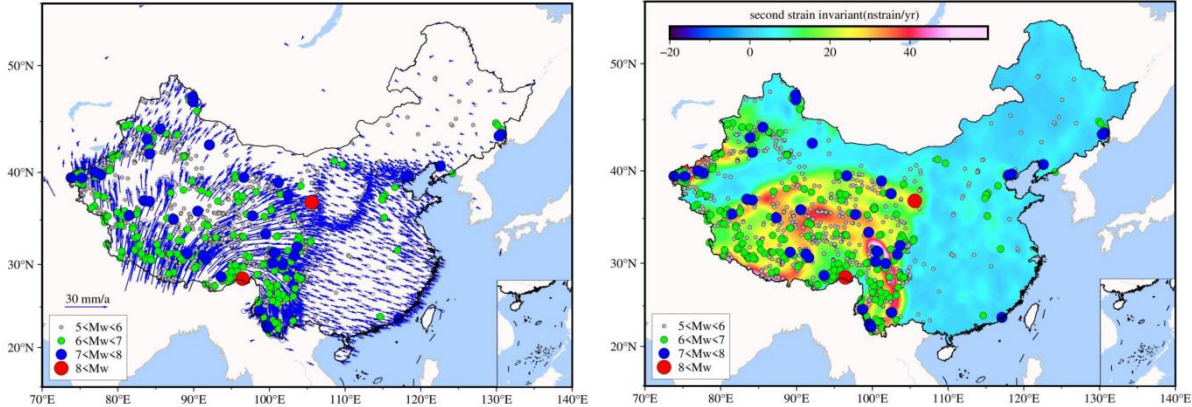


Figure 8. The distribution of strong earthquake and deformation strain field

According to the relationship between the above strong earthquake distribution and GNSS velocity field and the second strain invariant field, we can draw the following conclusions. First, strong earthquakes occur when the magnitude and direction of the GNSS velocity field change greatly. The change of velocity field is caused by the mutual compression of crustal structures of different active blocks. The stronger the regional velocity change, the higher the frequency of strong earthquakes. Secondly, strong earthquakes usually occur in areas with large strain rates and large changes in strain rates. All strong earthquakes with  $> 7$  are distributed in the region where the second strain rate invariance is greater than 20 nstrain/year.

## 7 The progress of CGCS2000 frame maintenance in millimeter level accuracy

Up to Date, the coordinate precisions of ITRF reference stations have already reached to mm level, even submillimeters, at reference epoch, but the coordinate maintenance precision of these stations are still at cm level due to non-linear movements related with geophysical phenomena. To enhance the accuracy of site location expressed, an enhanced method known as SSA-PD (Singular spectrum analysis with pseudo data) to address the phase shift issue of SSA and another method named SSA-P (Singular spectrum analysis for prediction) for predicting the coordinates of GPS sites at any specific time are proposed and put into use. For this purpose, the coordinate time series of China continuous operating reference stations spanning of ten years are used. After interpolation for missing data and gross data detection, all position time series were modeled with SSA-PD. Here only stations located in the plate of the South China subplate were taken as an example, the modeling results in U directions are shown in Figure 9.

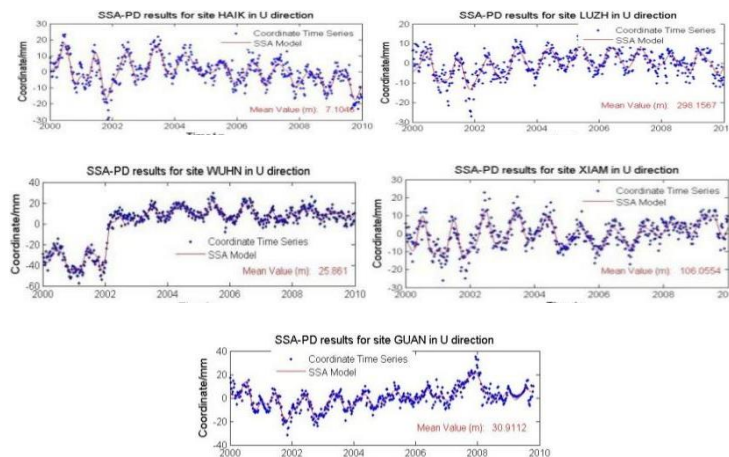


Figure 9. Modeling results for station nonlinear movements in the U directions in the South China subplate.

From the results analyzed, the original signals and modeled signals at most stations agreed well, and their differences - which were in fact the accuracies of the model results - were better than 3 mm, 2 mm, and 5 mm in the E, N, and U directions, respectively. Figure 9 also shows that similar trends and oscillation terms exist at the sites located in the same subplate, especially in the horizontal directions. Thus, it is possible for us to model the nonlinear movement at sites with a long period of time series and expand the nonlinear movement to the sites with a short period of observations, and then transform its position from the current epoch to any epoch



needed.

The time series of two stations with a distance of under 500 km had approximately the same amplitude and phase. If the distance between two stations was greater, both the amplitude and the phase drift at the two stations were not synchronized. It seems that only the nonlinear movement at two stations within a 500 km distance can be replaced in this way.

This another expanded method called SSA for prediction (SSA-P), for predicting the coordinates of GPS sites at any specific time was proposed. Its performance was assessed using 10-year GPS time series of weekly coordinates of 32 national GPS sites. The first 468 weekly samples were used to reconstruct the signals; the reconstructed model was then used to predict the next 52 weekly samples to validate the model's prediction results.

As vertical movements are much more complicated due to co-seismic and post-seismic deformations, global geophysical fluid dynamics, and so forth. It was found to be typical that the characteristic of the modeling based on earlier years could not be expanded forward to following years or had poor accuracy; thus, the accuracy of the modeling for the vertical component was usually poorer than that of the horizontal components, even though the accuracy of the modeling in the vertical direction was better than 5 mm.

In general, the results shown in Figure 10 indicate insignificant differences between the predicted signals and the real signals; the accuracy of the predicted results is quite stable, with an accuracy of about 3 mm at most stations.

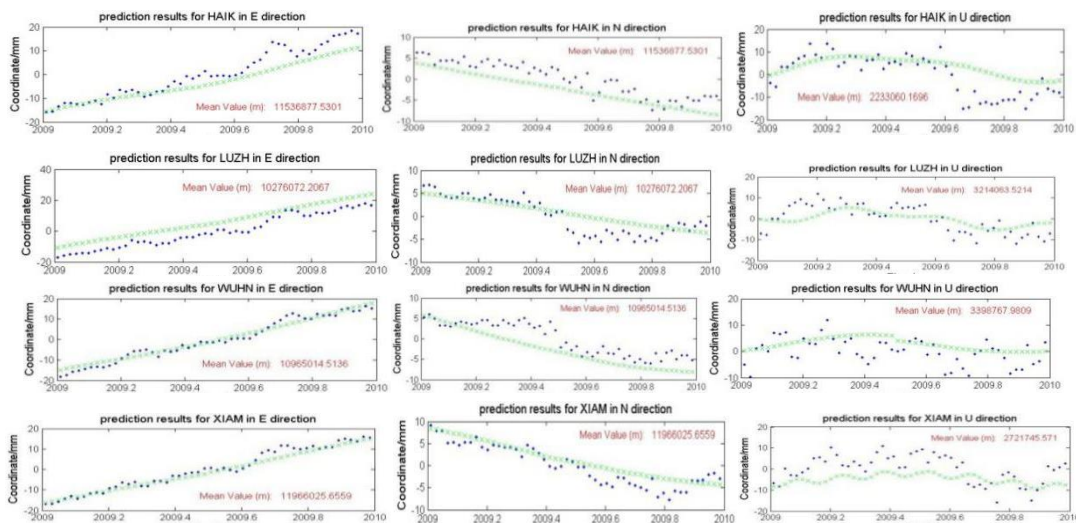


Figure 10. Prediction results for station nonlinear movements in the N, E, and U directions in the South China subplate.

The results for the performance assessment of SSA-P indicate that it is possible to obtain a high accuracy even when the noise level is larger than the oscillatory components.

The accuracy of the SSA-P used to predict the coordinates of the GPS sites in the horizontal and vertical directions was better than 5 mm and 1 cm, respectively, for most GPS sites, even though annual and semiannual signals in amplitude exist in the time series. However, the prediction results for the stations in the Lhasa and ChuanDian plates were poor, compared with those for the stations in other plates, resulting in the same conclusion as the fitted error from the plates.

## 8 The Preliminary Realization and Evaluation of CTRF2020

The current research of the international and regional coordinate reference framework is mainly realized by GPS technology. The launch of the last BDS3 satellite on June 23 of 2020 marked the completion of the global deployment of BDS. Therefore, it is urgent to study and establish the corresponding coordinate reference framework. We aim to preliminarily realize and evaluate the BDS3/COMPASS terrestrial reference framework (CTRF2020). CTRF2020 reference epoch is 2020.0, and it can be expressed with the coordinates and velocities of a series of reference sites at the epoch of 2020.0.

Firstly, the evaluation of the actual service performance of BDS in the global region reflects the high visibility and change trend of BDS satellite in recent three years, which provides basic input data for CTRF2020. Then, the BDS observations of about 100 global stations in the recent three years are calculated by PPP and NET solution, to obtain the global high-precision BDS coordinate time series. Then, the BDS time series of the two solutions are fitted and compared with the IGS14 velocity field. The results show that the series accuracy of PPP-BDS and NET-BDS solutions is equivalent, and there is an mm-level systematic deviation with IGS14 solutions. The horizontal series fitting accuracy of PPP-BDS and NET-BDS solutions is better than that of the vertical direction, the accuracy of NET-BDS solution is slightly better than PPP-BDS, and the difference of fitting accuracy is 0.12, 0.13, and 0.50 mm in the NEU direction. The velocity field accuracy of PPP-BDS and NET-BDS solution is the same, and the overall three-dimensional velocity difference is less than 0.2 mm/a. The velocity fields of PPP-BDS and NET-BDS solution have little difference from IGS14, and the overall difference is less than 0.5 mm/a. Finally, we give the limitations and improvement direction of CTRF2020. The preliminary realization and evaluation of CTRF2020 may be expected to provide a reference for the future realization of a comprehensive terrestrial reference framework dominated by BDS3 technology and supplemented by multi-source space geodetic technology.

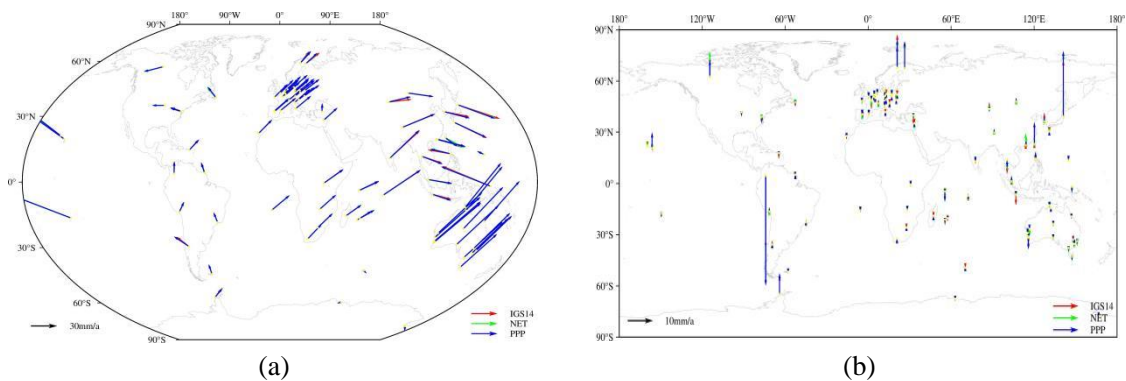


Figure 11. CTRF2020 horizontal and vertical velocity field.

We aim to preliminarily realize and evaluate the terrestrial reference framework based on BDS technology. The main research work includes three aspects:

(1) We evaluate the global actual service performance of BDS in recent years. By 2021, a total of 59 BDS satellites have been launched, the number of available BDS satellites in orbit has exceeded 40, and the number of visible BDS satellites in the global region has exceeded 10,

which indicates that the high visibility of BDS satellites in the global region in recent three years. This provides the necessary input conditions for CTRF2020, that is, long-term and reliable global BDS observation data.

(2) We fit and analyze the global BDS time series based on PPP-BDS and NET-BDS, respectively, and compare them with IGS14 velocity field. The results show that the series accuracy of PPP-BDS and NET-BDS solutions is equivalent, and there is a systematic error from IGS14 solution. The velocity parameters in BDS time series are not sensitive to periodic parameters, and whether the difference of velocity fitting solution of the periodic term is considered is within 0.1 mm/a. The BDS time series of the two modes can accurately reflect the station's linear motion rate and periodic change trend, and the periodic change trend in the vertical direction is usually more obvious than that in the horizontal direction. The horizontal series fitting accuracy of PPP-BDS and NET-BDS solutions is better than the vertical direction, and the series fitting accuracy of NET-BDS mode is slightly better than PPP-BDS. The difference in the NEU direction fitting accuracy between them is 0.12, 0.13, and 0.50 mm.

(3) We analyze and evaluate the accuracy and reliability of two kinds of velocity field models (PPP-BDS and NET-BDS) of CTRF2020. The results show that the three-dimensional velocity fields of PPP-BDS and NET-BDS are roughly the same in both numerical and direction, and the horizontal direction of CTRF2020 is close to IGS14 in both numerical and direction. However, there are some differences in the vertical direction. The velocity field accuracy of PPP-BDS and NET-BDS solution modes is the same, and the overall three-dimensional velocity difference is less than 0.2 mm/a. The velocity field of PPP-BDS and NET-BDS solution has little difference from that of IGS14, and the overall difference is less than 0.5 mm/a.

This research is limited to the processing and analysis of global BDS observations in the recent three years (2019–2021), and there are still several jobs to be developed and improved. First, at present, the number of global BDS continuous observation stations is still small, the spatial distribution is uneven, and the cumulative observation time is short, which also affects the accuracy and reliability of the preliminary velocity field product of CTRF2020 to a certain extent. Second, there is still a lack of integrated satellite orbit and clock error products of BDS, which leads to some inconsistency in the coordinates calculated by different analysis centers. Third, the integrated multi-source space geodetic technology is expected to further improve the stability and reliability of the framework. Fourth, although CTRF2020 adopts the analysis and evaluation technology of long-term time coordinate series of stations considering nonlinear factors, its results do not fully reflect the nonlinear variation parameters.

## 9 Summary

The research on the maintenance methods of regional reference frame based on GNSS has partly promoted the role of GNSS technology in dynamic monitoring and maintenance of regional reference frame and datum services, improved the theory and methods of regional reference frame maintenance, and provided technical support for the maintenance and use of regional reference frame. Relevant methods and technologies have played an important role in multiple national and provincial projects.

The current research of the international and regional coordinate reference framework is mainly realized by GPS technology. CTRF2020 aim to preliminarily realize and evaluate the

BDS3/COMPASS terrestrial reference framework (CTRF2020). CTRF2020 reference epoch is 2020.0, and it can be expressed with the coordinates and velocities of a series of reference sites at the epoch of 2020.0.

In general, the emergence and development of GNSS technology in the 1990s significantly promoted the research of tectonic movement and deformation monitoring into a new stage. With over 30 years of research, horizontal tectonic movement and main deformation characteristics in continental China have been clear, and the tectonic deformation in most areas has been accurately quantified. In the future, it is necessary to intensify the continuous GNSS observation further to obtain the three-dimensional tectonic movement information and its evolution characteristics with time. At the same time, it is necessary to strengthen the integration of GNSS and different geodetic technologies, and interdisciplinary research.

In addition, the dynamic maintenance of the millimeter level terrestrial reference frame still needs to consider the following issues: firstly, further improve the spatial observation data processing technology, weaken the impact of system errors, and obtain more accurate reference station coordinates, which is the foundation for improving the dynamic maintenance accuracy of the terrestrial reference frame; Secondly, the accuracy of nonlinear motion modeling of reference stations based on geophysical influence mechanisms and coordinate time series needs to be further improved; Thirdly, we need to further improve the implementation accuracy and stability of the epoch reference frame.

## Bibliography

- DANG Yamin, CHENG Chuanlu, YANG Qiang, et al. (2022) Vertical Deformation Characteristics Affected by Strong Earthquakes in Mount Qomolangma and Surrounding Areas. *Geomatics and Information Science of Wuhan University*, 2022, 47(1).
- DANG Yamin, GUO Chunxi, JIANG Tao, et al. (2021) 2020 height measurement and determination of Mount Qomolangma. *Acta Geodaetica et Cartographica Sinica*, 50(4).
- DANG Yamin, Yang Qiang, WANG Wei, et al. (2022) Analysis on 3D crustal deformation of Qinghai-Tibet Plateau and its surrounding areas based on block model. *Acta Geodaetica et Cartographica Sinica*, 2022,51(7) : 1192-1205. DOI: 10.11947/j. AGCS.2022.20220123.
- DANG Yamin,JIANG Tao, CHEN Junyong.(2022) Review on Research Progress of the Global Height Datum.*Geomatics and Information Science of Wuhan University*, 47(10):1576-1586.
- Guangwei, J. I. A. N. G., Panlong, W. A. N. G., Chunxi, G. U. O., Bin, W. A. N. G., & Yuanxi, Y. A. N. G. Short-term GNSS network solution and performance in large height difference region with tropospheric delay constraint. *Acta Geodaetica et Cartographica Sinica*, 51(11), 2255.
- Hou, Y., Wang, H., Wang, J., Ma, H., Ren, Y., Li, P., & Wang, Y. (2022). Studies and Analysis of Combining BDS-3/GNSS Ultra-Rapid Orbit Products from Different IGS Analysis Centers. *Remote Sensing*, 14(23), 6122.
- Hu, W. A. N. G., Yamin, D. A. N. G., Yangfei, H. O. U., Jinzhong, B. E. I., Jiexian, W. A. N. G., Guixia, B. A. I., ... & Shoujian, Z. H. A. N. G. (2020). Rapid and precise solution of the whole network of thousands of stations in China based on PPP network solution by UPD fixed technology. *Acta Geodaetica et Cartographica Sinica*, 49(3), 278.
- JIANG, G. W., WANG, B., WANG, Y. W., LI, K., & SUN, Y. Y. (2020). Establishment of regional terrestrial reference frame considering coordinate characteristic and stability. *Progress in Geophysics*, 35(1), 8-15.

- Jiang, G., Wang, P., Guo C., Wang, B., Yang Y. (2022). Short-term GNSS network solution and performance in large height difference region with tropospheric delay constraint. *Acta Geodaetica et Cartographica Sinica*, 51(11): 2255-2264.
- Pengfei Cheng a, Yingyan Cheng, Xiaoming Wang, Suqin Wu, Yantian Xu. Realization of an Optimal Dynamic Geodetic Reference Frame in China: Methodology and Applications[J]. *Engineering*,2020,6(08):879-917
- REN, Y., WANG, J., WANG, H., LIAN, L., HOU, Y., & WANG, Y. (2021). Construction of Velocity Field in Chinese Mainland Based on Local Seamless Delaunay Triangulation with Inverse Distance Weighting Method. *Geomatics and Information Science of Wuhan University*, 46(7), 1071-1080.
- Ren, Y., Lian, L., & Wang, J. (2021). Analysis of seismic deformation from global three-decade GNSS displacements: implications for a three-dimensional earth GNSS velocity field. *Remote Sensing*, 13(17), 3369.
- Ren, Y., Wang, H., Hou, Y., Wang, J., Cheng, Y., & Li, P. (2022, May). The Preliminary Realization and Evaluation of CTRF2020 Based on New BDS3 Technology. In *China Satellite Navigation Conference (CSNC 2022) Proceedings: Volume I* (pp. 57-69). Singapore: Springer Nature Singapore.
- Ren, Y., Wang, H., Lian, L., Wang, J., Cheng, Y., Zhang, Y., ... & Zhang, S. (2021). A method based on MTLs and ILSP for GNSS coordinate time series analysis with missing data. *Advances in Space Research*, 68(9), 3546-3561.
- Ren, Y., Wang, H., Wang, J., Lian, Li., Zhu, W., Wang, Y., & Zhang, S. (2020). The sub-block demarcation with K-Means plus plus in each province's interior and establishment analysis of the relative horizontal velocity field model in Mainland China. *CHINESE JOURNAL OF GEOPHYSICS-CHINESE EDITION*, 63(7), 2516-2533.
- Sun Fuping, Jia Yanfeng, Zhu Xinhui, Xiao Kai, Liu Jing. (2022). Advances in dynamic maintenance technology of mm-level terrestrial reference frame. *Geomatics and Information Science of Wuhan University*, 47(10): 1688-1700.
- Wang B., Jiang G., Sun Y., Hu W., Ma X.(2022). Regional reference frame maintenance considering anisotropy of plate motion. *Science of Surveying and Mapping*, 47(12):16-22.
- Wang X, Cheng Y, Wu S, Zhang K. An effective toolkit for the interpolation and gross error detection of GPS time series. *Surv Rev* 2015;48(348):202–11.
- Wang XM, Cheng YY, Wu SQ, Zhang KF. An enhanced singular spectrum analysis method for constructing nonsecular model of GPS site movement. *J Geophys Res Solid Earth* 2016;121(3):2193–211.
- Wang, H., Hou, Y., Dang, Y., Bei, J., Zhang, Y., Wang, J., ... & Gu, S. (2021). Long-term time-varying characteristics of UPD products generated by a global and regional network and their interoperable application in PPP. *Advances in Space Research*, 67(2), 883-901.
- Wang, H., Li, P., Wang, J., Ma, H., Hou, Y., & Ren, Y. (2022). Analysis of BDS-3 Real-Time Satellite Clock Offset Estimated in Global and Asia-Pacific and the Corresponding PPP Performances. *Remote Sensing*, 14(24), 6206.
- Wang, H., Ren, Y., Hou, Y., Wang, J., Zhang, Y., Cheng, Y., ... & Fang, S. (2022). The refinement of reprocessed GNSS three-decade displacement trajectory model with spectral analysis and hypothesis test. *Advances in Space Research*, 70(7), 1810-1829.
- Wang, H., Ren, Y., Wang, A., Wang, J., Cheng, Y., Fang, S., & Yang, Q. (2022). Two-Decade GNSS Observation Processing and Analysis with the New IGS Repro3 Criteria: Implications for the Refinement of Velocity Field and Deformation Field in Continental China. *Remote Sensing*, 14(15), 3719.
- Zhu Xinhui, Sun Fuping, Wang Ren. (2009). Global plate motion models based on ITRF2005. *Progress in Geophysics*, 24(3):859-865.
- Zhu Xinhui, Sun Fuping, Wang Ren. (2010). Development and comparison of current plate motion. *Journal of Geomatics Science and Technology*, 27(3): 184-188
- Zhu Xinhui, Sun Fuping. (2014). Establishment methods of modern crustal motion reference datum. Beijing: Sino Maps Press.

Zhu Xinhui, Yang Li, Sun Fuping, Wang Ren. (2014). Study on Reference Datum of Global Vertical Crustal Motion by SLR Techniques. *Acta Geodaetica et Cartographica Sinica*, 43(3): 240-247.

## Research progress in Earth Gravity

Heping Sun<sup>1, 2</sup>, Minzhang Hu<sup>3</sup>, Ziwei Liu<sup>3</sup>, Yiqing Zhu<sup>4</sup>, Shi Chen<sup>5</sup>, Miaomiao Zhang<sup>1</sup>, Hang Li<sup>1</sup>, Xiang Lei<sup>1</sup>, Jiangcun Zhou<sup>1</sup>, Xiaoming Cui<sup>1</sup>, Jianqiao Xu<sup>1</sup>, Xiaodong Chen<sup>1</sup>, Qianqian He<sup>6</sup>, Mingli Deng<sup>1</sup>, Linhai Wang<sup>5,7</sup>, Hongyan Lu<sup>5,7</sup>, Weimin Xu<sup>5,7</sup>, Jinling Yang<sup>8</sup>, Qiuyue Zheng<sup>9</sup>, Zhaohui Chen<sup>10</sup>, Lulu Jia<sup>5,7</sup>, Longwei Xiang<sup>11</sup>, Wen Shi<sup>5,7</sup>, Jiancheng Han<sup>5,7</sup>, Honglei Li<sup>5,7</sup>, Bei Zhang<sup>5,7</sup>, Yongbo Li<sup>5,7</sup>, Jiancang Zhuang<sup>12</sup>, Qianqian Li<sup>1</sup>, Lin Wu<sup>1</sup>, Lifeng Bao<sup>1,2</sup>

<sup>1</sup> Innovation Academy for Precision Measurement Science and Technology, Chinese Academy of Sciences

<sup>2</sup> University of Chinese Academy of Sciences

<sup>3</sup> Institute of Seismology, China Earthquake Administration

<sup>4</sup> Second Monitoring Center, China Earthquake Administration

<sup>5</sup> Institute of Geophysics, China Earthquake Administration

<sup>6</sup> East China University of Technology

<sup>7</sup> Beijing Baijiatuan Earth Sciences National Observation and Research Station

<sup>8</sup> Fujian Earthquake Agency

<sup>9</sup> Yunnan Earthquake Agency

<sup>10</sup> The First Monitoring and Application Center, China Earthquake Administration

<sup>11</sup> School of Geosciences, Yangtze University

<sup>12</sup> The Institute of Statistical Mathematics, Research Organization of Information and Systems, Tokyo, Japan

Gravity field is the most basic physical field generated by the material properties of the earth system. It reflects the spatial distribution, movement and change of materials determined by the interaction and dynamic process inside the Earth. Measuring gravity field is one of the three methods currently used to explore the internal structure of the Earth, including seismology and geomagnetism, and the gravity field provides a 'mirror' reflecting the internal structure of the Earth. Over the years, a variety of technical means have been used to detect the Earth's gravity field, including gravimeter, superconducting gravimeter, sea and air gravimeter, satellite gravity, satellite altimetry and so on, and have obtained a large number of gravity data, supporting numerous studies on the global change, resource detection, geological structure movement, water resources change and other related fields of research. Here is part of the progress in Earth gravity obtained by Chinese geodesy scientists from 2019 to 2023 from the following aspects, including

- (1) Continuous Gravity Network in Chinese Mainland
- (2) Application of Superconducting gravity measurement
- (3) Network adjustment for continental-scale gravity survey campaign and data quality control
- (4) Regional time-variable gravity field and its application
- (5) Research Progress on Novel Technologies for Gravity Inversion
- (6) Research Progress on marine gravity field determination
- (7) Application research on marine gravity field

## 1 Continuous Gravity Network in Chinese Mainland

Relative gravity measurement is an important technical means to study and explore global and regional geodynamic problems and the deep internal structure of the Earth. After decades of construction, China has built a comprehensive monitoring network of multi-source observation technology covering vast territory through major scientific projects according to the “Crustal Movement Observation Network of China” (CMONOC), the “China Digital Seismological Observation”, and the “China Seismic Background Field Detection Project”. The network comprehensively monitors crustal movement and the gravity field, atmosphere, ocean, and near-Earth space in the Chinese mainland and its adjacent area. to assist in earthquake prediction, national surveying and mapping, geoscience research, geodetic application and disaster weather prediction.

At present, China has established a continuous gravity network consisting of more than 80 stations that run various gravimeters including GWR superconducting gravimeter (SG), PET/gPhone, DZW, GS15 and TRG-1 types. The station distribution of more than 60 gPhone gravimeters and 7 SGs is listed in Figure 1 (Sun et al., 2022). As the gravity observation technology with the highest precision at present, China has invested huge efforts in the construction of SG network. Since 1985, when China's first SG was installed in the Institute of Geodesy and Geophysics in Wuhan, China has successively established seven SG stations until now. In 1997, Wuhan SG Station participated in the Global Geodynamics Program (GGP) implemented by Deep Earth Interior Committee of the International Union of Geodesy and Geophysics (IUGG) and the International Earth Tide Center (ICET) and the Asia-Pacific Space Geodynamics Program (APSG). Since then, Wuhan SG Station has been incorporated into the CMONOC and upgraded, and Lhasa and Lijiang SG stations have been successively established. At present, three SGs in Chinese Mainland including Wuhan, Lhasa, and Lijiang have participated in the International Geodynamics and Earth Tide Service (IGETS) implemented by the International Association of Geodesy (IAG) in 2016, and contributed to global geodynamics research joint with more than 40 SG stations around the world. In addition, the China SG Network also includes the instruments deployed in Wuhan, Lijiang and Beijing respectively by the China Earthquake Administration, Wuhan University and National Institute of Metrology. A series of subsequent SG stations are also under construction, which will provide more support for the research of time-varying gravity fields in the Chinese Mainland and global geodynamics in the future.

Since its establishment, continuous gravity network in in Chinese mainland has maintained a continuous and stable operation for a long time. It has accumulated a wealth of observation data and has played a very important role in exploring geodynamics and the internal structure of the Earth.



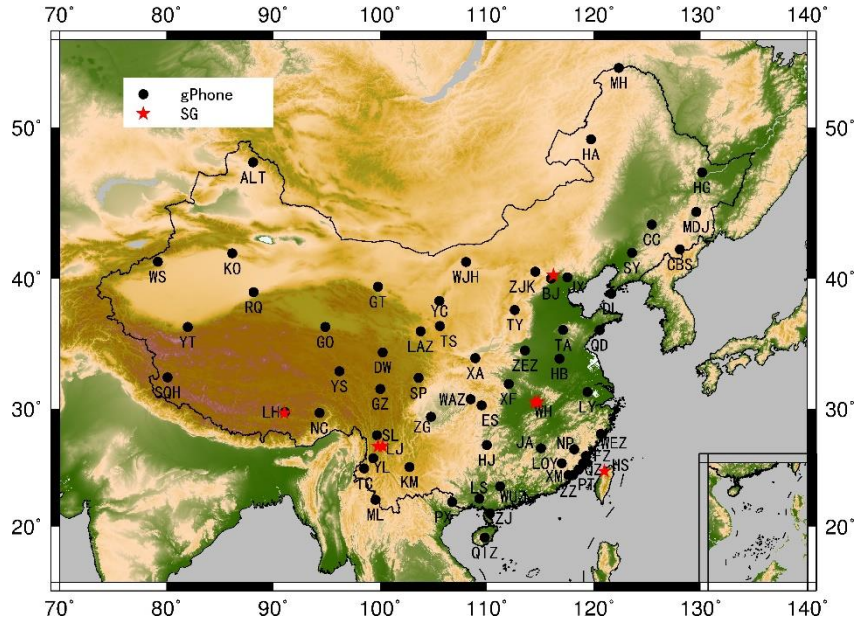


Figure 1. The distribution of 60 gPhone gravimeters and 7 Superconducting gravimeters (SGs: Wuhan (2), Lijiang (2), Lhasa (1), Beijing (1) and Hsinchu (1)) over China's mainland. gPhone stations are represented by the black solid circles while SG stations are represented by the red solid stars (Sun et al., 2022).

## 2 Application of Superconducting gravity measurement

### Application on Earth background noise

Based on the SG and gPhone gravity observations of the Crustal Movement Observation Network of China (CMONOC), the Innovation Academy for Precision Measurement Science and Technology (APM), Chinese Academy of Sciences, has carried out the application research of gravity technique in the study of Earth background noise. Earth background noise is some random waveform generated by non-seismic excitation sources recorded on the seismogram during seismically quiet periods. High-precision gravity technology is an effective method to detect weak signals from the Earth, so it has important application value in the study of Earth background noise.

The weak signal detection performance of gravimeter is closely related to the instrument noise level, which is determined by the observation performance of the instrument itself and the observation environment around the station. APM systematically evaluated noise levels of three IGETS SGs (OSG-065, OSG-057 and OSG-066) in Wuhan, Lhasa and Lijiang and 30 gPhone gravimeters covering mainland China belonging to the CMONOC, and the results are shown in Figure 2. Noise levels in the seismic and sub-seismic frequency bands were analyzed according to the power spectral density of the quietest period during seismically quiet periods (Figure 2). Compared with noise levels of other stations in the global SG network IGETS, the three SG stations in China all showed low noise and good observation quality in the seismic and sub-seismic frequency bands (Sun et al., 2019a; Li et al., 2020). Noise levels of 30 gPhone stations in mainland China were evaluated, and the results show that seismic noise magnitude (SNM) for most stations is in the range of 2~3, and attributed to complicated oceanic effects and active tectonic movement, noisier stations are mainly distributed along the coast and in the southeast of the Tibetan Plateau. This study also presents the Chinese low noise model (CLNM),

which represents the best working conditions of gPhone in mainland China.

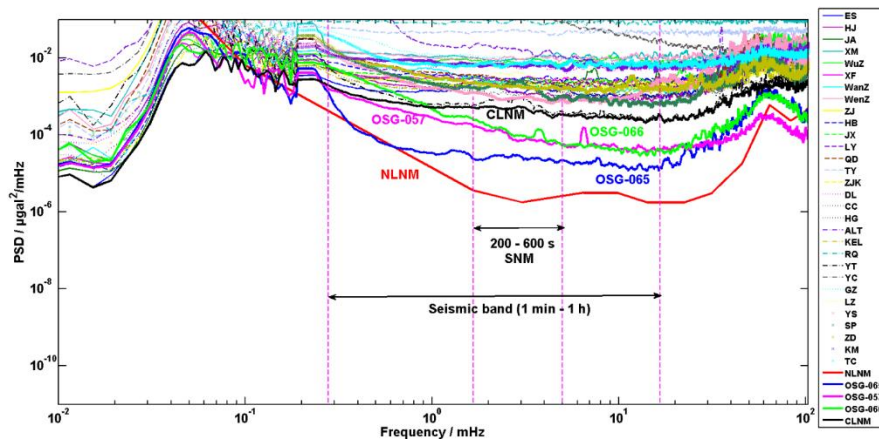


Figure 2. Power spectral densities of the quietest period for the 30 gPhone stations in the CMONOC network and three SG stations in the IGETS network. The black line (CLNM: Chinese Low Noise Model) is the lower envelope of the 30 gPhone stations, obtained similarly to the low noise model NLNM (red line) given by Peterson (1993). Figure 2 is quoted from Sun et al. (2022).

On this basis, we used SG stations of the global SG network IGETS to carry out the study of the Earth Hum signal, which is a very important type of the Earth background noise, including the long-period surface wave and background free oscillation signals that persist in the Earth even during seismically quiet periods. Using Lhasa, Canberra (Australia) and Syowa (Antarctica) stations, we extracted the background free oscillations from averaged power spectra between 0.3 and 5 mHz during seismically quiet periods. The spectral peaks of the background free oscillations are most clear at Canberra station, then at Lhasa station and finally at Syowa station which is very close to the coast and thus heavily affected by the ocean with high noise level. The excitation mechanism of background free oscillations has been controversial, with some early studies supporting the hypothesis of atmospheric excitation, but most later studies favoring the coupling between ocean infragravity waves and seafloor topography. Further analysis by the APM research team through four stations with low noise levels in Canberra (Australia), Bad Homburg (Germany), Kamioka (Japan) and Wuhan (China) showed that the excitation mechanism of background free oscillations below 5 mHz are associated with atmospheric and oceanic perturbations. In contrast to previous studies, the study found that the oceanic disturbance could play different roles in different periods (Sun et al., 2019a).

In the past two decades, the technique of surface wave signal extraction by seismic noise cross-correlation has been widely used in the study of crust and upper mantle structure. Broadband seismometer has the limitation of extracting long-period surface wave signals, so there are few studies on the deep interior structure of the Earth using this technique. In contrast, SG has high sensitivity, stability and observation accuracy, and can effectively record most kinds of seismic wave signals, which has incomparable advantages in the study of long-period seismology. The APM research team has selected the long-term observation data from stations of Canberra (CB), Black Forest (BF) and Sutherland (SU) from IGETS network. The three stations are also equipped with STS-1 seismometers. Long-period surface waves (2-7.5mHz, i.e. 133.3-500s) are successfully extracted by the noise auto-correlation method. The reliability of the results from SGs are verified by comparing with seismometers. It can be seen that both

the SG and the STS-1 seismometer can clearly record the surface waves propagating around the Earth for one circle (R1+R2) and two circles (R3+R4). The results of this study can be extended to the two-station noise cross-correlation, which provides a new idea for the study of the deep structure and dynamics of the Earth by combining gravitational and seismic techniques (Li et al., 2020).

**Application on Earth Tide and Geodynamics**

The long-term observations of the continuous gravity network provide an important basis for studying the response characteristics of Earth tide and geodynamic phenomena in Chinese mainland. This report mainly introduces our research on the regional characteristics of the tidal response in the Qinghai-Tibet Plateau and the time-varying characteristics of the liquid core resonance in the diurnal tides based on the SG observations from IGETS network.

**The tidal response in the Qinghai-Tibet Plateau**

The SG stations in Wuhan and Lijiang are almost at the same latitude as Lhasa, thus their Earth tide observation are almost equally affected by rotation and ellipticity. This provides excellent conditions for studying the impact of special tectonic environment on regional tidal deformation in the Qinghai-Tibet Plateau and its adjacent areas. According to long term observation, APM has established high-precision regional gravity tide datum in the three stations, and carried out detailed research on the oceanic tide and atmospheric loading effect in the station area (Sun et al., 2019; Liang et al., 2020). The scale factors of three SGs were all evaluated with a strategy of co-site comparison between the SGs and the FG-5 absolute gravimeter. We carried out a comparison analysis using two-year continuous gravity measurements recorded by the three stations (Figure 3). The tidal parameters show that no significant differences existed in the amplitude factors measured in Lhasa and Lijiang, but a remarkable difference was found when compared with the factors measured in Wuhan. The mean gravimetric amplitude factors of waves O1, K1, and M2 were about 0.27, 0.34, and 0.42% larger, respectively, than those measured in Wuhan (Sun et al., 2019b). The tidal gravity anomaly was about 0.34%, which we regarded as a local phenomenon unique to the Tibetan Plateau. In the Qinghai Tibet Plateau, the biggest regional disturbance comes from changes in the Plateau glaciers. However, glacier melting itself and its accompanying "crustal rebound" is a long-term process, which has little impact on the Earth's tidal deformation. The relatively large difference between the gravity tide observations and the theoretical model at Lhasa and Lijiang stations possibly comes from the interference of regional tectonic anomalies and active tectonic movement (Sun et al., 2019b; Sun et al., 2022).

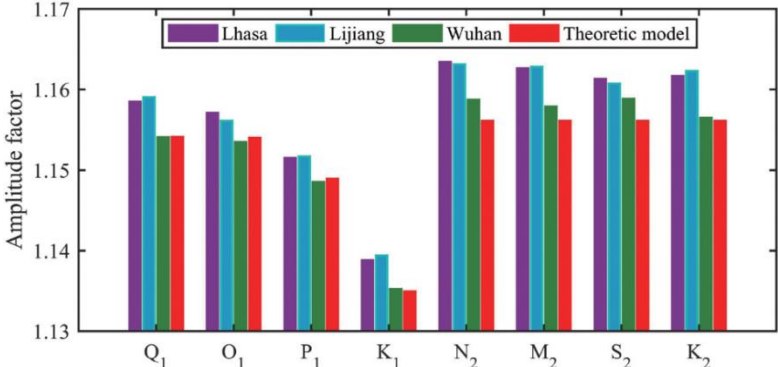


Figure 3. Comparison of the amplitude factors of diurnal and semidiurnal tidal waves observed in Lhasa, Lijiang, and Wuhan SG stations and the theoretical values from Mathews’s (2001) model (Sun et al., 2019b).

### **The liquid core resonance in the diurnal Earth tides**

The deep internal structure and internal dynamics of the Earth has always been the frontier hotspot in the field of geoscience research. The nearly diurnal free wobble (NDFW) of liquid core, also called free core nutation (FCN) in celestial frame, is a dynamic process originating from the core-mantle boundary. It involves a variety of geophysical information of the core-mantle couplings. The NDFW will lead to an obvious resonance enhancement in observations of diurnal tidal waves with near frequencies. The accurate separation of the tidal waves is an important means to detect this signal in the deep interior of the Earth. Previous research on NDFW parameters was limited to the low signal-to-noise ratio of  $\psi_1$  tidal wave which is most affected by the liquid core resonance. To explore whether NDFW has time-varying characteristics, we studied the reliability of liquid core resonance observed in different diurnal tidal waves under the current observation accuracy of SG. It is found that although K1 tidal wave is less affected by resonance compared with  $\psi_1$  tidal wave, it has higher observation signal-to-noise ratio due to its larger amplitude, which is more conducive to detecting the variation of liquid core resonance effect. We determined the accuracy limit of K1 tidal wave that can effectively detect the resonance change. On this basis, we analyzed the long-term observations from 20 SG stations of IGETS network and found a consistent temporal variation characteristics of liquid core resonance in the K1 wave tidal parameters from multiple stations that meet the accuracy limit. This variation was verified further by the results of VLBI observations. It is also found that the mechanism of this resonance change is closely related to the sudden change of geomagnetic field caused by the hydrodynamic phenomena of liquid core (Cui et al., 2020; Sun et al., 2022).

### **Application on regional gravity measurement**

APM is committed to the application of gravity observation technology in regional geophysical research. This report mainly introduces the application of superconductive gravity technique in the quantitative separation of the local vadose zone water storage changes, the application of hybrid gravimetry in the surface subsidence of Wuhan city and the observation experiment of deep underground (-848m) gravity field.

#### **Quantitative separation of the local vadose zone water storage changes**

The vadose zone is the porous medium between the ground surface and the groundwater level in the first unconfined aquifer. Quantitative study of vadose zone water storage changes (WSCVZ) is still a difficult problem. We proposed a new method for the quantitative separation of the local WSCVZ based on a single superconducting gravimeter (SG). This new method was verified through examples using the superconducting gravity observation data from Wuhan SG Station (May 2008 to April 2010) and groundwater level observation data. The quantitative separation results of the WSCVZ at Wuhan SG Station were compared with those obtained using the local hydrological modeling method and using the global GLDAS/Noah model. The results show good consistency, which indicates that the quantitative separation of the local WSCVZ can be achieved using the superconductive gravity technique and ground water level observations.

#### **Application of hybrid gravimetry in the surface subsidence**

Urban surface subsidence caused by groundwater exploitation, urban construction and other reasons is a potential hazard to public safety. We carried out experimental study of the surface subsidence in the city using the hybrid gravity measurement. We set up a gravity



observation network in the area with relatively large surface subsidence observed by InSAR in Wuhan (Figure 4, left). Seven campaign mobile gravity and GPS measurements were carried out between 2016 and 2017. The absolute gravity observation is used to control the long-term gravity change of the whole observation area, and the GLDAS land water model data is used to calculate and eliminate the overall land water gravity impact of the observation area. The seventh campaign result of gravity change relative to the first is shown in Figure 4 (right). Compared with the vertical surface deformation observed by D-InSAR, the results show that the gravity observation technology can obtain high-precision regional gravity changes in the city, and the mobile gravity can clearly observe the urban surface subsidence. Compared with InSAR observation technology, the gravity changes caused by different factors such as surface subsidence, water volume of the Yangtze River and groundwater are analyzed in detail. Some regional gravity changes have good correlation with the seasonal changes of the Yangtze River water. The research results show that the combination of multi-source observation technology is an effective way to explain the mechanism of urban surface subsidence (Chen et al., 2020).

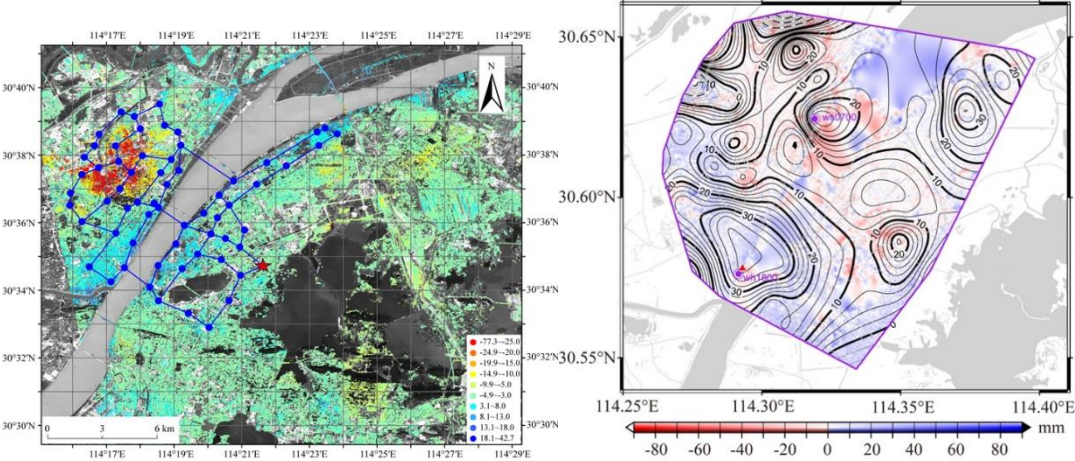


Figure 4. Left: Surface subsidence observed by InSAR and the mobile gravity observing network , Blue dots are gravity points. Red ★ point is the absolute gravity control point. Right: Comparison of the gravity change from the 1st campaign to the 7th covered on the vertical displacement observed by D-InSAR (Chen et al., 2020)

**Gravity Observation experiment in Huainan 848 m deep underground**

The deep underground environment is characterized by low background noise, low cosmic ray intensity, and low background radiation, and is an excellent platform for carrying out many major frontiers scientific experiment. The international deep underground laboratory has developed rapidly in recent years. APM and several research institutions in China have jointly carried out some preliminary observation experiments by relying on the space resources of underground coal mine tunnels in Huainan to build a deep multi-physical field observation and experiment platform. The experimental site, located at the junction of the southern source of the North China Craton and the lower Yangtze, is in Panyi Mine of Huainan Mining Group, about 15 km away from the urban area of Huainan (Figure 5\_left). The deep space consists of an underground horizontal layer with an altitude of - 848 m and several vertical shafts as shown in Figure 5 (right). This experiment was conducted in the horizontal layer of - 848 m. The LaCoste-Lomberg ET and Burris spring gravimeter were respectively deployed on the surface and in the tunnel of horizontal layer on January 18, 2020. Comparison of the original gravity recordings between the surface and the -848 m tunnel showed that the continuous gravity

observations are reliable, and the time-variant trends are consistent. The gravity noise underground and at the surface are analyzed with the power spectrum estimated from the quietest periods. The noise deep underground at the frequency band of 2–10 Hz is stronger than that at the surface, while the low-frequency band reverses and is more than 2 orders of magnitude lower than that at the surface. It fully demonstrates the low noise of underground environment at the deep geophysical experimental field in Huainan (Zhang et al., 2021; Wang et al., 2023).

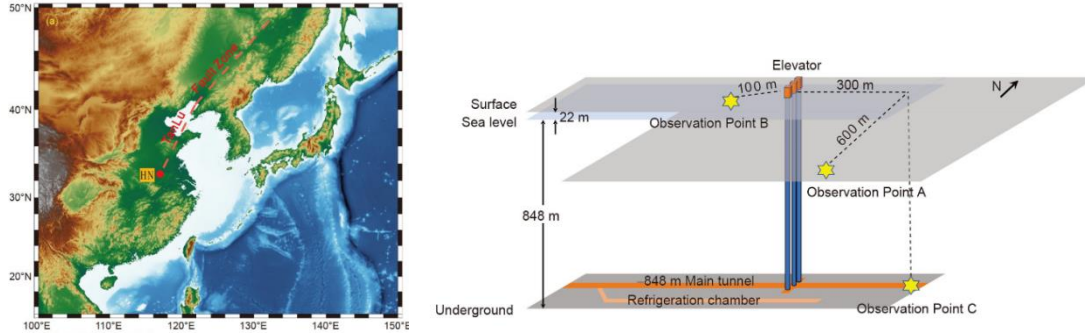


Figure 5. Huainan Deep Underground Lab. Left: the location of the lab; Right: layout of the observation system in the lab (Wang et al., 2023)

### 3 Network adjustment for continental-scale gravity survey campaign and data quality control

Spatiotemporal gravity signals from terrestrial hybrid repeated gravity observation have contributed to the understanding of the surface and subsurface mass redistribution, which reflects the crustal deformation and density changes. However, the disturbances of instrument performance and observation field source noise cause large uncertainty in the time-varying gravity signal. To quantify these uncertainties, based on the Bayesian principle and the Akaike's Bayesian information criterion (ABIC), Professor Chen's team has developed several advanced algorithms and models for the network adjustment, data quality control and multi-period gravity data assimilation. These methods can effectively determine the uncertainty in gravity observation data and obtain high-precision time-varying gravity signals.

To solve the problem of nonlinear drift of gravimeters in regional gravity measurements, Chen et al. (2019) proposed a new terrestrial scale gravity network adjustment method by means of objective Bayesian statistical inference. This method assumes that the variation of the drift rate is smooth function of lapsed time. We employed the ABIC to estimate these hyper-parameters. The drift rate change characteristics of each gravimeter can be obtained while estimating the gravity value, as shown in Figure 6. Compared with the linear drift model (Figure 6(b)), the residuals obtained by the Bayesian method using the nonlinear drift model exhibit the random characteristics of white noise (Figure 6(c)). On this basis, Wang et al. (2022) improved the Bayesian gravity adjustment method, using absolute and relative gravity observation data to estimate the scale factor of the relative gravimeter. As shown in Figure 6(d), compared with using the input scale factor, there is no correlation between the gravity difference and the mutual difference obtained by using the estimated scale factor. The improved method can effectively

reduce the residual and is conducive to improving the accuracy of the gravity value. Further, a data quality assessment process of residual analysis, correlation analysis, and cross-validation of absolute gravity measurement has been formed (Zheng et al., 2022).

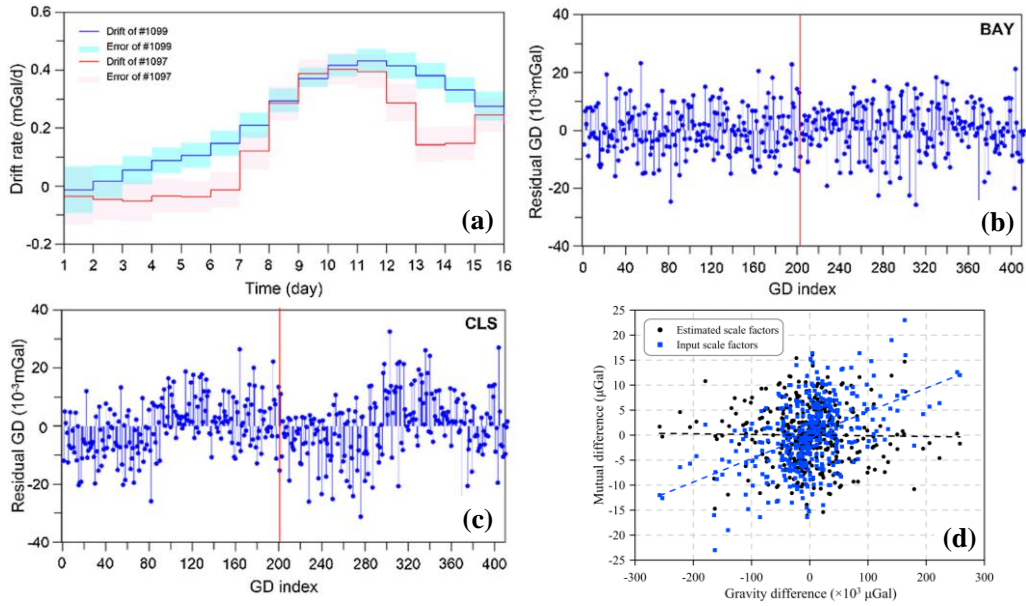


Figure 6. (a) The drift rate and uncertainty of two relative gravimeters estimated by Bayesian gravity adjustment. (b) and (c) the residuals obtained by Bayesian method and Classical adjustment respectively. (d) Comparison of the mutual difference between the estimated scale factors and the input scale factors.

The high-frequency features of the spatiotemporal gravity signals are related to near-surface field sources. Therefore, the low-frequency gravity changes potentially related to the deep source processes need to be extracted. Yang et al. (2021) and Chen et al. (2022) adopted a Bayesian apparent density source inversion (BADI) method with spatiotemporal smoothness constraints to effectively suppress the high-frequency fluctuations in the spatiotemporal gravity signals. The BADI method employs an equivalent apparent density model to build up a relationship between the deep field source body and the surface observed gravity changes. Then, the model-assimilated gravity changes can be derived from this apparent density model. We apply the method to the gravity observation data from 2014 to 2017 before the 2017 Jiuzhaigou MS7.0 earthquake. As shown in Figure 7(a, c, e), there are the high-frequency components in the gravity changes without assimilation. The model-assimilated values gravity values (b, d, f) have a consistent and stable changing trend.

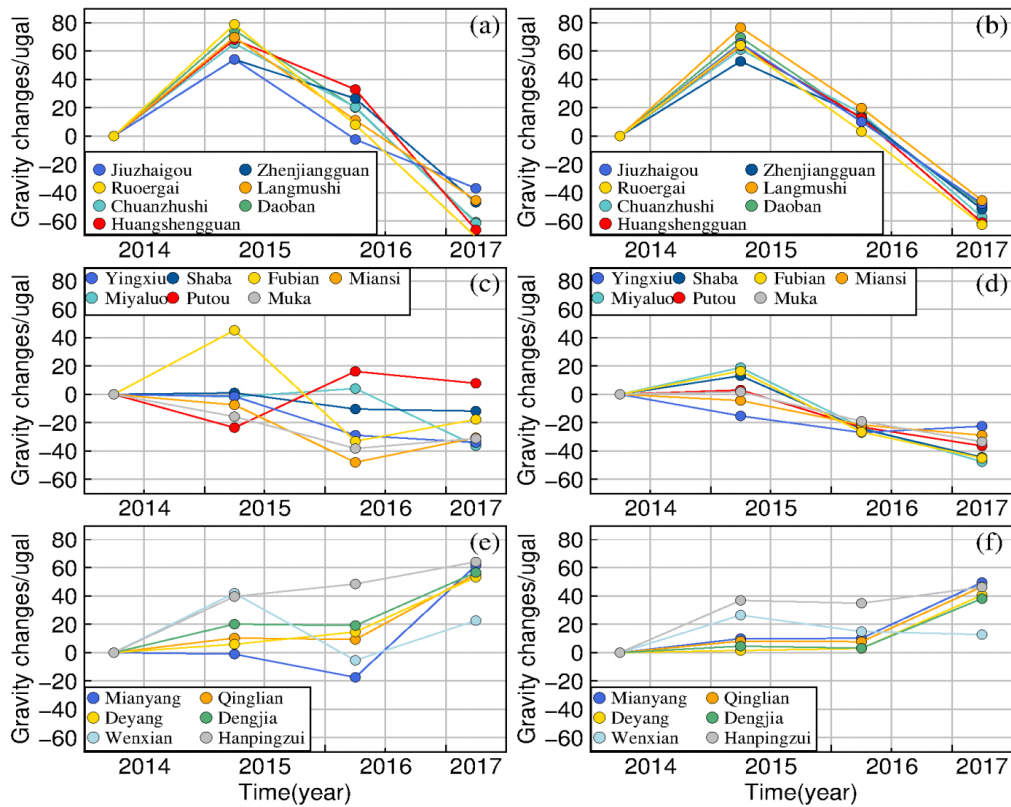


Figure 7. The time series of gravity value before and after processing by the Bayesian apparent density inversion method

#### 4 Regional time-variable gravity field and its application

Measuring the small variations in the Earth’s gravity field over time is an effective means to investigate issues related to mass changes, such as land subsidence, groundwater storage changes, and earthquake-induced mass migration. Terrestrial (ground-based) time-variable gravity measurement allows the detection and analysis of the regional and near-surface mass movement and migration because of its high accuracy and sensitivity to the sources of mass change in the Earth’s crust. Since 2000, the quality of terrestrial time-variable gravity measurements has been greatly improved because of the rapid development of the geophysical infrastructure in the Chinese mainland, represented by the “Crustal Movement Observation Network of China” project. These high-quality gravity measurements provide valuable information for time-variable gravity field modeling in China.



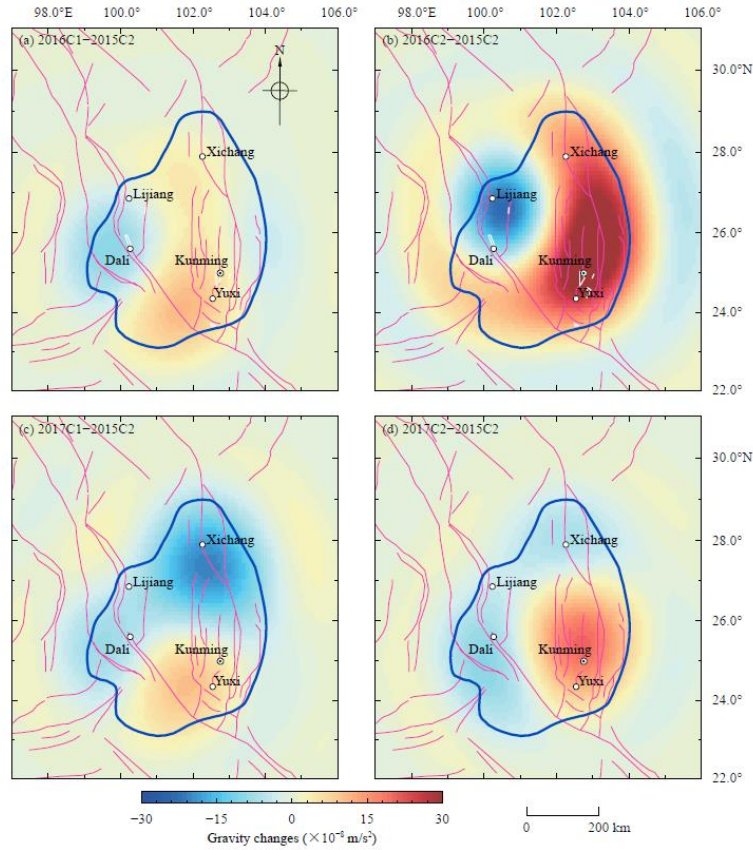


Figure 8. The spatial distribution of the degree 120 gravity field variations in the Sichuan-Yunnan region between 2016 and 2017 (with respect to 2015C2) determined using Slepian functions. The blue line indicates the boundary of the study area, and the magenta line indicates active faults.

Based on Slepian basis functions and terrestrial gravity measurements in the Sichuan-Yunnan region from 2015 to 2017, Han et al. (2021a) determined high-resolution (degree 120) time-variable gravity field (TVGF) solutions over this region (Figure 8). Figure 8a and Figure 8b show the gravity variations for 2016C1–2015C2 and 2016C2–2015C2 (C1 and C2 represent observations in the first half and second half of the year, respectively), while Figure 8c and Figure 8d show the cumulative gravity variations for 2017C1–2015C2 and 2017C2–2015C2, respectively. The spatial pattern in Figure 8b is correlated with the near-south tectonic structures along the Xichang-Yuxi line and the northwest-oriented Red River fault. This correlation indicates that the model results are tectonically sensitive. The gravity variations in Figure 8c shows that the increase around Xichang falls back, but the gravity increases around Kunming and Yuxi still exist. The results in Figure 8d show that the gravity increase around Xichang disappear while the gravity increases around Kunming and Yuxi continue to a larger extent. The degree 120 gravity solution in the Sichuan-Yunnan region will supplement the existing public geophysical models for the China Seismic Experimental Site, serving as a high-quality data product for regional crustal structure interpretation and seismic precursor identification.

Using a similar approach, Han et al. (2021b) determined high-resolution (degree 120) TVGF solutions in North China using Slepian functions and terrestrial gravity measurements from 2011 to 2013. Their comparison shows that the degree 120 results provide gravity variations with significantly higher spatial resolution and stronger signal strength compared with the GRACE-derived degree 60 results in the same region. The findings of this work could

benefit regional gravity field modeling, and the derived high-resolution TVGF solution could support water storage monitoring, tectonic activity analysis, and seismic risk assessment in North China.

The preparation and development of large earthquakes may cause transient changes of regional gravity field. High-precision repeated absolute gravimetry can obtain time variable gravity signals of mass changes inside the crust, providing a unique perspective on seismotectonic feature of strong continental earthquakes. For example, before the 2008 Mw 7.9 Wenchuan earthquake, a significant absolute gravity increase of several  $\mu\text{Gal}$  per year was observed near its epicenter (Zhang et al., 2020). However, due to the scarcity of absolute gravity data (lack of sufficient measurement stations), the mechanism behind this signal remains unknown.

Since 2010, the Crustal Movement Observation Network of China (CMONOC), a national network of crustal deformation monitoring originated from 1998, has expanded 25 absolute gravity stations to 101 (Han et al., 2020). These stations have been observed repeatedly every two or three years, greatly enriching high-precision absolute gravity data for earthquake research.

Based on absolute gravity observations by CMONOC for more than a decade in the northeastern Tibetan Plateau, an obvious and coincident gravity increase about 5 years before the 2022 Ms 6.9 Menyuan earthquake is observed at four stations around the epicenter, with the rate up to  $3.94 \mu\text{Gal}/\text{yr}$  at Minqin station (Jia et al., 2023). The observed gravity changes could not be reasonably explained by the land water storage change nor crustal vertical deformation and thus might be related to the processes in the crust. A disc-shaped equivalent source region is then modeled using MCMC method, based on the residual gravity rates. The disc has the radius of  $174.9 \pm 31.7$  km, thickness of  $1.9 \pm 0.6$  km, and depth of  $10.2 \pm 1.2$  km, with center ( $100.45^\circ\text{E}$ ,  $39.18^\circ\text{N}$ ) located at about 172 km northwest of the epicenter of the Menyuan earthquake.

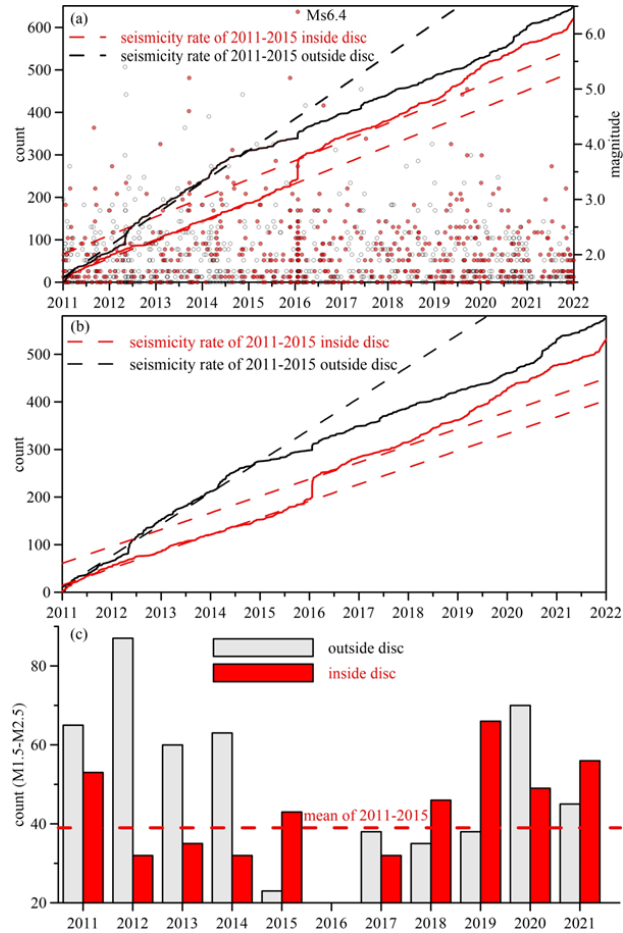


Figure 9. Seismicity in the modeled disc source region. (a) Cumulative curves for events with  $M \geq 1.5$ . The dots denote magnitude of the events. (b) Cumulative curves for events with magnitude from 1.5 to 2.5. The red and black solid curves in (a) and (b) represent the seismicity cumulative curves inside and outside the modeled disc respectively. To align with the cumulative count after the 2016 Ms 6.4 Menyuan earthquake, the top red dashed lines in (a) and (b) are shifted, keeping the same slopes as the bottom red lines. (c) Number of earthquakes per year with magnitude from 1.5 to 2.5, the red dashed line shows mean value from 2011 to 2015 inside disc.

To investigate the mechanism of gravity changes in the disc source region, the historical earthquake data in this area are analyzed. After the 2016 Ms 6.4 Menyuan earthquake (close to epicenter of the 2022 earthquake), the seismic frequency in 2017–2021 is higher than that in 2011–2015 in the source region (Figure 9a). The earthquake frequency increases gradually especially for the events of magnitude from 1.5 to 2.5 (Figure 9b). This is similar to the behavior of deep fluids migration. The number of earthquakes per year in the source region has increased yearly since 2017 (Figure 9c). Furthermore, the spatiotemporal distribution of epicenters inside disc is consistent with the fluid diffusion model, indicating that gravity increase could be related to the redistribution of deep fluid mass. In contrast, the seismicity is decreased rather than increased outside the source region. On the other hand, there are many low-velocity zones in upper and middle crust around the source region, facilitating fluid mass transport.

In general, based on the analysis of gravity change, near-surface processes, regional crustal structure, and seismic activity, multiple lines of evidence consistently show that there are deep fluids migrations before the 2022 Menyuan earthquake. Upwelling and migration of deep fluids (usually accompanied by regional gravity increases according to finite element modeling (Liu et al., 2022)) promote rock rupture through reducing the effective normal stress and the friction

coefficient. Then, this rupture leads to seismicity increases and potential triggering a large earthquake. Therefore, the observed gravity increases before the Menyuan earthquake could be related to fluid mass migration in the broad source region. Based on this explanation, a conceptual model for the fluid-driven seismicity and the simplified disc-shaped source is given in Figure 10. These results suggest that with the increasing availability of absolute gravimeters and the abundance of data, high-precision time-varying gravity observation may provide a geophysical method for monitoring regional crustal fluid environment and then determining the risk area with potential strong earthquakes.

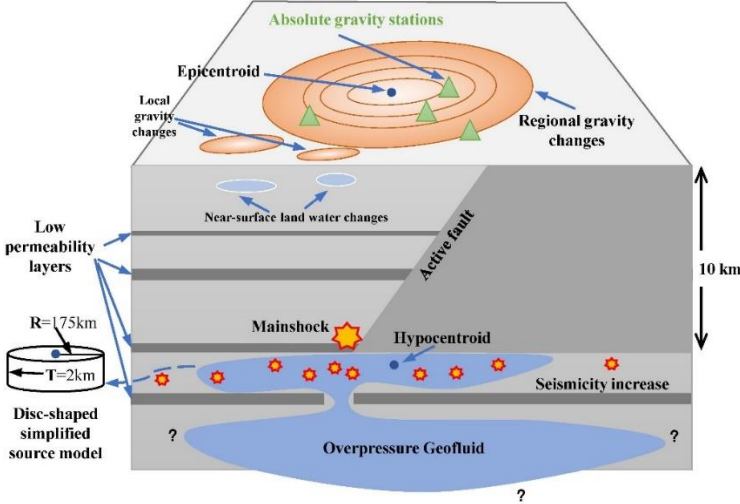


Figure 10. Sketch of deep mass transfer process and the disc-shaped source model of an earthquake. The hypocentroid is the center of mass of modeled disc and the epicentroid is surface projection of the hypocentroid.

### 5 Research Progress on Novel Technologies for Gravity Inversion

Gravity inversion, as one of the effective methods for studying the internal structure of the Earth, has the advantages of sensitivity to changes in subsurface material density, strong horizontal resolution, and low cost. However, it is also some drawbacks, such as low vertical resolution and strong non-uniqueness. Achieving high resolution, low non-uniqueness, and high reliability in detecting the Earth's internal structure are the main challenges for gravity inversion technology. The kernel issue for novel gravity inversion approach is how to address these problems by integrating the latest technological means. To address this issue, Chen Shi and his research team at the Institute of Geophysics of the China Earthquake Administration have developed advanced algorithms based on data assimilation and Bayesian uncertainty quantification theory. These algorithms have enabled the construction of finely detailed crustal density models for multiple seismic source regions in the Sichuan-Yunnan area, resulting in an improved level of understanding of these regions' structures.



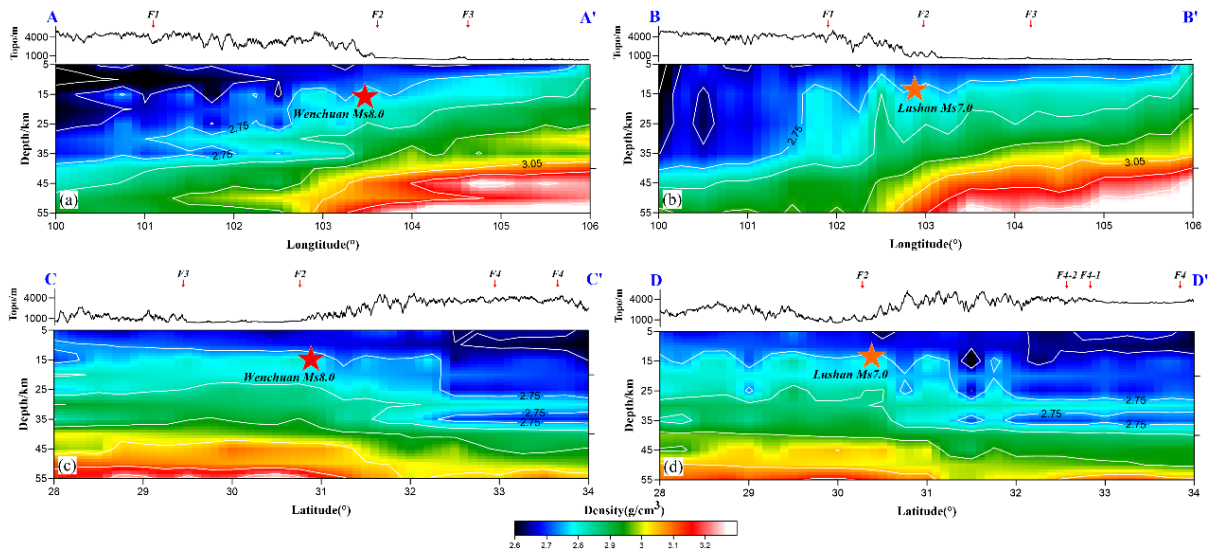


Figure 11. The density structure profiles below the epicenter area of Wenchuan earthquake and Lushan earthquake; (a) 31°N profile; (b) 30.3°N profile; (c) 103.4°E profile; (d) 103°E profile.

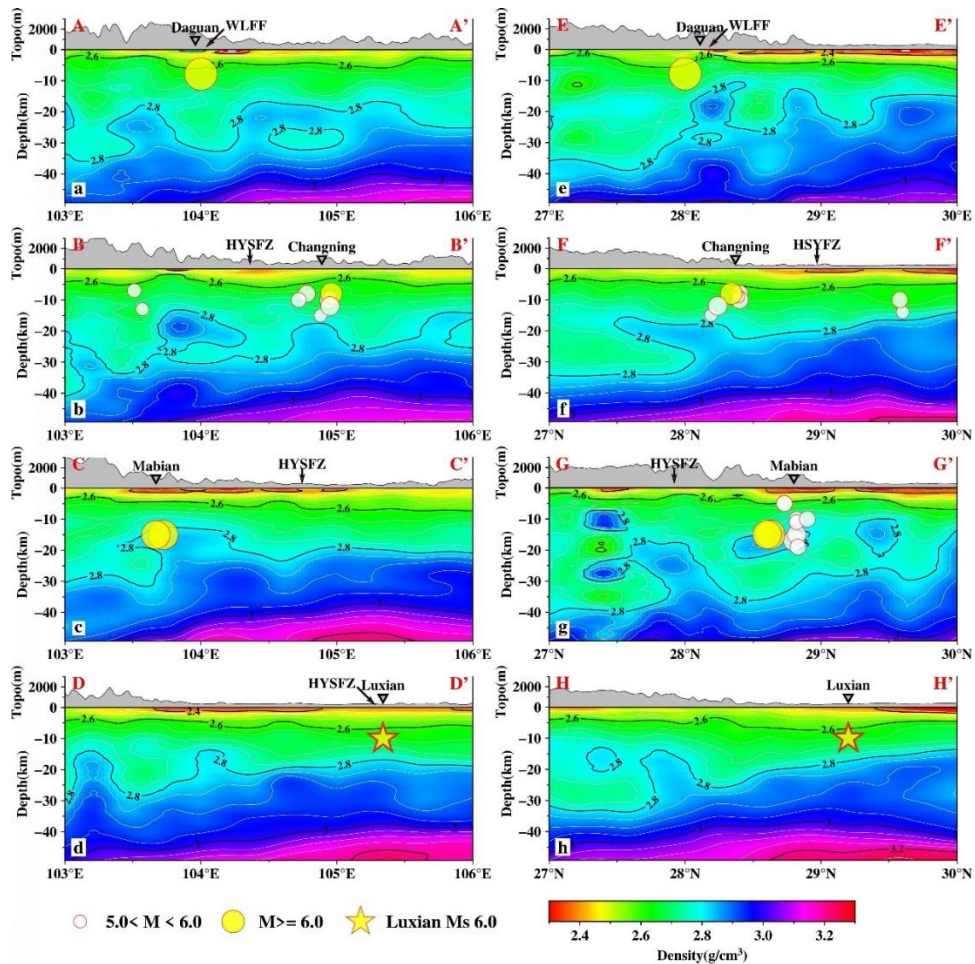


Figure 12. The density structure profiles below the epicenter area of Dagan earthquake, Changning earthquake, Maguan earthquake and Luxian earthquake; HYSFZ: Huaying Mountain Fault Zone; (a) 28.1°N profile; (b) 28.3°N profile; (c) 28.61°N profile; (d) 29.2°N profile; (e) 104°E profile; (f) 104.96°E profile; (g) 103.66°E profile; (h) 105.3°E profile.

Li et al. (2021) used the Bayesian assimilation gravity inversion method to construct the

three-dimensional crustal density model for the strong earthquake source area in the Longmenshan region. This method effectively solves the classic problem of bias in knowledge introduced by single or subjective constraints in traditional gravity inversion algorithms by introducing Bayesian parameter optimization criteria. Figure 11 shows the density structure profiles below the Wenchuan earthquake and Lushan earthquake source areas. The steep variation of the middle and upper crustal density interface below the Wenchuan earthquake and Lushan strong earthquake source areas is significant. Comparing Figure 11a and Figure 11b, the low-density layer of the middle crust below the subduction front of the Wenchuan earthquake fault may be the main cause of the different seismic mechanisms compared with the Lushan earthquake. Li et al. (2022) used the MCMC inversion method to construct the three-dimensional crustal density model for the strong earthquake source area in southern Sichuan. This method ingeniously combines prior knowledge and observation data while quantifying the uncertainty characteristics of parameters. Figure 12 shows the density structure profile below the Daguan earthquake, Changning earthquake, Maguan earthquake, and Luxian earthquake source areas. Comparing Figure 12g, Figure 12h with Figure 12a-f, the deep density structure of the source areas of the Daguan earthquake, Changning earthquake, and Mabian earthquake has strong heterogeneity, showing the physical properties of tectonic earthquakes, while such features are not obvious in the Luxian earthquake. Both above research results can provide basic methods guarantee and effective deep constraints for the study of the crustal structure and physical properties of potential strong earthquake risk sources.

## **6 Research Progress on marine gravity field determination**

### **Marine gravity field recovery from multi-source altimetry data**

Satellite altimetry is the main means to rapidly acquire global high-precision and high-resolution marine gravity field. It mainly obtains sea surface height data by microwave ranging, and uses the theoretical relationship between the external shape of the Earth and the gravity field to calculate the marine gravity field by using the corresponding algorithm. After decades of development, the satellite altimetry technology has developed from radar altimeter to synthetic aperture altimeter and interferometric radar altimeter, the measurement band has developed from Ku to Ka, the sampling rate has developed from 20 Hz to 40 Hz, the observation mode has developed from nadir satellite to wide swath satellite, the acquired data has developed from one-dimensional sea surface height along the orbit to two-dimensional strip sea surface height, the range accuracy has been improved, and the spatial and temporal resolution of the acquired data have been improved too. Currently, the spatial resolution of altimetry-derived marine gravity field can reach  $1' \times 1'$ , and the accuracy reaches 1-2 mGal in the local sea area (Andersen OB, and Knudsen P, 2019; Sandwell et al., 2021). The APM has evaluated the accuracy of the advanced gravity field models DTU13, DTU10, V24.1, and V27.1 published by two major international agencies in the offshore region of the South China Sea using Chinese coastal ship measurements of gravity data (whose distribution is shown in Figure 13), and the results show that the accuracy of the gravity field models in the sea areas, which are less affected by ocean currents, can reach 2-3 mGal (Li et al., 2021).

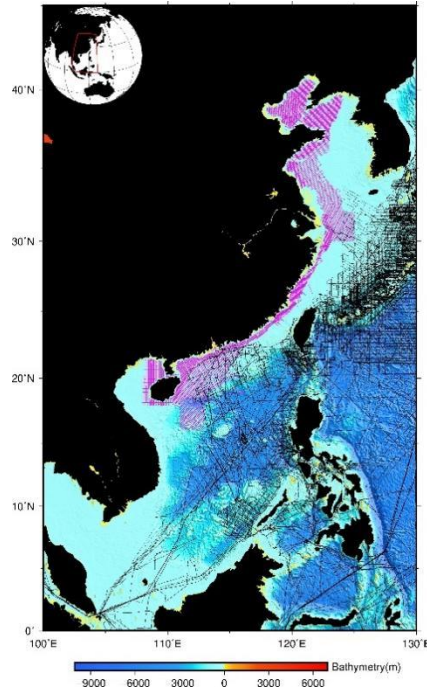


Figure 13. Geographic distribution of shipboard gravity measurements in the coastal region of China. The magenta lines are from the 908 Project, and the black lines are from the NCEI. The map was created by using GMT (<http://gmt.soest.hawaii.edu>). The background bathymetric data is from GEBCO (<https://download.gebco.net/>); its spatial resolution is resampled to  $1' \times 1'$ .

The methods of marine gravity field recovery from satellite altimetry are mainly contain gravity anomaly recovery from the geoid height (inverse Stokes method), and from deflection of the vertical (inverse Vening-Meinesz method, Laplace equation method). In terms of data sources, considering the limitations of single altimetric satellite in spatial coverage and measurement period, combining multi-source and multi-generation altimetric satellite data to recover the marine gravity field is the main method. For a long time, Chinese scholars have conducted a lot of researches on the combined inversion of multi-source and multi-generation altimetry data and the refinement of marine gravity field. Sun et al. (2022) outlined the development history of marine microwave altimetry satellites briefly, focusing on the results of global marine gravity field and global seafloor topography modeling using satellite altimetry, and compared the classic marine gravity fields and seafloor topography models. Zhang et al. (2021) determined the marine gravity fields in four selected regions (Northwest Atlantic, Hawaiian Sea, Mariana Trench region, and Aegean Sea) based on sea surface height (SSH) and sea surface slope (SSS), respectively, using data from the CryoSat-2, Jason-1/2, and SARAL/Altika geodetic missions. The results were evaluated, and showed that the SSH-based method is advantageous in robustly estimating marine gravity anomalies in coastal areas. The SSS-based method has an advantage in the region of moderate ocean depths (2000-4000 m) with seamounts and ridges, but has a significant disadvantage in the case of currents flowing in a north-south direction (e.g., the Western Boundary Current) or topography with north-south oriented trenches. In the deep ocean with flat seafloor topography, both methods have similar accuracy. Based on multiple geodetic missions (GMs) and precise repetition missions such as CryoSat-2, Jason-1/2, SARAL/Altika and HY-2A, Zhu et al. (2021) innovatively used an iterative method to determine the sea surface heights (SSHs) of SARAL/Altika altimetry data

with Ka band, and established the 1'×1' gravity anomaly model SCSGA V1.0. Its accuracy was evaluated using ship-measured gravity data. The result showed that the accuracy of SCSGA V1.0 is comparable to that of international advanced models, which provides high-quality data support for seafloor topographic inversion, seafloor tectonic motion study, and underwater gravity-assisted navigation using marine gravity fields.

### **New altimetry satellite for marine gravity field recovery**

The previous marine gravity field models are mainly from multi-source and multi-generation nadir altimetry satellite measurements. Since most of the altimetry satellites are polar orbiting satellites with large orbital inclination, the accuracy of the east-west component of the vertical deviation is significantly lower than that of the north-south component in most areas, and the time span of multi-source and multi-generation satellite data is affected by the time-varying information of the ocean, which limits the accuracy level of the ocean gravity field. In order to solve the above problems, scholars at home and abroad have proposed innovative altimetric satellite observation systems, such as SWOT (surface water ocean topography) and dual-satellite in tandem mode, aiming to achieve rapid acquisition of global coverage of two-dimensional sea surface height data, solving the high-precision vertical deviation north-south and east-west components simultaneously, so as to improve the resolution and accuracy of marine gravity field (Zhai et al., 2018; Bao and Xu, 2014). The successful launch of the SWOT satellite on December 16, 2022, kicked off the new system of altimetry satellites. Before acquiring the SWOT actual data, domestic and foreign scholars used simulated data to investigate the key techniques of marine gravity field recovery for the new altimetry data and achieved corresponding results. Jin et al. (2022) used the simulated single-period SWOT sea surface height data to calculate the vertical deviations in the South China Sea and parts of the Indian Ocean, and then compared with that calculated by one-year simulated sea surface height measurements from the Jason-1/GM (geodetic mission), Cryosat-2/LRM (low-rate mode), and SARAL/GM nadir altimeter missions. The results showed that the vertical deviation determined by single-period SWOT data is better than that determined by the combined dataset of Jason-1/GM, Cryosat-2/LRM and SARAL/GM data, which can significantly improve the accuracy of the east-west component of the vertical deviation. Yu et al. (2022) created a high-frequency SSH component using multibeam bathymetry data from the northern South China Sea, combined with mean sea level, to simulate SWOT surface height measurements. In addition, the SWOT SSH observation errors were simulated using the SWOT simulator to generate 19 21-day repetitive SWOT SSH observation periods (about 400 days), and two computational methods, the inverse Vening-Meinesz formula and the inverse Stokes integral, were used to calculate the marine gravity field in the South China Sea, and the results showed that the multi-period SWOT observations can provide high-quality marine gravity anomalies.

In terms of new satellite altimetry technology, APM has been conducting long-term research on related theories and key technologies. As early as 2014, APM took the lead in proposing a double-star companion altimetry satellite model, and gave a corresponding satellite orbit design scheme according to the basic requirements of satellite orbit design (Bao and Xu, 2014). Subsequent studies such as the demonstration of the calibration scheme of double-star altimetry and the demonstration of the ocean gravity field inversion scheme were carried out successively, which provided technical support for the new altimetry technology for marine



gravity field inversion.

### **Marine and airborne gravity measurement**

Marine and airborne gravity measurement is currently the main auxiliary method for obtaining the marine gravity field. This method primarily uses a gravimeter (or accelerometer) to measure the gravity acceleration of the sea surface while carried by a ship or aircraft. With high precision, it is suitable for measuring gravity information in wide ocean areas and inshore/reef regions where the precision of satellite altimetry for gravity field inversion is relatively low. The development of marine and airborne gravity measurement technology is closely related to the development of gravimeter equipment. In recent years, the successful development of new marine gravimeters and improvements in marine and airborne gravity data processing technology have led to the vigorous development of marine gravity measurement. Although the independent development of Chinese marine and airborne gravimeters started relatively late, significant achievements have been made in recent years with the investment of manpower and material resources. Currently, the marine and airborne gravimeter named CHZ-II developed by the APM and the SAG series gravimeters developed by the China Aerospace Science and Technology Corporation are gradually becoming practical.

With the development of marine gravity measurement technology, China's military oceanographic surveying and mapping department has carried out regular marine gravity measurement work using marine gravimeters. They have continuously conducted research on theoretical and technical methods for processing marine gravity measurement data, independently developed intelligent collection and processing equipment, constructed a complete and high-precision marine gravity measurement operation technology and equipment system, and formed a systematic and organized production operation capacity. With the development of independent marine gravimeters, domestic institutions have conducted multiple gravity measurement works and gravimeters platform comparison tests. In 2018, a multi-type marine gravity meter ship-to-ship comparison test was carried out in a partial area of the South China Sea on board the Xiangyanghong 6 research vessel (as shown in Figure 14). The marine and airborne gravimeter CHZ-II developed by the APM, together with six other gravimeters, including SAG-2M, SGA-WZ, ZL11, Russian GT-2M (No.39), and American LCR (No.S129), participated in the comparison, and six effective flight paths were obtained. By using methods such as repeat line comparison statistics, cross-point mismatch value statistics, and comparison of results from different gravimeters, the measurement accuracy of the six gravimeters was compared and analyzed. The results showed that all six gravity meters can meet the accuracy requirements of marine gravity measurement. The accuracy of domestic gravimeters is close to that of the GT-2M gravimeter and higher than that of the precision gravity meter LCR (Yuan et al., 2018).



Figure 14. Marine relative gravimeters: a CHZ-II; b ZL11; c SAG-2M; d SGA-WZ; e GT-2M; f LCR (Yuan et al., 2018)

Existing shipborne dynamic measurements are all relative gravity measurements, which measure the changes in gravity values of the moving carrier relative to fixed absolute gravity reference points. The problem of instrument zero drift during relative gravity measurement process affects the final measurement performance, and the lack of unified benchmarks between different measurement routes affects the fusion of shipborne data. The application of absolute gravimeters for dynamic measurement on moving carriers can provide same-site calibration for dynamic relative gravimeters, providing a new solution to the problems. With the development of cold atom interferometry technology, quantum dynamic absolute gravimeters have emerged, providing technical support for ocean dynamic absolute measurements.

In recent years, the APM, Zhejiang University of Technology, and China Shipbuilding Industry Group Co., Ltd. have respectively carried out research and development of quantum absolute gravimeters, track tests, lake tests, ocean mooring tests, and dynamic measurement experiments, solving a series of key technologies for cold atom dynamic absolute gravimeters and keeping up with the pace of foreign research. Among them, Zhejiang University has built a shipborne absolute gravity dynamic measurement system and conducted absolute gravity dynamic measurement experiments in a shipborne mooring state. According to the evaluation, the gravity measurement sensitivity in the shipborne mooring environment is  $16.6 \text{ mGal/Hz}^{-1/2}$ , and the resolution of gravity measurement within 1000 s integration time can reach 0.7 mGal. The stability of the system was evaluated through two weeks of absolute gravity measurement (Cheng Bing et al., 2021). The APM and the Naval University of Engineering jointly built an absolute dynamic gravity measurement system based on a cold atom gravimeter and an inertial stabilization platform, and adopted a combination of cold atom gravimeter and traditional accelerometer measurement methods to conduct shipborne dynamic measurement experiments. According to the evaluation, the internal agreement accuracy of the four repeated measurement lines is 2.272 mGal, and the external agreement accuracy of the four voyages is 2.331, 1.837, 3.988, and 2.589 mGal, respectively (Che Hao et al., 2022).

## **7 Application research on marine gravity field**

### **Application of marine gravity survey for seafloor topography inversion**

The bathymetry reflects the variations in the topography of the sea floor, and it is a fundamental parameter for conducting marine investigations and research. It provides important basic data for the study of oceanography, marine geology, marine geophysics, and marine biology. A precise model of the bathymetry helps to understand the external shape of the Earth, the movement of seafloor structures, and the evolution of the seafloor. It can be used for planning ship navigation routes, submarine navigation, deep-sea resource development, marine engineering construction, and marine environmental monitoring. It has important applications in marine science research, military oceanographic support, national economic development, and the protection of marine rights and interests.

The main method for rapidly measuring global seafloor topography is to use the marine gravity field to invert the seafloor topography. The theoretical basis for this method is the strong correlation between gravity anomalies and seafloor topography in a certain wave band. Based on this theory, many scholars have developed methods to invert seafloor topography using ocean gravity anomalies. So far, the commonly used methods for inverting seafloor topography from marine gravity anomalies include the admittance function method, least squares adjustment method, Smith and Sandwell (S&S) method, and gravity-geologic method (GGM). The APM has reviewed the development of domestic and foreign seafloor exploration technologies and model construction, discussed the current research status and major challenges of global seafloor topography fine modeling, and summarized the development trend of global seafloor topography fine modeling in the future. It is believed that the inversion of ocean gravity field based on satellite altimetry technology will still be the main technical means for fine modeling of global seafloor topography in the future. Moreover, new-generation altimetry satellites such as the tandem altimetry and the SWOT two-dimensional sea surface height measurement mission will provide data sources for further improving the accuracy of marine gravity field and seafloor topography models. Combining terrain complexity and optimizing seafloor topography inversion theory methods is expected to bring theoretical innovation, and exploring the use of artificial intelligence technology for fine modeling of seafloor topography deserves attention (Sun et al., 2022). With the development of artificial intelligence technology, scholars have continuously explored the combination of machine learning for seafloor topography inversion and have achieved good results (Annan and Wan, 2022; Wan et al., 2022). Annan and Wan (2022) used convolutional neural networks to invert the seafloor topography of the Guinea Gulf area by fusing vertical deflection data, gravity anomaly data, and vertical gravity gradient data and evaluated the accuracy. The results showed that the seafloor topography inverted by convolutional neural networks has higher accuracy.

### **Research on underwater gravity-assisted navigation**

Underwater gravity-assisted navigation has the characteristics of passive autonomy, stability, and strong anti-interference, and does not require the submarine to approach or float

to the surface to receive or transmit signals. It can realize the underwater concealed calibration of the navigation system, providing better protection for the safe and concealed navigation of submarines during long voyages. In the current international situation, China's marine strategy faces severe challenges. Developing underwater gravity-matching assisted navigation is of great strategic and practical significance for China to establish an underwater long-term passive autonomous navigation system, ensure underwater navigation safety, consolidate national defense security, break through island chain blockades, and maintain deterrence capability.

The underwater gravity-assisted navigation system mainly consists of the navigation reference map, gravity measurement sensor, dynamic measurement and data processing, matching positioning, and navigation information output. The gravity navigation reference map is the basic data source necessary for underwater gravity-assisted navigation positioning. It provides basic reference coordinates and foundational data support for matching navigation positioning. The accuracy and resolution of the reference map determine the overall effectiveness of matching navigation. The ocean gravity field can provide a high-precision, high-resolution navigation reference map for underwater gravity-assisted navigation. In recent years, domestic scholars have conducted a lot of research related to underwater matching navigation based on the ocean gravity field. Harbin Engineering University has conducted relevant research in gravity pattern matching positioning technology, contour matching algorithms, inertial navigation initial alignment based on gravity information, and simulation of gravity matching navigation systems. The Naval University of Engineering and the Naval Oceanographic and Hydrographic Research Institute have cooperated to conduct a series of studies on the generation technology of simulated gravity maps, the influence of gravity fields on inertial navigation, and the related algorithms/ICCP algorithms of gravity matching. The Information Engineering University has explored and researched the disturbance correction of gravity information in gravity-assisted inertial navigation, the UKF algorithm for inertial/gravity combined navigation, the reconstruction method for ocean gravity anomaly maps for navigation, and the improved method for the ICCP algorithm of gravity matching. The APM proposed inertial/gravity combined navigation positioning algorithms such as multi-mode adaptive estimation, minimum variance sum, and relative position constraints. They have also jointly conducted several sea trials of gravity matching assisted navigation with the Naval University of Engineering, the Oceanographic and Hydrographic Research Institute, and others. The positioning accuracy reached 1.9 nautical miles (as shown in Figure 15) (Liu et al., 2021). The above research provides a solid theoretical basis and technical support for the use of the ocean gravity field for underwater gravity-assisted navigation.

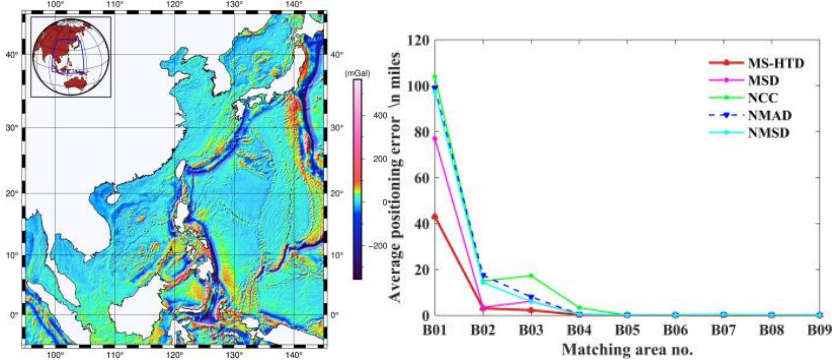


Figure 15. Average positioning error of matching navigation algorithm under different matching regions.

## **Research on seafloor tectonic movement**

Seafloor spreading is a geodynamic phenomenon closely related to the mass transfer of Earth's interior materials. It is also an important aspect of geodynamics and global change research, and has a significant impact on the interactions between Earth's layers. Investigating and analyzing seafloor spreading, revealing the evolution laws of the Earth as a whole or in specific regions, and predicting its trends, are hot topics in modern Earth science research. Essentially, the mass transfer caused by tectonic movements will inevitably lead to slight changes in the Earth's external gravity field. The Earth's gravity field is one of its inherent physical characteristics, reflecting the distribution, movement, and changing states of materials within the Earth's interior. Through differential observations of gravity fields at different times (including gravity anomalies, gravity gradients, vertical deflection, and geoid), information on the temporal and spatial distribution of the global gravity field can be obtained, and combined with plate tectonic theory, will provide accurate data for explaining and analyzing geodynamic phenomena and geophysical features of the Earth.

The APM utilizes the technical advantages of precise and quantitative geodetic measurements to detect rapid mass transfer phenomena in typical regions of the Earth's surface, such as the magma activity during submarine volcanic eruptions, through repeated observations of the ocean gravity field over multiple periods. Taking the submarine volcanic activity of Nishinoshima, Japan as an example, DEXP three-dimensional imaging technology was used to quickly image the magma distribution within the volcano, and the magma movement was analyzed by comparing the imaging results corresponding to the three periods before, during, and after the volcanic eruption. The research reveals the complex characteristics of magma movement during volcanic eruptions, including both lateral and vertical magma transport, and the magma chamber in the northeast is the main source of volcanic eruption materials (as shown in Figure 16). The research involves many disciplines, such as geodesy, geophysics, and geodynamics. The results provide a new research approach for a profound understanding of the characteristics and current activity status of oceanic plate tectonics, the formation process of oceanic islands, the explanation of geodynamic mechanisms, and the exploration of the mysteries within the Earth (Li et al., 2021).

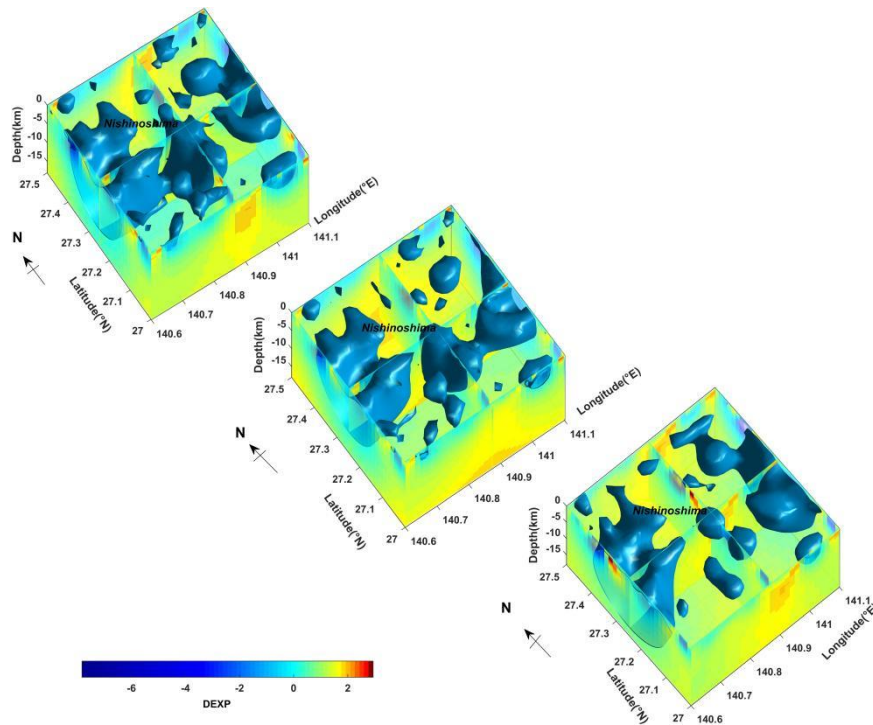


Figure 16. 3D DEXP image of the anomalous sources of the Nishinoshima from the detrend Bouguer gravity anomalies in 2013, 2014 and 2019 (Top: Before the eruption, 2013; Middle: During the eruption, 2014; Bottom: After the eruption, 2019).

## Bibliography

- Andersen, OB., Knudsen, P. (2019). The DTU17 global marine gravity field: first validation results. In: International association of geodesy symposia, Berlin, Heidelberg.
- Annan, R.F., Wan, X. (2022). Recovering Bathymetry of the Gulf of Guinea Using Altimetry-Derived Gravity Field Products Combined via Convolutional Neural Network. *Surv Geophys*, 43, 1541–1561.
- Bao, L., Xu, H. (2014). Twin-satellites Altimetry Mode and Its Orbit Design. *Acta Geodaetica et Cartographica Sinica*, 43(07):661-667.
- Chang, L., Qin, F., Wu, M. (2018). Gravity disturbance compensation for inertial navigation system. *IEEE Transactions on Instrumentation and Measurement*, 68(10), 3751-3765.
- Che, H., Li, A., Fang, J., Ge, G., Gao, W., Zhang, Y., Liu, C., Xu, J., Chang, L., Huang, C., Gong, W., Li, D., Chen, X., Qin, F. (2022). Ship-Borne Dynamic Absolute Gravity Measurement Experiment Based on Cold Atomic Gravimeter. *Acta Physica Sinica*, 71(11): 113701.
- Chen, S., Zhuang, J., Li, X., Lu, H., Xu, W. (2019). Bayesian approach for network adjustment for gravity survey campaign: methodology and model test. *Journal of Geodesy*, 93, 681-700.
- Chen, X., Li, H., Deng, M., Jiang, L., Sun, H., Li, D., Bai, L. (2020). Experimental study of the surface subsidence in the city using gravity observing techniques. *Chinese Journal of Geophysics*, 63(8), 2882-2892.
- Chen, Z., Chen, S., Zhang, B., Wang, L., Shi, L., Lu, H., Xu, W. (2022). Uncertainty quantification and field source inversion for the continental-scale time-varying gravity dataset: a case study in SE Tibet, China. *Pure and Applied Geophysics* 180, 683–702.
- Cheng, B., Zhou, Y., Chen, P., Zhang, K., Zhu, D., Wang, K., Weng, K., Wang, H., Peng, S., Wang, X., Wu, B., Lin, Q. (2021).

- Absolute Gravity Measurement Based on Atomic Gravimeter Under Ship-Borne Mooring State. *Acta Physica Sinica*, 70(4):7.
- Cui, X., Sun, H., Xu, J., Zhou, J., Chen, X. (2020). Relationship between free core nutation and geomagnetic jerks. *Journal of Geodesy*, 94, 1-13.
- Han, J., Chen, S., Chen, Z., Lu, H., Xu, W. (2021a). Determination of the degree 120 time-variable gravity field in the Sichuan-Yunnan region using Slepian functions and terrestrial measurements. *Earthquake Science* 34(3):211-221.
- Han, J., Chen, S., Lu, H., Xu, W. (2021b). Time-variable gravity field determination using Slepian functions and terrestrial measurements: A case study in North China with data from 2011 to 2013. *Chinese Journal of Geophysics* 64:1542-1557 (in Chinese).
- Han, Y., Wang, J., Xu, R. (2020). Fractal characteristics and earthquake monitoring capability of the CMONOC gravity network. *Earthquake Research in China* 36 (4): 879–887 (in Chinese).
- He, Q., Chen, X., Sun, H., Xu, J., Liu, Z., Zhou, S., Chen, Z. (2022). Quantitative separation of the local vadose zone water storage changes using the superconductive gravity technique. *Journal of Hydrology*, 609, 127734.
- Jia, L., Chen, S., Wang, L., Xiang, L., Lu, H., Shi, W. (2023). Gravity yearly transient change around the epicenter of 2022 Ms 6.9 Menyuan earthquake, China and seismotectonic implications. *Tectonophysics* 846: 229676.
- Jin, T., Zhou, M., Zhang, H., Li, J., Jiang, W., Zhang, S., Hu, M. (2022). Analysis of vertical deflections determined from one cycle of simulated SWOT wide-swath altimeter data. *Journal of Geodesy*, 96(4), 30.
- Li, H., Chen, S., Zhuang, J., Zhang, B., Shi, L. (2021). Gravity inversion method base on Bayesian-assimilation and its application in constructing crust density model of the Longmenshan region. *Chinese Journal of Geophysics* 64(4): 1236-1252.
- Li, H., Xu, J., Chen, X., Sun, H., Zhang, M., Zhang, L. (2020). Extracting long-period surface waves and free oscillations using ambient noise recorded by global distributed superconducting gravimeters. *Seismological research letters*, (4), 91.
- Li, H., Chen, X. D., Xu, J. Q. (2020). Comparison of noise levels between gravimeters and co-located seismometers at the seismic frequency band. *Geodesy and Geodynamics*, 40(8), 843-848.
- Li, Q., Bao, L., Shum, CK. (2020). Analysis of seafloor plate motion using ocean gravity field variations. *Chinese Journal of Geophysics*, 63(7): 2506-2515.
- Li, Q., Bao, L., Shum, C.K. (2021). Altimeter-derived marine gravity variations reveal the magma mass motions within the subaqueous Nishinoshima volcano, Izu–Bonin Arc, Japan. *Journal of Geodesy*, 95, 46.
- Li, Q., Bao, L., Wang, Y. (2021). Accuracy Evaluation of Altimeter-Derived Gravity Field Models in Offshore and Coastal Regions of China. *Frontiers in Earth Science*, 9(649).
- Li, Y., Chen, S., Li, H., Zhang, B. (2022). Contrastive analysis of the three-dimensional density structure characteristics of the focal area of moderate-strong earthquakes in southern Sichuan. *Chinese Journal of Geophysics* 65(11): 4326-4340.
- Liang, Y., Chen, X. D., Sun, H., Cui, X., Zhang, M., Niu, X. (2020). Gravity Tide Observation with OSG-066 and Their Applications at Lijiang Station, Yunnan Province, China. *Geodesy and Geodynamics*, 40(7): 713-719.
- Liu, H., Wu, L., Bao, L., Li, Q., Zhang, P., Wang, Y. (2022). Gravity matching navigation algorithm based on multiscale search and Hadamard transformed difference. *ISA transactions*, 128, 409-422.
- Liu, X., Chen, S., Xing, H. (2022). Gravity changes caused by crustal fluids invasion: A perspective from finite element modeling. *Tectonophysics* 833: 229335.
- Sandwell, D. T., Harper, H., Tozer, B., Smith, W. H. F. (2021). Gravity Field Recovery from Geodetic Altimeter Missions. *Adv. Space Res.* 68, 1059–1072.
- Sun, H., Cui, X., Xu, J., Ding, H., Zhang, M., Li, H., Wang, Z., Zhou, J., Chen, X. (2022). Progress of Research on the Earth's

Gravity Tides and its Application in Geodynamics in China. *Pure and Applied Geophysics*, 1-17.

- Sun, H., Li, Q., Bao, L., Wu, Z., Wu, L. (2022). Advancements and trends in high-resolution modeling of global seafloor topography. *Journal of Wuhan University: Information Science Edition*, 47(10): 1555-1567.
- Sun, H., Zhang, M., Xu, J., Chen, X. (2019a). Reanalysis of background free oscillations using recent SG data. *TAO: Terrestrial, Atmospheric and Oceanic Sciences*, Vol. 30, No. 6, 1-7.
- Sun, H., Zhang, H., Xu, J., Chen, X., Zhou, J., Zhang, M. (2019b). Influences of the Tibetan plateau on tidal gravity detected by using SGs at Lhasa, Lijiang and Wuhan Stations in China. *TAO: Terrestrial, Atmospheric and Oceanic Sciences*, Vol. 30, No. 1, 139-149.
- Sun, Z., Guan, B., Zhai, Z., Ouyang, M. (2022). Research progress of ocean satellite altimetry and its recovery of global marine gravity field and seafloor topography model. *Acta Geodaetica et Cartographica Sinica*, 51(6): 923-934.
- Wan, X., Liu, B., Sui, X., Annan, R. F., Hao, R., Min, Y. (2022). Bathymetry inversion using the deflection of the vertical: A case study in South China Sea. *Geodesy and Geodynamics*, 13(5), 492-502.
- Wang, B., Zhu, J., Deng, Z., Fu, M. (2018). A characteristic parameter matching algorithm for gravity-aided navigation of underwater vehicles. *IEEE Transactions on Industrial Electronics*, 66(2), 1203-1212.
- Wang, L., Chen, S., Zhuang, J., Xu, W. (2022). Simultaneous calibration of instrument scale factor and drift rate in network adjustment for continental-scale gravity survey campaign. *Geophysical Journal International*, 228(3), 1541-1555.
- Yang, J., Chen, S., Zhang, B., Zhuang, J., Wang, L., Lu, H. (2021). Gravity observations and apparent density changes before the 2017 Jiuzhaigou Ms7. 0 earthquake and their precursory significance. *Entropy*, 23(12), 1687.
- Wang, Y., Yang, Y., Sun, H., Xie, C., Zhang, Q., Cui, X., Chen, C., He, Y., Miao, Q., Mu, C., Guo, L., Teng, J. (2023). Observation and research of deep underground multi-physical fields—huainan 848 m deep experiment. *Science China Earth Sciences*, 66(1), 54-70.
- Yu, D., Hwang, C., Andersen, O.B., Chang, E.T., Gaultier, L. (2021). Gravity recovery from SWOT altimetry using geoid height and geoid gradient. *Remote Sensing of Environment*, 265, 112650.
- Yuan, Y., Gao, J., Wu, Z., Shen, Z., Wu, G. (2020). Performance estimate of some prototypes of inertial platform and strapdown marine gravimeters. *Earth Planets Space* 72, 89.
- Zhai, Z., Sun, Z., Xiao, Y., Li, F. (2018). Two-Satellites Tandem Mode Design and Accuracy Analysis of Gravity Field Inversion for Independent Marine Altimetry Satellite. *Geomatics and Information Science of Wuhan University*, 43(07):1030-1035.
- Zhang, M., Chen, X., Xu, J., Cui, X., Liu, M., Xing, L., Mu, C., Sun, H. (2021). A Preliminary Analysis of Gravity Noise Levels at the Deep Geophysical Experimental Field in Huainan. *Advances in Earth Science*, 36(5): 500-509.
- Zhang, S., Abulaitijiang, A., Andersen, O. B., Sandwell, D. T., Beale, J. R. (2021). Comparison and evaluation of high-resolution marine gravity recovery via sea surface heights or sea surface slopes. *Journal of Geodesy*, 95(6), 66.
- Zhang, Y., Chen, S., Xing, L., Liu, M., He, Z. (2020). Gravity changes before and after the 2008 Mw 7.9 Wenchuan earthquake at Pixian absolute gravity station in more than a decade. *Pure and Applied Geophysics* 177(1): 121-133.
- Zheng, Q., Yao, X., Chen, S., Yang, J., Liu, D., Chen, Z. (2022). Data quality assessment of time-variable surface microgravity surveys in the southeastern Tibetan Plateau. *Applied Sciences* 12(7), 3310.
- Zhu, C., Guo, J., Gao, J., Liu, X., Hwang, C., Yu, S., Yuan, J., Ji, B., Guan, B. (2020). Marine gravity determined from multi-satellite GM/ERM altimeter data over the South China Sea: SCSGA V1.0. *Journal of Geodesy*, 94, 1-16.



# Development Status of Chinese Gravimetry Satellite

Yun Xiao<sup>1,2</sup>, Yuanxi Yang<sup>1,2</sup>, Zhicai Luo<sup>3</sup>, Yunlong Wu<sup>4</sup>, Zongpeng Pan<sup>1,2</sup>, Hao Zhou<sup>3</sup>, Xiaogang Liu<sup>1,2</sup>, Zhongmiao Sun<sup>1,2</sup>, Zehua Guo<sup>5</sup>, Guodong Xu<sup>4</sup>, Sulan Liu<sup>4</sup>

<sup>1</sup> Xi'an research Institute of Surveying and Mapping, Shanxi, Xi'an 710054, China

<sup>2</sup> State Key Laboratory of Geo-Information Engineering, Shanxi, Xi'an 710054, China

<sup>3</sup> Institute of Geophysics and National Precise Gravity Measurement Facility (PGMF), Huazhong University of Science and Technology (HUST)

<sup>4</sup> School of Geography and Information Engineering, China University of Geosciences, Wuhan

<sup>5</sup> School of Geodesy and Geomatics, Wuhan University

## 1 Chinese First Satellite-to-Satellite Tracking Gravimetric Mission

The first pair of satellite to satellite tracking gravimetric satellites from China (Chinese Gravimetric mission) was successfully launched at the end of 2021. It adopts a hybrid measurement system of High-Low Satellite-to-Satellite Tracking (HL-SST) and Low-Low Satellite-to-Satellite Tracking (LL-SST) to obtain measurements of the global gravity field and its time-varying information, which can be used to study groundwater changes, glacier ablation, space micro-gravity fluctuations, ocean tides, earthquakes, etc. The data can be used for scientific research and engineering construction in the fields of natural resources, ocean, aerospace, and water conservancy, et al. The Chinese gravimetric satellite platform is designed to be ultra-silent, ultra-stable and ultra-accurate. In-orbit test results show that the working state of the platform is normal and all indicators meet the design requirements. This significantly improves the development level of the satellite platform and the level of space micro-gravity measurement, and will expand the prospect for scientific applications in various fields.

Chinese gravimetric satellite platform is designed and produced firstly, can provide an environment with low vibrations, stable temperature, precise space pointing and tiny deformation of the structure for the whole satellite, and ensures that the payloads of the inter-satellite ranging system and electrostatic suspension accelerometer work in suitable conditions.

The inter-satellite ranging system, electrostatic suspension accelerometer, BDS/GPS common mode receiver, star sensors, et al. are mounted. The inter-satellite ranging system is working in the dual-one way ranging configuration, and ranging noise level being better than  $3\mu\text{m}/\sqrt{\text{Hz}}$  in the frequency band of 0.025-0.1Hz. The accelerometer works with electrostatic suspension mode, which is highly sensitive to the residual thrust of the attitude control thruster, switching of the magnetic torque and other small vibrations. The spectrum analysis shows its high-sensitive axis noise level is being  $3\times 10^{-10}\text{m/s}^2/\sqrt{\text{Hz}}$  near the frequency 0.1Hz, and being  $1\times 10^{-9}\text{m/s}^2/\sqrt{\text{Hz}}$  for the less-sensitive axis. The three star sensors are designed integrally with the tiny deformation structure. The angles between star sensor boresights were calculated, then the average of the angles was removed, the standard deviation (STD) of residuals was better than 3". The center of mass detection and adjustment system reaches the accuracy level of 100 microns. The BDS/GPS common mode receiver observes BDS-3 signals and GPS signals simultaneously. The data from the BDS/GPS receiver is used for satellite Precise Orbit Determination (POD) and time synchronization. The achieved accuracy of the satellite orbits is

better than 2 cm determined from a comparison of the kinematic and reduced-dynamic orbits. Comparing the baseline of the KBR system with the POD yields RMS residuals of less than 1 mm.

The time-varying Earth gravity model with a maximum degree of 60 was recovered using satellite data from April 1, 2022 to August 30, 2022, being named Chinese Earth Gravity Field Model 22-01 (CEGM22S-01) (Figure 1). The model can well characterize global hydrological changes, such as the mass loss of Greenland and the terrestrial water storage changes of the Amazon River, and correlates strongly with the results of GRACE Follow-On with the root mean square (RMS) difference of 2 cm in global equivalent water height (Figure. 2.3.2). The model is converted into an equivalent water height which can be applied to Amazon terrestrial water storage monitoring.

With the accumulation of further satellite data, the continuous time-varying gravity field, space atmospheric density, space horizontal ionosphere, space magnetic field and other products can be produced, which will provide abundant information services for the fields of geophysics, geodesy, earthquake, water resources environment, ocean, national defense, etc.

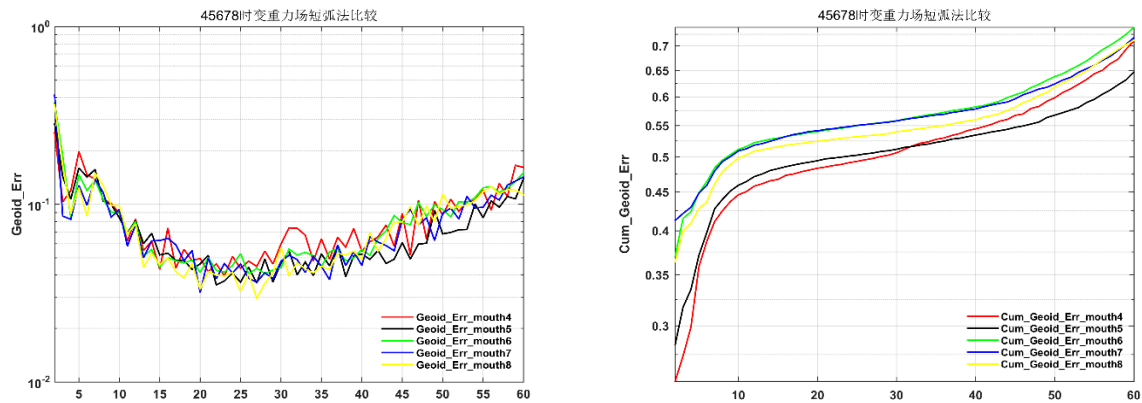


Figure 1. The degree error spectrum and accumulated error of the Chinese Earth Gravity Model CEGM22S-01 (Xiao et al., 2023).

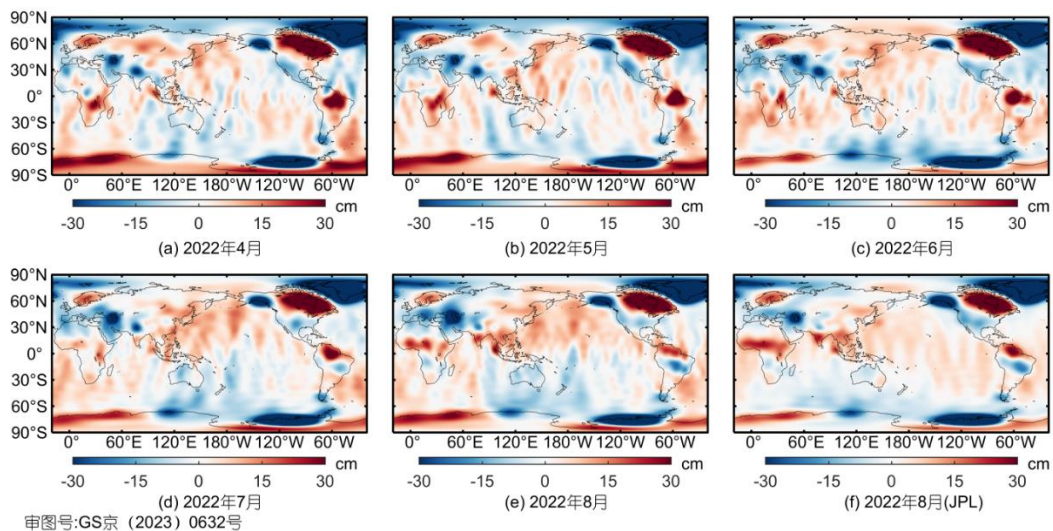


Figure 2. The power spectrum of the Chinese Earth Gravity Model CEGM22S-01 (Xiao et al., 2023)

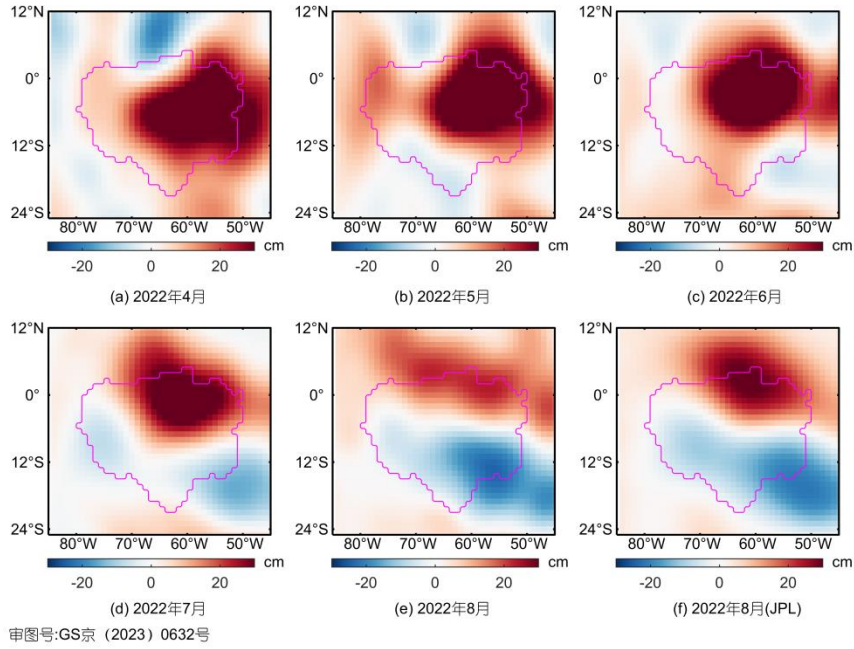


Figure 3. The inversion results of Amazon groundwater (Xiao et al., 2023)

## 2 Chinese Next Generation Gravimetric Mission

Tianqin (TQ) mission is a Chinese proposed project for space-based gravitational wave detection. The concept of TQ envisions an equilateral triangle constellation of three drag-free satellites orbiting the Earth with an orbital radius of about  $10^5$  km (Gong et al., 2021; Mei et al., 2021). To achieve the final goal of TQ mission, the TQ mission set a roadmap from TQ-1, TQ-2 to TQ-3.

The TQ-1 satellite, which is the first technology demonstration satellite for the TQ project, was launched on 20 December 2019. The first round of experiment had been carried out from 21 December 2019 until 1 April 2020. The residual acceleration of the satellite is found to be about  $1 \times 10^{-10} \text{ m/s}^2/\text{Hz}^{1/2}$  at 0.1 Hz and about  $5 \times 10^{-11} \text{ m/s}^2/\text{Hz}^{1/2}$  at 0.05 Hz, measured by an inertial sensor with a sensitivity of  $5 \times 10^{-12} \text{ m/s}^2/\text{Hz}^{1/2}$  at 0.1 Hz. The micro-Newton thrusters has demonstrated a thrust resolution of  $0.1 \mu\text{N}$  and a thrust noise of  $0.3 \mu\text{N}/\text{Hz}^{1/2}$  at 0.1 Hz. The residual noise of the satellite with drag-free control is  $3 \times 10^{-9} \text{ m/s}^2/\text{Hz}^{1/2}$  at 0.1 Hz. The noise level of the optical readout system is about  $30 \text{ pm}/\text{Hz}^{1/2}$  at 0.1 Hz. The temperature stability at temperature monitoring position is controlled to be about  $\pm 3 \text{ mK}$  per orbit, and the mismatch between the center-of-mass of the satellite and that of the test mass is measured with a precision of better than 0.1 mm. This successful mission has marked a new milestone in the development of the TQ project.

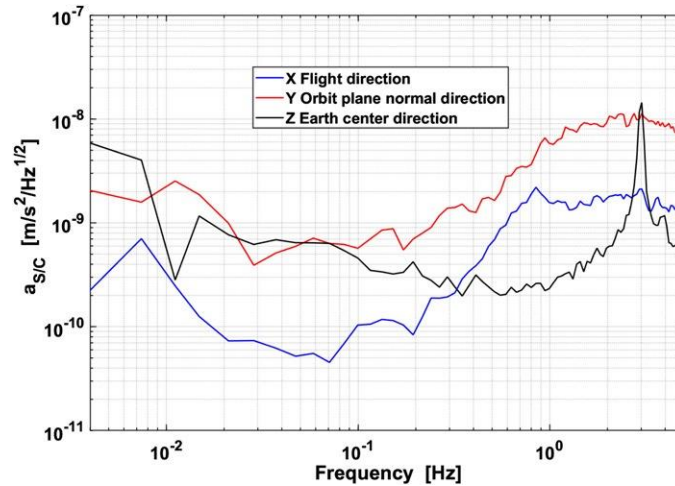


Figure 4. The actual acceleration level of the satellite measured by the inertial sensor onboard TQ-1. Note X is along the flight direction and Z points to the center of Earth.

Based on the successful TQ-1 mission, the TQ group has also focus on propose the TQ-2 mission. TQ-2 mission is designed as a totally experimental satellite for gravitational wave detection at low Earth orbit, which can detect the Earth's gravity field simultaneously. Therefore, it can be also regarded as the Chinese NGGM. For NGGM, the most promising NGGM is the Bender-type mission, which consists of a polar satellite pair and an inclined satellite pair. Due to the extra observations at the east-west direction derived from the inclined satellite pair, there are significant improvements in detecting temporal signals with higher accuracy and spatial-temporal resolution.

Based on the Bender-type NGGM concept, researchers have systematically analyzed the key mission design parameters and foreseen the extended application scopes in geosciences. In the context of Bender-type NGGM, the payload requirement is limited to approximately 20 nm/Hz<sup>1/2</sup> at the measurement bandwidth (MBW) of 0.01 ~ 1 Hz for laser ranging instrument (LRI), and 10<sup>-11</sup> m/s<sup>2</sup> at 0.001 ~ 0.1 Hz for accelerometer (ACC). Low frequency noise is also respectively limited to 1/f and 1/f<sup>2</sup> for LRI and ACCs due to unavoidable electronic noise. However, due to the complex payload manufacture procedures and volatile space observation environment, in reality LRI or ACCs noise may not be rigorously consistent with the designed noise models in frequency domain. Frequency dependent noise in *in-situ* observations always results in different MBW boundaries or different low frequency features. Therefore, Zhou et al. (2023) assesses the impacts of frequency dependent instrument noise for NGGM on determining temporal gravity field model. The results indicates that in the instrument noise only scenarios, a similar behavior is shown between the frequency spectrum of instrument's frequency dependent noise in terms of amplitude spectral density and the corresponding gravity solution in terms of geoid height error, while the frequency dependent instrument noise plays less role when the background force model errors are included. In the full noise contaminated scenarios, to achieve the scientific goal of Bender-type NGGM, it is feasible to shift the low MBW boundary from 0.001 Hz to 0.004 Hz for ACC, and from 0.01 Hz to 0.1 Hz for LRI (Figure 5 and Figure 6). The results are helpful to specify the requirement of manufacturing key payloads for the Bender-type NGGM.

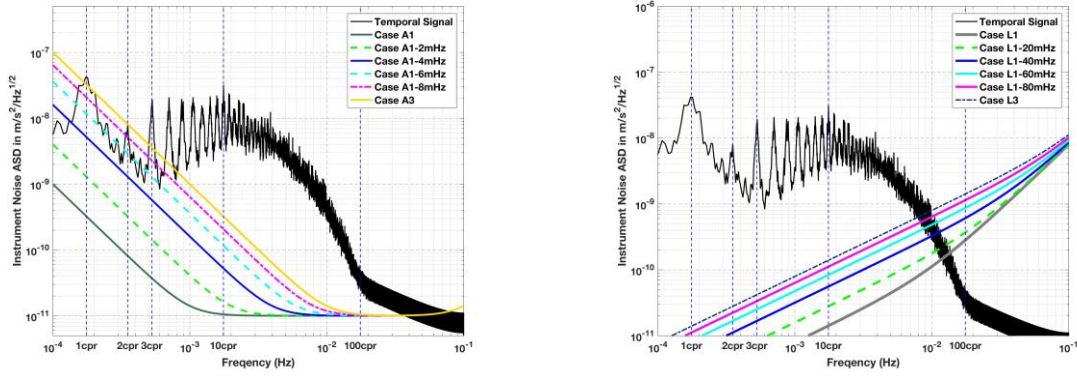


Figure 5. Amplitude spectral densities of accelerometer (left) and laser ranging interferometer (right) noise model considering different measurement bandwidths in terms of accelerations.

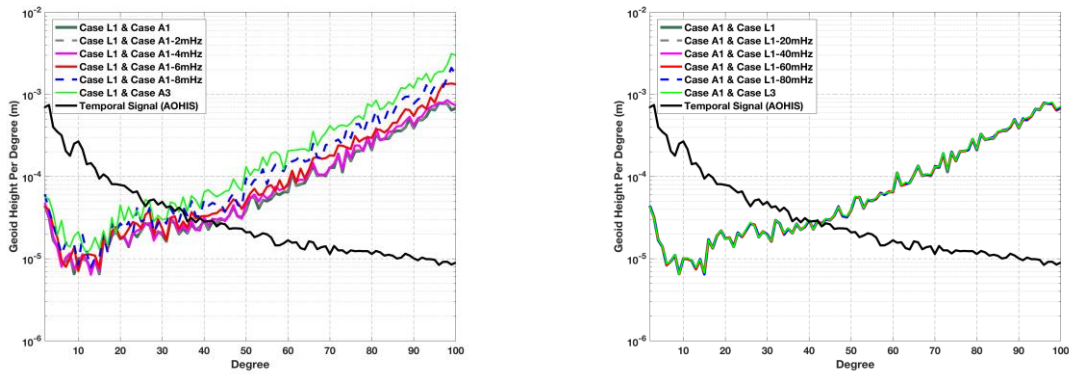


Figure 6. Geoid height errors per degree of gravity field solutions derived from the instrument noise model combinations considering different accelerometer (left) and laser ranging interferometer measurement bandwidths (right). Here non-tidal atmosphere and ocean aliasing error is fully considered, and the wiese-approach is applied to reduce the temporal aliasing error.

The prerequisite of implementing the Bender-type mission is to ensure the combination as well as the independency of the missions in the polar satellite formation (PSF) scenario as well as in the inclined satellite formation (ISF) scenario. To promote NGGM, Zhou et al. (2023a) implement a close-loop simulation study to evaluate the performance of the stand-alone ISF mission. In spectral domain, the ISF estimations show extremely poor quality for zonal and near-zonal coefficients due to the absence of observations over the polar regions, while the sectorial and near-sectorial coefficient estimations show approximately 71~77% noise reductions when compared with the PSF estimations. In spatial domain, the ISF mission presents its superior capability in detecting the Earth's mass variations within its observational areas than the PSF mission. The improvements of ISF are also obtained over the transition zones (50°N ~ 70°N and 50°S ~ 70°S) with 41% noise reductions. The simulation results demonstrate the feasibility of implementing a stand-alone mission in the inclined orbits, and the further possibility of promoting a Bender-type mission via a profound cooperation by two institutions.



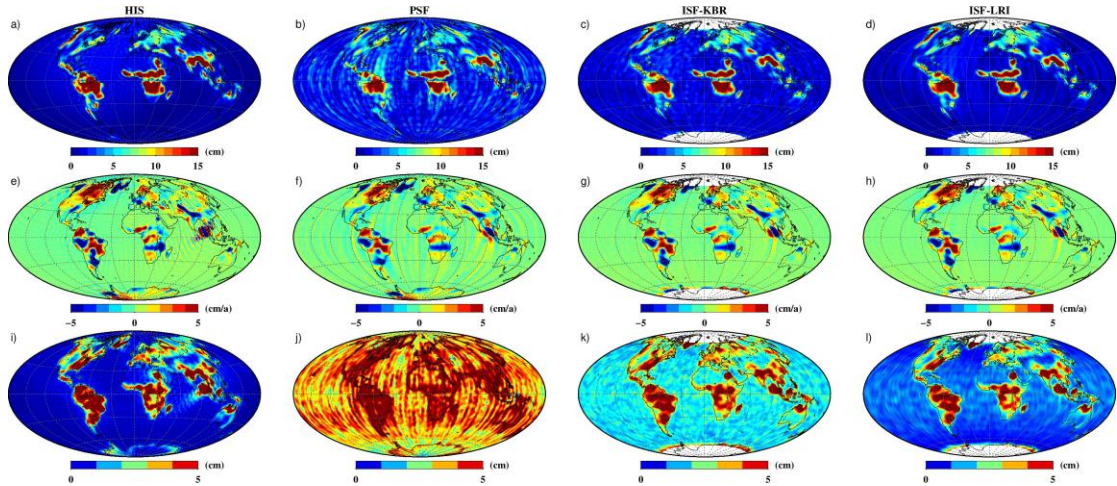


Figure 7. Annual amplitude (top), yearly trend (middle) and RMS residuals (bottom) derived from ESM HIS model (column 1), polar satellite formation(PSF, column 2), inclined satellite formation with K-band ranging system (ISF-KBR, column 3) and inclined satellite formation with laser ranging interferometer (ISF-LRI, column 4).

To proposal Chinese Bender-type NGGM, we also need to figure out the possibility of improve gravity field estimations via polar satellite formation. For the polar satellite formation, the errors in atmospheric and oceanic de-aliasing (AOD) model are still the key limitation especially taking advantages of improved laser ranging interferometer (LRI). Zhou et al. (2023b) explores the realistic assumption of continuously reducing AOD model error in global scale and regional scale (e.g., ocean, Greenland, Qinghai-Tibet plateau and South America) in the anticipated future. For this, using a realistic orbit scenario and error assumptions both for instrument and background model errors, the 5-year full-scale simulations are implemented in the context of 26 scenarios with different AOD model errors. The results demonstrate that when the AOD model errors are reduced in the global scale, the corresponding gain in temporal gravity field determination is significant, with 26.3-65.2% noise reduction in terms of mean RMS residuals over ocean in spatial domain (Figure 8). However, when the AOD model errors are reduced in the regional scale, the most notable noise reduction, with 22.9-43.9% noise reduction in spatial domain, is observed when the AOD model error decreases in ocean. The limited noise reductions (0.1% and 1.3% respectively in spectral and spatial domain) are observed in the temporal gravity field estimations if the AOD model is refined in other typical regions such as the Qinghai-Tibet plateau, the Greenland and the South America. Meanwhile, when the satellites passing over the AOD model refined regions, the along-orbit range rate analysis indicates that, there are visible differences by about 50.0 nm/s in terms of range rate residuals as well as 11.0-48.5 nm/s in terms of the mean RMS of range rate residuals. These results reflect the beneficial of reducing AOD model error in both global and regional scale for improving GRACE-type temporal gravity estimation, especially considering the development of LRI technology.

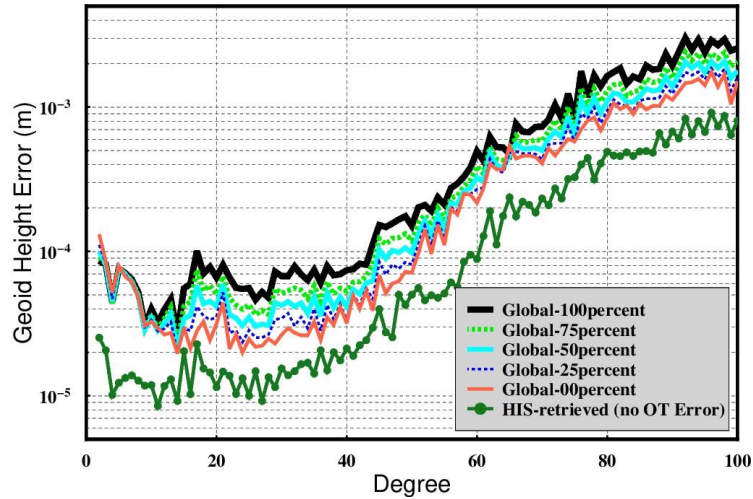


Figure 8. Geoid height error per degree of temporal gravity field models derived from different simulation scenarios where the different noise levels of global AOD models are considered.

In addition, to ensure the global observability of next generation gravimetric mission (NGGM), different agencies have to repeatedly launch satellites to about  $89.0^\circ$  orbit inclination. However, due to the poor isotropy of observation system, only minor improvement in terms of temporal gravity field estimation can be obtained via these repeatedly launched polar pair missions. To ensure the global observability as well as the isotropy of observation system, a near-polar pair mission rather than a polar mission is likely an optimal selection, especially considering that the Gravity Recovery and Climate Experiment (GRACE) Follow-On mission has been already in operation. Therefore, for the Chinese NGGM, Zhou et al. (2023c) design a closed-loop simulation to assess the performance of a near-polar mission at a near-circular orbit with about 500 km altitude for detecting the Earth's temporal gravity field. Based on the statistic results,  $85.0^\circ$  is selected as the optimal orbit inclination for the near-polar mission, which provides 37% noise reduction in terms of cumulative geoid height error in spectral domain, but also 31% noise reduction in terms of mean oceanic root-mean-square (RMS) error in spatial domain when compared to the  $89.0^\circ$  polar mission (89-PM). Although there are inevitable  $5.0^\circ$  polar gaps in the 85-NPM, the analysis result still demonstrates a comparable performance of the 85-NPM in tracking mass variations over the Antarctic, and even an outperformance with 12% noise reduction over the Greenland when compared to the 89-PM. The result confirms the feasibility of implementing a near-polar mission as a stand-alone mission or a complementary observation system for the repeatedly launched polar missions, which offers an alternative option of launching the Chinese NGGM satellites to an  $85.0^\circ$  inclination orbit instead of  $89.0^\circ$ .

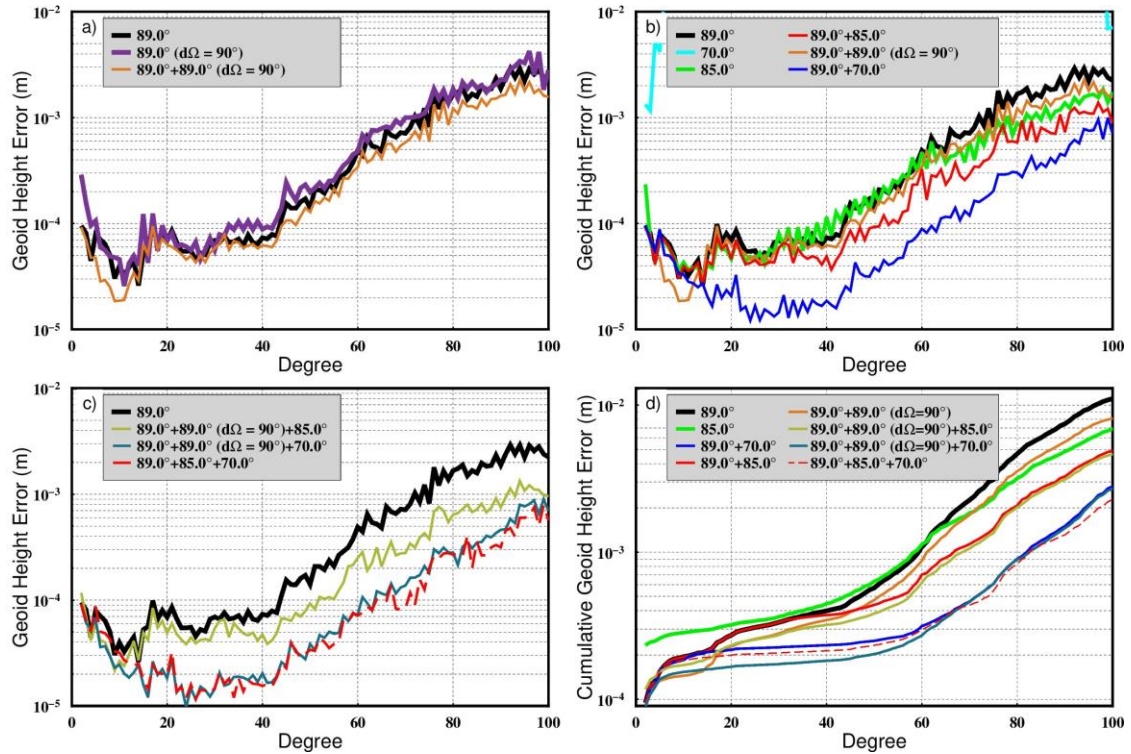


Figure 9. Geoid height error per degree (left) and cumulative geoid height error (right) from the simulation scenarios with different inclination combinations.

Based on the developed satellites and key payloads, the TQ group can provide an ultra-clean and stable environment for gravitational wave detection as well as Earth's gravity field determination. The new research results for satellite formations, key payloads and background force models also confirm the promising improvements of detecting high accuracy and high resolution Earth's gravity field via Chinese NGGM.

### 3 L1 level Construction of Satellite Gravity Gradiometry Observations

The L1 level construction method of high-precision satellite gravity gradiometry observations is an important basic data processing technology for promoting the national gravity satellite mission. Base on the GOCE satellite pre-processing technology and raw data, the L1 level construction method of satellite gravity gradiometry observation is studied and initially implemented in this work, which aim for the needs of the national gravity gradiometry satellite mission. The main steps include the conversion of the accelerometer voltage data, the reconstruction of the angular rate based on the combination of the star sensors, and the construction of the gravity gradient of the satellite. The results indicate that the accuracy of the accelerometer ultra-sensitive axis is  $10^{-10}$ - $10^{-11}$   $\text{m/s}^2/\text{Hz}^{1/2}$ , which achieve the designed accuracy requirements of the gradiometer. The optimal determination of the angular rate  $w_y$ 、 $w_z$  is improved by about 1 order of magnitude in the range of 10-100mHz at about  $10^{-6}$   $\text{rad/s/Hz}^{1/2}$ , which is effective in suppressing noise propagation caused by low precision angular velocity components in coordinate system conversions. The square root power spectrum of the angular rate reconstruction based on the Wiener filtering method in the 5-100 mHz band is enhanced by  $5.21$ - $6.56 \times 10^{-11}$   $\text{rad/s/Hz}^{1/2}$ , which indicates the necessity of solving the gravity gradient



based on high accuracy angular rate. Lastly, the calculated values for each component of the gravity gradient are of comparable accuracy to the official GOCE gravity gradient components. The trace of the gradient tensor is about  $10 \text{ mE/Hz}^{1/2}$  in the frequency range of 20-100 mHz, which validates our method. This work provides the technical support and reserve of independent raw data processing for promoting the national civil gravity gradiometry satellite mission.

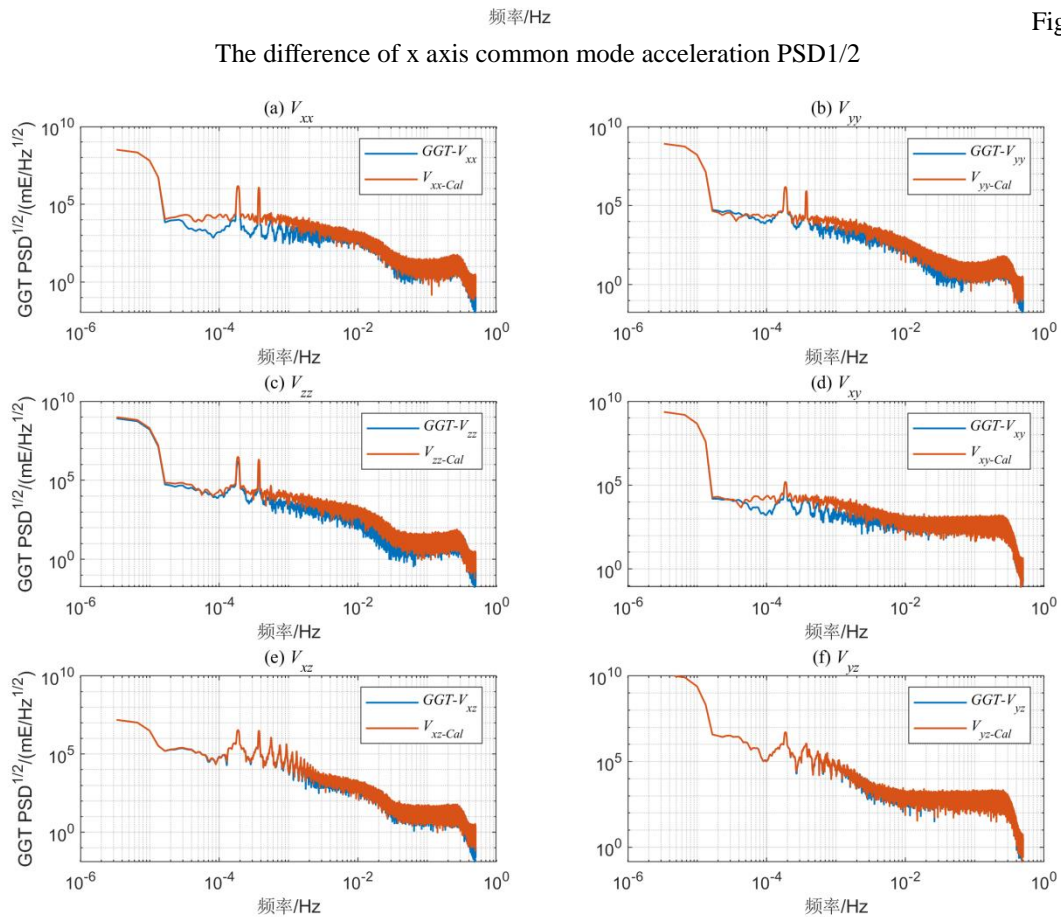


Figure 10.

Figure 11. PSD1/2 of calculated gradient trace and L1b\_GGT trace

## 4 The Data Processing Results of Chinese Gravimetry Satellite

Chinese first pair of gravimetry satellite has been in-orbit calibrated and verified completely. In-orbit test results show that the working state of the platform and payloads are normal and all indicators meet the design requirements. The achieved accuracy of the satellite orbits is better than 2 cm determined by combined BeiDou and GPS data. The stellar sensor accuracy 3" is tested by analysis residuals of angle between star sensor boresights.

The inter-satellite ranging system works in the dual-one way ranging configuration. Its performance is stable. The spectrum of range, range rate and range acceleration are showed in figure 12. noise The Range and range rate noise being less than  $3\mu\text{m}/\sqrt{\text{Hz}}$  and  $1\mu\text{m/s}/\sqrt{\text{Hz}}$  respectively in the frequency band of 0.025-0.1Hz. The electrostatic suspension accelerometer is working well. The accelerometer is highly sensitive to the residual thrust of the attitude control thruster, switching of the magnetic torque and other small vibrations. The spectrum

analysis shows its high-sensitive axis noise level is being  $3 \times 10^{-10} \text{m/s}^2/\sqrt{\text{Hz}}$  near the frequency 0.1Hz, and being  $1 \times 10^{-9} \text{m/s}^2/\sqrt{\text{Hz}}$  for the less-sensitive axis (Figure 13).

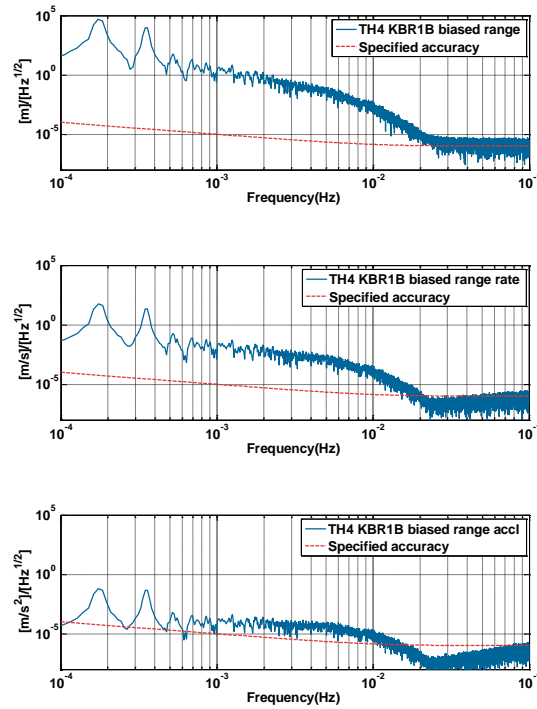


Figure 12. The spectrum of KBR biased range, range rate and range acceleration in the dual-one way ranging

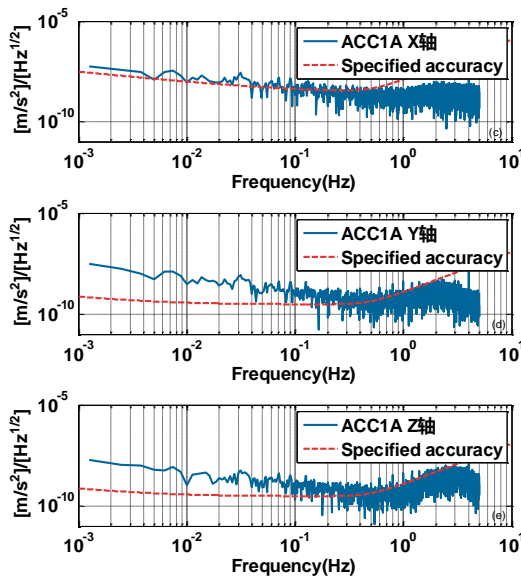


Figure 13. The accelerometer high-sensitive axis noise level being  $3 \times 10^{-10} \text{m/s}^2/\sqrt{\text{Hz}}$  near the frequency 0.1Hz, and being  $1 \times 10^{-9} \text{m/s}^2/\sqrt{\text{Hz}}$  for the less-sensitive axis

## Bibliography

Chen Q J, Shen Y Z, Francis O, et al. Tongji-Grace02s and Tongji-Grace02k: High-Precision Static GRACE-Only Global Earth's Gravity Field Models Derived by Refined Data Processing Strategies. *J Geophys Res Solid Earth*, 2018, 123(7):6111-6137

- Chen Q J, Shen Y Z, Zhang X F, et al. (2016). GRACE Data-based High Accuracy Global Static Earth's Gravity Field (in Chinese). *Acta Geodaetica et Cartographica Sinica*, 45 (4) : 396-403
- Ditmar P, Teixeira D E, Farahani H H. (2012). Understanding data noise in gravity field recovery on the basis of inter-satellite ranging measurements acquired by the satellite gravimetry mission GRACE. *J Geod.* 86(6): 441-465
- Feng W. (2013). Satellite gravity monitoring of regional land water and sea level changes (In Chinese). Doctor Dissertation. Beijing: University of Chinese Academy of Sciences
- Förste C, Bruinsma S L, Abrikosov O, et al. (2014). EIGEN-6C4-The latest combined global gravity field model including GOCE data up to degree and order 2190 of GFZ Potsdam and GRGS Toulouse. EGU General Assembly, held 27 April - 2 May, 2014 in Vienna, Austria, id.3707
- Gong, Y., Luo, J., Wang, B. (2021). Concepts and status of Chinese space gravitational wave detection projects. *Nature Astronomy*, 5, 881.
- Guo X, Ditmar P, Zhao Q L, Xiao Y. (2020). Improved recovery of temporal variations of the Earth's gravity field from satellite kinematic orbits using an epoch-difference scheme. *Journal of Geodesy*, 94(8):94-69
- GUO Zehua, WU Yunlong, XIAO Yun, HU Minzhang(2021) Reconstruction Method of Satellite Gravity Gradient Measurement Angular Velocity by Combining Star Tracker Quaternion. *Geomatics and Information Science of Wuhan University*, 46(9): 1336-1344
- Hsu H Z, Lü Y, Zhong M, et al.(2012). Satellite gravity and its application to monitoring geophysical environmental change (in Chinese). *Sci Sin Terrae*, 42: 843-853
- Kang Z, Bettadpur S, Nagel P, et al. (2020). GRACE-FL precise orbit determination and gravity recovery. *Journal of Geodesy*, 2020, 94(9): 1-17
- Kvas A, Brockmann J M, Krauss S, et al. GOCO06s—a satellite-only global gravity field model. *Earth System Science Data*, 2021, 13(1): 99-118
- Li J C, Fan C B, Chu Y X, et al. (2008). Using ICESAT Altimeter Data to Determine the Antarctic Ice Sheet Elevation Model (in Chinese). *Geomatics and Information Science of Wuhan University*, 2008(03):226-228,248
- Liang W, Xu X Y, Li J C, et al. (2018). The Determination of an Ultra-high Gravity Field Model SGG-UGM-1 by Combining EGM2008 Gravity Anomaly and GOCE observation Data (in Chinese). *Acta Geodaetica et Cartographica Sinica*, 47 (4) : 425-434
- Luo Z C, Li Q, Zhong B. (2012). Water Storage Variations in Heihe River Basin Recovered from GRACE Temporal Gravity Field (in Chinese). *Acta Geodaetica et Cartographica Sinica*, 41 (5) : 676-681
- Luo, J., Bai, Y., Cai, L., Cao, B., Chen, W., Chen, Y., et al. (2020). The first round result from the TianQin-1 satellite. *Classical and Quantum Gravity*, 37, 185013.
- Mei, J., Bai, Y., Bao, J., Barausse, E., Cai, L., Canuto, E., Cao, B., et al. (2021). The TianQin project: Current progress on science and technology. *Prog. Theor. Exp. Phys.*, 5, 05A107.
- Nie Y F, Shen Y Z, Chen Q J, et al. (2022). Hybrid-precision arithmetic for numerical orbit integration towards future satellite gravimetry missions. *Advance in Space Research*, 66(2020):671-688
- Nie Y F, Shen Y Z, Roland P, et al. (2022). Revisiting Force Model Error Modeling in GRACE Gravity Field Recovery. *Surveys in Geophysics*, doi.org/10.1007/s10712-022-09701-8.
- Ning J S, Wang Z T, Chao N F. (2016). Research status and progress of international new generation satellite gravity exploration program (in Chinese), *Geomatics and Information Science of Wuhan University*, 41(1):1-8
- Ning J S. (2001). Following the Developments of the World, Devoting to the Study on the Earth Gravity Field (in Chinese). *Geomatics and Information Science of Wuhan University*, 26(6): 471-474,486

- Pang Z X, Ji J F, Xiao Y, et al. (2012). Estimation of the Resolution of Earth's Gravity Field for GRACE Follow-On Using the Spectrum Method (in Chinese). *Acta Geodaetica et Cartographica Sinica*, 41 (3) : 333-338
- QU QingLiang, CHANG XiaoTao, ZHU GuangBin, YU ShengWen, ZHOU Miao, LIU Wei (2021) Calibration of satellite gravity gradients based on ground gravity data. *Chinese Journal of Geophysics* (in Chinese), 64(8): 2590-2598
- Ran J J, Xu H Z, Shen Y Z, et al. (2012). Expected Accuracy of the Global Gravity Field for Next GRACE Satellite Gravity Mission (in Chinese). *Chinese Journal of Geophysics*, 55 (9) :2898-2908
- Shen Y Z. (2017). Algorithm Characteristics of Dynamic Approach-based Satellite Gravimetry and its Improvement Proposals (in Chinese). *Acta Geodaetica et Cartographica Sinica*, 46 (10) : 1308-1315
- Siemes C. 2018. GOCE Level 1b gravity gradient processing algorithms. Technical Report ESA-EOPSM-GOCE-TN-3397, Paris, France: European Space Agency.
- Stummer C, Siemes C, Pail R, et al. 2012. Upgrade of the GOCE Level 1b gradiometer processor. *Advances in Space Research*, 49(4): 739-752
- Sun, H., Cui, X., Xu, J., Ding, H., Zhang, M., Li, H., Wang, Z., Zhou, J., Chen, X. (2022). Progress of Research on the Earth's Gravity Tides and its Application in Geodynamics in China. *Pure and Applied Geophysics*, 1-17.
- Sun, H., Li, Q., Bao, L., Wu, Z., Wu, L. (2022). Advancements and trends in high-resolution modeling of global seafloor topography. *Journal of Wuhan University: Information Science Edition*, 47(10): 1555-1567.
- Tapley B D, Bettadpur S, Ries J C, et al. (2004). GRACE measurements of mass variability in the Earth system. *science*, 305(5683): 503-505
- Wang C Q, Xu H Z, Zhong M, et al. (2015). An Investigation On GRACE Temporal Gravity Field Recovery Using the Dynamic Approach (in Chinese). *Chinese Journal of Geophysics*, 58 (3) :756-766
- WU YunLong, GUO ZeHua, XIAO Yun, MA Lin (2021) L1 level construction method of satellite gravity gradiometry observations. *Chinese Journal of Geophysics* (in Chinese), 64(12): 4437-4448
- Xiao Y, Xia Z R, Wang X T. (2006). Error Analyses for Recovery of the Earth's Gravity Field by HL-SST Technique (in Chinese). *Acta Geodaetica et Cartographica Sinica*, 35 (2) :106-111
- Xiao Y, Yang Y X, Pan Z P, Liu X G, Sun Z M. (2023). Performance and Application of the Chinese Satellite-to-Satellite Tracking Gravimetry System. *Chinese Science Bulletin*. Doi/10.1360/TB-2022-1057
- Xu H Z, Shen Y Z. (2001). Simulation of recovering the gravitational potential model from ephemerides of CHAMP (in Chinese). *Geomatics and Information Science of Wuhan University*, 26(6):483-486
- Xu T H, Yang Y X. Recovering the Gravity Potential Model from the Ephemerides and Accelerometer of CHAMP (in Chinese). (2004). *Acta Geodaetica et Cartographica Sinica*, 33 (2) :95-99
- Yang Y, Wang J, Lou L, et al. (2022). Development status and prospect of satellite-based surveying (in Chinese). *Space: Science and Technology*, 2022, doi:10.16708/j.cnki.1000-758X.2022.0031
- Zhou, H., Luo, Z., Zhou, Z., Yang, F., Pail, R., Tu, L., Yeh, H-C., Yang, S. (2021). What Can We Expect from the Inclined Satellite Formation for Temporal Gravity Field Determination? *Surveys in Geophysics*, 42, 699-726.
- Zhou, H., Tang, L., Tan, D., Duan, H., Pail, R., Luo, Z., Zhou, Z. (2023a). Impacts of frequency-dependent instrument noise for next-generation gravimetric mission on determining temporal gravity field model. *Journal of Geodesy*, 97(23), 1-25.
- Zhou, H., Wang, P., Pail, R., Guo, X., Wu, Y., Luo, Z. (2023c). Assessment of a near-polar pair mission for detecting the Earth's temporal gravity field. *Geophysical Journal International*, 234, 852-869.
- Zhou, H., Zheng, L., Pail, R., Liu, S., Qing T., Yang, F., Guo, X., & Luo, Z. (2023b). The impacts of reducing atmospheric and oceanic de-aliasing model error on temporal gravity field model determination. *Geophysical Journal International*,

234, 210-227.

# Progress in Earth Gravity Model and Vertical Datum

Tao Jiang<sup>1</sup>, Yonghai Chu<sup>2</sup>, Xinyu Xu<sup>2</sup>, Taoyong Jin<sup>2,15</sup>, Zhongmiao Sun<sup>3</sup>, Qiujie Chen<sup>4</sup>, Jinyun Guo<sup>5</sup>, Xiaoyun Wan<sup>6</sup>, Yihao Wu<sup>7</sup>, Yanguang Fu<sup>8</sup>, Lin He<sup>9</sup>, Xinwei Guo<sup>10</sup>, Yong Su<sup>11</sup>, Wei Liang<sup>2</sup>, Yongjun Jia<sup>12</sup>, Fukai Peng<sup>13</sup>, Lianjun Yang<sup>2</sup>

<sup>1</sup> Chinese Academy of Surveying and Mapping, Beijing, China

<sup>2</sup> School of Geodesy and Geomatics, Wuhan University, Wuhan, China

<sup>3</sup> Xi'an Research Institute of Surveying and Mapping, Xi'an, China

<sup>4</sup> Tongji University, Shanghai, China

<sup>5</sup> College of Geodesy and Geomatics, Shandong University of Science and Technology, Qingdao, China

<sup>6</sup> School of Land Science and Technology, China University of Geosciences, Beijing, China

<sup>7</sup> School of Earth Sciences and Engineering, Hohai University, Nanjing, China

<sup>8</sup> First Institute of Oceanography, Ministry of Natural Resources, Qingdao, China

<sup>9</sup> School of Resource Environmental Science and Engineering, Hubei University of Science and Technology, Xianning, China.

<sup>10</sup> Geodetic Data Processing Center of Ministry of Natural Resources, Xi'an, China

<sup>11</sup> Southwest Petroleum University, Chengdu, China

<sup>12</sup> National Satellite Ocean Application Service, Beijing, China

<sup>13</sup> College of Surveying and Geo-informatics, Tongji University, Shanghai, China

<sup>14</sup> School of Geodesy and Geomatics, Hubei LuoJia Laboratory, Wuhan University, Wuhan, China

## 1 Realization of the International Height Reference System in the region of Mount Qomolangma

For the first time, the orthometric height of Mount Qomolangma based on the International Height Reference System (IHRIS) is determined and released in the 2020 height measurement campaign of Mount Qomolangma. In order to realize the IHRIS in the region of Mount Qomolangma, the scheme of establishing high precision gravimetric geoid model in this area is adopted. Based on the spectral combination approach and data-driven spectral determination method, the gravimetric quasigeoid model in the area of Mount Qomolangma is computed from the combination of airborne and terrestrial gravity data. Optimal reference gravity model, its truncation degree and spherical cap integration radius are chosen through comprehensive test. The validation against highly accurate GNSS leveling measured height anomalies at 61 benchmarks indicates that the accuracy of the gravimetric quasigeoid model reaches 3.8 cm and the addition of airborne gravity data improves the model accuracy by 51.3 %. The interpolation method considering height difference correction is proposed for interpolating the height anomaly at the summit from the quasigeoid model. The rigorous formula for geoid–quasigeoid separation considering topographic masses is used for converting the height anomaly to the geoid undulation at the summit. Based on the IHRIS defined gravity potential value  $W_0$  and the GRS80 reference ellipsoid, and using the newly observed ground gravity at the summit, the high precision geoid undulation of Mount Qomolangma in the IHRIS is determined.

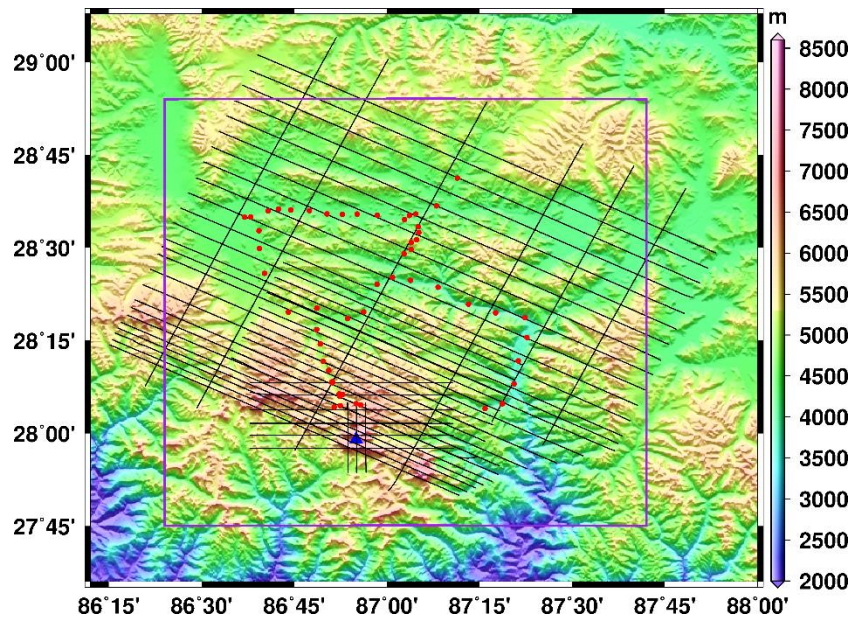


Figure 1. Airborne gravity survey lines and GNSS leveling points in the region of Mount Qomolangma (Blue triangle: Mount Qomolangma; Black Line: airborne gravity survey lines; Red point: GNSS leveling points; Purple rectangle: domain of quasigeoid model)

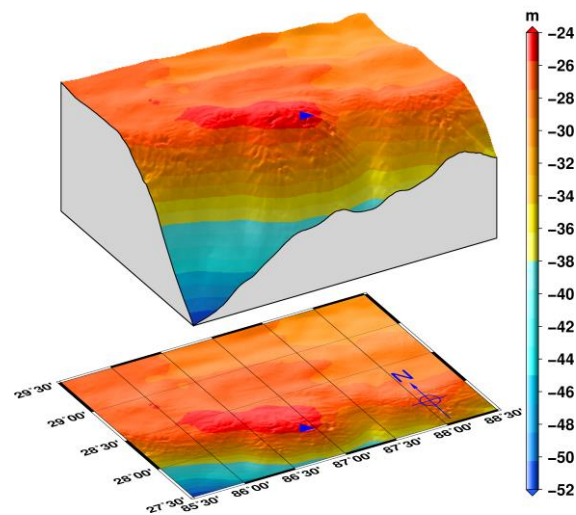


Figure 2. Gravimetric quasigeoid model computed from the combination of airborne and terrestrial gravity data (Blue triangle: Mount Qomolangma)

Table 1. Statistics of the differences between gravimetric geoid and GNSS leveling measured height anomalies (m)

Computation scheme	Min	Max	Mean	Std
Scheme 1 (Airborne + Ground)	0.148	0.333	0.270	0.038
Scheme 2 (Ground)	-0.129	0.270	0.169	0.078
Scheme 3 (Airborne + Ground)	0.166	0.371	0.314	0.048



## 2 The datum offset between the China's 1985 national vertical datum and global vertical datum

China's national height datum 1985, also known as China's national vertical datum 1985 (Abbreviated as CNVD1985) was determined in 1985 based on the tidal observation data of Qingdao gauge recording from 1952 to 1979. In order to eliminate the impact of the 18.6-year tidal long period, the data are divided into 10 groups, each with a data duration of 19 years. The moving average method with a sliding step of 1 year, is used to derive 10 groups of mean sea level (MSL), and then the average is taken as the mean sea level in the Yellow Sea, which is the zero-height level surface of CNVD1985. Although the MSL at the Qingdao tide gauge shows a sea level rising at the rate of 1.07 mm/yr from 1952 to 1980 and increased to 1.62 mm/yr from 1980 to 2011 (Wu et al., 2020), the height datum is usually regarded as a stable and constant reference for measuring height. From the point of view of gravity field and height datum, local MSL is a local tidal datum that is not consistent with global geoid.

As one of the equipotential surfaces of the Earth's gravity field, the geoid is an equipotential surface defined by a potential ( $W_0$ ) that fits best the undisturbed mean sea level in a least squares sense (Amin et al., 2019). It is the classical Gauss–Listing definition of geoid and is usually selected as the global vertical datum (GVD). In the past few decades, satellite technology has opened a new era of earth exploration from the space. The satellite altimetry and satellite gravimetry provide a new space technology that can directly measure the internal structure and the surface of the Earth. Several global mean sea surface (MSS) height models with a resolution of  $1' \times 1'$  or  $2' \times 2'$ , such as DTU15MSS, DTU18MSS, have been released due to the development of satellite altimetry technology and the accumulation of data. Satellite gravity has greatly improved the medium and long wavelength accuracy of the Earth's gravity field information (Jiang et al., 2020). High-resolution global gravity model (GGM), such as SGG-UGM-2 (Liang et al., 2020), can be combined with MSS to quantify the potential ( $W_0$ ).

The vertical datum offset can be defined as a geometric quantity (distance difference  $\Delta H$ ) or as a physical parameter (gravity potential difference  $\Delta W$ ), their relationship is expressed as  $\Delta H = -\Delta W/\gamma$ . Where, the gravity potential difference  $\Delta W$  is the potential ( $W_0^L$ ) of local vertical datum (CNVD1985) minus the potential ( $W_0$ ) of GVD, i.e.  $\Delta W = W_0^L - W_0$ ,  $\gamma$  is the normal gravity of Qingdao gauge station. So, the key problem of derive datum offset comes down to computing the  $W_0^L$  and  $W_0$ .

For the computation and analysis of the vertical datum offset, the following general parameters and model were adopted:

1. The geodetic reference system: GRS80, WGS84 and CGCS2000 (Table 2).
2. Mean sea surface: DTU15MSS. During the computation, the geodetic height of DTU15MSS must be transformed from T/P ellipsoid to GRS80, WGS84 and CGCS2000 ellipsoid. Only 33951 grid points with a bathymetry greater than 2000m are kept considering to reduce the impact of tide offshore.
3. Global gravity model: EGM2008 (Pavlis et al., 2012), EIGEN-6C4 (Förste et al., 2014) and SGG-UGM-1 (Liang et al., 2018).



Table 2. Basic parameters of the geodetic reference system

Geodetic reference system	Equatorial radius $a$ (m)	Reciprocal flattening $1/f$	geocentric gravitational constant $GM$ ( $m^3s^{-2}$ )	Angular velocity $\omega$ (rad/s)	Normal gravity potential $U_0$ ( $m^2s^{-2}$ )
GRS80	6378137	298.257222101	$3.986005000 \times 10^{14}$	$7.292115 \times 10^{-5}$	62636860.8500
WGS84	6378137	298.257223563	$3.986004418 \times 10^{14}$	$7.292115 \times 10^{-5}$	62636851.7146
CGCS2000	6378137	298.257222101	$3.986004418 \times 10^{14}$	$7.292115 \times 10^{-5}$	62636851.7149

Firstly, if the GPS/Leveling data of point  $P$  is available, the gravity potential  $W_0^L$  is computed by(Li et al.,2017):  $W_0^L = W^P + H^* \bar{\gamma}$ . Where,  $H^*$  is normal height of point  $P$  reference to CNVD1985 zero-height point,  $\bar{\gamma}$  is mean normal gravity along the normal gravity line passing point  $P$ . And the  $W^P$  is gravity potential of point  $P$ , which can be computed by spherical harmonic synthesis. The gravity potential ( $W_0^L$ ) of CNVD1985 zero-height point is computed based on 152 GPS/leveling measurements around Qingdao (Figure 3). We did not use nationwide GPS/leveling data for calculation as we did in other study(He & Chu & Xu & Zhang,2019), which was mainly due to the fact that the error would be larger if the distance between leveling points was too far away, while the error of leveling data around Qingdao would be small. Therefore, the precision of the local vertical datum potential calculated by using the level data around the reference point will be better.

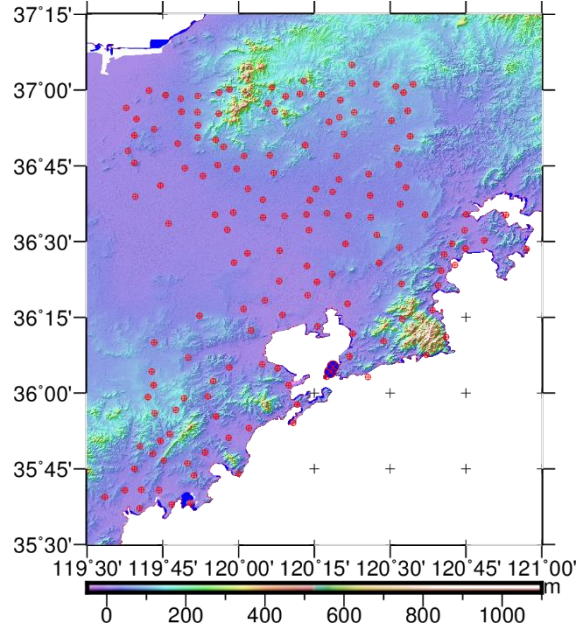


Figure 3. The distribution of GPS/leveling measurements around Qingdao

Then, a potential ( $W_0$ ) must be chose or computed for GVD. In the general formula of physical geodesy, it is usually specified that  $W_0 = U_0$ . This could make the formula or function simple and easy. A good method for the potential ( $W_0$ ) is computed it using MSS and GGM according to the definition of Gauss-Listing geoid, i.e.  $W_0 = W_{MSS}$ . For every grid point of DTU15MSS, the gravity potential  $W_{MSS}^i$  is computed by spherical harmonic synthesis and the final average is  $W_{MSS} = \frac{1}{N} \sum_{i=1}^N W_{MSS}^i$ . If the same GGM is used to compute the average of

$W_{MSS}$  for different geodetic reference system, the value from CGCS2000 and WGS84 are almost equal (Table 3) due to the parameters of these two reference systems are almost the same (Table 2). If keeping the same geodetic reference system, the value from EGM2008 and EIGEN-6C4 are almost equal, but the value from SGG-UGM-1 shows a slightly different. In any case, the numerical results calculated by the three GGMs are of comparable accuracy.

Two equipotential surfaces defined by  $U_0$  or  $W_{MSS}$  are selected as the GVD, the gravity potential difference between CNVD1985 and GVD can be expressed as  $\Delta W_1 = U_0 - W_0^L$  and  $\Delta W_2 = W_{MSS} - W_0^L$ . The corresponding geometric distance difference is obtained as  $\Delta H_1 = \Delta W_1/\gamma$  and  $\Delta H_2 = \Delta W_2/\gamma$ . We calculated the gravitational potential difference and datum offset, which are all listed in Table 3.

From the numerical results, we can find that the CNVD1985 is about 24.2cm (SGG-UGM-1, CGCS2000) below the GVD defined by  $U_0$ , but about 19.6cm above the GVD defined by Gauss-Listing geoid. There is a difference of about 1~3cm between the numerical results when using EGM2008, EIGEN-6C4, and SGG-UGM-1 models to calculate. The choice of geodetic reference system has almost no impact on the calculation results, which is obvious. Because the actual vertical datum definition is independent of the geodetic reference system. Although the equipotential surfaces defined by  $U_0$  has important theoretical significance, but it is inconsistent with the global mean sea level. So, Gauss-Listing geoid is the best choice for GVD.

Table 3. The gravity potential difference and vertical datum offset between Qingdao tide gauge and global datum defined by  $U_0$  or  $W_{MSS}$

GGM	Geodetic reference system	$W_0^L$ ( $m^2s^{-2}$ )	$U_0$ ( $m^2s^{-2}$ )	$W_{MSS}$ ( $m^2s^{-2}$ )	$\Delta W_1$ ( $m^2s^{-2}$ )	$\Delta H_1$ (m)	$\Delta W_2$ ( $m^2s^{-2}$ )	$\Delta H_2$ (m)
EGM2008	GRS80	62636862.9503	62636860.8500	62636865.1762	2.1003	-0.2144	-2.2259	0.2272
	WGS84	62636853.8143	62636851.7146	62636856.0389	2.0997	-0.2143	-2.2246	0.2270
	CGCS2000	62636853.8147	62636851.7149	62636856.0389	2.0998	-0.2143	-2.2242	0.2270
EIGEN-6C4	GRS80	62636863.1150	62636860.8500	62636865.1768	2.2650	-0.2312	-2.0618	0.2104
	WGS84	62636853.9790	62636851.7146	62636856.0396	2.2644	-0.2311	-2.0606	0.2103
	CGCS2000	62636853.9793	62636851.7149	62636856.0396	2.2647	-0.2311	-2.0603	0.2103
SGG-UGM-1	GRS80	62636863.2201	62636860.8500	62636865.1393	2.3701	-0.2419	-1.9192	0.1959
	WGS84	62636854.0841	62636851.7146	62636856.0021	2.3695	-0.2418	-1.9180	0.1957
	CGCS2000	62636854.0845	62636851.7149	62636856.0021	2.3696	-0.2418	-1.9176	0.1957

### 3 Geoid modeling from the combination of satellite gravity model, terrestrial and airborne gravity data

In 2017, The Joint Working Group (JWG) 0.1.2 (Strategy for the Realization of the International Height Reference System (IHRIS)) and JWG 2.2.2 (the 1 cm geoid experiment) of the International Association of Geodesy (IAG) jointly launched the Colorado geoid experiment. The goal of this experiment is to assess the repeatability of gravity potential values as IHRIS coordinates using different geoid modeling methods, and to compare and evaluate the corresponding gravimetric geoid models. In this frame, the National Geodetic Survey (NGS) of the United States of America (USA) provided the geodesy community with terrestrial, airborne

gravity and GPS (global positioning system) leveling data as well as digital elevation model (DEM) for a mountainous area of about 400 thousand km<sup>2</sup> in Colorado, which allowed the comparison of different methods and softwares for geoid computation using the same input dataset in this challenging area.

We used the spectral combination method for geoid determination in Colorado as our contribution to the geoid experiment. The gravimetric geoid model obtained from the combination of satellite gravity model GOCO06S and terrestrial gravity data agrees with the GPS leveling measured geoid heights at 194 benchmarks in 5.8 cm in terms of the standard deviation of discrepancies, and the standard deviation reduces to 5.3 cm after including the GRAV-D airborne gravity data collected at ~6.2 km altitude into the data combination. The contributions of airborne gravity data to the signal and accuracy improvements of the geoid models were quantified for different spatial distribution and density of terrestrial gravity data. The results demonstrate that, although the airborne gravity survey was flown at a high altitude, the additions of airborne gravity data improved the accuracies of geoid models by 13.4% - 19.8% in the mountainous area (elevations > 2000 m) and 12.7% - 21% (elevations < 2000 m) in the moderate area in the cases of terrestrial gravity data spacings are larger than 15 km.

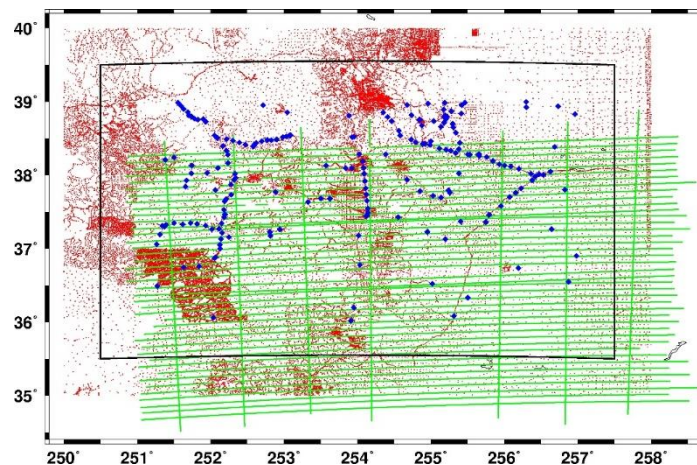


Figure 4. Distribution of terrestrial, airborne gravity and historic GPS leveling data in Colorado. Red points represent terrestrial gravity observations. Green lines represent GRAV-D airborne gravity data. Blue diamonds represent historic GPS leveling benchmarks. The computation area is bounded by the black rectangular.

Table 4. Statistics of the differences between the gravimetric geoid models based on different data combination modes and the GPS leveling measured geoid heights (unit: m)

Gravimetric geoid model	Min	Max	Mean	SD
EGM2008	0.625	1.008	0.847	0.061
EIGEN-6C4	0.575	0.999	0.851	0.067
XGM2019	0.563	1.034	0.836	0.075
GOCO06S + Terrestrial	0.703	1.029	0.864	0.058
GOCO06S + Terrestrial + Airborne	0.710	1.048	0.863	0.053

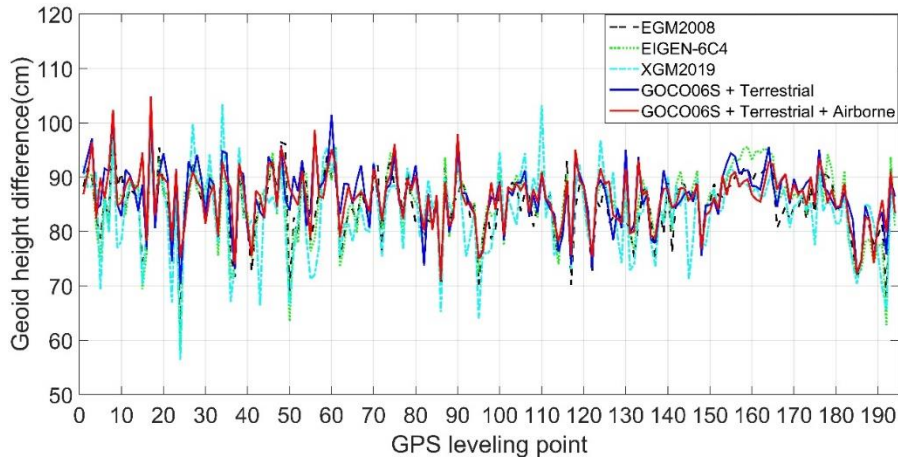


Figure 5. Differences between the gravimetric geoid models based on different data combination modes and the GPS leveling measured geoid heights. Results for EGM2008, EIGEN-6C4 and XGM2019 are included.

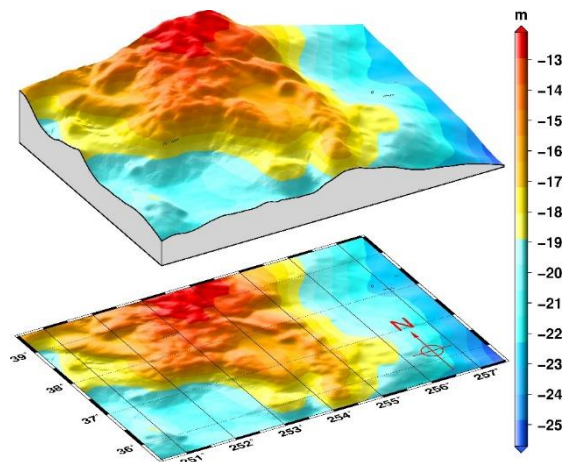


Figure 6. Gravimetric geoid model derived from the combination of satellite gravity model GOCO06S, terrestrial and GRAV-D airborne gravity data

Accurate knowledge of coastal gravity field is of importance for geodetic mean dynamic topography modelling, which is useful for studying coastal ecosystem processes and sea level change, as well as facilitating other offshore activities. However, coastal zones often present multiple challenges for quasi-geoid/geoid recovery. First, the satellite altimeter-derived data contain larger errors in coastal zones than in open seas, due to the land and calm water contamination on the return waveforms and degradation of the applied corrections. The poor data coverage in coastal boundary exacerbates this problem, which remains a barrier on coastal quasi-geoid/geoid determination. Airborne gravimetry provides seamless measurement both onshore and offshore with uniform accuracies, which can alleviate the mentioned problem of gravity field recovery in coastal areas.

We study the role of airborne data for gravity field recovery in a coastal region and the possibility to validate coastal gravity field model against recent altimetry data (CryoSat-2, Jason-1, and SARAL/Altika). Moreover, we combine airborne and ground-based gravity data for regional refinement and quantify and validate the contribution introduced by airborne data. Numerical experiments in the Gippsland Basin over the south-eastern coast of Australia show that the effects introduced by airborne gravity data appear as small-scale patterns on the centimetre scale in terms of quasi-geoid heights. Numerical results demonstrate that the



combination of airborne data improves the coastal gravity field, and the recent altimetry data can be potentially used to validate the high-frequency signals introduced by airborne data. The validations of different models against the recent altimeter-derived quasi-geoid heights demonstrate that the incorporation of airborne data improves the local quasi-geoid in coastal areas. The validation results are shown in Figure 4 and Table 4, the comparisons with other existing models show that QGland\_TSA (gravimetric quasi-geoid over the Gippsland Basin modelled with terrestrial (T), satellite altimetry (S), and airborne (A) gravity data) is of highest quality. QGland\_TS, AGQG2017, and EGM2008 have comparable accuracies, and all these three models are worse than QGland\_TSA, by the magnitudes of approximately 5–8 mm. The standard deviation (SD) of the misfit between altimeter-derived quasi-geoid heights and gravimetric quasi-geoid decreases from 0.028 to 0.023 m, when validating QGland\_TS and QGland\_TSA, respectively. The accuracies of EIGEN-6C4, GECO, and SGG-UGM-1 are between 3.4 and 3.7 cm, all of which are worse than the four models mentioned above. GOCO05c is of worst quality, and its accuracy decreases to 4.8 cm.

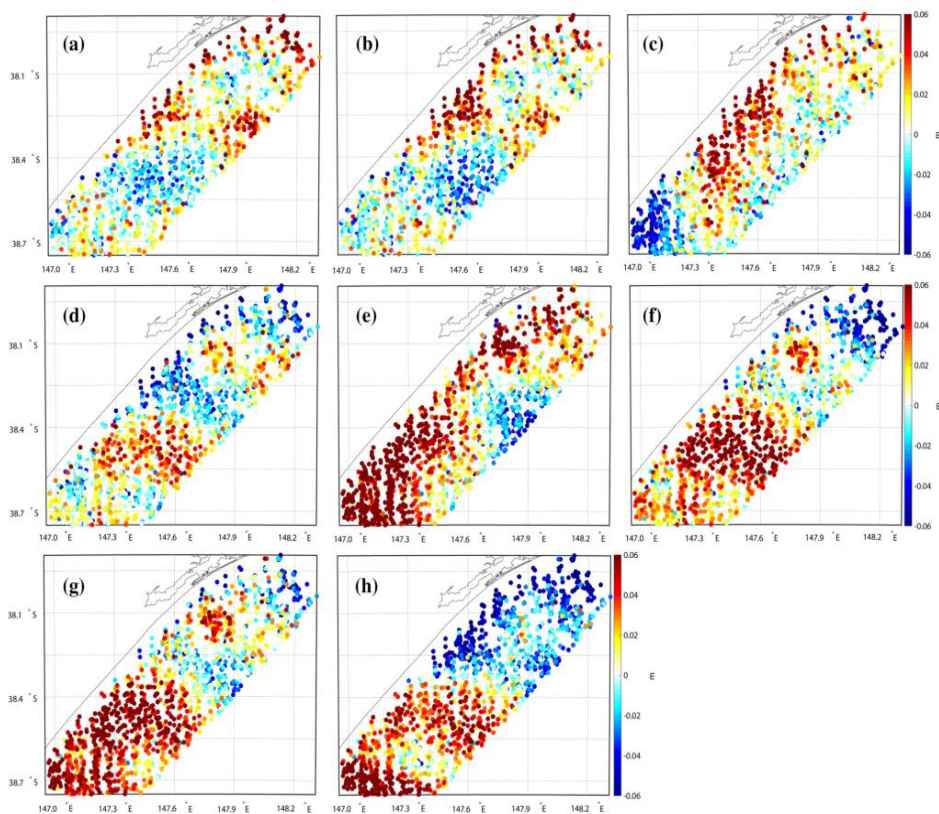


Figure 7. Evaluations of different gravimetric quasi-geoid models with the altimeter-derived quasi-geoid heights only located within the boundary of airborne survey. a QGland\_TSA, b QGland\_TS, c AGQG2017, d EGM2008, e EIGEN-6C4, f GECO, g SGG-UGM-1 and h GOCO05c. Note that the mean values of the misfit between gravimetric quasi-geoid models and altimeter-derived data are removed.

Table 5. Statistics of validations of different gravimetric quasi-geoids with the altimeter-derived quasi-geoid heights (units: m)

Quasi-geoid	Max	Min	SD
QGland_TSA	0.136	-0.169	0.023
QGland_TS	0.163	-0.189	0.028
AGQG2017	0.148	-0.179	0.031
EGM2008	0.171	-0.165	0.029
EIGEN-6C4	0.214	-0.127	0.037
GECO	0.150	-0.157	0.037
SGG-UGM-1	0.178	-0.138	0.034
GOCO05c	0.155	-0.194	0.048

## 4 Global Static Gravity Field Modeling

### Global static gravity field recovering from satellite observations

The satellite gravity models SWPU-GRACE2021S, GOSG02S, Tongji-GMMG2021S and WHU-SWPU-GOGR2022S are constructed based on GRACE and GOCE satellite observations by different organizations, such as Wuhan University, Tongji University, Southwest Petroleum University and Guangdong University of Technology.

SWPU-GRACE2021S model up to degrees and order (d/o) 180 is determined based on the dynamic approach with the GRACE data throughout the entire mission cycle of 15 years. GOSG02S up to d/o 300 is an improved GOCE-only model of GOSG01S derived from reprocessed GOCE data by combining the 300 d/o SGG (Satellite Gravity Gradient) normal equation via the direct least squares approach, 130 d/o SST-hl (Satellite-to-Satellite in high-low mode) normal equation via the point-wise acceleration approach. WHU-SWPU-GOGR2022S is determined by combining the normal equation of GOSG02S and that of SWPU-GRACE2021S via the VCE technique. Tongji-GMMG2021S is a combined model up to d/o 300 by combining 300 d/o GOCE gravity gradient normal equation via the direct method, the 180 d/o Tongji-Grace02s normal equation via the modified short-arc approach and the Kaula's regularization constraints.

The XGM2019 model and GPS/leveling data are used for precision analysis of, SWPU-GRACE2021S, GOSG02S, WHU-SWPU-GOGR2022S and Tongji-GMMG2021S in frequency domain and space domain respectively. The results show that the accuracy of GOSG02S and WHU-SWPU-GOGR2022S is comparable to GO\_CONS\_GCF\_2\_DIR\_R6, GO\_CONS\_GCF\_2\_TIM\_R6, GO\_CONS\_GCF\_2\_SPW\_R5, GOCO06s and Tongji-GMMG2021S that use the entire mission data of GOCE satellite and the accuracy differences are in the order of millimeters. The SWPU-GRACE2021S model has the same accuracy below degree/order 160 as the international mainstream of GRACE satellite gravity field models, i.e., ITSG-Grace2018s and Tongji-Grace02s.

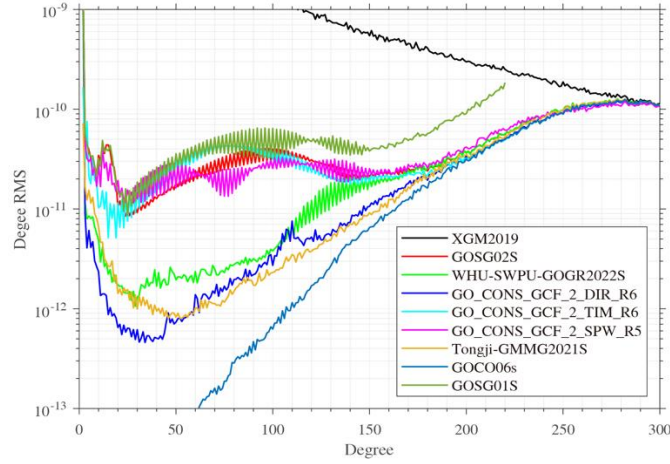


Figure 8. Degree Error RMS of models with respect to XGM2019.

Table 6. Statistical results of comparison with GPS/Leveling data in the USA (6169 points) and mainland China (649 points) (unit: m)

	<b>Model</b>	<b>Max</b>	<b>Min</b>	<b>Mean</b>	<b>STD</b>
USA	GOSG02S	1.046	-2.184	-0.562	0.441
	WHU-SWPU-GOGR2022S	1.050	-2.179	-0.561	0.440
	GO_CONS_GCF_2_DIR_R6	1.080	-2.196	-0.565	0.438
	GO_CONS_GCF_2_TIM_R6	1.038	-2.221	-0.554	0.432
	Tongji-GMMG2021S	1.068	-2.193	-0.561	0.437
	GOCO06s	1.001	-2.234	-0.557	0.435
China	GOSG02S	1.023	-1.690	0.073	0.388
	WHU-SWPU-GOGR2022S	1.024	-1.689	0.070	0.389
	GO_CONS_GCF_2_DIR_R6	0.969	-1.640	0.070	0.391
	GO_CONS_GCF_2_TIM_R6	0.963	-1.584	0.075	0.385
	Tongji-GMMG2021S	1.070	-1.665	0.072	0.389
	GOCO06s	0.953	-1.578	0.072	0.384

### Determination of high-resolution Earth's gravity field model

Based on the EHA-CT (the theory of the Ellipsoidal Harmonic Analysis and Coefficient Transformation) method, we develop a new  $5' \times 5'$  spatial resolution gravity field model SGG-UGM-2 up to degree 2190 and order 2160 by combining SGG (Satellite Gravity Gradient) and SST-hl (Satellite-to-Satellite in high-low mode) observations of GOCE (Gravity field and steady-state Ocean Circulation Explorer) mission, the ITSG-Grace2018 normal equation system, marine gravity anomalies recovered from satellite altimetry data and EGM2008-derived continental gravity data. The ellipsoidal harmonic coefficients of degrees 251—2159 are estimated by solving the block-diagonal form normal equations of the ground gravity anomalies (including the marine gravity data). The coefficients of degrees 2-250 are determined by combining the normal equations of satellite observations and ground gravity anomalies. The variance component estimation technique is used to estimate the relative weights of different observations.

The new SGG-UGM-2 model has a promising performance in the GPS/Leveling

validation and error analysis compared to EGM2008 in the frequency and spatial domains. The GPS/Leveling data in China and the USA are used to validate the model SGG-UGM-2, together with EIGEN-6C4, SGG-UGM-1, GECO and EGM2008. SGG-UGM-2 shows the best performance in the USA, as indicated by the statistics of the differences between model-derived quasi-geoidal/geoidal heights and GPS/Leveling data, and their histograms and empirical variograms. Due to the contribution of the new GRACE normal equation and the new marine gravity anomalies, SGG-UGM-2 has a slightly better performance than that of its predecessor SGG-UGM-1 in both mainland China, the USA and the coastal city Qingdao of China. This indicates that the methods used for developing SGG-UGM-2 are valid and can be used for developing future SGG-UGM series by individually processing available terrestrial gravity datasets (e.g. mainland China). In addition, the accuracy of the new model SGG-UGM-2 indicates that this model will provide an alternative for users.

Table 7. Statistical results of comparison with GPS/Leveling data in the USA (6169 points) and mainland China (649 points) (unit: m)

	Model	Max	Min	Mean	STD	RMS
USA	EGM2008	0.360	-1.396	-0.511	0.284	0.584
	SGG-UGM-1	0.317	-1.407	-0.511	0.280	0.583
	SGG-UGM-2	0.386	-1.394	-0.511	0.277	0.578
	GECO	0.313	-1.391	-0.513	0.281	0.585
	EIGEN-6C4	0.397	-1.392	-0.512	0.282	0.585
China	EGM2008	1.729	-1.535	0.239	0.240	0.339
	SGG-UGM-1	0.744	-0.618	0.246	0.162	0.294
	SGG-UGM-2	0.744	-0.603	0.246	0.161	0.292
	GECO	1.165	-0.847	0.244	0.180	0.303
	EIGEN-6C4	0.729	-0.698	0.243	0.157	0.289

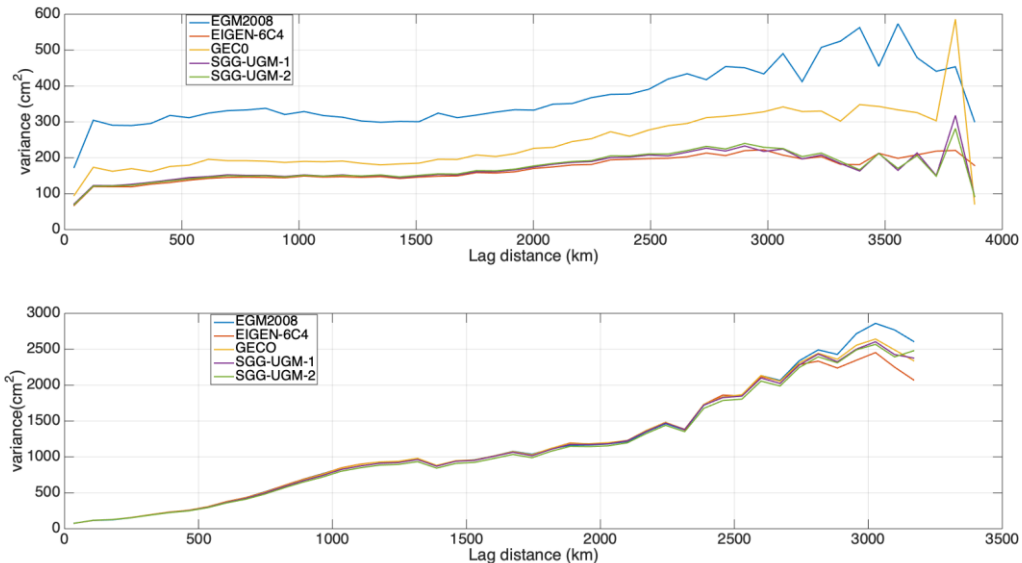


Figure 9. The empirical variograms of the differences with respect to the GPS/leveling data sets in China (top one) and USA (bottom one) for EGM2008, SGG-UGM-1, SGG-UGM-2, GECO and EIGEN-6C4.



## 5 Satellite Altimetry

### Altimetry Data Processing

Satellite altimetry is a key technology for obtaining global sea surface height. In 2021, China built the first ocean dynamic environment satellite constellation, which included the HY-2B, HY-2C, and HY-2D ocean dynamic environment satellites. The HY-2B satellite is a sun-synchronous orbit satellite. HY-2C and HY-2D satellites are non-sun-synchronous orbital satellites with inclinations of  $66^\circ$  (Figure 1).

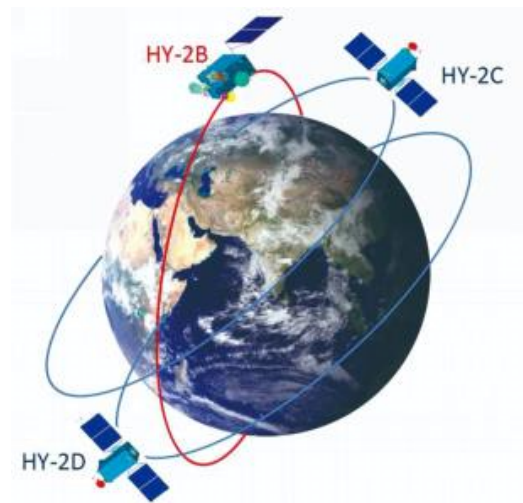


Figure 10. The orbits of HY-2B/2C/2D ([http://www.nsoas.org.cn/news/content/2021-05/25/23\\_8462.html](http://www.nsoas.org.cn/news/content/2021-05/25/23_8462.html))

The radar altimeters are one of the main payloads of China's ocean dynamic environment satellite constellation. In 2023, two synthetic aperture radar (SAR) altimeter satellites were launched. The second constellation of the ocean dynamic environment satellite under development is also equipped with SAR altimeter (Lin and Jia, 2022). In recent years, relying on the HY-2 series of altimetry satellites, China has carried out a lot of relevant exploration. The orbit determination and other geophysical and environmental corrections, such as atmospheric correction, sea state bias, tropospheric correction, etc., are crucial for the precision of altimetry data. In addition, satellite altimetry is easily affected by sea-land changes in offshore areas (or by the environment around lakes), which may introduce much noise into the waveform and hence increase the uncertainties of determining the distance between the satellite and the water body surface. Chinese researchers proposed several re-tracking methods based on waveform decontamination, realignment, denoising, and derivation to obtain high-precision altimetry observations in nearshore areas and lakes. They also evaluated the impact of different re-tracking algorithms on the SAR altimeter.

Several studies were implemented to improve the precise orbit determination (Guo et al., 2022b, 2023) and sea state bias correction of altimetry satellites (Peng and Deng, 2020a; Peng et al., 2022). Guan et al. (2020) discussed the necessity of ionospheric delay filtering for satellite altimetry. For waveform retracking, Wang and Huang (2021) presented an upgraded strategy for decontaminating waveforms to improve altimeter-derived coastal SSHs. Compared with the old decontamination strategy, one important improvement of the update method is the

realignment of waveforms prior to decontamination. Another is that they adopted gate-based outlier judging criteria, which enable outlier detectors to treat different parts of the waveform with different criteria. To reduce the smoothness of the effective signal and suppress background noise as much as possible, Li et al.(2020) proposed a piecewise adaptive-norm trend filtering method to take advantage of different norms in the regularized framework. The results verified that the method was superior to the other three commonly used waveform filtering methods, i.e., Gaussian filtering, wavelet transform, EMD and trend filtering methods. Li et al. (2020) proposed a new waveform retracking method that combines waveform denoising and waveform derivatives by analyzing the limitations of existing retracking methods. Yuan et al. (2020) proposed a processing strategy using SSA for waveform retracking, which can improve the accuracy of the mean sea surface model. Peng and Deng (2020b) proposed a modified Brown-peaky retracker to handle land-contaminated waveforms with land returns observed in the waveform trailing edge and developed a seamless combination of multiple retrackers to retrieve improved along-track sea surface height (Peng et al., 2021).

Moreover, for the SAR altimeter, Gao et al. (2021) selected four waveform retrackers, including ICE1, multi-threshold, SAMOSA, and IceSheet, to analyze their re-tracking accuracy within 20km near the coast using the in-situ sea level data from global tide gauge stations. The results show that the SAR multi-threshold retracker can retain the most valid data and obtain the highest correlation as well as the smallest root mean square error of the difference between the derived sea surface heights and the tide gauge sea levels within 6 km offshore.

### **Marine Gravity and Bathymetry Inversion**

Earth's gravity field can provide important basic geospatial information support for research and development in earth science. Satellite altimetry is the main technical means for ocean gravity field recovery. China has mainly carried out several aspects of work, including analyzing the impact of different inversion methods on the accuracy, fusing multi-satellite data with HY-2 series, inverting the near-shore gravity field, discussing the possible accuracy improvement brought by SWOT, researching multi-source gravity observation data fusion, and introducing deep learning into the inversion of the gravity field.

Ouyang (2022) and Sun et al. (2022) discussed the research progress of satellite altimetry and its recovery of global marine gravity field and of seabed topography model. Based on the marine vertical deflection and gravity anomaly obtained through satellite altimetry data, Wang and Huang (2021) assessed the marine geoid determined using different methods, including the Molodensky method, least square collocation, Stokes formula, two-dimensional spherical FFT, and the satellite altimetry leveling method. The results indicate that the marine geoid directly obtained through the Molodensky method is the best with the lowest standard deviation. After evaluating the performance of HY-2A/GM data in marine gravity field recovery (Wan et al., 2020a) and assessing the HY-2A/GM data by deriving the gravity field and bathymetry over the Gulf of Guinea (Wan et al., 2020b), Wan et al. (2022) developed a global marine gravity anomalies dataset, named Global Marine Gravity Anomaly Version 1 (GMGA1), from multi-satellite altimeter data. Compared to worldwide products such as DTU17, S&S V31.1, as well as values from EGM2008, EIGEN-6C4, and XGM2019e\_2159, GMGA1 has an accuracy of around 3.3 mGal. Hao et al. (2023) enhanced short-wavelength marine gravity anomaly using depth data and generated the Global Marine Gravity Anomaly Version 2 (GMGA2) dataset, whose accuracy is 0.7 mGal higher than GMGA1.

Zhang et al. (2020) calculated the 1'×1' marine gravity field model over the South China Sea area and the verifications with published models and shipborne gravimetric data showed that HY-2A GM data is capable of improving marine gravity field modeling. In a global context, Zhang(2022) constructed global marine gravity results and validating results showed that the HY-2 dataset is capable of improving marine gravity anomaly recoveries and the accuracy of NSOAS22 with incorporated HY-2 data is comparable to DTU21 and SS V31.1. Meanwhile, another global 1'×1' marine gravity field model is inverted based on the vertical deflection approach and the remove-restore procedure by introducing the EGM2008 as the reference model. The root-mean-square of differences at grids are respectively 3.4 mGal and 1.8 mGal with DTU and SIO SS series models (Zhang et al., 2020b). They also found that the SSH-based method (depending on geoid undulations) performs better in estimating marine gravity anomalies near the coast, while the SSS-based method (depending on vertical deflections) is more advantageous in regions with intermediate ocean depths and seamounts (Figure 2). However, the SSS-based method shows limitations in areas with north-south directional ocean currents and topography features. In the deep ocean, both methods have similar accuracy (Zhang et al., 2021). Several other studies on altimeter-derived gravity models were carried out on the regional scale (Zhu et al., 2020; Guo et al., 2022a; Ji et al., 2021; Zhu et al., 2019), and the global scale (Zhu et al., 2022).

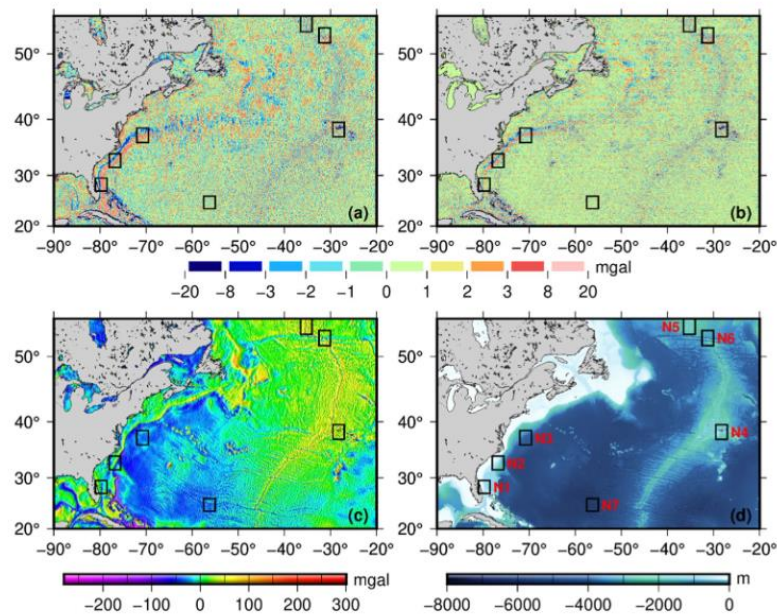


Figure 11. Residual marine gravity anomalies derived from SSS-based method and SSS-based method (Zhang et al. Journal of Geodesy, 2021)

Zhang et al. (2022) investigated the effect of the interpolation methods on accuracy when inverting the high spatial resolution marine gravity fields, especially in coastal areas where altimetry data is sparse. They presented an approach based on the ordinary kriging interpolation method, which uses the mean sea surface height as the constraint component in the vertical direction to improve the weight information of the ordinary kriging method and then improve the accuracy of the un-measured values. Compared to the ordinary kriging method, the experimental results show that this method can better assist in constructing marine gravity fields

at high spatial resolution in coastal regions. Li et al. (2021) compared several typical gravity models with shipboard gravity measurements in offshore and coastal regions of China. The root mean squares of deviations between gravity models and shipboard gravity are all more than 7 mGal in offshore regions and within the range of 9.5-10.2 mGal in coastal regions. Further analysis in coastal regions indicates that the new gravity models with new satellite missions including Jason-2, SARAL/Altika, and Envisat data have relatively higher accuracy, especially SARAL/Altika data, significantly improving the coastal gravity field. Yu and Hwang (2022) found that the altimeter-derived gravity anomalies showed an average gravity accuracy improvement of 9.5% by calibrated and scaled covariances of geoid gradients compared with that of the altimeter-derived gravity when using the initial variances. Through simulating SWOT SSH, they also found that multiple-cycle SWOT observations can deliver high-quality marine gravity anomalies (Yu et al., 2021). Taking the Surface Water and Ocean Topography (SWOT) wide-swath altimeter mission as an example, Jin et al. (2022) simulated one cycle of SWOT sea surface height measurements and compared it with the EGM2008 gravity field model. The vertical deflections determined by one cycle of SWOT data are better than those determined by the combined dataset of Jason-1/GM, Cryosat-2/LRM, and SARAL/GM data and can significantly improve the accuracy of east vertical deflection (Figure 3).

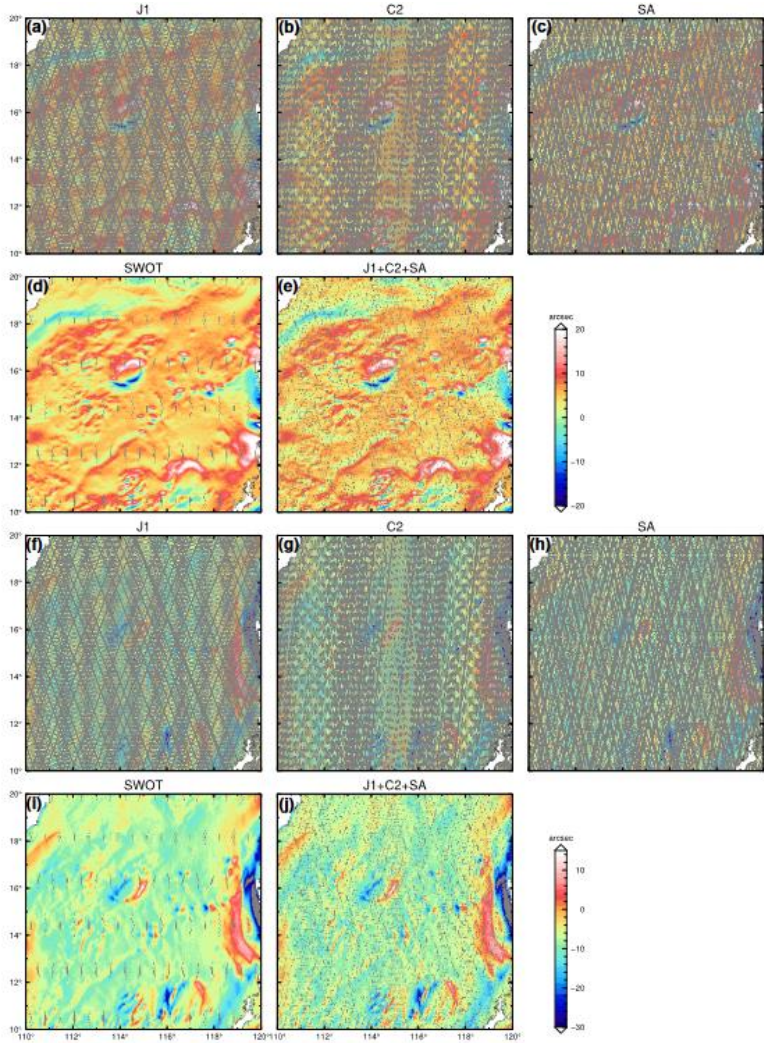


Figure 12. Vertical deflections from different SSH datasets in the South China Sea (Jin et al. Journal of Geodesy, 2022)



Regarding multi-source gravity data fusion, Zhao et al. (2022) improved the multi-surface function by introducing residual constraint factors to fuse the shipborne gravity data and satellite altimetry-derived gravity field model. Compared to the shipborne gravity data for verification, the improved method with residual constraint has the best accuracy, as well as the smallest extreme values and standard deviations. Furthermore, the improved method reduces the discrepancy between two kinds of data near the control shipborne measuring points and can extrapolate to the other areas to improve the accuracy of the satellite altimetry-derived gravity model with reasonably distributed residuals. Sun et al. (2021) developed a point-mass model with non-uniform point-mass density distribution based on iterative removal and recovery process. With the same shipborne gravity constraint, the fusion accuracy of the non-uniform density point-mass model can be improved by 12% compared with that of the uniform density point-mass model.

Annan and Wan (2022) recovered the bathymetry of the Gulf of Guinea using altimetry-derived gravity field products combined via a convolutional neural network. The spectral coherency analysis showed that the ship-borne depths correlated with the CNN-derived model better than with the other models. Wei et al. (2021) inverted bathymetry using HY-2A altimetry gravity data. An et al. (2022) proposed a GGM-based method using weighted averaging and distance factor to improve the accuracy of bathymetry modeling, by calculating short-wave gravity anomalies based on local seabed topography. Wan et al. (2023) computed altimetry-derived gravity gradients using the spectral method and verified their performance in bathymetry inversion using a back-propagation neural network, and the resultant bathymetries compare well with reference models from ship-borne depths, SRTM15+V2 and GEBCO\_2021. The effects of environmental correction errors and interferometric radar altimeter errors on marine gravity field inversion were discussed as well (Wan et al., 2020c, 2022b).

### **Sea Surface Height and its Change**

Global sea level change dataset is an important basis for understanding ocean dynamics, and satellite altimetry technology is currently the key technology for efficiently observing high-precision global sea surface. Domestic scholars have used deep learning to fuse altimetry and tide gauge data to improve the precision of coastal sea level changes. They also compared the accuracy of different mean dynamic topography (MDT) inversion methods. Furthermore, several products were generated, including a global mean sea surface height model, an Arctic mean sea surface height model and a global steric sea level change model.

Yang et al. (2021) proposed a fusion approach of altimetry and tide gauge data based on a deep belief network (DBN) method. They compared the fused sea level anomalies from the DBN method with those from the inverse distance weighted method, the kriging method, and the curvature continuous splines in tension method for different cases. The results show that the precision of the DBN method is better than that of the other three methods and is reduced by approximately 20% when the limited altimetry along-track data and in-situ tide gauge data are used. In addition, the sea level anomalies generated by the DBN model contain more spatial distribution information than others. Wu et al. (2022) compared the performances of the multivariate objective analysis (MOA) method with the rigorous least squares (LS) method. The results showed that the mean dynamic topography (MDT) derived from the LS method outperformed the MOA method, especially over coastal regions and ocean current areas. The

root mean square (RMS) of the discrepancies between the LS-derived MDT and the ocean reanalysis data was lower than the RMS of the discrepancies computed from the MOA method by a magnitude of 1–2 cm. Moreover, the geostrophic velocities calculated by the LS-derived MDT were more consistent with buoy data than those calculated by the MOA-derived solution by a magnitude of approximately 1 cm/s. After several regional sea surface case studies (Yuan et al., 2020b, 2021), Yuan et al. (2023) constructed a high-precision and high-resolution global MSS model SDUST2020 (Figure 4) from multi-source altimetry data of the past 30 years.

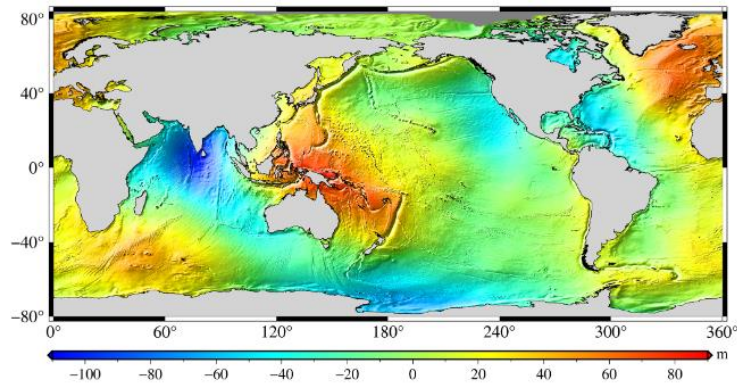


Figure 13. Global mean sea surface model SDUST 2020 (Yuan et al. Earth System Science Data, 2023)

By combining the measurements from ICESat and Cryosat-2 missions, Chen et al. (2022) published a new Arctic mean sea surface model named SUST22 (Figure 5), which has competitive precision and accuracy compared with other Arctic mean sea surface models.

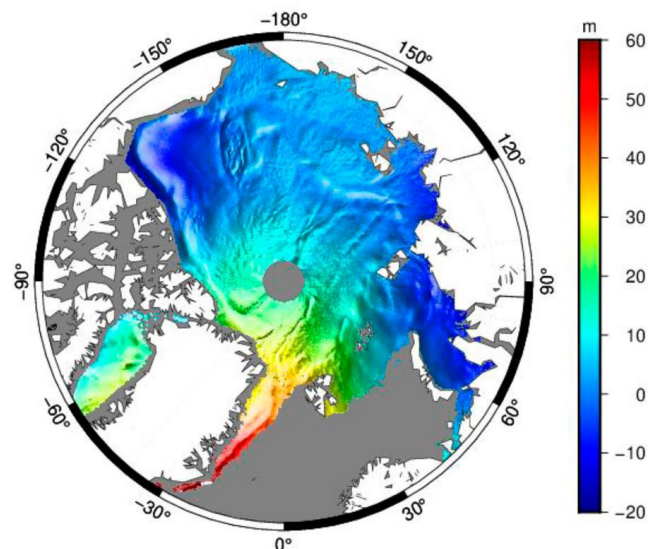


Figure 14. The Arctic mean sea surface model SUST22 (Chen et al. International Journal of Digital Earth, 2022)

In addition, Li et al. (2022) combined time-varying gravity data and satellite altimetry data to effectively determine the global steric sea level changes using sea level fingerprints and empirical orthogonal functions of the steric effect. Niu et al. (2020) used jointly the singular spectrum analysis and autoregressive moving average methods to predict sea level changes and crustal vertical changes in the near Japan seas, providing a new approach for predicting sea

level changes in the near sea.

### Ice Sheet and Water Level Changes

Satellite altimetry can also be applied in glaciology and hydrology. Several missions, such as Cryosat, Envisat, ICESat, SARAL, etc. were used to study the elevation and volume changes of ice sheets, and the water level changes of lakes, reservoirs, and other water bodies.

Sea ice is an important indicator of global climate change, and satellite altimetry can be used to obtain long-term and large-scale changes in sea ice. In recent years, several studies were using Cryosat, IceBridge, and Envisat to retrieve the ice thickness and ice freeboard variations in the Antarctic (Chen et al., 2019; Zhang et al., 2020; Gao et al., 2021), the Arctic (Zhang et al., 2019; Xiao et al., 2021; Zhang et al., 2021, 2022), and the Beaufort sea (Liu et al., 2019).

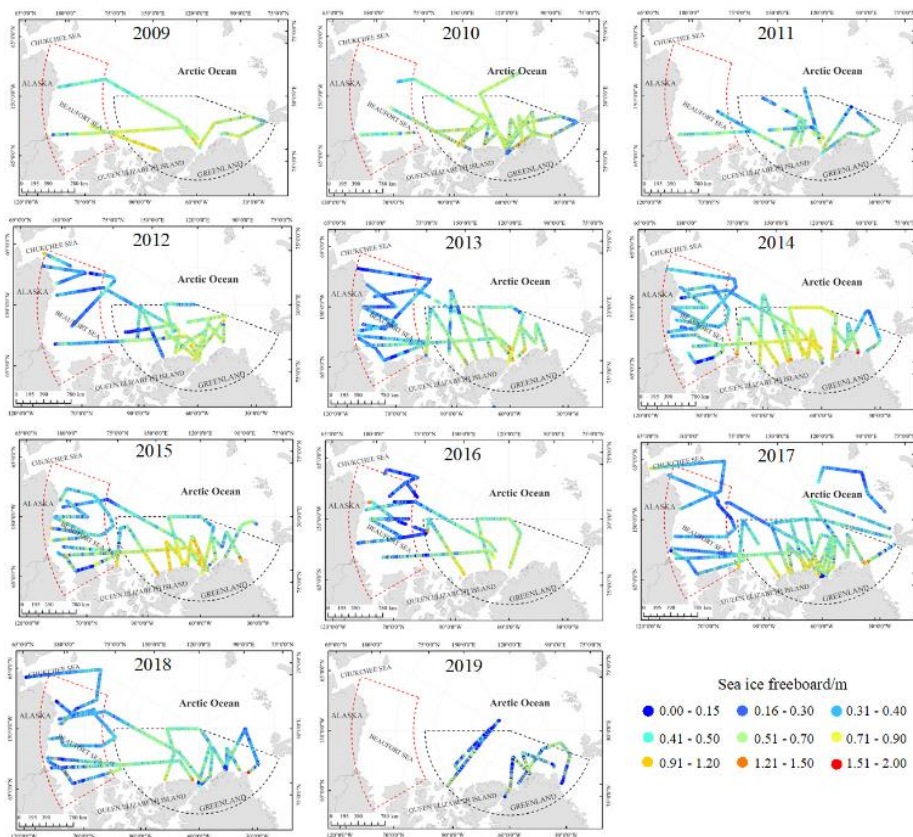


Figure 15. Arctic sea ice freeboard along the OIB flight lines from 2009 to 2019 (Zhang et al. IEEE Transactions on Geoscience and Remote Sensing, 2022)

In addition, Wang et al. (2022) used the laser altimetry ICESat-2 data to investigate the elevation and mass change of Svalbard from 2019 to 2021 by a hypsometric approach. The assessment shows that the Svalbard-wide elevation change rate is  $-0.775 \pm 0.225$  m/yr in 2019-2021, corresponding to the mass change of  $-14.843 \pm 4.024$  Gt/yr. Fan et al. (2022) obtained the time series of the ice surface elevation changes for 17 active lakes of the Antarctic using CryoSat-2 Baseline-D and ICESat-2 data from 2010 to 2020. Chen et al. (2020) combined the ICESat and CryoSat-2 altimeter datasets to monitor the activity of 17 glacial lakes in the Byrd glacier basin for 16 years. Then the water potential equation was used to obtain the drainage pathways map in the Byrd glacier basin, and subglacial lake activities were combined to analyze

the hydrological relationship among them. The results show that the subglacial lakes have a periodic pattern of water storage and drainage activities for about 2~3 years. With an improved slope correction and adjustment model, Chen and Zhang (2019) studied the elevation and volume change rate of the Greenland Ice Sheet between 2003 and 2009 using ICESat observations, and analyzed the melting status of each glacier drainage in detail. Chen et al. (2021) proposed a new elevation difference method for ice sheet elevation change determination with combined Cryosat-2 and ATM observations, and studied the volume change rate of the Greenland Ice Sheet, which showed obvious volume loss of  $-200.22 \text{ km}^3/\text{a}$  from 2010 to 2019.

Chao et al. (2019) used altimetry data from ENVISAT, ICESat, and SARAL to detect the water-level change in the Danjiangkou reservoir. The results show that the periodic signals between water levels from the altimetry mission, in situ observations and GRACE agree well with each other. For the lake areas, a modified retracker is used to determine heights from the first altimetric sub-waveform and applied to several lakes. Compared to the standard Ice retracker (0.11m), the new methodology can obtain lake levels with lower standard deviations (0.06m) (Yang, et al., 2021). Xu et al. (2022) employed ICESat and ICESat-2 altimetry data to obtain global water level changes for 22 008 lakes/reservoirs greater than  $1 \text{ km}^2$  (Figure 7). They found that across the globe, 78.84% of lakes exhibit a rising water level and the figure for reservoirs is 56.01%.

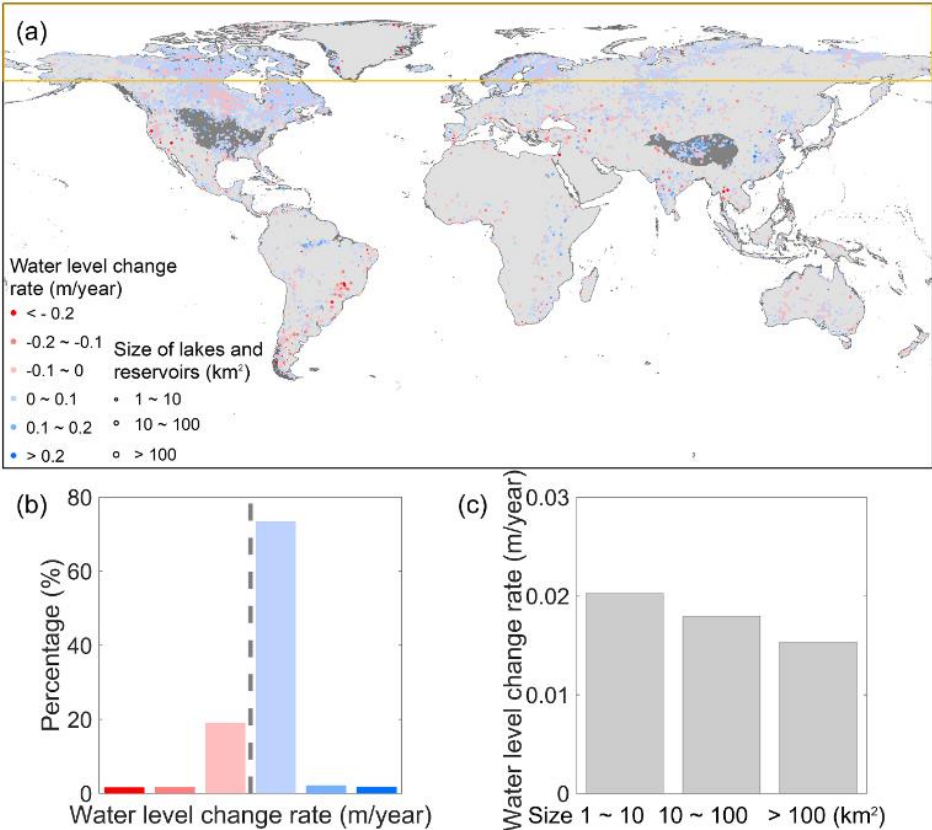


Figure 16. Global water level changes of 20776 lakes and 1232 reservoirs over 2003-2021 tracked by ICESat/ICESat-2 data (Xu et al. Environmental Research Letters, 2022)

To generate long-term and accurate lake level time series for the Tibetan lakes, Xu et al. (2022) presented a robust data processing strategy and constructed a 25-year-long lake level



time series of Ngangzi Co using the TOPEX/Poseidon-family altimeter data from October 1992 to December 2017. They found that the lake level increased by ~8 m from 1998–2017 and changed at different rates in the past 25 years. Based on ICESat/ICESat-2 altimetry and Landsat imagery, Xu et al. (2021) estimated trends in surface water levels of 52 water bodies (lakes and reservoirs) with areas larger than 1 km<sup>2</sup> in Australia. From 2003 to 2019, the area-weighted mean of water level change rates of them is -0.046 m/year, with 17 lakes (32.7%) with increasing water levels and 35 lakes (67.3%) decreasing with water levels.

## **6 Vertical datum transformation**

As sea level changes globally, accurate determination of the various vertical datums transformation plays an increasingly important role in analysis of sea level variation and ocean depth determination. Vertical datum transformation is the basic upon which to realize coastline definition and maritime features identification, and is of great importance for geospatial data expression under the same vertical datum.

From 2019 to 2023, We has made continuous breakthroughs and new progress in the vertical datum transformation between land and sea, mainly including three aspects as follows.

### **Construction and optimization of seamless chart datum model**

As the accuracy of the global ocean tide models in determining short-period tidal constituents has improved gradually, i.e., the EOT20 model shows an improvement of ~ 0.2 cm in the root-square sum value compared to FES2014 model in the global ocean. A series of researches on the construction of chart datum (CD) model were performed based on the previous studies.

The accuracy of the performance of seven global ocean tide models, i.e., DTU10, EOT11a, FES2014, GOT4.8, HAMTIDE12, OSU12 and TPXO8, were analyzed in the South China Sea. The accuracy was investigated using tidal results from 37 tide gauge stations. Results showed that the FES2014 model exhibiting slightly superior performance, with the root sum square value of the short-period tidal constituents was 9.35 cm. To figure out the accuracy of tide models in China seas, comparisons between the observations from the 33 tide gauge stations with continuous 3-year records and the three latest models, i.e., FES2014, EOT20, and TPXO9, were performed, which also indicated that the FES2014 model exhibiting slightly superior performance with the root sum square value of 7.91 cm. Meanwhile, these studies imply that the accuracy performance of the long-period tidal constituents has not received sufficient attention, which is vital to the establishment of the LNLW.

To construct LNLW model in China seas, the FES2014 tide model was adopted firstly. Statistical analysis on the distribution of the datum values of LNLW in the study area (15 °N–42 °N, 105°E–128 °E), showed that the LNLW values ranged from -22.72 to -446.74 cm. Comparison with results calculated from 16 tide gauge stations showed that the standard deviation was 13.02 cm. Owing to the Sa and Ssa tidal constituents provided by most global tide models are the simulation results of pure fluid dynamics (amplitude <1 cm), the TOPEX/Poseidon and Jason series satellite altimetry data have been adopted to construct the empirical model of Sa and Ssa tidal constituent, and then analyze the long-period tidal correction to the LNLW. It is indicated that the long-period tidal contribution should not be

neglected in LNLW construction. Furthermore, the latest CD datum has been constructed based on the combination of the empirical model and tide models. The spatial distribution of the LNLW value was shown in Figure 8.

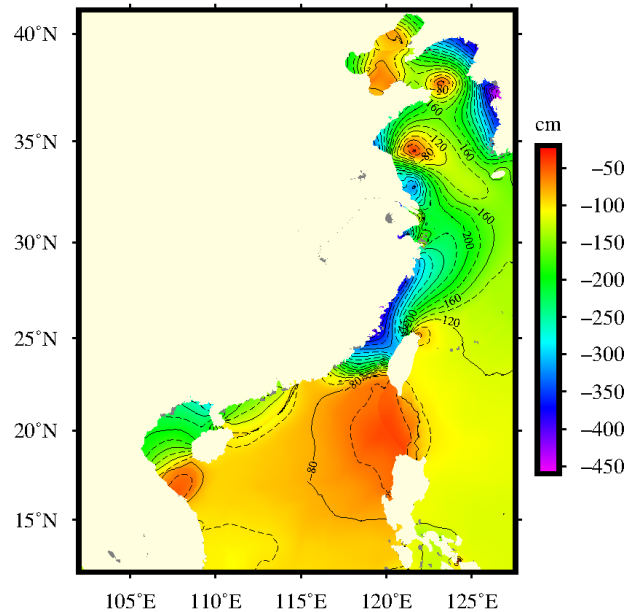


Figure 17. Spatial distribution of the lowest normal low water values in the China seas.

### Vertical datum transformation in regional and special sea area

In recent years, with the implementation of "land-sea overall planning" of China, some coastal cities in China, such as Qingdao, Shenzhen, and Tianjin have constructed the vertical datum transformation between land and sea, have constructed the regional separation model with 1'×1' resolution and conversion accuracy better than 15 cm. The Maritime Administration of the Ministry of Communications has also constructed the height and depth separation model in the Yellow Sea and Bohai Sea area.

The proposed technical route is as follows. A regional tide model is constructed, and then a LVLW model is constructed according to the definition. In addition, a sea surface topographic model like the geoid or CGCS2000 ellipsoid is also constructed. By superimposing LNLW model and sea surface topography model, and the construction of height and depth separation model is completed. Based on the above scheme, a high-resolution and high-precision separation model between the CGCS2000 ellipsoid, depth datum and quasi-geoid of Shandong Province was constructed, realizing the unification of the vertical datum of Shandong Province and its coastal regions.

We have also performed the vertical datum transformation in special sea areas. In the Yangtze estuarine waters, through the establishment of seamless CD and its transformant relationship with other vertical datums, combining with geoid, sea surface topography and three-dimensional numerical simulation of tidal wave motion. The standard error of the vertical datum transformation model was 12.4 cm. Although the Yangtze estuarine waters have complicated tidal wave characteristics and they are nearshore waters, which leads to poor accuracy of the mean sea surface topography model in this region, when the accuracy of satellite altimetry is further improved in the nearshore areas, the proposed method can be extended to nearshore and inland waters.

The transformation model of the geodetic height of the mean sea surface utilizes the

gridded MSS model and chart datum model based on the DTU15 model and the Atlantic Ocean 2008 tide model was obtained in the Great Wall Bay, and mean sea surface model, geoid model and CD model were combined to realized the vertical datum transformation in the Ross Sea and surrounding waters.

### **Developed and revised the technical specification**

The Technical specification for marine vertical datum transformation (CH/T 2021-2023), which is led by the First Institute of Oceanography, Ministry of Natural Resources, has been approved and issued of the National Technical Committee for Standardization of Geographic Information. It will come into effect on June 1, 2023. The specification stipulates the basic requirements of vertical datum transformation, data preprocessing, basic model construction, procedure of transformation, quality control and precision evaluation, the exchange of results and other contents. The specification provides technical guidance for the vertical datum transformation. Its implementation provides technical standard support for solving the transformation of land and sea datum and obtaining the achievements of land and sea seamless geographic information in our country.

## **7 Establishment of Vertical Movement Model of Chinese Mainland by Fusion**

### **Result of Leveling and GNSS**

Geodetic survey is one of the important methods to quantitatively study the vertical movement of the crust, among which leveling and GNSS are the most classic means of monitoring the vertical movement of the crust. By taking full advantage of the high precision of leveling data and the high spatial and temporal resolution of GNSS, a robust and reliable vertical movement model of the crust can be established. Single data source is analyzed. The method of analyzing, compensating and suppressing systematic errors in multi-phase leveling network data is analyzed, and a complete function model and stochastic model are established to improve the reliability of the calculation results. Heterogeneous data fusion is analyzed. It is proposed to use the functional model and random model to weaken the influence of systematic errors of heterogeneous data, including functional model compensation method and heterogeneous data weight ratio adjustment method. A process-based heterogeneous data fusion method is proposed, such as the joint adjustment method with the restriction that the geodetic height velocity is equal to the normal height velocity at the GNSS-leveling points. A result-based heterogeneous data fusion method is proposed. By analyzing the distance between the discrete control point and the grid point of GNSS and leveling vertical movement model, the grid point weight of different model is determined, and the grid value weighted fusion is realized. The establishment of the vertical movement model is analyzed. Based on the stable bedrock point, the effective stripping of the vertical movement of the surface and the crust is realized. The methods of establishing the vertical movement model of the ground are studied, including Inverse Distance Weighting Method, Kriging Method, Minimum Curvature Method, etc. The vertical movement model in Chinese mainland is established based on the Kriging method. Meanwhile, the spatial distribution characteristic of the vertical movement in the Chinese mainland is analyzed. According to fused vertical movement model, the characteristic

of vertical movement is analyzed: North China Plain and Jiangsu-shanghai area are severe subsiding, where the velocity of individual areas is up to 100 mm/a, the North-east of China and Tibet areas are uplifting, and the maximum velocity exceeds 5 mm/a in some local area, the vertical movement in other areas is relatively stable.

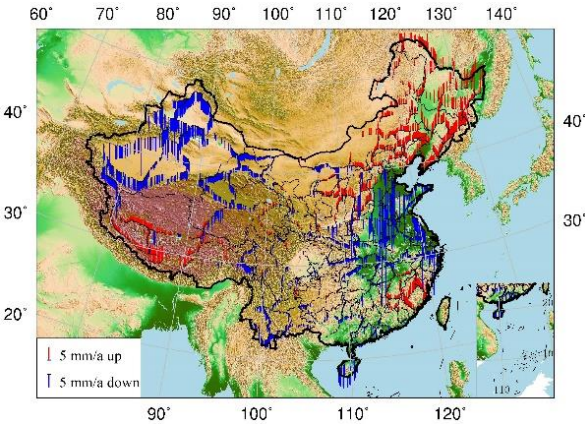


Figure 18. Vertical Velocity of Leveling Points

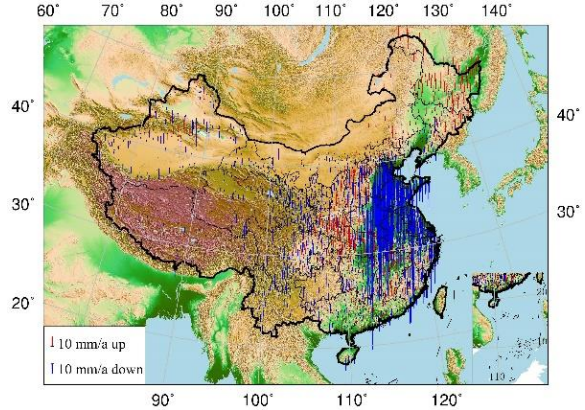


Figure 19. Vertical Velocity of GNSS Points

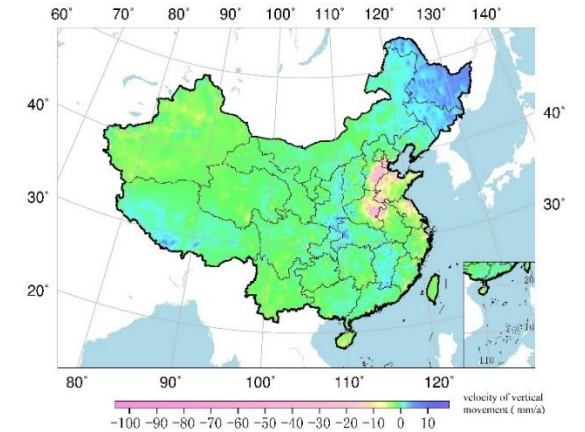


Figure 20. The vertical movement model of Chinese mainland by GNSS and Leveling data

**Bibliography**

Amin, H. , Sjöberg, L. E. , & Bagherbandi, M. A global vertical datum defined by the conventional geoid potential and the Earth ellipsoid parameters. Journal of Geodesy, 2019, 93: 1943-1961.

- An, D., J. Guo, Z. Li, B. Ji, X. Liu, and X. Chang. Improved Gravity-Geologic Method Reliably Removing the Long-Wavelength Gravity Effect of Regional Seafloor Topography: A Case of Bathymetric Prediction in the South China Sea. *IEEE Transactions on Geoscience and Remote Sensing*, 2022, 60:1-12.
- Annan, R. F., and X. Wan. Recovering Bathymetry of the Gulf of Guinea Using Altimetry-Derived Gravity Field Products Combined via Convolutional Neural Network. *Surveys in Geophysics*, 2022, 43(5):1541-1561.
- Chao, N., G. Chen, Z. Luo, X. Su, Z. Wang, and F. Li. Detecting Water Diversion Fingerprints in the Danjiangkou Reservoir from Satellite Gravimetry and Altimetry Data. *Sensors*, 2019, 19(16):3510.
- Chen, G., and S. Zhang. Elevation and Volume Change Determination of Greenland Ice Sheet Based on ICESat Observations. *Chinese Journal of Geophysics*, 2019, 62(7):2417-2428.
- Chen, G., S. Zhang, S. Liang, and J. Zhu. Elevation and Volume Changes in Greenland Ice Sheet From 2010 to 2019 Derived From Altimetry Data. *Frontiers in Earth Science*, 2021, 9:674983.
- Chen, G., Z. Zhang, S. K. Rose, O. B. Andersen, S. Zhang, and T. Jin. A New Arctic MSS Model Derived from Combined Cryosat-2 and ICESat Observations. *International Journal of Digital Earth*, 2022, 15(1):2202-2222.
- Chen, J., C. Zhou, and Q. Zhao. Subglacial lake activity and hydrological connection in the Byrd glacier basin during 2003-2018: analysis of multimission satellite altimetry monitoring results. *Acta Geodaetica et Cartographica Sinica*, 2020, 49(5):547-556.
- Chen J., Zhang X., Chen Q., Shen Y., Nie Y. (2022). Static Gravity Field Recovery and Accuracy Analysis Based on Reprocessed GOCE Level 1b Gravity Gradient Observations. *EGU General Assembly 2022*, Vienna, Austria, 23–27 May 2022, EGU22-6771, 10.5194/egusphere-egu22-6771.
- Chen Q., Shen Y., Francis O., Chen W., Zhang X., Hsu H. (2018). Tongji-grace02s and Tongji-grace02k: High-Precision Static GRACE-only Global Earth's Gravity Field Models Derived by Refined Data Processing Strategies. *Journal of Geophysical Research: Solid Earth*, 123(7), 6111-6137, 10.1029/2018JB015641.
- Chen, Y., Q. Ji, and X. Pang. Spatio-Temporal Variation of Antarctic Sea Ice Thickness Using Cryosat-2 Satellite Altimeter Data. *Journal of Glaciology and Geocryology*, 2019, 41(5):1214-1220.
- Dang, Y., Jiang, T., Guo, C., Chen, B., Zhang, C., Yang, Q., Wang, Z. (2023). Determining the new height of Mount Qomolangma based on the International Height Reference System. *Geo-spatial Information Science*, DOI: 10.1080/10095020.2022.2128901 (SCI).
- Dang, Y., Guo, C., Jiang, T., Zhang, Q., Chen, B., Jiang, G. (2020). Height measurement and determination of Mount Qomolangma. *Acta Geodaetica et Cartographica Sinica*, 50(4): 556-561.
- Dang, Y., Jiang, T., Chen, J. (2022). Review on Research Progress of the Global Height Datum. *Geomatics and Information Science of Wuhan University*, 47(10): 1576-1586.
- Ding S, Chen J. Preliminary building and application of seamless vertical datum of land and sea in Shandong province. *Bulletin of Surveying and Mapping*, 2019(S2): 293-297 . DOI: 10.13474/j.cnki.11-2246.2019.0647.
- Hao, R., X. Wan, and R. F. Annan. Enhanced Short-Wavelength Marine Gravity Anomaly Using Depth Data. *IEEE Transactions on Geoscience and Remote Sensing*, 2023, 61:1-9.
- He, L., Chu, Y., Xu, X., & Zhang, T. Evaluation of the GRACE/GOCE Global Geopotential Model on estimation of the geopotential value for the China vertical datum of 1985 (in Chinese). *Chinese J. Geophys*, 2019, 62(6): 2016-2026.
- Fan, Y., W. Hao, B. Zhang, C. Ma, S. Gao, X. Shen, and F. Li. Monitoring the Hydrological Activities of Antarctic Subglacial Lakes Using CryoSat-2 and ICESat-2 Altimetry Data. *Remote Sensing*, 2022, 14(4):898.
- Förste, C., Bruinsma, S. L., Abrikosov, O., Lemoine, J., Marty, J. C., Flechtner, F., Balmino, G., Barthelmes, F., & Biancale, R. EIGEN-6C4 The latest combined global gravity field model including GOCE data up to degree and order 2190 of

- GFZ Potsdam and GRGS Toulouse, 2014.
- Fu Y, Feng Y, Zhou D, et al. 2020. Accuracy assessment of global ocean tide models in the South China Sea using satellite altimeter and tide gauge data. *Acta Oceanologica Sinica*, 39(12): 1–10. DOI: 10.1007/s13131-020-1685-y;
- Fu Y, Zhou D, Feng Y, et al. Long-period solar annual and semiannual tidal contributions to the lowest normal low water in seas surrounding China. 2021, *Ocean Science, Discuss.* DOI: 10.5194/os-2021-3, 2021.
- Gao, Xianwen, T. Jin, and H. Huang. Analysis on the Accuracy of Waveform Retracking for the Coastal Synthetic Aperture Radar Altimeter Data. *Journal of Geodesy and Geodynamics*, 2021, 41(1):56-61.
- Gao, Xiang, X. Pang, and Q. Ji. Spatiotemporal Variation of Sea Ice Freeboard in the Antarctic Weddell Sea Based on CryoSat-2 Altimeter Data. *Geomatics and Information Science of Wuhan University*, 2021, 46(1):125-132.
- Guan, B., Z. Sun, X. Liu, and Z. Zhai. Necessity for Filtering for Ionospheric Delay in the Applications of Satellite altimetry. *Progress in Geophysics*, 2020, 35(6):2064-2067.
- Guo, C., Nie, J., Tian J., Wang, B., Jin, X., Zhao, D. (2020). Analysis of Vertical Deformation with the Adaptive Fusion of GNSS and Leveling Elevation Variation. *Geomatics and Information Science of Wuhan University*, 45(1):7-12
- Guo, C., Guo, X., Nie, J., Wang, B., Liu, X., Wang, H. (2021). Establishment of Vertical Movement Model of Chinese Mainland by Fusion Result of Leveling and GNSS. *Geomatics and Information Science of Wuhan University*, DOI: 10.13203/j.whugis20200167.
- Guo, J., H. Luo, C. Zhu, H. Ji, G. Li, and X. Liu. Accuracy Comparison of Marine Gravity Derived from HY-2A/GM and CryoSat-2 Altimetry Data: A Case Study in the Gulf of Mexico. *Geophysical Journal International*, 2022a, 230(2):1267-1279.
- Guo, J., L. Qi, X. Liu, X. Chang, B. Ji, and F. Zhang. High-Order Ionospheric Delay Correction of GNSS Data for Precise Reduced-Dynamic Determination of LEO Satellite Orbits: Cases of GOCE, GRACE, and SWARM. *GPS Solutions*, 2023, 27(1):13.
- Guo, J., G. Wang, H. Guo, M. Lin, H. Peng, X. Chang, and Y. Jiang. Validating Precise Orbit Determination from Satellite-Borne GPS Data of Haiyang-2D. *Remote Sensing*, 2022b, 14(10):2477.
- Guo, X., Guo, C., Nie, J., Wang, H., Tian J. (2021). Vertical Movement Model in Chinese Mainland Based on First Order Leveling Results. *Geomatics and Information Science of Wuhan University*, 47(3):361-368
- Jekeli, C., Hyo Jin, Y., & Jay Hyoun, K. The Offset of the South Korean Vertical Datum from a Global Geoid. *Journal of Civil Engineering*, 2012, 5(16): 816-821.
- Jiang, T., Dang, Y., Zhang, C. (2020). Gravimetric geoid modeling from the combination of satellite gravity model, terrestrial and airborne gravity data: a case study in the mountainous area, Colorado. *Earth Planets Space* 72, 189.
- Jiang, T., Dang, Y., Guo, C., Chen, B., Zhang, C. (2022). Realization of the international height reference system in the region of Mount Qomolangma. *Acta Geodaetica et Cartographica Sinica*, 51(8): 1757-1767.
- Ji, H., X. Liu, C. Zhu, J. Yuan, B. Ji, and J. Guo. On Performance of CryoSat-2 Altimeter Data in Deriving Marine Gravity over the Bay of Bengal. *Marine Geophysical Research*, 2021, 42(4):39.
- Jin, T., M. Zhou, H. Zhang, J. Li, W. Jiang, S. Zhang, and M. Hu. Analysis of Vertical Deflections Determined from One Cycle of Simulated SWOT Wide-Swath Altimeter Data. *Journal of Geodesy*, 2022, 96(4):30.
- Ke H, Zhao J, Zhou F, et al. Establishment of Sea - Land Vertical Datum Transformation for Hydrography Combining with Geoid, Sea Surface Topography and Numerical Simulation of Tidal Wave Motion in the Yangtze Estuarine Waters. *Geomatics and Information Science of Wuhan University*, 2022, 47(5): 731-737. DOI: 10.13203/j.whugis20200601.
- Ke H, Li F, Ai S, et al. Establishment of Chart Datum and Vertical Datum Transformation for Hydrography in the Chinese Great Wall Bay, Antarctic Peninsula. *Journal of Surveying Engineering*, 2020, 146(2): 05020003.

- Liang, W. , Li, J. , Xu, X. , Zhang, S. , & Zhao, Y. A High-Resolution Earth's Gravity Field Model SGG-UGM-2 from GOCE, GRACE, Satellite Altimetry, and EGM2008. *Engineering*, 2020, 6(8): 860-878.
- Liang, W. , Xu, X. , Li, J. , & Zhu, G. The determination of an ultra high gravity field model SGG-UGM-1 by combining EGM2008 gravity anomaly and GOCE observation data(In Chinese). *Acta Geodaetica et Cartographica Sinica*, 2018, 47(4): 425-434.
- Li, J. , Chu, Y. , & Xu, X. Determination of Vertical Datum Offset between the Regional and the Global Height Datum(in Chinese). *Acta Geodaetica et Cartographica Sinica*, 2017, 46(10): 1262-1273.
- Li, J, Fu, Y, Tang, Q, et al. Accuracy assessment of a seamless depth datum model established on the basis of the global ocean tide model. *Journal of Coastal Research, Special Issue No. 99*, pp. 74-78. 2020. Coconut Creek (Florida), ISSN 0749-0208.
- Li, L., M. Cai, X. Guan, and D. Chu. Piecewise Adaptive-Norm Trend Filtering Method for ICESat/GLAS Waveform Data Denoising. *IEEE Access*, 2020, 8:168965-168979.
- Li, Q., L. Bao, and Y. Wang. Accuracy Evaluation of Altimeter-Derived Gravity Field Models in Offshore and Coastal Regions of China. *Frontiers in Earth Science*, 2021, 9:722019.
- Li, Y., J. Guo, Y. Sun, J. Yuan, X. Chang, and H. Zhang. Inversion of Global Sea Level Change and Its Component Contributions by Combining Timevarying Gravity Data and Altimetry Data. *Acta Geodaetica et Cartographica Sinica*, 2022, 51(8):1768-1778.
- Li, Z., X. Liu, G. Jinyun, J. Yuan, Y. Niu, and J. Bing. A New Method of Satellite Radar Altimeter Waveform Retracking Based on Waveform Derivative. *Revista Internacional de Métodos Numéricos Para Cálculo y Diseño En Ingeniería*, 2020, 36.
- Lin, M., and Y. Jia. Past, Present and Future Marine Microwave Satellite Missions in China. *Remote Sensing*, 2022, 14(6):1330.
- Liu, S., F. Li, and Y. Yang. Inversion of Sea Ice Thickness Variation in Beaufort Sea from 2011 to 2017 Based on CryoSat-2 Data. *Journal of Geodesy and Geodynamics*, 2019, 39(12):1310-1316.
- Michael G H D, Gaia P, Denise D, et al. EOT20: a global ocean tide model from multi-mission satellite altimetry. *Earth System Science Data*, 2021, 13(8): 3869-3884.
- Niu, Y., J. Guo, J. Yuan, C. Zhu, M. Zhou, X. Liu, and B. Ji. Prediction of Sea Level Change in Japanese Coast Using Singular Spectrum Analysis And auto Regression Moving Average. *Chinese Journal of Geophysics*, 2020, 63(9):3263-3274.
- Ouyang, M. Research Progress and Prospects of Seabed Topography Inversion From altimetry Data. *Progress in Geophysics*, 2022, 37(6):2291-2300.
- Pavlis, N. K. , Holmes, S. A. , Kenyon, S. C. , & Factor, J. K. The development and evaluation of the Earth Gravitational Model 2008 (EGM2008). *Journal of Geophysical Research*, 2012, 117(B04): 1-38.
- Peng, F., and X. Deng. Improving Precision of High-Rate Altimeter Sea Level Anomalies by Removing the Sea State Bias and Intra-1-Hz Covariant Error. *Remote Sensing of Environment*, 2020a, 251:112081.
- Peng, F., and X. Deng. Validation of Sentinel-3A SAR Mode Sea Level Anomalies around the Australian Coastal Region. *Remote Sensing of Environment*, 2020b, 237:111548.
- Peng, F., X. Deng, and X. Cheng. Quantifying the Precision of Retracked Jason-2 Sea Level Data in the 0–5 Km Australian Coastal Zone. *Remote Sensing of Environment*, 2021, 263:112539.
- Peng, F., X. Deng, and X. Cheng. Australian Coastal Sea Level Trends Over 16 Yr of Reprocessed Jason Altimeter 20-Hz Data Sets. *Journal of Geophysical Research: Oceans*, 2022, 127(3):e2021JC018145.
- Sun, H., T. Jin, and C. Zhao. A Non-Uniform Density Distributed Point-Mass Method for the Fusion of Altimetric and Shipborne Gravity. *Journal of Geomatics*, 2021, 46(4):17-22.



- Sun W. Research on the vertical datum model construction in the Ross Sea and surrounding waters. 2022, Shandong University of Science and Technology.
- Sun, Z., B. Guan, Z. Zhai, and M. Ouyang. Research Progress of Ocean Satellite Altimetry and Its Recovery of Globalmarine Gravity Field and Seafloor Topography Model. *Acta Geodaetica et Cartographica Sinica*, 2022, 51(6):923-934.
- Wang, W., Guo, C., Ding, L., Zhao, H. (2019). Elevation Change Analysis of the National First Order Leveling Points in Recent 20 Years. *Acta Geodaetica et Cartographica Sinica*, 48(1):1-8
- Wu, F. , Zeng, A. , & Ming, F. Analyzing the long-term changes in China's National Height Datum. *Advances in Space Research*, 2020, 66: 1342-1350.
- Wu, Y., Abulaitijiang, A., Featherstone, W.E., McCubbine, J.C., Andersen, O.B. (2019). Coastal gravity field refinement by combining airborne and ground-based data. *Journal of Geodesy*, 93(12):2569-2584.
- Wan, X., R. F. Annan, S. Jin, and X. Gong. Vertical Deflections and Gravity Disturbances Derived from HY-2A Data. *Remote Sensing*, 2020a, 12(14):2287.
- Wan, X., R. F. Annan, and W. Wang. Assessment of HY-2A GM Data by Deriving the Gravity Field and Bathymetry over the Gulf of Guinea. *Earth, Planets and Space*, 2020b, 72(1):151.
- Wan, X., R. F. Annan, and Y. Y. Ziggah. Altimetry-Derived Gravity Gradients Using Spectral Method and Their Performance in Bathymetry Inversion Using Back-Propagation Neural Network. *Journal of Geophysical Research: Solid Earth*, 2023, 128(2):e2022JB025785.
- Wan, X., R. Hao, Y. Jia, X. Wu, Y. Wang, and L. Feng. Global Marine Gravity Anomalies from Multi-Satellite Altimeter Data. *Earth, Planets and Space*, 2022a, 74(1):165.
- Wan, X., S. Jin, B. Liu, S. Tian, W. Kong, and R. F. Annan. Effects of Interferometric Radar Altimeter Errors on Marine Gravity Field Inversion. *Sensors*, 2020c, 20(9):2465.
- Wan, X., F. Wang, H. Guo, and B. Liu. Impact of Errors in Environmental Correction on Gravity Field Recovery Using Interferometric Radar Altimeter Observations. *Remote Sensing*, 2022b, 14(24):6299.
- Wang, H., and Z. Huang. Waveform Decontamination for Improving Satellite Radar Altimeter Data Over Nearshore Area: Upgraded Algorithm and Validation. *Frontiers in Earth Science*, 2021, 9:748401.
- Wang, J., Y. Yang, C. Wang, and L. Li. Accelerated Glacier Mass Loss over Svalbard Derived from ICESat-2 in 2019–2021. *Atmosphere*, 2022, 13(8):1255.
- Wei, Z., J. Guo, C. Zhu, J. Yuan, X. Chang, and B. Ji. Evaluating Accuracy of HY-2A/GM-Derived Gravity Data With the Gravity-Geologic Method to Predict Bathymetry. *Frontiers in Earth Science*, 2021, 9:636246.
- Wu, Yihao, X. He, J. Huang, H. Shi, H. Wang, Yunlong Wu, and Y. Ding. Comparison of Mean Dynamic Topography Modeling from Multivariate Objective Analysis and Rigorous Least Squares Method. *Remote Sensing*, 2022, 14(21):5330.
- Xiao, F., S. Zhang, J. Li, T. Geng, Y. Xuan, and F. Li. Arctic Sea Ice Thickness Variations from CryoSat-2 Satellite Altimetry Data. *Science China Earth Sciences*, 2021, 64(7):1080-1089.
- Xu, N., Y. Ma, Z. Wei, C. Huang, G. Li, H. Zheng, and X. H. Wang. Satellite Observed Recent Rising Water Levels of Global Lakes and Reservoirs. *Environmental Research Letters*, 2022, 17(7):074013.
- Xu, N., Y. Ma, W. Zhang, and X. H. Wang. Surface-Water-Level Changes During 2003–2019 in Australia Revealed by ICESat/ICESat-2 Altimetry and Landsat Imagery. *IEEE Geoscience and Remote Sensing Letters*, 2021, 18(7):1129-1133.
- Yang, L., T. Jin, X. Gao, H. Wen, T. Schöne, M. Xiao, and H. Huang. Sea Level Fusion of Satellite Altimetry and Tide Gauge Data by Deep Learning in the Mediterranean Sea. *Remote Sensing*, 2021, 13(5):908.
- Yang, Y., P. Moore, Z. Li, and F. Li. Lake Level Change From Satellite Altimetry Over Seasonally Ice-Covered Lakes in the

- Mackenzie River Basin. *IEEE Transactions on Geoscience and Remote Sensing*, 2021, 59(10):8143-8152.
- Yu, D., and C. Hwang. Calibrating Error Variance and Scaling Global Covariance Function of Geoid Gradients for Optimal Determinations of Gravity Anomaly and Gravity Gradient from Altimetry. *Journal of Geodesy*, 2022, 96(9):61.
- Yu, D., C. Hwang, O. B. Andersen, E. T. Y. Chang, and L. Gaultier. Gravity Recovery from SWOT Altimetry Using Geoid Height and Geoid Gradient. *Remote Sensing of Environment*, 2021, 265:112650.
- Yuan, J., J. Guo, X. Liu, C. Zhu, Y. Niu, Z. Li, B. Ji, and Y. Ouyang. Mean Sea Surface Model over China Seas and Its Adjacent Ocean Established with the 19-Year Moving Average Method from Multi-Satellite Altimeter Data. *Continental Shelf Research*, 2020a, 192:104009.
- Yuan, J., J. Guo, Y. Niu, C. Zhu, and Z. Li. Mean Sea Surface Model over the Sea of Japan Determined from Multi-Satellite Altimeter Data and Tide Gauge Records. *Remote Sensing*, 2020b, 12(24):4168.
- Yuan, J., J. Guo, C. Zhu, C. Hwang, D. Yu, M. Sun, and D. Mu. High-Resolution Sea Level Change around China Seas Revealed through Multi-Satellite Altimeter Data. *International Journal of Applied Earth Observation and Geoinformation*, 2021, 102:102433.
- Yuan, J., J. Guo, C. Zhu, Z. Li, X. Liu, and J. Gao. SDUST2020 MSS: A Global 1' × 1' Mean Sea Surface Model Determined from Multi-Satellite Altimetry Data. *Earth System Science Data*, 2023, 15(1):155-169.
- Zhang, B., J. Liu, Z. Wang, T. Liu, and Q. Yang. Antarctic Ice-Shelf Thickness Changes from CryoSat-2 SARIn Mode Measurements: Assessment and Comparison with IceBridge and ICESat. *Journal of Earth System Science*, 2020, 129(1):127.
- Zhang, Shengjun, A. Abulaitijiang, O. B. Andersen, D. T. Sandwell, and J. R. Beale. Comparison and Evaluation of High-Resolution Marine Gravity Recovery via Sea Surface Heights or Sea Surface Slopes. *Journal of Geodesy*, 2021, 95(6):66.
- Zhang, S., O. B. Andersen, X. Kong, and H. Li. Inversion and Validation of Improved Marine Gravity Field Recovery in South China Sea by Incorporating HY-2A Altimeter Waveform Data. *Remote Sensing*, 2020a, 12(5):802.
- Zhang, Shengkai, T. Geng, C. Zhu, J. Li, X. Li, B. Zhu, L. Liu, and F. Xiao. Arctic Sea Ice Freeboard Estimation and Variations From Operation IceBridge. *IEEE Transactions on Geoscience and Remote Sensing*, 2022, 60:1-10.
- Zhang, S., J. Li, and X. Kong. Inversion of Global Marine Gravity Anomalies with Vertical Deflection Method Deduced from Laplace Equation. *Acta Geodaetica et Cartographica Sinica*, 2020b, 49(4):452-460.
- Zhang, Shengkai, Y. Xuan, J. Li, T. Geng, X. Li, and F. Xiao. Arctic Sea Ice Freeboard Retrieval from Envisat Altimetry Data. *Remote Sensing*, 2021, 13(8):1414.
- Zhang, Shengjun, R. Zhou, Y. Jia, T. Jin, and X. Kong. Performance of HaiYang-2 Altimetric Data in Marine Gravity Research and a New Global Marine Gravity Model NSOAS22. *Remote Sensing*, 2022, 14(17):4322.
- Zhang, S., C. Zhu, F. Xiao, L. Yuan, and J. Li. An Approach of Sea Ice Freeboard Retrieval with Operation IceBridge Airborne Topographic Mapper Data. *Journal of Geomatics*, 2019, 44(3):21-27.
- Zhang, W., J. Yan, and F. Li. An Improved Coastal Marine Gravity Field Based on the Mean Sea Surface Height Constraint Factor Method. *Remote Sensing*, 2022, 14(16):4125.
- Zhao, C., T. Jin, P. Qin, and L. Yang. An Improved Multi-Surface Function Method with Residual Constraint for the Fusion of Shipborne and Satellite Altimetry Derived Gravity Data. *Acta Geodaetica et Cartographica Sinica*, 2022:1-11.
- Zhu, C., J. Guo, J. Gao, X. Liu, C. Hwang, S. Yu, J. Yuan, B. Ji, and B. Guan. Marine Gravity Determined from Multi-Satellite GM/ERM Altimeter Data over the South China Sea: SCSGA V1.0. *Journal of Geodesy*, 2020, 94(5):50.
- Zhu, C., J. Guo, C. Hwang, J. Gao, J. Yuan, and X. Liu. How HY-2A/GM Altimeter Performs in Marine Gravity Derivation: Assessment in the South China Sea. *Geophysical Journal International*, 2019, 219(2):1056-1064.

- Zhu, C., J. Guo, J. Yuan, Z. Li, X. Liu, and J. Gao. SDUST2021GRA: Global Marine Gravity Anomaly Model Recovered from Ka-Band and Ku-Band Satellite Altimeter Data. *Earth System Science Data*, 2022, 14(10):4589-4606.
- Zhou D, Sun W, Fu H, et al. Accuracy assessment of three latest global ocean tide models in coastal areas of China. *Advances in Marine Science*, 2023, 41(1): 54-63.

# Temporal Gravity Field Modelling by Satellite Gravimetry

Zhicai Luo<sup>1</sup>, Qiuji Chen<sup>2</sup>, Bo Zhong<sup>3</sup>, Wei You<sup>4</sup>, Yong Su<sup>3,5</sup>, Hao Zhou<sup>1</sup>, Fan Yang<sup>1</sup>, Xiang Guo<sup>1</sup>, Qiong Li<sup>5</sup>, Xiancai Zou<sup>3</sup>, Yunzhong Shen<sup>2</sup>

<sup>1</sup> Institute of Geophysics and National Precise Gravity Measurement Facility (PGMF), Huazhong University of Science and Technology, Wuhan, China

<sup>2</sup> College of Surveying and Geo-informatics, Tongji University, Shanghai, China

<sup>3</sup> MOE Key Laboratory of Geospace Environment and Geodesy, School of Geodesy and Geomatics, Wuhan University, Wuhan, China

<sup>4</sup> Faculty of Geosciences and Environmental Engineering, Southwest Jiaotong University, Chengdu, China

<sup>5</sup> School of Civil Engineering and Geomatics, Southwest Petroleum University, Chengdu, China

The main activities and recent achievements on the data processing, theoretical and methodological development of temporal gravity field recovery have been summarized shortly in the report since 2019, which provided respectively by Huazhong University of Science and Technology (HUST team), Tongji University (TJU team), Wuhan University (WHU team), Southwest Jiaotong University (SWJTU team), and Southwest Petroleum University (SWPU team).

## 1 Research outcomes of the HUST team

The first representative work of the HUST team is the temporal gravity field model series. To reach the prelaunch baseline for GRACE mission, Zhou et al. (2019) developed two new hybrid processing strategies. One is for kinematic empirical parameters of range-rate observations, the other is for arc-specific parameters. For the kinematic empirical parameters, the proposed filter predetermined strategy is used to ensure the temporal signals while the pure predetermined strategy is applied to reduce the temporal noise. Based on the GRACE L1B V02 data and AOD RL05 model, the monthly gravity field models **HUST-Grace2019** shows the notable noise reduction of 19% in terms of cumulative geoid differences when compared to Center for Space Research (CSR) RL05 model (Figure 1). Furthermore, based on the new released dataset including GRACE L1B V03 and AOD RL06 model, the new **HUST-Grace2020** model is developed and it is included in the International Centre for Global Earth Models (ICGEM).

Meanwhile, the HUST team proposes a new concept for determining temporal gravity field models via a couple of high-low satellite-to-satellite tracking (HLSST) missions. As for the current HLSST mission consisting of a GNSS receiver and an accelerometer, it is expected to observe monthly (or weekly) gravity solution at the spatial resolution of about 1300 km (or 2000 km). As for satellite constellations, a significant improvement is expected by adding the second satellite or the third satellite with various inclinations. Moreover, the accuracy of weekly solution is expected to improve for three (or two) HLSST missions when compared to one HLSST mission. Due to the low financial costs, it is worthy to build a satellite constellation of HLSST missions to fill the possible gaps between the dedicated temporal gravity field detecting missions (Zhou et al., 2020).

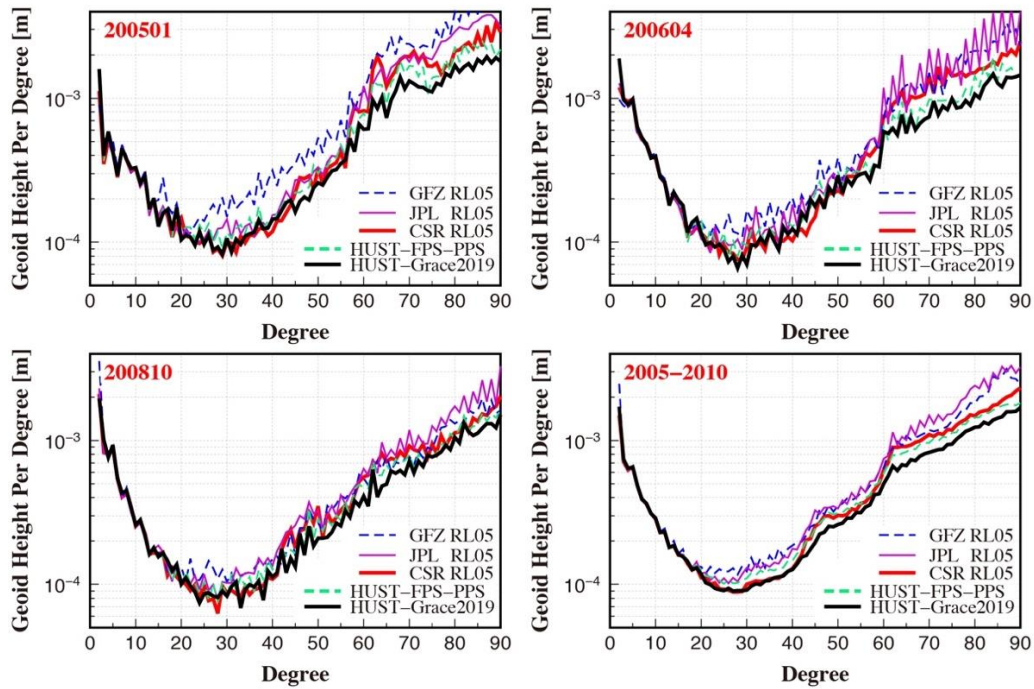


Figure 1. The geoid height per degree of GFZ RL05, JPL RL05, CSR RL05, HUST-FPS-PPS and HUST-Grace2019. The results in January 2005, April 2006 and October 2008 are presented, and that for the period January 2005 to December 2010 is also shown.

Another focus of the HUST team has been placed on the imperfect data processing from Level-1a to Level-1b. Typically, AOD (high-frequency non-tidal Atmosphere and Ocean De-aliasing) modelling, as one of the key prior model for temporal gravity recovery, has been seen as one major error source of the-state-of-the-art gravity mission, and likewise being a potential threaten to future gravity mission. On-going effort has been therefore made by HUST team in the past three years to refine the AOD modelling through densifying the vertical and time resolution of atmosphere mass with ERA-5 reanalysis data, and in this manner we have established a publicly available **HUST-ERA5** atmosphere de-aliasing product completely independent from the official RL06 but reaching better quality than RL06 (Yang et al., 2021), see Figure as below. Other efforts made by HUST team in terms of Level1a-to-Level1b include the refinement on attitude data processing, as which still remains non-negligible uncertainty so far. By fusing the star-cameras and gyroscope on-board, we has published a new attitude product **HUGG-01** (Yang et al., 2022). Evaluation of HUGG-01 against the official JPL-V04 has demonstrated an equivalent performance in the low-to-middle spectrum, with even a slightly lower noise level (in the high spectrum) than JPL-V04. Further analysis on KBR range-rate residuals and gravity recovery also indicates a minor discrepancy that is far below the sensitivity of the state-of-the-art satellite gravity mission, demonstrating a good agreement between HUGG-01 and JPL-V04.

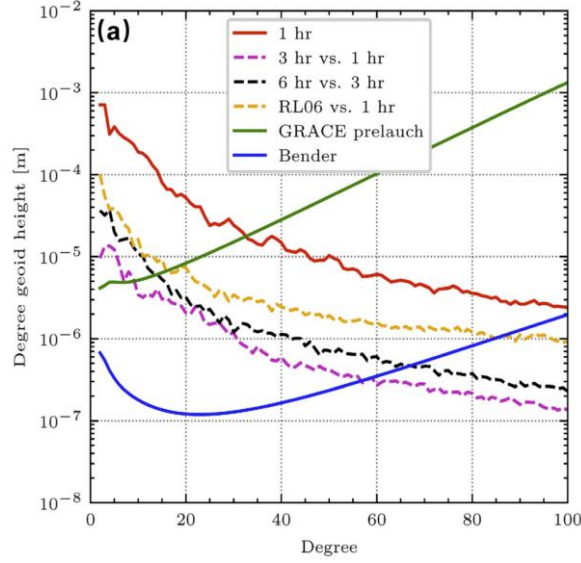


Figure 2. Evaluating 1-hourly HUST-ERA5 against RL06 in spectrum, with GRACE-prelaunch and Bender accuracy being as the reference.

## 2 Research outcomes of the TJU team

One of the most representative research outcomes is the development of an optimized short-arc approach (Figure 3), where the orbit integration length is successfully extended to 6 hours for a better signal-to-noise ratio and the colored noise of observation data is sufficiently taken into account by the filtering method. Based on the optimized short-arc approach, a refined GRACE monthly gravity field model series named **Tongji-Grace2018** has been produced, the quality of which is highly competitive to other state-of-art GRACE models (Chen et al., 2019). Moreover, considering the unconstrained time-variable GRACE spherical harmonic (SH) models are generally of low spatial resolution, especially after the indispensable filtering process, we developed a high-resolution SH model up to 180 degrees by incorporating spatial constraints determined from the filtered GRACE mass change estimates into the SH spectral domain. With this innovative regularization scheme, a time series of SH models named **Tongji-RegGrace2019** has been produced (Chen et al., 2021), which can be directly used without the need of any post-processing filtering. Comprehensive evaluations show that **Tongji-RegGrace2019** is of comparable quality in terms of both signal power and spatial resolution as the official Mascon solutions (Figure ).

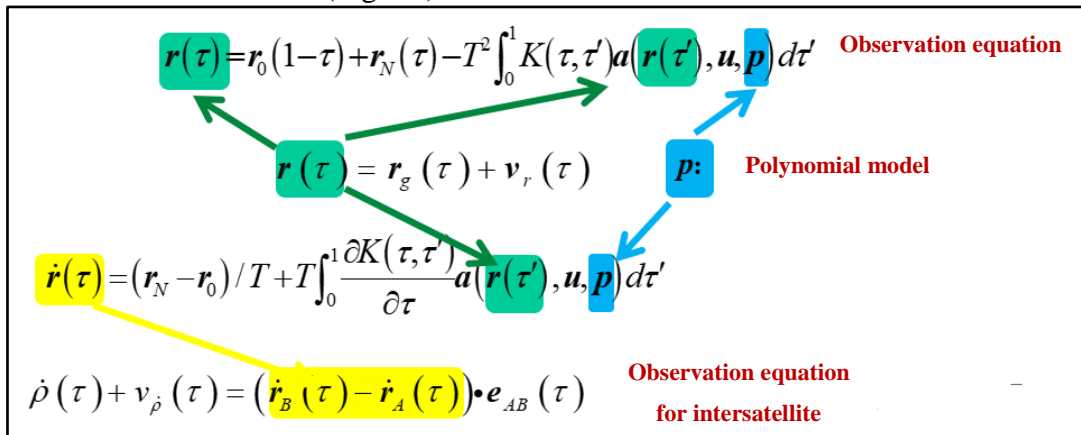


Figure 3. Optimized short-arc approach

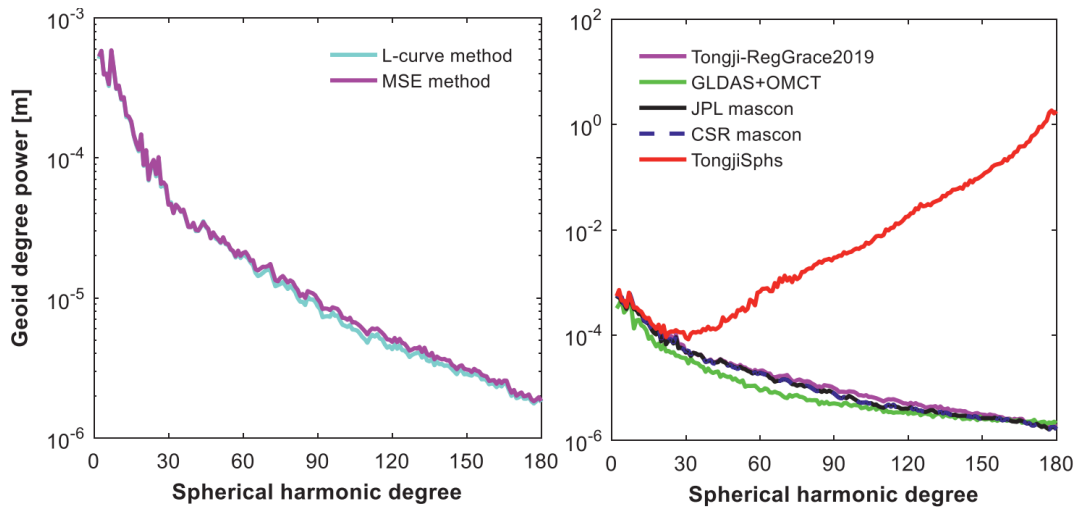


Figure 4. Geoid degree power of various models.

In addition, the team has focused on developing efficient methods for satellite geodetic data processing. On the one hand, an efficient variance component estimation (VCE) algorithm with rigorous trace calculation is proposed for large-scale least-squares problems, which is based on the local-global parameters partition scheme in satellite geodesy and is directly applicable to both the simplified yet common case where local parameters are unique to a single observation group and the generalized case where local parameters are shared by different groups of observations (Nie et al., 2022a). On the other hand, the team has systematically analyzed the connections and differences of four widely used noise-reduction approaches in GRACE gravity field recovery from both theoretical perspectives and numerical simulations, including the estimation of empirical accelerations (ACC method), the estimation of range-rate empirical parameters (KBR method), the use of fully populated covariance matrix (COV method) and the time series model-based filtering (FILT method). A unified theoretical framework is developed by the least-squares collocation model, which contributes to a deeper understanding of noise treatment in GRACE gravity field recovery (Nie et al., 2022b).

Combining the aforementioned theories and methods in processing observation data of low earth orbit (LEO) satellites prior to GRACE, a new time series of monthly gravity field models named **Tongji-LEO2021** has been developed and applied to directly quantify global mean ocean mass (GMOM) changes over the period January 1993 to December 2004 (Chen et al., 2022), since it is well-known that there are few time-variable gravity field models can be used before the GRACE era. In comparison to other measurements, Tongji-LEO2021-estimated GMOM change rates are nearly closed to the estimates from both Altimetry minus Steric observations and IGG-SLR-HYBRID solutions (Figure ), indicating that the new model is able to provide an independent and accurate measure for studying the earlier global sea-level change.



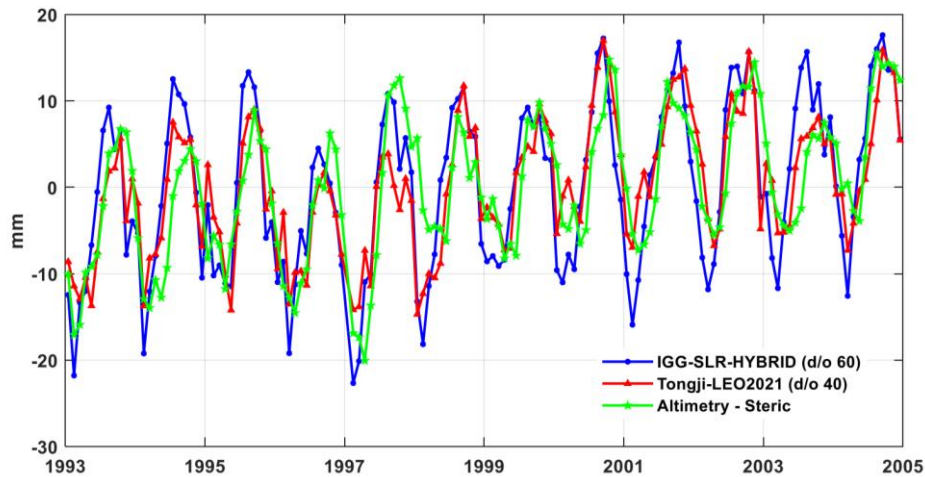


Figure 5. GMOM change estimates from Tongji-LEO2021, IGG-SLR-HYBRID solutions and Altimetry minus Steric observations covering the period January 1993 to December 2004.

### 3 Research outcomes of the WHU team

One of the WHU GRACE monthly gravity field solutions were produced using the classical dynamic approach. The first WHU time-series of monthly solutions (WHU RL01) were generated in 2017 based on the second release of GRACE Level-1B data. With the availability of the third release of the K-Band Ranging data and satellite attitude data (KBR1B RL03 and SCA1B RL03), the **WHU RL02** monthly solutions were produced. The background force models were also updated, mainly involving the static gravity fields (switch from EIGEN\_6C4 to GOCO06s) and the atmosphere and ocean de-aliasing products (from AOD1B RL05 to AOD1B RL06). Additionally, the GRACE kinematic orbits, which were taken as pseudo observations when compiling WHU RL02, were generated in-house with integrated single- and double-differenced carrier phase integer ambiguity resolution (Guo et al. 2020b). For parameter setups, the accelerometer biases were modeled with three-order polynomials and the scales were modeled with a fully populated matrix on daily basis to account for thermal variations. Finally, WHU RL02 adopted the frequency-dependent data weighting method for both KBRR and kinematic orbits, and it is also included in the ICGEM. Compared to WHU RL01, the signal-to-noise ratios (SNRs) of RL02 over 180 major river basins are improved by 16% on average (Figure ).

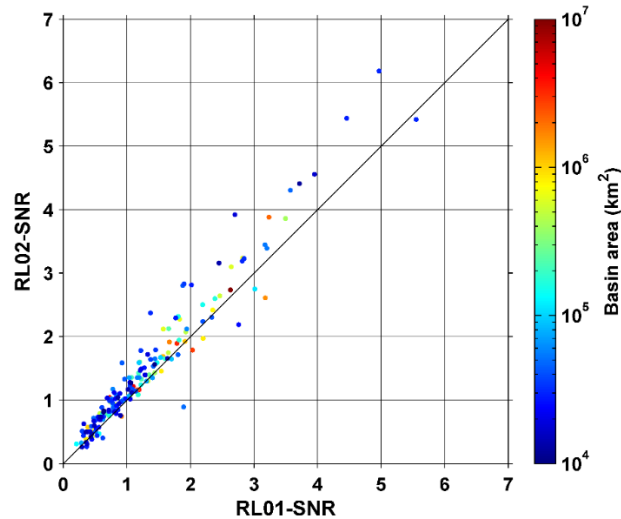


Figure 6. Signal-to-noise ratios over 180 major river basins

Another WHU GRACE monthly gravity field solutions are produced using the improved energy integral method. Based on the remove-compute-restore technique and improved energy balance equation, the precise geopotential difference (GPD) observations were estimated from GRACE Level-1B RL03 products according to the latest RL06 data processing standard (Zhong et al., 2022). To suppress the correlated noise of GRACE spherical harmonic (SH) solutions, we developed a series of constrained monthly gravity field solutions named **WHU-GRACE-GPD01s** from August 2002 to July 2016 using GRACE GPD observations (Zhong et al., 2023b). The constrained solutions were estimated using Kaula regularization, and the optimal regularization parameters were adaptively determined from GRACE data itself through variance component estimation. Extensive validations demonstrate that our constrained solutions are comparable to official spherical harmonic (SH) solutions (GFZ, JPL, and CSR RL06) (Figure ), and can be used without post-processing. The WHU-GRACE-GPD01s is also included in the ICGEM.

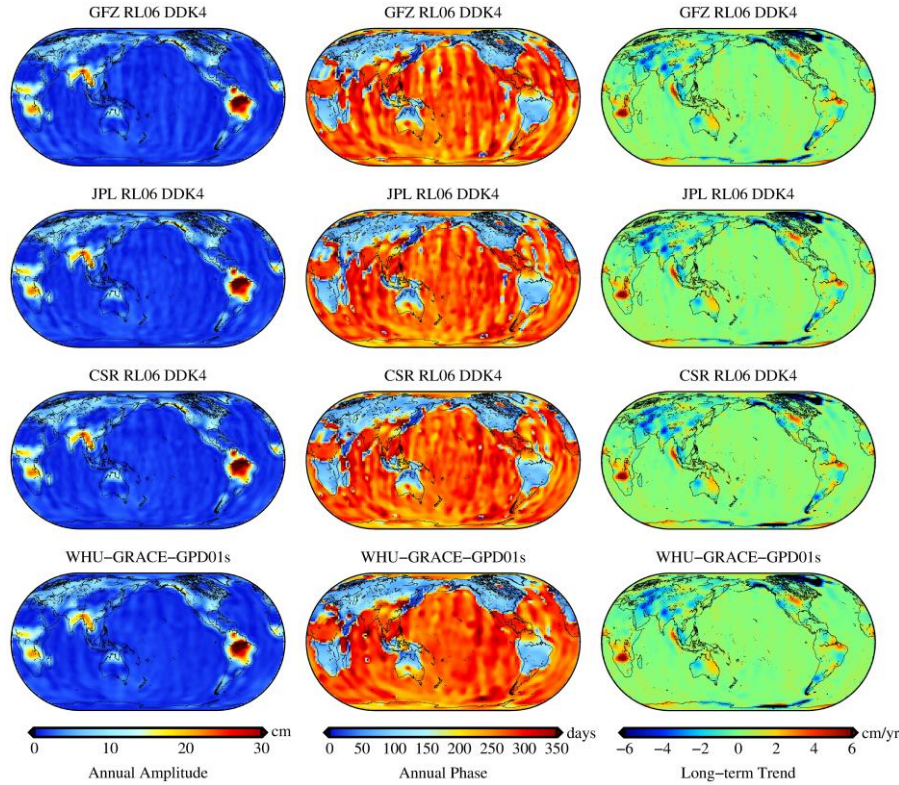


Figure 7. Annual amplitudes, annual phases, and long-term trends of global mass changes from the official unconstrained SH solutions (GFZ, JPL, and CSR RL06 with DDK4 filtering) and the constrained WHU-GRACE-GPD01s solutions over the period of January 2005 to December 2010.

To fill in the data gap between GRACE and GRACE Follow-On (GFO), other satellites' kinematic orbits derived from GPS-based high-low satellite-to-satellite tracking (hl-SST) data may be considered. We proposed an epoch-difference (ED) scheme in the context of the classical dynamic approach (CDA) to gravity field recovery. Compared to the traditional undifferenced (UD) scheme, the ED scheme can mitigate constant or slowly-varying systematic errors. To demonstrate the added value of the ED scheme, three sets of monthly gravity field solutions produced from six years of GRACE kinematic orbits are compared: two sets produced in-house (with the ED and UD scheme), and a set produced with the undifferenced scheme in the frame of the short-arc approach (SAA) (Zehentner and Mayer-Gürr 2015). As a reference, we use state-of-the-art ITSG-Grace2018 monthly gravity field solutions. A comparison in the spectral domain shows that the gravity field solutions suffer from a lower noise level when the ED scheme is applied, particularly at low-degree terms, with cumulative errors up to degree 20 being reduced by at least 20% (Figure ). In the spatial domain, the ED scheme notably reduces noise levels in the mass anomalies recovered (Figure ). In addition, the signals in terms of mean mass anomalies in selected regions become closer to those inferred from ITSG-Grace2018 solutions, while showing no evidence of any damping, when the ED scheme is used (Guo et al. 2020a).

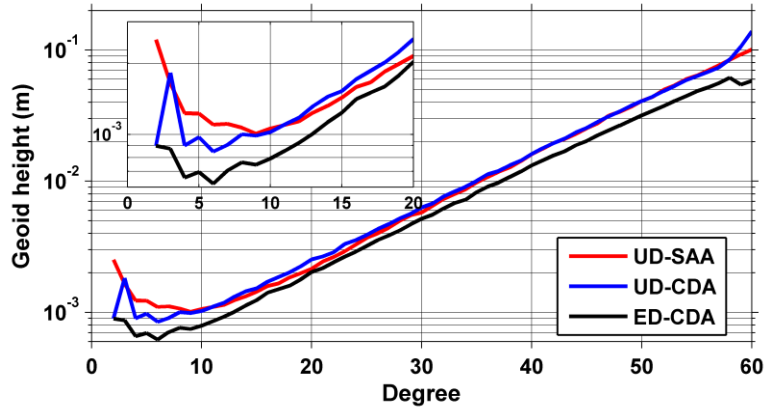


Figure 8. Geoid height errors per degree for different gravity field solutions (RMS values)

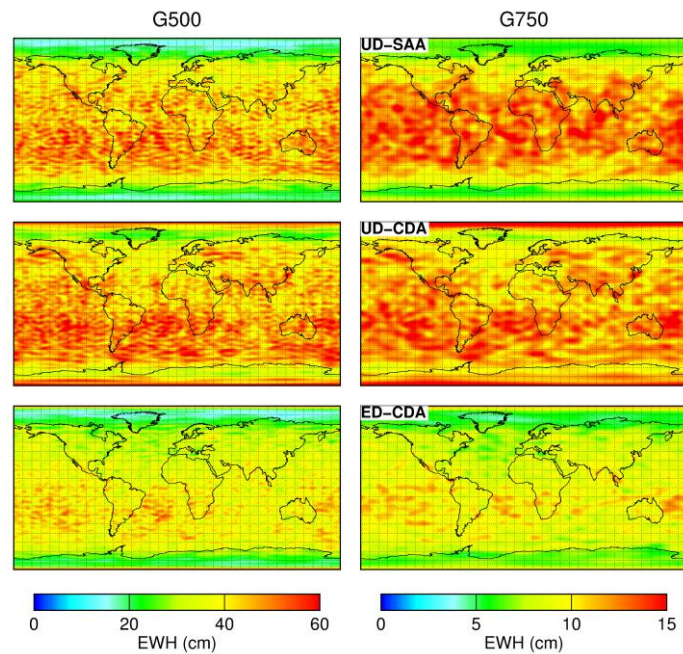


Figure 9. Geographical distribution of the gridded RMS differences with respect to ITSG2018 for different GPS-based solutions. The top, middle, and bottom rows show the results for the UD-SAA, UD-CDA, and ED-CDA solutions, respectively. G500/750: Gaussian smoothing filter with a 500/750 km radius.

In addition, the combination of high-low satellite-to-satellite tracking (HLSST) and satellite laser ranging (SLR) data is also investigated to determine the monthly gravity field solutions HLSST+SLR. The performance of the monthly HLSST+SLR solutions were evaluated in the spectral and spatial domains. Figure 10 shows that the accuracies of HLSST+SLR solutions are comparable to those from GRACE for SH coefficients below degree 10, and significantly improved compared to those of SLR-only and HLSST-only solutions (Zhong et al., 2021). It demonstrated that HLSST+SLR can be an alternative option to estimate temporal changes in the Earth gravity field, and can be used to monitor the large-scale mass transport during the data gaps between the GRACE and the GRACE follow-on missions.

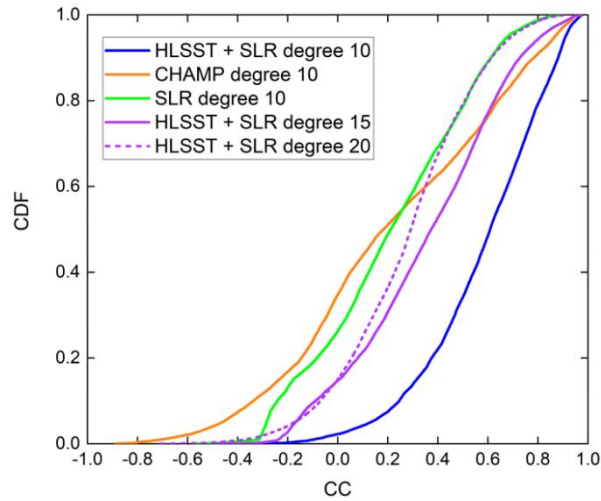


Figure 10. Cumulative distribution function (CDF) of spatial correlations from HLSST+SLR, CHAMP, SLR solutions with GRACE CSR. Note that the CC stands for coefficient correlation.

#### 4 Research outcomes of the SWJTU team

Precise orbits provide the necessary position information for gravity satellite missions with the support of the on-board Global Navigation Satellite System (GNSS) receiver. The generated purely kinematic orbits are subsequently used as pseudo-observations in gravity field recovery. In the past three years, the SWJTU team has been dedicated to processing and producing precise kinematic orbits as an important part of our gravity field recovery routine. As shown in Figure , the GRACE-FO kinematic orbits can achieve centimeter-level precision with respect to the JPL precise science orbit (PSO).

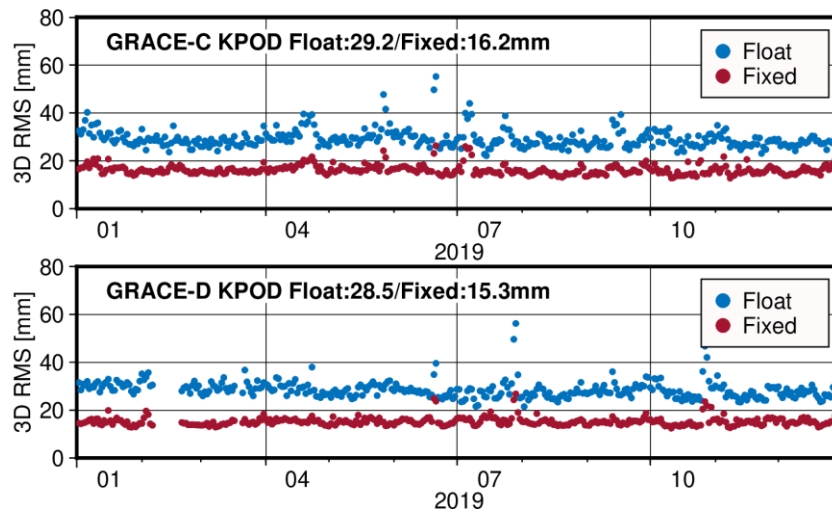


Figure 11. Daily RMS of orbit differences between GRACE-FO PSO products and orbits based on ambiguity float and fixed solutions.

Atmospheric and oceanic non-tidal high-frequency mass variations constitute a primary source of error that must be accurately modelled and removed before gravity field recovery. The SWJTU team utilized a first-generation atmospheric reanalysis dataset of China, CRA-40 (China Meteorological Administration’s Global Atmospheric Reanalysis), to establish an



atmospheric de-aliasing model called **CRA-40-AD**. For validation, CRA-40-AD displays comparable results with RL06 in geoid heights, as shown in Figure .

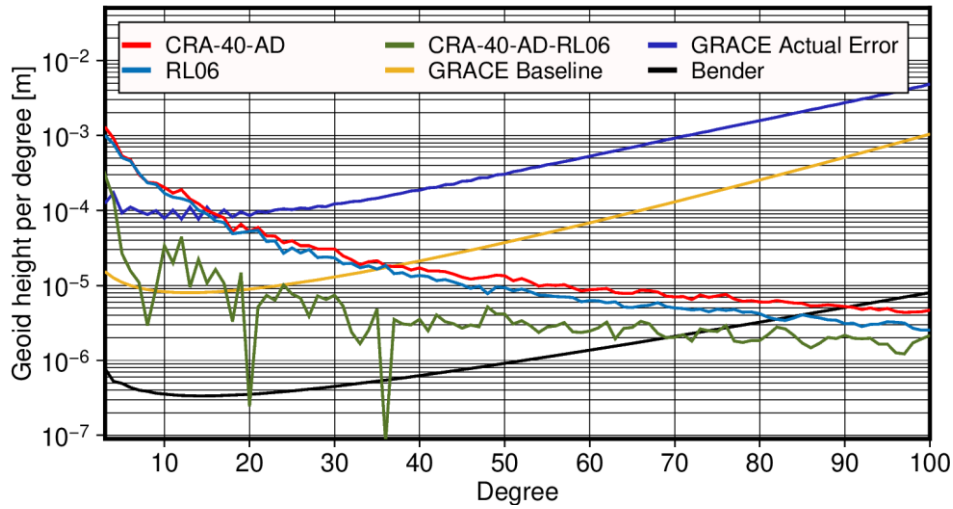


Figure 12. A comparison of geoid height per degree between CRA-40-AD and RL06, GRACE Baseline, Actual Error, and Bender Type curves are plotted as a reference.

Since 2019, the SWJTU team has been working on recovering a higher-precision temporal gravity field models with step-by-step improvements. In 2020, the **SWJTU-GRACE-RL02p** was derived based on original SWJTU-GRACE-RL01 with GRACE Level-1B RL03 data and a improved parametric strategy (Yu et al. 2021). Furthermore, we analyzed the residuals of SWJTU-GRACE-RL02p and considered the noises in calculated forces to decrease the correlations between residuals at different epochs to improve the quality of recoved models together with the determination of variance components of different observations. The new models present a better performance and the comparison of the two versions of models and official mdoels is shown in Figure .

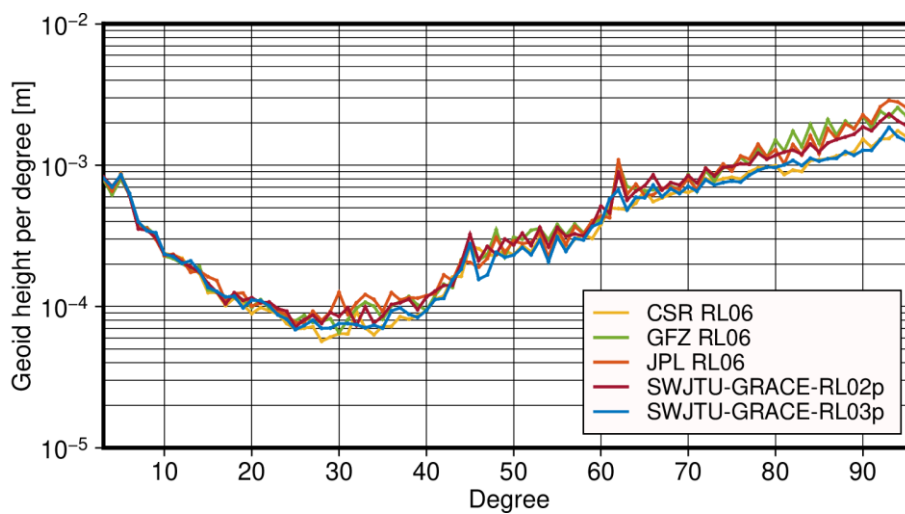


Figure 13. A comparison of geoid height per degree for 2009-03 with respect to EIGEN-6C4.

## 5 Research outcomes of the SWPU team

The SWPU team has extended the fundamental principle of the point mass model method and established a connection between satellite perturbation forces and surface mass changes in a rectangular coordinate system. By utilizing this improved method, we can directly compute surface mass changes using either gravity satellite observation data or a time-varying gravity field spherical harmonic coefficient model. The primary advantage of this method is its ability to enhance the theoretical model of the existing point mass model method. By including appropriate constraints in the computation of surface quality changes, the method can effectively reduce the impact of banded noise and signal leakage errors (Su et al., 2019). Furthermore, the team has meticulously processed the observation data over the entire lifecycle of GRACE and computed a 96 order monthly time-varying gravity field model **SWPU-GRACE2021** using dynamic methods. The model evaluation indicated that the overall accuracy of the model reached the sixth-generation official model's accuracy level, with the overall signal and noise levels conforming well with the CSR model (Su et al., 2022).

The team has also conducted investigations into the inversion of local surface mass changes using the Mascon method based on dynamic integration. This method is implemented by establishing a direct functional relationship between surface mass anomalies and satellite gravity observation data, thereby enabling the acquisition of high-precision and high-resolution inversion results of surface mass changes based on observation data and inversion region characteristics. To improve the ill-conditioned nature in the normal equation, spatiotemporal constraints (Mascon I) and prior information constraints (Mascon II) are introduced respectively. Taking the inversion of land surface mass changes in South America and Yangtze River Basin as examples, we utilized the GRACE Level-1B RL03 data and related mechanical models for 2005-2010 to calibrate orbit and accelerometer data, and obtained two sets of Mascon solution. By compared with the internationally released Mascon product (CSR/JPL Mascon RL06), Figure 14 shows that both constraint methods can yield relatively consistent inversion results, with the correlation coefficient of the Amazon basin reaching above 0.9. However, different Mascon solutions still exhibit certain differences in details. Without prior information, spatiotemporal correlation constraints can produce reliable Mascon inversion results. The Mascon solutions with different prior information models revealed that the inversion results do not rely on the prior model, but the detailed signals in the prior model have a certain impact on the inversion results. Hence, when abundant models or observation data exist in the study area, joint inversion of multi-source observation data can be conducted through prior information constraint methods (Li et al. 2020; Zhong et al., 2023a).



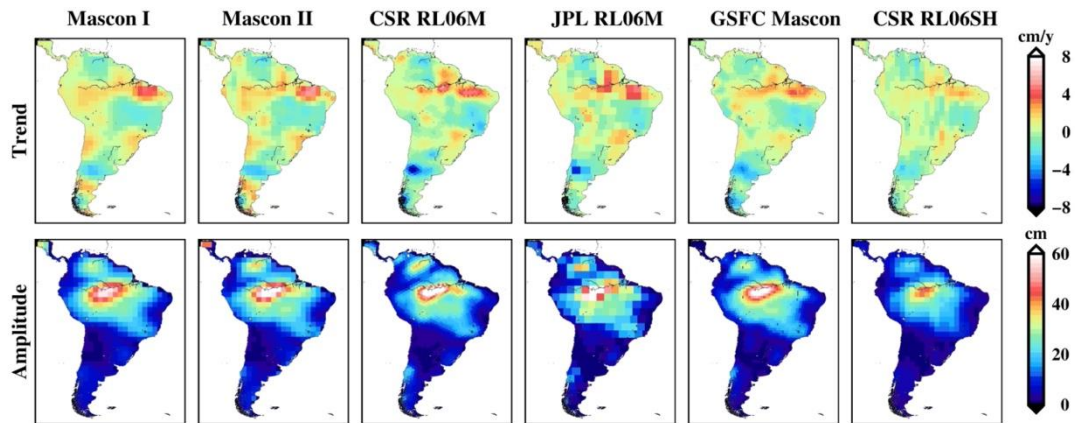


Figure 14. Spatial distribution of the amplitude and trend of land surface mass changes in South America from 2005 to 2010

## Bibliography

- Chen Q., Shen Y., Chen W., et al. (2019). An optimized short-arc approach: Methodology and application to develop refined time series of Tongji-Grace2018 GRACE monthly solutions. *Journal of Geophysical Research: Solid Earth*, 124(6), 6010-6038. <https://doi.org/10.1029/2018JB016596>.
- Chen Q., Shen Y., Kusche J., et al. (2021). High-Resolution GRACE Monthly Spherical Harmonic Solutions. *Journal of Geophysical Research: Solid Earth*, 126(1), e2019JB018892. <https://doi.org/10.1029/2019JB018892>.
- Chen Q., Wang F., Shen Y., et al. (2022). Monthly Gravity Field Solutions from Early LEO Satellites' Observations Contribute to Global Ocean Mass Change Estimates over 1993~2004. *Geophysical Research Letters*, e2022GL099917. <https://doi.org/10.1029/2022GL099917>.
- Guo X, Ditmar P, Zhao Q, Xiao Y (2020a). Improved recovery of temporal variations of the Earth's gravity field from satellite kinematic orbits using an epoch-difference scheme. *Journal of Geodesy*, 94(8). doi: 10.1007/s00190-020-01392-6.
- Guo X, Geng J, Chen X, Zhao Q (2020b). Enhanced orbit determination for formation-flying satellites through integrated single- and double-difference GPS ambiguity resolution. *GPS Solutions*, 24(1). doi: 10.1007/s10291-019-0932-1.
- Li Q, Luo Z C, Zhong B, et al. Mascon method based on different constraints for inversion of regional surface mass changes, Annual Meeting of Chinese Geoscience Union (CGU), Oct, 2020, Chongqing, China (in Chinese).
- Nie Y., Shen Y., Pail R., et al. (2022a). Revisiting Force Model Error Modeling in GRACE Gravity Field Recovery. *Surveys in Geophysics*, 43, 1169-1199. <https://doi.org/10.1007/s10712-022-09701-8>.
- Nie Y., Shen Y., Pail R., Chen Q. (2022b). Efficient variance component estimation for large-scale least-squares problems in satellite geodesy. *Journal of Geodesy*, 96, 13. <https://doi.org/10.1007/s00190-022-01599-9>
- Su Y, Zheng W L, Yu B. et al. (2019) Surface mass distribution derived from three-dimensional acceleration point-mass modeling approach with spatial constraint methods. *Chinese Journal of Geophysics* (in Chinese). 62(2): 508-519. doi: 10.6038/cjg2019L0770.
- Su Y, Li, J C, Zou, X C, Xu X Y, Wang C Q, Yu B, Li Q. (2022). SWPU-GRACE2021: a new temporal gravity model from GRACE. *GFZ Data Services*. <https://doi.org/10.5880/icgem.2022.001>.
- Yang F, Liang L, Wang C, Luo Z. (2022). Attitude Determination for GRACE-FO: Reprocessing the Level-1A SC and IMU Data. *Remote Sensing*. 14(1):126. <https://doi.org/10.3390/rs14010126>

- Yang, F., E. Forootan, C. Wang, J. Kusche, and Z. Luo. (2021). A New 1-Hourly ERA5-Based Atmosphere De-Aliasing Product for GRACE, GRACE-FO, and Future Gravity Missions, *Journal of Geophysical Research: Solid Earth*, 126 (9), e2021JB021, doi:10.1029/2021JB021926.
- Yu B, You W, Fan D-M, Su Y, Nigatu ZM (2021). A comparison of GRACE temporal gravity field models recovered with different processing details. *Geophysical Journal International* 227(2):1392-1417. <https://doi.org/10.1093/gji/ggab279>
- Zehentner N, Mayer-Gürr T (2015). Precise orbit determination based on raw GPS measurements. *Journal of Geodesy*, 90(3): 275-286. doi: 10.1007/s00190-015-0872-7.
- Zhong, B., Li, Q., Chen, J. & Luo, Z. (2022). A dataset of GRACE intersatellite geopotential differences from April 2002 to July 2016 (Version V2) [Dataset], Science Data Bank, doi: 10.11922/sciencedb.j00001.00365.
- Zhong B, Li Q, Li X P, et al. (2023a). Basin-scale terrestrial water storage changes inferred from GRACE-based geopotential differences: a case study of the Yangtze River Basin, China. *Geophysical Journal International*, 233(2):1318-1338.
- Zhong, B., Li, X., Chen, J. & Li, Q. (2023b). WHU-GRACE-GPD01s: A series of constrained monthly gravity field solutions derived from GRACE-based geopotential differences. *Earth and Space Science*, 10(4), e2022EA002699.
- Zhong, L., Sośnica, K., Weigelt, M., Liu, B. & Zou, X. (2021). Time-variable gravity field from the combination of HLSST and SLR. *Remote Sensing*, 13(17): 3491.
- Zhou, H., Zhou, Z. & Luo, Z. (2019). A new hybrid processing strategy to improve temporal gravity field solution. *Journal of Geophysical Research: Solid Earth*, 124(8), 9415-9432.
- Zhou, H., Zhou, Z., Luo, Z., Wang, K. & Wei, M. (2020). What can be expected from GNSS tracking of satellite constellations for temporal gravity field model determination? *Geophysical Journal International*, 222, 661-677.

# Progress and Achievements of Wide-area Real-time Precise Positioning

Xiaohong Zhang<sup>1</sup>, Yidong Lou<sup>1</sup>, Xingxing Li<sup>1</sup>, Shengfeng Gu<sup>1</sup>, Xin Li<sup>1</sup>, Pan Li<sup>1</sup>, Xiaodong Ren<sup>1</sup>, Xiaolei Dai<sup>1</sup>

<sup>1</sup> Wuhan University

## 1 Overview

Nowadays, there is an increasing demand for wide-area, real-time, and high-precision positioning in support of mass-market applications such as smartphones, the Internet of Things (IoT), and the automotive industry. From 2019 to 2023, many Chinese scholars have conducted extensive research on wide-area real-time precise positioning models, methods, and system applications, leading to a series of innovative achievements. These achievements can be broadly categorized into several aspects:

### (1) Real-time precise satellite orbit and clock

Real-time precise satellite orbit and clock corrections are prerequisites for wide-area real-time precise positioning. Numerous researchers have conducted research on orbit determination models, clock estimation models, ambiguity resolution, and efficiency improvement to provide precise and reliable orbit and clock products for real-time precise positioning.

### (2) Real-time FCB and precise atmospheric products

Real-time FCB and precise atmospheric products play a crucial role in achieving rapid and precise positioning. In the past four years, along with the construction and modernization of GNSS, especially the completion of BeiDou-3, Chinese researchers have made continuous progress in refining the real-time GNSS FCB estimation, global/regional precise ionospheric and tropospheric modeling, and providing high-quality FCB and atmospheric products to users for high-precision positioning applications.

### (3) Systems construction and commercial applications

Currently, China has established its wide-area real-time precision positioning system (such as SBAS and PPP-B2b) by providing precise satellite corrections via geostationary earth orbit (GEO) satellites. Besides, several Chinese companies are also devoted to constructing commercial high-precision systems (such as Qianxun XStar, Hi-Target Hi-RTP, UniStrong Atlas), to provide centimeter-level augmentation services in China and surrounding areas.

### (4) Future development: LEO augmentation

Presently, the rapid development of the LEO constellation brings innovative opportunities for satellite navigation. The fusion of LEO and GNSS, which brings significant improvement in satellite visibility and spatial geometry, is expected to further enhance the performance of PPP and finally provide a wide-area real-time and accurate positioning service. Therefore, Chinese scholars started to pay attention to LEO-augmented GNSS with the focus on its advantages for PPP rapid convergence, ambiguity resolution, global ionosphere modeling, etc.

## 2 Real-time GNSS Satellite Orbit Determination

### Ultra-rapid orbit determination

Due to the high accuracy of the satellite dynamical model, real-time GNSS satellite orbits are typically generated using predicted methods, such as the IGS ultra-rapid products. These orbits are extrapolated from batch least-squares (LSQ) POD solutions based on the latest available observations, and the accuracy and reliability depend on the stability of the satellite motion and force model, as well as the predicting duration. Various factors that impact the accuracy of precise orbit determination have been explored, such as the second- and third-order ionospheric corrections and different solar radiation pressure (SRP) models (Chen et al. 2019; Liu et al. 2019; Li et al. 2019, 2020; Yuan et al. 2020). Efficient processing strategies have also been developed to shorten the ultra-rapid updated time and improve orbit accuracy. Li et al. (2019) and Zhao et al. (2018) reduced the ultra-rapid updated time from 6h and 3h to 1h, resulting in an orbit improvement of about 20%~40%. The IGS analysis center of WHU has also released hourly-updated ultra-rapid orbit products, including GPS, GLONASS, Galileo, and BDS (<ftp://igs.gnsswhu.cn/pub/gps/products/MGEX>).

### Filter-based real-time orbit determination

In addition to the traditional batch LSQ and orbit prediction method, the filter-based method has been adopted in recent years to produce high-quality real-time orbit products. Duan et al. (2019) found that real-time POD results are more accurate than 6-h predicted orbits when the same tracking stations are involved. The filter-based method allows dynamic noise and orbit states to be tuned at each epoch, making it suitable for real-time POD of orbital maneuver satellites for stable and continuous orbit products (Dai et al. 2019). The ambiguity resolution (AR) method has been used for real-time POD in both double-differenced (DD) (Li et al. 2019) and undifferenced (UD) (Kuang et al. 2021; Dai et al. 2022) methods. Generally, AR improves the 3D RMS of filter-based orbit solutions by 40%~45%, with the average 3D RMS of the filter orbits being smaller than that of the ultra-rapid products from WHU (Figure 1). In terms of the convergence time and accuracy of kinematic PPP AR, the better performance of the filter orbit products is validated compared to the ultra-rapid orbit products (Lou et al. 2022).

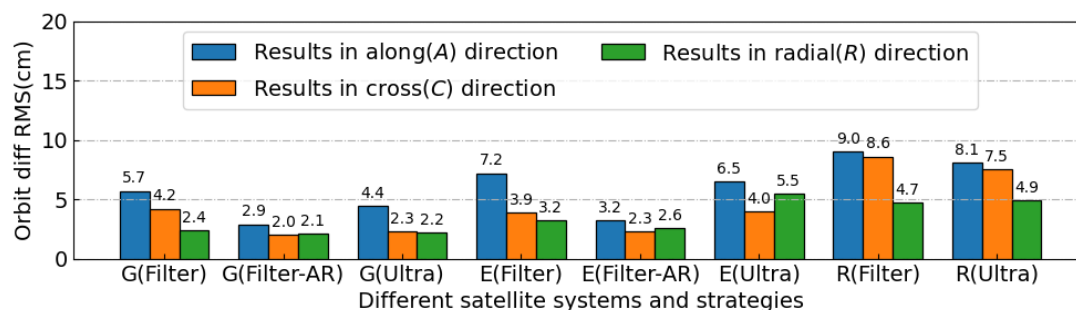


Figure 1. Average orbit accuracy of filtering solutions and ultra-rapid products from WHU for GPS, Galileo, and GLONASS satellites compared with the final products of CODE

### 3 Real-time GNSS Satellite Clock Estimation

#### Satellite clock estimation model

For the real-time clock estimation, three models are generally adopted, namely the undifferenced model (UD), epoch-differenced model (ED), and mixed model (MD). Two function models, namely the undifferenced model with all estimated parameters and the high-rate model introducing ambiguity estimates from the latest undifferenced model, were combined to improve the processing efficiency (Liu et al. 2019). A modified mixed-differenced approach for estimating multi-GNSS real-time clock offsets is presented, which further adds a satellite-differenced process and improves efficiency (Chen et al, 2018). Zhao et al. (2020) investigated the impacts of clock datum and initial clock of MD approach and proposed a flexible strategy for estimating real-time clock corrections, which consists of the clock prediction and the initial clock bias (ICB) bridging.

For traditional real time clock estimation, significant data discontinuity may arise an arbitrary clock jump between adjacent epochs. Shi et al. (2019) developed the oscillator noise model for the satellites of GPS, GLONASS, BDS, and Galileo according to the oscillator type as well as the block type, then introduced this oscillator noise model in real time multi-GNSS satellite clock estimation to improve the stability and smoothness of clock estimates.

#### Efficient processing method

A huge number of carrier-phase ambiguities estimated in the UD method significantly degrades the efficiency, in particular for multi-constellation or high-rate satellite clock estimation. Gong et al. (2018) utilized the square root information filter based on the QR factorization and ambiguity resolution to significantly reduce the computational load. The sequential least square adjustment with an adapted online quality control procedure was proposed to decrease the calculation time (Fu et al. 2019). Cao et al. (2022) developed a high-rate clock estimation algorithm without an external complex matrix library, which can be easily implemented in cross-platforms. Li et al (2022) introduced OpenMP and OpenBLAS to accelerate the processing of multi-GNSS clock estimation. Compared to the traditional serial strategy, the computation efficiency is significantly improved by more than 70% (Figure 2).

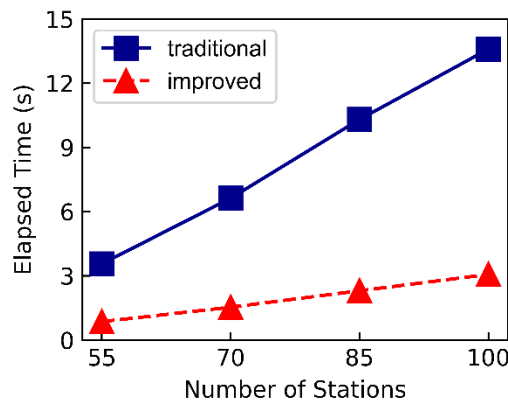


Figure 2. Elapsed time of quad-system clock estimation with 55-, 70-, 85-, and 100-station networks based on two computing strategies

### **Ambiguity fixed clock solution**

With the constraint of fixed ambiguities, the traditional float-ambiguity clock solution is further refined, resulting in ambiguity-fixed clock solution. An undifferenced ambiguity fixing algorithm is proposed for the classical real-time GNSS clock estimation without requiring modifications to the current data processing strategy and product consistency (Dai et al. 2019). Yang et al. (2019) developed an undifferenced ambiguity-fixed BDS satellite clock estimation method with triple-frequency ambiguity resolution, which contributes to both the initialization time and accuracy. Xie et al. (2023) proposed a dual-thread integer ambiguity resolution method, which realizes rapid re-convergence and high accuracy in multi-GNSS real-time clock estimation in case of the interruption.

## **4 Real-time FCB estimation**

### **Multi-GNSS FCB estimation**

The multi-GNSS FCB and integer clock estimation method is promoted. Li et al. (2019) developed a multi-GNSS integer recovery clock (MIRC) model that improves real-time clock estimates. The average computation time per epoch for 150 stations is improved by 97.1% compared to standard float clock estimation. Fu et al. (2022) proposed a Kalman filter-based online FCB determination method for satellite clock estimation, achieving wide-lane (WL) and narrow-lane (NL) FCB estimation accuracy of 0.004 cycles and 0.080 cycles, respectively. Hu et al. (2022) assessed BDS FCB and demonstrated that the inter-system bias between BDS-2 and BDS-3 should be taken into consideration in BDS PPP. Moreover, BDS-3 outperforms BDS-2 in FCB stability, positioning accuracy, and convergence time.

### **Multi-frequency FCB estimation**

The multi-frequency FCB is also investigated to fully exploit the multi-GNSS signal resource. Li et al. (2020) estimated phase and code biases of Galileo and BDS-3 binary offset carrier (BOC) signals, revealing Galileo E5a/E5b/E5ab signals and BDS-3 B2a/B2b signals exhibit the same phase biases with the resultant extra-wide-lane (EWL) FCBs very close to zero. Geng and Guo (2020) estimated the uncombined Galileo and BeiDou-3 multi-frequency phase biases and achieved single-epoch decimeter-level positioning using WL ambiguity resolution. Geng et al. (2020) estimated the triple-frequency GPS/BeiDou/Galileo/QZSS FCBs and found that EWL, WL, and NL FCBs were quite stable over time with standard deviations of less than 0.005, 0.025, and 0.030 cycles, respectively. The time-to-first-fix of triple-frequency PPP AR can be reduced from 9 min to 6 min compared with the legacy double-frequency solution. Jiang et al. (2022) estimated the multi-frequency phase OSB using the geometry-free and ionospheric-free (GF-IF) combination, achieving centimeter-level positioning accuracy with 3-h observation session. Furthermore, Geng et al. (2022) generated the GNSS OSB corrections for all-frequency PPP ambiguity resolution.

### **Real-time FCB estimation model refinement**

Chinese researchers also focused on refining the GNSS error correction model to improve the FCB quality. Qu et al. (2021) demonstrated that the IGS ultra-rapid orbits errors



significantly degrade the accuracy of real-time NL FCBs. Geng et al. (2021) identified the necessity of considering the differences in antenna phase center correction among frequencies in the Melbourne-Wübbena (MW) combination for WL FCB estimation. Cui et al. (2021) estimated receiver-type-dependent WL FCBs and discovered that deviations of up to 0.3 cycles can exist among different types of receivers. Shi et al. (2022) observed that signal distortion biases (SDBs) originating from receivers can significantly impact the FCB estimation of GPS and BDS, whereas the effect on Galileo is negligible (Figure 3). The application of SDBs led to an improvement of 46% and 13% in the accuracies of WL and NL FCBs, respectively. Furthermore, Zheng et al. (2023) reported that the correction of multipath errors resulted in a decrease in the mean RMS of NL FCB from 0.086 to 0.075 cycles.

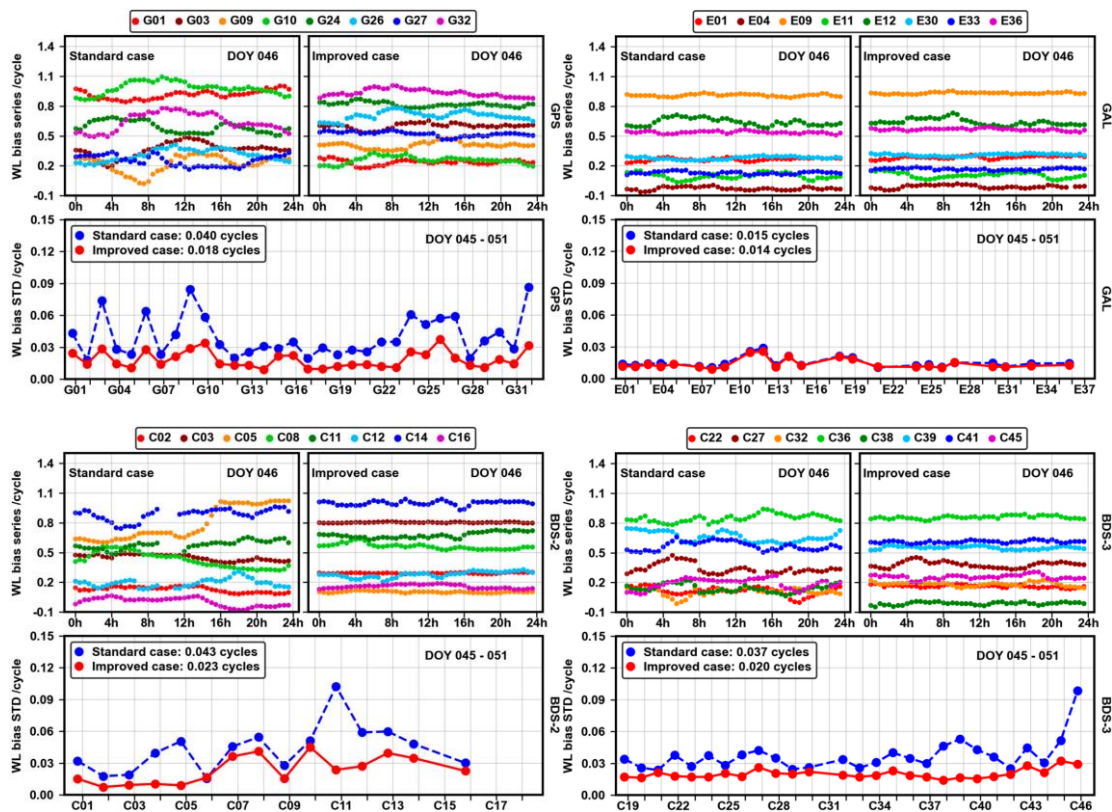


Figure 3. WL phase bias series on DOY 46, 2021 and the corresponding STDs across 7 days for GPS, Galileo, BDS-2, and BDS-3 before and after the calibration of signal distortion biases

## 5 Real-time ionospheric and tropospheric model

### Ionosphere modeling

High-precision ionospheric models require precise extraction of ionospheric total electron content (TEC) measurements. The PPP AR method was employed to extract ionospheric observations from phase observations based on undifferenced integer ambiguity (Ren et al. 2020), which improves the precision of the TEC observations by 91.7% and 67.3% compared to the traditional PL-C and UD-PPP methods. Besides, Xu et al (2022) applied GNSS dual-frequency measurements derived from smartphone in the analysis of the performance of



ionospheric TEC, which revealed that using consumer-level GNSS chipsets with optimal antennas in ionospheric studies is feasible.

In recent years, a series of novel ionosphere model such as two spherical harmonic regional real-time ionospheric model (Li et al 2019), Satellite-based Ionospheric Model (Li et al. 2022), Quasi-4-Dimension Ionospheric Modeling (Q4DIM, Gu et al 2022), Conventional Long Short-Term Memory (ConvLSTM)-based ionospheric model (Gao et al 2023), multi-layer VTEC model (Sui et al. 2023) was proposed. The results show that the proposed new models outperform the GIM and RIM products and significantly improve the convergence time of PPP. Currently, two institutions in China starts to provide real-time global ionospheric grid map, namely the Chinese Academy of Sciences (CAS, Li et al. 2020) and Wuhan University (WHU). Figure 4 gives an example of real-time global VTEC maps from CAS.

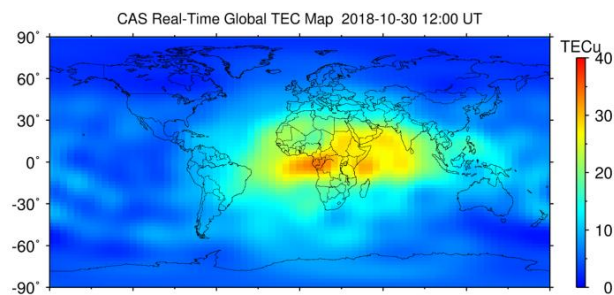


Figure 4. Real-time global VTEC maps from CAS on October 30, 2018, at 12:00 UT

## Troposphere modeling

With the rapid development of satellite navigation systems around the globe, the demand for real-time and high-accuracy troposphere models has been growing dramatically. The traditional Hopfield and Saastamoinen ZTD models are refined by adding annual and semi-annual periodic terms and using the Back-Propagation Artificial Neural Network (Yang et al. 2021). A new simplified zenith tropospheric delay model for GNSS real-time applications using numerical weather prediction data from the NCEP was established (Mao et al. 2021). Huang et al. (2023) derived an improved global grid ZTD model considering the height scale factor. To further improve the accuracy and spatial-temporal resolution of tropospheric products, a series of multi-source real-time tropospheric delay model that uses ground-based GNSS observations, meteorological data (such as ERA5), and empirical GPT2w models were developed (Yao et al. 2019; Xia et al. 2023; Lu et al. 2023).

## 6 Wide-area real-time precise positioning service

### BDS high-precision positioning service

The BDSBAS service broadcasts various wide-area differential corrections, including satellite orbit/clock corrections, ionospheric grids, and satellite partition comprehensive corrections, through the B1C signal of GEO satellites (Yang et al. 2022). Users in the BDS GEO coverage areas can achieve decimeter-level positioning in real-time and the experiment results show that the RMS of the positioning errors for static/kinematic dual-frequency PPP is 12 cm/16 cm and 18 cm/20 cm in the horizontal and vertical components, respectively. With

regard to the convergence performance, the horizontal and vertical positioning errors of kinematic PPP can converge to 0.5 m in less than 15 min and 20 min (Chen et al. 2021). PPP-B2b broadcasts precise orbit, clock offset, and DCB through BDS-3 GEO B2b\_I navigation message for PPP users over China. The typical broadcast interval is 48 seconds and 6 seconds for orbit and clock, respectively (Yang et al. 2022). As evaluated by Lan et al. (2022), the precision of PPP-B2b orbits are 9.42 cm, 21.26 cm, and 28.65 cm in the radial, along-track, and cross-track components, while the accuracy of PPP-B2b clock is 0.18 ns, which meets the real-time kinematic decimeter-level positioning needs of PPP users.

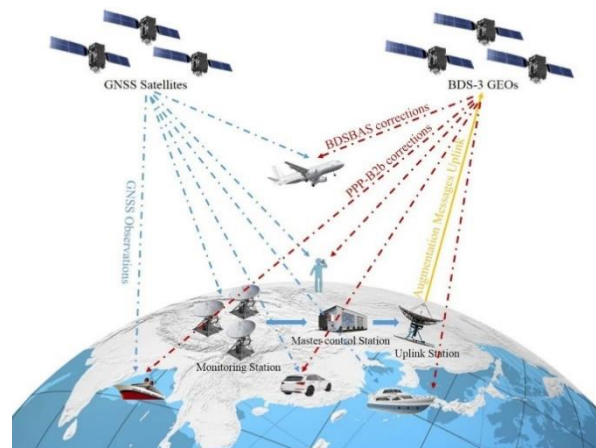


Figure 5. BDSBAS and PPP-B2b service of BDS-3

### Commercial high-precision positioning service

Besides the built-in high-precision positioning service of BDS, several commercial companies, such as Qianxun, Sixents Technology, and China Mobile have successively established their high-precision service system. All these companies can provide high-precision positioning service through several thousands of stations in China, and the users within this region can get a positioning precision of centimeters to millimeters (Shi et al. 2022). More recently, Qianxun has declared that instantaneous centimeter-level positioning can be achieved all over the world through their PPP-AR technology.

### Public high-precision positioning service

Attributed to the Real-Time Working Group (RTWG) of the International GNSS Service (IGS), Wuhan University has provided the real-time BDS/GNSS high precision orbit and clock for the worldwide PPP users. Li et al. (2022) compared SSR products from IGS RTS ACs (analysis centers), and the results indicated that Centre National D'Etudes Spatiales (CNES) and GNSS Research Center of Wuhan University (WHU) provide the most complete products with the best quality, with one-dimensional BDS orbit precision of MEO better than 10 cm and clock precision better than 0.35 ns. Concerning the potential applications of RTS for timing, Guo et al. (2022) further assessed the datum stability of WHU RT clock products, which is about  $3.05E-13/120$  s.

## 7 Performance of BDS-3 PPP-B2b Services

In addition to standard positioning, navigation, and timing (PNT) services, the BDS-3 also provides PPP service through B2b signals of GEO satellites (PPP-B2b). PPP-B2b service is a satellite-based service, which provides the precise orbits, clock offsets, and difference code bias (DCB) corrections of GPS and BDS-3 satellites to users in China and its surrounding areas ( $80^{\circ}\text{E}\sim 155^{\circ}\text{E}$ ,  $5^{\circ}\text{S}\sim 55^{\circ}\text{N}$ ). The central frequency of PPP-B2b signal is 1207.14 MHz and the bandwidth is 20.46 MHz (Yang et al. 2020, 2021, 2022).

### Service coverage of PPP-B2b service

The PPP-B2b service coverage is relatively even across all of Asia, with the best coverage in eastern China (Tao et al. 2021). The number of GPS and BDS-3 satellites that can match and recover real-time products is about 5~7, and the number of BDS-3 satellites is about 6~8. Overall, there are fewer GPS satellites available for PPP-B2b than BDS-3 satellites. Liu et al. (2022) indicated that the availability of PPP-B2b is highest in eastern China and decreases gradually toward the edge of the service area. In Wuhan, the average availability of GPS is not less than 80%, and the average availability of BDS-3 is about 90%. In order to improve the availability of satellite-based augmentation differential corrections, IGSO satellites can also be used to jointly broadcast the corrections of BDSBAS and PPP-B2b (Yang et al. 2022). The expected service coverage after the participation of the IGSO satellites is shown in Figure 6.

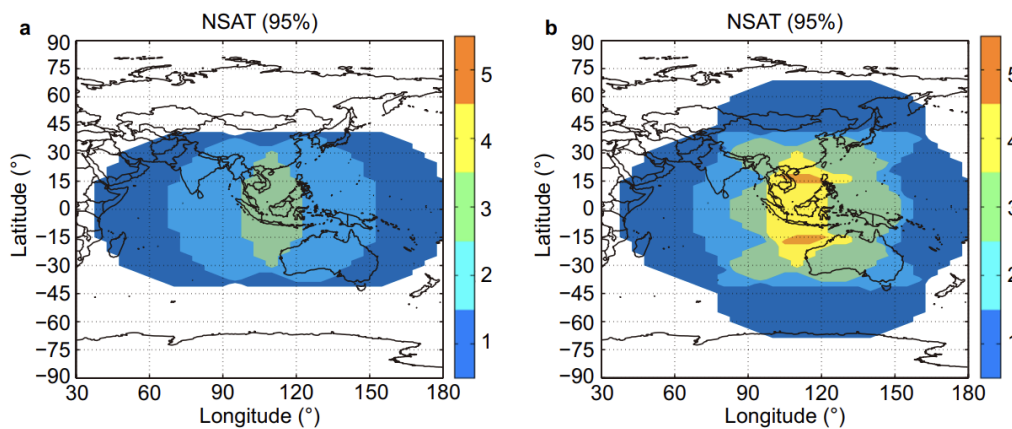


Figure 6. Visible satellites(a: 3GEO, b: 3 GEO+3 IGSO) with the elevation cut-of angle of  $40^{\circ}$ .

### Accuracy of orbit, clock, and bias products of PPP-B2b

In terms of orbit accuracy, the BDS-3 satellites are 6.5 cm, 24.0 cm, and 21.0 cm in radial, along-track, and cross-track components, while the accuracy of the IGSO orbit is slightly lower than that of the MEO orbit. Compared with the satellite orbit generated from broadcast ephemeris, the PPP-B2b real-time orbit error sequence is more continuous and smoother. Xu et al. (2021) indicated that the broadcast ephemeris is updated at regular intervals, and the orbits generated before and after the ephemeris update have significant jumps. The PPP-B2b real-time orbits effectively weaken such jumps. The STD values of real-time clock offset errors are below 0.18 and 0.15 ns for BDS-3 and GPS satellites (Ren et al. 2021). Tang et al. (2022) analyzed the accuracy of different types of DCBs. The result shows that the DCB(B1I) errors are smaller

than 2.0 ns, and the RMS of DCB for the remaining codes is 0.3 ns~0.7 ns.

### PPP performance of PPP-B2b

The PPP performance based on PPP-B2b signals was comprehensively evaluated. The results show that after convergence, the RMS of BDS-3 PPP is better than 0.15 and 0.2 m in the horizontal and vertical directions, respectively. The average convergence time is about 18 min (Yang et al. 2022). The positioning accuracy of the B1C/B2a combination is basically comparable to that of the B1I/B3I combination, but its convergence time is longer (Song et al. 2021). Zhou et al. (2022) examined the positioning performance of PPP-B2b augmented single frequency PPP (SF-PPP) with 7 GNSS stations for 15 consecutive days. By applying the PPP-B2b corrections, SF-PPP achieves better than 0.3 m and 0.6 m accuracy for the horizontal and vertical directions, respectively. The mean convergence time is close to the final precise product-based PPP solution.

Table 1. Accuracy (RMS) and convergence time of BDS PPP-B2b kinematic positioning

Positioning performance		WUHZ		BJF1		SHA1		KUN1	
		H	V	H	V	H	V	H	V
RMS (m)	DOY 248	0.077	0.125	0.080	0.124	0.061	0.075	0.087	0.118
	DOY 249	0.077	0.126	0.112	0.161	0.094	0.132	0.096	0.139
	DOY 250	0.077	0.136	0.116	0.132	0.093	0.122	0.107	0.111
	DOY 251	0.077	0.147	0.118	0.120	0.106	0.151	0.093	0.142
	DOY 252	0.056	0.138	0.079	0.114	0.068	0.116	0.090	0.129
	Average	0.073	0.134	0.101	0.130	0.085	0.119	0.094	0.128
Convergence time (min)		18.75		18.43		21.79		16.17	

## 8 LEO constellation augmented GNSS

An extended GNSS system with the LEO constellation transmitting navigation signals, which is called LEO enhanced Global Navigation Satellite Systems, consisting of high, medium, and low Earth orbit satellites, is proposed for the future precise positioning service (Li et al. 2019). To validate its advantages in accelerating the PPP convergence, the simulated LEO measurements are introduced to PPP processing in various challenging environments (Li et al. 2019; Li et al. 2022). As shown in Figure 7, with the augmentation of 60-, 96-, 192- and 288-satellite LEO constellation, the multi-GNSS PPP convergence time can be shortened from 9.6 to 7.0, 3.2, 2.1, and 1.3 min, respectively.

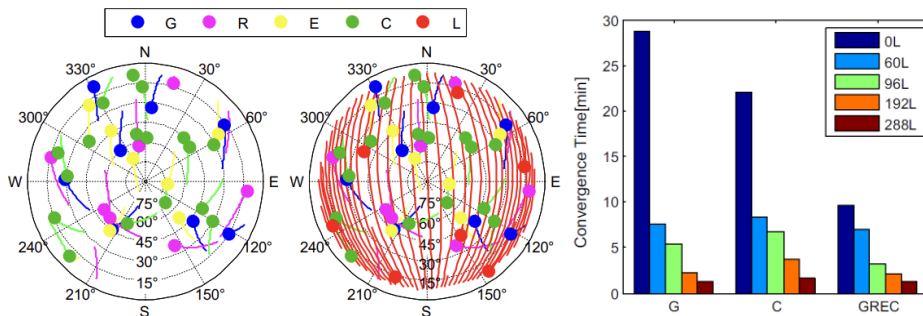


Figure 7. Sky plots of the multi-GNSS satellites without or with the augmentation of 192 LEO satellites (left panel); Average convergence time of LEO augmented PPP solutions(right panel)

The fusion of LEO constellation and GNSS can increase the number of visible satellites and optimize spatial geometry, which is expected to further improve the performance of PPP AR. Li et al. (2019) investigated the performance of LEO-augmented PPP AR with three types of LEO constellations. With observations of the 288-LEO constellation, the GREC fixed solutions can converge to 5 cm in all three directions within 1 min for all three stations.

Besides, the rapid development of LEO constellations provides a great opportunity to global ionospheric modeling, which is still not good over many regions (e.g., the oceans and the polar regions) due to the lack of ground-based GNSS stations. Ren et al. (2020) simulated observation data of three kinds of LEO constellations with 60, 96, and 192 satellites, and the results show that LEO observations can expand the coverage and increase the density of ionospheric pierce points (IPPs), thereby improving the precision of ionospheric modeling by 35.9%~50%.

Ge et al. (2022) comprehensively reviewed the current status of LEO-augmented GNSS, and analyzed the opportunities and challenges in terms of LEO constellation design, operation mode, and positioning performance, etc. Thanks to the fast geometric change brought by LEO satellites, LEO augmentation is expected to fundamentally solve the problem of the long convergence time of PPP without any augmentation. The convergence time can be shortened to within 1 min if appropriate LEO constellations are deployed. However, there are still some issues to overcome, such as the optimization of LEO constellation as well as the real-time LEO precise orbit and clock determination.

## Bibliography

- Andersen, OB., Knudsen, P. (2019). The DTU17 global marine gravity field: first validation results. In: International association of geodesy symposia, Berlin, Heidelberg.
- Chen Xinghan, Ge Maorong, Haroldo Antonio Marques, Schuh Harald. Evaluating the impact of higher-order ionospheric corrections on multi-GNSS ultra-rapid orbit determination[J]. *Journal of Geodesy*, 2019, 93(9): 1347-1365.
- Liu Yang, Liu Yanxiong, Tian Ziwen, Dai Xiaolei, Qing Yun, Li Menghao. Impact of ECOM Solar Radiation Pressure Models on Multi-GNSS Ultra-Rapid Orbit Determination[J]. *Remote Sensing*, 2019, 11(24).
- Li Xingxing, Yuan Yongqiang, Huang Jiande, Zhu Yiting, Wu Jiaqi, Xiong Yun, Li Xin, Zhang Keke. Galileo and QZSS precise orbit and clock determination using new satellite metadata[J]. *Journal of Geodesy*, 2019, 93(8): 1123-1136.
- Li Xingxing, Yuan Yongqiang, Zhu Yiting, Jiao Wenhai, Bian Lang, Li Xin, Zhang Keke. Improving BDS-3 precise orbit determination for medium earth orbit satellites[J]. *GPS Solutions*, 2020, 24(2): 53.
- Yuan Yongqiang, Li Xingxing, Zhu Yiting, Xiong Yun, Huang Jiande, Wu Jiaqi, Li Xin, Zhang Keke. Improving QZSS precise orbit determination by considering the solar radiation pressure of the L-band antenna[J]. *GPS Solutions*, 2020, 24(2): 50.
- Li Xingxing, Chen Xinghan, Ge Maorong, Schuh Harald. Improving multi-GNSS ultra-rapid orbit determination for real-time precise point positioning[J]. *Journal of Geodesy*, 2019, 93(1): 45-64.
- Zhao Qile, Xu Xiaolong, Ma Hongyang, Liu Jingnan. Real-time precise orbit determination of BDS/GNSS: method and service[J]. *Geomatics and Information Science of Wuhan University*, 2018, 43(12): 2157-2166.
- Duan Bingbing, Hugentobler Urs, Chen Junping, Inga Selmke, Wang Jiexian. Prediction versus real-time orbit determination for GNSS satellites[J]. *GPS Solutions*, 2019, 23(2): 39.

- Dai Xiaolei, Lou Yidong, Dai Zhiqiang, Qing Yun, Li Min, Shi Chuang. Real-time precise orbit determination for BDS satellites using the square root information filter[J]. *GPS Solutions*, 2019, 23(2): 45.
- Li Zongnan, Li Min, Shi Chuang, Fan Lei, Liu Yang, Song Weiwei, Tang Weiming, Zou Xuan. Impact of ambiguity resolution with sequential constraints on real-time precise GPS satellite orbit determination[J]. *GPS Solutions*, 2019, 23(3): 85.
- Kuang Kaifa, Li Jiancheng, Zhang Shoujian, Wei Hui, Cao Xinyun. Improve real-time GNSS orbit with epoch-independent undifferenced ambiguity resolution[J]. *Advances in Space Research*, 2021, 68(11): 4544-4555.
- Dai Xiaolei, Gong Xiaopeng, Li Chenglong, Qing Yun, Gu Shengfeng, Lou Yidong. Real-time precise orbit and clock estimation of multi-GNSS satellites with undifferenced ambiguity resolution[J]. *Journal of Geodesy*, 2022, 96(10) : 73.
- Lou Yidong, Dai Xiaolei, Gong Xiaopeng, Li Chenglong, Qing Yun, Liu Yang, Peng Yaquan, Gu Shengfeng. A review of real-time multi-GNSS precise orbit determination based on the filter method[J]. *Satellite Navigation*, 2022, 3(1): 15.
- Liu Teng, Zhang Baocheng, Yuan Yunbin, Zha Jiuping, Zhao Chuanbao. An efficient undifferenced method for estimating multi-GNSS high-rate clock corrections with data streams in real time[J]. *Journal of Geodesy*, 2019, 93(9): 1435-1456.
- Chen Liang, Zhao Qile, Hu Zhigang et al. GNSS global real-time augmentation positioning: Real-time precise satellite clock estimation, prototype system construction and performance analysis[J]. *Advances in Space Research*, 2018, 61(1), 367-384.
- Zhao Lewen, Dousa, Jan, Ye Shirong, Pavel Vaclavovic. A flexible strategy for handling the datum and initial bias in real-time GNSS satellite clock estimation[J]. *Journal of Geodesy*, 2020, 94, 1-11.
- Shi Chuang, Guo Shiwei, Gu Shengfeng, Yang Xinhao, Gong Xiaopeng, Deng Zhiguo, Ge Maorong, Harald Schuh. Multi-GNSS satellite clock estimation constrained with oscillator noise model in the existence of data discontinuity[J]. *Journal of Geodesy*, 2019, 93, 515-528.
- Gong Xiaopeng, Gu Shengfeng, Lou Yidong, Zheng Fu, Ge Maorong, Liu Jingnan. An efficient solution of real-time data processing for multi-GNSS network[J]. *Journal of Geodesy*, 2018, 92, 797-809.
- Fu Wenju, Huang Guanwen, Zhang Qin, Gu Shengfeng, Ge Maorong, Schuh Harad. Multi-GNSS real-time clock estimation using sequential least square adjustment with online quality control[J]. *Journal of Geodesy*, 2019, 93, 963-976.
- Cao Xinyun, Kuang Kaifa, Ge Yulong, Shen Fei, Zhang Soujian, Li Jiancheng. An efficient method for undifferenced BDS-2/BDS-3 high-rate clock estimation[J]. *GPS Solutions*, 2022, 26(3), 66.
- Li Xingxing, Li Yuhao, Xiong Yun, Wu Jiaqi, Zheng Hongjie, Li Linyang. An efficient strategy for multi-GNSS real-time clock estimation based on the undifferenced method[J]. *GPS Solutions*, 2023, 27(1), 23.
- Dai Zhiqiang, Dai Xiaolei, Zhao Qile, Liu Jingnan. Improving real-time clock estimation with undifferenced ambiguity fixing[J]. *GPS Solutions*, 2019, 23, 1-12.
- Yang Xinhao, Gu Shengfeng, Gong Xiaopeng, Song Weiwei, Lou Yidong, Liu Jingnan. Regional BDS satellite clock estimation with triple-frequency ambiguity resolution based on undifferenced observation[J]. *GPS Solutions*, 2019, 23, 1-11.
- Xie Wei, Huang Guanwen, Fu Wenju, Li Mengyuan, Du Shi, Tan Yue. Realizing rapid re-convergence in multi-GNSS real-time satellite clock offset estimation with dual-thread integer ambiguity resolution[J]. *GPS Solutions*, 2023, 27(1), 54.
- Li Xingxing, Xiong Yun, Yuan Yongqiang, Wu Jiaqi, Li Xin, Zhang Keke, Huang Jiaxin. Real-time estimation of multi-GNSS integer recovery clock with undifferenced ambiguity resolution[J]. *Journal of Geodesy*, 2019, 93(12): 2515-2528.
- Fu Wenju, Wang Jin, Wang Lei, Chen Ruizhi. A Kalman filter-based online fractional cycle bias determination method for real-time ambiguity-fixing GPS satellite clock estimation[J]. *Measurement*, 2022, 205: 112207.

- Hu Jiahuan, Li Pan, Zhang Xiaohong, Bisnath Sunil, Pan Lin. Precise point positioning with BDS-2 and BDS-3 constellations: ambiguity resolution and positioning comparison[J]. *Advances in Space Research*, 2022, 70(7) : 1830-1846.
- Li Xingxing, Li Xin, Liu Gege, Xie Weiliang, Guo Fei, Yuan Yongqiang, Zhang Keke, Feng Guolong. The phase and code biases of Galileo and BDS-3 BOC signals: effect on ambiguity resolution and precise positioning[J]. *Journal of Geodesy*, 2020, 94(1) : 9.
- Geng Jianghui, Guo Jiang. Beyond three frequencies: an extendable model for single-epoch decimeter-level point positioning by exploiting Galileo and BeiDou-3 signals[J]. *Journal of Geodesy*, 2020, 94(1) : 14.
- Geng Jianghui, Guo Jiang, Meng Xiaolin, Gao Kefu. Speeding up PPP ambiguity resolution using triple-frequency GPS/BeiDou/Galileo/QZSS data[J]. *Journal of Geodesy*, 2020, 94(1) : 6.
- Jiang Weiping, Liu Tianjun, Chen Hua, Song Chuanfeng, Chen Qusen, Geng Tao. Multi-frequency phase observable-specific signal bias estimation and its application in the precise point positioning with ambiguity resolution[J]. *GPS Solutions*, 2022, 27(1) : 4.
- Geng Jianghui, Wen Qiang, Zhang Qiyuan, Li Guangcai, Zhang Kunlun. GNSS observable-specific phase biases for all-frequency PPP ambiguity resolution[J]. *Journal of Geodesy*, 2022, 96(2) : 11.
- Qu Lizhong, Zhang Pu, Jing Changfeng, Du Mingyi, Wang Jian, Zhao Qile, Li Juanjuan. Estimating the Fractional Cycle Biases for GPS Triple-Frequency Precise Point Positioning with Ambiguity Resolution Based on IGS Ultra-Rapid Predicted Orbits[J]. *Remote Sensing*, 2021, 13(16).
- Geng Jianghui, Yang Songfeng, Guo Jiang. Assessing IGS GPS/Galileo/BDS-2/BDS-3 phase bias products with PRIDE PPP-AR[J]. *Satellite Navigation*, 2021, 2(1) : 17.
- Cui Bobin, Li Pan, Wang Jungang, Ge Maorong, Harald Schuh. Calibrating receiver-type-dependent wide-lane uncalibrated phase delay biases for PPP integer ambiguity resolution[J]. *Journal of Geodesy*, 2021, 95(7) : 82.
- Shi Chuang, Tian Yuan, Zheng Fu, Hu Yong. Accounting for Signal Distortion Biases for Wide-Lane and Narrow-Lane Phase Bias Estimation with Inhomogeneous Networks[J]. *Remote Sensing*, 2022, 14(1).
- Zheng Kai, Tan Lingmin, Liu Kezhong, Li Pan, Chen Mozi, Zeng Xuming. Multipath mitigation for improving GPS narrow-lane uncalibrated phase delay estimation and speeding up PPP ambiguity resolution[J]. *Measurement*, 2023, 206: 112243.
- Ren Xiaodong, Chen Jun, Li Xingxing, et al. Multi-GNSS contributions to differential code biases determination and regional ionospheric modeling in China[J]. *Advances in Space Research*, 2020, 65(1): 221-234.
- Li Wen, Li Zishen, Wang Ningbo, et al. A satellite-based method for modeling ionospheric slant TEC from GNSS observations: algorithm and validation[J]. *GPS Solutions*, 2022, 26(1): 14.
- Xu Li, Zhang Jiuping, Li Min, et al. Estimation of ionospheric total electron content using GNSS observations derived from a smartphone[J]. *GPS Solutions*, 2022, 26(4): 138.
- Li Zishen, Wang Ningbo, Wang Liang, Liu Ang, Yuan Hong, Zhang Kefei. Regional ionospheric TEC modeling based on a two-layer spherical harmonic approximation for real-time single-frequency PPP[J]. *Journal of Geodesy*, 2019, 93(9) : 1659-1671.
- Gu Shengfeng, Gan Chengkun, He Chengpeng, et al. Quasi-4-dimension ionospheric modeling and its application in PPP[J]. *Satellite Navigation*, 2022, 3(1): 24
- Gao Xin, Yao Yibin. A storm-time ionospheric TEC model with multichannel features by the spatiotemporal ConvLSTM network[J]. *Journal of Geodesy*, 2023, 97(1): 9.
- Sui Yun, Fu Haiyang, Wang Denghui, et al. Multi-layer Ionospheric Model Constrained by Physical Prior Based on GNSS Stations[J]. *IEEE Journal of Selected Topics in Applied Earth Observations and Remote Sensing*, 2023, 16: 1842-



1857.

- Li Zishen, Wang Ningbo, Hernández-Pajares Manuel, Yuan Yunbin, Krankowski Andrzej, Liu Ang, Zha Jiuping, Alberto García-Rigo, David Roma-Dollase, Yang Heng, Denis Laurichesse, Alexis Blot. IGS real-time service for global ionospheric total electron content modeling[J]. *Journal of Geodesy*, 2020, 94(3): 32.
- Yang Fei, Meng Xiaolin, Guo Jiming, Yuan Debao, Chen Ming. Development and evaluation of the refined zenith tropospheric delay (ZTD) models[J]. *Satellite Navigation*, 2021, 2(1):21.
- Mao Jian, Wang Qiang, Liang Yubin, Cui Tiejun. A new simplified zenith tropospheric delay model for real-time GNSS applications[J]. *GPS Solutions*, 2021, 25(2): 43.
- Huang Liangke, Zhu Ge, Peng Hua, Liu Lilong, Ren Chao. An improved global grid model for calibrating zenith tropospheric delay for GNSS applications[J]. *GPS Solutions*, 2023, 27(1): 17.
- Yao Yibin, Xu Xingyu, Xu Chaoqian, Peng Wenjie, Wan Yangyang. Establishment of a Real-Time Local Tropospheric Fusion Model[J]. *Remote Sensing*, 2019, 11(11): 1321.
- Xia Pengfei, Tong Mengxiang, Ye Shirong, Qian Jingye, Hu Fangxin. Establishing a high-precision real-time ZTD model of China with GPS and ERA5 historical data and its application in PPP[J]. *GPS Solutions*, 2022, 27(1) : 2.
- Lu Cuixian, Zhong Yaxin, Wu Zhilu, Zheng Yuxin, Wang Qiuyi. A tropospheric delay model to integrate ERA5 and GNSS reference network for mountainous areas: application to precise point positioning[J]. *GPS Solutions*, 2023, 27(2):81.
- Yang Yuanxi, Ding Qun, Gao Weiguang, Li Jinlong, Xu Yangyin, Sun Bijiao. Principle and performance of BDSBAS and PPP-B2b of BDS-3[J]. *Satellite Navigation*, 2022, 3(1) : 5.
- Chen Junping, Yu Chao, Zhou Jianhua, Wang Ahao, Zhang Yize, Song Ziyuan. Decimeter-level algorithm for satellite-based augmentation systems and performance analysis of BDS-2/BDS-3[J]. 2021, 51(1): 019507.
- Lan Ruohua, Yang Cheng, Zheng Yanli, Xu Qiaozhuang, Lv Jie, Gao Zhouzheng. Evaluation of BDS-3 B1C/B2b Single/Dual-Frequency PPP Using PPP-B2b and RTS SSR Products in Both Static and Dynamic Applications[J]. *Remote Sensing*, 2022, 14(22).
- Shi Junbo, Ouyang Chenhao, Yue Jinguang, Chen Ming, Guo Jiming. High-Precision Positioning Service Performance Analysis of Three BDS Ground-Based Augmentation Systems[J]. *Journal of Geodesy and Geodynamics*, 2022, 42(7) : 712-715,770.
- Li Bofeng, Ge Haibo, Bu Yuhang, Zheng Yanning, Yuan Leitong. Comprehensive assessment of real-time precise products from IGS analysis centers[J]. *Satellite Navigation*, 2022, 3(1) : 12.
- Guo Wenfei, Zuo Hongming, Mao Feiyu, Chen Jiaqi, Gong Xiaopeng, Gu Shengfeng, Liu Jingnan. On the satellite clock datum stability of RT-PPP product and its application in one-way timing and time synchronization[J]. *Journal of Geodesy*, 2022, 96(8) : 52.
- Yang Yuanxi, Gao Weiguang, Guo Shuren, Mao Yue, Yang Yufei. Introduction to BeiDou-3 navigation satellite system[J]. *Navigation*, 2019, 66(1) : 7-18.
- Yang Yuanxi, Liu Li, Li Jinlong, Yang Yufei, Zhang Tianqiao, Mao Yue, Sun Bijiao, Ren Xia. Featured services and performance of BDS-3[J]. *Science Bulletin*, 2021, 66(20): 2135-2143.
- Tao Jun, Liu Jingnan, Hu Zhigang, Zhao Qile, Chen Guo, Ju Boxiao. Initial Assessment of the BDS-3 PPP-B2b RTS compared with the CNES RTS[J]. *GPS Solutions*, 2021, 25(4) : 131.
- Liu Jinhua, Tang Chengpan, Zhou Shanshi, et al. The Bias in PPP-B2b real-time clock offset and the strategy to reduce it [J]. *Remote Sensing*, 2022, 14(18).
- Xu Yangyin, Yang Yuanxi, Li Jinlong. Performance evaluation of BDS-3 PPP-B2b precise point positioning service[J]. *GPS Solutions*, 2021, 25(4) : 142.

- Ren Zhiling, Gong Hang, Peng Jing, Tang Chengpan, Huang Xinming, Sun Guangfu. Performance assessment of real-time precise point positioning using BDS PPP-B2b service signal[J]. *Advances in Space Research*, 2021, 68(8) : 3242-3254.
- Tang Chengpan, Hu Xiaogong, Chen Jinping, Liu Li, Zhou Shanshi, Guo Rui, Li Xiaojie, He Feng, Liu Jinhua, Yang Jianhua. Orbit determination, clock estimation and performance evaluation of BDS-3 PPP-B2b service[J]. *Journal of Geodesy*, 2022, 96(9) : 60.
- Song Weiwei, Zhao Xinke, Lou Yidong, Sun Weibin, Zhao Zhengyu. Performance Evaluation of BDS-3 PPP-B2b Service[J]. *Geomatics and Information Science of Wuhan University*, 2021: 1-11.
- Zhou Haitao, Wang Lei, Fu Wenju, Han Yi, Li Tao, Li Wei, Chen Ruizhi. Real-time single-frequency precise point positioning using BDS-3 PPP-B2b corrections[J]. *Measurement*, 2022, 205: 112178.
- Li Bofeng, Ge Haibo, Ge Maorong, Nie Liangwei, Shen Yunzhong, Harald Schuh. LEO enhanced Global Navigation Satellite System (LeGNSS) for real-time precise positioning services[J]. *Advances in Space Research*, 2019, 63(1) : 73-93.
- Li Xingxing, Ma Fujian, Li Xin, Lv Hongbo, Bian Lang, Jiang Zihao, Zhang Xiaohong. LEO constellation-augmented multi-GNSS for rapid PPP convergence[J]. *Journal of Geodesy*, 2019, 93(5) : 749-764.
- Li Xin, Li Xingxing, Ma Fujian, Yuan Yongqiang, Zhang Keke, Zhou Feng, Zhang Xiaohong. Improved PPP Ambiguity Resolution with the Assistance of Multiple LEO Constellations and Signals[J]. *Remote sensing*, 2019, 11(4): 408.
- Li Min, Xu Tianhe, Guan Meiqian, Gao Fan, Jiang Nan. LEO-constellation-augmented multi-GNSS real-time PPP for rapid re-convergence in harsh environments[J]. *GPS Solutions*, 2022, 26: 1-12.
- Ren Xiaodong, Zhang Xiaohong, Schmidt M et al. (2020) Performance of GNSS global ionospheric modeling augmented by LEO constellation[J]. *Earth and Space Science* 7(1): e2019EA000898.
- Ge Haibo, Li Bofeng, Jia Song, Nie Liangwei, Wu Tianhao, Yang Zhe, Shang Jingzhe, Zheng Yanning, Ge Maorong. LEO enhanced global navigation satellite system (LeGNSS): Progress, opportunities, and challenges[J]. *Geo-spatial Information Science*, 2022, 25(1): 1-13.

# Development Status and Trend of Indoor Positioning and Navigation Technology

Baoguo Yu<sup>1,2</sup>, Lu Huang<sup>1,2</sup>, Yachuan Bao<sup>1,2</sup>, Haonan Jia<sup>1,2</sup>, Shuang Li<sup>1,2</sup>, Ruizhi Chen<sup>3</sup>, Xiaoji Niu<sup>3</sup>, Zhongliang Deng<sup>4</sup>, Jinzhong Bei<sup>5</sup>, Dehai Li<sup>5</sup>, Yunjia Wang<sup>6</sup>, Feng Lu<sup>7</sup>, Chun Liu<sup>8</sup>, Ling Pei<sup>9</sup>, Jian Wang<sup>10</sup>

<sup>1</sup> China Electronics Technology Group Network Communication Research Institute, Shijiazhuang City, Hebei Province

<sup>2</sup> State Key Laboratory of Satellite Navigation System and Equipment Technology, Shijiazhuang, Hebei

<sup>3</sup> Wuhan University Satellite Navigation and Positioning Technology Research Center, Wuhan,

<sup>4</sup> Beijing university of Posts and Telecommunications, Beijing

<sup>5</sup> China Academy of Surveying and Mapping Sciences, Beijing

<sup>6</sup> China University of Mining and Technology, Xuzhou, China

<sup>7</sup> Institute of Geographic Sciences and Resources, Chinese Academy of Sciences, Beijing

<sup>8</sup> School of Surveying, Mapping and Geographic Information, Tongji University, Shanghai, China

<sup>9</sup> Shanghai Jiao Tong University, Shanghai, China

<sup>10</sup> School of Geomatics and Urban Spatial Informatics, Beijing University of Civil Engineering and Architecture (BUCEA), Beijing, China

## 1 Introduction

The global satellite navigation system can provide all-weather, all-time, high-precision PNT (Positioning, Navigation, and Timing) services for various users on the surface and in near-Earth space, and has played an important role in many fields such as national security, national economy, and public life. However, it is still difficult for satellite navigation to provide accurate and reliable location services under signal shadowing environments. Therefore, extending navigation and positioning services from outdoors to indoors, developing high-precision indoor navigation and positioning technology, and labeling everything indoors with time and space are urgent needs of a modern smart society.

Compared with outdoor open space, the relationship between indoor channel environment and spatial topology is more complex, and GNSS spatial signals are attenuated due to building occlusion, resulting in the inability to effectively cover a large area in indoor environment. So academia and industry have explored a variety of indoor PNT theoretical methods and technical means. Although there are many types of indoor positioning and navigation information sources, they all have certain limitations. The fusion of different positioning information still faces the challenge of performance improvement brought about by environmental changes. The problems of wireless signal coverage, precise measurement, environmental perception, and map update brought about by the complex and changeable indoor environment are all difficulties faced by indoor and outdoor seamless positioning and navigation. These factors limit the large-scale application of related technologies in various indoor sheltered spaces and semi-sheltered spaces.

In general, the basic problems faced in the field of indoor and outdoor seamless positioning and navigation are mainly reflected in the following three aspects:

1) Architecture perspective. From the perspective of universal and unified space-time reference expression and Internet of Everything PNT service, no indoor and outdoor seamless navigation and positioning system and open standards for all applications and services have yet been established. Large-scale cross-domain promotion and ubiquitous unified applications are limited. So it is urgent to build a standardized architecture that is universal and applicable to most application scenarios.

2) System perspective. The current indoor positioning system side solutions are more oriented to local indoor environment applications, and a wide-area and large-scale network coverage capability has not been formed. Facing indoor spaces of different scales and environmental characteristics, it is an important development direction in the future to solve the system construction and deployment problems such as unified standards, low cost, easy implementation, wide coverage, and high concurrency. It is urgent to realize the breakthrough of a series of key technologies such as elastic and scalable networking of multi-mode base stations, integrated communication and navigation, and independent positioning by single base stations.

3) Application perspective. Different application scenarios have different user needs, and multiple factors such as cost, ease of use, reliability, real-time performance, and technology maturity must be considered comprehensively. Efforts should be made to solve problems such as chipification of user terminals, integration with outdoor positioning terminals, and application software ecology, and realize indoor positioning based on user multi-scenario roaming under unified system network deployment conditions.

Focusing on the above issues, this report summarizes the research status of indoor positioning and navigation technology in China, and focuses on the representative innovation achievements and applications of major scientific research institutions of indoor positioning technology in China in recent years. Finally, based on the challenges faced by the application and promotion of current indoor and outdoor seamless navigation and positioning systems, a trend analysis and prospect of future indoor integrated PNT systems are provided.

## **2 Development Status of Indoor Positioning Technology in China**

The international research and industrial application of indoor positioning technology are currently in a rising trend, and the research and application of positioning technologies such as WiFi, Bluetooth, ultra wideband, 5G/6G, pseudo-satellite, audio, visual, inertial, and geomagnetic technologies are continuously developing globally.

In terms of WiFi indoor positioning technology, Google has built a mobile terminal network positioning service platform based on WiFi technology, which can achieve rough indoor positioning. In terms of Bluetooth indoor positioning technology, in 2019, SIG (Special Interest Group) added the "direction finding" function in Bluetooth standard specification 5.1, which greatly improves the positioning accuracy and realizes an accuracy of sub meter level in line of sight environment. In terms of UWB indoor positioning technology, thanks to the anti-multipath and high-precision signal system advantages, a ranging accuracy of 10 centimeters and a positioning accuracy of 30 centimeters can be achieved in ideal indoor environments. Currently, the international standard for UWB signal system continues to iterate, and the latest IEEE 802.15.4ab is under development. In terms of 5G/6G high-precision indoor positioning,

3GPP has proposed clear requirements for 5G high-precision positioning in TS 22.261 standard, and some globally well-known companies such as Qualcomm and Huawei have proposed 5G meter level positioning solutions.

The rapid development of indoor positioning technology in China led to the early proposal of the "Xihe Plan" by the Ministry of Science and Technology of China, aiming to solve the problem of seamless indoor and outdoor navigation and positioning. Recently, with the joint efforts of the technology and industry sectors, especially with the support of the 13th Five Year National Key R&D Plan, China has made significant breakthroughs in multiple indoor positioning technologies. Representative achievements include: the team from the State Key Laboratory of Satellite Navigation System and Equipment Technology of China Electronics Technology Group proposed the Beidou pseudosatellite high-precision positioning system and algorithm for indoor environment. Based on the "Beidou commercial chip+IP soft core" and the Beidou pseudosatellite micro base station network, Beidou sub meter level indoor and outdoor continuous positioning has been achieved.



Figure 1. Beidou pseudosatellite indoor positioning micro base station and positioning terminal "spatiotemporal box"

The Beidou pseudosatellite indoor positioning technology adopts multi-channel broadcasting of navigation signals compatible with Beidou/GPS with different spread spectrum codes using the same clock source, combined with a pseudosatellite carrier phase and Doppler frequency shift fusion positioning algorithm based on nonlinear filtering, to solve the problems commonly faced by pseudosatellite micro base stations in indoor positioning environments, such as time synchronization, ambiguity resolution, clock drift estimation, near-far effect, and multipath. It features wide indoor coverage, sub meter level positioning and compatibility with Beidou system. High-precision indoor and outdoor continuous positioning is achieved, with static positioning accuracy better than 0.1m and dynamic positioning accuracy better than 0.5m (3-sigma).

The technological achievement has been successfully applied to large indoor environments such as airports and shopping malls. Especially during the Beijing 2022 Winter Olympics, in response to the needs of emergency command and scheduling, epidemic prevention and control, unmanned distribution, and security control, a Beidou pseudosatellite micro base station indoor and outdoor integrated positioning service network was constructed. The system was deployed at the National Ski Jumping Center in Zhangjiakou District (Snow Ruyi Stadium, as shown in Figure 2), providing fast positioning of personnel, vehicles, iron horses, robots, and other targets without dead corners within the accessible area of the entire venue, enabling adaptive seamless reception and switching between indoor Beidou micro base station signals and outdoor Beidou signals. The indoor and outdoor continuous positioning accuracy is better than 1 meter, solving

the international problem of high-precision seamless positioning technology for large-scale indoor and outdoor areas.



Figure 2. Application of Beidou pseudosatellite indoor and outdoor positioning system in Beijing 2022 Winter Olympics

Based on the 14th Five Year Plan National Key R&D Program project, the team led by Baoguo Yu has expanded indoor navigation and positioning technology to underground spaces. They have proposed a continuous positioning technology for both inside and outside tunnels based on Beidou micro base stations and multi-sensor fusion, solving the problems of large-scale long-distance networking, continuous and stable tracking of positioning signals in tunnels. They have achieved a positioning capability with accuracy better than 2m for high-speed moving targets (speed>80km/h) and an ultimate accuracy better than 0.5m in long tunnel environments. A technological leap for Beidou micro base stations from low-speed moving target positioning to high-speed moving target positioning is achieved, and the application scenarios of Beidou pseudosatellites are expanded.

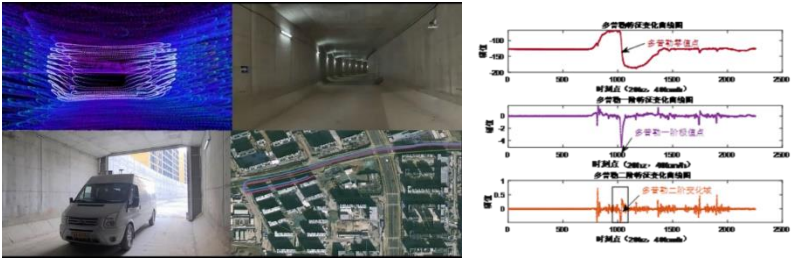


Figure 3. Test environment and results for continuous positioning of high-speed moving targets in underground space

To address the performance disadvantages of UWB indoor positioning technology in terms of service capacity, operating distance, and positioning networking, the Baoguo Yu team lead by Baoguo Yu has proposed a new HNav-UWB signal system, aiming to improve the measurement and positioning capabilities by signal layer design. The simulation shows that using ultra-low pulse repetition frequency and ultra-short frame structure design, the pulse repetition frequency can be as low as 915KHz, which greatly improves the ranging coverage and concurrent service capacity under low-power conditions. At the same time, the ULRP has concentrated energy and is more suitable for complex environments. The designed array-based single station positioning method adaptive to underground narrow and long spaces will significantly reduce the system deployment and application costs. The test results are shown in Figure 4.

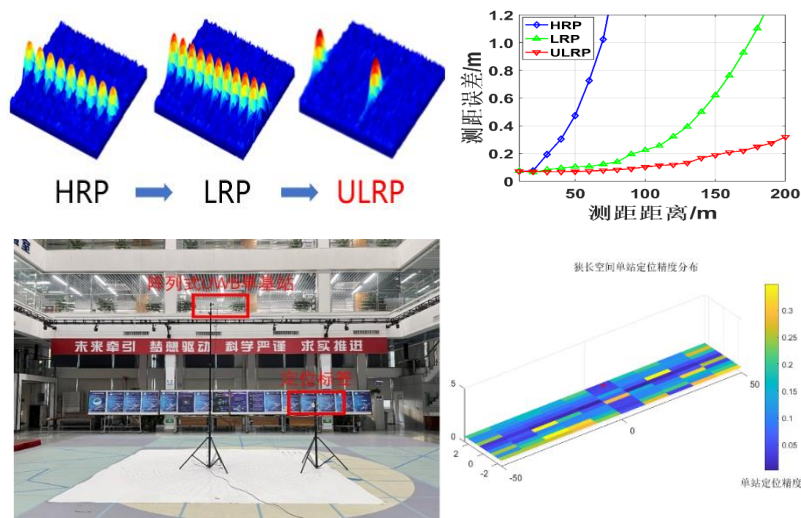


Figure 4. The proposed novel UWB signal system suitable for underground space and experimental results

Jinzhong Bei and Dehai Li of China Academy of Surveying and Mapping Sciences developed an indoor location cloud smart service platform and terminal application software, built an indoor location service system, broke through the adaptive interaction mechanism supported by user behavior pattern perception and platform knowledge model, developed a location cloud service system interconnection interface and operation overlay protocol, developed application systems for security monitoring and warning, emergency rescue and command, and public location service, and realized the transition expansion and practical application of the system in typical indoor scenarios.

The team of Ruizhi Chen at Wuhan University, China, has designed a weak audio signal detection method based on "coarse detection - signal normalization - fine detection - coarse difference rejection" mechanism, proposed and implemented a highly available audio signal robust detection algorithm based on time-frequency energy density matrix feature analysis and adaptive generalized correlation. With a breakthrough in the core technology of 50m long-distance high-precision ranging, the team have successfully developed and mass-produced the world's first audio positioning chip based on RISC-V architecture. On the basis of this chip, they built an integrated human-vehicle-object audio indoor positioning system across hardware and software platforms without changing any hardware or firmware of smartphones, realizing a high-precision, high-availability and wide-coverage indoor intelligence hybrid positioning system with positioning accuracy of 0.38 meters, location update rate of 20Hz and single base station signal coverage of 50 meters. The system has been deployed in indoor environments such as Nanjing South Station and Ezhou Airport in China, supporting applications such as smart security, smart logistics and smart communities, as shown in Figure 5.



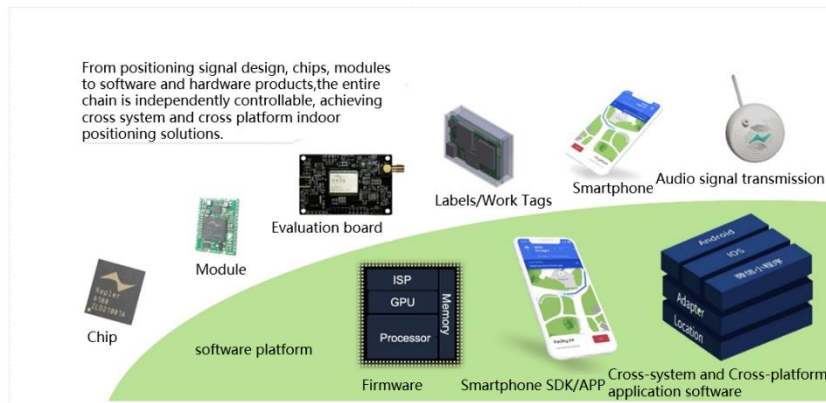


Figure 5. Cross-system and Cross-platform audio positioning software and hardware ecology

Zhongliang Deng's team at Beijing University of Posts and Telecommunications (BUPT), China, proposed the theory of embedded signal-to-noise positioning, designed the 5G common-band and in-band localization reference signal system, and broke through the bottleneck of high-precision time reference and multi-source heterogeneous feature fusion high-precision positioning for wireless network positioning. They developed the first 5G high-precision positioning international standard 3GPP TS 38.211 proposal, proposed a series of methods for heterogeneous multi-source cooperative positioning, broke through the bottleneck of high-precision time reference for wireless network positioning and multi-source heterogeneous feature fusion positioning, The 5G positioning capability in 5G R16 standard published in 2020 was improved to sub-meter level. Industrialized applications are implemented in the fields of smart senior care, safe production, and smart transportation, etc., which provides important technical support for the application of 5G positioning in the field of industrial Internet, as shown in Figure 6.

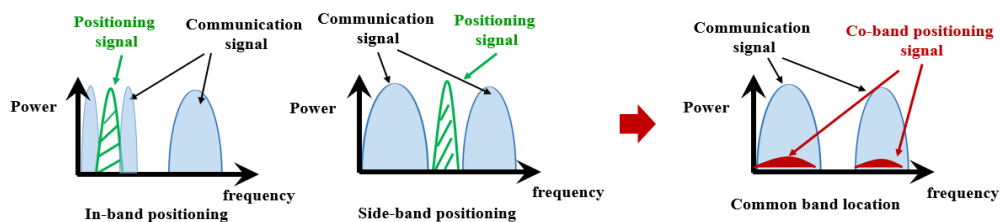


Figure 6. The principle of embedded signal-to-noise positioning

Indoor positioning technologies based on autonomous sensing typesensors have significant advantages in solving navigation and positioning problems in indoor non-cooperative environments. Usually, they can be broadly classified into two categories according to the source of information, one is to sense changes in carrier state information, such as inertial navigation, and the other is to sense changes in external environmental information, such as vision and LIDAR technologies. They have significant advantages in non-cooperative environments because they do not require early installation and deployment of infrastructure.

Baoguo Yu and Haonan Jia from the State Key Laboratory of Satellite Navigation System and Equipment Technology of CETC have developed a foot-worn positioning terminal (Figure

7) based on gyroscope, accelerometer, and barometer chips, with a weight of 50 g, dimensions of 47×33×26 mm, and power consumption of 200 mW. By embedding pedestrian motion pattern recognition, extended Kalman filter fusion algorithm based on zero velocity correction, and under purely autonomous navigation conditions, the positioning accuracy is 0.3%D, which is equivalent to walking of 1km with an error of less than 3m, and the speed measurement accuracy is better than 0.5m/s, realizing the autonomous, continuous and accurate positioning of personnel. Based on this technical achievement, the team won the championship in the 4th track competition of IPIN2022 International Indoor Positioning Competition.

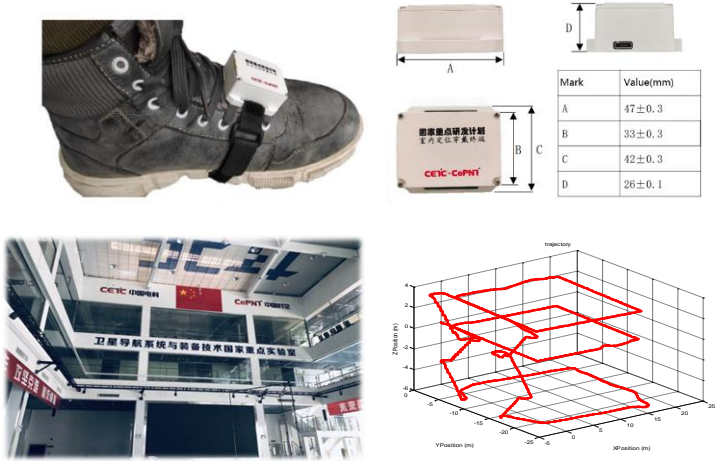


Figure 7. Pedestrian foot wearable positioning terminal and test results

Xiaoji Niu and Jian Kuang of Wuhan University designed a PDR scheme based on wearable inertial sensors, making full use of constrained information such as pedestrian motion patterns, human joint structures and environmental features to gradually reduce the dependence of PDR on gait assumptions from three aspects (e.g., Figure 8), such as single-foot inertial guidance, dual-foot inertial guidance and lower limb multiple inertial guidance. This method achieves the effect of improving the accuracy and robustness of autonomous pedestrian positioning in a length of about 1000m under a severe test scenario of no folding and no closure, and the positioning error is less than 1.5% of the walking distance.

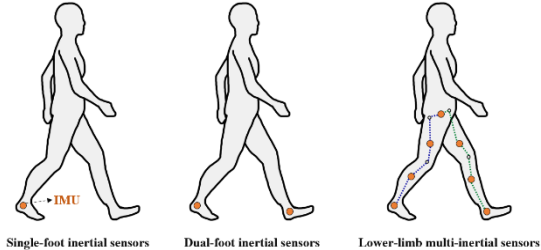


Figure 8. Single foot, dual-foot and lower limb multi-inertial guidance PDR solutions

To address the influence of complex dynamic scenes on visual positioning, Wang Yunjia et al. from China University of Mining and Technology established a robust indoor visual positioning algorithm that takes into account a wide range of indoor dynamic scenes. They used

MEMS inertial sensor built in smart phones to build the geometric constraints and parameter optimization models in the inertial information assisted visual positioning algorithm, and solved the problem of visual feature matching failure. The number of internal points in the PnP solution process is increased to improve the stability of visual positioning. The technical framework is shown in Figure 9.

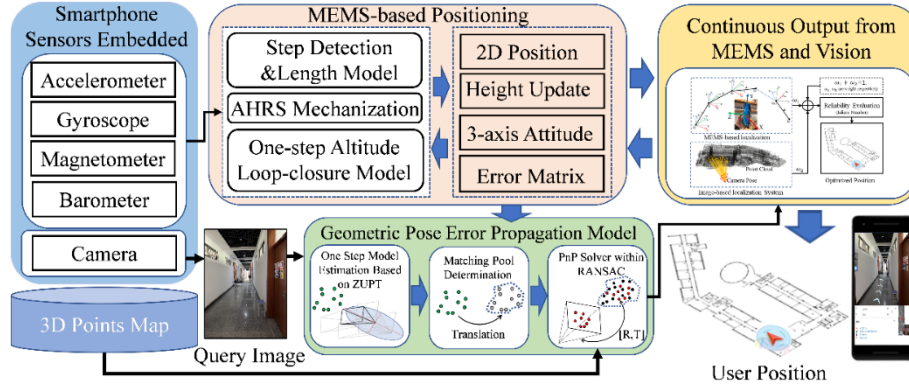


Figure 9. A robust positioning algorithm of indoor dynamic scene combining intelligent mobile MEMS and vision sensor

Ling Pei et al. of Shanghai Jiao Tong University have proposed a novel visual inertial odometer (VIO) method, which adopts structural regularity in an artificial environment and uses the Atlanta world model to describe the regularity. By fully exploring the structural lines consistent with each local world in Manhattan, the VIO method becomes more accurate and robust, and more flexible for different types of complex man-made environments. The proposed algorithm is compared with different existing advanced algorithms in multiple scenarios. The closed-loop error is 0.292% root mean square error, and the performance is more advanced. The test results are shown in Table 1.

Table 1. LOOP CLOSING ERROR OF DIFFERENT ALGORITHMS IN THREE INDOOR SCENES: RMSE ERROR (POS. [m]) MAX ERROR (DRIFT [m])

Seq. Name	Traveling Dist. [m]	OKVIS[5]		VINS[6](w/o loop)		Project Tango		Point-only		Point+Line		StructVIO	
		RMSE	Max.	RMSE	Max.	RMSE	Max.	RMSE	Max.	RMSE	Max.	RMSE	Max.
Soft-01	315.167	6.702	9.619	4.861	6.688	5.715	8.181	<b>2.153</b> <sup>2</sup>	2.728	2.262	2.842	<b>1.931</b> <sup>1</sup>	2.437
Soft-02	438.198	4.623	6.713	2.713	4.086	4.238	6.226	3.905	5.243	<b>1.468</b> <sup>2</sup>	2.026	<b>1.429</b> <sup>1</sup>	1.984
Soft-03	347.966	<b>4.505</b> <sup>2</sup>	6.223	7.270	9.832	167.825	228.630	6.515	8.119	8.618	10.790	<b>0.325</b> <sup>1</sup>	1.020
Soft-04	400.356	3.993	5.784	28.667	75.479	2.453	3.544	<b>1.550</b> <sup>1</sup>	2.028	4.051	5.262	<b>1.722</b> <sup>2</sup>	2.241
Mech-01	340.578	3.627	4.745	2.452	3.260	<b>1.948</b> <sup>2</sup>	2.726	3.298	3.961	4.323	5.181	<b>0.909</b> <sup>1</sup>	1.165
Mech-02	388.548	3.079	4.195	3.570	4.754	<b>1.596</b> <sup>2</sup>	2.217	1.663	2.108	2.317	2.927	<b>0.779</b> <sup>1</sup>	1.022
Mech-03	317.974	3.875	5.324	4.682	9.113	4.220	5.781	<b>2.384</b> <sup>2</sup>	3.020	4.193	5.272	<b>1.161</b> <sup>1</sup>	1.532
Mech-04	650.430	-	-	3.002	8.592	1.915	5.808	1.785	4.663	<b>1.425</b> <sup>2</sup>	3.729	<b>0.742</b> <sup>1</sup>	1.940
MicroA-01	257.586	2.485	3.382	<b>0.654</b> <sup>2</sup>	1.148	45.599	61.058	2.849	3.505	2.189	2.721	<b>0.642</b> <sup>1</sup>	1.225
MicroA-02	190.203	3.428	5.186	14.222	57.172	<b>1.145</b> <sup>1</sup>	1.692	1.964	2.514	<b>1.723</b> <sup>2</sup>	2.207	2.089	2.661
MicroA-03	388.730	0.078	0.779	<b>1.800</b> <sup>1</sup>	2.578	4.400	6.253	3.824	5.169	3.072	4.232	<b>1.884</b> <sup>2</sup>	2.892
MicroA-04	237.856	6.136	8.532	<b>0.994</b> <sup>2</sup>	1.765	55.200	75.318	2.056	2.897	2.406	2.879	<b>0.350</b> <sup>1</sup>	0.448
MicroB-01	338.962	2.898	4.025	<b>1.856</b> <sup>2</sup>	2.944	38.197	50.572	7.084	8.576	7.337	8.913	<b>1.477</b> <sup>1</sup>	1.902
MicroB-02	306.316	2.240	3.490	<b>1.030</b> <sup>2</sup>	2.431	5.660	8.652	2.521	3.714	3.197	4.610	<b>0.470</b> <sup>1</sup>	0.799
MicroB-03	485.291	-	-	2.132	3.368	<b>2.009</b> <sup>2</sup>	2.960	6.490	8.978	4.507	6.301	<b>0.445</b> <sup>1</sup>	0.675
MicroB-04	357.251	4.064	6.481	<b>1.332</b> <sup>2</sup>	2.068	13.962	22.028	5.078	7.713	1.977	3.074	<b>0.473</b> <sup>1</sup>	0.777
Mean Drift Err.(%)		1.078%		1.410%		6.180%		0.957%		<b>0.956%</b> <sup>2</sup>		<b>0.292%</b> <sup>1</sup>	
Median Drift Err.(%)		0.781%		<b>0.538%</b> <sup>2</sup>		0.900%		0.559%		0.570%		<b>0.176%</b> <sup>1</sup>	

Indoor high-precision mapping and real-time GIS are the application basis of high-

precision indoor positioning technology. In the past five years, Lu Feng et al. from the Institute of Geographic Sciences and Natural Resources Research of the Chinese Academy of Sciences proposed the indoor GIS framework under the support of the national key research and development project "Indoor Hybrid Intelligent Positioning and Indoor GIS Technology". It makes key technological breakthroughs such as high-precision indoor mapping and updating, automatic construction of indoor navigation network based on crowdsourcing trajectory, indoor mobile object management and location prediction, and indoor large-scale crowd pattern mining. It has developed high-precision indoor mapping technology and equipment, and formulated the crowdsourcing collaborative production technology and product standards for indoor navigation electronic maps. The application demonstration of location-based geographic information service in the indoor three-dimensional scene is carried out, as shown in Figure 10.

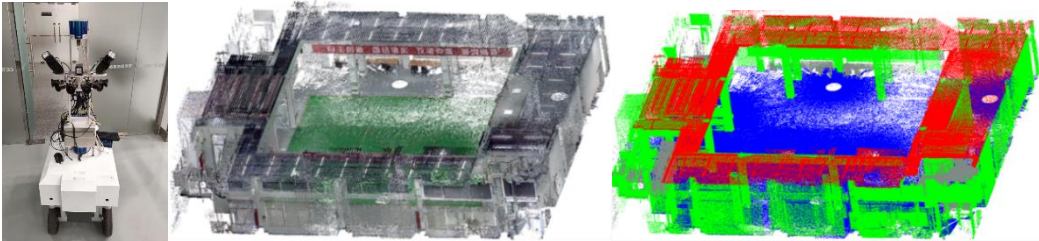


Figure 10. Results of semantic segmentation between light and small mobile indoor mapping platform and building interior

Liu Chun team of Tongji University is committed to the development of indoor mapping robot. They developed a high-precision time synchronization board, built an environment modeling and positioning navigation robot platform, integrated component recognition, semantic mapping, high-precision positioning, obstacle avoidance navigation and other functions on the platform. An average real-time positioning and orientation accuracy of 1km walking better than 15cm/0.1° is realized under the conditons of more than 30m long passage/corridor light texture in complex indoor scenes, and a standard visual map data set over 5000m<sup>2</sup> for typical scenes such as shopping malls, factories, communities and offices with accuracy better than 5cm is established. The coverage of 3D map construction is >90%, and the accuracy is better than 0.2m. The visual obstacle avoidance success rate is ≥95% (Figure 11), and the identification accuracy of more than 10 types of indoor and outdoor fixed facilities is ≥95%.



Figure 11. Laboratory mapping robot and test results

Wang Jian's team from Beijing University of Civil Engineering and Architecture proposed an indoor positioning method based on computer vision and coded graphics. Firstly, a series of



coded graphics for indoor object positioning were designed, and a method for calculating the spatial coordinates of coded graphics was proposed. Then, two kinds of spatial excising models based on unit weight and Tukey weight were constructed. Finally, the object positioning in indoor environment was achieved. The experimental results show that both models can calculate the object position well. The spatial excising model based on Tukey weight can correctly identify the residual of observed values, and obtain robust positioning results with high positioning accuracy. Thirty-nine coded graphics were posted in the test environment. The coded images were automatically obtained from twelve different sites when the object was moving. Each coded image consisted of five to eight coded graphics. The test results show that the position accuracy calculated by Tukey weight method is improved more significantly than that by unit weight method. The accuracy of plane minimum value is increased by 16.96%, the maximum value by 66.34%; the elevation minimum value is increased by 9.40% and the maximum value by 71.05%. The test scene and results are shown in Figure 12.

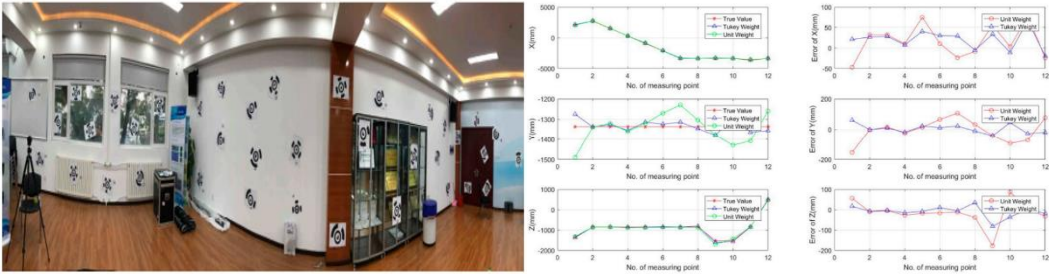


Figure 12. Test environment and results

### 3 Future development trends and suggestions

There are various existing indoor positioning technologies, while there are still problems in terms of positioning accuracy, scene generalization ability, indoor and outdoor continuity, and system capacity. So far, there is no single indoor positioning solution suitable for all indoor environments, so it is an important way to solve the problem of indoor positioning at present by designing an efficient multi-source information fusion solution, using a tight coupling of absolute positioning and relative positioning, autonomous positioning and wireless positioning, and integrating other heterogeneous information to obtain the optimal estimation of the position. At the same time, the current indoor positioning technology also faces problems such as different user needs, diverse application scenarios, complicated technical means, inconsistent standards and specifications, and no breakthrough in the general technical system. There is still a lack of a universal indoor positioning and navigation system that can be widely promoted.

In response to the above problems, the State Key Laboratory of Satellite Navigation System and Equipment Technology of China proposed an indoor and outdoor seamless PNT standardized architecture, which mainly includes the network layer, cloud processing layer and user layer. The network layer includes a public network for public users, a private network for professional users, and a mobile network for special users. The cloud processing layer includes a network map comprehensive management and control platform, a multi-information fusion intelligent control system, indoor and outdoor integrated GIS information, and a unified space-

time reference. The user layer includes smart terminals for mass users, integrated indoor and outdoor positioning chips, large-capacity and high-concurrency positioning service application software, etc., as shown in Figure 13.

### Indoor and outdoor seamless PNT system architecture

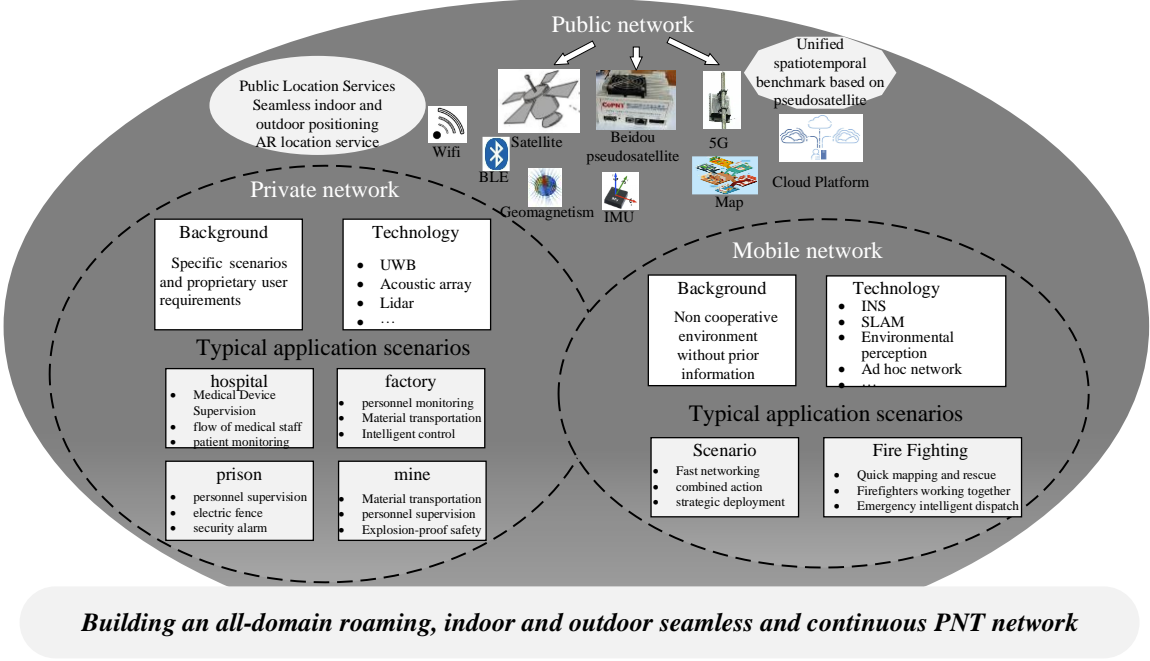


Figure 13. Architecture of seamless indoor and outdoor navigation and positioning system

Based on the seamless indoor and outdoor navigation positioning system architecture mentioned above, it is recommended to focus on the following three key tasks in the future:

1) Strengthen theoretical research on indoor positioning and navigation, and consolidate the foundation for the development of indoor high-precision positioning technology. With the improvement of indoor positioning service capabilities as the core, strengthen the theoretical foundation research of indoor high-precision navigation and positioning, and promote the coordinated development of technologies and equipment of hybrid positioning networks, integrated terminals, location service platforms, and standards.

2) Develop multi-source positioning information fusion technology and equipment, and establish a unified indoor positioning standard technology architecture. The fused use of multiple indoor positioning technologies with complementary characteristics will become the future development direction. Therefore, it is necessary to address the challenge of multi-source fusion positioning technology, and build a scalable and extensible general-purpose hardware integration mechanism, which can flexibly respond to the application requirements of complex scenarios. At the same time, it is necessary to establish a complete and unified indoor positioning standard technology architecture, coordinate indoor positioning resources, study a series of fusion positioning technology suitable for man-machine, universal terminal and map standards, and promote the integrated development of indoor positioning technology through standards.

3) Accelerate the practical application of indoor navigation and positioning technology,

and open up a new pattern for the development of integrated positioning, navigation and timing system. Facing the needs of large-scale indoor and outdoor seamless positioning public applications such as smart cities and emergency rescue in the future, through the development of standardized indoor geographic information and location service interface specifications, it is convenient for enterprises and individuals to customize personalized location services. A full-space intelligent location service ecosystem can be formed from the aspects of infrastructure and application modes, and large-scale, multi-scenario free roaming positioning among cities can be realized.

In summary, indoor positioning and navigation technology is an important cornerstone of the digitalization of the whole society in the future, and an important support for GNSS service expansion and capability improvement. In the future, a standardized indoor PNT infrastructure of "wide area + local area + triple play" will be formed, containing indoor high-precision positioning signals and information networks, a general technology engine for multi-user scenarios, and a standardized "cloud + terminal" service model. Facing the needs of most application scenarios, it is necessary to form relevant standard recommendations and provide ubiquitous, continuous, accurate, and intelligent indoor PNT services for public users, proprietary users, and special users on this basis. It will surely promote the rapid development of industrial manufacturing 2025, digital twins, and smart cities. At the same time, in terms of multi-system collaboration in the future, core interfaces with satellite Internet, 5G/6G mobile communication networks, and the Internet of Things will be formed to ensure that the indoor PNT system provides accurate spatio-temporal information services for various users. The continuous positioning, navigation and timing service performance of the global integrated PNT under the condition of GNSS shadowing will be greatly improved, and a more ubiquitous, fused and intelligent integrated space-time system and intelligent location service will be realized.

## Bibliography

- Chen Yang. Indoor positioning is an important cornerstone of digitalization of the whole society - interview with Wei Baoguo, chief scientist of China Electronics Technology Group, director of the State Key Laboratory of Satellite Navigation System and Equipment Technology [J]. *China Surveying and Mapping*, 2022, No. 212(02): 16-21.
- Niu X, Liu T, Kuang J, et al (2022). Pedestrian trajectory estimation based on foot-mounted inertial navigation system for multistory buildings in postprocessing mode. *IEEE Internet of Things Journal*, 2021, 9(9): 6879-6892.
- Zhang, Z., G. Chen, X. Wang & M. Shu (2021 a) DDRNet: Fast point cloud registration network for large-scale scenes. *Isprs Journal of Photogrammetry and Remote Sensing*, 175, 184-198.
- Li, Boying, Danping Zou, Daniele Sartori, Ling Pei, and Wenxian Yu. "Textslam: Visual slam with planar text features." In 2020 IEEE International Conference on Robotics and Automation (ICRA), pp. 2102-2108. IEEE, 2020.
- Zheng X, Zhang H, Wang Z, et al. Nonlinear state estimation with multisensor stochastic scheduling[J]. *IEEE Transactions on Systems, Man, and Cybernetics: Systems*, 2021, 52(5): 3349-3359.
- Danni. Audio Positioning, Curve Overtaking with Autonomous Indoor Positioning Technology——Interview with Chen Ruizhi, Director of State Key Laboratory of Surveying, Mapping and Remote Sensing Information Engineering, Wuhan University[J]. *China Surveying and Mapping*, 2022, No. 212(02): 12-15.
- Wan W, Yu T, Di K, et al. (2021) Visual Localization of the Tianwen-1 Lander Using Orbital, Descent and Rover Images.



Remote Sensing 13(17):3439-3450.

Pei, Ling, Kun Liu, Danping Zou, Tao Li, Qi Wu, Yifan Zhu, You Li, Zhe He, Yuwei Chen, and Daniele Sartori. "IVPR: An instant visual place recognition approach based on structural lines in Manhattan world." IEEE Transactions on Instrumentation and Measurement 69, no. 7 (2019): 4173-4187

Gan X, Yu B, Huang L, et al. Deep learning for weights training and indoor positioning using multi-sensor fingerprint[C]//2017 International Conference on Indoor Positioning and Indoor Navigation (IPIN). IEEE, 2017: 1-7.

Huang L, Yu B, Du S, et al. Multi-Level Fusion Indoor Positioning Technology Considering Credible Evaluation Analysis[J]. Remote Sensing, 2023, 15(2): 353.

Zhang Hengcai, et al. "Research Progress and Development Trend of Integrated PNT Scene Enhancement System." Journal of Wuhan University (Information Science Edition) 48.04(2023):491-505. doi:10.13203/j.whugis20220320.

Liu F, Zhang J, Wang J, et al. The indoor localization of a mobile platform based on monocular vision and coding images[J]. ISPRS International Journal of Geo-Information, 2020, 9(2): 122.

# Undifferenced and Uncombined GNSS Data Processing Activities

Baocheng Zhang<sup>1</sup>, Pengyu Hou<sup>1</sup>, Teng Liu<sup>1</sup>, Jiuping Zha<sup>1</sup>, Yunbin Yuan<sup>1</sup>

<sup>1</sup> State Key Laboratory of Geodesy and Earth's Dynamics, Innovation Academy for Precision Measurement Science and Technology, Chinese Academy of Sciences

## 1 Introduction

Pseudo-range (code) and carrier-phase (phase) observations provide the basic data for global navigation satellite system (GNSS) positioning, navigation and timing applications. GNSS data processing aims to estimate the parameters of interest using the code and phase observations. In addition to the global positioning system (GPS) and GLONASS observations used for several decades, the emergence of the European Galileo and the Chinese BeiDou navigation satellite system (BDS) provides more observations on multiple frequencies. In this multi-GNSS and multi-frequency context, an attractive choice is to directly process the undifferenced and uncombined (UDUC) data since it enables the simplest stochastic model and a unified functional model formulated with an arbitrary number of systems and frequencies.

In this contribution, we introduce the latest status of UDUC data processing activities in China, including single-station and multi-station data processing. UDUC data processing starts with original rank-deficient observation equations, with which one cannot estimate all parameters unbiasedly. One can turn to the S-system theory to address this rank deficiency problem, which selects a minimum number of parameters as the S-basis and formulates a full-rank model estimating linear functions of original parameters (Teunissen 1985). In the single-station case, we focus on the precise point positioning (PPP) technique which determines single-receiver positions using precise orbits and clocks (Zumberge et al. 1997). Another positioning technique, known as integer ambiguity resolution-enabled PPP or PPP-RTK, extends the PPP by further correcting satellite phase biases and atmospheric delays estimated in a multi-station network. We also introduce multi-station data processing in GNSS PPP-RTK (Wübbena et al. 2005).

## 2 Single-station UDUC PPP data processing

The PPP technique enables one to obtain precise positions by processing single-station GNSS data with the use of precise satellite orbits and clocks externally provided. This section introduces the formulation of UDUC PPP models for single-station data processing in recent years.

### Dual- and Multi-frequency PPP

Initial studies on UDUC PPP focused on processing of dual-frequency GPS data (Zhang et al. 2012). Researchers then combined multi-GNSS data to accelerate the convergence of UDUC PPP (Liu et al. 2017; Liu et al. 2018). To further improve the performances, one task of great importance is to process the emerging multi-frequency observations, e.g., BDS B1C, B2a, and B3I signals (Yang et al. 2019).

Liu et al. (2019) extended the dual-frequency UDUC PPP to a multi-frequency case. Compared with dual-frequency PPP, the addition of observations on more frequencies increases the size of rank deficiencies. These additional rank deficiencies stem from the ambiguities and phase biases on the third frequencies and beyond. Considering the same way adopted in the dual-frequency case, one can combine phase biases with ambiguities to eliminate the rank deficiency. The difference between dual-frequency and multi-frequency PPP lies in the estimability of code biases. There are no estimable code biases in the dual-frequency PPP model since code biases on the first two frequencies are selected as the S-basis, thereby entering into other estimable parameters. However, the multi-frequency PPP model needs to estimate the code biases on the third frequencies and beyond. We remark that multi-frequency UDUC PPP can obtain comparable results compared to ionospheric-free PPP (Li et al. 2015; Pan et al. 2019; Zhang et al. 2020).

UDUC PPP explicitly parameterizes ionospheric delays for estimation, implying its potentiality in ionospheric modeling. Liu et al. (2020) processed the GPS, BDS, GLONASS, and Galileo data on available triple frequencies and established an improved global vertical total electron content (VTEC) model with the spherical harmonic function. Moreover, they generated multi-GNSS differential code biases (DCBs) as by-products. Next to that, Liu and Zhang (2021) proposed a rigorous, flexible, and efficient approach to estimate code observable-specific biases (OSBs) using UDUC data. They processed one-month data and generated 32 types of code OSBs for GPS, GLONASS, BDS, Galileo and QZSS. Moreover, researches extended the concept of OSB from code to phase biases (Geng et al. 2022; Li et al. 2022).

### **Single-frequency PPP**

Although current GNSSs transmit multi-frequency signals, many low-cost mass-market receivers can only track single-frequency observations, demanding a single-frequency PPP model for data processing. To deal with the ionospheric delays, one can rely on external ionospheric products (e.g., global ionospheric map, GIM) and describe the uncertainty of products with a proper stochastic model, thereby formulating the ionosphere-weighted single-frequency PPP model. When ionospheric products are inaccessible, one can parameterize the ionospheric delays without any constrain in the UDUC observations and formulate the ionosphere-float model (Li et al. 2019; Zhang et al. 2018; Zhao et al. 2018).

With the addition of ionosphere pseudo-observations, there are no rank deficiencies related to ionospheric delays in the single-frequency UDUC observations. However, one size of rank deficiency exists between the receiver clock and satellite differential code bias. The satellite differential code bias appears in the single-frequency PPP model because the external satellite clocks contain the ionosphere-free combination of satellite code bias. To eliminate the rank deficiency, one can select the receiver clock of the first epoch as the S-basis and thus formulate the full-rank model estimating between-epoch time-differenced receiver clocks.

Ionosphere-float single-frequency PPP needs to deal with additional rank deficiencies due to the exclusion of ionosphere pseudo-observations. These rank deficiencies originate from ionospheric delays and satellite code biases, for which one can lump the ionospheric delays with satellite differential code biases. This implies that one can only estimate biased ionospheric delays with the ionosphere-float single-frequency model. Moreover, the estimable ionospheric delays are also biased by the receiver clock of the first epoch since the rank deficiency described in the ionosphere-weighted model before still exists in the ionosphere-float model and involves

ionosphere delays. With the establishment of the single-frequency ionosphere-float UDUC PPP, researchers have applied it to the ionosphere and troposphere retrieval using low-cost GNSS receivers (Li et al. 2019; Zhao et al. 2019). Moreover, Zhao et al. (2021) provided an open-source toolbox for processing multi-GNSS single-frequency data.

### **Modified PPP**

Single and multi-frequency PPP models introduced above implicitly assume that the receiver code biases stay constant over time. However, studies in recent years have shown that this assumption is not always valid, as the receiver code biases may vary with temperature change (Zhang et al. 2021b). This motivates researchers to modify the PPP model by considering time-varying receiver code biases.

Instead of one identical receiver code bias parameterized for all epochs, Zhang et al. (2021b) proposed a modified PPP model that parameterizes one receiver code bias in each epoch. However, one cannot estimate all receiver biases uniquely due to the rank deficiency between receiver clocks, receiver code biases, ionospheric delays, and ambiguities. For this, the modified PPP selects the receiver code bias of the first epoch as the S-basis. As a result, the full-rank modified PPP model estimates the receiver clock, ionospheric delay, and ambiguities lumped with the receiver code biases of the first epoch. Moreover, the modified PPP estimates from the second epoch the differential receiver code biases with respect to the first epoch. This implies that the temporal variations of the receiver code biases become estimable, and their adverse effects on PPP parameters, such as receiver clocks and ionospheric delays, are mitigated. Numerical tests conducted by Zhang et al. (2021b) showed that the modified PPP obtained more accurate slant total electron content (STEC) compared to the original PPP model with regard to the reference values of those derived from the geometry-free (GF) carrier phase observations (Ke et al. 2022; Li et al. 2020; Zhang et al. 2019). Concerning time transfer, the modified PPP is expected to improve the medium- and long-term frequency stability of receiver clocks.

## **3 Multi-station UDUC PPP-RTK data processing**

Although PPP can achieve high-accuracy positioning with a single-station receiver, it requires a long time (typically tens of minutes) to converge since it discards the integer nature of phase ambiguities and lacks atmosphere (troposphere and ionosphere) corrections. This motivates researchers to extend the PPP by correcting, in addition to satellite orbits and clocks, the satellite phase biases and atmospheric delays. Satellite phase biases play an important role in recovering the integer nature of ambiguities for single-receiver users, while correction of atmospheric delays makes fast integer ambiguity resolution achievable. This is the basic principle of PPP-RTK, which relies on a multi-station network to generate precise corrections (Wübbena et al. 2005). This section introduces multi-station data processing in PPP-RTK product generation.

### **Ionosphere-weighted PPP-RTK**

Multi-station PPP-RTK data processing can also adopt the ionosphere-weighted strategy. Instead of parameterizing the ionospheric delays without any constraints, ionosphere-weighted

PPP-RTK imposes a zero-mean constraint to between-receiver single-differenced ionospheric delays and considers the uncertainty of this constraint by a proper weighting scheme, as formerly done in relative positioning (Schaffrin and Bock 1988). This ionosphere-weighted strategy considers the spatial correction of ionospheric delays to formulate a stronger model than its ionosphere-float counterpart (Zha et al. 2021; Zhang et al. 2022b). In formulating the UDUC ionosphere-weighted PPP-RTK model, Zha et al. (2021) pointed out that adding ionospheric constraint reduces the rank deficiencies between ionospheric delays and receiver code biases from the number of receivers to only one. As a result, the estimable ionospheric delays of the ionosphere-weighted model are commonly affected by the differential code biases referring to a particular receiver assigned as the pivot, which eases the ionospheric interpolation on the user side. Experiments conducted on low and high solar activity days demonstrated that ionosphere-weighted PPP-RTK outperformed the ionosphere-float PPP-RTK regarding integer ambiguity resolution and positioning accuracy (Zha et al. 2021).

### **Phase-only PPP-RTK**

PPP-RTK commonly formulates its data processing model with both GNSS phase and code observations. The inclusion of code observations eases the rank deficiency problem and contributes to positioning if one cannot fix the phase ambiguities with a high success rate. In the case where rapid integer ambiguity resolution is possible, the contribution of code observations is marginal. Moreover, the unmodeled code-related errors, typically the code multipath, may reach several meters and deteriorate the positioning.

To avoid the adverse effects of unmodelled code-related code errors, Hou et al. (2022) formulated a phase-only PPP-RTK model with multi-frequency UDUC observations. Due to the exclusion of code observations, more rank deficiencies arise in the phase observation equations. One type of rank deficiency originates from the receiver clocks and receiver phase biases, for which one can select the receiver phase biases at the first frequency as the S-basis, resulting in estimable differential receiver phase biases at the second frequency and above. Another type stems from the satellite clocks, ionospheric delays, and satellite phase biases. Selecting the satellite phase biases at the first two frequencies can eliminate the rank deficiency. This implies that phase-only PPP-RTK only provides users with the satellite phase biases on the third frequencies and beyond since the satellite phase biases at the first two frequencies are lumped with satellite clocks. By correcting, among others, the satellite clocks and satellite phase biases, users can recover the integer nature of ambiguities at each frequency.

### **FDMA PPP-RTK**

PPP-RTK aims to recover the integer nature of ambiguities and fix them with a high success rate. Although we work with UDUC observations, only the double-differenced ambiguities are integer-estimable since we select part of ambiguities as the S-basis to address the rank deficiency problem. It is straightforward for code division multiple access (CDMA) systems to formulate double-differenced integer ambiguities. However, the GLONASS frequency division multiple access (FDMA) system defines different frequencies to identify satellites and thus cannot formulate double-differenced integer ambiguities, implying huge challenges in FDMA PPP-RTK. Fortunately, Teunissen (2019) proposed a new integer-estimable FDMA model which guarantees the integer nature of ambiguities and ensures a high success rate of partial ambiguity resolution.

Zhang et al. (2021a) presented a GLONASS PPP-RTK concept based on the integer-estimable FDMA model. They formulated a code-plus-phase GLONASS PPP-RTK model for homogeneous networks deployed with the same type of receivers, antennas, and firmware. In this case, the integer-frequency biases (IFBs) can be implicitly eliminated through re-parametrization, thereby preventing them from destroying the integer nature of ambiguities. For heterogeneous networks, they excluded the code observations and formulated a phase-only GLONASS PPP-RTK model that circumvents the unmodelled code IFBs. Although the phase-only GLONASS PPP-RTK model is too weak to achieve fast integer ambiguity resolution, one can combine GLONASS with other GNSSs to improve performances. Experiments conducted in both homogenous and heterogenous networks showed that the integration of GLONASS and GPS yielded an improvement of 8-34% in accuracy and led to a reduction of 25-50% in TTFB as compared with GPS-only PPP-RTK.

### **All-in-view PPP-RTK**

Due to the rank deficiency in UDUC observation equations, one cannot estimate the original satellite phase bias but only the biased one lumped with ambiguities. The number of ambiguities absorbed in the estimable satellite phase biases depends on the S-basis choices. A preferable S-basis choice shall prevent a large number of ambiguities from entering into satellite phase biases since the discontinuities of ambiguities will lead to jumps in satellite phase biases and eventually result in the re-estimation of user ambiguities. Hence, one commonly selects the phase biases and ambiguities pertaining to one receiver as the S-basis and formulates the estimable satellite phase biases containing only one ambiguity, provided that all network receivers track the same satellites. However, this common-view assumption implies a default exclusion of non-common-view satellites, resulting in degraded user positioning.

Zhang et al. (2022a) extended the PPP-RTK from common-view to all-in-view networks where at least one satellite is visible to all receivers. This relieves the stringent requirement of satellite visibility and can be guaranteed in most regional networks. The formulation of the all-in-view PPP-RTK model selects as the S-basis the phase biases and the ambiguities pertaining to one satellite that is tracked by all receivers. As a result, the estimable satellite phase biases always contain two ambiguities in all-in-view networks, thereby reducing to the best extent the jumps of satellite phase biases and the re-estimation of user ambiguities. In a network where enough common-view satellites were tracked, the results showed that the all-in-view PPP-RTK performed as well as the common-view PPP-RTK. This confirmed that the all-in-view PPP-RTK model is identical to the common-view model if processing the same common-view satellites. However, results in a network where many non-common-view satellites were tracked showed that all-in-view PPP-RTK improved the positioning accuracy and reduced the TTFB compared to the common-view PPP-RTK. This was because the all-in-view PPP-RTK utilized more satellites to formulate a stronger model.

## **Bibliography**

- Geng J, Wen Q, Zhang Q, et al. (2022) GNSS observable-specific phase biases for all-frequency PPP ambiguity resolution. *Journal of Geodesy* 96(2):1-18
- Hou P, Zhang B, Yasyukevich YV, et al. (2022) Multi-frequency phase-only PPP-RTK model applied to BeiDou data. *GPS*

- Ke C, Sheng C, Wang S (2022) Determination of receiver code bias variations with a modified geometry-free GNSS model. *Journal of Spatial Science* 67(1):79-89
- Li B, Ge H, Shen Y (2015) Comparison of ionosphere-free, UofC and uncombined PPP observation models. *Acta geodaetica et cartographica sinica* 44(7):734-740
- Li M, Yuan Y, Zhang X, et al. (2020) A multi-frequency and multi-GNSS method for the retrieval of the ionospheric TEC and intraday variability of receiver DCBs. *Journal of Geodesy* 94(10):1-14
- Li M, Zhang B, Yuan Y, et al. (2019) Single-frequency precise point positioning (PPP) for retrieving ionospheric TEC from BDS B1 data. *GPS Solutions* 23(1):1-11
- Li X, Li X, Jiang Z, et al. (2022) A unified model of GNSS phase/code bias calibration for PPP ambiguity resolution with GPS, BDS, Galileo and GLONASS multi-frequency observations. *GPS Solutions* 26(3):1-16
- Liu T, Yuan Y, Zhang B, et al. (2017) Multi-GNSS precise point positioning (MGPPP) using raw observations. *Journal of geodesy* 91(3):253-268
- Liu T, Zhang B (2021) Estimation of code observation-specific biases (OSBs) for the modernized multi-frequency and multi-GNSS signals: an undifferenced and uncombined approach. *Journal of Geodesy* 95(8):1-20
- Liu T, Zhang B, Yuan Y, et al. (2018) Real-Time Precise Point Positioning (RTPPP) with raw observations and its application in real-time regional ionospheric VTEC modeling. *Journal of Geodesy* 92(11):1267-1283
- Liu T, Zhang B, Yuan Y, et al. (2019) Multi-GNSS triple-frequency differential code bias (DCB) determination with precise point positioning (PPP). *Journal of Geodesy* 93(5):765-784
- Liu T, Zhang B, Yuan Y, et al. (2020) On the application of the raw-observation-based PPP to global ionosphere VTEC modeling: an advantage demonstration in the multi-frequency and multi-GNSS context. *Journal of Geodesy* 94(1):1-20
- Pan L, Zhang X, Liu J (2019) A comparison of three widely used GPS triple-frequency precise point positioning models. *GPS Solutions* 23(4):1-13
- Schaffrin B, Bock Y (1988) A unified scheme for processing GPS dual-band phase observations. *Bulletin Geodesique* 62(2):142-160
- Teunissen PJG (1985) Generalized inverses, adjustment, the datum problem and S-transformations. In: Grafarend EW, Sanso F (eds) *Optimization of Geodetic Networks*, Springer, Berlin
- Teunissen PJG (2019) A new GLONASS FDMA model *GPS Solutions* 23(4):1-19
- Wübbena G, Schmitz M, Bagge A (2005) PPP-RTK: precise point positioning using state-space representation in RTK networks. Paper presented at the Proc. ION GNSS 2005, The Institute of Navigation, Long Beach, CA, September 13-16
- Yang Y, Gao W, Guo S, et al. (2019) Introduction to BeiDou-3 navigation satellite system. *NAVIGATION, Journal of the Institute of Navigation* 66(1):7-18
- Zha J, Zhang B, Liu T, et al. (2021) Ionosphere-weighted undifferenced and uncombined PPP-RTK: theoretical models and experimental results. *GPS Solutions* 25(4):1-12
- Zhang B, Hou P, Odolinski R (2022a) PPP-RTK: from common-view to all-in-view GNSS networks. *Journal of Geodesy* 96(12):1-20
- Zhang B, Hou P, Zha J, et al. (2021a) Integer-estimable FDMA model as an enabler of GLONASS PPP-RTK. *Journal of Geodesy* 95(8):1-21
- Zhang B, Hou P, Zha J, et al. (2022b) PPP-RTK functional models formulated with undifferenced and uncombined GNSS observations. *Satellite Navigation* 3(1):1-15



- Zhang B, Ou J, Yuan Y, et al. (2012) Extraction of line-of-sight ionospheric observables from GPS data using precise point positioning. *Science China Earth Sciences* 55(11):1919-1928
- Zhang B, Teunissen PJG, Yuan Y, et al. (2018) Joint estimation of vertical total electron content (VTEC) and satellite differential code biases (SDCBs) using low-cost receivers. *Journal of Geodesy* 92(4):401-413
- Zhang B, Zhao C, Odolinski R, et al. (2021b) Functional model modification of precise point positioning considering the time-varying code biases of a receiver. *Satellite Navigation* 2(1):1-10
- Zhang X, Hu J, Ren X (2020) New progress of PPP/PPP-RTK and positioning performance comparison of BDS/GNSS PPP. *Acta Geodaetica et Cartographica Sinica* 49(9):1084-1100
- Zhang X, Zhang B, Yuan Y, et al. (2019) A refined carrier-to-code levelling method for retrieving ionospheric measurements from dual-frequency GPS data. *Measurement Science and Technology* 31(3)035010
- Zhao C, Yuan Y, Zhang B, et al. (2018) Ionosphere sensing with a low-cost, single-frequency, multi-GNSS receiver. *IEEE Transactions on Geoscience and Remote Sensing* 57(2):881-892
- Zhao C, Zhang B, Li W, et al. (2019) Simultaneous Retrieval of PWV and VTEC by Low-Cost Multi-GNSS Single-Frequency Receivers. *Earth and Space Science* 6(9):1694-1709
- Zhao C, Zhang B, Zhang X (2021) SUPREME: an open-source single-frequency uncombined precise point positioning software. *GPS Solutions* 25(3):1-8
- Zumberge J, Heflin M, Jefferson D, et al. (1997) Precise point positioning for the efficient and robust analysis of GPS data from large networks. *Journal of geophysical research: solid earth* 102(B3):5005-5017

# Progress and Achievements of Multi-sensor Fusion Navigation

Xingxing Li<sup>1</sup>, Xiaohong Zhang<sup>1</sup>, Xiaoji Niu<sup>2</sup>, Bijun Li<sup>3,4</sup>, Jian Wang<sup>5</sup>, Ling Pei<sup>6</sup>, Fangwen Yu<sup>7</sup>, Hongjuan Zhang<sup>3,4</sup>, Zhouzheng Gao<sup>8</sup>, Feng Zhu<sup>1</sup>, Weisong Wen<sup>9</sup>, Quan Zhang<sup>2</sup>, Tuan Li<sup>10,11</sup>, Tao Li<sup>6</sup>, Tong Hua<sup>6</sup>, Wenxian Yu<sup>6</sup>, Jianchi Liao<sup>1</sup>, Xin Li<sup>1</sup>, Houzeng Han<sup>5</sup>, Qiaozhuang Xu<sup>8</sup>, Jie Lv<sup>8</sup>, Cheng Yang<sup>8</sup>, Haitao Jiang<sup>10</sup>, Chuang Shi<sup>10</sup>

<sup>1</sup> School of Geodesy and Geomatics, Wuhan University, Wuhan, China

<sup>2</sup> Integrated & Intelligent Navigation Group, GNSS Research Center, Wuhan University, Wuhan, China

<sup>3</sup> State Key Laboratory of Information Engineering in Surveying, Mapping and Remote Sensing, Wuhan University, Wuhan, China

<sup>4</sup> Engineering Research Center for Spatio-Temporal Data Smart Acquisition and Application, Ministry of Education of China, Wuhan University

<sup>5</sup> School of Geomatics and Urban Spatial Informatics, Beijing University of Civil Engineering and Architecture, Beijing, China

<sup>6</sup> Shanghai Jiao Tong University, Shanghai, China

<sup>7</sup> Center for Brain-inspired Computing Research, Tsinghua University, Beijing, China

<sup>8</sup> School of Land Science and Technology, China University of Geosciences (Beijing), Beijing, China

<sup>9</sup> Department of Aeronautical and Aviation Engineering, The Hong Kong Polytechnic University

<sup>10</sup> School of Electronic and Information Engineering, Beihang University

<sup>11</sup> Advanced Research Institute of Multidisciplinary Sciences, Beijing Institute of Technology

## 1 Overview

Nowadays, the advent of a new technological era characterized by digitalization and intelligence has been permeating various industries. Numerous emerging domains, including mobile robotics, unmanned aerial vehicles (UAVs), and autonomous driving, are currently undergoing rapid developments. Real-time, high-precision, and all-scenario positioning services play a critical role in enabling a range of intelligent devices to execute tasks such as environmental perception, path planning, and behavior decision-making. Currently commonly used positioning technologies include dead reckoning (DR), inertial navigation system (INS), global navigation satellite system (GNSS), map matching (MM) positioning, visual/Lidar Simultaneous Localization and Mapping (SLAM) and so on. To address the inherent limitations of single positioning technology and achieve the desired performance of the positioning module, the utilization of a combination of heterogeneous and complementary sensors has become a common practice and the research of integrated navigation has become a hot topic. From 2019 to 2023, Chinese research institutes and related enterprises have been conducting extensive research on multi-sensor fusion navigation technology, resulting in a series of innovative achievements. These accomplishments can be broadly classified into multi-sensor fusion navigation models and methods, platforms and software, datasets, and applications, as described below.

## 2 Models and Methods

### GNSS/INS integration navigation

Before the integration of GNSS and INS, initializing the heading angle was a challenging task due to the inadequate performance of MEMS gyroscopes. Static alignment including coarse alignment and fine alignment is unable to achieve an accurate initialization of the heading angle for MEMS IMU. An optimization-based alignment (OBA) approach based on the least square estimation has been proposed, in which the constant direction cosine matrix (DCM) at the initial time is separated by attitude decomposition technique to construct the least square constraint optimization problem, then Davenport's q-method is used to solve this problem (Ouyang, et al. 2022). Zhang et al. (2020) developed a velocity-based optimization-based alignment method for low dynamic scenarios with low speed and low acceleration, which relies on the multiple-epochs velocity rather than the acceleration of the vehicle. An in-motion coarse alignment for GNSS-aided strapdown SINS is introduced based on Kalman filter (KF), and the simulation, vehicle test and lake trial are carried out (Huang et al. 2022). Besides, Huang et al. (2020) and Liu et al. (2022) employed the OBA method as a foundation and utilized GNSS observations to facilitate the alignment process. Additionally, the trajectory consistency was applied in IMU heading estimation. The IMU heading is calculated as the angle between the INS- and GNSS RTK-indicated position increment vectors in the horizontal direction based on the fact that the INS- and GNSS RTK-indicated trajectories are similar in shape (Chen et al. 2020).

In field environments, interruptions of satellite signals are common due to obstructions from buildings, foliage, and tunnels. The reliability of GNSS ambiguity resolution (AR) is affected by both the precision of observations and environmental factors. The fixing carrier phase integer ambiguities is a critical factor in achieving centimeter-level high-precision positioning through GNSS/INS integrated algorithms. Zhang et al. (2019) proposed an INS-aided integer ambiguity resolution enhancement method for precise point positioning (PPP) solutions in complex environment, which reveals the INS adding effect on PPP-AR from both the theoretical analysis and performance assessment. Ma et al. (2022) proposed a baseline vector constrained ILS ambiguity resolution method for moving-baseline based positioning and attitude determination scenes, which transformed the prior baseline length to a 3D baseline vector through the INS attitude information, used to assist ambiguity search and fix. The results show significant improvement on ambiguity resolution success rate and positioning precision, especially in the weak GNSS models with severe occlusion. Yang et al. (2019) proposed a robust unscented Kalman filter (UKF) based on the generalized maximum likelihood estimation (M-estimation) to improve the robustness of the integrated navigation system of GNSS and IMU. The proposed robust M-M unscented Kalman filter (RMUKF) applies the M-estimation principle to both functional model errors and measurement errors. In addition, an equivalent weight matrix, composed of the bi-factor shrink elements, is proposed in order to keep the original correlation coefficients of the predicted state unchanged.

### Land Vehicle Sensor and Dynamic Constraints Aided Positioning

The motion constraint is a kind of natural auxiliary information for land vehicle navigation,

which does not require the addition of auxiliary sensors and has the advantage of simple algorithm. The non-holonomic constraint (NHC) is a common auxiliary information based on the motion characteristics of civilian vehicles to improve the navigation accuracy of GNSS/INS integration on interruption of GNSS signal. Zhang et al. (2021) evaluated the navigation performance of multi-information integration based on a low-end inertial measurement unit (IMU) in precision agriculture by utilizing different auxiliary information (ie, GNSS real-time kinematic (RTK), NHC, and dual antenna GNSS), and a series of experiments with different operation scenes (e.g., open sky in wet and dry soils) were carried out for quantitative analysis.

The correct utilization of NHC requires a compensation of lever arm between the IMU center and the valid point of this constraint on the vehicle. The lever arm impact to NHC is investigate by two integrated navigation systems with different grade of IMUs, and analysis results show the forward lever arm is the most important influence factor, and the lever arm error should be controlled within sub-decimeter to ensure the accuracy and reliability of the NHC assistance (Zhang et al. 2020). Zhang et al. (2021) proposed an optimal mounting parameter estimation scheme based on the velocity vector observations is proposed, the quaternion-based optimal attitude determination method is used to estimate the mounting angle, and the weighted recursive least squares are applied to estimate the lever arm. Chen et al. (2020) designed a DR scheme using the attitude, derived incremental distance measurements from GNSS/INS smoothing solutions, and integrated the derived with the GNSS/INS position to estimate the pitch and heading mounting angles of the IMU.

The odometer and non-holonomic constraint are disturbed to a greater extent by more serious vibrations and bumping, and the distance increment model was applied to not only the odometer measurement but also the NHC constraint for superior robustness in the cases of carrier vibration, emergency stops, and passing speed bumps (Wang et al. 2022). Ouyang et al (2020) analyzed odometer pulse increment and pulse speed measurement models based on a navigation-level IMU for land vehicles. Gao et al. (2020) provided a tightly coupled integration mode among BDS triple-frequency PPP, INS, odometer, attitude measurements, and NHC, in which significant improvements on the accuracies of positioning and attitude determination can be obtained after adding odometer, attitude measurements, and NHC. Wu et al. (2021). compared the velocity and displacement increment measurement models of a wheel-mounted MEMS IMU-based dead reckoning system. Xu et al. (2023) analyzed the enhancements of low-cost INS, odometer, NHC, and dual-antenna attitudes on upgrading ambiguity fixing rate and reliability of single-frequency RTK.

### **Multi-sensor fusion navigation**

The rapid accumulation of inertial errors causes the positioning accuracy of GNSS/INS integration algorithms to inevitably diverge rapidly when the GNSS signal is obstructed for long periods of time or frequently. Visual-inertial navigation system (VINS) has become a practical solution for autonomous navigation due to its higher accuracy and lower cost. The integration of GNSS, INS and visual sensors provides significant benefits for navigation. On one hand, GNSS provides a spatial and temporal reference and helps in eliminating cumulative errors. On the other hand, in scenarios where GNSS signals are blocked, visual and inertial sensors can provide high-precision relative positioning information. Hu et al. (2023), Niu et al. (2022), Liao et al (2021) and Xu et al. (2022) fused stereo vision with GNSS/ SINS integration, where GNSS and stereo vision are loosely coupled and tightly coupled with SINS under the

earth-centered earth-fixed (ECEF) frame, respectively. The results show that with the support of stereo vision and SINS, GNSS accuracy can be considerably improved by 60%~80% in complex environments, which also outperforms the GNSS/SINS integration. Compared with loosely coupled integration, tightly coupled integration can utilize more complete sensor information to achieve more accurate positioning results. Li et al. (2022) and Li et al. (2022) proposed a centralized Extended Kalman Filter (EKF) to directly fuse raw data from GNSS carrier phase and pseudorange measurements, IMU, and visual features at the observation level. The system is integrated with the widely used high-precision GNSS models including PPP, real-time kinematic (RTK) and PPP-RTK to increase usability and flexibility. Li et al. (2022) proposed a tightly-coupled PPP/INS/Visual SLAM system that models and optimizes all raw data using a factor graph framework. To eliminate ionospheric effects and leverage carrier phase measurements, the system utilizes the ionosphere-free (IF) model through dual-frequency observations and incorporates phase ambiguity into the estimated states. Apart from positioning accuracy of the integrated navigation system, the integrity is important to ensure the safety of integrated navigation system. Integrity monitoring algorithm consists of fault detection and calculation of the protection level (PL). It provides the ability to alarm users when faults occur. Jiang et al. (2022) proposed an effective integrity monitoring (IM) scheme for GNSS/INS/vision integration based on error state extended Kalman filter (EKF) model. The corresponding PL was derived and vehicular field test was conducted to validate the effectiveness and performance of the proposed IM algorithm for the GNSS/INS/Vision integration. Results show that the proposed integrity monitoring algorithm is effective and can assure the integrity of the GNSS/INS/Vision integration at different fault modes.

The visual sensor is highly dependent on texture features, leading to a greater requirement for illumination and texture characteristics. In contrast, the laser sensor, as a distance sensor, primarily depends on the spatial structural features. As a result, laser sensors can achieve good complementarity with visual sensors. Li et al. (2023) proposes a navigation system tightly coupling PPP/INS/LiDAR with the DRANSAC-RAIM and the doppler iterative closet point algorithm (DICP) as its initialization procedure is established for accurate and reliable positioning in urban environments. Li et al (2023) develop a LiDAR sliding-window plane-feature tracking method to further improve PPP/INS/LiDAR integrated system. The vehicular experiments demonstrate that the GNSS/INS/LiDAR integration can maintain submeter level horizontal positioning accuracy in GNSS-challenging environments. Li et al (2023) achieved a tightly-coupled fusion of PPP/INS/Vision/LiDAR through a centralized EKF. The vehicle experiments results indicate that the PPP/INS/Vision/LiDAR integration can maintain sub-meter level positioning in GNSS difficult environments (Figure 1).

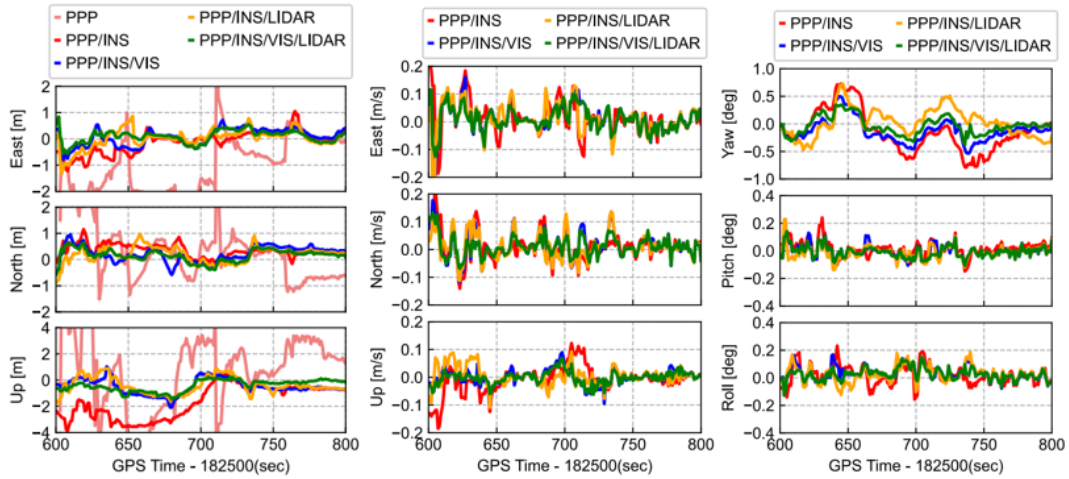


Figure 1. Position, velocity and attitude errors of PPP, PPP/INS, PPP/INS/Vision, PPP/INS/LiDAR and PPP/INS/Vision/LiDAR configurations

### High-Definition Map-based Localization for Intelligent Vehicle

In addition to real-time sensor observations, High definition (HD) map is also a common option for intelligent vehicles to achieve high-precision localization. The HD map is different from LiDAR cloud point map or occupancy grid map, which is much more lightweight to save and process. Some map standards have been proposed to formalize the HD map for intelligent vehicles, such as NDS, Lanelets, and OpenDrive, and they are broadly used in automotive enterprises, like Daimler, Toyota, and VOLKSWAGEN. Zhou et al. (2022) firstly generate a HD map of areas of interest from crowdsourced data as in Figure 2. In the first step, the lane mask propagation network (LMPNet) based on the feature pyramid network (FPN) is applied to road image sequences for lane detection. The lane markings are projected from a perspective space into a three-dimensional (3D) space to calculate the world coordinate of the lanes. The lane information collected via multiple crowdsourcing vehicles is discrete and has low accuracy. Therefore, data clustering and fitting are necessary. In the second step, an improved version of the density-based spatial clustering of applications with noise (DBSCAN) clustering algorithm is used to cluster the lanes extracted in the first step. The lane markings are more accurately described by utilizing a gradual fitting algorithm and a B-spline to fit the clustered data.

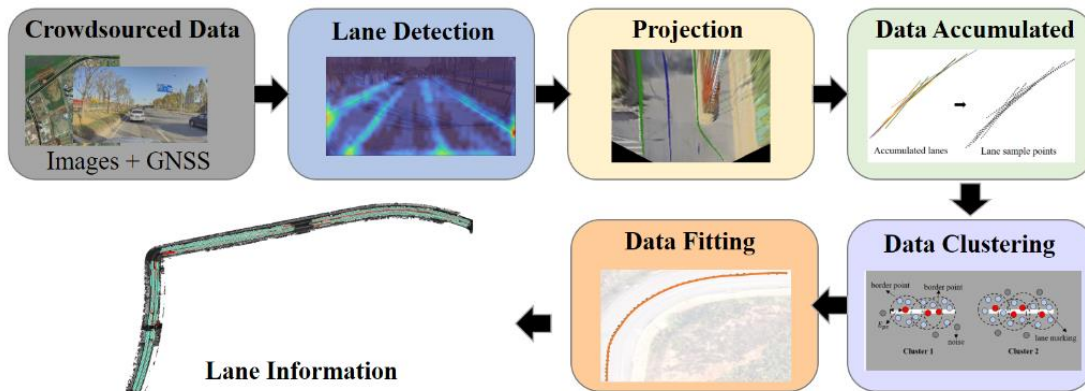


Figure 2. Extraction of lane information from multiple crowdsourcing vehicles

Lane markings can be used as topological and geometrical information in map-based localization methods, and the lateral vehicle-to-lane distance as can be used as the main measurement information in improving the positioning accuracy. Niu et al. (2023) proposed a multi-information integration method aided by lane distance to further eliminate lateral error. The lateral vehicle-to-lane distance measurements from camera-based systems, and the map-matching lane distance based on high-definition map were utilized to provide absolute lane distance measurement corrections in GNSS-denied environments. Xu et al. (2022) proposed a method to enhance GNSS/IMU integrated positioning by using a monocular camera and straight lane lines in HD maps. The positions are corrected by projecting lanes from OpenDRIVE maps onto the image, matching them with the visually detected ones, and minimizing the reprojected linear coefficients residuals. The tests demonstrate that positions in the lateral and up directions can be corrected to within 10 cm under current HD maps accuracy.

### **Brain-inspired Navigation**

In recent years, brain-inspired navigation has emerged as a cutting-edge topic in the field of multi-source fusion intelligent navigation, garnering essential attention from scholars. This approach involves the use of artificial neural networks to model the function or structure of navigation cells by drawing upon various neural mechanisms of spatial perception, representation, and navigation. With the integration of new neuromorphic sensors and computing chips, brain-inspired navigation enables the development of a new type of biologically-inspired intelligent navigation technology with brain-like performance, or even surpassing the navigation ability of the brain. This technology provides a promising technical route to overcome the limitations of traditional navigation technology in terms of intelligence, robustness, adaptability, and energy efficiency. Based on recent discoveries in neuroscience regarding the function and mechanism of navigational neural circuits, researchers have made essential progress in the theoretical methods and key technologies of brain-inspired navigation. Studies have been conducted on neural mechanisms, computational models, and navigation systems related to brain-inspired navigation, with some scholars providing systematic reviews (Cong M, et al., 2019; Yang C, et al., 2020; Guo C, et al., 2021; Liu J, et al., 2022; Meng Z, et al., 2023). In China, researchers have focused on developing computational models of navigation cells and methods for path integration, spatial mapping, path planning and navigation. In this section, we will analyze and summarize the research carried out by Chinese researchers in these areas.

Several computational models have been proposed based on the functional characteristics of spatial navigation cells. Gong Z, et al. (2021) introduced a theoretical model of three-dimensional grid cells that can adaptively represent two-dimensional and three-dimensional space according to different navigation modes. Meanwhile, Wang Y, et al. (2021) used computational modeling methods to analyze the activity patterns of grid cells encoding three-dimensional space. By employing a gravity-modulated oscillation model combined with animal body plane information, the firing field of grid cells on a curved surface can be generated. Another model was proposed by Han K, et al. (2020) based on differential Hebbian learning. This model spontaneously generates input associations of the Mexican hat model by modulating the firing rates of cells. By competitively and nonlinearly restricting the synaptic weights from place cells to grid cells, the hexagonal firing field distribution of grid cells is generated. Wang J, et al. (2020) proposed a dynamic multiscale grid cell model that can perform multiscale path



integration based on self-motion information. These computational models are essential in understanding the working principles and functional properties of navigation cells, and they can guide the development of brain-inspired navigation methods.

Path integration is a critical component of brain-inspired navigation that involves estimating a robot's position based on environmental and self-motion data. Constructing a path integration algorithm that combines the functional characteristics of navigational cells is a significant area of research in brain-inspired navigation. Several researchers have developed brain-inspired path integration algorithms by merging the grid cell to place cell model and the visual place cell model through information fusion to represent space. For example, Yang et al. (2020) proposed a vector-based method using multiscale grid cell models for unmanned aerial vehicles in large-scale space. They achieved multiscale path integration by introducing an exponentially increasing velocity gain factor in multiple attractor neural networks. Yang et al. (2022) built a multiscale three-dimensional grid cell model that supports path integration during four-degree-of-freedom motion in three-dimensional space. Zeng et al. (2020) proposed a Bayesian attractor network model that models head direction cell networks and grid cell networks, updating the neural encoding of each subnetwork in a Bayesian manner to improve the robustness of multimodal information integration. Zhao et al. (2021) presented a path integration model based on a novel stacking algorithm that enhances the accuracy of path integration by introducing multiscale grid cells. These path integration methods serve as a foundation for robot localization.

Creating maps is also an important research topic in brain-inspired navigation as they serve as the basis for implementing path planning and navigation control. Efficient encoding and construction of these maps is key. Zhao C, et al. (2020) proposed a cognitive map construction method that uses radial basis function neural networks to learn the mapping relationship between grid cells and place cells. The improved Q-learning algorithm is used to learn the Q-value of target-oriented place cells, which are used to represent space. The target-oriented direction information is then calculated based on the principle of centroid estimation, resulting in an accurate and reliable cognitive map. Zou Q, et al. (2020) developed a cognitive map learning framework for robots that adapts grid cells and place cells based on self-motion speed, continuously constructing a cognitive map of the environment during exploration. Chen M, et al. (2021) proposed a method for converting information from multiscale grid cells to place cells, constructing a bio-inspired SLAM algorithm that covers the entire spatial environment with multiscale grid cells and establishes a conversion relationship between these and place cells. Finally, Zhao D, et al. (2022) proposed a perception-motion integration neural network model that learns cognitive map representation by integrating perception and motion information. This model includes a deep neural network that represents environmental visual features, a recurrent neural network that encodes spatial information, and a neural network that decodes position information from spatial representation, allowing for effective updates to cognitive maps based on self-motion and visual information.

The path integration and map construction have been used in several navigation models to provide real-time position and map for robot navigation. Yu N, et al. (2019) proposed a navigation algorithm based on the cognitive mechanism of the hippocampus, updating the state of grid cells and place cells according to stripe cells. Gu Y, et al. (2021) developed a vector navigation method for large-scale space based on the oscillation interference model, improving

the robustness of vector navigation. Liao Y, et al. (2022) proposed a navigation method for two-dimensional space using spatial cells, correcting the error of path integration through a visual pathway computation model. Zhou Y, et al. (2022) constructed a bio-inspired target-oriented navigation model based on spatial exploration and cognitive map construction, generating a cognitive map and achieving target-oriented navigation. Chao L, et al. (2023) created an effective navigation path planning algorithm for unmanned aerial vehicles using spiking neural networks based on place cells.

Several systemic methods of brain-inspired SLAM and navigation for robots have been developed using navigation cell models. Yu et al. (2019) proposed a brain-inspired SLAM methods for 3D environments that uses 3D grid cells and multi-layer head direction cells to encode the robot's four degrees of freedom pose information, allowing for the construction of a 3D experience map that can be used for path planning and navigation control. Zeng T, et al. (2021) developed a compact brain-inspired cognitive mapping method that can generate the overall layout map of an environment while maintaining a small map size. Liu K, et al. (2022) developed a method based on neuromorphic chips that uses all-spiking neurons for path integration and map representation, enabling low-power and low-error spatial mapping. Tang H, et al. (2018) developed a brain-inspired cognitive navigation method for 2D indoor spaces that integrates cognitive mapping ability in the entorhinal cortex and episodic memory ability in the hippocampus to support robot execution of multiple tasks. In this model, a 3D continuous attractor network is used to model the functionality of the entorhinal cortex, and a recurrent spiking neural network is used to model the functionality of the hippocampus. Shen C, et al. (2019) proposed a brain-inspired navigation method that integrates inertial sensors to effectively reduce navigation errors, while Zou Q, et al. (2021) developed a self-learning system based on episodic memory that supports robot experience map learning, construction, and navigation, improving map construction and navigation efficiency and accuracy. Finally, Liu D, et al. (2022) proposed a robot navigation method based on experience and predictive maps that supports accurate construction of environment experience maps and path planning.

Indeed, the interdisciplinary collaboration between neuroscience, brain-inspired intelligence, robotics, and navigation is crucial for the development of brain-inspired navigation technology. The integration of knowledge from different fields can lead to the development of more advanced and efficient models and algorithms for robot navigation. By exploring the neural mechanisms of navigation, researchers can gain insights into how the human brain performs navigation tasks, and then apply these insights to develop new brain-inspired navigation technology that is highly robust, adaptive, and intelligent. Continued efforts in this direction can lead to the development of intelligent navigation systems that are capable of performing complex navigation tasks in various environments, such as search and rescue, logistics, and transportation.

### **3 Platform and Software**

In addition to the notable advancements made by Chinese scholars in multi-sensor fusion navigation Models and Methods, there has also been significant progress in the development of multi-source fusion navigation platforms and software. The purpose of these platforms and software is to enhance the reliability, accuracy, and robustness of navigation systems in

complex environments, thereby achieving high-precision navigation and positioning services tailored to different application scenarios. On the one hand, these platforms and software provides a foundational platform and toolset for scholars in related fields, including data input/output interfaces, visual interfaces, development interfaces and other features, that can effectively reduce the development difficulty and workload for researchers. On the other hand, they open up broader prospects for the development and application of multi-source fusion navigation algorithms.

The GREAT group in School of Geodesy and Geomatics at Wuhan University developed the Satellite Geodesy and Multi-source Navigation Software and Hardware Platform (GREAT software) as in Figure 3. The platform software not only supports common multi-sensor fusion navigation algorithms such as GNSS/INS integration, VINS, and GNSS/Visual/IMU/Lidar integration, but also provides a complete set of multi-frequency and multi-system GNSS post-processing and real-time products. The platform's hardware enables time synchronization of different sensors and support data collection of various sensors such as GNSS, IMU, Lidar, and Camera. A part of the platform's software, GREAT-UPD, has been open-sourced (Li et al. 2021).

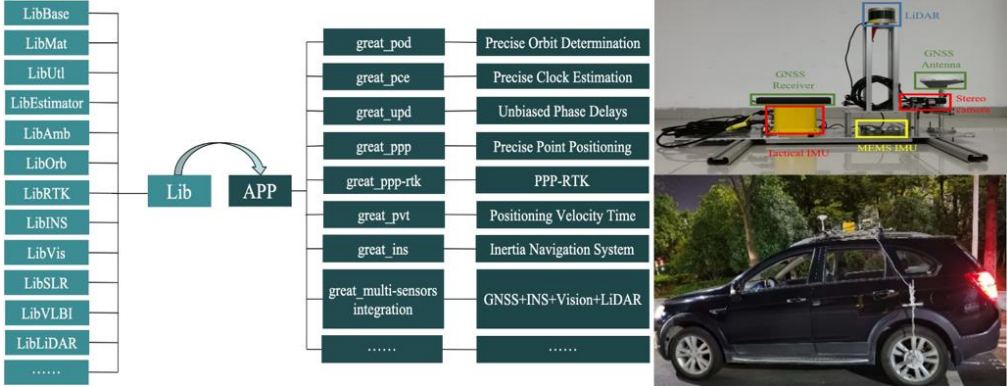


Figure 3. GREAT software: satellite geodesy and multi-source navigation software and hardware platform

The PLANET group in School of Geodesy and Geomatics at Wuhan University independently designed multi-sensor integration platforms SmartPNT-mate and SmartPNT-mini, which integrate GNSS, IMU, odometer, camera, LiDAR as well as high-precision time synchronization board and embedded AI edge computer. The group use hard synchronization to achieve microsecond-level time synchronization of various sensors and a millimeter-level spatial synchronization is achieved by precision design and machining, accurate calibration in laboratory and online dynamic estimation. Based on the SmartPNT-mate and SmartPNT-mini platforms, the group have collected multi-sensor data with a length of more than 1400 KM and a data volume of about 50TB in typical scenes, including open road sections, viaducts, urban canyons, avenues and tunnels.

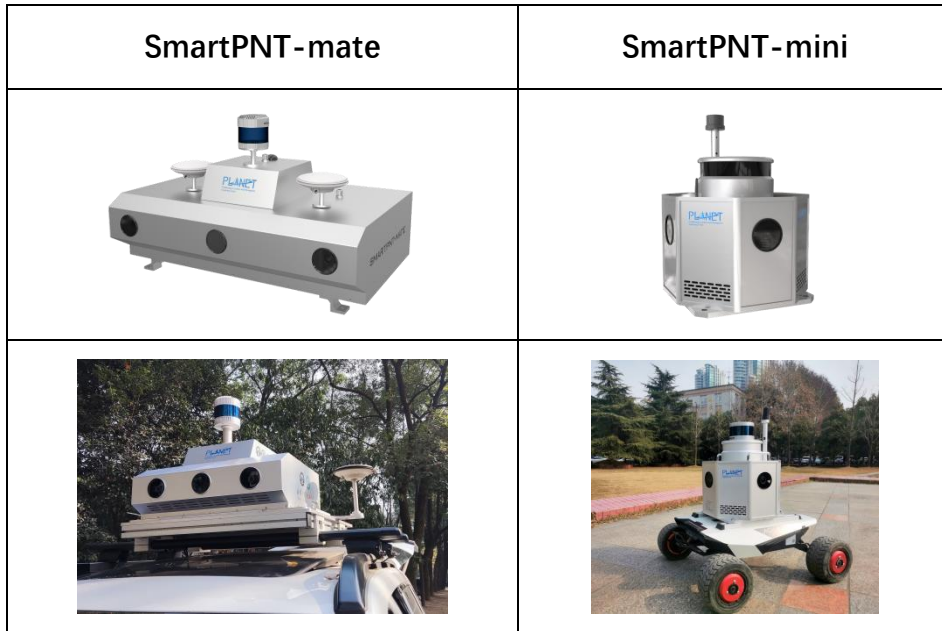


Figure 4. SmartPNT-mate and SmartPNT-mini hardware platform

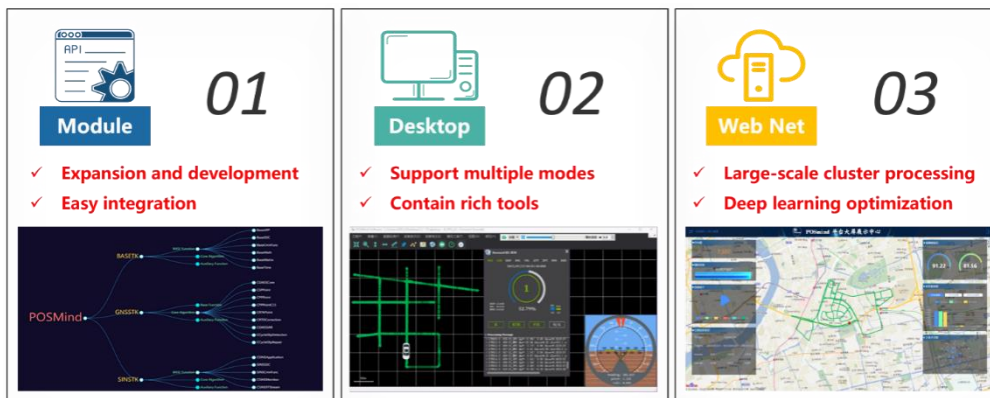


Figure 5. POSMind software system for PNT service

The Integrated & Intelligent Navigation Group (<http://i2nav.cn/>) at Wuhan University has made available an open-source platform for GNSS/INS integrated navigation systems based on both Extended Kalman Filter and graph optimization approaches. This platform aims to provide a general, modular, and easily extensible research environment for peers to develop and refine GNSS/INS integrated positioning algorithms. To mitigate the fragility of GNSS signals in complex environments, the research team has also proposed two novel algorithms, namely IC-GVINS (<https://github.com/i2Nav-WHU/IC-GVINS>) and Wheel-SLAM (<https://github.com/i2Nav-WHU/Wheel-SLAM>), which incorporate visual sensors and wheel encoders into the GNSS/INS integration system.

The team led by Prof. Ling Pei from Shanghai Jiao Tong University has developed an electronic system called S-Cube, which combines RTK capabilities, industrial cameras, high-precision inertial sensors, and multi-beam lidar as in Figure 6. The system is well suitable for academic research, particularly for the development and testing of SLAM algorithms. All sensors on the device are synchronized with a self-developed hardware platform, resulting in

millisecond-level time differences between each sensor. Furthermore, the device can also plug in different other sensors, like panoramic camera. To benefiting the multi-sensors navigation community, the code and hardware design will be open-sourced at <https://github.com/DreamWaterFound/S-Cube.git>.

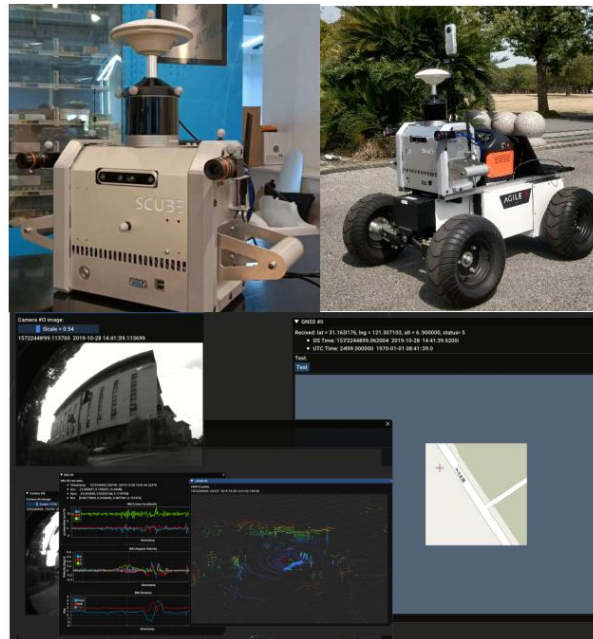


Figure 6. S-Cube: Plug-and-Play All-source Navigation Platform

## 4 Dataset

The assessment of precision is a critical aspect of the exploration of multi-sensor fusion navigation algorithms. As the number of required sensors and application scenarios increases in research, The acquisition of experimental data inevitably incurs substantial time and economic costs. Moreover, the use of disparate experimental data by various research institutions poses challenges in conducting impartial assessments of algorithmic performance. From 2019 to 2023, numerous public datasets were released by Chinese scholars. These datasets enabled many researchers worldwide to research without system and data limitations.

The integrated & intelligent navigation group at Wuhan university has opened source a vehicle GINS dataset for GNSS/INS integration applications (<https://github.com/i2Nav-WHU/awesome-gins-datasets>). The biggest feature of the dataset is that four different grades of MEMS IMUs are included, which provide an opportunity for the researchers to comprehensively evaluate their algorithms. The dataset was collected in an open-sky industrial area, where the GNSS RTK was well satisfied. The duration of the whole dataset is 1617 seconds, including the raw IMU data, GNSS RTK positioning results, and the ground-truth for each IMU.

Wen et al. (2020) provided the UrbanLoco: a mapping/localization dataset collected in highly-urbanized environments with a full sensor-suite.13 trajectories were collected in San Francisco and Hong Kong, covering a total length of over 40 kilometers. As shown in Figure 7, the dataset included a wide variety of urban terrains: urban canyons, bridges, tunnels, sharp



turns, etc. Moreover, the dataset incorporated information from various sensors, including LIDAR, cameras, IMU, and GNSS receivers.

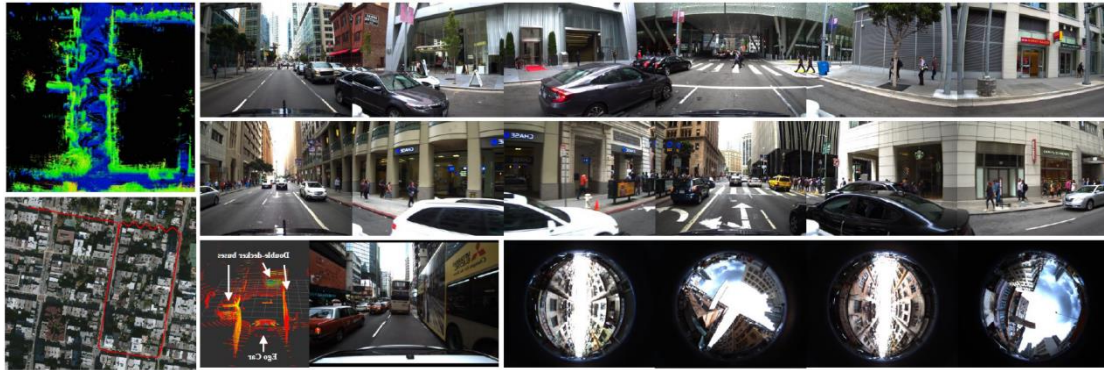


Figure 7. Urban terrains and sensor data of UrbanLoco

Yin et al. (2022) released M2DGR: a novel large-scale dataset collected by a ground robot with a full sensor-suite including six fish-eye and one sky-pointing RGB cameras, an infrared camera, an event camera, a Visual-Inertial Sensor, an inertial measurement unit, a LiDAR, a consumer-grade GNSS receiver and a GNSS-IMU navigation system with real-time kinematic signals (Figure 8). All those sensors were well-calibrated and synchronized, and their data were recorded simultaneously. The ground truth trajectories were obtained by the motion capture device, a laser 3D tracker, and an RTK receiver. The dataset comprises 36 sequences (about 1 TB) captured in diverse scenarios including both indoor and outdoor environments.

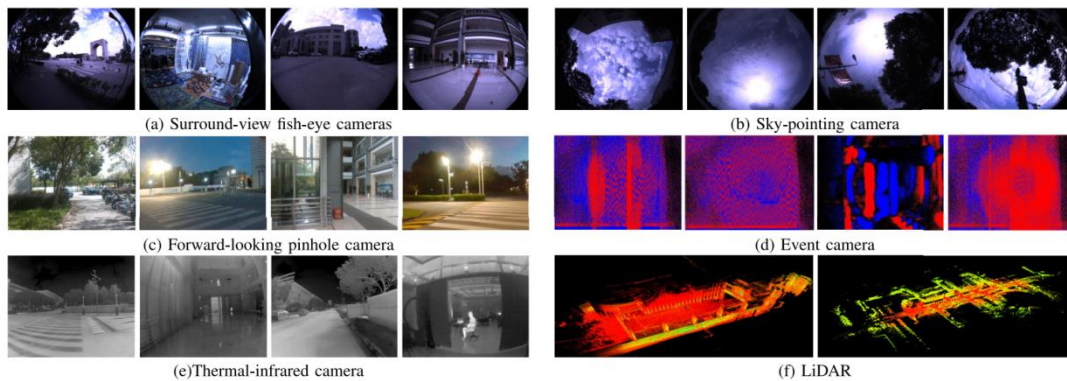


Figure 8. Typical scenarios and sensor data of M2DGR

## 5 Application

Multi-sensor fusion navigation can effectively overcome the limitations of single sensor navigation and provide high precision, reliability, and availability positioning services. The application prospects of multi-sensor fusion navigation are vast, encompassing traditional sectors such as transportation, agriculture, and urban construction, as well as emerging areas such as autonomous driving, UAVs, and intelligent robotics. From 2019 to 2023, Chinese

scholars have made significant achievements in the application of multi-sensor fusion navigation.

The achievements of the the integrated & intelligent navigation group (<http://i2nav.cn/>) in the application of multi-sensor fusion navigation are remarkable (Figure 9). They are manifested in the following aspects:

1) land vehicle navigation: The license of low-cost and high-precision vehicle-mounted integrated navigation scheme has been transferred to the mainstream Beidou /GNSS chip supplier in China. The high-precision and multi-source integrated navigation scheme has served frontline autonomous driving schemes. Relevant mass production navigation chips and modules have achieved an annual sales of 100,000 sets, and are widely used in autonomous driving, intelligent transportation, precision agriculture and other hot fields.

2) low-cost integrated hardware: INS-Probe, with independent intellectual property rights, can output 50Hz real-time high-precision position, speed and attitude information, and support sensor original observation output and post-processing calculation. INS-Probe supports external IMUs, GNSS, odometer and other sensors, and provides high precision time synchronization for cameras, Lidar and other sensors, realizing multi-source data fusion and positioning, and further improving system adaptability and robustness. It can provide a complete set of hardware and software solutions for low cost and high precision navigation applications such as unmanned vehicles, robots and UAVs.

3) pipeline measuring instrument: The pipeline measuring instrument series products were developed in collaboration with Guangzhou Datie Ruiwei Technology Co., LTD. (<http://dt-railway.com/>), whose accuracy and overall performance are at an international leading level and won the previous engineering comparison with the same type of products at home and abroad. The products have been successfully promoted in the gas, electric power, petrochemical and other industries.

4) railway track geometry measuring trolley system: A railway track geometry measuring trolley system based on INS was completed, and applied to Wuhan MAP Space Time Navigation Technology Co., LTD. (<http://www.whmpst.com/cn/>) and Guangzhou Datie Ruiwei Technology Co., LTD. (<http://dt-railway.com/>) for three models of inertial Rail vehicle inspection hardware and software products.

5) deeply coupled GNSS/INS receiver: Proprietary intellectual property GNSS/INS deep combination receiver software and hardware prototype support achievement transformation, can provide a full set of solutions. Deep combination software has been transformed to famous mobile phone terminal manufacturers, and deep combination hardware prototype has been transformed to aerospace research institute. In complex urban scenes, the positioning performance of deep combined receiver is better than that of Ublox integrated navigation product M8U. Under 100g/s ultra-high dynamic, the deep-depth combined receiver can output GNSS carrier phase stably.





Figure 9. The application of multi-source fusion navigation from integrated & intelligent navigation group

The team led by Prof. Jian Wang from Beijing University of Civil Engineering and Architecture have developed integrated navigation equipment for high precision automatic driving based GNSS/INS tightly coupled integration algorithm as in Figure 10. In urban environments, centimeter-level positioning results and high accuracy attitudes can be obtained. Combining with odometer information from the vehicle, the high precision positioning results can still be maintained in short GNSS outage duration. The GNSS/INS tightly coupled navigation equipment has been tested more than ten thousand times in urban environments, and it has been widely used in typical automatic driving application scenarios, such as automatic car, ports and fixed-route park area. At the same time, an automatic position and orientation system (POS) cloud processing platform has been developed for high-definition map production, the users can easily obtain the POS results by uploading the collected raw data combined with BDS ground-based augmentation system data.



Figure 10. GNSS/INS tightly coupled navigation equipment and automatic driving applications

## Bibliography

- Ouyang W, Wu Y. Optimization-based strapdown attitude alignment for high-accuracy systems: Covariance analysis with applications[J]. *IEEE Transactions on Aerospace and Electronic systems*, 2022, 58(5): 4053-4069.
- Zhang Q, Li S, Xu Z, et al. Velocity-based optimization-based alignment (VBOBA) of low-end MEMS IMU/GNSS for low dynamic applications[J]. *IEEE Sensors Journal*, 2020, 20(10): 5527-5539.
- Huang H, Wei J, Wang D, et al. In-Motion Initial Alignment Method Based on Vector Observation and Truncated Vectorized K-Matrix for SINS[J]. *IEEE Transactions on Instrumentation and Measurement*, 2022(71): 1-15.
- Huang Y, Zhang Z, Du S, et al. A high-accuracy GPS-aided coarse alignment method for MEMS-based SINS[J]. *IEEE Transactions on Instrumentation and Measurement*, 2020, 69(10): 7914-7932.
- Liu W, Cheng X, Ding P, et al. An optimal indirect in-motion coarse alignment method for GNSS-aided SINS[J]. *IEEE Sensors Journal*, 2022, 22(8): 7608-7618.
- Chen Q, Lin H, Guo R, et al. Rapid and accurate initial alignment of the low-cost MEMS IMU chip dedicated for tilted RTK receiver[J]. *GPS Solutions*, 2020(24): 1-13.
- Zhang X, Zhu F, Zhang Y, et al. The improvement in integer ambiguity resolution with INS aiding for kinematic precise point positioning[J]. *Journal of Geodesy*, 2019(93): 993–1010.
- Ma L, Zhu F, Liu W, et al. VC-LAMBDA: a baseline vector constrained LAMBDA method for integer least-squares estimation[J]. *Journal of Geodesy*, 2022(96): 59.
- Yang C, Shi W, Chen W. Robust M–M unscented Kalman filtering for GPS/IMU navigation [J]. *Journal of Geodesy*, 2019, 93:1093–1104.
- Zhang Q, Chen Q, Xu Z, et al. Evaluating the navigation performance of multi-information integration based on low-end inertial sensors for precision agriculture[J]. *Precision Agriculture*, 2021, 22(3): 627-646.
- Zhang Q, Hu Y, Niu X. Required lever arm accuracy of non-holonomic constraint for land vehicle navigation[J]. *IEEE Transactions on Vehicular Technology*, 2020, 69(8): 8305-8316.
- Zhang Q, Hu Y, Li S, et al. Mounting parameter estimation from velocity vector observations for land vehicle navigation[J]. *IEEE Transactions on Industrial Electronics*, 2021, 69(4): 4234-4244.
- Chen Q, Zhang Q, Niu X. Estimate the pitch and heading mounting angles of the IMU for land vehicular GNSS/INS integrated system[J]. *IEEE transactions on intelligent transportation systems*, 2020, 22(10): 6503-6515.
- Wang L, Niu X, Zhang T, et al. Accuracy and robustness of ODO/NHC measurement models for wheeled robot positioning[J]. *Measurement*, 2022(201): 111720.
- Ouyang W, Wu Y, Chen H. INS/odometer land navigation by accurate measurement modeling and multiple-model adaptive estimation[J]. *IEEE Transactions on Aerospace and Electronic Systems*, 2020, 57(1): 245-262.
- Gao Z, Ge M, Li Y et al. Modeling of multi-sensor tightly aided BDS triple-frequency precise point positioning and initial assessments [J]. *Information Fusion*, 2020, 55:184-198
- Wu Y, Niu X, Kuang J. A comparison of three measurement models for the wheel-mounted MEMS IMU-based dead reckoning system[J]. *IEEE Transactions on Vehicular Technology*, 2021, 70(11): 11193-11203.
- Xu Q, Gao Z, Lv J et al. Tightly Coupled Integration of BDS-3 B2b RTK, IMU, Odometer, and Dual-Antenna Attitude [J]. *IEEE Internet of Things Journal*, 2023, 10(7): 6415-6427.
- Hu J, Zhu F, Zhuo D, et al. Performance evaluation of Stereo Vision aided Loosely Coupled GNSS/SINS Integration for land vehicle navigation in Different Urban Environments[J]. *IEEE Sensors Journal*, 2023.

- Niu X, Tang H, Zhang T, et al. IC-GVINS: A Robust, Real-Time, INS-Centric GNSS-Visual-Inertial Navigation System[J]. *IEEE Robotics and Automation Letters*, 2022, 8(1): 216-223.
- Liao J, Li X, Wang X, et al. Enhancing navigation performance through visual-inertial odometry in GNSS-degraded environment[J]. *Gps Solutions*, 2021(25): 1-18.
- Xu Q, Lv J, Gao Z. Evaluation on Low-cost GNSS/IMU/Vision Integration System in GNSS-denied Environments[C]. 2022 IEEE 12th International Conference on Indoor Positioning and Indoor Navigation (IPIN). IEEE, 2022: 1-6.
- Li X, Li S, Zhou Y, et al. Continuous and Precise Positioning in Urban Environments by Tightly Coupled Integration of GNSS, INS and Vision[J]. *IEEE Robotics and Automation Letters*, 2022, 7(4): 11458-11465.
- Li X, Li X, Huang J, et al. Improving PPP-RTK in urban environment by tightly coupled integration of GNSS and INS[J]. *Journal of Geodesy*, 2021(95): 1-18.
- Li T, Pei L, Xiang Y, et al. P3-VINS: Tightly-Coupled PPP/INS/Visual SLAM Based on Optimization Approach[J]. *IEEE Robotics and Automation Letters*, 2022, 7(3): 7021-7027.
- Jiang H, Li T, Song D, et al. An effective integrity monitoring scheme for GNSS/INS/vision integration based on error state EKF model[J]. *IEEE Sensors Journal*, 2022, 22(7): 7063-7073.
- Li T, Pei L, Xiang Y, et al. P3-LINS: Tightly Coupled PPP-GNSS/INS/LiDAR Navigation System With Effective Initialization[J]. *IEEE Transactions on Instrumentation and Measurement*, 2023(72): 1-13.
- Li S, Wang S, Zhou Y, et al. Tightly Coupled Integration of GNSS, INS, and LiDAR for Vehicle Navigation in Urban Environments[J]. *IEEE Internet of Things Journal*, 2022, 9(24): 24721-24735.
- Li S, Li X, Wang H, et al. Multi-GNSS PPP/INS/Vision/LiDAR tightly integrated system for precise navigation in urban environments[J]. *Information Fusion*, 2023(90): 218-232.
- Zhou J, Guo Y, Bian Y, et al. Lane Information Extraction for High Definition Maps Using Crowdsourced Data[J]. *IEEE Transactions on Intelligent Transportation Systems*, 2022.
- Xu Q, Zhu F, Hu J, et al. An enhanced positioning algorithm module for low-cost GNSS/MEMS integration based on matching straight lane lines in HD maps[J]. *GPS Solutions*, 2023, 27(1): 22.
- Niu X, Peng Y, Dai Y, et al. Camera-Based Lane-Aided Multi-Information Integration for Land Vehicle Navigation[J]. *IEEE/ASME Transactions on Mechatronics*, 2023, 28(1): 152-163.
- Cong M, Zou Q, Liu D, et al. Review of robot navigation inspired by the localization cells' cognitive mechanism. *Journal of Mechanical Engineering*, 2019, 55(23): 1-12.
- Yang C, Liu J Y, Xiong Z, et al. Brain-inspired navigation technology integrating perception and action decision: a review and outlook[J]. *Acta Aeronautica et Astronautica Sinica*, 2020, 41(1): 30-44..
- Guo C, Luo B, Li F, et al. Review and verification for brain-like navigation algorithm. *Geomatics and Information Science of Wuhan University*, 2021, 46(12):1819-1831.
- Liu J, Luo Y, Guo C, et al. PNT intelligence and intelligent PNT. *Acta Geodaetica et Cartographica Sinica*, 2022, 51(6):811-828.
- Meng Z, Zhao D, Si B, Dai S. A survey on robot navigation based on mammalian spatial cognition. *Robot*, 2023, 1-17.
- Gong Z, Yu F. A Plane-Dependent Model of 3D Grid Cells for Representing Both 2D and 3D Spaces Under Various Navigation Modes[J]. *Frontiers in Computational Neuroscience*, 2021, 15: 739515.
- Wang Y, Xu X Y, Pan X C, et al. Grid cell activity and path integration on 2-D manifolds in 3-D space. *Nonlinear Dynamics*, 2021, 104(2): 1767-1780.
- Han K, Wu D, Lai L. A model of generating grid cell based on difference Hebbian learning in brain-inspired navigation. *Systems Engineering and Electronics*, 2020, 42(3):674-679.

- Wang J, Yan R, Tang H. Multi-Scale Extension in an entorhinal-hippocampal model for cognitive map building[J]. *Frontiers in Neurorobotics*, 2021, 14: 112.
- Yang C, Liu J, Xiong Z, et al. Brain-inspired vector navigation method based on model of multi-scale grid cells. *Journal of Chinese Inertial Technology*, 2022, 28(2):179-185.
- Yang C, Xiong Z, Liu J, et al. A 3D path integration approach based on multi-scale grid cells for large-scale navigation. *IEEE Transactions on Cognitive and Developmental Systems*, 2022, 14(03): 1009-1020.
- Zeng T, Tang F, Ji D, Si B. NeuroBayesSLAM: Neurobiologically inspired Bayesian integration of multisensory information for robot navigation. *Neural Network*, 2020, 126:21-35.
- Zhao C, Wu D, Han K, et al. Path integration model based on multi-scale grid cell. *Systems Engineering and Electronics*, 2020, 43(10): 2961-2967.
- Zhao C, Wu D, He J, et al. Navigation cognitive map construction based on improved Q-learning algorithm. *Journal of Air Force Engineering University: Natural Science Edition*, 2020, 21(2): 53–60.
- Zhao D, Zhang Z, Lu H, et al. Learning cognitive map representations for navigation by sensory–motor integration. *IEEE transactions on cybernetics*, 2022, 52(1):508-21.
- Zou Q, Cong M, Liu D, et al. Robotic episodic cognitive learning inspired by hippocampal spatial cells. *IEEE Robotics and Automation Letters*, 2020, 5(4):5573-5580.
- Yu N, Zhai Y, Yuan Y, et al. A bionic robot navigation algorithm based on cognitive mechanism of hippocampus. *IEEE Transactions on Automation Science and Engineering*, 2019, 16(4), 1640–1652.
- Gu Y, Zhao X, Dai C. Brain-like large-scale spatial vector navigation method based on grid cell model. *Control Theory & Applications*, 2021, 32(12): 2094-2100.
- Liao Y, Yu H, Yu N. A brain-like navigation method inspired by the spatial cells' cognitive mechanism. *Computers and Electrical Engineering*, 2022, 103:108305.
- Chen M, Tian D. Bionic slam algorithm based on multi-scale grid cell to place cell [J]. *Journal of Computer-Aided Design & Computer Graphics*, 2021, 33.
- Zhou Y, Wu D, Song Y, et al. Biological inspired goal-oriented navigation model based on spatial exploration and construction of cognitive map. *Journal of Electronics & Information Technology*, 2022.
- Chao L, Augenstein P, Roennau A, et al. Brain inspired path planning algorithms for drones. *Frontiers in Neurorobotics*, 2023, 17:29.
- Li X, Han X, Li X, et al. GREAT-UPD: An open-source software for uncalibrated phase delay estimation based on multi-GNSS and multi-frequency observations[J]. *GPS Solutions*, 2021(25): 1-9.
- Wen W, Zhou Y, Zhang G, et al. UrbanLoco: A full sensor suite dataset for mapping and localization in urban scenes[C]. 2020 IEEE international conference on robotics and automation (ICRA). IEEE, 2020: 2310-2316.
- Yin J, Li A, Li T, et al. M2dgr: A multi-sensor and multi-scenario slam dataset for ground robots[J]. *IEEE Robotics and Automation Letters*, 2021, 7(2): 2266-2273.
- Yu F, Shang J, Hu Y, et al. (2019) NeuroSLAM: A brain inspired SLAM system for 3D environments. *Biological Cybernetics*, 113(5-6):515-545.
- Zeng T, Si B. (2021) A brain-inspired compact cognitive mapping system. *Cognitive Neurodynamics*, 15:91-101.
- Liu K, Cui X, Kuang Y, et al. (2022) An all-neuron spiking 2-D path integration and map representation model implemented on neuromorphic chips. 2022 IEEE 16th International Conference on Solid-State & Integrated Circuit Technology (ICSICT), Nangjing, China, 1-3.
- Tang H, Yan R, Tan KC. (2018) Cognitive navigation by neuro-inspired localization, mapping, and episodic memory. *IEEE*

Transactions on Cognitive and Developmental Systems, 10(3):751–761.

Shen C, Liu X, Cao H, et al. (2019) Brain-like navigation scheme based on MEMS-INS and place recognition. Applied Sciences, 9(8):1708.

Zou Q, Cong M, Liu D, et al. (2021) A neurobiologically inspired mapping and navigating framework for mobile robots. Neurocomputing, 460: 181-194.

Liu D, Lyu Z, Zou Q, et al. (2022) Robotic navigation based on experiences and predictive map inspired by spatial cognition. IEEE/ASME Transactions on Mechatronics, 27(6):4316-26.

# Progress of Geodesy related Ionosphere

Zishen Li<sup>1,9</sup>, Ningbo Wang<sup>1</sup>, Liang Wang<sup>1</sup>, Xingliang Huo<sup>2</sup>, Xiaodong Ren<sup>3</sup>, Min Li<sup>2</sup>, Qiang Zhang<sup>3</sup>, Heng Yang<sup>11</sup>, Qi Liu<sup>13</sup>, Dongsheng Zhao<sup>4</sup>, Cheng Wang<sup>6</sup>, Ang Liu<sup>1</sup>, Andong Hu<sup>4</sup>, Ang Li<sup>1</sup>, Chengpan Tang<sup>5</sup>, Peng Chen<sup>12</sup>, Lei Wang<sup>3</sup>, Haiyang Fu<sup>7</sup>, Jiahao Zhong<sup>8</sup>, Ming Ou<sup>10</sup>, Wang Li<sup>14</sup>, Changyong He<sup>15</sup>

<sup>1</sup> Aerospace Information Research Institute, Chinese Academy of Sciences

<sup>2</sup> Innovation Academy for Precision Measurement Science and Technology, Chinese Academy of Sciences

<sup>3</sup> Wuhan University, Wuhan,

<sup>4</sup> China University of Mining and Technology

<sup>5</sup> Shanghai Astronomy Observatory

<sup>6</sup> Beihang University

<sup>7</sup> Fudan University

<sup>8</sup> Sun Yat-sen University

<sup>9</sup> Qilu Aerospace Information Research Institute

<sup>10</sup> China Research Institute of Radiowave Propagation

<sup>11</sup> Yangtze Normal University

<sup>12</sup> Xi'an University of Science and Technology

<sup>13</sup> Henan University

<sup>14</sup> Kunming University of Science and Technology

<sup>15</sup> Hunan University of Science and Technology

The ionosphere is the ionized part of the upper atmosphere of Earth, from about 40 km to 1000 km above sea level, and it plays an important role in atmospheric electricity and forms the inner edge of the magnetosphere. It has practical importance because, among other functions, it influences radio propagation, such as the Global Navigation Satellite System (GNSS), to distant places on Earth. Meanwhile, the GNSS, including BDS, GPS, Galileo and GLONASS, is also an essential technique for sensing the variation of ionosphere. During the years of 2019-2023, a large number of Chinese geodesy scientists, particularly more and more young researchers, devoted much efforts to the geodesy related ionosphere. Due to the very limited length, the achievements are carried out from the following six aspects, including

- (1) the ionospheric correction models for BDS and BDSBAS,
- (2) real-time global ionospheric monitoring and modeling,
- (3) the ionospheric 2D and 3D modeling based on GNSS and LEO satellites,
- (4) the ionospheric prediction based on artificial intelligence,
- (5) the monitoring and mitigation of ionospheric disturbances for GNSS users,
- (6) the ionospheric related data products and classical applications.

## 1 Ionospheric Correction Models for BDS-3 and BDSBAS

The application of space-based radio systems in L-band, like the Global Navigation Satellite System (GNSS), is severely affected by the signal propagation error induced by the

earth’s ionosphere. While the first order of ionospheric range error can be mitigated by forming the ionospheric-free linear combination of simultaneous GNSS measurements at two or more frequencies due to the dispersive nature of the ionosphere, a large number of single-frequency GNSS applications are reliant on the prior ionospheric information to correct the ionospheric path delay. Among them, ionospheric correction parameters transmitted in the navigation message of the Global Positioning System (GPS), Galileo and BeiDou are commonly used for the ionospheric error mitigation in single-frequency positioning (Yuan et al. 2019).

For BeiDou, different correction models are designed for single-frequency users of the regional BDS-2 and global BDS-3. BDS-2 adopts a Klobuchar-like model, which resembles GPS Ionospheric Correction Algorithm (ICA) but is formulated in a geographic coordinate system, to provide ionospheric correction service in the Asia-Pacific region (Wu et al. 2013). BDS-3 uses a newly designed broadcast ionospheric model BDGIM – BeiDou Global Ionospheric delay correction Model – to mitigate the ionospheric delay errors in single-frequency positioning (Yuan et al. 2019). In contrast to the Klobuchar-like model adopted in the regional BDS-2 system, the BDGIM describes global VTEC distributions with a simplified spherical harmonic expansion referring to a sun-fixed geomagnetic reference frame. The BDGIM is a two-dimensional ionospheric correction model, which relays on an elevation-dependent mapping function to convert ionospheric delays from vertical to slant directions. The nine broadcast parameters are designed to drive BDGIM, and they are transmitted in the BDS-3 navigation message with an update rate of 2 hours.

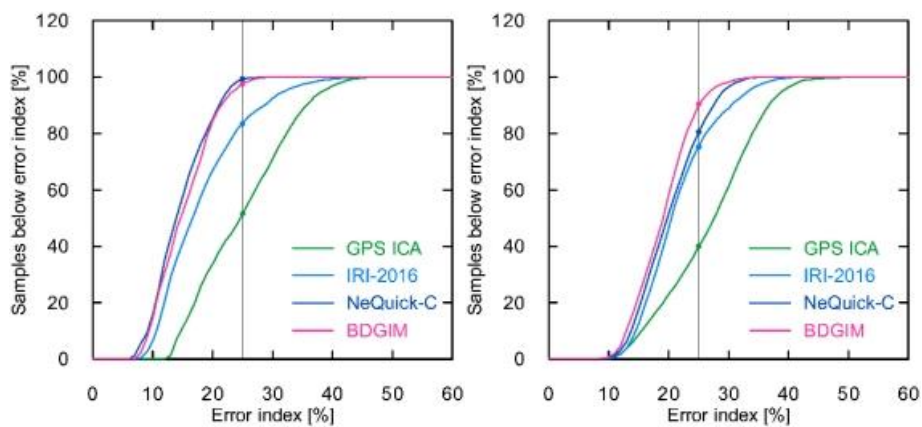


Figure 1. Cumulative distribution of different correction model errors compared to IGS-GIM (left) and Jason VTECs (right) covering solar maximum and minimum conditions. The vertical line denotes the targeted 25% error index (adapted from Wang et al. 2020).

The performance of the derived BDGIM had been assessed under different solar activities. BDGIM can achieve an overall correction capability of better than 75% for 98% of all observed samples compared to the IGS Global Ionospheric Maps (GIM) and 90% compared to Jason VTECs. In comparison with GPS ICA, BDGIM enables a 10–20% reduction of residual ionospheric errors. Furthermore, BDGIM exhibits a comparable performance with NeQuick-C model and about 5% better than the empirical IRI-2016 model. In the analysis of BDGIM performance under disturbed and quiet geomagnetic conditions, the model RMS error increases by 60% in GIM and Jason VTEC assessments, and the 3D positioning error increases by 17%



in the stand point positioning assessment (Wang et al. 2020). A notable degradation of model performance is found during the geomagnetic storm period. It can be an additional point to improve the model, especially considering the upcoming high solar conditions of the cycle 25.

For the BDS Satellite-based Augmentation System, i.e., BDSBAS, an adjusted Spherical Harmonics Adding KrigING method (SHAKING) approach was proposed for regional ionospheric VTEC modeling over China and its surrounding regions (Liu et al. 2021). In the SHAKING method, the VTEC information over the sparse observation data area is extrapolated by the Adjusted Spherical Harmonic (ASH) function, and the boundary distortion in regional VTEC modeling is corrected by the stochastic VTEC estimated using Kriging interpolation. Compared to the ASH-only solution, the quality of SHAKING generated regional ionospheric maps improves by 13-31% and 6-33% during high and low geomagnetic conditions, respectively. Compared to the inverse distance weighting (IDW) generated result, the significant quality improved of SHAKING-based VTEC maps is also observed, especially over the edge areas with an improvement of 60-80% (Liu et al. 2021). The GPS-L1 positioning augmented by BDSBAS corrections was also analyzed using the Huawei-P40 smartphone. Compared to the GPS-L1 stand positioning, the accuracy of BDSBAS augmented smartphone positioning increases by 27% in the horizontal component and 41% in a vertical component in the open-sky environment, and 50% improvement in both directions in the second experiment where the smartphone connects with an external geodetic GNSS antenna to reduce the negative effects of multipath errors (Liu et al. 2023).

## **2 Real-time Global Ionospheric Monitoring and Modelling**

### **Real-time global ionospheric modeling**

During the years of 2019-2023, the ionospheric associated analysis centers (IAAC) of China have continued to make significant contributions to the computation of real-time global ionospheric maps (RT-GIMs). Besides CAS, who had been working on the routine generation of RT-GIMs, Wuhan University (WHU) has also started RT-GIM computation and distribution. At CAS, an adjusted spherical harmonic expansion is used for its real-time regional ionospheric map computation (Li et al. 2019). The current implementation of the VTEC modelling approach of CAS relies on an approach that combines the periodical component and statistical part in the TEC modelling. At WHU, the global VTEC representation with a time resolution of 5 min uses the spherical harmonic expansion up to degree 12, and the real-time data streams of about 120 IGS Multi-GNSS stations (Zhang et al. 2018). WHU continues to encode its near-real-time TEC maps for real-time distribution in the RTCM format, which distributes the proposed RTCM SSR message type 1264 at 1 minute rate. As one of the analysis centers of the international GNSS Monitoring & Assessment System (iGMAS), Shanghai Astronomical Observatory (SHAO) has been actively participating in the space weather monitoring activities initiated by IAG, contributing to the integration of the real-time ionospheric map products of IGS and iGMAS for the Asia-Pacific region.

Li et al. (2019) described a two-layer two-SH approximation is applied to GPS and BDS for regional RT-TEC modelling and a significant improvement in the convergence time of precise point positioning is highlighted with the use of regional RT-ionospheric corrections. A

predicting-plus-modelling approach is employed for its RT-GIM computation using multi-GNSS streams of the IGS-RTS (Li et al. 2020). Wang et al. (2020) proposed an approach for NRT modeling of global ionospheric TEC by using the hourly IGS data based on a solar geomagnetic reference frame with spherical harmonic expansions up to a degree and order of 15. In the study of Han et al. (2022), the multi-GNSS multi-frequency observations from ground networks and space-borne ionospheric observations were assimilated to improve the real-time ionospheric modeling. Chen et al. (2022) provided an adaptive method for determining the Kalman filter process noise covariance matrix, which allows NRT modelling of the global VTEC from IGS hourly data. Yang et al. (2021) developed a new interpolation technique of RT-GIMs, i.e. Atomic Decomposition Interpolator of GIMs (ADIGIM), which minimizes the difference between observed VTEC measurement and weighted VTEC from historical GIMs in similar ionosphere conditions. Since January 2021, ADIGIM has been implemented in the RT-GIM modelling of UPC-IonSAT (one of classical IGS IAACs) by connecting the RT TOMographic IONosphere (RT-TOMION) model.

### Real-time Global Ionospheric Map combination

The first experimental combination of IGS RT-GIM has been generated by applying the weights given by the real-time dSTEC assessment technique to RT-GIMs provided by CAS, CNES and UPC-IonSAT since October 2018 (Li et al. 2020). The IGS RT-GIM is now generated using four RT ionospheric streams, which includes two Chinese centers, i.e. CAS and WHU, broadcasted in IGS-SSR message type 1264 and available from the IGS caster (products.igs-ip.net). A new version of IGS combined RT-GIM was developed at CAS with additional data streams from NRCAN since April 2021, compared to the legacy RT-GIM combination organized by UPC-IonSAT, supporting the IGS-SSR ionospheric message (Wang et al. 2022). An example of real-time global VTEC maps from CAS-combined and UPC-combined RT-GIMs are plotted in Figure 2, and similar global VTEC distributions can be found from both data sources. CAS combined RT-GIM streams are transmitted in both RTCM-SSR (IONO01IGS0) and IGS-SSR (IONO01IGS1) standards, which are freely accessible from the IGS data streaming server (products.igs-ip.net:2101) since January 2022.

Table 1. An overview of RT ionospheric streams used for RT-GIM combination and comparison

Analysis centers	Caster	Mountpoint	Interval / s	Format
CAS	products.igs-ip.net:2101	SSRC00CAS1	60	IGS-SSR
WHU	58.49.94.212:2101	IONO00WHU0	60	RTCM-SSR
CAS-combined	products.igs-ip.net:2101	IONO01IGS1	60	IGS-SSR

### RT-GIM assessment by different approaches

Since the quality of CNES RT-GIMs are investigated by RT-SF-PPP and IGS final maps (Nie et al. 2019), the performance of RT-GIMs of CAS, WHU, and IGS RT-GIM combination, were able to be evaluated in detail over 2 years by taking difference references, for instance the IGS final GIMs, JASON3 VTEC, and slant total electron content (dSTEC), and by the SF-PPP solutions. The results showed that the accuracy of the CAS RT-GIM is slightly better than that of the other two RT-GIMs (Ren et al. 2019). In addition, DORIS dSTEC assessment provides

an independent reference for the validation of RTGIM, which confirmed a better consistency with GNSS dSTEC assessments (Liu et al. 2023).

In summary, the performance of global VTEC representation in the available RT-GIMs has been assessed by IGS final product IGSG VTEC. During the testing period from 17/2/2022 to 13/03/2022 (see Figure 2), the results indicates that the RT-GIMs in particular the RT-GIM combination of CAS (marked by IONO01IGS1) turn out to be reliable sources of real-time global VTEC information.

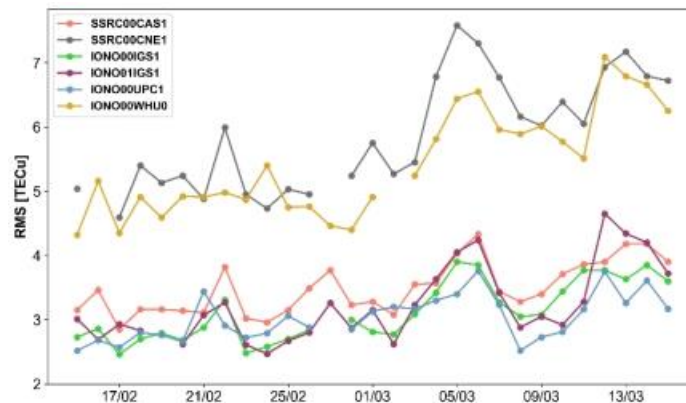


Figure 2. RMS series of different RT-GIMs (IONO01IGS1 for RT-GIM combination of CAS, IONO00IGS1 for RT-GIM combination of UPC-IonSAT, SSRC00CAS1 for CAS RT-GIM, SSRC00CNE1 for CNES RT-GIM, IONO00UPC1 for UPC-IonSAT RT-GIM, IONO00WHU0 for WHU RT-GIM) compared to IGS-GIM

### 3 Ionospheric 2D and 3D modeling based on GNSS and LEO satellites

A global ionosphere model with high accuracy and resolution is of great importance for ionospheric research and GNSS precise positioning applications. In the last 20 years, the accuracy and reliability of the global ionospheric model have benefited from the development of GNSS technology, but their performance is still not very good over many regions (e.g., the oceans and the polar regions) due to the lack of ground GNSS stations. Fortunately, the rapid development of low-Earth-orbit (LEO) satellite constellations provides a potential opportunity to address this issue. In 2019–2023, many Chinese researchers have been investigating global ionospheric 2D and 3D modeling by a combination of GNSS and LEO satellites through both simulated and real-data experiments.

Establishing high-precision and high-resolution ionospheric TEC models requires precise GNSS TEC measurements as well as LEO-based TEC measurements over the ocean. Ren et al. (2020a) used the PPP-Fixed method to extract ionospheric observations from phase observations based on zero-difference integer ambiguity. This method greatly improves the precision of the TEC observations. In the space-borne TEC retrieval, one of the main error sources that should be deducted is satellite and receiver differential code bias (DCB). Zhong et al. (2016a) proposed an improved DCB estimation method based on zero TEC assumption and optimized the parameter in the least square method for space-borne TEC determination. Based on space-borne GNSS observations, Zhong et al. (2016b, 2020) indicated that the long-term variations of GPS DCBs are primarily attributed to the satellite replacement under the zero-

mean constraint condition. With Chinese Fengyun satellite onboard observations, Li et al. (2017) estimated DCBs for both BDS and GPS, and Li et al. (2019) discussed the stability of DCBs for different solutions. Ren et al. (2020) estimated the LEO DCBs and generated the global topside ionospheric map using observations from multiple LEO satellites at different orbital altitudes. The mapping function is also fundamental in the space-borne TEC retrieval. Zhong et al. (2016c) evaluated different combinations of ionospheric effect height and mapping function for LEO satellites. Wu et al. (2021) proposed a new mapping Function based on the plasmaspheric scale height, and Wu et al. (2022) further analyzed the ionospheric horizontal gradients in the TEC mapping for space-borne TEC. Yuan et al. (2020, 2021) estimated LEO DCB and GPS DCB based on inequality constrained least square and multi-layer mapping function.

As an emerging remote sensing technique, GNSS reflectometry (GNSS-R) showed great potential in the ionospheric TEC monitoring and modeling over data-void or data-sparse regions. Wang and Morton (2021) investigated the feasibility of utilizing coherent GNSS-R measurements obtained by Spire CubeSats carrier phase data source to estimate slant TEC along the reflection signal path ionospheric and the results show that the slant TEC retrieved from GNSS-R measurements and from GIMs follow a similar trend. Furthermore, Liu et al. (2021) presented a simulation study of Arctic TEC mapping by integrating coherent GNSS-R measurements obtained from LEO CubeSat constellations with available ground-based GNSS observations. Ren et al. (2022) proposed an improved method which considers the influence of tropospheric delays and the topside ionospheric delays above the spaceborne GNSS-R receiver to estimate ionospheric TEC over oceans using the spaceborne GNSS-R technique.

Due to the emergence of LEO constellations, ionospheric research has gradually begun to differentiate between the top and bottom layers. LEO satellites typically orbit at altitudes ranging from 400 to 1400 km, which is around or above the ionospheric electron density maximum. The space-borne GNSS receivers bring great opportunities for the ionospheric sensing of the bottomside ionosphere (Li et al., 2022) and topside ionosphere (Ren et al., 2020b).

LEO satellites provide a great opportunity for global ionospheric modeling, however due to the limited number of LEO satellites available at present, Ren et al. (2020c) firstly simulated three kinds of designed LEO constellations with 60, 96, and 192 satellite data, the results show that LEO observations can expand the coverage and increase the density of ionospheric pierce points (IPPs), as shown in Figure 3.

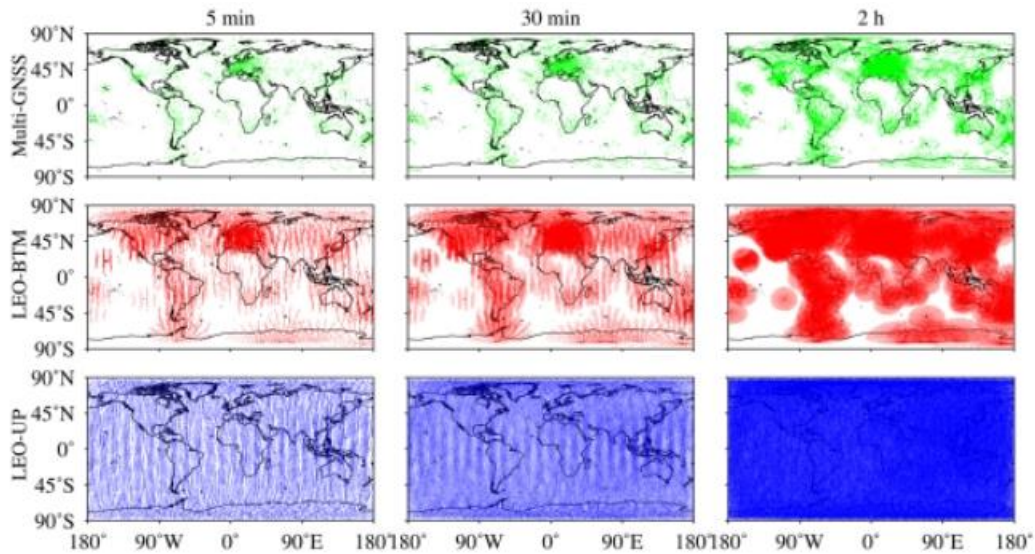


Figure 3. Distribution of ionospheric pierce points derived from Low-Earth-Orbiting (LEO) constellation with 192 satellites within different time spans, that is, 5 min, 30 min, and 2 hours, respectively.

Additionally, multi-source data such as GNSS data, satellite altimetry data, ionospheric occultation, and DORIS data can be used to generate a global ionospheric model with a significant improvement in accuracy (Hu et al., 2019; Han et al., 2022 ; Ren et al., 2021a ; Chen et al., 2021). To solve the problem that the satellite-based observation of ionospheric height cannot cover the whole ionospheric height range, Zhang et al. (2020) attributed the satellite altimetry and GNSS radio occultation products to a unified observation scale, and confirmed that the satellite-based ionospheric TEC products can be an effective supplement to the ground-based ionospheric TEC observation in ocean regions. An et al. (2019) attempted to fuse the ground GNSS with the IRI model and satellite altimetry. Shi et al. (2022) introduced the artificial neural network (ANN) to investigate the electron content at low latitudes. Using the ANN technique to combine the TEC from the IGS tracking station observations and the TEC measured by the COSMIC-2, the new model describes the ionospheric structure well.

In a global 3D ionospheric tomographic model, Zhou et al. (2020) used computer tomography to reconstruct three-dimensional electron density in the topside ionosphere using TEC observations from the Swarm-A/C satellites. Similarly, there are also limited space-borne measurements available for global ionospheric tomography. Thus, Ren et al. (2021b) investigated the potential improvements of GNSS-based ionospheric tomography at a global scale by combining the upcoming LEO constellations through simulation experiments. Wang et al. (2022) proposed using the ionospheric profile data of COSMIC-2 as the initial scale factor to constrain GNSS data. The work indicated that the fusion of GNSS and COSMIC-2 can improve the accuracy and spatial resolution of the 3-D tomographic modeling results. The combined GNSS-InSAR techniques will play an important role for imaging multiple scale ionospheric irregularities. Sui et al. (2020) verified the feasibility of three-dimensional tomography of the ionospheric electron density in the imaging area based on the Lutan-1 system and a possible combination of GNSS-InSAR technology for ionospheric parameter retrieval.

Ionospheric data assimilation is a now-casting technique to incorporate irregular ionospheric measurements into a certain background model, which is an effective and efficient way to overcome the limitation of the unbalanced data distribution and to improve the accuracy

of the model, so that the model and the data can be optimally combined with each other to produce a more reliable and reasonable system specification. Data assimilation technology has also been widely applied in ionospheric specification and prediction. Ou et al. (2022) adopted observation system simulation experiments (OSSE) to analyze the impacts of multi-source observations on ionospheric assimilation, and verified that space-based observations can improve the accuracy of ionospheric TEC and electron density. In particular, GNSS occultation can significantly improve the accuracy of nowcast and forecast of ionospheric electron density. The results also show that the existing observation system layout improves the data assimilation accuracy in the middle and low latitudes better than in the high latitudes. Ou et al. (2021) developed a near-real-time global ionospheric data assimilation and forecasting system (RT-GIDAM) based on a cloud computing platform. RT-GIDAM can realize the global ionospheric TEC and electron density nowcast and forecast in near real-time with higher spatio-temporal resolution ( $2.5^{\circ} \times 5^{\circ} \times 15\text{min}$ ). In order to improve the forecast accuracy of the ionosphere, He et al. (2019; 2020) constructed an EnKF ionosphere and thermosphere data assimilation algorithm through a sparse matrix method and found that the ionosphere forecast quality could be enhanced by optimizing the thermospheric neutral components via the EnKF method. The ionosphere electron density forecast accuracy can be improved by at least 10% for 24 hours.

#### **4 Ionospheric Predictions based on Artificial Intelligence**

Artificial Intelligence related approaches have been more widely used in ionospheric modeling by Chinese scholar since 2019 than ever, especially machine learning (ML) methods. ML approaches do not require a pre-defined base function in comparison with the traditional ionospheric modeling method, such as spherical harmonics. MLs can automatically construct a non-linear base function (using layers, unit, and activation functions) from a large amount of data. This can significantly reduce the model error during the model training.

Xia et al. (2021) developed a regional forecast model for TEC over China with a support vector machine. The variation of seasonal and local characteristics is also validated by the SVM model.

Li et al. (2021) developed an artificial neural network model for electron density is using the multi-observations, including COSMIC, FY-3C and Digisondes. Tang et al. (2020) investigated three machine learning models for TEC forecasting, including the long short-term memory (LSTM), autoregressive integrated moving average, and sequence-to-sequence models. Shi et al. (2022) adopted bidirectional long short-term memory (bi-LSTM) to forecast the ionospheric total electron content maps over China using long-term ground-based global positioning system observations from the Crustal Movement Observation Network of China. Yang et al. (2022) implemented pix2pixhd, one of the generative adversarial networks (GANs) to forecasting the one-day-ahead global TEC map.

LSTM has also been utilized in TEC map completion. Liu et al. (2020) uses LSTM to forecast the traditional coefficients to construct global ionospheric maps, and the typical ionospheric structures are sighted during geomagnetic events.

GAN, as developed for image completion initially, has proved to be effective tool in reconstructing global TEC maps. Pan et al. (2020, 2021) developed GANs named DCGAN-PB and SNP-GAN for global TEC completion. DCGAN-PB applies Poisson blending as a post-



processing procedure and shows a superior TEC completion performance over the traditional single-image inpainting methods such as TELEA and NS using the realistic MIT-TEC masks. While SNP-GAN, as a more enhanced tool, equips with an end-to-end generator, and robustness in different masks is the main advantage of SNP-GAN over DCGAN-PB. Moreover, SNP-GAN has shown the potential in uncovering meso-scale structures such as cusp. An illustration of results is shown in Figure 5. Our work show that the deep learning methods can learn from thousands of TEC maps in different conditions and extract useful features to overcome the challenges of effectively recovering the missing data in a large area not covered by the observation network. Chen et al. (2019, 2022) and Chen et al. (2021) also investigated several possibilities to improve the performance of GANs in global TEC completion, including take extra physical parameters into consideration and develop a new multi-step auxiliary prediction named MSAP.

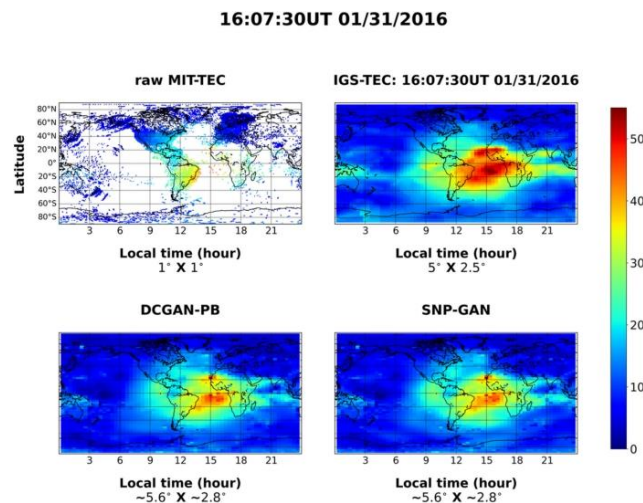


Figure 5. Global TEC maps at 16:07:30 UT on January 31, 2016. TEC peaks above the Atlantic ocean can be seen in all completed maps.

## 5 Monitoring and Modeling of Ionospheric Disturbances for GNSS users

Sudden changes in various space conditions, such as solar flare, geomagnetic storm and severe geological disasters, can cause evident ionospheric disturbances, resulting in plasma irregularities, which can disturb the trans ionospheric radio wave signals. For instance, the ground-based GNSS receivers can observe rapidly fluctuated carrier phase and amplitude signals if the radio wave strikes ionospheric irregularities. Monitoring and modeling ionospheric irregularities precisely is a key mean to correct its adverse impact on GNSS, making it become one of the heated research topics in the fields of both geodesy and space physics. This paper will initially summarize the recent research progress on monitoring and modeling of ionosphere by Chinese researchers, including monitoring network, monitoring methods, models and their applications in enhancing the accuracy of positioning and revealing the coupling relationship with space events.

China has established a three-dimensional monitoring network in recent years to monitor ionospheric disturbances. Since July 31, 2020, China has completed the construction of BeiDou navigation satellite system. Different from other existing navigation systems, BeiDou has Geostationary Orbit (GEO) satellites, which benefits the research of the ionospheric



disturbances (Hu et al. 2021), as the stationary IPPs of GEO satellites are free from the Doppler effect of the relative motion between satellites and receivers. Besides GEO, China has also launched a number low earth orbit (LEO) satellites with Langmuir probes, such as China Seismo-Electromagnetic Satellite (CSES) (Yan et al. 2020), FY3C and FY3D. On the ground, China has established multiple ionospheric monitoring networks, e.g., Crustal Movement Observation Network of China (CMONC) with more than 2000 stations, Meridian Project Phase II with 31 stations, BDSMART Space Atmospheric Monitoring Network with 55 stations led by Aerospace Information Research Institute (AIR), Chinese Academy of Sciences, and Ionospheric Observation Network for Irregularity and Scintillation in East/Southeast Asia (IONOISE) with 74 stations (Sun et al. 2020).

Supported by the development of instruments and networks, significant progress has achieved in the methods of monitoring ionospheric disturbance, especially in the application of GNSS geodetic receivers to ionospheric scintillation monitoring. Currently, GNSS receivers used in ionospheric monitoring can be divided into two types, the ionospheric scintillation monitoring receiver (ISMR) and the geodetic receiver. Two scintillation indices are available from ISMR, i.e. amplitude scintillation index ( $S_4$ ) and phase scintillation index ( $\sigma_\phi$ ). The distribution of ISMR is limited by its expensive price, while the accuracy of its scintillation indices is affected by the cut-off frequency of the Butterworth filter adopted in the detrending process. Although various studies have been carried out, it has not reached an agreement on the common cut-off frequency globally (Song et al. 2022), resulting in phase without amplitude scintillations in the Arctic region. Recently, low-cost and widely distributed GNSS geodetic receivers have been widely used in ionospheric scintillation monitoring, mainly benefitted from the wide application of ROTI (Yang et al. 2020). Besides ROTI, a variety of scintillation indices for geodetic receivers are also proposed, e.g.  $\sigma_{\phi f, \text{wavelet}}$  (Zhao et al. 2021) and  $SI_{\text{det}}$  (Luo et al. 2020), when ISMR is not available. The observations from geodetic receivers with 1s sampling interval is tried to provide nearly identical scintillation monitoring performance as ISMR, shown in Figure 6. For the data with 30s sampling interval, which is more generally available at all GNSS networks, existing scintillation indices still cannot provide accurate scintillation monitoring performance at the epoch level, where further research is needed.

Another important research direction of ionospheric disturbance is to model ionospheric scintillation, which is one of the key methods to eliminate the adverse effects of scintillation on positioning. Two types of approaches are usually adopted to model scintillation, i.e. the analytical model based on physical mechanisms and the data-driven model. The factors controlling the generation, evolution and changes between days are still unclear, limiting the accuracy of analytical model on the short-term variations (Li et al. 2021). With the accumulation of ionospheric monitoring data and the development of deep learning technology, existing research has established a number of data-driven ionospheric scintillation models (Liu et al. 2021). AIR has already provided the ROTI-based ionospheric scintillation model covering China as a free product with a time resolution of 5 minutes.

One application of ionospheric disturbance monitoring and modeling is to eliminate the adverse effects of scintillation on GNSS positioning. The following three approaches are usually adopted to improve the positioning accuracy under scintillation conditions. The first is

to correct cycle slips. Frequent cycle slips caused by scintillation will lead to excessive ambiguity resets, affecting the parameter calculation of both PPP and RTK technology (Zhao et al. 2019). However, determining the optimal threshold for judging cycle slip correctly is still a problem affect the performance of this method. The second method is to adjust the stochastic model adaptively according to the magnitude of scintillation (Luo et al. 2020), while it is difficult to apply in real-time applications due to the dependence on the processing efficiency of scintillation index. The third method is to eliminate the modeling residual error during the ionospheric active period with the model value. Recently, several Chinese companies, e.g. Qianxun and CHC Navigation, have released their product on GNSS positioning under the condition of strong ionospheric activity, which can basically ensure a fixed solution of RTK equipment.

Another application of ionospheric disturbance monitoring and modeling is to understand the coupling relationship between ionospheric disturbances and space events. As solar irradiation is the main energy in driving the ionospheric dynamic convection, significant attention has been paid to the remarkable ionospheric disturbances triggered by the sudden solar event, e.g. the X9.3 solar flare and the following G4 geomagnetic storm in September 2017 (Li et al. 2022, Ren et al. 2022), showing the increase of global daytime currents and the reduction of the eastward electric fields during the daytime from the equator to middle latitudes. The coupling relationships are also studied between the ionospheric disturbance and severe natural disasters, such as Nepal (2015), Ridgecrest (M7.1, 2019), Xinjiang (M6.2, 2016), Kaikoura (M7.8, 2016) and Fukushima (M6.9, 2016) earthquakes (Kong et al. 2018), showing either pre-seismic or co-seismic ionospheric disturbances. The destructive Tonga volcanic eruption attracts significant attention (Li et al. 2023), leading to a significant local ionospheric hole and the equatorial plasma bubbles across the wide Asia-Oceania area. Studies were also focused on the ionospheric disturbances caused by human activities, such as nuclear explosion and rocket launching (Liu et al. 2020), revealing the total electron content perturbation and its propagation speed.

Overall, this paper briefly summarized the outstanding achievements of Chinese researchers in monitoring and modeling ionospheric disturbances. In the past few years, China has established a space-ground based ionospheric disturbance monitoring network, including the BeiDou system, the LEO satellites and the ground GNSS receivers, especially those geodetic receivers benefitted from the development of the ionospheric scintillation indices. Regional ionospheric scintillation models were established and broadcasted as a product based on the long-term observations. The monitoring results and the established models were adopted to improve the positioning accuracy during the period with strong ionospheric activities and study the coupling relationship between ionospheric disturbances and solar-terrestrial events, natural disasters and human activities.

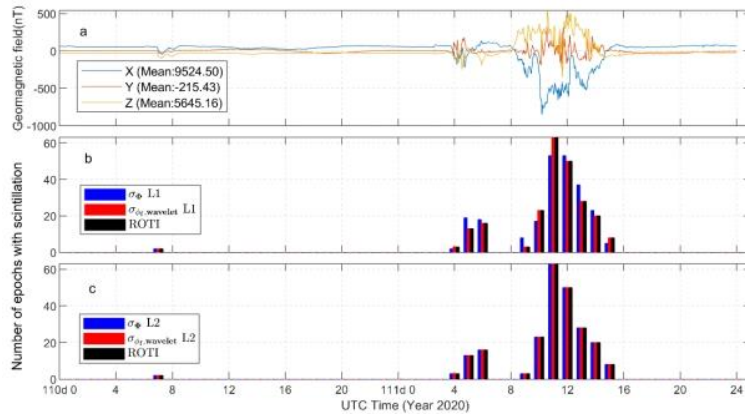


Figure 6. Scintillation monitoring performance with 1s sampling interval data from geodetic GNSS receiver

## 6 Ionospheric related Data Products and Classical Applications

### Ionospheric services for satellite navigation

Dual- or triple-frequency GNSS users can mitigate the ionospheric delay errors by forming the ionospheric-free (IF) linear combinations, but which will cause noise amplification as well as the loss of ionospheric delay information. A priori ionospheric information with high accuracy is required to correct the ionospheric delay in single-frequency PPP and can be used as virtual observations to constrain the parameters (Liu et al., 2023). Aside from terrestrial geodetic GNSS receivers, the mass-market smartphones might also benefit from the ionospheric augmentation service, e.g., BDSBAS ionospheric GIVD, GIMs, regional ionospheric maps (RIMs). Wang et al. (2021) proposed an PPP approach named Smart-PPP to achieve the sub-meter-level positioning accuracy for smart phone, as shown in Figure 8, in which the priori ionospheric information is introduced to eliminate ionospheric effects. Based on the investigations of Yi et al. (2021), smartphone PPP enjoys more beneficial effects from ionospheric constraints (IC) than low-cost and geodetic hardware, with a significant 30% horizontal improvement in the first epoch. Wang et al. (2020) find horizontal positioning accuracies of the smartphones with PPP-IC model are better than 1 m, while those with the SPP and the traditional PPP models are about 2 m. The ambiguity fixing success rate of the uncombined PPP models, which is proceed with high-precise ionospheric delay corrections, is slightly higher than that of the combined model (Wang et al., 2019). In additional, Zhao et al. (2021) also analyzed the reliability of GIM RMS maps for high-precision positioning by comparing the actual error of the differential STEC (dSTEC) with the RMS of the dSTEC derived from the RMS maps.

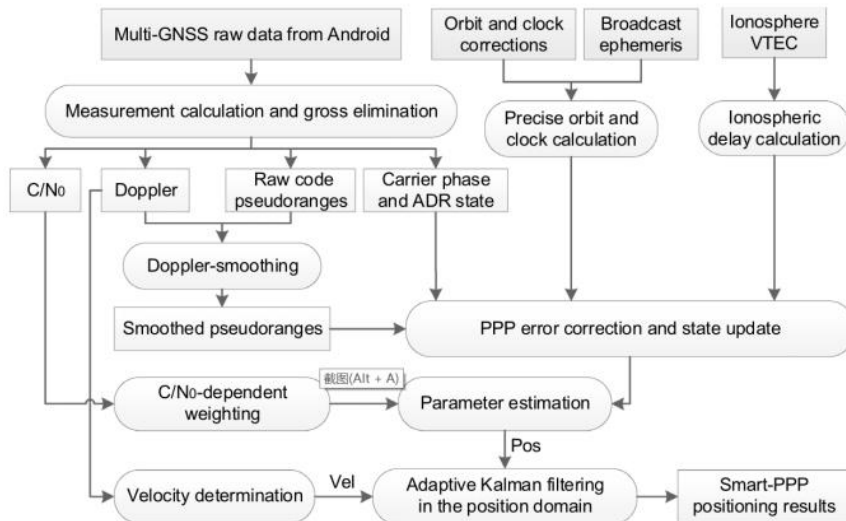


Figure 8. Flow diagram of PPP processing, in which the priori ionospheric information is introduced to eliminate ionospheric effects. After Wang et al. (2021).

## Ionospheric applications for Civil Aviation

In particular, International Civil Aviation Organization (ICAO) has also put forward new requirements for state monitoring of the ionosphere, which is used to promote migration to GNSS-based navigation from conventional (ground-based). The requirements defined by ICAO is that all the requirements (accuracy, integrity, continuity, and availability) with high safety (integrity) must be fulfilled together for operational systems. In the framework of ICAO, the ionospheric products are released for civil aviation, e.g., TEC Real Time Maps, global error of the NRT TEC map derived from errors of the GNSS measurement, TEC rate of the dynamic of the ionosphere, TEC-gradients, TEC-map prediction (1h - 24h), TEC-map Quality, 3D ionosphere reconstruction and model, scintillation measurement, ROTI (Rate of Change of TEC index), AATR (Along-Arc Tec Rate) or similar ionospheric index. In ICAO, the ionospheric TEC gradients research attracts more scholars' attention. Chang et al. (2021) gives the spatial decorrelation result on March 7, 2012, using the time-step method and the Brazilian GNSS network data, for the SLS-4000 GBAS. Jin et al. (2020) used the vertical ionospheric delay differences and residual differences at IPPs to perform the correlation analysis, and applied the annular data deprivation and three quadrants deprivation methods to create the undersampled threats over China region.

## Scientific applications with ionospheric products

The multi-source ionospheric data service also provides convenient conditions for studying the spatiotemporal characteristics of the ionosphere and carrying out corresponding scientific applications, which covers the following topics: ionospheric space weather, ionospheric structures and climatology, ionospheric dynamics and couplings, and planetary ionospheres (Liu et al., 2022b). The ionosphere space weather has significant temporal and spatial changes, which is generally controlled by the Sun's photoionization effect. Solar activity events can significantly affect the spatiotemporal variation of the ionosphere, e.g., solar eclipse, flare-enhanced ionospheric events, solar wind and so on (Zhang et al., 2020a, Jin et al., 2021,

Sun et al., 2021). A solar eclipse transiently shields the solar ionizing radiation falling into the atmosphere of the Earth, in which the rapid solar input reduction results in the ionospheric disturbances (Zhang et al., 2020a), as shown in Figure 9. The geomagnetic storms are mainly due to Coronal Mass Ejection (CME) or High-Speed Solar Winds (HSSWs), with the emission from sporadically rotating coronal holes during active geomagnetic days. These geomagnetic storms propagate significant energy inputs into the Earth's magnetosphere via solar winds, whose energy coupled with the Earth through many physical processes (e.g., field aligned currents, auroral electrojet, magnetospheric convection, etc.) in the auroral zone. The storm time ionospheric responses can easily be measured with the ground and space-based observations, e.g., GNSS, ionosondes, magnetometers and in situ multi-instrumental satellite systems.

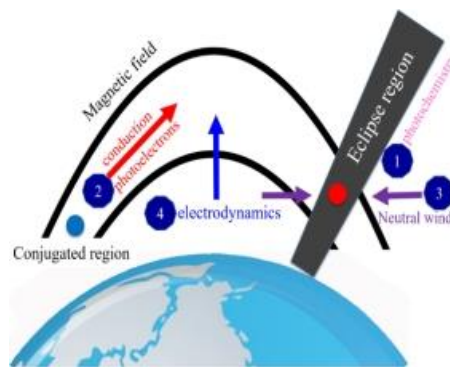


Figure 9. The related physical processes during the eclipse, including the photochemistry, interhemispheric photoelectron transport, thermal conduction, neutral wind, and electrodynamic. After Zhang et al.(2020a).

One application of ionospheric scientific exploration is to study ionospheric dynamics and couplings, including sudden stratosphere warming and lower atmospheric forcing, ionospheric dynamics, lithosphere-ionosphere coupling and solar wind-magnetosphere-polar ionosphere coupling (Huang et al., 2020 , Liu et al., 2022a). Based on the ROCSAT-1 satellite observations during 1999–2004, Zhang et al. (2020b) present the first analysis of the dependence of the afternoon downward plasma drifts on the season, longitude, solar activity, and lunar phase. Li et al. (2020a) investigated the responses of the ionosphere and the neutral winds in the mesospheric and lower thermospheric region to two SSWs, respectively. In the investigations of Li et al. (2022), effective ionospheric perturbations were reported immediately, respectively, two weeks and one week prior to these two earthquakes events, which reconfirms that ionospheric information can be utilized for short-term EQ prediction.

Another application covers ionospheric structures and climatology, which aims at ionospheric spatial structure and temporal variation (Chen et al., 2020 , Li et al., 2020b , Kuai et al., 2021 , Li et al., 2021 , Ma et al., 2021 , Liu et al., 2022a). The former mainly studies the uneven distribution of the ionosphere in the spatial dimension, which is represented by ionospheric climatology in equatorial ionization anomaly (EIA) and mid-latitude trough regions, topside ionosphere, night-time zonal ionospheric and polar region ionospheric. The latter takes the characteristics of the ionospheric morphology in the time dimension as the main research target, e.g., climatology of mid-latitude F2-layer bite-out, electron density enhancements, equatorial sunrise enhancement, ionospheric diurnal double-maxima (DDM) patterns and

ionospheric sensitivity to the solar Extreme Ultraviolet (EUV).

In addition, the mechanism of some ionospheric anomalies is also a hotspot of ionospheric scientific research, for examples, Es Layer, traveling ionospheric disturbances (TID), ionosphere and equatorial plasma bubbles (EPB), polar cap patches (Sun et al., 2020 , Xie et al., 2020 , Xu et al., 2020).

## Bibliography

- An X, Meng X, Jiang W et al (2019) Global ionosphere estimation based on data fusion from multisource: Multi-GNSS, IRI model, and satellite altimetry. *Journal of Geophysical Research: Space Physics*, 124(7), 6012-6028.
- Chang H, Yoon M, Pullen S, et al. 2021. Ionospheric spatial decorrelation assessment for GBAS daytime operations in Brazil[J]. *Navigation*, 68(2): 391-404.
- Chen P, Liu L, Liu H et al (2021). Accuracy evaluation of XUST's global ionospheric products. *Advances in Space Research*, 68(1), 201-213.
- Chen P., Liu H., Schmidt M., Yao Y., Yao W. (2021) Near Real-Time Global Ionospheric Modeling Based on an Adaptive Kalman Filter State Error Covariance Matrix Determination Method, *IEEE Transactions on Geoscience and Remote Sensing*, 60, 1-12, 2022, 5800812.
- Chen Y, Liu L, Le H, et al. 2020. Latitudinal Dependence of Daytime Electron Density Bite-Out in the Ionospheric F2-Layer[J]. *Journal of Geophysical Research: Space Physics*, 126(1).
- Chen, J., H. Fang, and Z. Liu (2021), The Application of a Deep Convolutional Generative Adversarial Network on Completing Global TEC Maps, *Journal of Geophysical Research: Space Physics*, 126.
- Chen, Z., M. Jin, Y. Deng, J. S. Wang, H. Huang, X. Deng, and C. M. Huang (2019), Improvement of a Deep Learning Algorithm for Total Electron Content Maps: Image Completion, *Journal of Geophysical Research: Space Physics*, 124(1), 790-800.
- Chen, Z., W. Liao, H. Li, J. Wang, X. Deng, and S. Hong (2022), Prediction of Global Ionospheric TEC Based on Deep Learning, *Space Weather*, 20(4), e2021SW002854.
- Han Y, Wang L, Chen R et al (2022). Toward real-time construction of global ionosphere map from ground and space-borne observations. *GPS Solutions*, 26(4), 147.
- He J, Yue X, Le, H et al (2020). Evaluation on the quasi-realistic ionospheric prediction using an ensemble Kalman filter data assimilation algorithm. *Space weather*, 18(3), e2019SW002410.
- He J, Yue X, Wang W et al (2019). EnKF ionosphere and thermosphere data assimilation algorithm through a sparse matrix method. *Journal of Geophysical Research: Space Physics*, 124(8), 7356-7365.
- Hu A, Li Z, Carter B et al (2019). Helmert-VCE-aided fast-WTLS approach for global ionospheric VTEC modelling using data from GNSS, satellite altimetry and radio occultation. *Journal of Geodesy*, 93, 877-888.
- Hu L, Lei J, Sun W, et al. (2021) Latitudinal variations of daytime periodic ionospheric disturbances from Beidou GEO TEC observations over China. *Journal of Geophysical Research: Space Physics* 126(3): e2020JA028809.
- Huang F, Lei J, Zhang R, et al. 2020. Prominent Daytime TEC Enhancements Under the Quiescent Condition of January 2017[J]. *Geophysical Research Letters*, 47(14).
- Jin B, Chen S, Li D, et al. 2020. Ionospheric Correlation Analysis and Spatial Threat Model for SBAS in China Region[J]. *Advances in Space Research*, 66(12): 2873-2887.
- Jin Y, Zhao B, Li G, et al. 2021. Inhibition of F3 Layer at Low Latitude Station Sanya During Recovery Phase of Geomagnetic

- Storms[J]. *Journal of Geophysical Research: Space Physics*, 126(12).
- Kong J, Yao Y, Zhou C (2018) Tridimensional reconstruction of the Co-Seismic Ionospheric Disturbance around the time of 2015 Nepal earthquake. *Journal of Geodesy* 92(13):1255–1266.
- Kuai J, Li Q, Zhong J, et al. 2021. The Ionosphere at Middle and Low Latitudes Under Geomagnetic Quiet Time of December 2019[J]. *Journal of Geophysical Research: Space Physics*, 126(6).
- Li G, Ning B, Otsuka Y, et al. (2021) Challenges to Equatorial Plasma Bubble and Ionospheric Scintillation Short-Term Forecasting and Future Aspects in East and Southeast Asia. *Surveys in Geophysics* 42(9):201–238.
- Li J, Chen Y, Liu L, et al. 2021. Occurrence of Ionospheric Equatorial Ionization Anomaly at 840 km Height Observed by the DMSP Satellites at Solar Maximum Dusk[J]. *Space Weather*, 19(5).
- Li M, Wang H, Liu J, et al. 2022. Two Large Earthquakes Registered by the CSES Satellite during Its Earthquake Prediction Practice in China[J]. *Atmosphere*, 13(5).
- Li N, Luan X, Lei J, et al. 2020a. Variations of Mesospheric Neutral Winds and Tides Observed by a Meteor Radar Chain Over China During the 2013 Sudden Stratospheric Warming[J]. *Journal of Geophysical Research: Space Physics*, 125(5).
- Li Q, Huang F, Zhong J, et al. 2020b. Persistence of the Long-Duration Daytime TEC Enhancements at Different Longitudinal Sectors During the August 2018 Geomagnetic Storm[J]. *Journal of Geophysical Research: Space Physics*, 125(11).
- Li R, Lei J, Kusche J, et al. (2023) Large-Scale Disturbances in the Upper Thermosphere Induced by the 2022 Tonga Volcanic Eruption. *Geophysical Research Letters* 50(3):e2022GL102265.
- Li T, Wang L, Fu W et al (2022). Bottomside ionospheric snapshot modeling using the LEO navigation augmentation signal from the Luojia-1A satellite. *GPS Solutions*, 26, 1-13.
- Li W, Li M, Shi C et al (2017). GPS and BeiDou differential code bias estimation using Fengyun-3C satellite onboard GNSS observations. *Remote Sensing*, 9(12), 1239.
- Li W, Zhao D, He C, et al. (2022) Spatial-Temporal Behaviors of Large-Scale Ionospheric Perturbations During Severe Geomagnetic Storms on September 7–8 2017 Using the GNSS, SWARM and TIE-GCM Techniques. *Journal of Geophysical Research: Space Physics* 127(3):e2021JA029830.
- Li X, Zhang W, Zhang K et al (2021). GPS satellite differential code bias estimation with current eleven low earth orbit satellites. *Journal of Geodesy*, 95(7), 76.
- Li Z, Wang N, Hernández-Pajares M, Yuan Y, Krankowski A, Liu A, Zha J, García-Rigo A, Roma-Dollase D, Yang H, Laurichesse D, Blot A (2020). IGS real-time service for global ionospheric total electron content modeling. *J. Geod.* 94 (3).
- Li Z, Wang N, Wang L, Liu A, Yuan H, Zhang K (2019). Regional ionospheric TEC modeling based on a two-layer spherical harmonic approximation for real-time single-frequency PPP. *J. Geod.* 93 (9): 1659–1671.
- Li, W., Zhao, D., He, C., Shen, Y., Hu, A., & Zhang, K. (2021). Application of a multi-layer artificial neural network in a 3-D global electron density model using the long-term observations of COSMIC, Fengyun-3C and Digisonde. *Space Weather*, 19, e2020SW002605.
- Liu A, Li Z, Wang N, et al. 2023. SHAKING: Adjusted spherical harmonics adding KrigING method for near real-time ionospheric modeling with multi-GNSS observations[J]. *Advances in Space Research*, 71(1): 67-79.
- Liu J, Zhang D, Hao Y, et al. 2022a. The time delay between the equatorial ionization anomaly and the equatorial electrojet in the eastern Asian and American sectors[J]. *Advances in Space Research*, 69(1): 187-196.
- Liu L, Lei J, Liu J. 2022b. Ionospheric Investigations Conducted by Chinese Mainland Scientists in 2020–2021[J]. *Chinese Journal of Space Science*, 42(4).
- Liu L, Morton Y J, Wang Y et al (2021). Arctic TEC Mapping Using Integrated LEO-Based GNSS-R and Ground-Based GNSS



- Observations: A Simulation Study. *IEEE Transactions on Geoscience and Remote Sensing*, 60, 1-10.
- Liu L, Morton YJ, Liu Y (2021) Machine learning prediction of storm-time high-latitude ionospheric irregularities from GNSS-derived ROTI maps. *Geophysical Research Letters* 48(20):e2021GL095561.
- Liu Y, Zhou C, Zhang X, et al. (2020) GNSS observations of ionospheric disturbances in response to the underground nuclear explosion in North Korea. *Chinese Journal of Geophysics* 63(4):1308–1317.
- Liu, A., Wang, N., Dettmering, D., Li, Z., Schmidt, M., Wang, L., & Yuan, H. (2023). Using DORIS Data for Validating Real-Time GNSS Ionosphere Maps. *Advances in Space Research*.
- Liu, A., Li, Z., Wang, N., Zhang, Y., Krankowski, A., & Yuan, H. (2022). SHAKING: adjusted Spherical Harmonics Adding KrigING method for near real-time ionospheric modeling with multi-GNSS observations. *Advances in Space Research*.
- Liu, B., Liu, A., Chen, L., Li, Z., Wang, N., Shao, B., & Wang, L. (2023). Smartphone-Based Positioning Augmented by BDSBAS Ionospheric Corrections. *IEEE Geoscience and Remote Sensing Letters*, 20, 1-5.
- Liu, L., Zou, S., Yao, Y., & Wang, Z. (2020). Forecasting global ionospheric TEC using deep learning approach. *Space Weather*, 18, e2020SW002501.
- Luo X, Gu S, Lou Y, et al. (2020) Amplitude scintillation index derived from C/N0 measurements released by common geodetic GNSS receivers operating at 1 Hz. *Journal of Geodesy* 94(2):27.
- Luo X, Gu S, Lou Y, et al. (2020) Better thresholds and weights to improve GNSS PPP under ionospheric scintillation activity at low latitudes. *GPS Solutions* 24(1):17.
- Ma H, Liu L, Chen Y, et al. 2021. Longitudinal Differences in Electron Temperature on Both Sides of Zero Declination Line in the Mid-latitude Topside Ionosphere[J]. *Journal of Geophysical Research: Space Physics*, 126(2).
- Nie, Z., Yang, H., Zhou, P. (2019) Quality assessment of CNES real-time ionospheric products. *GPS Solut* 23, 11.
- Ou M, Chen L, Wang Y et al (2022) Impact analysis of ground-based GNSS and space-based occultation observations on global ionospheric data assimilation. *Chinese journal of radio science*, 2022, 37(4): 619-628.
- Ou M, Chen L, Xu N et al (2021). A near real-time global ionospheric data assimilation and forecast system. In 2021 13th International Symposium on Antennas, Propagation and EM Theory (ISAPE), 1-3.
- Pan, Y., M. Jin, S. Zhang, and Y. Deng (2020), TEC Map Completion Using DCGAN and Poisson Blending, *Space Weather*, 18(5), e2019SW002390.
- Pan, Y., M. Jin, S. Zhang, and Y. Deng (2021), TEC Map Completion Through a Deep Learning Model: SNP-GAN, *Space Weather*, 19(11), e2021SW002810.
- Ren X, Chen J, Li X et al (2020a). Ionospheric total electron content estimation using GNSS carrier phase observations based on zero-difference integer ambiguity: methodology and assessment. *IEEE Transactions on Geoscience and Remote Sensing*, 59(1), 817-830.
- Ren X, Chen J, Zhang X (2021a). High-resolution and high-accuracy global ionosphere maps estimated by GNSS and LEO constellations: simulative and real data experimental results. In EGU General Assembly Conference Abstracts (pp. EGU21-10527).
- Ren X, Chen J, Zhang X et al (2020b). Mapping topside ionospheric vertical electron content from multiple LEO satellites at different orbital altitudes. *Journal of Geodesy*, 94, 1-17.
- Ren X, Liu H, Zhang J et al (2022). An Improved Method for Ionospheric TEC Estimation Using the Spaceborne GNSS-R Observations. *IEEE Transactions on Geoscience and Remote Sensing*, 60, 1-12.
- Ren X, Mei D, Liu H, et al. (2022) Investigation on horizontal and vertical traveling ionospheric disturbances propagation in global-scale using GNSS and Multi-LEO satellites. *Space Weather* 20(5):e2022SW003041.

- Ren X, Mei D, Zhang X et al (2021b). Electron density reconstruction by ionospheric tomography from the combination of GNSS and upcoming LEO constellations. *Journal of Geophysical Research: Space Physics*, 126(10), e2020JA029074.
- Ren X, Zhang X, Schmidt M et al (2020c). Performance of GNSS global ionospheric modeling augmented by LEO constellation. *Earth and Space Science*, 7(1), e2019EA000898.
- Ren, X., Chen, J., Li, X. (2019) Performance evaluation of real-time global ionospheric maps provided by different IGS analysis centers. *GPS Solut* 23, 113.
- Shi S, Wu S, Zhang K et al (2022). An investigation of a new artificial neural network-based TEC model using ground-based GPS and COSMIC-2 measurements over low latitudes. *Advances in Space Research*, 70(8), 2522-2540.
- Shi, S., Zhang, K., Wu, S., Shi, J., Hu, A., Wu, H., & Li, Y. (2022). An Investigation of Ionospheric TEC Prediction Maps Over China Using Bidirectional Long Short-Term Memory Method. *Space Weather*, 20(6), e2022SW003103.
- Song K, Meziane K, Kashcheyev A, et al. (2022) Multifrequency observation of high latitude scintillation: A comparison with the phase screen model. *IEEE Transactions on Geoscience and Remote Sensing* 60:1-9.
- Sui Y, Fu H, Wang K et al (2020). Tomography of Equatorial Ionization Anomaly based on GNSS-InSAR Techniques. In AGU Fall Meeting Abstracts, SA032-08.
- Sun W, Ning B, Hu L, et al. 2020. The Evolution of Complex Es Observed by Multi Instruments Over Low-Latitude China[J]. *Journal of Geophysical Research: Space Physics*, 125(8).
- Sun W, Wu B, Wu Z, et al. (2020) IONISE: An Ionospheric Observational Network for Irregularity and Scintillation in East and Southeast Asia. *Journal of Geophysical Research: Space Physics* 12(8): e2020JA028055.
- Sun Y Y, Chen C H, Qing H, et al. 2021. Nighttime Ionosphere Perturbed by the Annular Solar Eclipse on June 21, 2020[J]. *Journal of Geophysical Research: Space Physics*, 126(9).
- Tang, R., F. Zeng, Z. Chen, J. Wang, C. Huang, and Z. Wu (2020), The Comparison of Predicting Storm-Time Ionospheric TEC by Three Methods: ARIMA, LSTM, and Seq2Seq, *Atmosphere*, 11, 316.
- Wang G, Bo Y, Yu Q, et al. 2020. Ionosphere-Constrained Single-Frequency PPP with an Android Smartphone and Assessment of GNSS Observations[J]. *Sensors (Basel)*, 20(20).
- Wang J, Huang G, Yang Y, et al. 2019. FCB estimation with three different PPP models: equivalence analysis and experiment tests[J]. *Gps Solutions*, 23(4).
- Wang L, Li Z, Wang N, et al. 2021. Real-time GNSS precise point positioning for low-cost smart devices[J]. *Gps Solutions*, 25(2): 69.
- Wang N., Zhang Y., Krankowski A., Li Z., Li A., Kotulak K., Fron A. (2022) The Combined Real-Time Global Ionospheric Map for Operational Ionospheric Space Weather Monitoring, 2022 3rd URSI Atlantic and Asia Pacific Radio Science Meeting (AT-AP-RASC), Gran Canaria, Spain, 2022, 1-3,
- Wang Y, Morton Y J (2021). Ionospheric total electron content and disturbance observations from space-borne coherent GNSS-R measurements. *IEEE Transactions on Geoscience and Remote Sensing*, 60, 1-13.
- Wang Y, Yao Y B, Kong J, et al (2022) Analysis of the 3-D Evolution Characteristics of Ionospheric Anomalies During a Geomagnetic Storm Through Fusion of GNSS and COSMIC-2 Data [J]. *IEEE Transactions on Geoscience and Remote Sensing*, 60: 19.
- Wang Z., Xue K., Wang C., Zhang T., Fan L., Hu Z., Shi C., Jing G. (2020). Near real-time modeling of global ionospheric vertical total electron content using hourly IGS data, *Chinese J. Aeronaut.*
- Wang, N., Li, Z., Yuan, Y., & Huo, X. (2021). BeiDou Global Ionospheric delay correction Model (BDGIM): performance analysis during different levels of solar conditions. *GPS Solutions*, 25(3), 97.
- Wu M, Guo P, Xue J et al (2022). Analysis and Empirical Modeling of Ionospheric Horizontal Gradients in the TEC Mapping

- Onboard LEO Satellites. *IEEE Transactions on Geoscience and Remote Sensing*, 60, 1-14.
- Wu M, Guo P, Zhou W et al (2021). A new mapping function for spaceborne TEC conversion based on the plasmaspheric scale height. *Remote Sensing*, 13(23), 4758.
- Wu, X., Hu, X., Wang, G., Zhong, H., & Tang, C. (2013). Evaluation of COMPASS ionospheric model in GNSS positioning. *Advances In Space Research*, 51(6), 959-968.
- Xia, G., Liu, Y., Wei, T., Wang, Z., Zhou, C., Du, Z., et al. (2021). Ionospheric TEC forecast model based on support vector machine with GPU acceleration in the China region. *Advances in Space Research*, 68(3), 1377–1389.
- Xie H, Yang S, Zhao X, et al. 2020. Unexpected High Occurrence of Daytime F-Region Backscatter Plume Structures Over Low Latitude Sanya and Their Possible Origin[J]. *Geophysical Research Letters*, 47(22).
- Xu T, Hu Y, Deng Z, et al. 2020. Revisit to Sporadic E Layer Response to Presumably Seismogenic Electrostatic Fields at Middle Latitudes by Model Simulation[J]. *Journal of Geophysical Research: Space Physics*, 125(3).
- Yan R, Zhima Z, Xiong C, et al. (2020) Comparison of electron density and temperature from the CSES satellite with other space-borne and ground-based observations. *Journal of Geophysical Research: Space Physics* 125(10): e2019JA027747.
- Yang H., Monte-Moreno E., Hernández-Pajares M., David R.D. (2021) Real-time interpolation of global ionospheric maps by means of sparse representation. *J Geod*, 95, 71.
- Yang Z, Morton YTJ, Zakharenkova I, et al. (2020) Global view of Ionospheric disturbance impacts on kinematic GPS positioning solutions during the 2015 St. Patrick's Day storm. *Journal of Geophysical Research: Space Physics* 125(7): e2019JA027681.
- Yang, D., Q. Li, H. Fang, and Z. Liu (2022), One day ahead prediction of global TEC using Pix2pixhd, *Advances in Space Research*, 70(2).
- Yi D, Bisnath S, Naciri N, et al. 2021. Effects of ionospheric constraints in Precise Point Positioning processing of geodetic, low-cost and smartphone GNSS measurements[J]. *Measurement*, 183.
- Yuan L, Hoque M, Jin S (2021). A new method to estimate GPS satellite and receiver differential code biases using a network of LEO satellites. *GPS Solutions*, 25, 1-12.
- Yuan L, Jin S, Hoque M (2020). Estimation of LEO-GPS receiver differential code bias based on inequality constrained least square and multi-layer mapping function. *GPS Solutions*, 24(2), 57.
- Yuan, Y., Wang, N., Li, Z., & Huo, X. (2019). The BeiDou global broadcast ionospheric delay correction model (BDGIM) and its preliminary performance evaluation results. *Navigation*, 66(1), 55-69.
- Zhang R, Le H, Li W, et al. 2020a. Multiple Technique Observations of the Ionospheric Responses to the 21 June 2020 Solar Eclipse[J]. *Journal of Geophysical Research: Space Physics*, 125(12).
- Zhang R, Liu L, Yu Y, et al. 2020b. Westward Electric Fields in the Afternoon Equatorial Ionosphere During Geomagnetically Quiet Times[J]. *Journal of Geophysical Research: Space Physics*, 125(12).
- Zhang S, Huang L, Yin F et al (2020). Feasibility of the Data Fusion Between Space-Borne and Ground-Based TEC Products. *Geomatics and Information Science of Wuhan University*, 45(4), 557-564.
- Zhang, Q. and Zhao, Q. (2018) Global ionosphere mapping and differential code bias estimation during low and high solar activity periods with GIMAS software, *Remote Sens.-Basel*, 10, 705.
- Zhao D, Li W, Li C, et al. (2021) Extracting an ionospheric phase scintillation index based on 1 Hz GNSS observations and its verification in the Arctic region. *Acta Geodaetica et Cartographica Sinica* 50(3):368-383.
- Zhao D, Roberts GW, Hancock CM et al. (2019) A triple-frequency cycle slip detection and correction method applied on GPS and BDS. *GPS Solutions* 23(1):22.

- Zhao J, Hernández-Pajares M, Li Z, et al. 2021. Integrity investigation of global ionospheric TEC maps for high-precision positioning[J]. *Journal of Geodesy*, 95(3): 35.
- Zhong J, Lei J, Yue X (2020). Comment on Choi et al. Correlation between Ionospheric TEC and the DCB Stability of GNSS Receivers from 2014 to 2016. *Remote Sens.* 2019, 11, 2657. *Remote Sensing*, 12(21), 3496.
- Zhou K, Cai H, Song F et al (2020). Computerized ionospheric tomography study of three-dimensional electron density distribution in the top ionosphere based on Swarm satellites GPS/TEC observations. *Chinese Journal of Geophysics*, 63(9), 3219-3230.

# 2020 Qomolangma Height Survey

Yamin Dang<sup>1</sup>, Tao Jiang<sup>1</sup>, Chunxi Guo<sup>2</sup>, Bin Chen<sup>3</sup>, Chuanyin Zhang<sup>1</sup>, Qiang Yang<sup>1</sup>, Zhengtao Wang<sup>4</sup>

<sup>1</sup> Chinese Academy of Surveying and Mapping, Beijing, China

<sup>2</sup> Geodetic Data Processing Centre of Ministry of Natural Resources, Xi'an, China

<sup>3</sup> China Aero Geophysical Survey and Remote Sensing Center for Natural Resources, Beijing, China

<sup>4</sup> School of Geodesy and Geomatics, Wuhan University, Wuhan, China

Mount Qomolangma (MQ, known as Mount Everest in western countries) is located on the border between China and Nepal. It is not only the main peak of the Himalayas, but also the highest peak in the world, its height has attracted worldwide attention for a long time. In 2019, China and Nepal decided to jointly announce the new height of MQ. From 2019 to 2020, the height survey campaign of MQ was carried out and its latest height was precisely determined.

In previous campaigns of Qomolangma Height Survey (QHS) implemented by China in 1975 and 2005, the heights of MQ were referred to the mean sea level of Yellow Sea (Zhu 1976; Chen et al. 2001, 2006). The primary goal of 2020 QHS is to determine and announce the height of MQ through the cooperation between China and Nepal. However, the obstacle for determining the unique height of MQ is the inconsistency in height datum between the two countries, the 1985 National Height Datum of China is the mean sea level of the Yellow Sea and that of Nepal is the mean sea level of the Bay of Bengal in the Indian Ocean. Consequently, the key for 2020 QHS is to establish a high precision geoid model that realizing the common height datum recognized by both countries. We decided to establish a gravimetric geoid model in the area of MQ based on the IHRS, and use it as the datum of the height of MQ. However, high altitude and complex terrain in this region pose a great challenge for geoid modeling. Most places in this region are inaccessible for terrestrial gravity survey, yielding lots of gravity data gaps in areas with strong variations in topography and gravity field. The lack of gravity observations significantly limits the accuracy of geoid model, as well as the precision of the height of MQ. In the campaign of 2020 QHS, the science team carried out an airborne gravity survey over the area of MQ, performed terrestrial gravity measurements and BeiDou Navigation Satellite System (BDS) measurements at its peak, and combined a variety of geodetic technologies to precisely determine the new height of MQ.

## 1 Data collection of 2020 Qomolangma Height Survey

### Gravity data

#### 1 Airborne gravity data

During April-June 2020, 13 sorties of airborne gravity survey were implemented using the GT-2A airborne gravimeter. A King Air 350ER aircraft equipped with dual frequency GPS receivers is used to carry this gravimeter. The aircraft flew at a speed of 441.7 km/h relative to the ground and at the average altitude of 10 249 m (ellipsoidal height). Three ground GNSS stations were set up for the differential kinematic positioning of the aircraft coordinate. A total

of 5635.2 km flight trajectory was completed over the area of 12 700 km<sup>2</sup>, yielding 83 803 points of airborne gravity data with a sampling interval of 0.5 s. The airborne gravity data block is formed by 39 data lines in east-west direction and 9 inspection lines in north-south direction, resulting in 264 crossover points. The average spacing between data lines is 5 km, and is reduced to 2.5 km over the central area of MQ. An along track, time domain 100 s Kalman filtering was applied to smooth out the high frequency noises. The Root Mean Squares (RMS) of crossover differences is 1.1 mGal. The spatial distribution of airborne gravity survey lines are plotted in Figure (green lines).

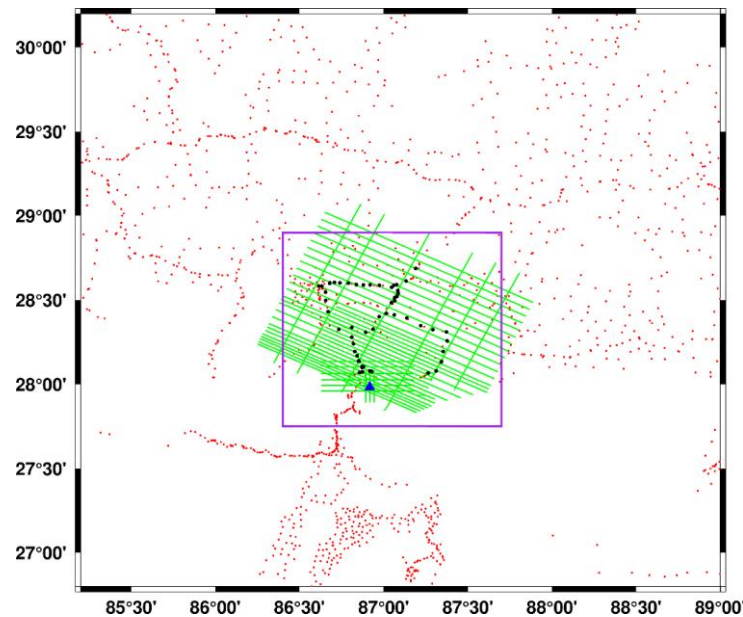


Figure 1. Distribution of airborne (green lines) and terrestrial (red points) gravity data, GNSS leveling data (black points), location of MQ (blue triangle), and the boundary of quasigeoid computation area (purple rectangle)

## 2 Terrestrial gravity data

Using the Z400 portable relative gravimeter specifically designed and developed for the 2020 campaign, the terrestrial gravity data at the peak of MQ was successfully collected for the first time. The Z400 relative gravimeter is designed and produced by Beijing Aodi Detection Instruments Co., Ltd, it only weights 4.5 kg, which makes it convenient to carry during mountaineering. Note that during the campaign of 2005 QHS, the highest altitude at which terrestrial gravity was observed is 7790 m above sea level (Guo et al. 2008).

Terrestrial gravity data at 210 points were newly collected in the 2020 campaign, which consist of 2 absolute gravity points, 6 control points and 202 data points. 2 points of absolute gravity values were determined using the FG5 absolute gravimeter with a precision better than 0.3  $\mu$ Gal, and gravity values at other points were acquired using round-trip relative gravity measurements by CG-6 gravimeters. Based on the relative gravity network adjustment, the standard error of gravity values at 6 control points and 202 data points is 5.2  $\mu$ Gal and 39.5  $\mu$ Gal, respectively. At all the gravity points, GNSS observations of 20~60 min are carried out to obtain the geodetic coordinates, and the average precision of the measured ellipsoidal heights is 5.7 cm.

## GNSS data

At 11:00 am on May 27, 2020, the Chinese survey mountaineering team successfully climbed to the peak of MQ. The surveyors located the highest point of snow surface by visual inspection and set up the survey target at this point. A GNSS antenna and 6 reflection prisms were installed on the top of the survey target. The surveyors carried out GNSS measurements at the peak using CHCNAV P5 receiver and Trimble ALLOY receiver. Both GNSS receivers were connected to the common antenna on the top of the survey target, which enables simultaneous GNSS data collection. The duration of valid observations for CHCNAV P5 receiver is 40 min 53 s and that for Trimble ALLOY receiver is 41 min 39 s. Both GPS and BDS data were collected with a sampling interval of 0.05 s. In the meantime, GPS and BDS measurements were conducted at 6 ground GNSS stations for more than 8 h. The spatial distribution of the peak GNSS network consisting of the peak point and the 6 ground stations are plotted in Figure 17.

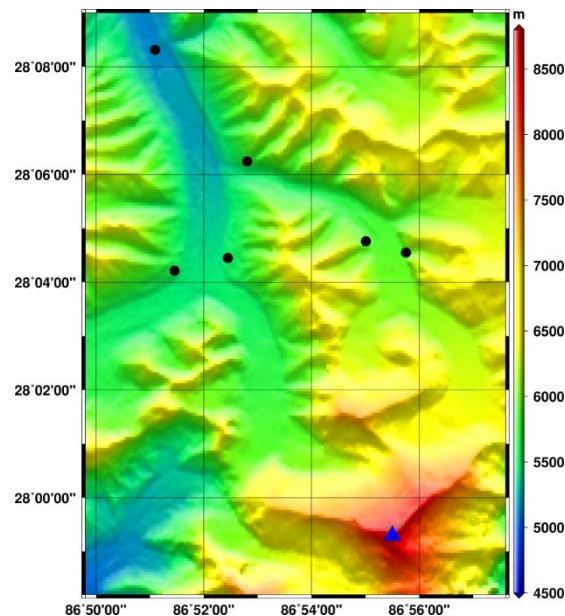


Figure 17. Distribution of the peak GNSS network. (Blue triangle: MQ; Black points: ground GNSS stations)

## Geodetic leveling and trigonometric height measurements

From November 2019 to June 2020, the geodetic leveling campaign along leveling routes of 800.2 km were carried out to transfer the 1985 National Height Datum of China to the 6 ground stations (Base Camp, Zhong Rong, III7, Xi Rong, Dong Rong 2 and Dong Rong 3) at the foot of MQ. The 6 ground stations are to be used for measuring the height of the peak by means of trigonometric leveling. The leveling network consists of 520 km first order leveling route, 253.1 km second order route, 8.6 km third order route and 18.5 km trigonometric leveling traverse, yielding 238 leveling points. The above-mentioned 61 GNSS stations are co-located with geodetic leveling measurements, see Figure 2 (black points) for the spatial distribution of these stations.

In addition, the intersection and trigonometric height measurements were carried out by observing the reflection prisms of the survey target erected at the peak from the 6 ground stations. The purpose of the intersection and trigonometric height measurements is to provide independent validation dataset for the GNSS derived geodetic coordinates of the peak of MQ.



## 2 Gravimetric quasigeoid modeling in the area of Mount Qomolangma

83803 points of airborne gravity disturbances, 3570 points of terrestrial gravity anomalies and the 3"×3" Shuttle Radar Topography Mission (SRTM) elevation data (Farr et al. 2007) are used for the determination of gravimetric quasigeoid models. The quasigeoid model is computed on a 1'×1' grid in the area bounded by  $27.75^\circ \leq \varphi \leq 28.9^\circ$  and  $86.4^\circ \leq \lambda \leq 87.7^\circ$  (Figure 1, purple rectangle).

Three computation schemes are used for gravimetric quasigeoid modeling. The scheme 1 computes the quasigeoid model using EIGEN-6C4 model and terrestrial gravity data, no airborne gravity data are used. The scheme 2 computes the quasigeoid model using EIGEN-6C4 model, terrestrial and airborne gravity data. The scheme 3 is based on the spectral combination approach, which combines airborne gravity disturbances and terrestrial gravity anomalies to compute the quasigeoid in one step, the explicit downward continuation of airborne gravity data is not needed (Sjöberg 1981; Wenzel 1982; Jiang and Wang 2016; Jiang 2018).

We validate the gravimetric quasigeoid models using the GNSS leveling derived height anomalies at the 61 benchmarks. Table 1 presents the statistics of the differences between the quasigeoid models based on three computation schemes and the GNSS leveling measured height anomalies.

Table 1. Statistics of the differences between gravimetric quasigeoid models and GNSS leveling measured height anomalies at 61 benchmarks (m)

Computation scheme	Min	Max	Mean	Std
Scheme 1 (EIGEN-6C4 + Terrestrial)	-0.129	0.270	0.169	0.078
Scheme 2 (EIGEN-6C4 +Terrestrial+ Airborne)	0.166	0.371	0.314	0.048
Scheme 3 (EIGEN-6C4 + Terrestrial + Airborne)	0.148	0.333	0.270	0.038

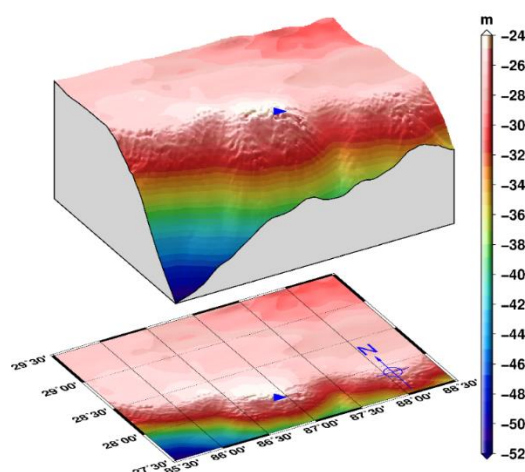


Figure 18. Gravimetric quasigeoid model based on the scheme 3. (Blue triangle: MQ)

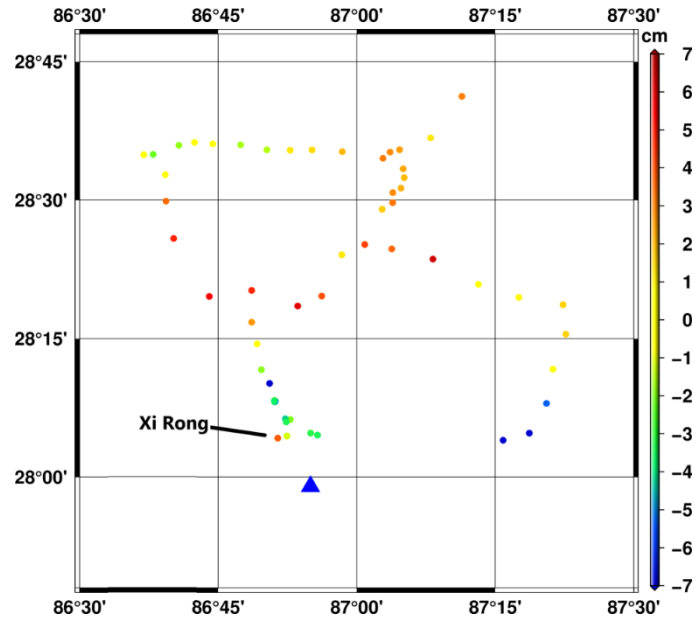


Figure 19. Differences between gravimetric quasigeoid model based on the scheme 3 and GNSS leveling derived height anomalies at 61 benchmarks. (blue triangle: MQ)

### 3 Determination of the IHR based orthometric height of the peak of Mount

#### Qomolangma

The orthometric height  $H$  of the peak of MQ can be written as follows:

$$H(\varphi, \lambda) = h(\varphi, \lambda) - N(\varphi, \lambda) \quad (1)$$

where  $(\varphi, \lambda, h)$  are the geodetic latitude, longitude and height of the peak point, which are precisely determined from GNSS measurements at the peak.  $N$  is the geoid undulation of the peak point, which is derived from the gravimetric quasigeoid model.

#### Determination of the geodetic coordinates of the peak of Mount Qomolangma

The software packages of GAMIT/GLOBK developed by Massachusetts Institute of Technology and GPAS (GNSS Processing and Analysis Software) developed by the Chinese Academy of Surveying and Mapping are used to process the BDS and GPS data of the peak GNSS network. Firstly, 14 GNSS reference stations from IGS (International GNSS Service), iGMAS (International GNSS Monitoring & Assessment System), MGEX (Multi-GNSS Experiment) and China BDS reference station network are selected as control stations for the baseline processing of the peak GNSS network, the relaxation constraints are applied to the station coordinates and satellite orbits, yielding the baseline results based on BDS and GPS observations, respectively. Secondly, 116 globally distributed IGS stations are selected as constraints for the adjustment of network consisting of the BDS and GPS derived baselines, the geodetic coordinates of the peak point in the ITRF2014 (International Terrestrial Reference System 2014) based on BDS, GPS and the combination of both systems are obtained, respectively. Table 2 lists the precisions of geodetic coordinates of the peak point derived from BDS, GPS and the combination of two systems. The standard error of the final geodetic coordinates of the peak point based on the combination of BDS and GPS observations is  $\pm 13.2$  mm in the horizontal direction (north and east) and  $\pm 9.4$  mm in

the vertical direction.

Table 2. Precisions of geodetic coordinates of the peak point (mm)

GNSS data	Horizontal direction		Vertical direction
	North	East	
BDS	8.6	20.3	13.2
GPS	6.5	14.7	13.3
BDS + GPS	5.2	12.1	9.4

The intersection and trigonometric height measurements also provide the geodetic coordinates of the peak point, which is an independent validation for the GNSS derived solution. By taking the weighted average of geodetic height values  $h_i (1 \leq i \leq 6)$  of the peak point measured from the 6 ground stations, the geodetic height  $h$  for the peak point with a standard error of  $\pm 4.2$  cm is finally obtained. Comparing the GNSS derived solution and the intersection derived solution, it is shown that the differences between the geodetic coordinates based on the two independent techniques are 4.2 cm for horizontal component, and 2.6 cm for geodetic height.

### Determination of geoid undulation of the peak of Mount Qomolangma

The geoid undulation of the peak of MQ is computed by

$$N = \zeta + \Delta + N_0 \quad (2)$$

where  $N$  is the geoid undulation of the peak,  $\zeta$  is the height anomaly of the peak interpolated from the local gravimetric quasigeoid model,  $\Delta$  is the geoid to quasigeoid separation,  $N_0$  is the zero-degree term of geoid undulation.

The interpolation of the height anomaly from quasigeoid model is tricky because of large topographic height differences in the area of MQ, the influence of height differences needs to be corrected. Considering the rugged terrain and strong variations in gravity field in this region, we use the rigorous model to compute the geoid to quasigeoid separation term  $\Delta$  (Flury and Rummel 2009, 2011).  $\Delta$  is determined to be -1.302 m using the observed gravity value at the peak and 3"×3" SRTM data in this area. The computation of the zero-degree term of geoid undulation  $N_0$  in Equation (2) involves the definition and selection of the specific height datum. Based on the IHRS and the GRS80 reference ellipsoid (Moritz 2000),  $N_0$  for the peak point is determined to be -0.177 m.

As a result, the final orthometric height on the snow surface of the peak of MQ in the IHRS is determined to be 8848.86 m with a precision of  $\pm 0.06$  m, while the precision is estimated from the errors in the geoid undulation and the geodetic height of the peak.

## Bibliography

- Dang, Y., Jiang, T., Guo, C., Chen, B., Zhang, C., Yang, Q., Wang, Z. (2023). Determining the new height of Mount Qomolangma based on the International Height Reference System. *Geo-spatial Information Science*, DOI: 10.1080/10095020.2022.2128901 (SCI).
- Dang, Y., Guo, C., Jiang, T., Zhang, Q., Chen, B., Jiang, G. (2020). Height measurement and determination of Mount Qomolangma. *Acta Geodaetica et Cartographica Sinica*, 50(4): 556-561.
- Flury, J., and R. Rummel. 2009. "On the geoid–quasigeoid separation in mountain areas." *Journal of Geodesy* 83: 829-847

- Flury, J., and R. Rummel. "On the computation of the geoid–quasigeoid separation." *Journal of Geodesy* 85: 185–186. doi:10.1007/s00190-011-0447-1.
- Förste, C., S. Bruinsma, O. Abrikosov, J. M. Lemoine, J. C. Marty, F. Flechtner, G. Balmino, F. Barthelmes, and R. Biancale. 2014. "EIGEN-6C4 The latest combined global gravity field model including GOCE data up to degree and order 2190 of GFZ Potsdam and GRGS Toulouse." GFZ Data Services, Potsdam, Germany. doi: 10.5880/icgem.2015.1.
- Hofmann, W. B., and H. Moritz. 2005. *Physical geodesy*. Wien New York: Springer.
- Ihde, J., L. Sánchez, R. Barzaghi, H. Drewes, C. Förste, T. Gruber, G. Liebsch, U. Marti, R. Pail, and M. Sideris. 2017. "Definition and proposed realization of the International Height Reference System (IHR)." *Surveys in Geophysics* 38 (3): 549-570.
- International Association of Geodesy. 2015. "IAG Resolutions Adopted by the IAG Council at the XXVIth IUGG General Assembly." Prague, Czech Republic. <https://iag.dgfi.tum.de/en/iag-and-iugg-resolutions/>.
- International Association of Geodesy. 2019. "IAG Resolutions Adopted by the IAG Council at the XXVIIIth IUGG General Assembly." Montreal, Canada. <https://office.iag-aig.org/iag-and-iugg-resolutions>.
- Jiang, T., and Y. M. Wang. 2016. "On the spectral combination of satellite gravity model, terrestrial and airborne gravity data for local gravimetric geoid computation." *Journal of Geodesy* 90 (12): 1405-1418
- Jiang, T. 2018. "On the contribution of airborne gravity data to gravimetric quasigeoid modelling: a case study over Mu Us area, China." *Geophysical Journal International* 215 (2): 1308.
- Jiang, T., Dang, Y., Guo, C., Chen, B., Zhang, C. (2022). Realization of the international height reference system in the region of Mount Qomolangma. *Acta Geodaetica et Cartographica Sinica*, 51(8): 1757-1767.
- Moritz, H. 2000. "Geodetic Reference System 1980." *Journal of Geodesy* 74: 128-133.
- Sánchez, L., J. Ågren, J. Huang, Y. Wang, J. Mäkinen, R. Pail, R. Barzaghi, G. S. Vergos, K. Ahlgren, and Q. Liu. 2021. "Strategy for the realisation of the International Height Reference System (IHR)." *Journal of Geodesy* 95. doi: 10.1007/s00190-021-01481-0.
- Sjöberg, L. 1981. "Least squares combination of satellite and terrestrial data in physical geodesy." *Annales Geophysicae* 37 (1): 25-30.
- Sánchez, L., and M. G. Sideris. 2017. "Vertical datum unification for the International Height Reference System (IHR)." *Geophysical Journal International* 209 (2): 570-586.
- Wenzel, H. G. 1982. "Geoid computation by least-squares spectral combination using intergral kernels." *The General IAG Meeting, Tokyo*, 438-453.

# Recent Advance in Geodetic Data Processing

Jianjun Zhu<sup>1</sup>, Leyang Wang<sup>2</sup>, Jun Hu<sup>1</sup>, Bofeng Li<sup>3</sup>, Haiqiang Fu<sup>1</sup>, Yibin Yao<sup>4</sup>

<sup>1</sup> School of Geosciences and Info-physics, Central South University, Changsha, China

<sup>2</sup> School of Geomatics, East China University of Technology, Nanchang, China

<sup>3</sup> College of Surveying and Geo-informatics, Tongji University, Shanghai, China

<sup>4</sup> School of Geodesy and Geomatics, Wuhan University, Wuhan, China

## 1 Data processing method

The classical hypothesis testing and reliability theory is only based on single alternative hypothesis, which is inconsistent with the practices. Yang et al. (2013) first extend the original outlier separability theory based on two alternative hypotheses to the general case where there are multiple alternative hypotheses, and then propose the new internal reliability index-minimal separability bias (MSB) that can control both the probability of missed detection and of wrong exclusion (Yang et al. 2017). Recently, Yang et al. (2021) further formulate the complete quality control indices and their algebraic estimation method for the unifying DIA estimators, by taking the uncertainty of the combined estimation-testing procedure into account and performing the propagation of uncertainty. Li et al. (2021) extent the hypothesis testing theory to ill-posed models, in which the overall-test statistics,  $w$ -test statistics and minimal detectable bias are all reformulated. Then, the bias-corrected  $w$ -test and overall-test statistics are both developed, so as to be approximated by a standard normal distribution and two non-central chi-square distributions, respectively.

In addition to the outlier, there is another important source of abnormal error, i.e., unmodeled error. Due to the spatiotemporal complexity of, and limited knowledge on systematic errors such as in GNSS signals, some residual observation errors cannot be eliminated or easily mitigated by differencing and combination of observations, model correction, and parameterization (Li et al. 2018; Zhang et al. 2019). Li et al. (2018) first propose a procedure to examine the significance of unmodeled errors based on a combined use of hypothesis tests. Zhang et al. (2019) propose a real-time site-specific unmodeled error detection method by using dual-frequency C/N<sub>0</sub>. Based on this, the stochastic model compensation approaches like composite model (Zhang et al. 2022) and functional model compensation approaches like multi-epoch partial parameterization (Zhang and Li 2020) are proposed. The results show that the theory and method for processing the unmodeled errors can further improve the precision and reliability of GNSS positioning and navigation.

For robust estimation problems, Yang et al. (2019) first prove that the traditional median variance estimate is biased when the sample number is small and then propose an unbiased median variance estimate to calibrate for the bias of the variance estimate. Using the unbiased median variance estimate, the M-estimator with IGGIII reduction factor is constructed to mitigate for the biases caused by the variance estimate. Liu et al. (2019) first deduce the weighted least-squares solution of partial errors-in-variables (PEIV) model, and a new RWTLS algorithm of correlated observation is proposed to solve the initial values of robust iterations by using the median parameter method. Then the median parameter method is used to determine

the initial value, and on this basis we propose a new robust estimated method, which is based on the standardized residual error and considered the influence of gross error both on observation and structure spaces. Yang and Shen (2020) develop a robust M estimation approach applied for three-dimensional (3D) correlated vector observations. A modified IGGIII bifactor reduction model is constructed, where the weight shrinking factor of the 3D vector observation is determined by a new test statistic that coincides with the estimated direction of the outlier vector. With the proposed bifactor reduction model, the outlying vector observation is down-weighted directly along a specific direction, rather than separately at the three components. Lü et al. (2020) proposes a new robust total least trimmed squares (TLTS) estimator without exhaustive evaluation for the EIV model, but the cofactor matrix of the independent variables needs to have a certain block structure. Tao et al. (2021) introduced the robust estimation into the total least-squares algorithm, developing a new robust weighted total least-squares algorithm, to eliminate the effect of outliers.

For variance component estimation (VCE) problems, Lü et al. (2019) introduced the variable projection principle and derived alternative formulae for the structured EIV model by applying Lagrange multipliers. Then, they applied least-squares variance component estimation (LS-VCE) is applied to estimate different (co)variance components in a structured EIV model. Liu et al. (2019) develop a VCE method termed the least-square variance-covariance component estimation method based on the equivalent conditional misclosure (LSV-ECM). Shi et al. (2020) proved that the maximum likelihood method cannot be used to estimate variance components for some stochastic models of routine measurement systems under some conditions, because the likelihood function is unbounded for such stochastic models. To further improve the quality of estimated values based on variance component estimation of the partial errors-in-variables (EIV) model, Wang et al. (2020) introduced the jackknife resampling method to perform bias calculation and bias correction. Wang et al. (2021) proposed a total solution based on EIV model, taking into account the observation errors of all variables. The variance covariance component estimation method is introduced into the solution of regression prediction model to correct the prior cofactor matrix of the random model and the non-common points to be predicted. To solve the problem of variance component estimation problem with large-scale observations, Nie et al. (2022) proposed an efficient VCE algorithm with rigorous trace calculation based on the local–global parameters partition scheme in satellite geodesy, which is directly applicable to both the simplified yet common case where local parameters are unique to a single observation group and the generalized case where local parameters are shared by different groups of observations.

For accuracy analysis of nonlinear function problems, Wang and his research group systematically researched the theories and methods of nonlinear adjustment precision estimation based on Sigma point. From the perspective of probability distribution of approximate function, Wang and his research group proposed the unscented transformation method based on deterministic Sigma point (Wang et al., 2020), the Sterling interpolation method based on deterministic Sigma point (Wang et al., 2019, 2021, 2022), the adaptive Monte Carlo method based on random Sigma point (Wang et al., 2019, 2021), Jackknife method based on resampled Sigma point (Wang et al., 2021), and Bootstrap method based on resampled Sigma point (Wang et al., 2021). These new theories and method of nonlinear adjustment precision estimation are constructed to solve the problem that the traditional approximate function

expression method relies on complex derivative operations. These theories and methods have been applied and proved in seismic fault parameter inversion, volcano Mogi model parameter inversion, volcano CDM model parameter inversion, GNSS baseline vector solution, digital elevation model, coordinate conversion, forward intersection, Gauss projection coordinate forward calculation, satellite clock error prediction, spatial straight line fitting, ellipse fitting and other measurement data processing fields. These researches are of great significance in both theory and application, which further improves and develops the geodetic data processing theory. In addition to this, Qu et al. (2019) proposes an adaptive relaxation algorithm based on the regularization method for stabilizing the nonlinear parameter estimation. Han et al. (2021) proposed a new first-order approximate (NFOA) precision estimation method to evaluate the posterior precision of weighted total least-squares estimates in an errors-in-variables model. A separable nonlinear least squares algorithm based on Moore-Penrose generalized inverse and solid matrix is proposed to solve the special structure of linear combination of nonlinear functions in the field of surveying and mapping.

For ill-posed problems, Song (2019) proposed a new iterative algorithm for rank-deficient adjustment models with inequality constraints, and proved its convergence. Wang et al. (2019) proposed the virtual observation method for solving the ill-posed problem of the PEIV model and the precision estimation method based on a second-order derivative approximate function method. Based on the mean square error (MSE) criterion, the regularization method reduces the parameter estimation variances of ill-posed models through introducing biases. When the uncertainty adjustment model is ill-posed, it is more seriously affected by the error of the coefficient matrix and the observation, Lu et al. (2019) applies ridge estimation method to ill-posed uncertainty adjustment model, derives an iterative algorithm to improve the stability and reliability of the result. To reduce the biases, Lin et al. (2020) proposed a bias reduction method. Based on this method, they proposed a bias-reduced regularization method to improve the MSE of regularized model parameter estimations. Truncated Singular Value Decomposition (TSVD) is an effective method commonly used in solving ill-posed geodetic problems. Lin et al. (2022) truncates small singular values in turn based on TSVD to acquire the changes of the variance and parameter estimation and analyzes the changes to determine the effects of the biases, which can avoid the calculation biases in the use of the true value of the parameters. Thereby, based on the theory of the minimum mean square error, the truncation parameter can be determined. In order to make the adjustment results unique and stable. Zhao et al. (2022) built a function model to solve inequality constraints, and based on the linear complementarity theory, proposed to use the potential function descent interior point algorithm to solve the rank deficient problem. Song et al. (2022) proposed a new ridge estimation method for solving rank-deficient least squares problems, in which a rank-deficient matrix is regarded as an almost rank-deficient. they gave an algebraic derivation that the optimal solution can in fact be obtained by solving a related regularized problem on the optimal worst-case residual. Then, they gave a new iterative algorithm to solve ridge parameter and prove its convergence.

For the total least squares problems, Wang et al. (2019) deduced the formulae of parameter solution for the MEIV model based on the principle of maximum likelihood estimation, and proposed two iterative algorithms. Zeng et al. (2019) proposed an ICTLS solution based on direct observation with constraints, which can restrict both independent and dependent variables. Making using of statistical properties of observations errors and coefficient matrix



error, Zhao et al. (2019) deduces a new computational formula of WTLS estimation for PEIV model based on Fisher Score algorithm. Meng et al. (2020) investigated the condition number of the minimum Frobenius norm solution of the multidimensional TLS problem, and provided a tight and computable upper bound estimation method. Sun et al. (2020) proposed the Frozen-Barycentre iteration method, which applies Samaski to the barycenter iteration method, realizes the conversion of internal iteration and external iteration, saves operation time by reducing derivative calculation, and improves the convergence efficiency of the barycenter iteration method. Based on the structural characteristics of the EIV model, Wang et al. (2020) divided the design matrix into a constant matrix and a random matrix, then rewrote the EIV model as a general structured model and reformulated it as an efficient WTLS algorithm, which only attaches a weight matrix to the random matrix to reduce the size of the matrices involved in the iterative process. Zeng et al. (2021) incorporated the second-order term into the constant term of the model based on the EIV model, thus representing the nonlinear general EIV model as a linear Gauss Helmert model, and deduced the linearized total least squares algorithm and approximate precision estimation formula of the general EIV model. Hu et al. (2021) put orthogonal geometric information as constraint conditions into weighted total least squares, and proposed a nonlinear equality constrained total least squares adjustment method with unknown corrected errors for constraint function. Based on the EIV model, Lü et al. (2021) construct an affine function by using the augmented matrix composed of coefficient matrix and observation vector, reconstruct the function model by using the variable projection method, and deduce a minimum double estimation algorithm for the structure population by using the Lagrangian method. Shi et al. (2021) proposed the uncertain total least squares estimation of linear regression model based on the least squares estimation and uncertainty theory. Based on the equality constrained nonlinear Gauss-Helmert (GH) model, Wang et al. (2020) used the Euler Lagrangian method to obtain the least squares solution of the nonlinear GH model with equality constraints, and then expressed it as the standard constrained least squares problem, introducing a unique sensitivity analysis method. Under the total least squares criterion, Xie et al. (2021) transformed the calculation of inequality constrained total least squares solution into a quadratic programming problem according to the Kuhn-Tucker condition of the optimal solution, and proposed an improved Jacobian iterative method to solve the quadratic programming problem. Xie et al. (2022) proposed the optimality conditions for inequality constrained weighted total least squares (ICWTLS) solution in inequality constrained PEIV model. Then they modified the existing linear approximation (LA) approach to make it suitable for cross-correlated data. The sequential quadratic programming (SQP) method is proposed based on the optimality conditions. Since the Hessian matrix is difficult to compute in the SQP algorithm and it converges slowly or even not converges when the Hessian matrix is indefinite positive, the damped quasi-Newton (DQN) SQP method is proposed. Considering coordinate errors of both control points and non-control points, and different weights between control points and non-control points, Zeng et al. (2022) proposed an extended weighted total least squares (WTLS) iterative algorithm of 3D similarity transformation based on Gibbs vector.

For multiplicative error model and mixed additive and multiplicative error model, Wang et al. (2020) and Wang et al. (2022) obtained the second-order accuracy information of the parameters of the multiplicative error model and the mixed additive and multiplicative error model by using Sterling method and SUT method without derivative calculation, respectively.

For ill-posed multiplicative error model, Wang et al. (2021) proposed to use the A-optimal design method to determine the regularization parameters of the ill-posed model, and established a more reliable parameter estimation method by combining the virtual observation iterative method. For mixed additive and multiplicative error model with constraints, Wang et al. (2022) constructed an exhaustive method for parameter estimation of ill-posed model with inequality constraints, and proved the effectiveness of the method in dealing with related problems. Shi et al. (2020) extended mixed additive and multiplicative error model to a more general generalized mixed additive and multiplicative error model with deterministic trend.

For most of the geodetic applications, the observables are real number and least squares-based adjustment has been widely used to reduce the error and obtain the optimal estimation. However, the observable of InSAR is recorded by a complex number which is related to interferometric phase and correlation. In such a case, complex least squares-based adjustment is needed. To develop the complex least squares-based adjustment, the critical problem is how to establish the least squares criteria and stochastic model for the complex number. Zhu et al. (2019) proposed a non-linear least squares adjustment method whose least squares criteria is the sum of squares of the module of the residual of complex observations is minimal. With this criterion, the adjustment should be conducted in complex domain. Cao et al. (2022) proposed that the complex observation can be divided into real and imaginary parts and complex least squares adjustment is then a joint adjustment of real and real and imaginary. As a result, the existing adjustment theory for real number can also be used to process the complex observable. For the stochastic model, Zhu et al. (2019) and Cao et al. (2022) suggested that standard deviation of the module of complex can be regarded as the weight of the complex observable.

## **2 Geodetic inversion**

The geodetic inversion method has been further developed. To determine the smoothing coefficient (also known as the regularization parameter) in the inversion of the coseismic slip distribution, a compromise curve between the model roughness and the residuals of the data fit is generally used (Wang et al., 2020). Based on the L-curve, the Eclectic Intersection curve was proposed as a new method to determine the smoothing coefficients by Wang et al. (2020). Compared with the L-curve method, the Eclectic Intersection curve method has the advantage of high computational efficiency, no dependence on data fit, and more suitable smoothing coefficients. In Zang et al. (2022), the performance of high-rate single GNSS and multi-GNSS fusion in early warning magnitude calculation, fast mass moment tensor inversion and static fault slip inversion is thoroughly investigated using data related to the Mw 7.4 magnitude earthquake in Mado County, Qinghai Province, China. Zhao et al. (2022) proposed a new method to determine coseismic slip distribution inversion for multi-observation types, which can simultaneously determine the relative weight ratio and regularization parameters of multiple observations.

At the same time, intelligent algorithms have been widely used in seismic inversion problems. Xu et al. (2015) proposed a Bayesian estimation-based method for fault parameter inversion, which can quantify the uncertainty of optimal model parameters through the posterior probability distribution of the parameter space. Yin et al. (2019) proposed a fault parameter inversion method based on the combination algorithm of a genetic algorithm and iterative least

squares algorithm, which can give consideration to the sensitivity and correlation of fault parameters. Wang et al. (2020) introduced a scale-free trace transformation (SUT) method based on a deterministic sampling strategy for nonlinear inversion and accuracy estimation of seismic fault parameters. Zhao et al. (2020) proposed an adaptive multi-start Gauss-Newton method (AMGNA) to invert seismic source parameters using multiple geodetic datasets. Wang et al. (2021) proposed a particle swarm optimization algorithm (BH-PSO) incorporating a black hole strategy. The BH-PSO method is less time-consuming than the simulated annealing (SA) method and has higher accuracy than the genetic algorithm (GA). Traditional genetic algorithm (GA) inversion results are unstable and easily fall into local optimum in an inversion of fault parameters (Wang et al., 2021). Wang et al. (2021) proposed a genetic Nelder-Mead neural network algorithm (GNMNA). GNMNA outperforms GA and NNA in terms of inversion accuracy and computational stability, and GNMNA has greater potential for application in complex seismic environments. Zhang et al. (2022) introduced a general variational inference algorithm, Automatic Differential Variational Inference (ADVI) to Bayesian slip inversion, and compares it to the classical Metropolis-Hastings (MH) sampling method. Zhao et al. (2021) proposed a deep learning approach of Earthquake Source Parameters Inversion using ResNet (abbreviated as ESPI-ResNet) from satellite InSAR data. Wang et al. (2021) introduced the Sterling interpolation method to estimate the accuracy of parametric nonlinear inversions in earthquakes and applied it to the Lushan and L'Aquila earthquakes.

The joint inversion of multiple data is still the trend of geodetic inversion. Interferometric synthetic aperture radar (InSAR) has become an important technique to study seismic cyclic deformation. To obtain the complete and accurate three-dimensional (3-D) surface displacements from heterogeneous InSAR displacement observations, Liu et al. (2018) proposed a strain model and variance component estimation-based method (SM-VCE), in which the robust variance component estimation (RVCE) algorithm is used to weight different InSAR observations. It has been proved that the SM-VCE method is obviously superior to the traditional InSAR empirical weighting method for obtaining 3-D displacements. In addition to the co-event 3-D displacements, Liu et al. (2022a) proposed a novel Kalman filter-based InSAR method (KFInSAR) to combine multiple InSAR time series observations to estimate the time-series 3-D displacements, in which each InSAR time series dataset is optimized with an iterative weighted least square (IWLS)-based error correction procedure (Liu et al., 2021a), and the decorrelation noise and atmospheric delay can be significantly decreased. Wang et al. (2019) used interferometric synthetic aperture radar data to analyze the isoseismic and postseismic displacement fields associated with the 2016 Central Petermann Ranges earthquake in Australia. Liu et al. (2019) developed a logarithmic model-based approach (LogSIM) for joint inversion of co-seismic and post-earthquake fault sliding using InSAR data from multiple platforms with different tracks. Wang et al. (2019) used GPS and InSAR coseismic deformation fields to jointly invert the sliding distribution model of the Koshien earthquake; analyzed the relationship between the Koshien earthquake and the Mino earthquake based on static Coulomb stress alteration in conjunction with previous research results; and also constructed a fault grid for seven major faults in southwestern Taiwan and obtained their stress alteration models. He et al. (2020) used rising and falling Sentinel-1 satellite interferometric synthetic aperture radar (InSAR) images to construct isoseismic displacements associated with the Mw 7.1 Anchorage earthquake, which showed a sub-circular deformation pattern with -4 cm of subsidence in the

line of sight direction. Wang et al. (2020) used three-dimensional co-seismic displacement fields from spatial imaging geodesy to invert the Mw7.8 Kaikoura, New Zealand earthquake. Yang et al. (2021) provided a new interpretation of the 2016 Mino earthquake based on synthetic aperture radar (SAR) satellite, high-speed GPS, and strong motion data. Yan et al. (2022a, b) proposed the improved spatiotemporal random effects (STRE) model and the multiresolution segmentation fusion (MRSF) method for InSAR and GNSS fusion, which can better reveal the spatial heterogeneity of deformation data and the slip distribution in Cascadia Subduction Zone and San Francisco Bay region, California. Liu et al. (2021b, 2022b, 2022c) estimate the 3-D co-seismic displacements of the 6<sup>th</sup> July 2019 Ridgecrest earthquake, California, the 22<sup>nd</sup> May 2021 Maduo earthquake, the 9<sup>th</sup> January 2022 Menyuan earthquake, China, etc. from InSAR and pixel-offset tracking observations based on the SM-VCE method, providing the valuable and accurate datasets for constraining the fault movements. Zhu et al. (2019) and Cao et al. (2022) estimated the forest height and sub-canopy topography with the complex least squares adjustment method from polarimetric InSAR data.

Antarctic basal water storage variation (BWSV) is the mass variation of liquid water under the Antarctic ice cap (Kang et al., 2021). Kang et al. (2021) proposed a stratified gravity density forward/inverse Antarctic BWSV estimation method and associated model based on multi-source satellite observation data. Many recent mass balances using the Gravity Recovery and Climate Experiment (GRACE) and satellite altimetry (including both radar and laser sensors) have used a large number of forward models with uncertainties (Gao et al., 2019). To minimize the considerable sources of error associated with the use of forward models, Gao et al. (2019) used multiple geodetic observations to estimate mass changes in the ice cap and present-day GIA, including GRACE and the Ice, Cloud, and Land Elevation Satellite (ICESat), and the Global Positioning System (GPS), using an improved Joint Inverse Estimation (JIE) method to solve for Antarctic GIA and ice trends simultaneously.

Shi et al. (2022) Analysis of land water reserves using GRACE time-varying gravity field data inversion and periodic characteristics of GLDAS and CPC results. By taking the Yellow River Basin as the study area to obtain the deficient equivalent water height and find that the water reserves in the study area as a whole decreased at a rate of  $-0.51 \pm 0.03 \text{ cm} \cdot \text{a}^{-1}$  from 2002 to 2020. The lag time of equivalent water height retrieved by GRACE is 2 ~ 3 months relative to precipitation, evapotranspiration, and soil temperature. It was verified by experiments that GRACE has a strong correlation with equivalent water height calculated by GLDAS and CPC, and both have obvious annual resonance periods.

## Bibliography

- Cao S, Fu H, Zhu J et al (2022) A Forest Height Joint Inversion Method Using Multibaseline PolInSAR Data. *IEEE Geoscience and Remote Sensing Letters*, 19: 2508105
- Gao C, Lu Y, Zhang Z et al (2019) A joint inversion estimate of Antarctic ice sheet mass balance using multi-geodetic data sets. *Remote Sensing* 11(6) 653.
- Han J, Zhang S, Li J (2021) New first-order approximate precision estimation method for parameters in an errors-in-variables model. *Journal of Surveying Engineering* 147(1):04020023.
- Hu C, Fang X, Zhao L (2020) Nonlinear equality constrained total least squares adjustment combined with orthogonal geometry

- information and its iterative algorithm. *Acta Geodaetica et Cartographica Sinica* 49(7):816-823.
- He P, Wen Y, Chen Y et al (2020) Coseismic rupture geometry and slip rupture process during the 2018 Mw 7.1 Anchorage, south-central Alaska earthquake: Intraplate normal faulting by slab tear constrained by geodetic and teleseismic data. *Earth and Space Science* 7(1): e2019EA000924.
- Kang J, Lu Y, Li Y et al (2021) Basal Water Storage Variations beneath Antarctic Ice Sheet Inferred from Multi-source Satellite Data. *The Cryosphere Discussions* 1-28.
- Li B., Zhang Z., Shen Y., Yang L. (2018) A procedure for the significance testing of unmodeled errors in GNSS observations. *Journal of Geodesy*, 92(10):1171-1186.
- Li B, Wang M, Shen Y (2021) The hypothesis testing statistics in linear ill-posed models. *Journal of Geodesy* 95(1):1-19.
- Lin D, Yao Y, Zheng D et al (2022) Determination of truncation parameter based on the differences of TSVD parameter estimates for ill-posed problems in geodesy. *Acta Geodaetica et Cartographica Sinica* 51(8):1787-1796.
- Lin D, Zhu J, Li C, et al (2020) Bias reduction method for parameter inversion of ill-posed surveying model. *Journal of Surveying Engineering* 146(3):04020011.
- Liu J, Hu J, Li Z, et al (2018) A method for measuring 3-d surface deformations with InSAR based on strain model and variance component estimation. *IEEE Transactions on Geoscience and Remote Sensing* 56(1):239–250.
- Liu J, Hu J, Bürgmann R, et al (2021a) A strain-model based InSAR time series method and its application to the Geysers geothermal field, California. *Journal of Geophysical Research: Solid Earth* 126(8):e2021JB021939.
- Liu J, Hu J, Li Z, et al (2021b) Estimation of 3D coseismic deformation with InSAR: an improved SM-VCE method by window optimization. *Acta Geodaetica et Cartographica Sinica* 50(9):1222-1239.
- Liu J, Hu J, Li Z, et al (2022a) Dynamic estimation of multi-dimensional deformation time series from InSAR based on Kalman filter and strain model. *IEEE Transactions on Geoscience and Remote Sensing* 60:1–16.
- Liu J, Hu J, Li Z, et al (2022b) Complete three-dimensional coseismic displacements due to the 2021 Maduo earthquake in Qinghai Province, China from Sentinel-1 and ALOS-2 SAR images. *SCIENCE CHINA Earth Sciences* 65:687–697.
- Liu J, Hu J, Li Z, et al (2022c) Three-dimensional surface displacements of the 8 January 2022 Mw6.7 Menyuan earthquake, China from Sentinel-1 and ALOS-2 SAR observations. *Remote Sensing* 14(6):1404.
- Lu T, Wu G, Zhou S (2019) Ridge estimation algorithm to ill-posed uncertainty adjustment model. *Acta Geodaetica et Cartographica Sinica* 48(4):403-411.
- Lü Z, Sui L (2021) Structured Total Least Squares Method Based on Variable Projection. *Geomatics and Information Science of Wuhan University* 46(3):388-394.
- Lü Z, Sui L (2020) The BAB algorithm for computing the total least trimmed squares estimator. *Journal of Geodesy* 94(12):1-14.
- Lü Z, Sui L (2019) Variance-covariance component estimation for structured errors-in-variables models with cross-covariances. *Studia Geophysica et Geodaetica* 63(4):485-508.
- Liu X, Xu W (2019) Logarithmic model joint inversion method for coseismic and postseismic slip: Application to the 2017 Mw 7.3 Sarpol Zahāb earthquake, Iran. *Journal of Geophysical Research: Solid Earth* 124(11):12034-12052.
- Liu Y, Wang J, Wang B et al (2019) Robust Weight Total Least Squares Algorithm of Correlated Observation Based on Median Parameter Method. *Geomatics and Information Science of Wuhan University* 44(03):378-384.
- Liu Z, Zhu D, Yu H et al (2019) Least-square variance-covariance component estimation method based on the equivalent conditional adjustment model. *Acta Geodaetica et Cartographica Sinica* 48(9):1088-1095.
- Meng L, Zheng B, Wei Y (2020) Condition numbers of the multidimensional total least squares problems having more than one solution. *Numerical Algorithms* 84(3):887-908.

- Nie Y, Shen Y, Pail R, et al (2022) Efficient variance component estimation for large-scale least-squares problems in satellite geodesy. *Journal of Geodesy* 96(2):1-15.
- Qu G, Sun Z, Su X et al (2019) Adaptive Relaxation Regularization Algorithm for Nonlinear Parameter Estimation. *Geomatics and Information Science of Wuhan University* 2019,44(10):1491-1497.
- Shi Y, Xu P (2020) Adjustment of Measurements with Multiplicative Random Errors and Trends. *IEEE Geoscience and Remote Sensing Letters* 18(11):1916-1920.
- Shi Y, Xu P (2020) Nonexistence of Maximum Likelihood Estimation of Variance Components in Some Stochastic Models. *Journal of Surveying Engineering* 146(2):06020001.
- Song Y, Li W, Deng C, et al (2022) A new ridge estimation method on rank-deficient adjustment model. *Acta Geodaetica et Geophysica*, 57(1):1-22.
- Song Y (2019) A new iterative algorithm for a rank-deficient adjustment model with inequality constraints. *Journal of geodesy* 93(12):2637-2649.
- Song Z, Fang T, Schonfeld P, et al (2021) Effect of point configurations on parameter estimation analysis of circles. *Journal of Surveying Engineering* 147(3):04021010.
- Shi H, Sun X, Wang S et al (2022) Total least squares estimation model based on uncertainty theory. *Journal of Ambient Intelligence and Humanized Computing* 1-7.
- Shi T, Liu X, Mu D et al (2022) Reconstructing gap data between GRACE and GRACE-FO based on multi-layer perceptron and analyzing terrestrial water storage changes in the Yellow River basin. *Chinese Journal of Geophysics* 65(7):2448-2463.
- Sun Z, Qu G, Su X et al (2020) Frozen-Barycentre Algorithm for Solving Distance Equations. *Geomatics and Information Science of Wuhan University* 45(9):1478-1484.
- Tao W, Hua X, Li P, et al (2021) An iterated reweighting total least squares algorithm formulated by standard least-squares theory. *Survey Review* 53(380):454-463.
- Wang B, Fang X, Liu C et al (2020) Data Snooping for the Equality Constrained Nonlinear Gauss–Helmert Model Using Sensitivity Analysis. *Journal of Surveying Engineering* 146(4):04020015.
- Wang J, Yan W, Zhang Q, et al (2021) Enhancement of Computational Efficiency for Weighted Total Least Squares. *Journal of Surveying Engineering* 147(4):04021019.
- Wang L, Chen T (2021) Virtual Observation Iteration Solution and A-Optimal Design Method for Ill-Posed Mixed Additive and Multiplicative Random Error Model in Geodetic Measurement. *Journal of Surveying Engineering* 147(4):04021016.
- Wang L, Chen T (2022) The SUT method for precision estimation of mixed additive and multiplicative random error model. *Acta Geodaetica et Cartographica Sinica* 51(11):2303-2316.
- Wang L, Chen T (2022) A method for mixed additive and multiplicative random error models with inequality constraints in geodesy. *Earth, Planets and Space* 74(1):1-15.
- Wang L, Ding R (2020) A parameter determination method of unscented transformation and its approximate ability analysis in the precision estimation of nonlinear measurement adjustment. *Measurement* 166:108065.
- Wang L, Ding R (2020) Inversion and precision estimation of earthquake fault parameters based on scaled unscented transformation and hybrid PSO/Simplex algorithm with GPS measurement data. *Measurement*, 153: 107422.
- Wang L, Gao H, Feng G (2019) Triggering relations and stress effects analysis of two  $M_w > 6$  earthquakes in southwest Taiwan based on InSAR and GPS data. *Acta Geodaetica et Cartographica Sinica* 48(10):1244-1253.
- Wang L, Jin X, Xu W et al (2021) A black hole particle swarm optimization method for the source parameters inversion:

- application to the 2015 Calbuco eruption, Chile. *Journal of Geodynamics* 146:101849.
- Wang L, Li Z (2021) Bootstrap method for inversion and precision estimation of earthquake source parameters. *Chinese Journal of Geophysics*, 64(6): 2001-2016.
- Wang L, Li Z (2021) Bootstrap method and the modified method based on weighted sampling for nonlinear model precision estimation. *Acta Geodaetica et Cartographica Sinica*, 50(7): 863-878.
- Wang L, Luo X (2021) Adaptive Quasi-Monte Carlo method for nonlinear function error propagation and its application in geodetic measurement. *Measurement* 186:110122.
- Wang L, Sun J (2021) Variance Components Estimation for Total Least-Squares Regression Prediction Model. *Geomatics and Information Science of Wuhan University* 46(2):280-288.
- Wang L, Xu R, Yu F (2022) Genetic Nelder-Mead neural network algorithm for fault parameter inversion using GPS data. *Geodesy and Geodynamics* 13(4):386-398.
- Wang L, Yu F, Li Z, et al (2020) Jackknife method for variance components estimation of partial EIV model. *Journal of Surveying Engineering*, 146(4):04020016.
- Wang L, Yu F (2021) Jackknife Resample Method for Precision Estimation of Total Least Squares. *Communications in Statistics - Simulation and Computation*, 50(5):1272-1289.
- Wang L, Zhao X (2020) Determination of Smoothing Factor for the Co-seismic Slip Distribution Inversion. *Acta Geodaetica et Cartographica Sinica* 3(1):25-35.
- Wang L, Zhao Y (2019) Adaptive Monte Carlo Method for Precision Estimation of Nonlinear Adjustment. *Geomatics and Information Science of Wuhan University*, 44(2): 206-213, 220.
- Wang L, Zou C (2019) Accuracy analysis and applications of the Sterling interpolation method for nonlinear function error propagation. *Measurement* 146:55-64.
- Wang L, Zou C (2021) Accuracy estimation of earthquake source geometry parameters by the Sterling interpolation method in the nonlinear inversion. *Journal of Surveying Engineering*, 147(1): 04020019.
- Wang L, Zou C (2022) Sterling Interpolation Method for Parameter Estimation and Precision Estimation in Multiplicative Error Model. *Geomatics and Information Science of Wuhan University*, 47(2): 219-225.
- Wang L, Wen G, Zhao Y (2019) Virtual observation method and precision estimation for ill-posed partial EIV model. *Journal of Surveying Engineering*, 145(4):04019010.
- Wang T, Jiao L, Tapponnier P, Shi X, & Wei S (2020) Space imaging geodesy reveals near circular, coseismic block rotation during the 2016 Mw 7.8 Kaikōura earthquake, New Zealand. *Geophysical Research Letters* 47(22), e2020GL090206.
- Wang S, Xu W, Xu C, Yin Z, Bürgmann R, Liu L, & Jiang G (2019) Changes in groundwater level possibly encourage shallow earthquakes in central Australia: The 2016 Petermann Ranges earthquake. *Geophysical Research Letters* 46: 3189–3198.
- Wang Q, Hu Y, Wang B (2019) The maximum likelihood estimation for multivariate EIV model. *Acta Geodaetica et Geophysica* 54(2):213-224.
- Xie J, Long S, Zhou C (2021) Classical Least Squares Method for Inequality Constrained PEIV Model. *Geomatics and Information Science of Wuhan University* 46(9):1291-1297.
- Xie J, Lin D, Long S (2022) Total least squares adjustment in inequality constrained partial errors-in-variables models: optimality conditions and algorithms. *Survey Review* 54(384):209-222.
- Xu W, Dutta R, Jónsson S (2015) Identifying active faults by improving earthquake locations with InSAR data and Bayesian estimation: the 2004 Tabuk (Saudi Arabia) earthquake sequence. *Bulletin of the Seismological Society of America* 105(2A): 765-775.



- Yan H, Dai W, Xie L, Xu W (2022a) Fusion of GNSS and InSAR time series using the improved STRE model: applications to the San Francisco Bay Area and Southern California. *Journal of Geodesy* 96(7):47.
- Yan H, Dai W, Liu H, Gao H, Neely WR, Xu W (2022b) Fusion of Spatially Heterogeneous GNSS and InSAR Deformation Data Using a Multiresolution Segmentation Algorithm and Its Application in the Inversion of Slip Distribution. *Remote Sensing* 14(14): 3293.
- Yin J, Xu C (2019) Inversion of Fault Parameters Based on Combinational Algorithm for Spherical Layered Model. *Geomatics and Information Science of Wuhan University* 44(9):1320-1327.
- Yang L., Wang J., Knight N.L., & Shen Y. (2013) Outlier separability analysis with a multiple alternative hypotheses test. *Journal of Geodesy*, 87(6): 591-604.
- Yang L, Li B, Shen Y, Rizos C (2017) Extension of internal reliability analysis regarding to separability analysis. *Journal of Surveying Engineering*, 143(3):04017002.
- Yang L, Shen Y, Li B (2019) M-estimation using unbiased median variance estimate. *Journal of Geodesy* 93(6):911-925.
- Yang L, Shen Y (2020) Robust M estimation for 3D correlated vector observations based on modified bifactor weight reduction model. *Journal of Geodesy*, 94: 31.
- Yang L, Shen Y, Li B, Rizos C (2021) Simplified algebraic estimation for the quality control of DIA estimator. *Journal of Geodesy*, 95:14.
- Yang, Y, Chen Q, Diao X, et al (2021) New interpretation of the rupture process of the 2016 Taiwan Meinong Mw 6.4 earthquake based on the InSAR, 1-Hz GPS and strong motion data. *Journal of Geodesy* 95: 1-21.
- Zeng H, He H, Chen L, et al (2022) Extended WTLS iterative algorithm of 3D similarity transformation based on Gibbs vector. *Acta Geodaetica et Geophysica* 57(1):43-61.
- Zhao X, Wang C, Zhang H et al (2021) Inversion of seismic source parameters from satellite InSAR data based on deep learning. *Tectonophysics* 821:229140.
- Zhao Y, Xu C (2020) Adaptive multistart Gauss–Newton approach for geodetic data inversion of earthquake source parameters. *Journal of Geodesy* 94(2):1-18.
- Zeng W, Fang X, Lin Y, et al (2019) On the errors-in-variables model with inequality constraints of dependent variables for geodetic transformation. *Survey Review* 51(365):166-171.
- Zeng W, Liu Z, Fang X et al (2021) Linearization Estimation Algorithm for Universal EIV Adjustment Model. *Geomatics and Information Science of Wuhan University* 46(9):1284-1290.
- Zhao J, Guo F, Li Q (2019) Fisher-Score Algorithm of WTLS Estimation for PEIV Model. *Geomatics and Information Science of Wuhan University* 44(02):214-220.
- Zhao S, Song Y, Li W (2022) A new algorithm for rank-deficient problems with inequality constraints. *Survey Review* 54(384):223-232.
- Zhao X, Xu C, Zhou L, Wen Y, Wang J, Zhao Y (2022) A new method applied for the determination of relative weight ratios under the TensorFlow platform when estimating coseismic slip distribution. *Journal of Geophysical Research: Solid Earth* 127, e2022JB024843.
- Zhang C, Chen T (2022) Bayesian slip inversion with automatic differentiation variational inference. *Geophysical Journal International* Pages 546–565.
- Zang J, Wen Y, Li Z, et al (2022) Rapid source models of the 2021 Mw 7.4 Maduo, China, earthquake inferred from high-rate BDS3/2, GPS, Galileo and GLONASS observations. *Journal of Geodesy* 96(9): 1-13.
- Zhang Z, Li B. Unmodeled error mitigation for single-frequency multi-GNSS precise positioning based on multi-epoch partial parameterization. *Measurement Science and Technology*, 2020, 31(2): 025008.

- Zhang Z, Li Y, He X, Chen W, Li B. A composite stochastic model considering the terrain topography for real-time GNSS monitoring in canyon environments, *Journal of Geodesy*, 2022, 96: 79.
- Zhang Z, Li B, Gao Y, Shen Y. Real-time carrier phase multipath detection based on dual-frequency C/N0 data. *GPS Solutions*, 2019, 23: 7.
- Zhu J, Xie Q, Zuo T et al (2019) Complex least squares adjustment to improve tree height inversion problem in PolInSAR. *Journal of Geodesy and Geoinformation Science* 2(1): 1-8

# Scientific Computation Platform for Geophysical Geodesy

*Chuanyin Zhang, Tao Jiang, Wei Wang, Baogui Ke*

<sup>1</sup> *Chinese Academy of Surveying and Mapping, Beijing, China*

Large scientific computing platform for geophysical geodesy the high-precision gravity field approximation and geoid calculation system PAGravf4.5 (steady state) and earth tide load effect and deformation monitoring and calculation system ETideLoad4.5 (time-varying) was developed by the gravity field and vertical datum team of the Chinese Academy of Surveying and Mapping, integrating 20 years of research results. Based on public welfare purposes, the scientific computing platform is committed to improving the technology and education environment where there is a severe shortage of such computing resources in domestic and foreign academic fields, showcasing the charm and potential of geodesy, reconstructing collaborative heterogeneous geodetic benchmarks (a geodetic system with deep fusion of multi-source heterogeneous Earth data and a geodetic framework with multiple heterogeneous Earth observation technologies), consolidating the effectiveness of geodetic applications, and supporting the intelligence of massive Earth observations.

## 1 Precise Approach of Earth Gravity Field and Geoid (PAGravf4.5)

PAGravf4.5 is a large Windows package for scientific computation rigorously based on stationary gravity field theory. Strictly according to physical geodesy, PAGravf4.5 constructs the unified analytical algorithm system of various terrain effects on various gravity field elements on the geoid or in the outer space outside the geoid to improve the geophysical gravity exploration and gravity field data processing. Scientifically constructs the gravity field approach system with the spatial domain integration algorithm based on boundary value theory and spectral domain radial basis function approach algorithm to realize the full element modelling on gravity field in full space outside geoid and fine gravity prospecting from various heterogeneous observations. And develops some ingenious physical geodetic algorithms to improve and unify the regional height datum, so as to consolidate and expand the applications of Earth gravity field.

User can design own schemes and processes, then organize flexibly the related programs and functions in PAGravf4.5, perform some scientific computations for various terrain effects outside geoid, full element modelling on gravity field, refinement of 1cm stationary geoid, fine gravity prospecting from heterogeneous observations, improvement of regional height datum and application of Earth gravity field.

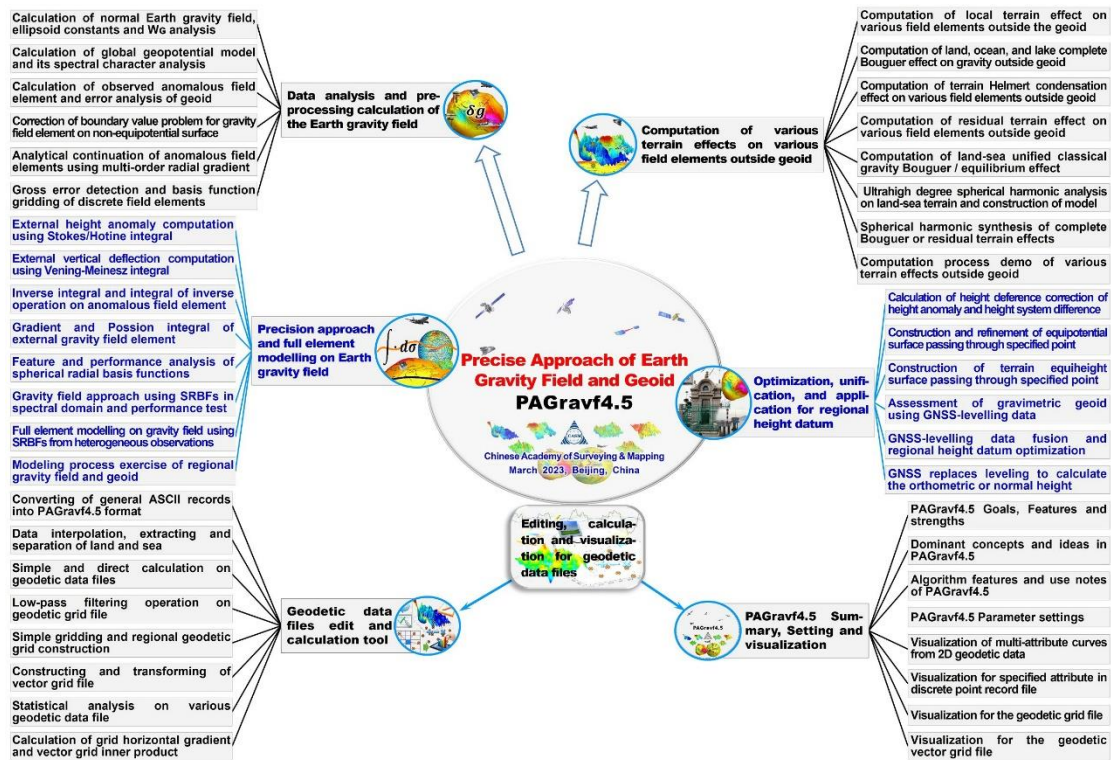


Figure 1. PAGrav4.5 Scientific Computing System Architecture

PAGrav4.5 has five subsystems, which includes data analysis and preprocessing calculation of Earth gravity field, computation of various terrain effects on various field elements outside geoid, precision approach and full element modelling on Earth gravity field, optimization, unification, and application for regional height datum as well as editing, calculation and visualization tools for geodetic data files. The scientific objectives of PAGrav4.5 mainly include the following three points:

(1) Solves the analytical compatibility and rigorous unified computation problems of various modes of terrain effects on various types of field elements, to fulfill the requirements of gravity field data processing in various cases and comprehensively improve the geophysical gravity exploration.

(2) Sets up the scientific and complete gravity field approach system with the positive-inverse integral in spatial domain and SRBF approach in spectral domain, to realize the full element analytical modelling in full space outside geoid from heterogeneous observations.

(3) Develops some ingenious physical geodetic algorithms based on the analytical relationship between Earth gravity field and height datum, to improve and unify the regional height datum, and consolidate and expand the applications of Earth gravity field.

## 2 Earth Tide, Load Effects and Deformation Monitoring Computation (ETideLoad4.5)

ETideLoad4.5 is a large scientific computing package for geophysical geodetic monitoring,

which adopts the scientific uniform numerical standards and analytic compatible geophysical algorithms accurately to compute various tidal and non-tidal effects on various geodetic variations outside the solid Earth, approaches the load deformation field and temporal gravity field from heterogeneous geodetic data, and then quantitatively monitors the land water, geological environment and ground stability variations, in order to support the deep fusion of heterogeneous geodetic data and collaborative monitoring of multi-geodetic technologies.

User can design own schemes and processes, then organize flexibly the related programs and functions from ETideLoad4.5, perform some scientific computations for various tidal or non-tidal effects, ground deformation field or temporal gravity field approach, land water, ground stability, or surface dynamic environment monitoring, and multi-source heterogeneous geodetic data deep fusion.

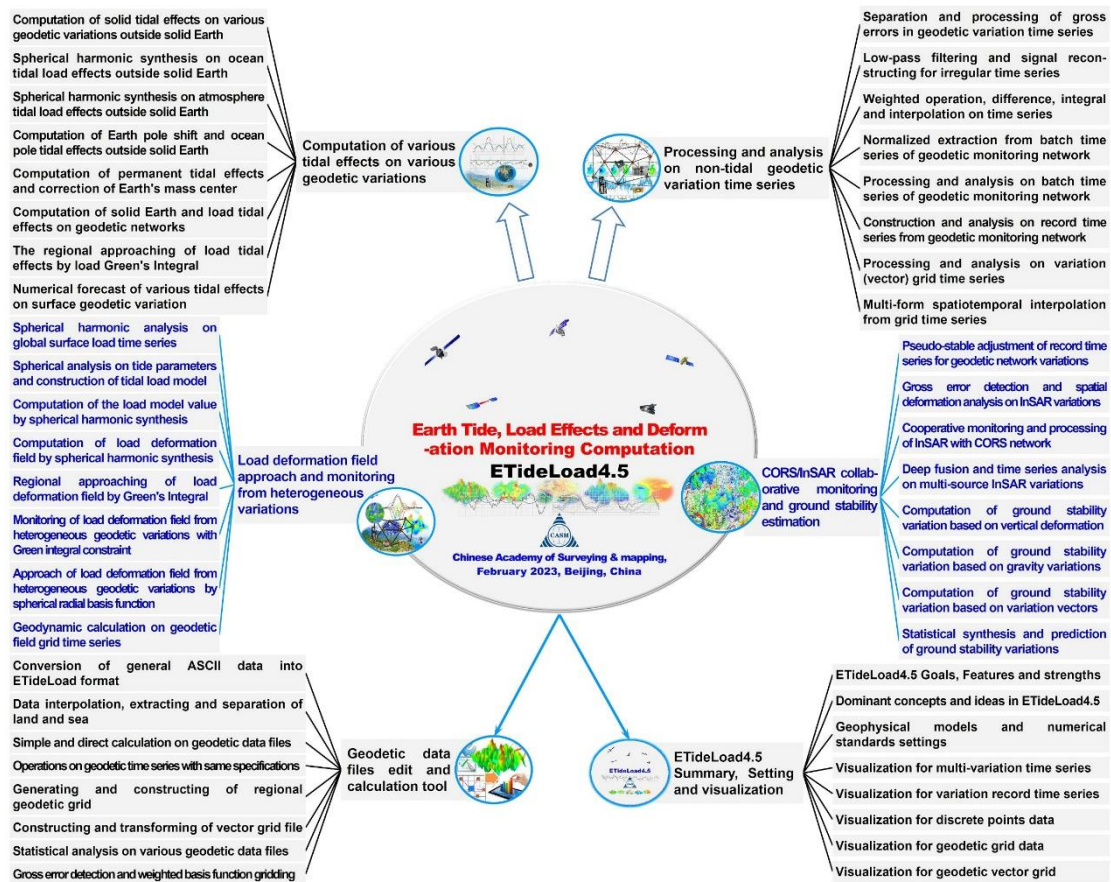


Figure 2. ETideLoad4.5 Scientific Computing System Architecture

ETideLoad4.5 is mainly composed of five subsystems: computation of various tidal effects on various geodetic variations, processing and analysis on non-tidal geodetic variation time series, load deformation field approach and monitoring from heterogeneous variations, CORS/InSAR collaborative monitoring and ground stability estimation, and geodetic data files edit and calculation tools, The scientific goals of ETideLoad4.5 mainly include the following three points:

(1) Using the consistent geophysical models and uniform numerical standards, accurately compute the various tidal and non-tidal effects on various geometric and physical geodetic variations on the ground and outside the solid Earth by constructing analytic compatible geodetic and geodynamic algorithms.

(2) Calculate and analyze the global and regional non-tidal load effects, and deeply fuse heterogeneous geodetic and surface load observations according to the theory of solid earth deformation, to realize the collaborative monitoring and high-precision approach of land water variations, load deformation field and time-varying gravity field.

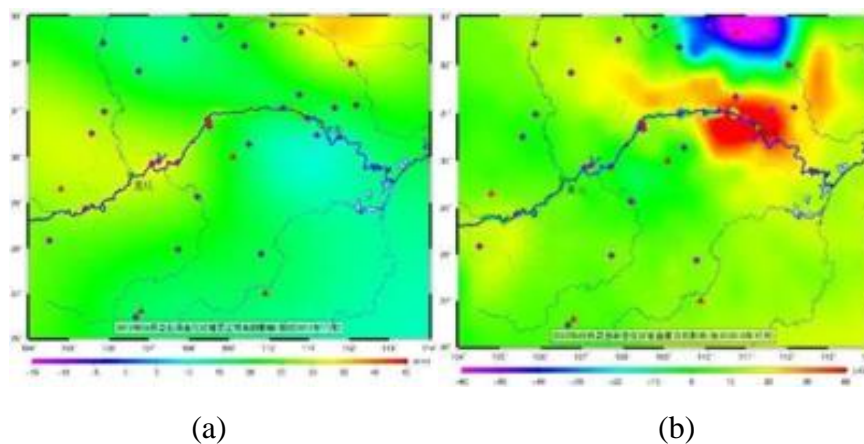
(3) Provide a set of scientific and practical geodetic geodynamic computation tools for construction of heterogeneous spatiotemporal geodetic frames, and deep fusion of heterogeneous Earth observations, collaborative monitoring of multi-geotechnologies, computation of solid Earth deformation, monitoring of surface hydrology environment, and surveying of geological disasters.

### 3 Typical Applications of Software

The scientific computing platform integrates classroom teaching, self-study exercises, applied computing and scientific research, and is suitable for senior undergraduate, graduate, scientific research and engineering technicians in geodesy and geosciences, geology and geophysics, surveying and mapping engineering and geographic information, aerospace and satellite dynamics, and earthquake and geodynamics. Mainly including several typical applications:

#### 1. Seamless and continuous monitoring of regional land water, ground deformation field, and gravity field changes.

From 2015 to 2016, using data from 26 CORS stations, 8 gravity stations, and 1 tilt station in the Three Gorges region and its surrounding areas (point distribution as shown in the figure), combined with daily average data from river hydrological stations and meteorological stations, as well as observation data from various satellite altimetry, Resource 3 satellite remote sensing, and GRACE satellite gravity, the load dynamics assimilation method was used to comprehensively determine the period from January 2010 to June 2015 in the Three Gorges region  $2^{\circ} \times 2^{\circ}$  Vertical deformation of the ground (a), ground gravity (b), ground tilt (c), and monthly variation of groundwater (d) grid time series.





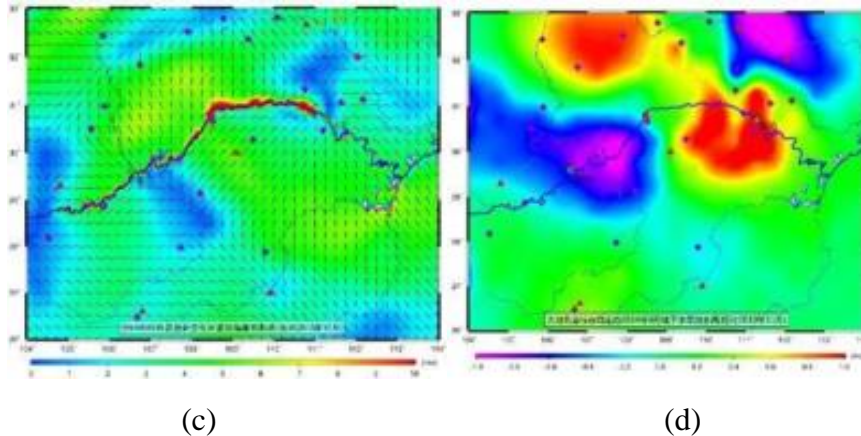


Figure 3. Three Gorges Region 2' x 2' Vertical ground deformation (a), ground gravity (b), ground tilt (c), and monthly variation of groundwater (d) grid time series

The results show that:

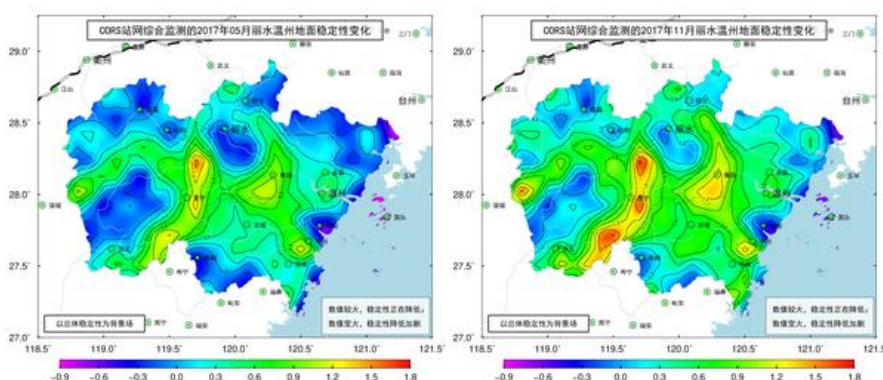
(1) the monitoring accuracy of ground vertical deformation is 5mm, and the monitoring accuracy of ground gravity change is 10  $\mu Gal$ . The comprehensive monitoring method of multiple elements of surface dynamic environment through multiple geodetic surveys is feasible.

(2) The annual variation amplitude of vertical ground deformation in the Three Gorges area is 36mm, the annual variation amplitude of geoid is 28mm, and the annual variation amplitude of ground gravity is 117  $\mu Gal$ .

(3) After the closure of the Yangtze River, the groundwater variation in the entire reservoir area has increased by nearly 0.5m<sup>3</sup> per square meter, and the impact area has expanded by over 150km from the centerline of the Yangtze River to both sides of the area.

## 2. Evaluation of Ground Stability Changes and Geological Disaster Monitoring and Warning Capability.

From 2017 to 2018, using continuous GNSS observation data from 38 CORS stations in and around Wenzhou, Lishui, Zhejiang Province from 2015 to 2017, combined with daily average atmospheric pressure data from 39 meteorological stations, using load deformation theory as dynamic constraints combined with known load removal recovery plans, calculated 1' x 1' Grid time series of monthly changes in ground vertical deformation, ground gravity, and ground stability in the Wenzhou area of Lishui from January 2015 to December 2017. Evaluate the ability of CORS station network to capture geological hazard precursors by quantitatively tracking changes in ground stability (as shown in the Figure 4).





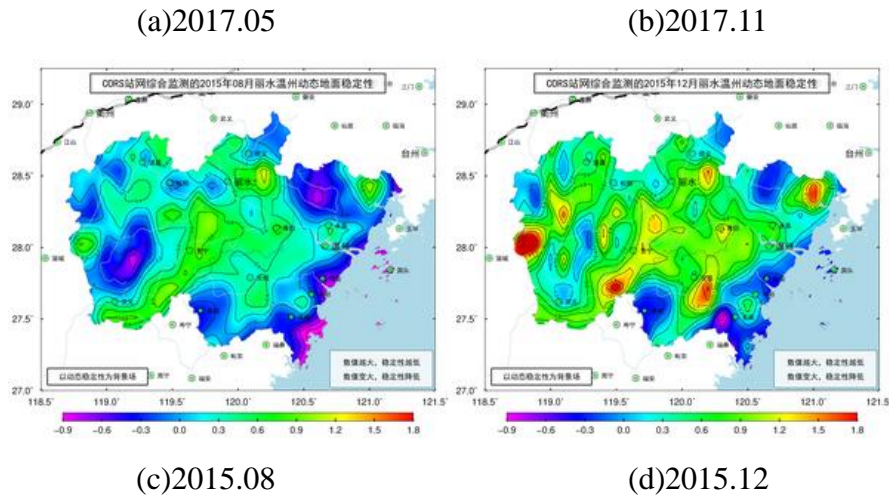


Figure 4. Comprehensive monitoring of dynamic ground stability in Lishui Wenzhou using CORS station network

The results show that:

(1) CORS network has the ability to continuously and quantitatively track and monitor the time and location of ground stability reduction, the duration of action, and the spatial impact distribution, as well as the ability to track and capture geological disaster processes and precursors.

(2) Before geological disasters occur, the CORS network can detect stability reduction signals in advance by continuously monitoring ground vertical deformation, ground gravity, and ground tilt changes, thereby capturing disaster precursors.

(3) The early capture rate of geological disaster precursors in the CORS station network in the Wenzhou area of Lishui can reach 92.5%.

**3. Ground subsidence and elevation benchmark monitoring and maintenance**

In 2016, a vertical benchmark monitoring and maintenance demonstration work was carried out in Shandong Province, combining CORS network, gravity satellite, and leveling network.

In 2017, a seamless and continuous monitoring of regional time-varying gravity field and groundwater reserve changes was carried out in the Hanzhong region of Shaanxi Province, in conjunction with the CORS network and gravity satellites.

In 2018, a comprehensive monitoring of land subsidence and regional elevation benchmark stability was carried out in Tianjin through multi-source and multiple geodetic surveys.

In 2019, land subsidence monitoring was carried out in Taizhou City, Zhejiang Province, using a joint time-series InSAR and CORS network.

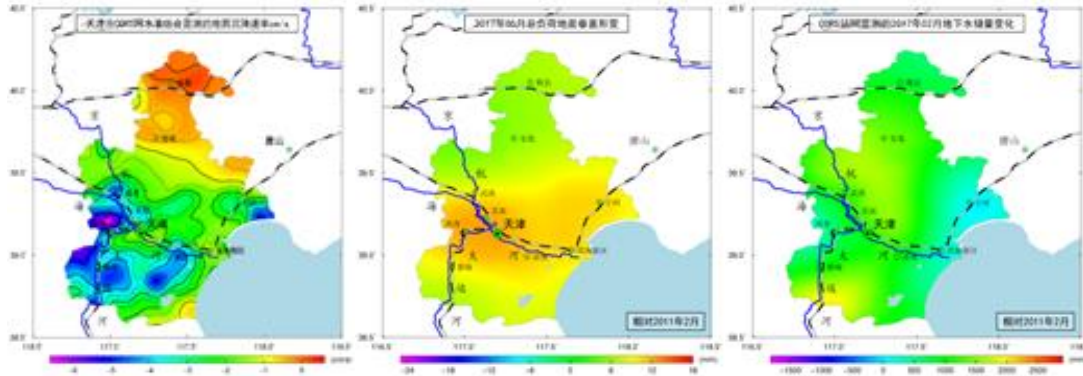


Figure 5. (a) Land subsidence rate of Tianjin CORS network leveling comprehensive monitoring(b) Vertical deformation of the load ground in June 2017(c) Monitoring changes in lunar groundwater reserves using CORS network

The results show:

(1) CORS station can not only directly and continuously monitor ground vertical deformation with millimeter level accuracy, but also, like the principle of monitoring global gravity field changes using GRACE satellite tracking satellites, can monitor small changes in regional gravity field with higher spatiotemporal resolution and sensitivity. Integrating various ground and satellite geodetic measurements can effectively improve the level of multi element monitoring of surface dynamic environment.

(2) In the vicinity of coastal zones and urban roads, InSAR monitoring is severely disturbed by surface non deformation information. After being unified with the CORS network's spatiotemporal monitoring benchmark, it can repair atmospheric delay errors, compensate for the impact of vertical deformation of load tides, and improve the ground's nonlinear and time-varying monitoring ability

#### 4. Regional linkage monitoring and numerical prediction of geological hazards

In 2021, 72 CORS stations, 44 groundwater monitoring stations, 41 river hydrological stations, as well as daily monitoring data of soil water and meteorology (with a time span from January 1, 2018 to December 31, 2020) were used in Baoshan and Dali cities in Yunnan Province (with an area of approximately 60000 square kilometers). The CORS network was used as a control to constrain assimilation of hydrological and meteorological observations and quantitatively monitor regional stability changes based on deformation dynamics and gravity field laws, Quantitative evaluation of geological hazard susceptibility has achieved numerical prediction of geological hazard risk (similar to meteorological and geological hazard trend prediction, replacing changes in meteorological elements with changes in ground stability).

(1) We have established a regional ground stability change and prediction grid time series model (with a spatial resolution of 1km and a time interval of 1 week), continuously monitoring the spatial distribution and temporal evolution trend of the entire region's hazardous areas, and achieving numerical prediction of geological hazard risk.

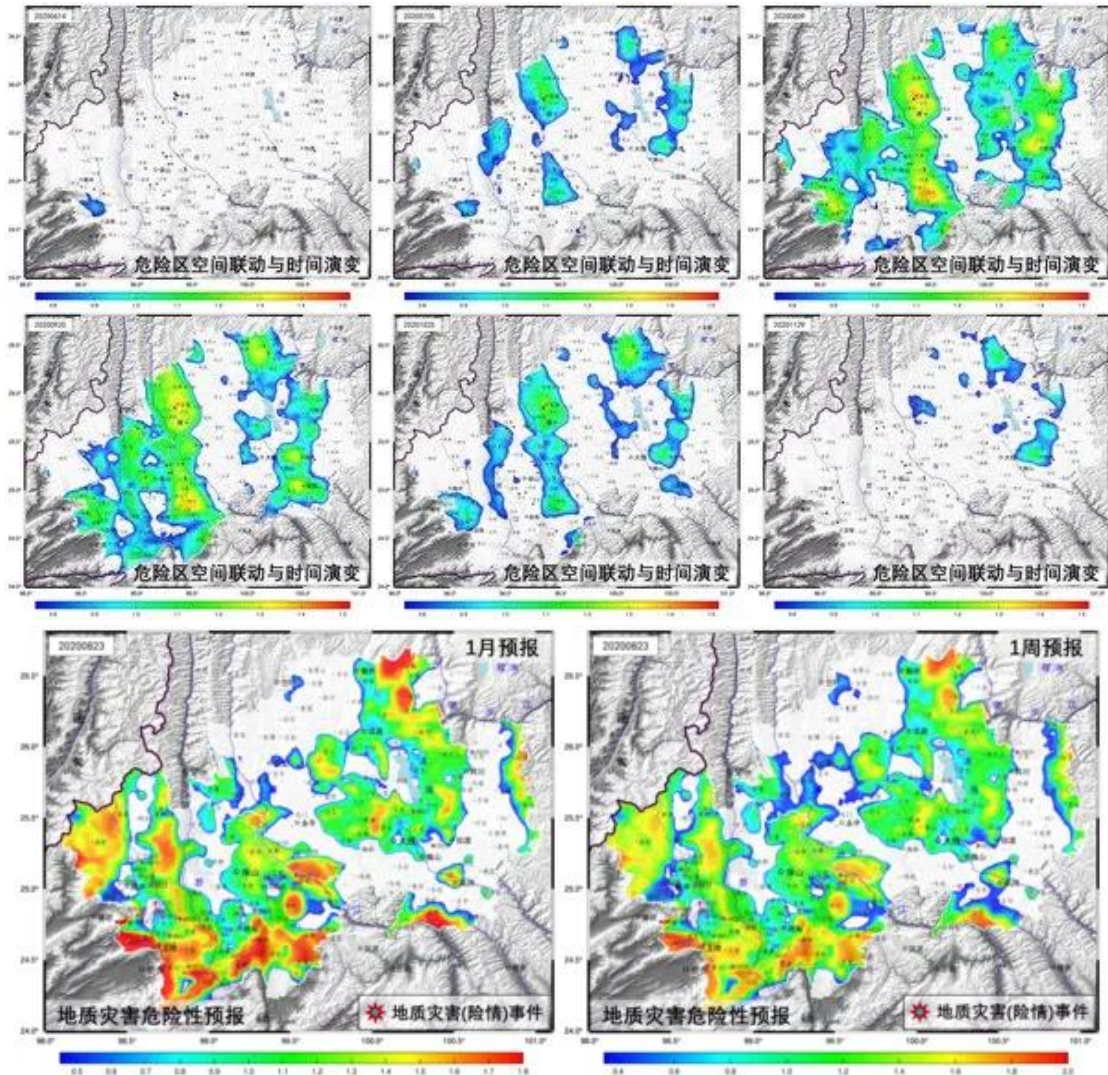


Figure 6. Spatial distribution and temporal evolution trend of hazardous areas and numerical prediction of geological hazard risk

The time of accelerated reduction of ground stability was used as the precursor of disasters, and the monitoring performance of ground stability changes was tested and verified using 197 actual disasters (dangerous situations) from 2018 to 2020. The results showed that 186 disasters showed precursor signals of accelerated ground stability reduction more than 2 days in advance, with a coincidence rate of 94.4%. Using 90 actual geological disasters (dangerous situations) that occurred in 2020 as verification, the 1-week, 2-week, and 1-month prediction rates were 92.2%, 83.3%, and 75.6%, respectively, as shown in Figure 6 (the color in the figure represents the geological hazard danger zone with rock and soil layers as the object. The bottom color scale is dimensionless, and the larger the value, the faster the stability decreases, and the greater the risk of geological disasters occurring here.)

(2) A numerical model for overall ground stability in the region was constructed to quantitatively evaluate the susceptibility of the entire region to geological hazards, and multiple potential geological hazard prone areas were identified.



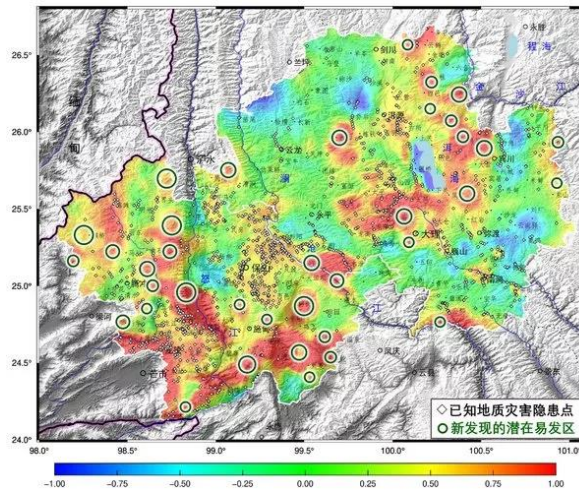


Figure 7. Numerical Model for Overall Ground Stability of Baoshan and Dali Cities in Yunnan Province

A comparative analysis was conducted between the overall stability model and the distribution of known geological hazard hazard points (as of December 2016). The results showed that 83% of known hazard points had poor stability in their basement; About 11% of areas with poor stability have no hidden danger points, and based on this, 37 new potential geological hazard prone areas have been interpreted.

# Seafloor Geodetic Positioning and Subsea Navigation Application

Shuqiang Xue<sup>1</sup>, Tianhe Xu<sup>2</sup>, Yanxiong Liu<sup>3</sup>, Xianping Qin<sup>4</sup>

<sup>1</sup> Chinese Academy of Surveying and Mapping, Beijing.

<sup>2</sup> Institute of Space Science, Shandong University, Weihai City, Shandong Province.

<sup>3</sup> First Institute of Oceanography, MNR, Qingdao City, Shandong Province.

<sup>4</sup> Xian Research Institute of Surveying and Mapping, Xian City, Shanxi Province.

## 1 Seafloor Geodetic positioning

The GNSS-A positioning accuracy of seafloor geodetic point is influenced by the trajectory of the surveying vessel. Circle trajectory is a commonly used surveying pattern in determining the position of seafloor geodetic point (Zeng et al. 2021). Compared with the circular measurement pattern for the positioning of seafloor control points, the accuracy of the circular and cross-track measurement pattern can be improved by 1.4 centimeters.

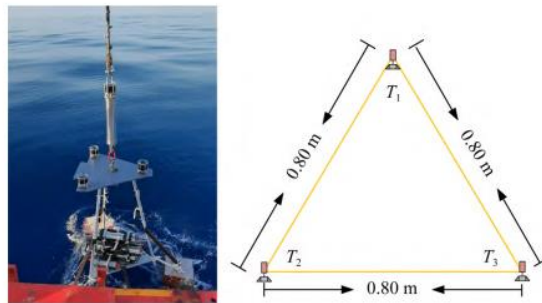


Figure.1 Schematic diagram of seafloor control point and beacon placement position on the station

The acoustic ray tracing algorithm is generally adopted in high-precision underwater positioning. To reduce the acoustic signal delay error and acoustic ray bending error in underwater positioning, the acoustic positioning algorithm based on the ray tracing has been widely applied. The algorithm needs to solve a large number of inverse problems, and therefore efficiently solving the inverse problem becomes critical to improve the whole efficiency of the underwater positioning algorithm.

Chinese scholars have proposed two kinds of  $p$ -order secant methods to improve the efficiency of traditional method (Yang et al. 2021), and the methods can be regarded as a generalization of the traditional secant method from two points to  $p$  points for rapidly solving the inverse problem. In the proposed methods, the calculation information in previous iterations is utilized to fit a polynomial model to speed up the algorithm convergence. The inverse problem is calculated by solving a polynomial equation approximating the function mapping from the emission angle to the radial distance of the ray. In the second-kind method, the inverse problem is however directly solved by approximating the function mapping from the radial distance to the emission angle. As the first-kind method needs to solve a  $p$ -order polynomial equation, the practicability of this method is limited to the complexity of solving the high-order equation, while the second-kind method can directly approximate the solution of the inverse problem, which is more practical and flexible.

In order to reduce the influence of sound ray bending and sound velocity variation errors on the submarine station parameters, an observation model considering sound ray bending and

sound velocity deviation parameters was established (Qin et al. 2023).

Table 1. Differences in horizontal coordinates between 2 D and 3D adjustments.

Case	Stations	Not estimating			Estimating		
		acoustic ray bending			acoustic ray bending		
		Session1	Session2	Session3	Session1	Session2	Session1
1	1 DDN(cm)	6.6	2.5	5.7	0.0	0.0	0.0
	1 DDE(cm)	7.2	2.7	6.3	0.0	0.0	0.1
	2 DDN(cm)	-2.6	-1.6	-2.5	0.0	0.0	0.0
	2 DDE(cm)	-7.6	-2.9	-6.6	-0.1	0.0	0.0
	3 DDN(cm)	-6.9	-2.7	-6.0	-0.1	0.0	0.0
	3 DDE(cm)	-3.3	-1.8	-3.1	0.0	0.0	0.0
	4 DDN(cm)	2.8	1.9	2.7	0.0	0.0	0.1
	4 DDE(cm)	3.7	2.0	3.4	0.0	0.0	0.0
2	1 DDN(cm)	7.7	3.8	6.6	0.0	0.0	0.1
	1 DDE(cm)	8.4	4.0	7.1	0.0	0.1	0.0
	2 DDN(cm)	-2.3	-0.3	-1.6	0.0	0.0	0.0
	2 DDE(cm)	-7.8	-4.2	-7.4	-0.1	0.0	0.0
	3 DDN(cm)	-7.1	-4.1	-6.8	-0.1	0.0	0.0
	3 DDE(cm)	-3.1	-0.5	-2.1	0.0	0.0	0.0
	4 DDN(cm)	1.7	0.6	1.9	0.0	0.0	0.1
	4 DDE(cm)	2.5	0.7	2.5	0.0	0.0	0.0

Table 1 shows that, the maximum difference of horizontal coordinates between 2 D and 3 D adjustments is 8.4 cm when the acoustic ray bending parameter is not estimated. If the acoustic ray bending parameter is introduced into the observation model and estimated together with the location parameters, the maximum difference of horizontal coordinates between 2 D and 3 D adjustment is reduced to 0.1 cm.

Table 2. Variations of vertical coordinates before and after adjustment.

Case	Stations	Not estimating			Estimating		
		acoustic ray bending			acoustic ray bending		
		Session1	Session2	Session3	Session1	Session2	Session1
(1)	1 DU(cm)	6.6	2.5	5.7	0.0	0.0	0.0
	2 DU(cm)	7.2	2.7	6.3	0.0	0.0	0.1
	3 DU(cm)	-2.6	-1.6	-2.5	0.0	0.0	0.0
	4 DU(cm)	-7.6	-2.9	-6.6	-0.1	0.0	0.0
(2)	1 DU(cm)	-6.9	-2.7	-6.0	-0.1	0.0	0.0
	2 DU(cm)	-3.3	-1.8	-3.1	0.0	0.0	0.0
	3 DU(cm)	2.8	1.9	2.7	0.0	0.0	0.1
	4 DU(cm)	3.7	2.0	3.4	0.0	0.0	0.0

As shown in Table 2, after adjustment with a ray bending parameter, the accuracy of vertical coordinates also significantly improved.

However, the traditional acoustic ray tracing method is usually based on the one-way acoustic propagation path without the consideration of the displacement of shipborne transducer during the process of acoustic signal propagation. Therefore, the systematic deviation will be introduced in the positioning for seafloor transponder, which will limit the positioning accuracy of seafloor points. To solve this problem, a layered constant gradient acoustic ray tracing underwater positioning algorithm considering round trip acoustic path is proposed (Yan et al. 2022). Combined with the actual propagation path of underwater acoustic signal, the round trip acoustic path.

Numerous errors are inevitable in marine surveying, including systematic errors and gross errors caused by GNSS dynamic positioning, inaccurate sound velocity profile measurements, and ocean ambient noise, and their interference will be directly reflected in the positioning results (Kuang et al. 2023).

Marine geodetic datum positioning is calculated by using the GNSS-A data. Based on the precise round-trip acoustic location model, Chinese scholars model the sound velocity error related to the deviation of sound velocity distribution (SVP) and time-varying error (Sun et al. 2023). To reduce the propagation error of the acoustic rays in the ocean, the SVP deviation and seafloor position parameters are resolved simultaneously by the Bayesian estimation using the round-trip acoustic travel time. The time-varying errors of SVP are corrected through symbolic regression using multi-gene genetic programming (MGGP) even without any accurate prespecified mathematical form of marine environmental variations.

First, the position and background SVP deviation is estimated by Bayesian estimation in the precise acoustic positioning model. Next, the time-varying sound velocity errors are modelled by symbolic function and determined by the MGGP approach using the acoustic travel time data. Finally, update the position vector again. These estimation steps are repeated until the position variation is below a convergence criterion.

Based on sound velocity profiles (SVPs) data, the equal gradient acoustic ray-tracing method is applied in high-precision position inversion. However, because of the discreteness of the SVPs used in the forementioned method, it ignores the continuous variation of sound velocity structure in time domain, which worsens the positioning accuracy. Chinese scholars consider the time domain variation of sound velocity structure and the cubic B-spline function is applied to characterize the perturbed sound velocity (Zhao et al. 2023).

Based on the ray-tracing theory, an inversion model of "stepwise iteration & progressive corrections" for both positioning and sound speed information is proposed, which conducts the gradual correction of seafloor geodetic station coordinates and disturbed sound velocity.

Robust Bayesian least squares the inversion model of iteration-gradual correction is carried out alternately by "fixed sound velocity - solution position" and "fixed position - estimated sound velocity", and the coordinates and sound velocity structure of the submarine station are modified gradually until the solution results meet the threshold requirements, so as to obtain the time-domain changes of the position of the submarine reference station and sound velocity structure. Quadratic polynomial (QP) method and cubic B-spline (CBS) function method are used to invert the structure of disturbed sound velocity. The spline function used by CBS sound velocity correction method has better smoothness and continuity, so it can obtain a better positioning result.

After modeling the spatio-temporal model of sound velocity disturbance with



cubic B-spline curve, Chinese scholars proposed to use the minimum norm condition to select the optimal hyper parameter (Zhuang et al. 2023), and realized the joint estimation of the coordinates of the seabed transponder and the spatio-temporal model of sound velocity. The simplest way to solve the two kinds of parameters of three-dimensional coordinate and sound velocity disturbance is to fix one kind of parameters to solve the other kind of parameters, which cannot guarantee the unbiased parameters. The Bayesian estimation is used to constrain the prior information of the parameters.

Similarly, Chinese scholars have used Bayesian estimation to simultaneously estimate the position of the submarine transponder and the horizontal gradient of sound velocity (Ming et al. 2023). Experimental results show that: at the same time, the method of solving the position of transponder and horizontal gradient of sound velocity is only applicable to the situation where the horizontal gradient of sound velocity changes little. Therefore, if this method is used to locate the seabed transponder, it is recommended to reduce the sailing time as far as possible to meet the assumption that the horizontal sound velocity structure remains approximately unchanged.

All the methods of sound velocity inversion require the constraints such as the real distance or the real terrain, which are often difficult to obtain in underwater positioning. To solve the problem of underwater high-accuracy position under the lack of measured sound velocity profile (SVP), some scholar proposes a self- constraint underwater positioning method without the assistance of measured sound velocity profiles (Zhao et al. 2023). Firstly, the model of incident angle and sound propagation distance is constructed. Then, by fitting the model coefficients, the reference depths of all observation epochs are obtained to be the depth constraint in the SVP inversion. Finally, the coordinates of underwater control points are accurately calculated with the inversion SVP.

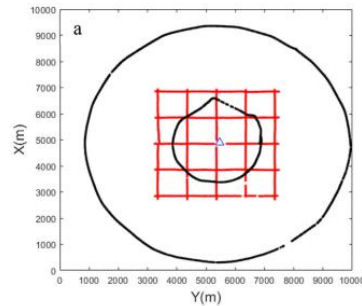


Figure 2. The three sailing routes (a)

Table 3. Variations of vertical coordinates before and after adjustment.

Route	Error(m)	Not estimating			Estimating		
		acoustic ray bending			acoustic ray bending		
		20m	60m	100m	20m	60m	100m
Cricle1	dx	0.02	0.02	0.02	0.01	0.01	0.01
	dy	0.02	0.01	0.00	0.01	0.03	0.01
	dz	0.91	0.51	0.36	0.45	0.69	0.45
Cricle2	dx	0.30	0.30	0.30	0.01	0.03	0.01
	dy	0.05	0.04	0.03	0.01	0.02	0.01
	dz	0.64	0.24	0.09	0.49	1.40	0.49

	dx	0.01	0.01	0.01	0.00	0.00	0.00
Grid	dy	0.00	0.00	0.00	0.00	0.00	0.00
	dz	1.01	0.83	1.05	0.50	0.53	0.50

The maximum horizontal positioning error is 0.05 m, which benefits from the symmetry of sailing tracks and the accurately retrieved SVP. The maximum vertical positioning error reaches 1.40 m and is larger than the horizontal positioning error, but the relative positioning error is very small in 3000 m depth. The positioning results show that the proposed method achieved high positioning accuracy without the measured SVP.

## 2 Subsea navigation applications.

Chinese scholars refer to GNSS tropospheric error processing method and propose GNSS acoustic position enhancement service method for underwater vehicle position enhancement service (Chen et al.2023)<sup>错误!未找到引用源。</sup>. The GNSS tropospheric error processing method is used

for reference, that is, the signal propagation time is first converted into distance, and then the distance is corrected by the projection function related to height Angle, the zenith tropospheric delay model and parameters, so as to support the high-precision position service. Based on the above method, the acoustic velocity correction information of submarine geodetic control points and surface buoys are used to invert the sea area to support the high-precision navigation calculation of underwater equipment.

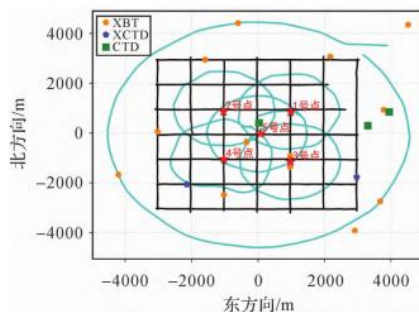


Figure 3. Distribution of seafloor reference stations, measured sound speed profiles and the ship's track lines

Table 4. Ship's navigation results based on the sound speed error correction model.

Track name (Time sorting)	Mean value of epoch-by-epoch accuracy			RMS of mutual difference with GNSS		
	E	N	U	E	N	U
Circle1	0.098	0.096	0.052	0.635	0.297	0.225
Circle2	0.278	0.267	0.192	0.579	0.438	0.420
Circle3	0.523	0.509	0.356	0.534	0.532	0.379
Circle4	0.299	0.292	0.191	0.482	0.333	0.237
Line	0.865	0.841	0.917	0.831	1.295	0.790
Circle5	0.378	0.367	0.196	0.519	0.343	0.200
Big circle	2.021	1.983	2.890	1.092	1.944	1.503

It can be seen that the accuracy of navigation results away from 3000m horizontal distance to the center of the submarine control network is decimeter level. In the test,

the navigation and positioning data (about 16000m in length) of a pilot line crossing the seabed control network on the sea surface were processed, and the mutual difference between the acoustic navigation result and GNSS positioning result was output. It shows that, with the increase of the horizontal distance between the survey ship and the center of the submarine control network, the accuracy of the three-dimensional results of acoustic navigation gradually increases within the range of 6000m, while it increases rapidly outside the range of 6000m. The accuracy of the results in the horizontal direction is about 10m and that in the vertical direction is greater than 40m at 10,000 m.

A rigorous method incorporates the time varying term of the sound velocity ranging error into the coefficient matrix of the underwater observation equation, and the transducer position error should be considered. Therefore, a Gauss-Helmert (GH) model is used for seafloor control point positioning . On this basis, considering the gross errors polluting of the observations, the robust estimation principle is introduced.

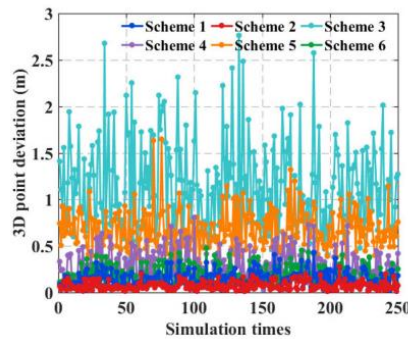


Figure 4. The 3D point deviations of each scheme.

Table 5. The statistical results of each scheme.

Statistics Method	Max	Min	RMS	STD
Scheme1	0.429	0.012	0.166	0.080
Scheme2	0.279	0.012	0.087	0.045
Scheme3	2.763	0.273	1.253	0.485
Scheme4	0.808	0.022	0.331	0.156
Scheme5	1.647	0.244	0.709	0.210
Scheme6	0.477	0.028	0.213	0.101

Scheme 1: When gross errors are not added, the general model is constructed, and the estimation is carried out based on the LS algorithm. Scheme 2: When gross errors are not added, the nonlinear GH model is constructed, and the estimation is carried out based on the WTLS algorithm. Scheme 3: When gross errors are added, the general model is constructed, and the estimation is carried out based on the LS algorithm. Scheme 4: When gross errors are added, the nonlinear GH model is constructed, and the estimation is carried out based on the WTLS algorithm. Scheme 5: When gross errors are added, the general model is constructed, and the estimation is carried out based on the robust LS algorithm. Scheme 6: When gross errors are added, the nonlinear GH model is constructed, and the estimation is carried out based on the robust WTLS algorithm.

In Scheme 6, the nonlinear GH model is adopted to address several kinds of error factors, and the transducer position error and the time-varying term of the sound velocity ranging error are combined into one unified error vector. The robust WTLS algorithm of the proposed model

accounts the anti-interference ability in both the structure and the observation spaces and can construct the equivalent covariance matrix of each observation independently. Hence, the influences of abnormal transducer position information and gross errors can be effectively resisted. Besides, Chinese scholars take into account the effect of transceiver separation (Xin et al. 2022), have suggested that based on the constant gradient sound ray tracing method, the optimal target coordinates can be obtained by searching according to the principle of minimum roundtrip delay difference. A Newton iterative solution algorithm based on round-trip time assignment according to sound distance is proposed to improve the computational efficiency.

## Bibliography

- Chen G X, Gao K F, Zhao J H, et al. 2023. The method of sound speed errors correction in GNSS-acoustic location service. *Acta Geodaetica et Cartographica Sinica*. (in chinese), 52(4):536-549.
- Kuang Y C, Lu Z P, Wang F C, et al. 2023. A Nonlinear Gauss-Helmert Model and Its Robust Solution for Seafloor Control Point Positioning, *Marine Geodesy*, 46:1, 16-42.
- Ma Y Y, Yang Y X, Zeng A M. 2022. GNSS-A straight-line survey pattern and trajectory combination optimization analysis. *Chinese Journal of Geophysics*. (in Chinese), 65(10):3797-3808.
- Ming F, Yang Y X, Zeng A M. 2023. Positioning accuracy of GNSS-A in deep sea based on Bayesian estimation. *Chinese Journal of Geophysics*. (in Chinese), 66(3):951-960.
- Qin X P, Yang Y X, Sun B J. 2023. A Robust Method to Estimate the Coordinates of Seafloor Stations by Direct-Path Ranging, *Marine Geodesy*, 46:1, 83-98.
- Sun D J, Yu M, Zheng C I, et al. 2023. Improved Seafloor Geodetic Positioning via Sound Velocity Correction Based on the Precise Round-Trip Acoustic Positioning Model, *Marine Geodesy*, 46:1, 43-61.
- Xin M Z, Ge M R, Yang F L, et al. 2022. A sound ray tracing positioning method for marine geodetic datum considering the effect of transceiver separation. *Chinese Journal of Geophysics*. (in Chinese), 65(10):3809-3817.
- Yang W L, Xue S Q, Liu Y X. 2021. P-order secant method for rapidly solving the ray inverse problem of underwater acoustic positioning. *Marine Geodesy*, 1-13.
- Yan F C, Wang Z J, Zhao S, et al. 2022. A layered constant gradient acoustic ray tracing underwater positioning algorithm considering round trip acoustic path. *Acta Geodaetica et Cartographica Sinica*. (in chinese), 51(1):31-40.
- Zeng A M, Yang Y X, Ming F, et al. 2021. Positioning model and analysis of the sailing circle mode of seafloor geodetic datum points. *Acta Geodaetica et Cartographica Sinica* (in chinese) ,
- Zhao S, Wang Z J, Nie Z X, et al. 2023. Precise positioning method for seafloor geodetic stations based on the temporal variation of sound speed structure. *Acta Geodaetica et Cartographica Sinica*. (in chinese), 52(1):41-50.  
50(07):939-952.
- Zhao J H, Liang W B, Ma J Y, et al. 2023. A Self-Constraint Underwater Positioning Method without the Assistance of Measured Sound Velocity Profile, *Marine Geodesy*, 46:1, 62-82.
- Zhang S Q, Yang Y X, Xu T H. 2023. Estimation of ocean sound velocity variation based on GNSS-A and its influence on positioning. *Chinese Journal of Geophysics* (in Chinese), 66(3):961-972.

# Progress on Hydrogeodesy

Wei Feng<sup>1</sup>, Shuang Yi<sup>2</sup>, Bo Zhong<sup>3</sup>, Qiujiu Chen<sup>4</sup>, Xiaodong Chen<sup>5</sup>, Yulong Zhong<sup>6</sup>, Yuanjin Pan<sup>3</sup>, Lin Liu<sup>7</sup>, Wei Wang<sup>8</sup>

<sup>1</sup> School of Geospatial Engineering and Science, Sun Yat-sen University, Zhuhai, China

<sup>2</sup> University of Chinese Academy of Sciences, Beijing, China

<sup>3</sup> School of Geodesy and Geomatics, Wuhan University, Wuhan, China

<sup>4</sup> College of Surveying and Geo-informatics, Tongji University, Shanghai, China

<sup>5</sup> Innovation Academy for Precision Measurement Science and Technology, Chinese Academy of Sciences, Wuhan, China

<sup>6</sup> School of Geography and Information Engineering, China University of Geosciences, Wuhan, China

<sup>7</sup> The Chinese University of Hong Kong, China

<sup>8</sup> Chinese Academy of Surveying and Mapping, Beijing, China

## 1 Satellite Gravity

Since the launch of Gravity Recovery and Climate Experiment (GRACE) and its successor, GRACE-Follow on (GRACE-FO), satellite gravimetry has revolutionized our understanding of mass transport and redistribution in the Earth system. Global observations of water and ice mass redistribution in the Earth system at monthly to decadal time scales are essential for understanding the climate variability and changes. GRACE and GRACE-FO have provided unprecedented insights into the Earth's water cycle, ice mass balance, and solid Earth deformation.

### Data processing

Low degree spherical harmonic coefficients are proved to be important to accurately estimated the changes in the Earth's surface mass, which however are missing or corrupted in GRACE/GRACE-FO gravity field models. The time variations of the three degree-1 coefficients, representing geocenter motions, do not exist as satellites always orbit around the center-of-mass of the Earth's system and insensitive to its motion with respect to the center-of-figure of the solid Earth. The time variations of the  $C_{20}$  coefficients ( $J_2$ ), representing the changes in the Earth's dynamic oblateness, are contaminated by large noise, partially originating from thermo-dependent systematic errors in the accelerometers. The time variations of the  $C_{30}$  coefficients are degraded during the end of the GRACE and so far the entire period of the GRACE-FO. To overcome these limitations, Sun et al. (2019, 2020, 2023) have developed and improved several methods to estimate these coefficients separately or simultaneously. The GRACE-OBP approach has been improved by identifying the optimal implementation parameters and considering the self-attraction and loading effects.

There are two major difficulties in the data processing of GRACE/GRACE-FO gravity satellites, namely, how to effectively filter out the strip noise and how to fill the 11 months of missing data between two generations of gravity satellites. For the filtering problem, Yi & Nico (2021) propose a new spatial filter based on autocorrelation in longitude direction and cross-correlation in latitude direction, using the singular spectrum analysis (SSA) technique, which can effectively remove the strip noise while maintaining the orthogonality with the physical

signal. For the gap-filling problem, Yi & Nico (2022) propose a method to fill the spherical harmonic coefficients based on SSA and cross-validation, which can extract the long-term and oscillatory variations from the available observations to obtain the gap-filling data with error estimates. Improved multichannel SSA was also used to fill the gap reliably between the two missions (Wang F. et al., 2021). Zhang et al. (2021) used the mass anomaly observed by Swarm mission to fill this gap.

GRACE intersatellite geopotential differences (GPD), as the gravimetric observables, can more directly reflect the surface mass changes compared with the geometric KBR range-rate observations. Based on the remove-compute-restore technique and improved energy balance equation, the precise GPD observations are estimated from GRACE Level-1B data (Zhong B. et al., 2020, 2022). The regional mass concentration (mascon) solutions over South America are estimated from the GPD data using a priori constraints (Zhong B. et al., 2020), and the influence of different external constraints on the estimation of regional mascon solutions are investigated (Zhong B. et al., 2021). Furthermore, to improve the reliability of regional mascon solutions and avoid the influence of external constraints, basin-scale terrestrial water storage anomalies (TWSA) in the Yangtze River Basin of China are estimated by using spatio-temporal constraints with the unconstrained spherical harmonic (SH) solutions (estimated from GPD data) as the a priori information (Zhong B. et al., 2023). In addition, Ferreira et al. (2020) also proposed a parameterization of TWSA based on the so-called improved point mass, which adopts the synthesized residual gravitational potential as observations. The approach allows the basis functions to be represented locally rather than globally, as well as the use of geophysical data constraints.

### **Terrestrial Water Storage Variations**

GRACE/GRACE-FO satellites have played a crucial role in studying the water cycle and water balance of various river basins in China. Zhong et al. (2020a, 2020b) used GRACE-derived terrestrial water storage change (TWSC) data and in-situ precipitation and runoff data to estimate evapotranspiration (ET) in West Liaohe River Basin (WLRB) and nine exorheic basins of China, respectively, based on the water balance equation. The results show that neglecting TWSC in the water balance leads to larger uncertainties in ET estimates, highlighting the importance of GRACE satellites in water balance studies. Bai et al. (2022) proposed a daily TWSA reconstruction framework and used it to improve the accuracy of TWSC estimates, which further led to better estimates of ET in nine exorheic basins of China. Qu et al. (2022) also employed WBE to estimate ET in the Yellow River Basin and investigate the annual, seasonal, and interannual variability of ET.

GRACE and GRACE-FO satellite data have also shown great potential in flood monitoring. Xiao et al. (2022) used GRACE and daily precipitation observations to reconstruct the daily water storage for the first time based on a statistical model to monitor the changes in terrestrial water storage during the "Henan 7.20 rainstorm" of China in 2021. The reconstructed daily TWSA has better potential for near-real-time flood monitoring for short-term events in a small region. Xie et al. (2022) reconstructed daily TWSA based on machine learning models to monitor flood events in the Yangtze River basin, which provides new opportunities for investigating submonthly water storage signals using GRACE and GRACE-FO satellite data. Furthermore, Xiong et al. (2022) established a novel standardized drought and flood potential index based on the ITSG-Grace2018 daily solution, which successfully detected 22 submonthly

exceptional floods and droughts in the Yangtze River basin. The index uses standardized anomalies of daily TWSA and daily precipitation to evaluate the potential of floods and droughts in a region.

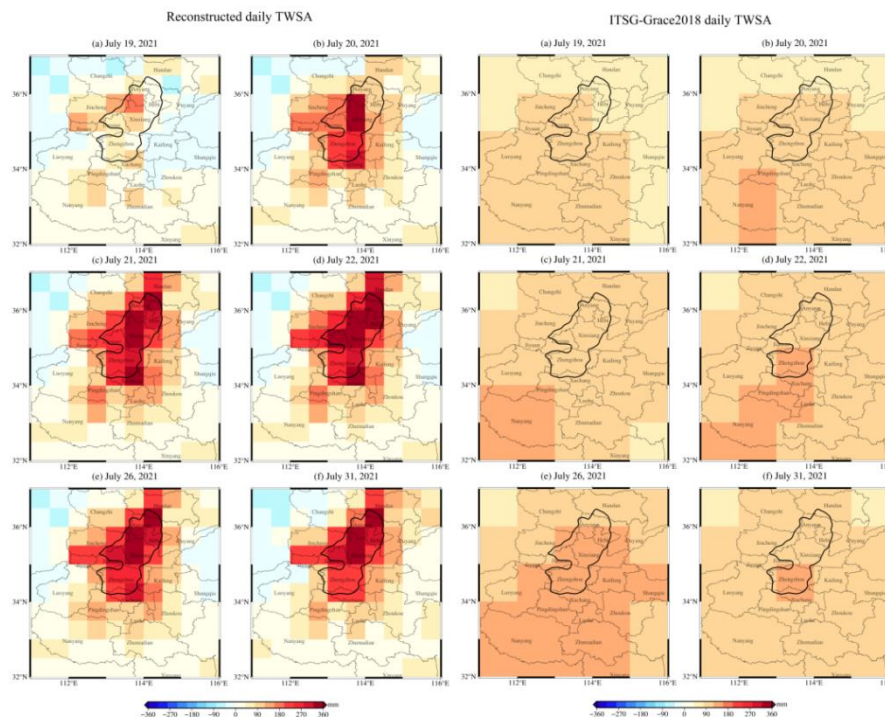


Figure 1 The left panels are the spatial distributions of reconstructed daily TWSA ( $0.5^\circ \times 0.5^\circ$ ), while the right panels are ITSG-Grace2018 daily TWSA ( $1^\circ \times 1^\circ$ ) with the seasonal cycle and the linear trend removed (Xiao et al. 2022).

## Cryosphere

Geodetic observations of cryospheric changes have continued to be advanced diversified in both methodological development and applications. Chinese geodesists have made growingly important contributions to the polar studies, with a strong focus on the Tibetan Plateau and its surrounding high-altitude regions, collected known as High Mountain Asia or the third pole, and the Greenland and Antarctica Ice Sheets.

Zhang et al. (2020) improved the estimates of secular variation of Greenland ice mass by introducing a stochastic process described using a forward-backward Kalman Filter into the time series analysis of GRACE data. They obtained an accelerated loss of Greenland ice mass of  $1.6 \text{ Gt/yr}^2$  during 2003-2017 and showed that this seemingly smaller acceleration than the reported ones from some of the previous studies was attributed to their better separation of acceleration from irregular interannual variations. Su et al. (2020) found that low-degree spherical harmonic coefficients, including degree-one terms and degree-two/three zonal terms, have a significant impact on estimating mass changes of the Greenland and Antarctic ice sheets using GRACE gravimetry. Ran et al. (2021) compared mascon products with mascon solutions computed in-house using a varying regularization parameter. They found that the observed discrepancies are likely dominated by differences in the applied regularization. They proposed an improved regularization scheme to estimate the mass change of the Greenland ice sheet. Liu et al. (2022) further developed the method and proposed a statistical model suitable for the reconstruction of GRACE-like high mountain glaciers (HMG) mass anomalies. Precipitation



and temperature are the only inputs. They reconstructed and evaluated the HMG mass anomaly time series in 14 HMG regions, and the results show high consistent with GRACE/GRACE-FO observations. Li et al., (2020), and Wang et al. (2023) reported that the inter-annual mass variations of Greenland and their spatial characteristics as observed from GRACE and GRACE-FO were correlated with large-scale atmospheric-ocean oscillations and warranted further investigations into the physical mechanisms.

## **2 Satellite Altimetry**

Traditional altimetry has successfully been used to measure global and regional sea level changes (e.g., Li et al., 2021; Chen et al. 2022; Wang et al. 2022). The large footprint limited its application on the alpine glacier. The ice tracking satellites ICESat & ICESat-2 and CryoSat-2 were the dominant approach to derive time-dependent elevation over glacier surfaces, due to their small footprint size.

Recently, Chinese scholars have estimated glacier mass balance in mountain regions by altimetry. Wang et al., (2021) combined ICESat and ICESat-2 data to survey the glacier thickness change in High Mountain Asia (HMA) over 2003-2019 and use independent gravity satellite data to fill the gap of ICESat. Shen et al., (2022) developed an elevation-aspect bin from elevation bin to estimate glaciers' inter-annual and intra-annual elevation changes based on ICESat & ICESat-2 over 2003-2020. Fan et al., (2022) calculated the elevation difference between ICESat-2 and NASA DEM to represent glacier mass balance over 2000-2021. Zhao et al., (2022) integrate ICESat, CryoSat-2, and ICESat-2 to provide high spatiotemporal glacier mass balance in southeastern Tibet. Wang and Sun (2022) used a new approach to obtain the complete seasonal cycle of glacier thickness changes in HMA.

## **3 GNSS/InSAR**

### **Mass loading and deformation**

GNSS data provides high precision measurements of the Earth's surface displacements, which can be used to study various geophysical phenomena, including mass loading. To solve the ill-posed problem of GNSS inversion for regional mass loading based on loading Green's function theory, some improved estimation strategies (e.g., construction of regularization constraint matrix, estimation of optimal regularization parameter) are presented to improve the reliability and stability of GNSS-derived TWS changes (Li et al., 2022a, 2022b, 2023). The GNSS-derived TWS changes present higher temporal (daily) and spatial (dozens of kilometers) resolution than the GRACE/GFO estimates where GNSS stations are densely distributed, and the GNSS-inferred TWSA can well bridge the data gap of GRACE/GFO estimates (Li et al., 2023; Jiang et al., 2021).

Wang et al. (2017) used the GNSS station network to monitor the changes in groundwater reserves in the Three Gorges area. The results were then compared with the water level from groundwater monitoring wells. Li et al. (2023) proposed a fusion method for inverting regional GWS changes by integrating GNSS and GRACE data. Regional GWSA are inverted by using loading Green's function method and the spherical harmonic function method, which use GNSS

and GRACE data, respectively. On this basis, the remove–restore theory in Earth’s gravity field is introduced to fuse the two results from GNSS and GRACE, thus obtaining more reliable spatiotemporal changes in regional GWS in the Shaanxi–Gansu–Ningxia of China.

Wang et al. (2022) examined mass load inversion using a combination of both horizontal and vertical GNSS displacements and found that including horizontal displacements led to approximately a 10% improvement in mass inversion for the current precision level of GNSS. Moreover, through synthetic experiments, they predicted a further improvement of approximately 20% to 30% with a higher GNSS precision level.

Pan et al. (2019) proposed a joint inversion method of GNSS and GRACE to estimate the partitioning of vertical deformation to glacial and tectonic sources. The results showed that the elastic effects of glacier melting accounted for 0.39 mm/year of the average ground uplift rate of  $0.72 \pm 0.12$  mm/year. In another study, Pan et al. (2023) found that the continuous water deficit throughout Tianshan and Pamir mainly located in glacier-covered areas, leading to spatial surface uplifting at rates of approximately 0.2–0.5 mm/yr. For Mainland China, Pan et al. (2021) used the GRACE/GRACE-FO products to isolate tectonic deformation signals at GPS sites within mainland China from 2002 to 2019. The results revealed the long-term spatial patterns of vertical tectonic motion in different blocks in mainland China. For the Tibetan Plateau, Jiao et al. (2019) found a rather poor correlation between satellite gravimetry and hydrological data in the interior basin. They separated the hydrological signal from satellite gravimetry using GNSS and other space geodesy data and concluded that the residual signals in the Tibetan Plateau should be attributed to deep tectonics.

### **Land Subsidence and Groundwater Depletion**

The InSAR technique, together with GNSS and GRACE, has been frequently used in quantifying land subsidence and investigating groundwater depletion. Tang et al. (2022) evaluated the effects of the water transfer from the Yellow River to Taiyuan basin and suggested that subsidence rates in the subsidence areas of the Taiyuan Basin reduced by up to ~70% in the period of 2017–2020 with respect to the period of 2007–2010. Similar studies were performed in SuZhou (Shi et al., 2021), Tianjin-Langfang (Shi et al., 2022), and Wuhan (Zhao et al., 2022). These studies provide crucial information for sustainable groundwater management practices.

Deep groundwater (confined groundwater) is the major water source in the North China Plain (NCP). Long-term deep groundwater overexploitation has resulted in substantial groundwater storage (GWS) depletion, which has been detected by GRACE (Feng et al. 2013, 2018). Quantifying the influence of long-term overexploitation on deep groundwater resources is extremely important to maintain the sustainability of the confined aquifer system. Bai et al. (2021) presented a new method to estimate the total exploitable GWS and the total GWS depletion since the 1960s, by combining use of the InSAR deformation, hydraulic head observations and hydrogeological data. The total exploitable GWS in Cangzhou was  $26.1 \pm 21.3$  km<sup>3</sup> and decreased by  $13.0 \pm 8.1$  km<sup>3</sup>~ $13.6 \pm 8.5$  km<sup>3</sup> until 2010, accounting for 49.8%~52.2% of the total amount. It is worth noting that 87.4%~87.9% of the total GWS depletion is irreversible, leading to a substantial permanent loss of groundwater storage capacity.

### **Cryosphere**

Frozen ground, defined by subsurface temperature, is not a typical target for geodesy but has

been recently tackled using InSAR and GNSS Reflectometry. Chen J. et al. (2022) combined InSAR ground deformation with an independent multivariate statistical method to isolate the cyclic seasonal component of the surface displacements related to active layer freeze and thaw from other signal components. Their results suggested a net increase of active layer water content of about 8 cm equivalent water thickness and widespread intensification of the surficial water cycle in central Tibet. By equaling the multi-year trends in surface subsidence as the volume change of ground ice, Wang L. et al. (2022) estimated a ground ice loss rate from permafrost degradation in the Selin Co basin, which contributed about 12% of the observed increase of lake volume in Selin Co.

GNSS-Interferometric Reflectometry (GNSS-IR), an unconventional method using reflected GNSS signals, enables estimates of snow depth around numerous geodetic-level continuous GNSS sites with a typical footprint of 1000 m<sup>2</sup>. Zhang Z.Y. et al. (2020) conducted the first comprehensive data mining study in which we screened seven major open-data GNSS networks to identify what sites are suitable for using GNSS-IR for permafrost studies. From the 186 continuously operating sites located in the Arctic permafrost areas, they identified 23 usable ones, the majority of which are located in northern Canada and Alaska. Applying GNSS-IR to 80 GNSS sites across northern China, Wan et al. (2022) generated the GSnow-CHINA product that includes snow depth time series at 2-to-24-hour intervals spanning 2013 to 2022. Such a new dataset is complementary to the current point measurements and remote sensing products, opening new opportunities for water resource management and regional climate modeling.

### 4 Surface Gravimetry

#### Estimation of regional water storage with superconducting gravimetry

He et al. (2022) proposed a new method for implementing the quantitative separation of the vadose zone water storage changes with superconducting gravimetry. The new method is validated with observations from a superconducting gravimeter (GWR-C032) at the National Geodetic Observation Station in Wuhan, China, and also with theoretical results computed by the local hydrological modeling method. Xing et al. (2022) assessed the local deep groundwater storage changes in a karst aquifer by using a more than 4-year record (2017–2021) of the superconducting gravimeter OSG-066 located at the Lijiang station.

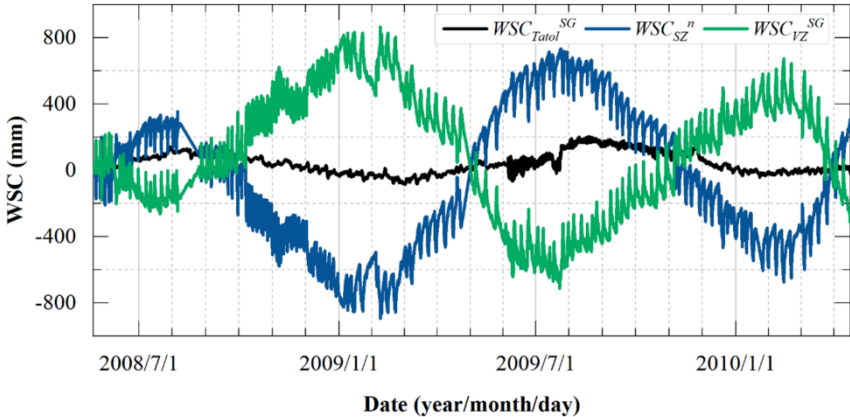


Figure2. Water storage changes at Wuhan SG Station quantitatively separated using the superconducting gravity technique. (He et al., 2022)

## Large Reservoirs and Basins

Wang et al. (2021) investigated the 2020 flood events and the spatio-temporal variations of Yangtze River of China using multiscale combination of GRACE and gPhone data. Wang et al. (2019) estimated the TWSA of China's Three Gorges Reservoir (TGR) using GRACE data and global hydrology models, and presented the main contribution of seepage variability to the difference between GRACE-based estimation and in-situ volume measurements. Ma et al. (2020) used Gaofen-1 (GF-1) satellite data and in-situ water level observations to developed a high-resolution dynamic model of TGR water storage. Wang et al. (2020) presented a framework to evaluate GRACE mascon products based on in-situ GPS measurements from the Yangtze River Basin (YRB) in China, and found more consistency between CSR mascon and in-situ observations.

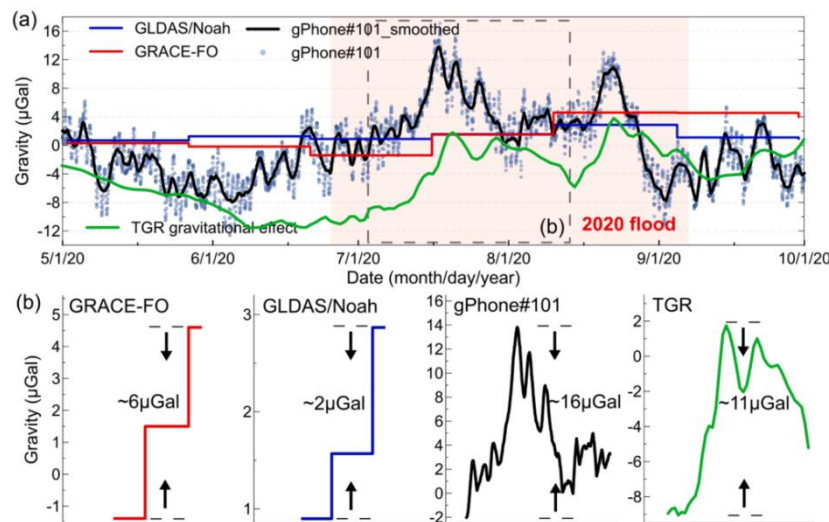


Figure3. The different gravity sensors and model, at gPhone#101 location, response to TWS changes in TGR during 2020 flood season (Wang et al., 2021).

## Bibliography

- Bai L, Jiang L, Zhao Y et al (2022). Quantifying the influence of long-term overexploitation on deep groundwater resources across Cangzhou in the North China Plain using InSAR measurements. *Journal of Hydrology* 605: 127368
- Bai H, Ming Z, Zhong Y et al (2022). Evaluation of evapotranspiration for exorheic basins in China using an improved estimate of terrestrial water storage change. *Journal of Hydrology* 610: 127885
- Chen Q, Wang F, Shen Y et al (2022). Monthly gravity field solutions from early LEO satellites' observations contribute to global ocean mass change estimates over 1993~2004. *Geophysical Research Letters* 49(21): e2022GL099917
- Chen J, Wu T, Liu L et al (2022). Increased Water Content in the Active Layer Revealed by Regional-Scale InSAR and Independent Component Analysis on the Central Qinghai-Tibet Plateau. *Geophysical Research Letters* 49(15): e2021GL097586
- Feng W, Shum C K, Zhong M et al (2018). Groundwater storage changes in China from satellite gravity: An overview. *Remote Sensing* 10(5): 674

- Feng W, Zhong M, Lemoine J M et al (2013). Evaluation of groundwater depletion in North China using the Gravity Recovery and Climate Experiment (GRACE) data and ground-based measurements. *Water Resources Research* 49(4): 2110-2118
- Ferreira V G, Yong B, Tourian M J et al (2020). Characterization of the hydro-geological regime of Yangtze River basin using remotely-sensed and modeled products. *Science of the Total Environment* 718: 137354
- Fan Y, Ke C Q, Zhou X et al (2023). Glacier mass-balance estimates over High Mountain Asia from 2000 to 2021 based on ICESat-2 and NASADEM. *Journal of Glaciology* 69(275): 500-512
- He Q, Chen X, Sun H et al (2022). Quantitative separation of the local vadose zone water storage changes using the superconductive gravity technique. *Journal of Hydrology* 609: 127734
- Jiang Z, Hsu Y J, Yuan L et al (2021). Characterizing spatiotemporal patterns of terrestrial water storage variations using GNSS vertical data in Sichuan, China. *Journal of Geophysical Research: Solid Earth* 126(12): e2021JB022398
- Jiao J, Zhang Y, Yin P et al (2019). Changing Moho Beneath the Tibetan plateau revealed by GRACE observations. *Journal of Geophysical Research: Solid Earth* 124(6): 5907-5923
- Li Z, Zhang Z, Scanlon B R et al (2022). Combining GRACE and satellite altimetry data to detect change in sediment load to the Bohai Sea. *Science of The Total Environment* 818: 151677
- Li W, Shum C K, Li F et al (2020). Contributions of Greenland GPS observed deformation from multisource mass loading induced seasonal and transient signals. *Geophysical Research Letters* 47(15): e2020GL088627
- Li W, Zhang C, Wang W et al (2023). Inversion of Regional Groundwater Storage Changes Based on the Fusion of GNSS and GRACE Data: A Case Study of Shaanxi–Gansu–Ningxia. *Remote Sensing* 15(2): 520
- Li X, Zhong B, Li J et al (2022). Analysis of terrestrial water storage changes in the Shaan-Gan-Ning Region using GPS and GRACE/GFO. *Geodesy and Geodynamics* 13(2): 179-188
- Li Xianpao, Zhong Bo, Liu Tao (2022). Simulation Analysis of Inverting Regional Surface Mass Variations Using GNSS Vertical Displacement. *Geomatics and Information Science of Wuhan University* 47(1): 45-54
- Li X, Zhong B, Li J et al (2023). Inversion of terrestrial water storage changes from GNSS vertical displacements using a priori constraint: A case study of the Yunnan Province, China. *Journal of Hydrology* : 129126
- Liu B, Zou X, Yi S et al (2022). Reconstructing GRACE-like time series of high mountain glacier mass anomalies. *Remote Sensing of Environment* 280: 113177
- Ma X, Wang L, Chen C et al (2020). Simulation of the dynamic water storage and its gravitational effect in the head region of three gorges reservoir using imageries of gaofen-1. *Remote Sensing* 12(20): 3353
- Pan Y, Chen R, Yi S et al (2019). Contemporary mountain-building of the Tianshan and its relevance to geodynamics constrained by integrating GPS and GRACE measurements. *Journal of Geophysical Research: Solid Earth* 124(11): 12171-12188
- Pan Y, Hammond W C, Ding H et al (2021). GPS Imaging of Vertical Bedrock Displacements: Quantification of Two-Dimensional Vertical Crustal Deformation in China. *Journal of Geophysical Research: Solid Earth* 126(4): e2020JB020951
- Pan Y, Jiang W, Ding H et al (2023). Intradecadal Fluctuations and Three-dimensional Crustal Kinematic Deformation of the Tianshan and Pamir derived from Multi-Geodetic Imaging. *Journal of Geophysical Research: Solid Earth* 128(1):e2022JB025325
- Qu W, Jin Z, Zhang Q et al (2022). Estimation of evapotranspiration in the yellow river basin from 2002 to 2020 based on GRACE and GRACE follow-on observations. *Remote Sensing* 14(3): 730
- Ran J, Ditmar P, Liu L et al (2021). Analysis and mitigation of biases in Greenland ice sheet mass balance trend estimates from

- GRACE mascon products. *Journal of Geophysical Research: Solid Earth* 126(7): e2020JB020880
- Shen C, Jia L, Ren S. (2022). Inter-and intra-annual glacier elevation change in high mountain Asia region based on ICESat-1&2 data using elevation-aspect bin analysis method. *Remote Sensing* 14(7): 1630
- Shi G, Ma P, Hu X et al (2021). Surface response and subsurface features during the restriction of groundwater exploitation in Suzhou (China) inferred from decadal SAR interferometry. *Remote Sensing of Environment* 256: 112327
- Shi X, Zhu T, Tang W et al (2022). Inferring decelerated land subsidence and groundwater storage dynamics in Tianjin–Langfang using Sentinel-1 InSAR. *International Journal of Digital Earth* 15(1): 1526-1546
- Su X, Guo J, Shum C K et al (2020). Increased low degree spherical harmonic influences on polar ice sheet mass change derived from GRACE Mission. *Remote Sensing* 12(24): 4178
- Sun Y, Li Y, Guo X et al (2023). Estimating C30 coefficients for GRACE/GRACE-FO time-variable gravity field models using the GRACE-OBP approach. *Journal of Geodesy* 97(3): 20
- Sun Y, Riva R (2020). A global semi-empirical glacial isostatic adjustment (GIA) model based on Gravity Recovery and Climate Experiment (GRACE) data. *Earth System Dynamics* 11(1): 129-137
- Sun Y, Riva R, Ditmar P et al (2019). Using GRACE to explain variations in the Earth's oblateness. *Geophysical Research Letters* 46(1): 158-168
- Tang W, Zhao X, Motagh M et al (2022). Land subsidence and rebound in the Taiyuan basin, northern China, in the context of inter-basin water transfer and groundwater management. *Remote Sensing of Environment* 269: 112792
- Wan W, Zhang J, Dai L et al (2022). A new snow depth data set over northern China derived using GNSS interferometric reflectometry from a continuously operating network (GSnow-CHINA v1. 0, 2013–2022). *Earth System Science Data* 14(8): 3549-3571
- Wang F, Shen Y, Chen Q et al (2021). Bridging the gap between GRACE and GRACE follow-on monthly gravity field solutions using improved multichannel singular spectrum analysis. *Journal of Hydrology* 594: 125972
- Wang F, Shen Y, Chen Q et al (2022). Revisiting sea-level budget by considering all potential impact factors for global mean sea-level change estimation. *Scientific Reports* 12(1): 10251
- Wang L, Kaban M K, Thomas M, et al (2019). The challenge of spatial resolutions for GRACE-based estimates volume changes of larger man-made lake: the case of China's Three Gorges Reservoir in the Yangtze River. *Remote Sensing* 11(1): 99
- Wang L, Chen C, Ma X et al (2020). Evaluation of GRACE mascon solutions using in-situ geodetic data: The case of hydrologic-induced crust displacement in the Yangtze River Basin. *Science of the Total Environment* 707: 135606
- Wang L, Peng Z, Ma X et al (2021). Multiscale gravity measurements to characterize 2020 flood events and their spatio-temporal evolution in Yangtze river of China. *Journal of Hydrology* 603: 127176
- Wang L, Zhao L, Zhou H et al (2022). Contribution of ground ice melting to the expansion of Selin Co (lake) on the Tibetan Plateau. *The Cryosphere* 16(7): 2745-2767
- Wang Q, Sun W. (2022). Seasonal Cycles of High Mountain Asia Glacier Surface Elevation Detected by ICESat-2. *Journal of Geophysical Research: Atmospheres* 127(23), e2022JD037501
- Wang Q, Yi S, Sun W. (2021). Continuous estimates of glacier mass balance in high mountain Asia based on ICESat-1, 2 and GRACE/GRACE follow-on data. *Geophysical Research Letters*, 48(2): e2020GL090954
- Wang S Y, Li J, Chen J et al (2022). On the improvement of mass load inversion with GNSS horizontal deformation: a synthetic study in Central China. *Journal of Geophysical Research: Solid Earth* 127(10): e2021JB023696
- Wang W, Zhang C, Liang S et al (2017). Monitoring of the temporal and spatial variation of groundwater storage in the Three Gorges area based on the CORS network. *Journal of Applied Geophysics* 146: 160-166

- Wang Z, Zhang B, Yao Y et al (2023). GRACE and mass budget method reveal decelerated ice loss in east Greenland in the past decade. *Remote Sensing of Environment* 286: 113450
- Xiao C, Zhong Y, Feng W et al (2022). Monitoring the Catastrophic Flood With GRACE-FO and Near-Real-Time Precipitation Data in Northern Henan Province of China in July 2021. *IEEE Journal of Selected Topics in Applied Earth Observations and Remote Sensing* 16: 89-101
- Xie J, Xu Y P, Yu H et al (2022). Monitoring the extreme flood events in the Yangtze River basin based on GRACE and GRACE-FO satellite data. *Hydrology and Earth System Sciences* 26(22): 5933-5954
- Xing L, Niu X, Bai L et al (2022). Monitoring groundwater storage changes in a Karst aquifer using superconducting gravimeter OSG-066 at the Lijiang station in China. *Pure and Applied Geophysics* 179(5): 1853-1870
- Xiong J, Yin J, Guo S (2021). Integrated flood potential index for flood monitoring in the GRACE era. *Journal of Hydrology* 603: 127115
- Yi S, Sneeuw N. (2021). Filling the data gaps within GRACE missions using singular spectrum analysis. *Journal of Geophysical Research: Solid Earth* 126(5): e2020JB021227
- Yi S, Sneeuw N. (2022). A novel spatial filter to reduce north–south striping noise in GRACE spherical harmonic coefficients. *Journal of Geodesy* 96(4): 23
- Zhang Z, Guo F, Zhang X. (2020). Triple-frequency multi-GNSS reflectometry snow depth retrieval by using clustering and normalization algorithm to compensate terrain variation. *GPS Solutions* 24: 1-18
- Zhang C, C.K. Shum, Ales B et al (2021). Rapid Mass Loss in West Antarctica Revealed by Swarm Gravimetry in the Absence of GRACE, *Geophys. Res. Lett.* 48, e2021GL095141. <https://doi.org/10.1029/2021GL095141>
- Zhang B, Liu L, Yao Y et al (2020). Improving the estimate of the secular variation of Greenland ice mass in the recent decades by incorporating a stochastic process, *Earth and Planetary Science Letters* 549, 116518
- Zhao F, Long D, Li X et al (2022). Rapid glacier mass loss in the Southeastern Tibetan Plateau since the year 2000 from satellite observations, *Remote Sensing of Environment* 270, 112853
- Zhao Y, Zhou L, Wang C et al (2022). Analysis of the spatial and temporal evolution of land subsidence in Wuhan, China from 2017 to 2021. *Remote Sensing* 14(13), 3142
- Zhong B, Li Q, Chen J, Luo Z (2022). A dataset of GRACE intersatellite geopotential differences from April 2002 to July 2016 (Version V2), *Science Data Bank*
- Zhong B, Li Q, Chen J et al (2020). Improved Estimation of Regional Surface Mass Variations from GRACE Intersatellite Geopotential Differences Using a Priori Constraints. *Remote Sensing* 12(16), 2553
- Zhong B, Li Q, Li X et al (2023). Basin-scale terrestrial water storage changes inferred from GRACE-based geopotential differences: A case study of the Yangtze River Basin, China. *Geophysical Journal International* 233(2): 1318–1338
- Zhong B, Tan J, Li Q et al (2021). Simulation analysis of regional surface mass anomalies inversion based on different types of constraints. *Geodesy and Geodynamics* 12(4): 298–307
- Zhong Y, Zhong M, Feng W et al (2020). Evaluation of the Evapotranspiration in the West Liaohe River Basin Based on GRACE Satellite and in Situ Measurements. *Geomatics and Information Science of Wuhan University* 45: 173-178
- Zhong Y, Zhong M, Mao Y et al (2020). Evaluation of Evapotranspiration for Exorheic Catchments of China during the GRACE Era: From a Water Balance Perspective. *Remote Sens.* 12(3): 511



# 2019-2022 CHINA NATIONAL REPORT on Geomagnetism and Aeronomy

For  
The 28th IUGG General Assembly  
Berlin, Germany, July 11-20, 2023

Chinese Committee for IAGA (CNC-IAGA)  
June, 2023

# Recent Advance in the Solar Wind Magnetosphere Ionosphere Link Explorer (SMILE) Mission

WANG Chi<sup>1\*</sup> BRANDUARDI-RAYMONT Graziella<sup>2</sup> ESCOUBET C P<sup>3</sup>

1 (State Key Laboratory of Space Weather, National Space Science Center, Chinese Academy of Sciences, Beijing 100190)

2 (Mullard Space Science Laboratory, University College London, London RH5 6NT)

3 (European Space Agency/European Space Research and Technology Centre, Noordwijk 2201 AZ)

\* E-mail: [cw@spaceweather.ac.cn](mailto:cw@spaceweather.ac.cn)

## Abstract

The SMILE (Solar wind Magnetosphere Ionosphere Link Explorer) mission is a joint space science mission between the European Space Agency (ESA) and the Chinese Academy of Sciences (CAS), aiming to understand the interaction of the solar wind with the Earth's magnetosphere in a global manner. The mission was adopted by CAS in November 2016 and by ESA in March 2019 with a target launch date in the early of 2025. We report the progress of SMILE mission by the end of 2022.

## Key words

SMILE, Soft X-ray Imager (SXI), Ultra-Violet Imager (UVI), Light Ion Analyzer (LIA), MAGnetometer (MAG)

## 1 Introduction

The SMILE<sup>[1]</sup> mission is a joint ESA and CAS space science mission, which aims at deepening our understanding of the interaction of the solar wind with the Earth's magnetosphere by making global images of the dayside magnetosheath and cusps of the magnetosphere, and the aurora at the North Pole simultaneously, while monitoring the in-situ plasma environment. The mission was adopted by CAS in November, 2016 and by ESA in March 2019.

CAS is responsible for the development of satellite Platform (PF), Telecommand and Telemetry, Science Application System (SAS) as well as Ground Support System (GSS), and provides MAGnetometer (MAG), Light Ion Analyzer (LIA) and Ultraviolet Imager (UVI) measurement instruments. ESA is responsible for the development of Payload Module (PLM), Launch

Vehicle, Launch Site, and science operation and ground receiving station supports when necessary, and also the development of the Soft X-ray Imager (SXI), intensifiers, mirrors with coating and calibration of UVI.

The SMILE Mission will use novel soft X-ray imaging technology to obtain, for the first time, the global image of the large-scale structures of the geospace. This is critical to quantitatively analyzing and understanding of the global feature of the magnetosphere.

The interaction of the solar wind with the Earth's atmosphere leads to the formation of the large structures of the magnetosphere, including the bow shock, magnetopause, and the cusp regions. The position and shape of the magnetopause and cusps change constantly as the Earth's magnetosphere responds to the varying solar wind dynamic pressures and interplanetary

magnetic field orientations. Both the fast and slow solar wind can be interrupted by large, fast-moving bursts of plasma called interplanetary Coronal Mass Ejections (CMEs). When a CME impacts the Earth's magnetosphere, it temporarily deforms the Earth's magnetic field, changing its direction and strength, and induces large electrical currents; this is called a geomagnetic storm and it is a global phenomenon. The southward interplanetary magnetic fields, as presented in a CME event, could induce magnetic reconnection in the Earth's magnetotail; this process accelerates protons and electrons downward toward the Earth's atmosphere, where they form the aurora, resulting in substorms.

The Scientific objectives of the SMILE mission are summarized as: (i) explore the fundamental modes of the dayside solar wind/magnetosphere interaction; (ii) understand the substorm cycle; (iii) determine how CME-driven storms arise and their relationship to substorms.

## 2 Modeling Update

The SMILE Modelling Working Group (MWG) performs studies on the predictions of X-ray signals and the reconstruction techniques from X-ray images to 3D magnetopause. Four approaches have been developed previously to derive the magnetopause position from X-ray images, including the Boundary Fitting Approach (BFA), Tangent Fitting Approach (TFA), Tangential Direction Approach (TDA), and Computed Tomography Approach (CTA). It is found that the 3D X-ray emissivity in the magnetosheath can be reconstructed based on the CTA, if tens of images are provided from different viewing geometries under the same or similar solar wind conditions (see Fig. 1)<sup>[2]</sup>. To obtain the images required to better perform the CTA, 87 different orbit locations are considered during one year to allow wide-angle coverage resulting from orbital precession. However the assumption that the magnetopause position does not change during the one year is not valid, preventing the application of CTA. This problem can be solved by dividing the solar wind conditions into several bins, and assuming that the magnetopause position corresponding to each solar wind bin is the same. An alternative way is through

machine learning techniques<sup>[3]</sup>. A 3D GAN network is applied to supplement 2D X-ray images collected at finite angles within limited orbital time during which the magnetopause is almost static. By deriving the information about cusps from the X-ray image, it is revealed that the tangent direction of the cusp boundary is the direction with the appreciable increase of local standard deviation in X-ray intensity<sup>[4]</sup>. The Instrument simulations are also performed to provide the photo

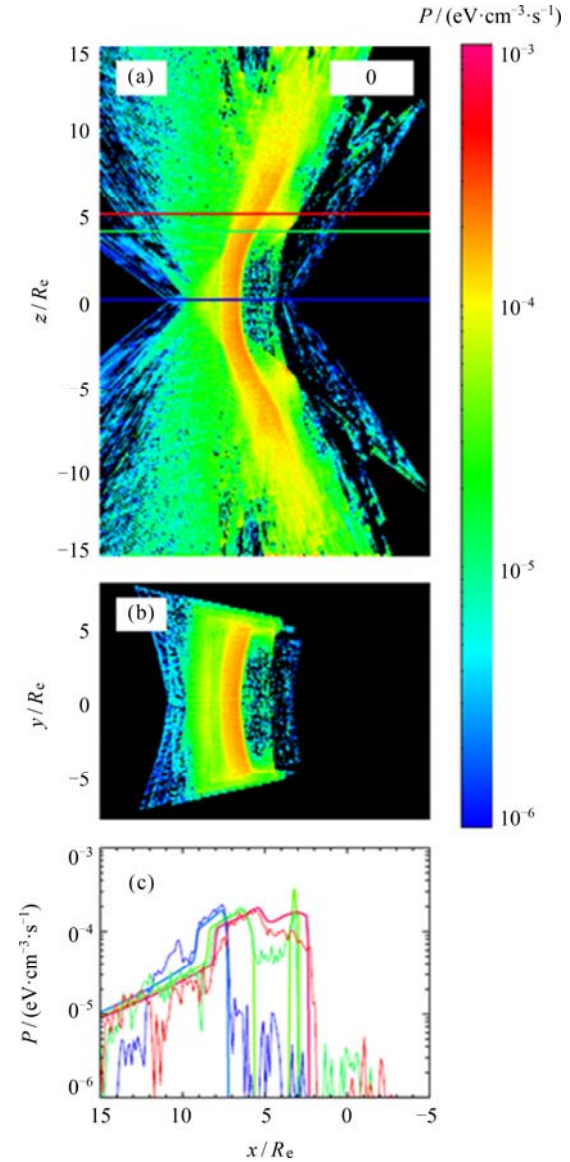


**Fig. 1** Reconstructed X-ray emissivity on the noon-midnight meridian plane (a), equatorial plane (b), and along the three lines marked in the top panel (c) based on the CT Approach

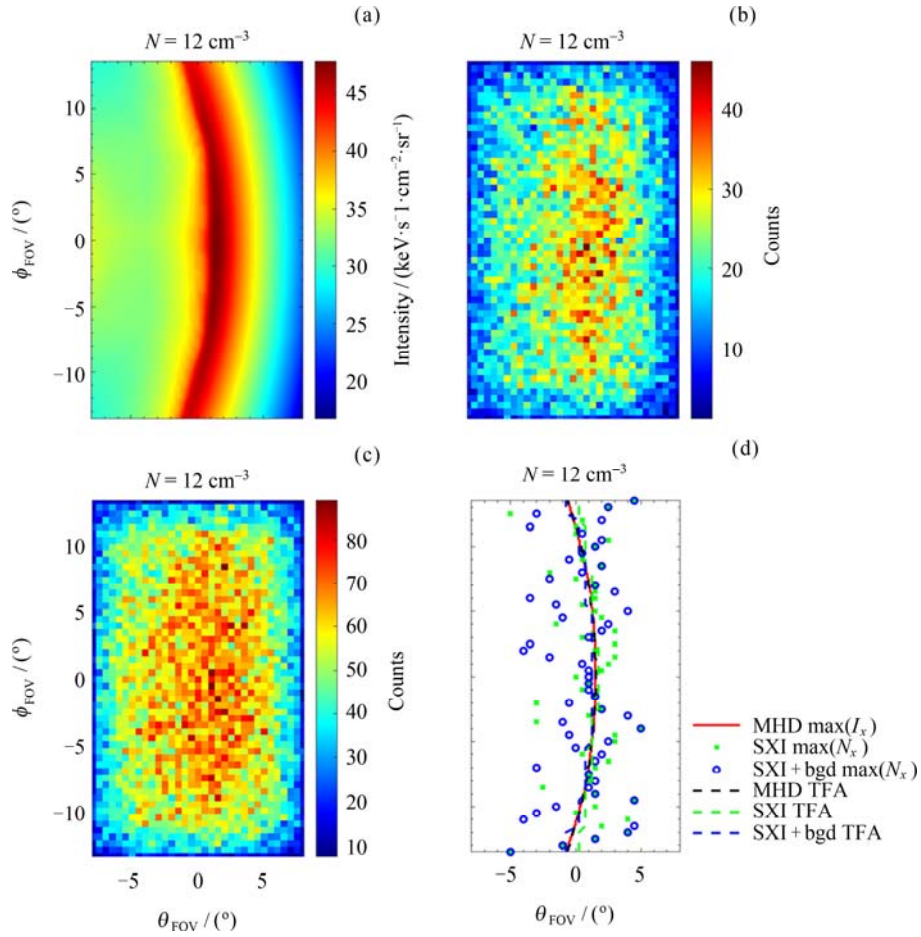


**Fig. 2** Instrument simulations of the X-ray photon counts. (a) X-ray image inside field of view of SXI. (b) SXI photon counts image corresponding to (a) without sky background. (c) SXI image after adding the constant sky background. (d) The X-ray maximum intensity of MHD and SXI photon counts images, and their best match curves by using TFA

counts images expected to be observed by the SXI instrument. The effectiveness of TFA is validated based on the simulated photon counts images (see Fig. 2)<sup>[5]</sup>.

### 3 Mission Update

#### 3.1 Satellite System

The science orbit is a highly elliptical orbit with the apogee altitude of about  $19 R_e$  and a perigee of about 5000 km. The inclination is  $73^\circ$  if launched with Vega-C as the baseline, or  $98.2^\circ$  with Ariane 62.

SMILE is a three-axis stabilized satellite which consists of Platform (PF) and Payload Module (PLM). The total mass of the satellite is less than 2250 kg including fuel that takes about 2/3 of the launch mass.

The science data will be downlinked by an X-band transmitter with a data volume of 47 Gbit per orbit. The telemetry and telecommand will go through Unified S-band TT&C system. The nominal life time is 3 years by launch and with the possibility to extend the mission

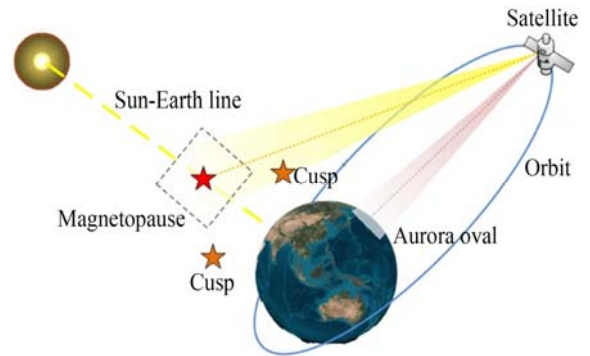


**Fig. 3** SMILE satellite HEO orbit

another 2 years. Fig. 3 and Fig. 4 show SMILE satellite HEO orbit and structure.

SXI for imaging magnetopause and cusps has passed Preliminary Design Review (PDR) and Structural Model (STM) environment test. The SXI Critical Design Review (CDR) was conducted in December of 2022 (see Fig. 5).

UVI to image the Earth aurora is jointly developed by



CAS and ESA. It's CDR is planned to be conducted in August of 2023 (see Fig. 6).

MAG to measure the magnetic field has finished PDR. MAG Engineering Model (EM) and MAG STM were delivered to Airbus for Assembly, Integration and Test (AIT) in 2021. MAG BOOM Qualification Model (QM) has been successfully deployed under the control of PLM in ESTEC (see Fig. 7). The CDR for MAG will be

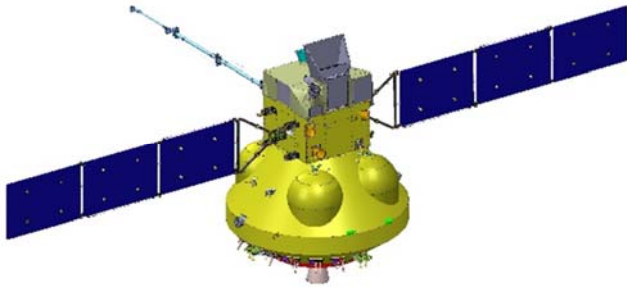


**Fig. 4** Diagram of the satellite structure



**Fig. 5** SXI STM on a shaker table at RAL, UK

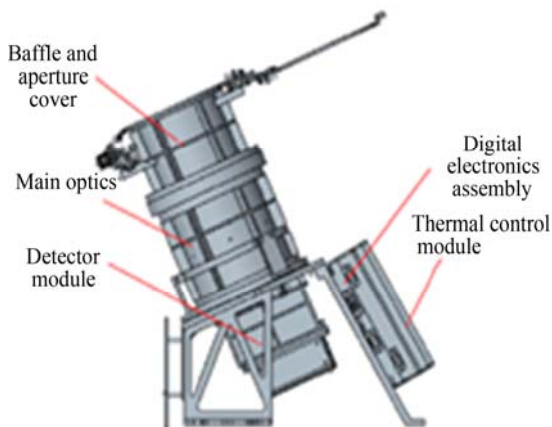


**Fig. 6** UVI assembly

conducted in January of 2023.

LIA instrument to monitor the in-situ plasma environment has passed PDR. LIA EM and Reduced EM (REM) have been delivered to PLM for the test (see Fig. 8). It's CDR was conducted in October of 2022.

Payload Module (PLM) which hosts SXI, UVI, MAG and X-band science downlink transmitter has finished PDR. PLM STM was integrated with instruments and has passed mechanical and thermal tests (see Fig. 9). PLM also has finished functional and electric tests with MAG and LIA. PLM STM was delivered to China in March of 2022. It is planned to begin PLM CDR at the beginning of 2023.

The Platform (PF) provides service for the whole satellite. PF also provides propellants and thruster for orbit maneuver from the insertion orbit to the HEO science orbit. PF also hosts two LIA sensors for  $4\pi$  space measurement. All the PF QM units have been delivered to PF and have passed electrical interface and functional tests (see Fig. 9). PF QM has been assembled and will pass the qualification level tests with PLM STM later (see Fig. 10). PF CDR will be conducted in January of 2023.



**Fig. 7** MAG BOOM deployment test in ESTEC



**Fig. 8** LIA electrical interface test in Airbus

Satellite STM has passed environment test in China in 2020. In April of 2022, Satellite QM AIT campaign started with PF QM and PLM STM in China. Satellite qualification level test has been performed from April to August of 2022. After satellite qualification level test, we finished the fitness and separation tests with launch adapter in ESTEC in September of 2022.

The electrical interface test will be performed in Madrid in June of 2023. The mission CDR is scheduled in the late of June, 2023. Fig. 11 showed satellite STM on the shaker.

### 3.2 Launch Vehicle

A single launch Vehicle is ESA's responsibility. The baseline is single launching in Kourou with Vega-C. Vega-C is a solid launch vehicle. The launch capability is no less than 2250 kg for 700 km circular injection orbit or 2300 kg for 450 km×700 km injection orbit.

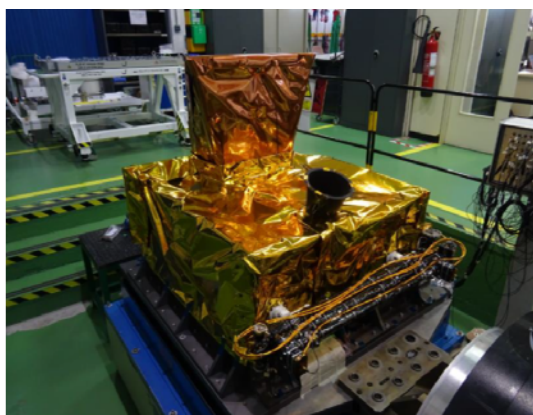


Fig. 9 PLM STM on shaker in ESTEC



Fig. 10 PF electrical interface test

### 3.3 Launch Site

SMILE will be launched in Kourou. ESA is responsible for the Launch Site and Launch service, and will provide the ground segment support and logistics.

### 3.4 TC/TM

China Satellite Launch and Tracking Control General (CLTC) will be responsible for the TC/TM of SMILE satellite. European Space Operation Center (ESOC) will be responsible for the TC/TM before the satellite's separation with the Launch Vehicle. In addition, ESA will also provide ground station support for orbit transfer from injection orbit to HEO science orbit and in case of emergency. Satellite QM to ground S-band interface compatibility test was successful in 2020 (see Fig. 12).

### 3.5 Ground Support System (GSS)

GSS has been constructed in China during the 12th Five-Year Plan Period and it will undergo some modifications according to the new requirements of the space science missions during the 13th Five-Year Plan Period. It is mainly responsible for the operation and management of the payloads, scientific data receiving, processing and distribution to the science community.

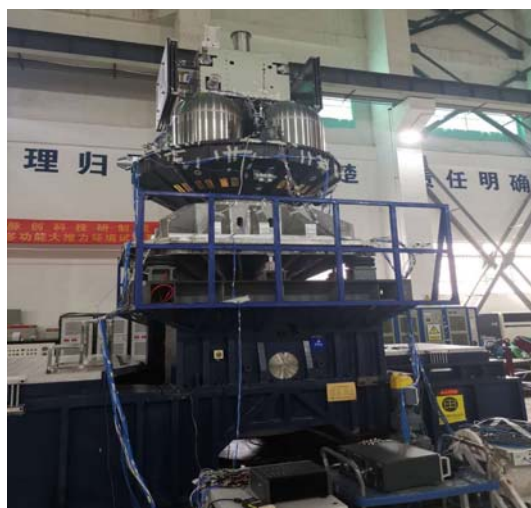


Fig. 11 Satellite STM on the shaker



Fig. 12 Satellite to ground S-band interface compatibility test

GSS has finished PDR. Some core software has finished requirement analysis and design. It has started joint test the Docker operation environment. The joint CDR for GSS was conducted in June of 2022.

### 3.6 Science Application System (SAS)

CAS will set up SAS located at NSSC, and ESA will set up Science Operation Center (SOC) located in European Space Astronomy Center (ESAC). Both parties will cooperate closely to make a scientific strategic plan and observation plan, monitor the execution of the plan, analyze the performance of the payloads in orbit, calibrate the payloads in orbit, produce quick look scientific data, and scientific data products.

SAS has finished PDR. Software is in the status of requirement analysis and design. A joint data products definition has been completed for SMILE.

## 4 Future Schedule

Based on Payload Instruments, PLM and PF PDRs, the joint Mission PDR was completed successfully in January 2020 in Netherlands, which is the third joint review of the SMILE mission, marking the kick-off of Phase C activities. PLM STM finished all the mechanical and the thermal tests and was shipped to IAMC for integration with QM Platform. S/C level QM test was completed in November 2022. All the scientific instruments, PLM and SC will finish CDR and a joint mission level CDR will be conducted in March 2023. SMILE satellite is planned to be launched around 2024–2025.

## Acknowledgments

This report is from Chinese Journal of Space Science, 2022, 42(4), and some progress are updated. SMILE Mission is a joint project with support from CAS and ESA. Thanks for the great support of CAS Strategic Priority Research Program and the ESA science program. Also thanks to the study and engineering teams for their cooperation and hard work: National Space Science Center, Innovation Academy for microsatellites of CAS, CLTC, Shanghai Institute of Space Propulsion, National Center for Space Weather, Polar Research Institute of China, *etc.* from Chinese side; University College London, University of Leicester, Bergen University, OEAW Space Research Institute, University of Liège, Institute National de Técnica Aeroespacial, Imperial College, Rutherford Appleton Laboratory, *etc.* from ESA side, as well as NASA Goddard Space Flight Center.

## References

- [1] WANG C, BRANDUARDI-RAYMONT G. Update on the ESA-CAS joint solar wind magnetosphere ionosphere link explorer (SMILE) mission[J]. *Chinese Journal of Space Science*, 2020, **40**(5): 700-703. DOI: 10.11728/cjss2020.05.700
- [2] JORGENSEN A M, XU R, SUN T, *et al.* A theoretical study of the tomographic reconstruction of magnetosheath X-ray emissions[J]. *Journal of Geophysical Research: Space Physics*, 2022, **127**(4): e2021JA029948
- [3] WANG R, LI D, SUN T. *et al.* A 3D magnetospheric CT reconstruction method based on 3D GAN and supplementary limited-angle 2D soft X-ray images. *Journal of Geophysical Research: Space Physics*, 128, e2022JA030424. <https://doi.org/10.1029/2022JA030424>
- [4] SUN T R, WANG X, WANG C. Tangent directions of the cusp boundary derived from the simulated soft X-ray image[J]. *Journal of Geophysical Research: Space Physics*, 2021, **126**(3): e2020JA028314. DOI: 10.1029/2020JA028314
- [5] GUO Y H, SUN T R, WANG C, *et al.* Deriving the magnetopause position from wide field-of-view soft X-ray imager simulation[J]. *Science China Earth Sciences*, 2022. DOI: 10.1007/s11430-021-9937-y



## Preface to the Special Issue on the National Report to the 28th IUGG General Assembly by CNC-IAMAS (2019–2022)<sup>※</sup>

Mu MU and Lei WANG

*Department of Atmospheric and Oceanic Sciences and Institute of Atmospheric Sciences,  
Fudan University, Shanghai 200438, China*

**Citation:** Mu, M. and L. Wang, 2023: Preface to the special issue on the National Report to the 28th IUGG General Assembly by CNC-IAMAS (2019–2022). *Adv. Atmos. Sci.*, <https://doi.org/10.1007/s00376-023-3003-z>.

---

The 28th General Assembly of the International Union of Geodesy and Geophysics (IUGG) will be held on 11–20 July 2023 in Berlin, Germany. The Chinese National Committee (CNC) for the International Association of Meteorology and Atmospheric Sciences (IAMAS) has invited leading Chinese scientists to review the progress and achievements in meteorology and atmospheric sciences in China since 2019, continuing its nearly 40 years tradition of submitting national reports to IUGG. The last four national reports were published as special issues in *Advances in Atmospheric Sciences* (AAS), the only associated journal of IAMAS, in 2007, 2012, and 2019, respectively. These special issues have received increasing global attention and are widely cited.

This newly prepared national report is also published as a special issue in AAS and consists of nine papers on Asian monsoon (Chen et al. 2023), atmospheric chemistry (Zhu et al. 2023), atmospheric electricity (Lyu et al. 2023), atmospheric predictability of weather and climate (Duan et al. 2023), high impact weather (Zhang et al. 2023), polar climate change and its interactions with the global climate system (Li et al. 2023), the role of stratospheric processes in climate change (Tian et al. 2023), seamless prediction (Ren et al. 2023), and the influences of human activity on regional climate over China (Duan et al. 2023). Although this report does not cover all topics of the atmospheric sciences, these papers are a good representation of the contributions made to the international community in meteorology and atmospheric sciences by Chinese scientists in the past four years. We sincerely appreciate the efforts of all the scientists involved in compiling this national report.

Chinese National Committee for IAMAS  
Mu MU, President  
Lei WANG, Secretary General

### REFERENCES

- Chen, W., and Coauthors, 2023: Recent advances in understanding multi-scale climate variability of the Asian monsoon. *Adv. Atmos. Sci.*, <https://doi.org/10.1007/s00376-023-2266-8>.
- Duan, J. P., H. Z. Zhu, L. Dan, and Q. H. Tang, 2023: Recent progress in studies of the influences of human activity on regional climate over China. *Adv. Atmos. Sci.*, <https://doi.org/10.1007/s00376-023-2327-z>.
- Duan, W. S., L. C. Yang, M. Mu, B. Wang, X. S. Shen, Z. Y. Meng, and R. Q. Ding, 2023: Recent advances in China on the predictability studies of weather and climate. *Adv. Atmos. Sci.*, <https://doi.org/10.1007/s00376-023-2334-0>.
- Li, X. C., and Coauthors, 2023: China's recent progresses in polar climate change and its interactions with the global climate system. *Adv. Atmos. Sci.*, <https://doi.org/10.1007/s00376-023-2323-3>.
- Lyu, W. T., and Coauthors, 2023: A review of atmospheric electricity research in China from 2019 to 2022. *Adv. Atmos. Sci.*, <https://doi.org/10.1007/s00376-023-2280-x>.
- Ren, H. L., and Coauthors, 2023: Seamless prediction in China: A review. *Adv. Atmos. Sci.*, <https://doi.org/10.1007/s00376-023-2335-z>.
- Tian, W. S., J. L. Huang, J. K. Zhang, F. Xie, W. K. Wang, and Y. F. Peng, 2023: Role of stratospheric processes in climate change: Advances and challenges. *Adv. Atmos. Sci.*, <https://doi.org/10.1007/s00376-023-2341-1>.

---

<sup>※</sup> This paper is a contribution to the special issue on the National Report to the 28th IUGG General Assembly by CNC-IAMAS (2019–2022).

Zhang, Q. H., R. M. Li, J. Z. Sun, F. Lu, J. Xu, and F. Zhang, 2023: A review of research on the record-breaking precipitation event in Henan Province, China, July 2021. *Adv. Atmos. Sci.*, <https://doi.org/10.1007/s00376-023-2360-y>.

Zhu, T., and Coauthors, 2023: Recent progress in atmospheric chemistry research in China: Establishing a theoretical framework for the “air pollution complex”. *Adv. Atmos. Sci.*, <https://doi.org/10.1007/s00376-023-2379-0>.

# Recent Advances in Understanding Multi-scale Climate Variability of the Asian Monsoon<sup>※</sup>

Wen CHEN<sup>1,2</sup>, Renhe ZHANG<sup>3</sup>, Renguang WU<sup>4</sup>, Zhiping WEN<sup>3</sup>, Liantong ZHOU<sup>2</sup>, Lin WANG<sup>2</sup>, Peng HU<sup>1,2</sup>, Tianjiao MA<sup>1,2</sup>, Jinling PIAO<sup>2</sup>, Lei SONG<sup>2</sup>, Zhibiao WANG<sup>2</sup>, Juncong LI<sup>3</sup>, Hainan GONG<sup>2</sup>, Jingliang HUANGFU<sup>2</sup>, and Yong LIU<sup>2</sup>

<sup>1</sup>Department of Atmospheric Sciences, Yunnan University, Kunming 650500, China

<sup>2</sup>Center for Monsoon System Research, Institute of Atmospheric Physics, Chinese Academy of Sciences, Beijing 100029, China

<sup>3</sup>Department of Atmospheric and Oceanic Sciences, Fudan University, Shanghai 200438, China

<sup>4</sup>Department of Atmospheric Sciences, School of Earth Sciences, Zhejiang University, Hangzhou 310058, China

(Received 18 September 2022; revised 15 January 2023; accepted 20 February 2023)

## ABSTRACT

Studies of the multi-scale climate variability of the Asian monsoon are essential to an advanced understanding of the physical processes of the global climate system. In this paper, the progress achieved in this field is systematically reviewed, with a focus on the past several years. The achievements are summarized into the following topics: (1) the onset of the South China Sea summer monsoon; (2) the East Asian summer monsoon; (3) the East Asian winter monsoon; and (4) the Indian summer monsoon. Specifically, new results are highlighted, including the advanced or delayed local monsoon onset tending to be synchronized over the Arabian Sea, Bay of Bengal, Indochina Peninsula, and South China Sea; the basic features of the record-breaking mei-yu in 2020, which have been extensively investigated with an emphasis on the role of multi-scale processes; the recovery of the East Asian winter monsoon intensity after the early 2000s in the presence of continuing greenhouse gas emissions, which is believed to have been dominated by internal climate variability (mostly the Arctic Oscillation); and the accelerated warming over South Asia, which exceeded the tropical Indian Ocean warming, is considered to be the main driver of the Indian summer monsoon rainfall recovery since 1999. A brief summary is provided in the final section along with some further discussion on future research directions regarding our understanding of the Asian monsoon variability.

**Key words:** Asian monsoon, multi-scale climate variability, monsoon onset, East Asian summer monsoon, East Asian winter monsoon, Indian summer monsoon

**Citation:** Chen, W., and Coauthors, 2023: Recent advances in understanding multi-scale climate variability of the Asian monsoon. *Adv. Atmos. Sci.*, **40**(8), 1429–1456, <https://doi.org/10.1007/s00376-023-2266-8>.

## Article Highlights:

- Advanced or delayed local monsoon onset synchronized over the tropical Asian regions (from the Arabian Sea to South China Sea)
- Different processes on multiple time-scales (from synoptic to decadal) all contributed to the record-breaking mei-yu in 2020
- Recent recovery of the East Asian winter monsoon intensity is possibly attributable to the Arctic Oscillation
- Recent recovery of the Indian summer monsoon rainfall is possibly attributable to the accelerated warming over South Asia

---

## 1. Introduction

Monsoon is a phenomenon of the annual cycle involving large differences in both wind and precipitation between summer and winter (e.g., Ramage, 1971; Huang et al., 2003). For example, East Asia features strong southerly winds and abundant rainfall in summer and strong northerly winds and

---

<sup>※</sup> This paper is a contribution to the special issue on the National Report to the 28th IUGG General Assembly by CNC-IAMAS (2019–2022).

\* Corresponding author: Wen CHEN  
Email: [chenwen-dq@ynu.edu.cn](mailto:chenwen-dq@ynu.edu.cn)

little rainfall in winter (Chen et al., 2019). Changes in monsoon intensity are crucial for people living in monsoon regions because water resources, agricultural harvests, transportation, and human lives are often affected by the natural hazards associated with anomalous monsoon activity. Hence, research on monsoon variability and its factors of influence has long been a top priority for Chinese meteorologists, and significant progress has been made over the past several decades (e.g., Tao and Chen, 1987; Ding, 1994; Zhang et al., 1996, 2017; Huang et al., 2004, 2012; He et al., 2007; Chen et al., 2013; Ding et al., 2015; Xue et al., 2015).

The Asian monsoon, which includes the East Asian and South Asian monsoon subsystems, is an important component of the global climate system (e.g., Tao and Chen, 1987). The East Asian summer monsoon (EASM) normally bursts in mid-May over the South China Sea (SCS) and propagates to North China, Korea and Japan in late July, featuring a typical summer rainband elongating zonally from the SCS to the Pacific. The onset of the South China Sea summer monsoon (SCSSM) signifies the start of the rainy season over East Asia. The northern boundary of the EASM is located in the transitional climate belt between the humid tropics and the arid midlatitudes, and this transition area has suffered from frequent meteorological disasters in recent decades due to the extremely fragile ecosystem with high sensitivity to climate change. In addition to research on monsoon intensity, numerous studies have been conducted in recent years on the SCSSM onset and the EASM northern boundary or transitional zone in East Asia. Attention has also been paid to the links between the EASM and the South Asian or Indian summer monsoon (ISM) in terms of both onset and intensity. Regarding the East Asian winter monsoon (EAWM), the work of many meteorologists has contributed to a better understanding of its variations across multiple time scales, including intraseasonal, interannual and interdecadal time scales. Moreover, the Asian summer monsoon (ASM) system is highly complex, with distinct spatial features over tropical South Asia and subtropical East Asia. Many achievements have been made in our understanding of the processes of the ISM variability in recent years, too.

This paper reviews recent advances in our understanding of the multi-scale climate variability of the Asian monsoon, with a main focus on the past several years. The remainder of this paper is organized as follows: Section 2 describes the progress that has been made on the SCSSM onset. Research achievements with respect to the EASM and EAWM are presented in sections 3 and 4, respectively. Section 5 summarizes the advancements in research on the ISM. And finally, section 6 provides a summary along with some suggestions for future research to address the unresolved scientific issues regarding our understanding of the Asian monsoon.

## 2. South China Sea summer monsoon onset

As the pivot of the entire Asian–Australian monsoon system, the SCSSM imposes substantial ecological and socioeconomic impacts worldwide via atmospheric telecon-

nections (Wang et al., 2009a; Yang et al., 2021; Chen et al., 2022a). The onset of the SCSSM marks the large-scale adjustment of the atmospheric circulation from the cold- to warm-season type (Chen et al., 2022a; Hu et al., 2022c), accompanied by the beginning of the major wet season (Hu et al., 2020b; Luo et al., 2020) and distinct changes in cloud and radiative features (Huang et al., 2020a). The recent review by Chen et al. (2022a) summarized the multi-scale variations of the SCSSM onset, including the interdecadal, interannual, intraseasonal, and synoptic scales. As a complement to Chen et al. (2022a), this part mainly focuses on research advances in the last few years.

### 2.1. Linkages among local monsoon onsets over the tropical ASM region

Climatologically, the onset of the tropical ASM consists of three different stages: monsoon onset over the Bay of Bengal and Indochina Peninsula in late April to early May; over the SCS and Arabian Sea in mid-May; and over the Indian subcontinent in late May to early June (Xiang and Wang, 2013; Liu et al., 2015; Bombardi et al., 2019, 2020; Hu et al., 2020a, 2021, 2022c). Most previous studies have mainly focused on the local monsoon onset of different sub-systems. However, recent studies have revealed that these local monsoon onsets are not independent, but instead closely connected to each other (Xing et al., 2016; Yang et al., 2021; Zeng et al., 2021; Hu et al., 2022a, c). For example, the monsoon onset over the Bay of Bengal exhibits an in-phase variation with that over the Arabian Sea (Hu et al., 2022a), India (Xing et al., 2016), and the SCS (Zeng et al., 2021), and the local monsoon onset over the Arabian Sea and India are also highly correlated (Hu et al., 2022a). As reviewed by Chen et al. (2022a), many studies have revealed the synchronized advancement of the tropical ASM onset after the mid-to-late 1990s. Based on the monthly mean rainfall and low-level winds in May, Hu et al. (2022c) revealed that the dominant mode of tropical ASM onset is characterized by coherent variations of local monsoon onset, i.e., the local monsoon onset tends to be synchronously advanced or delayed over the Arabian Sea, Bay of Bengal, Indochina Peninsula, and SCS.

The synchronized variation of local monsoon onsets can be attributed to both atmospheric internal processes and external forcings (Fig. 1). For example, accompanying an advanced monsoon onset over the Bay of Bengal, strong convective activity and latent heating appears therein, which is conducive to the breakdown and withdrawal of the subtropical high. As such, the monsoon onset over India and the SCS also tends to be earlier (Xing et al., 2016). Additionally, a synchronized delay of tropical ASM onset is more likely to occur during the easterly phase of the 30–80-day oscillation (Hu et al., 2022c). The spatial scale of the 30–80-day oscillation is greater than that of the ASM sub-systems (i.e., the Arabian Sea, Bay of Bengal, and SCS), and its timescale is longer than that of the local monsoon onset (i.e., in pentads or days). Thus, the 30–80-day oscillation is large enough to act as the background condition for the tropical ASM onset

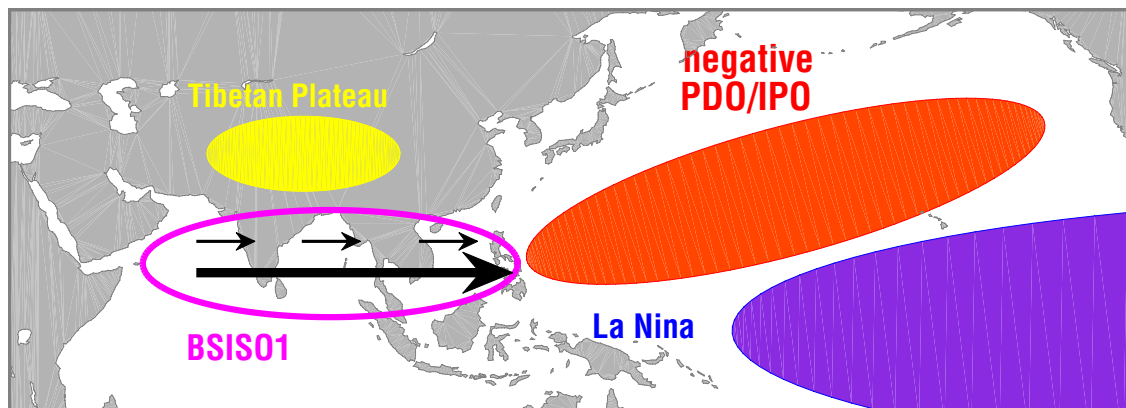


**Fig. 1.** Schematic of the dominant mode of the tropical ASM onset, featuring coherent variations of local monsoon onset. This mode can be attributed to both atmospheric internal processes (BSISO1) and external forcings (Tibetan Plateau, ENSO, and IPO).

(Hu et al., 2022c).

External forcings like the Tibetan Plateau's thermal condition, the El Niño–Southern Oscillation (ENSO), and the Interdecadal Pacific Oscillation (IPO) also play important roles in the simultaneously delayed or advanced tropical ASM onset. Based on observational datasets and model simulations, Hu et al. (2022a) revealed that the diabatic heating over the Tibetan Plateau leads to a westward movement of the South Asian high, which is favorable for a synchronized advanced monsoon onset over the Arabian Sea and India. ENSO is recognized as the most important interannual factor modulating the tropical ASM onset (Hu et al., 2022b, and references therein), and a preceding winter El Niño event tends to be followed by delayed monsoon onset over the Bay of Bengal (Wu and Mao, 2019), Indochina Peninsula (Hsu et al., 2014), SCS (Martin et al., 2019), and India (Ordoñez et al., 2016). Xiang and Wang (2013) investigated the interdecadal advanced tropical ASM onset after the mid-to-late 1990s. Their results revealed that the equatorial Rossby wave response to the La Niña-like mean state change can explain this advanced ASM onset (Xiang and Wang, 2013), which is associated with the positive-to-negative phase transition of IPO. Hu et al. (2022c) noticed that another interdecadal change in the ASM onset might have occurred after 2013/14. This recent delayed tropical ASM onset may also be attributable to the IPO, which exhibited a negative-to-positive phase transition in the early 2010s. In addition to the equatorial Rossby wave mechanisms mentioned by Xiang and Wang (2013), Hu et al. (2022c) suggested that the IPO may modulate the tropical ASM onset via a midlatitude Rossby wave train.

## 2.2. Interdecadal changes in SCSSM onset

In a recent review paper, Chen et al. (2022a) summarized the interdecadal change in the SCSSM onset around the mid-to-late 1990s. The mean SCSSM onset date has advanced by about half a month, which is not a local phenomenon but an integral part of the interdecadal advancement of the large-scale tropical ASM onset (Chen et al., 2022a; Hu et al.,

2022c). The interdecadal advancement of SCSSM onset is directly related to northwestward-propagating tropical disturbances, including vigorous tropical cyclone activities and enhanced intraseasonal oscillations (Hu et al., 2018; Chen et al., 2022a). Meanwhile, the primary source of this interdecadal shift is speculated to be the warm sea surface temperature (SST) anomalies in the western North Pacific (WNP; Yuan and Chen, 2013; Wang and Kajikawa, 2015; Chen et al., 2022a). However, some recent studies have provided other additional perspectives. For example, based on model simulations, Yu et al. (2016) suggested that the interdecadal advancement of SCSSM onset can be partly attributed to the urbanization of eastern China. Compared to previous studies focusing on the WNP, Lin and Zhang (2020) emphasized the important role of low-level zonal wind anomalies around Kalimantan Island, which is a response to the warm SST anomalies in the equatorial western Pacific. Apart from the tropical pathways like westward-propagating equatorial Rossby waves (Wang and Kajikawa, 2015; Chen et al., 2022a), the Pacific Ocean can also modulate the tropical ASM onset via the eastward-propagating Rossby wave train (Hu et al., 2022c). In addition to the tropical atmosphere and oceans, You et al. (2021) revealed that the warming in the mid-upper troposphere over subtropical East Asia can enhance the meridional temperature gradient, which was favorable for the interdecadal advancement of SCSSM onset in the mid-1990s. Moreover, some recent studies have suggested that the average date of SCSSM onset may have been delayed again in the early 2010s (Jiang and Zhu, 2021; Ai et al., 2022; Hu et al., 2022c). This recently delayed SCSSM onset may be attributable to the negative-to-positive phase transition of the IPO (Hu et al., 2022c) and the interdecadal warming of the tropical Indian Ocean (Ai et al., 2022). However, due to the relatively short time period, the robustness and mechanisms of the early-2010s interdecadal change in SCSSM onset still need further investigation.

In addition to the interdecadal changes in the mean monsoon onset date, recent studies have also investigated the interdecadal change in the relationship between ENSO and



SCSSM onset. Traditionally, ENSO is considered to be the most important factor controlling the SCSSM onset, and a preceding El Niño (La Niña) tends to be followed by a delayed (advanced) SCSSM onset (Zhu and Li, 2017; Martin et al., 2019). However, this relationship has broken down in recent years. For example, after the 2017/18 La Niña event, the SCSSM onset in 2018 was extremely late (Liu and Zhu, 2019; Deng et al., 2020); and after the 2018/19 El Niño event, the SCSSM onset in 2020 was extremely early (Hu et al., 2020a; Liu and Zhu, 2020). Several perspectives have been put forward to explain the recently weakened relationship between ENSO and SCSSM onset, including the interdecadal background changes (Hu et al., 2022c; Xu et al., 2022), ENSO diversity (Jiang and Zhu, 2021; Hu et al., 2022b), interference of other types of interannual variabilities (Ai et al., 2022; Cen et al., 2022; Hu et al., 2022b), and impacts of intraseasonal oscillations (Liu and Zhu, 2021; Hu et al., 2022b). Some studies have noted that the ENSO–SCSSM onset relationship is related to the background conditions, like the IPO or PDO (Pacific Decadal Oscillation; Hu et al., 2022c; Xu et al., 2022). Namely, the impacts of ENSO on the SCSSM onset are strong only during positive PDO phases (Xu et al., 2022). The modulation effects of the PDO on the ENSO–SCSSM onset linkage take place through affecting the anomalous WNP anticyclone (Xu et al., 2022). Jiang and Zhu (2021) suggested that the frequent occurrence of “cold tongue” La Niña is vital, but this perspective cannot explain the extremely early monsoon onset in 2019 following an El Niño event. Hu et al. (2022b) revealed that the anomalous Walker circulation associated with ENSO has been much weaker in recent years, and has thus been unable to deliver ENSO signals to the SCSSM onset. The changes in Walker circulation are closely related to the diversity of ENSO; namely, the frequent occurrence of central Pacific ENSO in recent years (Hu et al., 2022b). In addition, in recent years, the SCSSM onset has become more dominated by other SST signals, like the Northwest Indian Ocean (Ai et al., 2022) and the Victoria mode of North Pacific (Hu et al., 2022b). The Northwest Indian Ocean may modulate the SCSSM onset via suppressing the seasonal convection over the SCS and inducing eastward-propagating convective activities (Ai et al., 2022). The Victoria mode is the second empirical orthogonal function (EOF) mode of the extratropical Pacific Ocean SST (Ding et al., 2015), and can modulate the SCSSM onset via the large-scale divergent circulation (Hu et al., 2022b). Lastly, the influences of ENSO on the SCSSM onset may be contaminated by intraseasonal oscillation. For example, the vigorous quasi-biweekly oscillation in recent years may have disrupted the SCSSM onset from the slow-varying seasonal march modulated by ENSO (Liu and Zhu, 2021; Hu et al., 2022b), which may also have resulted in the weakened relationship between ENSO and SCSSM onset.

### 2.3. *The connections between SCSSM onset and rainfall anomalies*

The onset of the SCSSM is not only characterized by

steady changes in low-level zonal winds (from easterly to westerly), but also by sudden bursts of monsoonal convection (Chen et al., 2022a). One important application of the SCSSM onset is that it can be used to predict summertime rainfall anomalies. For example, corresponding to a late SCSSM onset, the total summer rainfall over subtropical East Asia (lower reaches of the Yangtze River valley and southern Japan) tends to increase (Huang et al., 2006; He and Zhu, 2015). This connection can be understood through two perspectives: the water vapor transport associated with the WNP anticyclone and the Pacific–Japan (PJ) pattern (Chen et al., 2022a). However, SCSSM onset mainly occurs in May (Hu et al., 2020a, 2022c; Chen et al., 2022a), and thus it has a much greater impact on the climate anomalies in early summer than in peak summer. Jiang et al. (2018) noticed that, accompanying a late SCSSM onset, there appears to be increased rainfall in the middle and lower reaches of the Yangtze River basin in May. However, these previous studies on the connections between SCSSM onset and rainfall anomalies mainly focused on the monthly or seasonal mean rainfall (He and Zhu, 2015; Jiang et al., 2018), and little attention was paid to extreme rainfall. In comparison, some recent studies have investigated the relationship between SCSSM onset and extreme rainfall over southern China and Southeast Asia.

Rainfall over southern China exhibits a typical double-peak evolution, with a major peak in mid-June and a second peak in mid-August (Sun et al., 2019; Hu et al., 2020b; Luo et al., 2020). As such, the rainy seasons in southern China can be classified into two distinct parts: the rainy season from April to June, known as the first rainy season or pre-summer flooding season; and the rainy season from July to September, known as the second rainy season or post-flooding season (Gu et al., 2018; Hu et al., 2020b; Luo et al., 2020). Recent studies have revealed that the SCSSM onset can greatly affect the rainfall properties of the first rainy season. Wu et al. (2020) revealed that the frequency of warm-sector heavy rainfall increases markedly from April to June, which is closely related to SCSSM onset. In contrast, the occurrence of frontal heavy rainfall exhibits less monthly variation during the first rainy season (Wu et al., 2020). In addition to the occurrence frequency, Li et al. (2020) reported that rainfall intensifies over southern China after the SCSSM onset, irrespective of the duration, which results from the favorable thermodynamic environment. Further details of related studies can be found in the recent review paper by Luo et al. (2020) and are therefore not repeated here.

In addition to the heavy rainfall over southern China, a recent study by Hu et al. (2022d) investigated the close linkage between the SCSSM onset and extreme rainfall over Southeast Asia in May. Usually, an early SCSSM onset is accompanied by a higher chance of extreme rainfall over Southeast Asia. The intensity of tropical synoptic-scale systems is thought to play an important role in this linkage (Hu et al. 2022d). Accompanying an advanced SCSSM onset,

the anomalous low-level cyclone over the SCS and the Philippine Sea increases the mid-troposphere humidity via moisture transport and the Ekman pumping effect. Besides, the barotropic energy conversion associated with this anomalous cyclone promotes the development of tropical synoptic-scale systems (Huangfu et al., 2017; Hu et al., 2022d). The combined effects of increased moisture and enhanced tropical disturbances can result in an increase in the occurrence of extreme rainfall in Southeast Asia.

### 3. East Asian summer monsoon

The EASM can affect not only the East Asian countries of China, Japan and Korea, but also other parts of the globe including India and North America through teleconnections (Srinivas et al., 2018; Zhou et al., 2020; Kosaka, 2021). In this section, we review several important issues, including the contributions of multi-scale factors to the super mei-yu in 2020, the close linkage between the summer monsoon rainfall in South Asia and East Asia, the climate variations over the EASM transitional zone, and the impacts of the Tibetan Plateau on the EASM.

#### 3.1. The record-breaking mei-yu in 2020: basic features and multi-scale processes

In early summer (from mid-June to mid-July), the convergence of monsoonal warm-humid airmass and cold airmass from mid and high latitudes creates a quasi-stationary front over East Asia (extending from central-eastern China to Japan), which is known as mei-yu in China, baiu in Japan, and changma in Korea (Ding, 2007; Ding et al., 2020). The variabilities of this planetary-scale mei-yu front can affect not only local regions including the Yangtze River valley and Japan (Ding et al., 2020), but also the global climate through teleconnections such as the PJ pattern (Nitta, 1987; Lu and Lin, 2009; Xu et al., 2019) and the circumglobal tele-

connection pattern (Ding and Wang, 2005; Zhou et al., 2020). The recent review by Ding et al. (2020) summarizes the multi-scale variabilities of the mei-yu and the related factors of influence.

In June–July 2020, a record-breaking mei-yu hit East Asia, which was characterized by a one-week-earlier onset, a half-month-later withdrawal, an extremely long duration, the strongest mean rainfall intensity, and frequent heavy rain-storm processes (Ding et al., 2021c; Niu et al., 2021). For example, the mei-yu season in 2020 lasted for 62 days, which was twice the climatological length. The accumulated rainfall reached 759.2 mm, which broke the record stretching back to the 1960s, and 18 national meteorological stations in China broke their historical records for daily rainfall (Ding et al., 2021c; Niu et al., 2021). More than 63 million people were affected by the floods, landslides and urban waterlogging associated with this super mei-yu, with 142 people reported dead or missing. The direct economic cost was estimated to be more than 178 billion RMB (Wei et al., 2020a; Ding et al., 2021c; Ge et al., 2022; Lu et al., 2022; Ma et al., 2022c). This super mei-yu was directly linked to anomalous circulation in the tropical and extratropical regions. On the one hand, an anomalous anticyclone was evident over the WNP during June–July, which transported abundant moisture to subtropical East Asia (Ding et al., 2021c; Wang et al., 2021b; Chen et al., 2022b) and excited the PJ pattern, thus affecting the mei-yu rainfall (Ding et al., 2021c; Qiao et al., 2021). On the other hand, the mid- and high-latitude circulation featured a “two ridge–one trough” pattern, and the excessive atmospheric blockings brought cold air-masses into the mei-yu region (Ding et al., 2021c; Qiao et al., 2021; Wang et al., 2021a). The above circulation anomalies can be attributed to the combined effects of the atmosphere, ocean, and sea ice. Figure 2 summarizes in detail the contributions of these factors to the super mei-yu, which we discuss in depth in the next two paragraphs, including climate

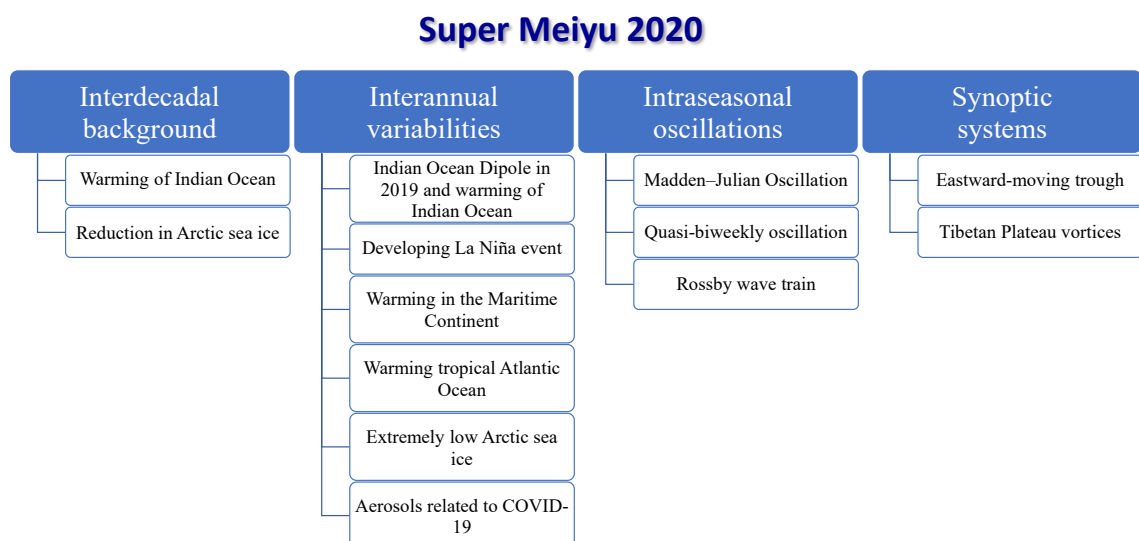


**Fig. 2.** Schematic of the multi-timescale (from interdecadal to synoptic) factors influencing the super mei-yu in 2020.



variabilities on the interannual–interdecadal timescales (e.g., SST and sea ice) and subseasonal timescales [e.g., the Madden–Julian Oscillation (MJO) and synoptic disturbances].

Unlike the extreme mei-yu in 1998, the super mei-yu in 2020 was not preceded by a strong El Niño event (Chen et al., 2021b; Cai et al., 2022). However, a very strong Indian Ocean dipole (IOD) was observed in the preceding autumn of 2019 (Takaya et al., 2020; Zhou et al., 2021). The combination of the 2019 IOD event and the decadal warming trend of the Indian Ocean resulted in a strong Indian Ocean warming in the early summer of 2020 (Guo et al., 2021; Tang et al., 2021; Chen et al., 2022b). The warming Indian Ocean excited equatorial Kelvin waves to the east, which is regarded as the major contributor to the anomalous cyclone over the WNP (Takaya et al., 2020; Chen et al., 2021b, 2022b; Ding et al., 2021b; Tang et al., 2021; Zhou et al., 2021; Cai et al., 2022). In addition, several studies have suggested that the developing La Niña in the equatorial central-eastern Pacific (Ding et al., 2021c; Chu et al., 2022), warming in the Maritime Continent (Tang et al., 2021; Zhao et al., 2022b), and the warm SST anomalies in the tropical Atlantic Ocean (Feng and Chen, 2021, 2022; Tang et al., 2021; Wang et al., 2021b; Zheng and Wang, 2021) also contributed to the anomalous WNP anticyclone. Specifically, the cold SST anomalies in the central-eastern Pacific excited an equatorial Rossby wave response and reinforced the WNP anticyclone (Pan et al., 2021; Tang et al., 2021), the active convections over the Maritime Continent promoted the WNP anticyclone via the local meridional circulation (Chu et al., 2022; Zhao et al., 2022b), and the Atlantic Ocean modulated the WNP anticyclone through an equatorial Kelvin wave response and the mass flow (Wang et al., 2021b). Note that the warm SST anomalies in the WNP seem to be a consequence of the anomalous anticyclone rather than its cause. In addition to the tropical oceans, Chen et al. (2021a) and Chen et al. (2022b) mainly emphasized the role of extremely low Arctic sea ice in the late spring and early summer, which mainly affected the super mei-yu via modulation of the atmospheric blockings and related cold-air activity. Interestingly, several studies have also revealed the impacts of reduced aerosols in the COVID-19 pandemic on the super mei-yu (Kripalani et al., 2022; Yang et al., 2022).

Apart from the above interannual variabilities and interdecadal backgrounds, some studies have also emphasized the prominent roles of high-frequency variabilities, including intraseasonal oscillations, synoptic-scale disturbances, mesoscale vortices, and the diurnal cycle. For example, Liang et al. (2021) and Zhang et al. (2021) noticed that an active phase of the MJO persisted in the Indian Ocean throughout June and July, and that the teleconnection associated with this MJO facilitated the super mei-yu in 2020. Ding et al. (2021a, c) revealed that the super mei-yu in 2020 exhibited remarkable quasi-biweekly oscillation, which may have been linked to the atmospheric blockings (Chen et al., 2021a, 2022b) and intraseasonal WNP anticyclone (Wang

et al., 2021b). The midlatitude Rossby wave train associated with the phase transition of the North Atlantic Oscillation is also believed to have been important, which is also on the intraseasonal timescale (Liu et al., 2020; Qiao et al., 2021). As for the synoptic- and mesoscale, the eastward movement of troughs (Ding et al., 2021a) and Tibetan Plateau vortices (Li et al., 2021a; Fu et al., 2022; Ma et al., 2022c) are regarded as prominent rainfall producers of this super mei-yu. Zeng et al. (2022) and Xia et al. (2021) investigated the diurnal cycles of the super mei-yu.

### 3.2. *Linkage between the summer monsoon rainfall over South Asia and East Asia*

The ASM system includes two separate yet closely related subsystems: the EASM and the South Asian summer monsoon (SASM). The EASM and SASM are different in many aspects (Roxy et al., 2015; Huang et al., 2017; Wu, 2017). For example, the SASM is related to the meridional land–sea thermal contrast, while the EASM is mainly associated with the zonal land–sea thermal contrast. As such, the SASM circulation is characterized by strong vertical easterly shear (i.e., easterly winds above westerly winds), while the EASM circulation features obvious vertical westerly shear (i.e., westerly winds throughout the troposphere). This may partly explain why the SASM region is dominated by cumulus clouds while the EASM region is a mix of cumulus and stratiform clouds (Huang et al., 2017). Despite the above differences, the SASM and EASM are also closely linked to each other. Many studies have shown that the summer monsoon rainfall over South Asia is positively correlated with that over northern China and negatively correlated with that over the Yangtze River basin and southern Japan (Wei et al., 2014b, 2015, 2019; Wu, 2017; Wu and Jiao, 2017; Stephan et al., 2019; Xue et al., 2022). In a previous review paper, Wu (2017) summarized two pathways of the linkage between the SASM and EASM on the interannual timescale. The “south pathway” is via the moisture transport over the low latitudes that involves the East Asia–Pacific (EAP) pattern (Huang and Sun, 1992; Huang, 2004) or PJ pattern (Nitta, 1987; Xu et al., 2019) and the movement of the western North Pacific subtropical high. Meanwhile, the “north pathway” is through the extratropical Silk Road pattern (SRP; Enomoto et al., 2003; Wang et al., 2017b, 2021c; Chowdary et al., 2019; Hu et al., 2020d) or the circumglobal teleconnection (CGT) pattern (Ding and Wang, 2005; Zhou et al., 2020) along the subtropical westerly jet, which is associated with the displacement of the South Asian high (Wei et al., 2014b, 2015, 2019; Xue and Chen, 2019; Xue et al., 2021). At the end of the review paper, Wu (2017) raised several important issues that were not well understood at that time. Subsequent works have further investigated these issues of the SASM–EASM linkage, including the impacts of ENSO and regional SST anomalies (Wu and Jiao, 2017; Ha et al., 2018; Liu and Huang, 2019), climate model performances (Preethi et al., 2017; Wu and Jiao, 2017; Woo et al., 2019), the linkage on the intraseasonal timescale (Wei et al., 2019), and the non-stationarity of the linkage (Lin et al., 2017; Wu

and Jiao, 2017; Wu et al., 2018; Sun and Ming, 2019; Stephan et al., 2019; Cen et al., 2022).

The connection between the SASM and EASM is not stationary, undergoing significant interdecadal changes. For example, the correlation between the summer rainfall in South Asia and northern China is rather strong before the 1970s but very weak in recent years (Wu, 2017; Wu and Jiao, 2017). Several hypotheses have been proposed to explain this interdecadal weakening relationship, which include external forcing such as SST, atmospheric internal variabilities, and stochastic processes. After removing the ENSO signal by partial correlation analysis, the interdecadal changes between summer rainfall over South Asia and northern China are still evident. As such, ENSO may make little contribution to the long-term change in this relationship (Wu, 2017; Wu and Jiao, 2017; Wu et al., 2018). This speculation was partly supported by an AGCM simulation forced by climatological SST and sea ice. The correlation between the SASM and northern China rainfall also exhibited remarkable interdecadal changes in the absence of ENSO (Wu et al., 2018). As such, the atmospheric internal variabilities may play important roles in the connection between the SASM and EASM. The forcing and the basic states are the two most important factors in determining atmospheric teleconnection. Regarding the forcing over South Asia, Wu and Jiao (2017) suggested that a combination of larger South Asian rainfall anomalies and more positive South Asian rainfall anomaly years may contribute to a stronger linkage between the SASM and northern China. This is because a higher mean rainfall background is favorable for a stronger dynamic response (Wu and Jiao, 2017). In addition to the forcing applied by heating, the atmospheric basic state is also very prominent. Lin et al. (2017) revealed that, after the 1970s, the subtropical westerly jet over East Asia shifted northward, which led to an increase in the wavelength of the stationary Rossby wave train (i.e., SRP/CGT). As such, the portion of the wave train over East Asia shifted eastward, and the anomalous anticyclone in the upper level also displaced eastward. This resulted in the eastward movement of rainfall anomalies from northern China to the Yellow Sea, and thus a weakening relationship between the SASM and northern China rainfall anomalies. A recent study by Xue et al. (2022) also indicated the movements of the westerly jet and the South Asian high are vital for the linkage between the SASM and northern China. In addition, Sun and Ming (2019) reported that mid- and high-latitude disturbances can also disrupt the connection between the SASM and the EASM. The summer North Atlantic Oscillation can affect the atmospheric circulation south of Lake Baikal, which is closely linked to central East Asian summer rainfall in recent years. When the signals of the circulation anomalies south of the Lake Baikal are removed, the linkage between the SASM and EASM becomes significant again after the 1970s. Last but not least, Monte Carlo simulations (Wu and Jiao, 2017; Wu et al., 2018) suggest the possibility that the interdecadal changes in the SASM and EASM linkage

being due to stochastic processes cannot be excluded.

In the review paper by Wu (2017), the SASM was considered a more active influencing factor, while the EASM was regarded as a passive recipient of influences. However, some recent studies have revealed the impacts and feedbacks of the EASM on the SASM. The EAP/PJ pattern is a dominant mode of the EASM variability (Nitta, 1987; Huang and Sun, 1992; Huang, 2004; Xu et al., 2019), which describes the out-of-phase variations of rainfall anomalies over the subtropical region (i.e., mei-yu) and tropical region (i.e., the monsoon trough). Based on observational analysis and model simulations, Srinivas et al. (2018) and Kosaka (2021) revealed the impacts of the PJ pattern on the SASM rainfall. These impacts include the atmospheric pathway and the oceanic pathway. When the PJ pattern is characterized by an anomalous anticyclone in the subtropics (e.g., Japan) and a cyclone over the tropics (e.g., WNP), the westward-extending anomalous cyclone and westerly winds can modulate the vertical motion via Ekman pumping effects. As such, the rainfall increases in central-eastern India but decreases in southern India (Srinivas et al., 2018; Kosaka, 2021). Such rainfall and circulation patterns resemble the first coupled mode between the vertically integrated water vapor transport over the SASM and EASM regions extracted by singular value decomposition (Liu and Huang, 2019). Apart from the atmospheric pathway, the anomalous westerly winds associated with the PJ pattern can reinforce the monsoonal southwesterly winds, thereby cooling the SST in the northern Indian Ocean. These cold SST anomalies can in turn change the evaporation and atmospheric circulation, which is the oceanic pathway of the PJ pattern affecting the SASM (Srinivas et al., 2018; Kosaka, 2021). In addition to the low-level circulation mentioned above, the South Asian high in the upper level is also vital for the linkage between the SASM and EASM. While previous studies mainly emphasized the impacts of latent heating over the SASM region on the displacement of the South Asian high (Wei et al., 2014b; Wu, 2017), some recent studies have revealed that the latent heating over the EASM region (e.g., Yangtze River valley and south of Japan) can also affect the location of the South Asian high (Wei et al., 2015, 2019; Zhou et al., 2020; Wang et al., 2021a), thus creating feedback to the rainfall over the SASM region. The displacement of the South Asian high is closely linked to the CGT pattern, which is a zonal wavenumber-5 teleconnection pattern in the upper troposphere. There are close interactions between the SASM and the CGT pattern (Ding and Wang, 2005, 2007). On the one hand, the SASM rainfall may excite a downstream Rossby wave train extending to East Asia and North America. On the other hand, the wave train excited in the jet exit region of the North Atlantic may affect the intensity and rainfall of the SASM (Ding and Wang, 2005, 2007). Recently, Zhou et al. (2020) revealed that the latent heating associated with the EASM can stimulate an upper-tropospheric teleconnection that resembles the CGT pattern. As such, the impacts and feedbacks of the EASM on the SASM may also be

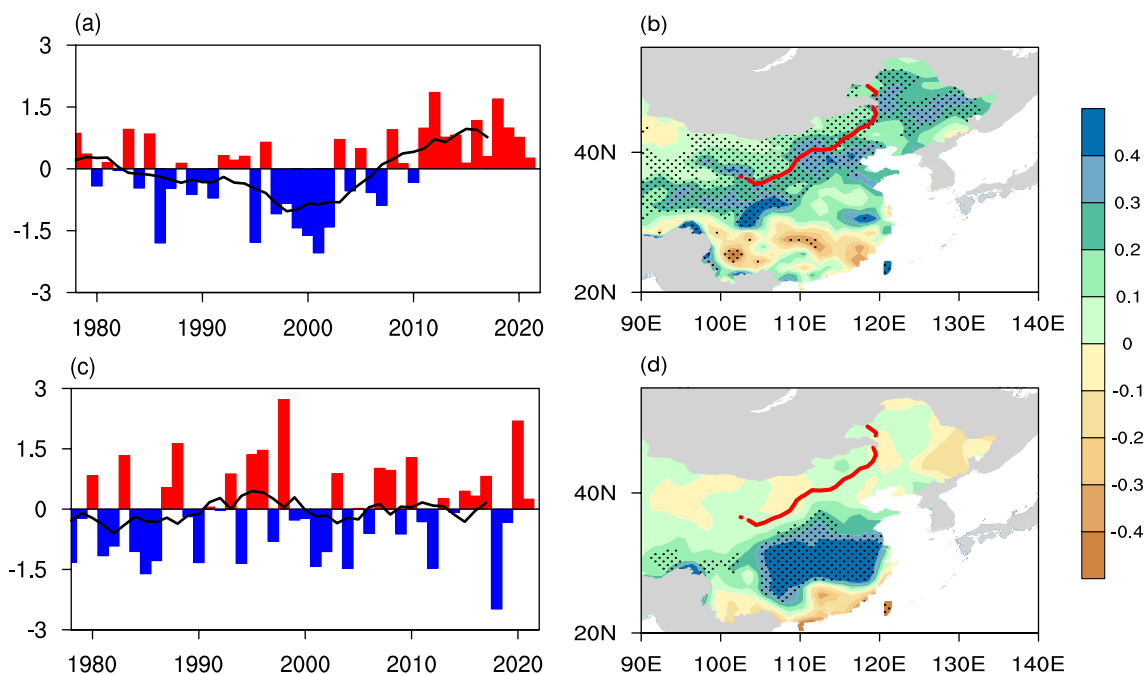


**Fig. 3.** Time series of the (a) EASM northern boundary index (bars) from 1979–2021 with the corresponding 9-yr running mean (black line), and (b) its regressed summer (June–August) precipitation pattern (units:  $\text{mm d}^{-1}$ ). (c, d) As in (a, b) but for the EASM intensity index. The dotted areas in (b, d) denote where the regressed anomalies are significant at the 95% confidence level, and the red lines represent the climatological mean position of the EASM northern boundary. The northern boundary index and intensity index of the EASM were calculated based on the definitions proposed by Chen et al. (2018) and Wang and Fan (1999), respectively.

achieved by the CGT pattern.

### 3.3. Dry–wet climate variations over the EASM transitional zone

In addition to intensity changes, the advancement of the EASM system can also exert a substantial influence on dry–wet conditions over a vast area of East Asia (Fig. 3). The EASM usually begins in southern China in May, and then marches northward in two stages before reaching its northernmost position in late July (Wang and LinHo, 2002; Ding and Chan, 2005; Chen et al., 2009; Yuan et al., 2012). The northernmost position of the EASM exhibits significant spatial fluctuations from year to year, thus forming a southwest–northeast-oriented belt between the arid and humid climate zone—the monsoon transitional zone (MTZ; Wang et al., 2017a, 2021e; Piao et al., 2021c; Zhao et al., 2021; Piao et al., 2022). The MTZ extends from the east of the Tibetan Plateau to Northeast China, and mainly covers semi-arid climate zones with rather low annual total precipitation amounts. Due to the scarcity of water resources, the MTZ is extremely sensitive and vulnerable to climate variability, especially to precipitation changes. Far from oceanic moisture sources, the formation of precipitation here is closely related local land processes, with the available water vapor contributed greatly by evaporation, according to methods under both Eulerian (Piao et al., 2018a, 2020) and Lagrangian frameworks (Wang et al., 2023).

Considering that more than half of the annual total precipitation occurs in the summertime, several studies have

mainly focused on summer precipitation variations and revealed their connections with SST anomalies over the tropical Pacific and northern Atlantic (Piao et al., 2017, 2018b; Zhao et al., 2019a, b). For example, it has been suggested that SST anomalies over the tropical central-eastern Pacific (TCEP) and tropical Northern Atlantic (TNA) can exert combined impacts on the interannual variation of summer precipitation via triggering an atmospheric wave train over Eurasia (Zhao et al., 2019b, 2020a, b); and only when opposite-sign SST anomalies appear over the TCEP and TNA are they both significantly correlated with the precipitation variation over the MTZ. This is because in opposite-sign (same-sign) cases, atmospheric anomalies induced by the TCEP SST anomalies are amplified (weakened) by those generated by the TNA SST changes (Zhao et al., 2020b). In addition to interannual variations, summer precipitation over the MTZ underwent remarkable interdecadal decreases in the late 1990s, along with prolonged drought conditions (Piao et al., 2017, 2021a). Observational results and sensitivity experiments show that the SST warming in the North Atlantic played an important role in this interdecadal change via inducing a wave-like teleconnection pattern from western Europe to Asia (Piao et al., 2017; Wang et al., 2017a).

Subsequent studies have projected future changes in precipitation over the MTZ and analyzed the main influencing factors (Piao et al., 2021b, c, 2022). The precipitation amount is expected to increase throughout the year according to both CMIP5 and CMIP6 model simulations, with the most significant changes identified in summer (Piao et al.,

2021c, 2022). Moisture budget analysis suggests that changes in vertical moisture advection and evaporation together dominate the precipitation increases, with the former factor playing a more important role. It is worth noting that changes in vertical moisture advection are mainly controlled by dynamic effects associated with atmospheric changes in CMIP6, but thermodynamic components related to humidity increase in CMIP5. This inconsistency between CMIP5 and CMIP6 results might be caused by the stronger warming gradient between the mid- high latitudes and the tropics projected in CMIP6 (Piao et al., 2021c). Based on 40-member ensemble projections of the National Center for Atmospheric Research's Community Climate System Model, version 3, Piao et al. (2021b) further indicated that the projected precipitation increases are under the combined impacts from external forcing and internal atmospheric variability. The internal atmospheric variability mainly holds dominant modes resembling those associated with the Arctic Oscillation (AO) and Polar-Eurasian pattern, causing large model spread via modulating vertical motions and water vapor transport over the MTZ.

### 3.4. Impacts of the Tibetan Plateau on the EASM

The Tibetan Plateau exerts a large impact on the EASM through orographic effects and interactions with the westerlies (e.g., Wu et al., 2007; Chen and Bordoni, 2014; Son et al., 2019, 2020; Kong and Chiang, 2020; Seok and Seo, 2021). As an elevated heat source and sink in the middle troposphere, the anomalous thermal state of the Tibetan Plateau modulates the land–sea thermal contrast and affects the climate over Asia (Duan and Wu, 2005; Wu et al., 2007). Snow anomalies over the Tibetan Plateau can induce anomalous heating or cooling in the atmospheric column through the snow–albedo effect and the snow–hydrological effect (Barnett et al., 1989; Yasunari et al., 1991). Consequently, Tibetan Plateau snow anomalies affect the atmospheric circulation and weather and climate in neighboring and remote regions. There have been numerous studies of the impacts of Tibetan Plateau snow anomalies on the EASM (e.g., Duan et al., 2018). Earlier studies focused mostly on the influence of the cold season (autumn–winter–spring) snow anomalies over the central–eastern Tibetan Plateau based on station snow observations. Utilizing satellite snow data, recent studies have detected the influence of the summer snow over the western Tibetan Plateau on the East Asian summer rainfall (e.g., Xiao and Duan, 2016; Wang et al., 2018).

Wang et al. (2018) summarized two pathways for the impacts of Tibetan Plateau summer snow anomalies on East Asian summer rainfall (Fig. 4). One is through a midlatitude atmospheric wave pattern induced by western Tibetan Plateau snow anomalies. More snow cover over the western Tibetan Plateau excites an upper-level wave pattern that extends to Northeast China (Fig. 4a). The anomalous southwesterlies to the south of an anomalous cyclone bring more moisture from the lower latitudes, leading to a band of excessive rainfall extending from the mid-to-lower Yangtze River to Japan. The other is through the tropical Indo-western

Pacific vertical circulation triggered by southern Tibetan Plateau snow anomalies (Fig. 4b). Anomalous cooling accompanying more snow cover over the southern Tibetan Plateau induces more convection through anomalous meridional overturning circulation. Anomalous convection over the Indian Ocean causes anomalous zonal overturning circulation with anomalous upper-level westerlies over the tropical Indian Ocean and anomalous upper-level convergence over the WNP. The suppressed convection over the WNP induces a meridional atmospheric circulation anomaly pattern with an anomalous lower-level cyclone over East Asia, inducing more rainfall extending from the middle-lower Yangtze River to Japan. When the amount of western and southern Tibetan Plateau snow is more than normal, their consistent impacts lead to more precipitation over the middle and lower reaches of the Yangtze River and subtropical WNP, and less precipitation over the northern Indian Ocean and tropical WNP (Wang et al., 2018).

## 4. The East Asian winter monsoon

The EAWM is an essential component of the global monsoon system in boreal winter and has widespread impacts on the weather and climate in the Asia-Pacific region and beyond (Fig. 5a; e.g., Chen et al., 2000; Chang et al., 2011; Wang and Lu, 2017; Yu et al., 2020; Ma and Chen, 2021). Its variations range from synoptic to interdecadal timescales and beyond, causing cold snaps, snowstorms, and haze in East Asia and strong tropical–extratropical interactions via the transportation of cold air masses (e.g., Wang et al., 2009b; Zhou et al., 2009; Wang and Chen, 2014; Ding et al., 2014; Abdillah et al., 2017; Yu et al., 2021; Zheng et al., 2022). This section reviews three aspects of recent EAWM studies: its interdecadal, long-term, and subseasonal variations.

### 4.1. Variations of the EAWM at the interdecadal timescale and beyond

The EAWM intensity has been found to have shifted from strong to weak around 1988 (Fig. 5b; Kang et al., 2006; Wang et al., 2009b; Miao et al., 2018; Miao and Wang, 2020; Miao and Jiang, 2021) and experienced significant strengthening after the early 21st century (Fig. 5b; Ding et al., 2014; Wang and Chen, 2014; Xiao et al., 2016). Accompanied by these decadal variations, the surface air temperature (SAT) over East Asia also experienced decadal fluctuations, with a significant warm period from the mid-1980s to the early 2000s and a cold period from the early 2000s to mid-2010s (Fig. 5c; Kang et al., 2006; Xiao et al., 2016). The weakening of the EAWM after the mid-1980s has been attributed to global warming because the East Asian wintertime SAT during this period shows a similar warming trend to the global mean SAT (e.g., Yang and Wu, 2013; Ding et al., 2014). However, the recovery of the EAWM intensity after the early 2000s in the presence of continuing greenhouse gas (GHG) emissions suggests an essential role of internal climate variability in the interdecadal variations of the



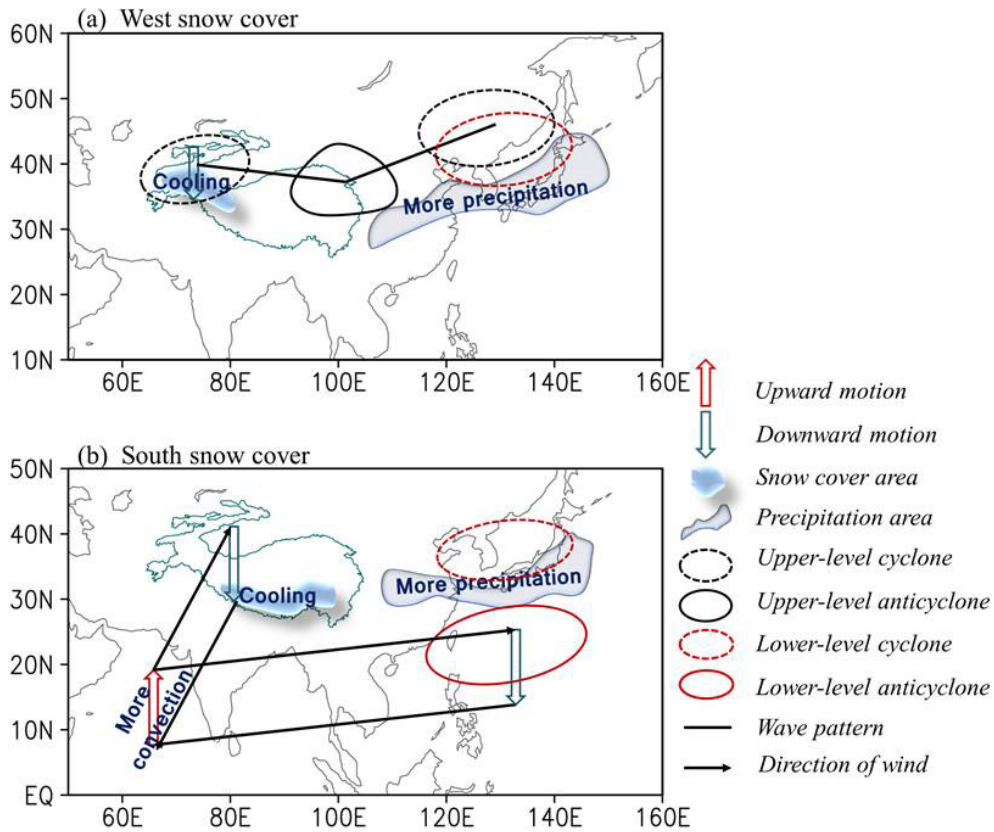


**Fig. 4.** Two pathways for the impacts of Tibetan Plateau summer snow anomalies on East Asian summer rainfall. One is a midlatitude atmospheric wave pattern associated with western Tibetan Plateau snow anomalies, and the other is tropical Indo-western Pacific vertical circulation triggered by southern Tibetan Plateau snow anomalies.

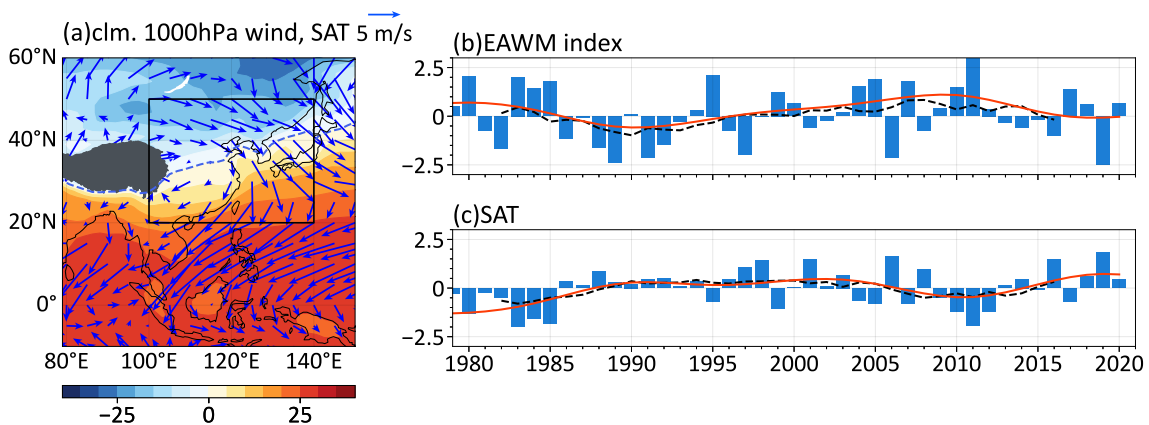


**Fig. 5.** (a) Climatological winter (December–January–February, DJF) mean 1000-hPa horizontal winds (vectors; units:  $m\ s^{-1}$ ) and SAT (color shading; units:  $^{\circ}C$ ). The blue dashed line indicates the  $0^{\circ}C$  isotherm. (b) Standardized DJF-mean EAWM index [bars; defined by Chen et al. (2000)] during 1979–2021. The black dashed line is the nine-point running average of the EAWM index. The red solid line is the low-frequency component of the EAWM index filtered by ensemble empirical mode decomposition (Wu and Huang, 2009). (c) As in (b) but for the area-mean SAT anomaly within  $20^{\circ}$ – $50^{\circ}N$  and  $100^{\circ}$ – $140^{\circ}E$  [box in (a)]. The data used in this figure are from NCEP–DOE Reanalysis II for the period 1979–2021.

EAWM intensity (e.g., Gong et al., 2019a, b, 2021; Wang et al., 2021b). The latter is highly consistent with that of the AO, the dominant mode of internal atmospheric variability over the extratropical Northern Hemisphere for approxi-

mately 100 years (Wang et al., 2021b). An interdecadal change in the AO from a positive to a negative phase can induce widespread cooling in northern East Asia, which offsets the forced warming by more than 70% in northern East

Asia during 1979–2018 (Gong et al., 2019a). This effect largely weakens the warming trend and even induces a cooling trend in some parts of northern East Asia, and is preceded by the multidecadal fluctuation of the internal component of autumn Arctic sea ice (Gong et al., 2021). The correlation coefficient between the AO and the internally induced winter SAT anomalies in northern East Asia is 0.9 when the variability shorter than 7 years is filtered out from the data. This means that the AO accounts for 81% of the total variance of the interdecadal change in internally induced SAT over northern East Asia (Gong et al., 2019a). Therefore, the AO is the most crucial internal climate variability determining the interdecadal fluctuation of the EAWM, especially for the northern part of East Asia. Although the AO is an atmospheric internal variability, external forcings can also exert an important influence on its long-term variations or trends. For example, some studies have revealed that an increase in GHGs can force a positive AO trend by strengthening the meridional temperature gradient (e.g., Shindell et al., 1999). It has also been suggested that the Arctic sea-ice loss or the increase in snow cover in the Eurasian continent may have contributed to the negative trend of the AO during 1980–2010 (e.g., Allen and Zender, 2011; Yang et al., 2016). In addition, the Indian Ocean warming has been documented as having played an important role in the positive trend of the AO from the late 1950s to the present day (Jeong et al., 2022). The external forcing of the long-term variations of the AO described above may be an important source of the interdecadal variations of the EAWM, which needs further investigation.

In addition to the EAWM intensity, the EAWM amplitude of interannual variability has also experienced multidecadal changes, such as a weakening after the 1980s. This timing is roughly consistent with that of the interdecadal weakening of the EAWM intensity because the large-scale warming after the mid-1980s was favorable to a reduction in the land–sea thermal contrast and a weakening of the intensity of the EAWM on the interannual time scale (He, 2013). Nevertheless, the amplitude of the interannual variability of the Siberian high's intensity in winter (December–February) did not weaken between 1958 and the present day. It was weak from the 1950s to the mid-1990s and became strong at the beginning of the 21st century, consistent with the interdecadal amplification of the EAWM intensity in the past two decades (e.g., Wang and Chen, 2014; Ding et al., 2014; Chen et al., 2021a). Also, the interdecadal enhancement of the interannual variability of the EAWM can be found not only in the Siberian high but also in other components of the EAWM. The underlying mechanism may involve the change in large-scale land–sea thermal contrast over East Asia since the mid-1990s. In fact, the phase changes of the interannual variability amplitudes of the land–sea thermal contrast index in the East Asian region are basically consistent with those of the Siberian high, which was weak from 1980 to the mid-1990s and strong afterward (Chen et al., 2021a). The land–sea thermal contrast is one of the most fundamental

and direct reasons for the formation of the EAWM. Due to the large ocean heat capacity, the temperature increase in the Northwest Pacific SST was smaller than that of the land in East Asia against the background of global warming from 1980 to the mid-1990s. Therefore, the thermal gradient between the sea and the land was reduced and this led to the weakening of the amplitude of the EAWM interannual variability. However, the global temperature entered a warming stagnation phase that lasted for more than 10 years after the late-1990s (Kosaka and Xie, 2013). During this period, the warming over land in East Asia slowed but the tropical eastern Pacific cooled on an interdecadal scale. The strengthening of the trade winds caused by the anomaly made Pacific surface seawater accumulate in the western Pacific, which in turn caused a significant acceleration in the warming of the upper ocean in the Northwest Pacific, thereby enhancing the sea–land thermal contrast in East Asia. This effect may have led to an increase in the EAWM amplitude of its interannual variability. If the internal variability of the climate system and the global warming caused by GHGs are superimposed in-phase in the next 10 to 20 years, and the warming re-enters an accelerating stage, the EAWM intensity of the interannual variability will likely increase again in the future.

#### 4.2. Subseasonal variations of the EAWM

Subseasonal variation of the EAWM largely manifests as an occurrence of cold events or the development of cold anomalies over East Asia associated with wind anomalies (e.g., Wang et al., 2021d). Many studies have shown that changes in the mid–high-latitude circulation systems contribute to temperature anomalies over East Asia (Ding and Krishnamurti, 1987; Jeong and Ho, 2005; Song and Wu, 2017). The intraseasonal variability of the EAWM is dominated by two Rossby wave trains over North Atlantic–Eurasia, with one propagating along the polar front jet and the other along the subtropical westerly jet (Jiao et al., 2019; An et al., 2022). Both of these wave trains can generate an anomalous anticyclone/cyclone over Japan and thereby impact the low-level winds and air temperature over East Asia. Further studies have indicated that the air pollution over the North China Plain in winter is closely related to the anomalous anticyclone over Northeast Asia, and thus is influenced by the two Rossby wave trains (An et al., 2020; Song et al., 2022). A case study showed that the formation of severe haze over the North China Plain during November–December 2015 can be attributed to the combined effect of the two Rossby wave trains over Eurasia (An et al., 2020).

Precursory signals have been detected in the stratosphere before the occurrence of cold events over East Asia. Song and Wu (2019d) found that changes in the stratospheric planetary wavenumber-1 are closely linked to cold anomalies over East Asia. The reflection of the planetary wavenumber-1 pattern leads to the downward propagation of stratospheric signals, which contributes to the development of the tropospheric Rossby wave train over Eurasia and thus leads to an enhancement of the Siberian high and cold anomalies over

East Asia. Moreover, Rossby wave breaking, which is characterized by an irreversible overturning of the potential temperature contours on the tropopause (McIntyre and Palmer, 1983), has also been found to be associated with cold anomalies over East Asia. Song and Wu (2021) indicated that anticyclonic wave breaking over western Siberia accompanied by a positive AO phase contributes to the development of the Rossby wave train over Eurasia and thus a strengthening of the Siberian high, which then leads to cold anomalies over East Asia. Cyclonic wave breaking over the North Pacific is connected with a westward retrogression of North Pacific blocking, during which the Siberian high is intensified, also causing cold anomalies over East Asia.

The EAWM has been shown to be influenced by tropical large-scale air–sea interaction. For example, it has been documented that the MJO can induce a poleward Rossby wave train and have an impact on the EAWM (Jeong et al., 2005; He et al., 2011). A previous study (Song and Wu, 2018) also indicated that both positive and negative phases of the AO can lead to cold events over East Asia but with differences in the location and extent of the cold anomalies. Another study found that the MJO-induced poleward Rossby wave train influencing East Asia can be modulated by the AO (Song and Wu, 2019a). The wave source over the Arabian Sea induced by the MJO convection is intensified by positive AO-related southeastward dispersion of wave energy, causing an enhancement of the poleward wave train triggered by phases 2 and 3 of the MJO, which leads to the development of an anomalous cyclone over midlatitude East Asia and cold anomalies there. The cooperative relationship of the MJO and the AO in influencing cold events over East Asia weakens in late winter in association with the weakened connection between the MJO and the AO, which is caused by the decrease in meridional heat fluxes and thus the weakened constructive interference with climatological stationary waves and decreasing of the poleward tropospheric eddy momentum and heat fluxes over the western Pacific (Song and Wu, 2019b). Moreover, the Quasi-Biennial Oscillation (QBO) in the tropical stratosphere can modulate the MJO during boreal winter, meaning the MJO-related temperature anomalies over East Asia are different in easterly and westerly QBO phases (Song and Wu, 2020).

Recent studies have also found that the intraseasonal variations of the EAWM show a close connection with tropical rainfall/convection over the western Pacific, which includes areas such as the SCS, the Maritime Continent, and the Philippine Sea (Jiao and Wu, 2019; Ma and Chen, 2021; Ma et al., 2022b). Statistical results show that the tropical convection over the western Pacific is enhanced for about six to eight days after the peak of strong intraseasonal EAWM events (Ma et al., 2022b). The anomalous convective heating over the Maritime Continent and the tropical Indian Ocean can also lead to the occurrence of cold events over East Asia (Song and Wu, 2019c). The anomalous tropical heating generates an anomalous overturning circulation cell, with ascending motion and convergence over the tropics and descending

motion over Siberia, which contributes to radiative cooling over Siberia and a southeastward intrusion of the Siberian high, resulting in cold anomalies over East Asia. This can also generate a Rossby wave train that propagates toward North America, where it induces temperature changes (Dong and Wang, 2022).

In addition, the ENSO–EAWM relationship has been found to be stronger during early winter (November–December) than late winter (January–February). This leads to a higher prediction skill for the EAWM in early winter than in late winter (Tian and Fan, 2020). The distinct ENSO–EAWM relationships between early and late winter have been suggested to be related to subseasonal changes in the teleconnections of ENSO over East Asia (Kim et al., 2018; Ma et al., 2022a). In early winter, El Niño is closely related to an anomalous anticyclone over Japan, which causes deceleration of the EAWM and a warmer East Asia (Fig. 6), with La Niña generally having opposite effects. In late winter, however, El Niño (La Niña) cannot induce a clear anticyclonic (cyclonic) anomaly over Japan, leading to weak impacts on the EAWM. Moreover, the early winter anomalous anticyclone/cyclone over Japan supports a strong impact of ENSO on haze pollution over the Beijing–Tianjin–Hebei region (Zhao et al., 2022a). The formation of the anomalous anticyclone/cyclone over Japan in early winter is related to two Rossby wave trains induced by ENSO. One propagates from the tropical Indian Ocean toward East Asia, and the other travels across the North Atlantic and Eurasia (An et al., 2022; Ma et al., 2022a). Numerical experiments suggest that the tropical Indian Ocean–East Asia wave train is mainly generated by precipitation heating in the tropical eastern Indian Ocean/western Pacific region (Fig. 6; Ma et al., 2022a).

Zhong and Wu (2022) investigated the subseasonal variations of the winter SAT over Eurasia using a seasonal-reliant EOF analysis. The first EOF mode was characterized by a persistent SAT anomaly throughout winter, while the second mode was characterized by a reversal of the SAT anomaly from early winter (November–December) to late winter (January–February). Their results were consistent with previous studies that applied the same approach to the SAT from station observations in China (Wei et al., 2014a, 2020b). The underlying mechanism involves internal dynamic processes within the atmosphere that resemble the Scandinavian teleconnection, which is maintained by both dynamic and thermal forcing effects of transient waves and the dispersion of stationary waves from the North Atlantic to Eurasia (Wei et al., 2020b). In contrast, it is loosely related to atmospheric external forcing and implies relatively low predictability of the two modes.

### 4.3. Interannual variations of the EAWM

The interannual variations of the EAWM have been studied extensively (e.g., Chen et al., 2019). Recent progress includes the impacts of Arctic sea ice (Ding et al., 2021b), the stratospheric QBO (Ma et al., 2021), and the COVID-19 pandemic on the winter climate. Arctic warming in the



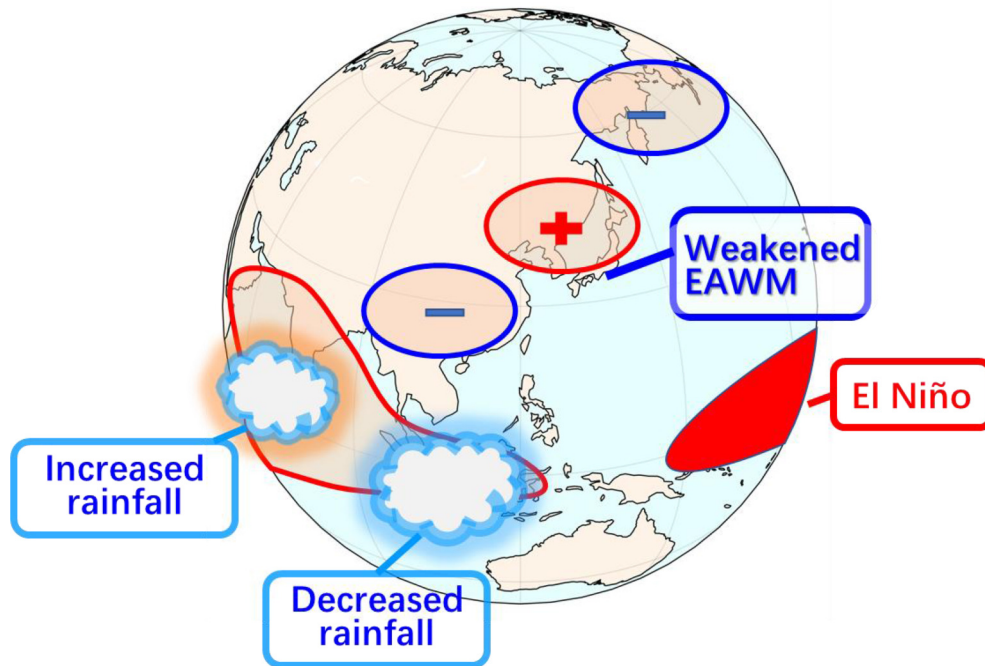


**Fig. 6.** Schematic of the possible roles of tropical Indian Ocean precipitation anomalies in the effects of ENSO on the EAWM. El Niño is typically accompanied by positive and negative precipitation anomalies in the tropical eastern and western Indian Ocean during early winter. This dipole precipitation anomaly, especially the eastern part, forces a Rossby wave train that propagates toward the pole. This Rossby wave train has an anomalous positive height center over Japan, leading to a weakening of the East Asian trough and hence a weakening of the EAWM.

Barents–Kara Sea (BKS) region is closely connected to cold winters over East Asia (e.g., [Kug et al., 2015](#); [Jang et al., 2019](#)). This warm BKS and cold East Asia SAT anomaly pattern is one of the dominant modes—namely, the third mode—of the winter SAT variability over the whole Northern Hemisphere extratropics ([Park et al., 2021](#)). The possible mechanism by which BKS warming is related to cooling in East Asia is suggested to take place through large-scale circulation patterns. BKS warming is accompanied by local development of an anomalous anticyclone and downstream development of an East Asian trough, which result in northerly flow and cold anomalies over East Asia ([Kug et al., 2015](#)). [Jang et al. \(2019\)](#) further showed that most current climate models can reasonably capture the above-mentioned warm BKS and cold East Asia relationship and the related physical processes. However, the causes of the close relationship remain controversial, with some suggesting it may be forced by Arctic sea-ice and SST anomalies, and others stating that it is contributed by internal atmospheric circulation (e.g., [Wang et al., 2020](#); [Dai and Deng, 2022](#); [Wang and Chen, 2022](#)).

Autumn sea-ice variability in the East Siberian–Chukchi–Beaufort Sea has been found to have strengthened in the past two decades, with its loss favoring a colder winter, including in central-western Eurasia and northeastern China, via a persistent Arctic anticyclonic anomaly and enhanced winter monsoon. Reduced sea-ice loss is believed to promote enhanced upward propagation of quasi-stationary

planetary waves and generate Eliassen–Palm flux convergence anomalies in both the upper troposphere and stratosphere, contributing to positive geopotential height anomalies in the Arctic ([Ding et al., 2021b](#)). In addition, previous studies have proposed that the QBO in the tropical stratosphere can affect tropospheric climate anomalies via three possible pathways—namely, the polar, subtropical, or tropical pathway. A recent study by [Ma et al. \(2021\)](#) showed that, during neutral ENSO winters (without El Niño or La Niña), the easterly phase of the QBO tends to be associated with a weakening of the EAWM through its effect on the subtropical westerly jet stream.

In addition, the short-term reduction in anthropogenic aerosol emissions during the COVID-19 pandemic may have affected the local East Asian atmospheric circulation and climate ([Lee et al., 2021](#)). CESM simulations also suggest that the reduction in aerosols in eastern China may have led to surface warming there, albeit the simulated warming is much weaker than the observed one. It is suggested that the direct radiative effect of aerosol, i.e., an increase in downward shortwave radiation, plays a key role in surface warming. Moreover, the initial surface warming can further drive an anomalous cyclone that advects warm and moist air to eastern China ([Lee et al., 2021](#)).

## 5. The Indian summer monsoon

Anomalies of the ISM greatly affect the Indian subconti-

ment and neighboring regions. In this section, we review the long-term changes in the ISM rainfall and factors, the influences of the Pacific, Indian and Atlantic SST anomalies on the interannual and interdecadal variations of the ISM rainfall. The interdecadal changes in the ISM-SST relationship are also covered.

### 5.1. Long-term changes in ISM rainfall

Changes in ISM rainfall have long been a concern in climatic studies. Research has shown that the ISM rainfall declined from 1950 to 1999 and recovered from 1999 to 2013 (e.g., Roxy et al., 2015; Jin and Wang, 2017; Roxy, 2017). The decline has been attributed to global warming, aerosol effects, deforestation, and a negative-to-positive phase transition of the IPO (Li et al., 2015; Paul et al., 2016; Chou et al., 2018). The accelerated warming over South Asia, which exceeded the tropical Indian Ocean warming, is considered to be the main driver of the ISM revival (Jin and Wang, 2017; Roxy, 2017).

The changes in ISM rainfall display spatial features. Varikoden et al. (2019) found an increasing (decreasing) trend in summer monsoon rainfall in the northern (southern) Western Ghats. They attributed this contrasting trend to a shift in the low-level westerlies over the region. Varikoden and Revadekar (2020) identified an increase in high-intensity rain events and a decrease in low-intensity rain events in the northeast regions of India. Maharana et al. (2021) linked the ISM rainfall changes to the spatial distribution of temperature and moisture changes over the Indian subcontinent. The recent weakening of the southwesterly flow was followed by a reduced northward moisture transport, leading to reduced rainfall over the Indo-Gangetic Plain and northeastern India, while the strengthening of the southwesterly flow was followed by enhanced northward moisture transport and hence increased rainfall over northwestern India.

The factors involved in these long-term ISM rainfall changes have been explored through observational analysis and numerical model experiments. Kumar and Singh (2021) suggested that the decadal trends in ISM rainfall over northeastern India and central India were controlled by long-term variations in the strength of El Niño events. Numerical experiments by Sandeep et al. (2020) showed that a weakening South Asian monsoon circulation is associated with a decline in the Atlantic Multidecadal Overturning Circulation, while precipitation exhibits contrasting responses that are dominated by a thermodynamic response. Through model simulations, Huang et al. (2020b) showed that the IPO contributed to the recent decline and recovery of ISM rainfall through moisture convergence anomalies associated with anomalous Walker circulation and meridional tropospheric temperature gradients along with the induced anomalous convection and zonal moisture advection. A positive-phase IPO appears to be related to decreased ISM rainfall through weakened Walker and Hadley circulations induced by warm SST anomalies over the TCEP, with the opposite occurring during negative phases of the IPO (Krishnamurthy and Krishnamurthy, 2014; Joshi and Kucharski, 2017).

Numerical model simulations have been conducted to understand the changes in the ISM and the roles of anthropogenic forcing. Li et al. (2021b) investigated the changes in ISM circulation and precipitation based on a large-ensemble simulation of the Canadian Earth System Model, version 2. It was found that the increase in global mean surface temperature weakened the large-ensemble mean ISM circulation but enhanced the precipitation and precipitable water. The decreased upper-level land–sea thermal contrast, which altered the meridional pressure gradient and consequently the upper-level winds, was found to be the main thermal driver of the weakening of the ISM circulation. The increase in ISM precipitation was mainly due to the positive contribution of the thermodynamic component. Ayantika et al. (2021) conducted numerical experiments with the IITM Earth System Model, version 2, to examine the individual and combined effects of GHGs and anthropogenic aerosol forcing on the response of ISM precipitation. The GHG forcing simulation showed an intensification of ISM precipitation, whereas a decrease in ISM precipitation and weakening of monsoon circulation was simulated in response anthropogenic aerosol forcing. Wang et al. (2019) investigated the physical mechanisms of anthropogenic aerosol-induced monsoon changes by decomposing the atmospheric change into a direct atmospheric response to radiative forcing and an SST-mediated change. They showed that the SST-mediated change dominated the aerosol-induced ISM response, with contributions from both the north–south interhemispheric SST gradient and the local SST cooling pattern over the tropical Indian Ocean.

### 5.2. Influences of Pacific Ocean SST anomalies on the ISM

ENSO is an important driver of the ISM variability (e.g., Yun and Timmermann, 2018; Hu et al., 2022e). ENSO influences the ISM through the Walker circulation and Hadley circulation. Kumar and Singh (2021) found significant spatiotemporal variation in the response of the ISM to El Niño. They identified a strengthening of the ISM over northeastern India during El Niño events. Schulte et al. (2021) found that the ENSO–ISM rainfall relationship is influenced by the SST anomaly gradient across the Niño-3 region. Roy et al. (2019) analyzed the ENSO–ISM rainfall connection in CMIP5 model simulations and found that practically no influence can be detected in any parts of India for pure Modoki ENSO events. Dandi et al. (2020) found that rainfall anomalies are negative over the southern Indian Peninsula and positive over the central parts of India during El Niño Modoki years. The atmospheric circulation over the WNP acts as a factor in determining the ISM rainfall anomaly pattern during El Niño Modoki years.

The ENSO–ISM relationship has experienced interdecadal changes in the past (Torrence and Webster, 1999; Krishnamurthy and Goswami, 2000; Kumar et al., 1999, 2006; Hu et al., 2022e), which, along with the plausible reasons why, continue to be a subject of recent studies (Feba et al., 2019; Roy et al., 2019; Dandi et al., 2020; Hrudya et al.,

2020, 2021; Pandey et al., 2020; Samanta et al., 2020; Seetha et al., 2020; Schulte et al., 2021; Srivastava et al., 2020; Fan et al., 2021; Kumar and Singh, 2021; Mahendra et al., 2021; Varikoden et al., 2022; Hu et al., 2022e). Pandey et al. (2020) separated the ENSO–ISM rainfall relationship into a “long-term” component and a “short-term” component. They found that the change in the ENSO–ISM rainfall relationship is mainly in the “long-term” component, which changes with an increase in GHG forcing, whereas the “short-term” component does not change appreciably.

The changes in the ENSO–ISM rainfall teleconnections display regional features. Mahendra et al. (2021) found that the ENSO teleconnection to rainfall over northern central India and the southern Indian Peninsula is stronger and more stable in all epochs, whereas the ENSO teleconnection to rainfall over central India and eastern central India has experienced large epochal changes. Seetha et al. (2020) found that the changes in the ENSO–ISM rainfall relationship are mostly pronounced in the ISM core zone. During 1931–1960, the effect of La Niña was more dominant owing to more La Niña events and larger Niño-3.4 SST anomalies. The rainfall during 1961–1990 and 1991–2015 was below normal because of strong El Niño events. These changes were associated with changes in the equatorial Walker and regional Hadley circulations, which modify the low-level monsoon winds and hence the moisture supply to the Indian subcontinent.

The impacts of ENSO on ISM rainfall and their interdecadal changes display subseasonal dependence. Hrudya et al. (2020) compared the impacts of ENSO on ISM rainfall during the onset (June), peak (July–August) and withdrawal (September) phases for the period 1951–2015 and explored the changes in the ENSO–monsoon relationship from earlier decades (1951–1980) to more recent decades (1986–2015). They identified noticeable changes in the ENSO–ISM relationship from the earlier to more recent decades during all three phases. During El Niño events, rainfall increased over most of India in the more recent decades during the onset phase, but decreased during the peak and withdrawal phases. During La Niña events, rainfall decreased over the monsoon core zone of India during all three phases. Srivastava et al. (2020) investigated the impact of ENSO on ISM rainfall during July and August and detected significant changes at multidecadal timescales in the relationship between ENSO and ISM rainfall during July and August. While the impact of ENSO was strong in August and weak in July during 1948–1980, August rainfall showed a weaker relationship to ENSO than July rainfall during the post-1980s.

The impacts of ENSO on the ISM appear to depend upon the equatorial Pacific SST anomaly pattern. Fan et al. (2021) found that the roles of the eastern Pacific (EP) and central Pacific (CP) types of ENSO on the ISM experienced notable multidecadal modulation in the late 1970s. They showed that CP-type ENSO plays a far more prominent role in producing anomalous ISM rainfall after the late 1970s, when the inverse relationship between EP-type ENSO and

the ISM weakened dramatically. Samanta et al. (2020) showed that half of the reduction in ISM rainfall during post-1980 La Niña events can be attributed to changes in the spatial pattern and intensity of those events.

### 5.3. Influences of Indian Ocean SST anomalies on the ISM

Another important factor of the ISM variability is the Indian Ocean SST anomalies (e.g., Ashok et al., 2001; Ummenhofer et al., 2011; Chowdary et al., 2015). Crétat et al. (2017) studied the impact of the Indian Ocean on ISM rainfall by removing the influences of the Pacific Ocean in model simulations. They found that the ISM rainfall variability was barely modified by the Indian Ocean, and the Indian Ocean did not force the monsoon circulation in the absence of ENSO. Vibhute et al. (2020) explored the decadal variability of tropical Indian Ocean SST and its association with ISM rainfall variability. They found a two-year lag correlation between the decadal-scale tropical Indian Ocean SST and Indian rainfall over the monsoon core zone.

The IOD is an important modulator of the variability of ISM rainfall (Ashok et al. 2004). Krishnaswamy et al. (2015) studied recent shifts in the impact of the IOD on ISM rainfall and found a strengthened impact of the IOD during the period 1942–2011. Then, in a subsequent study, Krishnaswamy et al. (2015) found that the influence of the IOD on mean ISM rainfall and extreme rainfall events has been strengthening in recent decades, but that of ENSO has been weakening. Hrudya et al. (2021) explored the changes in the IOD–ISM rainfall relationship from earlier (1951–1980) to more recent (1986–2015) decades during different phases of the ISM. Their analyses indicated that the IOD–ISM rainfall relationship strengthened during the withdrawal phase (September) over most of India in the more recent decades, but weakened during the onset phase (June). During the peak phase (July–August), the relationship changed from being out-of-phase (negative correlation) to in-phase (positive correlation) over most of the Indian subcontinent. During positive IOD events, an increase in rainfall over the Indian region was observed during all three phases in the more recent decades. During negative IOD events, a decrease in rainfall over the Indian subcontinent was observed during the peak and withdrawal phases.

The relationship between ISM rainfall and the IOD depends upon the distribution of IOD SST anomalies. Jiang et al. (2022) identified differences in the relationship between the ISM and IOD events according to their SST anomaly pattern: Type-W IOD events, with stronger SST anomalies in the western pole, are associated with a weak ISM from May to summer; Type-E IOD events, with stronger SST anomalies in the eastern pole, are associated with a strong ISM; and Type-C events, with comparable SST anomalies in both poles, are synchronous with weak ISM anomalies.

The role of the Indian Ocean in ISM rainfall may take place through its influence on the cycle of ENSO events. Through decoupled model experiments, Terray et al. (2021)



found that the Indian Ocean feedback to ENSO accelerated El Niño shifting to La Niña and modulated the length of ENSO events. This Indian Ocean feedback was mostly active during the decaying phase of El Niño, which was accompanied by a basin-wide warming in the Indian Ocean.

#### 5.4. Influences of Atlantic SST anomalies on the ISM

Studies have demonstrated the influence of the Atlantic Niño or Atlantic zonal mode (AZM) on the ISM (Kucharski et al. 2007, 2008, 2009; Nair et al., 2018; Sabeerali et al., 2019). The SST anomalies associated with the AZM modify the low-level convergence over India and thereby the ISM rainfall. Pottapinjara et al. (2014) showed that a warm (cold) AZM event leads to a decrease (an increase) in the number of monsoon depressions over the Bay of Bengal and thereby reduces (enhances) rainfall over India. The AZM induces a Kelvin wave-like response in tropospheric temperature that propagates to the east to reach the Indian Ocean and modulates the mid-tropospheric land-sea thermal gradient and thereby the ISM (Pottapinjara et al., 2014). Pottapinjara et al. (2021) used the Coupled Forecast System, version 2, to examine how well the model simulates this AZM-ISM link. The model simulations showed a Matsuno-Gill-type response to a warm AZM SST anomaly, with anomalous descending motion and reduced rainfall over India. Sabeerali et al. (2019) identified a strengthening in the relationship between ISM rainfall and the AZM in recent decades, which they attributed to the increase in the eastern equatorial Atlantic Ocean SST anomalies.

Recent studies have revealed an association between ISM rainfall and the Atlantic Multidecadal Oscillation (AMO) on multi-decadal timescales (Goswami et al., 2006; Zhang and Delworth, 2006; Wang et al., 2009c; Luo et al., 2011, 2018a, b; Krishnamurthy and Krishnamurthy, 2016). The AMO modulates the subseasonal change in the influences of North Atlantic SST anomalies on ISM rainfall (Borah et al., 2019; Rajesh and Goswami, 2020). The relationship between the ISM and the AMO is not stable over time (Malik et al., 2017). Luo et al. (2018c) detected a weakening of the ISM rainfall-AMO connection since the mid-1990s. Ahmad et al. (2022) investigated the AMO-ISM connection using CESM large-ensemble simulations and found an unstable connection in the 1800-year pre-industrial simulation, which they attributed to internal climatic processes. Their analysis suggests a substantial role played by subtropical WNP SSTs in modulating the link between the ISM and AMO.

A link has been found between the spring Atlantic meridional mode (AMM) and ISM rainfall (Vittal et al., 2020). Vittal et al. (2020) showed that ISM rainfall increases (decreases) during positive (negative) phases of the AMM. During a positive phase of the spring AMM, positive SST anomalies in the tropical North Atlantic Ocean strengthen anomalies of cyclonic circulation and convection over the Sahel region, which in turn modulate the winds over the western Indian Ocean, thereby cooling the SST there and strengthening the monsoon circulation over India.

## 6. Summary and discussion

This paper reviews the multi-scale climate variations and mechanisms of the Asian monsoon, with an emphasis on the latest research progress in the past several years. Previous studies on the EASM were primarily devoted to its onset over the SCS and its intensity, whereas attention in recent years has also been paid to its seasonal evolution (i.e., monsoon onset, withdrawal, and that between). For example, recent studies have investigated the climatological (Hu et al., 2019b), interdecadal (Hu et al., 2019a), interannual (Hu et al., 2019b, 2020b, c), and intraseasonal (Hu et al., 2019c) variations of SCSSM withdrawal. Since Chen et al. (2022a) already reviewed the progress made in the onset and withdrawal of the SCSSM, we mainly focus here on more recent advances, especially regarding monsoon onset. Results indicate that the local monsoon onset tends to be synchronously advanced or delayed over the Arabian Sea, Bay of Bengal, Indochina Peninsula, and SCS; and this synchronized variation of local monsoon onset can be attributed to both atmospheric internal processes (e.g., 30–80-day oscillation) and external forcings (e.g., ENSO, IPO, and the Tibetan Plateau thermal condition), depending on the time scale of the variations. Results also indicate that substantial achievements have been made in understanding the interdecadal change in the SCSSM onset around the mid-to-late 1990s. Moreover, it has been suggested that the average date of SCSSM onset was delayed again in the early 2010s. In addition, the relationship between SCSSM onset and extreme rainfall over southern China and Southeast Asia has been investigated.

Among the achievements in research on SCSSM onset, a particularly interesting result is the weakened relationship between ENSO and SCSSM onset in recent years. Conventionally, ENSO is regarded as the most important predictor of SCSSM onset (Zhu and Li, 2017; Martin et al., 2019). However, the weakened relationship between ENSO and SCSSM onset has driven us to look for other factors that may be of influence. Recent studies have highlighted the extratropical factors affecting SCSSM onset, including the midlatitude Rossby wave train (Liu and Zhu, 2019; Deng et al., 2020; Xu and Li, 2021), AO (Hu et al., 2021), Victoria mode (Hu et al., 2022b), PDO (Hu et al., 2022c), and quasi-biweekly oscillation originated from the Tibetan Plateau (Liu and Zhu, 2021). These factors need to be taken into account to create a new forecasting model that can hopefully overcome forecast errors like those in 2018 (Liu and Zhu, 2020) and 2019 (Hu et al., 2020a).

Regarding the EASM, the record-breaking mei-yu in 2020 has been extensively investigated, revealing the contributing factors at different time scales (interdecadal, interannual, subseasonal, synoptic, and diurnal). Among them, the warming Indian Ocean and the SST anomalies in both the tropical Pacific and Atlantic have been suggested as having contributed directly to this super mei-yu event. Also, the extremely low Arctic sea ice in late spring and early summer may have played a role. In addition to impacts from natural variability, the 2020 extreme summer rainfall might have

been related to the reduction in aerosols during the COVID-19 pandemic. Besides, the link between the summer monsoon rainfall over East Asia and South Asia has been further investigated. Recent advances include understanding the non-stationary and intraseasonal variation of their linkage. It is worth mentioning that earlier studies considered the SASM as a more active influencing factor, with the EASM as a passive recipient of influences. However, recent results have also revealed the impacts and feedbacks of the EASM on the SASM, with several mechanisms proposed.

In pace with the EASM reaching its northernmost position, the rainy season begins in the northern part of China, Korea, and Japan. A southward or northward shift of the summer monsoon northern boundary is often accompanied by summertime dry/wet climate anomalies in Northeast Asia. Since this summer monsoon northern boundary is generally located in the transitional climate belt between southern humid and northern arid regions, the MTZ has suffered from frequent meteorological disasters in recent decades due to the extremely fragile ecosystem with high sensitivity to climate change. Recent studies have investigated the summer precipitation variations and revealed the roles of SST anomalies over the tropical Pacific and North Atlantic on both interannual and interdecadal timescales. Moreover, future changes in MTZ precipitation have been projected, with its uncertainty analyzed by separating the external forcing and internal atmospheric variability. Preliminary observational studies have also found clear interdecadal changes in the EASM northern boundary over the past 70 years. However, climate model simulations suggest a northward extension of the EASM during the mid-Holocene and global warming scenarios (Piao et al., 2020; Wang et al., 2023). Hence, the issue of why the EASM northern boundary has not shown a persistent northward shift in the context of global warming should be addressed. Possible underlying mechanisms for the interdecadal variation in the EASM northern boundary also need to be investigated. It is commonly acknowledged that global warming will continue in the future even under a carbon-neutral scenario, posing a severe threat to ecological balance and sustainable development, especially over regions with fragile ecosystems and high sensitivity to climate change. Thus, further research on the interdecadal changes in the EASM northern boundary will not only advance our understanding of regional climate responses to global warming, but also provide important scientific support for national strategic decision-making in the short to medium term to address climate change.

Regarding the EAWM, significant advances have been made, especially in studies on its interdecadal, long-term, and subseasonal variations. Results suggest that the recovery of EAWM intensity after the early-2000s in the presence of continuing GHG emissions was dominated by internal climate variability (mostly the AO). Moreover, the interannual variability of the EAWM has also been found to have experienced multidecadal changes. However, the mechanisms underlying these changes in the EAWM system, including the Siberian

high, need further study in the future. On the subseasonal timescale, the wind variations over East Asia are associated with two Rossby wave trains propagating along the polar front jet and the subtropical jet, which have significant impacts on cold anomalies over this region. The influence of the MJO on the EAWM has been found to be modulated by both the AO and the QBO. The intraseasonal variations of the EAWM have also been shown to interact closely with tropical rainfall/convection over the western Pacific. The ENSO–EAWM relationship has been found to be stronger during early winter than late winter, and the mechanism is possibly related to subseasonal changes in the teleconnections of ENSO over East Asia.

As an important component of the Asian monsoon, research on the ISM has a long history, and many achievements have been made in ISM research in recent years. Specifically, the ISM revival around the end of the last century attracts a wide range of interest. Results suggest that the accelerated warming over South Asia, which exceeds the tropical Indian Ocean warming, was the main driver of the ISM rainfall recovery. Possible factors behind long-term ISM rainfall changes have been explored through observational analysis and numerical model experiments. Additionally, numerous studies have further investigated the influences on the ISM from Pacific Ocean, Indian Ocean, and Atlantic Ocean SST anomalies. In particular, the changes in the ENSO–ISM relationship and the plausible reasons have continued to be a key focus. Results indicate significant spatiotemporal variation in the ISM response to ENSO. Noticeable changes in the ENSO–ISM relationship have been identified from earlier to more recent decades during the onset, peak, and withdrawal phases. Similarly, the interdecadal changes of the relationship of the ISM with the IOD, AZM, and AMO have been explored. In addition, recent results show that the impacts of ENSO and the IOD on the ISM appear to depend upon the distribution of the equatorial Pacific and IOD SST anomaly pattern.

During the past several years, significant advances have been achieved in understanding the variations of the Asian monsoon at different temporal and spatial scales. It is noteworthy that there are complex interactions across both of these scales. A detailed understanding of the changes in the Asian monsoon requires an integrated investigation of these interactions. Moreover, we still face great challenges in predicting and projecting the Asian monsoon successfully, which mainly involves the use of climate models. Obviously, more studies are needed to evaluate the simulation abilities of current models in terms of the interdecadal and intraseasonal variations in the Asian monsoon. Finally, relatively little attention has been paid to the evolution of the EAWM compared with that of the EASM. The changes in EAWM evolution should be emphasized in future studies, which would enrich our understanding of the whole seasonal march of the Asian monsoon.

**Acknowledgements.** We thank the two anonymous reviewers for their constructive suggestions, which led to significant improve-

ments to the original manuscript. This study was supported by the National Natural Science Foundation of China (Grant Nos. 42230605 and 41721004).

## REFERENCES

- Abdillah, M. R., Y. Kanno, and T. Iwasaki, 2017: Tropical-extratropical interactions associated with East Asian cold air outbreaks. Part I: Interannual variability. *J. Climate*, **30**, 2989–3007, <https://doi.org/10.1175/JCLI-D-16-0152.1>.
- Ahmad, A., S. L. Li, F. F. Luo, and Y. Q. Gao, 2022: The unstable connection between Atlantic Multidecadal Oscillation and Indian Summer Monsoon in CESM-LE. *Climate Dyn.*, **58**, 1525–1537, <https://doi.org/10.1007/S00382-021-05976-6>.
- Ai, Y., N. Jiang, W. H. Qian, J. C.-H. Leung, and Y. Y. Chen, 2022: Strengthened regulation of the onset of the South China Sea summer monsoon by the Northwest Indian Ocean warming in the past decade. *Adv. Atmos. Sci.*, **39**, 943–952, <https://doi.org/10.1007/s00376-021-1364-8>.
- Allen R. J., and C. S. Zender, 2011: Forcing of the arctic oscillation by Eurasian snow cover. *J. Climate*, **24**, 6528–6539, <https://doi.org/10.1175/2011JCLI4157.1>.
- An, X. D., L. F. Sheng, Q. Liu, C. Li, Y. Gao, and J. P. Li, 2020: The combined effect of two westerly jet waveguides on heavy haze in the North China Plain in November and December 2015. *Atmospheric Chemistry and Physics*, **20**, 4667–4680, <https://acp.copernicus.org/articles/20/4667/2020/>.
- An, X. D., W. Chen, S. Fu, P. Hu, C. Li, and L. F. Sheng, 2022: Possible dynamic mechanisms of high- and low-latitude wave trains over Eurasia and their impacts on air pollution over the North China Plain in Early Winter. *J. Geophys. Res.*, **127**, e2022JD036732, <https://doi.org/10.1029/2022JD036732>.
- Ashok, K., Z. Y. Guan, and T. Yamagata, 2001: Impact of the Indian Ocean Dipole on the relationship between the Indian monsoon rainfall and ENSO. *Geophys. Res. Lett.*, **28**, 4499–4502, <https://doi.org/10.1029/2001GL013294>.
- Ashok, K., Z. Y. Guan, N. H. Saji, and T. Yamagata, 2004: Individual and combined influences of ENSO and the Indian Ocean Dipole on the Indian summer monsoon. *J. Climate*, **17**, 3141–3155, [https://doi.org/10.1175/1520-0442\(2004\)017<3141:IACIOE>2.0.CO;2](https://doi.org/10.1175/1520-0442(2004)017<3141:IACIOE>2.0.CO;2).
- Ayantika, D. C., R. Krishnan, M. Singh, P. Swapna, N. Sandeep, A. G. Prajeesh, and R. Vellore, 2021: Understanding the combined effects of global warming and anthropogenic aerosol forcing on the South Asian monsoon. *Climate Dyn.*, **56**, 1643–1662, <https://doi.org/10.1007/s00382-020-05551-5>.
- Barnett, T. P., L. Dümenil, U. Schlese, E. Roeckner, and M. Latif, 1989: The effect of Eurasian snow cover on regional and global climate variations. *J. Atmos. Sci.*, **46**(5), 661–686, [https://doi.org/10.1175/1520-0469\(1989\)046<0661:TEOESC>2.0.CO;2](https://doi.org/10.1175/1520-0469(1989)046<0661:TEOESC>2.0.CO;2).
- Bombardi, R. J., J. L. Kinter III, and O. W. Frauenfeld, 2019: A global gridded dataset of the characteristics of the rainy and dry seasons. *Bull. Amer. Meteor. Soc.*, **100**, 1315–1328, <https://doi.org/10.1175/BAMS-D-18-0177.1>.
- Bombardi, R. J., V. Moron, and J. S. Goodnight, 2020: Detection, variability, and predictability of monsoon onset and withdrawal dates: A review. *International Journal of Climatology*, **40**, 641–667, <https://doi.org/10.1002/joc.6264>.
- Borah, P., V. Venugopal, J. Sukhatme, P. Muddebihal, and B. N. Goswami, 2019: Role of the North Atlantic in Indian Monsoon Droughts. Available from <https://arxiv.org/abs/1911.10013>.
- Cai, Y. N., Z. S. Chen, and Y. Du, 2022: The role of Indian Ocean warming on extreme rainfall in central China during early summer 2020: Without significant El Niño influence. *Climate Dyn.*, **59**, 951–960, <https://doi.org/10.1007/s00382-022-06165-9>.
- Cen, S. X., W. Chen, S. F. Chen, L. Wang, Y. Y. Liu, and J. L. Huangfu, 2022: Weakened influence of El Niño–Southern Oscillation on the zonal shift of the South Asian High after the early 1980s. *International Journal of Climatology*, **42**, 7583–7597, <https://doi.org/10.1002/joc.7666>.
- Chang, C. P., M. M. Lu, and S. Wang, 2011: The East Asian winter monsoon. *The Global Monsoon System: Research and Forecast*. 2nd ed, C. P. Chang et al., Eds., World Scientific, 99–109, <https://doi.org/10.1142/8109>.
- Chen, J., W. Huang, L. Y. Jin, J. H. Chen, S. Q. Chen, and F. H. Chen, 2018: A climatological northern boundary index for the East Asian summer monsoon and its interannual variability. *Science China Earth Sciences*, **61**, 13–22, <https://doi.org/10.1007/s11430-017-9122-x>.
- Chen, J. Q., and S. Bordoni, 2014: Orographic effects of the Tibetan Plateau on the East Asian summer monsoon: An energetic perspective. *J. Climate*, **27**(8), 3052–3072, <https://doi.org/10.1175/JCLI-D-13-00479.1>.
- Chen, W., H. F. Graf, and R. H. Huang, 2000: The interannual variability of East Asian winter monsoon and its relation to the summer monsoon. *Adv. Atmos. Sci.*, **17**, 48–60, <https://doi.org/10.1007/s00376-000-0042-5>.
- Chen, W., L. Wang, Y. K. Xue, and S. F. Sun, 2009: Variabilities of the spring river runoff system in East China and their relations to precipitation and sea surface temperature. *International Journal of Climatology*, **29**, 1381–1394, <https://doi.org/10.1002/joc.1785>.
- Chen, W., J. Feng, and R. G. Wu, 2013: Roles of ENSO and PDO in the Link of the East Asian Winter Monsoon to the following Summer Monsoon. *J. Climate*, **26**, 622–635, <https://doi.org/10.1175/JCLI-D-12-00021.1>.
- Chen, W., L. Wang, J. Feng, Z. P. Wen, T. J. Ma, X. Q. Yang, and C. H. Wang, 2019: Recent progress in studies of the variabilities and mechanisms of the East Asian Monsoon in a changing climate. *Adv. Atmos. Sci.*, **36**, 887–901, <https://doi.org/10.1007/s00376-019-8230-y>.
- Chen, W., and Coauthors, 2021a: East Asian monsoon variability and its association with China’s climate under global warming. *Climate and Ecological Environment Evolution in China 2021: The Science Basis*, D. H. Qin and P. M. Zhai, Eds., Science Press. (in Chinese)
- Chen, W., P. Hu, and J. L. Huangfu, 2022a: Multi-scale climate variations and mechanisms of the onset and withdrawal of the South China Sea summer monsoon. *Science China Earth Sciences*, **65**, 1030–1046, <https://doi.org/10.1007/s11430-021-9902-5>.
- Chen, X. D., A. G. Dai, Z. P. Wen, and Y. Y. Song, 2021b: Contributions of Arctic sea - ice loss and East Siberian atmospheric blocking to 2020 record - breaking Meiyu - Baiu rainfall. *Geophys. Res. Lett.*, **48**, e2021GL092748, <https://doi.org/10.1029/2021GL092748>.
- Chen, X. D., Z. P. Wen, Y. Y. Song, and Y. Y. Guo, 2022b: Causes of extreme 2020 Meiyu-Baiu rainfall: A study of combined effect of Indian Ocean and Arctic. *Climate Dyn.*, **59**, 3485–3501, <https://doi.org/10.1007/S00382-022-06279-0>.



- Chou, C., D. Ryu, M.-H. Lo, H.-W. Wey, and H. M. Malano, 2018: Irrigation-induced land-atmosphere feedbacks and their impacts on Indian Summer Monsoon. *J. Climate*, **31**, 8785–8801, <https://doi.org/10.1175/JCLI-D-17-0762.1>.
- Chowdary, J. S., A. B. Bandgar, C. Gnanaseelan, and J. J. Luo, 2015: Role of tropical Indian Ocean Air-Sea interactions in modulating Indian summer monsoon in a coupled model. *Atmos. Sci. Lett.*, **16**, 170–176, <https://doi.org/10.1002/asl2.561>.
- Chowdary, J. S., K. M. Hu, G. Srinivas, Y. Kosaka, L. Wang, and K. K. Rao, 2019: The Eurasian Jet streams as conduits for East Asian monsoon variability. *Current Climate Change Reports*, **5**, 233–244, <https://doi.org/10.1007/s40641-019-00134-x>.
- Chu, Q. C., T. Lian, D. K. Chen, X. J. Wang, J. Feng, G. L. Feng, S. L. Qu, and Z. P. Zhang, 2022: The role of El Niño in the extreme Mei-Yu rainfall in 2020. *Atmospheric Research*, **266**, 105965, <https://doi.org/10.1016/j.atmosres.2021.105965>.
- Crétat, J., P. Terray, S. Masson, K. P. Sooraj, and M. K. Roxy, 2017: Indian Ocean and Indian summer monsoon: Relationships without ENSO in ocean-atmosphere coupled simulations. *Climate Dyn.*, **49**, 1429–1448, <https://doi.org/10.1007/s00382-016-3387-x>.
- Dai, A. G., and J. C. Deng, 2022: Recent Eurasian winter cooling partly caused by internal multidecadal variability amplified by Arctic sea ice-air interactions. *Climate Dyn.*, **58**, 3261–3277, <https://doi.org/10.1007/s00382-021-06095-y>.
- Dandi, R. A., J. S. Chowdary, P. A. Pillai, N. S. S. Sidhan, K. Koteswararao, and S. Ramakrishna, 2020: Impact of El Niño Modoki on Indian summer monsoon rainfall: Role of western north Pacific circulation in observations and CMIP5 models. *International Journal of Climatology*, **40**, 2117–2133, <https://doi.org/10.1002/joc.6322>.
- Deng, K. Q., S. Yang, D. J. Gu, A. L. Lin, and C. H. Li, 2020: Record-breaking heat wave in southern China and delayed onset of South China Sea summer monsoon driven by the Pacific subtropical high. *Climate Dyn.*, **54**, 3751–3764, <https://doi.org/10.1007/s00382-020-05203-8>.
- Ding, L. D., T. Li, and Y. Sun, 2021a: Subseasonal and synoptic variabilities of precipitation over the Yangtze River Basin in the summer of 2020. *Adv. Atmos. Sci.*, **38**, 2108–2124, <https://doi.org/10.1007/s00376-021-1133-8>.
- Ding, Q. H., and B. Wang, 2005: Circumglobal teleconnection in the northern Hemisphere summer. *J. Climate*, **18**, 3483–3505, <https://doi.org/10.1175/JCLI3473.1>.
- Ding, Q. H., and B. Wang, 2007: Intraseasonal teleconnection between the summer Eurasian wave train and the Indian monsoon. *J. Climate*, **20**, 3751–3767, <https://doi.org/10.1175/JCLI4221.1>.
- Ding, S. Y., B. Y. Wu, and W. Chen, 2021b: Dominant characteristics of early autumn arctic Sea Ice variability and its impact on Winter Eurasian Climate. *J. Climate*, **34**, 1825–1846, <https://doi.org/10.1175/JCLI-D-19-0834.1>.
- Ding, Y. H., 1994: *Monsoons over China*. Springer, 420 pp, <https://doi.org/10.1007/978-94-015-8302-2>.
- Ding, Y. H., 2007: The variability of the Asian summer monsoon. *J. Meteor. Soc. Japan*, **85B**, 21–54, <https://doi.org/10.2151/jmsj.85B.21>.
- Ding, Y. H., and T. N. Krishnamurti, 1987: Heat budget of the Siberian high and the winter monsoon. *Mon. Wea. Rev.*, **115**, 2428–2449, [https://doi.org/10.1175/1520-0493\(1987\)115<2428:HBOTSH>2.0.CO;2](https://doi.org/10.1175/1520-0493(1987)115<2428:HBOTSH>2.0.CO;2).
- Ding, Y. H., and J. C. L. Chan, 2005: The East Asian summer monsoon: An overview. *Meteorol. Atmos. Phys.*, **89**, 117–142, <https://doi.org/10.1007/s00703-005-0125-z>.
- Ding, Y. H., and Coauthors, 2014: Interdecadal variability of the East Asian winter monsoon and its possible links to global climate change. *J. Meteor. Res.*, **28**, 693–713, <https://doi.org/10.1007/s13351-014-4046-y>.
- Ding, Y. H., Y. J. Liu, Y. F. Song, and J. Zhang, 2015: From MONEX to the global monsoon: A review of monsoon system research. *Adv. Atmos. Sci.*, **32**, 10–31, <https://doi.org/10.1007/s00376-014-0008-7>.
- Ding, Y. H., P. Liang, Y. J. Liu, and Y. C. Zhang, 2020: Multiscale variability of Meiyu and its prediction: A new review. *J. Geophys. Res.*, **125**, e2019JD031496, <https://doi.org/10.1029/2019JD031496>.
- Ding, Y. H., Y. Y. Liu, and Z.-Z. Hu, 2021c: The record-breaking mei-yu in 2020 and associated atmospheric circulation and tropical SST anomalies. *Adv. Atmos. Sci.*, **38**, 1980–1993, <https://doi.org/10.1007/s00376-021-0361-2>.
- Dong, Z. Z., and L. Wang, 2022: Quasi-biweekly oscillation over the western North Pacific in boreal winter and its influence on the central North American air temperature. *J. Climate*, **35**(6), 1901–1913, <https://doi.org/10.1175/JCLI-D-21-0531.1>.
- Duan, A. M., and G.-X. Wu, 2005: Role of the Tibetan Plateau thermal forcing in the summer climate patterns over subtropical Asia. *Climate Dyn.*, **24**(7–8), 793–807, <https://doi.org/10.1007/s00382-004-0488-8>.
- Duan, A. M., Z. X. Xiao, and Z. Q. Wang, 2018: Impacts of the Tibetan Plateau winter/spring snow depth and surface heat source on Asian summer monsoon: A review. *Chinese Journal of Atmospheric Sciences*, **42**, 755–766, <https://doi.org/10.3878/j.issn.1006-9895.1801.17247>. (in Chinese with English abstract)
- Enomoto, T., B. J. Hoskins, and Y. Matsuda, 2003: The formation mechanism of the Bonin high in August. *Quart. J. Roy. Meteor. Soc.*, **129**, 157–178, <https://doi.org/10.1256/qj.01.211>.
- Fan, F. X., R. P. Lin, X. H. Fang, F. Xue, F. Zheng, and J. Zhu, 2021: Influence of the eastern Pacific and Central Pacific types of ENSO on the South Asian summer monsoon. *Adv. Atmos. Sci.*, **38**, 12–28, <https://doi.org/10.1007/s00376-020-0055-1>.
- Feba, F., K. Ashok, and M. Ravichandran, 2019: Role of changed Indo-Pacific atmospheric circulation in the recent disconnect between the Indian summer monsoon and ENSO. *Climate Dyn.*, **52**, 1461–1470, <https://doi.org/10.1007/s00382-018-4207-2>.
- Feng, J., and W. Chen, 2021: Roles of the North Indian Ocean SST and tropical North Atlantic SST in the latitudinal extension of the anomalous western North Pacific anticyclone during the El Niño decaying summer. *J. Climate*, **34**, 8503–8517, <https://doi.org/10.1175/JCLI-D-20-0802.1>.
- Feng, J., and W. Chen, 2022: Respective and combined Impacts of North Indian Ocean and tropical North Atlantic SST anomalies on the subseasonal evolution of anomalous western North Pacific anticyclones. *J. Climate*, **35**, 5623–5636, <https://doi.org/10.1175/JCLI-D-21-0799.1>.
- Fu, S. M., H. Tang, J. H. Sun, T. B. Zhao, and W. L. Li, 2022: Historical rankings and vortices' activities of the extreme Mei-Yu seasons: Contrast 2020 to previous Mei-Yu seasons. *Geo-*



- phys. Res. Lett.*, **49**, e2021GL096590, <https://doi.org/10.1029/2021GL096590>.
- Ge, Z.-A., L. Chen, T. Li, and L. Wang, 2022: How frequently will the persistent heavy rainfall over the Middle and Lower Yangtze River Basin in Summer 2020 happen under global warming. *Adv. Atmos. Sci.*, **39**, 1673–1692, <https://doi.org/10.1007/s00376-022-1351-8>.
- Gong, H. N., L. Wang, W. Chen, and R. G. Wu, 2019a: Attribution of the East Asian winter temperature trends during 1979–2018: Role of external forcing and internal variability. *Geophys. Res. Lett.*, **46**, 10 874–10 881, <https://doi.org/10.1029/2019GL084154>.
- Gong, H. N., L. Wang, W. Chen, and R. G. Wu, 2019b: Time-varying contribution of internal dynamics to wintertime land temperature trends over the northern Hemisphere. *Geophys. Res. Lett.*, **46**, 14 674–14 682, <https://doi.org/10.1029/2019GL086220>.
- Gong, H. N., L. Wang, W. Chen, and R. G. Wu, 2021: Evolution of the East Asian winter land temperature trends during 1961–2018: Role of internal variability and external forcing. *Environmental Research Letters*, **16**, 024015, <https://doi.org/10.1088/1748-9326/abd586>.
- Goswami, B. N., M. S. Madhusoodanan, C. P. Neema, and D. Sen Gupta, 2006: A physical mechanism for North Atlantic SST influence on the Indian summer monsoon. *Geophys. Res. Lett.*, **33**, L02706, <https://doi.org/10.1029/2005GL024803>.
- Gu, W., L. Wang, Z.-Z. Hu, K. M. Hu, and Y. Li, 2018: Interannual variations of the first rainy season precipitation over South China. *J. Climate*, **31**, 623–640, <https://doi.org/10.1175/JCLI-D-17-0284.1>.
- Guo, Y. Y., R. J. Zhang, Z. P. Wen, J. C. Li, C. Zhang, and Z. J. Zhou, 2021: Understanding the role of SST anomaly in extreme rainfall of 2020 Meiyu season from an interdecadal perspective. *Science China Earth Sciences*, **64**, 1619–1632, <https://doi.org/10.1007/s11430-020-9762-0>.
- Ha, K.-J., Y.-W. Seo, J.-Y. Lee, R. Kripalani, and K.-S. Yun, 2018: Linkages between the South and East Asian summer monsoons: A review and revisit. *Climate Dyn.*, **51**, 4207–4227, <https://doi.org/10.1007/s00382-017-3773-z>.
- He, J. H., and Z. W. Zhu, 2015: The relation of South China Sea monsoon onset with the subsequent rainfall over the subtropical East Asia. *International Journal of Climatology*, **35**, 4547–4556, <https://doi.org/10.1002/joc.4305>.
- He, J. H., H. Lin, and Z. W. Wu, 2011: Another look at influences of the Madden-Julian Oscillation on the wintertime East Asian weather. *J. Geophys. Res.*, **116**, D03109, <https://doi.org/10.1029/2010JD014787>.
- He, J. H., J. H. Ju, Z. P. Wen, J. M. Lü, and Q. H. Jin, 2007: A review of recent advances in research on Asian monsoon in China. *Adv. Atmos. Sci.*, **24**, 972–992, <https://doi.org/10.1007/s00376-007-0972-2>.
- He, S. P., 2013: Reduction of the East Asian winter monsoon interannual variability after the mid-1980s and possible cause. *Chinese Science Bulletin*, **58**, 1331–1338, <https://doi.org/10.1007/s11434-012-5468-5>.
- Hrudya, P. H., H. Varikoden, R. Vishnu, and J. Kuttippurath, 2020: Changes in ENSO-monsoon relations from early to recent decades during onset, peak and withdrawal phases of Indian summer monsoon. *Climate Dyn.*, **55**, 1457–1471, <https://doi.org/10.1007/s00382-020-05335-x>.
- Hrudya, P. P. V. H., H. Varikoden, and R. N. Vishnu, 2021: Changes in the relationship between Indian Ocean dipole and Indian summer monsoon rainfall in early and recent multi-decadal epochs during different phases of monsoon. *International Journal of Climatology*, **41**, E305–E318, <https://doi.org/10.1002/joc.6685>.
- Hsu, H.-H., T. J. Zhou, and J. Matsumoto, 2014: East Asian, Indochina and western North Pacific summer monsoon—an update. *Asia-Pacific Journal of Atmospheric Sciences*, **50**, 45–68, <https://doi.org/10.1007/s13143-014-0027-4>.
- Hu, D., A. M. Duan, and P. Zhang, 2022a: Association between regional summer monsoon onset in South Asia and Tibetan Plateau thermal forcing. *Climate Dyn.*, **59**, 1115–1132, <https://doi.org/10.1007/s00382-022-06174-8>.
- Hu, P., W. Chen, R. P. Huang, and D. Nath, 2018: On the weakening relationship between the South China Sea summer monsoon onset and cross-equatorial flow after the Late 1990s. *International Journal of Climatology*, **38**, 3202–3208, <https://doi.org/10.1002/joc.5472>.
- Hu, P., W. Chen, and S. F. Chen, 2019a: Interdecadal change in the South China Sea summer monsoon withdrawal around the mid-2000s. *Climate Dyn.*, **52**, 6053–6064, <https://doi.org/10.1007/s00382-018-4494-7>.
- Hu, P., W. Chen, S. F. Chen, and R. P. Huang, 2019b: Interannual variability and triggers of the South China Sea summer monsoon withdrawal. *Climate Dyn.*, **53**, 4355–4372, <https://doi.org/10.1007/s00382-019-04790-5>.
- Hu, P., W. Chen, R. P. Huang, and D. Nath, 2019c: Climatological characteristics of the synoptic changes accompanying South China Sea summer monsoon withdrawal. *International Journal of Climatology*, **39**, 596–612, <https://doi.org/10.1002/joc.5828>.
- Hu, P., W. Chen, S. F. Chen, and R. P. Huang, 2020a: Statistical analysis of the impacts of intra-seasonal oscillations on the South China Sea summer monsoon withdrawal. *International Journal of Climatology*, **40**, 1919–1927, <https://doi.org/10.1002/joc.6284>.
- Hu, P., W. Chen, S. F. Chen, Y. Y. Liu, and R. P. Huang, 2020b: Extremely early summer monsoon onset in the South China Sea in 2019 following an El Niño event. *Mon. Wea. Rev.*, **148**, 1877–1890, <https://doi.org/10.1175/MWR-D-19-0317.1>.
- Hu, P., W. Chen, S. F. Chen, Y. Y. Liu, R. P. Huang, and S. R. Dong, 2020c: Relationship between the South China Sea summer monsoon withdrawal and September–October rainfall over southern China. *Climate Dyn.*, **54**, 713–726, <https://doi.org/10.1007/s00382-019-05026-2>.
- Hu, P., W. Chen, S. F. Chen, Y. Y. Liu, L. Wang, and R. P. Huang, 2020d: Impact of the September silk road pattern on the South China Sea summer monsoon withdrawal. *International Journal of Climatology*, **40**, 6361–6368, <https://doi.org/10.1002/joc.6585>.
- Hu, P., W. Chen, S. F. Chen, Y. Y. Liu, L. Wang, and R. P. Huang, 2021: Impact of the March arctic oscillation on the South China Sea summer monsoon onset. *International Journal of Climatology*, **41**, E3239–E3248, <https://doi.org/10.1002/joc.6920>.
- Hu, P., W. Chen, S. F. Chen, L. Wang, and Y. Y. Liu, 2022b: The weakening relationship between ENSO and the South China Sea summer monsoon onset in recent decades. *Adv. Atmos. Sci.*, **39**, 443–455, <https://doi.org/10.1007/s00376-021-1208-6>.
- Hu, P., W. Chen, Z. B. Li, S. F. Chen, L. Wang, and Y. Y. Liu, 2022c: Close linkage of the South China Sea Summer mon-

- soon onset and extreme rainfall in may over Southeast Asia: Role of the synoptic-scale systems. *J. Climate*, **35**, 4347–4362, <https://doi.org/10.1175/JCLI-D-21-0740.1>.
- Hu, P., W. Chen, S. F. Chen, Y. Y. Liu, L. Wang, and R. P. Huang, 2022d: The leading mode and factors for coherent variations among the subsystems of tropical Asian summer monsoon onset. *J. Climate*, **35**(5), 1597–1612, <https://doi.org/10.1175/JCLI-D-21-0101.1>.
- Hu, P., W. Chen, L. Wang, S. F. Chen, Y. Y. Liu, and L. Y. Chen. 2022e: Revisiting the ENSO–monsoonal rainfall relationship: New insights based on an objective determination of the Asian summer monsoon duration. *Environmental Research Letters*, **17**(10): 104050, <https://doi.org/10.1088/1748-9326/ac97ad>.
- Huang, G., 2004: An index measuring the interannual variation of the East Asian summer monsoon—The EAP index. *Adv. Atmos. Sci.*, **21**, 41–52, <https://doi.org/10.1007/BF02915679>.
- Huang, M., J. D. Li, G. Zeng, and Y. K. Xie, 2020a: Regional characteristics of cloud radiative effects before and after the South China Sea summer monsoon onset. *J. Meteor. Res.*, **34**, 1167–1182, <https://doi.org/10.1007/s13351-020-0018-6>.
- Huang, R. H., and F. Y. Sun, 1992: Impacts of the tropical western Pacific on the East Asian summer monsoon. *J. Meteor. Soc. Japan*, **70**, 243–256, [https://doi.org/10.2151/jmsj1965.70.1B\\_243](https://doi.org/10.2151/jmsj1965.70.1B_243).
- Huang, R. H., L. T. Zhou, and W. Chen, 2003: The progresses of recent studies on the variabilities of the East Asian monsoon and their causes. *Adv. Atmos. Sci.*, **20**, 55–69, <https://doi.org/10.1007/BF03342050>.
- Huang, R. H., W. Chen, B. L. Yang, and R. H. Zhang, 2004: Recent advances in studies of the interaction between the East Asian winter and summer monsoons and ENSO cycle. *Adv. Atmos. Sci.*, **21**, 407–424, <https://doi.org/10.1007/BF02915568>.
- Huang, R. H., L. Gu, L. T. Zhou, and S. S. Wu, 2006: Impact of the thermal state of the tropical western Pacific on onset date and process of the South China Sea summer monsoon. *Adv. Atmos. Sci.*, **23**, 909–924, <https://doi.org/10.1007/s00376-006-0909-1>.
- Huang, R. H., J. L. Chen, L. Wang, and Z. D. Lin, 2012: Characteristics, processes, and causes of the Spatio-temporal variabilities of the East Asian monsoon system. *Adv. Atmos. Sci.*, **29**, 910–942, <https://doi.org/10.1007/s00376-012-2015-x>.
- Huang, R. H., Y. Liu, Z. C. Du, J. L. Chen, and J. L. Huangfu, 2017: Differences and links between the East Asian and South Asian summer monsoon systems: Characteristics and variability. *Adv. Atmos. Sci.*, **34**, 1204–1218, <https://doi.org/10.1007/s00376-017-7008-3>.
- Huang, X., and Coauthors, 2020b: The recent decline and recovery of Indian Summer monsoon rainfall: Relative roles of external forcing and internal variability. *J. Climate*, **33**, 5035–5060, <https://doi.org/10.1175/JCLI-D-19-0833.1>.
- Huangfu, J. L., R. H. Huang, and W. Chen, 2017: Relationship between the South China Sea summer monsoon onset and tropical cyclone genesis over the western North Pacific. *International Journal of Climatology*, **37**, 5206–5210, <https://doi.org/10.1002/joc.5141>.
- Jang, Y.-S., J.-S. Kug, and B.-M. Kim, 2019: How well do current climate models simulate the linkage between Arctic warming and extratropical cold winters. *Climate Dyn.*, **53**, 4005–4018, <https://doi.org/10.1007/s00382-019-04765-6>.
- Jeong, J. H., and C. H. Ho, 2005: Changes in occurrence of cold surges over east Asia in association with Arctic Oscillation. *Geophys. Res. Lett.*, **32**, L14704, <https://doi.org/10.1029/2005GL023024>.
- Jeong, Y. C., S. W. Yeh, Y. K. Lim, A. Santoso, and G. J. Wang, 2022: Indian Ocean warming as key driver of long-term positive trend of Arctic Oscillation. *npj Clim Atmos Sci*, **5**, 56, <https://doi.org/10.1038/s41612-022-00279-x>.
- Jiang, J. L., Y. M. Liu, J. Y. Mao, J. P. Li, S. W. Zhao, and Y. Q. Yu, 2022: Three types of positive Indian Ocean Dipoles and their relationships with the South Asian Summer Monsoon. *J. Climate*, **35**, 405–424, <https://doi.org/10.1175/JCLI-D-21-0089.1>.
- Jiang, N., and C. W. Zhu, 2021: Seasonal forecast of South China Sea summer monsoon onset disturbed by cold tongue La Niña in the past decade. *Adv. Atmos. Sci.*, **38**, 147–155, <https://doi.org/10.1007/s00376-020-0090-y>.
- Jiang, X. W., Z. Y. Wang, and Z. N. Li, 2018: Signature of the South China Sea summer monsoon onset on spring-to-summer transition of rainfall in the middle and lower reaches of the Yangtze River basin. *Climate Dyn.*, **51**, 3785–3796, <https://doi.org/10.1007/s00382-018-4110-x>.
- Jiao, Y., R. G. Wu, and L. Song, 2019: Individual and combined impacts of two Eurasian wave trains on intraseasonal East Asian winter monsoon variability. *J. Geophys. Res.*, **124**, 4530–4548, <https://doi.org/10.1029/2018JD029953>.
- Jiao, Y., and R. G. Wu, 2019, Propagation and influence on tropical precipitation of intraseasonal variation over mid-latitude East Asia in boreal winter. *Atmospheric and Oceanic Science Letters*, **12**(3), 155–161.
- Jin, Q. J., and C. E. Wang, 2017: A revival of Indian summer monsoon rainfall since 2002. *Nature Climate Change*, **7**, 587–594, <https://doi.org/10.1038/nclimate3348>.
- Joshi, M. K., and F. Kucharski, 2017: Impact of Interdecadal Pacific oscillation on Indian summer monsoon rainfall: An assessment from CMIP5 climate models. *Climate Dyn.*, **48**, 2375–2391, <https://doi.org/10.1007/s00382-016-3210-8>.
- Kang, L. H., W. Chen, and K. Wei, 2006: The interdecadal variation of winter temperature in China and its relation to the anomalies in atmospheric general circulation. *Climatic and Environmental Research*, **11**, 330–339, <https://doi.org/10.3969/j.issn.1006-9585.2006.03.009>. (in Chinese with English abstract)
- Kim, S., H. Y. Son, and J. S. Kug, 2018: Relative roles of equatorial central Pacific and western North Pacific precipitation anomalies in ENSO teleconnection over the North Pacific. *Climate Dyn.*, **51**, 4345–4355, <https://doi.org/10.1007/s00382-017-3779-6>.
- Kong, W. W., and J. C. H. Chiang, 2020: Interaction of the westerlies with the Tibetan Plateau in determining the Mei-Yu termination. *J. Climate*, **33**(1), 339–363, <https://doi.org/10.1175/JCLI-D-19-0319.1>.
- Kosaka, Y., 2021: Chapter 13 - Coupling of the Indian, western North Pacific, and East Asian summer monsoons. *Indian Summer Monsoon Variability*, J. Chowdary, A. Parekh, and C. Gnanaseelan, Eds., Elsevier, 263–286, <https://doi.org/10.1016/B978-0-12-822402-1.00002-8>.
- Kosaka, Y., and S.-P. Xie, 2013: Recent global-warming hiatus tied to equatorial Pacific surface cooling. *Nature*, **501**, 403–407, <https://doi.org/10.1038/nature12534>.
- Kripalani, R., K.-J. Ha, C.-H. Ho, J.-H. Oh, B. Preethi, M. Mujumdar, and A. Prabhu, 2022: Erratic Asian summer monsoon 2020: COVID-19 lockdown initiatives possible cause for

- these episodes. *Climate Dyn.*, **59**, 1339–1352, <https://doi.org/10.1007/s00382-021-06042-x>.
- Krishnamurthy, L., and V. Krishnamurthy, 2014: Influence of PDO on South Asian summer monsoon and monsoon-ENSO relation. *Climate Dyn.*, **42**, 2397–2410, <https://doi.org/10.1007/s00382-013-1856-z>.
- Krishnamurthy, L., and V. Krishnamurthy, 2016: Teleconnections of Indian monsoon rainfall with AMO and Atlantic tripole. *Climate Dyn.*, **46**, 2269–2285, <https://doi.org/10.1007/s00382-015-2701-3>.
- Krishnamurthy, V., and B. N. Goswami, 2000: Indian monsoon-ENSO relationship on interdecadal timescale. *J. Climate*, **13**, 579–595, [https://doi.org/10.1175/1520-0442\(2000\)013<0579:IMEROI>2.0.CO;2](https://doi.org/10.1175/1520-0442(2000)013<0579:IMEROI>2.0.CO;2).
- Krishnaswamy, J., S. Vaidyanathan, B. Rajagopalan, M. Bonell, M. Sankaran, R. S. Bhalla, and S. Badiger, 2015: Non-stationary and non-linear influence of ENSO and Indian Ocean Dipole on the variability of Indian monsoon rainfall and extreme rain events. *Climate Dyn.*, **45**, 175–184, <https://doi.org/10.1007/s00382-014-2288-0>.
- Kucharski, F., A. Bracco, J. H. Yoo, and F. Molteni, 2007: Low-frequency variability of the Indian monsoon-ENSO relationship and the tropical Atlantic: The “Weakening” of the 1980s and 1990s. *J. Climate*, **20**, 4255–4266, <https://doi.org/10.1175/JCLI4254.1>.
- Kucharski, F., A. Bracco, J. H. Yoo, and F. Molteni, 2008: Atlantic forced component of the Indian monsoon interannual variability. *Geophys. Res. Lett.*, **35**, L04706, <https://doi.org/10.1029/2007GL033037>.
- Kucharski, F., A. Bracco, J. H. Yoo, A. M. Tompkins, L. Feudale, P. Ruti, and A. Dell’Aquila, 2009: A Gill-Matsuno-type mechanism explains the tropical Atlantic influence on African and Indian monsoon rainfall. *Quart. J. Roy. Meteor. Soc.*, **135**, 569–579, <https://doi.org/10.1002/qj.406>.
- Kug, J.-S., J.-H. Jeong, Y.-S. Jang, B.-M. Kim, C. K. Folland, S.-K. Min, and S.-W. Son, 2015: Two distinct influences of Arctic warming on cold winters over North America and East Asia. *Nature Geoscience*, **8**, 759–762, <https://doi.org/10.1038/ngeo2517>.
- Kumar, K. K., B. Rajagopalan, and M. A. Cane, 1999: On the weakening relationship between the Indian monsoon and ENSO. *Science*, **284**, 2156–2159, <https://doi.org/10.1126/science.284.5423.2156>.
- Kumar, K. K., B. Rajagopalan, M. Hoerling, G. Bates, and M. A. Cane, 2006: Unraveling the mystery of Indian monsoon failure during El Niño. *Science*, **314**, 115–119, <https://doi.org/10.1126/science.1131152>.
- Kumar, P. K., and A. Singh, 2021: Increase in summer monsoon rainfall over the northeast India during El Niño years since 1600. *Climate Dyn.*, **57**, 851–863, <https://doi.org/10.1007/s00382-021-05743-7>.
- Lee, S.-S., J.-E. Chu, A. Timmermann, E.-S. Chung, and J.-Y. Lee, 2021: East Asian climate response to COVID-19 lockdown measures in China. *Scientific Reports*, **11**, 16852, <https://doi.org/10.1038/s41598-021-96007-1>.
- Li, L., C. W. Zhu, R. H. Zhang, and B. Q. Liu, 2021a: Roles of the Tibetan Plateau vortices in the record Meiyu rainfall in 2020. *Atmos. Sci. Lett.*, **22**, e1017, <https://doi.org/10.1002/asl.1017>.
- Li, X. Q., M. F. Ting, C. H. Li, and N. Henderson, 2015: Mechanisms of Asian summer monsoon changes in response to anthropogenic forcing in CMIP5 Models. *J. Climate*, **28**, 4107–4125, <https://doi.org/10.1175/JCLI-D-14-00559.1>.
- Li, Z. B., Y. Sun, T. Li, W. Chen, and Y. H. Ding, 2021b: Projections of South Asian summer monsoon under global warming from 1.5°C to 5°C. *J. Climate*, **34**, 7913–7926, <https://doi.org/10.1175/JCLI-D-20-0547.1>.
- Li, Z. H., Y. L. Luo, Y. Du, and J. C. L. Chan, 2020: Statistical characteristics of pre-summer rainfall over South China and associated synoptic conditions. *J. Meteor. Soc. Japan*, **98**, 213–233, <https://doi.org/10.2151/jmsj.2020-012>.
- Liang, P., Z.-Z. Hu, Y. H. Ding, and Q. W. Qian, 2021: The extreme Mei-yu season in 2020: Role of the madden-Julian oscillation and the cooperative influence of the Pacific and Indian Oceans. *Adv. Atmos. Sci.*, **38**, 2040–2054, <https://doi.org/10.1007/s00376-021-1078-y>.
- Lin, A. L., and R. H. Zhang, 2020: Climate shift of the South China Sea summer monsoon onset in 1993/1994 and its physical causes. *Climate Dyn.*, **54**, 1819–1827, <https://doi.org/10.1007/s00382-019-05086-4>.
- Lin, Z. D., R. Y. Lu, and R. G. Wu, 2017: Weakened impact of the Indian early summer monsoon on North China rainfall around the late 1970s: Role of basic-state change. *J. Climate*, **30**, 7991–8005, <https://doi.org/10.1175/JCLI-D-17-0036.1>.
- Liu, B. Q., and C. W. Zhu, 2019: Extremely Late Onset of the 2018 South China Sea summer monsoon following a La Niña event: Effects of triple SST anomaly mode in the North Atlantic and a weaker Mongolian cyclone. *Geophys. Res. Lett.*, **46**, 2956–2963, <https://doi.org/10.1029/2018GL081718>.
- Liu, B. Q., and C. W. Zhu, 2020: Boosting effect of tropical cyclone “Fani” on the onset of the South China Sea summer monsoon in 2019. *J. Geophys. Res.*, **125**, e2019JD031891, <https://doi.org/10.1029/2019JD031891>.
- Liu, B. Q., and C. W. Zhu, 2021: Subseasonal-to-seasonal predictability of onset dates of South China Sea summer monsoon: A perspective of meridional temperature gradient. *J. Climate*, **34**, 5601–5616, <https://doi.org/10.1175/JCLI-D-20-0696.1>.
- Liu, B. Q., Y. H. Yan, C. W. Zhu, S. M. Ma, and J. Y. Li, 2020: Record-breaking Meiyu rainfall around the Yangtze River in 2020 regulated by the subseasonal phase transition of the North Atlantic Oscillation. *Geophys. Res. Lett.*, **47**, e2020GL090342, <https://doi.org/10.1029/2020GL090342>.
- Liu, B. Q., Y. M. Liu, G. X. Wu, J. H. Yan, J. H. He, and S. L. Ren, 2015: Asian summer monsoon onset barrier and its formation mechanism. *Climate Dyn.*, **45**, 711–726, <https://doi.org/10.1007/s00382-014-2296-0>.
- Liu, Y., and R. H. Huang, 2019: Linkages between the South and East Asian monsoon water vapor transport during boreal summer. *J. Climate*, **32**, 4509–4524, <https://doi.org/10.1175/JCLI-D-18-0498.1>.
- Lu, C. H., Y. Sun, and X. B. Zhang, 2022: The 2020 Record-Breaking Mei-yu in the Yangtze River valley of China: The role of anthropogenic forcing and atmospheric circulation. *Bull. Amer. Meteor. Soc.*, **103**, S98–S104, <https://doi.org/10.1175/BAMS-D-21-0161.1>.
- Lu, R. Y., and Z. D. Lin, 2009: Role of subtropical precipitation anomalies in maintaining the summertime meridional teleconnection over the western North Pacific and East Asia. *J. Climate*, **22**, 2058–2072, <https://doi.org/10.1175/2008JCLI2444.1>.
- Luo, F. F., S. L. Li, and T. Furevik, 2011: The connection between the Atlantic Multidecadal Oscillation and the

- Indian Summer Monsoon in Bergen Climate Model Version 2.0. *J. Geophys. Res.*, **116**, D19117, <https://doi.org/10.1029/2011JD015848>.
- Luo, F. F., S. L. Li, Y. Q. Gao, N. Keenlyside, L. Svendsen, and T. Furevik, 2018a: The connection between the Atlantic multidecadal oscillation and the Indian summer monsoon in CMIP5 models. *Climate Dyn.*, **51**, 3023–3039, <https://doi.org/10.1007/s00382-017-4062-6>.
- Luo, F. F., S. L. Li, Y. Q. Gao, L. Svendsen, T. Furevik, and N. Keenlyside, 2018b: The connection between the Atlantic Multidecadal Oscillation and the Indian summer monsoon since the industrial revolution is intrinsic to the climate system. *Environmental Research Letters*, **13**, 094020, <https://doi.org/10.1088/1748-9326/aade11>.
- Luo, F. F., S. L. Li, and T. Furevik, 2018c: Weaker connection between the Atlantic Multidecadal Oscillation and Indian summer rainfall since the mid-1990s. *Atmos. Ocean. Sci. Lett.*, **11**, 37–43, <https://doi.org/10.1080/16742834.2018.1394779>.
- Luo, Y. L., R. D. Xia, and J. C. L. Chan, 2020: Characteristics, physical mechanisms, and prediction of pre-summer rainfall over South China: Research progress during 2008–2019. *J. Meteor. Soc. Japan*, **98**, 19–42, <https://doi.org/10.2151/jmsj.2020-002>.
- Ma, T. J., and W. Chen, 2021: Climate variability of the East Asian winter monsoon and associated extratropical–tropical interaction: A review. *Annals of the New York Academy of Sciences*, **1504**, 44–62, <https://doi.org/10.1111/nyas.14620>.
- Ma, T. J., W. Chen, J. L. Huangfu, L. Song, and Q. Y. Cai, 2021: The observed influence of the Quasi-Biennial Oscillation in the lower equatorial stratosphere on the East Asian winter monsoon during early boreal winter. *International Journal of Climatology*, **41**, 6254–6269, <https://doi.org/10.1002/joc.7192>.
- Ma, T. J., W. Chen, H. N. Gong, P. Hu, Y. Jiao, X. D. An, and L. Wang, 2022a: Linkage of strong intraseasonal events of the East Asian winter monsoon to the tropical convections over the western Pacific. *Remote Sensing*, **14**, 2993, <https://doi.org/10.3390/rs14132993>.
- Ma, T. J., and Coauthors, 2022b: Different ENSO teleconnections over East Asia in early and late winter: Role of precipitation anomalies in the tropical Indian Ocean and far western Pacific. *J. Climate*, **35**, 4319–4335, <https://doi.org/10.1175/JCLI-D-21-0805.1>.
- Ma, Y. Y., Z. Y. Hu, X. H. Meng, F. Liu, and W. J. Dong, 2022c: Was the record-breaking Mei-yu of 2020 enhanced by regional climate change. *Bull. Amer. Meteor. Soc.*, **103**, S76–S82, <https://doi.org/10.1175/BAMS-D-21-0187.1>.
- Maharana, P., R. Agnihotri, and A. P. Dimri, 2021: Changing Indian monsoon rainfall patterns under the recent warming period 2001–2018. *Climate Dyn.*, **57**, 2581–2593, <https://doi.org/10.1007/s00382-021-05823-8>.
- Mahendra, N., J. S. Chowdary, P. Darshana, P. Sunitha, A. Parekh, and C. Gnanaseelan, 2021: Interdecadal modulation of interannual ENSO-Indian summer monsoon rainfall teleconnections in observations and CMIP6 models: Regional patterns. *International Journal of Climatology*, **41**, 2528–2552, <https://doi.org/10.1002/joc.6973>.
- Malik, A., S. Brönnimann, A. Stickler, C. C. Raible, S. Muthers, J. Anet, E. Rozanov, and W. Schmutz, 2017: Decadal to multi-decadal scale variability of Indian summer monsoon rainfall in the coupled ocean-atmosphere-chemistry climate model SOCOL-MPIOM. *Climate Dyn.*, **49**, 3551–3572, <https://doi.org/10.1007/s00382-017-3529-9>.
- Martin, G. M., A. Chevuturi, R. E. Comer, N. J. Dunstone, A. A. Scaife, and D. Q. Zhang, 2019: Predictability of South China Sea summer monsoon onset. *Adv. Atmos. Sci.*, **36**, 253–260, <https://doi.org/10.1007/s00376-018-8100-z>.
- McIntyre, M. E., and T. N. Palmer, 1983: Breaking planetary waves in the stratosphere. *Nature*, **305**, 593–600, <https://doi.org/10.1038/305593a0>.
- Miao, J. P., and T. Wang, 2020: Decadal variations of the East Asian winter monsoon in recent decades. *Atmos. Sci. Lett.*, **21**, e960, <https://doi.org/10.1002/asl.960>.
- Miao, J. P., and D. B. Jiang, 2021: Multidecadal variations in the East Asian Winter Monsoon and their relationship with the Atlantic multidecadal oscillation since 1850. *J. Climate*, **34**, 7525–7539, <https://doi.org/10.1175/JCLI-D-21-0073.1>.
- Miao, J. P., T. Wang, H. J. Wang, Y. L. Zhu, and J. Q. Sun, 2018: Interdecadal weakening of the East Asian winter monsoon in the Mid-1980s: The roles of external forcings. *J. Climate*, **31**, 8985–9000, <https://doi.org/10.1175/JCLI-D-17-0868.1>.
- Nair, P. J., A. Chakraborty, H. Varikoden, P. A. Francis, and J. Kutippurath, 2018: The local and global climate forcings induced inhomogeneity of Indian rainfall. *Sci. Rep.*, **8**, 6026, <https://doi.org/10.1038/s41598-018-24021-x>.
- Nitta, T., 1987: Convective activities in the tropical western Pacific and their impact on the Northern Hemisphere summer circulation. *J. Meteor. Soc. Japan*, **65**, 373–390, [https://doi.org/10.2151/jmsj1965.65.3\\_373](https://doi.org/10.2151/jmsj1965.65.3_373).
- Niu, R. Y., P. M. Zhai, and G. R. Tan, 2021: Anomalous features of extreme Meiyu in 2020 over the Yangtze-Huai River Basin and attribution to large-scale circulations. *J. Meteor. Res.*, **35**, 799–814, <https://doi.org/10.1007/s13351-021-1018-x>.
- Ordoñez, P., D. Gallego, P. Ribera, C. Peña-Ortiz, and R. García-Herrera, 2016: Tracking the Indian summer monsoon onset back to the preinstrument period. *J. Climate*, **29**, 8115–8127, <https://doi.org/10.1175/JCLI-D-15-0788.1>.
- Pan, X., T. Li, Y. Sun, and Z. W. Zhu, 2021: Cause of extreme heavy and persistent rainfall over Yangtze River in summer 2020. *Adv. Atmos. Sci.*, **38**, 1994–2009, <https://doi.org/10.1007/s00376-021-0433-3>.
- Pandey, P., S. Dwivedi, B. N. Goswami, and F. Kucharski, 2020: A new perspective on ENSO-Indian summer monsoon rainfall relationship in a warming environment. *Climate Dyn.*, **55**, 3307–3326, <https://doi.org/10.1007/s00382-020-05452-7>.
- Park, H.-L., K.-H. Seo, B.-M. Kim, J.-Y. Kim, and S.-Y. S. Wang, 2021: Dominant wintertime surface air temperature modes in the northern Hemisphere extratropics. *Climate Dyn.*, **56**, 687–698, <https://doi.org/10.1007/s00382-020-05478-x>.
- Paul, S., S. Ghosh, R. Oglesby, A. Pathak, A. Chandrasekharan, and R. Ramsankaran, 2016: Weakening of Indian summer monsoon rainfall due to changes in land use land cover. *Scientific Reports*, **6**, 32177, <https://doi.org/10.1038/srep32177>.
- Piao, J. L., W. Chen, K. Wei, Y. Liu, H.-F. Graf, J.-B. Ahn, and A. Pogoreltsev, 2017: An abrupt rainfall decrease over the Asian inland plateau region around 1999 and the possible underlying mechanism. *Adv. Atmos. Sci.*, **34**, 456–468, <https://doi.org/10.1007/s00376-016-6136-5>.
- Piao, J. L., W. Chen, S. F. Chen, and K. Wei, 2018a: Intensified impact of North Atlantic oscillation in May on subsequent July Asian Inland Plateau precipitation since the late 1970s. *International Journal of Climatology*, **38**, 2605–2612,



- <https://doi.org/10.1002/joc.5332>.
- Piao, J. L., W. Chen, Q. Zhang, and P. Hu, 2018b: Comparison of moisture transport between Siberia and Northeast Asia on Annual and Interannual time scales. *J. Climate*, **31**, 7645–7660, <https://doi.org/10.1175/JCLI-D-17-0763.1>.
- Piao, J. L., W. Chen, S. F. Chen, H. N. Gong, and Q. Zhang, 2020: Summer water vapor Sources in Northeast Asia and East Siberia revealed by a moisture-tracing atmospheric model. *J. Climate*, **33**, 3883–3899, <https://doi.org/10.1175/JCLI-D-19-0516.1>.
- Piao, J. L., W. Chen, and S. F. Chen, 2021a: Water vapour transport changes associated with the interdecadal decrease in the summer rainfall over Northeast Asia around the late-1990s. *International Journal of Climatology*, **41**, E1469–E1482, <https://doi.org/10.1002/joc.6780>.
- Piao, J. L., W. Chen, and S. F. Chen, 2021b: Sources of the internal variability-generated uncertainties in the projection of Northeast Asian summer precipitation. *Climate Dyn.*, **56**, 1783–1797, <https://doi.org/10.1007/s00382-020-05557-z>.
- Piao, J. L., W. Chen, S. F. Chen, H. N. Gong, and L. Wang, 2021c: Mean states and future projections of precipitation over the monsoon transitional zone in China in CMIP5 and CMIP6 models. *Climatic Change*, **169**, 35, <https://doi.org/10.1007/s10584-021-03286-8>.
- Piao, J. L., W. Chen, L. Wang, and S. F. Chen, 2022: Future projections of precipitation, surface temperatures and drought events over the monsoon transitional zone in China from bias-corrected CMIP6 models. *International Journal of Climatology*, **42**, 1203–1219, <https://doi.org/10.1002/joc.7297>.
- Pottapinjara, V., M. S. Girishkumar, M. Ravichandran, and R. Murtugudde, 2014: Influence of the Atlantic zonal mode on monsoon depressions in the Bay of Bengal during boreal summer. *J. Geophys. Res.*, **119**, 6456–6469, <https://doi.org/10.1002/2014JD021494>.
- Pottapinjara, V., M. K. Roxy, M. S. Girishkumar, K. Ashok, S. Joseph, M. Ravichandran, and R. Murtugudde, 2021: Simulation of interannual relationship between the Atlantic zonal mode and Indian summer monsoon in CFSv2. *Climate Dyn.*, **57**, 353–373, <https://doi.org/10.1007/s00382-021-05712-0>.
- Preethi, B., M. Mujumdar, A. Prabhu, and R. Kripalani, 2017: Variability and teleconnections of South and East Asian summer monsoons in present and future projections of CMIP5 climate models. *Asia-Pacific Journal of Atmospheric Sciences*, **53**, 305–325, <https://doi.org/10.1007/s13143-017-0034-3>.
- Qiao, S. B., and Coauthors, 2021: The longest 2020 Meiyu season over the past 60 years: Subseasonal perspective and its predictions. *Geophys. Res. Lett.*, **48**, e2021GL093596, <https://doi.org/10.1029/2021GL093596>.
- Rajesh, P. V., and B. N. Goswami, 2020: Four-dimensional structure and sub-seasonal regulation of the Indian summer monsoon multi-decadal mode. *Climate Dyn.*, **55**, 2645–2666, <https://doi.org/10.1007/s00382-020-05407-y>.
- Ramage, C. S., 1971: *Monsoon Meteorology*. Academic Press, 296 pp.
- Roxy, M. K., 2017: Land warming revives monsoon. *Nature Climate Change*, **7**, 549–550, <https://doi.org/10.1038/nclimate3356>.
- Roxy, M. K., K. Ritika, P. Terray, R. Murtugudde, K. Ashok, and B. N. Goswami, 2015: Drying of Indian subcontinent by rapid Indian Ocean warming and a weakening land-sea thermal gradient. *Nature Communications*, **6**, 7423, <https://doi.org/10.1038/ncomms8423>.
- Roy, I., R. G. Tedeschi, and M. Collins, 2019: ENSO teleconnections to the Indian summer monsoon under changing climate. *International Journal of Climatology*, **39**, 3031–3042, <https://doi.org/10.1002/joc.5999>.
- Sabeerali, C. T., R. S. Ajayamohan, H. K. Bangalath, and N. Chen, 2019: Atlantic zonal mode: An emerging source of Indian Summer Monsoon variability in a warming world. *Geophys. Res. Lett.*, **46**, 4460–4467, <https://doi.org/10.1029/2019GL082379>.
- Samanta, D., B. Rajagopalan, K. B. Karnauskas, L. Zhang, and N. F. Goodkin, 2020: La Niña's diminishing fingerprint on the Central Indian summer monsoon. *Geophys. Res. Lett.*, **47**, e2019GL086237, <https://doi.org/10.1029/2019GL086237>.
- Sandeep, N., P. Swapna, R. Krishnan, R. Farneti, A. G. Prajeesh, D. C. Ayantika, and S. Manmeet, 2020: South Asian monsoon response to weakening of Atlantic meridional overturning circulation in a warming climate. *Climate Dyn.*, **54**, 3507–3524, <https://doi.org/10.1007/s00382-020-05180-y>.
- Schulte, J., F. Policelli, and B. Zaitchik, 2021: A continuum approach to understanding changes in the ENSO–Indian monsoon relationship. *J. Climate*, **34**, 1549–1561, <https://doi.org/10.1175/JCLI-D-20-0027.1>.
- Seetha, C. J., H. Varikoden, C. A. Babu, and J. Kuttippurath, 2020: Significant changes in the ENSO–monsoon relationship and associated circulation features on multidecadal timescale. *Climate Dyn.*, **54**, 1491–1506, <https://doi.org/10.1007/s00382-019-05071-x>.
- Seok, S.-H., and K.-H. Seo, 2021: Sensitivity of East Asian summer monsoon precipitation to the location of the Tibetan Plateau. *J. Climate*, **34**(22), 8829–8840, <https://doi.org/10.1175/JCLI-D-21-0154.1>.
- Shindell, D. T., R. L. Miller, G. A. Schmidt, and L. Pandolfo, 1999: Simulation of recent northern winter climate trends by greenhouse-gas forcing. *Nature*, **399**, 452–455, <https://doi.org/10.1038/20905>.
- Son, J.-H., K.-H. Seo, and B. Wang, 2019: Dynamical control of the Tibetan Plateau on the East Asian summer monsoon. *Geophys. Res. Lett.*, **46**(13), 7672–7679, <https://doi.org/10.1029/2019GL083104>.
- Son, J.-H., K.-H. Seo, and B. Wang, 2020: How does the Tibetan Plateau dynamically affect downstream monsoon precipitation. *Geophys. Res. Lett.*, **47**(23), e2020GL090543, <https://doi.org/10.1029/2020GL090543>.
- Song, L., and R. G. Wu, 2017: Processes for occurrence of strong cold events over eastern China. *J. Climate*, **30**, 9247–9266, <https://doi.org/10.1175/JCLI-D-16-0857.1>.
- Song, L., and R. G. Wu, 2018: Comparison of intraseasonal East Asian Winter cold temperature anomalies in positive and negative phases of the arctic oscillation. *J. Geophys. Res.*, **123**, 8518–8537, <https://doi.org/10.1029/2018JD028343>.
- Song, L., and R. G. Wu, 2019a: Impacts of MJO convection over the maritime continent on eastern China cold temperatures. *J. Climate*, **32**, 3429–3449, <https://doi.org/10.1175/JCLI-D-18-0545.1>.
- Song, L., and R. G. Wu, 2019b: Different cooperation of the arctic oscillation and the Madden-Julian oscillation in the East Asian cold events during early and late winter. *J. Geophys. Res.*, **124**, 4913–4931, <https://doi.org/10.1029/2019JD030388>.
- Song, L., and R. G. Wu, 2019c: Combined effects of the MJO and the arctic oscillation on the intraseasonal eastern China winter temperature variations. *J. Climate*, **32**, 2295–2311,

- <https://doi.org/10.1175/JCLI-D-18-0625.1>.
- Song, L., and R. G. Wu, 2019d: Precursory signals of East Asian winter cold anomalies in stratospheric planetary wave pattern. *Climate Dyn.*, **52**, 5965–5983, <https://doi.org/10.1007/s00382-018-4491-x>.
- Song, L., and R. G. Wu, 2020: Modulation of the QBO on the MJO-related surface air temperature anomalies over Eurasia during boreal winter. *Climate Dyn.*, **54**, 2419–2431, <https://doi.org/10.1007/s00382-020-05122-8>.
- Song, L., and R. G. Wu, 2021: Two types of rossby wave breaking events and their influences on East Asian winter temperature. *J. Geophys. Res.*, **126**, e2020JD033917, <https://doi.org/10.1029/2020JD033917>.
- Song, L. Y., S. F. Chen, W. Chen, J. P. Guo, C. L. Cheng, and Y. Wang, 2022: Distinct evolutions of haze pollution from winter to the following spring over the North China Plain: Role of the North Atlantic sea surface temperature anomalies. *Atmospheric Chemistry and Physics*, **22**, 1669–1688, <https://doi.org/10.5194/acp-22-1669-2022>.
- Srinivas, G., J. S. Chowdary, Y. Kosaka, C. Gnanaseelan, A. Parekh, and K. V. S. R. Prasad, 2018: Influence of the Pacific–Japan pattern on Indian summer monsoon rainfall. *J. Climate*, **31**, 3943–3958, <https://doi.org/10.1175/JCLI-D-17-0408.1>.
- Srivastava, G., A. Chakraborty, and R. S. Nanjundiah, 2020: Multi-decadal variations in ENSO–Indian summer monsoon relationship at sub-seasonal timescales. *Theor. Appl. Climatol.*, **140**, 1299–1314, <https://doi.org/10.1007/s00704-020-03122-6>.
- Stephan, C. C., N. P. Klingaman, and A. G. Turner, 2019: A mechanism for the recently increased interdecadal variability of the Silk Road pattern. *J. Climate*, **32**(3), 717–736, <https://doi.org/10.1175/JCLI-D-18-0405.1>.
- Sun, J. H., Y. C. Zhang, R. X. Liu, S. M. Fu, and F. Y. Tian, 2019: A review of research on warm-sector heavy rainfall in China. *Adv. Atmos. Sci.*, **36**, 1299–1307, <https://doi.org/10.1007/s00376-019-9021-1>.
- Sun, J. Q., and J. Ming, 2019: Possible mechanism for the weakening relationship between Indian and central East Asian summer rainfall after the late 1970s: Role of the mid-to-high-latitude atmospheric circulation. *Meteorol. Atmos. Phys.*, **131**, 517–524, <https://doi.org/10.1007/s00703-018-0586-5>.
- Takaya, Y., I. Ishikawa, C. Kobayashi, H. Endo, and T. Ose, 2020: Enhanced Meiyu–Baiu rainfall in early summer 2020: Aftermath of the 2019 super IOD event. *Geophys. Res. Lett.*, **47**, e2020GL090671, <https://doi.org/10.1029/2020GL090671>.
- Tang, S. L., J.-J. Luo, J. Y. He, J. Y. Wu, Y. Zhou, and W. S. Ying, 2021: Toward understanding the extreme floods over Yangtze River valley in June–July 2020: Role of tropical oceans. *Adv. Atmos. Sci.*, **38**, 2023–2039, <https://doi.org/10.1007/s00376-021-1036-8>.
- Tao, S. Y., and L. X. Chen, 1987: A review of recent research on the East Asian summer monsoon in China. *Monsoon Meteorology*, C. P. Chang and T. N. Krishnamurti, Eds., Oxford University Press, 60–92.
- Terray, P., K. P. Sooraj, S. Masson, and C. Prodhomme, 2021: Anatomy of the Indian Summer Monsoon and ENSO relationships in state-of-the-art CGCMs: Role of the tropical Indian Ocean. *Climate Dyn.*, **56**, 329–356, <https://doi.org/10.1007/s00382-020-05484-z>.
- Tian, B. Q., and K. Fan, 2020: Different prediction skill for the East Asian winter monsoon in the early and late winter season. *Climate Dyn.*, **54**, 1523–1538, <https://doi.org/10.1007/s00382-019-05068-6>.
- Torrence, C., and P. J. Webster, 1999: Interdecadal changes in the ENSO–monsoon system. *J. Climate*, **12**, 2679–2690, [https://doi.org/10.1175/1520-0442\(1999\)012<2679:ICITM>2.0.CO;2](https://doi.org/10.1175/1520-0442(1999)012<2679:ICITM>2.0.CO;2).
- Ummenhofer, C. C., A. Sen Gupta, Y. Li, A. S. Taschetto, and M. H. England, 2011: Multi-decadal modulation of the El Niño–Indian monsoon relationship by Indian Ocean variability. *Environmental Research Letters*, **6**, 034006, <https://doi.org/10.1088/1748-9326/6/3/034006>.
- Varikoden, H., and V. Revadekar, 2020: On the extreme rainfall events during the southwest monsoon season in Northeast regions of the Indian subcontinent. *Meteorological Applications*, **27**, e1822, <https://doi.org/10.1002/met.1822>.
- Varikoden, H., J. V. Revadekar, J. Kuttippurath, and C. A. Babu, 2019: Contrasting trends in southwest monsoon rainfall over the western Ghats region of India. *Climate Dyn.*, **52**, 4557–4566, <https://doi.org/10.1007/s00382-018-4397-7>.
- Varikoden, H., P. P. V. H. Hrudya, R. N. Vishnu, and J. Kuttippurath, 2022: Changes in the ENSO–ISMR relationship in the historical and future projection periods based on coupled models. *International Journal of Climatology*, **42**, 2225–2245, <https://doi.org/10.1002/joc.7362>.
- Vibhute, A., S. Halder, P. Singh, A. Parekh, J. S. Chowdary, and C. Gnanaseelan, 2020: Decadal variability of tropical Indian Ocean sea surface temperature and its impact on the Indian summer monsoon. *Theor. Appl. Climatol.*, **141**, 551–566, <https://doi.org/10.1007/s00704-020-03216-1>.
- Vittal, H., G. Villarini, and W. Zhang, 2020: Early prediction of the Indian summer monsoon rainfall by the Atlantic Meridional Mode. *Climate Dyn.*, **54**, 2337–2346, <https://doi.org/10.1007/s00382-019-05117-0>.
- Wang, B., and Z. Fan, 1999: Choice of South Asian summer monsoon indices. *Bull. Amer. Meteor. Soc.*, **80**, 629–638, [https://doi.org/10.1175/1520-0477\(1999\)080<0629:COSASM>2.0.CO;2](https://doi.org/10.1175/1520-0477(1999)080<0629:COSASM>2.0.CO;2).
- Wang, B., and Y. Kajikawa, 2015: Reply to “Comments on ‘Interdecadal Change of the South China Sea Summer Monsoon Onset’”. *J. Climate*, **28**, 9036–9039, <https://doi.org/10.1175/JCLI-D-15-0173.1>.
- Wang, B., and LinHo, 2002: Rainy season of the Asian–Pacific summer monsoon. *J. Climate*, **15**, 386–398, [https://doi.org/10.1175/1520-0442\(2002\)015<0386:RSOTAP>2.0.CO;2](https://doi.org/10.1175/1520-0442(2002)015<0386:RSOTAP>2.0.CO;2).
- Wang, B., F. Huang, Z. W. Wu, J. Yang, X. H. Fu, and K. Kikuchi, 2009a: Multi-scale climate variability of the South China Sea monsoon: A review. *Dyn. Atmos. Oceans*, **47**, 15–37, <https://doi.org/10.1016/j.dynatmoce.2008.09.004>.
- Wang, H. J., J. H. Sun, S. M. Fu, and Y. C. Zhang, 2021a: Typical circulation patterns and associated mechanisms for persistent heavy rainfall events over Yangtze–Huaihe River Valley during 1981–2020. *Adv. Atmos. Sci.*, **38**, 2167–2182, <https://doi.org/10.1007/s00376-021-1194-8>.
- Wang, H., S. P. Xie, Y. Kosaka, Q. Y. Liu, and Y. Du, 2019: Dynamics of Asian summer monsoon response to anthropogenic aerosol forcing. *J. Climate*, **32**, 843–858, <https://doi.org/10.1175/JCLI-D-18-0386.1>.
- Wang, L., and W. Chen, 2014: An intensity index for the East Asian winter monsoon. *J. Climate*, **27**, 2361–2374, <https://doi.org/10.1175/JCLI-D-13-00086.1>.
- Wang, L., and M.-M. Lu, 2017: The East Asian winter monsoon. *The Global Monsoon System: Research and Forecast*. 3rd

- ed, C. P. Chang et al., Eds., 51–61, [https://doi.org/10.1142/9789813200913\\_0005](https://doi.org/10.1142/9789813200913_0005).
- Wang, L., R. H. Huang, L. Gu, W. Chen, and L. H. Kang, 2009b: Interdecadal variations of the East Asian winter monsoon and their association with quasi-stationary planetary wave activity. *J. Climate*, **22**, 4860–4872, <https://doi.org/10.1175/2009JCLI2973.1>.
- Wang, L., W. Chen, G. Huang, and G. Zeng, 2017a: Changes of the transitional climate zone in East Asia: Past and future. *Climate Dyn.*, **49**, 1463–1477, <https://doi.org/10.1007/s00382-016-3400-4>.
- Wang, L., P. Q. Xu, W. Chen, and Y. Liu, 2017b: Interdecadal variations of the Silk Road pattern. *J. Climate*, **30**(24), 9915–9932, <https://doi.org/10.1175/JCLI-D-17-0340.1>.
- Wang, L., H. N. Gong, and X. Q. Lan, 2021b: Interdecadal variation of the Arctic Oscillation and its influence on climate. *Transactions of Atmospheric Sciences*, **44**, 50–60, <https://doi.org/10.13878/j.cnki.dqkxxb.20201030001>. (in Chinese with English abstract)
- Wang, L., P. Q. Xu, and J. S. Chowdary, 2021c: Teleconnection along the Asian Jet stream and its association with the Asian summer monsoon. *Indian Summer Monsoon Variability: El Niño-Teleconnections and Beyond*, J. Chowdary et al., Eds., Elsevier, 287–298, <https://doi.org/10.1016/B978-0-12-822402-1.00009-0>.
- Wang, L., C. Zheng, and Y. Y. Liu, 2021d: Understanding the East Asian winter monsoon in 2018 from the intraseasonal perspective. *Climate Dynamics*, **57**, 2053–2062, <https://doi.org/10.1007/s00382-021-05793-x>.
- Wang, Q. L., L. Wang, G. Huang, J. L. Piao, and C. Chotamonsak, 2021e: Temporal and spatial variation of the transitional climate zone in summer during 1961–2018. *International Journal of Climatology*, **41**, 1633–1648, <https://doi.org/10.1002/joc.6902>.
- Wang, Q. L., G. Huang, L. Wang, J. L. Piao, T. J. Ma, P. Hu, C. Chotamonsak, and A. Limsakul, 2023: Mechanism of the summer rainfall variation in Transitional Climate Zone in East Asia from the perspective of moisture supply during 1979–2010 based on the Lagrangian method. *Climate Dyn.*, **60**, 1225–1238, <https://doi.org/10.1007/s00382-022-06344-8>.
- Wang, S., and W. Chen, 2022: Impact of internal variability on recent opposite trends in wintertime temperature over the Barents–Kara Seas and central Eurasia. *Climate Dyn.*, **58**, 2941–2956, <https://doi.org/10.1007/s00382-021-06077-0>.
- Wang, S., D. Nath, W. Chen, and T. J. Ma, 2020: CMIP5 model simulations of warm Arctic-cold Eurasia pattern in winter surface air temperature anomalies. *Climate Dyn.*, **54**, 4499–4513, <https://doi.org/10.1007/s00382-020-05241-2>.
- Wang, Y. M., S. L. Li, and D. H. Luo, 2009c: Seasonal response of Asian monsoonal climate to the Atlantic Multidecadal Oscillation. *J. Geophys. Res.*, **114**, D02112, <https://doi.org/10.1029/2008JD010929>.
- Wang, Z. B., R. G. Wu, S.-F. Chen, G. Huang, G. Liu, and L.-H. Zhu, 2018: Influence of western Tibetan Plateau summer snow cover on East Asian summer rainfall. *J. Geophys. Res.*, **123**(5), 2371–2386, <https://doi.org/10.1002/2017JD028016>.
- Wei, K., C. J. Ouyang, H. T. Duan, Y. L. Li, M. X. Chen, J. Ma, H. C. An, and S. Zhou, 2020a: Reflections on the catastrophic 2020 Yangtze River basin flooding in southern China. *The Innovation*, **1**, 100038, <https://doi.org/10.1016/j.xinn.2020.100038>.
- Wei, W., L. Wang, Q. L. Chen, and Y. Y. Liu, 2014a: Interannual variations of early and late winter temperatures in China and Their Linkage. *Chinese Journal of Atmospheric Sciences*, **38**, 524–536, <https://doi.org/10.3878/j.issn.1006-9895.1401.13320>. (in Chinese with English abstract)
- Wei, W., L. Wang, Q. L. Chen, Y. Y. Liu, and Z. Li, 2020b: Definition of Early and Late winter and associated interannual variations of surface air temperature in China. *Chinese Journal of Atmospheric Sciences*, **44**, 122–137, <https://doi.org/10.3878/j.issn.1006-9895.1904.18238>. (in Chinese with English abstract)
- Wei, W., R. H. Zhang, M. Wen, X. Y. Rong, and T. Li, 2014b: Impact of Indian summer monsoon on the South Asian High and its influence on summer rainfall over China. *Climate Dyn.*, **43**, 1257–1269, <https://doi.org/10.1007/s00382-013-1938-y>.
- Wei, W., R. H. Zhang, M. Wen, B.-J. Kim, and J.-C. Nam, 2015: Interannual variation of the South Asian high and its relation with Indian and East Asian summer monsoon rainfall. *J. Climate*, **28**, 2623–2634, <https://doi.org/10.1175/JCLI-D-14-00454.1>.
- Wei, W., R. H. Zhang, S. Yang, W. H. Li, and M. Wen, 2019: Quasi-biweekly oscillation of the South Asian high and its role in connecting the Indian and East Asian summer rainfalls. *Geophys. Res. Lett.*, **46**, 14 742–14 750, <https://doi.org/10.1029/2019GL086180>.
- Woo, S., G. P. Singh, J.-H. Oh, and K.-M. Lee, 2019: Possible teleconnections between East and South Asian summer monsoon precipitation in projected future climate change. *Meteorol. Atmos. Phys.*, **131**, 375–387, <https://doi.org/10.1007/s00703-017-0573-2>.
- Wu, G. X., and Coauthors, 2007: The influence of mechanical and thermal forcing by the Tibetan Plateau on Asian climate. *Journal of Hydrometeorology*, **8**(4), 770–789, <https://doi.org/10.1175/JHM609.1>.
- Wu, N. G., X. Ding, Z. P. Wen, G. X. Chen, Z. Y. Meng, L. X. Lin, and J. Z. Min, 2020: Contrasting frontal and warm-sector heavy rainfalls over South China during the early-summer rainy season. *Atmos. Res.*, **235**, 104693, <https://doi.org/10.1016/j.atmosres.2019.104693>.
- Wu, R., and Y. Jiao, 2017: The impacts of the Indian summer rainfall on North China summer rainfall. *Asia-Pacific Journal of Atmospheric Sciences*, **53**, 195–206, <https://doi.org/10.1007/s13143-017-0013-8>.
- Wu, R. G., 2017: Relationship between Indian and East Asian summer rainfall variations. *Adv. Atmos. Sci.*, **34**, 4–15, <https://doi.org/10.1007/s00376-016-6216-6>.
- Wu, R. G., K. M. Hu, and Z. D. Lin, 2018: Perspectives on the non-stationarity of the relationship between Indian and East Asian summer rainfall variations. *Atmos. Ocean. Sci. Lett.*, **11**, 104–111, <https://doi.org/10.1080/16742834.2018.1387758>.
- Wu, X. F., and J. Y. Mao, 2019: Decadal Changes in interannual dependence of the bay of Bengal summer monsoon onset on ENSO modulated by the pacific decadal oscillation. *Adv. Atmos. Sci.*, **36**, 1404–1416, <https://doi.org/10.1007/s00376-019-9043-8>.
- Wu, Z. H., and N. E. Huang, 2009: Ensemble empirical mode decomposition: A noise-assisted data analysis method. *Advances in Adaptive Data Analysis*, **1**, 1–41, <https://doi.org/10.1142/S1793536909000047>.
- Xia, R. D., Y. L. Luo, D.-L. Zhang, M. X. Li, X. H. Bao, and J. S.



- Sun, 2021: On the diurnal cycle of heavy rainfall over the Sichuan basin during 10–18 August 2020. *Adv. Atmos. Sci.*, **38**, 2183–2200, <https://doi.org/10.1007/s00376-021-1118-7>.
- Xiang, B. Q., and B. Wang, 2013: Mechanisms for the advanced Asian summer monsoon onset since the mid-to-late 1990s. *J. Climate*, **26**, 1993–2009, <https://doi.org/10.1175/JCLI-D-12-00445.1>.
- Xiao, X., W. Chen, G. Z. Fan, and D. W. Zhou, 2016: Possible external forcing factors for the interdecadal change in the East Asian winter monsoon around the late 1990s. *Climatic and Environmental Research*, **21**, 197–209, <https://doi.org/10.3878/j.issn.1006-9585.2015.15169>. (in Chinese with English abstract)
- Xiao, Z. X., and A. M. Duan, 2016: Impacts of Tibetan Plateau snow cover on the interannual variability of the East Asian summer monsoon. *J. Climate*, **29**(23), 8495–8514, <https://doi.org/10.1175/JCLI-D-16-0029.1>.
- Xing, N., J. P. Li, and L. N. Wang, 2016: Effect of the early and late onset of summer monsoon over the Bay of Bengal on Asian precipitation in May. *Climate Dyn.*, **47**, 1961–1970, <https://doi.org/10.1007/s00382-015-2944-z>.
- Xu, L., and Z.-L. Li, 2021: Impacts of the wave train along the Asian Jet on the South China Sea summer monsoon onset. *Atmosphere*, **12**, 1227, <https://doi.org/10.3390/atmos12091227>.
- Xu, M., H. M. Xu, J. Ma, and J. C. Deng, 2022: Impact of Pacific Decadal Oscillation on interannual relationship between El Niño and South China Sea summer monsoon onset. *International Journal of Climatology*, **42**, 2739–2753, <https://doi.org/10.1002/joc.7388>.
- Xu, P. Q., L. Wang, W. Chen, J. Feng, and Y. Y. Liu, 2019: Structural changes in the Pacific–Japan pattern in the late 1990s. *J. Climate*, **32**, 607–621, <https://doi.org/10.1175/JCLI-D-18-0123.1>.
- Xue, X., and W. Chen, 2019: Distinguishing interannual variations and possible impacted factors for the northern and southern mode of South Asia High. *Climate Dyn.*, **53**, 4937–4959, <https://doi.org/10.1007/s00382-019-04837-7>.
- Xue, X., W. Chen, S. F. Chen, and D. W. Zhou, 2015: Modulation of the connection between boreal winter ENSO and the South Asian high in the following summer by the stratospheric quasi-biennial oscillation. *J. Geophys. Res.*, **120**, 7393–7411, <https://doi.org/10.1002/2015JD023260>.
- Xue, X., W. Chen, S. F. Chen, S. S. Sun, and S. S. Hou, 2021: Distinct impacts of two types of South Asian highs on East Asian summer rainfall. *International Journal of Climatology*, **41**(S1), E2718–E2740, <https://doi.org/10.1002/joc.6876>.
- Xue, X., W. Chen, and S. F. Chen, 2022: Distinct impacts of two types of South Asian high on the connection of the summer rainfall over India and North China. *International Journal of Climatology*, **42**, 8056–8072, <https://doi.org/10.1002/joc.7692>.
- Yang, L. N., and B. Y. Wu, 2013: Interdecadal variations of the East Asian winter surface air temperature and possible causes. *Chinese Science Bulletin*, **58**, 3969–3977, <https://doi.org/10.1007/s11434-013-5911-2>.
- Yang, S., R. G. Wu, M. Q. Jian, J. Huang, X. M. Hu, Z. Q. Wang, and X. W. Jiang, 2021: *Climate Change in Southeast Asia and Surrounding Areas*. Springer, <https://doi.org/10.1007/978-981-15-8225-7>.
- Yang, X.-Y., X. J. Yuan, and M. F. Ting, 2016: Dynamical link between the Barents–Kara Sea Ice and the Arctic oscillation. *J. Climate*, **29**, 5103–5122, <https://doi.org/10.1175/JCLI-D-15-0669.1>.
- Yang, Y., and Coauthors, 2022: Abrupt emissions reductions during COVID-19 contributed to record summer rainfall in China. *Nature Communications*, **13**, 959, <https://doi.org/10.1038/s41467-022-28537-9>.
- Yasunari, T., A. Kitoh, and T. Tokioka, 1991: Local and remote responses to excessive snow mass over Eurasia appearing in the northern spring and summer climate—A study with the MRI-GCM. *J. Meteor. Soc. Japan*, **69**(4), 473–487, [https://doi.org/10.2151/jmsj1965.69.4\\_473](https://doi.org/10.2151/jmsj1965.69.4_473).
- You, J. L., M. Q. Jian, S. Gao, and J. J. Cai, 2021: Interdecadal change of the winter-spring tropospheric temperature over Asia and its impact on the South China Sea summer monsoon onset. *Frontiers in Earth Science*, **8**, 599447, <https://doi.org/10.3389/feart.2020.599447>.
- Yu, R., Z. H. Jiang, and H. Y. Ma, 2016: A numerical study on the impact of urban land-use change over eastern China on the onset of the South China Sea monsoon. *Chinese Journal of Atmospheric Sciences*, **40**, 504–514, <https://doi.org/10.3878/j.issn.1006-9895.1504.15116>. (in Chinese with English abstract)
- Yu, T. T., J. Feng, and W. Chen, 2020: Evaluation of CMIP5 models in simulating the respective impacts of East Asian winter monsoon and ENSO on the western North Pacific anomalous anticyclone. *International Journal of Climatology*, **40**, 805–821, <https://doi.org/10.1002/joc.6240>.
- Yu, T. T., W. Chen, J. Feng, K. M. Hu, L. Song, and P. Hu, 2021: Roles of ENSO in the link of the East Asian summer monsoon to the ensuing winter monsoon. *J. Geophys. Res.*, **126**, e2020JD033994, <https://doi.org/10.1029/2020JD033994>.
- Yuan, F., and W. Chen, 2013: Roles of the tropical convective activities over different regions in the earlier onset of the South China Sea summer monsoon after 1993. *Theor. Appl. Climatol.*, **113**, 175–185, <https://doi.org/10.1007/s00704-012-0776-x>.
- Yuan, F., W. Chen, and W. Zhou, 2012: Analysis of the role played by circulation in the persistent precipitation over South China in June 2010. *Adv. Atmos. Sci.*, **29**, 769–781, <https://doi.org/10.1007/s00376-012-2018-7>.
- Yun, K. S., and A. Timmermann, 2018: Decadal monsoon-ENSO relationships reexamined. *Geophys. Res. Lett.*, **45**, 2014–2021, <https://doi.org/10.1002/2017GL076912>.
- Zeng, W. X., G. X. Chen, L. Q. Bai, Q. Liu, and Z. P. Wen, 2022: Multiscale processes of heavy rainfall over East Asia in summer 2020: Diurnal cycle in response to synoptic disturbances. *Mon. Wea. Rev.*, **150**, 1355–1376, <https://doi.org/10.1175/MWR-D-21-0308.1>.
- Zeng, Z. J., Y. Y. Guo, and Z. P. Wen, 2021: Interdecadal change in the relationship between the bay of Bengal summer monsoon and South China Sea summer monsoon onset. *Frontiers in Earth Science*, **8**, 610982, <https://doi.org/10.3389/feart.2020.610982>.
- Zhang, R., and T. L. Delworth, 2006: Impact of Atlantic multi-decadal oscillations on India/Sahel rainfall and Atlantic hurricanes. *Geophys. Res. Lett.*, **33**, L17712, <https://doi.org/10.1029/2006GL026267>.
- Zhang, R. H., A. Sumi, and M. Kimoto, 1996: Impact of El Niño on the East Asian monsoon: A diagnostic study of the '86/87 and '91/92 events. *J. Meteor. Soc. Japan*, **74**, 49–62, [https://doi.org/10.2151/jmsj1965.74.1\\_49](https://doi.org/10.2151/jmsj1965.74.1_49).
- Zhang, R. H., Q. Y. Min, and J. Z. Su, 2017: Impact of El Niño

- on atmospheric circulations over East Asia and rainfall in China: Role of the anomalous western North Pacific anticyclone. *Science China Earth Sciences*, **60**, 1124–1132, <https://doi.org/10.1007/s11430-016-9026-x>.
- Zhang, W. J., Z. C. Huang, F. Jiang, M. F. Stuecker, G. S. Chen, and F. F. Jin, 2021: Exceptionally persistent Madden - Julian Oscillation activity contributes to the extreme 2020 East Asian summer monsoon rainfall. *Geophys. Res. Lett.*, **48**, e2020GL091588, <https://doi.org/10.1029/2020GL091588>.
- Zhao, W., W. Chen, S. F. Chen, S. L. Yao, and D. Nath, 2019a: Inter - annual variations of precipitation over the monsoon transitional zone in China during August–September: Role of sea surface temperature anomalies over the tropical Pacific and North Atlantic. *Atmos. Sci. Lett.*, **20**, e872, <https://doi.org/10.1002/asl.872>.
- Zhao, W., S. F. Chen, W. Chen, S. L. Yao, D. Nath, and B. Yu, 2019b: Interannual variations of the rainy season withdrawal of the monsoon transitional zone in China. *Climate Dyn.*, **53**, 2031–2046, <https://doi.org/10.1007/s00382-019-04762-9>.
- Zhao, W., W. Chen, S. F. Chen, D. Nath, and L. Wang, 2020a: Interdecadal change in the impact of North Atlantic SST on August rainfall over the monsoon transitional belt in China around the late 1990s. *Theor. Appl. Climatol.*, **140**, 503–516, <https://doi.org/10.1007/s00704-020-03102-w>.
- Zhao, W., W. Chen, S. F. Chen, S. L. Yao, and D. Nath, 2020b: Combined impact of tropical central - eastern Pacific and North Atlantic sea surface temperature on precipitation variation in monsoon transitional zone over China during August–September. *International Journal of Climatology*, **40**, 1316–1327, <https://doi.org/10.1002/joc.6231>.
- Zhao, W., W. Chen, S. F. Chen, H. N. Gong, and T. J. Ma, 2021: Roles of anthropogenic forcings in the observed trend of decreasing late-summer precipitation over the East Asian transitional climate zone. *Scientific Reports*, **11**, 4935, <https://doi.org/10.1038/S41598-021-84470-9>.
- Zhao, W., and Coauthors, 2022a: Distinct Impacts of ENSO on Haze pollution in the Beijing–Tianjin–Hebei region between early and late winters. *J. Climate*, **35**, 687–704, <https://doi.org/10.1175/JCLI-D-21-0459.1>.
- Zhao, Y. H., J. B. Cheng, G. L. Feng, R. Zhi, Z. H. Zheng, and Z. P. Zhang, 2022b: Analysis of the atmospheric direct dynamic source for the westerly extended WPSH and record-breaking Plum Rain in 2020. *Climate Dyn.*, **59**, 1233–1251, <https://doi.org/10.1007/s00382-022-06186-4>.
- Zheng, F., and Coauthors, 2022: The 2020/21 Extremely cold winter in China influenced by the synergistic effect of La Niña and Warm Arctic. *Adv. Atmos. Sci.*, **39**, 546–552, <https://doi.org/10.1007/s00376-021-1033-y>.
- Zheng, J. Y., and C. Z. Wang, 2021: Influences of three oceans on record-breaking rainfall over the Yangtze River Valley in June 2020. *Science China Earth Sciences*, **64**, 1607–1618, <https://doi.org/10.1007/s11430-020-9758-9>.
- Zhong, W. G., and Z. W. Wu, 2022: Subseasonal variations of Eurasian wintertime surface air temperature: Two distinct leading modes. *Climate Dyn.*, **59**, 85–108, <https://doi.org/10.1007/s00382-021-06118-8>.
- Zhou, F. L., R. H. Zhang, and J. P. Han, 2020: Influences of the East Asian summer rainfall on circumglobal teleconnection. *J. Climate*, **33**, 5213–5221, <https://doi.org/10.1175/JCLI-D-19-0325.1>.
- Zhou, W., J. C. L. Chan, W. Chen, J. Ling, J. G. Pinto, and Y. P. Shao, 2009: Synoptic-scale controls of persistent low temperature and icy weather over southern China in January 2008. *Mon. Wea. Rev.*, **137**, 3978–3991, <https://doi.org/10.1175/2009MWR2952.1>.
- Zhou, Z.-Q., S.-P. Xie, and R. Zhang, 2021: Historic Yangtze flooding of 2020 tied to extreme Indian Ocean conditions. *Proceedings of the National Academy of Sciences of the United States of America*, **118**, e2022255118, <https://doi.org/10.1073/pnas.2022255118>.
- Zhu, Z. W., and T. Li, 2017: Empirical prediction of the onset dates of South China Sea summer monsoon. *Climate Dyn.*, **48**, 1633–1645, <https://doi.org/10.1007/s00382-016-3164-x>.

## A Review of Atmospheric Electricity Research in China from 2019 to 2022<sup>※</sup>

Weitao LYU<sup>1,2</sup>, Dong ZHENG<sup>1,2,6</sup>, Yang ZHANG<sup>1,2</sup>, Wen YAO<sup>1,2</sup>, Rubin JIANG<sup>3,6</sup>, Shanfeng YUAN<sup>3</sup>,  
Dongxia LIU<sup>3,6</sup>, Fanchao LYU<sup>4</sup>, Baoyou ZHU<sup>5</sup>, Gaopeng LU<sup>5</sup>, Qilin ZHANG<sup>6</sup>, Yongbo TAN<sup>6</sup>,  
Xuejuan WANG<sup>6</sup>, Yakun LIU<sup>7</sup>, Shaodong CHEN<sup>8</sup>, Lyuwen CHEN<sup>8</sup>, Qingyong LI<sup>9</sup>, and Yijun ZHANG<sup>10</sup>

<sup>1</sup>State Key Laboratory of Severe Weather, Chinese Academy of Meteorological Sciences, Beijing 100081, China

<sup>2</sup>Laboratory of Lightning Physics and Protection Engineering, Chinese Academy of Meteorological Sciences,  
Beijing 100081, China

<sup>3</sup>Key Laboratory of Middle Atmosphere and Global Environment Observation, Institute of Atmospheric Physics,  
Chinese Academy of Sciences, Beijing 100029, China

<sup>4</sup>Key Laboratory of Transportation Meteorology of China Meteorological Administration,  
Nanjing Joint Institute for Atmospheric Sciences, Nanjing 210041, China

<sup>5</sup>Chinese Academy of Sciences Key Laboratory of Geospace Environment, School of Earth and Space Sciences,  
University of Science and Technology of China, Hefei 230026, China

<sup>6</sup>Collaborative Innovation Center on Forecast and Evaluation of Meteorological Disasters (CIC-FEMD), Nanjing  
University of Information Science & Technology, Nanjing 210044, China

<sup>7</sup>Department of Electrical Engineering, Shanghai Jiao Tong University, Shanghai 200030, China

<sup>8</sup>Institute of Tropical and Marine Meteorology, China Meteorological Administration, Guangzhou 510641, China

<sup>9</sup>Beijing Key Lab of Transportation Data Analysis and Mining, Beijing Jiaotong University, Beijing 100044, China

<sup>10</sup>Department of Atmospheric and Oceanic Sciences and Institute of Atmospheric Sciences,  
Fudan University, Shanghai 200438, China

(Received 24 October 2022; revised 4 January 2023; accepted 10 January 2023)

### ABSTRACT

Atmospheric electricity is composed of a series of electric phenomena in the atmosphere. Significant advances in atmospheric electricity research conducted in China have been achieved in recent years. In this paper, the research progress on atmospheric electricity achieved in China during 2019–22 is reviewed focusing on the following aspects: (1) lightning detection and location techniques, (2) thunderstorm electricity, (3) lightning forecasting methods and techniques, (4) physical processes of lightning discharge, (5) high energy emissions and effects of thunderstorms on the upper atmosphere, and (6) the effect of aerosol on lightning.

**Key words:** atmospheric electricity, thunderstorm, lightning, lightning detection, lightning physics

**Citation:** Lyu, W. T., and Coauthors, 2023: A review of atmospheric electricity research in China from 2019 to 2022. *Adv. Atmos. Sci.*, **40**(8), 1457–1484, <https://doi.org/10.1007/s00376-023-2280-x>.

### Article Highlights:

- Advanced lightning detection and location techniques have been rapidly developed and broadly utilized in China.
- The understanding of many aspects of atmospheric electricity has been consistently deepened in recent years.
- Several new findings in atmospheric electricity research conducted in China suggest future directions.

---

<sup>※</sup> This paper is a contribution to the special issue on National Report to the 28th IUGG General Assembly by CNC-IAMAS (2019–2022).

\* Corresponding author: Weitao LYU  
Email: [wltu@ustc.edu](mailto:wltu@ustc.edu)

## 1. Introduction

Atmospheric electricity is an important branch of atmospheric science research that combines a broad range of electrical phenomena in the atmosphere. In China, there are sev-

eral lightning research groups (LRGs) devoted to atmospheric electricity, and significant progress has been made by LRGs in recent decades. Qie (2012) and Qie and Zhang (2019) reviewed the research progress in atmospheric electricity achieved in China during the periods 2006–10 and 2011–18, respectively. Qie et al. (2015) reviewed research that focused primarily on ground-based thunderstorm and lightning field experiments conducted in different regions of China during 2005–14. Zhang et al. (2016) reviewed the research advances on the discharge processes of artificially triggered and natural lightning, as well as the advances in lightning protection technology testing conducted during the period 2006–15 in Guangdong, China. Qie et al. (2021b) reviewed the research advances resulting from the “Dynamical-microphysical-electrical Processes in Severe Thunderstorms and Lightning Hazards (STORM973)” project, during which the main focus was the collection of field observations in the Beijing metropolitan region over the period 2014–18.

In the last few years, most advancements resulting from the study of atmospheric electricity in China were related to a project sponsored by the National Key Research and Development Program of China: “Research on Thunderstorm Electrification-discharge Processes and Lightning Effects”. The goals of this project are to: 1) develop a real-time three-dimensional (3D) lightning channel mapping system with a high resolution, 2) observe thunderstorm electrification-discharge processes collaboratively in China, 3) reveal the relationship between multiple characteristics of lightning activities and thunderstorm structure, 4) develop a seamless lightning forecasting and warning operational demonstration platform by leveraging artificial intelligence techniques, 5) analyze the effects of grounded objects on the lightning striking process, multi-dimensional electromagnetic radiation features, and coupling mechanisms of the lightning process, and 6) establish an experimental research platform for lightning damage and protection.

In this paper, the atmospheric electricity research progress achieved in China during 2019–22 is reviewed focusing on the following aspects: (1) lightning detection and location techniques, (2) thunderstorm electricity, (3) lightning forecasting methods and techniques, (4) physical processes of lightning discharge, (5) high energy emissions and effects of thunderstorms on the upper atmosphere, and (6) the effect of aerosol on lightning.

## 2. Lightning detection and location techniques

### 2.1. Lightning location networks based on VLF/LF signals

Total lightning positioning based on Very Low Frequency/Low Frequency (VLF/LF) signals has the advantages of long detection distance and strong anti-interference performance. In China, in addition to the cloud-to-ground lightning (CG) location network based on VLF/LF signals being built

by the business department (Zhang et al., 2022c), several LRGs have also built their own total lightning location networks and are constantly developing new positioning techniques. Since 2010, different location networks have been continuously operating in the scientific research fields, including the Low-Frequency E-field Detection Array (LFEDA) of the Chinese Academy of Meteorological Sciences (CAMS), Beijing Lightning NETWORK (BLNET) of Institute of Atmospheric Physics (IAP), Chinese Academy of Sciences (CAS), and hybrid baseline total flash positioning network of University of Science and Technology of China (USTC).

For thunderstorm and lightning research, starting from 2014, the CAMS LRG has built a lightning detection array based on LF electric field fast antennas, named as LFEDA. Through waveform post-processing positioning, it can obtain the 3D location of LF sources with high efficiency and positioning accuracy (~100 m, evaluated by triggered lightning). In recent years, Zhang et al. (2021f) upgraded the original hardware setup of LFEDA and developed a new generation of the real-time LFEDA (RT\_LFEDA) substations based on the FPGA real-time signal processing technique, as shown in Fig. 1. The new setup has the advantages of lower power consumption (10–24 W), higher integration, and faster data processing speed. Each substation is used to digitize and extract VLF/LF signal characteristics in real time and save the original waveforms. The Time of Arrival (TOA) or 3D algorithm developed with the graphical processing unit (GPU) is used for real-time positioning.

The IAP LRG built a multi-band lightning 3D positioning network in Beijing (BLNET) around 2010. In 2015, the sensitivity of sensors, the operation efficiency of software, and the detection performance of the network were improved by updating the hardware, station network layout, and positioning algorithm of BLNET (Wang et al., 2020a; Yuan et al., 2020). Ma et al. (2021c) then upgraded the location technique, and a 3D total lightning positioning network of eight stations was deployed in Binzhou, Shandong Province. The system synchronously digitized the signals of derivation of electric field change, the fast and slow electric field, through a multi-channel data acquisition card controlled by the industrial computer. The TOA particle swarm optimization (PSO) positioning algorithm is adopted based on waveform post-processing, which has a high positioning accuracy verified by triggered lightning.

The USTC LRG has been building a spheric detection array in the Jianghuai region (JASA). Five stations in the Jianghuai region and a remote station located in Conghua (~950 km away) were deployed before 2019 to investigate narrow bipolar events (NBE) activities in the relatively low latitude region (Liu et al., 2021b). Since 2019, the network has been expanded to 13 stations with multiple baselines ranging from 100–200 km to about 1000 km and is designed to geolocate the large-scale lightning flashes during thunderstorms over the eastern coastal areas of China. The network adopts a GPU parallel processing technique with real-time positioning capability.



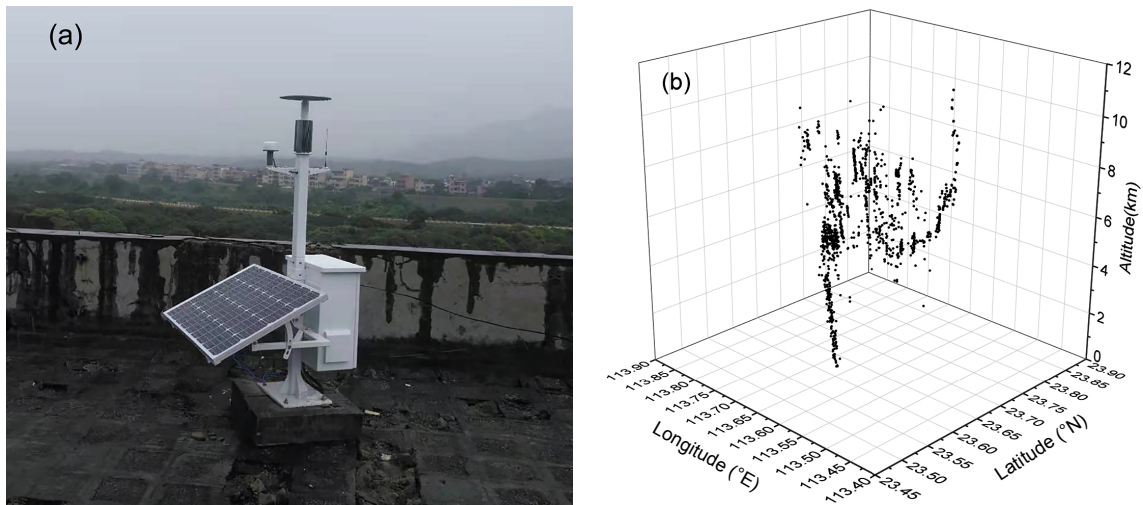


**Fig. 1.** The (a) new, low power consumption substation of RT\_LFEDA and (b) positioning results for a lightning flash.

## 2.2. Total lightning location techniques based on VLF/LF signals

How to improve the performance of total lightning location system (LLS) operating at VLF/LF band has always been a research focus. Different techniques have been adopted to improve the precision.

The CAMS LRG developed a positioning algorithm combining time reversal and the TOA method when LFEDA was built in the early stage (Chen et al., 2019b; Zhang et al., 2021f). Compared with the traditional TOA method, this method can obtain higher-quality 3D positioning results with fewer matching stations (as low as four stations), poor signal-to-noise ratio, and lower time accuracy, which is beneficial to the positioning of long-distance weak signals.

Other location techniques have also been applied to the LF total lightning location problem, which improves the matching ability of the pulses from the same discharge source. For example, Fan et al. (2021a) applied the empirical mode decomposition (EMD) technique in LFEDA, which achieves LF signal filtering and high-frequency noise reduction. After waveform correlation matching by gradually reducing the window, the optimal solution was solved by the traditional time of arrival method, and the positioning number was increased by more than five times. Furthermore, based on the waveforms obtained by the 3D lightning radiation source location system established in Datong County, Qinghai Province, Wang et al. (2021g) combined the Pearson correlation method with EMD to match the electric field pulse of lightning discharge, and a better performance (nearly seven times of sources were located) was achieved compared to the pulse-peak feature matching method.

Compared with waveform-based localization, feature-based localization is fast, but the precision is low and needs to be improved. Wang et al. (2021c) proposed a fast and refined positioning method based on deep learning features that can significantly improve the matching ability of multi-stations signals and the location speed. The locating results

for a natural lightning flash using this method are shown in Fig. 2. Compared to the pulse-peak feature matching and waveform cross-correlation matching methods (TOA-TR methods), this new method has a higher matching efficiency (increased by more than 50%).

## 2.3. Lightning location techniques based on VHF signals

Compared with the LF positioning technique, the Very High Frequency (VHF) positioning technique has natural advantages in depicting lightning channels. Zhang et al. (2020f) developed the continuous interferometer (CINTF) system in 2016. It consists of three VHF broadband discone antennas arranged at the vertices of an equilateral triangle of 20 m and a high-speed acquisition system. In the first few years since the system's inception, the signals of the three antennas were filtered and digitized continuously with a sampling rate of  $200 \text{ MS s}^{-1}$ , and a maximum record length of 2 s was achieved. Recently, the system has been upgraded to achieve a  $400\text{-MS s}^{-1}$  sampling rate and a maximum record length of 4 s. The correlation time delay method was used to calculate the elevation, azimuth, and other information. It can achieve high-precision positioning with sub-microsecond resolution.

Chen et al. (2022c) further developed a calibration method for the source positioning error of CINTF at close range and validated this method with rocket-triggered lightning experiments. During the initial stage of an upward positive leader (UPL), the calibrated altitude positioning errors of CINTF are approximately 11 m, 14 m, and 20 m, when the source elevation angles are  $40^\circ$ ,  $50^\circ$ , and  $60^\circ$ , respectively, which suggests an error increasing with the source ascending. Based on the calibrated observation results, Chen et al. (2022c) investigated the development characteristics of the initial stage of the UPL and discussed the possible physical mechanisms.

A lightning broadband VHF interferometer has been deployed in Lhasa since 2019 by the IAP LRG. Li et al.

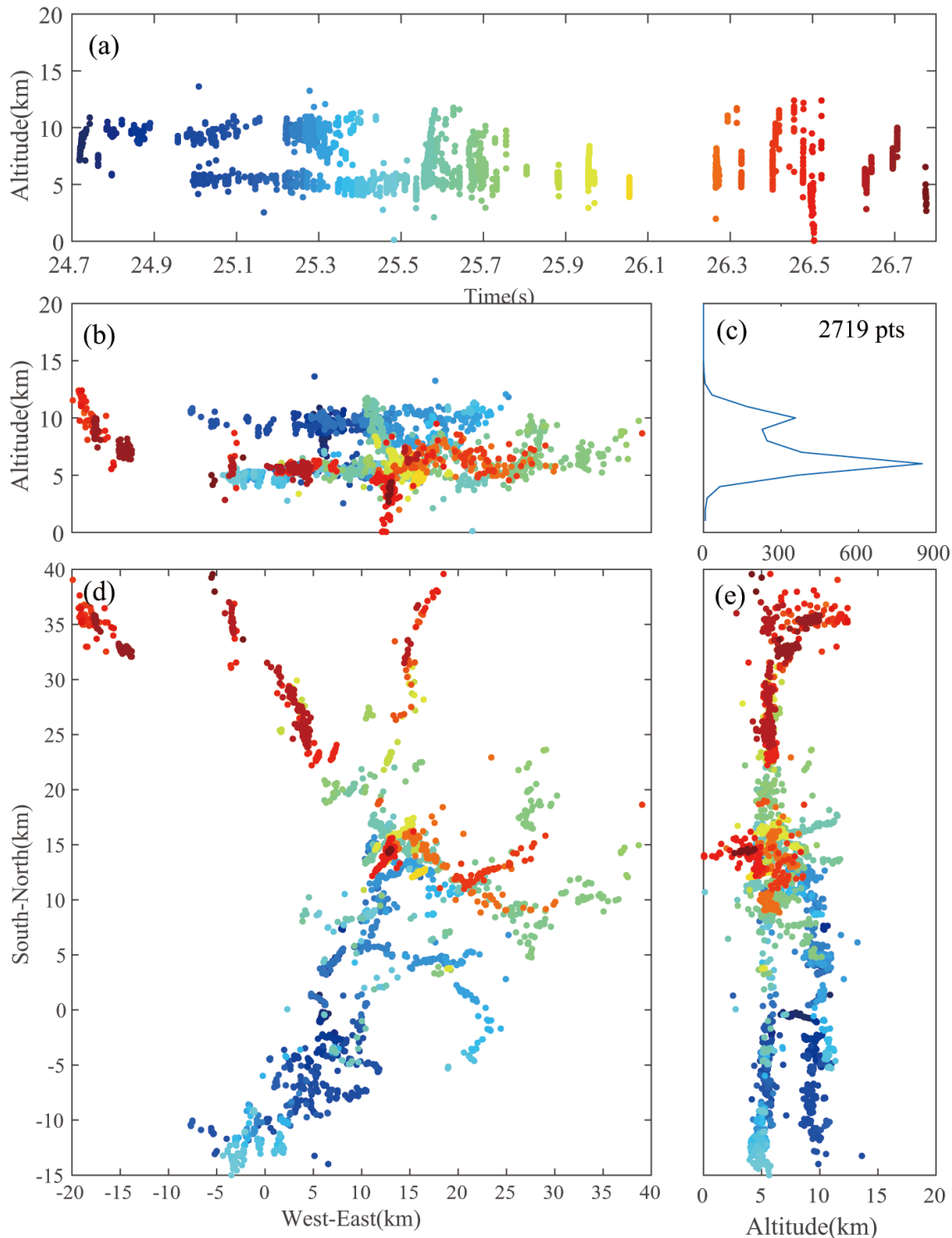


**Fig. 2.** Positioning results based on encoding features for a natural lightning flash. (a) Source altitude development, where the blue to red colors illustrate the beginning to the end of the flash. (b) North-south vertical projection. (c) Source height distribution. (d) Plan view. (e) East-west vertical projection of lightning radiation sources. [Reprinted from (Wang et al., 2021c)].

(2021b) introduced a new hybrid algorithm in this interferometer to image the two-dimensional (2D) lightning channels. The new algorithm combines the time difference of arrival (TDOA) and the electromagnetic time reversal (EMTR) technique, so it was named the TDOA-EMTR technique. Differ-

ent from the traditional EMTR technique, FFT spectrum metrics were used to remove the low-power points in each time window. Results show that TDOA-EMTR can improve positioning efficiency by more than a factor of three to four.

Wang et al. (2020d) used a method similar to Stock and

Krehbiel (2014) to improve the performance of the interferometer by using multiple baselines. Seven antennas are used to form an “L” shape interferometer (also known as a continuous VHF imaging array), and a method of applying multisignal classification to estimate the direction of arrival of a lightning VHF radiation source is proposed. This method improves the precision of traditional continuous interferometer positioning.

A dual-band location system operating at VLF-LF/VHF ranges was developed and reported by Liu et al. (2019c). It consists of 14 sensors operating at both VLF-LF and VHF ranges and covers an area of approximately 100 km in diameter in Chongqing, China. They suggest that the link between the sources of different frequency ranges can be investigated and a more complete picture of lightning channels can be described with sources from different frequency bands.

VHF positioning data can provide a variety of information with post processing. Li et al. (2021e, 2022) developed the lightning extension channel construction method and channel morphology characterization method based on 3D radiation source location data from the Lightning Mapping Array (LMA). These methods reduce the number of incorrect connections to obtain a more realistic discharge scale and are used to reveal the characteristics of charge-level distributions.

#### 2.4. *Satellite-based lightning optical monitoring technique*

China’s first geostationary satellite lightning imager, i. e., the Lightning Mapping Imager (LMI) onboard the Fengyun-4A, which was launched in December 2016, provides unprecedented lightning detection over China and its neighboring regions. The LMI can continuously detect total lightning over a large area and provide important information for the early warning of severe storms (Yang et al., 2017).

Cao et al. (2021) compared the optical signatures and spatial distribution characteristics of lightning observed by the LMI and the Lightning Imaging Sensor (LIS) on the International Space Station and found that fewer and shorter lightning flashes were observed by LMI. The number of LMI groups and the peak area of lightning density are consistent with reports from the China lightning locations network. The statistical results for duration, brightness, and coverage area of the LMI in different regions were also given based on the 2019 LMI lightning dataset. For isolated thunderstorm clusters, Liu et al. (2021f) found that the horizontal detection error of the LMI is about 15 km when comparing with the ground-based lightning observations. And LMI detection is relatively less efficient during the daytime and increases to a higher value from 1300 Beijing Time to midnight (Li et al., 2021c).

Hui et al. (2020) studied the influence of lightning light radiation characteristics on the detection capacity of the LMI and found that flashes detected by the LMI exhibit higher optical radiance but shorter durations than flashes detected by the LIS onboard Tropical Rainfall Measuring Mission (TRMM). The LMI has detected fewer lightning events

over the Tibetan Plateau (TP) and presents a lower detection efficiency there. However, it has advantages in revealing the higher intra-cloud lightning ratio in intense convection (Zhang et al., 2020d).

The performance of the FY-4A LMI was evaluated during multiple convective events over the Beijing area by Chen et al. (2021). They suggest that the spatial distributions of lightning from the LMI and BLNET are consistent with each other. However, the number of flashes detected by the LMI was roughly one order of magnitude less than that of the BLNET.

#### 2.5. *Electric field sounding technique*

The electric field sonde is a key tool used to study the charge distribution of thunderstorms. In recent years, the IAP LRG has constructed a thunderstorm electric–meteorological integrated sounding system based on the developed double-metal sphere electric field sonde in combination with the weather radiosonde. The integrated sounding system performs synchronous measurement of the electric field, temperature, and humidity in thunderstorm clouds. In the summer of 2019, a field experiment was conducted in the North China Plain, and Zhang et al. (2021b) presented the distribution characteristics of the electric field and charge structure in thunderstorm clouds in this area for the first time.

### 3. Thunderstorm electricity

Dynamical and microphysical processes in thunderstorms determine the intensity, type, polarity, and even channel propagation characteristics of lightning activity by influencing the charging process and the structure of charge distribution. The electrical activity may also affect the dynamic and microphysical field in thunderstorms (Lian et al., 2020).

#### 3.1. *Lightning activity in different types of thunderstorms*

##### 3.1.1. *Mesoscale convective system*

Mesoscale convective systems (MCSs) typically cover a spatial scale from tens to hundreds of kilometers and yield active lightning flashes. Liu et al. (2021a) reported that three types of MCSs accounted for about 73% of linear MCSs occurring in Beijing, including linear leading convective lines with a trailing stratiform region (TS), leading stratiform region with a trailing convective region (LS), and leading convective lines with a parallel stratiform region (PS). They also found that lightning mainly occurred in the linear convective region of TS, LS, and PS MCSs; at the dissipating stage, the lightning increased in the stratiform region of TS MCSs; fewer lightning flashes occurred in the LS MCSs; and the ratio of positive CG (PCG) lightning to CG lightning was high in PS MCSs. PS MCSs generally had the highest ratio of PCG to CG lightning, followed by the LS and TS MCSs. Zhao et al. (2021a) found that the positions where the lightning channels propagate are mainly dominated by the graupel and ice crystal particles in the convective



regions of MCSs, by dry snow first and ice crystal particles second in the stratiform regions of MCSs. In typical MCSs, the lightning frequency may be positively correlated with the volume of the regions with reflectivity greater than 30 dBZ or 40 dBZ (Liu et al., 2021a; Yu et al., 2022). Meanwhile, Chen et al. (2020c) noted that, in a rapidly developing MCS, the flash rate increased much faster than storm volume growth. In MCSs, only small regions were associated with more than two flash initiations in six minutes (Wang et al., 2022a). These regions were found to be primarily distributed in a stable altitude ranging from 9 km to 13 km, while only a few of these regions were at a lower altitude near the melting level. Wang et al. (2022a) suggested that the spatial relationship of these lower regions to the reflectivity core was different to that of the main altitude regions.

Cells merging is common in the convective lines of MCSs. Lu et al. (2021) found that, during the merging process of cells, the total flash rate slightly decreased at the beginning, sharply increased later, and peaked when the merging process was completed. The cloud bridge was found to be one of the regions where lightning events increased the most, which benefited from the increase and expansion of ice particles at the middle-upper levels. The simulation performed by Lu et al. (2022) suggested that the charge distribution in the cloud evolved from a staggered charge pocket pattern into a vertically stratified five-layer pattern during the merge stage.

Lightning activity in the stratiform regions of MCSs has recently been an area of focus. It is reported that more than 90% of flashes in the stratiform region of MCSs propagated above bright-band areas (Wang et al., 2019b), and most of the stratiform flashes had a single-layer structure in their channel extension area (Wang et al., 2020b). Usually, most of the stratiform flashes were initiated within a certain distance from the reflectivity core and near/in the melting layer (Wang et al., 2020b). Wang et al. (2021b) further reported that the negative leaders of stratiform flashes mainly propagated within a height range of 9–12 km in most MCSs, especially small or developing MCSs, and propagated more frequently in a low-altitude range (5–7 km) in the MCSs with a large and developed stratiform region.

### 3.1.2. Hailstorms

Hailstorms usually produce strong lightning activity accompanied with hailfall and a high proportion of PCG lightning (Liu et al., 2020a, c; Zheng et al., 2021a). For example, Sun et al. (2020) reported that the ratio of PCG lightning rapidly increased before the hailfall and reached a peak of 58% in a hailstorm, which should be due to the inverted tripolar charge structures (Zheng et al., 2021a).

Lightning data can provide useful information for hailfall warnings. The  $2\sigma$  lightning jump algorithm can provide a mean lead time of around 30 min for predicting the occurrence of hailfall, but it also exhibits a relatively high false alarm rate exceeding 30% when using total lightning data and 50% when using CG lightning data (Tian et al., 2019, 2021; Sun et al., 2020). A new method was proposed by Tian et al.

(2022) that combines the hydrometeor classification results of dual-polarization radar and the  $2\sigma$  lightning jump algorithm. They suggested that the evolution of large hail, graupel and small hail, rain and hail, and ice crystal grid point numbers in a thunderstorm can be used to effectively identify valid and invalid lightning jumps, thus improving hail warning performance. From a test based on 17 hail cases, they found that the new method decreased the false alarm rate from 58.5% to 29.2% and increased the critical success index from 41.5% to 70.8%.

### 3.1.3. Tropical cyclones

In terms of number and intensity of tropical cyclones (TCs), the northwest Pacific is the most active basin. TCs contribute approximately 4.9% of all lightning in this area, and the regions with highest contributions are located in the northern South China Sea and the ocean northeast of the Philippines. Meanwhile, the dominant lightning contributors are TCs of tropical storm strength (Zhang et al., 2020e). Furthermore, in the northwest Pacific region, TCs contribute more lightning activity during La Niña periods compared with El Niño periods (Zhang et al., 2020e, 2021e).

There is a strong correlation between lightning frequency and the timing of the TC maximum sustained wind speed. Kong et al. (2021) reported that the maximum lightning frequency occurred about 25–49 hours before the maximum intensity in terms of wind speed. Lightning in the inner-core or eyewall may have a higher ratio of intra-cloud lightning (Zhang et al., 2020d) and present an active phenomenon with a sharp increase in frequency (i.e., lightning outbreak) during the rapid intensification (RI) stage (Zhang et al., 2019b). RI lightning outbreaks occur primarily in the downshear quadrants and inside the radius of maximum wind (RMW) (Zhang et al., 2019b). For landing TCs, the dominant factor for producing lightning and convective asymmetry is the vertical wind shear. Zhang et al. (2022a) analyzed the lightning activities in both weak ( $< 32.7 \text{ m s}^{-1}$ ) and strong ( $\geq 32.7 \text{ m s}^{-1}$ ) TCs. They suggest that the lightning asymmetries were enhanced when the shear magnitude increased. This implies that lightning is an indicator of intense convection and TC intensity. And thus, lightning data may be assimilated into numerical models to understand the deep convection in TCs and to predict their evolution (Zhang et al., 2020c).

## 3.2. Lightning properties and their associations with thunderstorm structure

Different studies report lightning spatiotemporal size parameters for different locations (You et al., 2019a, b; Zheng and Zhang, 2021) or for different-type thunderstorms (Zheng et al., 2018, 2019b). In most studies, a negative correlation between flash spatial extent and flash rate for various types of thunderstorms has been suggested, that is, the thunderstorms with relatively weak convection tend to have lower flash frequency and greater flash-length compared to those with relatively strong convection. Zheng and Zhang (2021) reported a more complicated relationship between flash rate and flash size through the comparison of the thun-

derstorm and lightning features among the TP, Central and Eastern China (CEC), and the Himalayas (SHF). Combined with the concept suggested by Bruning and MacGorman (2013), Zheng and Zhang (2021) put forward a new perspective (Fig. 3). Below a certain convection intensity threshold, the enhancement of convection will reinforce the charging rate and amplify the area of the high-density charge region, which causes the common increase in flash rate and spatial extent; if the convection exceeds the threshold, the strong air-flow may break up the charge regions and help form small, staggered charge regions (like the pattern of charge pockets suggested by Bruning and MacGorman), which contributes to the high-frequency but small-spatial-extent flashes, i.e., negative correlation between flash rate and length. However, the relationship between flash duration and thunderstorm structure is still obscure. Flash duration also shows weak correlation with the flash length and radiance (You et al., 2019b).

Zheng et al. (2018, 2019a) suggested that flash initial leader (IL) properties may be related to thunderstorm structure. They found that the ILs of flashes in supercells were characterized by shorter propagation distance, more tilted direction, and slower average speed, relative to those in normal thunderstorms. These differences were attributed to the fact that supercells tend to be predominated by the pattern of charge pockets, and normal thunderstorms tend to be predominated by a horizontally broad and vertically layered charge distribution pattern. They further found that the IL properties of the flashes initiated in strong and weak dynamic regions may also be different. In supercells, the ILs initiated in the regions with relatively weak dynamic processes tended to have a greater average propagation speed than those initiated in the regions with relatively strong

dynamic process, which was opposite of the situation in normal thunderstorms. A proposed explanation is that, in supercells, the large, horizontally broad charge regions in the weak dynamic areas provide stronger ambient electric fields than the small, staggered charge regions in the strong dynamic areas. Meanwhile, in a normal thunderstorm, the strong and weak dynamic areas may both be predominated by horizontally broad charge regions. Also, strong dynamic areas had larger charging rates, and therefore, greater ambient electric fields.

### 3.3. Charge structure

Charge structure is the bridge connecting the dynamic and microphysical processes of thunderstorms and lightning activity, and new knowledge about charge structure has recently been gained. In situ electric field sonde experiments have been conducted, and they suggest an inhomogeneous and complex charge distribution pattern within the clouds (Yu et al., 2021; Zhang et al., 2021b, d). Xu et al. (2020) suggested that the charged ice phase particles transported by the backward flow behind the convective line into the stratiform region were the main charge source; meanwhile, the in situ charging of noninductive collisional and melting processes also contributed to the formation of charge structure. By using a new explicit lightning model implemented within WRF-ARW and a cloud model featuring explicit inductive and noninductive charging processes, Gan et al. (2020), Zhang et al. (2021c), and Zou et al. (2023) explored the charge structures and the formation mechanisms of thunderstorms in South and North China. As for the formation of inverted charge structure, which typically exists in severe thunderstorms, Xu et al. (2019) suggested that a strong updraft ( $>16 \text{ m s}^{-1}$ ), large liquid water content ( $>2 \text{ g m}^{-3}$ ),

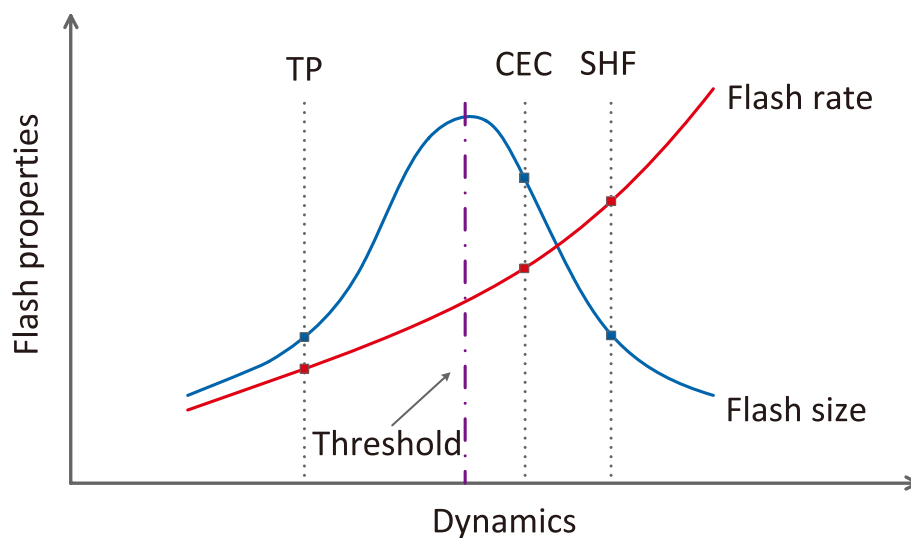


**Fig. 3.** A conceptual diagram suggested by Zheng and Zhang (2021) to describe the variation of the flash rate and size with the enhancement of thunderstorm dynamical process. Vertical grey dashed lines mark the possible situations of the thunderstorms over the Tibetan Plateau (TP), Central and Eastern China (CEC), and the southern foothills of the Himalayas (SHF). The suggested dynamic intensity threshold (purple dotted dashed line) splits the upward and downward variation tendency of flash size.

and high graupel rime accretion rate ( $>4.5 \text{ g m}^{-2} \text{ s}^{-1}$ ) above the  $-20^\circ\text{C}$  layer might cause positive charging of graupel and negative charging of ice crystals.

Some studies have further explored charge structures of distinctive thunderstorms. Zheng et al. (2019b) first documented the inverted dipolar and inverted tripolar charge structures in winter thunderstorms. Wang et al. (2021a) indicated that the high PCG percentage in Hokuriku winter thunderstorms was caused by the inverted charge structure rather than the various deformations. In a rainstorm dominated by warm precipitation, Liu et al. (2020c) noted that the charge accumulation regions indicated by the relatively active lightning deviated from the charging region indicated by the relatively strong convection. They suggested that, with weak convection in the rainstorm, the charges were transferred from where they originated (i.e., convection core) faster than the charging rate, causing a relatively low charge density in the convection core; meanwhile, the transferred charged particles might aggregate in regions away from the convection core and form relatively high charge density locally, therefore producing relatively frequent flashes. TP thunderstorms have been found to be prone to a larger-than-usual lower positive charge center (LPCC) (Qie et al., 2005, 2009). Wang et al. (2019a), by means of numerical modeling, suggested that weak convection and a low freezing level are essential for LPCC formation; meanwhile, the prominence of the LPCC benefits from weakened charge density in the upper positive charge region, but the charge density in the LPCC of a TP thunderstorm is not significantly different from that in the LPCC of a typical plain thunderstorm.

The association of the charge structure with the lightning discharges is important. By coupling an improved stochastic lightning parameterization for upward lightning into a thunderstorm model, Tan et al. (2019) investigated the relationship between the electrical environment characteristics of thunderstorms and the initiation of upward lightning. It was found that when self-initiated upward lightning started, the corresponding bottom charge region was closer to the ground and its charge was comparable to that of the upper charge region. The model suggested that with a greater concentration of the bottom charge region came a higher weighted height of the bottom charge region. In addition, Zheng et al. (2021b) quantitatively evaluated the effect of upward lightning discharges on space charges and potential and electrostatic fields using the thunderstorm model. They also analyzed the neutralization process of the deposited opposite-polarity charge in the lightning channel and its effect on the space charge structure and subsequent lightning discharges. Xu et al. (2021) analyzed the effects of the horizontal distribution characteristics of thunderstorm charge structure on lightning type as well as discharge behavior. They proposed that a compact upper positive charge region and a uniform main negative charge region favored the initiation of positive cloud-to-ground flashes, while the horizontal offset of the high concentration charge center in the upper positive charge region was conducive to the occurrence of bolt-from-the-blue flashes.

### 3.4. Climatology of thunderstorms and lightning

Thunderstorms and lightning flashes are coupled weather phenomena that exist within larger weather systems. They are affected by and have an impact on climate change. Some studies have focused on their climatological characteristics.

#### 3.4.1. Thunderstorm activity

Using the FY-2E black body temperature (TBB) and cloud classification products, as well as the lightning data provided by the World Wide Lightning Location Network (WWLLN), Ma et al. (2021a) created a thunderstorm feature dataset (TFD) covering the full-disc observation range of the FY-2E satellite and analyzed the thunderstorm activity over the Chinese mainland and the adjacent seas. They reported that the most frequent thunderstorm activity occurred in South China, Southwest China, the Eastern and Central TP, and the South China Sea and the weakest thunderstorm activity occurred in Northwest China. They also reported the differences in monthly and diurnal variations and cloud area between the thunderstorms occurring over the Chinese mainland and the adjacent seas.

Thunderstorms occurring over the TP have been investigated in several studies. Generally, TP thunderstorms feature weak convection, small horizontal extent, and low flash frequency and flash density, and they predominantly occur during May–September and in the afternoon (Zheng et al., 2020; Zheng and Zhang, 2021). Based on data from the Precipitation Radar (PR) aboard the TRMM satellite, Qie et al. (2022b) reported that TP thunderstorms increased in size and intensity from west to east, the thunderstorm frequency was the highest in the central TP, and the thunderstorm lightning-yielding ability was the strongest over the east TP in June. Using the TFD (Ma et al., 2021a), Du et al. (2022) revealed three high-frequency thunderstorm activity centers in the southeast, south-central, and southwest regions of the TP, respectively.

Furthermore, thundersnow is a special kind of thunderstorm that combines snowfall and lightning. A 10-year climatology of thundersnow in China was developed based on observations during 2008–2017 (Xu et al., 2022b). They found thundersnow events to be widely distributed across China, while the regions of high-frequency thundersnow events are located in the TP and northeastern China.

#### 3.4.2. Lightning activity

Lightning activity across most of China's mainland was investigated by Xu et al. (2022c). Over China's mainland area, lightning activity generally decreases from south to north and from east to west, with a mean CG density of  $0.9 \text{ fl km}^{-2} \text{ yr}^{-1}$  and maximum CG densities of more than  $10 \text{ fl km}^{-2} \text{ yr}^{-1}$ . However, differences in the spatiotemporal distributions may be revealed by using different observations, such as WWLLN and LIS, as suggested by Ma et al. (2021b). Both WWLLN and LIS show intense lightning activity over the central and southeastern TP during the period from May to September. LIS indicated very intense lightning

activity over the northeastern TP, while WWLLN indicated relatively weak lightning activity. And WWLLN indicated a high-density center of lightning activity over the southwestern TP, which is not suggested by LIS. Li et al. (2020) suggested a new parameter that is a product of rainfall, the Bowen ratio, and surface specific humidity, and found it showed a better correlation with lightning activity than rainfall alone or other parameters over the TP.

#### 3.4.3. *Climate change in lightning activity*

Focusing on lightning activity in the South Asia Region over the past two decades, Qie et al. (2021a) identified a clear increase in lightning density with an increasing rate of  $0.096 \text{ fl km}^{-2} \text{ yr}^{-1}$ . They suggest that the surface latent heat flux along the west coast of the Indian subcontinent can explain 52% of the lightning variance and may contribute to a  $0.025 \text{ fl km}^{-2} \text{ yr}^{-1}$  increase. Furthermore, Qie et al. (2022a) suggested that in the TP region, lightning activity has exhibited a significant increase in the last two decades in both the OTD/LIS and WWLLN observations, with an average rate of  $0.072 \pm 0.069 \text{ fl km}^{-2} \text{ yr}^{-1}$  during 1996–2013.

## 4. Lightning forecasting and data assimilation

### 4.1. *Lightning nowcasting and warning methods and techniques*

Lightning nowcasting and warning play vital roles in lightning disaster reduction. Accurate and timely lightning forecasting is still a big challenge. Different from the traditional lightning nowcasting methods that mainly refer to the precipitation structural parameters of the thunderstorm, Zhao et al. (2021b) analyzed the differences in the characteristics of vertical turbulence between thunderstorms and non-thunderstorms. They found that, at the first flash stage, the eddy dissipation rate of thunderstorms can reach  $0.19 \text{ m}^2 \text{ s}^{-3}$ , and the achievable height of turbulence can exceed the  $-30^\circ \text{C}$  layer; in contrast, during the whole non-thunderstorm lifetime, the corresponding maximums are  $0.12 \text{ m}^2 \text{ s}^{-3}$  and about the  $-10^\circ \text{C}$  layer (hard to exceed this layer), respectively. The first radar echoes of thunderstorms and non-thunderstorms were investigated by Zhao et al. (2022). They found that thunderstorms and non-thunderstorms show different characteristics of liquid/ice particles in different height layers in their first radar echoes, and non-thunderstorms tend to feature larger echo intensities below the  $-10^\circ \text{C}$  level. These results indicate that we can warn of the occurrence of lightning earlier, even when the storm first appears.

Based on BLNET total lightning data and radar observations, Srivastava et al. (2022) proposed a thunderstorm tracking algorithm to identify and validate convective cells. By applying a neighborhood and smoothing technique, the boundaries of convective cells were distinguished. Then the identified cells were extrapolated to forecast the lightning activity area. Their results show that the algorithm has accuracies of 63%, 80%, and 91% for 30 min, 15 min, and 5 min

lead times, respectively.

Quantitative and diagnostic relationships have also been established based on tracking entire thunderstorm cells. By using 3D total lightning location data and continuous-waver radar data (vertical detection), Cui et al. (2022) investigated the relationship between lightning occurrence and the precipitation cloud column (PCC) structure at a fixed position. They found the prominent differences in the structure between the PCC with and without lightning and indicated that the hydrometeor size and diversity at a specific spatial grid box should be the key parameter determining the lightning occurrence in PCCs.

### 4.2. *Very short-range lightning forecasting methods and techniques*

Very short-range lightning forecasting has more lead time. Existing prediction methods rely on numerical weather prediction (NWP) models, and the forecast performance fundamentally depends on the physical parameterization schemes.

Using the Weather Research and Forecasting (WRF) model coupled with electrification and discharge schemes (WRF-Electric), Xu et al. (2022a) carried out numerical experiments for lightning prediction in North China. Their results indicate that lightning activity regions can be predicted well by WRF-Electric, particularly for the 6–12-hour period. However, compared with the observations, the predicted lightning activity region was relatively more concentrated and the flash density was higher. They suggest that the lightning initial threshold should be modified according to the resolution of the model in the discharge parameterization process, and the neutralization charge magnitude in a single discharge should refer to the observations.

### 4.3. *Application of artificial intelligence in lightning forecasting*

In recent years, artificial intelligence has been applied in many fields, and lots of machine learning techniques have been developed. Some machine learning techniques were also introduced into lightning forecasting.

Zhou et al. (2020) developed a new CG nowcasting algorithm using a semantic segmentation deep learning network they named LightningNet. In this technique, both Himawari-8 satellite and radar echo data were used, and the 2D convolution in the semantic segmentation network was replaced with 3D convolution to obtain the lightning occurrence probability. For 0–1-h lightning nowcasting, the evaluation results show that the probability of detection, the false alarm ratio, and the threat score of LightningNet reached 0.633, 0.386, and 0.453, respectively.

Cui et al. (2022) established quantitative and diagnostic relationships based on grid box correspondence by using 3D total lightning location data and continuous-waver radar data (vertical detection). By using the Light Gradient Boosting Machine algorithm, they developed a lightning diagnosis program integrating multiple radar parameters. Evaluation results show that the algorithm has a lightning occurrence



hit rate of 93.5% and a threat score of 0.421.

Geng et al. (2019) proposed a data-driven model for lightning prediction based on neural networks named LightNet. The dual encoders in LightNet were designed to extract the simulation spatiotemporal features of WRF data and recent observation of lightning data to attempt to calibrate the simulation products and assist the prediction. Experiments show that LightNet can significantly improve 6-hour predictions and achieve an equitable threat score three times better than the previous designs. Geng et al. (2021) further established a multi-source data-driven forecasting framework based on deep neural networks including a lightning scenario. This scenario may be heterogeneous in spatial and temporal domains. Evaluation results show that with more data sources, a higher forecasting score is achieved, and a better performance compared to the formerly established 6-hour lightning forecasting schemes is obtained.

For 12-hour lightning forecasts, Lin et al. (2019) proposed an attention-based dual-source spatiotemporal neural network (ADSNet). In the forecasting procedure, this model draws on the advantage of the RNN and deploys a channel-wise attention mechanism to adaptively enhance the valuable information carried in the simulation data. The attention mechanism can not only improve forecasting performance, it can also endow the model with interpretability for the contributions of various inputted parameters. A bidirectional spatiotemporal propagator for encoding the forward and backward trend information of WRF data, LightNet+, was designed by Zhou et al. (2022). Compared with previous single-direction encoders, LightNet+ can fully analyze and utilize the temporal dependencies in the simulation data. Evaluation results show that LightNet+ can improve equitable threat scores by 10% compared to ADSNet.

By using a semantic segmentation deep learning network, Zhou et al. (2021) merged multi-source observation data and high-resolution NWP data and found that it can yield a good 2–6-h lightning forecast. A multiple input and output lightning nowcasting model, Convolutional Long- and Short-Term Memory Lightning Forecast Net (CLSTM-LFN), was constructed by Guo et al. (2022) to improve 0–3-h lightning nowcasting performance.

#### 4.4. Lightning data assimilation

Lightning data can be introduced into weather models to improve forecasts of severe weather because of the close relationship between lightning and strong convection. Since lightning cannot be directly modeled, it needs to be converted into a variable used in the model.

Some studies have used lightning data to modulate the dynamic parameters of models. Chen et al. (2020d) did experiments to assimilate lightning data from the LMI aboard the FY-4A geostationary satellite in combination with radar data. The LMI data was found to add benefits to the assimilation of radar data by reducing wind errors and promoting updraft development at locations where lightning was observed. Wang et al. (2020c) designed a lightning data dynamic nudging method to adjust the dynamic field in con-

vective clouds based on the relationship between lightning and vertical velocity. They found that the lightning data dynamic nudging did not significantly change the intensity of the updraft of the investigated squall line relative to the simulation without assimilation; but it did expand the spatial distribution of positive vertical velocity at 700 hPa by approximately 2% and therefore extend the spatial distribution of rainfall greater than 40 mm h<sup>-1</sup>. The positive effect could last for 2–3 h. Xiao et al. (2021a, b) assimilated total lightning data in a four-dimensional variational (4DVAR) system for the purpose of very short-term convective forecasting. They used the total lightning rate to modulate the vertical velocity and found that the assimilation improved the model's dynamical states by enhancing the convergence and updraft in and near the convective system. Furthermore, it was proposed that the simultaneous application of lightning data and radar data in the assimilation could produce better results. Gan et al. (2021) developed a total lightning data assimilation (LDA) scheme at the cloud-resolving scale that assimilates total lightning data through the ensemble square root filter (EnSRF) method based on the relationship of the maximum vertical velocity with the flash rate. The LDA scheme improves forecasting by improving the water vapor field, providing a warm and moist environment, and increasing convergence at low levels and divergence at upper levels.

Lightning data also can be used to modulate the microphysical parameters of models. Chen et al. (2019a) suggested an LDA scheme for nudging water contents modulated by the total lightning rate in the WRF model and tested it for two severe squall line cases in Beijing. The LDA scheme caused the simulated surface cold pool to agree well with the observations, therefore resulting in significantly-improved quantitative precipitation forecasts. Liu et al. (2021e) improved upon forecasting precipitation in leeward slope areas by using lightning data to yield pseudo-water vapor. Zhang et al. (2020c) used the lightning data from the WWLLN to modulate the WRF (Weather Research and Forecasting) model's relative humidity for Super Typhoon Haiyan in 2013 and found significant improvement in the intensity forecast of the typhoon by assimilating inner-core lightning but only faint improvement in the rainband by assimilating the lightning there. Sun et al. (2022) introduced LMI lightning data to retrieve graupel mixing ratio fields. Their assimilation experiments for two oceanic mesoscale convective systems based on the WRF model via nudging terms exhibited that most of the convective cells missed by the control experiments were recovered.

Chen et al. (2020b) used LMI lightning data to yield a proxy of radar reflectivity and then assimilated the proxy reflectivity in the Rapid-refresh Multi-scale Analysis and Prediction System-Short Term system. They reported that the positive effect of the cycling assimilation of proxy reflectivity on rainfall forecasts is similar to the parallel experiments that directly assimilated radar reflectivity. The application of this method in mountainous cases proved that it can be used as a substitute in the areas where radar data are missing.

## 5. Physics processes of lightning discharge

### 5.1. Characteristics of positive and negative leaders in lightning

Qie et al. (2019) provided a detailed comparison of the development of positive, negative, and recoil leaders. They summarized the propagating characteristics of rare positive recoil leaders through pre-conditioned channels in both tower lightning and rocket-triggered lightning and clarified the intermittent propagation of the positive leader during its the initial and sustained development. Jiang et al. (2020b) investigated the intermittent propagation of UPL and upward negative leaders in rocket-triggered lightning and found an abrupt luminous crown blooming due to a step of UPL. The clustered space leaders resulted in negative channel branching, while the residual structure in positive leaders just resulted in an individual step. In laboratory lightning-like discharges, Huang et al. (2022) observed and analyzed the step of positive leaders led by a separate luminous structure. They found that a streamer-like common zone connects the primary channel with a separate luminous structure, which exhibits bidirectional development.

Yuan et al. (2019) documented the positive leader branching feature that occurs during the propagation of a UPL. Nearby bidirectional leaders with clear asymmetrical channel extensions at opposite ends were observed (Fig. 4). By connecting with the lateral side of the progressing main positive channel, new branches of positive leaders were formed. It is suggested this kind of side discharge, together with head-splitting, are considered as two important branching mechanisms of positive leaders.

Using synchronous multi-frequency radio sensors, Yuan et al. (2020) observed and analyzed the origin of an uncommon three-stroke PCG flash with different terminations. Their results revealed that the downward positive leader preceding the positive return strokes possibly developed either from different decayed leaders or from the opposite end of a developing in-cloud negative leader. For active

horizontal negative channels, Yuan et al. (2021a) found two kinds of side breakdowns from these channels during a PCG flash. They suggested that the inception of the positive leader is independent of the disconnection or current cutoff on the negatively charged channel.

Wu et al. (2021) presented a detailed analysis of the formation of an in-cloud channel branch that extended toward the ground and finally developed into a PCG return stroke. The initiation and propagation characteristics of four vertical bidirectional leaders that made connection to the previously formed aloft horizontal channel were analyzed. It was found that the connection of the upper negative end of the bidirectional leaders to the aloft horizontal channel led to the abrupt elongation of the lower positive end.

In a recent study, Wu et al. (2022) reported the optical characteristic of needles in a PCG flash for the first time (Fig. 5). It was found that all the needles in this case were observed during the later stage and continuing current period of the return stroke. These needles initiated near the previously formed predominantly horizontal channel and extended almost perpendicular to the horizontal channel. Flickering events, which are recoil-type streamers (or leaders) retracing the needle-created channels show repetitive features. Wu et al. (2022) suggested that the needles in this PCG flash are induced by the radial motion of negative charge from the hot core into the surrounding corona sheath of the positive leader channel, when the core is rapidly recharged by the processes of return-stroke and continuing current with its radial electric field reversed.

Jiang et al. (2022) documented a unique intracloud lightning flash with abundant positive leader branches extending from one position. The recoil leaders' activation and the promotion effect on the breakdown of negative-end were discussed. They found that the positive leaders, which were accompanied by frequent recoil leaders, exhibited a noticeable transition signature from the stable and smooth extension stage to the active developing stage. And the back-and-forth interaction from the opposite ends was associated with the

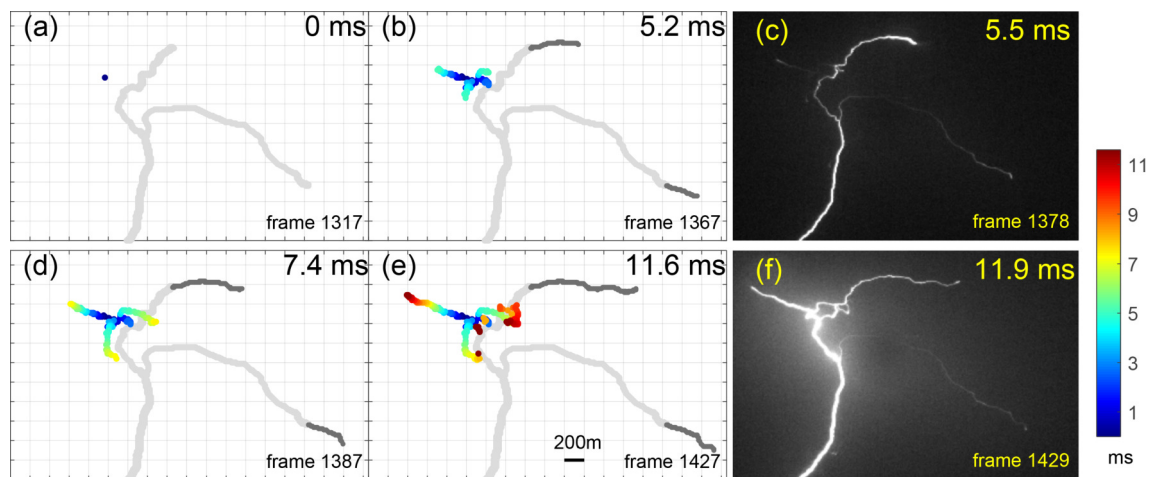


**Fig. 4.** The development of a bidirectional leader: (a) inception, (b–d) bidirectional propagation, (e) connection of the bidirectional leader to the existing positive channel, and (f) after connection. [Reprinted from (Yuan et al., 2019)].

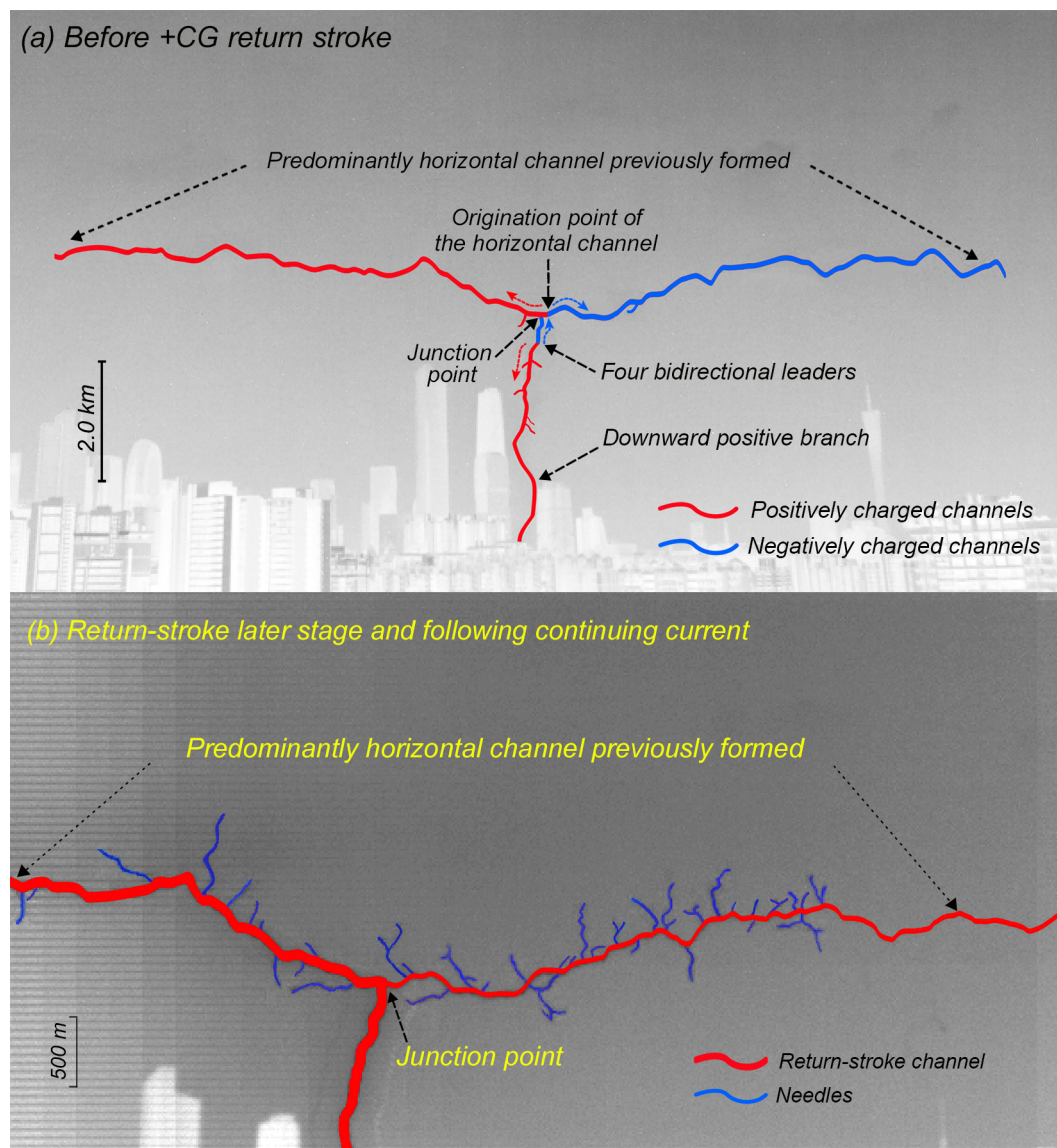


**Fig. 5.** (a) Composite image of 30 selected frames obtained by a high-speed video camera operating at 20 000 frames per second. (b) Composite image of 400 selected frames obtained by a high-speed video camera operating at 50 000 frames per second showing needles. [Adapted from (Wu et al., 2022)].

activation and propagation of long recoil leaders with regular electromagnetic pulse trains.

Considering the limitations of the stochastic lightning parameterization scheme, Zheng et al. (2022) established a new self-sustained electrical neutrality lightning discharge parameterization scheme, which simulated the dynamic aspect of channel development for the first time, including conducting, extinguishing, and reactivation. The new scheme can also simulate the evolution of the channel nonlinear electrical parameters, maintain the complete electrical neutrality of the entire discharge channel, etc., which agrees well with the current knowledge of the lightning discharge process. Therefore, it may become an effective tool for subsequent exploration of discharge phenomena associated with the dynamic development of lightning channels.

## 5.2. Characteristics of tall-object lightning discharge

Compared with the ground or low objects, the top of ground-based tall objects (such as tall buildings, tall trees, tall towers, windmills, and power transmission towers) is more likely to reach the initiation threshold of the upward leader due to the enhancement distortion of electric fields, which makes tall objects not only easy to be struck by downward lightning, but also able to initiate upward lightning. Tall objects are an important platform for lightning observation and research because of their relatively high probability of lightning occurrence.

In recent years, Chinese researchers have carried out some observation campaigns and studies on tall-object lightning: the LRG of the CAMS and the Guangzhou Institute of Tropical and Marine Meteorology, China Meteorological



Administration have established the Tall-Object Lightning Observatory in Guangzhou (TOLOG) and began conducting a comprehensive tall-object lightning observation experiment from 2009 (e.g., Lü et al., 2020); the IAP LRG began observing lightning associated with the 325-m-high meteorological tower in Beijing from 2012 (e.g., Jiang et al., 2021b); and the Shenzhen Meteorological Bureau and Hongkong Polytechnic University have conducted observation of lightning associated with the 356-m-high Shenzhen Meteorological Gradient Tower in the southern coastal area of China (e.g., Gao et al., 2020).

### 5.2.1. Characteristics of the tall-object lightning attachment process

Generally, the lightning attachment process can be separated into two phases: the initiation and propagation of one or more upward leaders from grounded objects toward the downward propagating leaders and the so-called breakthrough phase (BTP, also known as the final jump) (Rakov and Tran, 2019). Because the attachment process determines the location of the lightning grounding point (lightning return stroke position) and the area impacted by the strike, it is a crucial aspect of lightning physics and lightning protection to understand. For the lightning attachment process, tall objects can play the role of “Magnifying Glass” (Lü et al., 2020).

By using high-speed video cameras operating at 20 kilo

frames per second (kfps) and 525 kfps, Qi et al. (2019) documented video recordings with the highest framing rate to-date of the attachment process in a natural CG flash. Several important parameters, including the average inter-step interval, step length, and 2D propagation speed of the downward negative leader (DNL) and that of the UPL were statistically analyzed. It is interesting to note that the last step of the DNL contacting the UCL was captured by the high-speed video camera operating at 525 kfps. As shown in Fig. 6, the 2D length of the final imaged gap between the DNL tip and UCL tip analyzed in this case was estimated to be about 13 m.

Jiang et al. (2021b) investigated the fine structure of the breakthrough phase in a natural lightning flash striking the Beijing 325-m meteorology tower. The high-speed video images with a framing rate of 380 kfps recorded two consecutive frames for the BTP (Fig. 7). From these high-rate frames, they found a new route scenario during the BTP, which is the conversion from the previously high-impedance common streamer zone (CSZ) to a hot plasma channel. The route appeared when the bright tips of the DNL and UCL were at least 23 m apart. A space leader-like luminous segment was captured in the route.

Srivastava et al. (2019) reported the intermittent propagation of a UCL connecting a DNL in a negative CG strike to the Beijing 325-m meteorology tower. The DNL and UCL exhibited different intermittent features with temporally

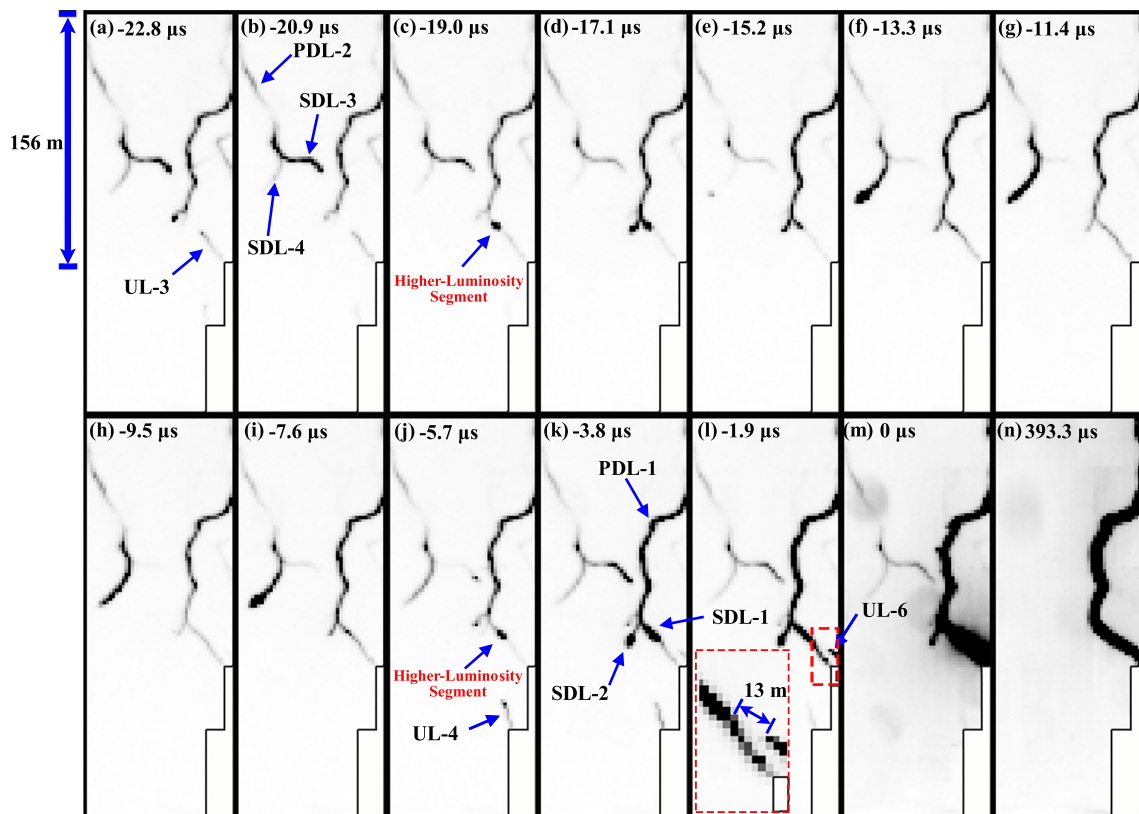


**Fig. 6.** Sequential high-speed video camera (framing rate: 525 kfps) images of a natural negative CG flash [Reprinted from (Qi et al., 2019)]. (UL: Upward Leader; PDL: Primary branch of Downward Leader; SDL: Secondary branch of Downward Leader).

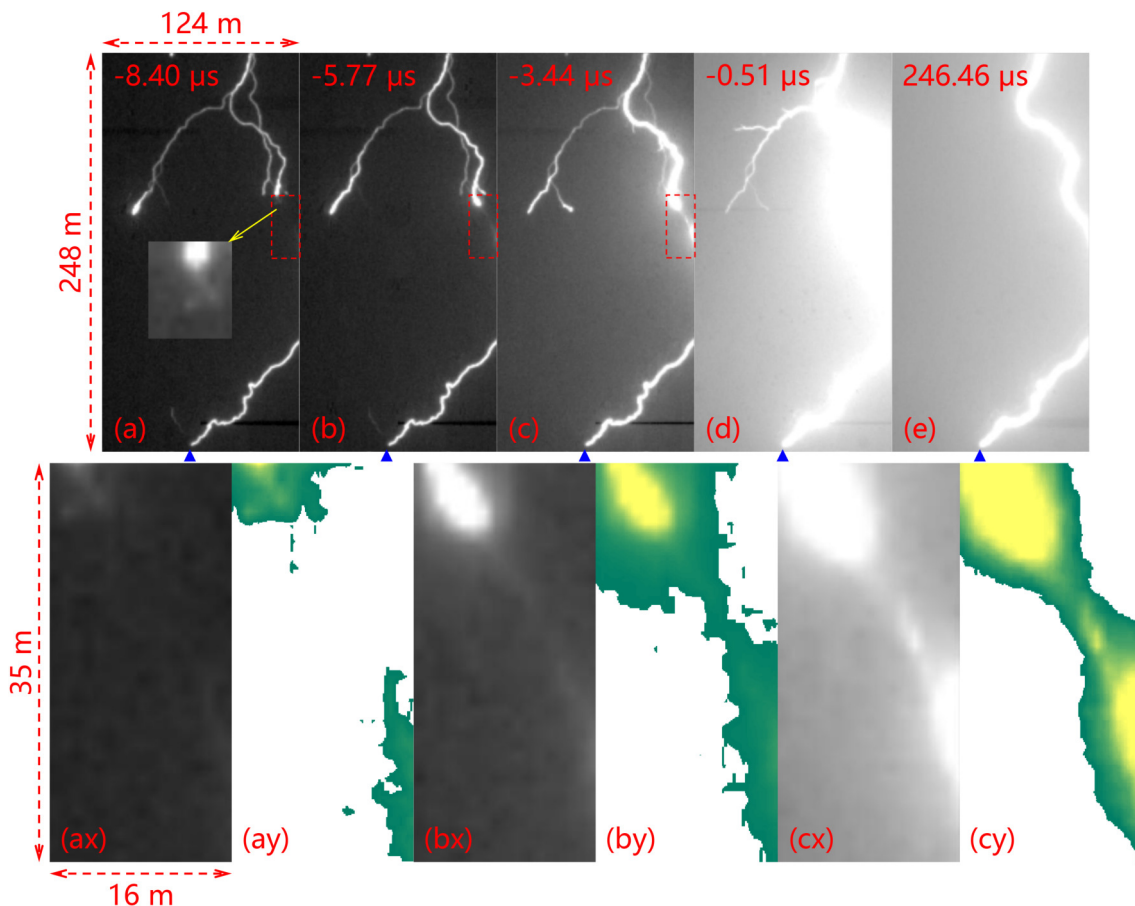


**Fig. 7.** High-speed (380 kfps) video recordings of the attachment process in a natural CG flash show the formation of the route and the leader-like luminous segment in the route. (a)–(e) show the full view and the lower panel shows an expanded view of the red rectangle area in (a)–(c). (ax), (bx), and (cx) are grey and (ay), (by), and (cy) are pseudo-color. [Adapted from (Jiang et al., 2021b)].

inconsistent steps, suggesting independent stepping development. However, they also suggest that when the DNL and UCL are very close in space, the DNL can induce and support the development of the UCL.

Qi et al. (2020, 2021) analyzed the high-speed video recordings of CG flashes striking a cluster of tall buildings (height of 100 m to 600 m) in the TOLOG field of view. The results show that the height and the top geometry of the tall objects are two essential factors that affect the 2D striking distances (SD) of the first return stroke. Combining the results with the peak current data of return strokes provided by LLS, they also indicated that the correlation between the SD and the LLS-inferred peak current appeared to be poor.

### 5.2.2. Characteristics of upward lightning

Using high-speed video observations and BLNET data from the summer seasons of 2012–20 in Beijing, Yuan et al. (2021b) analyzed the detailed characteristics of a total of 25 tower-initiated upward flashes. Twenty-one of the upward flashes were triggered by nearby PCG. They suggested that the positive change of the local electric field or continuing current period during the return stroke may favor the inception of the UPL.

Wu et al. (2019a, b) investigated the upward lightning flashes triggered from tall objects by two single-stroke PCG flashes with high peak current (+310 kA and +141 kA, respectively), which were usually followed by long continuing currents. The results show that the initiation of upward flashes triggered from tall objects by the high peak-current PCGs could be caused by the combined effects of the PCG return stroke, its associated continuing current, and the in-cloud K processes.

Many studies show that upward lightning is usually triggered by a downward PCG. However, Jiang et al. (2021a) reported the first documented downward PCG initiated by upward negative lightning, which demonstrated a new scenario for the initiation of PCG. The optical and electric field change data measured at TOLOG show that an upward lightning (negative) was first triggered from the tip of the 600-m-high Canton Tower by a distant PCG, and then the upward lightning served to facilitate the intracloud discharges that supplied positive charges for a downward PCG.

Using a highly sensitive magnetic field (B-field) antenna, Fan et al. (2021b) examined the electromagnetic characteristics of a UPL that ascended from the Canton Tower. It was found that before the inception of sustained

UPL, electric field (E-field) and B-field pulses with small amplitudes are superposed on the E-field and B-field changes. The time scale of pulses and the inter-pulse interval are similar to those associated with the precursors of rocket-triggered lightning. However, the UPL of the upward lightning initiated from the Canton Tower extended significantly in the first several milliseconds, with the initial average 2D velocity being one order of magnitude faster than that of rocket-triggered lightning, indicating that the initiation and development of a UPL triggered from a tall object benefits from the substantial E-field enhancement caused by nearby discharges.

The upward leaders in upward flashes are often followed by an initial continuous current (ICC), which typically lasts for a few hundred milliseconds. When the channels of a UPL or return stroke decay, recoil leaders (RLs) may initiate in or near the decayed channel. RLs usually develop inside the cloud, which makes the optical observation of RLs challenging, and thus the initiation and development of RL are still unclear. Wu et al. (2020) presented a detailed study of RLs in an upward flash. The initial position and propagation of RLs were analyzed, and it was found that each dart/dart-stepped leader initiated near the positive extremity of the preceding bidirectional attempted leader. Based on 20-kfps high-speed video recordings, Wu et al. (2021) further analyzed the abrupt elongation phenomenon of the positive end of the bidirectional leader. It was found that the positive end of the dart/dart-stepped leader extended abruptly via connection between the floating channel and the positive channel tip.

### 5.2.3. Characteristics of tall-object lightning return strokes

Tall objects play an “Amplifier” role on the lightning electromagnetic field (Lü et al., 2020): the higher the tall object, the larger the LLS-inferred peak current of strokes recorded in the vicinity of the tall object; numerical simulation of the tall object on the electromagnetic field of the lightning return stroke also shows that the higher the tall object is, the more significant the enhancement effect is.

Huang et al. (2021b) analyzed the waveform characteristics of optical pulses from a total of 66 subsequent return strokes in 28 upward lightning flashes. They found that the optical pulse of the subsequent return stroke in upward lightning has the shortest values, and the half-peak width of the optical pulse of the subsequent return stroke in upward lightning is lower than that of the subsequent return stroke in downward lightning.

Using a Rogowski coil installed at a height of 492 m on the 600-m Canton Tower, Chen et al. (2022a) collected lightning current direct measurements of tower-initiated flashes on the Canton Tower for the first time (Fig. 8). They analyzed the current waveforms of three single-stroke downward flashes and two multiple-stroke upward flashes, as well as the luminosity of the corresponding return strokes. For subsequent strokes in the same upward flash, the maximum peak current was found to be proportional to the square of the initial

peak luminosity. Note that all five flashes analyzed by Chen et al. (2022a) were negative polarity. Based on a comparison of the directly measured and LLS-inferred peak currents of the strokes, it is indicated that LLS-inferred peak currents of subsequent return strokes are overestimated compared to the first return stroke.

### 5.2.4. Effects of tall objects on the lightning process

Comparing to the lower objects, tall objects could be struck by lightning (either downward and upward lightning) with higher probability, so tall objects are “Hot Spots” of lightning flashes (Lü et al., 2020). Based on TOLOG optical data from 2009 to 2014, Wu et al. (2019c) analyzed the distribution characteristics of 119 downward CG flashes in the northwest of Canton Tower within 3 km. The results show that 44% (52/119) of downward CG flashes occurred on the four tallest buildings in the area. Except for the Canton Tower flashes, the attraction that downward CG flashes expe-

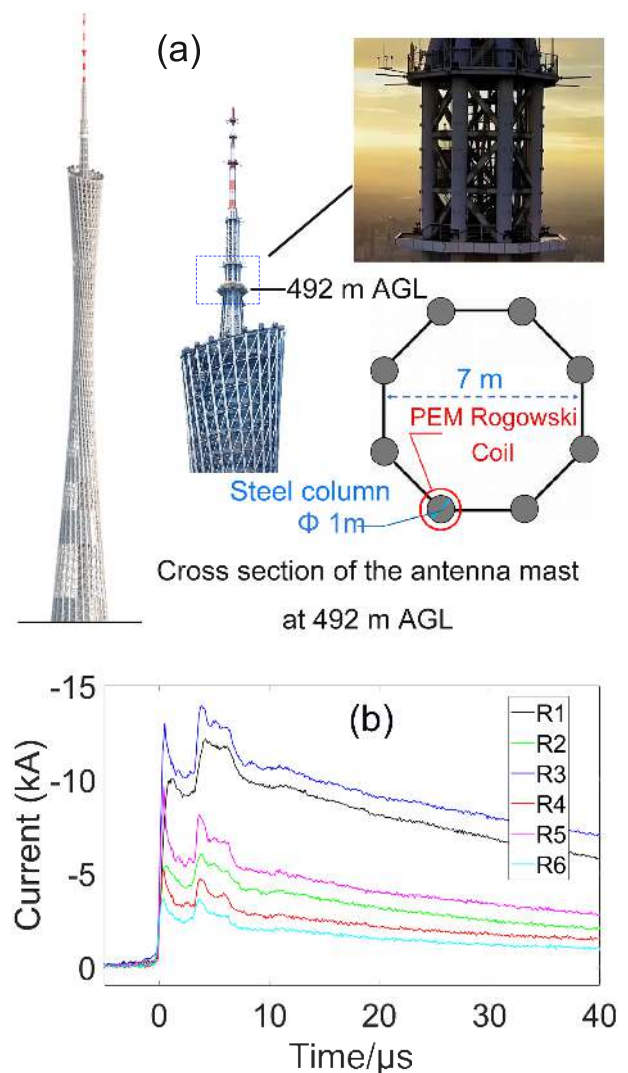


**Fig. 8.** Diagram for the placement of the Rogowski coil installed on the Canton Tower (a) and current waveforms of the return strokes in an upward lightning flash (b). [Reprinted from (Chen et al., 2022a), with permission from Elsevier].



rience toward Canton Tower makes it that downward CG flashes rarely occur within the vicinity of 1 km.

The observation area of TOLOG can be used as a “Calibration Field” for LLS (Lü et al., 2020). By using data from Guangdong–Hongkong–Macao LLS (GHMLLS) for the period 2014–18, Chen et al. (2020a) investigated the lightning “Hot Spot” caused by the 600-m-high Canton Tower, the 390-m-high CITIC Plaza, and the 308-m-high GF Securities Head-quarters, which are all relatively isolated in Guangzhou city. The number of strokes within a 200-m radius of the Canton Tower lightning “Hot Spot” was found to be about four times higher than that of the other two tall objects. It is speculated that upward lightning flashes account for the majority of Canton Tower flashes, while those flashes hitting the other two tall objects are mainly downward type.

Recently, the lightning location records of GHMLLS near several supertall structures in Shenzhen were analyzed by Zhang et al. (2022b). It was found that the higher the tall-object height is, the more lightning flashes that are recorded nearby, and the higher the proportion of records classified as in-cloud lightning is, which implies that higher objects are more likely to suffer more lightning strokes, especially subsequent strokes contained in upward lightning flashes.

Modeling the electrification and discharge process is another effective way to examine the effects of tall objects on lightning processes. Jiang et al. (2020a) presented an improved stochastic model to simulate the development of lightning leaders based on optical observations. The propagation of DNL and UCL, their attachment process, and the distribution of lightning strike points under different tall-object situations were analyzed. The results show that as the tall-object height increases, the relative strike frequency of lightning to the object increases with a decreasing rate. They also suggest that tall objects may cause lightning flashes to strike themselves and may attract nearby flashes to strike the ground close to the tall objects.

### 5.3. Characteristics of rocket-triggered lightning discharge

Employing comprehensive measurements collected from rocket-triggered lightning, subsequent leaders with intensive chaotic pulse trains (CPTs) were analyzed in detail and compared with normal dart leaders and dart-stepped leaders occurring in one flash by Pu et al. (2019). They found that the CPT leaders were accompanied by energetic radiation and emitted much stronger radiation at broadband radio frequencies and optical bands than normal leaders. The results suggested that the large product of return stroke charge and the leader velocity could be a reliable proxy/indicator for CPT.

Li et al. (2019) examined the underground magnetic field data near the channel of triggered lightning. By comparing the microsecond-scale magnetic pulses during the upward leader as simultaneously detected in the subsurface space and at 2-m soil depth, the magnetic signal was found to be modified by the soil medium, with a typical attenuation

of more than 55% and a pulse peak delay of about 0.6  $\mu$ s. The component of the magnetic field with relatively high frequency would attenuate faster than that with relatively low frequency.

From an altitude-triggered lightning flash striking a 30-m tower during the SHandong Triggering Lightning Experiment (SHATLE), Liu et al. (2020b) observed the attachment process with a circuitous “S” shaped route between the lower extremity of the triggering wire and the upper tip of the tower. They found that the DNL and the tower tip “missed” each other, but then both turned horizontal and eventually connected during the break through phase, with a total channel length of 25.3 m, close to a factor of two times the direct distance (13 m) between the wire tip and tower tip. It is interesting to note that the first eight return strokes of the lightning flash developed through the “S” shaped channel, while the last one altered the attachment route by directly bridging the gap between the wire tip and the tower tip, which may be caused by the long inter-stroke interval facilitating the channel cooling and the conductivity decreasing (Fig. 9).

Ma et al. (2020) investigated the characteristics and mechanisms of ICC pulses and M-components in rocket-triggered lightning. In two special cases, they found that multiple current surges were superimposed on the extremely long-lasting ICC and continuing current (CC) process. These current surges can maintain the grounding channel and extend the branches of the in-cloud channel, thus lengthening the time scale of the ICC/CC process, which may reduce the possibility of a return stroke thereafter. By checking the in-cloud discharge behaviors based on the VHF radiation source mapping, ground E-field changes, and the simultaneous current data, they also identified a new scenario leading to an M-component that involves a short-term interruption (or weakening of breakdown) of the upward return stroke wave and then reactivation promoted by the residual charge.

During the SHATLE field experiments in 2014 and 2015, and the Guangdong Comprehensive Observation Experiment on Lightning Discharge in 2018, Fan et al. (2019) documented a kind of magnetic pulse burst (MPB) during the ICC in rocket-triggered negative lightning. MPB sources could originate from the breakdown near the leader tip and have an average peak current on the order of kA. *B*-field measurements at the nearby site exhibit slow variations with small MPBs superposing on them. They suggest that the appearance of MPBs may indicate the enhancement of both the charge transfer and the channel brightness.

An altitude-triggered lightning flash was observed during the Guangdong Comprehensive Observation Experiment on Lightning Discharge in 2021. Fan et al. (2022) documented the low-medium frequency *B*-field measurements associated with an altitude-triggered lightning flash for the first time. The propagation of UPL during the inception of attempted DNL is revealed by *B*-field signals with microsecond resolution. The results show that the bidirectional leaders develop in an uncoordinated manner, and the measurements indicate

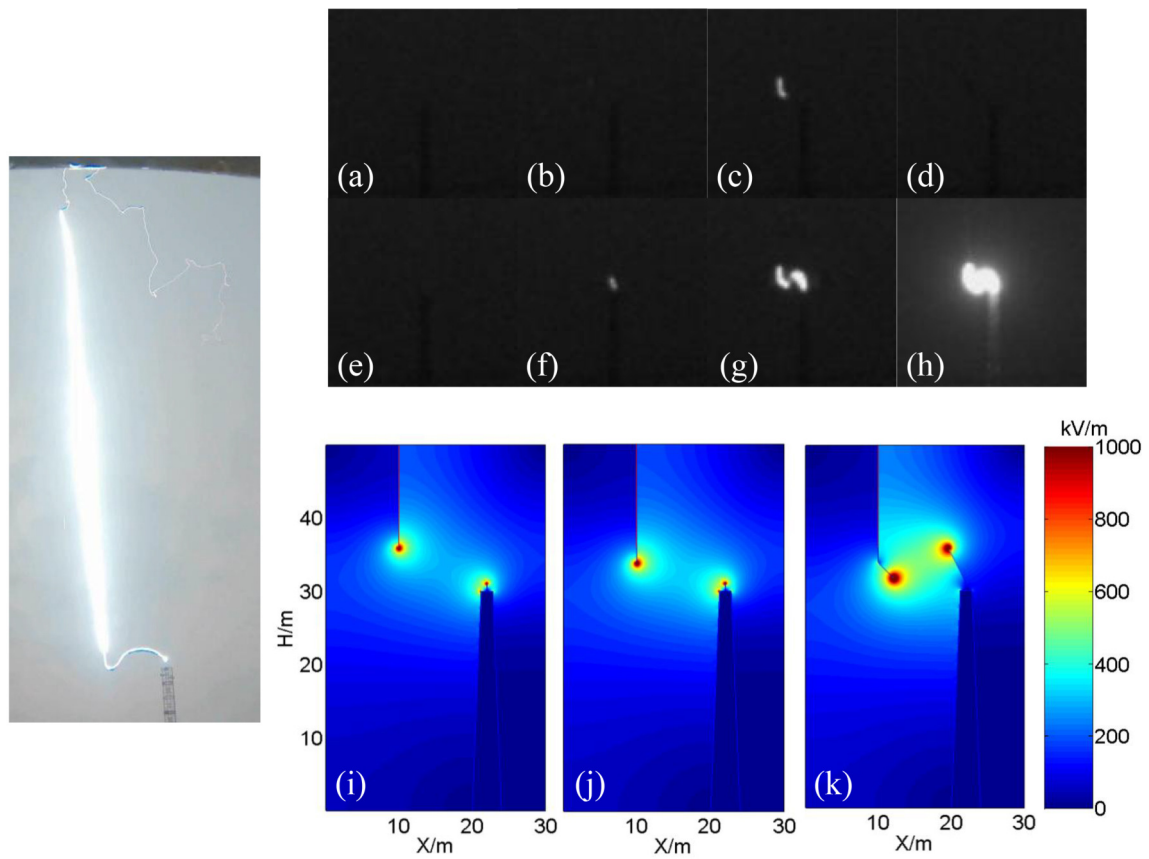


**Fig. 9.** (left) Still photograph of the circuitously attached discharge to the tower, (a)–(h) high-speed video frames of the leader behaviors for the attachment, and (i)–(k) simulated electrostatic field at three instants for initiation and attachment of leaders. [Adapted from (Liu et al., 2020b), with permission from Elsevier].

that the stepping of DNL was much more frequent than that of UPL during the stage of sustained propagation.

Tang et al. (2020) analyzed the characteristics of a triggered bipolar lightning flash with two current polarity reversals. Measurements suggest that the polarity of charge transferred to the ground varies from negative to positive and then reverse to negative (negative-positive-negative). Another example of current polarity reversal during the initial stage of a rocket-triggered lightning flash is documented by Li et al. (2021a).

Using observations from CINTF, Chen et al. (2022c) investigated the development of UPL in its initial stage and discussed its possible mechanisms. A kind of precursor current pulse (PCP), which is generated by a weak positive upward breakdown and a subsequent strong negative downward breakdown, was analyzed in detail. They found that the self-sustaining development of the UPL usually associated with the PCP cluster and the initial PCP cluster, which will stop immediately when the PCP cluster disappears. Li et al. (2021d) examined the characteristics of upward negative precursors in positive rocket-triggered lightning. They suggest that the precursors were actually the un-sustained development of upward leaders, which produced the initial channel segment at the wire tip and eventually extinguished.

#### 5.4. Spectral characteristics of a lightning flash

Spectral observations can record the emission spectrum of the lightning channel and can be used to retrieve physical information from inside the channel. Lightning spectral measurements with high spatial and temporal resolution have been used to reveal the details of lightning channels (Zhang et al., 2019a, 2020b; An et al., 2019, 2021a, b; Wang et al., 2019c, 2021d, 2022b, c; Liu et al., 2019a, b, 2021d, 2022; Wan et al., 2021; Chen et al., 2022b).

Zhang et al. (2019a) investigated the variation characteristics of return stroke current along the discharge channel, and three types of variation trends with height were found. The attenuation factor is roughly positively correlated with the intensity of discharge. They also suggest that the current tends to decay exponentially during the strong discharge process.

Using a high-speed slitless spectrograph, Liu et al. (2019a) analyzed the channel core of a natural negative CG, confirmed the lightning channel corona sheath model, and suggested that ionic lines are mainly radiated from the channel core. An et al. (2021b) calculated the corona sheath radius of the lightning return stroke channel and investigated the distribution of electrical conductivity along the channel radial direction. The relationship between the radius and electrical

conductivity of the channel was investigated. It was found that the electrical conductivity decays steeply to about  $500 \text{ S m}^{-1}$  and then more slowly as the radius increases. Positive correlations between the radius of the corona sheath and the quantity of leader charge and the diameter of the leader channel were also found. In other studies, An et al. (2019) and Wang et al. (2022c) analyzed the temperature distribution along the channel radial direction and the relationship between the initial radius and the discharge parameters.

An accurate spectral diagnosis is important in revealing the physical mechanisms of the discharge processes. The atmospheric attenuation, grating efficiency, and optical response of the camera can affect the lightning spectrum observation. Instead of the traditional Boltzmann plot method for calculating the lightning channel temperature, Liu et al. (2019a, b) used the Saha-Boltzmann plot method to determine the temperature of the return stroke channel. Wan et al. (2021) investigated the effects of atmospheric attenuation on the measured spectrum of lightning channels and calculated the corrected temperature of the channel. The result showed that the corrected channel temperature of the return stroke (calculated by the ionic lines) could be 10 000 K higher than the uncorrected value. They suggest that the temperature of the lightning channel calculated by the atomic lines was barely affected by the atmospheric attenuation. It should be noted that the total intensity of ionic lines and the electrical conductivity could increase with height, as indicated by An et al. (2021a) from the investigation of two downward PCG flashes. This also suggests that the current intensity of PCG increases with height.

Based on the TOLOG spectra data of a lightning flash striking the 600-m-high Canton Tower, Wang et al. (2022b) presented an experimental verification of the opacity thickness of lightning in the near-infrared spectrum for the first time. The results show that singly ionized radiation in the visible wavelength range apparently persists for approximately 320–400  $\mu\text{s}$ , and it coexists with neutral radiation for approximately 240–320  $\mu\text{s}$ , which means that the lightning channel exhibits a hot part radiating ionized lines and a cold part radiating neutral lines at the same time.

The properties of the lightning leader could influence the physical processes of the return stroke. Chen et al. (2022b) analyzed the effects of leader charge on the current intensity and spectral property of return strokes. They found that the return stroke current intensity mainly depends on the total charges deposited during the previous leader process. The radius of channel core is closely related to the current intensity, which can be reflected by the intensity of the singly ionized lines in the spectrum. Zhang et al. (2020b) also documented the electrical conductivity and the transmission properties of lightning leaders. They found that the 2D speed of the leader is proportionate to the corresponding conductivity. Meanwhile, the value of the 2D speed could be significantly affected by the propagation direction of the leader tip.

## 6. High energy emissions and effects of thunderstorms on the upper atmosphere

### 6.1. Terrestrial Gamma-ray Flashes

Terrestrial Gamma-ray Flashes (TGFs) are high-energy emissions with photon energy up to tens of MeV that were discovered firstly by satellite-based and then by ground-based gamma-ray detectors. Since their discovery around the 1990s, TGFs have attracted substantial attention in the lightning community, although studies from China are still limited. Details on spaceborne and ground-based observation platforms and other worldwide TGF-related studies can be found in the recent review papers by Lu et al. (2020) and Lyu et al. (2023). It is suggested that TGFs are a natural high-energy phenomenon associated with lightning discharges that occur frequently during thunderstorms. However, TGF production mechanisms, their associated processes, and their effects on human activity are still unclear. It is found that gamma rays in thunderstorms propagate in either an upward (usually detected by satellite-based detectors) or downward (usually detected by ground-based detectors) direction.

#### 6.1.1. Upward TGFs

Upward TGFs are usually generated within milliseconds of the initiation of upward negative leaders, and they may produce a kind of distinct radio emission because of the generation and propagation of a large number of high-energy electrons. Satellite-based gamma-ray detectors play a substantial role in the detection and observation of upward TGFs. The Insight-Hard X-ray Modulation Telescope (Insight-HXMT) (Zhang et al., 2020a) and Gravitational wave high-energy Electromagnetic Counterpart All-sky Monitor (GECAM) (Lv et al., 2018) are two platforms currently operating in China that can monitor high energy photons. Xian et al. (2021) analyzed the thermal structure of the environmental atmosphere associated with TGFs. A higher tropopause altitude was found in the TGF-related storms compared with the climatology values, and the land–ocean difference in the thermal structure of TGF-producing storms for subtropical and tropical thunderstorms is slightly different. Zhang et al. (2020a, 2021a) examined the low-frequency (LF) emissions associated with TGFs detected by Fermi and Insight-HXMT. They found that most TGFs were produced during the mature stage of the strong convection, but not in the strongest convection regions (Zhang et al., 2021a). The occurrence contexts of TGFs relative to the production of narrow bipolar events (NBEs) were analyzed, and TGFs that occurred both before and after lightning initiation were found, which may support different TGF production mechanisms (Zhang et al., 2021a).

By investigating five years of satellite-based gamma-ray observations and ground-based radio measurements, Lyu et al. (2021) demonstrated the close connection between upward TGFs and a distinct type of in-cloud discharge, which they named energetic in-cloud pulses (EIPs).

The identification of TGFs from the independent search of positive EIPs (+EIPs) implies a high-to-certain probability of almost all EIPs being TGFs. The work by Lyu et al. (2021) not only provides strong evidence of the connection between +EIPs and TGFs, but also experimentally demonstrates the detection of a subset of TGFs from radio signals alone.

### 6.1.2. Downward TGFs

Downward TGFs observed by ground-based gamma-ray detectors are found to be associated with several different types of lightning processes, such as DNLs or UPLs, the initial continuing current stage of rocket-triggered lightning flashes, and return stroke processes. Li et al. (2019) used an NaI (T1) detector and found that photons with low energy (X-ray) were associated with the development of stepped leaders of triggered lightning. Zhang et al. (2023) designed a distributed Thunderstorm Energetic Radiation Observation System (TEROS) to detect high-energy photons up to tens of MeV and found that energetic radiations were observed during the leader phases of five rocket-triggered lightning experiments. Compared to upward TGFs, fewer downward TGFs have been observed all over the world. With the recently designed TEROS, more details about the production of downward TGFs will become known as research in China progresses.

Based on ground-based radio measurements as well as satellite-based and ground-based gamma-ray detector observations, the studies focusing on TGF production, the relationship between gamma ray production and the occurrence of lightning discharges as well as thunderstorm circumstances have recently become areas of focus in the fields of atmospheric electricity and high energy atmospheric physics. We expect that a benefit of the development of state-of-art instruments of high temporal and spatial resolutions combined with satellite-based and ground-based measurements will be new insights into the processes and mechanisms of TGFs.

## 6.2. Transient luminous events (TLEs)

### 6.2.1. Sprites and halos

Yang et al. (2018a) analyzed the parent CGs of positive and negative sprites observed in different thunderstorm regions with various lightning activity and thunderstorm structures and discussed the different conditions needed for inducing different polarity sprites. They found that negative sprites are associated with intense and deep convection, while positive sprites are mostly associated with stratiform regions without strong convection. Pan et al. (2021) documented in detail the characteristics and lightning activity of an MCS that produced only one sprite event and found that sprites tend to be produced early in the maturity-to-dissipation stage of MCSs, with an increasing percentage of +CG to total CG. By investigating more than 1000 halo/sprite producing lightning strokes during hurricane Matthew, Huang et al. (2021a) found that the halo/sprite production during Matthew could be separated into two regions: the inner core,

which is favorable for negative halos; and the outer rainbands, which are productive for both positive and negative halo/sprite strokes. Their results also suggested a comparable feature between the outer rainbands of Matthew and the trailing stratiform region of continental MCSs.

Wang et al. (2020e) analyzed the occurrence of sprites over the southern foot of the TP by comparing the lightning detection data from WWLLN and the observations from Imager of Sprites and Upper Atmospheric Lightning (ISUAL) aboard the FORMOSAT-2 satellite. The location accuracy of ISUAL for sprites and that of WWLLN for lightning discharges in this region are examined for a total of 17 sprites. Based on the characteristics of parent lightning strokes and the meteorological context of thunderstorms derived from the FY-2 cloud-top brightness temperature data, they found that not only MCSs, but also small-scale convective systems, can produce sprites over the southern TP area.

Using the ISUAL and WWLLN data, Wang et al. (2021f) documented an extremely rare case of a negative sprite observed near the northern border of Bogotá, Colombia. A distinct “sprite current” feature was identified during the observed sprite-producing negative CG stroke. From the charge transfer analysis, they found that the sprite and the intense sprite current might have been produced by and linked to the extraordinarily long charge transfer time after the parent negative CG stroke and the plasma irregularities in the mesosphere.

Lu et al. (2018) investigated the possible relationships between halos and sprites and confirmed the association of positive halos and sprites, as well as the connection between negative sprites and halos. Statistical analysis shows that the majority of ISUAL-observed halos are pure events without any discernible streamer development. They suggest that since streamer development may depend on the impulse charge transfer of a particular time scale, many negative CG strokes may only produce halos even though the associated impulse charge moment changes exceed the threshold for sprite production.

### 6.2.2. Gigantic jets

In general, gigantic jets (GJs) are usually produced over strong tropical or tropical-like thunderstorms with convective surges or overshooting tops. In previous studies, it has been suggested that few non-GJ type TLEs were observed during the lifetime of GJ-producing summer thunderstorms. However, Yang et al. (2018b) found that MCSs provide favorable conditions not only for GJs but also for sprites. He et al. (2019) documented the first observed positive polarity GJ, which was recorded near the Yellow Sea over the Chinese mainland during a storm dominated by negative CG flashes. It was produced in a thunderstorm context consistent with a typical summer thunderstorm, and during a CG-increasing period when overshooting appears. Yang et al. (2020) analyzed a GJ in southern China in terms of its morphology, meteorology, storm evolution, lightning, and narrow bipolar events. It was found that the GJ initiated in the



region with the coldest cloud top brightness temperature and near the strong convection region. Three NBEs were generated within 30 s before and after the GJ. Based on the observations from ISUAL, magnetic field radio measurements, and lightning locations from WWLLN, Wang et al. (2021e) documented six negative red sprites produced in a tropical thunderstorm that later evolved into Hurricane Harvey (2017), and analyzed the parent stroke characteristics. They found that tropical marine meteorological systems are more likely to be the main production convection systems of negative sprites. It is interesting to note that another 18 GJs were also observed during the sprite-producing storm. They also indicated that the thundercloud charge structures of oceanic sprite-producing thunderstorms could be different from those of continental storms, as revealed from the meteorological context of storms producing both GJs and sprites.

### 6.2.3. Blue discharges and the associated NBEs

The luminous features of NBEs remain unclear, although radio emissions reflecting their existence have been reported for decades. NBEs have been thought to be relatively “dark” (nonluminous) compared to other normal lightning discharges. Based on the spectral measurements of the Atmosphere-Space Interactions Monitor (ASIM) on the International Space Station and simultaneous radio observations from ground-based radio sensors, the luminous signatures of nine negative and three positive NBEs were documented by Liu et al. (2021b). They found that NBEs of both positive and negative polarities are associated with 337-nm optical emissions, but with weak or no detectable emissions at 777.4 nm, which suggests that NBEs are associated with streamer breakdown (Fig. 10a). For negative NBEs, the optical strength is almost linearly correlated with the peak current of the associated NBEs (Fig. 10b). These findings provide new insights into the means of measuring the occurrences and strength of cloud-top discharges near the tropopause.

Liu et al. (2021c) investigated the meteorological and electrical conditions of two midlatitude thunderstorms producing thirteen blue discharges observed simultaneously by ISUAL and a ground-based lightning detection array. They found that blue discharges tend to cluster within a bounded area near the convective surge area with low cloud top temperatures ( $\sim 195$  K). Based on the outbreak of negative NBEs at altitudes between 16 km and 18 km, they suggest the existence of a strong and high upper positive charge layer due to the intense convective updraft and the production of upward positive blue discharges because of the favorable charge structures.

### 6.3. Ionospheric perturbation caused by lightning during thunderstorms

Studies show that lightning activity during thunderstorms enables electric coupling effects with the lower ionosphere. By investigating the total electron content (TEC) and its direction of propagation associated with thunderstorms using the method of polynomial filtering, Ogunsua et al. (2020) documented evidence of deviations in the ionospheric. They

found that the internal dynamics of the equatorial ionosphere were suppressed by large thunderstorm effects during the daytime. Furthermore, single a lightning stroke can have an impact on both the daytime and nighttime lower ionosphere. By investigating the skywave features of lightning sferics versus the lightning source peak currents, Qin et al. (2020) found a direct and fast nonlinear coupling between lightning-generated electromagnetic fields and the lower ionosphere. The signature of radio sferics can also be used to retrieve the properties of the ionosphere. Qin et al. (2019) introduced a modified ray-theory based model and its comparison with a finite difference time domain model for lightning sferic transmission in the earth-ionosphere waveguide. With this new model, a quantitatively better performance was achieved, and the lightning sferics could be modeled in frequencies down to 3 kHz, 5 kHz, and 7 kHz for distances of up to 500 km, 800 km, and 1000 km, respectively.

## 7. Effect of aerosol on lightning

Combining the lightning data from BLNET and PM2.5 data from 35 automatic air-monitoring stations in Beijing, Sun et al. (2020) investigated the potential effects of aerosol on lightning activity in this metropolitan region. It was found that the peak lightning activity under relatively polluted conditions occurred four hours later than that under relatively clean conditions, and the total flashes during the peak lightning activity period was doubled. The detailed relationship between the lightning flashes and the content of PM2.5 was analyzed. A significant positive correlation when PM2.5 was lower than  $130 \mu\text{g m}^{-3}$ , and a negative correlation when PM2.5 exceeded  $150 \mu\text{g m}^{-3}$  was found. However, the relationship was very weak when PM2.5 ranged between  $130 \mu\text{g m}^{-3}$  and  $150 \mu\text{g m}^{-3}$ .

To further investigate the effects of aerosols on electrification and lightning activity in the metropolitan Beijing area, Sun et al. (2021) conducted a WRF Model simulation of a multicell thunderstorm with a two-moment bulk microphysical scheme and bulk lightning model. The results show that fewer lightning discharges are produced in the continental regions where aerosol concentrations are low because of reduced latent heat in the upper levels being released, weaker updraft speed, smaller ice particle concentrations, and lower charging rates. However, lightning activity is significantly enhanced during the developing and mature stages under polluted conditions.

## 8. Concluding remarks

Although significant advancements in the study of atmospheric electricity in China have been achieved in recent years, some interesting and important questions still require further research: (1) the mechanism of electrification and charge structure formation of natural thunderstorms; (2) the initiation mechanism of natural lightning discharge; (3) the application of precise lightning location information in light-

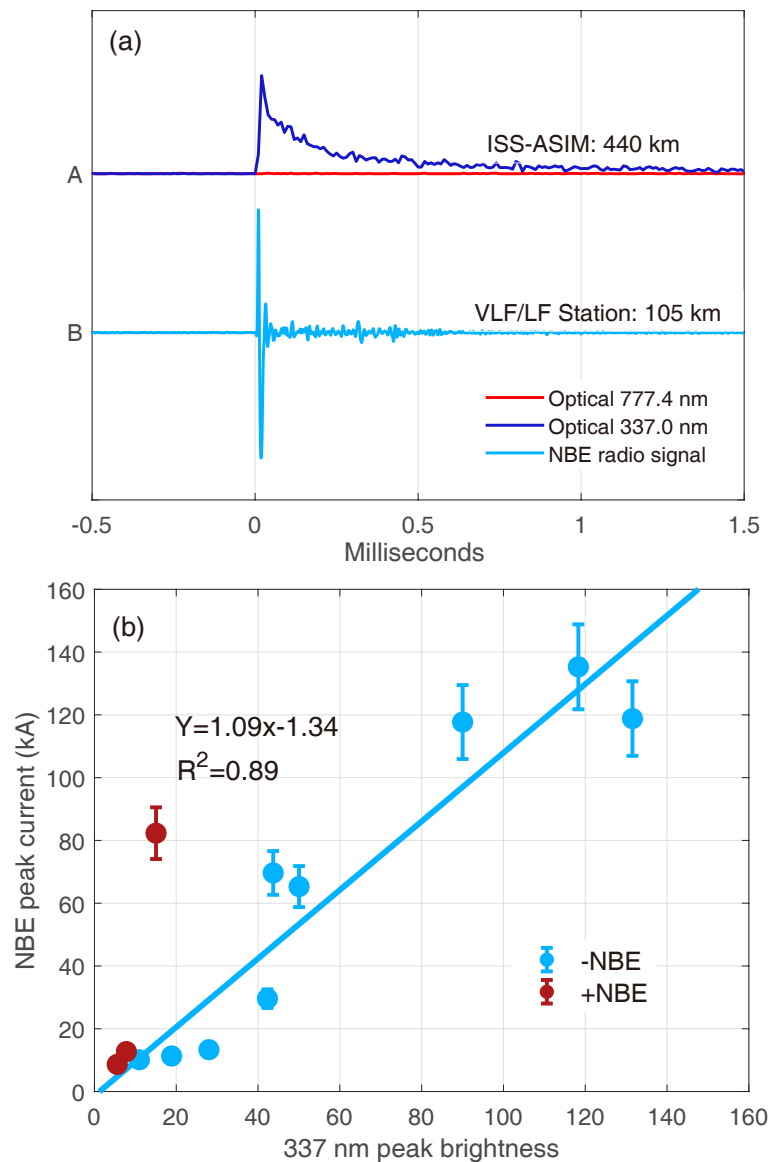


**Fig. 10.** (a) Comparison between the ASIM blue emissions and the VLF/LF sferic signal for a negative NBE. (b) Correlations between the 337-nm peak brightness of blue emission and peak current of NBEs. [Adapted from (Liu et al., 2021b)].

ning parameterization and severe weather forecasting; (4) the detection, inversion, and application techniques of discharge parameters for total lightning; (5) the mechanism of TGFs; (6) the mechanism of leader propagation and attachment to elevated objects on the ground and to the flat ground; (7) the application of artificial intelligence or other new techniques to lightning detection, analysis, and forecasting.

**Acknowledgements.** This research was supported by the National Key Research and Development Program of China (Grant No. 2017YFC1501500). The authors would like to express special thanks to Prof. Xiushu QIE, Dr. Bin WU, Dr. Qi QI, Dr. Wenjuan ZHANG, Dr. Fei WANG, Dr. Liangtao XU, and Dr. Tianxue ZHENG for preparing this paper.

## REFERENCES

- An, T. T., P. Yuan, G. R. Liu, J. Y. Cen, X. J. Wang, M. Zhang, and Y. Y. An, 2019: The radius and temperature distribution along radial direction of lightning plasma channel. *Physics of Plasmas*, **26**, 013506, <https://doi.org/10.1063/1.5059363>.
- An, T. T., P. Yuan, R. R. Chen, N. Zhang, R. B. Wan, M. Zhang, and G. R. Liu, 2021a: Evolution of discharge characteristics along the positive cloud-to-ground lightning channel. *J. Geophys. Res.: Atmos.*, **126**, e2020JD033478, <https://doi.org/10.1029/2020JD033478>.
- An, T. T., P. Yuan, R. B. Wan, R. R. Chen, G. R. Liu, J. Y. Cen, and X. J. Wang, 2021b: Conductivity characteristics and corona sheath radius of lightning return stroke channel. *Atmospheric Research*, **258**, 105649, <https://doi.org/10.1016/j.atmosres.2021.105649>.
- Bruning, E. C., and D. R. MacGorman, 2013: Theory and observa-

- tions of controls on lightning flash size spectra. *J. Atmos. Sci.*, **70**(12), 4012–4029, <https://doi.org/10.1175/JAS-D-12-0289.1>.
- Cao, D. J., F. Lu, X. H. Zhang, and J. Yang, 2021: Lightning activity observed by the FengYun-4A lightning mapping imager. *Remote Sensing*, **13**(15), 3013, <https://doi.org/10.3390/rs13153013>.
- Chen, L. H., P. Yuan, T. T. An, H. Deng, B. Y. Chen, and F. C. Su, 2022b: The influence of leader charge on current intensity and spectral characteristics of return strokes. *Atmospheric Research*, **280**, 106399, <https://doi.org/10.1016/j.atmosres.2022.106399>.
- Chen, L. W., W. T. Lü, Y. J. Zhang, Y. Ma, Q. Qi, and B. Wu, 2020a: Detection results of Guangdong-Hongkong-Macao lightning location system for tall-object lightning. *Journal of Applied Meteorological Science*, **31**(2), 165–174, <https://doi.org/10.11898/1001-7313.20200204>. (in Chinese with English abstract)
- Chen, L. W., and Coauthors, 2022a: Return-stroke current measurement at the Canton Tower and preliminary analysis results. *Electric Power Systems Research*, **206**, 107798, <https://doi.org/10.1016/j.epr.2022.107798>.
- Chen, Y. D., Z. Yu, W. Han, J. He, and M. Chen, 2020b: Case study of a retrieval method of 3D proxy reflectivity from FY-4A lightning data and its impact on the assimilation and forecasting for severe rainfall storms. *Remote Sensing*, **12**(7), 1165, <https://doi.org/10.3390/rs12071165>.
- Chen, Z. F., Y. Zhang, Y. F. Fan, J. X. Wang, W. T. Lyu, D. Zheng, and W. J. Pang, 2022c: Close observation of the evolution process during initial stage of triggered lightning based on continuous interferometer. *Remote Sensing*, **14**, 863, <https://doi.org/10.3390/rs14040863>.
- Chen, Z. F., Y. Zhang, D. Zheng, Y. J. Zhang, X. P. Fan, Y. F. Fan, L. T. Xu, and W. T. Lyu, 2019b: A method of three-dimensional location for LFEDA combining the time of arrival method and the time reversal technique. *J. Geophys. Res.: Atmos.*, **124**(12), 6484–6500, <https://doi.org/10.1029/2019JD030401>.
- Chen, Z. X., X. Qie, D. X. Liu, and Y. J. Xiong, 2019a: Lightning data assimilation with comprehensively nudging water contents at cloud-resolving scale using WRF model. *Atmospheric Research*, **221**, 72–87, <https://doi.org/10.1016/j.atmosres.2019.02.001>.
- Chen, Z. X., X. S. Qie, J. Z. Sun, X. Xiao, Y. X. Zhang, D. J. Cao, and J. Yang, 2021: Evaluation of Fengyun-4A Lightning Mapping Imager (LMI) performance during multiple convective episodes over Beijing. *Remote Sensing*, **13**, 1746, <https://doi.org/10.3390/rs13091746>.
- Chen, Z. X., X. Qie, Y. Yair, D. X. Liu, X. Xiao, D. F. Wang, and S. F. Yuan, 2020c: Electrical evolution of a rapidly developing MCS during its vigorous vertical growth phase. *Atmospheric Research*, **246**, 105201, <https://doi.org/10.1016/j.atmosres.2020.105201>.
- Chen, Z. X., J. Z. Sun, X. S. Qie, Y. Zhang, Z. M. Ying, X. Xiao, and D. J. Cao, 2020d: A method to update model kinematic states by assimilating satellite-observed total lightning data to improve convective analysis and forecasting. *J. Geophys. Res.: Atmos.*, **125**, e2020JD033330, <https://doi.org/10.1029/2020JD033330>.
- Cui, Y. X., D. Zheng, Y. J. Zhang, Z. Ruan, F. Li, W. Yao, Q. Meng, and C. H. Zhao, 2022: Association of lightning occurrence with precipitation cloud column structure at a fixed position. *Atmospheric Research*, **267**, 105989, <https://doi.org/10.1016/j.atmosres.2021.105989>.
- Du, Y. X. Y., and Coauthors, 2022: Thunderstorm activity over the Qinghai–Tibet Plateau Indicated by the combined data of the FY-2E geostationary satellite and WWLLN. *Remote Sensing*, **14**, 2855, <https://doi.org/10.3390/rs14122855>.
- Fan, X., and Coauthors, 2021a: Application of ensemble empirical mode decomposition in low-frequency lightning electric field signal analysis and lightning location. *IEEE Trans. Geosci. Remote Sens.*, **59**(1), 86–100, <https://doi.org/10.1109/TGRS.2020.2991724>.
- Fan, Y. F., Y. Zhang, G. P. Lu, W. T. Lyu, H. Y. Liu, L. T. Xu, and D. Zheng, 2022: First measurements of low-medium frequency magnetic radiation for an altitude-triggered lightning flash. *Geophys. Res. Lett.*, **49**, e2022GL098867, <https://doi.org/10.1029/2022GL098867>.
- Fan, Y. F., and Coauthors, 2019: Measurements of magnetic pulse bursts during initial continuous current of negative rocket-triggered lightning. *J. Geophys. Res.: Atmos.*, **124**, 11 710–11 721, <https://doi.org/10.1029/2019JD031237>.
- Fan, Y. F., and Coauthors, 2021b: Electromagnetic characteristics of upward leader initiated from the Canton Tower: A comparison with rocket-triggered lightning. *J. Geophys. Res.: Atmos.*, **126**, e2021JD034998, <https://doi.org/10.1029/2021JD034998>.
- Gan, M. J., F. X. Guo, Q. Li, Z. Liu, K. Zhang, and B. B. Cai, 2020: Numerical simulation of charge structure evolution characteristics of a thunderstorm cell at mature stage during a squall line event in Guangdong. *Journal of Tropical Meteorology*, **36**(4), 562–576, <https://doi.org/10.16032/j.issn.1004-4965.2020.052>. (in Chinese with English abstract)
- Gan, R. H., Y. Yang, X. B. Qiu, R. C. Wang, X. X. Qiu, and L. J. Zhu, 2021: Assimilation of the maximum vertical velocity converted from total lightning data through the EnSRF method. *J. Geophys. Res.: Atmos.*, **126**(9), e2020JD034300, <https://doi.org/10.1029/2020JD034300>.
- Gao, Y., M. L. Chen, W. T. Lyu, Q. Qi, Z. L. Qin, Y. P. Du, and Y. J. Zhang, 2020: Leader charges, currents, ambient electric fields, and space charges along downward positive leader paths retrieved from ground measurements in metropolis. *J. Geophys. Res.: Atmos.*, **125**(19), e2020JD032818, <https://doi.org/10.1029/2020JD032818>.
- Geng, Y. L. A., and Coauthors, 2019: LightNet: A dual spatiotemporal encoder network model for lightning prediction, *Proc. 25th ACM SIGKDD International Conference on Knowledge Discovery & Data Mining*, Anchorage, AK, USA, ACM, 2439–2447, <https://doi.org/10.1145/3292500.3330717>.
- Geng, Y. L. A., and Coauthors, 2021: A deep learning framework for lightning forecasting with multi-source spatiotemporal data. *Quart. J. Roy. Meteor. Soc.*, **147**, 4048–4062, <https://doi.org/10.1002/qj.4167>.
- Guo, S. C., J. Y. Wang, R. H. Gan, Z. D. Yang, and Y. Yang, 2022: Experimental study of cloud-to-ground lightning nowcasting with multisource data based on a video prediction method. *Remote Sensing*, **14**, 604, <https://doi.org/10.3390/rs14030604>.
- He, Q. J., J. Yang, G. P. Lu, Z. X. Chen, Y. Wang, M. Sato, and X. S. Qie, 2019: Analysis of the first positive polarity gigantic jet recorded near the Yellow Sea in mainland China. *Journal of Atmospheric and Solar-Terrestrial Physics*, **190**, 6–15, <https://doi.org/10.1016/j.jastp.2019.04.015>.
- Huang, A. J., J. Yang, S. A. Cummer, F. Lyu, and N. Y. Liu,

- 2021a: Examining the capacity of hurricane Matthew (2016) in spawning halo/sprite-producible lightning strokes during its lifetime. *J. Geophys. Res.: Atmos.*, **126**, e2021JD035097, <https://doi.org/10.1029/2021JD035097>.
- Huang, S. X., and Coauthors, 2022: Separate luminous structures leading positive leader steps. *Nature Communications*, **13**(1), 3655, <https://doi.org/10.1038/s41467-022-31409-x>.
- Huang, X. L., W. T. Lü, B. Wu, X. B. Sun, Y. Ma, L. W. Chen, Q. Qi, and H. Y. Liu, 2021b: Characteristics of optical pulsed induced by lightning return strokes to tall structures in Guangzhou. *Journal of Tropical Meteorology*, **37**(3), 439–449, <https://doi.org/10.16032/j.issn.1004-4965.2021.042>. (in Chinese with English abstract)
- Hui, W., F. X. Huang, and R. X. Liu, 2020: Characteristics of lightning signals over the Tibetan Plateau and the capability of FY-4A LMI lightning detection in the Plateau. *International Journal of Remote Sensing*, **41**(12), 4605–4625, <https://doi.org/10.1080/01431161.2020.1723176>.
- Jiang, R. J., and Coauthors, 2020a: Simulation of cloud-to-ground lightning strikes to structures based on an improved stochastic lightning model. *Journal of Atmospheric and Solar-Terrestrial Physics*, **203**, 105274, <https://doi.org/10.1016/j.jastp.2020.105274>.
- Jiang, R. J., and Coauthors, 2021a: First documented downward positive cloud-to-ground lightning initiated by an upward negative lightning. *J. Geophys. Res.: Atmos.*, **126**, e2021JD034566, <https://doi.org/10.1029/2021JD034566>.
- Jiang, R. B., S. F. Yuan, X. S. Qie, M. Y. Liu, and D. F. Wang, 2022: Activation of abundant recoil leaders and their promotion effect on the negative-end breakdown in an intracloud lightning flash. *Geophys. Res. Lett.*, **49**, e2021GL096846, <https://doi.org/10.1029/2021GL096846>.
- Jiang, R. B., and Coauthors, 2020b: Luminous crown residual vs. bright space segment: Characteristic structures for the intermittent positive and negative leaders of triggered lightning. *Geophys. Res. Lett.*, **47**, e2020GL088107, <https://doi.org/10.1029/2020GL088107>.
- Jiang, R. B., and Coauthors, 2021b: Fine structure of the breakthrough phase of the attachment process in a natural lightning flash. *Geophys. Res. Lett.*, **48**, e2020GL091608, <https://doi.org/10.1029/2020GL091608>.
- Kong, X. Z., Y. Zhao, Z. F. Qiu, X. Y. Tao, and W. J. Zhang, 2021: A simple method for predicting intensity change using the peak time lag between lightning and wind in tropical cyclones. *Geophys. Res. Lett.*, **48**(2), e2020GL088872, <https://doi.org/10.1029/2020GL088872>.
- Li, F. Q., and Coauthors, 2021a: A rocket-triggered lightning flash containing negative-positive-negative current polarity reversal during its initial stage. *J. Geophys. Res.: Atmos.*, **126**, e2020JD033187, <https://doi.org/10.1029/2020JD033187>.
- Li, F. Q., and Coauthors, 2021b: A new hybrid algorithm to image lightning channels combining the time difference of arrival technique and electromagnetic time reversal technique. *Remote Sensing*, **13**(22), 4658, <https://doi.org/10.3390/rs13224658>.
- Li, J. L., X. K. Wu, J. Yang, R. B. Jiang, T. Yuan, J. Y. Lu, and M. Y. Sun, 2020: Lightning activity and its association with surface thermodynamics over the Tibetan Plateau. *Atmospheric Research*, **245**, 105118, <https://doi.org/10.1016/j.atmosres.2020.105118>.
- Li, P. F., G. F. Zhai, W. J. Pang, W. Hui, W. J. Zhang, J. Chen, and L. T. Zhang, 2021c: Preliminary research on a comparison and evaluation of FY-4A LMI and ADTD data through a moving amplification matching algorithm. *Remote Sensing*, **13**(1), 11, <https://doi.org/10.3390/rs13010011>.
- Li, X., and Coauthors, 2019: Underground measurement of magnetic field pulses during the early stage of rocket-triggered lightning. *J. Geophys. Res.: Atmos.*, **124**(6), 3168–3179, <https://doi.org/10.1029/2018JD029682>.
- Li, X., and Coauthors, 2021d: On the transition from precursors to the initial upward positive leader in negative rocket-triggered lightning. *J. Geophys. Res.: Atmos.*, **126**, e2020JD033926, <https://doi.org/10.1029/2020JD033926>.
- Li, Y. R., Y. Zhang, Y. J. Zhang, and P. R. Krehbiel, 2021e: A new method for connecting the radiation sources of lightning discharge extension channels. *Earth and Space Science*, **8**, e2021EA001713, <https://doi.org/10.1029/2021EA001713>.
- Li, Y. R., Y. Zhang, Y. J. Zhang, and P. R. Krehbiel, 2022: Analysis of the configuration relationship between the morphological characteristics of lightning channels and the charge structure based on the localization of VHF radiation sources. *Geophys. Res. Lett.*, **49**, e2022GL099586.
- Lian, C. H., and Coauthors, 2020: Influence of electrical activity on dynamical and microphysical processes in thunderstorms. *Chinese Journal of Atmospheric Sciences*, **44**(1), 138–149, <https://doi.org/10.3878/j.issn.1006-9895.1903.18240>. (in Chinese with English abstract)
- Lin, T. Y., and Coauthors, 2019: Attention-based dual-source spatiotemporal neural network for lightning forecast. *IEEE Access*, **7**, 15 8296–15 8307, <https://doi.org/10.1109/ACCESS.2019.2950328>.
- Liu, D. X., X. S. Qie, Y. C. Chen, Z. L. Sun, and S. F. Yuan, 2020a: Investigating lightning characteristics through a supercell storm by comprehensive coordinated observations over North China. *Adv. Atmos. Sci.*, **37**(8), 861–872, <https://doi.org/10.1007/s00376-020-9264-x>.
- Liu, D. X., M. Y. Sun, D. B. Su, W. J. Xu, H. Yu, and Y. C. Chen, 2021a: A five-year climatological lightning characteristics of linear mesoscale convective systems over North China. *Atmospheric Research*, **256**, 105580, <https://doi.org/10.1016/j.atmosres.2021.105580>.
- Liu, F. F., and Coauthors, 2021b: Optical emissions associated with narrow bipolar events from thunderstorm clouds penetrating into the stratosphere. *Nature Communications*, **12**(1), 6631, <https://doi.org/10.1038/s41467-021-26914-4>.
- Liu, F. F., and Coauthors, 2021c: Meteorological and electrical conditions of two mid-latitude thunderstorms producing blue discharges. *J. Geophys. Res.: Atmos.*, **126**(8), e2020JD033648, <https://doi.org/10.1029/2020JD033648>.
- Liu, G. R., P. Yuan, T. T. An, J. Y. Cen, and X. J. Wang, 2019a: A visible channel core and the channel structure below the connection point for natural cloud-to-ground lightning. *Applied Physics Letters*, **115**, 064103, <https://doi.org/10.1063/1.5111845>.
- Liu, G. R., P. Yuan, T. T. An, D. X. Sun, J. Y. Cen, and X. J. Wang, 2019b: Using Saha-Boltzmann plot to diagnose lightning return stroke channel temperature. *J. Geophys. Res.: Atmos.*, **124**, 4689–4698, <https://doi.org/10.1029/2018JD028620>.
- Liu, G. R., T. T. An, R. B. Wan, P. Yuan, X. J. Wang, J. Y. Cen, H. T. Cheng, and Z. Y. Guo, 2021d: Study on the characteristic parameters of lightning return stroke channel core based on spectroscopy. *Spectroscopy and Spectral Analysis*, **41**(10),



- 3269–3275. (in Chinese with English abstract)
- Liu, G. R., and Coauthors, 2022: Diagnosis of lightning return stroke channel temperature according to different band spectra. *Acta Physica Sinica*, **71**(10), 109201, <https://doi.org/10.7498/aps.71.20211673>. (in Chinese with English abstract)
- Liu, H. Y., W. S. Dong, L. Cai, L. F. Li, B. Q. Qin, and L. Yang, 2019c: Initial results of a dual band 3-D lightning locating system. *Proceedings of the CSEE*, **39**(12), 3561–3568, <https://doi.org/10.13334/j.0258-8013.pcsee.181285>. (in Chinese with English abstract)
- Liu, M. Z., and Coauthors, 2020b: Circuitous attachment process in altitude-triggered lightning striking a 30-m-high tower. *Atmospheric Research*, **244**, 105049, <https://doi.org/10.1016/j.atmosres.2020.105049>.
- Liu, P., Y. Yang, Y. Xin, and C. H. Wang, 2021e: Impact of lightning data assimilation on forecasts of a leeward slope precipitation event in the western margin of the Junggar Basin. *Remote Sensing*, **13**(18), 3584, <https://doi.org/10.3390/rs13183584>.
- Liu, Y., H. B. Wang, Z. Li, and Z. H. Wang, 2021f: A verification of the lightning detection data from FY-4A LMI as compared with ADTD-2. *Atmospheric Research*, **248**, 105163, <https://doi.org/10.1016/j.atmosres.2020.105163>. <https://doi.org/10.1016/j.atmosres.2020.105163>.
- Liu, Z., D. Zheng, F. X. Guo, Y. Zhang, Y. J. Zhang, C. Wu, H. N. Chen, and S. Y. Han, 2020c: Lightning activity and its associations with cloud structures in a rainstorm dominated by warm precipitation. *Atmospheric Research*, **246**, 105120, <https://doi.org/10.1016/j.atmosres.2020.105120>.
- Lu, G. P., and Coauthors, 2018: On the causative strokes of halos observed by ISUAL in the vicinity of North America. *Geophys. Res. Lett.*, **45**(19), 10 781–10 789, <https://doi.org/10.1029/2018GL079594>.
- Lu, G. P., and Coauthors, 2020: Terrestrial gamma-ray flashes as the high-energy effect of tropospheric thunderstorms in near-Earth space. *Scientia Sinica Physica, Mechanica & Astronomica*, **50**(12), 129506, <https://doi.org/10.1360/SSPMA-2020-0303>. (in Chinese with English abstract)
- Lu, J. Y., and Coauthors, 2021: Lightning activity during convective cell mergers in a squall line and corresponding dynamical and thermodynamical characteristics. *Atmospheric Research*, **256**, 105555, <https://doi.org/10.1016/j.atmosres.2021.105555>.
- Lu, J. Y., and Coauthors, 2022: Effects of convective mergers on the evolution of microphysical and electrical activity in a severe squall line simulated by WRF coupled with explicit electrification scheme. *J. Geophys. Res.: Atmos.*, **127**(16), e2021JD036398, <https://doi.org/10.1029/2021JD036398>.
- Lü, W. T., L. W. Chen, Y. Ma, Q. Qi, B. Wu, and R. J. Jiang, 2020: Advances of observation and study on tall-object lightning in Guangzhou over the last decade. *Journal of Applied Meteorological Science*, **31**(2), 129–145, <https://doi.org/10.11898/1001-7313.20200201>. (in Chinese with English abstract)
- Lv, P., S. L. Xiong, X. L. Sun, J. G. Lv, and Y. G. Li, 2018: A low-energy sensitive compact gamma-ray detector based on LaBr3 and SiPM for GECAM. *Journal of Instrumentation*, **13**(08), P08014–P08014. doi: <http://dx.doi.org/10.1088/1748-0221/13/08/P08014>.
- Lyu, F. C., S. A. Cummer, M. Briggs, D. M. Smith, B. Mailyan, and S. Lesage, 2021: Terrestrial gamma-ray flashes can be detected with radio measurements of energetic in-cloud pulses during thunderstorms. *Geophys. Res. Lett.*, **48**, e2021GL093627, <https://doi.org/10.1029/2021GL093627>.
- Lyu, F. C., Y. J. Zhang, G. P. Lu, B. Y. Zhu, H. B. Zhang, W. Xu, S. L. Xiong, and W. T. Lyu, 2023: Review of recent observations and research progresses of terrestrial gamma-ray flashes during thunderstorms. *Science China Earth Sciences*, **66**, <https://doi.org/10.1007/s11430-022-1026-y>.
- Ma, R. Y., D. Zheng, W. Yao, and W. J. Zhang, 2021a: Thunderstorm feature dataset and characteristics of thunderstorm activities in China. *Journal of Applied Meteorological Science*, **32**(3), 358–369, <https://doi.org/10.11898/1001-7313.20210308>. (in Chinese with English abstract)
- Ma, R. Y., D. Zheng, Y. J. Zhang, W. Yao, W. J. Zhang, and D. Cuomu, 2021b: Spatiotemporal lightning activity detected by WWLLN over the Tibetan Plateau and its comparison with LIS lightning. *J. Atmos. Oceanic Technol.*, **38**(3), 511–523, <https://doi.org/10.1175/JTECH-D-20-0080.1>.
- Ma, Z. L., and Coauthors, 2020: Characteristics of impulsive currents superimposing on continuous/continuing current of rocket-triggered lightning. *IEEE Transactions on Electromagnetic Compatibility*, **62**, 1200–1208, <https://doi.org/10.1109/TEMC.2019.2924993>.
- Ma, Z. L., and Coauthors, 2021c: A low frequency 3D lightning mapping network in North China. *Atmospheric Research*, **249**, 105314, <https://doi.org/10.1016/j.atmosres.2020.105314>.
- Ogunsua, B. O., A. Srivastava, J. Bian, X. Qie, D. Wang, R. Jiang, and J. Yang, 2020: Significant day-time ionospheric perturbation by thunderstorms along the West African and Congo sector of equatorial region. *Scientific Reports*, **10**, 8466, <https://doi.org/10.1038/s41598-020-65315-3>.
- Pan, C., J. Yang, K. Liu, and Y. Wang, 2021: Comprehensive analysis of a coast thunderstorm that produced a sprite over the Bohai Sea. *Atmosphere*, **12**(6), 718, <https://doi.org/10.3390/atmos12060718>.
- Pu, Y. J., S. A. Cummer, F. C. Lyu, M. Briggs, B. Mailyan, M. Stanbro, and O. Roberts, 2019: Low frequency radio pulses produced by terrestrial gamma-ray flashes. *Geophys. Res. Lett.*, **46**(12), 6990–6997, <https://doi.org/10.1029/2019GL082743>.
- Qi, Q., W. T. Lü, B. Wu, Y. Ma, L. W. Chen, and R. J. Jiang, 2020: Two-dimensional optical observation of striking distance of lightning flashes to two buildings in Guangzhou. *Journal of Applied Meteorological Science*, **31**(2), 156–164, <https://doi.org/10.11898/1001-7313.20200203>. (in Chinese with English abstract)
- Qi, Q., W. T. Lyu, Y. Ma, B. Wu, L. W. Chen, R. J. Jiang, Y. N. Zhu, and V. A. Rakov, 2019: High-speed video observations of natural lightning attachment process with framing rates up to half a million frames per second. *Geophys. Res. Lett.*, **46**, 12 580–12 587, <https://doi.org/10.1029/2019GL085072>.
- Qi, Q., W. T. Lyu, D. H. Wang, B. Wu, Y. Ma, L. W. Chen, F. C. Lyu, and R. J. Jiang, 2021: Two-dimensional striking distance of lightning flashes to a cluster of tall buildings in Guangzhou. *J. Geophys. Res.: Atmos.*, **126**, e2021JD034613, <https://doi.org/10.1029/2021JD034613>.
- Qie, K., X. S. Qie, and W. S. Tian, 2021a: Increasing trend of lightning activity in the South Asia region. *Science Bulletin*, **66**(1), 78–84, <https://doi.org/10.1016/j.scib.2020.08.033>.
- Qie, X. S., 2012: Progresses in the atmospheric electricity researches in China during 2006–2010. *Adv. Atmos. Sci.*, **29**(5), 993–1005, <https://doi.org/10.1007/s00376-011-11>

- 95-0.
- Qie, X. S., and Y. J. Zhang, 2019: A review of atmospheric electricity research in China from 2011 to 2018. *Adv. Atmos. Sci.*, **36**(9), 994–1014, <https://doi.org/10.1007/s00376-019-8195-x>.
- Qie, X. S., T. L. Zhang, G. S. Zhang, T. L. Zhang, and X. Z. Kong, 2009: Electrical characteristics of thunderstorms in different plateau regions of China. *Atmospheric Research*, **91**, 244–249, <https://doi.org/10.1016/j.atmosres.2008.04.014>.
- Qie, X. S., and Coauthors, 2015: A review of atmospheric electricity research in China. *Adv. Atmos. Sci.*, **32**(2), 169–191, <https://doi.org/10.1007/s00376-014-0003-z>.
- Qie, X. S., and Coauthors, 2019: Propagation of positive, negative, and recoil leaders in upward lightning flashes. *Earth and Planetary Physics*, **3**(2), 102–110, <https://doi.org/10.26464/epp2019014>.
- Qie, X. S., and Coauthors, 2021b: Understanding the dynamical-microphysical-electrical processes associated with severe thunderstorms over the Beijing metropolitan region. *Science China Earth Sciences*, **64**(1), 10–26, <https://doi.org/10.1007/s11430-020-9656-8>.
- Qie, X. S., and Coauthors, 2022a: Significantly increased lightning activity over the Tibetan Plateau and its relation to thunderstorm genesis. *Geophys. Res. Lett.*, **49**, e2022GL099894, <https://doi.org/10.1029/2022GL099894>.
- Qie, X. S., and Coauthors, 2022b: Regional differences of convection structure of thunderclouds over the Tibetan Plateau. *Atmospheric Research*, **278**, 106338, <https://doi.org/10.1016/j.atmosres.2022.106338>.
- Qie, X. S., T. L. Zhang, C. P. Chen, G. S. Zhang, T. Zhang, and W. Z. Wei, 2005: The lower positive charge center and its effect on lightning discharges on the Tibetan Plateau. *Geophys. Res. Lett.*, **32**, L05814, <https://doi.org/10.1029/2004GL022162>.
- Qin, Z. L., S. A. Cummer, M. L. Chen, F. C. Lyu, and Y. P. Du, 2019: A comparative study of the ray theory model with the finite difference time domain model for lightning Sferic transmission in earth-ionosphere waveguide. *J. Geophys. Res.: Atmos.*, **124**(6), 3335–3349, <https://doi.org/10.1029/2018JD029440>.
- Qin, Z. L., and Coauthors, 2020: Prima facie evidence of the fast impact of a lightning stroke on the lower ionosphere. *Geophys. Res. Lett.*, **47**, e2020GL090274, <https://doi.org/10.1029/2020gl090274>.
- Rakov, V. A., and M. D. Tran, 2019: The breakthrough phase of lightning attachment process: From collision of opposite-polarity streamers to hot-channel connection. *Electric Power Systems Research*, **173**, 122–134, <https://doi.org/10.1016/j.epr.2019.03.018>.
- Srivastava, A., R. B. Jiang, S. F. Yuan, X. Qie, D. F. Wang, H. B. Zhang, Z. L. Sun, and M. Y. Liu, 2019: Intermittent propagation of upward positive leader connecting a downward negative leader in a negative cloud-to-ground lightning. *J. Geophys. Res.: Atmos.*, **124**, 13 763–13 776, <https://doi.org/10.1029/2019JD031148>.
- Srivastava, A., and Coauthors, 2022: Lightning nowcasting with an algorithm of thunderstorm tracking based on lightning location data over the Beijing area. *Adv. Atmos. Sci.*, **39**(1), 178–188, <https://doi.org/10.1007/s00376-021-0398-2>.
- Stock, M., and P. Krehbiel, 2014: Multiple baseline lightning interferometry—Improving the detection of low amplitude VHF sources. Preprints, 2014 International Conf. on Lightning Protection (ICLP), Shanghai, China, IEEE, 293–300, <https://doi.org/10.1109/ICLP.2014.6973139>.
- Sun, H., H. L. Wang, J. Yang, Y. T. Zeng, Q. L. Zhang, Y. B. Liu, J. Y. Gu, and S. Y. Huang, 2022: Improving forecast of severe oceanic mesoscale convective systems using FY-4A lightning data assimilation with WRF-FDDA. *Remote Sensing*, **14**(9), 1965, <https://doi.org/10.3390/rs14091965>.
- Sun, M. Y., and Coauthors, 2020: Lightning activity of a severe thunderstorm with several hail-fall stages in Beijing metropolitan region. *Chinese Journal of Atmospheric Sciences*, **44**(3), 601–610, <https://doi.org/10.3878/j.issn.1006-9895.1910.19134>. (in Chinese with English abstract)
- Sun, M. Y., and Coauthors, 2021: Aerosol effects on electrification and lightning discharges in a multicell thunderstorm simulated by the WRF-ELEC model. *Atmospheric Chemistry and Physics*, **21**, 14 141–14 158, <https://doi.org/10.5194/acp-21-14141-2021>.
- Tan, Y. B., T. X. Zheng, and Z. Shi, 2019: Improved lightning model: Application to discuss the characteristics of upward lightning. *Atmospheric Research*, **217**, 63–72, <https://doi.org/10.1016/j.atmosres.2018.10.011>.
- Tang, G. Y., Z. L. Sun, R. B. Jiang, F. Q. Li, M. Y. Liu, K. Liu, and X. S. Qie, 2020: Characteristics and mechanism of a triggered lightning with two polarity reversals of charges transferred to ground. *Acta Physica Sinica*, **69**(18), 189201, <https://doi.org/10.7498/aps.69.20200374>. (in Chinese with English abstract)
- Tian, Y., W. Yao, J. L. Yin, X. S. Qie, H. W. Cao, J. Li, S. F. Yuan, and D. F. Wang, 2021: Comparison of the performance of different lightning jump algorithms in Beijing. *Journal of Applied Meteorological Science*, **32**(2), 217–232, <https://doi.org/10.11898/1001-7313.20210207>. (in Chinese with English abstract)
- Tian, Y., and Coauthors, 2019: Total lightning signatures of thunderstorms and lightning jumps in hailfall nowcasting in the Beijing area. *Atmospheric Research*, **230**, 104646, <https://doi.org/10.1016/j.atmosres.2019.104646>.
- Tian, Y., and Coauthors, 2022: A method for improving the performance of the  $2\sigma$  lightning jump algorithm for nowcasting hail. *Atmospheric Research*, **280**, 106404, <https://doi.org/10.1016/j.atmosres.2022.106404>.
- Wan, R. B., P. Yuan, T. T. An, G. R. Liu, X. J. Wang, W. S. Wang, X. Huang, and H. Deng, 2021: Effects of atmospheric attenuation on the lightning spectrum. *J. Geophys. Res.: Atmos.*, **126**, e2021JD035387, <https://doi.org/10.1029/2021JD035387>.
- Wang, D. F., and Coauthors, 2020a: Beijing broadband lightning network and the spatiotemporal evolution of lightning flashes during a thunderstorm. *Chinese Journal of Atmospheric Sciences*, **44**(4), 851–864, <https://doi.org/10.3878/j.issn.1006-9895.1910.19161>. (in Chinese with English abstract)
- Wang, D. H., D. Zheng, T. Wu, and N. Takagi, 2021a: Winter positive cloud-to-ground lightning flashes observed by LMA in Japan. *IEEE Transactions on Electrical and Electronic Engineering*, **16**, 402–411, <https://doi.org/10.1002/tee.23310>.
- Wang, F., H. Y. Liu, W. S. Dong, Y. J. Zhang, W. Yao, and D. Zheng, 2019b: Radar reflectivity of lightning flashes in stratiform regions of mesoscale convective systems. *J. Geophys. Res.: Atmos.*, **124**, 14 114–14 132, <https://doi.org/10.1029/2019JD031238>.
- Wang, F., Y. J. Zhang, H. Y. Liu, W. S. Dong, W. Yao, and D.



- Zheng, 2020b: Vertical reflectivity structures near lightning flashes in the stratiform regions of mesoscale convective systems. *Atmospheric Research*, **242**, 104961, <https://doi.org/10.1016/j.atmosres.2020.104961>.
- Wang, F., Y. J. Zhang, W. S. Dong, H. Y. Liu, F. Li, and W. Yao, 2021b: Characteristics of negative leader propagation area of lightning flashes initiated in the stratiform regions of mesoscale convective systems. *J. Geophys. Res.: Atmos.*, **126**, e2020JD033336, <https://doi.org/10.1029/2020JD033336>.
- Wang, F., Y. J. Zhang, X. H. Deng, H. Y. Liu, W. S. Dong, and W. Yao, 2022a: Characteristics of regions with high-density initiation of flashes in mesoscale convective systems. *Remote Sensing*, **14**, 1193, <https://doi.org/10.3390/rs14051193>.
- Wang, F., X. H. Deng, Y. J. Zhang, Y. J. Li, G. S. Zhang, L. T. Xu, and D. Zheng, 2019a: Numerical simulation of the formation of a large lower positive charge center in a Tibetan Plateau thunderstorm. *J. Geophys. Res.: Atmos.*, **124**, 9561–9593, <https://doi.org/10.1029/2018JD029676>.
- Wang, H., D. H. Chen, J. F. Yin, D. S. Xu, G. F. Dai, and L. W. Chen, 2020c: An improvement of convective precipitation nowcasting through lightning data dynamic nudging in a cloud-resolving scale forecasting system. *Atmospheric Research*, **242**, 104994, <https://doi.org/10.1016/j.atmosres.2020.104994>.
- Wang, J. X., Y. Zhang, Y. D. Tan, Z. F. Chen, D. Zheng, Y. J. Zhang, and Y. F. Fan, 2021c: Fast and fine location of total lightning from low frequency signals based on deep-learning encoding features. *Remote Sensing*, **13**, 2212, <https://doi.org/10.3390/rs13112212>.
- Wang, T., L. H. Shi, S. Qiu, Z. Sun, and Y. T. Duan, 2020d: Continuous broadband lightning VHF mapping array using MUSIC algorithm. *Atmospheric Research*, **231**, 104647, <https://doi.org/10.1016/j.atmosres.2019.104647>.
- Wang, X. J., P. Yuan, and Q. L. Zhang, 2019c: Study on the resistance and thermal effects of current in lightning return stroke channel by spectroscopy. *Spectroscopy and Spectral Analysis*, **39**(12), 3718–3723, [https://doi.org/10.3964/j.issn.1000-0593\(2019\)12-3718-06](https://doi.org/10.3964/j.issn.1000-0593(2019)12-3718-06). (in Chinese with English abstract)
- Wang, X. J., W. Q. Xu, H. T. Wang, J. Yang, P. Yuan, Q. L. Zhang, L. Y. Hua, and Y. K. Zhang, 2021d: Spectral features, temperature and electron density properties of lightning M-component. *Acta Physica Sinica*, **70**(9), 099202, <https://doi.org/10.7498/aps.70.20201875>. (in Chinese with English abstract)
- Wang, X. J., and Coauthors, 2022b: First experimental verification of opacity for the lightning near-infrared spectrum. *Geophys. Res. Lett.*, **49**, e2022GL098883, <https://doi.org/10.1029/2022GL098883>.
- Wang, X. J., and Coauthors, 2022c: Spectral analysis and study on the channel temperature of lightning continuing current process. *Spectroscopy and Spectral Analysis*, **42**(7), 2069–2075. (in Chinese with English abstract)
- Wang, Y. H., Y. C. Min, Y. L. Liu, and G. Zhao, 2021g: A new approach of 3D lightning location based on Pearson correlation combined with empirical mode decomposition. *Remote Sensing*, **13**(19), 3883, <https://doi.org/10.3390/rs13193883>. <https://doi.org/10.3390/rs13193883>.
- Wang, Y. P., G. P. Lu, K.-M. Peng, M. Ma, S. A. Cummer, A. B. Chen, and B. Y. Zhu, 2021f: Space-based observation of a negative sprite with an unusual signature of associated sprite current. *J. Geophys. Res.: Atmos.*, **126**, 2020JD033686, <https://doi.org/10.1029/2020JD033686>. <https://doi.org/10.1029/2020JD033686>.
- Wang, Y. P., and Coauthors, 2021e: Ground observation of negative sprites over a tropical thunderstorm as the embryo of Hurricane Harvey (2017). *Geophys. Res. Lett.*, **48**(14), e2021GL094032, <https://doi.org/10.1029/2021GL094032>.
- Wang, Z. J., G. P. Lu, Y. P. Wang, A. J. Huang, and H. B. Zhang, 2020e: Observational analysis of red sprites by ISUAL instrument over the southern Tibetan Plateau. *Chinese Journal of Atmospheric Sciences*, **44**(1), 93–104, <https://doi.org/10.3878/j.issn.1006-9895.1909.18232>. (in Chinese with English abstract)
- Wu, B., W. T. Lü, Q. Qi, Y. Ma, L. W. Chen, and R. J. Jiang, 2020: High-speed video observations on abrupt elongations of the positive end of bidirectional leader. *Journal of Applied Meteorological Science*, **31**(2), 146–155, <https://doi.org/10.11898/1001-7313.20200202>. (in Chinese with English abstract)
- Wu, B., W. T. Lü, Q. Qi, Y. Ma, L. W. Chen, Z. G. Su, and S. S. Wu, 2019a: Optical and electric field observations of two concurrent upward flashes triggered by a positive cloud-to-ground flash. *Journal of Applied Meteorological Science*, **30**(3), 257–266, <https://doi.org/10.11898/1001-7313.20190301>. (in Chinese with English abstract)
- Wu, B., W. T. Lü, Q. Qi, Y. Ma, L. W. Chen, Y. J. Zhang, Y. N. Zhu, and V. A. Rakov, 2019b: Synchronized two-station optical and electric field observations of multiple upward lightning flashes triggered by a 310-kA +CG flash. *J. Geophys. Res.: Atmos.*, **124**, 1050–1063, <https://doi.org/10.1029/2018JD029378>.
- Wu, B., W. T. Lü, Q. Qi, Y. Ma, L. W. Chen, R. J. Jiang, Y. N. Zhu, and V. A. Rakov, 2021: A positive cloud-to-ground flash caused by a sequence of bidirectional leaders that served to form a ground-reaching branch of a pre-existing horizontal channel. *J. Geophys. Res.: Atmos.*, **126**, e2020JD033653, <https://doi.org/10.1029/2020JD033653>.
- Wu, B., and Coauthors, 2022: High-speed video observations of needles in a positive cloud-to-ground lightning flash. *Geophys. Res. Lett.*, **49**, e2021GL096546, <https://doi.org/10.1029/2021GL096546>.
- Wu, S. S., W. T. Lü, Q. Qi, B. Wu, L. W. Chen, Z. G. Su, R. J. Jiang, and C. X. Zhang, 2019c: Characteristics of downward cloud-to-ground lightning flashes around Canton Tower based on optical observations. *Journal of Applied Meteorological Science*, **30**(2), 203–210, <https://doi.org/10.11898/1001-7313.20190207>. (in Chinese with English abstract)
- Xian, T., G. P. Lu, H. B. Zhang, Y. P. Wang, S. L. Xiong, Q. B. Yi, J. Yang, and F. C. Lyu, 2021: Implications of GNSS-Inferred Tropopause Altitude Associated with Terrestrial Gamma-ray Flashes. *Remote Sensing*, **13**(1939), 1–12. doi: <https://doi.org/10.3390/rs13101939>.
- Xiao, X., J. Z. Sun, X. S. Qie, Z. M. Ying, L. Ji, M. X. Chen, and L. N. Zhang, 2021b: Lightning data assimilation scheme in a 4DVAR system and its impact on very short-term convective forecasting. *Mon. Wea. Rev.*, **149**(2), 353–373, <https://doi.org/10.1175/MWR-D-19-0396.1>.
- Xiao, X., and Coauthors, 2021a: Evaluating the performance of lightning data assimilation from BLNET observations in a 4DVAR-based weather nowcasting model for a high-impact weather over Beijing. *Remote Sensing*, **13**(11), 2084, <https://doi.org/10.3390/rs13112084>.

- [doi.org/10.3390/rs13112084](https://doi.org/10.3390/rs13112084).
- Xu, D. W., and Coauthors, 2021: Numerical simulation on the effects of the horizontal charge distribution on lightning types and behaviors. *J. Geophys. Res.: Atmos.*, **126**(18), e2020JD034375, <https://doi.org/10.1029/2020JD034375>.
- Xu, L. T., L. L. Xue, and I. Geresdi, 2020: How does the melting impact charge separation in squall line? A bin microphysics simulation study *Geophys. Res. Lett.*, **47**(21), e2020GL090840, <https://doi.org/10.1029/2020GL090840>.
- Xu, L. T., S. Chen, and W. Yao, 2022a: Evaluation of lightning prediction by an electrification and discharge model in long-term forecasting experiments. *Advances in Meteorology*, **2022**, 4583030, <https://doi.org/10.1155/2022/4583030>.
- Xu, L. T., Y. J. Zhang, F. Wang, and X. Cao, 2019: Simulation of inverted charge structure formation in convective regions of mesoscale convective system. *J. Meteor. Soc. Japan*, **97**(6), 1119–1135, <https://doi.org/10.2151/jmsj.2019-062>.
- Xu, L. T., W. J. Zhang, X. Cao, J. H. Zhao, and Y. J. Zhang, 2022b: A 10-year thundersnow climatology over China. *Geophys. Res. Lett.*, **49**(19), e2022GL100734, <https://doi.org/10.1029/2022GL100734>.
- Xu, M. Y., and Coauthors, 2022c: Lightning climatology across the Chinese continent from 2010 to 2020. *Atmospheric Research*, **275**, 106251, <https://doi.org/10.1016/j.atmosres.2022.106251>.
- Yang, J., Z. Q. Zhang, C. Y. Wei, F. Lu, and Q. Guo, 2017: Introducing the new generation of Chinese geostationary weather satellites, Fengyun-4. *Bull. Amer. Meteor. Soc.*, **98**(8), 1637–1658, <https://doi.org/10.1175/BAMS-D-16-0065.1>.
- Yang, J., N. Y. Liu, M. Sato, G. P. Lu, Y. Wang, and G. L. Feng, 2018a: Characteristics of thunderstorm structure and lightning activity causing negative and positive sprites. *J. Geophys. Res.: Atmos.*, **123**, 8190–8207, <https://doi.org/10.1029/2017JD026759>.
- Yang, J., M. Sato, N. Y. Liu, G. P. Lu, Y. Wang, and Z. C. Wang, 2018b: A gigantic jet observed over an mesoscale convective system in midlatitude region. *J. Geophys. Res.: Atmos.*, **123**(2), 977–996, <https://doi.org/10.1002/2017JD026878>.
- Yang, J., and Coauthors, 2020: Analysis of a gigantic jet in southern China: Morphology, meteorology, storm evolution, lightning, and narrow bipolar events. *J. Geophys. Res.: Atmos.*, **125**, e2019JD031538, <https://doi.org/10.1029/2019JD031538>.
- You, J., D. Zheng, W. Yao, and Q. Meng, 2019a: Spatio-temporal scale and optical radiance of flashes over East Asia and Western Pacific Areas. *Journal of Applied Meteorological Science*, **30**(2), 191–202, <https://doi.org/10.11898/1001-7313.20190206>. (in Chinese with English abstract)
- You, J., D. Zheng, Y. J. Zhang, W. Yao, and Q. Meng, 2019b: Duration, spatial size and radiance of lightning flashes over the Asia-Pacific region based on TRMM/LIS observations. *Atmospheric Research*, **223**, 98–113, <https://doi.org/10.1016/j.atmosres.2019.03.013>.
- Yu, H., T. L. Zhang, Y. Chen, W. T. Lü, X. P. Zhao, and J. Chen, 2021: Vertical electrical field during decay stage of local thunderstorm near coastline in tropical island. *Acta Physica Sinica*, **70**(10), 109201, <https://doi.org/10.7498/aps.70.20201634>. (in Chinese with English abstract)
- Yu, H., and Coauthors, 2022: Relationship between lightning activities and radar echoes of squall line convective systems. *Chinese Journal of Atmospheric Sciences*, **46**(4), 835–844, <https://doi.org/10.3878/j.issn.1006-9895.2101.20243>. (in Chinese with English abstract)
- Yuan, S. F., R. B. Jiang, X. S. Qie, and D. F. Wang, 2021a: Side discharges from the active negative leaders in a positive cloud-to-ground lightning flash. *Geophys. Res. Lett.*, **48**, e2021GL094127, <https://doi.org/10.1029/2021GL094127>.
- Yuan, S. F., R. B. Jiang, X. S. Qie, Z. L. Sun, D. F. Wang, and A. Srivastava, 2019: Development of side bidirectional leader and its effect on channel branching of the progressing positive leader of lightning. *Geophys. Res. Lett.*, **46**, 1746–1753, <https://doi.org/10.1029/2018GL080718>.
- Yuan, S. F., X. S. Qie, R. B. Jiang, D. F. Wang, Z. L. Sun, A. Srivastava, and E. Williams, 2020: Origin of an uncommon multiple-stroke positive cloud-to-ground lightning flash with different terminations. *J. Geophys. Res.: Atmos.*, **125**(15), e2019JD032098, <https://doi.org/10.1029/2019JD032098>.
- Yuan, S. F., X. S. Qie, R. B. Jiang, D. F. Wang, Y. Wang, C. X. Wang, A. Srivastava, and Y. Tian, 2021b: In-cloud discharge of positive cloud-to-ground lightning and its influence on the initiation of tower-initiated upward lightning. *J. Geophys. Res.: Atmos.*, **126**, e2021JD035600, <https://doi.org/10.1029/2021JD035600>.
- Zhang, H. B., G. P. Lu, F. C. Lyu, M. R. Ahmad, X. Qie, S. A. Cummer, S. L. Xiong, and M. S. Briggs, 2020a: First measurements of low-frequency Sferics associated with terrestrial gamma-ray flashes produced by equatorial thunderstorms. *Geophys. Res. Lett.*, **47**, e2020GL089005, <https://doi.org/10.1029/2020GL089005>.
- Zhang, H. B., and Coauthors, 2021a: On the terrestrial gamma-ray flashes preceding narrow bipolar events. *Geophys. Res. Lett.*, **48**, e2020GL092160, <https://doi.org/10.1029/2020gl092160>.
- Zhang, H. B., and Coauthors, 2021b: The charge structure in a thunderstorm based on three-dimensional electric field sonde. *Chinese Journal of Geophysics*, **64**(4), 1155–1166, <https://doi.org/10.6038/cjg202100187>. (in Chinese with English abstract)
- Zhang, K., and Coauthors, 2021c: Simulation study of characteristics and causes of charge structure in rainstorm dominated by warm cloud precipitation. *Journal of Tropical Meteorology*, **37**(3), 478–489, <https://doi.org/10.16032/j.issn.1004-4965.2021.046>. (in Chinese with English abstract)
- Zhang, M., P. Yuan, G. R. Liu, X. J. Wang, J. Y. Cen, and T. T. An, 2019a: The current variation along the discharge channel in cloud-to-ground lightning. *Atmospheric Research*, **225**, 121–130, <https://doi.org/10.1016/j.atmosres.2019.04.001>.
- Zhang, N., P. Yuan, T. T. An, M. Zhang, and R. R. Chen, 2020b: The conductivity and propagation property of lightning leader tip. *Atmospheric Research*, **245**, 105099, <https://doi.org/10.1016/j.atmosres.2020.105099>.
- Zhang, R., W. J. Zhang, Y. J. Zhang, J. N. Feng, and L. T. Xu, 2020c: Application of lightning data assimilation to numerical forecast of super typhoon Haiyan (2013). *J. Meteor. Res.*, **34**, 1052–1067, <https://doi.org/10.1007/s13351-020-9145-3>.
- Zhang, T. L., and Coauthors, 2021d: Sounding observation of vertical electric field in eyewall of Typhoon Wipha (No. 1907) during landing period. *Acta Physica Sinica*, **70**(13), 139201, <https://doi.org/10.7498/aps.70.20202183>. (in Chinese with English abstract)
- Zhang, W. J., S. A. Rutledge, W. X. Xu, and Y. J. Zhang, 2019b: Inner-core lightning outbreaks and convective evolution in Super Typhoon Haiyan (2013). *Atmospheric Research*, **219**, 123–139, <https://doi.org/10.1016/j.atmosres.2018.12.028>.
- Zhang, W. J., Y. J. Zhang, D. Zheng, and W. T. Lyu, 2020e: Quan-

- tifying the contribution of tropical cyclones to lightning activity over the Northwest Pacific. *Atmospheric Research*, **239**, 104906, <https://doi.org/10.1016/j.atmosres.2020.104906>.
- Zhang, W. J., Y. J. Zhang, D. Zheng, W. T. Lü, and L. T. Xu, 2021e: An overview on the research of lightning activity in tropical cyclones. *Journal of Marine Meteorology*, **41**(3), 1–10, <https://doi.org/10.19513/j.cnki.issn2096-3599.2021.03.001>. (in Chinese with English abstract)
- Zhang, W. J., Y. J. Zhang, S. J. Shu, D. Zheng, and L. T. Xu, 2022a: Lightning distribution in tropical cyclones making landfall in China. *Frontiers in Earth Science*, **10**, 940205, <https://doi.org/10.3389/feart.2022.940205>.
- Zhang, W. J., W. Hui, W. Lyu, D. J. Cao, P. F. Li, D. Zheng, X. Fang, and Y. J. Zhang, 2020d: FY-4A LMI observed lightning activity in super Typhoon Mangkhut (2018) in comparison with WWLLN data. *J. Meteor. Res.*, **34**, 336–352, <https://doi.org/10.1007/s13351-020-9500-4>.
- Zhang, X., and Coauthors, 2023: Study of the characteristics of rocket-triggered lightning energetic radiation and its relationships with the discharge parameters. *Science China Earth Sciences*, **66**, <https://doi.org/10.1007/s11430-022-1025-0>.
- Zhang, Y., Z. F. Chen, J. X. Wang, Y. F. Fan, D. Zheng, W. T. Lü, and Y. J. Zhang, 2020f: Observation of the whole discharge process during a multi-stroke triggered lightning by continuous interferometer. *Journal of Applied Meteorological Science*, **31**(2), 197–212, <https://doi.org/10.11898/1001-7313.20200207>. (in Chinese with English abstract)
- Zhang, Y., J. X. Wang, D. Zheng, W. T. Lyu, Y. J. Zhang, Y. F. Fan, X. P. Fan, and W. Yao, 2021f: Progress of observation and study on CMA\_FEBLS low frequency three-dimensional total lightning flash detection technology in the last decade. *Journal of Tropical Meteorology*, **37**(3), 298–308, <https://doi.org/10.16032/j.issn.1004-4965.2021.028>. (in Chinese with English abstract)
- Zhang, Y., and Coauthors, 2022b: Evaluation of GHMLLS performance characteristics based on observations of artificially triggered lightning. *Journal of Applied Meteorological Science*, **33**(3), 329–340, <https://doi.org/10.11898/1001-7313.20220307>. (in Chinese with English abstract)
- Zhang, Y. J., and Coauthors, 2016: A review of advances in lightning observations during the past decade in Guangdong, China. *J. Meteor. Res.*, **30**(5), 800–819, <https://doi.org/10.1007/s13351-016-6928-7>.
- Zhang, Y. J., and Coauthors, 2022c: Advances in lightning monitoring and location technology research in China. *Remote Sensing*, **14**(5), 1293, <https://doi.org/10.3390/rs14051293>.
- Zhao, C. H., D. Zheng, Y. J. Zhang, X. T. Liu, Y. Zhang, W. Yao, and W. J. Zhang, 2021a: Characteristics of cloud microphysics at positions with flash initiations and channels in convection and stratiform areas of two squall lines. *Journal of Tropical Meteorology*, **37**(3), 358–369, <https://doi.org/10.16032/j.issn.1004-4965.2021.035>. (in Chinese with English abstract)
- Zhao, C. H., D. Zheng, Y. J. Zhang, X. T. Liu, Y. Zhang, W. Yao, and W. J. Zhang, 2021b: Turbulence characteristics of thunderstorms before the first flash in comparison to non-thunderstorms. *Geophys. Res. Lett.*, **48**, e2021GL094821, <https://doi.org/10.1029/2021GL094821>.
- Zhao, C. H., Y. J. Zhang, D. Zheng, X. T. Liu, Y. Zhang, X. P. Fan, W. Yao, and W. J. Zhang, 2022: Using polarimetric radar observations to characterize first echoes of thunderstorms and nonthunderstorms: A comparative study. *J. Geophys. Res.: Atmos.*, **127**(23), e2022JD036671, <https://doi.org/10.1029/2022JD036671>.
- Zheng, D., and Y. J. Zhang, 2021: New insights into the correlation between lightning flash rate and size in thunderstorms. *Geophys. Res. Lett.*, **48**, e2021GL096085, <https://doi.org/10.1029/2021GL096085>.
- Zheng, D., Y. J. Zhang, and Q. Meng, 2018: Properties of negative initial leaders and lightning flash size in a cluster of supercells. *J. Geophys. Res.: Atmos.*, **123**, 12 857–12 876, <https://doi.org/10.1029/2018JD028824>.
- Zheng, D., D. H. Wang, Y. J. Zhang, T. Wu, and N. Takagi, 2019b: Charge regions indicated by LMA lightning flashes in Hokuriku's winter thunderstorms. *J. Geophys. Res.: Atmos.*, **124**, 7179–7206, <https://doi.org/10.1029/2018jd030060>.
- Zheng, D., W. J. Zhang, W. Yao, L. T. Xu, and F. Wang, 2021a: Research progress of lightning activity in thunderstorms. *Journal of Tropical Meteorology*, **37**(3), 289–297, <https://doi.org/10.16032/j.issn.1004-4965.2021.027>. (in Chinese with English abstract)
- Zheng, D., D. D. Shi, Y. Zhang, Y. J. Zhang, W. T. Lyu, and Q. Meng, 2019a: Initial leader properties during the preliminary breakdown processes of lightning flashes and their associations with initiation positions. *J. Geophys. Res.: Atmos.*, **124**, 8025–8042, <https://doi.org/10.1029/2019jd030300>.
- Zheng, D., and Coauthors, 2020: Lightning and deep convective activities over the Tibetan Plateau. *National Science Review*, **7**, 487–488, <https://doi.org/10.1093/nsr/nwz182>.
- Zheng, T. X., Y. B. Tan, and Y. R. Wang, 2021b: Numerical simulation to evaluate the effects of upward lightning discharges on thunderstorm electrical parameters. *Adv. Atmos. Sci.*, **38**(3), 446–459, <https://doi.org/10.1007/s00376-020-0154-z>.
- Zheng, T. X., Y. B. Tan, H. C. Wang, Z. Shi, W. T. Lyu, B. Wu, Y. K. Zhang, 2022: A self-sustained charge neutrality intra-cloud lightning parameterization containing channel decay and reactivation. *Geophys. Res. Lett.*, **49**(23), e2022GL100849, <https://doi.org/10.1029/2022GL100849>.
- Zhou, K. H., Y. G. Zheng, and T. B. Wang, 2021: Very short-range lightning forecasting with NWP and observation data: A deep learning approach. *Acta Meteorologica Sinica*, **79**(1), 1–14, <https://doi.org/10.11676/qxxb2021.002>. (in Chinese with English abstract)
- Zhou, K. H., Y. G. Zheng, W. S. Dong, and T. B. Wang, 2020: A deep learning network for cloud-to-ground lightning nowcasting with multisource data. *J. Atmos. Oceanic Technol.*, **37**(5), 927–942, <https://doi.org/10.1175/JTECH-D-19-0146.1>.
- Zhou, X. Y., Y. L. A. Geng, H. M. Yu, Q. Li, L. T. Xu, W. Yao, D. Zheng, and Y. J. Zhang, 2022: LightNet+: A dual-source lightning forecasting network with bi-direction spatiotemporal transformation. *Applied Intelligence*, **52**, 11 147–11 159, <https://doi.org/10.1007/s10489-021-03089-5>.
- Zou, D. K., F. X. Guo, Z. W. Zhang, Y. Chu, X. Lu, Z. Liu, and Z. Y. Wu, 2023: Relationship between lower positive charge center and warm cloud depth in thunderstorms over Qinghai-Xizang Plateau. *Plateau Meteorology*, **42**(1), 68–81, <https://doi.org/10.7522/j.issn.1000-0534.2022.00023>. (in Chinese with English abstract)

• Review •

## China's Recent Progresses in Polar Climate Change and Its Interactions with the Global Climate System<sup>✱</sup>

Xichen LI<sup>1</sup>, Xianyao CHEN<sup>2,3</sup>, Bingyi WU<sup>4,5</sup>, Xiao CHENG<sup>6</sup>, Minghu DING<sup>7</sup>, Ruibo LEI<sup>8</sup>, Di QI<sup>9</sup>, Qizhen SUN<sup>10</sup>, Xiaoyu WANG<sup>2,3</sup>, Wenli ZHONG<sup>2,3</sup>, Lei ZHENG<sup>6</sup>, Meijiao XIN<sup>1,11</sup>, Xiaocen SHEN<sup>1</sup>, Chentao SONG<sup>1,11</sup>, and Yurong HOU<sup>1,11</sup>

<sup>1</sup>*Institute of Atmospheric Physics, Chinese Academy of Sciences, Beijing 100029, China*

<sup>2</sup>*Frontier Science Center for Deep Ocean Multispheres and Earth System and Physical Oceanography Laboratory, Ocean University of China, Qingdao 266100, China*

<sup>3</sup>*Qingdao National Laboratory for Marine Science and Technology, Qingdao 266061, China*

<sup>4</sup>*Department of Atmospheric and Oceanic Sciences/Institute of Atmospheric Sciences, Fudan University, Shanghai 200438, China*

<sup>5</sup>*CMA-FDU Joint Laboratory of Marine Meteorology, Shanghai 200438, China*

<sup>6</sup>*School of Geospatial Engineering and Science, Southern Marine Science and Engineering Guangdong Laboratory (Zhuhai), Sun Yat-sen University, Zhuhai 519082, China*

<sup>7</sup>*State Key Laboratory of Severe Weather, Chinese Academy of Meteorological Sciences, Beijing 100081, China*

<sup>8</sup>*Key Laboratory for Polar Science of the MNR, Polar Research Institute of China, Shanghai 200136, China*

<sup>9</sup>*Polar and Marine Research Institute, Jimei University, Xiamen 361021, China*

<sup>10</sup>*Polar Research and Forecasting Division, National Marine Environmental Forecasting Center, Beijing 100081, China*

<sup>11</sup>*College of Earth and Planetary Sciences, University of Chinese Academy of Sciences, Beijing 100049, China*

(Received 1 November 2022; revised 12 February 2023; accepted 23 February 2023)

### ABSTRACT

During the recent four decades since 1980, a series of modern climate satellites were launched, allowing for the measurement and record-keeping of multiple climate parameters, especially over the polar regions where traditional observations are difficult to obtain. China has been actively engaging in polar expeditions. Many observations were conducted during this period, accompanied by improved Earth climate models, leading to a series of insightful understandings concerning Arctic and Antarctic climate changes. Here, we review the recent progress China has made concerning Arctic and Antarctic climate change research over the past decade. The Arctic temperature increase is much higher than the global-mean warming rate, associated with a rapid decline in sea ice, a phenomenon called the Arctic Amplification. The Antarctic climate changes showed a zonally asymmetric pattern over the past four decades, with most of the fastest changes occurring over West Antarctica and the Antarctic Peninsula. The Arctic and Antarctic climate changes were driven by anthropogenic greenhouse gas emissions and ozone loss, while tropical–polar teleconnections play important roles in driving the regional climate changes and extreme events over the polar regions. Polar climate changes may also feedback to the entire Earth climate system. The adjustment of the circulation in both the troposphere and the stratosphere contributed to the interactions between the polar climate changes and lower latitudes. Climate change has also driven rapid Arctic and Southern ocean acidification. Chinese researchers have made a series of advances in understanding these processes, as reviewed in this paper.

**Key words:** polar climate change, recent progress in China, Arctic amplification, tropical-polar interactions, global sea level rise, stratospheric circulation

**Citation:** Li, X. C., and Coauthors, 2023: China's recent progresses in polar climate change and its interactions with the global climate system. *Adv. Atmos. Sci.*, **40**(8), 1401–1428, <https://doi.org/10.1007/s00376-023-2323-3>.

### Article Highlights:

- Chinese researchers have made substantial progress in researching polar climate change and its interactions with the global climate system.

✱ This paper is a contribution to the special issue on the National Report to the 28th IUGG General Assembly by CNC-IAMAS (2019–2022).

\* Corresponding author: Xichen LI  
Email: [lixichen@mail.iap.ac.cn](mailto:lixichen@mail.iap.ac.cn)



- A series of interactions and feedback contribute to the Arctic amplification and the regionality and seasonality of the Antarctic change.
  - Lower latitudes largely impact the Arctic and Antarctic climate changes, which feedback to the changes in the Earth's system.
  - Anomalous circulation and sea-ice melt are responsible for the rapid ocean acidification in the Arctic Ocean and Southern Ocean.
- 

## 1. Introduction

In the recent four decades since the satellite era, many dramatic climate changes have been observed over the Arctic and Antarctic regions (Zhang, 2015; Yao et al., 2017; Yu et al., 2018a; Wang et al., 2019d; Francis and Wu, 2020; Li et al., 2021b). These polar climate changes affect changes in the global climate system (Chen and Tung, 2018; Luo et al., 2019; Chen et al., 2020a; Chen and Luo, 2021; Wu and Li, 2022; Yuan et al., 2022). The climate changes over the Arctic and the Antarctic are characterized by different features. The Arctic climate change is much faster than that of the globe, a phenomenon known as the Arctic amplification (Wu, 2017; Dai et al., 2019). The surface air temperature trend over the Arctic region is at least two to four times as fast as the global mean warming rate (Wu, 2017; Wei et al., 2016), which results in a rapid decline and altered physical properties of the Arctic sea ice (Lei and Wei, 2020).

The climate-related changes around the Antarctic show a zonally asymmetric pattern, with the strongest changes happening around the West Antarctic (Ding et al., 2011; Wang et al., 2019b, d; Li et al., 2021b; Zhang et al., 2021c). The surface warming around the West Antarctic and the Antarctic Peninsula is about two to three times that of the global mean rate, whereas the warming trend over the East Antarctic has not been significant in recent decades (Yuan et al., 2015; Turner et al., 2020; Li et al., 2021b). The overall Antarctic sea-ice extent had been increasing before 2014, known as the Antarctic sea-ice paradox (Li et al., 2014; Yuan et al., 2017; Yu et al., 2018a; Wang et al., 2019c; Li et al., 2021b), except that the sea-ice extent around the Amundsen-Bellinghousen seas had dramatically decreased (Li et al., 2014; Yu et al., 2018a). However, this positive sea-ice trend reversed after 2015, as was followed by rapid declines around the entirety of Antarctica (Wang et al., 2019d; Li et al., 2021b; Ding et al., 2022a).

The polar climate changes interact with the climate variability over the lower latitudes. First, tropical-polar teleconnections influence polar climate changes (Ding et al., 2011, 2014; Li et al., 2014, 2015b, 2019c, 2021b). On interannual time scales, El Niño dominates the tropical Antarctic teleconnection (Yuan and Martinson, 2001; Ding et al., 2011; Li et al., 2021b; Zhang et al., 2021b), with the Indian Ocean Dipole mode also playing an important role (Rao and Ren, 2020; Yu et al., 2022). On decadal and longer time scales, the Pacific Decadal Oscillation (PDO) and the Atlantic Multi-decadal Oscillation (AMO) both contribute to the

Antarctic multi-decadal changes (Li et al., 2014, 2015a, b, 2021b). In particular, the positive phase of the AMO since the early 1980s and the following negative phase of the PDO since the late 1990s both served to deepen the Amundsen Sea Low (Li et al., 2014, 2021b). These circulation changes contribute to the asymmetric Antarctic climate changes, including the rapid warming over the West Antarctic, the sea-ice paradox, and the accelerated ice shelf melting around the West Antarctic. The climate variability over the tropics and the mid-latitudes may also contribute to the Arctic changes through both atmospheric bridges and oceanic pathways (Ding et al., 2014; Hu et al., 2016; Wu, 2017; Luo et al., 2019; Liu et al., 2021b; Xiao and Ren, 2021; Wu and Ding, 2022). The tropical Pacific decadal variability may cause rapid warming around northeastern Canada and Greenland (Ding et al., 2014), while the AMO may also contribute to the evolution of the Arctic Amplification (Fang et al., 2022). On the other hand, the North Atlantic warming may drive a warmer Arctic Ocean as well as an Arctic sea-ice decline (Wang et al., 2017a; Zhang et al., 2022e) through oceanic processes, known as the Arctic Atlantification. The thinner and younger Arctic sea ice is more sensitive to atmospheric and oceanic forcing, which leads to the fact that the Arctic sea ice is physically more like the Antarctic sea ice, leading to the phenomenon of Antarctification of Arctic sea ice (Granskog et al., 2020). A strengthened Siberian high well corresponds to a systematic northward shift of atmospheric circulation over northern Eurasia, the North Atlantic, and northern North America, leading to significant increases in the atmospheric total energy transport into the Barents-Kara Seas (Wu and Ding, 2022). Therefore, atmospheric circulation anomalies in the middle and lower latitudes play important roles in generating Arctic warm anomalies (Wu, 2017).

The Arctic and Antarctic climate changes may feedback to the lower latitudes and contribute to changes in the Earth's climate system (Gong et al., 2017; Wu and Francis, 2019; Chen et al., 2020b; Dou et al., 2020; Wu et al., 2022a; Yuan et al., 2022). The rapid warming over the Arctic is usually associated with cooling over the land areas of the mid-latitudes in the Northern Hemisphere, known as the Warm Arctic Cold Continents pattern (Sun et al., 2016b; Wu, 2017; Guan et al., 2020), or the Warm Arctic Cold Eurasian pattern (Overland et al., 2011; Wu et al., 2011; Luo et al., 2016; Xu et al., 2018). In particular, the Arctic climate variability may largely contribute to the climate variability around East Asia, impacting the surface temperature (Li et

al., 2019b; Zhang et al., 2020; Bi et al., 2022), the precipitation (Zhang et al., 2021f; Wu and Li, 2022) and the air pollution (Ji and Fan, 2019b; Liu et al., 2020b) around China. On the other hand, it is reported that the variability of the Southern Ocean SST and the Antarctic sea ice may also influence the tropical convection and inter-hemispheric energy balance (Xiang et al., 2018), as well as precipitation over southern China (Dou et al., 2020; Yuan et al., 2022). Finally, both the Greenland ice sheet and the Antarctic ice sheet experienced accelerated melting during the past three decades (Zhang et al., 2021c), largely contributing to the global mean sea level rise (Chen et al., 2014, 2017), as well as the freshwater cycle over the high-latitude oceans.

In this paper, we first review the recent research progress of the observed Arctic and Antarctic climate changes in section 2. We then review the tropical–polar teleconnections and their contributions to polar climate changes in section 3. The impacts of the polar climate changes on the lower latitudes are reviewed in section 4. The dynamics related to stratospheric processes are then summarized in section 5, followed by a conclusion and discussion.

## 2. Recently observed polar climate changes

New techniques have recently been developed, which largely increased our capability to monitor the climate changes over the polar regions, especially during the modern satellite era since 1979. A series of dramatic climate changes have been observed over the polar regions. The Arctic climate changes are characterized by rapid surface warming, accompanied by the accelerated melting of both land and sea ice, a process known as Arctic amplification. The Antarctic climate changes exhibit clear regionally and season-

ally dependent features, with the strongest changes usually occurring around West Antarctica. The recent progress in the observed Arctic and Antarctic climate changes are reviewed as follows.

### 2.1. The Arctic Amplification

During the past four decades, the Arctic has experienced rapid climate change. The surface air temperature over the Arctic has increased rapidly in all seasons (Fig. 1). The warming rate over the Arctic region is more than four times faster than that of global warming, a phenomenon termed Arctic amplification. Some regions, like Svalbard Island, can experience warming four times greater than the global average (Wei et al., 2016). This Arctic warming is usually accompanied by anomalous cooling over the mid- and high-latitudes of North America and the Eurasian continent and an anomalous warming over the North Pacific, North Africa, and the lower latitudes of North America and Asia (Wu, 2017) (Fig. 1).

The rapid warming over the Arctic region is associated with an accelerated sea-ice decline (Ding et al., 2017; Luo et al., 2021) (Fig. 2). Recent studies indicated that the summertime atmospheric warming and moistening over the Arctic region, synchronized by an atmospheric circulation adjustment over the high-latitude northern hemisphere, may increase the downwelling longwave radiation over the polar region, contributing to the Arctic sea-ice loss, especially in summer (Ding et al., 2017; Luo et al., 2021; Liang et al., 2022; Shen et al., 2022b). Similarly, the SST anomalies over the mid- and high-latitude North Pacific and North Atlantic may drive anomalous advection of both temperature and water vapor and enhance water vapor and cloud radiative feedback processes, thus contributing to the accelerated Arctic sea-ice decline in boreal autumn (Yu and Zhong, 2018).

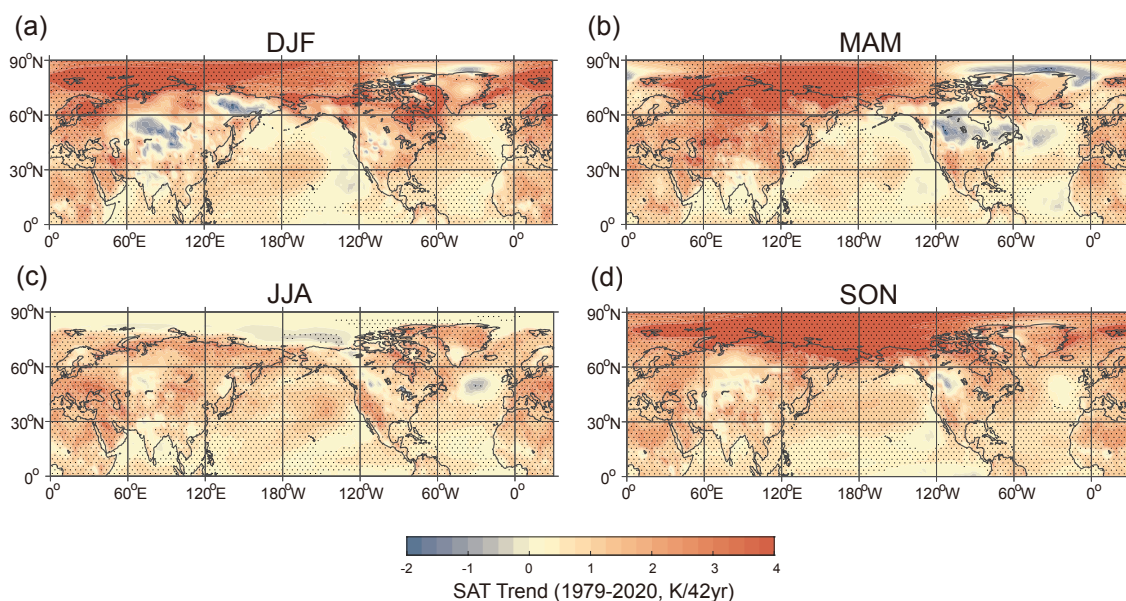


**Fig. 1.** The seasonal surface air temperature (SAT) trend over the Northern Hemisphere from 1979 to 2020. The color shadings in (a–d) show the SAT trend for boreal winter (DJF, a), spring (MAM, b), summer (JJA, c), and autumn (SON, d), respectively. Dotted regions are significant at  $p < 0.05$  based on a Mann-Kendall test.



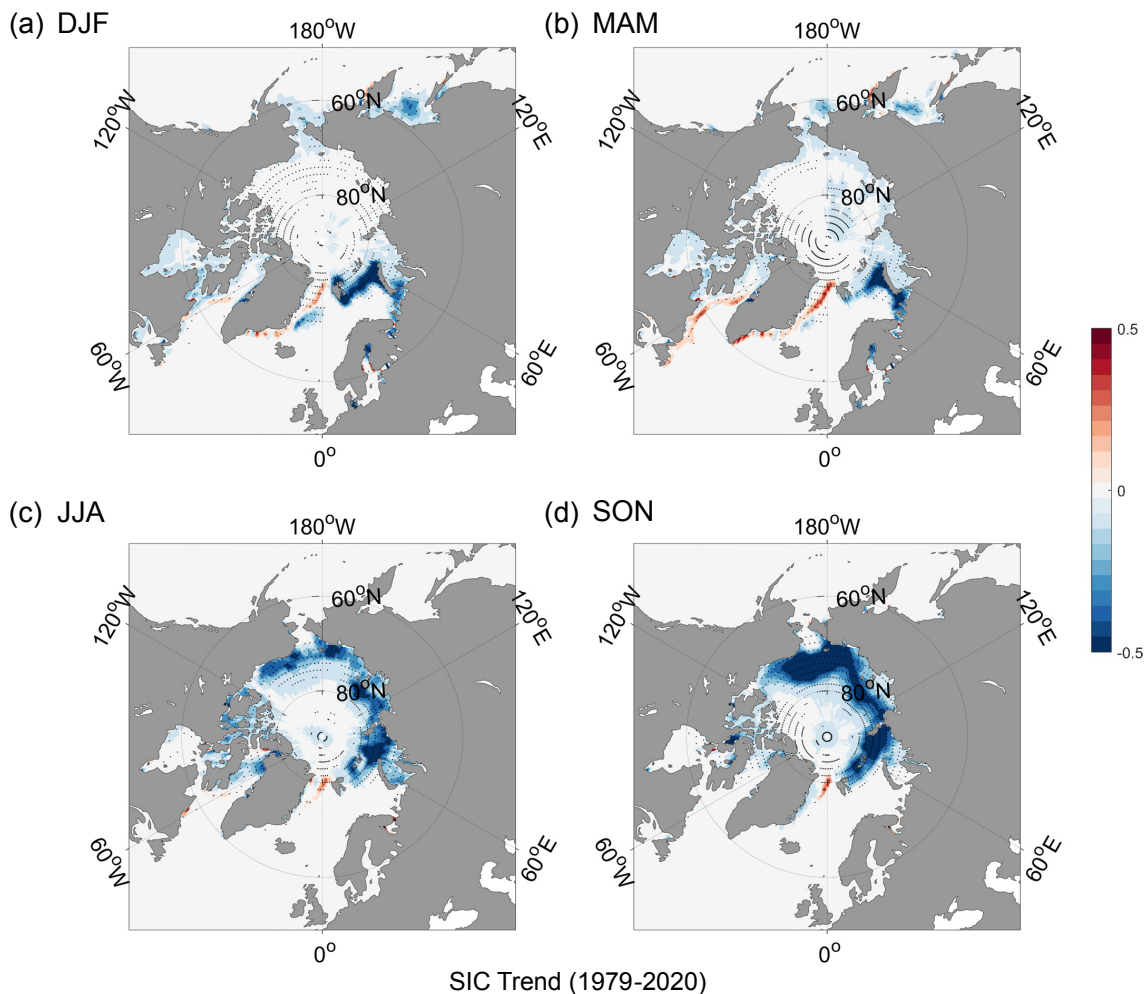


**Fig. 2.** The seasonal Arctic sea-ice concentration (SIC) trend from 1979 to 2020. The color shadings in (a–d) show the SIC trend for boreal winter (DJF, a), spring (MAM, b), summer (JJA, c), and autumn (SON, d), respectively. Dotted regions are significant at  $p < 0.05$  based on a Mann-Kendall test.

Additionally, increased snowfall or rain-on-ice events, associated with increased warm air mass intrusions from low latitudes, together with thinner sea ice (Liang et al., 2022), would have the net effect of enhancing the precipitation contribution to the sea-ice mass balance. Thinner sea ice and additional ice, in turn, promote an increasing winter ocean-to-ice heat flux in the Arctic Ocean (Zhong et al., 2022) and delay the onset of winter basal growth of sea ice (Lei et al., 2022). Moreover, the Arctic sea-ice loss shows a strong regional feature. For example, a positive phase of the Arctic dipole may intensify the ice-albedo feedback, thus contributing to rapid sea-ice loss over the Pacific sector of the Arctic Ocean in boreal summer (Lei et al., 2016). In addition, recent studies (Francis and Wu, 2020) indicated that cold anomalies have frequently occurred in the middle and lower levels of the troposphere over the Arctic region since 2005. Such atmospheric changes may have led to a slowdown of the Arctic sea-ice decline over the recent decade (Francis and Wu, 2020).

The Arctic amplification was reported to be associated with a series of physical processes and feedback (Xiao et al.,

2020a; Fang et al., 2022), including an intensified transport of heat and moisture between the Arctic and lower latitudes (Wang et al., 2020e; Xu et al., 2021c; Wang and Chen, 2022), and an increase in the outgoing longwave radiation induced by the recent Arctic sea-ice loss (Dai et al., 2019). The rapid surface warming and sea-ice decline are also partially attributed to the strengthened subsidence flow associated with an intensified polar cell (Qian et al., 2016). In addition, the decline of the Arctic sea ice and its associated surface warming may influence the atmospheric lapse rate and thus adjust the stability of the boundary layer over the Arctic region (Zhang et al., 2021d). By modulating the lower tropospheric stability, the Arctic sea ice may also impact the pathway of liquid water, leading to an adjustment of the low-level clouds (Yu et al., 2019b). Such feedback between the sea ice and the atmosphere may further contribute to Arctic amplification, especially during the initial ice-freezing season (Zhang et al., 2021d).

An important consequence of the Arctic amplification is the accelerated melting of the Greenland ice sheet and the associated freshwater discharge, which has significantly

raised the sea level and affected ocean stratification (Yan et al., 2013, 2014; Ran et al., 2021). The Greenland ice sheet, especially the glaciers on its edge, has experienced severe melting in the past decades (Yang et al., 2019b; Zhang et al., 2022c), primarily due to the warm sub-surface water intrusion from the Atlantic Ocean.

Recently, the surface melting and flow of the glaciers are accelerating, which also contributes to the accelerated mass loss and internal structure change of the Greenland Ice Sheet (Liu et al., 2016; Wang et al., 2019a; Huai et al., 2020; Chen and Luo, 2021; Wang and Luo, 2022; Luo and Lin, 2023). The surface mass balance of the Greenland ice sheet is tightly associated with the surface temperature and precipitation changes. The ice surface temperature in the northwest portion of the Greenland Ice Sheet has increased since the 21st century with a strong seasonal feature (Hall et al., 2013; Huai et al., 2021), accelerating the surface melting in this region (Wei et al., 2022). The total precipitation over Greenland shows a positive long-term trend, with the peak season having shifted during the past decade (Ding et al., 2020; Huai et al., 2022).

The melting of the Greenland ice sheet has released large amounts of freshwater into the North Atlantic Ocean, leading to an adjustment of the ocean circulation (Hu et al., 2011). Simulations show that the Atlantic Meridional Overturning Circulation (AMOC) is weakened due to this freshwater discharge, which may also affect global climate by adjusting meridional heat transport (Yang et al., 2016a; Yu et al., 2016; Liu et al., 2018). Similar ocean circulation adjustments have occurred over the Arctic Ocean, associated with increased sea-ice melt, Arctic river discharge, and changes in atmospheric and oceanic circulations. For example, an anomalous accumulation of freshwater in the western Arctic Ocean leads to a spin-up of the Beaufort Gyre (Zhong et al., 2019b) and the redistribution of Pacific water in the deep basin (Zhong et al., 2019a). The transport of water masses from the East Siberian Sea into the Makarov Basin associated with the cyclonic Arctic circulation may contribute to the development of the halocline in the Makarov Basin (Wang et al., 2021c).

## 2.2. Asymmetric Antarctic climate changes

During the past four decades, coincident with the modern satellite era, Antarctica has experienced a series of dramatic climate changes (Wang et al., 2017b, 2019d; Zhang et al., 2021c), showing strong zonally asymmetric features (Li et al., 2021b). These changes involve rapid surface warming in West Antarctica and the Antarctic Peninsula (Gao et al., 2018; Ding et al., 2020; Lin et al., 2020; Xu et al., 2021a), an opposite trend of snow accumulation between the Antarctic Peninsula and the western part of West Antarctica (Wang et al., 2017b), a pre-2014 expansion of the Antarctic sea-ice extent (Yu et al., 2018a; Wang et al., 2019c), followed by a rapid sea-ice decline (Wang et al., 2019d), and the accelerated land-ice melting (Wang et al., 2019b; Zhang et al., 2021c) especially around the West Antarctic.

Since the second half of the 20th century, the surface

air temperature trends over the Antarctic have been characterized by a seesaw-like pattern, with rapid warming over the West Antarctic and the Antarctic Peninsula (Fig. 3a) (Ding et al., 2011; Li et al., 2021b) and mild cooling over mainland East Antarctica (Fig. 3a). The warming trend over the West Antarctic was about twice the global warming rate (Li et al., 2014, 2015a, b, 2021b). At the same time, the East Antarctic has experienced negligible warming or even a weak cooling trend (Fig. 3a) (Li et al., 2014, 2015a, b). Recently, scattered station observations show some reversed temperature trends since the beginning of the 21st century (Figs. 3b–e), including the disappearance (vanishing) of the rapid warming over the Antarctic Peninsula and the West Antarctic (Figs. 3b, c), accompanied by rapid warming of the South Pole since the early 2000s (Figs. 3d, e) (Turner et al., 2020; Li et al., 2021b).

The snow accumulation rate over the Antarctic also shows a strong regional dependence. Observations based on ice cores reveal a positive trend in the accumulation rate over the Antarctic Peninsula since the 1950s, whereas that over the western part of West Antarctica has significantly decreased during 1900–2010 (Wang et al., 2017b, 2019b, 2020g). Moreover, the snow melting rate over the Ross Sea region has dramatically decreased in the past several decades (Li et al., 2017b; Zheng et al., 2020). During the same period, both the intensity and frequency of the extreme precipitation events over the Antarctic region have increased significantly, largely due to global warming caused by anthropogenic greenhouse gas emissions (Ren, 2002; Xiao et al., 2008; Yu et al., 2018b).

The ocean heat content in the Southern Ocean has increased over the past several decades (Gao et al., 2018; Guo et al., 2019; Xu et al., 2021a), with much of the ocean warming concentrated in the high latitudes of the Southern Oceans (Gao et al., 2018). This increase is tightly associated with the thickening, deepening, and warming of the Subantarctic Mode Water (SAMW) (Gao et al., 2018; Xu et al., 2021a), as well as the shallowing and freshening (Yao et al., 2017) of the Antarctic Intermediate Water. In contrast, although there is extensive warming in the sub-surface Southern Ocean, the surface water shows a cooling trend (Song, 2020), which is primarily attributed to the changes in the surface heat flux between the ocean and the atmosphere. Moreover, sea spray over the Southern Ocean may intensify the heat and moisture exchange between the atmosphere and ocean, resulting in a reduction of the surface air temperature (Song et al., 2022).

The changes in Antarctic sea ice show strong regional and seasonal features (Li et al., 2014, 2015a, b). The improvement of both the observational techniques (Lei et al., 2009; Shi et al., 2021b; Liao et al., 2022) and the numerical model experiments (Shu et al., 2020; Shi et al., 2021a) help us to better understand the complexity of the Antarctic sea-ice changes. Unlike Arctic sea ice, which experienced a rapid decline in the past decades, the total Antarctic sea-ice extent increased until 2015 (Fig. 4) (Yu et al., 2018a; Wang et al.,

2019c). The sea-ice concentration around the West Antarctic is accompanied by a redistributed total (areal) expansion, with significant declines over the Weddell Sea, the Bellingshausen Sea, and the Amundsen Sea, but dramatic increases

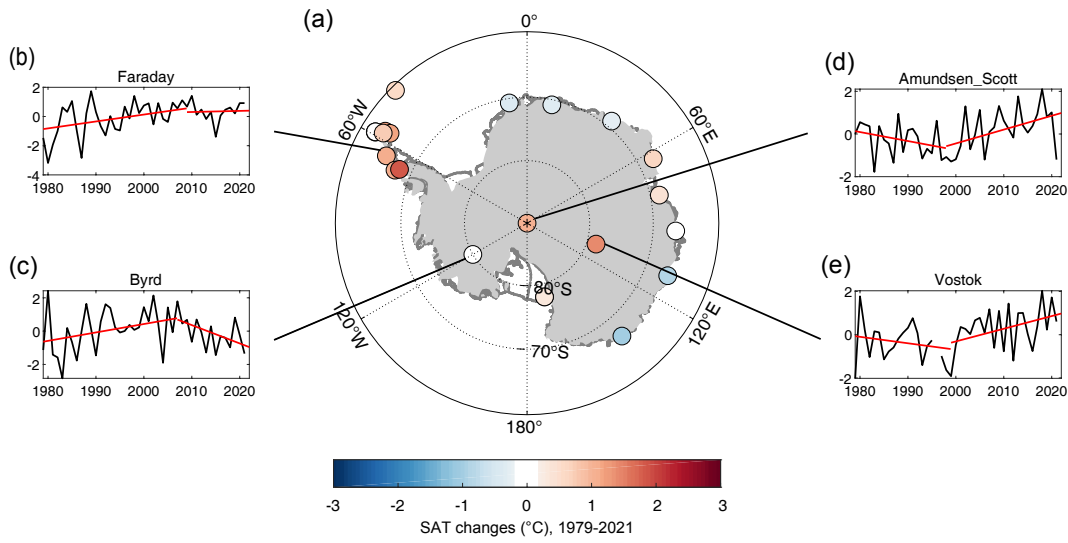


**Fig. 3.** The Antarctic surface air temperature (SAT) changes based on station observations during 1979–2021. The color dots in (a) depict the observed SAT changes. The black curves in (b–e) show the time series of the annual mean SAT for the (b) Faraday, (c) Byrd, (d) Amundsen-Scott, and (e) Vostok stations. The red lines in (b–e) show the linear SAT trends.

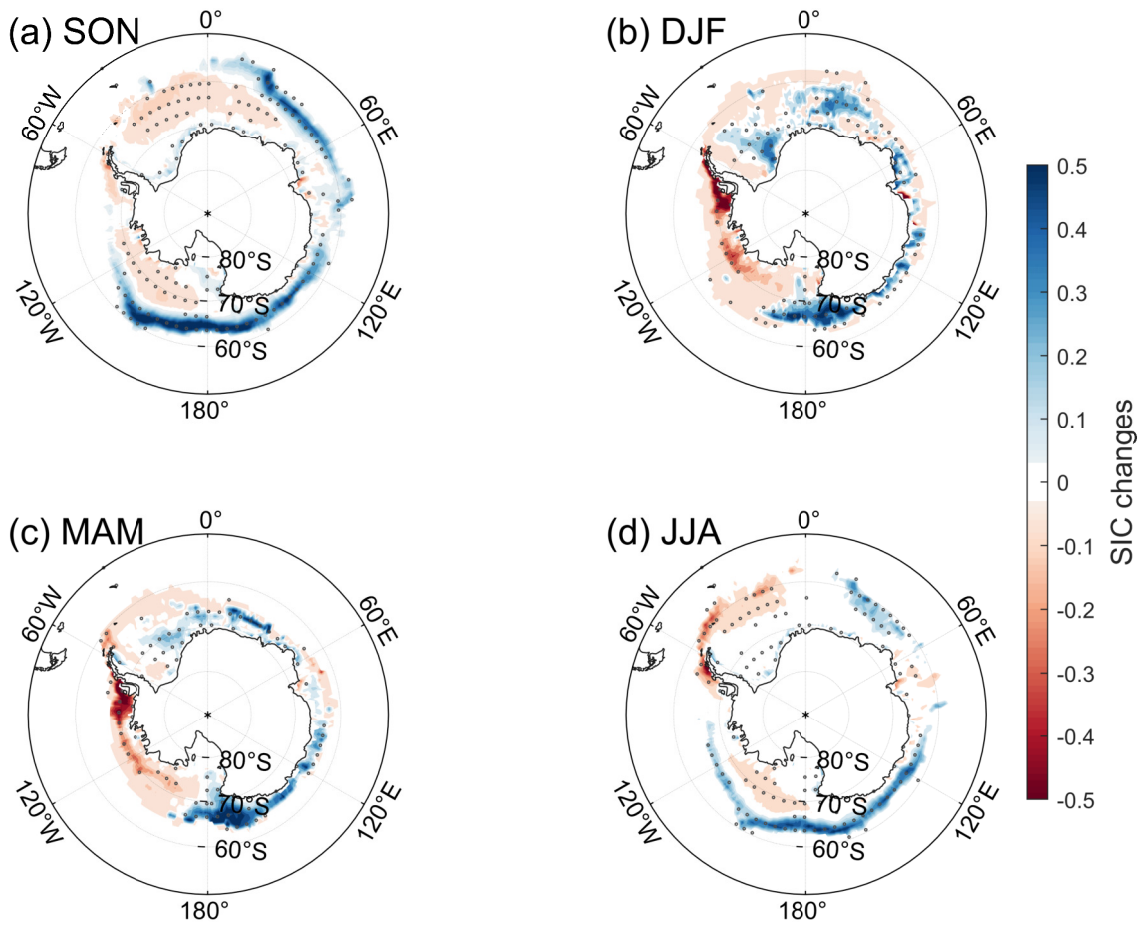


**Fig. 4.** The seasonal Antarctic sea-ice concentration (SIC) changes from 1979 to 2014. The color shadings in (a–d) show the SIC changes for austral spring (SON, a), summer (DJF, b), autumn (MAM, c), and winter (JJA, d), respectively. Dotted regions are significant at  $p < 0.1$ .

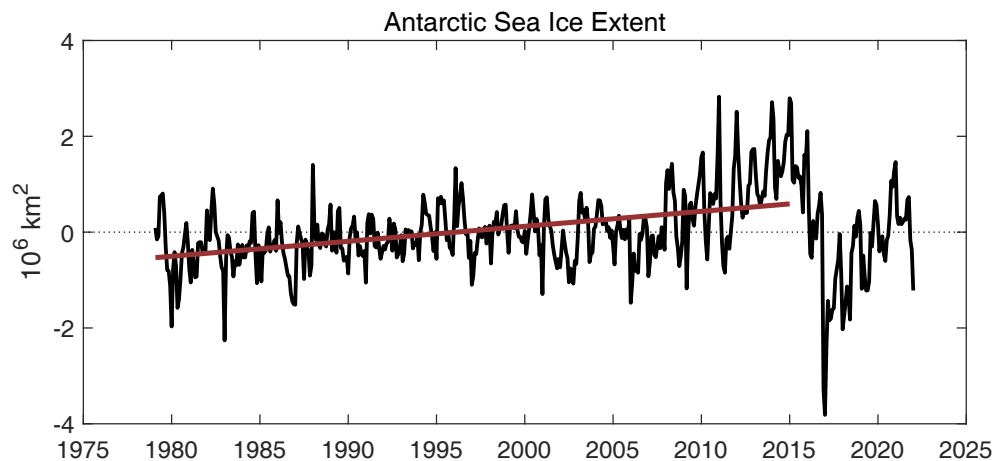


**Fig. 5.** The monthly Antarctic sea-ice extent (SIE) anomalies during 1979–2021. The red line shows the SIE trend from 1979 to 2014.

over the Ross Sea (Fig. 4) (Li et al., 2014, 2015a, b, 2021b; Wang et al., 2019c). After 2015, the Antarctic sea ice experienced a rapid decline (Fig. 5), with the annual mean total extent of the sea ice decreased by at least  $1.6 \times 10^6$  km<sup>2</sup> (Wang et al., 2019d). The sea-ice changes around Antarctica may further contribute to the ocean heat content and oceanic stratification. For example, in recent decades, many polynyas (Wang et al., 2017c; Hou and Shi, 2021; Wang et al., 2021d, 2022d) are triggered (formed) over the Ross Sea, the Prydz Bay, and the Weddell Sea regions, mainly driven by the strengthened wind forcing. These processes favor the formation of Antarctic sea ice, releasing more salinity and further intensifying deep oceanic convection (Guo et al., 2016; Ma et al., 2020b) through the brine effect, contributing to a warming of the Antarctic bottom water (Wang et al., 2017c).

Over the past several decades, the melting rate of the Antarctic ice sheets has accelerated. This change shows a clear zonally asymmetric feature, with the strongest melting around West Antarctica (Zhang et al., 2021c; Li et al., 2022). Recent studies indicated that the West Antarctic Ice Sheet experienced a rapid mass loss (Wang et al., 2019b; Zhang et al., 2021c), with a strong seasonal feature (Yang et al., 2016b), primarily due to the warm water intrusion from the sub-surface Southern Oceans. The mass loss over the East Antarctica is relatively weak (Zhang et al., 2021c).

The complexity of the Antarctic climate changes is primarily attributed to a combined effect of the anthropogenic ozone loss and greenhouse gas increase (Thompson et al., 2011; Swart et al., 2018; Li et al., 2021b), atmospheric circulation changes (Wang et al., 2019d, 2022d; Zhang et al., 2021c), cloud-radiation feedback (Wang et al., 2019c), as well as the atmosphere–sea ice–ocean interaction (Li et al., 2014; Ma et al., 2020b), the sea ice–ocean coupling (Ma et al., 2020b; Shi et al., 2021a), and the sea ice–ice shelf coupling (Guo et al., 2019), etc.

Notably, the adjustment of the atmospheric circulation over the high-latitude Southern Hemisphere plays an essential role in modulating these complicated climate changes over

the Antarctic region, mainly through atmospheric thermal advection (Li et al., 2021b) and mechanical forcing (Wang et al., 2019d; Zhang et al., 2021c, 2022d). Over the past four decades, the atmospheric circulation changes over the Antarctic have been characterized by a positive phase of the Southern Annular Mode (SAM) and a deepening of the Amundsen Sea Low (ASL) (Ding et al., 2020). The former was mainly driven by the depletion of stratospheric ozone and increased CO<sub>2</sub> concentrations (Thompson et al., 2011; Swart et al., 2018; Li et al., 2021b), whereas the latter was more closely related to tropical–polar teleconnections (Li et al., 2021b), largely contributing to the climate changes over the West Antarctic including both the rapid warming and the sea-ice redistribution (Ding et al., 2011; Li et al., 2017b, 2021b; Wang et al., 2019d; Guo et al., 2020; Zhang et al., 2021c). Furthermore, the interannual variability of the surface wind over Antarctica and the Southern Ocean is tightly associated with the Southern Hemisphere large-scale circulation modes (Yu and Zhong, 2019b), while the extreme strong wind events are more prevalent over the coastal region around East Antarctica (Yu and Zhong, 2019a).

### 2.3. Progresses in observational techniques

Because of the unique geological location and the harsh environment, climate observations over the polar regions are difficult to obtain. For a long time, limited observations and relatively low-quality measurements restricted our capability to retrieve the climate change signals over the polar regions. Over the past four decades, a series of modern climate satellites were launched. Meanwhile, China engaged itself in polar expeditions, with a series of new techniques developed to better detect the changing polar environment (Cheng et al., 2022), including a series of polar expeditions with the two icebreakers (“Xuelong” and “Xuelong 2”). A satellite (BNU-1) has been launched recently to provide timely observations and monitor the rapid changes in polar regions (Zhang et al., 2021g). Sled car-based and airplane-based radars have been used to observe the environment under the ice sheet (Sun et al., 2009; Cui et al., 2020).



Unmanned aerial systems (UASs) have also been used to resolve the detailed surface features of polar sea ice (Li et al., 2019a) and obtain atmosphere profiles over the Southern Ocean, which may benefit numerical weather forecasts (Sun et al., 2020). Along the PANDA (Prydz Bay-Amery Ice Shelf-Dome A) Transect, CHINARE (Chinese National Antarctic Research Expedition) deployed ~650 stakes to monitor the surface mass balance from the coastal Zhongshan Station to Dome A (Minghu et al., 2011; Ding et al., 2015), the summit of East Antarctica. In addition, Automatic Weather Stations (AWSs), applied to extremely cold environments, have also been installed along PANDA Transect. Currently, 12 AWSs operate continuously and provide near real-time data to the public (Ding et al., 2022b).

A series of new techniques have been developed to better observe the sea-ice properties over the polar regions (Lei et al., 2009, 2017, 2022; Wu and Liu, 2018; Chen et al., 2022c). A high-precision ice thickness measuring device was invented and applied to observe the landfast ice mass balance in East Antarctica (Lei et al., 2009). Based on the measured data, the influence of tides on sea-ice growth was obtained. A new type of sea Ice Mass balance Buoy (IMB), an unmanned ice station, has been developed, which has been applied to the construction of the buoy array during the Multidisciplinary drifting Observatory for the Study of Arctic Climate (MOSAIC) expedition in 2019/20 (Lei et al., 2022). Compared with the traditional IMB, upper-ocean observations have increased, allowing for the observation and assessment of the effects of the subcooled water under winter ice and the summer freshwater layer on the growth and ablation of sea ice (Zhang et al., 2022c). Combining the ship-based and ice-based observational systems, especially the measurement technology of underwater robots, a three-dimensional observation system for measuring the morphological parameters of sea ice is constructed (Lei et al., 2017). A satellite-based sea-ice navigation system (SatSINS) has been developed (Hui et al., 2017a), which integrates remotely sensed and in-situ observations to optimize the marine navigational routes in sea ice-covered waters. Wang et al. (2022f) compared the sea-ice motion products from the Ocean and Sea Ice Satellite Application Facility and indicated that eleven Arctic sea-ice motion products are of reasonably high quality if the uncertainties are appropriately considered. By combining observations from multiple satellites, a recent study revealed that the sea-ice melting time is linked to the evolution of the summer sea ice (Zheng et al., 2021).

The assessment of the total mass balance of the Arctic and Antarctic ice sheets has also been significantly improved (Wang et al., 2021a), largely due to the launch of altimetry and gravity satellites (Cheng et al., 2015; Xiao et al., 2020b), which have great implications for analyzing the global mean sea level rise. Although the GRACE data tends to underestimate the ice mass loss (Gao et al., 2019a), combining these satellite measurements with the in-situ observations may improve the quality of these mass-balance datasets. Additionally, Yuan et al. (2020) developed an algorithm based

on the convolutional neural network to detect the supraglacial lakes over the Greenland ice sheet.

One of the most important examples of progress is a better estimation of the ice flow and the surface melting over the Antarctic and Greenland ice sheets using satellite-based measurements. Cheng and Xu (2006) developed a technique based on four-pass differential synthetic aperture radar (SAR) interferometry aboard the JERS-1 and ERS satellite platforms to retrieve the motion of Antarctic glaciers. This method has been used to detect and validate the ice flow of Grove Mountain and several East Antarctic Glaciers (Cheng et al., 2007). Recently Li et al. (2018) further retrieved the velocity of ice flow over the Antarctic ice sheet using MODIS-based Mosaic datasets. Hui et al. (2017b) produced a database (Antarctic Land Cover Database for the Year 2000, Antarctica LC2000) based on combining computer-aided and manual interpretation methods to classify the land-cover types over Antarctica. Liao et al. (2019) developed an algorithm to derive the snow depth and ice thickness from the SIMBA (Snow and Ice Mass Balance Array) ice mass balance buoy data. In addition, Zheng et al. (2022) developed a new strategy to quantify the daily surface melting over the Greenland ice sheet based on satellite observations.

Based on ICESat-1/GLAS satellite observations, Liu et al. (2014) developed a method to detect the peak stress points where an ice shelf is most likely to break. This method has been used to investigate the mechanism of ice-shelf retreat (Liu et al., 2015) and detect the ice crevasses around the Antarctic ice sheet. Qi et al. (2021) built an iceberg calving product over all Antarctic ice shelves based on this method, which identifies every calving event larger than 1 km<sup>2</sup> in the past 15 years.

#### 2.4. Rapid acidification in the Arctic Ocean and Southern Ocean

With the climate change in the past decades, the Arctic Ocean has shown widespread ocean acidification and aragonite undersaturation ( $\Omega_{\text{arag}} < 1$ ). Based on the observations of the Arctic Ocean (47 Arctic research cruises) over the past three decades (1994–2021), Qi et al. (2017) illustrated that low  $\Omega_{\text{arag}}$  water had expanded northwards to 85°N and deepened to a 250-m depth in the Western Arctic Ocean, and concluded that the Pacific Winter Water (PWW) transport, upon converging and deepening as a result of the intensification of the Beaufort Current eddies, is primarily responsible for the expansion of acidified waters in the upper Arctic Ocean. Later, by estimating changes in pH and  $\Omega_{\text{arag}}$  of the Arctic surface seawater, Qi et al. (2022a) reported a rapid acidification of the Arctic Ocean with a rate 3~4 times higher than other ocean basins. Meanwhile, the mechanism “ice melt-driven enhanced anthropogenic CO<sub>2</sub> acidification” was unveiled (Qi et al., 2022a): sea-ice melt exposes seawater to the atmosphere and promotes the rapid uptake of atmospheric CO<sub>2</sub>, lowering its alkalinity and buffer capacity, thus leading to sharp declines in pH and  $\Omega_{\text{arag}}$  (Fig.6).

As the most productive sea, the Chukchi Sea has been found to contribute more than 50% of the carbon sink in the

Arctic Ocean, and the carbon absorption at the surface is still increasing year after year (Tu et al., 2021). However, severe ocean acidification was observed in the subsurface water of the Chukchi Sea. A control mechanism was proposed that the biological activities driven by the Pacific Ocean inflowing water lead to the acidification of subsurface water in the Chukchi Sea (Qi et al., 2020a, 2022b). These results are expected to provide important background information for the ecological assessment of the Chukchi Sea.

In addition, Wu et al. (2021) developed and improved a walk-around pH observation system that adapts to low-temperature environments. Simultaneously, a high-quality dataset was produced by compiling and revising data from twelve Arctic scientific expeditions, thirty-five Antarctic scientific expeditions, and international databases. With that, they further demonstrated the mechanism of the Arctic Ocean acidification, revealing that the Arctic melt-ice dilution and sea-air  $\text{CO}_2$  exchange induced the rapid acidification of the water column, wherein aragonite saturation (a biological indicator of acidification) first decreased to a biohazard threshold (Wu et al., 2021). Aided by the comparison of Southern Ocean data from BGC-Argo and ship-collected datasets, a tool CORS (integrated analysis of seawater dissolved gases  $\text{CO}_2$  and  $\text{O}_2$ ) was developed as a quality control for ocean float data. They found that carbon sinks in the high-latitude region of the Southern Ocean were underestimated by 50% by BGC-Argo and proposed that data quality control and correction are necessary for some automatic observation platforms such as buoys (Wu et al., 2022b).

### 3. Impacts of Tropics and mid-latitudes on polar climate

Climate variability over the tropics and mid-latitudes plays a crucial role in driving Arctic and Antarctic climate changes on intra-seasonal to multi-decadal time scales (Wu, 2017; Wang et al., 2018; Li et al., 2019c, 2021b; Dou and Zhang, 2022; Wu and Ding, 2022). In the Southern Hemisphere, atmospheric bridges, especially Rossby wave dynamics, play a key role in these teleconnections (Ding et al., 2011; Li et al., 2014, 2021b; Zhang et al., 2021b). The large-scale anomalous circulation driven by these teleconnections largely contributes to the asymmetric Antarctic climate

changes through a series of atmosphere-ice-ocean interactions (Yuan and Martinson, 2000; Li et al., 2014; Yu et al., 2018a; Zhang et al., 2021b). In the Northern Hemisphere, both atmospheric and oceanic processes are crucial in linking the Arctic climate system and the lower latitudes (Hall et al., 2013; Li et al., 2015b; Liu et al., 2018; Wang et al., 2021a).

#### 3.1. Tropics and mid-latitudes impact Antarctic climate

Recently, a series of studies indicated that the tropical and mid-latitude climate variability might be contributing to the Antarctic climate changes (Li et al., 2021b; Zhang et al., 2021b; Chen et al., 2022a; Wang et al., 2022c) on interannual, decadal, and longer timescales. The physical pathways linking the Antarctic climate changes and the lower latitudes are complex (Yang et al., 2020; Zhang et al., 2021b, e; Dou and Zhang, 2022), although most of these teleconnections are through the atmospheric bridges, in particular the adjustment of the three-cell circulation, the jets system, and of stationary Rossby waves (Li et al., 2021b; Zhang et al., 2021b, e). In this section, we review how climate variability over lower latitudes may impact the atmospheric circulation adjustment over the high latitudes of the Southern Hemisphere (Li et al., 2020a, 2021b; Zhang et al., 2021b), and how these large-scale circulation changes further contribute to the asymmetric climate changes over the Antarctic through a series of atmosphere-ice-ocean interactions (Li et al., 2021b; Zhang et al., 2021e; Dou and Zhang, 2022).

On interannual time scales, ENSO plays a dominant role in contributing to climate variability over the high-latitude Southern Hemisphere. During the El Niño events, the warm sea surface temperature (SST) anomaly over the eastern tropical Pacific generally triggers a Rossby wave train emanating from the tropical Pacific to the South American region, inducing a shallow Amundsen Sea Low (ASL) (Yuan and Martinson, 2000, 2001; Li et al., 2020a; Li et al., 2021b) (Fig. 7a). The changes of ASL further impact the Antarctic surface air temperature (Li et al., 2021b) and sea ice (Yuan and Martinson, 2001; Yuan and Li, 2008; Li et al., 2014, 2020a; Zhang et al., 2021b, e) through wind forcing and thermal advection (Li et al., 2014, 2020a). A recent study indicated that the Rossby wave train triggered by the central Pacific El Niño shifted to the west by about  $20^\circ$  compared to an eastern Pacific El Niño (Zhang et al., 2021b). In addition, based on CMIP6 simulation results, the projected South-

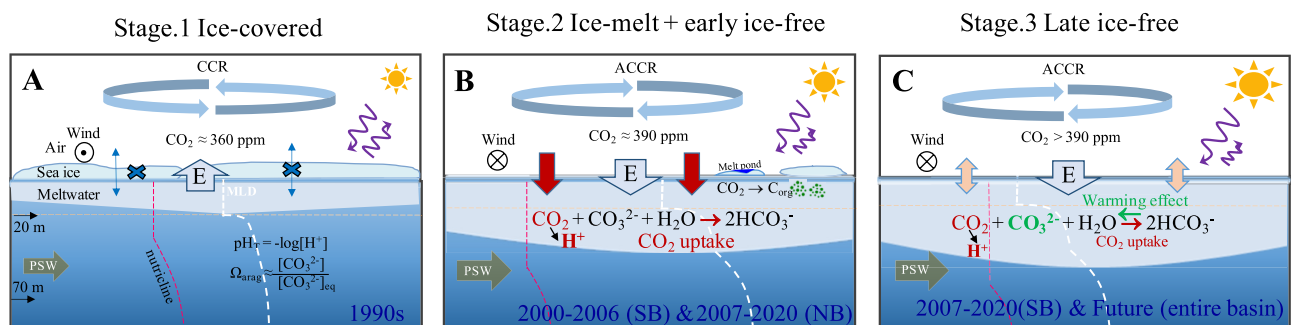


Fig. 6. Conceptual model illustrating warming and climate change-driven sea-ice retreat and associated changes in  $\text{CO}_2$ -system.



ern Ocean warming in the 21st century is tightly associated with changes in the amplitude of ENSO events (Wang et al., 2022a). Meanwhile, the amplitude of the Antarctic dipole is expected to be reduced under greenhouse warming, which is predominantly attributed to the opposing roles of increased ENSO variability and decreased SAM variability (Li et al., 2021a).

The mechanisms outlined above operate not only for the ENSO-polar connection but also for tropical-polar connections from other ocean basins (Li et al., 2014; Rao and Ren, 2020; Yang et al., 2020; Chen et al., 2022a). For example, Rossby wave trains can be generated by convective heating associated with the tropical Indian Ocean (Rao and Ren, 2020; Yu et al., 2022), the Maritime Continent (Chen et al., 2022a), and the tropical and North Atlantic (Li et al., 2014). In addition, these mechanisms operate on various time scales. The negative trend of the South Pacific Oscillation index in austral autumn, triggered by an anomalous wave train from the Indian Ocean to the Southern Ocean, can, in part, induce decreased SIC in the Bellingshausen Sea and increased SIC over the Ross Sea (Yu et al., 2021). On intra-seasonal timescales, Rossby wave trains excited by the Madden-Julian Oscillation (Yang et al., 2020) propagate to southern high latitudes and can influence temperature and sea ice in as quickly as a few days to a week (Wang et al., 2022b, c).

On decadal and longer time scales, the Interdecadal Pacific Oscillation (IPO) (Ding et al., 2011) and the Atlantic Multidecadal Oscillation (AMO) (Li et al., 2014, 2021b) play a key role in driving the multi-decadal changes over the Antarctic through similar mechanisms, namely the adjustment of the stationary Rossby wave trains (Li et al., 2021b) (Fig. 7b). During the positive phase of the IPO, the anomalous warm SST over the eastern tropical Pacific triggers a Rossby wave train that induces a shallow ASL (Ding et al.,

2011; Li et al., 2021b). During the positive phase of the AMO, the north and tropical Atlantic warming generates a Rossby wave train, which is guided around the Southern Oceans by the subtropical jet, ultimately influencing the atmospheric circulation around Antarctica, intensifying the SAM, and deepening the ASL (Li et al., 2014, 2015a, b, 2021b).

Notably, these interannual and interdecadal teleconnections are not independent of one another but rather closely interact (Ding et al., 2016; Dou and Zhang, 2022). In addition, interdecadal shifts exist in these interactions, including the interdecadal changes in the lagged relationship between the summer Pacific–South American (PSA) pattern and subsequent ENSO events in the following summer (Ding et al., 2016), as well as the weakening of the ENSO–Antarctic dipole relationship over the past two decades (Dou and Zhang, 2022).

Moreover, midlatitude climate variability may also influence the Antarctic climate (Wen et al., 2021; Zhang et al., 2021e). Recent studies have revealed that the warm (cool) SST anomalies in the western South Atlantic can increase the SIC over the eastern Ross Sea in austral spring while, at the same time, decreasing the SIC over the northwestern Weddell Sea (Zhang et al., 2021e). In addition, the model simulation shows that long-term changes in the Antarctic bottom water (AABW) can be affected by remote forcing from topographic changes of the Tibetan Plateau and also through Rossby wave dynamics (Wen et al., 2021). In particular, increased anthropogenic aerosol concentration in the Northern Hemisphere can induce atmospheric circulation changes in Southern Hemisphere, weakening the subtropical and the subpolar jets in austral winter (Wang et al., 2020b).

These teleconnections modify the large-scale circulation over the high-latitude Southern Hemisphere and subsequently impact the Antarctic climate variability through a series of atmosphere-ice-ocean interactions (Yuan and Martinson,

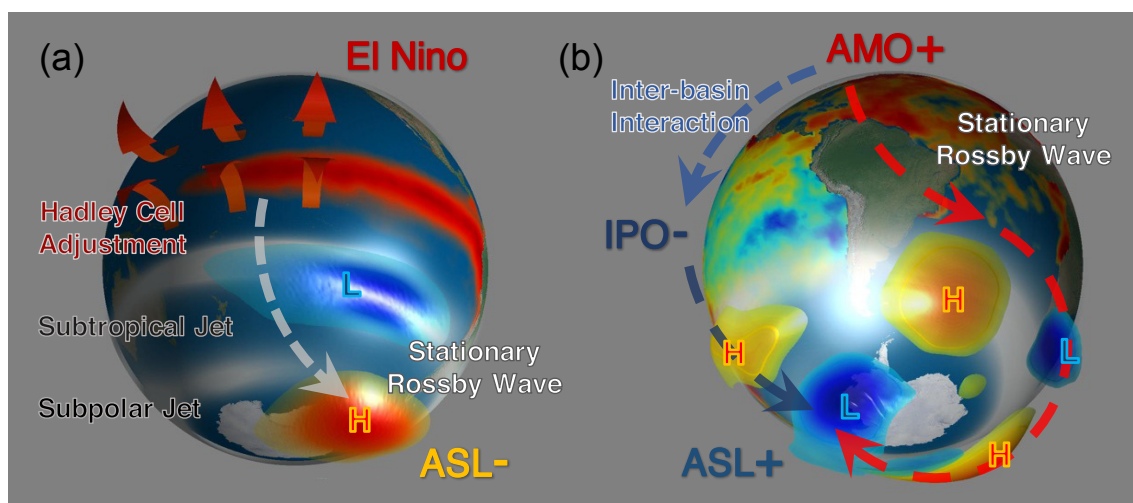


**Fig. 7.** Teleconnection patterns triggered by interannual and decadal sea surface temperature variability, respectively. (a) Schematic of tropical–Antarctic atmospheric teleconnection patterns induced by El Niño events. (b) Schematic of the atmospheric teleconnection patterns induced by a positive phase of the Atlantic Multidecadal Oscillation (AMO; red arrow) and a negative phase of the Interdecadal Pacific Oscillation (IPO; blue arrow).

2001; Li et al., 2014, 2021b; Zhang et al., 2021e). The Antarctic SIC is strongly influenced by the remote forcing from the tropical and midlatitudes (Li et al., 2014, 2020a; Zhang et al., 2021b, e; Dou and Zhang, 2022). La Niña events (Li et al., 2020a; Zhang et al., 2021b), the negative phase of IPO (Li et al., 2020a), and a positive phase of AMO (Li et al., 2014) lead to a deepening of the ASL through a Rossby wave train, and vice versa. The deepened ASL can further increase the SIC over the western Ross Sea and decrease the SIC over the Amundsen, Bellingshausen, and Weddell Seas (Li et al., 2014, 2020a; Zhang et al., 2021b), a phenomenon known as the Antarctic sea-ice dipole. Moreover, the Antarctic SIC is also modulated by the Southern Annular Mode (SAM) (Zhang et al., 2018b; Li et al., 2020a, 2021a), which is closely related to the Antarctic internal variability (Wang et al., 2020f).

The tropical-polar teleconnections may also contribute to the ocean bottom pressure (OBP) in the South Pacific, with a positive OBP anomaly related to the positive phase of the second Pacific South American mode (PSA2) (Qin et al., 2022). Temperature extremes on the Antarctic Peninsula are closely related to the intraseasonal oscillations and the fast synoptic-scale Rossby wave (Wang et al., 2022c). Additionally, tropical volcanic eruptions (Wu et al., 2018; Liu et al., 2020a) may also impact the Antarctic surface temperature by increasing sulfur aerosols in the Antarctic stratosphere (Wu et al., 2018).

### 3.2. Tropics and mid-latitudes impact Arctic climate

The tropics and the mid-latitude climate variability may impact Arctic climate changes through atmospheric and oceanic pathways (Ding et al., 2014; Feng and Wu, 2015; Hu et al., 2016; Liu et al., 2021b; Fang et al., 2022; Wu and Ding, 2022), whose process is even more complicated than that of the tropical–Antarctic teleconnection.

The tropical SST variability may contribute to the Arctic SAT changes on interannual and decadal time scales through atmospheric bridges. The tropical Pacific decadal variability may generate stationary Rossby wave trains and influence the atmospheric circulation around the high-latitude Atlantic (Ding et al., 2014), contributing to a prominent surface and tropospheric warming around Northeastern Canada and Greenland since 1979. The SST cooling in the tropical central and eastern Pacific may also contribute to the recently observed Arctic warming anomalies (Wu, 2017). Recent studies indicated that the East Pacific El Niño events may have led to a cooling anomaly over the Barents-Kara Seas in February, while the Central Pacific events usually contribute to an SAT warming over northeastern Canada and Greenland (Li et al., 2019c). The equatorial Pacific warming related to Central Pacific El Niño events could inhibit summer Arctic warming and sea-ice melting by deepening the tropospheric Arctic polar vortex and enhancing the circumpolar westerly wind (Hu et al., 2016). The AMO may contribute to the evolution of the Arctic Amplification on multi-decadal and longer timescales (Fang et al., 2022). On the other hand, a recent study reveals a multidecadal seesaw of

the cold wave frequency between central Eurasia and Greenland, which is likely driven by the AMO (Liu et al., 2022).

The atmospheric teleconnections may also impact the Arctic sea-ice extent. The decline of summer-time Arctic sea ice has accelerated over the past four decades, which is, in part, driven by thermal advection and the mechanical forcing associated with the negative phases of the Arctic Oscillation and the PDO, as well as the positive phases of the NAO, the Arctic Dipole, and the AMO (Cai et al., 2021). It has been suggested that the recent persistent positive PNA pattern has led to increased heat and moisture fluxes, accelerating the sea-ice decline over the western Arctic Ocean (Liu et al., 2021b). In contrast, the phase changes of the PDO may affect the Arctic dipole pattern, modulating the variations of summertime SIC over the Pacific sector. In particular, the PDO recently shifted to its positive phase, which may temporarily slow down the observed decline of the summertime SIC within the Pacific sector of the Arctic Ocean (Bi et al., 2021). In addition, the Arctic sea-ice variability during the melt season is tightly associated with the phase change of the AMO (Yu et al., 2019a). On the other hand, the enhancement of North Atlantic westerly winds associated with the SST dipole to the south and north of the Gulf Stream Extension may promote long-lived Ural blocking and high-latitude European blocking, further contributing to the loss of sea ice in the Barents-Kara Seas and also to Eurasian cooling (Luo et al., 2019).

Oceanic processes represent an important pathway by which features in the tropics and mid-latitudes can induce Arctic climate changes (Zhang, 2015; Shu et al., 2019, 2021; Zhang et al., 2022e). Zhang (2015) revealed that three key factors, including the oceanic heat transport from the Atlantic and the Pacific Oceans and the Arctic Dipole pattern, have played a crucial role in driving the summer-time Arctic sea-ice decline in recent decades. The Atlantic water is particularly important in the thermal balance of the Arctic Ocean (Shu et al., 2019). North Atlantic warming is usually associated with a warmer Arctic Ocean and sea-ice declines (Zhang et al., 2022e). The Barents-Kara Seas releases most of the ocean heat that originates from the North Atlantic and is a known cooling machine of the Arctic Ocean. It has been reported that this cooling machine has expanded poleward, a phenomenon termed the poleward shift of the Arctic Atlantification (Shu et al., 2021). The transport of heat and salinity from the Pacific also significantly contributes to the climate variability of the Arctic Ocean. For example, the variability of the Bering Strait inflow largely contributes to the recent freshening of the Arctic Ocean (Shu et al., 2018).

On the other hand, the Arctic Ocean may feedback upon the Atlantic and the Pacific by adjusting their ocean circulations. In particular, the freshwater outflow from the Arctic Ocean plays an important role in modulating the Atlantic Meridional Overturning Circulation (AMOC). A recent study (Chen and Tung, 2018) indicated that the role of AMOC may be altered in the presence of greenhouse-gas heating. Usually, the AMOC transports surface heat northwards,

heating Europe and North America. Under global warming, the AMOC may start to store heat in the deeper Atlantic, buffering the surface warming for the planet as a whole (Chen and Tung, 2018). On the other hand, according to CMIP model simulations, the projected decline of anthropogenic aerosols may also potentially weaken the AMOC, leading to enhanced oceanic heat uptake in the subpolar North Atlantic (Ma et al., 2020c).

Simulation experiments forced by winter Eurasian regional ground albedo changes consistently demonstrate that regional cooling directly contributes to Arctic warm anomalies. Sometimes the cooling can enhance the Siberian high and generate positive 500-hPa height anomalies over and around the Ural Mountains through atmospheric subsidence anomalies and wave-energy propagation, ultimately leading to warm anomalies over the Barents-Kara Seas (Wu and Ding, 2022).

#### 4. Polar changes contribute to a changing global climate system

Climate change over the Arctic and Antarctic regions may both impact the lower latitudes, primarily through the adjustment of the large-scale atmospheric circulations and associated atmosphere-ice-ocean interactions. Both the Greenland and Antarctic ice sheets experienced accelerated melting during the past three decades, contributing to a rise in global

mean sea level. These global impacts of the polar climate changes are reviewed as follows.

##### 4.1. Arctic changes impact lower-latitudes

Rapid warming and sea-ice loss over the Arctic are associated with anomalous cooling over the mid- and high-latitude continental areas of the Northern Hemisphere for boreal winter and spring. This dipole-like, anomalous SAT pattern is pronounced from interannual to multi-decadal timescales, known as the “warm Arctic cold continental” pattern (Luo et al., 2016; Wu, 2017; Gu et al., 2018; Ding et al., 2021). In particular, the cooling over the central Eurasian continent is linked to warming in the Arctic, named the “warm Arctic-cold Eurasia” pattern (Xu et al., 2019; Dai and Song, 2020; Dai and Deng, 2022) (Fig. 8). The Arctic sea-ice loss, especially those over the Barents-Kara seas (Fig. 2a), releases additional heat and moisture from the ocean to the atmosphere, which can increase Siberian snow cover and further enhance the Siberian high (Wu et al., 2011; Zuo et al., 2016). This anticyclonic circulation anomaly transports cold air from the Arctic to the mid-latitude Eurasian continent (Fig. 1a and Fig. 8). The retreat of the Barents-Kara sea ice can trigger a surface temperature dipole pattern between Eurasia and North America by adjusting the mid- and high-latitude atmospheric circulation in boreal winter (Hou et al., 2022). In addition, the anomalous snowfall over northern Eurasia may mediate the effect of the Arctic sea ice on Eurasian cooling (Xu et al., 2018). The autumn sea-ice loss over the Arctic

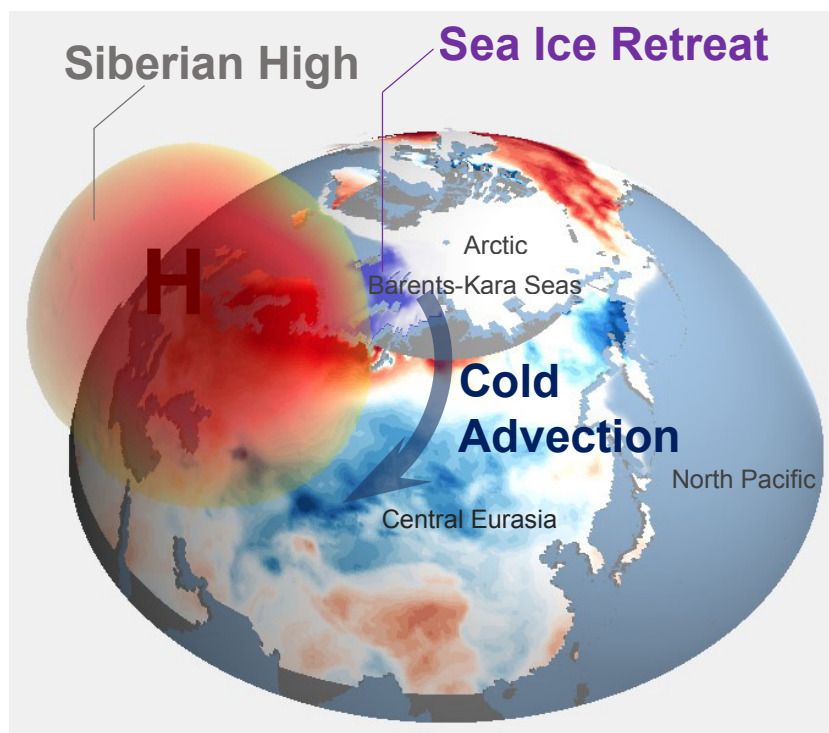


**Fig. 8.** Schematic diagram of the mechanism for the Warm Arctic–Cold Eurasia (WACE) pattern associated with sea-ice loss over the Barents-Kara Seas in boreal winter. Declines in sea-ice heat the surface and tropospheric atmosphere and excite an anomalous high-pressure center over northern Siberia, driving cold advection from the Arctic to central Eurasia.



Ocean may contribute to an anomalous “north-south” dipole mode of the snow cover over the mid-to-high latitude Eurasian continent, potentially contributing to the winter-springtime cold events over mid-latitude Eurasia (Zhang et al., 2019a, 2022g). Moreover, the phase changes of the AMO may influence the effect of the Arctic sea-ice loss on the anomalous cooling over Siberia (Luo et al., 2017; Chen et al., 2021).

In particular, the Arctic sea-ice loss may change winter weather patterns and the frequency of extreme cold events over the Eurasian continent. During wintertime, the intensity of the tripole wind pattern and the frequency of its extremely negative phase over Eurasia is significantly correlated with autumn Arctic sea-ice anomalies (Wu et al., 2013). The reduction of the meridional temperature gradient associated with Arctic sea-ice loss leads to the vertical propagation of planetary wave energy, a weakening of the stratospheric polar vortex, and the genesis of an atmospheric blocking system over the Ural regions (Luo et al., 2018). The winter warming in the Barents-Kara seas and the associated sea-ice declines may contribute to a large increase in the mean duration of the Ural blocking events, thus affecting the recent winter Eurasian cold extreme events (Luo et al., 2018). The Arctic atmospheric circulation anomalies during the summertime and the Arctic sea-ice declines may also impact the intraseasonal evolution of extreme cold events over Eurasia (Wu et al., 2017). Notably, the zonal movement of the Ural blocking exerts important feedback on the sea-ice variability in the Barents-Kara seas (Chen et al., 2018). The Arctic polar vortex shifted persistently towards the Eurasian continent in February over the past three decades, which induced a cooling anomaly over the mid-latitude Eurasian continent (Zhang et al., 2016). In addition, the phase change of the PDO may contribute to the influence of the Arctic sea-ice loss on the extreme winter events over the Eurasian continent (Zhang et al., 2022d). Recent studies have shown that in recent decades, the linkage between the Arctic sea-ice variability, the Arctic Oscillation, and the Eurasian extreme cold events has significantly intensified (Chen et al., 2019; He et al., 2019; Ding and Wu, 2021).

Recent studies revealed a seesaw pattern of extreme temperature events on sub-seasonal timescales (Ma and Zhu, 2020), with a cold event over East Asia accompanied by a warm event in North America, usually lasting for several weeks (Sung et al., 2021). In addition, increased wildfire events over the western U.S. in boreal autumn are fueled by more fire-favorable weather associated with Arctic sea-ice declines during the preceding months on both interannual and interdecadal time scales, inducing regional circulation changes accompanied by a poleward shift of the polar jet stream (Zou et al., 2021).

It has been reported that an increase of the winter sea-ice extent over the Greenland-Barents Seas may trigger an atmospheric wave train propagating southeastward from high-latitude Eurasia towards the subtropical North Pacific, with cyclonic wind anomalies over the subtropical North

Pacific, to include the induction of an El Niño event in the following winter (Chen et al., 2020a). One recent study (Chen et al., 2020b) found that the relationship between the spring Arctic Oscillation and winter-time ENSO events has weakened since the early 1990s. The boreal winter Arctic Oscillation is also reported to have an interannual relationship with the summer SST anomalies over the western tropical Indian Ocean (Gong et al., 2017) and may impact October East African precipitation (Gong et al., 2016).

Additionally, the Arctic-midlatitude linkage also displays strong phasic fluctuations (or decadal fluctuations), and Arctic sea-ice loss may be conducive to the alternative occurrence of warm Arctic-cold Eurasia (2007/2008–2012/2013) and warm Arctic-warm Eurasia (2013/2014–2018/2019) events (Wu et al., 2022a).

The Arctic changes may impact climate variability over East Asia. It is reported that the Arctic Oscillation may work together with the ENSO system, contributing to the occurrence of cold events over East Asia during boreal winter (Song and Wu, 2022). Both the negative phase of the Arctic Oscillation in El Niño winters and the Ural blocking in La Niña winters are followed by a Rossby wave train over Eurasia continents that strengthens the Siberian high, leading to cold anomalies over East Asia (Song and Wu, 2022). The winter sea-ice loss over the Barents-Kara Seas also largely contributes to the hiatus of winter warming in China (Li et al., 2019b). The interactions between the Arctic sea-ice anomalies and the SST anomalies in the equatorial central-eastern Pacific are important in influencing the East Asian winter monsoon system (Sun et al., 2016a; Zhang et al., 2020). In addition, the widespread North Atlantic-Arctic warming could modulate and interact with the atmospheric background flow over the North Atlantic-Arctic Ocean, which further enhances the quasi-stationary Rossby waves and results in a strengthening of the East Asian winter monsoon and cooling over East Asia (Zhang et al., 2022e).

In addition, declines in Arctic sea ice play an important role in the summer atmospheric circulation and the extreme climate events over East Asia (Wu and Li, 2022). The Arctic sea-ice loss may intensify the East Asia summer monsoon (Wu and Li, 2022), deepening the low-pressure system over the Eurasian continent and increasing the frequency of the heat waves and heavy precipitation over the mid-latitudes of East Asia (Wu and Li, 2022). The winter-time Arctic sea-ice variability plays an important role in the influence of the North Atlantic Oscillation on the East Asia summer-time precipitation (Zhang et al., 2021f). The combined effects of Indian Ocean warming and Arctic sea-ice loss also contributed to a record-breaking Meiyu-Baiu rainfall over East Asia in June-July 2020 through enhanced mid-tropospheric westerlies and anomalous meridional wind convergence (Chen et al., 2022b). In addition, the anomalous cooling over the mid- and low-level troposphere over the Arctic region favors a heat wave event over East Asia and Europe in boreal summer (Wu and Francis, 2019).

Furthermore, extreme cold events over the Tibetan

Plateau are affected by Rossby wave trains triggered by Arctic sea-ice loss (Bi et al., 2022), and they are regulated by sea-ice variability in the Beaufort and Laptev Seas (Bi et al., 2022). The Arctic sea-ice loss may also trigger stationary Rossby wave trains, propagating to the Tibetan Plateau area and impacting its air pollution by changing the atmospheric advection (Bi et al., 2022).

The winter sea-ice cover over the Barents Sea has been reported to have an interannual linkage with the spring Normalized Difference Vegetation Index over Eurasia (Ji and Fan, 2019a). They are also important predictors of dust weather frequency in East Asia, particularly over northern China (Ji and Fan, 2019b; Liu et al., 2020b). In addition, the positive phase of the preceding wintertime Arctic polar vortex intensity tends to increase the spring Normalized Difference Vegetation Index in Europe and Lake Baikal but may lead to a significant decrease in this parameter over Siberia (Li et al., 2017a).

#### 4.2. Antarctic changes impact lower latitudes

The Antarctic climate variability may also largely impact the lower latitude climate (Bai et al., 2016; Xiang et al., 2018; Fu et al., 2019; Jiang et al., 2022). Antarctic climate changes can directly affect tropical climate variability through atmospheric bridges (Xiang et al., 2018; Jiang et al., 2022). For example, the Antarctic sea ice significantly impacts the global air temperature by changing the intensity of atmospheric baroclinic disturbances to modify wave energy transmission (Jiang et al., 2022). Antarctic ozone depletion also plays an important role in increasing the Southern Hemisphere extratropical precipitation (Bai et al., 2016). On the other hand, the Antarctic climate variability can transport energy to the upper-layer ocean over the mid-high latitude Southern Hemisphere, affecting SST variability, which further triggers the remote climate effect through atmospheric teleconnections (Hwang et al., 2017; Xiang et al., 2018; Yang et al., 2018; Fu et al., 2019).

The Southern Oceans, a major region for global heat uptake, has a pronounced influence on global-scale atmospheric circulations, tropical SST variability, and tropical precipitation (Hwang et al., 2017). In addition, the Southern Ocean may affect the position of the ITCZ from the perspective of global energy balance (Xiang et al., 2018). Perturbing the Southern Ocean with an external heat forcing may drive cross-equatorial ocean heat transport and lead to a shift of the ITCZ (Liu et al., 2021a). In addition, based on the CMIP6 simulation results, the projected changes of the extratropical surface heat flux associated with the AMOC and Southern Ocean SIC play an important role in the tropical climate response to global warming (Geng et al., 2022). Antarctic Intermediate Water, originating from the Southern Oceans, also has a potential impact on interannual and interdecadal variability of the Indonesian Throughflow (Yang et al., 2018), as well as the oceanic climate variability around the western boundary current (Fu et al., 2019).

Antarctic climate variability also has a pronounced impact on the weather and climate systems around China

(Fang et al., 2019; Chang et al., 2020; Dou et al., 2020; Yuan et al., 2022). An interdecadal dipole pattern between the summer geopotential heights in Northeast Asia and the Antarctic (Fig. 9) has been revealed in a recent study (Fang et al., 2019), which provides important evidence that the atmospheric circulation around the Antarctic may influence China. The Antarctic Oscillation may impact the precipitation and temperature of Southern China, especially around the Yangtze River Basin (Fig. 10) (Dou et al., 2020; Yuan et al., 2022). In spring, the enhanced atmosphere-ocean heat flux associated with the Antarctic Oscillation may intensify a meridional Indian Ocean tripole mode and thus strengthen precipitation over the Maritime Continent area, further influencing the summer precipitation in Southern China (Fig. 10) through atmospheric bridges (Dou et al., 2020). In addition, the autumn Antarctic Oscillation may regulate both the dry-cold northerly advection and the moist-warm southerly advection in both the troposphere and the stratosphere, further influencing the winter precipitation and temperature of Southern China (Yuan et al., 2022). Moreover, the winter-time haze pollution in central-eastern China is closely related to the tropospheric and stratospheric polar vortices in the Southern Hemisphere in August and September (Chang et al., 2020).

#### 4.3. Polar climate changes contribute to global sea level rise

One of the most important effects of polar climate changes is their impact on the global mean sea level rise. During the last two decades, the melting of ice sheets and the increase of the ocean heat content dominated the trend of the global mean sea level rise (Li et al., 2013; Chen et al.,

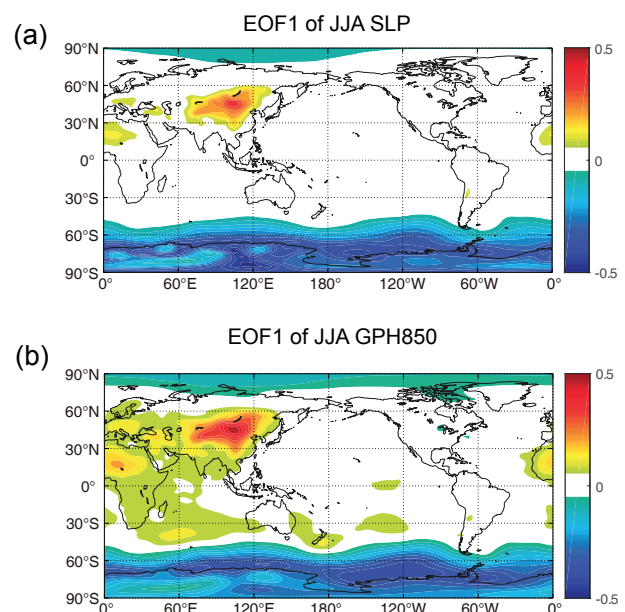


**Fig. 9.** The first Principal Component Analysis (PCA) mode of the low-passed ( $f < 0.1$ ) decadal sea level pressure (SLP, a) and 850-hPa geopotential height (GPH850, b) anomalies during 1948–2021 for boreal summer (JJA). [Reprinted from (Fang et al., 2019), reproduced with permission from Springer Nature].

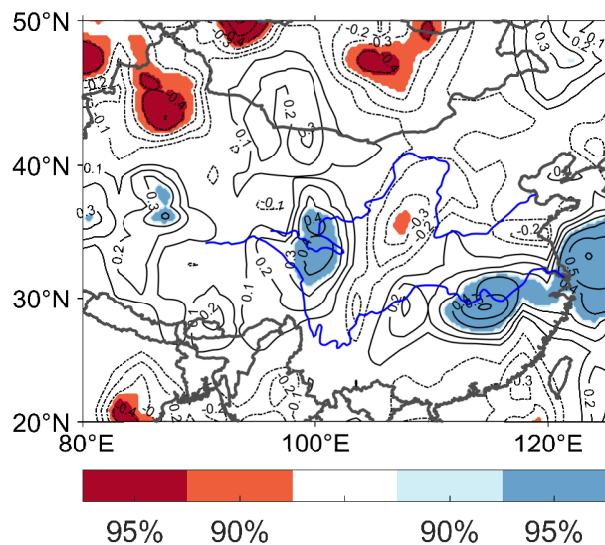


**Fig. 10.** The correlation pattern between the boreal summer (JJA) precipitation over China and the SAM index in May during 1988–2012. The positive (negative) correlation coefficients are shown in solid (dashed) contours. The color shadings reflect the degree of statistical significance using the students' *t*-test. [Reprinted from (Dou et al., 2020), reproduced with permission from Springer Nature].

2014; Yi et al., 2015; Chen et al., 2017; Yi et al., 2017). Recent studies indicated that the GMSL experienced an acceleration from 1993 to 2014, whose ratio increased from  $2.2 \pm 0.3 \text{ mm yr}^{-1}$  (1993) to  $3.3 \pm 0.3 \text{ mm yr}^{-1}$  (2014), with the peak value occurring in 2004 and a slight deceleration happening in the recent decade (Chen et al., 2014, 2017). Over the past two decades, ice sheet melting over the polar region mainly contributed to the GMSL rise (Chen et al., 2017). An accelerated mass loss has been observed around the Greenland and Antarctic ice sheets (Gao et al., 2015; Zheng et al., 2022). At present levels, the polar ice sheet melting plays a more important role in the acceleration of the global sea level rise, in comparison to that of the seawater expansion caused by the increased ocean heat content (Xie et al., 2016b; Chen et al., 2017).

Over the past two decades, glacial melt around the Greenland ice sheet has been dramatically accelerated. Greenland is one of the largest contributors to the global sea level rise (Chen et al., 2017). From 1993 to 2014, the acceleration of global mean sea level rise has been faster than in previous decades, which can be largely attributed to the freshwater discharge from the Greenland ice sheet, whose contribution increased from 5% of the global sea level change rate (1993) to more than 25% (Chen et al., 2017). Recent studies indicated that the oceanic warm water intrusion dominates the accelerated basal melting of the Jakobshavn Glacier, one of the largest outlet glaciers in Greenland (Wang et al., 2020c). In addition, the glacial melt around Greenland may also be driven by a positive phase of the summer North Atlantic Oscillation (Ruan et al., 2019)

Due to the rapid melting and collapse of the West Antarctic ice shelf, the contribution of the Antarctic ice sheet to

sea level rise has increased from  $0.08$  ( $-0.10$  to  $0.27$ )  $\text{mm yr}^{-1}$  in 1992–2001 to  $0.40$  ( $0.20$ – $0.61$ )  $\text{mm yr}^{-1}$  in 2002–2011, whereas the enhanced Antarctic ice sheet mass loss was partially offset by increased snowfall over East Antarctica (Ding et al., 2017). The long-term mass loss of the Antarctic ice sheet is primarily attributed to oceanic basal melting rather than the surface mass balance, noting that the strongest basal melting occurred around the West Antarctic and the Antarctic Peninsula (Gao et al., 2019b; Zhang et al., 2021a). On the other hand, the mass loss of the East Antarctic ice sheet is mainly concentrated near the Poinsett Cape, which is much weaker than that of the West Antarctic ice sheet (Li et al., 2016). Under the background of global warming, the size of the Antarctic ice sheet may continue to decrease, considering that the frequency of the ice calving events continues to increase all around the Antarctic (Li et al., 2016, 2020b; Gao et al., 2019b; Qi et al., 2020b, 2021).

In addition to these regional effects, the increase in ocean heat content (Chen et al., 2013; Chen and Tung, 2018) and the tropical–polar teleconnection may also impact the glacial melt around the Arctic and the Antarctic (Li et al., 2021b), and thus further contribute to the global mean sea level rise. Moreover, it has been reported that the mountain glaciers in Alaska are also melting rapidly due to the recent climatic change, which greatly contributes to the global sea level rise (Jin and Feng, 2016).

## 5. The role of the stratospheric circulation

The stratospheric climate variability is key in the Arctic and Antarctic climate systems. It directly interacts with the variabilities in the troposphere and further mediates the interactions between the polar climate systems and the lower latitudes in both hemispheres, therefore largely impacting the global climate system (Fig. 11).

The stratospheric polar vortex (SPV) is the dominant stratospheric circulation system, usually active from autumn to spring in each hemisphere. Its variability can dramatically affect the tropospheric circulation, including the southern/northern annular mode and the Amundsen Sea Low, etc. Better estimation of the SPV may help to improve forecast skill and future projections of the polar climate system (Rao et al., 2021).

In the Northern Hemisphere, the stratospheric circulation anomalies associated with SPV changes can directly descend into the troposphere through stratosphere–troposphere coupling processes, including wave–mean flow interaction and the reflection of planetary waves (Gong et al., 2018; Wang and Ting, 2022). This interaction may significantly affect the climate and weather conditions over the Northern Hemisphere, leading to anomalous cold-air outbreaks (Cheung et al., 2016; Huang et al., 2021a), widespread precipitation (Zhang et al., 2022a), atmospheric environmental conditions (e.g.,  $\text{PM}_{2.5}$  concentration) (Huang et al., 2021b; Lu et al., 2021), and even tropical deep convection (Wang et al., 2020a). Accordingly, it



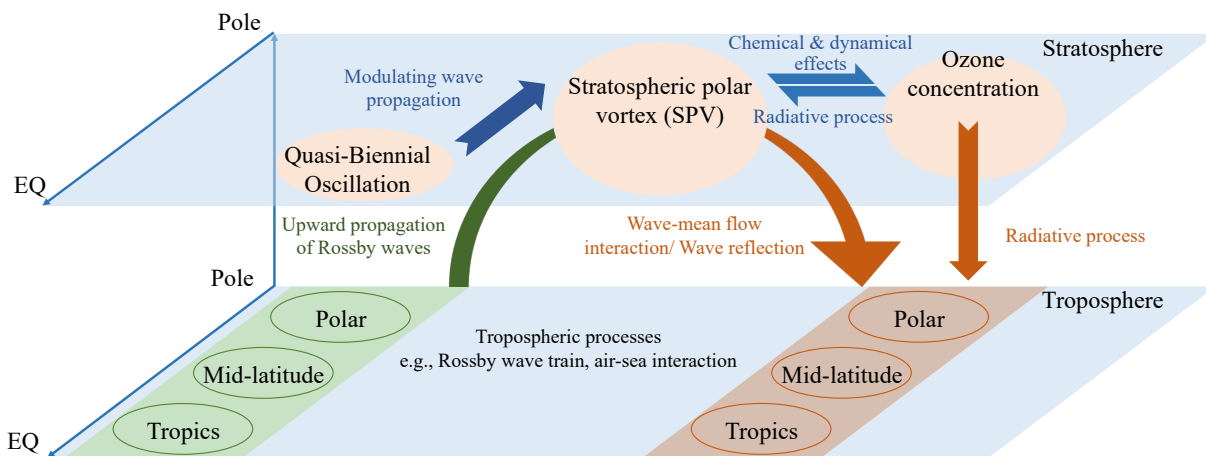


**Fig. 11.** Schematic diagram showing the influence of the stratospheric circulation on the global climate system. The stratospheric circulation interacts with the troposphere in a coupled way. The green arrow shows how the tropospheric circulation affects the stratosphere. Through tropospheric processes, circulation anomalies in the polar, mid-latitudes, and tropics can affect the upward propagation of the Rossby waves, further affecting the polar stratospheric circulation. In addition, stratospheric processes can also affect polar circulations, as shown by the blue arrows. The orange arrows show the influence of the stratospheric circulation on the troposphere. Stratospheric circulation anomalies can directly affect mid-latitudes and the polar regions through wave-mean flow interaction, wave reflection processes, and radiative processes and proceed to further affect tropical regions through tropospheric processes.

serves as an important pathway linking the circulations over the Arctic, extratropics, and tropical regions (Ding et al., 2021; Xu et al., 2021b). However, the interaction between the stratospheric and tropospheric circulation anomalies over the Northern Hemisphere largely depends on the circulation condition in both the stratosphere and the troposphere (Yu and Ren, 2019; Zhang et al., 2019b; Xu et al., 2022).

Given that the Northern Hemispheric SPV exerts such an important impact on the global climate system, many efforts have been devoted to exploring the possible causes of its variation on different timescales. On the subseasonal timescale, the Madden-Julian Oscillation can significantly affect the SPV through Rossby wave dynamics (Yang et al., 2019a; Ma et al., 2020a). On the interannual timescale, both the equatorial stratospheric Quasi-Biennial Oscillation (QBO) and El Niño-Southern Oscillation can influence the SPV by modulating the wave propagation and affecting the intensity of tropospheric wave forcing, respectively (Dai and Tan, 2016; Zhou et al., 2018; Zhang et al., 2022f). On decadal timescales, the SST anomalies over the North Atlantic and the central North Pacific may significantly enhance the intensification of the SPV (Hu et al., 2018, 2019). Meanwhile, the SPV has shifted towards the Eurasian continent in recent decades, largely due to the recently observed declines of Arctic sea ice, especially around the Barents-Kara Seas (Zhang et al., 2016).

Although the Southern Hemispheric SPV is less volatile compared to its Northern Hemispheric counterpart, recent studies provide evidence showing that it can still exert remarkable impacts on the tropospheric circulation (Shen et al., 2020a; Wang et al., 2020d). In particular, extremely weak SPV events can sometimes occur attributed to the joint effect of the QBO and anomalous tropospheric

waves (Rao et al., 2020; Shen et al., 2020b). The anomalous circulation further descends into the troposphere and persists for months, significantly influencing the hemispheric-scale weather condition and the Antarctic sea-ice extent (Wang et al., 2021b; Shen et al., 2022a).

A main driver of the observed high-latitude stratospheric climate change is the variation of the stratospheric ozone concentration, particularly the ozone hole depletion and its recent recovery over the high latitudes of the Southern Hemisphere. In the Southern Hemisphere, the stratospheric ozone concentration has shown preliminary signs of recovery since the early 2000s (Bian et al., 2012; Hu et al., 2022b). Its recovery has been suggested to contribute to stratospheric warming in recent years and may be responsible for the more frequent occurrence of weak SPV events (Xia et al., 2020a; Shen et al., 2022a). In addition, the Antarctic ozone anomaly greatly impacts the Antarctic sea-ice extent via the radiative process and the ice-albedo feedback (Xia et al., 2020b).

In the Northern Hemisphere, the stratospheric ozone anomaly impacts the tropospheric climate variability through two main pathways. The ozone concentration change can directly influence the atmospheric temperature through its radiative forcing (Xia et al., 2021). It may also induce hemispheric-scale circulation change in the troposphere by modulating the SPV (Xie et al., 2016a). The physical processes by which changes in ozone concentration impact the polar atmospheric circulation are complicated. The Arctic sea-ice concentration, the background circulation over the mid-latitudes and tropics, as well as the hydrological cycle may all influence the processes through their adjustment of the local circulation, the atmosphere-ocean interaction, and the meridional overturning circulation (Xie et al., 2017;

Hu et al., 2022a; Wang et al., 2022e; Zhang et al., 2022b). Many studies have also attempted to identify possible factors influencing stratospheric polar ozone concentrations on different timescales. It has been found that tropospheric circulation anomalies, including SST anomalies, sea-ice loss, and the MJO, can all contribute to the observed ozone variability (Tian et al., 2017; Zhang et al., 2018a; Yang et al., 2020).

## 6. Conclusion and Discussion

In the past four decades since the modern satellite era, a series of polar climate changes have been observed. These changes include a rapid Arctic warming that is more than twice as fast as the global warming rate, known as the Arctic Amplification, and zonally asymmetric climate changes over the Antarctic, with the fastest surface warming, sea- and land-ice melting all happening around the West rather than the East Antarctic.

These polar climate changes on the multi-decadal scale have been primarily driven by anthropogenic greenhouse gas increases and ozone loss, while the regional features of the polar climate changes and the more frequent extreme events are largely attributed to the tropical–polar teleconnections. On the other hand, polar climate changes significantly impact the Earth's climate system in several aspects. First, the accelerated melting of the Greenland and Antarctic ice sheets is a primary cause of global-mean sea level rise. In addition, the Arctic warming tends to cool the land areas over the mid-latitude Northern Hemisphere. The Arctic and Antarctic sea-ice changes may also impact the precipitation and large-scale circulation over the tropics and mid-latitudes. The adjustment of the atmospheric circulation in both the troposphere and the stratosphere, as well as the oceanic processes, all contribute to the interactions between the polar climate changes and climate variability over lower latitudes.

An important mission of the polar climate investigation is to improve observational systems around the Arctic and the Antarctic, as many of the polar climate changes and their associated variability last for decades or longer. Thus, long-lasting, high-quality measurements over high latitudes are needed to investigate these variations. However, unlike tropical and mid-latitude regions, observations over polar regions are comparatively difficult to obtain because of the harsh environment. Although the assessment of many variables, including the temperatures of the ocean and atmosphere, sea level, and sea-ice concentrations, have become available during the modern satellite era, most satellites do not fly over the North or South Pole, leaving a big gap in the observation coverage. The lack of polar satellite observations leads to observational and reanalysis datasets with compromised quality and reliability around the Arctic and Antarctic regions, which need to be improved in future investigations.

Considering that the decadal and multi-decadal variability over the tropics and the mid-latitudes, including the

PDO and AMO, all contributed to Arctic and Antarctic climate changes, the phase change of these modes of decadal variability may also lead to a phase change of the polar climate changes. For example, the zonally asymmetric Antarctic climate change, with the West warming and East cooling, may potentially switch in the future following the phase reversals of the AMO and the PDO. The interaction between the long-term trend and the decadal/multi-decadal variability may largely contribute to future polar climate changes and consequently influence the predictability and the projection of the Earth's climate system, which represents an issue that warrants further investigation.

In addition, regarding the interactions between the polar climate and the lower latitude climate variability, we found that more attention was paid to the impact of the Arctic Amplification on lower latitudes and the contributions of the tropics (and mid-latitudes) to the Antarctic climate. The converse effects of the Antarctic on the lower latitudes and the impacts of the tropics on the Arctic climate changes involve multiple interactions between the ocean, the atmosphere, and the cryosphere, which is relatively more complicated and less understood. Such linkages also require further investigation in future studies.

**Acknowledgements.** X. LI was supported by the National Key Research and Development Program of China (2018YFA0605703), the National Natural Science Foundation of China (No. 41976193 and No. 42176243). X. CHEN was supported by the National Key Research and Development Program of China (2019YFC1509100) and the National Science Foundation of China (No. 41825012). B. WU was supported by the Major Program of the National Natural Science Foundation of China (41790472), the National Key Basic Research Project of China (2019YFA0607002), and the National Natural Science Foundation of China (41730959). X. CHENG was funded by the Innovation Group Project of Southern Marine Science and Engineering Guangdong Laboratory (Zhuhai) (Grant No. 311021008). M. DING was supported by the National Natural Science Foundation of China (42122047 and 42105036) and the Basic Research Fund of the Chinese Academy of Meteorological Sciences (2021Y021 and 2021Z006). Q. SUN was supported by the National Key R&D Program of China (No. 2022YFE0106300).

## REFERENCES

- Bai, K. X., N. B. Chang, and W. Gao, 2016: Quantification of relative contribution of Antarctic ozone depletion to increased austral extratropical precipitation during 1979–2013. *J. Geophys. Res.: Atmos.*, **121**, 1459–1474, <https://doi.org/10.1002/2015JD024247>.
- Bi, H. B., Y. H. Wang, Y. Liang, W. F. Sun, X. Liang, Q. L. Yu, Z. H. Zhang, and X. L. Xu, 2021: Influences of summertime Arctic Dipole atmospheric circulation on sea ice concentration variations in the Pacific Sector of the Arctic during different Pacific Decadal Oscillation phases. *J. Climate*, **34**, 3003–3019, <https://doi.org/10.1175/JCLI-D-19-0843.1>.
- Bi, M., Q. Q. Li, S. Yang, D. Guo, X. Y. Shen, and X. T. Sun, 2022: Effects of Arctic sea ice in autumn on extreme cold

- events over the Tibetan Plateau in the following winter: Possible mechanisms. *Climate Dyn.*, **58**, 2281–2292, <https://doi.org/10.1007/s00382-021-06007-0>.
- Bian, L. G., Z. Lin, X. D. Zheng, Y. F. Ma, and L. H. Lu, 2012: Trend of Antarctic ozone hole and its influencing factors. *Advances in Climate Change Research*, **3**, 68–75, <https://doi.org/10.3724/SP.J.1248.2012.00068>.
- Cai, Q. Q., D. Beletsky, J. Wang, and R. B. Lei, 2021: Interannual and decadal variability of Arctic summer sea ice associated with atmospheric teleconnection patterns during 1850–2017. *J. Climate*, **34**, 9931–9955, <https://doi.org/10.1175/JCLI-D-20-0330.1>.
- Chang, L. Y., Z. W. Wu, and J. M. Xu, 2020: Potential impacts of the Southern Hemisphere polar vortices on central-eastern China haze pollution during boreal early winter. *Climate Dyn.*, **55**, 771–787, <https://doi.org/10.1007/s00382-020-05294-3>.
- Chen, J. X., X. M. Hu, S. Yang, S. H. Lin, and Z. N. Li, 2022a: Influence of convective heating over the maritime continent on the West Antarctic climate. *Geophys. Res. Lett.*, **49**, e2021GL097322, <https://doi.org/10.1029/2021GL097322>.
- Chen, S. F., R. G. Wu, and W. Chen, 2019: Enhanced impact of Arctic sea ice change during boreal autumn on the following spring Arctic oscillation since the mid-1990s. *Climate Dyn.*, **53**, 5607–5621, <https://doi.org/10.1007/s00382-019-04886-y>.
- Chen, S. F., R. G. Wu, W. Chen, and B. Yu, 2020a: Influence of winter Arctic sea ice concentration change on the El Niño–Southern Oscillation in the following winter. *Climate Dyn.*, **54**, 741–757, <https://doi.org/10.1007/s00382-019-05027-1>.
- Chen, S. F., R. G. Wu, W. Chen, and B. Yu, 2020b: Recent weakening of the linkage between the spring Arctic Oscillation and the following winter El Niño–Southern Oscillation. *Climate Dyn.*, **54**, 53–67, <https://doi.org/10.1007/s00382-019-04988-7>.
- Chen, X. D., and D. H. Luo, 2021: Impact of Greenland blocking on midlatitude extreme cold weather: Modulation of Arctic sea ice in western Greenland. *Science China Earth Sciences*, **64**, 1065–1079, <https://doi.org/10.1007/s11430-020-9782-2>.
- Chen, X. D., D. H. Luo, S. B. Feldstein, and S. Lee, 2018: Impact of winter Ural blocking on Arctic sea ice: Short-time variability. *J. Climate*, **31**, 2267–2282, <https://doi.org/10.1175/JCLI-D-17-0194.1>.
- Chen, X. D., Z. P. Wen, Y. Y. Song, and Y. Y. Guo, 2022b: Causes of extreme 2020 Meiyu–Baiu rainfall: A study of combined effect of Indian Ocean and Arctic. *Climate Dyn.*, **59**, 3485–3501, <https://doi.org/10.1007/S00382-022-06279-0>.
- Chen, X. Y., and K.-K. Tung, 2018: Global surface warming enhanced by weak Atlantic overturning circulation. *Nature*, **559**, 387–391, <https://doi.org/10.1038/s41586-018-0320-y>.
- Chen, X. Y., Y. Feng, and N. E. Huang, 2014: Global sea level trend during 1993–2012. *Global and Planetary Change*, **112**, 26–32, <https://doi.org/10.1016/j.gloplacha.2013.11.001>.
- Chen, X. Y., Y. L. Zhang, M. Zhang, Y. Feng, Z. H. Wu, F. L. Qiao, and N. E. Huang, 2013: Intercomparison between observed and simulated variability in global ocean heat content using empirical mode decomposition, part I: Modulated annual cycle. *Climate Dyn.*, **41**, 2797–2815, <https://doi.org/10.1007/s00382-012-1554-2>.
- Chen, X. Y., and Coauthors, 2017: The increasing rate of global mean sea-level rise during 1993–2014. *Nature Climate Change*, **7**, 492–495, <https://doi.org/10.1038/nclimate3325>.
- Chen, Y., X. Zhao, X. P. Pang, and Q. Ji, 2022c: Daily sea ice concentration product based on brightness temperature data of FY-3D MWRI in the Arctic. *Big Earth Data*, **6**, 164–178, <https://doi.org/10.1080/20964471.2020.1865623>.
- Chen, Y. N., D. H. Luo, and L. H. Zhong, 2021: North Atlantic multidecadal footprint of the recent winter warm Arctic–cold Siberia pattern. *Climate Dyn.*, **57**, 121–139, <https://doi.org/10.1007/s00382-021-05698-9>.
- Cheng, X., and G. H. Xu, 2006: The integration of JERS-1 and ERS SAR in differential interferometry for measurement of complex glacier motion. *J. Glaciol.*, **52**, 80–88, <https://doi.org/10.3189/172756506781828881>.
- Cheng, X., X. W. Li, Y. Shao, and Z. Li, 2007: DINSAR measurement of glacier motion in Antarctic Grove Mountain. *Chinese Science Bulletin*, **52**, 358–366, <https://doi.org/10.1007/s11434-007-0054-y>.
- Cheng, X., S. S. Fan, L. Zheng, and J. L. Zhou, 2022: Critical technologies for detection of polar environment. *Bulletin of Chinese Academy of Sciences*, **37**, 921–931, <https://doi.org/10.16418/j.issn.1000-3045.20220626001>. (in Chinese with English abstract)
- Cheng, Y. C., O. Andersen, and P. Knudsen, 2015: An improved 20-year Arctic Ocean altimetric sea level data record. *Marine Geodesy*, **38**, 146–162, <https://doi.org/10.1080/01490419.2014.954087>.
- Cheung, H. H. N., W. Zhou, M. Y. T. Leung, C. M. Shun, S. M. Lee, and H. W. Tong, 2016: A strong phase reversal of the Arctic Oscillation in midwinter 2015/2016: Role of the stratospheric polar vortex and tropospheric blocking. *J. Geophys. Res.: Atmos.*, **121**, 13 443–13 457, <https://doi.org/10.1002/2016JD025288>.
- Cui, X. B., and Coauthors, 2020: Bed topography of princess Elizabeth land in east Antarctica. *Earth System Science Data*, **12**, 2765–2774, <https://doi.org/10.5194/essd-12-2765-2020>.
- Dai, A. G., and M. R. Song, 2020: Little influence of Arctic amplification on mid-latitude climate. *Nature Climate Change*, **10**, 231–237, <https://doi.org/10.1038/s41558-020-0694-3>.
- Dai, A. G., and J. C. Deng, 2022: Recent Eurasian winter cooling partly caused by internal multidecadal variability amplified by Arctic sea ice–air interactions. *Climate Dyn.*, **58**, 3261–3277, <https://doi.org/10.1007/S00382-021-06095-Y>.
- Dai, A. G., D. H. Luo, M. R. Song, and J. P. Liu, 2019: Arctic amplification is caused by sea-ice loss under increasing CO<sub>2</sub>. *Nature Communications*, **10**, 121, <https://doi.org/10.1038/s41467-018-07954-9>.
- Dai, Y., and B. K. Tan, 2016: The western Pacific pattern precursor of major stratospheric sudden warmings and the ENSO modulation. *Environmental Research Letters*, **11**, 124032, <https://doi.org/10.1088/1748-9326/aa538a>.
- Ding, M. H., C. D. Xiao, and D. H. Qin, 2022a: Explosive warming event in Antarctica on 18 March 2022 and its possible causes. *Climate Change Research*, **18**, 384–388, <https://doi.org/10.12006/j.issn.1673-1719.2022.068>. (in Chinese with English abstract)
- Ding, M. H., W. Han, T. Zhang, X. Y. Yue, J. Fyke, G. Liu, and C. D. Xiao, 2020: Towards more snow days in summer since 2001 at the Great Wall Station, Antarctic Peninsula: The role of the amundsen sea low. *Adv. Atmos. Sci.*, **37**, 494–504, <https://doi.org/10.1007/s00376-019-9196-5>.
- Ding, M. H., C. D. Xiao, C. J. Li, D. H. Qin, B. Jin, G. T. Shi, A. H. Xie, and X. B. Cui, 2015: Surface mass balance and its cli-

- mate significance from the coast to Dome A, East Antarctica. *Science China Earth Sciences*, **58**, 1787–1797, <https://doi.org/10.1007/s11430-015-5083-9>.
- Ding, M. H., and Coauthors, 2022b: The PANDA automatic weather station network between the coast and Dome A, East Antarctica. *Earth System Science Data*, **14**, 5019–5035, <https://doi.org/10.5194/ESSD-14-5019-2022>.
- Ding, Q. H., E. J. Steig, D. S. Battisti, and M. Küttel, 2011: Winter warming in West Antarctica caused by central tropical Pacific warming. *Nature Geoscience*, **4**, 398–403, <https://doi.org/10.1038/ngeo1129>.
- Ding, Q. H., J. M. Wallace, D. S. Battisti, E. J. Steig, A. J. E. Gallant, H.-J. Kim, and L. Geng, 2014: Tropical forcing of the recent rapid Arctic warming in northeastern Canada and Greenland. *Nature*, **509**, 209–212, <https://doi.org/10.1038/nature13260>.
- Ding, Q. H., and Coauthors, 2017: Influence of high-latitude atmospheric circulation changes on summertime Arctic sea ice. *Nature Climate Change*, **7**, 289–295, <https://doi.org/10.1038/nclimate3241>.
- Ding, R. Q., J. P. Li, Y.-H. Tseng, K.-J. Ha, S. Zhao, and J.-Y. Lee, 2016: Interdecadal change in the lagged relationship between the Pacific–South American pattern and ENSO. *Climate Dyn.*, **47**, 2867–2884, <https://doi.org/10.1007/s00382-016-3002-1>.
- Ding, S. Y., and B. Y. Wu, 2021: Linkage between autumn sea ice loss and ensuing spring Eurasian temperature. *Climate Dyn.*, **57**, 2793–2810, <https://doi.org/10.1007/s00382-021-05839-0>.
- Ding, S. Y., B. Y. Wu, and W. Chen, 2021: Dominant characteristics of early autumn Arctic sea ice variability and its impact on Winter Eurasian climate. *J. Climate*, **34**, 1825–1846, <https://doi.org/10.1175/JCLI-D-19-0834.1>.
- Dou, J., and R. H. Zhang, 2022: Weakened relationship between ENSO and Antarctic sea ice in recent decades. *Climate Dyn.*, **60**, 1313–1327, <https://doi.org/10.1007/s00382-022-06364-4>.
- Dou, J., Z. W. Wu, and J. P. Li, 2020: The strengthened relationship between the Yangtze River Valley summer rainfall and the Southern Hemisphere annular mode in recent decades. *Climate Dyn.*, **54**, 1607–1624, <https://doi.org/10.1007/s00382-019-05078-4>.
- Fang, K. Y., and Coauthors, 2019: An interdecadal climate dipole between Northeast Asia and Antarctica over the past five centuries. *Climate Dyn.*, **52**, 765–775, <https://doi.org/10.1007/s00382-018-4161-z>.
- Fang, M., X. Li, H. W. Chen, and D. L. Chen, 2022: Arctic amplification modulated by Atlantic Multidecadal Oscillation and greenhouse forcing on multidecadal to century scales. *Nature Communications*, **13**, 1865, <https://doi.org/10.1038/S41467-022-29523-X>.
- Feng, C., and B. Y. Wu, 2015: Enhancement of winter Arctic warming by the Siberian high over the past decade. *Atmospheric and Oceanic Science Letters*, **8**, 257–263, <https://doi.org/10.3878/AOSL20150022>.
- Francis, J. A., and B. Y. Wu, 2020: Why has no new record-minimum Arctic sea-ice extent occurred since September 2012? *Environmental Research Letters*, **15**, 114034, <https://doi.org/10.1088/1748-9326/abc047>.
- Fu, Y., C. Z. Wang, P. Brandt, and R. J. Greatbatch, 2019: Interannual variability of Antarctic intermediate water in the tropical North Atlantic. *J. Geophys. Res.: Oceans*, **124**, 4044–4057, <https://doi.org/10.1029/2018JC014878>.
- Gao, C. C., Y. Lu, Z. Z. Zhang, and H. L. Shi, 2019a: A joint inversion estimate of Antarctic ice sheet mass balance using multi-geodetic data sets. *Remote Sensing*, **11**, 653, <https://doi.org/10.3390/rs11060653>.
- Gao, C.-C., Y. Lu, Z.-Z. Zhang, H.-L. Shi, and C.-D. Zhu, 2015: Ice sheet mass balance in Antarctica measured by GRACE and its uncertainty. *Chinese Journal of Geophysics*, **58**, 780–792, <https://doi.org/10.6038/cjg20150308>. (in Chinese with English abstract)
- Gao, C. C., Y. Lu, H. L. Shi, Z. Z. Zhang, C. Y. Xu, and B. Tan, 2019b: Detection and analysis of ice sheet mass changes over 27 Antarctic drainage systems from GRACE RL06 data. *Chinese Journal of Geophysics*, **62**, 864–882, <https://doi.org/10.6038/cjg2019M0586>. (in Chinese with English abstract)
- Gao, L. B., S. R. Rintoul, and W. D. Yu, 2018: Recent wind-driven change in Subantarctic Mode Water and its impact on ocean heat storage. *Nature Climate Change*, **8**, 58–63, <https://doi.org/10.1038/s41558-017-0022-8>.
- Geng, Y.-F., S.-P. Xie, X.-T. Zheng, S.-M. Long, S. M. Kang, X. P. Lin, and Z.-H. Song, 2022: CMIP6 intermodel spread in interhemispheric asymmetry of tropical climate response to greenhouse warming: Extratropical ocean effects. *J. Climate*, **35**, 4869–4882, <https://doi.org/10.1175/JCLI-D-21-0541.1>.
- Gong, D. Y., D. Guo, R. Mao, J. Yang, Y. Q. Gao, and S. J. Kim, 2016: Interannual modulation of East African early short rains by the winter Arctic Oscillation. *J. Geophys. Res.: Atmos.*, **121**, 9441–9457, <https://doi.org/10.1002/2016JD025277>.
- Gong, D.-Y., and Coauthors, 2017: Boreal winter Arctic Oscillation as an indicator of summer SST anomalies over the western tropical Indian Ocean. *Climate Dyn.*, **48**, 2471–2488, <https://doi.org/10.1007/s00382-016-3216-2>.
- Gong, H. N., L. Wang, W. Chen, and D. Nath, 2018: Multidecadal fluctuation of the wintertime Arctic oscillation pattern and its implication. *J. Climate*, **31**, 5595–5608, <https://doi.org/10.1175/JCLI-D-17-0530.1>.
- Granskog, M. A., P. Assmy, and N. Koç, 2020: Emerging traits of sea ice in the atlantic sector of the Arctic. *Climate Change and the White World*, P. S. Goel, R. Ravindra, and S. Chattopadhyay, Eds., Springer, 3–10, [https://doi.org/10.1007/978-3-030-21679-5\\_1](https://doi.org/10.1007/978-3-030-21679-5_1).
- Gu, S., Y. Zhang, Q. G. Wu, and X. Q. Yang, 2018: The linkage between Arctic sea ice and midlatitude weather: In the perspective of energy. *J. Geophys. Res.: Atmos.*, **123**, 11 536–11 550, <https://doi.org/10.1029/2018JD028743>.
- Guan, W. N., X. N. Jiang, X. J. Ren, G. Chen, and Q. H. Ding, 2020: Role of atmospheric variability in driving the “warm-arctic, cold-continent” pattern over the North America sector and sea ice variability over the Chukchi-Bering sea. *Geophys. Res. Lett.*, **47**, e2020GL088599, <https://doi.org/10.1029/2020GL088599>.
- Guo, G. J., J. X. Shi, and Y. T. Jiao, 2016: Turbulent mixing in the upper ocean of the northwestern Weddell Sea, Antarctica. *Acta Oceanologica Sinica*, **35**, 1–9, <https://doi.org/10.1007/s13131-016-0816-y>.
- Guo, G. J., L. B. Gao, and J. X. Shi, 2020: Modulation of dense shelf water salinity variability in the western Ross Sea associated with the Amundsen Sea Low. *Environmental Research Letters*, **16**, 014004, <https://doi.org/10.1088/1748-9326/abc995>.



- Guo, G. J., J. X. Shi, L. B. Gao, T. Tamura, and G. D. Williams, 2019: Reduced sea ice production due to upwelled oceanic heat flux in Prydz Bay, East Antarctica. *Geophys. Res. Lett.*, **46**, 4782–4789, <https://doi.org/10.1029/2018GL081463>.
- Hall, D. K., J. C. Comiso, N. E. DiGirolamo, C. A. Shuman, J. E. Box, and L. S. Koenig, 2013: Variability in the surface temperature and melt extent of the Greenland ice sheet from MODIS. *Geophys. Res. Lett.*, **40**, 2114–2120, <https://doi.org/10.1002/grl.50240>.
- He, S. P., H. J. Wang, Y. Q. Gao, and F. Li, 2019: Recent intensified impact of December Arctic Oscillation on subsequent January temperature in Eurasia and North Africa. *Climate Dyn.*, **52**, 1077–1094, <https://doi.org/10.1007/s00382-018-4182-7>.
- Hou, S. S., and J. X. Shi, 2021: Variability and formation mechanism of polynyas in Eastern Prydz Bay, Antarctica. *Remote Sensing*, **13**, 5089, <https://doi.org/10.3390/rs13245089>.
- Hou, Y. R., and Coauthors, 2022: A surface temperature dipole pattern between Eurasia and North America triggered by the Barents–Kara sea-ice retreat in boreal winter. *Environmental Research Letters*, **17**, 114047, <https://doi.org/10.1088/1748-9326/ac9ecd>.
- Hu, A. X., G. A. Meehl, W. Q. Han, and J. J. Yin, 2011: Effect of the potential melting of the Greenland Ice Sheet on the Meridional Overturning Circulation and global climate in the future. *Deep Sea Research Part II: Topical Studies in Oceanography*, **58**, 1914–1926, <https://doi.org/10.1016/j.dsr2.2010.10.069>.
- Hu, C. D., S. Yang, Q. G. Wu, Z. N. Li, J. W. Chen, K. Q. Deng, T. T. Zhang, and C. Y. Zhang, 2016: Shifting El Niño inhibits summer Arctic warming and Arctic sea-ice melting over the Canada Basin. *Nature Communications*, **7**, 11721, <https://doi.org/10.1038/ncomms11721>.
- Hu, D. Z., Z. Y. Guan, W. S. Tian, and R. C. Ren, 2018: Recent strengthening of the stratospheric Arctic vortex response to warming in the central North Pacific. *Nature Communications*, **9**, 1697, <https://doi.org/10.1038/s41467-018-04138-3>.
- Hu, D. Z., Z. Y. Guan, M. C. Liu, and W. H. Feng, 2022a: Dynamical mechanisms for the recent ozone depletion in the Arctic stratosphere linked to North Pacific sea surface temperatures. *Climate Dyn.*, **58**, 2663–2679, <https://doi.org/10.1007/s00382-021-06026-x>.
- Hu, D. Z., Z. Y. Guan, Y. P. Guo, C. H. Lu, and D. C. Jin, 2019: Dynamical connection between the stratospheric Arctic vortex and sea surface temperatures in the North Atlantic. *Climate Dyn.*, **53**, 6979–6993, <https://doi.org/10.1007/s00382-019-04971-2>.
- Hu, Y. H., W. S. Tian, J. K. Zhang, T. Wang, and M. Xu, 2022b: Weakening of Antarctic stratospheric planetary wave activities in early austral spring since the early 2000s: A response to sea surface temperature trends. *Atmospheric Chemistry and Physics*, **22**, 1575–1600, <https://doi.org/10.5194/acp-22-1575-2022>.
- Huai, B. J., M. R. van den Broeke, and C. H. Reijmer, 2020: Long-term surface energy balance of the western Greenland Ice Sheet and the role of large-scale circulation variability. *The Cryosphere*, **14**, 4181–4199, <https://doi.org/10.5194/tc-14-4181-2020>.
- Huai, B. J., M. R. van den Broeke, C. H. Reijmer, and J. Cappellen, 2021: Quantifying rainfall in Greenland: A combined observational and modeling approach. *J. Appl. Meteorol. Climatol.*, **60**, 1171–1188, <https://doi.org/10.1175/JAMC-D-20-0284.1>.
- Huai, B. J., M. R. van den Broeke, C. H. Reijmer, and B. Noël, 2022: A daily, 1-km resolution Greenland rainfall climatology (1958–2020) from statistical downscaling of a regional atmospheric climate model. *J. Geophys. Res.: Atmos.*, **127**, e2022JD036688, <https://doi.org/10.1029/2022JD036688>.
- Huang, J. L., P. Hitchcock, A. C. Maycock, C. M. McKenna, and W. S. Tian, 2021a: Northern hemisphere cold air outbreaks are more likely to be severe during weak polar vortex conditions. *Communications Earth & Environment*, **2**, 147, <https://doi.org/10.1038/s43247-021-00215-6>.
- Huang, W., Y. Y. Yu, Z. C. Yin, H. S. Chen, and M. Gao, 2021b: Appreciable role of stratospheric polar vortex in the abnormal diffusion of air pollutant in North China in 2015/2016 winter and implications for prediction. *Atmospheric Environment*, **259**, 118549, <https://doi.org/10.1016/J.ATMOSENV.2021.118549>.
- Hui, F. M., T. C. Zhao, X. Q. Li, M. Shokr, P. Heil, J. C. Zhao, L. Zhang, and X. Cheng, 2017a: Satellite-based sea ice navigation for Prydz Bay, East Antarctica. *Remote Sensing*, **9**, 518, <https://doi.org/10.3390/rs9060518>.
- Hui, F. M., and Coauthors, 2017b: AntarcticaLC2000: The new Antarctic land cover database for the year 2000. *Science China Earth Sciences*, **60**, 686–696, <https://doi.org/10.1007/s11430-016-0029-2>.
- Hwang, Y. T., S. P. Xie, C. Deser, and S. M. Kang, 2017: Connecting tropical climate change with Southern Ocean heat uptake. *Geophys. Res. Lett.*, **44**, 9449–9457, <https://doi.org/10.1002/2017GL074972>.
- Ji, L. Q., and K. Fan, 2019a: Interannual linkage between wintertime sea-ice cover variability over the Barents Sea and springtime vegetation over Eurasia. *Climate Dyn.*, **53**, 5637–5652, <https://doi.org/10.1007/s00382-019-04884-0>.
- Ji, L. Q., and K. Fan, 2019b: Climate prediction of dust weather frequency over northern China based on sea-ice cover and vegetation variability. *Climate Dyn.*, **53**, 687–705, <https://doi.org/10.1007/s00382-018-04608-w>.
- Jiang, S. Y., H. B. Hu, W. Perrie, N. Zhang, H. K. Bai, and Y. H. Zhao, 2022: Different climatic effects of the Arctic and Antarctic ice covers on land surface temperature in the Northern Hemisphere: Application of Liang-Kleeman information flow method and CAM4.0. *Climate Dyn.*, **58**, 1237–1255, <https://doi.org/10.1007/s00382-021-05961-z>.
- Jin, S. G., and G. P. Feng, 2016: Uncertainty of grace-estimated land water and glaciers contributions to sea level change during 2003–2012. Preprints, 2016 IEEE International Geoscience and Remote Sensing Symposium (IGARSS), Beijing, China, IEEE, 6189–6192, <https://doi.org/10.1109/IGARSS.2016.7730617>.
- Lei, R. B., and Z. X. Wei, 2020: Exploring the Arctic Ocean under Arctic amplification. *Acta Oceanologica Sinica*, **39**, 1–4, <https://doi.org/10.1007/s13131-020-1642-9>.
- Lei, R. B., Z. J. Li, J. M. Qin, and Y. F. Cheng, 2009: Investigation of new technologies for in-situ ice thickness observation. *Advances in Water Science*, **20**, 287–292, <https://doi.org/10.3321/j.issn:1001-6791.2009.02.021>. (in Chinese with English abstract)
- Lei, R. B., X. Tian-Kunze, M. Leppäranta, J. Wang, L. Kaleschke, and Z. H. Zhang, 2016: Changes in summer sea ice, albedo, and partitioning of surface solar radiation in the Pacific sector of Arctic Ocean during 1982–2009. *J. Geophys. Res.: Oceans*, **121**, 5470–5486, <https://doi.org/10.1002/2016JCO11831>.

- Lei, R. B., X. Tian-Kunze, B. R. Li, P. Heil, J. Wang, J. B. Zeng, and Z. X. Tian, 2017: Characterization of summer Arctic sea ice morphology in the 135°–175°W sector using multi-scale methods. *Cold Regions Science and Technology*, **133**, 108–120, <https://doi.org/10.1016/j.coldregions.2016.10.009>.
- Lei, R. B., and Coauthors, 2022: Seasonality and timing of sea ice mass balance and heat fluxes in the Arctic transpolar drift during 2019–2020. *Elementa: Science of the Anthropocene*, **10**, 000089, <https://doi.org/10.1525/elementa.2021.000089>.
- Li, F., L.-X. Yuan, S.-K. Zhang, Y.-D. Yang, D. C. E., and W.-F. Hao, 2016: Mass change of the Antarctic ice sheet derived from ICESat laser altimetry. *Chinese Journal of Geophysics*, **59**, 93–100, <https://doi.org/10.6038/cjg20160108>. (in Chinese with English abstract)
- Li, J., J. C. Zuo, M. X. Chen, W. Tan, and Y. Q. Yang, 2013: Assessing the global averaged sea-level budget from 2003 to 2010. *Acta Oceanologica Sinica*, **32**, 16–23, <https://doi.org/10.1007/s13131-013-0361-x>.
- Li, J., K. Fan, J. J. Xu, A. M. Powell, and F. Kogan, 2017a: The effect of preceding wintertime Arctic polar vortex on springtime NDVI patterns in boreal Eurasia, 1982–2015. *Climate Dyn.*, **49**, 23–35, <https://doi.org/10.1007/s00382-016-3324-z>.
- Li, R. X., Y. Cheng, H. T. Cui, M. L. Xia, X. H. Yuan, Z. Li, S. L. Luo, and G. Qiao, 2022: Overestimation and adjustment of Antarctic ice flow velocity fields reconstructed from historical satellite imagery. *The Cryosphere*, **16**, 737–760, <https://doi.org/10.5194/tc-16-737-2022>.
- Li, S. J., W. J. Cai, and L. X. Wu, 2020a: Attenuated interannual variability of austral winter Antarctic sea ice over recent decades. *Geophys. Res. Lett.*, **47**, e2020GL090590, <https://doi.org/10.1029/2020GL090590>.
- Li, S. J., W. J. Cai, and L. X. Wu, 2021a: Weakened Antarctic dipole under global warming in CMIP6 models. *Geophys. Res. Lett.*, **48**, e2021GL094863, <https://doi.org/10.1029/2021GL094863>.
- Li, T., Y. Liu, and X. Cheng, 2020b: Recent and imminent calving events do little to impair Amery ice shelf's stability. *Acta Oceanologica Sinica*, **39**, 168–170, <https://doi.org/10.1007/s13131-020-1600-6>.
- Li, T., Y. Liu, T. Li, F. M. Hui, Z. Q. Chen, and X. Cheng, 2018: Antarctic surface ice velocity retrieval from MODIS-based mosaic of Antarctica (MOA). *Remote Sensing*, **10**, 1045, <https://doi.org/10.3390/rs10071045>.
- Li, T., and Coauthors, 2019a: Resolving fine-scale surface features on polar sea ice: A first assessment of UAS photogrammetry without ground control. *Remote Sensing*, **11**, 784, <https://doi.org/10.3390/rs11070784>.
- Li, X. C., D. M. Holland, E. P. Gerber, and C. Yoo, 2014: Impacts of the north and tropical Atlantic Ocean on the Antarctic Peninsula and sea ice. *Nature*, **505**, 538–542, <https://doi.org/10.1038/nature12945>.
- Li, X. C., E. P. Gerber, D. M. Holland, and C. Yoo, 2015a: A Rossby wave bridge from the tropical Atlantic to West Antarctica. *J. Climate*, **28**, 2256–2273, <https://doi.org/10.1175/JCLI-D-14-00450.1>.
- Li, X. C., D. M. Holland, E. P. Gerber, and C. Yoo, 2015b: Rossby waves mediate impacts of tropical oceans on West Antarctic atmospheric circulation in austral winter. *J. Climate*, **28**, 8151–8164, <https://doi.org/10.1175/JCLI-D-15-0113.1>.
- Li, X. C., and Coauthors, 2021b: Tropical teleconnection impacts on Antarctic climate changes. *Nature Reviews Earth & Environment*, **2**, 680–698, <https://doi.org/10.1038/S43017-021-00204-5>.
- Li, X. W., X. D. Wang, C. Wang, and L. Zhang, 2017b: Antarctic snow melt detection based on the synergy of SSM/I and QuikSCAT. *Antarctic Science*, **29**, 561–568, <https://doi.org/10.1017/S0954102017000268>.
- Li, X. X., Z. W. Wu, and Y. J. Li, 2019b: A link of China warming hiatus with the winter sea ice loss in Barents–Kara Seas. *Climate Dyn.*, **53**, 2625–2642, <https://doi.org/10.1007/s00382-019-04645-z>.
- Li, Z. Y., W. J. Zhang, M. F. Stuecker, H. M. Xu, F.-F. Jin, and C. Liu, 2019c: Different effects of two ENSO types on Arctic surface temperature in boreal winter. *J. Climate*, **32**, 4943–4961, <https://doi.org/10.1175/JCLI-D-18-0761.1>.
- Liang, Y., H. B. Bi, H. J. Huang, R. B. Lei, X. Liang, B. Cheng, and Y. H. Wang, 2022: Contribution of warm and moist atmospheric flow to a record minimum July sea ice extent of the Arctic in 2020. *The Cryosphere*, **16**, 1107–1123, <https://doi.org/10.5194/tc-16-1107-2022>.
- Liao, S. T., H. Luo, J. F. Wang, Q. Shi, J. L. Zhang, and Q. H. Yang, 2022: An evaluation of Antarctic sea-ice thickness from the Global Ice-Ocean Modeling and Assimilation System based on in situ and satellite observations. *The Cryosphere*, **16**, 1807–1819, <https://doi.org/10.5194/TC-16-1807-2022>.
- Liao, Z. L., and Coauthors, 2019: Snow depth and ice thickness derived from SIMBA ice mass balance buoy data using an automated algorithm. *International Journal of Digital Earth*, **12**, 962–979, <https://doi.org/10.1080/17538947.2018.1545877>.
- Lin, J. T., C. H. Lin, P. K. Rajesh, J. Yue, C. Y. Lin, and T. Matsuo, 2020: Local-time and vertical characteristics of quasi-6-day oscillation in the ionosphere during the 2019 Antarctic sudden stratospheric warming. *Geophys. Res. Lett.*, **47**, e2020GL090345, <https://doi.org/10.1029/2020GL090345>.
- Liu, B., B. Wang, J. Liu, D. L. Chen, L. Ning, M. Yan, W. Y. Sun, and K. F. Chen, 2020a: Global and polar region temperature change induced by single mega volcanic eruption based on community earth system model simulation. *Geophys. Res. Lett.*, **47**, e2020GL089416, <https://doi.org/10.1029/2020GL089416>.
- Liu, F. K., Y. Y. Luo, J. Lu, and X. Q. Wan, 2021a: The role of ocean dynamics in the cross-equatorial energy transport under a thermal forcing in the southern ocean. *Adv. Atmos. Sci.*, **38**, 1737–1749, <https://doi.org/10.1007/s00376-021-1099-6>.
- Liu, J., and Coauthors, 2020b: Impact of Arctic amplification on declining spring dust events in East Asia. *Climate Dyn.*, **54**, 1913–1935, <https://doi.org/10.1007/s00382-019-05094-4>.
- Liu, J. P., Z. Q. Chen, J. Francis, M. R. Song, T. Mote, and Y. Y. Hu, 2016: Has arctic sea ice loss contributed to increased surface melting of the Greenland ice sheet? *J. Climate*, **29**, 3373–3386, <https://doi.org/10.1175/JCLI-D-15-0391.1>.
- Liu, Y., X. Cheng, F. M. Hui, X. W. Wang, F. Wang, and C. Cheng, 2014: Detection of crevasses over polar ice shelves using Satellite Laser Altimeter. *Science China Earth Sciences*, **57**, 1267–1277, <https://doi.org/10.1007/s11430-013-4796-x>.
- Liu, Y., J. C. Moore, X. Cheng, R. M. Gladstone, J. N. Bassis, H. X. Liu, J. H. Wen, and F. M. Hui, 2015: Ocean-driven thinning



- enhances iceberg calving and retreat of Antarctic ice shelves. *Proceedings of the National Academy of Sciences of the United States of America*, **112**, 3263–3268, <https://doi.org/10.1073/pnas.1415137112>.
- Liu, Y. G., R. Hallberg, O. Sergienko, B. L. Samuels, M. Harrison, and M. Oppenheimer, 2018: Climate response to the melt-water runoff from Greenland ice sheet: Evolving sensitivity to discharging locations. *Climate Dyn.*, **51**, 1733–1751, <https://doi.org/10.1007/s00382-017-3980-7>.
- Liu, Y. S., C. Sun, Z. Q. Gong, J. P. Li, and Z. Shi, 2022: Multi-decadal seesaw in cold wave frequency between central Eurasia and Greenland and its relation to the Atlantic Multidecadal Oscillation. *Climate Dyn.*, **58**, 1403–1418, <https://doi.org/10.1007/s00382-021-05967-7>.
- Liu, Z. F., and Coauthors, 2021b: Acceleration of western Arctic sea ice loss linked to the Pacific North American pattern. *Nature Communications*, **12**, 1519, <https://doi.org/10.1038/s41467-021-21830-z>.
- Lu, Q., J. Rao, D. Guo, M. Yu, and Y. Y. Yu, 2021: Downward propagation of sudden stratospheric warming signals and the local environment in the Beijing-Tianjin-Hebei region: A comparative study of the 2018 and 2019 winter cases. *Atmospheric Research*, **254**, 105514, <https://doi.org/10.1016/j.atmosres.2021.105514>.
- Luo, B. L., L. X. Wu, D. H. Luo, A. G. Dai, and I. Simmonds, 2019: The winter midlatitude-Arctic interaction: Effects of North Atlantic SST and high-latitude blocking on Arctic sea ice and Eurasian cooling. *Climate Dyn.*, **52**, 2981–3004, <https://doi.org/10.1007/s00382-018-4301-5>.
- Luo, D. H., X. D. Chen, A. G. Dai, and I. Simmonds, 2018: Changes in atmospheric blocking circulations linked with winter Arctic warming: A new perspective. *J. Climate*, **31**, 7661–7678, <https://doi.org/10.1175/JCLI-D-18-0040.1>.
- Luo, D. H., Y. Q. Xiao, Y. Yao, A. G. Dai, I. Simmonds, and C. L. F. Franzke, 2016: Impact of Ural blocking on winter warm Arctic-cold Eurasian anomalies. Part I: Blocking-induced amplification. *J. Climate*, **29**, 3925–3947, <https://doi.org/10.1175/JCLI-D-15-0611.1>.
- Luo, D. H., Y. N. Chen, A. G. Dai, M. Mu, R. H. Zhang, and S. Ian, 2017: Winter Eurasian cooling linked with the Atlantic multidecadal oscillation. *Environmental Research Letters*, **12**, 125002, <https://doi.org/10.1088/1748-9326/aa8de8>.
- Luo, R., Q. H. Ding, Z. W. Wu, I. Baxter, M. Bushuk, Y. Y. Huang, and X. Q. Dong, 2021: Summertime atmosphere-sea ice coupling in the Arctic simulated by CMIP5/6 models: Importance of large-scale circulation. *Climate Dyn.*, **56**, 1467–1485, <https://doi.org/10.1007/s00382-020-05543-5>.
- Luo, X., and T. Lin, 2023: A Semi-Empirical Framework for ice sheet response analysis under Oceanic forcing in Antarctica and Greenland. *Climate Dyn.*, **60**, 213–226, <https://doi.org/10.1007/s00382-022-06317-x>.
- Ma, J., W. Chen, D. Nath, and X. Q. Lan, 2020a: Modulation by ENSO of the relationship between stratospheric sudden warming and the Madden-Julian oscillation. *Geophys. Res. Lett.*, **47**, e2020GL088894, <https://doi.org/10.1029/2020GL088894>.
- Ma, L. B., B. Wang, and J. Cao, 2020b: Impacts of atmosphere-sea ice-ocean interaction on Southern Ocean deep convection in a climate system model. *Climate Dyn.*, **54**, 4075–4093, <https://doi.org/10.1007/s00382-020-05218-1>.
- Ma, S. M., and C. W. Zhu, 2020: Opposing trends of winter cold extremes over Eastern Eurasia and North America under recent Arctic warming. *Adv. Atmos. Sci.*, **37**, 1417–1434, <https://doi.org/10.1007/s00376-020-0070-2>.
- Ma, X. F., W. Liu, R. J. Allen, G. Huang, and X. C. Li, 2020c: Dependence of regional ocean heat uptake on anthropogenic warming scenarios. *Science Advances*, **6**, eabc0303, <https://doi.org/10.1126/sciadv.abc0303>.
- Minghu, D., X. Cunde, L. Yuansheng, R. Jiawen, H. Shugui, J. Bo, and S. Bo, 2011: Spatial variability of surface mass balance along a traverse route from Zhongshan station to Dome A, Antarctica. *J. Glaciol.*, **57**, 658–666, <https://doi.org/10.3189/002214311797409820>.
- Overland, J. E., K. R. Wood, and M. Y. Wang, 2011: Warm Arctic—cold continents: Climate impacts of the newly open Arctic Sea. *Polar Research*, **30**, 15787, <https://doi.org/10.3402/polar.v30i0.15787>.
- Qi, D., and Coauthors, 2017: Increase in acidifying water in the western Arctic Ocean. *Nature Climate Change*, **7**, 195–199, <https://doi.org/10.1038/nclimate3228>.
- Qi, D., and Coauthors, 2020a: Coastal acidification induced by biogeochemical processes driven by sea-ice melt in the western Arctic ocean. *Polar Science*, **23**, 100504, <https://doi.org/10.1016/j.polar.2020.100504>.
- Qi, D., and Coauthors, 2022a: Climate change drives rapid decadal acidification in the Arctic Ocean from 1994 to 2020. *Science*, **377**, 1544–1550, <https://doi.org/10.1126/science.abc0383>.
- Qi, D., and Coauthors, 2022b: Rapid acidification of the Arctic Chukchi Sea waters driven by anthropogenic forcing and biological carbon recycling. *Geophys. Res. Lett.*, **49**, e2021GL097246, <https://doi.org/10.1029/2021GL097246>.
- Qi, M. Z., Y. Liu, Y. J. Lin, F. M. Hui, T. Li, and X. Cheng, 2020b: Efficient location and extraction of the iceberg calved areas of the Antarctic ice shelves. *Remote Sensing*, **12**, 2658, <https://doi.org/10.3390/rs12162658>.
- Qi, M. Z., Y. Liu, J. P. Liu, X. Cheng, Y. J. Lin, Q. Y. Feng, Q. Shen, and Z. T. Yu, 2021: A 15-year circum-Antarctic iceberg calving dataset derived from continuous satellite observations. *Earth System Science Data*, **13**, 4583–4601, <https://doi.org/10.5194/essd-13-4583-2021>.
- Qian, W. H., K. J. Wu, J. C. H. Leung, and J. Shi, 2016: Long-term trends of the Polar and Arctic cells influencing the Arctic climate since 1989. *J. Geophys. Res.: Atmos.*, **121**, 2679–2690, <https://doi.org/10.1002/2015JD024252>.
- Qin, J. H., X. H. Cheng, C. C. Yang, N. S. Ou, and X. Q. Xiong, 2022: Mechanism of interannual variability of ocean bottom pressure in the South Pacific. *Climate Dyn.*, 2103–2116, <https://doi.org/10.1007/S00382-022-06198-0>.
- Ran, J. J., P. Ditmar, L. Liu, Y. Xiao, R. Klees, and X. Y. Tang, 2021: Analysis and mitigation of biases in Greenland ice sheet mass balance trend estimates from GRACE mascon products. *J. Geophys. Res.: Solid Earth*, **126**, e2020JB020880, <https://doi.org/10.1029/2020JB020880>.
- Rao, J., and R. C. Ren, 2020: Modeling study of the destructive interference between the tropical Indian Ocean and eastern Pacific in their forcing in the southern winter extratropical stratosphere during ENSO. *Climate Dyn.*, **54**, 2249–2266, <https://doi.org/10.1007/s00382-019-05111-6>.
- Rao, J., C. I. Garfinkel, I. P. White, and C. Schwartz, 2020: The Southern Hemisphere minor sudden stratospheric warming in September 2019 and its predictions in S2S models. *J. Geophys. Res.: Atmos.*, **125**, e2020JD032723, <https://doi.org/10.1029/2020JD032723>.

- 1029/2020JD032723.
- Rao, J., C. I. Garfinkel, T. W. Wu, Y. X. Lu, Q. Lu, and Z. Q. Liang, 2021: The January 2021 sudden stratospheric warming and its prediction in subseasonal to seasonal models. *J. Geophys. Res.: Atmos.*, **126**, e2021JD035057, <https://doi.org/10.1029/2021JD035057>.
- Ren, J. W., 2002: Mass Balance in the Lambert Glacier Basin and Variability of the Antarctic Ice Sheet. *Progr. Natur. Sci.*, **12**, 1064–1069.
- Ruan, R. M., and Coauthors, 2019: Decelerated Greenland Ice Sheet melt driven by positive summer North Atlantic oscillation. *J. Geophys. Res.: Atmos.*, **124**, 7633–7646, <https://doi.org/10.1029/2019JD030689>.
- Shen, X. C., L. Wang, and S. Osprey, 2020a: Tropospheric forcing of the 2019 Antarctic sudden stratospheric warming. *Geophys. Res. Lett.*, **47**, e2020GL089343, <https://doi.org/10.1029/2020GL089343>.
- Shen, X. C., L. Wang, and S. Osprey, 2020b: The Southern Hemisphere sudden stratospheric warming of September 2019. *Science Bulletin*, **65**, 1800–1802, <https://doi.org/10.1016/j.scib.2020.06.028>.
- Shen, X. C., L. Wang, S. Osprey, S. C. Hardiman, A. A. Scaife, and J. Ma, 2022a: The life cycle and variability of Antarctic weak Polar vortex events. *J. Climate*, **35**, 2075–2092, <https://doi.org/10.1175/JCLI-D-21-0500.1>.
- Shen, Z. L., A. M. Duan, D. L. Li, and J. X. Li, 2022b: Quantifying the contribution of internal atmospheric drivers to near-term projection uncertainty in September Arctic Sea Ice. *J. Climate*, **35**, 3427–3443, <https://doi.org/10.1175/JCLI-D-21-0579.1>.
- Shu, Q., Q. Wang, Z. Y. Song, and F. L. Qiao, 2021: The poleward enhanced Arctic Ocean cooling machine in a warming climate. *Nature Communications*, **12**, 2966, <https://doi.org/10.1038/S41467-021-23321-7>.
- Shu, Q., F. L. Qiao, Z. Y. Song, J. C. Zhao, and X. F. Li, 2018: Projected freshening of the Arctic Ocean in the 21st century. *J. Geophys. Res.: Oceans*, **123**, 9232–9244, <https://doi.org/10.1029/2018JC014036>.
- Shu, Q., Q. Wang, J. Su, X. Li, and F. L. Qiao, 2019: Assessment of the Atlantic water layer in the Arctic Ocean in CMIP5 climate models. *Climate Dyn.*, **53**, 5279–5291, <https://doi.org/10.1007/s00382-019-04870-6>.
- Shi, Q., Q. H. Yang, L. J. Mu, J. F. Wang, F. Massonnet, and M. R. Mazloff, 2021a: Evaluation of sea-ice thickness from four reanalyses in the Antarctic Weddell Sea. *The Cryosphere*, **15**, 31–47, <https://doi.org/10.5194/tc-15-31-2021>.
- Shu, Q., Q. Wang, Z. Y. Song, F. L. Qiao, J. C. Zhao, M. Chu, and X. F. Li, 2020: Assessment of sea ice extent in CMIP6 with comparison to observations and CMIP5. *Geophys. Res. Lett.*, **47**, e2020GL087965, <https://doi.org/10.1029/2020GL087965>.
- Shi, Q., J. Su, G. Heygster, J. X. Shi, L. Z. Wang, L. Z. Zhu, Q. L. Lou, and V. Ludwig, 2021b: Step-by-step validation of Antarctic ASI AMSR-E sea-ice concentrations by MODIS and an aerial image. *IEEE Trans. Geosci. Remote Sens.*, **59**, 392–403, <https://doi.org/10.1109/tgrs.2020.2989037>.
- Song, L., and R. G. Wu, 2022: Different processes of occurrence of cold events over East Asia in El Niño and La Niña winters. *Climate Dyn.*, **58**, 3139–3154, <https://doi.org/10.1007/S00382-021-06082-3>.
- Song, X. Z., 2020: Explaining the zonal asymmetry in the air-sea net heat flux climatology over the Antarctic Circumpolar Current. *J. Geophys. Res.: Oceans*, **125**, e2020JC016215, <https://doi.org/10.1029/2020JC016215>.
- Song, Y. J., F. L. Qiao, J. P. Liu, Q. Shu, Y. Bao, M. Wei, and Z. Y. Song, 2022: Effects of sea spray on large-scale climatic features over the Southern Ocean. *J. Climate*, **35**, 4645–4663, <https://doi.org/10.1175/JCLI-D-21-0608.1>.
- Sun, B., and Coauthors, 2009: The Gamburtsev mountains and the origin and early evolution of the Antarctic Ice Sheet. *Nature*, **459**, 690–693, <https://doi.org/10.1038/nature08024>.
- Sun, C. H., S. Yang, W. J. Li, R. N. Zhang, and R. G. Wu, 2016a: Interannual variations of the dominant modes of East Asian winter monsoon and possible links to Arctic sea ice. *Climate Dyn.*, **47**, 481–496, <https://doi.org/10.1007/s00382-015-2851-3>.
- Sun, L. T., J. Perlwitz, and M. Hoerling, 2016b: What caused the recent “Warm Arctic, Cold Continents” trend pattern in winter temperatures? *Geophys. Res. Lett.*, **43**, 5345–5352, <https://doi.org/10.1002/2016GL069024>.
- Sun, Q. Z., T. Vihma, M. O. Jonassen, and Z. H. Zhang, 2020: Impact of assimilation of radiosonde and UAV observations from the Southern Ocean in the Polar WRF Model. *Adv. Atmos. Sci.*, **37**, 441–454, <https://doi.org/10.1007/s00376-020-9213-8>.
- Sung, M.-K., S.-W. Son, C. Yoo, J. Hwang, and S.-I. An, 2021: Seesawing of winter temperature extremes between East Asia and North America. *J. Climate*, **34**, 4423–4434, <https://doi.org/10.1175/JCLI-D-20-0789.1>.
- Swart, N. C., S. T. Gille, J. C. Fyfe, and N. P. Gillett, 2018: Recent Southern Ocean warming and freshening driven by greenhouse gas emissions and ozone depletion. *Nature Geoscience*, **11**, 836–841, <https://doi.org/10.1038/s41561-018-0226-1>.
- Thompson, D. W. J., S. Solomon, P. J. Kushner, M. H. England, K. M. Grise, and D. J. Karoly, 2011: Signatures of the Antarctic ozone hole in Southern Hemisphere surface climate change. *Nature Geoscience*, **4**, 741–749, <https://doi.org/10.1038/ngeo1296>.
- Tian, W. S., and Coauthors, 2017: The relationship between lower-stratospheric ozone at southern high latitudes and sea surface temperature in the East Asian marginal seas in austral spring. *Atmospheric Chemistry and Physics*, **17**, 6705–6722, <https://doi.org/10.5194/acp-17-6705-2017>.
- Tu, Z. B., C. F. Le, Y. Bai, Z. P. Jiang, Y. X. Wu, Z. X. Ouyang, W. J. Cai, and D. Qi, 2021: Increase in CO<sub>2</sub> uptake capacity in the Arctic Chukchi Sea during summer revealed by satellite-based estimation. *Geophys. Res. Lett.*, **48**, e2021GL093844, <https://doi.org/10.1029/2021GL093844>.
- Turner, J., G. J. Marshall, K. Clem, S. Colwell, T. Phillips, and H. Lu, 2020: Antarctic temperature variability and change from station data. *International Journal of Climatology*, **40**, 2986–3007, <https://doi.org/10.1002/joc.6378>.
- Wang, F. Y., W. S. Tian, F. Xie, J. K. Zhang, and Y. Y. Han, 2018: Effect of Madden-Julian oscillation occurrence frequency on the interannual variability of Northern Hemisphere stratospheric wave activity in winter. *J. Climate*, **31**, 5031–5049, <https://doi.org/10.1175/JCLI-D-17-0476.1>.
- Wang, F. Y., Y. Y. Han, S. Y. Zhang, and R. H. Zhang, 2020a: Influence of stratospheric sudden warming on the tropical intraseasonal convection. *Environmental Research Letters*, **15**, 084027, <https://doi.org/10.1088/1748-9326/ab98b5>.
- Wang, G. J., and Coauthors, 2022a: Future Southern Ocean warming linked to projected ENSO variability. *Nature Climate*

- Change*, **12**, 649–654, <https://doi.org/10.1038/s41558-022-01398-2>.
- Wang, H. J., and D. H. Luo, 2022: North Atlantic footprint of summer Greenland ice sheet melting on interannual to interdecadal time scales: A Greenland blocking perspective. *J. Climate*, **35**, 1939–1961, <https://doi.org/10.1175/JCLI-D-21-0382.1>.
- Wang, H., S. P. Xie, X. T. Zheng, Y. Kosaka, Y. Y. Xu, and Y. F. Geng, 2020b: Dynamics of Southern Hemisphere atmospheric circulation response to anthropogenic aerosol forcing. *Geophys. Res. Lett.*, **47**, e2020GL089919, <https://doi.org/10.1029/2020GL089919>.
- Wang, J. P., J. A. Church, X. B. Zhang, J. M. Gregory, L. Zanna, and X. Y. Chen, 2021a: Evaluation of the local sea-level budget at tide gauges since 1958. *Geophys. Res. Lett.*, **48**, e2021GL094502, <https://doi.org/10.1029/2021GL094502>.
- Wang, K. J., X. Cheng, Z. Q. Chen, F. M. Hui, Y. Liu, and Y. Tian, 2020c: Ocean contributes to the melting of the Jakobshavn Glacier front. *Science China Earth Sciences*, **63**, 405–411, <https://doi.org/10.1007/s11430-019-9394-6>.
- Wang, L., and M. Ting, 2022: Stratosphere-troposphere coupling leading to extended seasonal predictability of summer North Atlantic oscillation and boreal climate. *Geophys. Res. Lett.*, **49**, e2021GL096362, <https://doi.org/10.1029/2021GL096362>.
- Wang, L., S. C. Hardiman, P. E. Bett, R. E. Comer, C. Kent, and A. A. Scaife, 2020d: What chance of a sudden stratospheric warming in the southern hemisphere? *Environmental Research Letters*, **15**, 104038, <https://doi.org/10.1088/1748-9326/aba8c1>.
- Wang, S., and W. Chen, 2022: Impact of internal variability on recent opposite trends in wintertime temperature over the Barents–Kara Seas and central Eurasia. *Climate Dyn.*, **58**, 2941–2956, <https://doi.org/10.1007/S00382-021-06077-0>.
- Wang, S., M. H. Ding, G. Liu, and W. Chen, 2022b: Processes and mechanisms of persistent extreme rainfall events in the Antarctic Peninsula during Austral summer. *J. Climate*, **35**, 3643–3657, <https://doi.org/10.1175/JCLI-D-21-0834.1>.
- Wang, S., W. Chen, S. F. Chen, D. Nath, and L. Wang, 2020e: Anomalous winter moisture transport associated with the recent surface warming over the Barents–Kara seas region since the mid-2000s. *International Journal of Climatology*, **40**, 2497–2505, <https://doi.org/10.1002/joc.6337>.
- Wang, S., M. H. Ding, G. Liu, T. Wei, W. Q. Zhang, W. Chen, T. F. Dou, and C. D. Xiao, 2022c: On the drivers of temperature extremes on the Antarctic Peninsula during austral summer. *Climate Dyn.*, **59**, 2275–2291, <https://doi.org/10.1007/S00382-022-06209-0>.
- Wang, S., and Coauthors, 2017a: Climate characteristics in Ny-Ålesund, Arctic. *Journal of Glaciology and Geocryology*, **39**, 479–489, <https://doi.org/10.7522/j.issn.1000-0240.2017.0054>.
- Wang, S. Y., J. P. Liu, X. Cheng, T. Kerzenmacher, Y. Y. Hu, F. M. Hui, and P. Braesicke, 2021b: How do weakening of the stratospheric Polar Vortex in the southern hemisphere affect regional Antarctic sea ice extent? *Geophys. Res. Lett.*, **48**, e2021GL092582, <https://doi.org/10.1029/2021GL092582>.
- Wang, T., W. S. Tian, J. K. Zhang, M. Xu, T. Lian, D. Z. Hu, and K. Qie, 2022e: Surface ocean current variations in the North Pacific related to Arctic stratospheric ozone. *Climate Dyn.*, **59**, 3087–3111, <https://doi.org/10.1007/s00382-022-06271-8>.
- Wang, T. J., H. Wei, and J. G. Xiao, 2022d: Dynamic linkage between the interannual variability of the spring Ross Ice Shelf Polynya and the atmospheric circulation anomalies. *Climate Dyn.*, **58**, 831–840, <https://doi.org/10.1007/s00382-021-05936-0>.
- Wang, X., R. T. Chen, C. Li, Z. Q. Chen, F. M. Hui, and X. Cheng, 2022f: An intercomparison of satellite derived Arctic Sea Ice motion products. *Remote Sensing*, **14**, 1261, <https://doi.org/10.3390/rs14051261>.
- Wang, X. D., Z. K. Wu, and X. W. Li, 2019a: Near-surface snowmelt detection on the Greenland ice sheet from FengYun-3 MWRI data. *Cluster Computing*, **22**, 8301–8308, <https://doi.org/10.1007/s10586-018-1743-9>.
- Wang, X. Q., Z. R. Zhang, X. Z. Wang, T. Vihma, M. Zhou, L. J. Yu, P. Uotila, and D. V. Sein, 2021d: Impacts of strong wind events on sea ice and water mass properties in Antarctic coastal polynyas. *Climate Dyn.*, **57**, 3505–3528, <https://doi.org/10.1007/s00382-021-05878-7>.
- Wang, X. Y., J. P. Zhao, V. B. Lobanov, D. Kaplunenko, Y. N. Rudykh, Y. He, and X. Y. Chen, 2021c: Distribution and transport of water masses in the East Siberian Sea and their impacts on the Arctic Halocline. *J. Geophys. Res.: Oceans*, **126**, e2020JC016523, <https://doi.org/10.1029/2020JC016523>.
- Wang, Y., G. Huang, and K. M. Hu, 2020f: Internal variability in multidecadal trends of surface air temperature over antarctica in austral winter in model simulations. *Climate Dyn.*, **55**, 2835–2847, <https://doi.org/10.1007/s00382-020-05412-1>.
- Wang, Y. H., X. J. Yuan, H. B. Bi, Y. Liang, H. J. Huang, Z. H. Zhang, and Y. X. Liu, 2019c: The contributions of winter cloud anomalies in 2011 to the summer sea-ice rebound in 2012 in the Antarctic. *J. Geophys. Res.: Atmos.*, **124**, 3435–3447, <https://doi.org/10.1029/2018JD029435>.
- Wang, Y. T., S. G. Hou, M. H. Ding, and W. J. Sun, 2020g: On the performance of twentieth century reanalysis products for Antarctic snow accumulation. *Climate Dyn.*, **54**, 435–455, <https://doi.org/10.1007/s00382-019-05008-4>.
- Wang, Y. T., B. J. Huai, E. R. Thomas, M. R. van den Broeke, J. M. van Wessem, and E. Schlosser, 2019b: A new 200-year spatial reconstruction of West Antarctic surface mass balance. *J. Geophys. Res.: Atmos.*, **124**, 5282–5295, <https://doi.org/10.1029/2018JD029601>.
- Wang, Y. T., and Coauthors, 2017b: Snow accumulation variability over the West Antarctic Ice Sheet since 1900: A comparison of ice core records with ERA-20C reanalysis. *Geophys. Res. Lett.*, **44**, 11 482–11 490, <https://doi.org/10.1002/2017GL075135>.
- Wang, Z. M., J. Turner, Y. Wu, and C. Y. Liu, 2019d: Rapid decline of total Antarctic sea ice extent during 2014–16 controlled by wind-driven sea ice drift. *J. Climate*, **32**, 5381–5395, <https://doi.org/10.1175/JCLI-D-18-0635.1>.
- Wang, Z. M., Y. Wu, X. Lin, C. Y. Liu, and Z. L. Xie, 2017c: Impacts of open-ocean deep convection in the Weddell Sea on coastal and bottom water temperature. *Climate Dyn.*, **48**, 2967–2981, <https://doi.org/10.1007/s00382-016-3244-y>.
- Wei, T., B. Noël, M. H. Ding, and Q. Yan, 2022: Spatiotemporal variations of extreme events in surface mass balance over Greenland during 1958–2019. *International Journal of Climatology*, **42**, 8008–8023, <https://doi.org/10.1002/JOC.7689>.
- Wei, T., M. H. Ding, B. Y. Wu, C. G. Lu, and S. J. Wang, 2016: Variations in temperature-related extreme events (1975–2014) in Ny-Ålesund, Svalbard. *Atmos. Sci. Lett.*, **17**, 102–108, <https://doi.org/10.1002/asl.632>.



- Wen, Q., C. Y. Zhu, Z. X. Han, Z. Y. Liu, and H. J. Yang, 2021: Can the topography of Tibetan Plateau affect the Antarctic bottom water? *Geophys. Res. Lett.*, **48**, e2021GL092448, <https://doi.org/10.1029/2021GL092448>.
- Wu, B. Y., 2017: Winter atmospheric circulation anomaly associated with recent Arctic winter warm anomalies. *J. Climate*, **30**, 8469–8479, <https://doi.org/10.1175/JCLI-D-17-0175.1>.
- Wu, B. Y., and J. A. Francis, 2019: Summer Arctic cold anomaly dynamically linked to East Asian heat waves. *J. Climate*, **32**, 1137–1150, <https://doi.org/10.1175/JCLI-D-18-0370.1>.
- Wu, B. Y., and Z. K. Li, 2022: Possible impacts of anomalous Arctic sea ice melting on summer atmosphere. *International Journal of Climatology*, **42**, 1818–1827, <https://doi.org/10.1002/joc.7337>.
- Wu, B. Y., and S. Y. Ding, 2022: Cold-Eurasia contributes to Arctic warm anomalies. *Climate Dyn.*, <https://doi.org/10.1007/s00382-022-06445-4>.
- Wu, B. Y., J. Z. Su, and R. H. Zhang, 2011: Effects of autumn-winter Arctic sea ice on winter Siberian High. *Chinese Science Bulletin*, **56**, 3220–3228, <https://doi.org/10.1007/s11434-011-4696-4>.
- Wu, B. Y., K. Yang, and J. A. Francis, 2017: A cold event in Asia during January–February 2012 and its possible association with Arctic sea ice loss. *J. Climate*, **30**, 7971–7990, <https://doi.org/10.1175/JCLI-D-16-0115.1>.
- Wu, B. Y., Z. K. Li, J. A. Francis, and S. Y. Ding, 2022a: A recent weakening of winter temperature association between Arctic and Asia. *Environmental Research Letters*, **17**, 034030, <https://doi.org/10.1088/1748-9326/ac4b51>.
- Wu, B. Y., D. Handorf, K. Dethloff, A. Rinke, and A. X. Hu, 2013: Winter weather patterns over Northern Eurasia and Arctic Sea ice loss. *Mon. Wea. Rev.*, **141**, 3786–3800, <https://doi.org/10.1175/MWR-D-13-00046.1>.
- Wu, S. L., and J. Liu, 2018: Comparison of Arctic sea ice concentration datasets. *Haiyang Xuebao*, **40**, 64–72, <https://doi.org/10.3969/j.issn.0253-4193.2018.11.007>. (in Chinese with English abstract)
- Wu, X., S. Griessbach, and L. Hoffmann, 2018: Long-range transport of volcanic aerosol from the 2010 Merapi tropical eruption to Antarctica. *Atmospheric Chemistry and Physics*, **18**, 15 859–15 877, <https://doi.org/10.5194/acp-18-15859-2018>.
- Wu, Y. X., D. Qi, Z. X. Ouyang, L. Cao, R. A. Feely, H. M. Lin, W. J. Cai, and L. Q. Chen, 2021: Contrasting controls of acidification metrics across environmental gradients in the North Pacific and the adjunct Arctic Ocean: Insight from a transregional study. *Geophys. Res. Lett.*, **48**, e2021GL094473, <https://doi.org/10.1029/2021GL094473>.
- Wu, Y. X., and Coauthors, 2022b: Integrated analysis of carbon dioxide and oxygen concentrations as a quality control of ocean float data. *Communications Earth & Environment*, **3**, 92, <https://doi.org/10.1038/S43247-022-00421-W>.
- Xia, Y., W. X. Xu, Y. Y. Hu, and F. Xie, 2020a: Southern-Hemisphere high-latitude stratospheric warming revisit. *Climate Dyn.*, **54**, 1671–1682, <https://doi.org/10.1007/s00382-019-05083-7>.
- Xia, Y., Y. Y. Hu, J. P. Liu, Y. Huang, F. Xie, and J. T. Lin, 2020b: Stratospheric ozone-induced cloud radiative effects on Antarctic Sea Ice. *Adv. Atmos. Sci.*, **37**, 505–514, <https://doi.org/10.1007/s00376-019-8251-6>.
- Xia, Y., Y. Y. Hu, Y. Huang, C. F. Zhao, F. Xie, and Y. K. Yang, 2021: Significant contribution of severe ozone loss to the Siberian-Arctic Surface warming in spring 2020. *Geophys. Res. Lett.*, **48**, e2021GL092509, <https://doi.org/10.1029/2021GL092509>.
- Xiang, B. Q., M. Zhao, Y. Ming, W. D. Yu, and S. M. Kang, 2018: Contrasting impacts of radiative forcing in the Southern Ocean versus southern tropics on ITCZ position and energy transport in one GFDL climate model. *J. Climate*, **31**, 5609–5628, <https://doi.org/10.1175/JCLI-D-17-0566.1>.
- Xiao, C. D., and Coauthors, 2008: Surface characteristics at Dome A, Antarctica: First measurements and a guide to future ice-coring sites. *Annals of Glaciology*, **48**, 82–87, <https://doi.org/10.3189/172756408784700653>.
- Xiao, D., and H. L. Ren, 2021: Interdecadal changes in synoptic transient eddy activity over the Northeast Pacific and their role in tropospheric Arctic amplification. *Climate Dyn.*, **57**, 993–1008, <https://doi.org/10.1007/s00382-021-05752-6>.
- Xiao, H. X., F. Zhang, L. J. Miao, X. S. Liang, K. Wu, and R. Q. Liu, 2020a: Long-term trends in Arctic surface temperature and potential causality over the last 100 years. *Climate Dyn.*, **55**, 1443–1456, <https://doi.org/10.1007/s00382-020-05330-2>.
- Xiao, K., M. X. Chen, Q. Wang, X. Z. Wang, and W. H. Zhang, 2020b: Low-frequency sea level variability and impact of recent sea ice decline on the sea level trend in the Arctic Ocean from a high-resolution simulation. *Ocean Dynamics*, **70**, 787–802, <https://doi.org/10.1007/s10236-020-01373-5>.
- Xie, F., J. K. Zhang, W. J. Sang, Y. Li, Y. L. Qi, C. Sun, Y. Li, and J. C. Shu, 2017: Delayed effect of Arctic stratospheric ozone on tropical rainfall. *Atmospheric Science Letters*, **18**, 409–416, <https://doi.org/10.1002/asl.783>.
- Xie, F., and Coauthors, 2016a: A connection from Arctic stratospheric ozone to El Niño–Southern oscillation. *Environmental Research Letters*, **11**, 124026, <https://doi.org/10.1088/1748-9326/11/12/124026>.
- Xie, H., and Coauthors, 2016b: A comparative study of changes in the Lambert Glacier/Amery Ice Shelf system, East Antarctica, during 2004–2008 using gravity and surface elevation observations. *J. Glaciol.*, **62**, 888–904, <https://doi.org/10.1017/jog.2016.76>.
- Xu, L. X., Y. Ding, and S. P. Xie, 2021a: Buoyancy and wind driven changes in Subantarctic Mode Water during 2004–2019. *Geophys. Res. Lett.*, **48**, e2021GL092511, <https://doi.org/10.1029/2021GL092511>.
- Xu, M., W. S. Tian, J. K. Zhang, T. Wang, and K. Qie, 2021b: Impact of sea ice reduction in the Barents and Kara Seas on the variation of the East Asian trough in late winter. *J. Climate*, **34**, 1081–1097, <https://doi.org/10.1175/JCLI-D-20-0205.1>.
- Xu, Q. B., W. Chen, and L. Song, 2022: Two leading modes in the evolution of major sudden stratospheric warmings and their distinctive surface influence. *Geophys. Res. Lett.*, **49**, e2021GL095431, <https://doi.org/10.1029/2021GL095431>.
- Xu, X. P., S. P. He, F. Li, and H. J. Wang, 2018: Impact of northern Eurasian snow cover in autumn on the warm Arctic–cold Eurasia pattern during the following January and its linkage to stationary planetary waves. *Climate Dyn.*, **50**, 1993–2006, <https://doi.org/10.1007/s00382-017-3732-8>.
- Xu, X. P., S. P. He, Y. Q. Gao, B. T. Zhou, and H. J. Wang, 2021c: Contributors to linkage between Arctic warming and East Asian winter climate. *Climate Dyn.*, **57**, 2543–2555, <https://doi.org/10.1007/s00382-021-05820-x>.
- Xu, X. P., S. P. He, Y. Q. Gao, T. Furevik, H. J. Wang, F. Li, and F. Ogawa, 2019: Strengthened linkage between midlatitudes

- and Arctic in boreal winter. *Climate Dyn.*, **53**, 3971–3983, <https://doi.org/10.1007/s00382-019-04764-7>.
- Yan, Q., H. J. Wang, O. M. Johannessen, and Z. S. Zhang, 2014: Greenland ice sheet contribution to future global sea level rise based on CMIP5 models. *Adv. Atmos. Sci.*, **31**, 8–16, <https://doi.org/10.1007/s00376-013-3002-6>.
- Yan, Q., Z. S. Zhang, Y. Q. Gao, H. J. Wang, and O. M. Johannessen, 2013: Sensitivity of the modeled present-day Greenland Ice Sheet to climatic forcing and spin-up methods and its influence on future sea level projections. *J. Geophys. Res.: Earth Surf.*, **118**, 2174–2189, <https://doi.org/10.1002/jgrf.20156>.
- Yang, C. Y., T. Li, X. H. Xue, S.-Y. Gu, C. Yu, and X. K. Dou, 2019a: Response of the northern stratosphere to the Madden-Julian oscillation during boreal winter. *J. Geophys. Res.: Atmos.*, **124**, 5314–5331, <https://doi.org/10.1029/2018JD029883>.
- Yang, C. Y., A. K. Smith, T. Li, D. E. Kinnison, J. Li, and X. K. Dou, 2020: Can the Madden-Julian oscillation affect the antarctic total column ozone? *Geophys. Res. Lett.*, **47**, e2020GL088886, <https://doi.org/10.1029/2020GL088886>.
- Yang, L. N., L. Zhou, S. J. Li, and Z. X. Wei, 2018: Spreading of the South Pacific tropical water and Antarctic intermediate water over the maritime continent. *J. Geophys. Res.: Oceans*, **123**, 4423–4446, <https://doi.org/10.1029/2018JC013831>.
- Yang, Q., T. H. Dixon, P. G. Myers, J. Bonin, D. Chambers, M. R. Van Den Broeke, M. H. Ribergaard, and J. Mortensen, 2016a: Recent increases in Arctic freshwater flux affects Labrador Sea convection and Atlantic overturning circulation. *Nature Communications*, **7**, 10525, <https://doi.org/10.1038/ncomms10525>.
- Yang, Y., L. Zhijun, M. Leppäranta, B. Cheng, L. Q. Shi, and R. B. Lei, 2016b: Modelling the thickness of landfast sea ice in Prydz Bay, East Antarctica. *Antarctic Science*, **28**, 59–70, <https://doi.org/10.1017/S0954102015000449>.
- Yang, Y. D., F. Li, C. Hwang, M. H. Ding, and J. J. Ran, 2019b: Space-time evolution of Greenland ice sheet elevation and mass from envisat and GRACE data. *J. Geophys. Res.: Earth Surf.*, **124**, 2079–2100, <https://doi.org/10.1029/2018JF004765>.
- Yao, W. J., J. X. Shi, and X. L. Zhao, 2017: Freshening of Antarctic intermediate water in the south atlantic ocean in 2005–2014. *Ocean Science*, **13**, 521–530, <https://doi.org/10.5194/os-13-521-2017>.
- Yi, S., K. Heki, and A. Qian, 2017: Acceleration in the global mean sea level rise: 2005–2015. *Geophys. Res. Lett.*, **44**, 11 905–11 913, <https://doi.org/10.1002/2017GL076129>.
- Yi, S., W. K. Sun, K. Heki, and A. Qian, 2015: An increase in the rate of global mean sea level rise since 2010. *Geophys. Res. Lett.*, **42**, 3998–4006, <https://doi.org/10.1002/2015GL063902>.
- Yu, L., Y. Q. Gao, and O. H. Otterå, 2016: The sensitivity of the Atlantic meridional overturning circulation to enhanced freshwater discharge along the entire, eastern and western coast of Greenland. *Climate Dyn.*, **46**, 1351–1369, <https://doi.org/10.1007/s00382-015-2651-9>.
- Yu, L. J., and S. Y. Zhong, 2018: Changes in sea-surface temperature and atmospheric circulation patterns associated with reductions in Arctic sea ice cover in recent decades. *Atmospheric Chemistry and Physics*, **18**, 14 149–14 159, <https://doi.org/10.5194/acp-18-14149-2018>.
- Yu, L. J., and S. Y. Zhong, 2019a: Strong wind speed events over Antarctica and its surrounding oceans. *J. Climate*, **32**, 3451–3470, <https://doi.org/10.1175/JCLI-D-18-0831.1>.
- Yu, L. J., and S. Y. Zhong, 2019b: The interannual variability of surface winds in Antarctica and the surrounding oceans: A climatological analysis using the ERA-Interim reanalysis data. *J. Geophys. Res.: Atmos.*, **124**, 9046–9061, <https://doi.org/10.1029/2019JD030328>.
- Yu, L. J., S. Y. Zhong, M. Y. Zhou, B. Sun, and D. H. Lenschow, 2018a: Antarctic summer sea ice trend in the context of high-latitude atmospheric circulation changes. *J. Climate*, **31**, 3909–3920, <https://doi.org/10.1175/JCLI-D-17-0739.1>.
- Yu, L. J., S. Y. Zhong, M. Y. Zhou, D. H. Lenschow, and B. Sun, 2019a: Revisiting the linkages between the variability of atmospheric circulations and Arctic melt-season sea ice cover at multiple time scales. *J. Climate*, **32**, 1461–1482, <https://doi.org/10.1175/JCLI-D-18-0301.1>.
- Yu, L. J., S. Y. Zhong, T. Vihma, C. Sui, and B. Sun, 2021: Sea ice changes in the Pacific sector of the Southern Ocean in austral autumn closely associated with the negative polarity of the South Pacific Oscillation. *Geophys. Res. Lett.*, **48**, e2021GL092409, <https://doi.org/10.1029/2021GL092409>.
- Yu, L. J., S. Y. Zhong, T. Vihma, C. Sui, and B. Sun, 2022: The impact of the Indian Ocean basin mode on antarctic sea ice concentration in interannual time scales. *Geophys. Res. Lett.*, **49**, e2022GL097745, <https://doi.org/10.1029/2022GL097745>.
- Yu, L. J., Q. H. Yang, T. Vihma, S. Jagovkina, J. P. Liu, Q. Z. Sun, and Y. B. Li, 2018b: Features of extreme precipitation at Progress Station, Antarctica. *J. Climate*, **31**, 9087–9105, <https://doi.org/10.1175/JCLI-D-18-0128.1>.
- Yu, Y. Y., and R. C. Ren, 2019: Understanding the variation of stratosphere-troposphere coupling during stratospheric northern annular mode events from a mass circulation perspective. *Climate Dyn.*, **53**, 5141–5164, <https://doi.org/10.1007/s00382-019-04675-7>.
- Yu, Y. Y., P. C. Taylor, and M. Cai, 2019b: Seasonal variations of Arctic low-level clouds and its linkage to sea ice seasonal variations. *J. Geophys. Res.: Atmos.*, **124**, 12 206–12 226, <https://doi.org/10.1029/2019JD031014>.
- Yuan, J. W., Z. H. Chi, X. Cheng, T. Zhang, T. Li, and Z. Q. Chen, 2020: Automatic extraction of supraglacial lakes in southwest greenland during the 2014–2018 melt seasons based on convolutional neural network. *Water*, **12**, 891, <https://doi.org/10.3390/w12030891>.
- Yuan, N. M., M. H. Ding, J. Ludescher, and A. Bunde, 2017: Increase of the Antarctic Sea Ice Extent is highly significant only in the Ross Sea. *Scientific Reports*, **7**, 41096, <https://doi.org/10.1038/srep41096>.
- Yuan, N. M., M. H. Ding, Y. Huang, Z. T. Fu, E. Xoplaki, and J. Luterbacher, 2015: On the long-term climate memory in the surface air temperature records over Antarctica: A nonnegligible factor for trend evaluation. *J. Climate*, **28**, 5922–5934, <https://doi.org/10.1175/JCLI-D-14-00733.1>.
- Yuan, X. J., and D. G. Martinson, 2000: Antarctic sea ice extent variability and its global connectivity. *J. Climate*, **13**, 1697–1717, [https://doi.org/10.1175/1520-0442\(2000\)013<1697:ASIEVA>2.0.CO;2](https://doi.org/10.1175/1520-0442(2000)013<1697:ASIEVA>2.0.CO;2).
- Yuan, X. J., and D. G. Martinson, 2001: The Antarctic dipole and its predictability. *Geophys. Res. Lett.*, **28**, 3609–3612, <https://doi.org/10.1029/2001GL012969>.
- Yuan, X. J., and C. H. Li, 2008: Climate modes in southern high latitudes and their impacts on Antarctic sea ice. *J. Geophys.*

- Res.: Oceans*, **113**, C06S91, <https://doi.org/10.1029/2006JC004067>.
- Yuan, Z. X., J. Qin, S. L. Li, S. J. Huang, Y. Mbululo, and A. Rehman, 2022: Impact of boreal autumn Antarctic oscillation on winter wet-cold weather in the middle-lower reaches of Yangtze River Basin. *Climate Dyn.*, **58**, 329–349, <https://doi.org/10.1007/s00382-021-05906-6>.
- Zhang, B., Y. B. Yao, L. Liu, and Y. J. Yang, 2021a: Interannual ice mass variations over the Antarctic ice sheet from 2003 to 2017 were linked to El Niño–Southern Oscillation. *Earth and Planetary Science Letters*, **560**, 116796, <https://doi.org/10.1016/j.epsl.2021.116796>.
- Zhang, C., T. M. Li, and S. L. Li, 2021b: Impacts of CP and EP El Niño events on the Antarctic sea ice in Austral Spring. *J. Climate*, **34**, 9327–9348, <https://doi.org/10.1175/JCLI-D-21-0002.1>.
- Zhang, C. Y., J. K. Zhang, M. Xu, S. Y. Zhao, and X. F. Xia, 2022a: Impacts of stratospheric Polar Vortex shift on the East Asian trough. *J. Climate*, **35**, 5605–5621, <https://doi.org/10.1175/JCLI-D-21-0235.1>.
- Zhang, C. Y., and Coauthors, 2021c: Rapid mass loss in West Antarctica revealed by swarm gravimetry in the absence of GRACE. *Geophys. Res. Lett.*, **48**, e2021GL095141, <https://doi.org/10.1029/2021GL095141>.
- Zhang, J. K., W. S. Tian, M. P. Chipperfield, F. Xie, and J. L. Huang, 2016: Persistent shift of the Arctic polar vortex towards the Eurasian continent in recent decades. *Nature Climate Change*, **6**, 1094–1099, <https://doi.org/10.1038/nclimate3136>.
- Zhang, J. K., and Coauthors, 2018a: Stratospheric ozone loss over the Eurasian continent induced by the polar vortex shift. *Nature Communications*, **9**, 206, <https://doi.org/10.1038/s41467-017-02565-2>.
- Zhang, J. K., and Coauthors, 2022b: Responses of Arctic sea ice to stratospheric ozone depletion. *Science Bulletin*, **67**, 1182–1190, <https://doi.org/10.1016/j.scib.2022.03.015>.
- Zhang, L., M. H. Ding, T. F. Dou, Y. Huang, J. M. Lv, and C. D. Xiao, 2021d: The shallowing surface temperature inversions in the Arctic. *J. Climate*, **34**, 4159–4168, <https://doi.org/10.1175/JCLI-D-20-0621.1>.
- Zhang, L., B. L. Gan, X. C. Li, H. Wang, C. Y. Wang, W. J. Cai, and L. X. Wu, 2021e: Remote influence of the midlatitude South Atlantic variability in spring on Antarctic summer sea ice. *Geophys. Res. Lett.*, **48**, 2020GL090810, <https://doi.org/10.1029/2020GL090810>.
- Zhang, P., Z. W. Wu, and R. Jin, 2021f: How can the winter North Atlantic Oscillation influence the early summer precipitation in Northeast Asia: Effect of the Arctic sea ice. *Climate Dyn.*, **56**, 1989–2005, <https://doi.org/10.1007/s00382-020-05570-2>.
- Zhang, P., Z. W. Wu, J. P. Li, and Z. N. Xiao, 2020: Seasonal prediction of the northern and southern temperature modes of the East Asian winter monsoon: The importance of the Arctic sea ice. *Climate Dyn.*, **54**, 3583–3597, <https://doi.org/10.1007/s00382-020-05182-w>.
- Zhang, Q. L., B. J. Huai, M. R. van den Broeke, J. Cappelen, M. H. Ding, Y. T. Wang, and W. J. Sun, 2022c: Temporal and spatial variability in contemporary Greenland warming (1958–2020). *J. Climate*, **35**, 2755–2767, <https://doi.org/10.1175/JCLI-D-21-0313.1>.
- Zhang, R., 2015: Mechanisms for low-frequency variability of summer Arctic sea ice extent. *Proceedings of the National Academy of Sciences of the United States of America*, **112**, 4570–4575, <https://doi.org/10.1073/pnas.1422296112>.
- Zhang, R. H., W. S. Tian, J. K. Zhang, J. L. Huang, F. Xie, and M. Xu, 2019b: The corresponding tropospheric environments during downward-extending and nondownward-extending events of stratospheric northern annular mode anomalies. *J. Climate*, **32**, 1857–1873, <https://doi.org/10.1175/JCLI-D-18-0574.1>.
- Zhang, R. H., W. Zhou, W. S. Tian, Y. Zhang, Z. C. Liu, and P. K. Y. Cheung, 2022f: Changes in the relationship between ENSO and the winter Arctic stratospheric polar vortex in recent decades. *J. Climate*, **35**, 5399–5414, <https://doi.org/10.1175/JCLI-D-21-0924.1>.
- Zhang, R. N., R. H. Zhang, and G. K. Dai, 2022d: Intraseasonal contributions of Arctic sea-ice loss and Pacific decadal oscillation to a century cold event during early 2020/21 winter. *Climate Dyn.*, **58**, 741–758, <https://doi.org/10.1007/s00382-021-05931-5>.
- Zhang, R. N., R. H. Zhang, and C. H. Sun, 2022e: Modulation of the interdecadal variation of atmospheric background flow on the recent recovery of the EAWM during the 2000s and its link with North Atlantic–Arctic warming. *Climate Dyn.*, **59**, 561–578, <https://doi.org/10.1007/S00382-022-06152-0>.
- Zhang, R. N., C. H. Sun, R. H. Zhang, W. J. Li, and J. Q. Zuo, 2019a: Role of Eurasian snow cover in linking winter-spring Eurasian coldness to the autumn Arctic sea ice retreat. *J. Geophys. Res.: Atmos.*, **124**, 9205–9221, <https://doi.org/10.1029/2019JD030339>.
- Zhang, X. W., B. Y. Wu, and S. Y. Ding, 2022g: Influence of spring Arctic sea ice melt on Eurasian surface air temperature. *Climate Dyn.*, **59**, 3305–3316, <https://doi.org/10.1007/s00382-022-06267-4>.
- Zhang, Y., Z. H. Chi, F. M. Hui, T. Li, X. Y. Liu, B. G. Zhang, X. Cheng, and Z. Q. Chen, 2021g: Accuracy evaluation on geolocation of the Chinese First Polar Microsatellite (Ice Pathfinder) imagery. *Remote Sensing*, **13**, 4278, <https://doi.org/10.3390/rs13214278>.
- Zhang, Z. R., P. Uotila, A. Stössel, T. Vihma, H. L. Liu, and Y. S. Zhong, 2018b: Seasonal southern hemisphere multi-variable reflection of the southern annular mode in atmosphere and ocean reanalyses. *Climate Dyn.*, **50**, 1451–1470, <https://doi.org/10.1007/s00382-017-3698-6>.
- Zheng, L., X. Cheng, Z. Q. Chen, and Q. Liang, 2021: Delay in Arctic sea ice freeze-up linked to early summer sea ice loss: Evidence from satellite observations. *Remote Sensing*, **13**, 2162, <https://doi.org/10.3390/rs13112162>.
- Zheng, L., C. X. Zhou, T. J. Zhang, Q. Liang, and K. Wang, 2020: Recent changes in pan-Antarctic region surface snowmelt detected by AMSR-E and AMSR2. *The Cryosphere*, **14**, 3811–3827, <https://doi.org/10.5194/tc-14-3811-2020>.
- Zheng, L., X. Cheng, X. Y. Shang, Z. Q. Chen, Q. Liang, and K. Wang, 2022: Greenland Ice Sheet daily surface melt flux observed from space. *Geophys. Res. Lett.*, **49**, e2021GL096690, <https://doi.org/10.1029/2021GL096690>.
- Zhong, W. L., M. Steele, J. L. Zhang, and S. T. Cole, 2019a: Circulation of Pacific winter water in the Western Arctic Ocean. *J. Geophys. Res.: Oceans*, **124**, 863–881, <https://doi.org/10.1029/2018JC014604>.
- Zhong, W. L., J. L. Zhang, M. Steele, J. P. Zhao, and T. Wang, 2019b: Episodic extrema of surface stress energy input to the western Arctic ocean contributed to step changes of freshwater content in the beaufort gyre. *Geophys. Res. Lett.*, **46**,



12 173–12 182, <https://doi.org/10.1029/2019GL084652>.

- Zhong, W. L., S. T. Cole, J. L. Zhang, R. B. Lei, and M. Steele, 2022: Increasing winter ocean-to-ice heat flux in the Beaufort Gyre Region, Arctic ocean over 2006–2018. *Geophys. Res. Lett.*, **49**, e2021GL096216, <https://doi.org/10.1029/2021GL096216>.
- Zhou, X., J. P. Li, F. Xie, Q. L. Chen, R. Q. Ding, W. X. Zhang, and Y. Li, 2018: Does Extreme El Niño have a different effect on the stratosphere in boreal winter than its moderate counterpart? *J. Geophys. Res.: Atmos.*, **123**, 3071–3086, <https://doi.org/10.1002/2017JD028064>.
- Zou, Y. F., P. J. Rasch, H. L. Wang, Z. W. Xie, and R. D. Zhang, 2021: Increasing large wildfires over the western United States linked to diminishing sea ice in the Arctic. *Nature Communications*, **12**, 6048, <https://doi.org/10.1038/s41467-021-26232-9>.
- Zuo, J. Q., H.-L. Ren, B. Y. Wu, and W. J. Li, 2016: Predictability of winter temperature in China from previous autumn Arctic sea ice. *Climate Dyn.*, **47**, 2331–2343, <https://doi.org/10.1007/s00382-015-2966-6>.

# Recent Progress in Studies on the Influences of Human Activity on Regional Climate over China<sup>※</sup>

Jianping DUAN<sup>1,2</sup>, Hongzhou ZHU<sup>2,3</sup>, Li DAN<sup>2</sup>, and Qihong TANG<sup>4,3</sup>

<sup>1</sup>State Key Laboratory of Earth Surface and Ecological Resources, Faculty of Geographical Science, Beijing Normal University, Beijing 100875, China

<sup>2</sup>CAS Key Laboratory of Regional Climate-Environment for Temperate East Asia, Institute of Atmospheric Physics, Chinese Academy of Sciences, Beijing 100029, China

<sup>3</sup>University of Chinese Academy of Sciences, Beijing 100049, China

<sup>4</sup>Key Laboratory of Water Cycle and Related Land Surface Processes, Institute of Geographic Sciences and Natural Resources Research, Chinese Academy of Sciences, Beijing 100101, China

(Received 14 December 2022; revised 18 April 2023; accepted 19 April 2023)

## ABSTRACT

The influences of human activity on regional climate over China have been widely reported and drawn great attention from both the scientific community and governments. This paper reviews the evidence of the anthropogenic influence on regional climate over China from the perspectives of surface air temperature (SAT), precipitation, droughts, and surface wind speed, based on studies published since 2018. The reviewed evidence indicates that human activities, including greenhouse gas and anthropogenic aerosol emissions, land use and cover change, urbanization, and anthropogenic heat release, have contributed to changes in the SAT trend and the likelihood of regional record-breaking extreme high/low temperature events over China. The anthropogenically forced SAT signal can be detected back to the 1870s in the southeastern Tibetan Plateau region. Although the anthropogenic signal of summer precipitation over China is detectable and anthropogenic forcing has contributed to an increased likelihood of regional record-breaking heavy/low precipitation events, the anthropogenic precipitation signal over China is relatively obscure. Moreover, human activities have also contributed to a decline in surface wind speed, weakening of monsoon precipitation, and an increase in the frequency of droughts and compound extreme climate/weather events over China in recent decades. This review can serve as a reference both for further understanding the causes of regional climate changes over China and for sound decision-making on regional climate mitigation and adaptation. Additionally, a few key or challenging scientific issues associated with the human influence on regional climate changes are discussed in the context of future research.

**Key words:** human activity, regional climate, China

**Citation:** Duan, J. P., H. Z. Zhu, L. Dan, and Q. H. Tang, 2023: Recent progress in studies on the influences of human activity on regional climate over China. *Adv. Atmos. Sci.*, **40**(8), 1362–1378, <https://doi.org/10.1007/s00376-023-2327-z>.

### Article Highlights:

- Recent evidence of the human influences on regional climate over China is reviewed based on studies published since 2018.
- Human activity has contributed to changes in SAT, wind speed, precipitation, droughts, and compound extreme climate/weather events.
- Anthropogenic forcing of regional climate changes can be climatic factor-, region-, period-, and event-dependent.

---

## 1. Introduction

In addition to natural climate variations, human activity has induced prominent influences on regional climate over China in recent decades (Zhai et al., 2018; Sun et al., 2022), and the anthropogenic signal on temperature seasonality has been tracked back to the late 19th century in the Tibetan

---

<sup>※</sup> This paper is a contribution to the special issue on National Report to the 28th IUGG General Assembly by CNC-IAMAS (2019–2022).

\* Corresponding author: Jianping DUAN  
Email: [duanjp@bnu.edu.cn](mailto:duanjp@bnu.edu.cn)

Plateau (TP) region (Duan et al., 2019; Yin et al., 2022). Human activities are characterized mainly by the emissions of industrialization-induced greenhouse gas (GHG) and anthropogenic aerosols (AA), land use and cover change (LUCC), urbanization, and some other aspects (e.g., anthropogenic heat release, AHR) (Fig. 1). The emissions of GHG and AA have altered atmospheric components and influenced radiative forcing, ultimately affecting the global or regional climate, while LUCC and urbanization have changed the physical properties of the underlying surfaces, induced land-atmosphere interactions, and ultimately influenced the regional climate. It is unequivocal that the human influence has greatly warmed the atmosphere, ocean and land (IPCC, 2021). However, the anthropogenic forcing effect can differ regionally. For example, some regions suffer more from global warming (Xie et al., 2019), and the regional climate responses to anthropogenic forcing also differ (Li et al., 2022a). Typically, SAT changes over China seem more sensitive to external forcing than those over the United States owing to the stronger climate memory, and this has led to substantially different warming trends between China and the United States (Li et al., 2022a). Therefore, a systematic review of the evidence of anthropogenic influences on regional climate can not only deepen our understanding of the regional anthropogenic climate effect, but can also serve as a reference for regional climate mitigation and adaptation.

China has the largest population in the world and has experienced rapid economic development and industrialization in recent decades; the anthropogenic influences on the regional climate of China have drawn great attention. Many studies have indicated that anthropogenic forcing has contributed to both the rapid increase in SAT trends and the increased frequency and intensity of SAT extremes over China during recent decades (Chen et al., 2019a, Chen et al., 2021, Li et al., 2022a; Sun et al., 2022). Although the anthropogenic signal of regional precipitation might be obscured by the strong internal variability, some studies have revealed an effect of anthropogenic warming on the mean and extreme precipitation trends via enhancing the water cycle over China in recent decades (Zhai et al., 2018; Li et al., 2021c). Moreover, anthropogenic forcing has triggered droughts, weakened monsoon precipitation, and surface wind speed (SWS) changes over China (Fig. 1). These changes resulting from human activity, especially for extreme event changes, have brought potential or direct threats to human societies in China (Wang et al., 2018b; Yuan et al., 2019; Li et al., 2021b). Sound regional- or national-level decision-making for disaster prevention and mitigation depends on the reliable detection of anthropogenic forcings of mean and extreme climate changes.

Human activity-induced regional climate changes may cover many aspects. In this paper, we mainly review the anthropogenic effects on regional SAT, precipitation, drought, SWS, and monsoon-related precipitation changes over China (Fig. 1). According to the journal's requirement that this paper should focus on progress mainly over the last five years, the evidence reviewed is derived from references

published since 2018.

## 2. Methods employed in detection and attribution studies

Before reviewing the research progress on the anthropogenic influences on regional climate changes over China, the key methods used for detection and attribution studies are first summarized. For the detection and attribution of trends in climate changes, multivariate analysis and Bayesian inference are used most. The optimal fingerprinting method, the most popular method in detection and attribution studies, is a multivariate analysis method, while Bayesian inference methods can integrate multiple sources of data for attribution (Zhai et al., 2018).

The so-called "fingerprint" is the climate system that generates unique responses to various external forcings, just as every person has a unique fingerprint (Hasselmann, 1993, Allen and Tett, 1999). These responses can be obtained from simple physical arguments based on the forcing pattern or the mean response to a particular forcing scenario among an ensemble of climate model runs (Allen and Tett, 1999). Generalized linear regression is usually utilized to achieve the optimal fingerprinting method (Allen and Tett, 1999; Allen and Stott, 2003; Stott et al., 2003).

With the development of attribution methods, regularized optimal fingerprinting (ROF) was developed to obtain more objective and accurate implementation in the area of detection and attribution (Ribes et al., 2013). The main difference of ROF from the classical optimal fingerprinting method is that ROF uses a regularized estimate of the internal variability covariance matrix to improve the estimation of residuals (Ribes et al., 2013).

The most commonly used climate event attribution method is calculating an event's probability related to anthropogenic forcing. The core idea of this probability approach is the "control variable method". For example, based on the distribution of climate variables or of an index characterizing the corresponding extreme events in two sets of simulations (one containing all forcings, and the other containing only the natural forcing), the contribution of the human influence to the risk of change in a certain extreme event can be calculated. The probability of a certain extreme event simulated with all forcings is denoted as  $P_1$ , and the probability of the same event under only the natural forcing is denoted as  $P_0$ . Then, the ratio  $P_1/P_0$  is the risk ratio, and  $(1 - P_1/P_0)$  is the fraction of attributable risk, which is used to measure the extent of human influence on the extreme event (Otto, 2017; Zhai et al., 2018). The other method of event attribution is the "storyline approach" (Shepherd, 2016), which mainly deduces the event of interest. In summary, experiments should be designed with possible physical influencing factors, and some of them are taken as preconditions (mostly large-scale circulations), and the question of to what extent climate change has altered the magnitude of this specific event is finally answered deterministically (Shepherd, 2016).

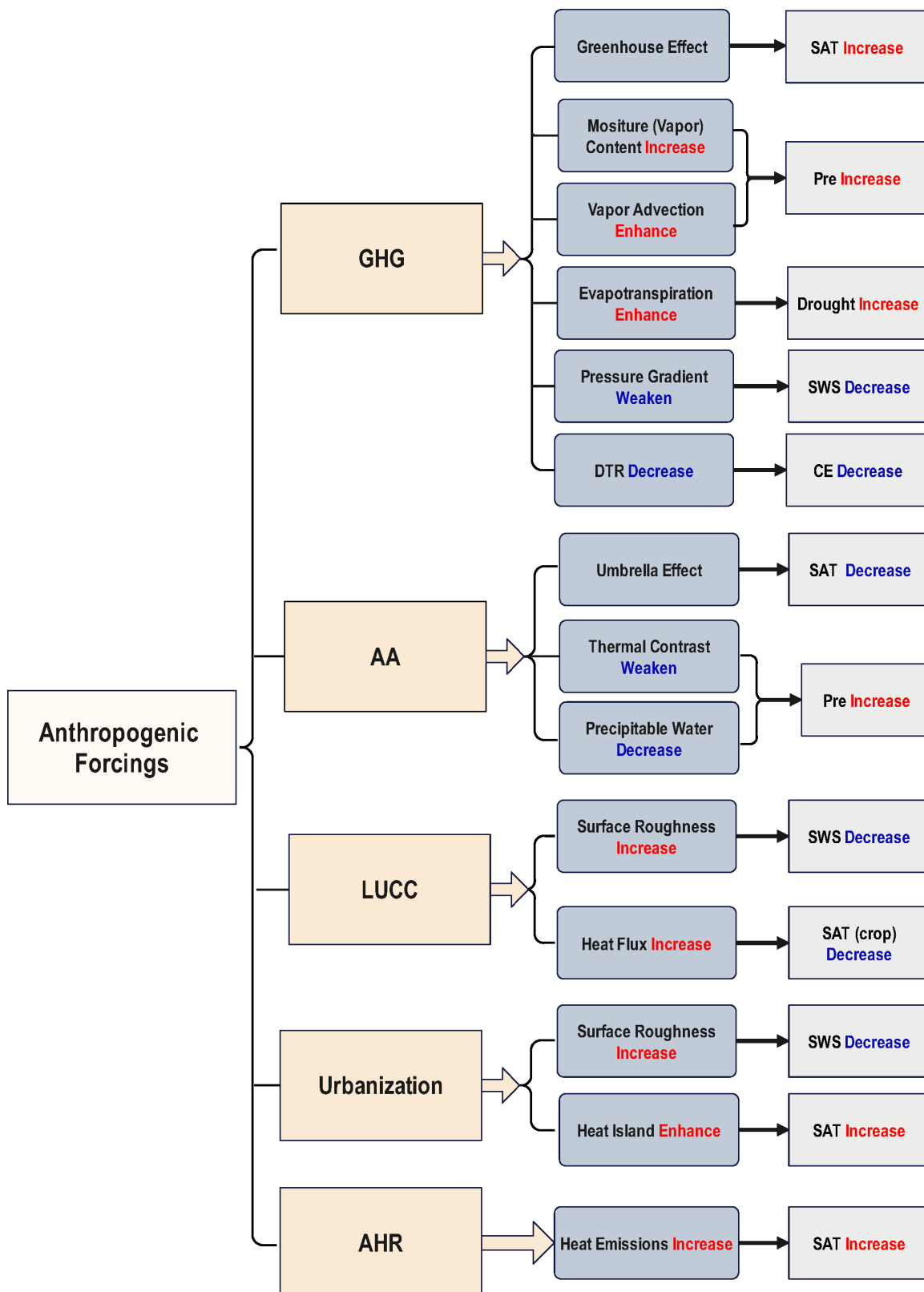


**Fig. 1.** Schematic of the influence of human activities on regional climate changes over China. Among the physical mechanisms, the pressure gradient refers to the atmospheric pressure difference between the high- and mid-latitude zone. The umbrella effect, representing the direct effect of aerosols, refers to aerosol particles that weaken surface solar radiation by reflecting and absorbing solar radiation. GHG, greenhouse gas; AA, anthropogenic aerosols; LUCC, land use cover change; AHR, anthropogenic heat release; SAT, surface air temperature; Pre, precipitation; SWS, surface wind speed; CE, compound events; DTR, diurnal temperature range.

Most of the following reviewed studies used the optimal fingerprinting or ROF method and an event probability method for detection and attribution in trends of climate changes and extreme climate events, respectively.

### 3. Anthropogenic influences on SAT trends and extremes over China

#### 3.1. Anthropogenic influences on SAT trends over China

Anthropogenic forcing has been identified as the dominant factor for the rapid SAT increase over China in recent decades (Allabakash and Lim, 2022; Sun et al., 2022) (Table 1). During the period 1961–2005, the SAT over China increased by  $0.78^{\circ}\text{C} \pm 0.27^{\circ}\text{C}$ , with warming of  $0.25^{\circ}\text{C} (10 \text{ yr})^{-1}$  and  $0.17^{\circ}\text{C} (10 \text{ yr})^{-1}$  resulting from GHG emissions and other anthropogenic factors, respectively (Allabakash and Lim, 2022). Compared to other parts of China, the TP has shown a greater warming rate in recent decades ( $1.23^{\circ}\text{C}$  from 1961–2005) (Zhou and Zhang, 2021), and GHG forcing has contributed an increase of  $1.37^{\circ}\text{C}$  according to best estimates (Zhou and Zhang, 2021). GHG forcing was the major contributor to the increased warming, and AA induced a cooling effect and offset part of the warming resulting from the GHG effect over the whole of China and in a few subregions (Jia et al., 2020; Zhou and Zhang, 2021) (Fig. 2). In addition to GHG and AA, LUCC and urbanization also influenced the local or regional SAT trends over China (Du et al., 2019; Jin et al., 2021; Yang et al., 2021; Zhang et al., 2022a) (Fig. 2). LUCC has generally induced significant SAT decreases in cropland areas and significant SAT increases in urbanized areas over China (Jin et al., 2021; Yang et al., 2021). Urbanization contributed to an increase of  $0.49^{\circ}\text{C}$  in the annual SAT over the whole of China from 1961 to 2013 (Sun et al., 2022). Urbanization also contributed to the diurnal temperature range trends by more than 25% in both winter and summer, and positively affected the surface sunshine duration by approximately 29.4% in winter and 11.9% in summer, over China from 1951 to 2020 (Zhang et al., 2022a). Moreover, the urban drying island effect in recent periods over eastern China, resulting from the decreased cloud cover, induced a mitigation effect on the urban heat island effect (Du et al., 2019).

Apart from the increased SAT, human activity has also contributed to a significant weakening of the SAT seasonality on the TP (Duan et al., 2017, 2019) and over China (Qian and Zhang, 2015). This mainly features a significant reduction in the winter–summer SAT difference, driven by the combined effect of increased GHGs and AAs with a meridional difference (Duan et al., 2019). In particular, anthropogenic forcing–induced SAT seasonality weakening has been tracked back to the 1870s on the TP (Duan et al., 2019). A detection and attribution study (Duan et al., 2019) using tree ring–based reconstructions of the summer–winter temperature difference indicates that the anthropogenic signal is

detectable since the 1870s and can be supported by natural climate proxy evidence (Fig. 3).

#### 3.2. Anthropogenic influences on SAT extremes over China

Anthropogenic forcing has influenced the intensity, frequency and occurrence likelihood of extreme temperature events in many regions of China (Chen et al., 2019a; Yin et al., 2019; Lu et al., 2020b; Liu et al., 2022). In view of the whole of China, both intensity and frequency indices of extreme temperature showed continuous warming from 1951 to 2018, and more intense and more frequent warm extremes and less intense and less frequent cold extremes were observed in most regions (Hu and Sun, 2022). GHG forcing accounted for approximately 1.6 (1.1 to 2) times the observed warming reflected in the changes in most indices, while AA offset approximately 35% (10%–60%) of GHG-induced warming for warm extremes, and land use and ozone may have made very small positive contributions to extreme temperatures (the effect of ozone was separated from the GHG effect) (Hu and Sun, 2022). Anthropogenic forcing is also a critical factor affecting the observed decadal changes in temperature extremes over China since the mid-1990s (Chen and Dong, 2019) and has contributed to the increased frequency, intensity, and spatial extent of regional daytime and nighttime heatwaves (HWs) over China in recent decades (Lu et al., 2018; Wang et al., 2018b; Yin and Sun, 2018; Su and Dong, 2019; Wang et al., 2022b). These changes were driven both directly by the strengthened greenhouse effect and indirectly by the related land–atmosphere and circulation feedbacks (Su and Dong, 2019). Estimations have indicated that the increased probability of the hottest day occurring over more than 75% of the observed areas in China could be attributed to anthropogenic forcing (Chen et al., 2021), and the GHG effect changed the frequencies of summer days and tropical nights by  $+3.48 \pm 1.45 \text{ d} (10 \text{ yr})^{-1}$  and  $+2.99 \pm 1.35 \text{ d} (10 \text{ yr})^{-1}$  over eastern China from 1960 to 2012, respectively (Wang et al., 2018b). Nevertheless, local AA emissions may be a factor affecting the spatially heterogeneous extreme temperature trends in China (Chen and Dong, 2019).

Many case-based quantitative attribution studies have also demonstrated that anthropogenic forcing was the dominant factor affecting the increased frequency and intensity of extreme high-temperature events over China in recent decades (Fig. 4, Table 2). Anthropogenic forcing explained approximately 42% of the SAT warming and 60% (40%) of the increases in maximum (minimum) temperature, respectively, corresponding to extreme summer heat in western China in 2015 (Chen et al., 2019a). Simulation-based attribution results show that, given the external forcing at the 1961–2015 level and regardless of the sea surface boundary conditions, there is a 21-fold increase in the likelihood of 2015-like heat events in Northwest China due to anthropogenic forcing (Zhang et al., 2022d). Anthropogenic forcing has made the occurrence likelihood of July 2017–like HW events over eastern China increase by a factor of 4.8 (Sparrow

**Table 1.** Quantitative contributions of anthropogenic forcings to regional climate changes over China obtained from references published since 2018. See Table 3 for abbreviation definitions.

Climatic/ environmental factor	Region (site)	Period	Season	Quantitative contribution (forcing factor)	Reference
SAT trend	Whole of China	1961–2013	Annual	↑0.49°C (urbanization)	Sun et al. (2022)
	TP	1961–2005	Annual	↑1.37°C (GHG)	Zhou and Zhang (2021)
	WC	1958–2015	Annual	↑ (GHG)	Wang et al. (2018)
	WC (WBGT)	1961–2010	Summer	↑1.178°C (ANT)	Li et al. (2020a)
	EC (WBGT)	1961–2010	Summer	↑0.708°C (ANT)	Li et al. (2020a)
Precipitation trend	Whole of China (trend in extreme)	1961–1990	Annual	↑ (GHG); ↓ (AA); hard to separate from NAT	Dong et al. (2022)
	Whole of China	1961–2012	Summer	↑ (GHG)	Lu et al. (2020a)
	SEC	1961–2014	Summer	↑ (GHG); ↓ (AA)	Guo et al. (2023)
	NWC	1961–2014	Summer	↑ (AA)	Guo et al. (2023)
	NEC	1961–2014	Summer	↓ (ANT)	Guo et al. (2023)
	SWC	1961–2014	Summer	↓ (AA)	Guo et al. (2023)
	NSTP	1961–2013	Summer	↑ (ANT)	Zhao et al. (2022)
	STP	1961–2013	Summer	↓ (ANT)	Zhao et al. (2022)
	NC	1994–2011	Summer	↑ (GHG); ↓ (AA)	Zhang et al. (2020a)
	SC	1994–2011	Summer	↑ (GHG)	Zhang et al. (2020a)
	SWC	1993–2007	Autumn	↓ (AA)	Huo et al. (2021)
	EC	1956–2003	Annual	↑ (GHG); ↓ (AA)	Ma et al. (2017b)
	TCZ	1951–2005	Late summer	↓ (AA)	Zhao et al. (2021)
	SC/Shenzhen (rural)	1979–2020	Annual	↑ (urbanization)	Zhang et al. (2020d)
	CP-SFND	1961–2013	Annual	↑ (ANT)	Zhou et al. (2021a)
Drought trend	Whole of China (flash drought)	1959–2005	Annual	↑77 ± 26% (GHG)	Yuan et al. (2019)
	NC/YRB	1960–2010	Annual	↑ (reservoir operation)	Omer et al. (2020)
	SEPTP	1959–2015	Autumn	↑ (anthropogenic warming)	Ma et al. (2017a)
	WC/YIRB	1961–2017	Annual	↑ (reservoir impoundment)	Liang et al. (2021)
	NC	1961–1015	Autumn	↑ (anthropogenic warming)	Zhang et al. (2022e)
	SC	1961–1015	Autumn	↑ (rainfall change by anthropogenic factors)	Zhang et al. (2022e)
	NC/BTH (VPD)	1951–2017	Annual	↑ ≥ 30% (urbanization)	Wang et al. (2022a)
	EC/YRD (VPD)	1951–2017	Annual	↑ ≥ 30% (urbanization)	Wang et al. (2022a)
	SC/PRD (VPD)	1951–2017	Annual	↑ ≥ 30% (urbanization)	Wang et al. (2022a)
	WC/SCB (VPD)	1951–2017	Annual	↑ ≥ 30% (urbanization)	Wang et al. (2022a)
SWS	Whole of China	1981–2021	Annual	↓ (GHG; LUCC)	Zha et al. (2021)
	EC	1991–2015	Annual	↓ (LUCC)	Li et al. (2018c)
	NWC	1980–2012	Annual	↓ (ANT)	Zheng et al. (2018)
	NC/BTH	1980–2018	Annual	↓ 0.37 m s <sup>-1</sup> yr <sup>-1</sup> (urbanization)	Wang et al. (2020a)
CE	SWC	1967–2010	Summer	↑ (ANT)	Wu et al. (2022)
	NEC	1951–2014	Summer	↑ (ANT; GHG)	Li et al. (2022b)
	EC	1961–2018	Summer	↑ (GHG); ↓ (urbanization)	Yu and Zhai (2020)
	EC	1965–2014	Summer	↑ (GHG)	Wang et al. (2022b)

et al., 2018) and the frequency of July 2017–like HWs in central eastern China become approximately 1 in 5 years under current climate conditions (Chen et al., 2019b). Due to the combined influences of anthropogenically forced warming (~78%) and urbanization (~17%), July and August 2018–like HW events in Northeast China have become a one-in-60-year event in urban regions and a one-in-80-year event in rural regions (Zhou et al., 2020). Simultaneously, anthropogenic warming has made 30-day persistent nighttime

HWs like the event of summer 2018 in Northeast China become about a one-in-60-year event (compared to about a one-in-a-500-year event naturally) (Ren et al., 2020). Moreover, anthropogenic forcing has also contributed to extreme warm events in spring, such as the 2018 event that occurred over eastern China, and has increased the chance of this event occurring by tenfold (Lu et al., 2020b). Aside from GHG-induced warming, urbanization, the effects of energy consumption (i.e., AHR) and urban development have also



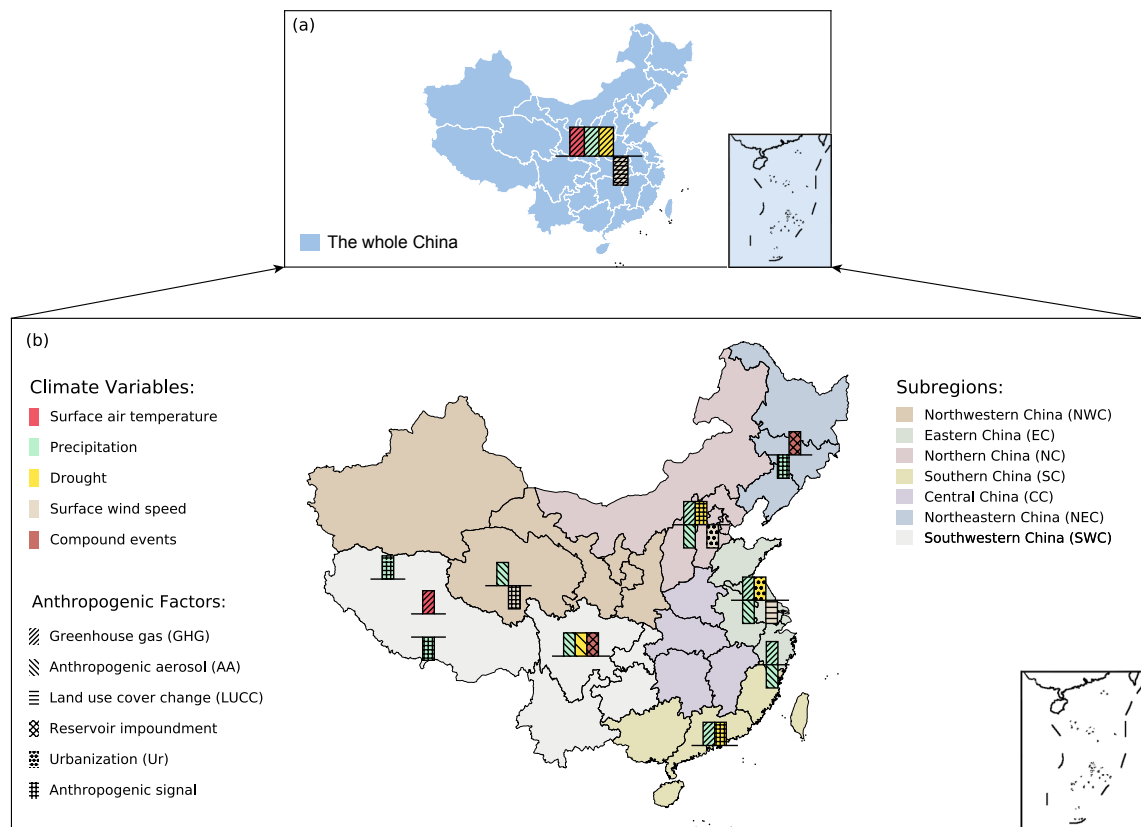


**Fig. 2.** The dominant anthropogenic factors influencing the trend of regional climate changes (including a few climatic parameters) over (a) the whole of China and (b) in a few subregions of China based on study results obtained from references published since 2018. The upward/downward histograms indicate uptrends/downtrends. For the quantitative contributions and further detailed information, please see Table 1. Panel (a) highlights the influences of different anthropogenic factors [legend provided in the lower-left corner of panel (b)] on different climate variables [legend provided in the upper-left corner of panel (b)] over the whole of China (i.e., the nationwide scale). Panel (b) highlights the influences of different anthropogenic factors [legend in the lower-left of panel (b)] on different climate variables [legend in the upper-left of panel (b)] over the subregions [legend in the upper-right of panel (b)].

contributed to hot extremes over China (Chen and Dong, 2019; Sun et al., 2019; Yang et al., 2019, 2021; Liu et al., 2021; Wang et al., 2021a). Urbanization has contributed about 30%–40% of the nighttime high temperature extremes since 1960 over eastern China (Sun et al., 2019). AHR can drastically aggravate urban heat stress (Yang et al., 2021), and has contributed an annual increase of 0.02–0.19 days of extreme heat events in Beijing city center (Liu et al., 2021). It was revealed that urban development increased the total thermal discomfort hours by 27% in the urban areas of the Yangtze River Delta during the period 2009–2013, with AHR and urban land use contributing nearly equal amounts (Yang et al., 2019). The mean contributions of urbanization to the maximum daily maximum temperature, high-temperature days, and hot-night days were 68%, 45% and 27%, respectively, in Beijing, Tianjin and Shijiazhuang (Wang et al., 2021c).

Simultaneously, anthropogenic forcing has significantly decreased regional extreme low-temperature events over China (Table 2). Although the reduced trend of cold events

in southeastern China cannot be attributed with high confidence to any anthropogenic signal alone (Freychet et al., 2021), human influence can clearly be detected in the changes in cold spell durations (Lu et al., 2018), icy days, and frosty nights at the whole-China scale (Wang et al., 2018b; Yin and Sun, 2018). Due to anthropogenic-induced warming, the likelihoods of 2019-like early spring cold events occurring over the southeastern TP (Duan et al., 2021) and of April 2020-like cold events occurring over Northeast China (Yu et al., 2022) have reduced by about 80%. For the record-breaking three-day cold events since 1961 that occurred in January 2021 across eastern China, human activities have reduced the likelihood of such events by about 50% (Liu et al., 2020). Moreover, anthropogenically induced warming also partly contributed to the rapid switches between warm and cold extremes in winter (volatile winters) in China, leading to increased volatile winters in Northeast, Northwest, Southwest, Southeast China, and the Yangtze River Valley after 1980 (Chen et al., 2019c).

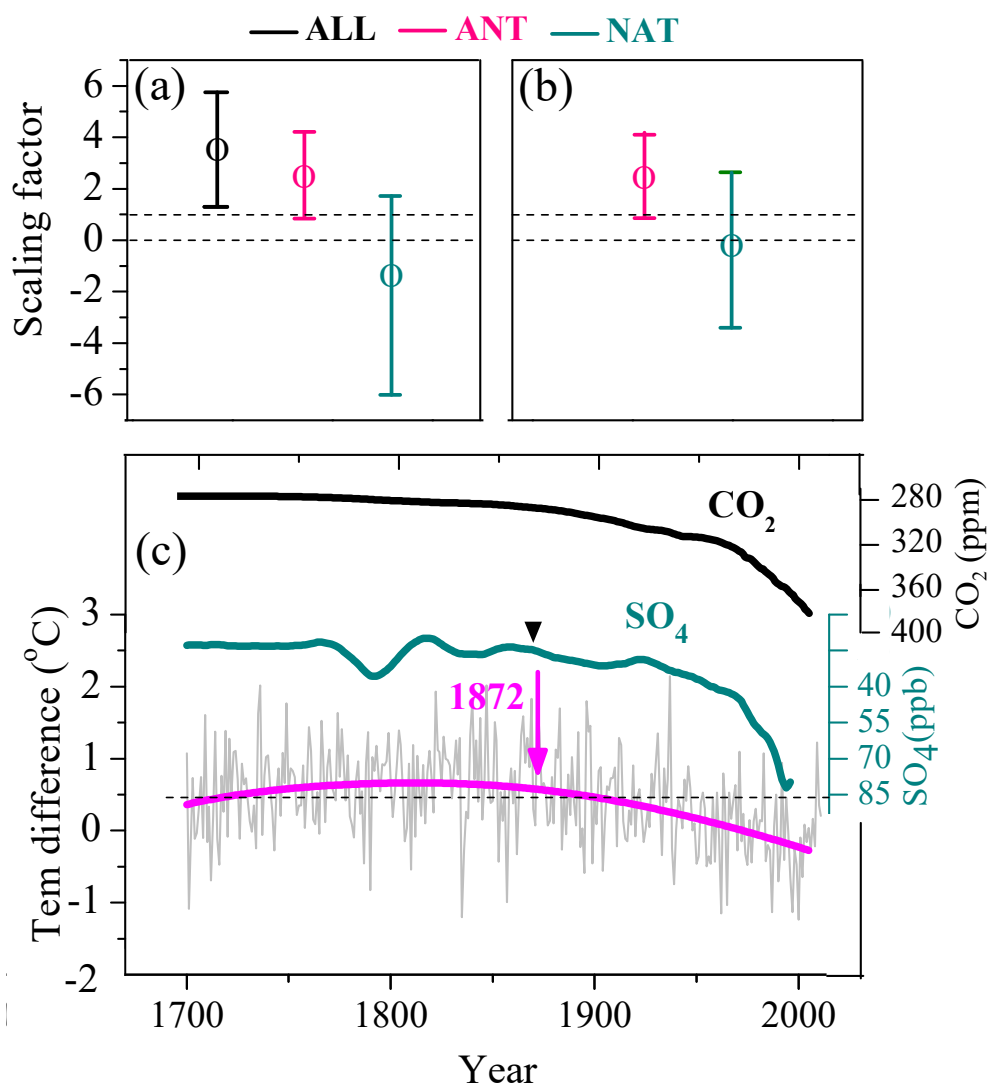


**Fig. 3.** The (a, b) detectable anthropogenic signal and (c) natural evidence for the influence of anthropogenic forcing on temperature seasonality in the TP region since the 1870s. ALL, ANT and NAT mean all forcing, anthropogenic forcing and natural forcing, respectively. Panels (a) and (b) are the scaling factors and corresponding 90% confidence intervals derived from one-signal and two-signal detection and attribution analysis, respectively. The data used in (a, b) are derived from Fig. 4 of Duan et al. (2019). “Tem difference” (grey line) in (c) means the summer minus winter temperature difference, and the pink line is its 50-year Gaussian smoothing. CO<sub>2</sub> (thick black line) and sulfate (dark cyan) concentrations are increasing downwards. The black triangle and the pink arrow in (c) indicate the corresponding turning points. The data used in (c) are derived from Fig. 2 of Duan et al. (2019).

## 4. Anthropogenic influences on regional precipitation and droughts over China

### 4.1. Anthropogenic influences on precipitation trends over China

The signal of anthropogenic forcing of precipitation over China might be region-, season-, period- or intensity-dependent. The anthropogenic signal can be detected in the observed changes in summer precipitation over China and in heavy precipitation over eastern China/the whole of China in recent decades, while external forcings cannot be

detected for moderate or light precipitation individually (Lu et al., 2020a) (Fig. 2, Table 1). Anthropogenic signals also cannot be detected in the trends of either the annual mean or the annual extreme precipitation over China from 1961 to 2010 (Li et al., 2021c). Moreover, it is difficult to separate the contributions of anthropogenic and natural forcings of annual extreme precipitation in northern and southern China in the period 1961–2020 and decompose the anthropogenic component into specific components (e.g., GHG) driving changes in Chinese precipitation (Dong et al., 2022). Regionally, an anthropogenic signal was detected in the changes in

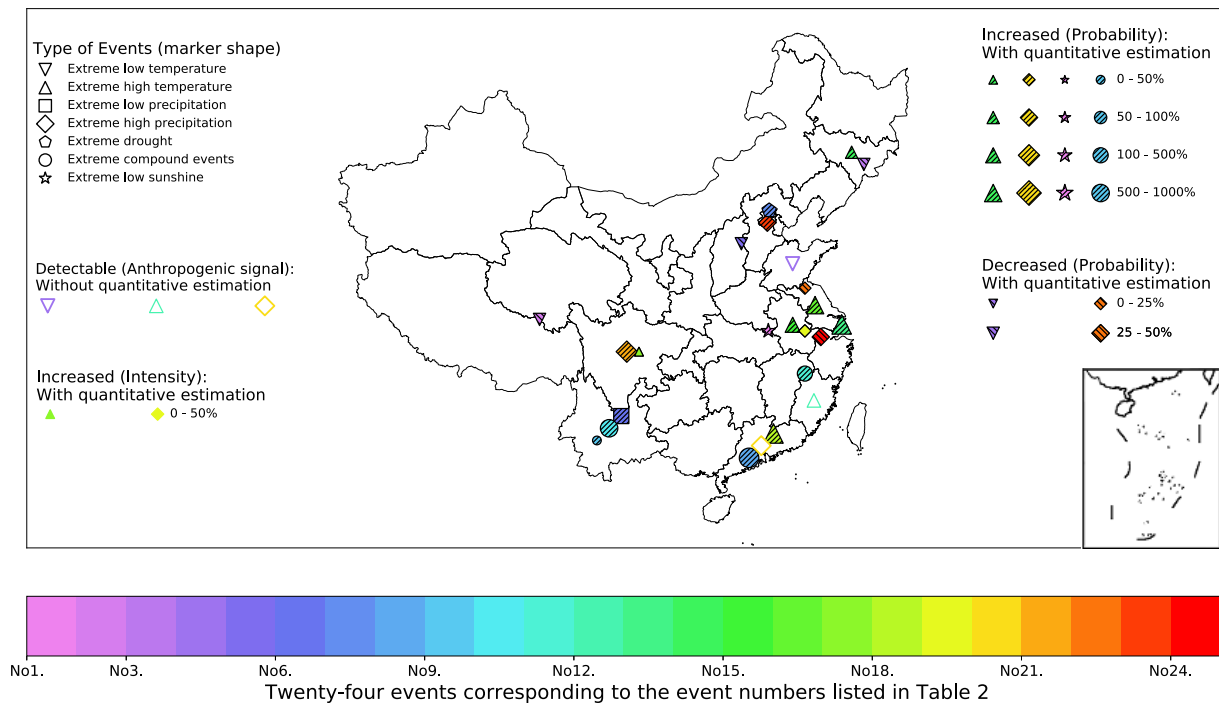


**Fig. 4.** Anthropogenic forcing–induced changes in the occurrence likelihoods of record-breaking climate/weather events that occurred in China in recent years from study results published since 2018. The marker shape in the top-left denotes the type of event, and the open markers in the middle-left indicate detectable anthropogenic signals without quantitative estimations. The solid markers in the bottom-left, upper-right and middle-right indicate detectable anthropogenic signals with quantitative estimations of increased intensity, increased probability, and decreased probability, respectively. The different colors denote the different events listed in Table 2. The color bar shows 24 events corresponding to the event numbers listed in Table 2.

summer precipitation trends over the northern TP, while the change over the southern TP was controlled mainly by internal variability (Zhao et al., 2022). GHGs were identified as the critical factor affecting the increased precipitation frequencies over southern and northeastern China, while AA contributed to the decreased precipitation frequency over northern China (Zhang et al., 2020a). AA also contributed significantly to the decreasing autumn precipitation trends over Southwest China from 1961 to 2007 and over Southeast China in 2020 (Huo et al., 2021; Tan et al., 2022), as well as the reduction in decadal changes in summer rainfall over the northern IndoChina Peninsula since the mid-1990s (Luo et al., 2019). Moreover, anthropogenic forcing has altered the occurrences of daily circulation patterns governing precipitation over eastern China and contributed to shaping the contrasting north–south precipitation trends (Zhou et al., 2021a).

#### 4.2. Anthropogenic influences on precipitation extremes over China

In addition to the effects of anthropogenic forcing on the trend and spatial patterns of precipitation over China, human activity has also affected precipitation extremes over China (Zhai et al., 2018; Duan et al., 2022; Sun et al., 2022). GHG forcing plays an important role in affecting the upward trend of intensified precipitation extremes over China, and AA forcing partly offsets the GHG effect (Xu et al., 2022). In Southeast and Northwest China, GHG and AA

forcings have contributed to the increase in summer extreme precipitation through different processes (Guo et al., 2023). Moreover, anthropogenic forcing positively influenced the temporal inequality of precipitation extremes over China, especially in southern China, during the period 1961–2005 (Duan et al., 2022). Anthropogenic forcing has already decreased the occurrence probability of snowfall relative to natural forcing in some parts of China in recent decades (Chen et al., 2020). At relatively small spatial scales, anthropogenic forcing has likely played a role in increasing the risk of extreme rainfall north of the Yangtze by a factor of 1.64 (Li et al., 2018a) and caused a greater variance in precipitation extremes in the period 1986–2012 than 1960–1985 in the provinces of Zhejiang and Guangdong (Gao et al., 2018; Liu et al., 2020). When the relative humidity (RH) is less than 80% or greater than 85%, increased AA emissions tend to inhibit or enhance precipitation in the middle reaches of the Yangtze River (Bai et al., 2020). However, when RH is between 80% and 85%, AA has little influence on the change in precipitation. A record-breaking (since 1961) heavy rainstorm occurred in Beijing on 19–20 July 2016 (Luo et al., 2020). Although the pattern of synoptic systems (western Pacific subtropical high and cold vortex) has been identified as the key cause of this event, AA also influenced mixed-phase microphysical processes contributing to the heavy rainstorm (Guo et al., 2019). AA also tends to delay and prolong the period with the highest frequency of precipitation start times in the northern China Plain,

**Table 2.** Quantitative contributions of anthropogenic forcings to regional record-breaking climate/weather events over China obtained from references published since 2018. See Table 3 for abbreviation definitions.

Number	Extreme event(s)	Region (site)	Duration	Quantitative contribution (forcing factor)	Reference
1	extreme low sunshine	YRD	Jan–Feb 2019	↑ 3.1 times; ↑ 1.3 times (probability) (AA; GHG)	He et al. (2021)
2	extreme low temperature	TP	Feb–Mar 2019	↓ 80% (probability) (human activity)	Duan et al. (2021)
3	extreme low temperature	NEC	19–25 Apr 2022	↓ 80% (probability) (human activity)	Yu et al. (2022)
4	extreme low temperature	NC	21–25 Jan 2016	↓ 89% (probability) (human activity)	Sun et al. (2018)
5	extreme low temperature	EC	6–8 Jan 2021	detectable (human activity)	Liu et al. (2022)
6	extreme low precipitation	SWC	Apr–Jun 2019	↑ ~6 times (probability) (human activity)	Lu et al. (2021)
7	extreme drought	NC/Beijing	Winter 2017	↑ 1.29 times (probability) (human activity)	Du et al. (2020)
8	extreme compound events	SC	Apr–May 2018	↑ 17 times (probability) (human activity)	Zhang et al. (2020b)
9	extreme compound events	SWC/Yunnan	Spring–early summer 2019	↑ 43% (probability) (human activity)	Wang et al. (2021b)
10	extreme compound events	SWC	May–Jun 2019	↑ 7.21 times (probability) (anthropogenic warming)	Du et al. (2021)
11	extreme compound events (wet–dry)	SC	Summer 2020	↑ 3.51 times (probability) (anthropogenic warming)	Du et al. (2022)
12	extreme high temperature (warming winter)	NC/SEC	Winter 2016	↓ detectable (water vapor / aerosols)	Zhang et al. (2022b)
13	extreme high temperature	EC/Shanghai	Jul 2017	↑ ≥ 10 times (probability) (anthropogenic warming)	Chen et al. (2019b)
14	extreme high temperature	NEC	Jul–Aug 2018	↑ 78% (probability) (anthropogenic)	Zhou et al. (2020)
15	extreme high temperature	CEC	21–25 Jul 2017	↑ 4.8 times (probability) (human activity)	Sparrow et al. (2018)
16	extreme high temperature	EC	Spring 2018	↑ 10 times (probability) (human activity)	Lu et al. (2020b)
17	extreme high temperature	WC	Summer 2015	↑ 42% (intensity) (GHG)	Chen and Dong (2018)
18	extreme high temperature	SC	Sep 2021	↑ 50 times (probability) (anthropogenic warming)	Wang and Sun (2022)
19	extreme high precipitation	EC/Yangtze River	Dec 2018–Feb 2019	↓ 19% (intensity) (anthropogenic warming)	Hu et al. (2021)
20	extreme high precipitation	SC/	14–16 Dec 2013	↑ detectable (AA)	Liu et al. (2021)
21	extreme high precipitation	Guangdong SWC/Sichuan	11–20 Aug 2020	↑ 2 times (probability) (human activity)	Qian et al. (2022)
22	extreme high precipitation	EC	Summer 2020	↓ 46% (probability) (human activity)	Zhou et al. (2021b)
23	extreme high precipitation	NC/Beijing	Winter 2020	↑ 52.9% (probability) (human activity)	Pei et al. (2022)
24	extreme high precipitation	YRB	June, July 2020	↓ 54% (probability) (human activity)	Lu et al. (2022)

Yangtze River Delta, and Pearl River Delta regions (Sun and Zhao, 2021). AA also influenced the warm rain and mixed-phase microphysical processes contributing to the heavy rainstorm that occurred in Beijing on 19–20 July 2016 (Guo et al., 2019).

Anthropogenic signals have also been detected in regional precipitation over China in many case-based quantitative detection and attribution studies (Fig. 4, Table 2). Anthropogenic forcing has increased the likelihood of April to June 2019–like precipitation deficit events in southwestern China by 10% by increasing the probability of anomalous high pressure in southwestern China (Lu et al., 2021). How-

ever, anthropogenic forcing reduced the likelihood of March to July 2019–like heavy precipitation events in southern China by about 60% (Li et al., 2021b) and reduced the likelihood of the rainfall amount in the extended rainy winter of 2018/19 over the middle and lower reaches of the Yangtze River of China by ~19% (Hu et al., 2021). Anthropogenic forcing has reduced the probability of summer persistent heavy rainfall in central western China similar to 2018 by ~47% but increased that of daily rainfall extremes by ~1.5 times (Zhang et al., 2020c). An anthropogenic signal is detectable in the more water vapor pattern (increase by ~100%) that contributed to the high precipitation event that

**Table 3.** Abbreviations used in Tables 1 and 2.

Abbreviation	Full name	Abbreviation	Full name
BTH	Beijing–Tianjin–Hebei	SEC	Southeastern China
CE	Compound Events	SEPTP	Southeastern Periphery of the Tibetan Plateau
CP/SFND	circulation patterns /southern flood–northern drought	STP	Southern Tibetan Plateau
EC	Eastern China	SWC	Southwestern China
NC	Northern China	TCZ	transitional climate zone
NEC	Northeastern China	TP	Tibetan Plateau
N/STP	North/South Tibetan Plateau	VPD	Vapor Deficit
NWC	Northwestern China	WBGT	Wet Bulb Globe Temperature Index
PRD	Pearl River Delta	WC	Western China
SAT	Surface Air Temperature	YIRB	Yalong River Basin
SC	Southern China	YeRB	Yellow River Basin
SCB	Sichuan Basin	YRD	Yangtze river delta

occurred in North China in February 2020 (Pei et al., 2022), and in the intensified daily and subdaily precipitation extremes observed in eastern China since 1970 (Chen et al., 2021). Anthropogenically forced climate change doubled the occurrence probability of 11 to 20 August 2020–like record-breaking persistent heavy rainfall events in southwestern China (Qian et al., 2022). Moreover, extensive urbanization exerted thermal and dynamic influences on precipitation in China, decreasing the total precipitation over and downwind of Beijing city by 11% in summer during 2005–2012 (Wang et al., 2018a) and significantly increasing the hourly precipitation intensity over the Pearl River Delta during 1994–2016 compared to that during 1971–1993 (Wu et al., 2019). The enhanced local AHR combined with global warming (Wen et al., 2020) led to an ~20% to more than 100% increase in the probability of hourly precipitation with a magnitude of 20–100 mm h<sup>-1</sup> occurring over urban locations in China (Fung et al., 2021). Additionally, another study indicated that the anthropogenic influence cannot be significantly detected over China in the observational record or simulations from 1961 to 2012 based on field significance tests (Li et al., 2018b). The above evidence from references published since 2018 indicates that the anthropogenic signal in regional precipitation over China is obscure compared to the signal in the regional SAT, and can be region-, season-, period-, intensity- or model-dependent; the influencing mechanisms are also highly complex.

#### 4.3. Anthropogenic influences on monsoon-related precipitation over China

In addition to the direct influence of human activity on regional precipitation over China, anthropogenic forcing also affects Chinese precipitation indirectly by influencing monsoons. Model simulations have indicated that anthropogenic forcing, especially AA, played a dominant role in the weakened monsoon circulation and the observed decrease in interdecadal precipitation over the South China Sea in the late 20th century (Lin et al., 2020). AA-induced tropospheric cooling over Asian land regions led to anomalous descending motion between 20° and 40°N and reduced the land–sea thermal contrast, resulting in weakened East Asian

summer monsoon (EASM) precipitation over eastern China observed in recent decades (Wang et al., 2019; Zhao et al., 2021). AA forcing significantly exacerbated the weakening of the EASM (Wang et al., 2020b), and the aerosol-induced fast atmospheric response dominated the weakening of the EASM and the decreased precipitation over eastern China (Mu and Wang, 2021). In contrast, GHG forcing led to a wetting trend in the transitional climate zone by inducing southerly wind anomalies, thereby offsetting the effect of AA forcing (Zhao et al., 2021). Black carbon aerosol emissions from different sectors resulted in a regional warming effect over China, leading to an enhanced summer monsoon circulation and a subsequent decrease/increase in rainfall over northeastern/southern China (Zhuang et al., 2019).

#### 4.4. Anthropogenic effects on regional droughts over China

Due to the effects of anthropogenic forcing on SAT and precipitation over China, anthropogenic activities have also contributed to drought events, including meteorological and hydrological droughts, over China (Fig. 4, Tables 1 and 2). The effects of human activity on droughts over China are mainly in the form of GHG-induced warming, increased AA emissions, urbanization, and human water use (Ma et al., 2019; Jiao et al., 2020; Huang et al., 2022). Anthropogenic warming was found to be conducive to the robust increases in the dry and warm meteorological conditions of the autumn drought event over the southeastern periphery of the TP in 2009 (Ma et al., 2017a) and severe droughts in Northwestern China (Ma et al., 2019). Anthropogenic climate change has increased the probability of the 2020 extreme SPEI (Standardized Precipitation Evapotranspiration Index) occurring over the southern coastal regions of China by 3.51 times and explained 71.5% of the attributable risk (Du et al., 2021). Increased GHGs accounted for 77% ± 26% of the upward trend in the flash drought frequency from 1961 to 2005 over China (Yuan et al., 2019). Furthermore, anthropogenic forcing–triggered droughts have increased the fire risk over China. For example, anthropogenic warming has increased the likelihood of the extreme FWI (fire weather index) over Southwest China in 2019 by 7.21 times (Du et



al., 2021).

Although AA has caused humidification over many parts of the globe, a notable aridification effect resulting from AA has occurred over a large part of China (Zhang et al., 2018). Moreover, urbanization has intensified droughts over China. An estimation showed that urbanization has contributed more than 30% to the total increase in atmospheric aridity in Chinese urban core areas (Wang et al., 2022a). However, in the Yangtze River Basin (YaRB), urbanization seems to have alleviated extreme drought conditions (1.14%) while increasing the drought duration and severity (9.02%) (Huang et al., 2022; Wang et al., 2022a). On the other hand, human activities, mainly referring to water management, industrial water usage and reservoir regulation, have exerted a substantial effect on hydrological drought over China (Jiao et al., 2020), but the effects of human activities vary with location. Due to the large amount of irrigation water and high evapotranspiration, human activities have induced a change from a positive correlation to a negative correlation between meteorological and hydrological droughts in the mid-stream region of the Heihe River basin, especially during the warm and irrigation seasons (Ma et al., 2019). In the YaRB and the Yellow River Basin (YeRB), human activities have exerted positive and negative effects on the spatiotemporal characteristics of hydrological droughts, respectively (Jiao et al., 2020; Omer et al., 2020). Specifically, reservoir operations decreased the multiyear monthly discharge but increased the low flow in severe drought years in the middle and lower sub-basins of the YaRB (Jiao et al., 2020). Similarly, in the YeRB, agricultural practices and afforestation intensified soil-moisture drought, while grassland restoration had a positive impact on the agricultural drought severity (Omer et al., 2020). In the Yalong River basin (YIRB), anthropogenic disturbances, mainly referring to the construction of large reservoirs, have led to a dramatic decrease in RH in the past decade, far beyond its previous periodic amplitude range (Liang et al., 2021).

## 5. Influences of anthropogenic forcing on compound extreme weather/climate events over China

Anthropogenic forcing has contributed to compound extreme events, especially compound dry and hot events (CDHEs) and compound daytime and nighttime HWs over China (Fig. 4, Tables 1, 2). Over most regions of China, especially southwestern and northeastern China, anthropogenic forcings, mainly GHG emissions, have increased the likelihood or severity of CDHEs in recent decades (Li et al., Li et al., 2020b, 2022b; Wu et al., 2022). GHG-induced warming increased the likelihood of the CDHEs that occurred in spring to early summer 2019 in Yunnan Province by about 140% (123%–157%) (Wang et al., 2021b). GHG forcing has also produced prominent impacts in terms of an increased frequency, intensity and spatial extent of compound daytime and nighttime HWs over China, while AA forcing

has influenced HWs mainly during the daytime (Wang et al., 2022b; Wang et al., 2018b; Su and Dong, 2019). In addition, urbanization has played an important role in compound maximum daily maximum temperature and minimum daily minimum temperature events in a few regions of China, with contributions ranging from 11% to 41% and 14% to 29%, respectively (Yang et al., 2022). Urban compound daytime and nighttime hot extremes across eastern China increased by  $1.76 \text{ d (10 yr)}^{-1}$  from 1961 to 2014, and the attributable fractions were estimated as 0.51 (urbanization), 1.63 (GHGs) and 0.54 (other anthropogenic forcings)  $\text{d (10 yr)}^{-1}$  (Wang et al., 2021a). Urbanization has also moderated the changes in CDHEs in eastern China (Yu and Zhai, 2020; Yang et al., 2022).

## 6. Influence of human activities on SWS over China

In addition to affecting the SAT, precipitation and drought, human activities have also resulted in changes in SWS over China (Fig. 2, Table 1). Some studies have demonstrated that human activity has been an important factor contributing to regional near-surface wind speed declines over China in recent decades (Bian et al., 2018; Li et al., 2018c; Ao et al., 2020; Wang et al., 2020a, Zhang et al., 2021). The mechanisms by which human activities contribute to the decline in SWS over China may include the following: (1) the high-latitude rapid warming in recent decades weakened the annual and seasonal meridional air temperature gradients and then resulted in slowed SWSs in northern China (Zhang et al., 2021); (2) LUCC led to an increased surface roughness, contributing to a reduction in near-surface wind speeds over China (Zha et al., 2021), especially in urban areas. Related to anthropogenically induced warming, the SWS showed a significant declining trend of  $-0.103 \text{ m s}^{-1} \text{ (10 yr)}^{-1}$  annually, and showed similar seasonal changes in the central and eastern parts of northern China, from 1961 to 2016 (Zhang et al., 2021). In Northwest China, human activities also contributed to the annual and seasonal (except winter) SWS decreases observed during 1980–2012 (Zheng et al., 2018). Urbanization contributed to an annual SWS decline of approximately  $-0.37 \text{ m s}^{-1}$ , with the largest declines exceeding  $-1.0 \text{ m s}^{-1}$  in some highly urbanized areas in the Beijing–Tianjin–Hebei region over the period 1980–2018 (Wang et al., 2020a). Urbanization induced an annual SWS decline of  $-0.13 \text{ m s}^{-1} \text{ (10 yr)}^{-1}$  during the period 1972–2012 at Shijiazhuang Station, contributing 86.0% of the total SWS decline at the station (Bian et al., 2018). Additionally, urbanization has contributed approximately 73.3% to the annual and seasonal SWS declines observed in Liaoning Province over the past 40 years (Ao et al., 2020).

## 7. Summary and future research

Based on the evidence obtained from studies published



since 2018, some achievements are summarized as follows. Human activities, including GHG and AA emissions, urbanization, LUCC, and AHR, have contributed significantly to the SAT trend and extreme changes over China, and the anthropogenic signal can be tracked back to the 1870s in the TP region. The anthropogenic signal affecting precipitation over China is relatively obscure and can be dependent on the period, season, event intensity, spatial scope, or even model simulation. Anthropogenic forcing has also weakened monsoon precipitation, triggered regional droughts, and contributed to the decline in SWS over China. Moreover, anthropogenic forcing, especially GHG-induced warming, has intensified regional compound extreme climate/weather events (e.g., compound dry and hot events and compound daytime and nighttime HWs) over China in recent decades.

While the achievements mentioned above constitute great advancements, further studies have also covered the following points that, whilst challenging, should be considered in future research:

(1) In addition to the significant contribution of anthropogenic forcing to regional climate changes over China, decadal- and multidecadal-scale climate fluctuations may also contribute to those changes simultaneously. Quantitatively attributing regional climate changes to anthropogenic forcing and decadal or multidecadal climate fluctuations is still challenging because sometimes superimposed or counteracting effects occur between these factors.

(2) Many attribution studies have provided quantitative, confirming, and distinct evidence that anthropogenic forcing has influenced the regional climate over China in recent decades, while evidence for earlier periods is relatively rare due to the limited length of observational records. In view of the multitude of climate proxy data available over the TP and eastern China, such as tree rings, ice cores, and historical documents, the detection and attribution of anthropogenic signals based on the combined use of observations, climate proxy data and model simulations could provide further understanding or confirmational evidence regarding the influences of human activity on regional climate changes over China.

(3) To achieve the target of carbon neutrality, clean energy (e.g., hydropower) might be utilized more widely in the future, and this would induce very strong local human activities (e.g., to develop hydropower by building large reservoirs). Specifically, large dams (e.g., the Three Gorges Dam) have significantly influenced the regional climate (e.g., SAT, precipitation and moisture) and atmospheric circulation (Li et al., 2019; 2021a, 2021d, Chen et al., 2022). Apart from hydropower, solar energy is also a promising application (Yang et al., 2018). Solar energy exerts a significant influence, especially through changes in LUCC, on local climate (e.g., surface temperature and albedo) (Hua et al., 2022; Xia et al., 2022; Yang et al., 2022). Such strong local human activity certainly induces a great effect on the regional climate. Assessing and quantifying the influence of human activities on regional climate conditions is a popular and challenging scientific issue.

(4) Compared to general extreme climate/weather events, studies on the influence of human activity on compound extreme climate/weather events are still scarce. China, with the largest population worldwide, is highly vulnerable to meteorological disasters under climate change (IPCC AR6). In view of the great effect of compound extreme climate/weather events on human health/life and crops/plants (Wang et al., 2021a; Zhang et al., 2022c), further studies on the effects of human activity in terms of compound extreme climate/weather events might be a key scientific issue in the future.

**Acknowledgements.** This work was supported by the National Natural Science Foundation of China (Grant No. 41875113).

## REFERENCES

- Allabakash, S., and S. Lim, 2022: Anthropogenic influence of temperature changes across East Asia using CMIP6 simulations. *Scientific Reports*, **12**, 11896, <https://doi.org/10.1038/S41598-022-16110-9>.
- Allen, M. R., and S. F. B. Tett, 1999: Checking for model consistency in optimal fingerprinting. *Climate Dyn.*, **15**, 419–434, <https://doi.org/10.1007/s003820050291>.
- Allen, M. R., and P. A. Stott, 2003: Estimating signal amplitudes in optimal fingerprinting, part I: Theory. *Climate Dyn.*, **21**, 477–491, <https://doi.org/10.1007/s00382-003-0313-9>.
- Ao, X., Q. F. Zhai., Y. Cui, L. D. Shen, X. Y. Zhou, C. Y. Zhao, and L. Zhu, 2020: Analysis of urbanization effect on near-surface wind speed change in Liaoning province. *Meteorological Monthly*, **46**(9), 1153–1164, <https://doi.org/10.7519/j.issn.1000-0526.2020.09.003>. (in Chinese with English abstract)
- Bai, Y. Q., H. X. Qi, T. L. Zhao, Y. Zhou, L. Liu, J. Xiong, Z. M. Zhou, and C. G. Cui, 2020: Simulation of the responses of rainstorm in the Yangtze River Middle Reaches to changes in anthropogenic aerosol emissions. *Atmos. Environ.*, **220**, 117081, <https://doi.org/10.1016/j.atmosenv.2019.117081>.
- Bian, T., G. Y. Ren, and L. X. Zhang, 2018: Significant urbanization effect on decline of near-surface wind speed at Shijiazhuang station. *Climate Change Research*, **14**(1), 21–30, <https://doi.org/10.12006/j.issn.1673-1719.2017.030>. (in Chinese with English abstract)
- Chen, H. P., J. Q. Sun, and W. Q. Lin, 2020: Anthropogenic influence would increase intense snowfall events over parts of the Northern Hemisphere in the future. *Environmental Research Letters*, **15**, 114022, <https://doi.org/10.1088/1748-9326/abbc93>.
- Chen, W., and B. W. Dong, 2018: Drivers of the severity of the extreme hot summer of 2015 in western China. *Journal of Meteorological Research*, **32**, 1002–1010, <https://doi.org/10.1007/s13351-018-8004-y>.
- Chen, W., and B. W. Dong, 2019: Anthropogenic impacts on recent decadal change in temperature extremes over China: Relative roles of greenhouse gases and anthropogenic aerosols. *Climate Dyn.*, **52**, 3643–3660, <https://doi.org/10.1007/s00382-018-4342-9>.
- Chen, W., B. W. Dong, L. Wilcox, F. F. Luo, N. Dunstone, and E. J. Highwood, 2019a: Attribution of recent trends in temperature extremes over China: Role of changes in anthropogenic

- aerosol emissions over Asia. *J. Climate*, **32**, 7539–7560, <https://doi.org/10.1175/JCLI-D-18-0777.1>.
- Chen, Y., and Coauthors, 2019b: Anthropogenic warming has substantially increased the likelihood of July 2017-Like heat waves over central Eastern China. *Bull. Amer. Meteor. Soc.*, **100**(1), S91–S95, <https://doi.org/10.1175/BAMS-D-18-0087.1>.
- Chen, Y., Z. Liao, and P. M. Zhai, 2019c: Coincidence of increasingly volatile winters in China with Arctic sea-ice loss during 1980–2018. *Environmental Research Letters*, **14**, 124076, <https://doi.org/10.1088/1748-9326/ab5c99>.
- Chen, Y., W. Li, X. L. Jiang, P. M. Zhai, and Y. L. Luo, 2021: Detectable Intensification of hourly and daily scale precipitation extremes across eastern China. *J. Climate*, **34**, 1185–1201, <https://doi.org/10.1175/JCLI-D-20-0462.1>.
- Chen, Z. Y., Z. X. Liu, L. R. Yin, and W. F. Zheng, 2022: Statistical analysis of regional air temperature characteristics before and after dam construction. *Urban Climate*, **41**, 101085, <https://doi.org/10.1016/j.uclim.2022.101085>.
- Dong, S. Y., Y. Sun, and X. B. Zhang, 2022: Attributing observed increase in extreme precipitation in China to human influence. *Environmental Research Letters*, **17**, 095005, <https://doi.org/10.1088/1748-9326/ac888e>.
- Du, J. Z., K. C. Wang, S. J. Jiang, B. S. Cui, J. K. Wang, C. F. Zhao, and J. P. Li, 2019: Urban dry island effect mitigated urbanization effect on observed warming in China. *J. Climate*, **32**, 5705–5723, <https://doi.org/10.1175/JCLI-D-18-0712.1>.
- Du, J. Z., K. C. Wang, B. S. Cui, S. J. Jiang, and G. C. Wu, 2020: Attribution of the record-breaking consecutive dry days in winter 2017/18 in Beijing. *Bull. Amer. Meteor. Soc.*, **101**, S95–S102, <https://doi.org/10.1175/BAMS-D-19-0139.1>.
- Du, J. Z., K. C. Wang, and B. S. Cui, 2021: Attribution of the extreme drought-related risk of wildfires in spring 2019 over Southwest China. *Bull. Amer. Meteor. Soc.*, **102**, S83–S90, <https://doi.org/10.1175/BAMS-D-20-0165.1>.
- Du, J. Z., K. Q. Fu, K. C. Wang, and B. S. Cui, 2022: Anthropogenic influences on 2020 extreme dry-wet contrast over South China. *Bull. Amer. Meteor. Soc.*, **103**(3), S68–S75, <https://doi.org/10.1175/BAMS-D-21-0176.1>.
- Duan, J. P., and Coauthors, 2017: Weakening of annual temperature cycle over the Tibetan Plateau since the 1870s. *Nature Communications*, **8**, 14008, <https://doi.org/10.1038/ncomms14008>.
- Duan, J. P., and Coauthors, 2019: Detection of human influences on temperature seasonality from the nineteenth century. *Nature Sustainability*, **2**, 484–490, <https://doi.org/10.1038/s41893-019-0276-4>.
- Duan, J. P., and Coauthors, 2021: Anthropogenic influences on the extreme cold surge of early spring 2019 over the Southeastern Tibetan Plateau. *Bull. Amer. Meteor. Soc.*, **102**, S111–S116, <https://doi.org/10.1175/BAMS-D-20-0215.1>.
- Duan, W. L., and Coauthors, 2022: Changes in temporal inequality of precipitation extremes over China due to anthropogenic forcings. *npj Climate and Atmospheric Science*, **5**, 33, <https://doi.org/10.1038/s41612-022-00255-5>.
- Freychet, N., S. F. B. Tett, A. A. Abatan, A. Schurer, and Z. Feng, 2021: Widespread persistent extreme cold events over South-East China: Mechanisms, trends, and attribution. *J. Geophys. Res.*, **126**, e2020JD033447, <https://doi.org/10.1029/2020JD033447>.
- Fung, K. Y., C.-Y. Tam, T. C. Lee, and Z. Q. Wang, 2021: Comparing the influence of global warming and urban anthropogenic heat on extreme precipitation in urbanized Pearl River Delta area based on dynamical downscaling. *Geophys. Res. Atmos.*, **126**, e2021JD035047, <https://doi.org/10.1029/2021JD035047>.
- Gao, L., J. Huang, X. W. Chen, Y. Chen, and M. B. Liu, 2018: Contributions of natural climate changes and human activities to the trend of extreme precipitation. *Atmospheric Research*, **205**, 60–69, <https://doi.org/10.1016/j.atmosres.2018.02.006>.
- Guo, C. W., H. Xiao, H. L. Yang, and W. Wen, 2019: Effects of anthropogenic aerosols on a heavy rainstorm in Beijing. *Atmosphere*, **10**, 162, <https://doi.org/10.3390/atmos10040162>.
- Guo, Y., B. W. Dong, and J. S. Zhu, 2023: Anthropogenic impacts on changes in summer extreme precipitation over China during 1961–2014: Roles of greenhouse gases and anthropogenic aerosols. *Climate Dyn.*, **60**, 2633–2643, <https://doi.org/10.1007/s00382-022-06453-4>.
- Hasselmann, K., 1993: Optimal fingerprints for the detection of time-dependent climate change. *J. Climate*, **6**, 1957–1971, [https://doi.org/10.1175/1520-0442\(1993\)006<1957:OFFTDO>2.0.CO;2](https://doi.org/10.1175/1520-0442(1993)006<1957:OFFTDO>2.0.CO;2).
- He, Y. Y., K. C. Wang, and D. Qi, 2021: Roles of anthropogenic forcing and natural variability in the record-breaking low sunshine event in January–February 2019 over the Middle-Lower Yangtze Plain. *Bull. Amer. Meteor. Soc.*, **102**, S75–S81, <https://doi.org/10.1175/BAMS-D-20-0185.1>.
- Hu, T., and Y. Sun, 2022: Anthropogenic influence on extreme temperatures in China based on CMIP6 models. *International Journal of Climatology*, **42**, 2981–2995, <https://doi.org/10.1002/joc.7402>.
- Hu, Z. Y., and Coauthors, 2021: Was the extended rainy winter 2018/19 over the Middle and Lower Reaches of the Yangtze River driven by anthropogenic forcing. *Bull. Amer. Meteor. Soc.*, **102**(1), S67–S73, <https://doi.org/10.1175/BAMS-D-20-0127.1>.
- Hua, Y. P., J. Chai, L. Chen, and P. X. Liu, 2022: The influences of the desert photovoltaic power station on local climate and environment: A case study in Dunhuang photovoltaic industrial park, Dunhuang city, China in 2019. *Atmosphere*, **13**, 1235, <https://doi.org/10.3390/atmos13081235>.
- Huang, S. Z., X. Zhang, L. Yang, N. C. Chen, W.-H. Nam, and D. Niyogi, 2022: Urbanization-induced drought modification: Example over the Yangtze River Basin, China. *Urban Climate*, **44**, 101231, <https://doi.org/10.1016/j.uclim.2022.101231>.
- Huo, F., Z. H. Jiang, H. Y. Ma, Z. H. Li, and Y. P. Li, 2021: Reduction in autumn precipitation over Southwest China by anthropogenic aerosol emissions from Eastern China. *Atmospheric Research*, **257**, 105627, <https://doi.org/10.1016/j.atmosres.2021.105627>.
- IPCC, 2021: *Climate Change 2021: The Physical Science Basis. Contribution of Working Group I to the Sixth Assessment Report of the Intergovernmental Panel on Climate Change*. Cambridge University Press.
- Jia, A. L., S. L. Liang, D. D. Wang, B. Jiang, and X. T. Zhang, 2020: Air pollution slows down surface warming over the Tibetan Plateau. *Atmospheric Chemistry and Physics*, **20**, 881–899, <https://doi.org/10.5194/acp-20-881-2020>.
- Jiao, D. L., D. J. Wang, and H. Y. Lv, 2020: Effects of human activities on hydrological drought patterns in the Yangtze River Basin, China. *Natural Hazards*, **104**, 1111–1124, <https://doi.org/10.1007/s11069-020-04206-2>.

- Jin, X. L., P. H. Jiang, H. Y. Du, D. S. Chen, and M. C. Li, 2021: Response of local temperature variation to land cover and land use intensity changes in China over the last 30 years. *Climatic Change*, **164**, 34, <https://doi.org/10.1007/s10584-021-02955-y>.
- Li, C., Y. Sun, F. Zwiers, D. Q. Wang, X. B. Zhang, G. Chen, and H. Wu, 2020a: Rapid warming in summer wet bulb globe temperature in China with human-induced climate change. *J. Climate*, **33**, 5697–5711, <https://doi.org/10.1175/JCLI-D-19-0492.1>.
- Li, C. X., and Coauthors, 2018a: Attribution of extreme precipitation in the lower reaches of the Yangtze River during May 2016. *Environmental Research Letters*, **13**, 014015, <https://doi.org/10.1088/1748-9326/aa9691>.
- Li, H. X., H. P. Chen, B. Sun, H. J. Wang, and J. Q. Sun, 2020b: A detectable anthropogenic shift toward intensified summer hot drought events over Northeastern China. *Earth and Space Science*, **7**, e2019EA000836, <https://doi.org/10.1029/2019EA000836>.
- Li, Q., X. G. Liu, Y. L. Zhong, M. M. Wang, and M. X. Shi, 2021a: Precipitation changes in the Three Gorges Reservoir Area and the relationship with water level change. *Sensors*, **21**, 6110, <https://doi.org/10.3390/s21186110>.
- Li, Q. X., and Coauthors, 2022a: Different climate response persistence causes warming trend unevenness at continental scales. *Nature Climate Change*, **12**, 343–349, <https://doi.org/10.1038/s41558-022-01313-9>.
- Li, R. K., and Coauthors, 2021b: Anthropogenic influences on heavy precipitation during the 2019 extremely wet rainy season in Southern China. *Bull. Amer. Meteor. Soc.*, **102**, S103–S109, <https://doi.org/10.1175/BAMS-D-20-0135.1>.
- Li, W., Z. H. Jiang, X. B. Zhang, and L. Li, 2018b: On the emergence of anthropogenic signal in extreme precipitation change over China. *Geophys. Res. Lett.*, **45**, 9179–9185, <https://doi.org/10.1029/2018GL079133>.
- Li, W., Y. Chen, and W. L. Chen, 2021c: The emergence of anthropogenic signal in mean and extreme precipitation trend over China by using two large ensembles. *Environmental Research Letters*, **16**, 014052, <https://doi.org/10.1088/1748-9326/abd26d>.
- Li, W., Z. H. Jiang, L. Z. X. Li, J.-J. Luo, and P. M. Zhai, 2022b: Detection and attribution of changes in summer compound hot and dry events over Northeastern China with CMIP6 models. *Journal of Meteorological Research*, **36**, 37–48, <https://doi.org/10.1007/s13351-022-1112-8>.
- Li, X., J. Sha, and Z.-L. Wang, 2021d: Influence of the Three Gorges Reservoir on climate drought in the Yangtze River Basin. *Environmental Science and Pollution Research*, **28**, 29 755–29 772, <https://doi.org/10.1007/s11356-021-12704-4>.
- Li, Y., L. G. Wu, X. Y. Chen, and W. C. Zhou, 2019: Impacts of Three Gorges Dam on regional circulation: A numerical simulation. *J. Geophys. Res.*, **124**, 7813–7824, <https://doi.org/10.1029/2018JD029970>.
- Li, Z. Q., L. L. Song, H. Ma, J. J. Xiao, K. Wang, and L. Chen, 2018c: Observed surface wind speed declining induced by urbanization in East China. *Climate Dyn.*, **50**, 735–749, <https://doi.org/10.1007/s00382-017-3637-6>.
- Liang, Y. N., Y. P. Cai, X. Wang, C. H. Li, and Q. Liu, 2021: Projected climate impacts of large artificial reservoir impoundment in Yalong River Basin of southwestern China. *Journal of Hydrometeorology*, **22**, 2179–2191, <https://doi.org/10.1175/JHM-D-21-0042.1>.
- Lin, Z. X., B. W. Dong, and Z. P. Wen, 2020: The effects of anthropogenic greenhouse gases and aerosols on the inter-decadal change of the South China Sea summer monsoon in the late twentieth century. *Climate Dyn.*, **54**, 3339–3354, <https://doi.org/10.1007/s00382-020-05175-9>.
- Liu, B., and Coauthors, 2021: Increases in anthropogenic heat release from energy consumption lead to more frequent extreme heat events in urban cities. *Adv. Atmos. Sci.*, **38**, 430–445, <https://doi.org/10.1007/s00376-020-0139-y>.
- Liu, Y. J., C. Li, Y. Sun, F. Zwiers, X. B. Zhang, Z. H. Jiang, and F. Zheng, 2022: The January 2021 cold air outbreak over Eastern China: Is there a human fingerprint. *Bull. Amer. Meteor. Soc.*, **103**, S50–S54, <https://doi.org/10.1175/BAMS-D-21-0143.1>.
- Liu, Z., Y. Ming, C. Zhao, N. C. Lau, J. P. Guo, M. Bollasina, and S. H. L. Yim, 2020: Contribution of local and remote anthropogenic aerosols to a record-breaking torrential rainfall event in Guangdong Province, China. *Atmospheric Chemistry and Physics*, **20**, 223–241, <https://doi.org/10.5194/acp-20-223-2020>.
- Lu, C. H., Y. Sun, and X. B. Zhang, 2018: Multimodel detection and attribution of changes in warm and cold spell durations. *Environmental Research Letters*, **13**, 074013, <https://doi.org/10.1088/1748-9326/aacb3e>.
- Lu, C. H., F. C. Lott, Y. Sun, P. A. Stott, and N. Christidis, 2020a: Detectable anthropogenic influence on changes in summer precipitation in China. *J. Climate*, **33**, 5357–5369, <https://doi.org/10.1175/JCLI-D-19-0285.1>.
- Lu, C. H., Y. Sun, N. Christidis, and P. A. Stott, 2020b: Contribution of global warming and atmospheric circulation to the hottest spring in Eastern China in 2018. *Adv. Atmos. Sci.*, **37**, 1285–1294, <https://doi.org/10.1007/s00376-020-0088-5>.
- Lu, C. H., J. Jiang, R. D. Chen, S. Ullah, R. Yu, F. C. Lott, S. F. B. Tett, and B. W. Dong, 2021: Anthropogenic influence on 2019 May–June extremely low precipitation in southwestern China. *Bull. Amer. Meteor. Soc.*, **102**, S97–S102, <https://doi.org/10.1175/BAMS-D-20-0128.1>.
- Lu, C. H., Y. Sun, and X. B. Zhang, 2022: The 2020 record-breaking Mei-yu in the Yangtze River Valley of China: The role of anthropogenic forcing and atmospheric circulation. *Bull. Amer. Meteor. Soc.*, **103**(3), S98–S104, <https://doi.org/10.1175/BAMS-D-21-0161.1>.
- Luo, F. F., B. W. Dong, F. X. Tian, and S. L. Li, 2019: Anthropogenically forced decadal change of South Asian summer monsoon across the Mid - 1990s. *J. Geophys. Res.*, **124**, 806–824, <https://doi.org/10.1029/2018JD029195>.
- Luo, L., H. Xiao, H. L. Yang, H. N. Chen, J. Guo, Y. Sun, and L. Feng, 2020: Raindrop size distribution and microphysical characteristics of a great rainstorm in 2016 in Beijing, China. *Atmospheric Research*, **239**, 104895, <https://doi.org/10.1016/j.atmosres.2020.104895>.
- Ma, F., L. F. Luo, A. Z. Ye, and Q. Y. Duan, 2019: Drought characteristics and propagation in the semiarid Heihe River Basin in Northwestern China. *Journal of Hydrometeorology*, **20**, 59–77, <https://doi.org/10.1175/JHM-D-18-0129.1>.
- Ma, S. M., T. J. Zhou, O. Angéilil, and H. Shiogama, 2017a: Increased chances of drought in southeastern periphery of the Tibetan Plateau induced by anthropogenic warming. *J. Climate*, **30**, 6543–6560, <https://doi.org/10.1175/JCLI-D-16-0636.1>.
- Ma, S., and Coauthors, 2017b: Detectable Anthropogenic Shift



- toward Heavy Precipitation over Eastern China. *Journal of Climate*, **30**, 1381–1396, <https://doi.org/10.1175/JCLI-D-16-0311.1>.
- Mu, J. Y., and Z. L. Wang, 2021: Responses of the East Asian summer monsoon to aerosol forcing in CMIP5 models: The role of upper - tropospheric temperature change. *International Journal of Climatology*, **41**, 1555–1570, <https://doi.org/10.1002/joc.6887>.
- Omer, A., M. Zhuguo, Z. Y. Zheng, and F. Saleem, 2020: Natural and anthropogenic influences on the recent droughts in Yellow River Basin, China. *Science of the Total Environment*, **704**, 135428, <https://doi.org/10.1016/j.scitotenv.2019.135428>.
- Otto, F. E. L., 2017: Attribution of weather and climate events. *Annual Review of Environment and Resources*, **42**, 627–646, <https://doi.org/10.1146/annurev-environ-102016-060847>.
- Pei, L., Z. W. Yan, D. L. Chen, and S. G. Miao, 2022: The contribution of human-induced atmospheric circulation changes to the record-breaking winter precipitation event over Beijing in February 2020. *Bull. Amer. Meteor. Soc.*, **103**, S55–S60, <https://doi.org/10.1175/BAMS-D-21-0153.1>.
- Qian, C., and X. B. Zhang, 2015: Human influences on changes in the temperature seasonality in mid- to high-latitude land areas. *J. Climate*, **28**, 5908–5921, <https://doi.org/10.1175/JCLI-D-14-00821.1>.
- Qian, C., Y. B. Ye, W. X. Zhang, T. J. Zhou, 2022: Heavy rainfall event in Mid-August 2020 in Southwestern China: Contribution of anthropogenic forcings and atmospheric circulation. *Bull. Amer. Meteor. Soc.*, **103**(3), S111–S117, <https://doi.org/10.1175/BAMS-D-21-0233.1>.
- Ren, L. W., and Coauthors, 2020: Anthropogenic influences on the persistent night-time heat wave in Summer 2018 over Northeast China. *Bull. Amer. Meteor. Soc.*, **101**, S83–S88, <https://doi.org/10.1175/BAMS-D-19-0152.1>.
- Ribes, A., S. Planton, and L. Terray, 2013: Application of regularised optimal fingerprinting to attribution. Part I: Method, properties and idealised analysis. *Climate Dyn.*, **41**, 2817–2836, <https://doi.org/10.1007/s00382-013-1735-7>.
- Shepherd, T. G., 2016: A common framework for approaches to extreme event attribution. *Current Climate Change Reports*, **2**, 28–38, <https://doi.org/10.1007/s40641-016-0033-y>.
- Sparrow, S., and Coauthors, 2018: Attributing human influence on the July 2017 Chinese heatwave: The influence of sea-surface temperatures. *Environmental Research Letters*, **13**, 114004, <https://doi.org/10.1088/1748-9326/aae356>.
- Stott, P. A., M. R. Allen, and G. S. Jones, 2003: Estimating signal amplitudes in optimal fingerprinting. Part II: Application to general circulation models. *Climate Dyn.*, **21**, 493–500, <https://doi.org/10.1007/s00382-003-0314-8>.
- Su, Q., and B. W. Dong, 2019: Recent decadal changes in heat waves over China: Drivers and mechanisms. *J. Climate*, **32**, 4215–4234, <https://doi.org/10.1175/JCLI-D-18-0479.1>.
- Sun, Y., and C. F. Zhao, 2021: Distinct impacts on precipitation by aerosol radiative effect over three different megacity regions of eastern China. *Atmospheric Chemistry and Physics*, **21**, 16 555–16 574, <https://doi.org/10.5194/acp-21-16555-2021>.
- Sun, Y., T. Hu, X. B. Zhang, H. Wan, P. Stott, and C. H. Lu, 2018: Anthropogenic influence on the Eastern China 2016 super cold surge. *Bull. Amer. Meteor. Soc.*, **99**, S123–S127, <https://doi.org/10.1175/BAMS-D-17-0092.1>.
- Sun, Y., T. Hu, X. B. Zhang, C. Li, C. H. Lu, G. Y. Ren, and Z. H. Jiang, 2019: Contribution of global warming and urbanization to changes in temperature extremes in Eastern China. *Geophys. Res. Lett.*, **46**, 11 426–11 434, <https://doi.org/10.1029/2019GL084281>.
- Sun, Y., X. B. Zhang, Y. H. Ding, D. L. Chen, D. H. Qin, and P. M. Zhai, 2022: Understanding human influence on climate change in China. *National Science Review*, **9**, nwab113, <https://doi.org/10.1093/nsr/nwab113>.
- Tan, X. Z., X. X. Wu, Z. Q. Huang, S. M. Deng, M. C. Hu, and T. Y. Gan, 2022: Detection and attribution of the decreasing precipitation and extreme drought 2020 in southeastern China. *J. Hydrol.*, **610**, 127996, <https://doi.org/10.1016/j.jhydrol.2022.127996>.
- Wang, Y., Y. Sun, T. Hu, D. Qin, and L. Song, 2018: Attribution of temperature changes in Western China. *Int. J. Climatol.*, **38**, 742–750, <https://doi.org/10.1002/joc.5206>.
- Wang, D.-Q., and Y. Sun, 2022: Effects of anthropogenic forcing and atmospheric circulation on the record-breaking wet bulb heat event over southern China in September 2021. *Advances in Climate Change Research*, **13**, 778–786, <https://doi.org/10.1016/j.accre.2022.11.007>.
- Wang, H., S.-P. Xie, Y. Kosaka, Q. Y. Liu, and Y. Du, 2019: Dynamics of Asian summer monsoon response to anthropogenic aerosol forcing. *J. Climate*, **32**, 843–858, <https://doi.org/10.1175/JCLI-D-18-0386.1>.
- Wang, J., J. M. Feng, and Z. W. Yan, 2018a: Impact of extensive urbanization on summertime rainfall in the Beijing region and the role of local precipitation recycling. *J. Geophys. Res.*, **123**, 3323–3340, <https://doi.org/10.1002/2017JD027725>.
- Wang, J., S. F. B. Tett, Z. W. Yan, and J. M. Feng, 2018b: Have human activities changed the frequencies of absolute extreme temperatures in eastern China. *Environmental Research Letters*, **13**, 014012, <https://doi.org/10.1088/1748-9326/aa9404>.
- Wang, J., J. M. Feng, Z. W. Yan, and J. L. Zha, 2020a: Urbanization impact on regional wind stilling: A modeling study in the Beijing-Tianjin-Hebei region of China. *J. Geophys. Res.*, **125**, e2020JD033132, <https://doi.org/10.1029/2020JD033132>.
- Wang, J., and Coauthors, 2021a: Anthropogenic emissions and urbanization increase risk of compound hot extremes in cities. *Nature Climate Change*, **11**, 1084–1089, <https://doi.org/10.1038/s41558-021-01196-2>.
- Wang, P., and Coauthors, 2022a: Amplification effect of urbanization on atmospheric aridity over China under past global warming. *Earth's Future*, **10**, e2021EF002335, <https://doi.org/10.1029/2021EF002335>.
- Wang, S. S., J. P. Huang, and X. Yuan, 2021b: Attribution of 2019 extreme spring-early summer hot drought over Yunnan in Southwestern China. *Bull. Amer. Meteor. Soc.*, **102**, S91–S96, <https://doi.org/10.1175/BAMS-D-20-0121.1>.
- Wang, X. X., X. M. Lang, and D. B. Jiang, 2022b: Detectable anthropogenic influence on summer compound hot events over China from 1965 to 2014. *Environmental Research Letters*, **17**, 034042, <https://doi.org/10.1088/1748-9326/ac4d4e>.
- Wang, Y. J., Y. Y. Ren, L. C. Song, and Y. Xiang, 2021c: Responses of extreme high temperatures to urbanization in the Beijing–Tianjin–Hebei urban agglomeration in the context of a changing climate. *Meteorological Applications*, **28**, e2024, <https://doi.org/10.1002/met.2024>.
- Wang, Z. L., J. Y. Mu, M. L. Yang, and X. C. Yu, 2020b: Reexamining the mechanisms of East Asian summer monsoon changes in response to Non-East Asian anthropogenic

- aerosol forcing. *J. Climate*, **33**, 2929–2944, <https://doi.org/10.1175/JCLI-D-19-0550.1>.
- Wen, J. P., J. Chen, W. S. Lin, B. L. Jiang, S. S. Xu, and J. Lan, 2020: Impacts of anthropogenic heat flux and urban Land-Use change on frontal rainfall near coastal regions: A case study of a rainstorm over the Pearl River Delta, South China. *J. Appl. Meteorol. Climatol.*, **59**, 363–379, <https://doi.org/10.1175/JAMC-D-18-0296.1>.
- Wu, M. W., Y. L. Luo, F. Chen, and W. K. Wong, 2019: Observed link of extreme hourly precipitation changes to urbanization over coastal South China. *J. Appl. Meteorol. Climatol.*, **58**, 1799–1819, <https://doi.org/10.1175/JAMC-D-18-0284.1>.
- Wu, X. Y., Z. C. Hao, Y. Zhang, X. Zhang, and F. H. Hao, 2022: Anthropogenic influence on compound dry and hot events in China based on coupled model intercomparison project phase 6 models. *International Journal of Climatology*, **42**, 4379–4390, <https://doi.org/10.1002/joc.7473>.
- Xia, Z. L., Y. J. Li, W. Zhang, R. S. Chen, S. C. Guo, P. Zhang, and P. J. Du, 2022: Solar photovoltaic program helps turn deserts green in China: Evidence from satellite monitoring. *Journal of Environmental Management*, **324**, 116338, <https://doi.org/10.1016/j.jenvman.2022.116338>.
- Xie, Y. K., J. P. Huang, and Y. Ming, 2019: Robust regional warming amplifications directly following the anthropogenic emission. *Earth's Future*, **7**, 363–369, <https://doi.org/10.1029/2018EF001068>.
- Xu, H. W., H. P. Chen, and H. J. Wang, 2022: Detectable human influence on changes in precipitation extremes across China. *Earth's Future*, **10**, e2021EF002409, <https://doi.org/10.1029/2021EF002409>.
- Yang, B., and Coauthors, 2019: Modeling the impacts of urbanization on summer thermal comfort: The role of urban land use and anthropogenic heat. *J. Geophys. Res.*, **124**, 6681–6697, <https://doi.org/10.1029/2018JD029829>.
- Yang, J. N., X. Y. Li, W. Peng, F. Wagner, and D. L. Mauzerall, 2018: Climate, air quality and human health benefits of various solar photovoltaic deployment scenarios in China in 2030. *Environmental Research Letters*, **13**, 064002, <https://doi.org/10.1088/1748-9326/aabe99>.
- Yang, S., S. W. Li, B. Chen, Z. M. Xie, and J. Peng, 2021: Responses of heat stress to temperature and humidity changes due to anthropogenic heating and urban expansion in south and North China. *Frontiers in Earth Science*, **9**, 673943, <https://doi.org/10.3389/feart.2021.673943>.
- Yang, Y., N. Zhao, Y. W. Wang, and M. X. Chen, 2022: Variations in summertime compound heat extremes and their connections to urbanization in China during 1980–2020. *Environmental Research Letters*, **17**, 064024, <https://doi.org/10.1088/1748-9326/ac61c5>.
- Yin, H., and Y. Sun, 2018: Detection of anthropogenic influence on fixed threshold indices of extreme temperature. *J. Climate*, **31**, 6341–6352, <https://doi.org/10.1175/JCLI-D-17-0853.1>.
- Yin, H., Y. Sun, and M. G. Donat, 2019: Changes in temperature extremes on the Tibetan Plateau and their attribution. *Environmental Research Letters*, **14**, 124015, <https://doi.org/10.1088/1748-9326/ab503c>.
- Yin, H., Y. Sun, and M.-Y. Li, 2022: Reconstructed temperature change in late summer over the eastern Tibetan Plateau since 1867 CE and the role of anthropogenic forcing. *Global and Planetary Change*, **208**, 103715, <https://doi.org/10.1016/j.gloplacha.2021.103715>.
- Yu, H. Y., and Coauthors, 2022: Attribution of April 2020 exceptional cold spell over Northeast China. *Bull. Amer. Meteor. Soc.*, **103**, S61–S67, <https://doi.org/10.1175/BAMS-D-21-0175.1>.
- Yu, R., and P. M. Zhai, 2020: Changes in compound drought and hot extreme events in summer over populated eastern China. *Weather and Climate Extremes*, **30**, 100295, <https://doi.org/10.1016/j.wace.2020.100295>.
- Yuan, X., L. Y. Wang, P. L. Wu, P. Ji, J. Sheffield, and M. Zhang, 2019: Anthropogenic shift towards higher risk of flash drought over China. *Nature Communications*, **10**, 4661, <https://doi.org/10.1038/s41467-019-12692-7>.
- Zha, J. L., D. M. Zhao, J. Wu, and C. Shen, 2021: Terrestrial near-surface wind speed variations in China: Research progress and prospects. *Journal of Meteorological Research*, **35**, 537–556, <https://doi.org/10.1007/s13351-021-0143-x>.
- Zhai, P. M., B. Q. Zhou, and Y. Chen, 2018: A review of climate change attribution studies. *Journal of Meteorological Research*, **32**, 671–692, <https://doi.org/10.1007/s13351-018-8041-6>.
- Zhang, B., B. W. Dong, and R. H. Jin, 2020a: Forced decadal changes in summer precipitation characteristics over China: The roles of greenhouse gases and anthropogenic aerosols. *Journal of Meteorological Research*, **34**, 1226–1241, <https://doi.org/10.1007/s13351-020-0060-4>.
- Zhang, G. F., and Coauthors, 2021: Uneven warming likely contributed to declining near-surface wind speeds in Northern China between 1961 and 2016. *J. Geophys. Res.*, **126**, e2020JD033637, <https://doi.org/10.1029/2020JD033637>.
- Zhang, H., C. Zhou, and S. Y. Zhao, 2018: Influences of the internal mixing of anthropogenic aerosols on global aridity change. *Journal of Meteorological Research*, **32**, 723–733, <https://doi.org/10.1007/s13351-018-7155-1>.
- Zhang, L. X., T. J. Zhou, X. L. Chen, P. L. Wu, N. Christidis, and F. C. Lott, 2020b: The late spring drought of 2018 in South China. *Bull. Amer. Meteor. Soc.*, **101**, S59–S64, <https://doi.org/10.1175/BAMS-D-19-0202.1>.
- Zhang, S. Q., G. Y. Ren, Y. Y. Ren, and S. KealdrupTysa, 2022a: Linkage of extreme temperature change with atmospheric and locally anthropogenic factors in China mainland. *Atmospheric Research*, **277**, 106307, <https://doi.org/10.1016/j.atmosres.2022.106307>.
- Zhang, T. T., Y. Deng, J. W. Chen, S. Yang, P. Gao, and H. N. Zhang, 2022b: Disentangling physical and dynamical drivers of the 2016/17 record-breaking warm winter in China. *Environmental Research Letters*, **17**, 074024, <https://doi.org/10.1088/1748-9326/ac79c1>.
- Zhang, T. Y., and Coauthors, 2022c: Climate change may outpace current wheat breeding yield improvements in North America. *Nature Communications*, **13**, 5591, <https://doi.org/10.1038/s41467-022-33265-1>.
- Zhang, W. X., and Coauthors, 2020c: Anthropogenic influence on 2018 summer persistent heavy rainfall in Central Western China. *Bull. Amer. Meteor. Soc.*, **101**, S65–S70, <https://doi.org/10.1175/BAMS-D-19-0147.1>.
- Zhang, W. X., L. W. Ren, and T. J. Zhou, 2022d: Understanding differences in event attribution results arising from modeling strategy. *Journal of Meteorological Research*, **36**, 49–60, <https://doi.org/10.1007/s13351-022-1109-3>.
- Zhang, X. Y., J. H. Yu, L. Z. X. Li, and W. Li, 2022e: Role of anthropogenic climate change in autumn drought trend over

- China from 1961 to 2014. *Journal of Meteorological Research*, **36**, 251–260, <https://doi.org/10.1007/s13351-022-1178-3>.
- Zhang, L., X. Chen, and R. Lai, 2020d: Urban signatures of sub-daily extreme precipitation events over a metropolitan region. *Atmospheric Research*, **246**, 105204, <https://doi.org/10.1016/j.atmosres.2020.105204>.
- Zhao, D., L. X. Zhang, and T. J. Zhou, 2022: Detectable anthropogenic forcing on the long-term changes of summer precipitation over the Tibetan Plateau. *Climate Dyn.*, **59**, 1939–1952, <https://doi.org/10.1007/s00382-022-06189-1>.
- Zhao, W., W. Chen, S. F. Chen, H. N. Gong, and T. J. Ma, 2021: Roles of anthropogenic forcings in the observed trend of decreasing late-summer precipitation over the East Asian transitional climate zone. *Sci Rep*, **11**, 4935, <https://doi.org/10.1038/s41598-021-84470-9>.
- Zheng, J. L., B. F. Li, Y. N. Chen, Z. S. Chen, and L. S. Lian, 2018: Spatiotemporal variation of upper-air and surface wind speed and its influencing factors in northwestern China during 1980–2012. *Theor. Appl. Climatol.*, **133**, 1303–1314, <https://doi.org/10.1007/s00704-017-2346-8>.
- Zhou, B. Q., P. M. Zhai, S. F. B. Tett, and F. C. Lott, 2021a: Detectable anthropogenic changes in daily-scale circulations driving summerrainfall shifts over eastern China. *Environmental Research Letters*, **16**, 074044, <https://doi.org/10.1088/1748-9326/ac0f28>.
- Zhou, C. L., D. L. Chen, K. C. Wang, A. G. Dai, and D. Qi, 2020: Conditional attribution of the 2018 summer extreme heat over northeast China: Roles of urbanization, global warming, and warming-induced circulation changes. *Bull. Amer. Meteor. Soc.*, **101**, S71–S76, <https://doi.org/10.1175/BAMS-D-19-0197.1>.
- Zhou, T. J., and W. X. Zhang, 2021: Anthropogenic warming of Tibetan Plateau and constrained future projection. *Environmental Research Letters*, **16**, 044039, <https://doi.org/10.1088/1748-9326/abede8>.
- Zhou, T. J., L. W. Ren, and W. X. Zhang, 2021b: Anthropogenic influence on extreme Meiyu rainfall in 2020 and its future risk. *Science China Earth Sciences*, **64**, 1633–1644, <https://doi.org/10.1007/s11430-020-9771-8>.
- Zhuang, B. L., and Coauthors, 2019: The direct effects of black carbon aerosols from different source sectors in East Asia in summer. *Climate Dyn.*, **53**, 5293–5310, <https://doi.org/10.1007/s00382-019-04863-5>.



• Review •

# Recent Advances in China on the Predictability of Weather and Climate<sup>✉</sup>

Wansuo DUAN<sup>1,2</sup>, Lichao YANG<sup>\*1</sup>, Mu MU<sup>3</sup>, Bin WANG<sup>1</sup>, Xueshun SHEN<sup>4</sup>, Zhiyong MENG<sup>5</sup>, and Ruiqiang DING<sup>6</sup>

<sup>1</sup>*LASG, Institute of Atmospheric Physics, Chinese Academy of Sciences, Beijing 100029, China*

<sup>2</sup>*Collaborative Innovation Center on Forecast and Evaluation of Meteorological Disasters (CIC-FEMD), Nanjing University of Information Science & Technology, Nanjing 210044, China*

<sup>3</sup>*Department of Atmospheric and Oceanic Sciences/Institute of Atmospheric Sciences, Fudan University, Shanghai 200438, China*

<sup>4</sup>*CMA Earth System Modeling and Prediction Center, China Meteorological Administration, Beijing 100081, China*

<sup>5</sup>*CMA Tornado Key Laboratory, Department of Atmospheric and Oceanic Sciences, School of Physics, Peking University, Beijing 100871, China*

<sup>6</sup>*Faculty of Geographical Science, Beijing Normal University, Beijing 100875, China*

(Received 4 November 2022; revised 27 March 2023; accepted 7 April 2023)

## ABSTRACT

This article summarizes the progress made in predictability studies of weather and climate in recent years in China, with a main focus on advances in methods to study error growth dynamics and reduce uncertainties in the forecasting of weather and climate. Specifically, it covers (a) advances in methods to study weather and climate predictability dynamics, especially those in nonlinear optimal perturbation methods associated with initial errors and model errors and their applications to ensemble forecasting and target observations, (b) new data assimilation algorithms for initialization of predictions and novel assimilation approaches to neutralize the combined effects of initial and model errors for weather and climate, (c) applications of new statistical approaches to climate predictions, and (d) studies on meso- to small-scale weather system predictability dynamics. Some of the major frontiers and challenges remaining in predictability studies are addressed in this context.

**Key words:** predictability, target observation, data assimilation, ensemble forecasting

**Citation:** Duan, W. S., L. C. Yang, M. Mu, B. Wang, X. S. Shen, Z. Y. Meng, and R. Q. Ding, 2023: Recent advances in China on the predictability of weather and climate. *Adv. Atmos. Sci.*, **40**(8), 1521–1547, <https://doi.org/10.1007/s00376-023-2334-0>.

## Article Highlights:

- The CNOP method has been successful in field campaigns for targeting observations associated with real-time forecasts of tropical cyclones.
- The DRP-4DVar data assimilation method, proposed by Chinese scientists, has greatly reduced the initial shock phenomenon in decadal predictions.
- Emerging methods such as complex networks and AI are expected to significantly enhance the prediction capabilities of weather and climate events.

## 1. Introduction

High-impact weather and climate events [e.g., typhoons,

rainstorms, monsoon, El Niño–Southern Oscillation (ENSO), and Indian Ocean Dipole (IOD) events] have serious adverse effects on society, the economy, and people’s lives in China and elsewhere across the globe, and thus predicting such events has always been a key concern of governments and the general public. Although initial errors due to insufficient observations at present, and model errors due to imperfect descriptions of atmospheric and oceanic processes, inevitably exist in numerical forecasts, governments and the

✉ This paper is a contribution to the special issue on the National Report to the 28th IUGG General Assembly by CNC-IAMAS (2019–2022).

\* Corresponding author: Lichao YANG  
Email: [yanglc@mail.iap.ac.cn](mailto:yanglc@mail.iap.ac.cn)

public still expect relevant agencies to provide high quality weather forecasting and climate prediction services in a timely manner. A key question posed to meteorologists, therefore, is how can we maximize the forecasting capability for weather and climate using current numerical prediction systems?

To address this question, one first needs to recognize the reasons and mechanisms responsible for prediction uncertainties and identify the major sources of forecast uncertainties. Thereafter, one can then study how to effectively reduce those forecast uncertainties. Such studies belong to the research field of predictability (Mu et al., 2004b, 2017a). Since a high forecast skill is closely related and important to everyone's lives, the predictability of high-impact weather and climate events has long been recognized as a frontier research topic in the atmospheric and oceanic sciences. Indeed, it is listed as the core research subject in the "World Weather Research Program" (<https://public.wmo.int/en/programmes/world-weather-research-programme>) and the "World Climate Research Program" (<https://www.wcrp-climate.org/clivar>).

Studies on predictability dynamics generally provide useful guidance to improve the forecasting skills for weather and climate (Palmer et al., 1998; Mu et al., 2002; Duan and Mu, 2015). They generally focus on estimation of the predictability time, identification of the predictability sources and associated uncertainties, and recognition of the mechanism responsible for error growth (Kalnay, 2002; Mu et al., 2017a; Duan and Mu, 2018). These concerns are often explored by investigating the growth dynamics of forecast errors caused by initial and/or model uncertainties. Then, an effective forecasting strategy can be constructed to predict the weather and climate events of concern.

Data assimilation (DA) is recognized as one of the most important forecast strategies to reduce the prediction uncertainties induced by initial errors (Bauer et al., 2015). It combines a limited number of observations with numerical models and their respective error statistics to provide an improved estimate (or analysis) of the present state (Tala-Grand, 1997). Bauer et al. (2015) pointed out that the advances in numerical weather prediction (NWP) have undergone a quiet revolution in the past 30 years, resulting in the forecasting skill having increased by nearly 30% during this period, and the improvement is even more substantial in the Southern Hemisphere. Such a breakthrough was achieved through exploiting satellite data and the variational DA approach (Bauer et al., 2015). It is obvious that DA plays an important role in achieving high-quality forecasts in modern NWP.

In addition to advanced DA methods, targeted observations are essential to obtain a high-quality forecast (Mu et al., 2015; Parsons et al., 2017). Actually, if an advanced DA approach together with additional targeted observations (Snyder, 1996) is used to predict high-impact weather or climate events, a more accurate initial state can be obtained, and their forecasting skill can be increased to a large extent. In tar-

geted observation strategies, to better predict an event occurring in an area (i.e., the verification area) at a given future time  $t_1$ , additional observations are deployed at a much earlier time  $t_0$  (i.e., the target time;  $t_0 < t_1$ ) in a few key areas (i.e., sensitive areas), where the additional observations are expected to make a larger contribution to reducing the forecast errors in the verification area; and assimilating these observations will provide a more reliable initial state and then a more accurate prediction (Snyder, 1996). Theoretically, if the initial perturbations that cause the largest perturbation growth can be identified, the initial errors located in the areas where the perturbations are concentrated are generally thought of as contributing more to the forecast errors, and thus preferentially assimilating additional targeted observations in these areas will reduce initial error effects much more effectively and improve the forecast skill greatly [see the reviews by Majumdar (2016) and Mu et al. (2015)]. Targeted observation strategies have been implemented in field campaigns associated with high-impact-weather forecasts (Langland et al., 1999; Wu et al., 2005, 2007). In the 21st century, targeted observation has become one of the main components of the new international atmospheric science program advocated by the World Meteorological Organization (WMO)—namely, the Observing System Research and Predictability Experiment (THORPEX; WMO, 2004)—and has achieved great success in field campaigns for typhoon forecasting (Parsons et al., 2017). A new Tropical Pacific Observing System (TPOS2020; <https://tropicalpacific.org/>) plan has been proposed to optimize the Tropical Atmosphere/Ocean observational network/Triangle Trans-Ocean Buoy Network (TRITON) to address the challenge of ENSO predictions posed by El Niño diversity (Cravatte et al., 2016; Kessler et al., 2021); furthermore, Chen et al. (2018) stated that a targeted observation strategy would be useful for refining observational networks. These findings certainly emphasize the importance of implementing targeted observation strategies in high-impact-weather and climate predictions.

Tennekes (1991) pointed out that a complete forecast includes not only a deterministic forecast but also an estimation of its uncertainty. Therefore, reliable estimation of uncertainties is indispensable for complete forecasts. Ensemble forecasting is a useful method that provides estimation of uncertainties by evaluating ensemble spread (Du et al., 2018; Duan et al., 2019). The idea of ensemble forecasting is that the perturbations that reflect the uncertainties of the initial states are superimposed on the initial condition in the control run to generate an initial ensemble, and then the forecast error of the ensemble mean can be quantified using the spread of the forecast ensemble (Leith, 1974). These members can also be used to calculate the probability for the occurrence of the weather or climate events of concern [see the review by Kriz (2019)]. Since the analysis errors in the control forecasts often grow quickly, the perturbations for ensemble forecasting should present fast-growing dynamical behaviors; in this situation, the optimally growing perturbations are useful for improving the ensemble forecast skill. Due to the abun-

dance of forecast products of ensemble forecasting, this method plays an irreplaceable role in numerical prediction and has been listed as one of the main development strategies of current numerical prediction by the WMO (Majumdar et al., 2021).

Consequently, a complete high-quality forecast should contain an accurate forecast result and a reliable estimation of its uncertainties. To produce an accurate forecast result, in addition to using a superior numerical model, one should also use advanced DA methods and targeted observations. Furthermore, a reliable ensemble forecast system is also essential to obtain an effective estimation of the forecast uncertainties. Therefore, to greatly improve the forecasting skill for high-impact weather and climate events, meteorologists should synthesize theoretical and practical research on targeted observations, DA, and ensemble forecasting under the framework of an advanced numerical model, based on the guidance of theoretical studies on predictability dynamics. In recent years, Chinese scientists have made great progress in this field and some of their results have been implemented in operational centers in China. This paper summarizes this progress, as well as future prospects, especially on major frontiers and challenges in research on methods to study error growth dynamics and to reduce the uncertainties in forecasting weather and climate.

## 2. Advances in studies of nonlinear optimal perturbations for weather and climate predictability dynamics

Consensus has been reached that the best methods for predicting geophysical dynamical systems are optimization methods (e.g., DA); however, such methods for estimating forecast uncertainty remain controversial (Smith et al., 1999). Currently, there are two approaches to optimization methods for error growth estimations. One is to solve the optimally growing initial perturbation during a given period of prediction, while the other searches for the optimally growing perturbations during a time period before the initialization of prediction. One representative example in the former approach is that of singular vectors (SVs, Lorenz, 1965), and one in the latter approach is Lyapunov vectors (Toth and Kalnay, 1993). However, these two approaches are both linear and do not contain the effects of nonlinearity that exist in atmospheric and oceanic motions or land surface processes (Mu, 2000; Kalnay, 2002). In this section, we summarize the advances made in studies of nonlinear optimal perturbations achieved by Chinese scientists via these two approaches.

### 2.1. Conditional nonlinear optimal perturbation: applications to ensemble forecasting and targeted observations

As mentioned above, SVs (Lorenz, 1965) are traditional approaches to estimating the growth of initial errors, and work by simplifying nonlinear systems to be linear and allowing exploration of the initial error that causes the largest pre-

diction error during a given time period. Although SVs have been widely used to address the error growth dynamics of atmospheric and oceanic predictability and even to yield initial perturbations of ensemble forecasting for weather and climate events and identify sensitive areas for targeted observation (Mu et al., 2015, Majumdar, 2016; Duan and Mu, 2018), they do not consider the modulation effect on optimal perturbations of nonlinear processes (Mu, 2000; Sévellec and Fedorov, 2013; Winkler et al., 2020). To overcome this limitation, Mu et al. (2003) proposed a novel approach of conditional nonlinear optimal perturbation (CNOP) in the field of atmospheric sciences. Similar optimal perturbation also subsequently appeared in the fields of fluid mechanics (see Pringle and Kerswell, 2010; Kerswell et al., 2014). Such perturbations often describe the initial perturbation that satisfies a certain constraint condition and have the largest departure from the reference state at a given future time. The CNOP has been applied to find the optimal precursor (OPR) for the occurrence of high-impact oceanic-atmospheric environmental events such as ENSO and IOD events (Duan et al., 2004; Duan and Zhao, 2014; Mu et al., 2017b; Yang et al., 2020), as well as explore the optimally growing initial errors (OGEs) for targeted observations associated with the forecasts of tropical cyclones (TCs; Mu et al., 2009; Qin et al., 2013; Qin and Mu, 2014), the season-dependent predictability barrier for ENSO and IOD events (Mu et al., 2007; Duan et al., 2009; Feng and Duan, 2014; Duan and Mu, 2018; Liu et al., 2018a), and the stability and sensitivity analyses of both thermohaline circulation and terrestrial ecosystems (Mu et al., 2004a; Sun and Mu, 2014; Zu et al., 2016). All these works not only reveal the important role of considering nonlinear effects, but also provide useful guidance for improving weather and climate predictions. In particular, in recent years, the CNOP has been extended to applications in ensemble forecasting for weather and climate forecasting and field campaigns for targeted observations associated with TC forecasting; furthermore, it has been extended from the original CNOP representing the OGEs [for convenience, hereafter referred to as CNOP-I (Mu et al., 2003, 2010)] to the additional CNOP-P for addressing the influences of optimal model parametric error (Mu et al., 2010), CNOP-B for revealing the boundary uncertainties that have the largest effect on forecasts (Wang and Mu, 2015), and CNOP-F [i.e., the nonlinear forcing singular vector (NFSV) proposed in Duan and Zhou (2013)] for exploring combined effects of various model errors. Thus, a family of CNOPs has been achieved, including CNOP-I, -P, -B and -F (Wang et al., 2020a). All these perturbations fully consider the effects of nonlinear physical processes and have been shown to represent the optimally growing mode in their respective scenarios. To facilitate readers, we summarize the CNOP family and their respective benefits in Table 1.

#### 2.1.1. Ensemble forecasting

In applications of CNOPs, CNOP-I was recently applied to ensemble forecasting, and orthogonal CNOPs (i.e., O-CNOPs), which is a new approach to yield initial per-

**Table 1.** The CNOP family and their respective benefits.

CNOP type	Representation	Benefit	References
CNOP-I	The initial perturbation that satisfies a certain physical constraint but causes the largest evolution of state perturbation at the prediction time	CNOP-I version: more accurately identifies the sensitive area for targeted observation O-CNOPs version: more reasonably depicts initial uncertainty in ensemble forecasting	Mu et al. (2007); Qin et al. (2023); Jiang et al. (2022) Duan and Huo (2016); Huo et al. (2019); Huo and Duan (2019); Zhang and Tian (2022)
CNOP-P	The parameter perturbation that yields the largest evolution of state perturbation at the prediction time	CNOP-P version: identifies the most sensitive parameter or the optimal multi-parameter combination for targeted observation and ensemble forecasting	Mu et al. (2010); Duan and Zhang (2010); Sun and Mu (2017a, b); Wang et al. (2020b)
CNOP-B	The boundary perturbation that causes the largest evolution of state perturbation at the prediction time	CNOP-B version: reveals the boundary condition error that exerts the largest effect on the prediction error	Wang and Mu (2015); Ma et al. (2022)
CNOP-F (also NFSV)	The tendency perturbation that yields the largest evolution of the state perturbation at the prediction time	CNOP-F version: more reasonably identifies the area that contributes a much larger model error effect on the prediction error O-NFSVs version: generates mutually independent tendency perturbations to address the effects of different kinds of model uncertainties in ensemble forecasting C-NFSVs version: produces dynamically coordinated initial and model perturbations to deal with the combined effect of initial and model uncertainties in ensemble forecasting	Duan and Zhou (2013); Zhao and Duan (2014) Zhang et al. (2022a); Xu et al. (2022b) Duan et al. (2022a)

turbations for ensemble forecasting, were proposed (Duan and Huo, 2016). O-CNOPs have been used to provide skillful forecasts for TC tracks. For example, Huo et al. (2019) demonstrated that the ensembles generated by O-CNOPs, as compared with those made by traditional SVs, Bred Vectors (BVs), and Random Perturbations (RPs), can present much larger spreads; moreover, they tend to appear on both sides of real TC tracks and have high prediction reliability for TC tracks, ultimately providing much higher forecasting skill for TC tracks (Huo and Duan, 2019).

CNOP-P, which was proposed to address optimal parametric perturbation, has also been used in ensemble forecasting, based on its recognized sensitivity to parameter uncertainties. As is well known, a convection-allowing model cannot yet well resolve convective cells as well as turbulence diffusion and has limitations in forecasting severe weather events. Even if ensemble techniques are used, the ensembles generated by the stochastically perturbed physics tendencies (SPPT; Buizza et al., 1999) used in operational centers still face new scientific challenges, especially the problem of under-dispersion. To address this under-dispersion issue, Wang et al. (2020b) applied the CNOP-P approach to the Global and Regional Assimilation and Prediction Enhanced System (GRAPES), which is a convection-scale ensemble prediction model, to detect the most sensitive model parameters. They then formulated the model uncertainty by adding a group of stochastic perturbations on these sensitive parameters and conducted ensemble forecast experiments on relevant variables of convective scales. They showed that these new members, as compared with those generated only by the SPPT, bring about much larger spread for humidity and temperature over the troposphere and yield much more reliable

forecasting skill for near-surface variables and precipitation. In view of this, we conclude that CNOP-P is more applicable than SPPT in describing model uncertainties for convective-scale forecasting. Of course, it is easily recognized that CNOP-P only accounts for the effect of model parameter errors, and there are other model error sources that also severely influence weather and climate predictions; furthermore, these model errors are interactive. Considering this situation, Xu et al. (2022a) further adopted the CNOP-F approach [i.e., the NFSV in Duan and Zhou (2013)] for measuring the combined effect of various model errors to explore the ensemble forecast of convective scales [also see Xu et al. (2022b)]. They superimposed the NFSV on the SPPT perturbations and formulated new tendency perturbations (denoted by SPPT\_NFSV) for ensemble forecasts. With these new perturbations, Xu et al. (2022b) conducted ensemble experiments using the GRAPES convection-scale ensemble prediction model as adopted in Wang et al. (2020b). They illustrated that the overall probabilistic skills were significantly improved at the 99.99% significance level as estimated by a Student's *t*-test, and have an advantage over the SPPT (Fig. 1). Particularly, they demonstrated that the use of the NFSV enhances the forecasting skill for precipitation accuracy. It is inferred that additional state-independent nonlinear perturbations (e.g., the NFSV) superimposed on the SPPT can better represent model uncertainties in convection-scale ensemble forecasts and ultimately contribute to a more comprehensive characterization of model error for convective-scale forecasts.

In addition, the CNOP-F (i.e., NFSV) was also extended to yield a group of combined modes of initial and model perturbations that are mutually independent and can

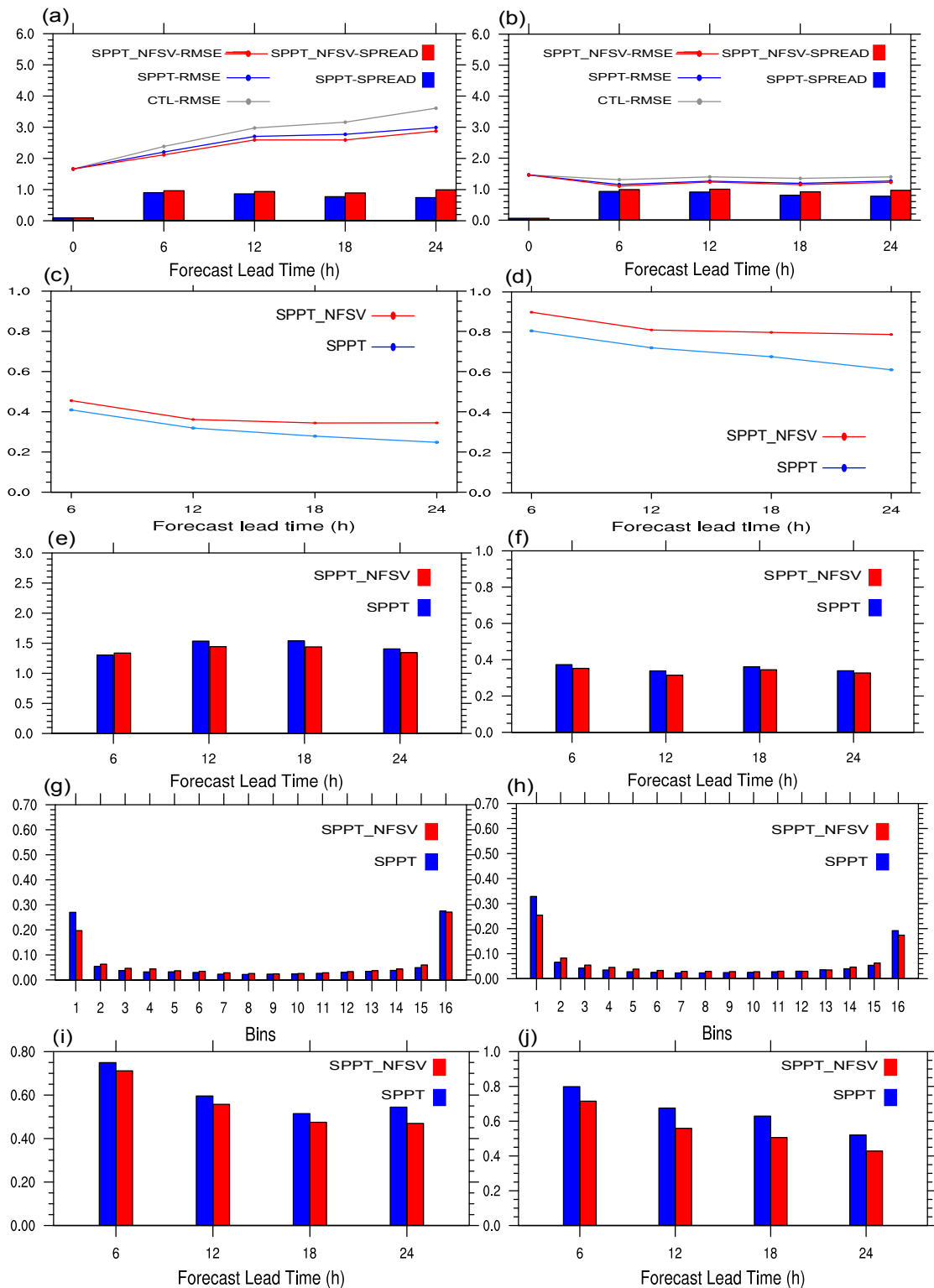


**Fig. 1.** The probabilistic skill for 500-hPa zonal wind (left column) and temperature (right column). Panels (a) and (b) show the domain-averaged RMSE of the control forecast (gray line), the SPPT\_NFSV experiment (red line), and the SPPT experiment (blue line), together with the ensemble spread for the SPPT\_NFSV (red bar) and the SPPT (blue bar). Panels (c) and (d) represent the spread-error consistency, and (e) and (f) show the continuous ranked probability score. Panels (g) and (h) are Talagrand rank histograms, and (i) and (j) show the outlier scores. The model adopted height-based terrain-following coordinates with 51 vertical levels and covered the domain of South China (19.99°–25.99°N, 106.5°–117°E) with a horizontal resolution of 0.03°. The forecasts were integrated for 24 h, initialized at 0000 UTC of each day during the period 1–30 May 2020 over South China. [Reprinted from (Xu et al., 2022b)].



cause the largest departure from the control forecast in their respective sub-phases, which offers a novel ensemble forecasting method of C-NFSVs (Duan et al., 2022a). The C-NFSVs reveal the important role of the dynamically coordinated growth of initial and model perturbations in improving the ensemble forecasting skill, thus yielding much more reliable ensembles compared with O-CNOPs for measuring only initial error effects in terms of spatiotemporal variability (Duan et al., 2022a). C-NFSVs are under investigation for TC track and intensity forecasting with encouraging preliminary results. It is expected that future papers will address the usefulness of C-NFSVs in producing much more realistic forecasts for high-impact weather and climate events.

### 2.1.2. Targeted observations

Another type of application of CNOPs is to provide the sensitive area for targeted observations associated with high-impact weather and climate events by revealing their precursory disturbance and/or fastest-growing initial errors. Although CNOP-I has always been used to explore the OPRs and OGEs and their growth dynamics for some typical weather and climate events since it was proposed in 2003 (Mu et al., 2003), as summarized in section 2.1, its applications in recent years have been focused on identifying sensitive areas for targeted observations by OPRs and OGEs, especially for the forecasting of high-impact oceanic–atmospheric environmental events. For example, CNOP-I was applied to identify the OPRs for the sudden shifts in the Antarctic circumpolar current transport through the Drake Passage (Zhou et al., 2021), the occurrence of large meanders in the track of the Kuroshio (Liu et al., 2018b), the initiation of the primary Madden–Julian Oscillation (MJO; Wei et al., 2019), and the determination of El Niño types (Duan et al., 2018; Hou et al., 2019, Hou et al., 2023); plus, it was also used to determine the OGEs for predictions of the oceanic flows in the Kuroshio extension (Geng et al., 2020; Wang et al., 2020c), and the sea surface height, with a key focus on the role of mesoscale eddies, as well as forecasts of high-impact weather events such as TCs (Qin et al., 2013; Jiang et al., 2022), heavy rainfall (Yu and Meng, 2016, 2022; Zhang and Tian, 2022), and the southwest vortex (Chen et al., 2021). All these identified OPRs or OGEs provide useful indications for the sensitive areas for targeted observations associated with corresponding weather and climate event forecasting. Particularly, motivated by the important role of the meteorological initial field in air quality forecasts, Yang et al. (2022) made a first attempt at applying CNOP-I to determine the sensitive area for targeted observations associated with improving PM<sub>2.5</sub> forecasts in a heavy air pollution event that did not have a warning issued in time by the Beijing Municipal Ecological and Environmental Monitoring Center. In particular, greater improvements in PM<sub>2.5</sub> forecasts were obtained by assimilating targeted observations in the sensitive areas, relative to those after assimilating the additional observations in the key areas suggested by previous studies. Therefore, even if the strategy of targeted observation was initially proposed for forecasting high-impact weather and

ocean events, the study of Yang et al. (2022) suggests that this strategy, especially when determined by the CNOP-I, is also useful in greatly improving air quality forecasts.

In addition, the similarities between OPRs and OGEs and their application in targeted observations in recent applications of CNOP-I should be particularly emphasized. Specifically, when oceanic–atmospheric ENSO events and IOD events were explored using the CNOP-I method, they were shown to have similar OPRs and OGEs in terms of spatial variability; plus, their large perturbation values were demonstrated to often be concentrated within a small area (Mu et al., 2014, 2017b; Hu and Duan, 2016). Therefore, when additional observations are carried out over these areas and assimilated into the initial fields, one can not only improve the accuracy of the initial fields and then decrease the prediction errors, but also detect the precursory signals of the events in advance, which may substantially improve the forecasting skill for such events (Mu et al., 2014). It is clear that these studies provide support for a new approach in identifying the sensitive area for targeted observations by considering the similarity between the OPRs and OGEs.

Another great advance in targeted observations is that CNOP-I has been applied in several realistic TC field campaigns to determine the observation area of the Fengyun-4A satellite (FY-4) and locations of dropsondes. From 2020 to 2022, a total of eight field campaigns were implemented by using FY-4 and/or dropsondes (Chan et al., 2022; Feng et al., 2022; Qin et al., 2023). Six TCs, including Higos (202007), Maysak (202009), Chan-Hom (202014), Conson (2022113), Chanthu (202114) and Mulan (202207), were observed using FY-4 from the China Meteorological Administration (CMA), and simultaneously, these TCs were also observed using dropsondes from Hong Kong Observatory. Particularly, in TC Mulan from 8 to 10 August 2022 over the South China Sea, the first ever ground–space–sky observing system experiment (OSE) of a TC with enhanced observations, including GIIRS microwave soundings, round-trip radiosondes and aircraft-launched dropsondes, was conducted through collaboration between meteorological authorities and research institutes on mainland China with the meteorological service in Hong Kong. Furthermore, these data were assimilated in real time into the operational numerical prediction system of the CMA (Chan et al., 2022). The observational and forecast results were presented in “the CMA weather conferences”, which demonstrated that assimilating the additional data collected in this way shows a positive impact on TC forecasts of both track and intensity (see Fig. 2), as well as improves the forecasting skill for heavy rain in southern China.

CNOP-I was also applied to identify the sensitive area for targeted observations in an oceanic field campaign conducted in summer 2019 for prediction of the vertical thermal structure in continental shelf seas in the Yellow Sea (Hu et al., 2021; Liu et al., 2021). It was found that the sensitive area is northeast–southwest-oriented to the northeast of the verification area. The associated targeted observations obtained in the field campaign further helped in refining the



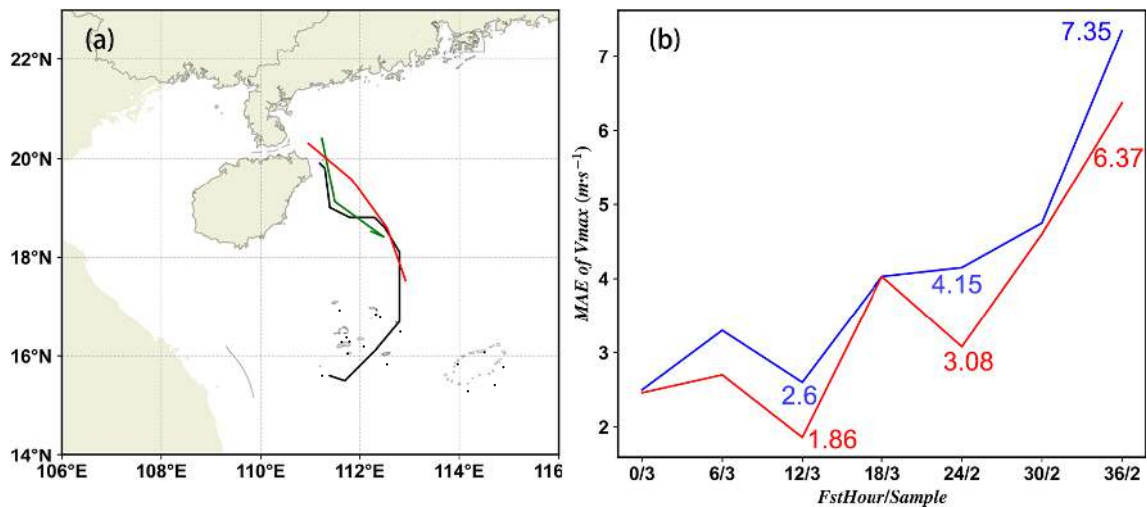


**Fig. 2.** (a) The track forecasts before (red) and after (green) assimilating additional observations, and the best track (black) of TC Mulan, which is often derived using the available observations and represents a subjectively smoothed representation of a TC's location and intensity over its lifetime. (b) The forecast errors of the maximum wind speed ( $V_{max}$ ) before (blue) and after (red) assimilating additional observations. The forecast was initialized at 0600 UTC 8 August 2022 with a lead time of 36 h. [Reprinted from (Chan et al. 2022), Reproduced with permission from Springer Nature].

structure of the initial vertical thermal structure, thereby greatly improving predictions of the vertical thermal structure at a lead time of 7 days. Liu et al. (2021) also extended CNOP-I to a new application in the field campaign for vertical thermal structure predictions favorable for recognizing circulation patterns and enhancing fishing and submarine expeditions.

The above discussion shows that targeted observations determined by CNOP-I have been transferred from theoretical studies of OSSEs (observing system simulation experiments) to OSEs. The use of CNOP-I in these OSEs represents a realistic implementation of self-developed targeted observation technology in China to support meteorological or oceanic observational campaigns in order to improve atmospheric and oceanic forecasts. But is there a particular kind of weather or climate event that is not sensitive to targeted observations? A study on the sensitive area for targeted observation of a heavy rain event in South China in June 2008 attempted to answer this question (Huang and Meng, 2014). Specifically, the authors expressed a perspective that designing a particular observation plan based on an estimated target area could be unnecessary or useless for heavy rainfall forecasts when the focus is on forecasting a heavy rain case by using a piece-by-piece DA targeting strategy. Whether or not such a perspective still holds for most other rainfall cases may need further investigation, especially by using the CNOP-I approach, which considers the interaction among the region-dependent uncertainties of the initial field and then automatically determines the most sensitive initial error.

### 2.1.3. Analyses of sensitivities and uncertainties

Sensitivities to initial fields and model parameters are one of the reasons for prediction uncertainties. Studies on

parametric sensitivity are especially important for the simulation and prediction of land surface processes. It is known that the parametric errors depicting climate change uncertainties are one of the main model error sources that severely influence the prediction skill for land surface processes. Scientists often explore the effects of climate change uncertainties by superimposing on the climatology a time-invariant perturbation without consideration of the effect of climate variability. However, Sun and Mu (2013) superimposed the parameter perturbations featured by CNOP-P to explore the response of the uncertainties in land surface process prediction and found that the resultant perturbations provided a possible climate change scenario including the changes in both the climatology and climate variability possibly induced by the frequency of occurrence of extreme events. Furthermore, these perturbations, compared with the traditional way, have helped to fully address the impact of climate change on the simulated net primary production and soil carbon in China (Sun and Mu, 2013, 2017a). Sun and Mu (2017b) also demonstrated that the use of CNOP-P reveals the possibility of the terrestrial ecosystem as a carbon sink in China. In addition, Sun and Mu (2017a) applied CNOP-P to identify a subset of physical parameters whose accuracy was much more important in reducing prediction uncertainties. They applied this new strategy to simulating and predicting the net primary production in arid and semi-arid regions over the Tibetan Plateau and revealed significant effects of nonlinear interactions among parameters on projecting the sensitivity of a group of parameters, which compensated for the deficiencies of traditional approaches and also greatly helped in determining the parameter set that should be preferentially calibrated by additional observations to improve the simulation and prediction (Sun et al., 2020). These works indicate that the idea

of targeted observation for improving initial fields can be extended to calibrate the values of sensitive parameters by digesting additional observations.

Another factor that causes prediction uncertainties is the boundary condition error; and Wang and Mu (2015), as mentioned in section 2, proposed the CNOP-B approach to explore the boundary condition errors that have the largest impact on forecast uncertainties. Furthermore, they applied CNOP-B to an ocean ecosystem model and identified two nutrient errors at the bottom boundary of the water column. These two nutrient errors have similar spatial pattern but opposite signs, and have significantly asymmetric nonlinear effects on the simulated deep chlorophyll maximum [which is a ubiquitous phenomenon in oligotrophic waters in the global ocean (Navarro and Ruiz, 2013)]. More recently, Ma et al. (2022) further used the CNOP-B method to investigate the effect of Arctic Sea ice uncertainties (as a boundary) on the prediction of atmospheric Ural blocking events. They found that the use of CNOP-B allows one to identify the uncertainties in the sea-ice concentration of the Greenland Sea, Barents Sea, and Okhotsk Sea as the dominant contributors to the forecast uncertainties of strong and long-lasting Ural blocking formation in four pentads. Furthermore, the local characteristics of perturbation distribution provided by these boundary uncertainties are able to provide the area where the additional observations should be preferentially implemented for the sea-ice concentration in order to

improve the forecasting skill of Ural blocking events.

**2.2. Nonlinear local Lyapunov exponents: applications to estimate the predictability time and yield ensemble forecasting members**

As mentioned in section 2, one approach to obtaining the optimal initial perturbations is to evaluate the evolution of initial perturbations during the time period before the prescribed time interval of prediction. The vectors derived from the Lyapunov exponents are the representatives. The traditional Lyapunov vectors and relevant Lyapunov exponents are established under the framework of linear systems and, similar to SVs, limitations exist in revealing the effect of non-linearity on predictability. To address this issue, Ding and Li (2007) proposed the nonlinear local Lyapunov exponent (NLLE) method, theoretically inherited from the Lyapunov exponent in a linear framework. The NLLE measures the growth rates of initial errors averaged over a given time period in a nonlinear dynamical system and can be used to quantify an averaged predictable time of the system. Over the past decade, the NLLE has been applied to determine the predictable times of weather and climate on various time scales. For different reference states of weather or climate events of concern, their respective analogous states can be extracted from the historical observational time series according to a locally dynamical analogs algorithm proposed by Li and Ding (2011), and then the error growth between the refer-

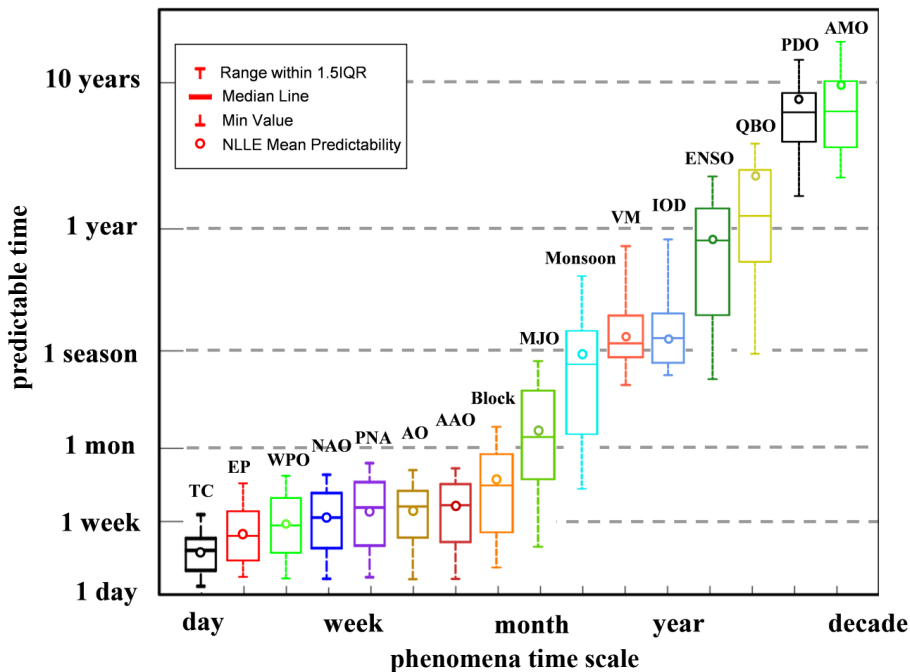


**Fig. 3.** A diagram of the predictable time range of weather and climate systems at various time scales estimated using the NLLE method. The weather and climate phenomena include TC track, eastern Pacific oscillation (EP), western Pacific Oscillation (WPO), North Atlantic Oscillation (NAO), Pacific–North American teleconnection (PNA), Arctic Oscillation (AO), Antarctic Oscillation (AAO), Blocking High (Block), Madden–Julian Oscillation MJO, monsoon, Victoria Mode (VM), Indian Ocean Dipole (IOD), El Niño–Southern Oscillation (ENSO), Quasi-Biweekly Oscillation (QBO), Pacific Decadal Oscillation (PDO), and Atlantic Multidecadal Oscillation (AMO).

ence states and analogous states can be estimated, with the predictable time range ultimately being determined according to the spread of the time when the error growths are saturated. Such an idea has been adopted to estimate the predictable time ranges of TC tracks (Zhong et al., 2018a, b, 2021), the quasi-biweekly oscillation (QBO; Shi and Ding, 2012), the MJO (Ding et al., 2010, 2011; Lu et al., 2020), the East Asian summer monsoon (Ai et al., 2017; Li et al., 2018), ENSO (Hou et al., 2018a, Hou et al., 2022), and the Pacific Decadal Oscillation (PDO, Ding et al., 2016). By combining these studies in terms of predictable time, a predictability diagram ranging from synoptic to decadal time scales was obtained. For convenience, we plot this in Fig. 3. It is obvious that the predictable time of weather and climate phenomena depends on their time scale, with the predictable times increasing with the timescale length. This predictability diagram serves as a useful reference for improving seamless predictions.

The above studies provide a means to understand how far forward one can predict atmospheric and oceanic motions and associated weather and climate events. Li et al. (2019) named such predictability as “forward predictability”. In fact, for a weather or climate event that has happened, the back-tracking time with which one can trace it is also useful for understanding the predictable time and improving predictions (Mu et al., 2002). This predictable time was termed “backward predictability” by Li et al. (2019). The NLE method was also applied to explore the backward predictability and, eventually, a backward NLE method was developed to determine the backward predictability of extreme weather and climate events, e.g., an extreme high-temperature event (Li et al., 2019, 2020, 2021a; Li and Ding, 2022). This method can quantitatively provide the maximum lead time for predictions of specific states or extreme weather and climate events. In addition, to examine the effects of different external forcing (e.g., ENSO events, the PDO) on the atmospheric predictability, a conditional NLE was also introduced to separate the effect of each external forcing on the predictability, which can therefore quantitatively estimate the relative contribution of each external forcing to the predictability of the nonlinear dynamical system (Li and Ding, 2011). Combining these NLEs may provide insight into predictability dynamics and the effect of external forcing, which serves as a reference to evaluate the skillful lead times of numerical weather forecasting and climate predictions.

In addition, the vectors corresponding to the NLEs were named the nonlinear local Lyapunov vectors (NLLVs), which represent a group of vectors of orthogonal directions in phase space and have different growth rates with time. NLLVs have been used to yield ensemble forecasting members through a hierarchy of models (Feng et al., 2014, 2016; Hou et al., 2018b). They have been demonstrated as able to perform better and more reliably than BVs in ensemble forecasting (Feng et al., 2014). A comparison of the ensemble forecasting skills of NLLVs and Ensemble Transform Kalman filter (ETKF) schemes suggested that the skill

achieved by NLLVs is comparable to that made by the ETKF, but the former can be computed far more easily and with less computation time (Feng et al., 2014). Consequently, NLLVs not only have potential for improving the ensemble forecasting skill, but are also easily implemented in complex models, which shows a potential for application in operational forecasts.

It should be noted that NLLVs are different from O-CNOPs as reviewed in section 2.1, although they can both be applied in ensemble forecasts to address the effect of initial uncertainties. The former searches for the optimally growing initial perturbations before the initialization time of the forecasts to estimate the growing-type perturbations employed in the ensemble forecast, whereas the latter directly estimates the growing-type perturbations during the forecast period. In other words, one method concerns the lasting effect of historical information on the present state estimation, while the other directly estimates the present state according to the evolutionary behavior of initial uncertainties during the forecast period. Actually, these two kinds of information are both important for estimation of the present state and forecasting of the future state. It is therefore inferred that combining NLLVs and O-CNOPs may lead to a better ensemble forecasting skill, which is worth investigating in the future.

### 3. New DA algorithms and novel assimilation approaches to address the combined effect of initial and model errors

Four-dimensional variational (4DVar) and the Ensemble Kalman filter (EnKF) are two commonly used DA methods for providing high-quality initial conditions for operational forecasts (Evensen, 1994; Talagrand, 1997). A few major operational NWP centers around the world have successfully applied 4DVar, EnKF, or a hybrid of both, to generate global and/or regional analyses and/or reanalyses. In terms of 4DVar, there are still two main challenges that have to be faced in real-time forecasts: one is the high computational cost, and the other is the lack of a global flow-dependent background error covariance (BEC) matrix [hereafter referred to as the “B matrix” (Liu et al., 2011)]. One of the strategies to address these difficulties is to develop a four-dimensional ensemble variational (4DEnVar) algorithm by referring to the idea of EnKF, which adopts a pure ensemble covariance predicted dynamically in DA cycles as per the EnKF to provide the flow-dependent B matrix for the 4DVar cost, and obtains the analysis without tangent linear and adjoint models (Liu et al., 2008; Tian et al., 2008). Thus, 4DVar becomes much more easily realized and economical owing to the 4DEnVar algorithm, and has been applied in some operational centers with high forecast skill (Buehner et al., 2010a, b; Kleist and Ide, 2015; Lorenc et al., 2015). Despite the progress made with this algorithm, it has not yet been applied operationally in most of the world’s major NWP centers, including the CMA. Furthermore, relevant challenges regarding the flow-dependent B matrix and the localization

for dealing with spurious correlation between the model and observation still need to be faced, due to limited ensemble sizes and the difficulties of reasonably determining the vertical coordinates of satellite radiance observations and the localization radius, for instance. Therefore, one has to develop a corresponding 4DEnVar algorithm based on specific forecast models, such as the CMA Global Forecast System of GRAPES (GRAPES-GFS) in China. Although the hybrid 4DVar-EnKF DA method has gained great attention and become a research trend, the EnKF itself is still a popular DA method presently. Furthermore, many studies have explored its efficiency and effectiveness in simulations and predictions of weather and climate. One of the main difficulties in implementing the EnKF is that one has to generate an ensemble to estimate the forecast-error statistics in performing DA. The large ensembles in the EnKF always mean more numerical integration, and it therefore comes at huge computational cost. However, the limited ensemble members are usually insufficient to represent the statistics of background flows at different time scales, especially the slow-varying part, which can lead to filter drift due to the misfit of slow-varying signals and a decrease in the DA efficiency. Moreover, it is known that model error is another major source of forecast errors (Duan and Zhou, 2013; Duan and Mu, 2018). Concerning the approaches to reduce model error effects, one has to improve numerical models by updating and/or improving physical parameterization schemes, or increase their spatiotemporal resolutions. However, model errors have diverse sources; moreover, they are nonlinearly interactive. Therefore, it is difficult to separate and debug them to reduce their negative effects. Although the stochastic physical perturbations used in ensemble forecasts can partly consider model errors in the ensemble covariance of 4DEnVar, they are unable to reduce the model errors in DA significantly. To overcome the above difficulties in using DA, Chi-

nese scientists have invested great effort in recent years in the development of new 4DVar and EnKF algorithms and novel DA approaches in order to reduce model error effects (see the overview in Table 2).

### 3.1. New 4DVar algorithms and their applications

#### 3.1.1. DRP-4DVar DA

Dimension-Reduced-Projection 4DVar (DRP-4DVar; Wang et al., 2010; Liu et al., 2011) is one of the representative 4DEnVar methods developed by Chinese scientists. This algorithm uses a limited numbers of ensemble forecasting members to project the optimization problem in model space onto a low-dimensional subspace spanned by these ensemble members; and the necessary localization is directly applied to the ensemble samples based on the leading eigenvectors of the localization correlation function in zonal, meridional and vertical directions, rather than being applied to the Kalman Gain matrix as the EnKF does (Wang et al., 2018). As a result, the DRP-4DVar algorithm is not only time-saving and easily implemented, but also realizes low dependence in the B matrix that is applicable either inside the assimilation window (implicitly) or from window to window (explicitly) (Wang et al., 2010).

DRP-4DVar has been successfully applied in regional and global weather forecasts. The high-quality initial conditions produced by this algorithm have led to obvious improvements in predicting regional heavy rainfall and typhoons in China (e.g., Liu et al., 2009; Zhao et al., 2012). In particular, a 4DEnVar DA system for medium-range numerical weather forecasts in GRAPES-GFS has been developed in recent years (Zhu et al., 2022). This DA system has two unique advantages. First, the system dynamically estimates the BEC during the DA cycle instead of adopting a pre-estimated static BEC as 4DVar does; and second, an inflation

**Table 2.** Overview of the improvements in DA methods achieved by Chinese scientists.

New DA method	Key idea	Benefit	References
DRP-4DVar	Project the optimization problem in model space on a low-dimensional subspace spanned by a limited number of ensemble members	Time-saving, easily implemented, and includes a global flow-dependent B matrix.	Wang et al. (2010); Zhao et al. (2012)
NLS-4DVar	Converts the 4DEnVar optimization problem into a nonlinear least-squares problem able to be solved using an efficient Gauss–Newton iteration scheme, and uses a multigrid interactive technique to correct multi-scale errors	Time-saving and includes the nonlinear effects involved in the cost function	Tian and Feng (2015); Tian et al. (2018)
NFSV-DA	Solves the tendency perturbation to minimize the distance between forecasts and observation	Able to address the combined effect of both initial and model errors	Tao and Duan (2019); Duan et al. (2022b)
Modified EnKF	EnOI version: perform IAUs to introduce assimilation increments calculated by EnOI to model integrations	Able to suppress the effect of shortwave noise in the assimilation runs	Wu et al. (2018)
	EnKF-MGA version: uses adaptive multigrid analysis to draw out multiscale information of background error statistics	Adapts to a broader range of impact radii, shortens the spin-up period, and yields smaller assimilation error	Wu et al. (2015)
	MSHea-EnKF version: uses long-term simulations and the frequency split technique to address the low-frequency background error statistics	Consumes few computer resources and provides comparable performances to the standard EnKF	Yu et al. (2019)



technique, by which the current predictions of the ensemble covariance are initiated from the linear combinations of previous analysis increments produced by the 4DVar system and balanced RPs generated using the static climate BEC, is utilized to alleviate the underestimation problem of the B matrix during the DA cycle (Zhu et al., 2022). The system, with all its advantages, created resultant smaller errors in the ensemble mean analysis and better skill in the ensemble mean forecast than 4DVar in a single analysis and deterministic forecast (Zhu et al., 2022). In fact, the DRP-4DVar embedded in GRAPES-GFS can be used not only to conduct ensemble DA independently, but also to provide flow-dependent ensemble covariance for the 4DVar system, by which an ensemble 4DVar (En4DVar) DA system for GRAPES-GFS was additionally established. Furthermore, this En4DVar system achieved a more accurate analysis and higher forecast skill than the 4DVar in GRAPES-GFS. It should be noted that using the DRP-4DVar (4DVar) approach to provide the ensemble covariance for the En4DVar system differs from most of the presently available En4DVar systems internationally, which estimate the dynamic covariance via the EnKF-class algorithms or the 4DVar approach. Therefore, this is a novel algorithm for generating the dynamic ensemble covariance for En4DVar.

In addition to its applications in regional and global NWP, DRP-4DVar has also been applied in the initialization of decadal climate predictions by the Flexible Global Ocean–Atmosphere–Land System model, gridpoint version 2 (FGOALS-g2), developed by LASG, Institute of Atmospheric Physics, Chinese Academy of Sciences (He et al., 2017, 2020a, b). Actually, it is one of the world's first 4DVar-based initialization systems for decadal predictions. Due to better dynamically coordinated behavior between the initial conditions of different component models obtained by DRP-4DVar in the coupled framework of FGOALS-g2, the tough initial shock problem was greatly alleviated. Furthermore, a much higher decadal prediction skill for surface air temperature anomalies was achieved (He et al., 2017; Fig. 4). In addition, since DRP-4DVar has the ability to incorporate the constraint of air–sea–land interactions during the process of initialization, a high prediction skill for the PDO, East Asian summer monsoon, Sahel rainfall, and surface air temperature and precipitation over the Tibetan Plateau and Europe has also been attained on interannual to decadal time scales [for further details, readers are referred to He et al. (2020a, b), Li et al. (2021b, c), and Shi et al. (2021, 2022)].

Enlightened by these studies, ongoing projects are focusing on investigating the ability of DRP-4DVar for initializing the difficult but urgent issue of subseasonal-to-seasonal (S2S) prediction. Furthermore, in view of the great advantages of DRP-4DVar, it is expected that high skill in S2S predictions (e.g., the MJO, monsoon) and related extreme events (e.g., extreme precipitation, heatwaves) will be achieved. Of course, with these potential applications, more challenging problems for the 4DVar algorithm may be

revealed, and more effort will be needed to optimize the performance of 4DVar in predicting high-impact weather and climate events.

### 3.1.2. NLS-4DVar DA

The nonlinear least-squares 4DVar (NLS-4DVar) algorithm, which was proposed by Chinese scientists and attracted a lot of attention due to its success, is another 4DVar DA approach. The idea of NLS-4DVar is to convert the 4DVar optimization problem into a nonlinear least-squares problem that can be solved using an efficient Gauss–Newton iteration scheme, and then the nonlinear effect including the 4DVar cost function can be handled naturally and accurately (Tian and Feng, 2015; Tian et al., 2018). Based on this, a multigrid NLS-4DVar was further developed to correct multi-scale errors and enhance assimilation performance with reduced computational costs via the multigrid iterative algorithm of NLS-4DVar (Zhang and Tian, 2018). In addition, Tian et al. (2021) considered the influence of both initial and model errors and provided an integral correction 4DVar algorithm to correct them simultaneously and then reduce the impact of model errors on the performance of DA (Zhang and Tian, 2022).

With the above progress regarding NLS-4DVar algorithms, these methods have also been applied in meteorological and environmental simulations and forecasts. Specifically, Zhang et al. (2020a) constructed the SNAP system (i. e., the system of multigrid NLS-4DVar DA for NWP) by embedding the multigrid NLS-4DVar in the Weather Research and Forecasting (WRF) model. This system borrows the data processing and observation operator modules from the operational Gridpoint Statistical Interpolation and has the ability to assimilate multi-source and multi-scale observations from conventional, satellite and Doppler radar observations (Zhang et al., 2020a, b; Zhang and Tian, 2021). Furthermore, Zhang et al. (2021, 2022a) applied NLS-4DVar to the atmospheric chemical transmission model WRF-CMAQ (WRF- Community Multiscale Air Quality Modeling System) and constructed a joint assimilation system that can simultaneously optimize initial conditions and emission fluxes for improving PM<sub>2.5</sub> concentration forecasts. In addition, a Tan-Tracker global CO<sub>2</sub> flux inversion system was established to optimize the terrestrial and ocean carbon fluxes through assimilating space-based and/or ground-based CO<sub>2</sub> observations using NLS-4DVar, where a novel dual-pass strategy was proposed for initialization (Jin et al., 2021). Recently, NLS-4DVar was further upgraded to a big data–driven version, which provides superior performance to the standard NLS-4DVar without additional computational costs (Tian and Zhang, 2019).

All these applications of NLS-4DVar have shown that this approach greatly reduces the computational cost and performs well in simulations or forecasts for relevant climate events based on realistic forecast models. It is therefore expected that NLS-4DVar will make important contributions to operational forecast systems, especially in terms of meso- and micro-scale systems, because of its ability in handling

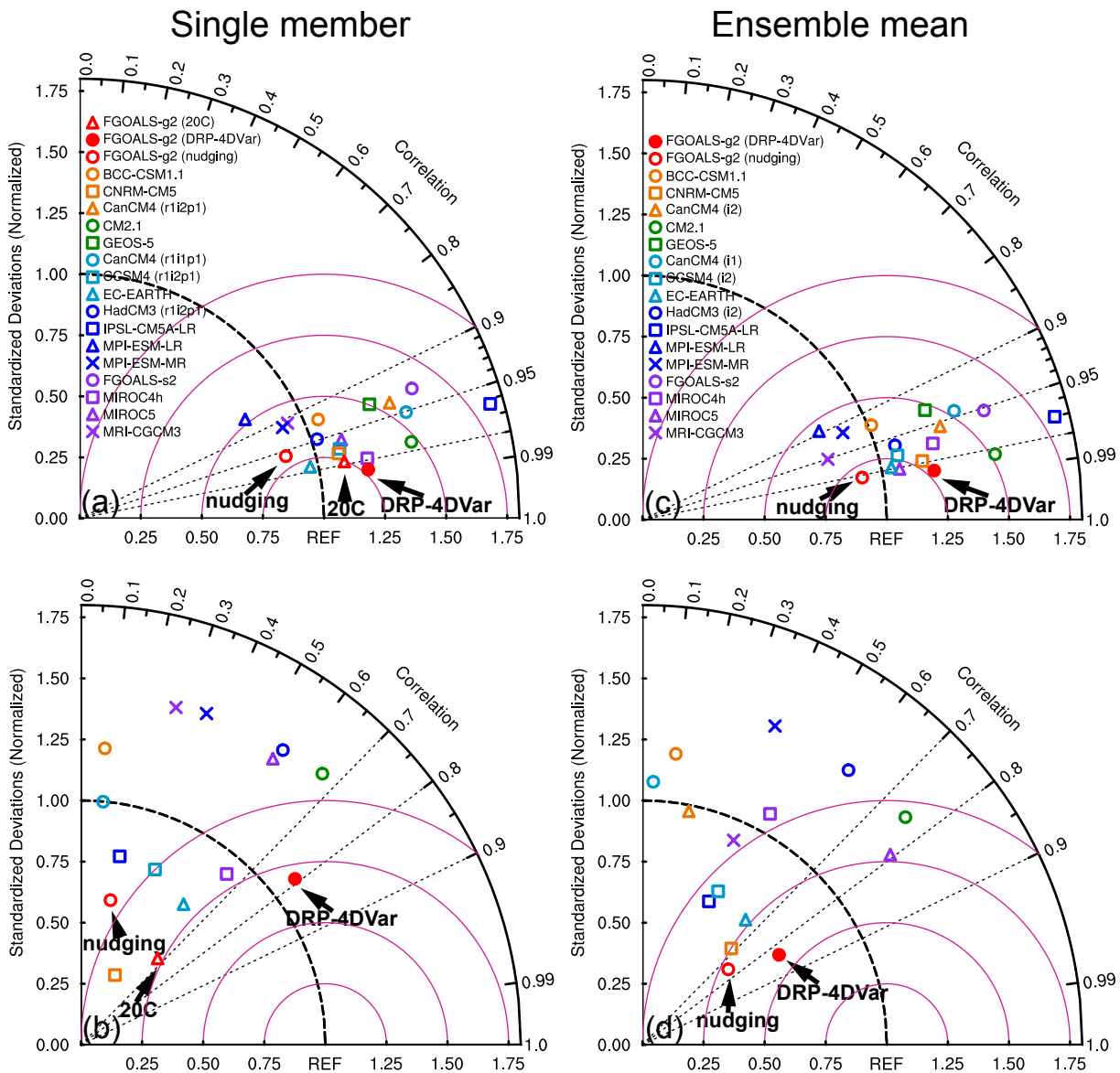


**Fig. 4.** Taylor diagrams for the 10-year averaged global mean surface air temperature anomaly (SATA), with trend (top) and without trend (bottom). The first member is shown on the left and the ensemble mean of the first three members is shown on the right. Each circle represents one model. The radial coordinate means the standard deviation of the SATA normalized by the standard deviation of the corresponding observed SATA. The red filled circle and red open circle correspond to the DRP-4DVar and nudging results based on the hindcasts from the FGOALS system, respectively. The red open triangles are for the 20th historical simulation (20C) made by the FGOALS system without any initialization. The violet semicircles represent the RMSE of the hindcasts, which is also normalized by the observed standard deviation. The correlation between the hindcast and observation is indicated by the azimuthal variable. For the single member, the simulation from the historical experiment by FGOALS-g2 is also plotted. Only the models with positive correlations are shown. [Reprinted from (He et al, 2017)].

the strong nonlinearity that exists in these systems.

### 3.2. Improvement of the EnKF scheme

The EnKF, as discussed above, is limited in terms of its multiscale representation of BEC. To address this issue, Wu et al. (2015) developed an adaptive compensatory approach to improve the performance of the EnKF in the multiscale analysis (MSA). The approach adaptively triggers a multigrid analysis (MGA) to extract multiscale information from the observational residual after the EnKF without inflation is com-

pleted at each analysis step. In this way, the MGA can extract multiscale information through refining the analysis grid; furthermore, it does not introduce any correlation scale. Particularly, Wu et al. (2015) demonstrated that the MGA also helps reduce the computational cost of the original MSA by 93%; and on the assimilation quality, they illustrated that the EnKF with the adaptive MGA shows an incremental improvement over the original EnKF-MSA and the adaptive EnKF-MGA works for a broader range of impact radii than the standard EnKF (i.e., the EnKF with inflation). For



extreme impact radii, the adaptive EnKF-MGA causes much smaller assimilation error than the standard EnKF; particularly, it shortens the spin-up period by 53%. Regarding the accurate representation of the slow-varying part of background error statistics, Yu et al. (2019) designed a multi-timescale, high-efficient approximate EnKF (MSHea-EnKF) to increase the representation of low-frequency background error statistics and then enhance its computational efficiency. MSHea-EnKF uses model simulations over a long period to construct background statistics and adopts the frequency split technique to address different time scales; thus, the performance of coupled DA on large-scale dynamics can be expected to improve. In fact, Yu et al. (2019) adopted a hybrid coupled ocean circulation model and showed that MSHea-EnKF only requires a small fraction of computing resources to present a comparable performance to the standard EnKF. This new EnKF scheme allows one to assimilate multisource observations into any high-resolution coupled Earth system model that is intractable with current computing power for weather and climate analysis and predictions.

Given the huge computational cost of the EnKF, the Ensemble Optimization Interpolation (EnOI) approach is also used in realistic numerical forecasts. The EnKF adopts the B matrix derived from a real-time computed ensemble, while EnOI just uses a B matrix estimated by a statistic historical ensemble and can be regarded as an approximation to the EnKF. However, EnOI has only one forward integration and remarkably reduces the computational costs in the EnKF (Oke et al., 2002; Evensen, 2003), consequently often being applied in operational forecasts. Recently, Wu et al. (2018) developed an initialization scheme for FGOALS based on EnOI. In this scheme, the observed oceanic temperature and salinity profiles from the EN4 dataset produced by the Hadley Center (Good et al., 2013) and the grid sea surface temperature (SST) from HadISST (Rayner et al., 2003) are assimilated to the model with an assimilation window width of 1 month. The feature of this initialization scheme is that it adopts a combination of EnOI and the incremental analysis update (IAU), where the assimilation increments are calculated by EnOI and then introduced into the model integration by the IAU. Compared with the traditional EnOI method that directly adds analysis increments to model states, the EnOI-IAU approach gradually superimposes the analysis increments generated by EnOI to model tendency equations during the model integration, which enhances constraints of the assimilation on the time dimension of the model and ultimately greatly suppresses the shortwave noise in the assimilation runs (Bloom et al., 1996). Based on this scheme, Wu et al. (2018) built a decadal climate prediction system, referred to as IAP-DecPreS, which was used to conduct decadal prediction experiments serving the Climate Prediction Project (DCPP; Boer et al., 2016), and showed significant predictive skill for SST anomalies in the North Atlantic and subtropical Pacific (Hu et al., 2023). In addition, Hu et al. (2019) adopted IAP-DecPreS to study the impacts of initialization

approaches and full-field and anomaly assimilation on the seasonal to interannual climate prediction skill (see also Hu et al., 2020). They demonstrated that the anomaly assimilation scheme greatly reduced the model initial shocks in predictions and thus improved the seasonal to interannual prediction skill for ENSO and Indian Ocean basin modes.

The EnKF, as emphasized above, is hugely expensive in computational terms, but with the advances in computing capacity, it will benefit from improved computational platforms, and we could therefore profit further from these new EnKF schemes. Accordingly, we can easily achieve more ensemble members and make higher quality assimilation. It may also be possible, in the near future, to have a global EnKF configuration that approaches a higher spatial model resolution. As shown above, the hybrid 4Dvar and EnKF approach makes it possible to implement a global flow-dependent B matrix and enhance the assimilation performance. Alongside this, if 4DVar is reasonably combined with more advanced and newly developed EnKF schemes as above, then higher quality initial fields and higher forecasting skill can be expected.

### 3.3. NFSV-DA and its applications

As discussed above, DA plays a key role in current weather forecasting and climate prediction. However, the classical DA methods, as reviewed in sections 3.1 and 3.2, were mainly established on the assumption of a perfect model with only initial error effects considered. In recent years, Duan and Zhou (2013), as reviewed in section 2, proposed the NFSV approach to reveal the model error that causes the largest prediction error. Actually, the NFSV suggests adopting a total tendency perturbation for depicting the combined effect of different kinds of model error sources. Inspired by the NFSV, Duan et al. (2022b) formulated an NFSV data assimilation (NFSV-DA) approach for neutralizing not only the initial error effect but also the model error effect (Tao and Duan 2019; Tao et al., 2020). It should be noted that NFSV-DA, which is different from the above NFSV that consists of a maximum problem that solves the total tendency perturbation that causes the largest departure from a reference state, is relevant to a minimization problem that calculates the optimal tendency perturbation to offset the prediction errors caused by initial and model errors by assimilating a limited number of observations. This is the exact reason why it is regarded as a DA approach.

NFSV-DA has been applied to El Niño predictions. Particularly, it helped to make a breakthrough in alleviating the effect of the “spring predictability barrier” phenomenon for ENSO (Tao and Duan, 2019). Results have also shown that NFSV-DA has great capacity in revealing which type of El Niño will occur in predictions. Figure 5 provides the predictions for central (CP) El Niño events made by an intermediate ENSO model (ICM; Zhang et al., 2003) and its corrected version by NFSV-DA. [For eastern Pacific (EP) El Niño events, readers can refer to Fig. 4 in Tao et al. (2020)]. Furthermore, NFSV-DA has been applied in real-time predictions of El Niño events in recent years. Together with ICM (Zhang et

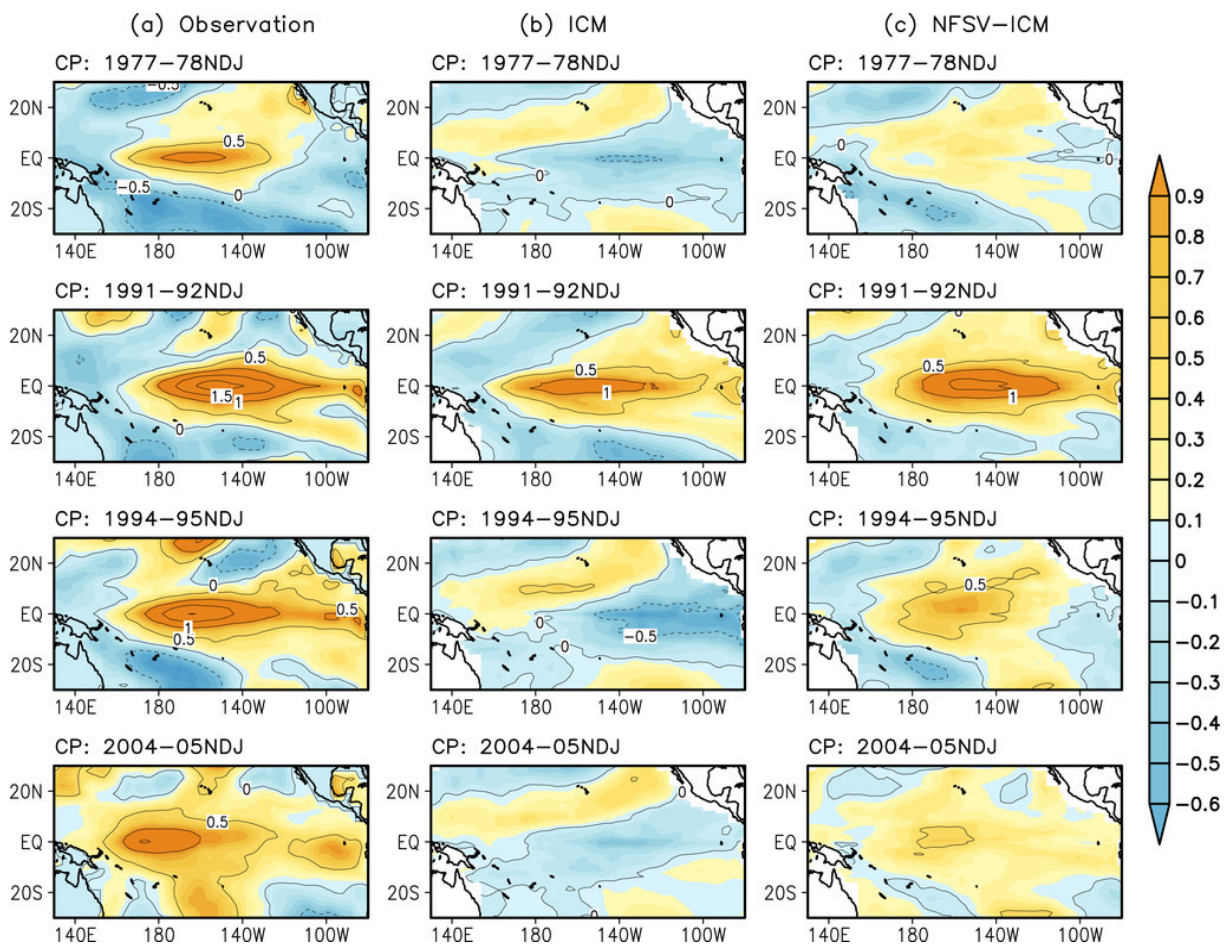


**Fig. 5.** The winter SST pattern of central Pacific (CP) El Niño in the (a) observations, (b) ICM predictions and (c) NFSV-ICM predictions, where the lead time is six months. [Reprinted from (Tao and Duan, 2019), © American Meteorological Society. Used with permission].

al., 2003), NFSV-DA shows superiority in predicting the 2015/16 strong El Niño event and its subsequent double La Niña variability from 2016 to 2018. For the 2019 CP El Niño event, many models predicted a strong EP El Niño event at the beginning of the year; and for the following 2021/22 La Niña event, quite a few models did not make successful forecasts. However, NFSV-DA performs well in predicting the warm and cold phases and even the types of those events (Duan et al., 2022b).

Despite NFSV-DA having been applied successfully in the prediction of El Niño, it remains unknown whether it might be useful when applied to the forecasting of other weather and climate events. Therefore, more weather and climate phenomena should be investigated to explore the robustness and usefulness of NFSV-DA in improving predictions. It is anticipated that NFSV-DA could prove highly effective when applied in numerical weather forecasting and climate predictions.

#### 4. Statistical approaches to improving prediction skill

In addition to numerical predictions of weather and cli-

mate, significant progress has also been made by Chinese scientists in studies of data-driven predictions made by statistical approaches, including traditional statistics, emerging complex networks, and machine learning (ML). They have identified the sources of climate predictability via a complex network and conducted prediction experiments on high-impact climate events. In addition, they have also proposed new statistical prediction methods for achieving high levels of forecasting skill. Besides these advances, the progress made in the use of ML in climate predictions is also summarized in this section.

##### 4.1. An approach to identify sources of climate predictability considering the impact of climate memory

In the past few years, a number of studies have been carried out to explore the possible relationships between climate patterns/variables of concern and external forcing, as well as the dynamical mechanisms of different interactions of coupled systems, but little attention has been paid to the effects of climate memory. In view of the potential mix of different predictable sources, neglecting the effects of climate memory may induce uncertainties in the subsequent climate predic-

tion. In order to quantify the effects of climate memory and increase the prediction skill, Yuan et al. (2014) proposed a strategy for identifying predictable sources [also see Yuan et al. (2019)]. Specifically, this strategy adopts the recently proposed fractional integral statistical model, which is a generalized version of the classical stochastic climate model proposed by Hasselmann (1976), to decompose a given climatic time series into the memory part  $M(t)$  and the residual part  $\varepsilon(t)$ ; and then, by calculating the variance explained by  $M(t)$ , the climate memory effects—in other words, the contributions of climate memory to predictability—can be quantified. Regarding the residual part  $\varepsilon(t)$ , the strategy can further use a variance decomposition method to extract the relatively slow-varying covariance matrix, which may contain signals related to external forcing and dynamical interactions of multiple climate processes; and in this way, different predictable sources on multiple time scales can be obtained.

With the above strategy, Nian et al. (2020) analyzed the seasonal predictability in observational monthly surface air temperatures over China from 1960 to 2017. They found that the climate memory component, as expected, contributes to a large portion of the seasonal predictability in the temperature records; and after removing the memory component, the residual predictability stems mainly from teleconnections, where the residual predictability is closely related to SST anomalies in the eastern tropical Pacific and the northern Indian Ocean in summer. It is obvious that the strategy and its application to the seasonal predictability of surface air temperature provides a new way to estimate climate predictability, and more importantly, by employing this strategy, the different predictability sources can be better recognized. Meanwhile, it is also necessary to emphasize the different climate memories over the corresponding temporal scale since the long-term persistence of some climate variables [i.e., precipitation (Yang and Fu, 2019)] is process dependent. It is obvious that these predictability sources can be regarded as the predictors to predict the relevant climate phenomenon by a statistical model or, as recently popular, a deep learning model. It is therefore expected that this strategy to identify the predictability sources can be further used to carry out real predictions and improve prediction skill.

#### 4.2. Complexity-based forecasting of climate phenomena

The novel complexity-based technique of climate networks has been developed rapidly and implemented to advance our knowledge of the Earth system, especially with respect to extreme climate events. The key idea of the method is that the locations in a longitude–latitude spatial grid can be regarded as nodes in the climate network and the connections between the time series at different nodes are recognized as edges (Tsonis and Roebber, 2004; Donges et al., 2009). Using statistical filtering facilities, one can interactively filter for nodes and edges, thereby highlighting structures of particular importance for matter and energy flow in the climate system, which promotes a deeper understanding of climate science and even substantially improves the prediction of high-impact climate events [see the review by Fan et

al. (2021)]. Here, we highlight the applications of climate networks in improving the forecasting skill of the Indian summer monsoon.

The Indian summer monsoon is an intense rainy season lasting from June to September and delivers more than 70% of the country's annual rainfall. Despite the development of sophisticated statistical and dynamical climate models, a relatively long-term and reliable prediction of the Indian summer monsoon rainfall (ISMR) has remained a challenging problem. Fan et al. (2022) constructed a series of dynamical climate networks based on the global near-surface air temperature (NSAT) field, showing that there are characteristics of the directed and weighted climate networks that can serve as efficient long-term predictors for ISMR forecasting. Specifically, they uncovered the Southwest Atlantic as a hotspot for predicting the Indian precipitation, due to the strong connection through the chain of main atmospheric circulation patterns. Based on this, Fan et al. (2022) developed a climate network prediction method for ISMR, which produced a forecasting skill of 0.54 (Pearson correlation) with a 5-month lead time by using the previous calendar year's data (Fig. 6). This level of skill is higher than that of operational forecast models, even with quite a short lead time. It is clear that the climate network method can capture useful predictors for ISMR and provide much higher forecast skill. This network approach allows the all-India rainfall to be predicted, as well as the rainfall in different homogeneous Indian regions, which is crucial for the country's agricultural production.

The climate network approach was also successfully applied to improving the forecasting skill for IOD events (Lu et al., 2022) and exploring the weakening tropical circulations (Geng et al., 2021), the relationship between the CO<sub>2</sub> concentration and surface air temperature (Ying et al., 2021), and the transportation and clustering of PM<sub>2.5</sub> concentrations (Ying et al., 2022). Although the application of climate networks has achieved successes in climate predictions, improvement of the prediction level is still limited.

A promising methodology that has emerged in recent years and could play an instrumental role in demystifying climate change is ML. Due to the enhanced data availability, ML has been shown to have ability in making up for the deficiency of traditional forecast methods. Owing to the limited prediction skill for the IOD achieved by traditional dynamical and statistical methods, Ling et al. (2022) developed a multi-task deep learning model named MTL-NET to challenge the current IOD prediction skill. The deep learning method can extend reliable IOD predictions out to 7 months ahead, which exceeds the original 3 months in the traditional predictions. By investigating the precursors revealed by MTL-NET for strong IOD events, their studies also help us deepen our understanding of the nonlinear mechanisms of the IOD, and of the complex climate variabilities in the Earth system. Aside from helping enhance prediction levels, ML may also have potential in reducing computational costs in ensemble forecasts. Since the computational cost of large ensemble members is always a challenge in the real-



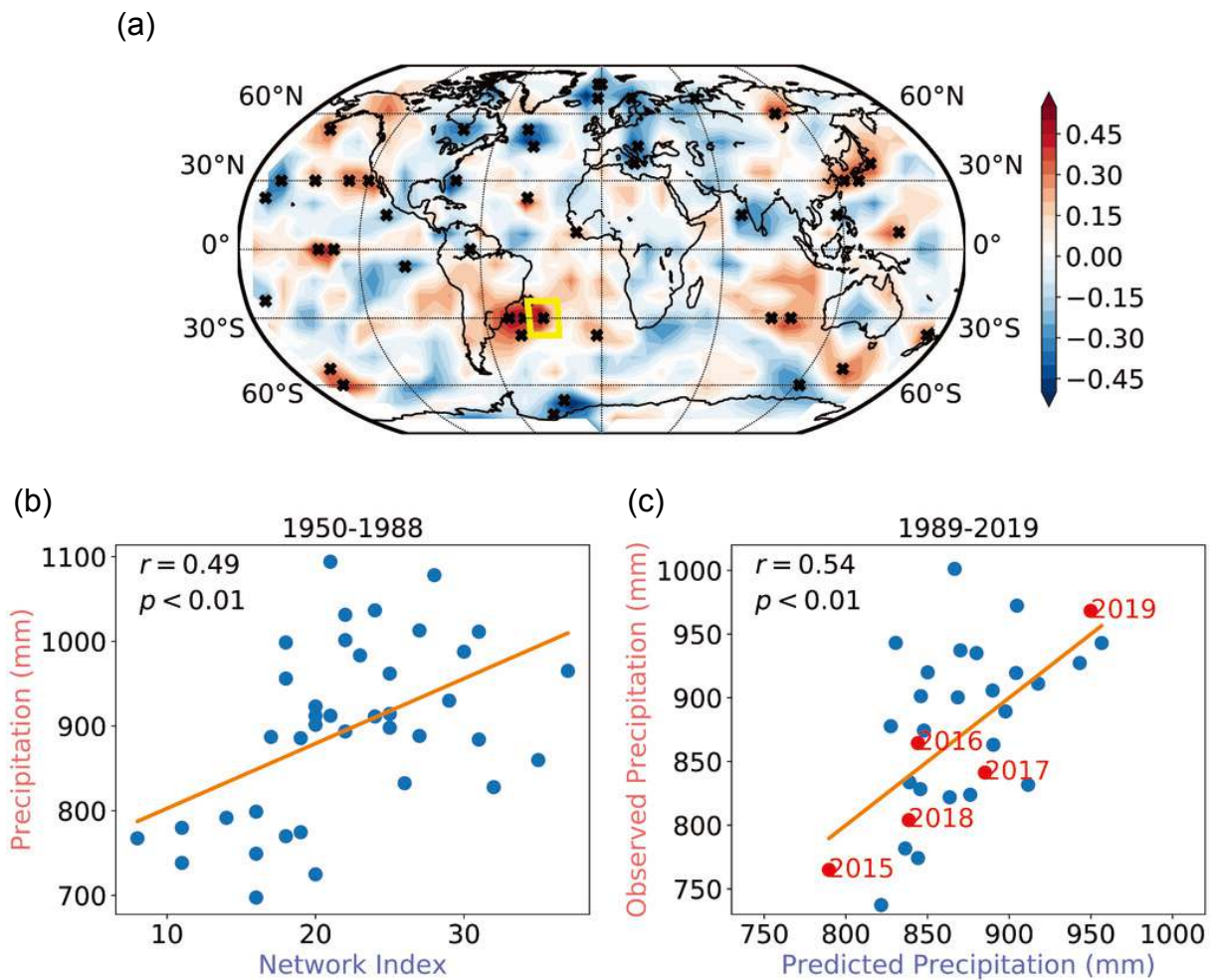


**Fig. 6.** (a) The correlation coefficients between observed All Indian Rainfall Index (AIRI) in summer (June–September, JJAS) and the network predictor during the training period (1950–88) for all nodes. The regions with statistical significance exceeding the 95% confidence level (Student's *t*-test) are marked in black. The region with the maximal correlation coefficient is marked by the yellow box. (b) Scatterplot between the observed JJAS AIRI and the optimized network predictor (i.e., only using the NSAT information in the yellow box) in the training period. (c) Scatterplot between the observed JJAS AIRI and the predicted AIRI during the forecast period (1989–2019). [Reprinted from (Fan et al., 2022), © American Meteorological Society. Used with permission].

time operational chain of ensemble forecasts, Duan et al. (2022a) applied deep learning to learn the dependence relationship of the control runs and ensemble forecasting members, and then expected to produce efficient ensemble members in real-time forecasts. The numerical results showed that the ensemble forecasts made by the deep learning models could not only reduce the computational costs in real-time forecasts, but also achieve comparable forecasting skill to the original ensemble forecast system. Therefore, the application of ML may be a new research topic of interest in ensemble forecasting.

As an emerging method of climate prediction, climate networks show ability in identifying spatial information about cooperativity and provide a new possibility of revealing precursory signals of climate or even entire causal chains of climate phenomena. However, some latent processes and relationships of climate systems cannot yet be identified by the climate network method, and the relevant climate prediction

level is still limited from this perspective. However, the promise of ML is superior to that of the climate network method in learning the complex nonlinear relationships in data. Therefore, combining the climate network method with ML may have the potential to deepen the physical understanding and improve the prediction skill of weather and climate events.

#### 4.3. The year-to-year increment prediction approach and its role in enhancing climate predictions

Fan et al. (2008) proposed the year-to-year increment prediction approach (referred to as the DY approach) based on the quasi-biennial oscillation of climate variables. The DY includes both the predictand and predictor in the year-to-year increment, rather than only the predictor in the anomaly of the traditional climate prediction approach. The DY can then amplify the signal against that in traditional anomaly prediction; plus, it can capture multi-timescale vari-

abilities of climate variables. As a result, the DY not only shows high predictive skill for the interannual variability of climate variables, but also reproduces their interdecadal variability (Fan et al., 2008). In recent years, Fan et al. (2012), based on the DY, combined dynamic model predictions and further proposed a new idea of statistical–dynamical hybrid climate prediction approach. Furthermore, the idea was realized in predictions of summer precipitation over China (Liu and Fan, 2012; Dai and Fan, 2021), spring drought in China (Tian and Fan, 2022), the summer extreme precipitation frequency in the Yangtze River basin (Tian and Fan, 2020), and the number of landfalling TCs in summer in China (Tian and Fan, 2019). Moreover, satisfying levels of prediction skill benefiting from available predictors and, particularly, from inheriting the contribution of dynamical coupled model predictions for large-scale atmospheric circulation anomalies, were achieved not only for mid–high-latitude climate systems such as Arctic sea ice, Eurasian snow cover, and SST over the North Pacific, but also tropical climate systems such as ENSO and SST over the tropical Indian and Atlantic oceans.

It is clear that the DY, which uses the difference in a variable between the current year and preceding year, is able to provide higher prediction skills of the interannual and decadal component, as compared with traditional anomaly prediction, especially when it is inherited from the superiority of a dynamically coupled model in predicting large-scale circulations. Evidently, this further illustrates the great strength of the statistical–dynamical hybrid approach in climate predictions. Consequently, it can be expected that this approach will play a more important role in climate predictions, especially in the forecasting of high-impact climate events.

## 5. Predictability dynamics associated with meso- to small-scale weather systems

The above sections have reviewed the advances made in predictability studies associated with the identification of optimally growing errors and the development of dynamical and statistical methods to reduce the prediction uncertainties of weather and climate. In fact, in the evolution of prediction errors, the errors of different variables and at different temporal and spatial scales interact with each other, and thus revealing the key factors that have large impacts on these prediction uncertainties and identifying the dominant scale responsible for error growth will have important implications on improving the forecast skill for weather and climate events. In recent years, Chinese scientists have made contributions towards understanding these aspects of error growth and multi-scale interactions, particularly in meso- to small-scale weather systems, which range from several meters to around 2000 km spatially, and from seconds to days temporally, which in particular can encompass certain types of disastrous weather events, such as squall lines, supercells and convection (Orlanski, 1975). Such studies can help us to optimize

observational networks, assimilation algorithms, and model configurations in order to maximize the forecasting accuracy for various types of disastrous weather and climate events. Studies on meso- to small-scale error growth carried out by Chinese scientists can be summarized into two aspects, as follows:

One aspect is the identification of the key factors for an accurate forecast through either ensemble-based sensitive analysis or DA. Studies show that the formation of a squall line in China is most sensitive to the initial moisture, with a linear response to the initial moisture error (Wu et al., 2013), which is different from the nonlinear response in squall lines over the United States. The mesoscale convective vortex (MCV) has been demonstrated to be a key factor in producing extremely heavy rainfall in China (Yu and Meng, 2016; Zhang et al., 2022b), and operational models carry larger uncertainty in predicting the behavior of MCVs owing to the juxtaposition between the direction of MCV movement and the low-level jet (Zhang and Meng, 2018). In addition to MCVs, the predictability of TCs has also been examined, revealing that the TC intensity forecast error is closely related to the intensity (as well as the rate of intensity change) of TCs and a number of environmental parameters (Zhang et al., 2014). A TC's intensity and precipitation forecast largely depends on the initial relationship between the TC intensity and location and the initial steering flow (Zhu et al., 2016).

Another aspect is to understand the error growth dynamics. A pioneering study on storm-scale predictability revealed that small yet realistic uncertainties in boundary layer and topographical influence, or errors much smaller than what can be observed, may lead to considerable differences in the initiation and subsequent organization and intensity of the mesoscale convective system and its embedded supercells (Zhang et al., 2015, 2016). The forecast errors remained nearly unchanged even when the initial perturbations were reduced by 90%, which suggests an inherently limited predictability for lead times as short as 3–6 h.

The relative importance of errors at different spatial scales has been a hot topic in error growth dynamics. There has been disagreement on whether small-scale or large-scale error is more important. The former claims that small-amplitude, small-scale errors will grow up-scale, saturate at smaller scales, and transfer to progressively larger scales, while the latter claims that errors grow up-amplitude at all model-resolved scales simultaneously rather than transfer up-scale. This disagreement is actually equivalent because the important scale should be determined by the dominant error growth dynamics. In this regard, how sensitive the forecast error growth is to different amplitudes and horizontal scales of flow-dependent unobservable initial uncertainties in a high-resolution convection-permitting ensemble forecast on a real high-impact rainfall event in China was examined by Zhang et al. (2022b). The dominance of up-scale rather than up-amplitude error growth was demonstrated under the regime of  $k^{-5/3}$  power spectra by revealing the inability of

large-scale errors to grow until the amplitude of small-scale errors has increased to an adequate amplitude. An apparent transfer of the fastest growing scale from smaller to larger scales with a slower growth rate at larger scales was revealed. In addition, initial perturbations with different structures have different error growth features at larger scales in different variables in a regime transitioning from the  $k^{-5/3}$  to  $k^{-3}$  power law; and the error growth featured by the CNOP-type initial error mentioned in section 2 tends to be more up-amplitude relative to perturbations of the NCEP's Global Ensemble Forecast System or sub-grid-scale perturbations.

## 6. Summary and discussion

The advances made in predictability studies in China in recent years have been reviewed in this article, mainly from the perspectives of new methods for targeted observation, DA, ensemble forecasting, and statistical predictions and their applications to weather and climate predictions. The article emphasizes the great progress made in studies of nonlinear optimal perturbations for targeted observations and ensemble forecasting, and a family of CNOPs are presented, including CNOP-I for measuring the initial error effect, CNOP-P for estimating the model parametric error effect, CNOP-B for evaluating uncertainties in boundary conditions, and CNOP-F for investigating the combined effect of various model errors (see section 2). Among the many studies on the sensitive areas for targeted observations associated with the forecasting of high-impact ocean-atmosphere environmental events, several field campaigns for the forecasting of TCs and predictions of the vertical thermal structure in continental shelf seas in the Yellow Sea are highlighted to demonstrate the real-time implementation of the CNOP-I technique independently developed in China to support meteorological and oceanic observational campaigns for the needs of weather and climate predictions. In ensemble forecasting, CNOPs have been found to be able to represent initial uncertainties for TC track forecasting through orthogonal CNOP-Is, and to estimate model parametric uncertainties and even the combined effect of different kinds of model errors for convection-scale forecasting using CNOP-P and -F, respectively (see section 2.1). Another approach, the NLLE, was proposed to quantify the predictable time of atmospheric and oceanic motions and associated weather and climate, and a predictability diagram from daily weather, through monthly, sub-seasonal, and seasonal, to interannual and even decadal climate phenomena was achieved for reference in improving the level of seamless predictions. Furthermore, the vectors featured by the NLLE (i.e., NLLVs), were applied to provide the lasting effect on initial uncertainties of the ensemble forecasting of past information, which favored a better performance and higher reliability than that of traditional BVs and presented a skill comparable to the ETKF; due to the features of NLLVs in the form of easier realization and less computational time, this approach prevails over the ETKF in terms of ensemble forecast performance (see section 2.2). All

these methods on targeted observation and ensemble forecasting indicate that fully considering the nonlinear effects is necessary in order to correct prediction biases. Concerning DA, new 4DVar and EnKF algorithms for initialization and approaches to reduce the combined effect of model and initial errors are reviewed (see section 3). These new algorithms include DRP- and NLS-4DVar, both of which are focused on 4DVar to address the challenge of 4DVar posed by the flow-dependent B matrix and computational efficiency problem (see section 3.1). The former algorithm projects the optimization problem in model space onto a low-dimensional subspace, using a particular localization technique to deal with spurious correlation between the model field and observations, and was eventually embedded in GRAPES-GFS to provide flow-dependent ensemble covariance for 4DVar, which ultimately led to the establishment of an En4DVar DA system for GRAPES-GFS. This latter algorithm focuses on another perspective to treat the nonlinear effect included in the 4DVar cost function by considering nonlinear least-squares. It furthermore uses a multigrid interactive technique to correct multi-scale errors and reduce the computational cost, which was eventually applied in quite a few models to address relevant practical concerns. Besides 4DVar algorithms, Chinese scientists have also developed new EnKF schemes to reduce the computational costs and address the multiscale background error statistics (see section 3.2). With the newly-developed adaptive EnKF-MGA, it is possible to address the multiscale information from the observational residual by adaptively triggering an MGA, thus producing smaller assimilation errors and shortening the spin-up period; but with the further improved MSHea-EnKF, it is possible to use long-term simulations and the frequency split technique to derive the low-frequency background error statistic and use less computing resource to provide comparable performances to the standard EnKF.

Along with the development of dynamical forecasting, statistical approaches are also thriving in terms of acquiring high levels of forecast skill for high-impact weather and climate events (see section 4). Chinese scientists have continued to invest great effort in exploring new and effective statistical forecasts methodologies. Particularly, based on the classical stochastic climate model, a fractional integral statistical model was built to quantify the predictable sources and help us to purposely design better prediction models (see section 4.1). Meanwhile, the network theory, which emerged from complex system science, has been recently applied in climate science, providing critical predictive power for scientific challenges, which is sometimes even superior to dynamical forecasts (see section 4.2). Chinese scientists have also tried using ML algorithms to improve IOD predictions and increase the efficiency of ensemble forecasting in real-time forecasts, eventually showing that ML has the ability to make up for the deficiency of traditional forecast methods. In addition, different from the traditional statistical prediction approach based on climate anomalies, a year-to-year increment prediction approach (DY approach) was proposed,



**Table 3.** Main advances in predictability studies in China in recent years.

Forecast strategy	Old methods and limitations	New methods and advantages	Highlights of applications
Targeted observation	Methods: SV, ETKF Limitations: <ul style="list-style-type: none"> <li>• Linear approximation to nonlinear initial error growth</li> <li>• Only adaptive to initial field</li> </ul>	<ul style="list-style-type: none"> <li>• CNOP-I: identifies the sensitive area for targeted observation using nonlinear model</li> <li>• CNOP-P: reveals sensitive parameters for targeted observations</li> <li>• CNOP-B: recognizes the most sensitive perturbation on boundary condition</li> <li>• CNOP-F (NFSV): discloses the most disturbing tendency error</li> </ul>	<ul style="list-style-type: none"> <li>• Field campaigns of targeted observations for forecasting of TCs and predictions of vertical thermal structure in continental shelf seas in the Yellow Sea: assimilating targeted observations obviously improves the forecast skill of concerned state (Qin et al., 2023; Chan et al., 2022; Liu et al., 2021)</li> </ul>
Data assimilation	Method: 4DVar Limitations: <ul style="list-style-type: none"> <li>• High computational costs</li> <li>• Lack of global flow-dependent B matrix</li> <li>• Insufficient handling of nonlinear effect involved in cost function</li> <li>• Only addresses initial error effect</li> </ul> Method: EnKF Limitations: <ul style="list-style-type: none"> <li>• High computational cost</li> <li>• Inaccurate representation of background flow statistics at different time scales</li> </ul>	<ul style="list-style-type: none"> <li>• DRP-4DVar: includes global flow-dependent B matrix and reduces computation time</li> <li>• NLS-4DVar: addresses the nonlinear effect including the cost function and saves on computational resources</li> <li>• NFSV-DA: deals with combined effect of initial errors and different kinds of model errors</li> <li>• EnKF-MGA: improves performance of EnKF in multiscale analysis and reduces computational cost</li> <li>• MSHea-EnKF: increases representation of low-frequency background error statistics and enhances computational efficiency</li> </ul>	<ul style="list-style-type: none"> <li>• Predictions of decadal climate using DRP-4DVar: one of the world's first 4DEnVar-based initialization systems for decadal predictions and greatly alleviated tough initial shock problem (He et al., 2017)</li> <li>• Establishment of a Tan-Tracker global CO<sub>2</sub> flux inversion system using NLS-4DVar (Jin et al., 2021)</li> <li>• Predictions of El Niño types using NFSV-DA: achieves a lead time of 6 months to recognize El Niño type in ENSO predictions (Tao et al., 2020; Duan et al., 2022b)</li> </ul>
Ensemble forecasting	Method: SVs Limitations: <ul style="list-style-type: none"> <li>• Linear approximation to nonlinear error growth</li> <li>• Only adaptive to estimation of initial uncertainties</li> </ul> Method: BVs Limitation: non-orthogonality of BVs	<ul style="list-style-type: none"> <li>• O-CNOPs: represents fully nonlinear initial perturbations for ensemble forecasting</li> <li>• C-NFSVs: estimates combined effect of initial and model errors</li> <li>• NLLVs: provides mutually orthogonal initial perturbations for ensemble forecasts</li> </ul>	<ul style="list-style-type: none"> <li>• TC track forecasting through O-CNOPs and convection-scale forecasting using CNOP-P and -F: achieves higher forecast skill than traditional methods (Huo et al., 2019; Wang et al., 2020b; Xu et al., 2022b)</li> <li>• Provision of a predictability diagram from daily weather, through monthly, subseasonal and seasonal to interannual and even decadal climate phenomena using the NLE (present study)</li> </ul>
Statistical prediction methods	Traditional statistical approaches cannot recognize complex and nonlinear relationships in data very well.	<ul style="list-style-type: none"> <li>• Climate networks and ML algorithms: compensate for deficiencies of traditional dynamical and statistical forecast methods</li> </ul>	<ul style="list-style-type: none"> <li>• Prediction of Indian summer monsoon rainfall using climate network: achieves much higher prediction skill than that of operational forecast models, even with quite a short lead time (Fan et al., 2022)</li> <li>• Predictions of IOD using ML algorithm: extends reliable IOD predictions out to 7 months ahead, which exceeds the original 3 months in traditional predictions (Ling et al., 2022)</li> </ul>

which amplifies the climate signal and shows high prediction skill for interannual and interdecadal climate variabilities (see section 4.3). Nevertheless, the dynamical and statistical approaches have their respective advantages and limitations. How to effectively combine the dynamical and statistical approaches and improve the forecast skill may be a prospective research subject in need of further study.

It is clear that Chinese scientists have made some outstanding contributions to the development of new methods that address the forecasting uncertainties for weather and cli-

mate. To facilitate readers, we summarize in Table 3 these contributions from the perspective of targeted observation, DA, ensemble forecasting, and statistical predictions. In this context, the hot topics related to the importance of errors at the different spatial scales of meso- to small-scale weather systems are also highlighted (see section 5). An apparent transfer of the fastest growing scale from smaller to larger scales with a slower growth rate at larger scales was revealed under the regime of  $k^{-5/3}$  power spectra, and the dominant role of up-scale rather than up-amplitude error growth

was demonstrated. The error growth featured by the CNOP-I error was shown to be more up-amplitude in a regime transitioning from the  $k^{-5/3}$  to  $k^{-3}$  power law, relative to perturbations of the NCEP's Global Ensemble Forecast System or sub-grid-scale perturbations. These studies contribute to addressing the controversy regarding whether small-scale or large-scale error is more important in meso- to small-scale weather systems. Furthermore, understanding the error growth dynamics can help to optimize observational networks, assimilation algorithms, and model configurations in order to maximize the forecasting accuracy of various disastrous weather events.

Besides these above advances, there studies have also been conducted on controversial issues of predictability, and these should be mentioned here. For example, on the issue "whether the approaching limit of predictability for TC track prediction is near or has already been reached", proposed by Landsea and Cangialosi (2018), Zhou and Toth (2020) and Yu et al. (2022) used TC forecast data in the Atlantic basin and in the western North Pacific basin, respectively, to explore what the past trend was in the reduction of TC forecast track error, and how such errors may be further reduced in future decades. Both showed that the improvements of TC track forecast skills in the past 10 years have mainly been due to the reduction in analysis errors rather than the reduction in the error growth rate. They also pointed out that if the current trend continues, a further two-day improvement in TC track forecast lead times may be projected for the coming 20 years in the Atlantic basin, and 15 years in the western North Pacific basin. It is therefore clear that we have not yet reached the limit of TC track predictability in both basins.

Although great progress has been made in the predictability and even practical forecasting of weather and climate, there are greater requirements for numerical weather forecasting and climate prediction related to disaster prevention and national security with the development of society and the progress of technology. For example, it is necessary to strengthen the development of seamless forecasting systems from traditional weather scales to decadal climate scales, the development of coupled forecasting systems from single atmosphere to multi-spherical interactions between the atmosphere, sea, land and ecology, and the coordinated development of an observation–assimilation–model forecasting system instead of an independent observation system or numerical forecast model. These requirements undoubtedly pose new challenges to the study of predictability for high-impact weather and climate events, particularly in the study of targeted observation, DA, and ensemble forecasting with the consideration of multiple temporal and spatial scales and their associated interactions. Although international communities have developed various strategies to deal with the above challenges and made progress—particularly, a few NWP centers have established weather forecasting and climate prediction systems that are able to address some of the new challenges to certain extent—their DA systems, ensemble forecast-

ing systems and other technologies are not open to the public. Therefore, in order to meet the new requirements in forecasting and predictions in China, Chinese scientists must try to study multi-scale error analysis theory for dealing with multi-scale problems in DA and ensemble forecasting, establish new theories that accurately quantify the sensitivities in observations and uncertainties, improve current hybrid assimilation techniques or develop new filtering techniques based on current particle or mixed filtering algorithms, and construct new models that incorporate the advantages of big data analysis and artificial intelligence. It is expected that a much advanced numerical forecasting system can be established in China in the near future, thus addressing the challenges of numerical weather forecasting and climate predictions due to the effects of multiple temporal and spatial scales and their interactions.

**Acknowledgements.** The authors greatly appreciate the useful comments and suggestions of the editor and two anonymous reviewers. The authors would also like to thank Drs. Ke FAN, Xiangjun TIAN, Guodong SUN, Qiang WANG, Feifan ZHOU, Jingfang FAN, Juanjuan LIU, Naiming YUAN, Guokun DAI, Xinrong WU, Bo WU, and Ms. Lu WANG and Zhizhen XU for providing materials. This article was sponsored by the National Natural Science Foundation of China (Grant Nos. 41930971, 42105061 and 42030604).

## REFERENCES

- Ai, S. C., Q. L. Chen, J. P. Li, R. Q. Ding, and Q. J. Zhong, 2017: Baseline predictability of daily east Asian summer monsoon circulation indices. *Asia-Pacific Journal of Atmospheric Sciences*, **53**, 243–256, <https://doi.org/10.1007/s13143-017-0031-6>.
- Bauer, P., A. Thorpe, and G. Brunet, 2015: The quiet revolution of numerical weather prediction. *Nature*, **525**, 47–55, <https://doi.org/10.1038/nature14956>.
- Bloom, S. C., L. L. Takacs, A. M. Da Silva, and D. Ledvina, 1996: Data assimilation using incremental analysis updates. *Mon. Wea. Rev.*, **124**, 1256–1271, [https://doi.org/10.1175/1520-0493\(1996\)124<1256:DAUIAU>2.0.CO;2](https://doi.org/10.1175/1520-0493(1996)124<1256:DAUIAU>2.0.CO;2).
- Boer, G. J., and Coauthors, 2016: The decadal climate prediction project (DCPP) contribution to CMIP6. *Geoscientific Model Development*, **9**, 3751–3777, <https://doi.org/10.5194/gmd-9-3751-2016>.
- Buehner, M., P. L. Houtekamer, C. Charette, H. L. Mitchell, and B. He, 2010a: Intercomparison of variational data assimilation and the ensemble Kalman filter for global deterministic NWP. Part I: Description and single-observation experiments. *Mon. Wea. Rev.*, **138**(5), 1550–1566, <https://doi.org/10.1175/2009mwr3157.1>.
- Buehner, M., P. L. Houtekamer, C. Charette, H. L. Mitchell, and B. He, 2010b: Intercomparison of variational data assimilation and the ensemble Kalman filter for global deterministic NWP. Part II: One-month experiments with real observations. *Mon. Wea. Rev.*, **138**(5), 1567–1586, <https://doi.org/10.1175/2009mwr3158.1>.
- Buizza, R., M. Milleer, and T. N. Palmer, 1999: Stochastic representation of model uncertainties in the ECMWF ensemble pre-

- diction system. *Quart. J. Roy. Meteor. Soc.*, **125**, 2887–2908, <https://doi.org/10.1002/qj.49712556006>.
- Chan, P. W., W. Han, B. Mak, X. H. Qin, Y. Z. Liu, R. Y. Yin, and J. C. Wang, 2022: Ground-space-sky observing system experiment during tropical cyclone Mulan in August 2022. *Adv. Atmos. Sci.*, **40**, 194–200, <https://doi.org/10.1007/s00376-022-2267-z>.
- Chen, D. K., N. Smith, and W. Kessler, 2018: The evolving ENSO observing system. *National Science Review*, **5**, 805–807, <https://doi.org/10.1093/nsr/nwy137>.
- Chen, G., B. Wang, and J. J. Liu, 2021: Study on the sensitivity of initial perturbations to the development of a vortex observed in Southwest China. *J. Geophys. Res.*, **126**, e2021JD034715, <https://doi.org/10.1029/2021JD034715>.
- Cravatte, S., W. S. Kessler, N. Smith, S. E. Wijffels, and Contributing Authors, 2016: First Report of TPOS 2020. GOOS-215, 200 pp. [Available online at <http://tpos2020.org/first-report/>.]
- Dai, H. X., and K. Fan, 2021: An effective downscaling model for operational prediction of summer precipitation over China. *Atmospheric Research*, **257**, 105621, <https://doi.org/10.1016/j.atmosres.2021.105621>.
- Ding, R. Q., and J. P. Li, 2007: Nonlinear finite-time Lyapunov exponent and predictability. *Physics Letters A*, **364**, 396–400, <https://doi.org/10.1016/j.physleta.2006.11.094>.
- Ding, R. Q., J. P. Li, and K. H. Seo, 2010: Predictability of the Madden-Julian oscillation estimated using observational data. *Mon. Wea. Rev.*, **138**, 1004–1013, <https://doi.org/10.1175/2009mwr3082.1>.
- Ding, R. Q., J. P. Li, and K. H. Seo, 2011: Estimate of the predictability of boreal summer and winter intraseasonal oscillations from observations. *Mon. Wea. Rev.*, **139**, 2421–2438, <https://doi.org/10.1175/2011mwr3571.1>.
- Ding, R. Q., J. P. Li, F. Zheng, J. Feng, and D. Q. Liu, 2016: Estimating the limit of decadal-scale climate predictability using observational data. *Climate Dyn.*, **46**, 1563–1580, <https://doi.org/10.1007/s00382-015-2662-6>.
- Donges, J. F., Y. Zou, N. Marwan, and J. Kurths, 2009: Complex networks in climate dynamics. *The European Physical Journal Special Topics*, **174**(1), 157–179, <https://doi.org/10.1140/epjst/e2009-01098-2>.
- Du, J., and Coauthors, 2018: Ensemble methods for meteorological predictions. *Handbook of Hydrometeorological Ensemble Forecasting*, Q. Duan et al., Eds., Springer, 1–52.
- Duan, W. S., and F. F. Zhou, 2013: Non-linear forcing singular vector of a two-dimensional quasi-geostrophic model. *Tellus A*, **65**, 18452, <https://doi.org/10.3402/tellusa.v65i0.18452>.
- Duan, W. S., and P. Zhao, 2014: Revealing the most disturbing tendency error of Zebiak-Cane model associated with El Nino predictions by nonlinear forcing singular vector approach. *Climate Dyn.*, **44**, 2351–2367, <https://doi.org/10.1007/s00382-014-2369-0>.
- Duan, W. S., and M. Mu, 2015: Dynamics of nonlinear error growth and the “spring predictability barrier” for El Nino predictions. *Climate Change: Multidecadal and Beyond*, C. P. Chang et al., Eds. World Scientific, 81–96, [https://doi.org/10.1142/9789814579933\\_0005](https://doi.org/10.1142/9789814579933_0005).
- Duan, W. S., and Z. H. Huo, 2016: An approach to generating mutually independent initial perturbations for ensemble forecasts: Orthogonal conditional nonlinear optimal perturbations. *J. Atmos. Sci.*, **73**, 997–1014, <https://doi.org/10.1175/JAS-D-15-0138.1>.
- Duan, W. S., and M. Mu, 2018: Predictability of El Niño-southern oscillation events, Oxford Research Encyclopedia of Climate Science, 28. <https://doi.org/10.1093/acrefore/978019028620.013.80>.
- Duan, W. S., M. Mu, and B. Wang, 2004: Conditional nonlinear optimal perturbations as the optimal precursors for El Nino-southern oscillation events. *J. Geophys. Res.*, **109**, D23105, <https://doi.org/10.1029/2004JD004756>.
- Duan, W. S., and R. Zhang, 2010: Is model parameter error related to spring predictability barrier for El Nino events? Results from a theoretical model. *Adv. Atmos. Sci.*, **27**, 1003–1013, <https://doi.org/10.1007/s00376-009-9166-4>.
- Duan, W. S., X. C. Liu, K. Y. Zhu, and M. Mu, 2009: Exploring the initial errors that cause a significant “spring predictability barrier” for El Niño events. *J. Geophys. Res.*, **114**, C04022.
- Duan, W. S., X. Q. Li, and B. Tian, 2018: Towards optimal observational array for dealing with challenges of El Niño-Southern Oscillation predictions due to diversities of El Niño. *Climate Dyn.*, **51**, 3351–3368, <https://doi.org/10.1007/s00382-018-4082-x>.
- Duan, W. S., Y. Wang, Z. H. Huo, and F. F. Zhou, 2019: Ensemble forecast methods for numerical weather forecast and climate prediction: Thinking and prospect. *Climatic and Environmental Research*, **24**(3), 396–406, <https://doi.org/10.3878/j.issn.1006-9585.2018.18133>. (in Chinese with English abstract)
- Duan, W. S., J. J. Ma, and S. Vannitsem, 2022a: An ensemble forecasting method for dealing with the combined effects of the initial and model errors and a potential deep learning implementation. *Mon. Wea. Rev.*, **150**, 2959–2976, <https://doi.org/10.1175/MWR-D-22-0007.1>.
- Duan, W. S., R. Feng, L. C. Yang, and L. Jiang, 2022b: A new approach to data assimilation for numerical weather forecasting and climate prediction. *Journal of Applied Analysis and Computation*, **12**(3), 1007–1021, <https://doi.org/10.11948/20220098>.
- Evensen, G., 1994: Sequential data assimilation with a nonlinear quasi-geostrophic model using Monte Carlo methods to forecast error statistics. *J. Geophys. Res.*, **99**, 10143–10162, <https://doi.org/10.1029/94JC00572>.
- Evensen, G., 2003: The Ensemble Kalman Filter: Theoretical formulation and practical implementation. *Ocean Dynamics*, **53**, 343–367, <https://doi.org/10.1007/s10236-003-0036-9>.
- Fan, J. F., J. Meng, J. Ludescher, X. S. Chen, Y. Ashkenazy, J. Kurths, S. Havlin, and H. J. Schellnhuber, 2021: Statistical physics approaches to the complex Earth system. *Physics Reports*, **896**, 1–84, <https://doi.org/10.1016/j.physrep.2020.09.005>.
- Fan, J. F., J. Meng, J. Ludescher, Z. Y. Li, E. Surovyatkina, X. S. Chen, J. Kurths, and H. J. Schellnhuber, 2022: Network-based approach and climate change benefits for forecasting the amount of Indian monsoon rainfall. *J. Climate*, **35**, 1009–1020, <https://doi.org/10.1175/JCLI-D-21-0063.1>.
- Fan, K., H. J. Wang, and Y. J. Choi, 2008: A physically-based statistical forecast model for the middle-lower reaches of the Yangtze River Valley summer rainfall. *Chinese Science Bulletin*, **53**(4), 602–609, <https://doi.org/10.1007/s11434-008-0083-1>.
- Fan, K., Y. Liu, and H. P. Chen, 2012: Improving the prediction of the East Asian summer monsoon: New approaches. *Wea. Forecasting*, **27**(4), 1017–1030, <https://doi.org/10.1175/WAF-D-11-00092.1>.
- Feng, J., R. Q. Ding, D. Q. Liu, and J. P. Li, 2014: The application

- of nonlinear local Lyapunov vectors to ensemble predictions in Lorenz systems. *J. Atmos. Sci.*, **71**, 3554–3567, <https://doi.org/10.1175/Jas-D-13-0270.1>.
- Feng, J., R. Q. Ding, J. P. Li, and D. Q. Liu, 2016: Comparison of nonlinear local Lyapunov vectors with bred vectors, random perturbations and ensemble transform Kalman filter strategies in a barotropic model. *Adv. Atmos. Sci.*, **33**, 1036–1046, <https://doi.org/10.1007/s00376-016-6003-4>.
- Feng, J., X. H. Qin, C. Q. Wu, P. Zhang, L. Yang, X. S. Shen, W. Han, and Y. Z. Liu, 2022: Improving typhoon predictions by assimilating the retrieval of atmospheric temperature profiles from the FengYun-4A's Geostationary Interferometric Infrared Sounder (GIIRS). *Atmospheric Research*, **280**, 106391, <https://doi.org/10.1016/j.atmosres.2022.106391>.
- Feng, R., and W. S. Duan, 2014: The spatial patterns of initial errors related to the “winter predictability barrier” of the Indian Ocean dipole. *Atmos. Ocean. Sci. Lett.*, **7**, 406–410, <https://doi.org/10.3878/j.issn.1674-2834.14.0018>.
- Geng, Y., Q. Wang, M. Mu, and K. Zhang, 2020: Predictability and error growth dynamics of the Kuroshio Extension state transition process in an eddy-resolving regional ocean model. *Ocean Modelling*, **153**, 101659, <https://doi.org/10.1016/j.oceanmod.2020.101659>.
- Geng, Z. J., Y. W. Zhang, B. Lu, J. F. Fan, Z. M. Zhao, and X. S. Chen, 2021: Network-synchronization analysis reveals the weakening tropical circulations. *Geophys. Res. Lett.*, **48**, e2021GL093582, <https://doi.org/10.1029/2021GL093582>.
- Good, S. A., M. J. Martin, and N. A. Rayner, 2013: EN4: Quality controlled ocean temperature and salinity profiles and monthly objective analyses with uncertainty estimates. *J. Geophys. Res.*, **118**, 6704–6716, <https://doi.org/10.1002/2013JC009067>.
- Hasselmann, K., 1976: Stochastic climate models Part I. Theory. *Tellus*, **28**, 473–485, <https://doi.org/10.1111/j.2153-3490.1976.tb00696.x>.
- He, Y. J., and Coauthors, 2017: Reduction of initial shock in decadal predictions using a new initialization strategy. *Geophys. Res. Lett.*, **44**(16), 8538–8547, <https://doi.org/10.1002/2017GL074028>.
- He, Y. J., and Coauthors, 2020a: A DRP-4DVar-based coupled data assimilation system with a simplified off-line localization technique for decadal predictions. *Journal of Advances in Modeling Earth Systems*, **12**(4), e2019MS001768, <https://doi.org/10.1029/2019MS001768>.
- He, Y. J., and Coauthors, 2020b: A new DRP-4DVar-based coupled data assimilation system for decadal predictions using a fast online localization technique. *Climate Dyn.*, **54**(7), 3541–3559, <https://doi.org/10.1007/s00382-020-05190-w>.
- Hou, M. Y., W. S. Duan, and X. F. Zhi, 2019: Season-dependent predictability barrier for two types of El Niño revealed by an approach to data analysis for predictability. *Climate Dyn.*, **53**, 5561–5581, <https://doi.org/10.1007/s00382-019-0488-w>.
- Hou, M. Y., Y. M. Tang, W. S. Duan, and Z. Q. Shen, 2023: Toward an optimal observational array for improving two flavors of El Niño predictions in the whole Pacific. *Climate Dyn.*, **60**, 831–850, <https://doi.org/10.1007/s00382-022-06342-w>.
- Hou, Z. L., J. P. Li, R. Q. Ding, C. Karamperidou, W. S. Duan, T. Liu, and J. Feng, 2018a: Asymmetry of the predictability limit of the warm ENSO phase. *Geophys. Res. Lett.*, **45**, 7646–7653, <https://doi.org/10.1029/2018gl077880>.
- Hou, Z. L., J. P. Li, R. Q. Ding, J. Feng, and W. S. Duan, 2018b: The application of nonlinear local Lyapunov vectors to the Zebiak–Cane model and their performance in ensemble prediction. *Climate Dyn.*, **51**, 283–304, <https://doi.org/10.1007/s00382-017-3920-6>.
- Hou, Z. L., J. P. Li, R. Q. Ding, and J. Feng, 2022: Investigating decadal variations of the seasonal predictability limit of sea surface temperature in the tropical Pacific. *Climate Dyn.*, **59**, 1079–1096, <https://doi.org/10.1007/s00382-022-06179-3>.
- Hu, H. Q., J. Y. Liu, L. L. Da, W. H. Guo, K. Liu, and B. L. Cui, 2021: Identification of the sensitive area for targeted observation to improve vertical thermal structure prediction in summer in the Yellow Sea. *Acta Oceanologica Sinica*, **40**(7), 77–87, <https://doi.org/10.1007/s13131-021-1738-x>.
- Hu, J. Y., and W. S. Duan, 2016: Relationship between optimal precursory disturbances and optimally growing initial errors associated with ENSO events: Implications to target observations for ENSO prediction. *J. Geophys. Res.*, **121**, 2901–2917, <https://doi.org/10.1002/2015JC011386>.
- Hu, S., B. Wu, T. J. Zhou, and Z. Guo, 2019: A comparison of full-field and anomaly initialization for seasonal prediction of Indian Ocean basin mode. *Climate Dyn.*, **53**(9–10), 6089–6104, <https://doi.org/10.1007/s00382-019-04916-9>.
- Hu, S., T. J. Zhou, and B. Wu, 2020: Improved ENSO prediction skill resulting from reduced climate drift in IAP-DecPreS: A comparison of full-field and anomaly initialization. *Journal of Advances in Modeling Earth Systems*, **12**(2), e2019MS001759, <https://doi.org/10.1029/2019MS001759>.
- Hu, S., T. J. Zhou, B. Wu, and Coauthors, 2023: Seasonal Prediction of the Record-Breaking Northward Shift of the Western Pacific Subtropical High in July 2021. *Adv. Atmos. Sci.*, **40**, 410–427, <https://doi.org/10.1007/s00376-022-2151-x>.
- Huang, L., and Z. Y. Meng, 2014: Quality of the target area for metrics with different nonlinearities in a mesoscale convective system. *Mon. Wea. Rev.*, **142**, 2379–2397, <https://doi.org/10.1175/MWR-D-13-00244.1>.
- Huo, Z. H., and W. S. Duan, 2019: The application of the orthogonal conditional nonlinear optimal perturbations method to typhoon track ensemble forecasts. *Science China Earth Sciences*, **62**, 376–388, <https://doi.org/10.1007/s11430-018-9248-9>.
- Huo, Z. H., W. S. Duan, and F. F. Zhou, 2019: Ensemble forecasts of tropical cyclone track with orthogonal conditional nonlinear optimal perturbations. *Adv. Atmos. Sci.*, **36**(2), 231–247, <https://doi.org/10.1007/s00376-018-8001-1>.
- Jiang, L., W. S. Duan, and H. L. Liu, 2022: The most sensitive initial error of sea surface height anomaly forecasts and its implication for target observations of mesoscale eddies. *J. Phys. Oceanogr.*, **52**, 723–740, <https://doi.org/10.1175/JPO-D-21-0200.1>.
- Jin, Z., X. J. Tian, R. Han, Y. Fu, X. Li, H. Q. Mao, and C. H. Chen, 2021: A global CO<sub>2</sub> flux dataset (2015–2019) inferred from OCO-2 retrievals using the Tan-Tracker inversion system. *Earth System Science Data Discussion*, <https://doi.org/10.5194/essd-2021-210>.
- Kalnay, E., 2002: *Atmospheric Modeling, Data Assimilation and Predictability*. Cambridge University Press, <https://doi.org/10.1017/CBO9780511802270>.
- Kerswell, R. R., C. C. T. Pringle, and A. P. Willis, 2014: An optimization approach for analysing nonlinear stability with transition to turbulence in fluids as an exemplar. *Reports on Progress in Physics*, **77**(8), 085901, <https://doi.org/10.1088/>



- 0034-4885/77/8/085901.
- Kessler, W. S., and Coauthors, 2021: Final Report of TPO 2020. GOOS-268, 83 pp. Available from <https://tropicalpacific.org/tpos2020-project-archive/reports/>.
- Kleist, D. T., and K. Ide, 2015: An OSSE-based evaluation of hybrid variational–ensemble data assimilation for the NCEP GFS. Part II: 4DEnVar and hybrid variants. *Mon. Wea. Rev.*, **143**(2), 452–470, <https://doi.org/10.1175/mwr-d-13-00350.1>.
- Kriz, K. A., 2019: Ensemble forecasting. *The Palgrave Handbook of Government Budget Forecasting*, D. Williams and T. Calabrese, Eds., Springer, 413–426, [https://doi.org/10.1007/978-3-030-18195-6\\_21](https://doi.org/10.1007/978-3-030-18195-6_21).
- Landsea, C. W., and J. P. Cangialosi, 2018: Have we reached the limits of predictability for tropical cyclone track forecasting. *Bull. Amer. Meteor. Soc.*, **99**, 2237–2243, <https://doi.org/10.1175/BAMS-D-17-0136.1>.
- Langland, R. H., and Coauthors, 1999: The North Pacific Experiment (NORPEX-98): Targeted observations for improved North American weather forecasts. *Bull. Amer. Meteor. Soc.*, **80**, 1363–1384, [https://doi.org/10.1175/1520-0477\(1999\)080<1363:TNPEXT>2.0.CO;2](https://doi.org/10.1175/1520-0477(1999)080<1363:TNPEXT>2.0.CO;2).
- Leith, C. E., 1974: Theoretical skill of Monte Carlo forecasts. *Mon. Wea. Rev.*, **102**, 409–418, [https://doi.org/10.1175/1520-0493\(1974\)102<0409:TSOMCF.2.0.CO;2](https://doi.org/10.1175/1520-0493(1974)102<0409:TSOMCF.2.0.CO;2).
- Li, B. S., R. Q. Ding, J. P. Li, Y. D. Xu, and J. Li, 2018: Asymmetric response of predictability of East Asian summer monsoon to ENSO. *SOLA*, **14**, 52–56, <https://doi.org/10.2151/sola.2018-009>.
- Li, F. F., B. Wang, Y. J. He, W. Y. Huang, S. M. Xu, L. Liu, J. J. Liu, and L. J. Li, 2021b: Important role of North Atlantic air–sea coupling in the interannual predictability of summer precipitation over the eastern Tibetan Plateau. *Climate Dyn.*, **56**(5), 1433–1448, <https://doi.org/10.1007/s00382-020-05542-6>.
- Li, F. F., and Coauthors, 2021c: Improved decadal predictions of East Asian summer monsoon with a weakly coupled data assimilation scheme. *International Journal of Climatology*, **41**(12), 5550–5571, <https://doi.org/10.1002/joc.7141>.
- Li, J. P., and R. Q. Ding, 2011: Temporal–spatial distribution of atmospheric predictability limit by local dynamical analogs. *Mon. Wea. Rev.*, **139**, 3265–3283, <https://doi.org/10.1175/MWR-D-10-05020.1>.
- Li, X., and R. Q. Ding, 2022: The backward nonlinear local Lyapunov exponent and its application to quantifying the local predictability of extreme high-temperature events. *Climate Dyn.*, <https://doi.org/10.1007/s00382-022-06469-w>.
- Li, X., R. Q. Ding, and J. P. Li, 2019: Determination of the backward predictability limit and its relationship with the forward predictability limit. *Adv. Atmos. Sci.*, **36**, 669–677, <https://doi.org/10.1007/s00376-019-8205-z>.
- Li, X., R. Q. Ding, and J. P. Li, 2020: Quantitative comparison of predictabilities of warm and cold events using the backward nonlinear local Lyapunov exponent method. *Adv. Atmos. Sci.*, **37**, 951–958, <https://doi.org/10.1007/s00376-020-2100-5>.
- Li, X., J. Feng, R. Q. Ding, and J. P. Li, 2021a: Application of backward nonlinear local Lyapunov exponent method to assessing the relative impacts of initial condition and model errors on local backward predictability. *Adv. Atmos. Sci.*, **38**, 1486–1496, <https://doi.org/10.1007/s00376-021-0434-2>.
- Ling, F. H., J. J. Luo, Y. Li, T. Tang, L. Bai, W. L. Ouyang, and T. Yamagata, 2022: Multi-task machine learning improves multi-seasonal prediction of the Indian Ocean Dipole. *Nature Communications*, **13**, 7681, <https://doi.org/10.1038/s41467-022-35412-0>.
- Liu, C. S., Q. N. Xiao, and B. Wang, 2008: An ensemble-based four-dimensional variational data assimilation scheme. Part I: Technical formulation and preliminary test. *Mon. Wea. Rev.*, **136**(9), 3363–3373, <https://doi.org/10.1175/2008MWR2312.1>.
- Liu, C. S., Q. N. Xiao, and B. Wang, 2009: An ensemble-based four-dimensional variational data assimilation scheme. Part II: Observing system simulation experiments with Advanced Research WRF (ARW). *Mon. Wea. Rev.*, **137**, 1687–1704, <https://doi.org/10.1175/2008MWR2699.1>.
- Liu, D., W. S. Duan, R. Feng, and Y. M. Tang, 2018a: Summer predictability barrier of Indian ocean dipole events and corresponding error growth dynamics. *J. Geophys. Res.*, **123**, 3635–3650, <https://doi.org/10.1029/2017JC013739>.
- Liu, J. J., B. Wang, and Q. N. Xiao, 2011: An evaluation study of the DRP-4-DVar approach with the Lorenz-96 model. *Tellus A*, **63**, 256–262, <https://doi.org/10.1111/j.1600-0870.2010.00487.x>.
- Liu, K., W. H. Guo, L. L. Da, J. Y. Liu, H. Q. Hu, and B. L. Cui, 2021: Improving the thermal structure predictions in the Yellow Sea by conducting targeted observations in the CNOP-identified sensitive areas. *Scientific Reports*, **11**, 19518, <https://doi.org/10.1038/s41598-021-98994-7>.
- Liu, X., M. Mu, and Q. Wang, 2018b: The nonlinear optimal triggering perturbation of the Kuroshio large meander and its evolution in a regional ocean model. *J. Phys. Oceanogr.*, **48**(8), 1771–1786, <https://doi.org/10.1175/JPO-D-17-0246.1>.
- Liu, Y., and K. Fan, 2012: Improve the prediction of summer precipitation in the Southeastern China by a hybrid statistical downscaling model. *Meteorol. Atmos. Phys.*, **117**(3–4), 121–134, <https://doi.org/10.1007/s00703-012-0201-0>.
- Lorenc, A. C., N. E. Bowler, A. M. Clayton, S. R. Pring, and D. Fairbairn, 2015: Comparison of hybrid-4DEnVar and hybrid-4DVar data assimilation methods for global NWP. *Mon. Wea. Rev.*, **143**(1), 212–229, <https://doi.org/10.1175/mwr-d-14-00195.1>.
- Lorenz, E. N., 1965: A study of the predictability of a 28-variable atmospheric model. *Tellus*, **17**, 321–333, <https://doi.org/10.3402/tellusa.v17i3.9076>.
- Lu, D. Y., R. Q. Ding, and J. P. Li, 2020: The predictability limit of the amplitude and phase of the Madden-Julian oscillation. *Atmospheric Science Letters*, **21**, e968, <https://doi.org/10.1002/asl.1968>.
- Lu, Z. H., W. J. Dong, B. Lu, N. M. Yuan, Z. G. Ma, M. I. Bogachev, and J. Kurths, 2022: Early warning of the Indian Ocean Dipole using climate network analysis. *Proceedings of the National Academy of Sciences of the United States of America*, **119**, e2109089119, <https://doi.org/10.1073/pnas.2109089119>.
- Ma, X. Y., M. Mu, G. K. Dai, Z. Han, C. X. Li, and Z. N. Jiang, 2022: Influence of Arctic sea ice concentration on extended-range prediction of strong and long-lasting Ural blocking events in winter. *J. Geophys. Res.*, **127**, e2021JD036282, <https://doi.org/10.1029/2021JD036282>.
- Majumdar, S. J., 2016: A Review of Targeted Observations. *Bull. Amer. Meteor. Soc.*, **97**, 2287–2303, <https://doi.org/10.1175/BAMS-D-14-00259.1>.
- Majumdar, S. J., and Coauthors, 2021: Multiscale forecasting of

- high-impact weather: Current status and future challenges. *Bull. Amer. Meteor. Soc.*, **102**(3), E635–E659, <https://doi.org/10.1175/BAMS-D-20-0111.1>.
- Mu, M., 2000: Nonlinear singular vectors and nonlinear singular values. *Science in China Series D: Earth Sciences*, **43**, 375–385, <https://doi.org/10.1007/BF02959448>.
- Mu, M., W. S. Duan, and J. C. Wang, 2002: The predictability problems in numerical weather and climate prediction. *Adv. Atmos. Sci.*, **19**(2), 191–204, <https://doi.org/10.1007/s00376-002-0016-x>.
- Mu, M., W. S. Duan, and B. Wang, 2003: Conditional nonlinear optimal perturbation and its applications. *Nonlinear Processes in Geophysics*, **10**, 493–501, <https://doi.org/10.5194/npg-10-493-2003>.
- Mu, M., L. Sun, and H. A. Dijkstra, 2004a: The sensitivity and stability of the ocean's thermohaline circulation to finite-amplitude perturbations. *J. Phys. Oceanogr.*, **34**, 2305–2315, [https://doi.org/10.1175/1520-0485\(2004\)034<2305:TSASOT>2.0.CO;2](https://doi.org/10.1175/1520-0485(2004)034<2305:TSASOT>2.0.CO;2).
- Mu, M., W. S. Duan, and J. F. Chou, 2004b: Recent advances in predictability studies in China (1999–2002). *Adv. Atmos. Sci.*, **21**(3), 437–443, <https://doi.org/10.1007/BF02915570>.
- Mu, M., W. S. Duan, and B. Wang, 2007: Season-dependent dynamics of nonlinear optimal error growth and El Niño–Southern Oscillation predictability in a theoretical model. *J. Geophys. Res.*, **112**(D10), D10113, <https://doi.org/10.1029/2005JD006981>.
- Mu, M., F. F. Zhou, and H. L. Wang, 2009: A method for identifying the sensitive areas in targeted Observations for tropical cyclone prediction: Conditional Nonlinear optimal perturbation. *Mon. Wea. Rev.*, **137**, 1623–1639, <https://doi.org/10.1175/2008MWR2640.1>.
- Mu, M., W. Duan, Q. Wang, and R. Zhang, 2010: An extension of conditional nonlinear optimal perturbation approach and its applications. *Nonlinear Processes in Geophysics*, **17**, 211–220, <https://doi.org/10.5194/npg-17-211-2010>.
- Mu, M., Y. S. Yu, H. Xu, and T. T. Gong, 2014: Similarities between optimal precursors for ENSO events and optimally growing initial errors in El Niño predictions. *Theor. Appl. Climatol.*, **115**(3–4), 461–469, <https://doi.org/10.1007/s00704-013-0909-x>.
- Mu, M., W. S. Duan, D. K. Chen, and W. D. Yu, 2015: Target observations for improving initialization of high-impact ocean-atmospheric environmental events forecasting. *National Science Review*, **2**, 226–236, <https://doi.org/10.1093/nsr/nwv021>.
- Mu, M., W. S. Duan, and Y. M. Tang, 2017a: The predictability of atmospheric and oceanic motions: Retrospect and prospects. *Science China Earth Sciences*, **60**, 2001–2012, <https://doi.org/10.1007/s11430-016-9101-x>.
- Mu, M., R. Feng, and W. S. Duan, 2017b: Relationship between optimal precursors for Indian Ocean Dipole events and optimally growing initial errors in its prediction. *J. Geophys. Res.*, **122**(2), 1141–1153, <https://doi.org/10.1002/2016JC012527>.
- Navarro, G., and J. Ruiz, 2013: Hysteresis conditions the vertical position of deep chlorophyll maximum in the temperate ocean. *Global Biogeochemical Cycles*, **27**, 1013–1022, <https://doi.org/10.1002/gbc.20093>.
- Nian, D., N. M. Yuan, K. R. Ying, G. Liu, Z. T. Fu, Y. J. Qi, and C. L. E. Franzke, 2020: Identifying the sources of seasonal predictability based on climate memory analysis and variance decomposition. *Climate Dyn.*, **55**, 3239–3252, <https://doi.org/10.1007/s00382-020-05444-7>.
- Oke, P. R., J. S. Allen, R. N. Miller, G. D. Egbert, and P. M. Kosro, 2002: Assimilation of surface velocity data into a primitive equation coastal ocean model. *J. Geophys. Res.*, **107**(C9), 3122, <https://doi.org/10.1029/2000JC000511>.
- Orlanski, I., 1975: A rational subdivision of scales for atmospheric processes. *Bull. Amer. Meteor. Soc.*, **56**, 527–530, <https://doi.org/10.1175/1520-0477-56.5.527>.
- Palmer, T. N., R. Gelaro, J. Barkmeijer, and R. Buizza, 1998: Singular vectors, metrics, and adaptive observations. *J. Atmos. Sci.*, **55**, 633–653, [https://doi.org/10.1175/1520-0469\(1998\)055<0633:SVMAAO>2.0.CO;2](https://doi.org/10.1175/1520-0469(1998)055<0633:SVMAAO>2.0.CO;2).
- Parsons, D. B., and Coauthors, 2017: THORPEX research and the science of prediction. *Bull. Amer. Meteor. Soc.*, **98**(4), 807–830, <https://doi.org/10.1175/BAMS-D-14-00025.1>.
- Pringle, C. C. T., and R. R. Kerswell, 2010: Using nonlinear transient growth to construct the minimal seed for shear flow turbulence. *Physical Review Letters*, **105**, 154502, <https://doi.org/10.1103/PhysRevLett.105.154502>.
- Qin, X. H., and M. Mu, 2014: Can adaptive observations improve tropical cyclone intensity forecasts. *Adv. Atmos. Sci.*, **31**(2), 252–262, <https://doi.org/10.1007/s00376-013-3008-0>.
- Qin, X. H., W. S. Duan, and M. Mu, 2013: Conditions under which CNOP sensitivity is valid for tropical cyclone adaptive observations. *Quart. J. Roy. Meteor. Soc.*, **139**, 1544–1554, <https://doi.org/10.1002/qj.2109>.
- Qin, X. H., W. S. Duan, P. W. Chan, B. Y. Chen, and K. N. Huang, 2023: Effects of dropsonde data in field campaigns on forecasts of tropical cyclones over the western North Pacific in 2020 and the role of CNOP sensitivity. *Adv. Atmos. Sci.*, **40**, 791–803, <https://doi.org/10.1007/s00376-022-2136-9>.
- Rayner, N. A., D. E. Parker, E. B. Horton, C. K. Folland, L. V. Alexander, D. P. Rowell, E. C. Kent, and A. Kaplan, 2003: Global analyses of sea surface temperature, sea ice, and night marine air temperature since the late nineteenth century. *J. Geophys. Res.*, **108**, 4407, <https://doi.org/10.1029/2002JD002670>.
- Sévellec, F., and A. V. Fedorov, 2013: Model bias reduction and the limits of oceanic decadal predictability: Importance of the deep ocean. *J. Climate*, **26**(11), 3688–3707, <https://doi.org/10.1175/JCLI-D-12-00199.1>.
- Shi, P. F., and Coauthors, 2021: Significant land contributions to interannual predictability of East Asian summer monsoon rainfall. *Earth's Future*, **9**(2), e2020EF001762, <https://doi.org/10.1029/2020EF001762>.
- Shi, P. F., and Coauthors, 2022: Contributions of weakly coupled data assimilation-based land initialization to interannual predictability of summer climate over Europe. *J. Climate*, **35**(2), 517–535, <https://doi.org/10.1175/JCLI-D-20-0506.1>.
- Shi, Z., and R. Q. Ding, 2012: Estimating the predictability of the Quasi-Biweekly Oscillation using the nonlinear local Lyapunov exponent approach. *Atmos. Ocean. Sci. Lett.*, **5**, 389–392, <https://doi.org/10.1080/16742834.2012.11447023>.
- Smith, L. A., C. Ziehmann, and K. Fraedrich, 1999: Uncertainty dynamics and predictability in chaotic systems. *Quart. J. Roy. Meteor. Soc.*, **125**, 2855–2886, <https://doi.org/10.1002/qj.49712556005>.
- Snyder, C., 1996: Summary of an informal workshop on adaptive observations and FASTEX. *Bull. Amer. Meteor. Soc.*, **77**, 953–961, <https://doi.org/10.1175/1520-0477-77.5.953>.



- Sun, G. D., and M. Mu, 2013: Understanding variations and seasonal characteristics of net primary production under two types of climate change scenarios in China using the LPJ model. *Climatic Change*, **120**, 755–769, <https://doi.org/10.1007/s10584-013-0833-1>.
- Sun, G. D., and M. Mu, 2014: The analyses of the net primary production due to regional and seasonal temperature differences in eastern China using the LPJ model. *Ecological Modelling*, **289**, 66–76, <https://doi.org/10.1016/j.ecolmodel.2014.06.021>.
- Sun, G. D., and M. Mu, 2017a: A new approach to identify the sensitivity and importance of physical parameters combination within numerical models using the Lund–Potsdam–Jena (LPJ) model as an example. *Theor. Appl. Climatol.*, **128**, 587–601, <https://doi.org/10.1007/s00704-015-1690-9>.
- Sun, G. D., and M. Mu, 2017b: Projections of soil carbon using the combination of the CNOP-P method and GCMs from CMIP5 under RCP4.5 in North–South Transect of Eastern China. *Plant and Soil*, **413**, 243–260, <https://doi.org/10.1007/s11104-016-3098-4>.
- Sun, G. D., M. Mu, and Q. L. You, 2020: Identification of key physical processes and improvements for simulating and predicting net primary production over the Tibetan Plateau. *J. Geophys. Res.*, **125**, e2020JD033128, <https://doi.org/10.1029/2020JD033128>.
- Talagrand, O., 1997: Assimilation of observations, an introduction (Special Issue: Data assimilation in meteorology and oceanography: Theory and practice). *J. Meteor. Soc. Japan*, **75**(1), 191–209, [https://doi.org/10.2151/jmsj1965.75.1b\\_191](https://doi.org/10.2151/jmsj1965.75.1b_191).
- Tao, L. J., and W. S. Duan, 2019: Using a nonlinear forcing singular vector approach to reduce model error effects in ENSO forecasting. *Wea. Forecasting*, **34**(5), 1321–1342, <https://doi.org/10.1175/WAF-D-19-0050.1>.
- Tao, L. J., W. S. Duan, and S. Vannitsem, 2020: Improving forecasts of El Niño diversity: A nonlinear forcing singular vector approach. *Climate Dyn.*, **55**, 739–754, <https://doi.org/10.1007/s00382-020-05292-5>.
- Tennekes H., 1991. Karl Popper and the accountability of numerical weather forecasting. ECMWF Workshop Proceedings. New Developments in Predictability. London: ECMWF.
- Tian, B. Q., and K. Fan, 2019: Seasonal climate prediction models for the number of landfalling tropical cyclones in China. *J. Meteor. Res.*, **33**(5), 837–850, <https://doi.org/10.1007/s13351-019-8187-x>.
- Tian, B. Q., and K. Fan, 2020: Climate prediction of summer extreme precipitation frequency in the Yangtze River valley based on sea surface temperature in the southern Indian Ocean and ice concentration in the Beaufort Sea. *International Journal of Climatology*, **40**(9), 4117–4130, <https://doi.org/10.1002/joc.6446>.
- Tian, B. Q., and K. Fan, 2022: New downscaling prediction models for spring drought in China. *International Journal of Climatology*, **42**, 6960–6975, <https://doi.org/10.1002/joc.7623>.
- Tian, X. J., and X. B. Feng, 2015: A non-linear least squares enhanced POD-4DVar algorithm for data assimilation. *Tellus A Dyn. Meteorol. Oceanogr.*, **67**, 25340, <https://doi.org/10.3402/tellusa.v67.25340>.
- Tian, X. J., and H. Q. Zhang, 2019: A big data-driven nonlinear least squares four-dimensional variational data assimilation method: Theoretical formulation and conceptual evaluation. *Earth and Space Science*, **6**, 1430–1439, <https://doi.org/10.1029/2019EA000735>.
- Tian, X. J., Z. H. Xie, and A. G. Dai, 2008: An ensemble-based explicit four-dimensional variational assimilation method. *J. Geophys. Res.*, **113**, D21124, <https://doi.org/10.1029/2008JD010358>.
- Tian, X. J., H. Q. Zhang, X. B. Feng, and Y. F. Xie, 2018: Nonlinear least squares En4DVar to 4DVar methods for data assimilation: Formulation, analysis, and preliminary evaluation. *Mon. Wea. Rev.*, **146**, 77–93, <https://doi.org/10.1175/MWR-D-17-0050.1>.
- Tian, X. J., H. Q. Zhang, X. B. Feng, and X. Li, 2021: i4DVar: An integral correcting four-dimensional variational data assimilation method. *Earth and Space Science*, **8**, e2021EA001767, <https://doi.org/10.1029/2021EA001767>.
- Toth, Z., and E. Kalnay, 1993: Ensemble forecasting at NMC: The generation of perturbations. *Bull. Amer. Meteor. Soc.*, **74**(12), 2317–2330, [https://doi.org/10.1175/1520-0477\(1993\)074<2317:EFANTG>2.0.CO;2](https://doi.org/10.1175/1520-0477(1993)074<2317:EFANTG>2.0.CO;2).
- Tsonis, A. A., and P. J. Roebber, 2004: The architecture of the climate network. *Physica A: Statistical Mechanics and its Applications*, **333**, 497–504, <https://doi.org/10.1016/j.physa.2003.10.045>.
- Wang, B., J. J. Liu, S. D. Wang, W. Cheng, J. Liu, C. S. Liu, Q. N. Xiao, and Y. H. Kuo, 2010: An economical approach to four-dimensional variational data assimilation. *Adv. Atmos. Sci.*, **27**(4), 715–727, <https://doi.org/10.1007/s00376-009-9122-3>.
- Wang, B., J. J. Liu, L. Liu, S. M. Xu, and W. Y. Huang, 2018: An approach to localization for ensemble-based data assimilation. *PLoS One*, **13**(1), e0191088, <https://doi.org/10.1371/journal.pone.0191088>.
- Wang, L., X. S. Shen, J. J. Liu, and B. Wang, 2020b: Model uncertainty representation for a convection-allowing ensemble prediction system based on CNOP-P. *Adv. Atmos. Sci.*, **37**(8), 817–831, <https://doi.org/10.1007/s00376-020-9262-z>.
- Wang, Q., and M. Mu, 2015: A new application of conditional nonlinear optimal perturbation approach to boundary condition uncertainty. *J. Geophys. Res.*, **120**, 7979–7996, <https://doi.org/10.1002/2015JC011095>.
- Wang, Q., M. Mu, and G. D. Sun, 2020a: A useful approach to sensitivity and predictability studies in geophysical fluid dynamics: Conditional non-linear optimal perturbation. *National Science Review*, **7**(1), 214–223, <https://doi.org/10.1093/nsr/nwz039>.
- Wang, Q., M. Mu, and S. Pierini, 2020c: The fastest growing initial error in prediction of the Kuroshio Extension state transition processes and its growth. *Climate Dyn.*, **54**(3–4), 1953–1971, <https://doi.org/10.1007/s00382-019-05097-1>.
- Wei, Y. T., M. Mu, H. L. Ren, and J. X. Fu, 2019: Conditional nonlinear optimal perturbations of moisture triggering primary MJO initiation. *Geophys. Res. Lett.*, **46**, 3492–3501, <https://doi.org/10.1029/2018GL081755>.
- Winkler, J., M. Denhard, and B. A. Schmitt, 2020: Krylov methods for adjoint-free singular vector based perturbations in dynamical systems. *Quart. J. Roy. Meteor. Soc.*, **146**, 225–239, <https://doi.org/10.1002/qj.3668>.
- WMO, 2004: THORPEX international science plan. Version 3, WMO/TD-No. 1246, WWRP/THORPEX-No. 02, 55 pp. Available from [https://library.wmo.int/index.php?lvl=notice\\_display&id=7301#ZDZuGvkyY18](https://library.wmo.int/index.php?lvl=notice_display&id=7301#ZDZuGvkyY18).
- Wu, B., T. J. Zhou, and F. Zheng, 2018: EnOI-IAU initialization scheme designed for decadal climate prediction system IAP-DecPreS. *Journal of Advances in Modeling Earth Systems*,

- 10(2), 342–356, <https://doi.org/10.1002/2017MS001132>.
- Wu, C. C., and Coauthors, 2005: Dropwindsonde observations for Typhoon Surveillance near the Taiwan Region (DOT-STAR): An overview. *Bull. Amer. Meteor. Soc.*, **86**, 787–790, <https://doi.org/10.1175/BAMS-86-6-791>.
- Wu, C. C., J. H. Chen, P. H. Lin, and K. H. Chou, 2007: Targeted observations of tropical cyclone movement based on the adjoint-derived sensitivity steering vector. *J. Atmos. Sci.*, **64**, 2611–2626, <https://doi.org/10.1175/JAS3974.1>.
- Wu, D. C., Z. Y. Meng, and D. C. Yan, 2013: The predictability of a squall line in South China on 23 April 2007. *Adv. Atmos. Sci.*, **30**, 485–502, <https://doi.org/10.1007/s00376-012-2076-x>.
- Wu, X. R., W. Li, G. J. Han, L. X. Zhang, C. X. Shao, C. J. Sun, and L. L. Xuan, 2015: An adaptive compensatory approach of the fixed localization in the EnKF. *Mon. Wea. Rev.*, **143**, 4714–4735, <https://doi.org/10.1175/MWR-D-15-0060.1>.
- Xu, Z. Z., J. Chen, M. Mu, G. K. Dai, and Y. N. Ma, 2022a: A nonlinear representation of model uncertainty in a convective-scale ensemble prediction system. *Adv. Atmos. Sci.*, **39**, 1432–1450, <https://doi.org/10.1007/s00376-022-1341-x>.
- Xu, Z. Z., J. Chen, M. Mu, L. J. Tao, G. K. Dai, J. Z. Wang, and Y. N. Ma, 2022b: A stochastic and non-linear representation of model uncertainty in a convective-scale ensemble prediction system. *Quart. J. Roy. Meteor. Soc.*, **148**, 2507–2531, <https://doi.org/10.1002/qj.4322>.
- Yang, L. C., and Z. T. Fu, 2019: Process-dependent persistence in precipitation records. *Physica A: Statistical Mechanics and its Applications*, **527**, 121459, <https://doi.org/10.1016/j.physa.2019.121459>.
- Yang, L. C., W. S. Duan, Z. F. Wang, and W. Y. Yang, 2022: Toward targeted observations of the meteorological initial state for improving the PM<sub>2.5</sub> forecast of a heavy haze event that occurred in the Beijing-Tianjin-Hebei region. *Atmospheric Chemistry and Physics*, **22**, 11429–11453, <https://doi.org/10.5194/acp-22-11429-2022>.
- Yang, Z. Y., X. H. Fang, and M. Mu, 2020: The optimal precursor of El Niño in the GFDL CM2p1 model. *J. Geophys. Res.*, **125**, e2019JC015797, <https://doi.org/10.1029/2019JC015797>.
- Ying, N., W. P. Wang, J. F. Fan, D. Zhou, Z. G. Han, Q. H. Chen, Q. Ye, and Z. G. Xue, 2021: Climate network approach reveals the modes of CO<sub>2</sub> concentration to surface air temperature. *Chaos: An Interdisciplinary Journal of Nonlinear Science*, **31**, 031104, <https://doi.org/10.1063/5.0040360>.
- Ying, N., W. S. Duan, Z. D. Zhao, and J. F. Fan, 2022: Complex network analysis of fine particulate matter (PM<sub>2.5</sub>): Transport and clustering. *Earth System Dynamics*, **13**, 1029–1039, <https://doi.org/10.5194/esd-13-1029-2022>.
- Yu, H., Chen, G., Zhou, C., Wong, W. and Coauthors, 2022: Are We Reaching the Limit of Tropical Cyclone Track Predictability in the Western North Pacific?. *Bull. Amer. Meteor. Soc.*, **103**, E410–E428, <https://doi.org/10.1175/BAMS-D-20-0308.1>.
- Yu, H. Z., and Z. Y. Meng, 2016: Key synoptic-scale features influencing the high-impact heavy rainfall in Beijing, China, on 21 July 2012. *Tellus A Dyn. Meteorol. Oceanogr.*, **68**, 31045, <https://doi.org/10.3402/tellusa.v68.31045>.
- Yu, H. Z., and Z. Y. Meng, 2022: The impact of moist physics on the sensitive area identification for heavy rainfall associated weather systems. *Adv. Atmos. Sci.*, **39**(5), 684–696, <https://doi.org/10.1007/s00376-021-0278-9>.
- Yu, X., and Coauthors, 2019: A multi-timescale EnOI-like high-efficiency approximate filter for coupled model data assimilation. *Journal of Advances in Modeling Earth Systems*, **11**, 45–63, <https://doi.org/10.1029/2018MS001504>.
- Yuan, N. M., Z. T. Fu, and S. D. Liu, 2014: Extracting climate memory using fractional integrated statistical model: A new perspective on climate prediction. *Scientific Reports*, **4**, 6577, <https://doi.org/10.1038/srep06577>.
- Yuan, N. M., Y. Huang, J. P. Duan, C. W. Zhu, E. Xoplaki, and J. Luterbacher, 2019: On climate prediction: How much can we expect from climate memory. *Climate Dyn.*, **52**, 855–864, <https://doi.org/10.1007/s00382-018-4168-5>.
- Zhang, H. Q., and X. J. Tian, 2018: A multigrid nonlinear least squares four-dimensional variational data assimilation scheme with the advanced research weather research and forecasting model. *J. Geophys. Res.*, **123**, 5116–5129, <https://doi.org/10.1029/2017JD027529>.
- Zhang, H. Q., and X. J. Tian, 2021: Evaluating the forecast impact of assimilating ATOVS radiance with the regional system of multigrid NLS-4DVar Data Assimilation for Numerical Weather Prediction (SNAP). *Journal of Advances in Modeling Earth Systems*, **13**, e2020MS002407, <https://doi.org/10.1029/2020MS002407>.
- Zhang, H. Q., and X. J. Tian, 2022: Integral correction of initial and model errors in system of multigrid NLS-4DVar data assimilation for numerical weather prediction (SNAP). *Quart. J. Roy. Meteor. Soc.*, **148**, 2490–2506, <https://doi.org/10.1002/qj.4313>.
- Zhang, H. Q., X. J. Tian, W. Cheng, and L. P. Jiang, 2020a: System of multigrid nonlinear least-squares four-dimensional variational data assimilation for numerical weather prediction (SNAP): System formulation and preliminary evaluation. *Adv. Atmos. Sci.*, **37**, 1267–1284, <https://doi.org/10.1007/s00376-020-9252-1>.
- Zhang, L., X. J. Tian, H. Q. Zhang, and F. Chen, 2020b: Impacts of multigrid NLS-4DVar-based Doppler radar observation assimilation on numerical simulations of landfalling Typhoon Haikui (2012). *Adv. Atmos. Sci.*, **37**, 873–892, <https://doi.org/10.1007/s00376-020-9274-8>.
- Zhang, M. R., and Z. Y. Meng, 2018: Impact of synoptic-scale factors on rainfall forecast in different stages of a persistent heavy rainfall event in South China. *J. Geophys. Res.*, **123**(7), 3574–3593, <https://doi.org/10.1002/2017JD028155>.
- Zhang, R. H., S. E. Zebiak, R. Kleeman, and N. Keenlyside, 2003: A new intermediate coupled model for El Niño simulation and prediction. *Geophys. Res. Lett.*, **30**, 2012, <https://doi.org/10.1029/2003GL018010>.
- Zhang, S., X. J. Tian, H. Q. Zhang, X. Han, and M. G. Zhang, 2021: A nonlinear least squares four-dimensional variational data assimilation system for PM<sub>2.5</sub> forecasts (NASM): Description and preliminary evaluation. *Atmospheric Pollution Research*, **12**, 122–132, <https://doi.org/10.1016/j.apr.2021.03.003>.
- Zhang, S., X. J. Tian, X. Han, M. G. Zhang, H. Q. Zhang, and H. Q. Mao, 2022a: Improvement of PM<sub>2.5</sub> forecast over China by the joint adjustment of initial conditions and emissions with the NLS-4DVar method. *Atmos. Environ.*, **271**, 118896, <https://doi.org/10.1016/j.atmosenv.2021.118896>.
- Zhang, Y. J., Z. Y. Meng, F. Q. Zhang, and Y. H. Weng, 2014: Predictability of tropical cyclone intensity evaluated through 5-yr forecasts with a convection-permitting regional-scale Model in the Atlantic Basin. *Wea Forecasting*, **29**,

- 1003–1023, <https://doi.org/10.1175/WAF-D-13-00085.1>.
- Zhang, Y. J., F. Q. Zhang, D. Stensrud, and Z. Y. Meng, 2015: Practical Predictability of the 20 May 2013 Tornadoic Thunderstorm Event in Oklahoma: Sensitivity to Synoptic Timing and Topographical Influence. *Mon. Wea. Rev.*, **143**, 2973–2997, <https://doi.org/10.1175/MWR-D-14-00394.1>.
- Zhang, Y. J., F. Q. Zhang, D. J. Stensrud, and Z. Y. Meng, 2016: Intrinsic predictability of the 20 May 2013 tornadoic thunderstorm event in Oklahoma at storm scales. *Mon. Wea. Rev.*, **144**, 1273–1298, <https://doi.org/10.1175/MWR-D-15-0105.1>.
- Zhang, Y. J., H. Z. Yu, M. R. Zhang, Y. W. Yang, and Z. Y. Meng, 2022b: Uncertainties and error growth in forecasting the record-breaking rainfall in Zhengzhou, Henan on 19–20 July 2021. *Science China Earth Sciences*, **65**(10), 1903–1920, <https://doi.org/10.1007/s11430-022-9991-4>.
- Zhao, P., and W. S. Duan, 2014: Time-dependent nonlinear forcing singular vector-type tendency error of the Zebiak-Cane model. *Atmos. Oceanic Sci. Lett.*, **7**, 395–399, <https://doi.org/10.3878/j.issn.1674-2834.14.0026>.
- Zhao, Y., B. Wang, and J. J. Liu, 2012: A DRP-4DVar data assimilation scheme for typhoon initialization using sea level pressure data. *Mon. Wea. Rev.*, **140**(4), 1191–1203, <https://doi.org/10.1175/MWR-D-10-05030.1>.
- Zhong, Q. J., J. P. Li, L. F. Zhang, R. Q. Ding, and B. S. Li, 2018a: Predictability of tropical cyclone intensity over the western North Pacific using the IBTrACS dataset. *Mon. Wea. Rev.*, **146**, 2741–2755, <https://doi.org/10.1175/Mwr-D-17-0301.1>.
- Zhong, Q. J., L. F. Zhang, J. P. Li, R. Q. Ding, and J. Feng, 2018b: Estimating the predictability limit of tropical cyclone tracks over the western North Pacific using observational data. *Adv. Atmos. Sci.*, **35**, 1491–1504, <https://doi.org/10.1007/s00376-018-8008-7>.
- Zhong, Q. J., J. P. Li, S. W. Li, Y. Wang, R. Q. Ding, and L. F. Zhang, 2021: Influence of sea surface temperature on the predictability of idealized tropical cyclone intensity. *Journal of Tropical Meteorology*, **27**, 355–367, <https://doi.org/10.46267/j.1006-8775.2021.031>.
- Zhou, F. F., and Z. Toth, 2020: On the prospects for improved tropical cyclone track forecasts. *Bull. Amer. Meteor. Soc.*, **101**, E2058–E2077, <https://doi.org/10.1175/BAMS-D-19-0166.1>.
- Zhou, L., Q. Wang, M. Mu, and K. Zhang, 2021: Optimal precursors triggering sudden shifts in the Antarctic circumpolar current transport through Drake Passage. *J. Geophys. Res.*, **126**, e2021JC017899, <https://doi.org/10.1029/2021JC017899>.
- Zhu, L., and Coauthors, 2016: Prediction and predictability of high-impact western pacific landfalling tropical cyclone vicente(2012)through convection-permitting ensemble assimilation of doppler radar velocity. *Mon. Wea. Rev.*, **144**, 21–43, <https://doi.org/10.1175/MWR-D-14-00403.1>.
- Zhu, S. J., and Coauthors, 2022: A four-dimensional ensemble-variational (4DEnVar) data assimilation system based on GRAPES-GFS: System description and primary tests. *Journal of Advances in Modeling Earth Systems*, **14**(7), e2021MS002737, <https://doi.org/10.1029/2021MS002737>.
- Zu, Z. Q., M. Mu, and H. A. Dijkstra, 2016: Optimal initial excitations of decadal modification of the Atlantic meridional overturning circulation under the prescribed heat and freshwater flux boundary conditions. *J. Phys. Oceanogr.*, **46**(7), 2029–2047, <https://doi.org/10.1175/JPO-D-15-0100.1>.

• Review •

## Seamless Prediction in China: A Review<sup>※</sup>

Hong-Li REN<sup>\*1,2</sup>, Qing BAO<sup>3</sup>, Chenguang ZHOU<sup>4</sup>, Jie WU<sup>5</sup>, Li GAO<sup>6</sup>, Lin WANG<sup>1</sup>, Jieru MA<sup>1</sup>, Yao TANG<sup>3</sup>, Yangke LIU<sup>3</sup>, Yujun WANG<sup>1</sup>, and Zuosen ZHAO<sup>7</sup>

<sup>1</sup>State Key Laboratory of Severe Weather, and Institute of Tibetan Plateau Meteorology,  
Chinese Academy of Meteorological Sciences, Beijing 100081, China

<sup>2</sup>Collaborative Innovation Center on Forecast and Evaluation of Meteorological Disasters (CIC-FEMD),  
Nanjing University of Information Science and Technology, Nanjing 210044, China

<sup>3</sup>State Key Laboratory of Numerical Modeling for Atmospheric Sciences and Geophysical Fluid Dynamics,  
Institute of Atmospheric Physics, Chinese Academy of Sciences, Beijing 100029, China

<sup>4</sup>Department of Atmospheric Science, School of Environmental Studies,  
China University of Geosciences, Wuhan 430074, China

<sup>5</sup>China Meteorological Administration Key Laboratory for Climate Prediction Studies, National Climate Center,  
China Meteorological Administration, Beijing 100081, China

<sup>6</sup>Ensemble Forecasting Division, CMA Earth System Modeling and Prediction Center (CEMC), Beijing 100081, China

<sup>7</sup>School of Atmospheric Sciences, Chengdu University of Information Technology, Chengdu 610225, China

(Received 4 November 2022; revised 27 March 2023; accepted 10 April 2023)

### ABSTRACT

Seamless prediction is a weather–climate integrated prediction covering multiple time scales that include days, weeks, months, seasons, years, and decades. Seamless prediction can provide different industries with information such as weather conditions and climate variations from the next few days to years, which have important impacts on economic and social development and important reference value for short-, medium- and long-term decision-making and planning of the country. Therefore, seamless prediction has received widespread attention from the international scientific community recently. As Chinese scientists have also carried out relevant research, this paper reviews the research in China on developments and applications of seamless prediction methods and prediction systems in recent years. Among them, the main progress of seamless prediction methods studies is reviewed from four aspects: short- and medium-range weather forecasting, subseasonal-to-seasonal, seasonal-to-interannual, and decadal climate prediction. In terms of development and application of seamless prediction systems, the main achievements made by meteorological operational departments, scientific institutes, and universities in China in recent years are reviewed. Finally, some of the issues in seamless prediction that need further study are discussed.

**Key words:** seamless prediction, weather–climate integrated prediction, prediction system

**Citation:** Ren, H.-L., and Coauthors, 2023: Seamless prediction in China: A review. *Adv. Atmos. Sci.*, **40**(8), 1501–1520, <https://doi.org/10.1007/s00376-023-2335-z>.

### Article Highlights:

- Some representative and the latest prediction methods on multiple time scales from weather to climate in China are summarized.
- Separate weather and climate prediction systems and two weather–climate integrated prediction systems have been developed in China.
- Future directions including model improvements, initialization, and prediction methods of seamless prediction in China are discussed.

---

<sup>※</sup> This paper is a contribution to the special issue on the National Report to the 28th IUGG General Assembly by CNC-IAMAS (2019–2022).

\* Corresponding author: Hong-Li REN  
Email: [renhl@cma.gov.cn](mailto:renhl@cma.gov.cn)

## 1. Introduction

There has been a growing desire to obtain weather and climate information on time scales from several days to



weeks, months, seasons, years, and decades. The weather and climate prediction business aims to provide society and government with products of different time scales. It is a challenging project to establish seamless prediction of weather and climate, and is one of the main tasks of modern weather and climate prediction. This is also an important part of “weather forecasting, climate prediction and long-term climate prediction” proposed by the World Climate Research Program (WCRP, 2005). The concept of “seamless prediction” was first presented in 2005 and first used by Palmer et al. (2008), referring to predictions across the range of weather and climate time scales. Since then, seamless prediction has attracted wide attention (Brown et al., 2012; Hoskins, 2013; Kumar and Murtugudde, 2013; Delworth et al., 2020; Ruti et al., 2020). The Working Group on Subseasonal to Interdecadal Prediction (WGSIP) contributes to WCRP studies on predictability and prediction on a wide range of time scales from several weeks to seasons, years, and decades. WGSIP promotes scientific research and an international programme of seamless prediction. Traditionally, weather and climate prediction issues are seen as different disciplines. However, integrated modeling and seamless prediction across multiple time scales stem from a recognition that the evolution of weather and climate are linked by the same physical processes in the atmosphere–ocean–land–cryosphere system operating across multiple spatial and temporal scales (Brown et al., 2012). Establishing a weather–climate integrated prediction system is also an important development direction of seamless prediction (Hurrell et al., 2009; Brown et al., 2012).

Seamless prediction covers short- and medium-range, subseasonal-to-seasonal (S2S), seasonal-to-interannual (S2I), and decadal time scales. With the efforts of Chinese scientists and meteorological operational departments in the past three decades, short- and medium-range weather forecasts and S2I climate prediction in China have developed relatively maturely. A representative achievement in short- and medium-range weather forecasts is the four-dimensional variational (4DVar) assimilation system independently developed by the Numerical Weather Prediction Centre (NWPC) of the China Meteorological Administration (CMA), making it one of the few national forecast centers in the world with independent development and operational application of a 4DVar assimilation system (Shen et al., 2021). In terms of S2I climate prediction, meteorological operational departments, scientific institutes, and some Chinese universities have developed several prediction systems (Bao et al., 2013, 2019; Liu et al., 2015, 2021a; Ren et al., 2017; He et al., 2020a; Song et al., 2021). Based on these systems and some international advanced systems (Saha et al., 2014; Takaya et al., 2018; Johnson et al., 2019), the National Climate Center (NCC) of the CMA developed the China Multi-Model Ensemble prediction system (CMME), which performs well in global and regional climate prediction (Ren et al., 2019b). Extended-range forecasting lies between medium-range weather forecasting and short-term climate prediction, and decadal prediction lies between interannual climate predic-

tion and long-term climate change projection, both of which are essential components of seamless prediction. In recent years, the sources of predictability, initialization schemes, and prediction methods of extended-range and decadal prediction have become the focus of international research. Chinese researchers have also participated extensively and made important contributions. For example, several extended-range forecast methods and decadal prediction initialization schemes have been proposed (Ren et al., 2014a; Hsu et al., 2015; Wu et al., 2018a, 2022). Multiple S2S and decadal prediction systems have been developed and used for operational prediction (Liu et al., 2017; Wu et al., 2018a). These systems participated in the international S2S Prediction Project and Decadal Forecast Exchange, separately. Research on different time scales lays a solid foundation for developing a seamless prediction system.

Since the concept of seamless prediction was proposed, several international research and operational centers have used the seamless approach to develop weather–climate integrated prediction systems that provide forecasts with multiple time scales (Vitart et al., 2008; Brown et al., 2012; Ham et al., 2019a; Delworth et al., 2020). For example, the European Centre for Medium-Range Weather Forecasts (ECMWF) developed a combined medium-range and monthly coupled forecasting system (Vitart et al., 2008), and the UK Met Office developed the Met Office Unified Model for weather and climate prediction (MetUM; Brown et al., 2012). These achievements indicate that seamless prediction has transitioned from concept to practice. In recent years, the CMA and the Institute of Atmospheric Physics of the Chinese Academy of Sciences (CAS-IAP) have independently developed weather–climate integrated prediction systems—namely, the CMA Climate Prediction System version 3 (CMA-CPSv3) and CAS Flexible Global Ocean–Atmosphere–Land System model finite-volume 2 (FGOALS-f2). The development of these systems demonstrates that China has taken a significant step towards developing seamless prediction systems providing forecasts from weather to climate scales.

In the past three decades, Chinese researchers have made many achievements in weather and climate prediction, as well as some significant progress in weather–climate integrated prediction. This paper reviews the main research achievements of prediction methods and systems on different time scales in seamless prediction in China over the past 30 years, including the recent achievements in weather–climate integrated prediction. A summary and discussion of future research directions in seamless prediction are provided in the final section.

## 2. Progress of seamless prediction methods

### 2.1. Progress of short- and medium-range weather forecasts

The short- and medium-range weather forecast is the main component of the traditional weather forecast, which

has the characteristics of a long development time, solid foundation, and high level of maturity (Dai et al., 2016; Xiu, 2019). The uncertainty of the initial value is the primary source of forecast error in numerical weather prediction (NWP). A high-quality initial value of a model is formed by a specific data assimilation scheme based on meteorological observation data and background field information at the initial time. Therefore, data assimilation is a key technology for NWP (Gong, 2013). Advanced data assimilation technology is considered one of the important reasons for improving NWP skills (Bannister, 2017). With multi-year research efforts, CMA-NWPC realized the operational implementation of its 4DVar assimilation system in 2018 (Zhang et al., 2019). Its subsequent application has great significance for global medium-range weather forecasts in China and demonstrates that operational NWP assimilation technology in China has reached the forefront of the international NWP field. The 4DVar assimilation system can significantly increase the types of available observation data, improve the quality of global analyses, and further improve NWP skills (Zhang et al., 2019; Shen et al., 2021). Currently, the observation data of the NWP data assimilation system mostly come from satellite data. However, bias correction of satellite data is one of the critical factors affecting the assimilation effect of satellite data. In terms of satellite data bias correction technology, Zhang et al. (2018) developed a dynamic bias correction scheme suitable for satellite radiance data. This scheme is used in actual business and can effectively solve the drift of observation data caused by the aging of satellite detection instruments, degradation of the bias correction equation coefficients, and seasonal changes.

Precipitation forecasting is the key to short- and medium-range weather forecasts. Improving the accuracy of precipitation forecasts has long been the focus of meteorological business and scientific research. In recent years, NWP has changed from a single-value forecast to an ensemble forecast, and from a deterministic forecast to a probabilistic forecast. Chinese researchers have used different parametric schemes to confirm that ensemble forecasting can improve the skills of precipitation forecasts (Chen et al., 2003; Li et al., 2007). However, due to the existence of initial value error, the approximation of numerical calculation, and the imperfection of the physical processes in the NWP model, there are often certain systematic and random errors in precipitation forecast results. Therefore, it is vital to correct model outputs to obtain more accurate precipitation forecast results. Four methods are usually used for post-processing precipitation forecasts, including quantitative precipitation correction and integration methods, probabilistic forecast processing, statistical downscaling, and stepwise correction based on segmented hierarchical clustering (Bi et al., 2016; Gao et al., 2023). They are also important ways to improve precipitation forecasts in practice. In addition to precipitation elements, other continuous variables such as temperature, wind, and visibility adopt the same correction method: on the basis of the model background field and urban stations' guidance forecasts, the grid-point forecast is gradually approximated to

the stations' guidance forecasts to form the final refined grid forecast products by considering the stepwise interpolation analysis method of refined geographic information correction (Jin et al., 2019).

## 2.2. Progress of S2S prediction

The extended-range forecast is a crucial component of establishing a seamless prediction system. The error source of weather forecasts is mainly the initial value, and the error source of climate prediction is mainly the boundary value. The extended-range forecast lies between the weather forecast and short-term climate prediction, which constitute both an initial value problem and boundary value problem. In 2013, the World Meteorological Organization (WMO) identified the extended-range forecast as one of the most critical tasks and proposed the international S2S Prediction Project, which focuses on the sources of S2S predictability.

The difficulty of S2S prediction is the lack of predictability sources. Many studies have pointed out that the Madden–Julian Oscillation (MJO) plays a critical role in bridging weather and climate, and its activities (propagation, intensity, and phase evolution) have essential effects on weather and climate (Zhang, 2005; Jia et al., 2011; Hsu et al., 2016). Therefore, the MJO has long been considered the most important predictability source for S2S prediction (Brunet et al., 2010; Robertson et al., 2015). However, MJO signals are weaker in boreal summer than in other seasons (Wheeler and Hendon, 2004; Zhang, 2005). Boreal Summer Intraseasonal Oscillation (BSISO) is the most remarkable large-scale convection and circulation mode in the Asian summer monsoon region (Wu et al., 2016). The East Asia–Pacific (EAP) teleconnection pattern is the dominant mode of circulation variability over East Asia in boreal summer (Lin et al., 2018; Wu et al., 2020b). They are important predictability sources of subseasonal variability in boreal summer (Wang et al., 2009; Lee et al., 2013; Hsu et al., 2020a). Sudden stratospheric warming (SSW) is the most intense circulation evolution phenomenon in the stratospheric polar region in boreal winter. Many studies have noted that the downward propagation of the Northern Annular Mode signal during SSW from the stratosphere to the troposphere can increase the predictability of surface weather on subseasonal time scales (Tripathi et al., 2015; Domeisen et al., 2020a, b). In addition, external forcing factors with “memory” characteristics, such as the ocean, soil moisture, and snow, are also predictability sources for S2S prediction (Koster et al., 2011; Jeong et al., 2013; Yuan et al., 2015).

S2S prediction methods mainly include physical statistical models, dynamical models, and dynamical–statistical approaches. Physical statistical models are generally established by the linear or nonlinear relationship between meteorological elements (prediction variables) and large-scale signals (prediction factors). In recent years, Chinese researchers have established several physical statistical models to carry out S2S prediction research; for example, the Low-Frequency Synoptic Map (Li et al., 2018), Extended Complex Autoregressive model (Yang, 2018), and Spatial-Temporal Projec-



tion Model (STPM, Hsu et al., 2015, 2020b). Among them, the STPM method uses the coupling mode of the evolution of prediction factors and variables with time and space to establish a statistical model, which effectively extracts and utilizes the low-frequency components and historical information in the observation data and is widely used in the subseasonal prediction of precipitation (Hsu et al., 2015; Zhu and Li, 2017a), tropical convective activities (Zhu et al., 2015), tropical cyclones (Zhu et al., 2017), winter surface air temperature and extremely cold days (Zhu and Li, 2017b), and summer surface air temperature and heat waves (Zhu and Li, 2018), showing higher forecast skill than traditional statistical models. Pan et al. (2020) confirmed that the STPM method could also be used for S2I prediction, such as ENSO evolution prediction. To date, the STPM method has also been applied to the operational prediction system of the CMA. Hsu et al. (2020b) pointed out that, although the STPM method can provide highly skilled and stable S2S prediction products, its ability to predict the intensity and process of extreme weather needs to be further improved.

In the past decade, dynamic models have become the most powerful tool for S2S prediction. Since 2013, the CMA-NCC has successively developed the Beijing Climate Center Atmospheric General Circulation Model version 2.2 (BCC-AGCM2.2) and the Beijing Climate Center Climate System Model version 1.2 (BCC-CSM1.2), which fills the gap between the medium-range weather forecast and short-term climate prediction. The Beijing Climate Center Sub-seasonal to Seasonal prediction system version 1 (BCC-S2Sv1) was established based on BCC-CSM1.2, which is the first model in China to participate in Phase I of the S2S Prediction Project. The widely used metric to measure the MJO and its prediction is the Real-time Multivariate MJO (RMM) index developed by Wheeler and Hendon (2004). The main characteristics of the MJO, such as intensity, periodicity, spatial structure, and temporal evolution, can be well simulated by BCC-S2Sv1 (Zhao et al., 2015). However, the prediction skill of the MJO (RMM) index is only about 16 days for the submitted dataset (Liu et al., 2017), which is relatively lower than most of the other participants in the S2S Prediction Project (Lim et al., 2018). To improve the prediction skills for the MJO, Chinese researchers have carried out a lot of research work, such as improving the initial conditions of dynamical models and optimizing ensemble prediction strategies. Liu et al. (2017) stated that improving atmospheric and oceanic initial conditions can increase the MJO prediction skill to 21–22 days. Introducing a moderate moisture initialization scheme could also extend the MJO prediction skill by about 2–3 days and enable a more reliable subseasonal prediction of extratropical circulation and precipitation through a more realistic description of MJO-related teleconnections (Wu et al., 2020a). Moreover, by combining the perturbations of multiple parameters that are mainly responsible for cloud and convection parameterization schemes, MJO prediction can be further enhanced during lead times of 2–3 weeks, as well as an improved spectrum, intensity, spatial structure,

and propagation of the MJO (Liu et al., 2019). In terms of optimizing ensemble prediction strategies, several studies have shown that the lagged average forecasting (LAF) scheme (Ren et al., 2017), an ensemble of different initialization schemes (Ren et al., 2016; Wu et al., 2020a), and the multi-model ensemble (MME) of several S2S project models (Wang et al., 2020b), are helpful for improving MJO prediction. As the number of models participating in the S2S Prediction Project increases, the MME will be recognized as an important development direction in S2S prediction. In addition to MJO prediction, the submitted dataset shows that the prediction skills for the EAP teleconnection during May–September and BSISO index are about 10 days and 9 days, respectively (Bo et al., 2020; Wu et al., 2020b). Bo et al. (2020) showed that optimizing atmospheric and oceanic initial conditions can also increase the prediction skill for the BSISO index to 12 days.

Dynamical–statistical prediction methods have been widely used for S2S prediction in recent years. The prediction skills of dynamical models can be further improved by effectively combining dynamical models and empirical/statistical methods. Ren et al. (2014a) proposed the Dynamical-Analogue Ensemble Method to effectively reduce prediction errors and increase prediction skills for the monthly mean and daily atmospheric circulation forecasts. Wu et al. (2018b) established a seasonal rolling MJO dynamical–statistical downscaling precipitation prediction model based on the forecasted MJO information by a dynamical model and achieved higher prediction skills than in the original dynamical model’s forecast. In addition, Wu et al. (2022) recently developed a dynamical–statistical prediction model that improves the prediction skills for the MJO (RMM) and BSISO indices to 22–23 days and 10–13 days, respectively, both of which are largely improved compared with the original dynamical model forecasts (Jie et al., 2017; Liu et al., 2017).

Since 2019, the CMA and CAS-IAP have successively developed the latest generation of climate prediction systems. The third-generation climate prediction system was developed by the CMA (CMA-CPSv3). The S2S prediction sub-system of CMA-CPSv3 (BCC-S2Sv2) has participated in Phase II of the S2S Prediction Project. Compared with BCC-S2Sv1, BCC-S2Sv2 has significantly improved the prediction skill for the MJO (RMM) index, which is about 23 days for the submitted dataset. Version 1.3 of the FGOALS-f2 (FGOALS-f2-V1.3) subseasonal-to-decadal (S2D) prediction system was developed by the State Key Laboratory of Numerical Modeling for Atmospheric Sciences and Geophysical Fluid Dynamics (LASG) at CAS-IAP. The S2S prediction subsystem of the FGOALS-f2-V1.3 S2D system also participated in Phase II of the S2S Prediction Project, which was launched in January 2019. Based on the MJO (RMM) index calculated by ECMWF, the prediction skill for the MJO for the submitted dataset is about 23 days, as determined by the maximum lead time with an anomaly correlation coefficient (ACC) exceeding 0.5. They have reached the advanced inter-

national level for MJO prediction.

### 2.3. Progress of S2I prediction

Primary sources of S2I predictability consist of slowly evolving boundary conditions, such as sea surface temperature (SST), land surface conditions (moisture and snow cover), and sea-ice variations (Zuo et al., 2016; Acosta Navarro et al., 2020). Quasi-Biennial Oscillation (QBO; Marshall and Scaife, 2009; Portal et al., 2022) and stratospheric states (Butler et al., 2016; Nie et al., 2019) are considered the upper boundary conditions to affect S2I prediction. It has been well recognized that El Niño–Southern Oscillation (ENSO) is considered the most important source of S2I predictability, which is the primary mode of interannual variability and affects temperature and precipitation anomalies in various regions through global teleconnection.

S2I prediction methods also mainly include physical statistical models, dynamical models, and dynamical–statistical approaches. In recent years, supported by high-performance computing, big data, and advanced algorithms, machine learning has provided new ideas for S2I prediction. In terms of physical statistical models, Liu and Chan (2003) developed a statistical prediction model based on ENSO-related indices and predicted reasonably the annual number of land-falling tropical cyclones. Ren et al. (2019c) and Wang et al. (2019) developed different statistical prediction models based on the comprehensive use of external precursors and effectively improved the prediction skill of ENSO. Fan et al. (2008) proposed an interannual incremental prediction method, which chooses the year-to-year increment for a quantity as the object that is to be predicted. This unique statistical model is considered an efficient prediction approach and is widely used in S2I prediction of summer rainfall in eastern China, temperature in northeastern China, activity of western North Pacific typhoons, Atlantic hurricanes, and the winter North Atlantic Oscillation (NAO) (Fan et al., 2008; Fan, 2009, 2010; Fan and Wang, 2009; Huang et al., 2014; Tian and Fan, 2015), showing increased prediction skills and application prospects.

With the continuous improvement of physical processes in dynamical models and the rapid development of high-performance computing, some Chinese universities, meteorological operational departments, and scientific institutes have developed several relatively complex dynamical models in recent years, such as a global atmosphere–ocean coupled model (He et al., 2020a), atmosphere–ocean–land–ice coupled climate system models (Li et al., 2013a; Ren et al., 2017; Bao et al., 2019; Wu et al., 2021), and atmosphere–ocean–land–ice–wave coupled climate system models (Bao et al., 2020b; Song et al., 2020). Several studies have demonstrated that these dynamical models have good prediction skills for climate phenomenon, such as precipitation (Wu et al. 2017; He et al., 2020a; Liu et al., 2021c; Wang et al., 2022a), SST (Zhao et al., 2019; Song et al., 2020, 2022; Ying et al., 2022), sea surface height (Wang et al., 2023), and tropical cyclones (Lang and Wang, 2008; Li et al., 2021b), as well as major climate variability modes, such as

ENSO (Luo et al., 2008b; Ren et al., 2017, 2019a; Cheng et al., 2022), the Indian Ocean Dipole (IOD; Luo et al., 2007, 2008a; Ren et al., 2017), and the primary East Asian summer circulation patterns (Ren et al., 2017; Zhou et al., 2020a). However, the existence of model errors in a single dynamical model, which leads to limited prediction ability, means the MME has been found to be an effective approach to improve S2I prediction (Palmer et al., 2000; Wang et al., 2009, 2020a, 2022a). In recent years, several major international research and operational centers, such as the ECMWF, the Asia-Pacific Economic Cooperation Climate Center (APCC), and the National Centers for Environmental Prediction (NCEP), have developed their own MME prediction systems for dynamical seasonal climate prediction. To fill the gap in the field of operational MME prediction in China, the NCC/CMA developed a Chinese operational MME prediction system, the aforementioned CMME, based on a combination of several Chinese operational climate prediction systems and imported prediction data of international advanced climate models (Ren et al., 2019b). The CMME system is presently applied to real-time climate prediction at the NCC/CMA, which provides monthly and seasonal predictions of several climate variability modes, such as ENSO and the IOD, as well as climate anomalies of temperature, precipitation, and so on. On the other hand, many studies have shown that improving the initial conditions of dynamical models can achieve higher prediction skills. Nie et al. (2019) stated that the upper-stratospheric zonal wind anomaly on the initial date plays a significant role in the winter prediction of the NAO and Arctic Oscillation (AO). Ren and Nie (2021) further significantly improved the prediction skill for the winter AO relative to current multi-model dynamical predictions through constructing a linear empirical model based on the previous-summer tropical oceanic temperature and Arctic sea-ice signals. Song et al. (2020) and Yang et al. (2020) developed different data assimilation frameworks to predict SST and Arctic sea ice, respectively, and pointed out that realistic initial conditions can significantly increase the seasonal prediction skill. Liu et al. (2021b) highlighted the role of sea-ice assimilation for global analysis and developed the first atmosphere–ocean–ice coupled data assimilation scheme in China. This scheme is currently applied in CMA-CPSv3 and can generate stable and reliable initial conditions of the atmosphere, ocean, and sea ice, which are used for weather and climate prediction.

Based on dynamical model prediction, empirically correcting model outputs by using historical information can also improve the prediction skills of dynamical models (Ren and Chou, 2005). Chinese researchers have used several dynamical–statistical prediction methods, such as empirical orthogonal function analysis, singular value decomposition, the Pattern Project Method (Kug et al., 2007), and the Stepwise Pattern Project Method (Kug et al., 2008), to improve the S2I prediction skills for precipitation in China and ENSO (Qin et al., 2011; Kang et al., 2012; Su et al., 2013; Shi et al., 2016; Wang et al., 2017, 2020a). In recent years, based on dynamical models and historical data, a dynamical

–statistical prediction method of analogue correction of errors (ACE) was developed and applied (Ren and Chou, 2005, 2006, 2007a, b; Ren et al., 2009; Li et al., 2013b). Ren et al. (2014b) and Liu and Ren (2017) applied the ACE method to predict ENSO and achieved better prediction results. The ACE method is considered to be a pioneering prediction method in recent years (Xiao et al., 2012), and has been recognized by international scholars (Plenković et al., 2018, 2020; Yang et al., 2018). In addition, Chinese researchers have established a variety of dynamical–statistical downscaling models based on the close relationship between prediction variables and factors from the atmosphere, ocean, or sea ice in different seasons, which have effectively improved the S2I prediction skills for regional climate, such as precipitation (Chen et al., 2012; Liu and Fan, 2012, 2013; Liu and Ren, 2015; Liu et al., 2018, 2021c; Wang et al., 2022b), temperature (Dai et al., 2018; Liu et al., 2022a), and tropical cyclones (Sun and Chen, 2011).

Recently, the rapid progress in machine learning has shown strong potential in S2I prediction. For example, Ham et al. (2019b) established a statistical model based on a deep learning approach and reported good prediction skill for ENSO at lead times of up to 1.5 years. Chinese researchers have conducted a lot of research mainly on two aspects: machine learning prediction models, and improving dynamical prediction by using machine learning methods. Due to the low cost of statistical models and the high capability of machine learning in processing data, many researchers have established statistical models based on machine learning methods to predict climate state variables and climate variability modes, such as summer rainfall, winter temperature, drought conditions, SST, and the IOD (Wu et al., 2006; Feng et al., 2020; Zheng et al., 2020; He et al., 2021a; Jiang et al., 2021; Liu et al., 2022b). On the other hand, many researchers have tried to correct the error of dynamical prediction by using machine learning methods. For example, Wang et al. (2021) developed a machine learning and dynamical hybrid seasonal prediction method that significantly improves the dynamical prediction skill for summer rainfall in China. Jin et al. (2022) proposed a hybrid model that combines a convolutional neural network and ridge regression to predict the seasonal precipitation anomaly over China. These studies show that machine learning methods can not only mine nonlinear relationships, but correct the error of dynamical models and achieve higher S2I prediction skills. Machine learning will be a promising method for improving climate prediction. It is worth noting, however, that the lack of training data is a factor that limits the performance of machine learning prediction models (He et al., 2021b). Nevertheless, this does not mean that having enough “big data” can develop a high-performance prediction model. Establishing a machine learning prediction model based on climate dynamics is essential to realize its potential in climate prediction (He et al., 2021b; Yang et al., 2022).

#### 2.4. Progress of decadal prediction

In recent years, decadal climate prediction for the next

year to the next 10–30 years has been a hot topic of research in the international climate science community because of its potential value in dealing with the economic and social problems associated with climate change. The focus of decadal climate prediction is the average climate state for many years in the future, especially the next 2–5 years’ average prediction for the near-term climate. Phase 5 of the Coupled Model Intercomparison Project (CMIP5) listed decadal prediction as one of the core experiments (Taylor et al., 2012), and prediction results were used in the fifth Assessment Report of the Intergovernmental Panel on Climate Change (Kirtman et al., 2013). CMIP6 established the Decadal Climate Prediction Project (Boer et al., 2016) around the problem of decadal climate prediction.

Decadal climate prediction is considered to be a combination of an initial value problem and an external forcing condition problem, and its predictability depends on internal variabilities in the climate system and changes of external forcing (Palmer et al., 2008; Meehl et al., 2009, 2014; Zhou and Wu, 2017). External forcing, including changes in atmospheric compositions associated with human activity or volcanic eruptions, solar variations, and others, can be done by historical simulations or Representative Concentration Pathway projections in dynamical models (Taylor et al., 2012). The prediction of internal variabilities, such as the Pacific Decadal Oscillation (PDO) and Atlantic Multidecadal Oscillation (AMO), depends on the accurate estimation of initial climate states, which is crucial and challenging in decadal climate prediction (Wu et al., 2015; Zhou and Wu, 2017).

Initialization enables the dynamical model to obtain the internal variability signals of the climate systems from observation data. Several studies have shown that initialized decadal prediction has higher prediction skills than uninitialized prediction (Meehl et al., 2009; Xin et al., 2018, 2019). The initialization scheme is key to determining the level of decadal climate prediction skills. In recent years, Chinese researchers have used several assimilation methods, such as nudging (Gao et al., 2012; Wei et al., 2016; Han et al., 2017; Wu et al., 2018c; Xin et al., 2018), Incremental Analysis Updates (IAUs; Wu and Zhou, 2012; Wu et al., 2015), 3DVar (Wang et al., 2013), Dimension-Reduced Projection 4DVar (He et al., 2017, 2020b), Ensemble Optimum Interpolation (EnOI, Wei et al., 2017; Xin et al., 2019), and EnOI-IAU (Wu et al., 2018a; Zhou et al., 2020b), to carry out research on decadal climate prediction. Among them, the EnOI and EnOI-IAU methods are considered to be relatively efficient assimilation methods and have been successfully applied in the decadal climate prediction business.

In previous studies, the initialization of most models just assimilated the temperature and salinity of the oceanic surface and subsurface due to the heat flux and memory of the ocean (Meehl et al., 2021). As noted in Bellucci et al. (2015), the initialization of other components, such as sea ice, the land surface, stratosphere, and aerosols in the climate system, may have a potential impact on decadal climate prediction. However, these components cannot be adequately ini-



tialized due to the lack of reliable data, and their effects on decadal climate prediction have yet to be further explored.

### 3. Development and application of seamless prediction systems

#### 3.1. Prediction systems of the CMA

In the past three decades, the operational departments of the CMA have been committed to developing operational prediction systems for weather and climate prediction to meet the needs of national and social development. In terms of weather forecasting, the CMA has developed multiple numerical forecasting systems for weather forecasting at different time scales and in different regions. In terms of climate prediction, the CMA developed several climate prediction systems based on models with different spatiotemporal resolutions in the early stage, which were used for S2S, S2I, and decadal prediction. In recent years, the CMA has successfully developed a weather–climate integrated prediction system based on a common model, which is an important component of the seamless prediction system. This section reviews the development and application of the CMA models in the past three decades from two aspects: separate NWP and climate prediction systems, and weather–climate integrated prediction systems.

##### 3.1.1. Separate NWP and climate prediction systems

With the support of the “Tenth Five-Year Plan” and a national key scientific and technology project entitled “Innovative Research on China’s Meteorological Numerical Forecasting System”, the CMA has cooperated with many other institutes to develop and establish a multi-scale general data assimilation and NWP system, named the Global/Regional Assimilation Prediction System (GRAPES; Xue and Chen, 2008). Since then, with continued support from the “Eleventh Five-Year Plan” and “Twelfth Five-Year Plan”, scientific and technology project, and the GRAPES-specific project of the CMA, the CMA has made continuous improvements to the GRAPES models (Shen et al., 2020, 2021). In terms of short-range and nowcasting weather forecasts, the CMA established a mesoscale NWP system (GRAPES-Meso; Xu et al., 2017) and further developed a regional typhoon forecasting system (GRAPES-TYM; Qu et al., 2022). These systems play an important role in the daily weather forecast business. In terms of medium-range weather forecasts, the Global Medium-Range Numerical Weather Prediction System (GRAPES-GFS; Zhang and Shen, 2008; Shen et al., 2017) was established, which is the first global weather forecast system with independent development, stable operation, and good forecast results in China. In addition, ensemble prediction is considered an important component of the NWP system. The CMA established a regional mesoscale ensemble prediction system (GRAPES-REPS; Chen and Li, 2020) and a global medium-range ensemble prediction system (GRAPES-GEPS; Chen and Li, 2020; Gao et al., 2020), which both provide probabilistic forecast

products and play an important role in weather probabilistic forecasting. To date, the CMA has gradually established a complete operational NWP system with deterministic and ensemble prediction from the regional to the global scale, and cultivated a research and development team for the entire NWP business chain, including observation data preprocessing, quality control, data assimilation, dynamic model framework and physical processes improvement, model parallel computing, model system integration, and prediction product post-processing (Shen et al., 2021).

In terms of climate prediction system development and application, three generations of climate prediction systems have been established by the CMA for operational use since 1995. The first generation of the CMA Climate Prediction System (CMA-CPSv1) was developed from 1995 to 2004, which consists of two sub-systems with different time scales: monthly dynamical extended-range forecasting and seasonal prediction. Among them, the seasonal prediction sub-system was developed based on the Beijing Climate Center ocean–atmosphere Coupled Model version 1.0 (BCC-CM1.0), which participated in CMIP3. CMA-CPSv1 played an important role in China’s short-term climate prediction business and climate change research after operational application (Ding et al., 2002, 2004; Zhang et al., 2004; Li et al., 2005). The second generation of the CMA Climate Prediction System (CMA-CPSv2) was developed from 2005 to 2015, which added a new S2S prediction sub-system compared with CMA-CPSv1. In 2005, the CMA began to develop an ocean–atmosphere–land–ice coupled climate system model to improve the ability in climate change simulation and short-term climate prediction. With the efforts of decades-long research, several versions of fully coupled climate models were developed, including the Beijing Climate Center Climate Prediction Model version 1.1 (BCC-CSM1.1), BCC-CSM1.1m, and BCC-CSM1.2. BCC-CSM1.1 and BCC-CSM1.1m both participated in CMIP5. However, the horizontal and vertical resolution of BCC-CSM1.2 is the highest (T106L40, approximately 110 km) among them. It was used in the S2S prediction sub-system and participated in Phase I of the S2S Prediction Project. BCC-CSM1.1m, with a medium horizontal resolution and lower vertical resolution (T106L26), was used in the seasonal prediction sub-system and CMME prediction. CMA-CPSv2 has been able to provide real-time monthly, seasonal and interannual climate prediction products since its operational application in 2015, which can meet the public and society’s demands for climate prediction products in the next month to a year. CMA-CPSv2 has a good prediction ability for ENSO, with a lead time of over eight months, as well as for the East Asian, South Asian, Southeast Asian, North Pacific, and Indian summer monsoon indices (Liu et al., 2014, 2015; Ren et al., 2017). Wu et al. (2017) compared the prediction ability of CMA-CPSv2 and CMA-CPSv1 for seasonal temperature, precipitation and circulation, and pointed out that CMA-CPSv2 has higher prediction skills. In terms of decadal climate prediction, BCC-CSM1.1, with a coarse horizontal and vertical

resolution (T42L26, approximately 280 km), participated in the Decadal Prediction Experiment in CMIP5 (Xin et al., 2012). Historical hindcasts showed that BCC-CSM1.1 has reasonable decadal prediction skills for SST in the tropical Atlantic, western Pacific, and Indian oceans (Han et al., 2017), the AO (Wu et al., 2018c), AMO (Wei et al., 2017), and near-surface air temperature in East Asia (Xin et al., 2019). However, the decadal climate prediction system needs to be further developed in future research to meet the requirements of operational use.

### 3.1.2. Weather–climate integrated prediction system

Since 2010, the CMA has been developing the second version of its climate system model (BCC-CSM2). BCC-CSM2-HR is the high-resolution version of BCC-CSM2, with a T266 horizontal resolution (approximately 45 km) in the atmosphere, and participated in the High-Resolution Model Intercomparison Project (HighResMIP) in CMIP6 (Wu et al., 2021). Based on this model, the CMA developed its third-generation climate prediction system (CMA-CPSv3) from 2010 to 2020, which consists of three sub-systems: a high-resolution climate model sub-system, a multi-layer coupling assimilation sub-system, and an ensemble prediction sub-system. Compared with the previous generation, the current high-resolution climate model sub-system of CMA-CPSv3 combines many significant scientific and technical improvements for the model resolutions and physical process parameterizations in the atmosphere, land, ocean, and sea ice. The simulation performance for temperature, precipitation, ENSO, the MJO, and QBO has been significantly improved (Wu et al., 2021). The multi-layer coupling assimilation sub-system of CMA-CPSv3 realizes the coordinated assimilation of multi-source data from the ocean, sea ice, and atmosphere. Based on the combination of EnOI and Local Ensemble Transform Kalman Filter algorithms, an ocean ensemble assimilation method was built to assimilate ocean temperature/salinity profiles, SST, and sea level anomaly (SLA) observation data at a daily frequency. Also, OI-based sea-ice assimilation and atmospheric nudging were implemented to incorporate daily sea-ice concentration observation data and 6-hourly atmospheric multi-variable reanalysis data (Liu et al., 2021b). The ensemble prediction sub-system of CMA-CPSv3 consists of 21 ensemble members, which can draw on the best of others and eliminate the forecast uncertainties caused by observation, analysis errors, and the inherent chaos of the atmospheric system. CMA-CPSv3 is a weather–climate integrated prediction system, which can provide prediction products with several time scales. Regarding its weather forecasts, CMA-CPSv3 operates every day and releases daily temperature and precipitation for the next 7 days and weekly average temperature and precipitation for the next 30 days. In terms of S2S prediction, CMA-CPSv3 operates every day and hindcasts twice every week, which integrates for up to 60 days. In addition, CMA-CPSv3 operates once every month to release S2I prediction products and integrates for up to 7 months. Liang et al. (2022) evaluated the seasonal prediction performance of

CMA-CPSv3 for the Asian summer monsoon and stated that CMA-CPSv3 has higher prediction skills for summer rainfall, summer monsoon indices, the western North Pacific subtropical high, ENSO, and the IOD than CMA-CPSv2. Overall, CMA-CPSv3 has reached an advanced international level for MJO prediction and is significantly superior to previous seasonal prediction systems in predicting climate phenomena and anomalies of precipitation and surface temperature in China on seasonal scales.

### 3.2. Prediction systems of CAS-IAP

In recent years, CAS-IAP has also paid more attention to the operational use of scientific research models. With multi-year research efforts, CAS-IAP has developed a weather–climate integrated prediction system, named the FGOALS-f2 ensemble forecast display platform, which can provide short- and medium-range weather forecasts and S2S, S2I and decadal climate prediction products. In addition, CAS-IAP also developed a decadal climate prediction system in 2018, and its prediction results are published on the “Decadal Forecast Exchange” platform. This section reviews the progress of CAS-IAP in operational prediction in recent years from two aspects: its weather–climate integrated prediction system and decadal prediction system.

#### 3.2.1. Weather–climate integrated prediction system

Jointly funded by the Alliance of International Science Organizations in the Belt and Road Region and a National Natural Science Foundation of China major research project entitled “the Earth–Atmosphere Coupling System on the Qinghai–Tibet Plateau and its Global Climate Effect”, CAS-IAP developed the FGOALS-f2 ensemble forecast display platform based on the FGOALS-f2-V1.3 S2D prediction system (Bao et al., 2019; He et al., 2019; Li et al., 2021b). The prediction model used is FGOALS-f2, which is a climate system model representing the interaction between the atmosphere, oceans, land, and sea ice. The atmospheric component of FGOALS-f2 is FAMIL2, which is characterized by a scale-aware convection scheme (Bao and Li, 2020) and FV3 dynamic core (Zhou et al., 2015). The resolution of the prediction system is approximately 100 km for both atmospheric and ocean grids. The nudging technique is adopted as the initialization method for both the atmospheric and oceanic components (Bao et al., 2019; Li et al., 2021b). The S2S prediction sub-system provides real-time S2S prediction products of temperature, precipitation and circulation to CMME-S2S. Regarding the seasonal climate prediction sub-system, the prediction sub-system uses the LAF method to generate two members on each day, which are integrated for up to 12 months, and the forecast frequency is once per day. The seasonal prediction products have participated in CMME-S2D, which includes monthly and seasonal-average prediction data. Historical hindcasts show that the FGOALS-f2-V1.3 prediction system has reasonable prediction skills for ENSO (~0.83 at a 6-month lead time), the IOD (~0.56 at a 5-month lead time) (the initial time for predicting ENSO and the IOD is 20 July during 1981–2017), and tropical cyclone frequency

( $\sim 0.6$  and  $\sim 0.61$  in the western Pacific and North Atlantic, respectively) (Bao et al., 2019; Li et al., 2021b).

The FGOALS-f2 ensemble forecast display platform covers the S2D timescales from weather to climate. The prediction products include tropical cyclones, the MJO, ENSO, Arctic sea ice, and global potential vorticity, as well as temperature and precipitation from daily to decadal scales. The prediction products cover global and regional areas, such as the Tibetan Plateau, the Arctic, and “the Belt and Road” countries and regions. The platform provides forecasting services for disaster risk reduction in countries and regions along the Belt and Road. Compared with the traditional prediction system, the FGOALS-f2 system not only provides effective prediction services for disaster prevention and mitigation in China, but is actively oriented to major national needs and strategies such as national sustainable development, the Belt and Road, and Arctic resource development.

### 3.2.2. Decadal prediction system

In 2012, CAS-IAP built the initial version of its decadal prediction system based on FGOALS-g1 (Wen et al., 2007) and the IAU initialization scheme (Wu and Zhou, 2012; Wu et al., 2015), which is one of the earliest decadal prediction systems in China. In recent years, based on the IAU initialization scheme, CAS-IAP has developed the EnOI-IAU initialization scheme (Wu et al., 2018a; Zhou et al., 2020b) and established its Decadal Prediction System (IAP-DecPreS; Wu et al., 2018a) based on FGOALS-s2 (Bao et al., 2013). The crucial part of IAP-DecPreS is an initialization scheme for the oceanic component of a coupled general circulation model. EnOI-IAU can initialize the coupled model via assimilating raw observational oceanic temperature profiles, which is of great help in improving the timeliness of prediction. IAP-DecPreS is currently the only system in China to share prediction results with the Decadal Forecast Exchange platform, which is organized by the Met Office with the participation of multiple countries. Historical hindcasts show that IAP-DecPreS has good prediction skills for SST anomalies related to the PDO and AMO (Wu et al., 2018a; Zhou et al., 2020b).

Recently, the decadal prediction sub-system of the FGOALS-f2-V1.3 S2D system was developed and run at LASG, CAS-IAP. The decadal hindcast experiments with eight ensemble members were conducted starting every year over the period 1981–2015. The model was integrated from 1976 with an initial condition taken from the 40-year Global Reanalysis (Li et al., 2021a) datasets, which assimilated the air temperature at each pressure layer, the zonal and meridional winds, specific humidity, and surface pressure, and SST was assimilated as well. The external boundary conditions were consistent with the CMIP6 historical simulations. Given the need to serve the forecasting demands during China’s rainy season, every decadal experiment was initialized from 20 March and integrated for 129 months. The hindcast dataset not only provides the climate state of the model, but supports real-time forecasts based on relevant skill evaluation. In 2022, the decadal prediction sub-system carried out

real-time forecasts for the next 10 years, and the forecast results were adopted by the NCC to serve the operational work of the disaster risk reduction of the near-term climate prediction. The model outputs contain multiple and sufficient monthly mean atmospheric and oceanic variables.

### 3.3. Prediction systems of other institutes in China

In recent years, several Chinese universities and scientific institutes have also developed their own climate prediction systems, such as the First Institute of Oceanography–Climate Prediction System (FIO-CPS; Song et al., 2021), the Chinese Academy of Meteorological Sciences Climate System Model (CAMS-CSM, Rong et al., 2018; Liu et al., 2021a) climate prediction system, and the Climate Forecast System of Nanjing University of Information Science and Technology (NUIST-CFS; He et al., 2020a; Ying et al., 2022). These prediction systems participated in CMME-S2D and CMME-ENSO, as well as a national climate trend prediction conference for summer and winter–spring.

Two versions of climate prediction systems have been established by the First Institute of Oceanography (FIO) for operational use. The first version (FIO-CPS v1.0) was developed based on the First Institute of Oceanography–Earth System Model version 1.0 (FIO-ESM v1.0, Qiao et al., 2013), which is an Earth System model characterized by a coupled wave model. FIO-ESM v1.0 participated in CMIP5 and showed good simulation performance for the basic patterns and variability of the atmosphere and ocean, including ENSO (Qiao et al., 2013, Song et al., 2014). FIO-CPS v1.0 uses the ensemble adjustment Kalman filter initialization method to assimilate the daily SST and SLA and uses the three-dimensional ocean temperature perturbation method to generate 10 members, which are integrated for up to 6 months (Chen et al., 2016). The hindcast results of FIO-CPS v1.0 show that it has high SST prediction skill over the North Pacific for two seasons in advance, which transfers fairly well to precipitation prediction (Zhao et al., 2019; Song et al., 2020). The new version (FIO-CPS v2.0) was developed based on the First Institute of Oceanography–Earth System Model version 2.0 (FIO-ESM v2.0; Bao et al., 2020b), which participated in CMIP6. There are some significant scientific and technical improvements in the physical process parameterizations and model resolutions of every component in FIO-ESM v2.0. This latest version can simulate the climatological states of the atmosphere and ocean fairly well. The patterns of temperature, precipitation, and SST are greatly improved compared to those of FIO-ESM v1.0 (Bao et al., 2020b). FIO-CPS v2.0 adopts the nudging initialization method to assimilate the upper-ocean temperature in the mixed layer. Similar to FIO-CPS v1.0, FIO-CPS v2.0 uses the three-dimensional ocean temperature perturbation method mentioned above to generate 10 members, but their prediction time extends to 13 months (Song et al., 2021). Compared with FIO-CPS v1.0, FIO-CPS v2.0 has higher prediction skill for SST anomalies, especially over the equatorial Pacific (Song et al., 2022). The ACC score for ENSO is around 0.78 at a 6-month lead time in FIO-CPS v2.0 (Song



et al., 2021).

CAMS-CSM was developed by the Chinese Academy of Meteorological Sciences (CAMS), which is an ocean–atmosphere–land–ice fully coupled climate system model (Rong et al., 2018). CAMS-CSM participated in CMIP6 (Rong et al., 2019, 2021) and showed good simulation performance for climatological mean states and seasonal cycles including temperature, precipitation, SST, and sea ice (Rong et al., 2018, 2021; Wei et al., 2018). The major climate variability modes are also reasonably captured by CAMS-CSM, such as the MJO, BSISO, ENSO, AO, PDO, East Asian summer monsoon, and Northern and Southern Hemisphere annular modes (Rong et al., 2018, 2021; Wei et al., 2018; Hua et al., 2019; Lu and Ren, 2019; Nan et al., 2019; Qi et al., 2019; Ren et al., 2019d). The climate prediction system based on CAMS-CSM adopts a nudging initialization scheme to assimilate reanalysis data of the atmosphere and ocean, which include the 55-year Japanese Reanalysis Project reanalysis data (Kobayashi et al., 2015) and NCEP Global Ocean Data Assimilation System reanalysis data (Behringer and Xue, 2004). The prediction system uses the LAF method to generate eight members, which are integrated for up to six months. Liu et al. (2021a) evaluated the seasonal prediction skills of the CAMS-CSM climate prediction system and stated that the system has good prediction skills for ENSO, IOD, temperature, and precipitation anomalies. The ACC score for ENSO is around 0.75 at a 6-month lead time, and for the IOD it is around 0.51 at a 2-month lead time.

NUIST-CFS1.0 was developed based on the SINTEX-F model, which is an ocean–atmosphere fully coupled climate model (Luo et al., 2005a). It has been confirmed that the SINTEX-F model has good simulation and prediction performance for both ENSO and the IOD (Luo et al., 2005b, 2007, 2008a, b). NUIST-CFS1.0 adopts a nudging initialization scheme to assimilate the observed weekly average OISST (Optimum Interpolation Sea Surface Temperature) values to generate realistic and atmosphere–ocean well-balanced initial conditions. NUIST-CFS1.0 is separately perturbed by three different coupled physics schemes and initialization schemes to constitute an ensemble of nine members (He et al., 2020a; Asfaw and Luo, 2022). They are integrated for up to 24 months and their forecast frequency is once per month (on the first day of each month). The hindcast results of NUIST-CFS1.0 show that it has high prediction skills for tropical SST anomalies. In particular, ENSO is skillfully predicted up to 1.5–2 years in advance, and the IOD can be predicted one to two seasons in advance (He et al., 2020a; Ying et al., 2022). In addition, NUIST-CFS1.0 has reasonable prediction performance for the climatological mean states of summer temperature and precipitation in China (He et al., 2020a).

#### 4. Summary and future prospects

Over the past three decades, Chinese researchers have conducted a lot of research on weather and climate predic-

tion. Figure 1 summarizes the main progress of seamless prediction methods and systems in China in the past 30 years and shows potential development directions in future research. Among them, there are many landmark or unique methods and systems for weather forecasting or climate prediction. For example, the operational application of the 4DVar assimilation system demonstrates that the operational NWP assimilation technology in China has reached the forefront of the international NWP field. GRAPES-GFS is the first global weather forecast system with independent development, stable operation, and good forecast results in China. CMME filled the gap in the field of operational MME prediction in China. The ACE method has been recognized and had a profound impact on the subsequent analogue-based prediction method. BCC-S2Sv1 was the first model in China to participate in the S2S Prediction Project, and IAP-DecPreS is currently the only model in China to share prediction results with the Decadal Forecast Exchange platform. Since the concept of seamless prediction was proposed in 2005, Chinese meteorological operational departments and scientific institutes have developed two weather–climate integrated prediction systems—namely, CMA-CPSv3 (developed by the CMA) and FGOALS-f2-V1.3 (developed by CAS-IAP). The operational implementation of these two systems signifies that China has taken a significant step towards seamless prediction.

However, as our understanding of seamless prediction has deepened, more new issues and challenges have gradually been exposed. There are still some systematic biases in prediction models (Zhang et al., 2020b; Wu et al., 2021). The improvement of prediction models depends heavily on our understanding of physical processes and mechanisms and how they work in the climate system. Therefore, more reasonable physics-based parameterization schemes need to be developed and improved in future work. Traditional NWP primarily uses a high-resolution atmospheric model and does not consider the coupling with the ocean and sea ice. In contrast, traditional climate prediction uses an atmosphere–ocean–land–ice coupled climate model, but the resolution is lower than that of NWP models. Improving the resolution of the prediction model will be of great significance to the application of a seamless prediction system. The resolutions of CMA-CPSv3 and FGOALS-f2-V1.3 are 45 km and 100 km, respectively, which cannot meet the requirements of a refined weather forecast. The next-generation high-resolution Earth System model of the CMA is currently being developed. CAS FGOALS-f3-H (Bao et al., 2020a) participated in CMIP6 HighResMIP, and the resolution reached C384 (approximately 25 km), which provided a solid model basis for the future development of high-resolution refined seamless prediction.

Traditionally, separated data assimilation schemes are applied to the uncoupled models, and their products are used to initialize the corresponding components in the coupled model (Saha et al., 2006; MacLachlan et al., 2015; Takaya et al., 2018). There are also some models that used

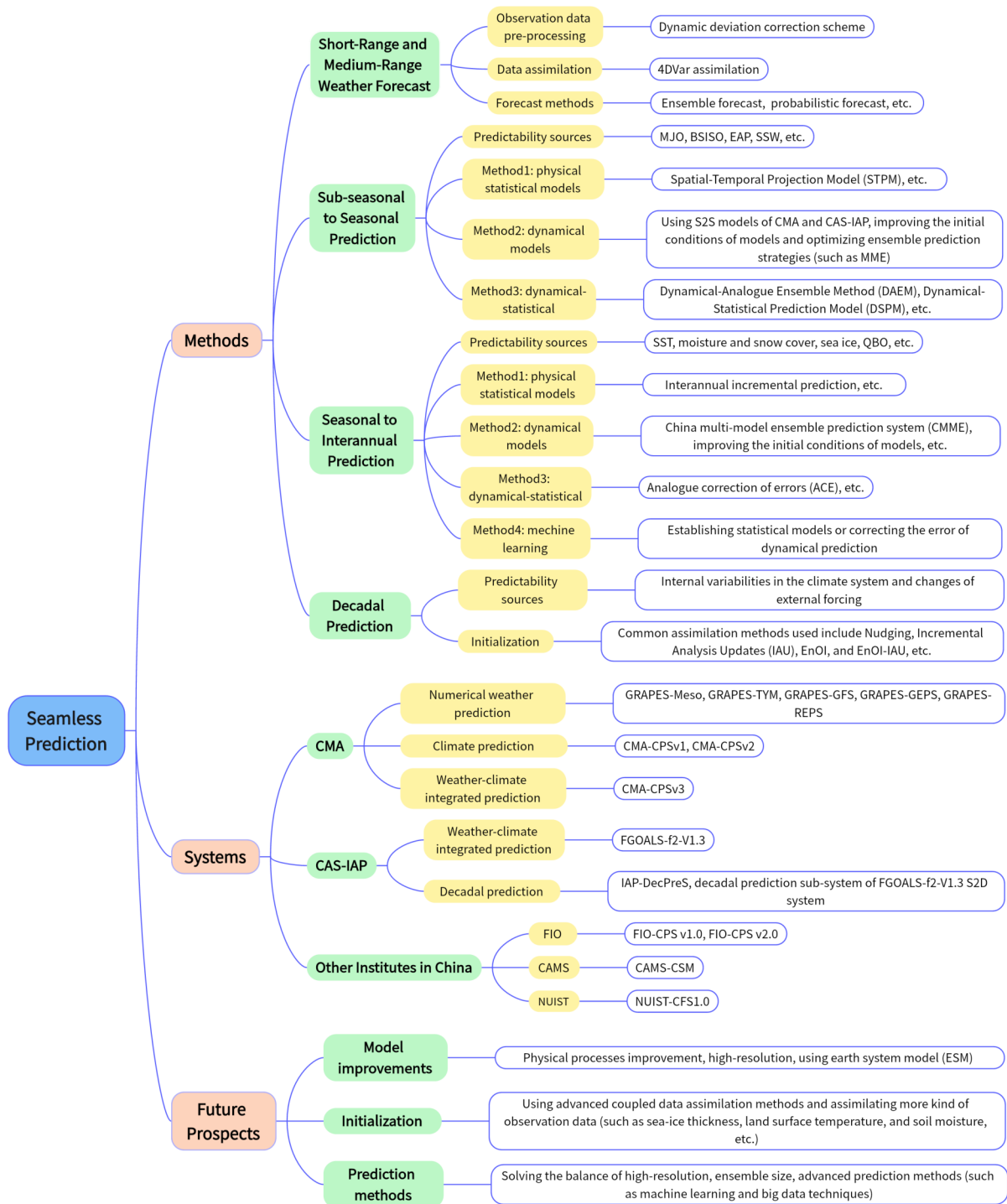


**Fig. 1.** Schematic of the main progress in seamless prediction methods and systems in China in the past 30 years, as well as development directions in future research.

reanalysis products from external sources to initialize individual model components (Liu et al., 2015; Xin et al., 2018). In recent years, coupled data assimilation schemes were developed to reduce the possible inconsistency caused by uncoupled data assimilation. The coupled data assimilation sub-system of CMA-CPSv3 assimilates multisource observations of ocean, sea ice, and atmosphere. Some other important observation data, such as sea-ice thickness, land surface tem-

perature, and soil moisture, need to be considered in future studies (Liu et al., 2021b).

Ensemble size is an important aspect that determines prediction skills and reliability. In general, the more ensemble members, the higher the prediction skill. The consequences of computing costs need to be considered when using more ensemble members (Meehl et al., 2021). Machine learning and big data techniques provide new possi-

bilities to complement and improve seamless prediction systems (Ruti et al., 2020). The prediction skills of seamless prediction systems will largely depend on the balance between a high resolution, large ensemble size, advanced prediction methods, and advanced data assimilation schemes.

The original use of the term “seamless” (Palmer et al., 2008) referred to predictions across the range of weather and climate time scales. Since then, the definition has evolved toward the idea of predicting “the spatiotemporal continuum of the interactions among weather, climate, and the Earth system” (Brunet et al., 2010). That means that the development of seamless prediction will extend from the physical climate system towards a comprehensive view of the Earth system by including interactions with the biogeophysical components (Hazeleger et al., 2012). The “Science Summit on Seamless Research for Weather, Climate, Water, and Environment” was organized by the WMO in 2017 and emphasized the importance of seamless earth system prediction (Ruti et al., 2020). In recent years, the CMA and CAS-IAP have successively developed earth system models—namely, BCC-ESM1 (Wu et al., 2020c) and CAS-ESM (Zhang et al., 2020a)—which both participated in CMIP6. However, there is still much research to be done in the transition from “weather and climate” to “weather, climate and Earth system” for seamless prediction, both in theory and practice. For example, considering land use and anthropogenic effects in seamless earth system prediction will effectively improve the prediction ability of extreme weather events (Ruti et al., 2020), which is one of the focuses of S2S prediction in recent years. In summary, Chinese researchers should persist with their efforts to develop and improve seamless prediction.

**Acknowledgements.** This work was jointly supported by the National Natural Science Foundation of China (Grant Nos. U2242206, 42175015, and 41975094) and the Basic Research and Operational Special Project of CAMS (Grant No. 2021Z007).

## REFERENCES

- Acosta Navarro, J. C., and Coauthors, 2020: Link between autumnal Arctic sea ice and northern hemisphere winter forecast skill. *Geophys. Res. Lett.*, **47**, e2019GL086753, <https://doi.org/10.1029/2019GL086753>.
- Asfaw, T. G., and J.-J. Luo, 2022: Seasonal prediction of summer precipitation over East Africa using NUIST-CFS1.0. *Adv. Atmos. Sci.*, **39**, 355–372, <https://doi.org/10.1007/s00376-021-1180-1>.
- Bannister, R. N., 2017: A review of operational methods of variational and ensemble-variational data assimilation. *Quart. J. Roy. Meteor. Soc.*, **143**, 607–633, <https://doi.org/10.1002/qj.2982>.
- Bao, Q., and J. Li, 2020: Progress in climate modeling of precipitation over the Tibetan Plateau. *National Science Review*, **7**, 486–487, <https://doi.org/10.1093/nsr/nwaa006>.
- Bao, Q., X. F. Wu, J. X. Li, L. Wang, B. He, X. C. Wang, Y. M. Liu, and G. X. Wu, 2019: Outlook for El Niño and the Indian Ocean dipole in autumn-winter 2018–2019. *Chinese Science Bulletin*, **64**, 73–78, <https://doi.org/10.1360/N972018-00913>. (in Chinese with English abstract)
- Bao, Q., and Coauthors, 2013: The flexible global ocean-atmosphere-land system model, spectral version 2: FGOALS-s2. *Adv. Atmos. Sci.*, **30**, 561–576, <https://doi.org/10.1007/s00376-012-2113-9>.
- Bao, Q., and Coauthors, 2020a: CAS FGOALS-f3-H and CAS FGOALS-f3-L outputs for the high-resolution model intercomparison project simulation of CMIP6. *Atmospheric and Oceanic Science Letters*, **13**, 576–581, <https://doi.org/10.1080/16742834.2020.1814675>.
- Bao, Y., Z. Y. Song, and F. L. Qiao, 2020b: FIO-ESM version 2.0: Model description and evaluation. *J. Geophys. Res.: Oceans*, **125**, e2019JC016036, <https://doi.org/10.1029/2019JC016036>.
- Behringer, D. W., and Y. Xue, 2004: Evaluation of the global ocean data assimilation system at NCEP: The Pacific Ocean. Preprints, Eighth Symposium on Integrated Observing and Assimilation Systems for Atmosphere, Oceans, and Land Surface, AMS 84th Annual Meeting, Seattle, Washington, Washington State Convention and Trade Center, 11–15.
- Bellucci, A., and Coauthors, 2015: Advancements in decadal climate predictability: The role of nonoceanic drivers. *Rev. Geophys.*, **53**, 165–202, <https://doi.org/10.1002/2014RG000473>.
- Bi, B. G., K. Dai, Y. Wang, J. L. Fu, Y. Cao, and C. H. Liu, 2016: Advances in techniques of quantitative precipitation forecast. *Journal of Applied Meteorological Science*, **27**, 534–549, <https://doi.org/10.11898/1001-7313.20160503>. (in Chinese with English abstract)
- Bo, Z. K., X. W. Liu, W. Z. Gu, A. N. Huang, Y. J. Fang, T. W. Wu, W. H. Jie, and Q. P. Li, 2020: Impacts of atmospheric and oceanic initial conditions on boreal summer intraseasonal oscillation forecast in the BCC model. *Theor. Appl. Climatol.*, **142**, 393–406, <https://doi.org/10.1007/s00704-020-03312-2>.
- Boer, G. J., and Coauthors, 2016: The Decadal Climate Prediction Project (DCPP) contribution to CMIP6. *Geoscientific Model Development*, **9**, 3751–3777, <https://doi.org/10.5194/gmd-9-3751-2016>.
- Brown, A., S. Milton, M. Cullen, B. Golding, J. Mitchell, and A. Shelly, 2012: Unified modeling and prediction of weather and climate: A 25-year journey. *Bull. Amer. Meteor. Soc.*, **93**, 1865–1877, <https://doi.org/10.1175/BAMS-D-12-00018.1>.
- Brunet, G., and Coauthors, 2010: Collaboration of the weather and climate communities to advance subseasonal-to-seasonal prediction. *Bull. Amer. Meteor. Soc.*, **91**, 1397–1406, <https://doi.org/10.1175/2010BAMS3013.1>.
- Butler, A. H., and Coauthors, 2016: The Climate-system Historical Forecast Project: Do stratosphere-resolving models make better seasonal climate predictions in boreal winter? *Quart. J. Roy. Meteor. Soc.*, **142**, 1413–1427, <https://doi.org/10.1002/qj.2743>.
- Chen, H., X. Q. Yin, Y. Bao, and F. L. Qiao, 2016: Ocean satellite data assimilation experiments in FIO-ESM using ensemble adjustment Kalman filter. *Science China Earth Sciences*, **59**, 484–494, <https://doi.org/10.1007/s11430-015-5187-2>.
- Chen, H. P., J. Q. Sun, and H. J. Wang, 2012: A statistical downscaling model for forecasting summer rainfall in China from DEMETER Hindcast datasets. *Wea. Forecasting*, **27**,

- 608–628, <https://doi.org/10.1175/WAF-D-11-00079.1>.
- Chen, J., and X. L. Li, 2020: The review of 10 years development of the GRAPES global/regional ensemble prediction. *Advances in Meteorological Science and Technology*, **10**, 9–18, 29, <https://doi.org/10.3969/j.issn.2095-1973.2020.02.003>. (in Chinese with English abstract)
- Chen, J., J. S. Xue, and H. Yan, 2003: The uncertainty of mesoscale numerical prediction of South China heavy rain and the ensemble simulations. *Acta Meteorologica Sinica*, **61**, 432–446, <https://doi.org/10.11676/qxxb2003.042>. (in Chinese with English abstract)
- Cheng, Y. J., and Coauthors, 2022: Investigating the ENSO prediction skills of the Beijing Climate Center climate prediction system version 2. *Acta Oceanologica Sinica*, **41**, 99–109, <https://doi.org/10.1007/s13131-021-1951-7>.
- Dai, H. X., K. Fan, and B. Q. Tian, 2018: A hybrid downscaling model for winter temperature over northeast China. *International Journal of Climatology*, **38**, e349–e363, <https://doi.org/10.1002/joc.5376>.
- Dai, K., Y. Cao, Q. F. Qian, S. Gao, S. R. Zhao, Y. Chen, and C. H. Qian, 2016: Situation and tendency of operational technologies in short- and medium-range weather forecast. *Meteorological Monthly*, **42**, 1445–1455, <https://doi.org/10.7519/j.issn.1000-0526.2016.12.002>. (in Chinese with English abstract)
- Delworth, T. L., and Coauthors, 2020: SPEAR: The next generation GFDL modeling system for seasonal to multidecadal prediction and projection. *Journal of Advances in Modeling Earth Systems*, **12**, e2019MS001895, <https://doi.org/10.1029/2019MS001895>.
- Ding, Y. H., Y. M. Liu, Y. J. Song, and Q. Q. Li, 2002: Research and experiments of the dynamical model system for short-term climate prediction. *Climate and Environmental Research*, **7**, 236–246, <https://doi.org/10.3878/j.issn.1006-9585.2002.02.11>. (in Chinese with English abstract)
- Ding, Y. H., and Coauthors, 2004: Advance in seasonal dynamical prediction operation in China. *Acta Meteorologica Sinica*, **62**, 598–612, <https://doi.org/10.11676/qxxb2004.059>. (in Chinese with English abstract)
- Domeisen, D. I. V., and Coauthors, 2020a: The role of the stratosphere in subseasonal to seasonal prediction: 1. Predictability of the stratosphere. *J. Geophys. Res.: Atmos.*, **125**, e2019JD030920, <https://doi.org/10.1029/2019JD030920>.
- Domeisen, D. I. V., and Coauthors, 2020b: The role of the stratosphere in subseasonal to seasonal prediction: 2. Predictability arising from stratosphere-troposphere coupling. *J. Geophys. Res.: Atmos.*, **125**, e2019JD030923, <https://doi.org/10.1029/2019JD030923>.
- Fan, K., 2009: Predicting winter surface air temperature in northeast China. *Atmospheric and Oceanic Science Letters*, **2**, 14–17, <https://doi.org/10.1080/16742834.2009.11446770>.
- Fan, K., 2010: A prediction model for Atlantic named storm frequency using a year-by-year increment approach. *Wea. Forecasting*, **25**, 1842–1851, <https://doi.org/10.1175/2010WAF222406.1>.
- Fan, K., and H. J. Wang, 2009: A new approach to forecasting typhoon frequency over the western North Pacific. *Wea. Forecasting*, **24**, 974–986, <https://doi.org/10.1175/2009WAF222194.1>.
- Fan, K., H. J. Wang, and Y. J. Choi, 2008: A physically-based statistical forecast model for the middle-lower reaches of the Yangtze River valley summer rainfall. *Chinese Science Bulletin*, **53**, 602–609, <https://doi.org/10.1007/s11434-008-0083-1>.
- Feng, P. Y., and Coauthors, 2020: Using large-scale climate drivers to forecast meteorological drought condition in growing season across the Australian wheatbelt. *Science of the Total Environment*, **724**, 138162, <https://doi.org/10.1016/j.scitotenv.2020.138162>.
- Gao, F., X. G. Xin, and T. W. Wu, 2012: A study of the prediction of regional and global temperature on decadal time scale with BCC\_CSM1.1 model. *Chinese Journal of Atmospheric Sciences*, **36**, 1165–1179, <https://doi.org/10.3878/j.issn.1006-9895.2012.11243>. (in Chinese with English abstract)
- Gao, L., P. F. Ren, F. Zhou, J. W. Zheng, and H. L. Ren, 2020: Evaluations and ensemble approaches of Western-Pacific subtropical high and South-Asian high ensemble forecasting in GRAPES-GEPS. *Advances in Earth Science*, **35**, 715–730, <https://doi.org/10.11867/j.issn.1001-8166.2020.060>. (in Chinese with English abstract)
- Gao, L., Z. S. Zhao, J. Qin, Q. L. Chen, and H. K. Cai, 2023: Stepwise correction of ECMWF ensemble forecasts of severe rainfall in China based on segmented hierarchical clustering. *Frontiers in Earth Science*, **10**, 1079225, <https://doi.org/10.3389/feart.2022.1079225>.
- Gong, J. D., 2013: Data assimilation: A key technology for NWP—technical review of data assimilation in ECMWF. *Advances in Meteorological Science and Technology*, **3**, 6–13, <https://doi.org/10.3969/j.issn.2095-1973.2013.03.001>. (in Chinese with English abstract)
- Ham, S., A.-Y. Lim, S. Kang, H. Jeong, and Y. Jeong, 2019a: A newly developed APCC ScoPS and its prediction of East Asia seasonal climate variability. *Climate Dyn.*, **52**, 6391–6410, <https://doi.org/10.1007/s00382-018-4516-5>.
- Ham, Y.-G., J. H. Kim, and J.-J. Luo, 2019b: Deep learning for multi-year ENSO forecasts. *Nature*, **573**, 568–572, <https://doi.org/10.1038/s41586-019-1559-7>.
- Han, Z. Y., B. Wu, and X. G. Xin, 2017: Decadal prediction skill of the global sea surface temperature in the BCC\_CSM1.1 climate model. *Advances in Earth Science*, **32**, 396–408, <https://doi.org/10.11867/j.issn.1001-8166.2017.04.0396>. (in Chinese with English abstract)
- Hazeleger, W., and Coauthors, 2012: EC-Earth V2.2: Description and validation of a new seamless earth system prediction model. *Climate Dyn.*, **39**, 2611–2629, <https://doi.org/10.1007/s00382-011-1228-5>.
- He, B., and Coauthors, 2019: CAS FGOALS-f3-L model datasets for CMIP6 historical atmospheric model intercomparison project simulation. *Adv. Atmos. Sci.*, **36**, 771–778, <https://doi.org/10.1007/s00376-019-9027-8>.
- He, C. T., J. F. Wei, Y. Y. Song, and J.-J. Luo, 2021a: Seasonal prediction of summer precipitation in the middle and lower reaches of the Yangtze River valley: Comparison of machine learning and climate model predictions. *Water*, **13**, 3294, <https://doi.org/10.3390/w13223294>.
- He, J. Y., J. Y. Wu, and J.-J. Luo, 2020a: Introduction to climate forecast system version 1.0 of Nanjing University of Information Science and Technology. *Trans. Atmos. Sci.*, **43**, 128–143, <https://doi.org/10.13878/j.cnki.dqkxb.20191110007>. (in Chinese with English abstract)
- He, S. P., H. J. Wang, H. Li, and J. Z. Zhao, 2021b: Machine learn-



- ing and its potential application to climate prediction. *Transactions of Atmospheric Sciences*, **44**, 26–38, <https://doi.org/10.13878/j.cnki.dqkxxb.20201125001>. (in Chinese with English abstract)
- He, Y. J., and Coauthors, 2017: Reduction of initial shock in decadal predictions using a new initialization strategy. *Geophys. Res. Lett.*, **44**, 8538–8547, <https://doi.org/10.1002/2017GL074028>.
- He, Y. J., and Coauthors, 2020b: A new DRP-4DVar-based coupled data assimilation system for decadal predictions using a fast online localization technique. *Climate Dyn.*, **54**, 3541–3559, <https://doi.org/10.1007/s00382-020-05190-w>.
- Hoskins, B., 2013: The potential for skill across the range of the seamless weather-climate prediction problem: A stimulus for our science. *Quart. J. Roy. Meteor. Soc.*, **139**, 573–584, <https://doi.org/10.1002/qj.1991>.
- Hsu, P.-C., J. Y. Lee, and K. J. Ha, 2016: Influence of boreal summer intraseasonal oscillation on rainfall extremes in Southern China. *International Journal of Climatology*, **36**, 1403–1412, <https://doi.org/10.1002/joc.4433>.
- Hsu, P.-C., Y. X. Zang, Z. W. Zhu, and T. Li, 2020b: Subseasonal-to-seasonal (S2S) prediction using the spatial-temporal projection model (STPM). *Transactions of Atmospheric Sciences*, **43**, 212–224, <https://doi.org/10.13878/j.cnki.dqkxxb.20191028002>. (in Chinese with English abstract)
- Hsu, P.-C., T. M. Li, L. J. You, J. Y. Gao, and H.-L. Ren, 2015: A spatial-temporal projection model for 10–30 day rainfall forecast in South China. *Climate Dyn.*, **44**, 1227–1244, <https://doi.org/10.1007/s00382-014-2215-4>.
- Hsu, P.-C., Y. T. Qian, Y. Liu, H. Murakami, and Y. X. Gao, 2020a: Role of abnormally enhanced MJO over the Western Pacific in the formation and subseasonal predictability of the record-breaking Northeast Asian heatwave in the summer of 2018. *J. Climate*, **33**, 3333–3349, <https://doi.org/10.1175/JCLI-D-19-0337.1>.
- Hua, L. J., L. Chen, X. Y. Rong, J. Li, G. Zhang, and L. Wang, 2019: An assessment of ENSO stability in CAMS climate system model simulations. *J. Meteor. Res.*, **33**, 80–88, <https://doi.org/10.1007/s13351-018-8092-8>.
- Huang, Y. Y., H. J. Wang, and K. Fan, 2014: Improving the prediction of the summer Asian-Pacific oscillation using the interannual increment approach. *J. Climate*, **27**, 8126–8134, <https://doi.org/10.1175/JCLI-D-14-00209.1>.
- Hurrell, J., G. A. Meehl, D. Bader, T. L. Delworth, B. Kirtman, and B. Wielicki, 2009: A unified modeling approach to climate system prediction. *Bull. Amer. Meteor. Soc.*, **90**, 1819–1832, <https://doi.org/10.1175/2009BAMS2752.1>.
- Jeong, J.-H., H. W. Linderholm, S.-H. Woo, C. Folland, B.-M. Kim, S.-J. Kim, and D. L. Chen, 2013: Impacts of snow initialization on subseasonal forecasts of surface air temperature for the cold season. *J. Climate*, **26**, 1956–1972, <https://doi.org/10.1175/JCLI-D-12-00159.1>.
- Jia, X. L., L. J. Chen, F. M. Ren, and C. Y. Li, 2011: Impacts of the MJO on winter rainfall and circulation in China. *Adv. Atmos. Sci.*, **28**, 521–533, <https://doi.org/10.1007/s00376-010-9118-z>.
- Jiang, W., Y. Y. Liu, P. Chen, and Z. W. Zhang, 2021: Prediction of summer precipitation in Jiangsu province based on precursor factors: A deep neural network approach. *Acta Meteorologica Sinica*, **79**, 1035–1048, <https://doi.org/10.11676/qxxb2021.057>. (in Chinese with English abstract)
- Jie, W. H., F. Vitart, T. W. Wu, and X. W. Liu, 2017: Simulations of the Asian summer monsoon in the sub-seasonal to seasonal prediction project (S2S) database. *Quart. J. Roy. Meteor. Soc.*, **143**, 2282–2295, <https://doi.org/10.1002/qj.3085>.
- Jin, R. H., and Coauthors, 2019: Progress and challenge of seamless fine gridded weather forecasting technology in China. *Meteorological Monthly*, **45**, 445–457, <https://doi.org/10.7519/j.issn.1000-0526.2019.04.001>. (in Chinese with English abstract)
- Jin, W. X., Y. Luo, T. W. Wu, X. M. Huang, W. Xue, and C. Q. Yu, 2022: Deep learning for seasonal precipitation prediction over China. *J. Meteor. Res.*, **36**, 271–281, <https://doi.org/10.1007/s13351-022-1174-7>.
- Johnson, S. J., and Coauthors, 2019: SEAS5: The new ECMWF seasonal forecast system. *Geoscientific Model Development*, **12**, 1087–1117, <https://doi.org/10.5194/gmd-12-1087-2019>.
- Kang, H. W., C. W. Zhu, Z. Y. Zuo, and R. H. Zhang, 2012: Statistical downscaling of pattern projection using multi-model output variables as predictors. *Acta Meteorologica Sinica*, **70**, 192–201, <https://doi.org/10.11676/qxxb2012.019>. (in Chinese with English abstract)
- Kirtman, B., and Coauthors, 2013: Near-term climate change: Projections and predictability. *Climate Change 2013: The Physical Science Basis. Contribution of Working Group I to the Fifth Assessment Report of the Intergovernmental Panel on Climate Change*, T. F. Stocker et al., Eds., Cambridge University Press, Cambridge, United Kingdom and New York, NY, USA, 953–1028.
- Kobayashi, S., and Coauthors, 2015: The JRA-55 reanalysis: General specifications and basic characteristics. *J. Meteor. Soc. Japan*, **93**, 5–48, <https://doi.org/10.2151/jmsj.2015-001>.
- Koster, R. D., and Coauthors, 2011: The second phase of the global land-atmosphere coupling experiment: Soil moisture contributions to subseasonal forecast skill. *Journal of Hydrometeorology*, **12**, 805–822, <https://doi.org/10.1175/2011JHM1365.1>.
- Kug, J. S., J. Y. Lee, and I. S. Kang, 2007: Global sea surface temperature prediction using a multimodel ensemble. *Mon. Wea. Rev.*, **135**, 3239–3247, <https://doi.org/10.1175/MWR3458.1>.
- Kug, J. S., J. Y. Lee, and I. S. Kang, 2008: Systematic error correction of dynamical seasonal prediction of sea surface temperature using a stepwise pattern project method. *Mon. Wea. Rev.*, **136**, 3501–3512, <https://doi.org/10.1175/2008MWR2272.1>.
- Kumar, A., and R. Murtugudde, 2013: Predictability, uncertainty and decision making: A unified perspective to build a bridge from weather to climate. *Current Opinion in Environmental Sustainability*, **5**, 327–333, <https://doi.org/10.1016/j.cosust.2013.05.009>.
- Lang, X. M., and H. J. Wang, 2008: Can the climate background of western North Pacific typhoon activity be predicted by climate model? *Chinese Science Bulletin*, **53**, 2392–2399, <https://doi.org/10.1007/s11434-008-0266-9>.
- Lee, J. Y., B. Wang, M. C. Wheeler, X. H. Fu, D. E. Waliser, and I.-S. Kang, 2013: Real-time multivariate indices for the boreal summer intraseasonal oscillation over the Asian summer monsoon region. *Climate Dyn.*, **40**, 493–509, <https://doi.org/10.1007/s00382-012-1544-4>.
- Li, C. X., T. B. Zhao, C. X. Shi, and Z. Q. Liu, 2021a: Assessment

- of precipitation from the CRA40 dataset and new generation reanalysis datasets in the global domain. *International Journal of Climatology*, **41**, 5243–5263, <https://doi.org/10.1002/joc.7127>.
- Li, J., Y. S. Liao, B. Zhang, and T. Y. Shen, 2007: The preliminary application of ensemble prediction in flash flood forecasting. *Plateau Meteorology*, **26**, 854–861. (in Chinese with English abstract)
- Li, J. X., and Coauthors, 2021b: Dynamical seasonal prediction of tropical cyclone activity using the FGOALS-f2 ensemble prediction system. *Wea. Forecasting*, **36**, 1759–1778, <https://doi.org/10.1175/WAF-D-20-0189.1>.
- Li, L. J., and Coauthors, 2013a: The flexible global ocean-atmosphere-land system model, Grid-point Version 2: FGOALS-g2. *Adv. Atmos. Sci.*, **30**, 543–560, <https://doi.org/10.1007/s00376-012-2140-6>.
- Li, W. J., Z. H. Zheng, and C. H. Sun, 2013b: Improvements to dynamical analogue climate prediction method in China. *Chinese Journal of Atmospheric Sciences*, **37**, 341–350, <https://doi.org/10.3878/j.issn.1006-9895.2012.12311>. (in Chinese with English abstract)
- Li, W. J., and Coauthors, 2005: Research and operational application of dynamical climate model prediction system. *Journal of Applied Meteorological Science*, **16**, 1–11, <https://doi.org/10.3969/j.issn.1001-7313.2005.z1.001>. (in Chinese with English abstract)
- Li, Z. Y., Z. X. Sun, J. Y. Zhang, and Z. P. Wu, 2018: Application of low-frequency synoptic map in forecasting heavy rainfall in Guizhou province. *Meteorological Science and Technology*, **46**, 999–1003, <https://doi.org/10.19517/j.1671-6345.20170561>. (in Chinese with English abstract)
- Liang, X. Y., Q. P. Li, and T. W. Wu, 2022: Dynamical seasonal prediction of the Asian summer monsoon in the China meteorological administration climate prediction system version 3. *Frontiers in Earth Science*, **10**, 934248, <https://doi.org/10.3389/feart.2022.934248>.
- Lim, Y., S.-W. Son, and D. Kim, 2018: MJO prediction skill of the subseasonal-to-seasonal prediction models. *J. Climate*, **31**, 4075–4094, <https://doi.org/10.1175/JCLI-D-17-0545.1>.
- Lin, X. Z., C. F. Li, R. Y. Lu, and A. A. Scaife, 2018: Predictable and unpredictable components of the summer East Asia–Pacific teleconnection pattern. *Adv. Atmos. Sci.*, **35**, 1372–1380, <https://doi.org/10.1007/s00376-018-7305-5>.
- Liu, B., and Coauthors, 2021a: Seasonal prediction skills in the CAMS-CSM climate forecast system. *Climate Dyn.*, **57**, 2953–2970, <https://doi.org/10.1007/s00382-021-05848-z>.
- Liu, J., L. J. Chen, and Y. Liu, 2022a: A statistical downscaling prediction model for winter temperature over Xinjiang based on the CFSv2 and sea ice forcing. *International Journal of Climatology*, **42**, 8552–8567, <https://doi.org/10.1002/joc.7747>.
- Liu, J., Y. M. Tang, X. S. Song, and Z. L. Sun, 2022b: Prediction of the Indian Ocean dipole using deep learning method. *Chinese Journal of Atmospheric Sciences*, **46**, 590–598, <https://doi.org/10.3878/j.issn.1006-9895.2105.21048>. (in Chinese with English abstract)
- Liu, K. S., and J. C. L. Chan, 2003: Climatological characteristics and seasonal forecasting of tropical cyclones making landfall along the South China coast. *Mon. Wea. Rev.*, **131**, 1650–1662, <https://doi.org/10.1175/2554.1>.
- Liu, X., and Coauthors, 2021b: Development of coupled data assimilation with the BCC climate system model: Highlighting the role of sea-ice assimilation for global analysis. *Journal of Advances in Modeling Earth Systems*, **13**, e2020MS002368, <https://doi.org/10.1029/2020MS002368>.
- Liu, X. W., and Coauthors, 2014: Relationships between interannual and intraseasonal variations of the Asian–Western Pacific summer monsoon hindcasted by BCC\_CSM1.1(m). *Adv. Atmos. Sci.*, **31**, 1051–1064, <https://doi.org/10.1007/s00376-014-3192-6>.
- Liu, X. W., and Coauthors, 2015: Performance of the seasonal forecasting of the Asian summer monsoon by BCC\_CSM1.1(m). *Adv. Atmos. Sci.*, **32**, 1156–1172, <https://doi.org/10.1007/s00376-015-4194-8>.
- Liu, X. W., and Coauthors, 2017: MJO prediction using the sub-seasonal to seasonal forecast model of Beijing Climate Center. *Climate Dyn.*, **48**, 3283–3307, <https://doi.org/10.1007/s00382-016-3264-7>.
- Liu, X. W., and Coauthors, 2019: Validity of parameter optimization in improving MJO simulation and prediction using the sub-seasonal to seasonal forecast model of Beijing Climate Center. *Climate Dyn.*, **52**, 3823–3843, <https://doi.org/10.1007/s00382-018-4369-y>.
- Liu, Y., and K. Fan, 2012: Prediction of spring precipitation in China using a downscaling approach. *Meteorol. Atmos. Phys.*, **118**, 79–93, <https://doi.org/10.1007/s00703-012-0202-z>.
- Liu, Y., and K. Fan, 2013: A new statistical downscaling model for autumn precipitation in China. *International Journal of Climatology*, **33**, 1321–1336, <https://doi.org/10.1002/joc.3514>.
- Liu, Y., and H.-L. Ren, 2015: A hybrid statistical downscaling model for prediction of winter precipitation in China. *International Journal of Climatology*, **35**, 1309–1321, <https://doi.org/10.1002/joc.4058>.
- Liu, Y., and H.-L. Ren, 2017: Improving ENSO prediction in CFSv2 with an analogue-based correction method. *International Journal of Climatology*, **37**, 5035–5046, <https://doi.org/10.1002/joc.5142>.
- Liu, Y., H.-L. Ren, A. A. Scaife, and C. F. Li, 2018: Evaluation and statistical downscaling of East Asian summer monsoon forecasting in BCC and MOHC seasonal prediction systems. *Quart. J. Roy. Meteor. Soc.*, **144**, 2798–2811, <https://doi.org/10.1002/qj.3405>.
- Liu, Y., H.-L. Ren, N. P. Klingaman, J. P. Liu, and P. Q. Zhang, 2021c: Improving long-lead seasonal forecasts of precipitation over Southern China based on statistical downscaling using BCC\_CSM1.1m. *Dyn. Atmos. Oceans*, **94**, 101222, <https://doi.org/10.1016/j.dynatmoce.2021.101222>.
- Lu, B., and H.-L. Ren, 2019: ENSO features, dynamics, and teleconnections to East Asian climate as simulated in CAMS-CSM. *J. Meteor. Res.*, **33**, 46–65, <https://doi.org/10.1007/s13351-019-8101-6>.
- Luo, J.-J., S. Masson, E. Roeckner, G. Madec, and T. Yamagata, 2005a: Reducing climatology bias in an ocean–atmosphere CGCM with improved coupling physics. *J. Climate*, **18**, 2344–2360, <https://doi.org/10.1175/JCLI3404.1>.
- Luo, J.-J., S. Masson, S. Behera, S. Shingu, and T. Yamagata, 2005b: Seasonal climate predictability in a coupled OAGCM using a different approach for ensemble forecasts. *J. Climate*, **18**, 4474–4497, <https://doi.org/10.1175/>



JCLI3526.1.

- Luo, J.-J., S. Masson, S. Behera, and T. Yamagata, 2007: Experimental forecasts of the Indian Ocean dipole using a coupled OAGCM. *J. Climate*, **20**, 2178–2190, <https://doi.org/10.1175/JCLI4132.1>.
- Luo, J.-J., S. Masson, S. K. Behera, and T. Yamagata, 2008b: Extended ENSO predictions using a fully coupled ocean–atmosphere model. *J. Climate*, **21**, 84–93, <https://doi.org/10.1175/2007JCLI1412.1>.
- Luo, J.-J., S. Behera, Y. Masumoto, H. Sakuma, and T. Yamagata, 2008a: Successful prediction of the consecutive IOD in 2006 and 2007. *Geophys. Res. Lett.*, **35**, L14S02, <https://doi.org/10.1029/2007GL032793>.
- MacLachlan, C., and Coauthors, 2015: Global Seasonal forecast system version 5 (GloSea5): A high-resolution seasonal forecast system. *Quart. J. Roy. Meteor. Soc.*, **141**, 1072–1084, <https://doi.org/10.1002/qj.2396>.
- Marshall, A. G., and A. A. Scaife, 2009: Impact of the QBO on surface winter climate. *J. Geophys. Res.: Atmos.*, **114**, D18110, <https://doi.org/10.1029/2009JD011737>.
- Meehl, G. A., and Coauthors, 2009: Decadal prediction: Can it be skillful? *Bull. Amer. Meteor. Soc.*, **90**, 1467–1485, <https://doi.org/10.1175/2009BAMS2778.1>.
- Meehl, G. A., and Coauthors, 2014: Decadal climate prediction: An update from the trenches. *Bull. Amer. Meteor. Soc.*, **95**, 243–267, <https://doi.org/10.1175/BAMS-D-12-00241.1>.
- Meehl, G. A., and Coauthors, 2021: Initialized Earth System prediction from subseasonal to decadal timescales. *Nature Reviews Earth & Environment*, **2**, 340–357, <https://doi.org/10.1038/s43017-021-00155-x>.
- Nan, S. L., J. L. Yang, Y. Bao, J. Li, and X. Y. Rong, 2019: Simulation of the Northern and Southern Hemisphere annular modes by CAMS-CSM. *J. Meteor. Res.*, **33**, 934–948, <https://doi.org/10.1007/s13351-019-8099-9>.
- Nie, Y., A. A. Scaife, H.-L. Ren, R. E. Comer, M. B. Andrews, P. Davis, and N. Martin, 2019: Stratospheric initial conditions provide seasonal predictability of the North Atlantic and Arctic Oscillations. *Environmental Research Letters*, **14**, 034006, <https://doi.org/10.1088/1748-9326/ab0385>.
- Palmer, T. N., Č. Branković, and D. S. Richardson, 2000: A probability and decision-model analysis of PROVOST seasonal multi-model ensemble integrations. *Quart. J. Roy. Meteor. Soc.*, **126**, 2013–2033, <https://doi.org/10.1002/qj.49712656703>.
- Palmer, T. N., F. J. Doblas-Reyes, A. Weisheimer, and M. J. Rodwell, 2008: Toward seamless prediction: Calibration of climate change projections using seasonal forecasts. *Bull. Amer. Meteor. Soc.*, **89**, 459–470, <https://doi.org/10.1175/BAMS-89-4-459>.
- Pan, X., Z. W. Zhu, and T. M. Li, 2020: Forecasts of ENSO evolution using spatial-temporal projection model. *International Journal of Climatology*, **40**, 6301–6314, <https://doi.org/10.1002/joc.6581>.
- Plenković, I. O., L. D. Monache, K. Horvath, and M. Hraštinski, 2018: Deterministic wind speed predictions with analogue-based methods over complex topography. *J. Appl. Meteorol. Climatol.*, **57**, 2047–2070, <https://doi.org/10.1175/JAMC-D-17-0151.1>.
- Plenković, I. O., I. Schicker, M. Dabernig, K. Horvath, and E. Keresturi, 2020: Analog-based post-processing of the ALADIN-LAEF ensemble predictions in complex terrain. *Quart. J. Roy. Meteor. Soc.*, **146**, 1842–1860, <https://doi.org/10.1002/qj.3769>.
- Portal, A., P. Ruggieri, F. M. Palmeiro, J. García-Serrano, D. I. V. Domeisen, and S. Gualdi, 2022: Seasonal prediction of the boreal winter stratosphere. *Climate Dyn.*, **58**, 2109–2130, <https://doi.org/10.1007/s00382-021-05787-9>.
- Qi, Y. J., R. H. Zhang, X. Y. Rong, J. Li, and L. Li, 2019: Boreal summer intraseasonal oscillation in the Asian–Pacific monsoon region simulated in CAMS-CSM. *J. Meteor. Res.*, **33**, 66–79, <https://doi.org/10.1007/s13351-019-8080-7>.
- Qiao, F. L., Z. Y. Song, Y. Bao, Y. J. Song, Q. Shu, C. J. Huang, and W. Zhao, 2013: Development and evaluation of an earth system model with surface gravity waves. *J. Geophys. Res.: Oceans*, **118**, 4514–4524, <https://doi.org/10.1002/jgrc.20327>.
- Qin, Z. K., Z. H. Lin, H. Chen, and Z. B. Sun, 2011: The bias correction methods based on the EOF/SVD for short-term climate prediction and their applications. *Acta Meteorologica Sinica*, **69**, 289–296, <https://doi.org/10.11676/qxxb2011.024>. (in Chinese with English abstract)
- Qu, A. X., S. H. Ma, and J. Zheng, 2022: Development and preliminary test of CMA-TYM hybrid En3DVar scheme. *Meteorological Monthly*, **48**, 299–310, <https://doi.org/10.7519/j.issn.1000-0526.2021.091801>. (in Chinese with English abstract)
- Robertson, A. W., A. Kumar, M. Peña, and F. Vitart, 2015: Improving and promoting subseasonal to seasonal prediction. *Bull. Amer. Meteor. Soc.*, **96**, ES49–ES53, <https://doi.org/10.1175/BAMS-D-14-00139.1>.
- Ren, H.-L., and J. F. Chou, 2005: Analogue correction method of errors by combining both statistical and dynamical methods together. *Acta Meteorologica Sinica*, **63**, 988–993, <https://doi.org/10.3321/j.issn:0577-6619.2005.06.015>. (in Chinese with English abstract)
- Ren, H.-L., and J. F. Chou, 2006: Introducing the updating of multi-reference states into dynamical analogue prediction. *Acta Meteorologica Sinica*, **64**, 315–324, <https://doi.org/10.3321/j.issn:0577-6619.2006.03.006>. (in Chinese with English abstract)
- Ren, H.-L., and J. F. Chou, 2007a: Study progress in prediction strategy and methodology on numerical model. *Advances in Earth Science*, **22**, 376–385, <https://doi.org/10.3321/j.issn:1001-8166.2007.04.007>. (in Chinese with English abstract)
- Ren, H.-L., and J. F. Chou, 2007b: Study on strategy and method of dynamic similarity prediction. *Science in China Series D: Earth Sciences*, **37**, 1101–1109, <https://doi.org/10.3969/j.issn.1674-7240.2007.08.014>. (in Chinese)
- Ren, H.-L., and Y. Nie, 2021: Skillful prediction of winter Arctic Oscillation from previous summer in a linear empirical model. *Science China Earth Sciences*, **64**, 27–36, <https://doi.org/10.1007/s11430-020-9665-3>.
- Ren, H.-L., J. Q. Zuo, and Y. Deng, 2019c: Statistical predictability of Niño indices for two types of ENSO. *Climate Dyn.*, **52**, 5361–5382, <https://doi.org/10.1007/s00382-018-4453-3>.
- Ren, H.-L., J. F. Chou, J. P. Huang, and P. Q. Zhang, 2009: Theoretical basis and application of an analogue-dynamical model in the Lorenz system. *Adv. Atmos. Sci.*, **26**, 67–77, <https://doi.org/10.1007/s00376-009-0067-3>.
- Ren, H.-L., P. Q. Zhang, W. J. Li, and L. J. Chen, 2014a: The dynamical-analogue ensemble method for improving opera-

- tional monthly forecasting. *Acta Meteorologica Sinica*, **72**, 723–730, <https://doi.org/10.11676/qxxb2014.055>. (in Chinese with English abstract)
- Ren, H.-L., Y. Liu, F.-F. Jin, Y.-P. Yan, and X. W. Liu, 2014b: Application of the analogue-based correction of errors method in ENSO prediction. *Atmospheric and Oceanic Science Letters*, **7**, 157–161, <https://doi.org/10.3878/j.issn.1674-2834.13.0080>.
- Ren, H.-L., J. Wu, C. B. Zhao, Y. J. Cheng, and X. W. Liu, 2016: MJO ensemble prediction in BCC-CSM1.1(m) using different initialization schemes. *Atmospheric and Oceanic Science Letters*, **9**, 60–65, <https://doi.org/10.1080/16742834.2015.1116217>.
- Ren, H.-L., and Coauthors, 2017: Prediction of primary climate variability modes at the Beijing Climate Center. *J. Meteor. Res.*, **31**, 204–223, <https://doi.org/10.1007/s13351-017-6097-3>.
- Ren, H.-L., and Coauthors, 2019a: Seasonal predictability of winter ENSO types in operational dynamical model predictions. *Climate Dyn.*, **52**, 3869–3890, <https://doi.org/10.1007/s00382-018-4366-1>.
- Ren, H.-L., and Coauthors, 2019b: The China multi-model ensemble prediction system and its application to flood-season prediction in 2018. *J. Meteor. Res.*, **33**, 540–552, <https://doi.org/10.1007/s13351-019-8154-6>.
- Ren, P. F., L. Gao, H.-L. Ren, X. Y. Rong, and J. Li, 2019d: Representation of the Madden–Julian oscillation in CAMS-CSM. *J. Meteor. Res.*, **33**, 627–650, <https://doi.org/10.1007/s13351-019-8118-x>.
- Rong, X. Y., J. Li, H. M. Chen, Y. F. Xin, J. Z. Su, L. J. Hua, and Z. Q. Zhang, 2019: Introduction of CAMS-CSM model and its participation in CMIP6. *Climate Change Research*, **15**, 540–544, <https://doi.org/10.12006/j.issn.1673-1719.2019.186>. (in Chinese with English abstract)
- Rong, X. Y., J. Li, H. M. Chen, J. Z. Su, L. J. Hua, Z. Q. Zhang, and Y. F. Xin, 2021: The CMIP6 historical simulation datasets produced by the climate system model CAMS-CSM. *Adv. Atmos. Sci.*, **38**, 285–295, <https://doi.org/10.1007/s00376-020-0171-y>.
- Rong, X. Y., and Coauthors, 2018: The CAMS climate system model and a basic evaluation of its climatology and climate variability simulation. *J. Meteor. Res.*, **32**, 839–861, <https://doi.org/10.1007/s13351-018-8058-x>.
- Ruti, P. M., and Coauthors, 2020: Advancing research for seamless earth system prediction. *Bull. Amer. Meteor. Soc.*, **101**, E23–E35, <https://doi.org/10.1175/BAMS-D-17-0302.1>.
- Saha, S., and Coauthors, 2006: The NCEP climate forecast system. *J. Climate*, **19**, 3483–3517, <https://doi.org/10.1175/jcli3812.1>.
- Saha, S., and Coauthors, 2014: The NCEP climate forecast system version 2. *J. Climate*, **27**, 2185–2208, <https://doi.org/10.1175/JCLI-D-12-00823.1>.
- Shen, X. S., J. J. Wang, Z. C. Li, D. H. Chen, and J. D. Gong, 2020: China's independent and innovative development of numerical weather prediction. *Acta Meteorologica Sinica*, **78**, 451–476, <https://doi.org/10.11676/qxxb2020.030>. (in Chinese with English abstract)
- Shen, X. S., Q. Y. Chen, J. Sun, W. Han, J. D. Gong, Z. C. Li, and J. J. Wang, 2021: Development of operational global medium-range forecast system in National Meteorological Centre. *Meteorological Monthly*, **47**, 645–654, <https://doi.org/10.7519/j.issn.1000-0526.2021.06.001>. (in Chinese with English abstract)
- Shen, X. S., and Coauthors, 2017: Development and operation transformation of GRAPES global middle-range forecast system. *Journal of Applied Meteorological Science*, **28**, 1–10, <https://doi.org/10.11898/1001-7313.20170101>. (in Chinese with English abstract)
- Shi, H. B., J. Chang, and J. P. Liang, 2016: Application of pattern projection downscaling method in the prediction of summer precipitation in Yellow River Basin. *Meteor. Mon.*, **42**, 1364–1371, <https://doi.org/10.7519/j.issn.1000-0526.2016.11.008>. (in Chinese with English abstract)
- Song, Y. J., Y. D. Zhao, X. Q. Yin, Y. Bao, and F. L. Qiao, 2020: Evaluation of FIO-ESM v1.0 seasonal prediction skills over the North Pacific. *Frontiers in Marine Science*, **7**, 504, <https://doi.org/10.3389/fmars.2020.00504>.
- Song, Y. J., Q. Shu, Y. Bao, X. D. Yang, and Z. Y. Song, 2021: The short-term climate prediction system FIO-CPS v2.0 and its prediction skill in ENSO. *Frontiers in Earth Science*, **9**, 759339, <https://doi.org/10.3389/feart.2021.759339>.
- Song, Y. J., Z. Y. Song, M. Wei, Q. Shu, Y. Bao, and F. L. Qiao, 2022: The ENSO prediction in 2021 winter based on the FIO-CPS v2.0. *Advances in Marine Science*, **40**, 165–174, <https://doi.org/10.12362/j.issn.1671-6647.of2021001>. (in Chinese with English abstract)
- Song, Z. Y., H. L. Liu, C. Z. Wang, L. P. Zhang, and F. L. Qiao, 2014: Evaluation of the eastern equatorial Pacific SST seasonal cycle in CMIP5 models. *Ocean Science*, **10**, 837–843, <https://doi.org/10.5194/os-10-837-2014>.
- Su, H. J., Q. G. Wang, J. Yang, and Z. H. Qian, 2013: Error correction on summer model precipitation of China based on the singular value decomposition. *Acta Physica Sinica*, **62**, 109202, <https://doi.org/10.7498/aps.62.109202>. (in Chinese with English abstract)
- Sun, J. Q., and H. P. Chen, 2011: Predictability of western North Pacific typhoon activity and its factors using DEMETER coupled models. *Chinese Science Bulletin*, **56**, 3474–3479, <https://doi.org/10.1007/s11434-011-4640-7>.
- Takaya, Y., and Coauthors, 2018: Japan Meteorological Agency/Meteorological Research Institute-Coupled Prediction System version 2 (JMA/MRI-CPS2): Atmosphere–land–ocean–sea ice coupled prediction system for operational seasonal forecasting. *Climate Dyn.*, **50**, 751–765, <https://doi.org/10.1007/s00382-017-3638-5>.
- Taylor, K. E., R. J. Stouffer, and G. A. Meehl, 2012: An overview of CMIP5 and the experiment design. *Bull. Amer. Meteor. Soc.*, **93**, 485–498, <https://doi.org/10.1175/BAMS-D-11-00094.1>.
- Tian, B. Q., and K. Fan, 2015: A skillful prediction model for winter NAO based on Atlantic Sea surface temperature and Eurasian snow cover. *Wea. Forecasting*, **30**, 197–205, <https://doi.org/10.1175/WAF-D-14-00100.1>.
- Tripathi, O. P., and Coauthors, 2015: The predictability of the extratropical stratosphere on monthly time-scales and its impact on the skill of tropospheric forecasts. *Quart. J. Roy. Meteor. Soc.*, **141**, 987–1003, <https://doi.org/10.1002/qj.2432>.
- Vitart, F., and Coauthors, 2008: The new VarEPS–monthly forecasting system: A first step towards seamless prediction. *Quart. J. Roy. Meteor. Soc.*, **134**, 1789–1799, <https://doi.org/10.1002/qj.2432>.

- 10.1002/qj.322.
- Wang, B., and Coauthors, 2009: Advance and prospectus of seasonal prediction: Assessment of the APCC/CLIPAS 14-model ensemble retrospective seasonal prediction (1980–2004). *Climate Dyn.*, **33**, 93–117, <https://doi.org/10.1007/s00382-008-0460-0>.
- Wang, B., and Coauthors, 2013: Preliminary evaluations of FGOALS-g2 for decadal predictions. *Adv. Atmos. Sci.*, **30**, 674–683, <https://doi.org/10.1007/s00376-012-2084-x>.
- Wang, G. J., H.-L. Ren, J. P. Liu, and X. Y. Long, 2023: Seasonal predictions of sea surface height in BCC-CSM1.1m and their modulation by tropical climate dominant modes. *Atmospheric Research*, **281**, 106466, <https://doi.org/10.1016/j.atmosres.2022.106466>.
- Wang, J. L., J. Yang, H.-L. Ren, J. X. Li, Q. Bao, and M. N. Gao, 2021: Dynamical and machine learning hybrid seasonal prediction of summer rainfall in China. *J. Meteor. Res.*, **35**, 583–593, <https://doi.org/10.1007/s13351-021-0185-0>.
- Wang, L., H.-L. Ren, J. S. Zhu, and B. H. Huang, 2020a: Improving prediction of two ENSO types using a multi-model ensemble based on stepwise pattern projection model. *Climate Dyn.*, **54**, 3229–3243, <https://doi.org/10.1007/s00382-020-05160-2>.
- Wang, L., H.-L. Ren, Q. L. Chen, B. Tian, and Y. Liu, 2017: Statistical correction of ENSO prediction in BCC\_CSM1.1m based on stepwise pattern projection method. *Meteor. Mon.*, **43**, 294–304, <https://doi.org/10.7519/j.issn.1000-0526.2017.03.005>. (in Chinese with English abstract)
- Wang, L., H.-L. Ren, X. D. Xu, B. H. Huang, J. Wu, and J. P. Liu, 2022a: Seasonal-interannual predictions of summer precipitation over the Tibetan Plateau in North American multimodel ensemble. *Geophys. Res. Lett.*, **49**, e2022GL100294, <https://doi.org/10.1029/2022GL100294>.
- Wang, N., H.-L. Ren, Y. Liu, Y. Deng, X. X. Meng, J. Wu, and F. Zhou, 2022b: Multi-predictor ensembles improving seasonal prediction of summer rainfall over the Bohai Sea Rim based on statistical downscaling of BCC\_CSM1.1 m. *Atmospheric Research*, **275**, 106221, <https://doi.org/10.1016/j.atmosres.2022.106221>.
- Wang, Q. Y., and Coauthors, 2019: Tropical cyclones act to intensify El Niño. *Nature Communications*, **10**, 3793, <https://doi.org/10.1038/s41467-019-11720-w>.
- Wang, Y., H.-L. Ren, F. Zhou, J.-X. Fu, Q. L. Chen, J. Wu, W. H. Jie, and P. Q. Zhang, 2020b: Multi-model ensemble sub-seasonal forecasting of precipitation over the maritime continent in boreal summer. *Atmosphere*, **11**, 515, <https://doi.org/10.3390/atmos11050515>.
- WCRP, 2005: Strategic framework 2005–2015: Coordinated observation and prediction of the Earth system. WCRP-123 and WMO/TD-No. 1291. Available online at: [https://www.wcrp-climate.org/documents/WCRP\\_stratgImple\\_LowRes.pdf](https://www.wcrp-climate.org/documents/WCRP_stratgImple_LowRes.pdf).
- Wei, L. X., X. G. Xin, B. Y. Cheng, T. W. Wu, Q. Guo, and Y. H. Li, 2016: Hindcast of China climate with decadal experiment by BCC-CSM1.1 climate model. *Climate Change Research*, **12**, 294–302, <https://doi.org/10.12006/j.issn.1673-1719.2015.196>. (in Chinese with English abstract)
- Wei, M., Q. Q. Li, X. G. Xin, W. Zhou, Z. Y. Han, Y. Luo, and Z. C. Zhao, 2017: Improved decadal climate prediction in the North Atlantic using EnOI-assimilated initial condition. *Science Bulletin*, **62**, 1142–1147, <https://doi.org/10.1016/j.scib.2017.08.012>.
- Wei, T., J. Li, X. Y. Rong, W. J. Dong, B. Y. Wu, and M. H. Ding, 2018: Arctic climate changes based on historical simulations (1900–2013) with the CAMS-CSM. *J. Meteor. Res.*, **32**, 881–895, <https://doi.org/10.1007/s13351-018-7188-5>.
- Wen, X. Y., T. J. Zhou, S. W. Wang, B. Wang, H. Wan, and J. Li, 2007: Performance of a reconfigured atmospheric general circulation model at low resolution. *Adv. Atmos. Sci.*, **24**, 712–728, <https://doi.org/10.1007/s00376-007-0712-7>.
- Wheeler, M. C., and H. H. Hendon, 2004: An all-season real-time multivariate MJO index: Development of an index for monitoring and prediction. *Mon. Wea. Rev.*, **132**, 1917–1932, [https://doi.org/10.1175/1520-0493\(2004\)132<1917:AARMMI>2.0.CO;2](https://doi.org/10.1175/1520-0493(2004)132<1917:AARMMI>2.0.CO;2).
- Wu, A. M., W. W. Hsieh, and B. Y. Tang, 2006: Neural network forecasts of the tropical Pacific sea surface temperatures. *Neural Networks*, **19**, 145–154, <https://doi.org/10.1016/j.neunet.2006.01.004>.
- Wu, B., and T. J. Zhou, 2012: Prediction of decadal variability of sea surface temperature by a coupled global climate model FGOALS\_gl developed in LASG/IAP. *Chinese Science Bulletin*, **57**, 2453–2459, <https://doi.org/10.1007/s11434-012-5134-y>.
- Wu, B., T. J. Zhou, and F. Zheng, 2018a: EnOI-IAU initialization scheme designed for decadal climate prediction system IAP-DecPreS. *Journal of Advances in Modeling Earth Systems*, **10**, 342–356, <https://doi.org/10.1002/2017MS001132>.
- Wu, B., X. L. Chen, F. F. Song, Y. Sun, and T. J. Zhou, 2015: Initialized decadal predictions by LASG/IAP climate system model FGOALS-s2: Evaluations of strengths and weaknesses. *Advances in Meteorology*, **2015**, 904826, <https://doi.org/10.1155/2015/904826>.
- Wu, J., H.-L. Ren, C. B. Zhao, P. Q. Zhang, and Y. J. Wu, 2016: Research and application of operational MJO monitoring and prediction products in Beijing Climate Center. *Journal of Applied Meteorological Science*, **27**, 641–653, <https://doi.org/10.11898/1001-7313.20160601>. (in Chinese with English abstract)
- Wu, J., H.-L. Ren, S. Zhang, Y. Liu, and X. W. Liu, 2017: Evaluation and predictability analysis of seasonal prediction by BCC second-generation climate system model. *Chinese Journal of Atmospheric Sciences*, **41**, 1300–1315, <https://doi.org/10.3878/j.issn.1006-9895.1703.16256>. (in Chinese with English abstract)
- Wu, J., H.-L. Ren, X. F. Xu, and L. Gao, 2018b: Seasonal modulation of MJO's impact on precipitation in China and its dynamical-statistical downscaling prediction. *Meteorological Monthly*, **44**, 737–751, <https://doi.org/10.7519/j.issn.1000-0526.2018.06.002>. (in Chinese with English abstract)
- Wu, J., H. L. Ren, B. Lu, P. Q. Zhang, C. B. Zhao, and X. W. Liu, 2020a: Effects of moisture initialization on MJO and its teleconnection prediction in BCC subseasonal coupled model. *J. Geophys. Res.: Atmos.*, **125**, e2019JD031537, <https://doi.org/10.1029/2019JD031537>.
- Wu, J., P. Q. Zhang, L. Li, H.-L. Ren, X. W. Liu, A. A. Scaife, and S. Zhang, 2020b: Representation and predictability of the East Asia-Pacific teleconnection in the Beijing Climate Center and UK Met Office subseasonal prediction systems. *J. Meteor. Res.*, **34**, 941–964, <https://doi.org/10.1007/s13351-020-0040-8>.
- Wu, J., H.-L. Ren, P. Q. Zhang, Y. Wang, Y. Liu, C. B. Zhao,



- and Q. P. Li, 2022: The dynamical-statistical subseasonal prediction of precipitation over China based on the BCC new-generation coupled model. *Climate Dyn.*, **59**, 1213–1232, <https://doi.org/10.1007/s00382-022-06187-3>.
- Wu, L. Q., Q. Q. Li, Y. H. Ding, L. J. Wang, X. G. Xin, and M. Wei, 2018c: Preliminary assessment on the hindcast skill of the Arctic Oscillation with decadal experiment by the BCC\_CSM1.1 climate model. *Advances in Climate Change Research*, **9**, 209–217, <https://doi.org/10.1016/j.accre.2018.12.001>.
- Wu, T. W., and Coauthors, 2020c: Beijing Climate Center Earth System Model version 1 (BCC-ESM1): Model description and evaluation of aerosol simulations. *Geoscientific Model Development*, **13**, 977–1005, <https://doi.org/10.5194/gmd-13-977-2020>.
- Wu, T. W., and Coauthors, 2021: BCC-CSM2-HR: A high-resolution version of the Beijing climate center climate system model. *Geoscientific Model Development*, **14**, 2977–3006, <https://doi.org/10.5194/gmd-14-2977-2021>.
- Xiao, Z. N., B. Liu, H. Liu, and D. Zhang, 2012: Progress in climate prediction and weather forecast operations in China. *Adv. Atmos. Sci.*, **29**, 943–957, <https://doi.org/10.1007/s00376-012-1194-9>.
- Xin, X. G., T. W. Wu, and J. Zhang, 2012: Introduction of CMIP5 experiments carried out by BCC climate system model. *Progressus Inquisitiones de Mutatione Climatis*, **8**, 378–382, <https://doi.org/10.3969/j.issn.1673-1719.2012.05.010>. (in Chinese with English abstract)
- Xin, X. G., F. Gao, M. Wei, T. W. Wu, Y. J. Fang, and J. Zhang, 2018: Decadal prediction skill of BCC-CSM1.1 climate model in East Asia. *International Journal of Climatology*, **38**, 584–592, <https://doi.org/10.1002/joc.5195>.
- Xin, X. G., M. Wei, Q. Q. Li, W. Zhou, Y. Luo, and Z. C. Zhao, 2019: Decadal prediction skill of BCC-CSM1.1 with different initialization strategies. *J. Meteor. Soc. Japan*, **97**, 733–744, <https://doi.org/10.2151/jmsj.2019-043>.
- Xiu, S. Y., 2019: Current situation and trend of short-term and medium-term digital weather forecasting technology. *Agriculture and Technology*, **39**, 157–158, <https://doi.org/10.19754/j.nyyjs.20191130061>. (in Chinese)
- Xu, C. L., J. J. Wang, and L. P. Huang, 2017: Evaluation on QPF of GRAPES-Meso4.0 model at convection-permitting resolution. *Acta Meteorologica Sinica*, **75**, 851–876, <https://doi.org/10.11676/qxxb2017.068>. (in Chinese with English abstract)
- Xue, J. S., and D. H. Chen, 2008: *Scientific Design and Application of GRAPES Numerical Prediction System*. Science Press, 383 pp. (in Chinese)
- Yang, C. Y., J. P. Liu, and S. M. Xu, 2020: Seasonal Arctic Sea ice prediction using a newly developed fully coupled regional model with the assimilation of satellite sea ice observations. *Journal of Advances in Modeling Earth Systems*, **12**, e2019MS001938, <https://doi.org/10.1029/2019MS001938>.
- Yang, J., M. Astitha, L. D. Monache, and S. Alessandrini, 2018: An analog technique to improve storm wind speed prediction using a dual NWP model approach. *Mon. Wea. Rev.*, **146**, 4057–4077, <https://doi.org/10.1175/MWR-D-17-0198.1>.
- Yang, Q. M., 2018: A study of the extended-range forecast for the low frequency temperature and high temperature weather over the lower reaches of Yangtze River valley in summer. *Advances in Earth Science*, **33**, 385–395, <https://doi.org/10.11867/j.issn.1001-8166.2018.04.0385>. (in Chinese with English abstract)
- Yang, S. X., F. H. Ling, W. S. Ying, S. Yang, and J.-J. Luo, 2022: A brief overview of the application of artificial intelligence to climate prediction. *Transactions of Atmospheric Sciences*, **45**, 641–659, <https://doi.org/10.13878/j.cnki.dqkxxb.20210623003>. (in Chinese with English abstract)
- Ying, W. S., H. P. Yan, and J.-J. Luo, 2022: Seasonal predictions of summer precipitation in the middle-lower reaches of the Yangtze River with global and regional models based on NUIST-CFS1.0. *Adv. Atmos. Sci.*, **39**, 1561–1578, <https://doi.org/10.1007/s00376-022-1389-7>.
- Yuan, Y., C. Y. Li, and J. Ling, 2015: Different MJO activities between EP El Niño and CP El Niño. *Scientia Sinica Terrae*, **45**, 318–334. (in Chinese with English abstract)
- Zhang, C. D., 2005: Madden-Julian oscillation. *Rev. Geophys.*, **43**, RG2003, <https://doi.org/10.1029/2004RG000158>.
- Zhang, H., X. M. Wang, and D. Wang, 2018: 1D Var dynamic bias correction of satellite radiance. *Documentation of Numerical Weather Prediction Center of CMA*, **25**. (in Chinese with English abstract)
- Zhang, H., and Coauthors, 2020a: Description and climate simulation performance of CAS-ESM version 2. *Journal of Advances in Modeling Earth Systems*, **12**, e2020MS002210, <https://doi.org/10.1029/2020MS002210>.
- Zhang, L., and Coauthors, 2019: The operational global four-dimensional variational data assimilation system at the China Meteorological Administration. *Quart. J. Roy. Meteor. Soc.*, **145**, 1882–1896, <https://doi.org/10.1002/qj.3533>.
- Zhang, P. Q., Q. Q. Li, L. N. Wang, Y. M. Liu, X. L. Shi, and T. W. Wu, 2004: Development and application of dynamic climate model prediction system in China. *Science & Technology Review*(7), 17–21, <https://doi.org/10.3321/j.issn:1000-7857.2004.07.006>.
- Zhang, R. H., and X. S. Shen, 2008: On the development of the GRAPES—A new generation of the national operational NWP system in China. *Chinese Science Bulletin*, **53**, 3429–3432, <https://doi.org/10.1007/s11434-008-0462-7>.
- Zhang, R.-H., and Coauthors, 2020b: A review of progress in coupled ocean-atmosphere model developments for ENSO studies in China. *Journal of Oceanology and Limnology*, **38**, 930–961, <https://doi.org/10.1007/s00343-020-0157-8>.
- Zhao, C. B., H.-L. Ren, L. C. Song, and J. Wu, 2015: Madden-Julian Oscillation simulated in BCC climate models. *Dyn. Atmos. Oceans*, **72**, 88–101, <https://doi.org/10.1016/j.dynatmoce.2015.10.004>.
- Zhao, Y. D., X. Q. Yin, Y. J. Song, and F. L. Qiao, 2019: Seasonal prediction skills of FIO-ESM for North Pacific sea surface temperature and precipitation. *Acta Oceanologica Sinica*, **38**, 5–12, <https://doi.org/10.1007/s13131-019-1366-x>.
- Zheng, G., X. F. Li, R.-H. Zhang, and B. Liu, 2020: Purely satellite data-driven deep learning forecast of complicated tropical instability waves. *Science Advances*, **6**, eaba1482, <https://doi.org/10.1126/sciadv.aba1482>.
- Zhou, F., H.-L. Ren, Z.-Z. Hu, M.-H. Liu, J. Wu, and C.-Z. Liu, 2020a: Seasonal predictability of primary East Asian summer circulation patterns by three operational climate prediction models. *Quart. J. Roy. Meteor. Soc.*, **146**, 629–646, <https://doi.org/10.1002/qj.3697>.
- Zhou, L.-J., and Coauthors, 2015: Global energy and water bal-

- ance: Characteristics from Finite-volume Atmospheric Model of the IAP/LASG (FAMIL1). *Journal of Advances in Modeling Earth Systems*, **7**, 1–20, <https://doi.org/10.1002/2014MS000349>.
- Zhou, T. J., and B. Wu, 2017: Decadal climate prediction: Scientific frontier and challenge. *Advances in Earth Science*, **32**, 331–341, <https://doi.org/10.11867/j.issn.1001-8166.2017.04.0331>. (in Chinese with English abstract)
- Zhou, T. J., B. Wu, and S. Hu, 2020b: Decadal prediction system IAP-DecPreS and its predictive skill. *Transactions of Atmospheric Sciences*, **43**, 159–168, <https://doi.org/10.13878/j.cnki.dqkxxb.20191210001>. (in Chinese with English abstract)
- Zhu, Z. W., and T. M. Li, 2017a: The statistical extended-range (10–30-day) forecast of summer rainfall anomalies over the entire China. *Climate Dyn.*, **48**, 209–224, <https://doi.org/10.1007/s00382-016-3070-2>.
- Zhu, Z. W., and T. M. Li, 2017b: Statistical extended-range forecast of winter surface air temperature and extremely cold days over China. *Quart. J. Roy. Meteor. Soc.*, **143**, 1528–1538, <https://doi.org/10.1002/qj.3023>.
- Zhu, Z. W., and T. M. Li, 2018: Extended-range forecasting of Chinese summer surface air temperature and heat waves. *Climate Dyn.*, **50**, 2007–2021, <https://doi.org/10.1007/s00382-017-3733-7>.
- Zhu, Z. W., T. M. Li, P.-C. Hsu, and J. H. He, 2015: A spatial–temporal projection model for extended-range forecast in the tropics. *Climate Dyn.*, **45**, 1085–1098, <https://doi.org/10.1007/s00382-014-2353-8>.
- Zhu, Z. W., T. M. Li, L. Bai, and J. Y. Gao, 2017: Extended-range forecast for the temporal distribution of clustering tropical cyclogenesis over the western North Pacific. *Theor. Appl. Climatol.*, **130**, 865–877, <https://doi.org/10.1007/s00704-016-1925-4>.
- Zuo, J. Q., H.-L. Ren, B. Y. Wu, and W. J. Li, 2016: Predictability of winter temperature in China from previous autumn Arctic Sea ice. *Climate Dyn.*, **47**, 2331–2343, <https://doi.org/10.1007/s00382-015-2966-6>.

# Role of Stratospheric Processes in Climate Change: Advances and Challenges<sup>✉</sup>

Wenshou TIAN<sup>\*1</sup>, Jinlong HUANG<sup>1</sup>, Jiankai ZHANG<sup>1</sup>, Fei XIE<sup>2</sup>, Wuke WANG<sup>3,4</sup>, and Yifeng PENG<sup>1</sup>

<sup>1</sup>College of Atmospheric Sciences, Lanzhou University, Lanzhou 730000, China

<sup>2</sup>School of Systems Science, Beijing Normal University, Beijing 100875, China

<sup>3</sup>Department of Atmospheric Science, China University of Geosciences, Wuhan 430078, China

<sup>4</sup>Centre for Severe Weather and Climate and Hydro-Geological Hazards, Wuhan 430078, China

(Received 14 November 2022; revised 8 February 2023; accepted 3 March 2023)

## ABSTRACT

In this review, instead of summarizing all the advances and progress achieved in stratospheric research, the main advances and new developments in stratosphere–troposphere coupling and stratospheric chemistry–climate interactions are summarized, and some outstanding issues and grand challenges are discussed. A consensus has been reached that the stratospheric state is an important source of improving the predictability of the troposphere on sub-seasonal to seasonal (S2S) time scales and beyond. However, applying stratospheric signals in operational S2S forecast models remains a challenge because of model deficiencies and the complexities of the underlying mechanisms of stratosphere–troposphere coupling. Stratospheric chemistry, which controls the magnitude and distribution of many important climate-forcing agents, plays a critical role in global climate change. Convincing evidence has been found that stratospheric ozone depletion and recovery have caused significant tropospheric climate changes, and more recent studies have revealed that stratospheric ozone variations can even exert an impact on SSTs and sea ice. The climatic impacts of stratospheric aerosols and water vapor are also important. Although their quantitative contributions to radiative forcing have been reasonably well quantified, there still exist large uncertainties in their long-term impacts on climate. The advances and new levels of understanding presented in this review suggest that whole-atmosphere interactions need to be considered in future for a better and more thorough understanding of stratosphere–troposphere coupling and its role in climate change.

**Key words:** stratosphere, the stratosphere–troposphere coupling, stratospheric chemistry–climate interactions, stratospheric ozone

**Citation:** Tian, W. S., J. L. Huang, J. K. Zhang, F. Xie, W. K. Wang, and Y. F. Peng, 2023: Role of stratospheric processes in climate change: Advances and challenges. *Adv. Atmos. Sci.*, **40**(8), 1379–1400, <https://doi.org/10.1007/s00376-023-2341-1>.

## Article Highlights:

- This review reveals the vital importance of the stratosphere in improving subseasonal-to-seasonal forecasting of the atmosphere
- The advances and progress achieved imply an essential need for modern-era atmospheric research being extended to the whole atmosphere

## 1. Introduction

Benefiting from continuously increasing amounts of data and more complex climate models, significant progress has been made during the past several decades in understanding Earth's climate, both past and future. A series of climate

change assessment reports produced by the Intergovernmental Panel on Climate Change (IPCC) confirm that increases in greenhouse gases (GHGs) and aerosols have been dominant external forcings of climate change during the last two centuries. However, the magnitude and significance of observed climate changes are still under wide debate, and our physical understanding of many components of the climate system and their role in climate change remains incomplete (IPCC, 2001, 2014, 2021).

Among the roles of the various components of the climate system in climate change, that of stratospheric processes has been one of the hottest topics in the past three decades. In

<sup>✉</sup> This paper is a contribution to the special issue on National Report to the 28th IUGG General Assembly by CNC-IAMAS (2019–2022).

\* Corresponding author: Wenshou TIAN  
Email: [wstian@lzu.edu.cn](mailto:wstian@lzu.edu.cn)



1992, a project named Stratosphere–Troposphere Processes and their Role in Climate (SPARC) was founded as a core project of the World Climate Research Programme. This project aims to understand how atmospheric chemical and physical processes in the stratosphere interact with Earth's climate system. After 30 years of implementation of this project, the importance of the stratosphere in modulating and regulating climatic variability and trends is now widely recognized, and some great advances have been achieved despite grand challenges still remaining (SPARC, 2022).

In a recent comprehensive research overview by Baldwin et al. (2019), the progress made in understanding the stratosphere and mesosphere in the past 100 years was presented with a large coverage of various directions and aspects in this area. Meanwhile, some other recent review papers have presented more detailed descriptions of the advances made on some specific topics or issues (e.g., Kidston et al., 2015; Butler et al., 2019; Baldwin et al., 2021, Haynes et al., 2021; Butchart, 2022). After 100 years of research, our understanding of the dynamical and chemical processes in the stratosphere has advanced greatly. In addition, it is now widely accepted that stratospheric processes have important impacts on tropospheric weather and climate on various time scales, and climate models with a well-resolved stratosphere can give more accurate climate predictions.

Despite the significant progress in understanding stratospheric processes, their role in climate changes remains an issue of debate. The pathways, time scales and underlying mechanisms through which stratospheric processes impact tropospheric weather and climate still need to be further elucidated. In this review, we do not intend to detail all advances and progress made in stratospheric research; rather, we will focus on the coupling between the stratosphere and troposphere and discuss how and to what extent stratospheric processes modulate tropospheric weather or shape climatic variability and trends. In doing so, we also intend to highlight issues of current scientific interest in stratospheric research. In section 2, the impacts of thermodynamic and dynamic processes on weather and climate change are discussed. In section 3, the impacts of stratospheric chemical processes on the troposphere are presented. A summary and concluding remarks are given in section 4.

## 2. Role of thermodynamic and dynamic processes

It is well-known that the variations in the stratospheric circulation are strongly governed by the tropospheric processes below. However, the stratosphere is far from being a passive bystander to tropospheric influences. In fact, a two-way coupling exists between the stratosphere and troposphere. The diverse variabilities of the stratospheric circulation and thermal state can exert an influence on the troposphere below at different time scales. Therefore, knowledge of the stratospheric states has been identified as important for improving the predictability of the troposphere on sub-sea-

sonal to seasonal (S2S) timescales and beyond (e.g., Sigmund et al., 2013; Rao et al., 2019, 2020a, b; Domeisen et al., 2020a; Huang et al., 2021). In addition to its role in S2S forecasting, a consensus has been reached by the scientific community that stratospheric processes should be well represented in climate models in order to accurately evaluate future climate change (e.g., Baldwin et al., 2019), thereby highlighting the importance of such processes in climatic variability.

### 2.1. Synoptic and S2S timescale impacts

The largest dynamical variability at S2S timescales occurs in the polar stratosphere where the stratospheric polar vortex (SPV) exists. The SPV is formed mainly through radiative cooling. More specifically, the strong contrast in stratospheric air temperatures between the poles and low latitudes leads to the formation of a circumpolar vortex in both hemispheres. The SPV in the Northern Hemisphere exhibits a larger variability compared to its counterpart in the Southern Hemisphere, due to stronger wave forcing that is closely related to larger mountain ranges and greater land–sea contrast in the Northern Hemisphere (e.g., Held et al., 2002; Rao and Ren, 2020). The strength and position of the SPV is largely influenced by planetary-scale Rossby waves, which propagate vertically into the polar stratosphere and break (Charney and Drazin, 1961; Matsuno, 1971). In extreme cases, the effects of planetary wave breaking lead to a dramatic weakening of the SPV with a reversal of the climatological westerlies, which is well-known as sudden stratospheric warming (SSW; Schoeberl, 1978; Quiroz, 1986; Baldwin et al., 2021). SSW occurs more frequently in the Northern Hemisphere than in the Southern Hemisphere; for instance, it occurs roughly six times per decade in the Northern Hemisphere (e.g., Charlton and Polvani, 2007; Hu et al., 2014; Butler et al., 2015), with more events in January and February, whereas only one major event (in September 2002) has been observed since the modern satellite era in the Southern Hemisphere (Krüger et al., 2005). Note that in early September 2019 there was a similar event in the Southern Hemisphere, but it did not meet the established criteria for a major SSW (Rao et al., 2020b).

As the most dramatic form of SPV variability, SSW events have important impacts on tropospheric weather and climate, particularly in the Northern Hemisphere. The stratospheric anomalies associated with SSW extend downwards into the lowermost stratosphere, where they last for one to two months on average, and thence to the surface, affecting tropospheric weather (Baldwin and Dunkerton, 2001; Hitchcock and Simpson, 2014; Karpechko et al., 2017; Zhang et al., 2019b). Composites of the Northern Annular Mode (NAM), as presented in previous studies (e.g., Baldwin and Dunkerton 2001, Hitchcock and Simpson, 2014; Rao et al., 2019; Liang et al., 2022b; Lu et al., 2022), remain the common approach to diagnosing the coupling between the stratosphere and troposphere following SSW. Here, we update these composite results with 46 SSW events based on ERA5 reanalysis data, as shown in Fig. 1. The canonical tropospheric

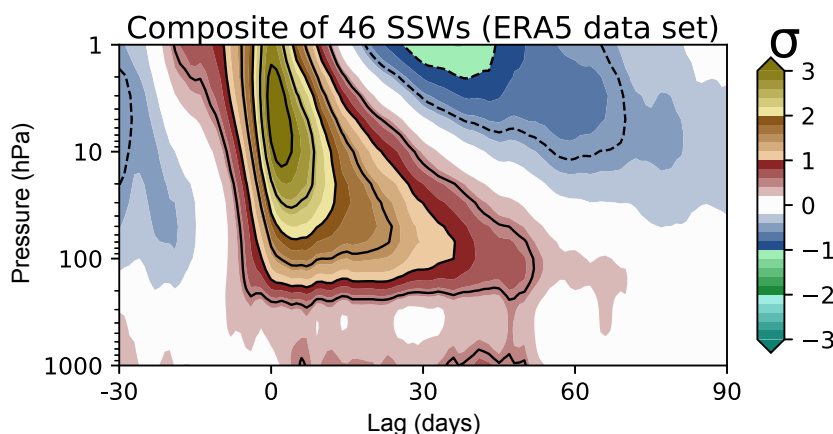


**Fig. 1.** Composite normalized anomaly of polar-cap-averaged ( $60^{\circ}$ – $90^{\circ}$ N) geopotential height following 46 SSW events according to ERA5 reanalysis data for the period 1950–2020. SSW is defined according to the method of Charlton and Polvani (2007). The polar-cap-averaged geopotential height anomaly is commonly used as the NAM index (Baldwin and Thompson, 2009).

response to SSW is a negative phase of the NAM, corresponding to an equatorward shift of storm tracks, severe cold-air outbreaks, and heavy snowfall over most of the midlatitude Northern Hemisphere (Baldwin and Dunkerton, 2001; Charlton and Polvani, 2007; Kolstad et al., 2010; Wang and Chen, 2010; Yu et al., 2015, 2018; Kretschmer et al., 2018; Huang and Tian, 2019; Rao et al., 2019; Domeisen and Butler, 2020; Huang et al., 2021).

Despite corroborative evidence that the SPV can exert an impact on tropospheric weather, the dynamical mechanisms by which circulation anomalies associated with SSW induce changes to surface weather are still under investigation. Several mechanisms have been proposed in the literature, but no consensus has been reached. Some studies have argued that SSW affects tropospheric weather mainly through modulating the Arctic Oscillation or North Atlantic Oscillation (NAO) in the troposphere (Baldwin and Dunkerton, 2001; Charlton and Polvani, 2007; Scaife et al., 2016; Baldwin et al., 2021), whereas others have reported that SSW can induce changes in tropospheric weather regimes, such as tropospheric blocking and eddy-driven jets (e.g., Maycock et al., 2020; Huang et al., 2017), as well as the hemispheric transport of cold airmasses at mid–high latitudes (Huang et al., 2021), and hence changes in weather patterns. In addition, previous studies have linked the mass or pressure changes at the surface to SPV variations (e.g., Yu et al., 2014; Yu and Ren, 2019; Zhang and Tian, 2019). Other mechanisms have been proven to be of importance to the dynamical coupling between the stratosphere and troposphere, such as tropospheric modulations of stratospheric potential vorticity anomalies (e.g., Hoskins et al., 1985; Hartley et al., 1998), the “downward control” principle (e.g., Haynes et al., 1991), stratospheric influence on tropospheric baroclinic instability (e.g., Wittman et al., 2007), and stratospheric reflection of planetary waves vertically propagating from the troposphere (e.g., Perlwitz and Harnik, 2003). However, none of the abovementioned mechanisms is always active in the coupling

between the polar stratosphere and troposphere.

The impacts of the SPV on tropospheric weather and climate are by now well recognized, and so the forecasting community has suggested that SSW provides useful information for improving the forecasting skill for surface weather in the Northern Hemisphere on S2S timescales (e.g., Sigmond et al., 2013; Rao et al., 2019, 2020a, b; Domeisen et al., 2020a; Huang et al., 2021), and even on synoptic timescales (Huang et al., 2022). For a comprehensive discussion on how our improved understanding of the state of the stratosphere and its dynamical links to the troposphere has helped to enhance the predictability of the troposphere on S2S timescales, readers are referred to the review by Butler et al. (2019). However, applying this skill in forecast models, including S2S and operational models, remains a challenge, partly because of the complexity of the physical mechanisms responsible for the impacts of SSW on surface weather in the northern extratropics (see above discussion). Another reason is that robust forecasting of the stratosphere on subseasonal timescales has not yet been achieved (e.g., Domeisen et al., 2020b). More recently, the SNAPSI (Stratospheric Nudging And Predictable Surface Impacts) project has been initiated by the SPARC community (Hitchcock et al., 2022), which aims to further our understanding of the role of SPV disturbances in the surface predictability of S2S models. The dynamics of the SPV and its corresponding influences on the troposphere have been intensively investigated over several decades, and whilst we do not review all developments here, we do highlight the relevant challenges that are of importance to address in the future. For a detailed review of the dynamics of the SPV and its tropospheric influences, readers are referred to the recent reviews by, for example, Kidston et al. (2015), Baldwin et al. (2019, 2021), Butler et al. (2019), and Butchart (2022).

In the tropical lower stratosphere, a dominant feature exists in the zonal wind field called the Quasi-Biennial Oscillation (QBO), which was discovered during the 1960s and

1970s (Reed et al., 1961; Angell and Korshover, 1964; Belmont and Dartt, 1968). The QBO is characterized by a regular downward mitigation of easterly and westerly flow over a period of roughly 28 months (e.g., Ebdon, 1960; Ebdon and Veryard, 1961; Baldwin et al., 2001; Tian et al., 2006), and two QBO disruptions have been respectively observed in 2015/16 and 2019/20 (e.g., Osprey et al., 2016; Anstey et al., 2022). So far, the QBO has been theoretically well understood; the transition of equatorial winds is a result of the upward propagation of tropospheric atmospheric waves (e.g., gravity waves, mixed Rossby–gravity waves, and Kelvin waves) in the tropics into the stratosphere, which deposit momentum into the stratospheric mean flow and in turn drive the easterly–westerly transition (Lindzen and Holton, 1968; Wallace and Kousky, 1968; Holton and Lindzen, 1972). Although the QBO is a tropical stratospheric phenomenon, its influences are not confined to the tropical stratosphere, but reach instead to the high latitudes. Gray et al. (2018) summarized three possible pathways for the QBO impacting the troposphere below, as shown in Fig. 2.

One of QBO's impacts in the tropics is its modulation of the Madden–Julian Oscillation (MJO; Madden and Julian, 1972; Zhang, 2005), which is the dominant mode of intraseasonal variability in the tropical troposphere and has an important influence on global weather and climate. Studies have found a robust QBO–MJO connection, e.g., the MJO is much stronger and persists about 10 days longer in the QBO easterly phase than in the QBO westerly (Yoo and Son, 2016; Son et al., 2017). In addition, the S2S forecast skill for the MJO is improved by one week during the QBO easterly

phase relative to the westerly phase (Marshall et al., 2017; Lim et al., 2019). Despite the robustness of the QBO–MJO connection, there is no consensus as to the mechanisms responsible for the QBO's impacts on the MJO (e.g., Martin et al., 2021). Several mechanisms have been proposed to explain the links, such as QBO-related temperature stratification effects, radiative effects, and its impacts on wave propagation (e.g., Son et al., 2017; Abhik et al., 2019; Densmore et al., 2019; Sakaeda et al., 2020), but their relative importance and robustness are still under scrutiny. In addition to its impacts on the MJO, the QBO has been found to impact tropical deep convection and precipitation via its influence on tropical tropopause temperatures or static stability, as evidenced by both observational and modeling studies (Giorgetta et al., 1999; Collimore et al., 2003; Garfinkel and Hartmann, 2011; Nie and Sobel, 2015; Gray et al., 2018; Rao et al., 2020a, b, c; Huangfu et al., 2021; Wang et al., 2021; Anstey et al., 2022).

The QBO can also induce a meridional circulation at subtropical latitudes, which can influence the horizontal temperature gradient and vertical wind shear near the tropospheric subtropical jet. The modified horizontal temperature gradient/vertical wind shear can further affect the life cycle of synoptic-scale and planetary-scale waves over midlatitudes in the troposphere, which thus helps extend the influence of the QBO down to the surface (Ruti et al., 2006; Garfinkel and Hartmann, 2011; Gray et al., 2018).

The QBO can also modulate the strength of the SPV, particularly in the Northern Hemisphere (e.g., Chen and Wei, 2009; Garfinkel et al., 2012; Zhang et al., 2019a, 2020b;

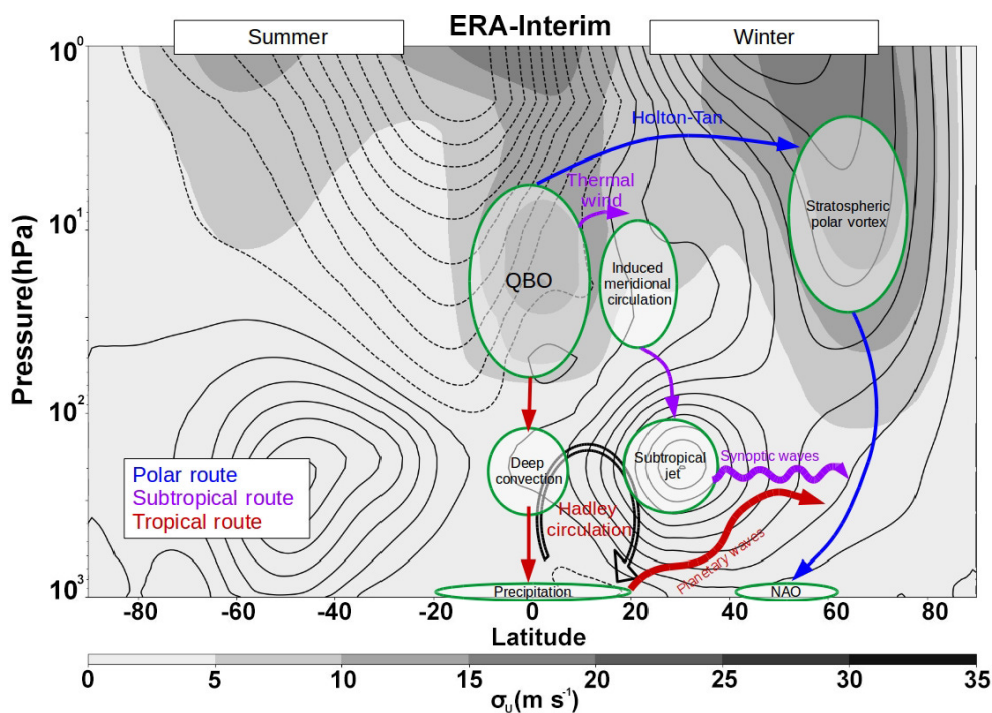


**Fig. 2.** Schematic of the three primary routes (tropical, subtropical, polar) for the QBO impacting the troposphere. Contours show the winter (December–February) averaged, zonal-mean zonal winds for the period 1979–2016 from the ERA-Interim dataset. [Reprinted from Gray et al. (2018)].

Rao et al., 2020a), and subsequently influences tropospheric circulation and surface weather patterns. The SPV tends to be colder and stronger during westerly QBO, but warmer and more disturbed during easterly QBO; this is well-known as the Holton–Tan effect (Holton and Tan, 1980, 1982), i.e., during easterly QBO, vertically propagating planetary waves from the extratropical troposphere in winter are refracted away from the subtropical region and redirected towards the polar stratosphere where they break and in turn weaken the polar vortex, and vice versa for westerly QBO. Some studies have indicated that the Holton–Tan effect was weakened during 1977–97 (e.g., Lu et al., 2008, 2014), whereas it is projected to strengthen in the future according to the results of CMIP5/6 models (Rao et al., 2020c), suggesting that the Holton–Tan effect has not been steady over time. In addition, the QBO has been reported to have impacts on stationary planetary wave activity in winter in the Northern Hemisphere, and subsequently on East Asian climate (e.g., Chen and Li, 2007; Ma et al., 2021). For a detailed summary of the QBO’s impacts on the troposphere, readers are referred to the reviews by Haynes et al. (2021) and Butchart (2022).

A prominent meridional circulation in the stratosphere that bridges the tropical stratosphere and the polar stratosphere is the Brewer–Dobson (BD) circulation (see Fig. 3), which is also referred to as the global mass circulation and features tropospheric air entering into the stratosphere in the tropics, moving upwards and polewards, and then descending in the middle and high latitudes (e.g., Dobson and Harrison, 1926; Brewer, 1949; Dobson, 1956; Butchart, 2014). The BD circulation is driven by the breaking or dissipation of the waves propagating from the troposphere in the midlatitudes, and thus is also expressed by the wave-driven circula-

tion (Andrews and McIntyre, 1976, 1978a, b; Boyd, 1976).

More model-based evidence is now emerging that a changing BD circulation may play a significant role in the dynamical coupling between the stratosphere and troposphere, with implications for surface climate and weather (e.g., Baldwin et al., 2007; Karpechko and Manzini, 2012; Scaife et al., 2012). Changes in the BD circulation have been found to be closely connected to changes in the intensity and location of the tropospheric jet stream (e.g., Thompson and Solomon, 2002), surface pressure changes over middle and high latitudes (e.g., Zhang and Tian, 2019), tropospheric storm tracks (e.g., Scaife et al., 2012; Kidston et al., 2015), and precipitation (e.g., Karpechko and Manzini, 2012). As shown in Fig. 3, the QBO, the BD circulation, and the SPV are also dynamically connected. For instance, during easterly QBO, planetary waves are refracted by the critical line and redirected towards the polar regions, where they break, and an anomalous BD circulation that pumps polewards and then descends over the pole is thus induced. The descending branch of this anomalous BD circulation can cause anomalous adiabatic warming over the pole and a subsequent weakening of the SPV. It has been found that easterly QBO together with a weakened SPV are conducive to an increased likelihood of extreme cold-air outbreaks occurring, and vice versa (e.g., Thompson et al., 2002).

Apart from large-scale stratospheric processes, some small- and mesoscale processes in the lowermost midlatitude stratosphere (e.g., tropopause folding, stratospheric potential vorticity intrusion, isentropic mixing) also play a role in tropospheric weather and climate changes (Fig. 3). Luo et al. (2013) found that frequent tropopause folds over the mei-yu area in China lead to a strong downward transport of air-masses from the lower stratosphere to the upper troposphere

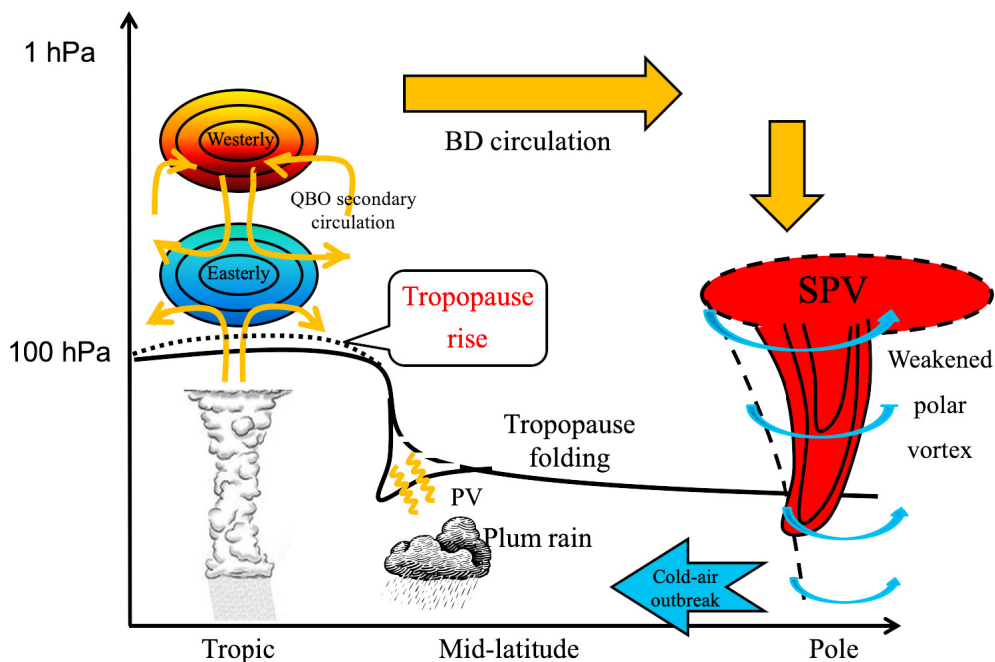


**Fig. 3.** Schematic of stratospheric dynamical processes (e.g., the QBO, BD circulation, SPV, and tropopause folding) that can exert important influences on tropospheric weather and climate.



before the onset of mei-yu precipitation, suggesting that strong potential vorticity intrusion from the lower stratosphere could provide useful information for estimating the onset of the mei-yu season in China. In addition, tropopause folds are closely associated with surface wind gust extremes (e.g., Škerlak et al., 2015), rapid cyclogenesis (e.g., Wernli et al., 2002), and even the initiation of severe mesoscale weather systems like strong convection (e.g., Russell et al., 2012; Antonescu et al., 2013). A recent model-based study reported a statistically significant change in the tropopause fold frequency in both hemispheres under future climate change (Akritidis et al., 2019). As for small-scale isentropic mixing processes, their impacts on tropospheric weather and climate take place mainly through changing the tracer distributions in the upper troposphere and lower stratosphere, and hence exert an indirect impact via chemical–radiative coupling. However, this issue has not been well addressed to date, due to the complexity of the coupled chemical–radiative–dynamic processes involved and a lack of high-resolution tracer observations.

## 2.2. Role of stratospheric thermodynamics in climatic variability and trends

Owing to increases in anthropogenic emissions of GHGs and ozone depleting substances (ODSs), the stratosphere has experienced a significant cooling trend during the past several decades (e.g., Ramaswamy et al., 2001; Randel et al., 2009; Ren et al., 2015). However, due to limitations in data, there are large uncertainties in the magnitude of linear trends estimated from different data sources. For instance, the global-mean temperature trend in the middle stratosphere (25–45 km) estimated from NOAA data is almost twice that from UK Met Office data (Thompson et al., 2012). This uncertainty in the trend of stratospheric temperature is also apparent when comparing observations and hindcast model simulations (Thompson et al., 2012). A recent study revisited this issue and indicated that the latest satellite-based data show better consistency with each other and better agreement with observations (Maycock et al., 2018). Nevertheless, the well-known stratospheric cooling and tropospheric warming due to increasing concentrations of GHGs will change meridional and horizontal temperature gradients of the atmosphere, as well as vertical temperature gradients, and in turn affect stratospheric processes (e.g., ozone depletion, BD circulation, the polar vortex) owing to the thermodynamic feedback, which further impacts the weather and climate in the troposphere.

Although there is still debate on what causes the change in the BD circulation, the scientific community has reached a broad consensus that there is an acceleration rate of roughly 2.0%–3.2% (10 yr)<sup>-1</sup> (i.e., varying with the GHG scenario considered) in the BD circulation in response to stratospheric cooling and tropospheric warming (e.g., Rind et al., 1990; Austin, 2002; Butchart et al., 2010; Lin and Fu, 2013; Fu et al., 2019). In addition, the mechanisms behind the strengthened BD circulation are still under investigation. Apart from the mechanism that increasing wave activities in

the troposphere due to tropospheric warming could lead to a strengthening of the BD circulation, Shepherd and McLandress (2011) argued that GHG-induced tropospheric warming pushes the critical layers within the subtropical lower stratosphere upwards, which allows more wave activities to penetrate into the subtropical lower stratosphere and then strengthen the BD circulation. Changing BD circulation has contributed to an increase in column ozone at midlatitudes (e.g., Mahfouf et al., 1994; Shepherd, 2008; Li et al., 2009), faster removal of ODSs (e.g., Butchart and Scaife, 2001; Douglass et al., 2008; Butchart, 2014), and an increasing ozone flux from the stratosphere into the troposphere (e.g., Hegglin and Shepherd, 2009; Neu et al., 2014). Finally, the dynamic coupling between the stratosphere and troposphere is also influenced by a changing BD circulation (e.g., Zhang and Tian, 2019), with important implications for surface weather and climate.

Observed variability and long-term changes in the properties of the polar vortex have also been widely discussed (e.g., Kim et al., 2014; Zhang et al., 2016; Seviour, 2017; Hu et al., 2018). Previous studies have reported an observed strengthening of the Antarctic polar vortex during austral spring (e.g., Zuev and Savelieva, 2019), whereas there are no recent studies about projected changes in the Antarctic polar vortex. In general, ozone recovery will likely lead to a weakening of the Antarctic polar vortex, while increases in GHGs will tend to strengthen it. However, as mentioned earlier, the SPV has large dynamical variabilities. Consequently, determining the SPV trend is rather challenging. Kim et al. (2014) showed that the Arctic polar vortex experienced a weakening trend in midwinter over the past three decades. However, Hu et al. (2018) reported that the SPV has been strengthened since the last decade. These discrepancies are due either to the different lengths of data recorders used in these studies, or the analysis of vortex strength at different altitudes.

As for the changes in SPV position, Zhang et al. (2016) found that the Arctic SPV in February shifted towards Eurasia during 1980–2016. Moreover, notably, the extent of the polar vortex shift in the last decade (2010s) compared to the 1980s was smaller than before (Zhang et al., 2020a), suggesting that there is a decadal variability in the SPV position, which is related to the internal variability in the climate system (Seviour, 2017; Zhao et al., 2022). In addition, various climate variabilities could influence the SPV position (Huang et al., 2018; Zhang et al., 2019a). The above results suggest that future changes in the strength and position of the Arctic SPV deserve further investigation.

Recent studies have presented corroborative evidence that the weakening and shift of the Arctic polar vortex has contributed to observed cooling in midlatitude Eurasia in boreal winter (e.g., Zhang et al., 2016; Garfinkel et al., 2017; Huang et al., 2018; Kretschmer et al., 2018; Xu et al., 2021; Liang et al., 2022a). Overall, the future changes in the strength of the Arctic polar vortex diverge widely across climate models, with no agreement as to the sign of the change, and a demonstration of large uncertainties (e.g., Karpechko

et al., 2022). In addition, the mechanisms responsible for the projected changes in the Arctic polar vortex remain unclear. To add confidence to the projections of the wintertime Arctic polar vortex strength and position, more effort is thus needed to understand the mechanisms and to narrow the large intermodel spread in projections.

Considering the prominent role of SSW in improving the S2S forecast skill of surface weather, several previous studies have focused on their potential future change. However, there does not exist a consistent trend in SSW events (e.g., Mitchell et al., 2013; Kim et al., 2017; Ayarzagüena et al., 2018, 2020; Charlton-Perez et al., 2018; Rao and Garfinkel, 2021a). Several possible reasons have been proposed to explain the discrepancy: (1) the opposing effects of the projected ozone recovery and increasing GHG concentrations on the Arctic stratosphere (e.g., Hu and Tung, 2003; Ayarzagüena et al., 2013; Hu et al., 2015); (2) the various criteria used to define SSW, since the frequency of SSW is sensitive to the different definitions of SSW (e.g., Butler et al., 2015; Palmeiro et al., 2015; Butler and Gerber, 2018). A recent study analyzed SSW changes in the future using new simulations performed under CMIP6. It was found that most models show a statistically significant trend in the frequency of SSW, but large disagreement exists on the sign of this trend (Ayarzagüena et al., 2020).

Beside the processes mentioned above, there may be other changes in response to tropospheric warming and stratospheric cooling, which awaits the results of further studies. For example, some studies have investigated the projected changes in QBO and suggest that the QBO amplitude in the lower stratosphere has decreased (Kawatani and Hamilton, 2013; Schirber et al., 2015; Naoe et al., 2017; Rao et al., 2020c). Considering our incomplete understanding of

changes in wave forcing contributing to the QBO, it is still difficult to draw a robust conclusion about its future changes or whether there will be more frequent QBO interruptions under the future climate.

### 3. The stratospheric chemistry and climate interaction

#### 3.1. Stratospheric chemical composition changes

Atmospheric chemistry plays a critical role in modulating global climate. Climatic impacts of stratospheric ozone, which is both radiatively and chemically active, have been well documented in the literature (e.g., de F. Forster and Shine, 1997; Son et al., 2009, 2010; Hu et al., 2015; Nowack et al., 2015, 2018; Xie et al., 2016; Maleska et al., 2020; Zhang et al., 2020a; Friedel et al., 2022; Oh et al., 2022). Apart from ozone, ODSs, aerosols, water vapor, and GHGs in the stratosphere all have an impact on global climate through radiative or chemical processes and chemical–radiative–dynamic feedbacks. A conceptual model of the interactions among the various major chemical components in the stratosphere is shown in Fig. 4.

Due to the emissions of ODSs such as chlorofluorocarbons (CFCs), the quantity of global stratospheric ozone decreased between the late 1970s and early 1990s. On a near-global scale, upper-stratospheric ozone is now recovering owing to the effects of the Montreal Protocol and its amendments on ODS levels (Chipperfield et al., 2017; WMO, 2022). However, ozone in the lower stratosphere, between 60°S and 60°N, has continued to decline since 1998, which has been attributed to various dynamical variabilities in the climate system (Ball et al., 2018; Chipperfield et

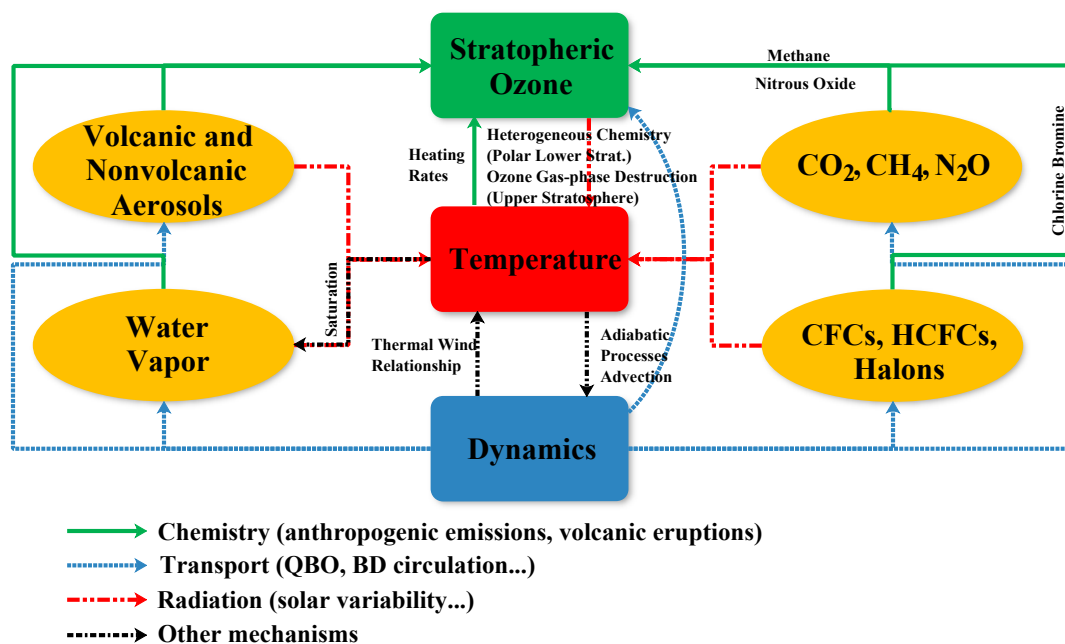


Fig. 4. Schematic of the interactions between stratospheric chemical components and temperature. [Adapted from WMO (2011)].



al., 2018; Zhang et al., 2018). The opposite trends of the upper- and lower-stratospheric ozone have resulted in an insignificant total column ozone (TCO) trend since the 2000s. The latest WMO ozone assessment (WMO, 2022) reported that various datasets show an increase of  $0.3\% \pm 0.3\%$   $(10 \text{ yr})^{-1}$  in the near-global mean ( $60^{\circ}\text{S}$ – $60^{\circ}\text{N}$ ) TCO for the period 1996–2020.

Observations show an increase in global stratospheric water vapor in the 2000s (Yue et al., 2019; Konopka et al., 2022). Long-term changes and the interannual variability of stratospheric water vapor are not only controlled by the oxidation of methane ( $\text{CH}_4$ ), but also related to tropical cold point temperatures and overshooting convections that are both influenced by climate change (Sherwood and Dessler, 2000; Holton and Gettelman, 2001; Rosenlof, 2003; Tian and Chipperfield, 2006; Solomon et al., 2010). Stratospheric aerosols are formed when particles and their precursor gases enter the stratosphere.

The stratospheric aerosol loading and aerosol optical depth (AOD) can increase by one order of magnitude or more and reside for one to three years when a large volcanic eruption injects massive quantities of sulfur dioxide ( $\text{SO}_2$ ) into the stratosphere (Robock, 2000; Kremser et al., 2016; Aubry et al., 2021). Both historic and recent trends in stratospheric aerosols can be largely attributed to volcanic eruptions (Deshler et al., 2003; Vernier et al., 2011).

Solar radiation warms the stratosphere, mainly through absorption of solar radiation by ozone, stratospheric aerosols, and molecular oxygen. Meanwhile, stratospheric aerosols and GHGs, including water vapor ( $\text{H}_2\text{O}$ ), ozone, carbon dioxide ( $\text{CO}_2$ ),  $\text{CH}_4$ , nitrous oxide ( $\text{N}_2\text{O}$ ), CFCs, hydrochlorofluorocarbons, and brominated chlorofluorocarbons (halons), can absorb and re-emit outgoing long wave radiation from the troposphere. As mentioned earlier, a significant cooling trend has been observed in the stratosphere owing to increasing concentrations of GHGs. On the other hand, there are various photochemical reactions, gas-phase chemical reactions, and heterogeneous chemical processes that take place among the above chemical species. These chemical processes cause changes in the magnitudes and spatial distributions of chemically and radiatively active tracer gases, which in turn induce temperature and circulation changes in the stratosphere via coupled radiative–dynamical processes. Therefore, complex chemical–radiative–dynamical feedbacks exist in the stratosphere. In the following section, the feedback effects of stratospheric ozone, aerosols and water vapor on the climate system are discussed.

### 3.2. Climate forcing of stratospheric ozone

Stratospheric ozone plays an important role in the global radiative balance of Earth's atmosphere because it can heat the stratosphere by absorbing solar ultraviolet radiation and has a strong infrared radiation absorption band at  $9.6 \mu\text{m}$ , which can change the stratospheric temperature by absorbing and emitting longwave radiation. The anthropogenic emissions of ODSs in the 20th century led to a significant depletion of stratospheric ozone. There has since

been an expected global recovery of mid- and upper-stratospheric ozone under the control of the Montreal Agreement, but a trend of decreasing lower-stratospheric ozone still exists (WMO, 2022). Stratospheric ozone changes exert a direct radiative forcing on the surface climate. de F. Forster and Shine (1997) calculated an annually and globally averaged radiative forcing of stratospheric ozone of  $-0.22 \pm 0.03 \text{ W m}^{-2}$  for the period 1979–96, when stratospheric ozone depletion was at its strongest. The IPCC's Fifth Assessment Report estimated a global mean effective radiative forcing of  $-0.05 \pm 0.10 \text{ W m}^{-2}$  for the period 1750–2011, which is relatively smaller than that of  $\text{CO}_2$  ( $2.16 \pm 0.25 \text{ W m}^{-2}$ ).

Although the above studies suggest that the radiative forcing of stratospheric ozone is marginal, the representation of stratospheric ozone in chemistry–climate models may have a first-order impact on estimates of effective climate sensitivity (e.g., Tian and Chipperfield, 2005; Nowack et al., 2015). Romanowsky et al. (2019) found that including interactive stratospheric ozone chemistry in climate models leads to a significant improvement in their representation of the stratosphere–troposphere coupling induced by Arctic sea-ice loss, as compared to simulations without interactive chemistry, and consequently the reproduction of more realistic mid-latitude atmospheric responses. It has been suggested that climate–ozone feedback may amplify the climatic impacts of stratospheric ozone, since changes in ozone could induce changes in atmospheric circulation and planetary wave propagation through radiative–dynamical feedbacks (Nathan and Cordero, 2007; Albers and Nathan, 2013; Hu et al., 2015). Ozone-induced changes in planetary wave propagation and breaking may act directly on the tropospheric climate through the “downward control” theory (Haynes et al., 1991) or cause convergence and divergence anomalies in the upper tropospheric eddy heat flux and eddy momentum flux (Zhang et al., 2020a), indirectly changing the meridional overturning circulations in the troposphere (Limpasuvan and Hartmann, 2000; Rao and Garfinkel, 2020, 2021b).

The Antarctic ozone hole can exert significant impacts on the atmospheric circulations and the surface climate in the Southern Hemisphere. Because of its radiative cooling effects, stratospheric ozone depletion results in a strengthening of the SPV over the Antarctic. Such a strengthened SPV causes the tropospheric Southern Annular Mode (SAM) to shift toward its positive phase (Thompson et al., 2011), which establishes a linkage between the SPV changes and the surface climate (Son et al., 2010; Thompson et al., 2011). The positive phase of SAM is accompanied with a strengthening of the westerly winds at high latitudes, a southward shift of the subtropical jet stream, and a southward expansion of the Hadley cell in austral summer (Son et al., 2010; Min and Son, 2013; Solomon and Polvani, 2016). Corresponding to such changes in large-scale circulations, a poleward shift of storm track in the Southern Hemisphere was also reported (Grise et al., 2014), with an increase in occurrence probability of cyclones at southern high latitudes (Lynch et al., 2006). The stratospheric ozone depletion may

also favor more Rossby wave breaking events in austral summer on the equatorward side of the southern mid-latitude jet (Ndarana et al., 2012). In addition, the Antarctic ozone hole could also result in an increase in subtropical precipitation and a shift of the subtropical dry zones toward the South Pole in austral summer (Son et al., 2009; Kang et al., 2011; Polvani et al., 2011).

The Antarctic ozone hole may also influence the Antarctic sea ice. Some studies have suggested that the increase in Antarctic sea-ice extent from 1979 to 2015 could be explained by stratospheric ozone depletion and its associated atmospheric circulation changes (Hall and Visbeck, 2002; Turner et al., 2009). However, other model-based studies have argued that the Antarctic ozone hole may have led to higher surface temperatures in the Southern Ocean and thus a decrease in the Antarctic sea ice (Sigmond and Fyfe, 2010; Bitz and Polvani, 2012; Xia et al., 2020). Such contradicting responses of sea ice to stratospheric ozone changes may be due to processes operating on different timescales (Ferreira et al., 2015). On shorter time-scales (months to years), the Antarctic ozone hole leads to anomalous equatorward Ekman transport, reducing the SST around Antarctica in summer. Consequently, sea ice freeze-up the following winter is earlier, and the sea-ice edge, year-round, is situated more to the north than normal. On longer time-scales (years to decades), the surface cooling is replaced by warming associated with enhanced Ekman pumping of relatively warm water beneath the mixed layer, which reduces the Antarctic sea ice (Ferreira et al., 2015). The impacts of stratospheric ozone depletion on sea ice take place not only through ozone-induced changes in surface winds and ocean drifts, but also in relation to increases in cloud in the upper troposphere (Xia et al., 2018, 2020). It is worth noting that stratospheric ozone depletion is unlikely to be the primary driver of the observed Antarctic sea-ice trend (Solomon et al., 2015; Landrum et al., 2017; Seviour et al., 2019). More details about the climatic impacts of the Antarctic ozone hole are discussed in the review by Thompson et al. (2011) and the assessment by WMO (2022).

It is well recognized that the Antarctic ozone hole is recovering as a result of the Montreal Protocol (WMO, 2022). Banerjee et al. (2020) found a “pause” or even a weak “reversal” of the Southern Hemispheric climate trend since the early 2000s due to stratospheric ozone recovery. Their findings provide clear evidence that humans can positively influence Earth’s climate through international cooperation, i.e., the Montreal Protocol has slowed the rate of climate change related to stratospheric ozone depletion. Following that study, other researchers have also reported the climate change trend related to ozone recovery. Zambri et al. (2021) found that the post-2001 increase in ozone has led to significant changes in the trends of stratospheric temperature and circulation over the Southern Hemisphere. Ivanciu et al. (2022) further indicated that the weakening of residual circulation, the equatorward shift and weakening of surface westerly winds, and a decrease in the transport of the Antarctic Circum-

polar Current in the near future are also related to stratospheric ozone recovery. However, not all the climate changes over the Southern Hemisphere in recent decades are associated with Antarctic stratospheric ozone changes. Hu et al. (2022) reported that a weakening of stratospheric planetary wave activities during September since the early 2000s is a response to increases in SST rather than the ozone recovery.

To date, the impacts of Arctic stratospheric ozone changes on the climate system remain insufficiently understood. Using the UK Met Office’s model, Cheung et al. (2014) found that considering stratospheric ozone variability does not significantly improve the weather forecasting skill for the troposphere during spring. In addition, Rao and Garfinkel (2020) indicated that, in models, a good ozone forecast does not ensure a good forecast of surface weather. However, other studies, using chemistry–climate models with coupled chemical–radiative–dynamical processes, have found that Arctic stratospheric ozone depletion can cause positive-phase anomalies in the NAO, a poleward shift of the tropospheric jet stream in the North Atlantic, and warming anomalies over Eurasia (Smith and Polvani, 2014; Calvo et al., 2015; Ivy et al., 2017; Friedel et al., 2022). It has also been reported that springtime Arctic stratospheric ozone depletion can cause an increase in precipitation over northern Europe and the northwestern United States, and a decrease over southern Europe, Eurasia and central China (Xie et al., 2018; Ma et al., 2019; Friedel et al., 2022). These climate responses are closely related to a strengthened SPV and a delayed break-up of the SPV, which result from a cooling of the SPV due to stratospheric ozone depletion. In addition, stratospheric ozone depletion may also affect the position of the Arctic SPV and favor a shift of the SPV towards Siberia (Zhang et al., 2020a).

The changes in the polar vortex associated with Arctic stratospheric ozone depletion may further affect the cryosphere and ocean. A recent study found that strengthening of the Arctic SPV in association with stratospheric ozone depletion may induce reductions in the Arctic sea-ice concentration and sea-ice thickness over the Kara Sea, Laptev Sea and East Siberian Sea from spring to summer (Zhang et al., 2022). Arctic stratospheric ozone depletion may further affect the climate over the North Pacific Ocean. Xie et al. (2017) found that a decrease in Arctic stratospheric ozone in early spring tends to induce a negative North Pacific Oscillation (NPO) anomaly in April via southward propagation of Rossby waves from high latitudes. Wang et al. (2022) proposed that Arctic stratospheric ozone depletion favors negative NPO anomalies through the interactions between synoptic-scale eddies and the mean flow over the North Pacific. The relative contributions of the two abovementioned mechanisms need to be further evaluated in future studies. Furthermore, ozone-related negative NPO anomalies force positive Victoria mode–like SST anomalies in the North Pacific through modulating the surface heat flux (Xie et al., 2017) and surface ocean current (Wang et al., 2022), which then induces El Niño-like SST anomalies 20 months

later (Xie et al., 2016). The main climatic impacts of polar stratospheric ozone depletion on tropospheric and surface climate are summarized in Fig. 5.

### 3.3. Climatic impacts of stratospheric water vapor

Although the concentrations of stratospheric water vapor are rather small, it too can modulate the radiative energy budget of the climate system (de F. Forster and Shine, 1999; Solomon et al., 2010; Dessler et al., 2013; Hegglin et al., 2014). Considering the uncertainty due to calculation methods and various forcings, the total stratospheric water vapor forcing reported by the IPCC's Sixth Assessment Report is  $0.05 \pm 0.05 \text{ W m}^{-2}$ . In addition, tropospheric temperature increases may cause more water vapor to enter the stratosphere, implying the existence of feedback between stratospheric water vapor and tropospheric climate (Garfinkel et al., 2021). Dessler et al. (2013) estimated the strength of this feedback in a chemistry–climate model to be  $0.3 \text{ W (m}^2 \text{ K)}^{-1}$ , which would be a significant contribution to the overall climate sensitivity. However, some studies have argued that its associated surface warming effect is not as significant as previously thought, which is due to compensating effects of cloud feedbacks induced by water vapor (Huang et al., 2020; Li and Newman, 2020). On the other hand, increases in stratospheric water vapor could reduce the temperature in the stratosphere since it is also a GHG. However, studies have reported that estimated radiative cooling rates of water vapor in the stratosphere vary considerably among different numerical models (Huang et al., 2016, 2020; Banerjee et al., 2019; Li and Newman, 2020; Wang and Huang, 2020). For example, de F. Forster and Shine (2002) found that an average

increase of 0.7 ppmv in stratospheric water vapor could result in a maximum stratospheric cooling of approximately 0.8 K. Following that study, Tian et al. (2009) took the chemical–radiative–dynamical feedbacks of stratospheric water vapor into account and estimated that a 2.0 ppmv increase in stratospheric water vapor can cause a maximum cooling of 4.0 K. Maycock et al. (2014) estimated that the net increase in stratospheric water vapor from 1980 to 2010 cooled the lower stratosphere by up to approximately 0.2 K  $(10 \text{ yr})^{-1}$  in global and annual mean terms, which was approximately 40% of the observed cooling trend over this period.

Furthermore, stratospheric water vapor changes could significantly affect ozone concentrations in the stratosphere (Kirk-Davidoff et al., 1999; Vogel et al., 2011; Rosenlof, 2018). Increased stratospheric water vapor improves the  $\text{HO}_x$  level and thereby decreases ozone in the upper and lower stratosphere (Dvortsov and Solomon, 2001; Ito and Matsuzaki, 2015). Stratospheric water vapor also affects ozone indirectly by cooling the stratosphere, which in turn modulates the rates of gas-phase reactions (Dessler et al., 2013; Gilford et al., 2016). In addition, increased water vapor may enhance the areas of polar stratospheric cloud particles and increase the heterogeneous reaction rates, leading to more chlorine activation and stronger polar ozone loss (Tian et al., 2009; Vogel et al., 2011; Drdla and Müller, 2012). The above processes may change ozone–climate feedbacks and give rise to further climate changes.

### 3.4. Climatic impacts of GHGs in the stratosphere

Changes in GHGs, including  $\text{CO}_2$ ,  $\text{CH}_4$ ,  $\text{N}_2\text{O}$  and halocar-

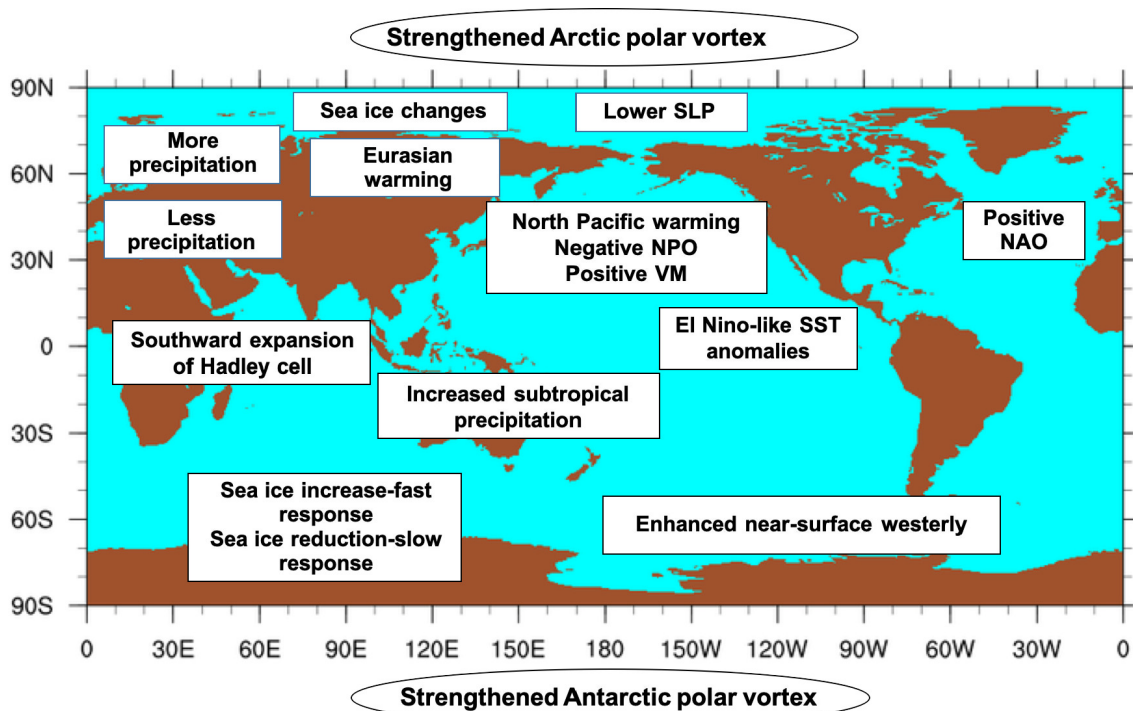


Fig. 5. Schematic of the tropospheric and surface climate changes associated with Antarctic or Arctic stratospheric ozone depletion.



bons, could also alter the chemical composition and chemical–radiative–dynamical feedback processes in the stratosphere. First, halocarbons are the major gases responsible for stratospheric ozone depletion, while  $\text{N}_2\text{O}$  increases  $\text{NO}_x$  concentrations after stratospheric photolysis and also decreases stratospheric ozone. WMO (2022) documented that the ozone depletion potential of anthropogenic  $\text{N}_2\text{O}$  emissions in 2020 were more than two times as large as that of all CFCs in that year. In the future, as halocarbons continue to decrease, the contribution of  $\text{N}_2\text{O}$  to stratospheric ozone depletion may be more important (Wang et al., 2014).  $\text{CH}_4$  can be photolyzed in the upper stratosphere, increasing the concentration of  $\text{HO}_x$  and thus ozone depletion. An increase in GHGs would reduce the stratospheric temperature and weaken the rate of gas-phase chemical reactions, leading to a “super-recovery” of stratospheric ozone (Shepherd, 2008; Li et al., 2009; Chipperfield et al., 2017). Furthermore, greater quantities of GHGs may increase the frequency of planetary waves entering the stratosphere and accelerate the BD circulation in the stratosphere (Rind et al., 1990; Butchart, 2014; Hardiman et al., 2014), thereby affecting the distributions of stratospheric chemical components. As a result, stratospheric ozone changes and chemical–climate interactions in the future are likely to be highly complex. Multiple chemistry–climate models project that the stratospheric ozone recovery will depend on the future climate change scenario (Dhomse et al., 2018; Keeble et al., 2021). However, it is worth mentioning that there is large uncertainty in future projections of Arctic stratospheric ozone changes. Most chemistry–climate model simulations indicate that increases in GHGs will mean Arctic ozone recovers to its 1980 level earlier than Antarctic ozone does, by slowing down the gas-phase chemical depletion rate of ozone and enhancing the BD circulation (WMO, 2022). However, the cooling effects in the polar lower stratosphere induced by increasing GHGs, combined with increasing stratospheric water vapor, may increase the probability of polar stratospheric cloud occurrence, enhance heterogeneous chemistry, and deplete polar ozone (Tian et al., 2009; Vogel et al., 2011; von der Gathen et al., 2021). von der Gathen et al. (2021) showed that local maxima of polar stratospheric cloud formation potential in the Arctic tends to increase in the future under high GHG emission scenarios.

### 3.5. Climatic impacts of stratospheric aerosols

Stratospheric sulfate aerosols are highly reflective in the visible and ultraviolet bands, which reduces the amount of solar radiation reaching Earth’s surface at timescales of months to years. Previous studies have reported a significant negative effective radiative forcing of about  $-20 \text{ W m}^{-2}$  per unit of stratospheric AOD during volcanically active periods (Gregory et al., 2016; Larson and Portmann, 2016; Schmidt et al., 2018; Marshall et al., 2020), although this may not be a linear relationship for large eruptions (Marshall et al., 2020). Consequently, a general surface cooling can be observed after a volcanic eruption, and this surface cooling can last two to three years after a large eruption (Robock and Mao, 1995). For example, global mean air temperatures

were reduced by up to  $0.5^\circ\text{C}$  at the surface and  $0.6^\circ\text{C}$  in the troposphere following the eruption of Mount Pinatubo (Parker et al., 1996). Yu et al. (2016) estimated that stratospheric aerosols have led to a radiative forcing of  $-0.072 \text{ W m}^{-2}$  since 1850. However, a warmer winter after eruptions in Northern Hemispheric continents has also been reported, which is a result of the enhanced pole-to-equator temperature gradient and thereby a stronger polar vortex (Robock and Mao, 1992; Robock, 2000). However, the significance of this warming is doubtful and uncertain, and some recent studies have argued, based on models with a relatively higher resolution, that the warming of Northern Hemispheric continents is very small for eruptions such as Pinatubo or Krakatau (Polvani et al., 2019; Azoulay et al., 2021; DallaSantana and Polvani, 2022).

Stratospheric aerosols may also affect regional and global precipitation. For instance, it was reported that monsoon precipitation tends to decrease following large eruptions in the same hemisphere (Trenberth and Dai, 2007; Joseph and Zeng, 2011; Iles et al., 2013; Man et al., 2014; Yang et al., 2022), while significantly intensified monsoon precipitation is found when large volcanic forcing occurs in the other hemisphere or the tropics (Liu et al., 2016, 2022). But what causes this hemispheric asymmetric response of precipitation to volcanic forcing? Stratospheric aerosols emitted by large eruptions can reduce the incoming shortwave radiation and weaken the land–sea thermal contrast in the same hemisphere, leading to decreases in monsoon rainfall (Iles et al., 2013; Man et al., 2014; Yang et al., 2022). On the other hand, an eruption occurring in one hemisphere enhances the hemispheric thermal contrast and drives cross-equatorial flows that converge into the monsoon trough, favoring more precipitation in the counter hemisphere (Liu et al., 2016). Overall, the precipitation response to volcanic aerosols in the stratosphere is the result of a complex combination of multiple processes including radiative and dynamical effects, which remain poorly understood.

In addition, stratospheric aerosols may modulate stratospheric ozone–climate interactions through chemical–radiative–dynamical coupling processes. Volcanic aerosols might provide an additional surface area density for heterogeneous chemistry, thus accelerating the hydrolysis of dinitrogen pentoxide and the release of active halogens, which would decrease the stratospheric ozone (e.g., Aquila et al., 2013; Tilmes et al., 2018; Kilian et al., 2020). On the other hand, volcanic sulfate aerosols heat the lower stratosphere and accelerate the BD circulation that transports more ozone to higher latitudes (Aquila et al., 2012, 2013; Muthers et al., 2015; Kilian et al., 2020).

## 4. Concluding remarks

This review summarizes the main advances in stratosphere–troposphere coupling and stratospheric chemistry–climate interactions, and discusses some relevant outstanding issues and grand challenges. These new advances and devel-

opments in stratospheric processes and their role in climate changes imply that climate prediction skill could be improved on sub-seasonal, seasonal, decadal, and even multi-decadal time scales when stratospheric processes and signals are taken into account. The SPV/SSW, QBO, BDC, and stratospheric air intrusion, in particular, have important impacts on tropospheric weather and climate at various time scales ranging from synoptic to interannual. At even longer time scales, the changes in stratospheric composition, particularly that of ozone, aerosols and water vapor, can modulate global climatic variability and trends via complex chemical–radiative–dynamic feedbacks, and are hence potentially useful for improving the long-term predictability of Earth’s climate. However, applying stratospheric information in operational S2S forecast models remains a challenge, partly because of the complexity of the physical mechanisms responsible for the stratosphere–troposphere coupling. Another reason is that better forecasting of the stratosphere on S2S time scales has not yet been achieved. The latest generation chemistry–climate models are still unable to reproduce well important aspects of the chemical and physical climate of the stratosphere. For instance, because of the relatively coarse spatial and temporal grid resolutions of some chemistry–climate models, stratospheric gravity waves that occur on scales smaller than the model resolution cannot be resolved, which to some degree introduces uncertainty and potential bias (e.g., Wang et al., 2023). In addition, in most models, the QBO’s period and amplitude are not well simulated. For aspects of stratospheric chemistry, previous studies have identified that the latest generation chemistry–climate models have difficulty in simulating polar stratospheric clouds and heterogeneous reactions that take place on modeled polar stratospheric cloud surfaces.

Some of the mechanisms through which stratospheric processes modulate tropospheric weather and climate have been revealed in recent years. Stratosphere–troposphere coupling works at various time scales, and different coupled processes have different mechanisms and pathways depending

on the time scale. At synoptic to sub-seasonal time scales, robust evidence exists that SPV anomalies, SSW events in particular, correlate closely with tropospheric weather and climate changes at lead times of more than at least 15 days. At interannual time scales, the QBO plays a dominant role in stratosphere–troposphere interaction, especially in the tropics. BD circulation, which is the primary control of stratosphere–troposphere mass exchange (STE), can also act as a dynamical bridge between the tropical and polar stratosphere. Despite the above knowledge, the thermodynamic mechanisms by which temperature and circulation anomalies in the stratosphere impact surface weather and climate are still not fully understood, and more studies are needed in the future.

There also exists convincing evidence that the stratosphere itself is cooling with increasing concentrations of GHGs, while stratospheric ozone has stopped its decline since the 2000s. In response to the increased concentrations of GHGs and the ozone decline since the 1980s, some climatic factors and processes have exhibited evident trends both in the stratosphere and troposphere. The depletion of ozone in the Antarctic, in particular, has induced significant climate changes in the Southern Hemisphere. In recent years, it has been revealed that variations in Arctic stratospheric ozone have also had important impacts on the weather and climate in the Northern Hemisphere. Arctic stratospheric ozone variations could even cause changes in SSTs and ocean currents over the North Pacific. On the other hand, a slow recovery signal in stratospheric ozone has been noted in the past two decades, but its recovery process and significance still possess many uncertainties and close attention should be paid to the climatic impacts of the ozone recovery in the future. Meanwhile, the several extreme low events of the Arctic stratospheric ozone have been observed in recent years. Whether or not extremes of Arctic stratospheric ozone will appear more frequently and whether those extremes will exert an impact on the weather and climate in the Northern Hemisphere should be carefully monitored.

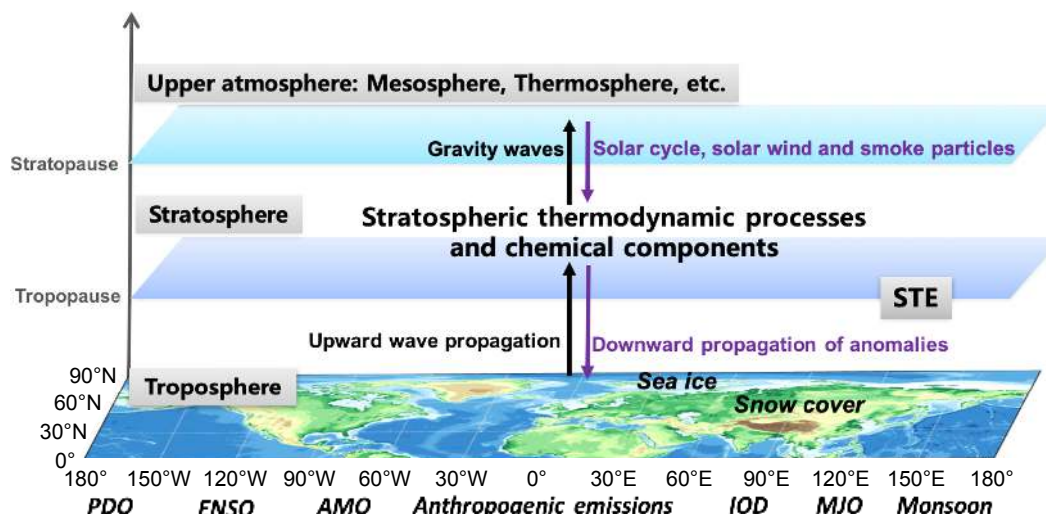


Fig. 6. Schematic of the role of the stratosphere in whole-atmosphere interactions at different time scales.



Apart from ozone, the climatic impact of stratospheric water vapor and aerosols has emerged as another hot topic in recent years. Stratospheric water vapor is increasing with climate warming, while stratospheric aerosols have large variability owing to highly varying natural and anthropogenic emissions. So far, the quantitative contributions of stratospheric aerosols and water vapor to radiative forcing have been reasonably well quantified, but large uncertainties in their short-term and long-term impacts on climate remain. The climatic impacts of stratospheric aerosols and water vapor, including the potential for catastrophic climate impacts following a major volcanic event, and stratospheric smoke from extreme fires, have become a challenging issue.

Finally, from these new advances and knowledge with respect to the role of stratospheric processes in climate, we can see that stratosphere–troposphere coupling is also modulated by land surface and oceanic processes (e.g., snow cover and sea ice), the atmospheric processes above the middle atmosphere, the solar cycle, solar wind, and the meteoric rise in smoke particles (see Fig. 6). The interactions of the whole atmosphere need to be considered in future for a better and more thorough understanding of stratosphere–troposphere coupling. The most important issues worth our attention at present include (1) developing high-top models with good presentation of the stratosphere and even the upper atmosphere for the purpose of applying stratospheric information in operational S2S forecasting; (2) close monitoring of short-term and long-term changes in stratospheric constituents for the purpose of improving climate predictions and projections; and (3) in-depth investigations of atmospheric processes in the upper atmosphere, including the stratosphere and beyond, for the purpose of developing/improving whole-atmosphere climate models.

**Acknowledgements.** This work was supported by the National Natural Science Foundation of China (Grant Nos. 42175089, 42121004 and 42142038).

**Open Access** This article is licensed under a Creative Commons Attribution 4.0 International License, which permits use, sharing, adaptation, distribution and reproduction in any medium or format, as long as you give appropriate credit to the original author(s) and the source, provide a link to the Creative Commons licence, and indicate if changes were made. The images or other third party material in this article are included in the article's Creative Commons licence, unless indicated otherwise in a credit line to the material. If material is not included in the article's Creative Commons licence and your intended use is not permitted by statutory regulation or exceeds the permitted use, you will need to obtain permission directly from the copyright holder. To view a copy of this licence, visit <http://creativecommons.org/licenses/by/4.0/>.

## REFERENCES

- Abhik, S., H. H. Hendon, and M. C. Wheeler, 2019: On the sensitivity of convectively coupled equatorial waves to the Quasi-Biennial Oscillation. *J. Climate*, **32**, 5833–5847, <https://doi.org/10.1175/JCLI-D-19-0010.1>.
- Akritidis, D., A. Pozzer, and P. Zanis, 2019: On the impact of future climate change on tropopause folds and tropospheric ozone. *Atmospheric Chemistry and Physics*, **19**, 14 387–14 401, <https://doi.org/10.5194/acp-19-14387-2019>.
- Albers, J. R., and T. R. Nathan, 2013: Ozone loss and recovery and the preconditioning of upward-propagating planetary wave activity. *J. Atmos. Sci.*, **70**, 3977–3994, <https://doi.org/10.1175/JAS-D-12-0259.1>.
- Andrews, D. G., and M. E. McIntyre, 1976: Planetary waves in horizontal and vertical shear: The generalized Eliassen-Palm relation and the mean zonal acceleration. *J. Atmos. Sci.*, **33**, 2031–2048, [https://doi.org/10.1175/1520-0469\(1976\)033<2031:PWIHAV>2.0.CO;2](https://doi.org/10.1175/1520-0469(1976)033<2031:PWIHAV>2.0.CO;2).
- Andrews, D. G., and M. E. McIntyre, 1978a: Generalized Eliassen-Palm and Charney-Drazin theorems for waves on Axisymmetric mean flows in compressible atmospheres. *J. Atmos. Sci.*, **35**, 175–185, [https://doi.org/10.1175/1520-0469\(1978\)035<0175:GEPACD>2.0.CO;2](https://doi.org/10.1175/1520-0469(1978)035<0175:GEPACD>2.0.CO;2).
- Andrews, D. G., and M. E. McIntyre, 1978b: On wave-action and its relatives. *J. Fluid Mech.*, **89**, 647–664, <https://doi.org/10.1017/S0022112078002785>.
- Angell, J. K., and J. Korshover, 1964: Quasi-biennial variations in temperature, total ozone, and tropopause height. *J. Atmos. Sci.*, **21**, 479–492, [https://doi.org/10.1175/1520-0469\(1964\)021<0479:QBVITT>2.0.CO;2](https://doi.org/10.1175/1520-0469(1964)021<0479:QBVITT>2.0.CO;2).
- Anstey, J. A., and Coauthors, 2022: Impacts, processes and projections of the Quasi-Biennial Oscillation. *Nature Reviews Earth & Environment*, **3**, 588–603, <https://doi.org/10.1038/s43017-022-00323-7>.
- Antonescu, B., G. Vaughan, and D. M. Schultz, 2013: A five-year radar-based climatology of tropopause folds and deep convection over Wales, United Kingdom. *Mon. Wea. Rev.*, **141**, 1693–1707, <https://doi.org/10.1175/MWR-D-12-00246.1>.
- Aquila, V., L. D. Oman, R. S. Stolarski, P. R. Colarco, and P. A. Newman, 2012: Dispersion of the volcanic sulfate cloud from a Mount Pinatubo–like eruption. *J. Geophys. Res.: Atmos.*, **117**, D06216, <https://doi.org/10.1029/2011JD016968>.
- Aquila, V., L. D. Oman, R. Stolarski, A. R. Douglass, and P. A. Newman, 2013: The response of ozone and nitrogen dioxide to the eruption of Mt. Pinatubo at Southern and Northern Mid-latitudes. *J. Atmos. Sci.*, **70**, 894–900, <https://doi.org/10.1175/JAS-D-12-0143.1>.
- Aubry, T. J., J. Staunton-Sykes, L. R. Marshall, J. Haywood, N. L. Abraham, and A. Schmidt, 2021: Climate change modulates the stratospheric volcanic sulfate aerosol lifecycle and radiative forcing from tropical eruptions. *Nature Communications*, **12**, 4708, <https://doi.org/10.1038/s41467-021-24943-7>.
- Austin, J., 2002: A three-dimensional coupled chemistry–climate model simulation of past stratospheric trends. *J. Atmos. Sci.*, **59**, 218–232, [https://doi.org/10.1175/1520-0469\(2002\)059<0218:ATDCCC>2.0.CO;2](https://doi.org/10.1175/1520-0469(2002)059<0218:ATDCCC>2.0.CO;2).
- Ayazragüena, B., U. Langematz, S. Meul, S. Oberländer, J. Abalichin, and A. Kubin, 2013: The role of climate change and ozone recovery for the future timing of major stratospheric warmings. *Geophys. Res. Lett.*, **40**, 2460–2465, <https://doi.org/10.1002/grl.50477>.
- Ayazragüena, B., and Coauthors, 2018: No robust evidence of future changes in major stratospheric sudden warmings: A

Abhik, S., H. H. Hendon, and M. C. Wheeler, 2019: On the sensitivity of convectively coupled equatorial waves to the Quasi-Biennial Oscillation. *J. Climate*, **32**, 5833–5847, <https://doi.org/10.1175/JCLI-D-19-0010.1>.

- multi-model assessment from CCM1. *Atmospheric Chemistry and Physics*, **18**, 11 277–11 287, <https://doi.org/10.5194/acp-18-11277-2018>.
- Ayarzagüena, B., and Coauthors, 2020: Uncertainty in the response of sudden stratospheric warmings and stratosphere-troposphere coupling to quadrupled CO<sub>2</sub> concentrations in CMIP6 models. *J. Geophys. Res.: Atmos.*, **125**, e2019JD032345, <https://doi.org/10.1029/2019JD032345>.
- Azoulay, A., H. Schmidt, and C. Timmreck, 2021: The Arctic polar vortex response to volcanic forcing of different strengths. *J. Geophys. Res.: Atmos.*, **126**, e2020JD034450, <https://doi.org/10.1029/2020JD034450>.
- Baldwin, M. P., and T. J. Dunkerton, 2001: Stratospheric harbingers of anomalous weather regimes. *Science*, **294**, 581–584, <https://doi.org/10.1126/science.1063315>.
- Baldwin, M. P., and D. W. J. Thompson, 2009: A critical comparison of stratosphere–troposphere coupling indices. *Quart. J. Roy. Meteor. Soc.*, **135**, 1661–1672, <https://doi.org/10.1002/qj.479>.
- Baldwin, M. P., M. Dameris, and T. G. Shepherd, 2007: How will the stratosphere affect climate change? *Science*, **316**, 1576–1577, <https://doi.org/10.1126/science.1144303>.
- Baldwin, M. P., and Coauthors, 2001: The Quasi-Biennial Oscillation. *Rev. Geophys.*, **39**, 179–229, <https://doi.org/10.1029/1999RG000073>.
- Baldwin, M. P., and Coauthors, 2019: 100 years of progress in understanding the stratosphere and mesosphere. *Meteor. Monogr.*, **59**, 27.1–27.62, <https://doi.org/10.1175/AMSMONOGRAPHS-D-19-0003.1>.
- Baldwin, M. P., and Coauthors, 2021: Sudden stratospheric warmings. *Rev. Geophys.*, **59**, e2020RG000708, <https://doi.org/10.1029/2020RG000708>.
- Ball, W. T., and Coauthors, 2018: Evidence for a continuous decline in lower stratospheric ozone offsetting ozone layer recovery. *Atmospheric Chemistry and Physics*, **18**, 1379–1394, <https://doi.org/10.5194/acp-18-1379-2018>.
- Banerjee, A., J. C. Fyfe, L. M. Polvani, D. Waugh, and K.-L. Chang, 2020: A pause in Southern Hemisphere circulation trends due to the Montreal Protocol. *Nature*, **579**, 544–548, <https://doi.org/10.1038/s41586-020-2120-4>.
- Banerjee, A., G. Chiodo, M. Previdi, M. Ponater, A. J. Conley, and L. M. Polvani, 2019: Stratospheric water vapor: An important climate feedback. *Climate Dyn.*, **53**, 1697–1710, <https://doi.org/10.1007/s00382-019-04721-4>.
- Belmont, A. D., and D. G. Dartt, 1968: Variation with longitude of the Quasi-Biennial Oscillation. *Mon. Wea. Rev.*, **96**, 767–777, [https://doi.org/10.1175/1520-0493\(1968\)096<0767:VWLOTQ>2.0.CO;2](https://doi.org/10.1175/1520-0493(1968)096<0767:VWLOTQ>2.0.CO;2).
- Bitz, C. M., and L. M. Polvani, 2012: Antarctic climate response to stratospheric ozone depletion in a fine resolution ocean climate model. *Geophys. Res. Lett.*, **39**, L20705, <https://doi.org/10.1029/2012GL053393>.
- Boyd, J. P., 1976: The noninteraction of waves with the zonally averaged flow on a spherical earth and the interrelationships on eddy fluxes of energy, heat and momentum. *J. Atmos. Sci.*, **33**, 2285–2291, [https://doi.org/10.1175/1520-0469\(1976\)033<2285:TNOWWT>2.0.CO;2](https://doi.org/10.1175/1520-0469(1976)033<2285:TNOWWT>2.0.CO;2).
- Brewer, A. W., 1949: Evidence for a world circulation provided by the measurements of helium and water vapour distribution in the stratosphere. *Quart. J. Roy. Meteor. Soc.*, **75**, 351–363, <https://doi.org/10.1002/qj.49707532603>.
- Butchart, N., 2014: The Brewer–Dobson circulation. *Rev. Geophys.*, **52**, 157–184, <https://doi.org/10.1002/2013RG000448>.
- Butchart, N., 2022: The stratosphere: A review of the dynamics and variability. *Weather and Climate Dynamics*, **3**, 1237–1272, <https://doi.org/10.5194/wcd-3-1237-2022>.
- Butchart, N., and A. A. Scaife, 2001: Removal of chlorofluorocarbons by increased mass exchange between the stratosphere and troposphere in a changing climate. *Nature*, **410**, 799–802, <https://doi.org/10.1038/35071047>.
- Butchart, N., and Coauthors, 2010: Chemistry–climate model simulations of twenty-first century stratospheric climate and circulation changes. *J. Climate*, **23**, 5349–5374, <https://doi.org/10.1175/2010JCLI3404.1>.
- Butler, A., and Coauthors, 2019: Sub-seasonal predictability and the stratosphere. *Sub-Seasonal to Seasonal Prediction*, A. W. Robertson and F. Vitart, Eds., Elsevier, 223–241, <https://doi.org/10.1016/B978-0-12-811714-9.00011-5>.
- Butler, A. H., and E. P. Gerber, 2018: Optimizing the definition of a sudden stratospheric warming. *J. Climate*, **31**, 2337–2344, <https://doi.org/10.1175/JCLI-D-17-0648.1>.
- Butler, A. H., D. J. Seidel, S. C. Hardiman, N. Butchart, T. Birner, and A. Match, 2015: Defining sudden stratospheric warmings. *Bull. Amer. Meteor. Soc.*, **96**, 1913–1928, <https://doi.org/10.1175/BAMS-D-13-00173.1>.
- Calvo, N., L. M. Polvani, and S. Solomon, 2015: On the surface impact of Arctic stratospheric ozone extremes. *Environmental Research Letters*, **10**, 094003, <https://doi.org/10.1088/1748-9326/10/9/094003>.
- Charlton, A. J., and L. M. Polvani, 2007: A new look at stratospheric sudden warmings. Part I: Climatology and modeling benchmarks. *J. Climate*, **20**, 449–469, <https://doi.org/10.1175/JCLI3996.1>.
- Charlton-Perez, A. J., L. Ferranti, and R. W. Lee, 2018: The influence of the stratospheric state on North Atlantic weather regimes. *Quart. J. Roy. Meteor. Soc.*, **144**, 1140–1151, <https://doi.org/10.1002/qj.3280>.
- Charney, J. G., and P. G. Drazin, 1961: Propagation of planetary-scale disturbances from the lower into the upper atmosphere. *J. Geophys. Res.*, **66**, 83–109, <https://doi.org/10.1029/JZ066i001p00083>.
- Chen, W., and T. M. Li, 2007: Modulation of northern hemisphere wintertime stationary planetary wave activity: East Asian climate relationships by the Quasi-Biennial Oscillation. *J. Geophys. Res.: Atmos.*, **112**, D20120, <https://doi.org/10.1029/2007JD008611>.
- Chen, W., and K. Wei, 2009: Interannual variability of the winter stratospheric polar vortex in the Northern Hemisphere and their relations to QBO and ENSO. *Adv. Atmos. Sci.*, **26**, 855–863, <https://doi.org/10.1007/s00376-009-8168-6>.
- Cheung, J. C. H., J. D. Haigh, and D. R. Jackson, 2014: Impact of EOS MLS ozone data on medium-extended range ensemble weather forecasts. *J. Geophys. Res.: Atmos.*, **119**, 9253–9266, <https://doi.org/10.1002/2014JD021823>.
- Chipperfield, M. P., and Coauthors, 2017: Detecting recovery of the stratospheric ozone layer. *Nature*, **549**, 211–218, <https://doi.org/10.1038/nature23681>.
- Chipperfield, M. P., and Coauthors, 2018: On the cause of recent variations in lower stratospheric ozone. *Geophys. Res. Lett.*, **45**, 5718–5726, <https://doi.org/10.1029/2018GL078071>.
- Collimore, C. C., D. W. Martin, M. H. Hitchman, A. Huesmann, and D. E. Waliser, 2003: On the relationship between the QBO and tropical deep convection. *J. Climate*, **16**, 2552–2568, [https://doi.org/10.1175/1520-0442\(2003\)016<2552-2568](https://doi.org/10.1175/1520-0442(2003)016<2552-2568).

552:OTRBTQ>2.0.CO;2.

- DallaSanta, K., and L. M. Polvani, 2022: Volcanic stratospheric injections up to 160Tg(S) yield a Eurasian winter warming indistinguishable from internal variability. *Atmospheric Chemistry and Physics*, **22**, 8843–8862, <https://doi.org/10.5194/acp-22-8843-2022>.
- de F. Forster, P. M., and K. P. Shine, 1997: Radiative forcing and temperature trends from stratospheric ozone changes. *J. Geophys. Res.: Atmos.*, **102**, 10 841–10 855, <https://doi.org/10.1029/96JD03510>. <https://doi.org/10.1029/96JD03510>.
- de F. Forster, P. M., and K. P. Shine, 1999: Stratospheric water vapour changes as a possible contributor to observed stratospheric cooling. *Geophys. Res. Lett.*, **26**, 3309–3312, <https://doi.org/10.1029/1999GL010487>.
- de F. Forster, P. M., and K. P. Shine, 2002: Assessing the climate impact of trends in stratospheric water vapor. *Geophys. Res. Lett.*, **29**, 10-1–10-4, <https://doi.org/10.1029/2001GL013909>.
- Densmore, C. R., E. R. Sanabia, and B. S. Barrett, 2019: QBO influence on MJO amplitude over the maritime continent: Physical mechanisms and seasonality. *Mon. Wea. Rev.*, **147**, 389–406, <https://doi.org/10.1175/MWR-D-18-0158.1>.
- Deshler, T., M. E. Hervig, D. J. Hofmann, J. M. Rosen, and J. B. Liley, 2003: Thirty years of in situ stratospheric aerosol size distribution measurements from Laramie, Wyoming (41°N), using balloon-borne instruments. *J. Geophys. Res.: Atmos.*, **108**, 4167, <https://doi.org/10.1029/2002JD002514>.
- Dessler, A. E., M. R. Schoeberl, T. Wang, S. M. Davis, and K. H. Rosenlof, 2013: Stratospheric water vapor feedback. *Proceedings of the National Academy of Sciences of the United States of America*, **110**, 18 087–18 091, <https://doi.org/10.1073/pnas.1310344110>.
- Dhomse, S. S., and Coauthors, 2018: Estimates of ozone return dates from Chemistry–Climate Model Initiative simulations. *Atmospheric Chemistry and Physics*, **18**, 8409–8438, <https://doi.org/10.5194/acp-18-8409-2018>.
- Dobson, G. M. B., 1956: Origin and distribution of the polyatomic molecules in the atmosphere. *Proceedings of the Royal Society of London. Series A. Mathematical and Physical Sciences*, **236**, 187–193, <https://doi.org/10.1098/rspa.1956.0127>.
- Dobson, G. M. B., and D. N. Harrison, 1926: Measurements of the amount of ozone in the earth's atmosphere and its relation to other geophysical conditions. *Proceedings of the Royal Society of London. Series A, Containing Papers of a Mathematical and Physical Character*, **110**, 660–693, <https://doi.org/10.1098/rspa.1926.0040>.
- Domeisen, D. I. V., and A. H. Butler, 2020: Stratospheric drivers of extreme events at the Earth's surface. *Communications Earth & Environment*, **1**, 59, <https://doi.org/10.1038/s43247-020-00060-z>.
- Domeisen, D. I. V., and Coauthors, 2020a: The role of the stratosphere in subseasonal to seasonal prediction: 2. Predictability arising from stratosphere-troposphere coupling. *J. Geophys. Res.: Atmos.*, **125**, e2019JD030923, <https://doi.org/10.1029/2019JD030923>.
- Domeisen, D. I. V., and Coauthors, 2020b: The role of the stratosphere in subseasonal to seasonal prediction: 1. Predictability of the stratosphere. *J. Geophys. Res.: Atmos.*, **125**, e2019JD030920, <https://doi.org/10.1029/2019JD030920>.
- Douglass, A. R., R. S. Stolarski, M. R. Schoeberl, C. H. Jackman, M. L. Gupta, P. A. Newman, J. E. Nielsen, and E. L. Fleming, 2008: Relationship of loss, mean age of air and the distribution of CFCs to stratospheric circulation and implications for atmospheric lifetimes. *J. Geophys. Res.: Atmos.*, **113**, D14309, <https://doi.org/10.1029/2007JD009575>.
- Drdla, K., and R. Müller, 2012: Temperature thresholds for chlorine activation and ozone loss in the polar stratosphere. *Ann. Geophys.*, **30**, 1055–1073, <https://doi.org/10.5194/angeo-30-1055-2012>.
- Dvortsov, V. L., and S. Solomon, 2001: Response of the stratospheric temperatures and ozone to past and future increases in stratospheric humidity. *J. Geophys. Res.: Atmos.*, **106**, 7505–7514, <https://doi.org/10.1029/2000JD900637>.
- Ebdon, R. A., 1960: Notes on the wind flow at 50 mb in tropical and sub-tropical regions in January 1957 and January 1958. *Quart. J. Roy. Meteor. Soc.*, **86**, 540–542, <https://doi.org/10.1002/qj.49708637011>.
- Ebdon, R. A., and R. G. Veryard, 1961: Fluctuations in equatorial stratospheric winds. *Nature*, **189**, 791–793, <https://doi.org/10.1038/189791a0>.
- Ferreira, D., J. Marshall, C. M. Bitz, S. Solomon, and A. Plumb, 2015: Antarctic Ocean and sea ice response to ozone depletion: A two-time-scale problem. *J. Climate*, **28**, 1206–1226, <https://doi.org/10.1175/JCLI-D-14-00313.1>.
- Friedel, M., G. Chiodo, A. Stenke, D. I. V. Domeisen, S. Fueglistaler, J. G. Anet, and T. Peter, 2022: Springtime arctic ozone depletion forces northern hemisphere climate anomalies. *Nature Geoscience*, **15**, 541–547, <https://doi.org/10.1038/s41561-022-00974-7>.
- Fu, Q., S. Solomon, H. A. Pahlavan, and P. Lin, 2019: Observed changes in Brewer–Dobson circulation for 1980–2018. *Environmental Research Letters*, **14**, 114026, <https://doi.org/10.1088/1748-9326/ab4de7>.
- Garfinkel, C. I., and D. L. Hartmann, 2011: The Influence of the Quasi-Biennial Oscillation on the troposphere in winter in a hierarchy of models. Part I: Simplified dry GCMs. *J. Atmos. Sci.*, **68**, 1273–1289, <https://doi.org/10.1175/2011JAS3665.1>.
- Garfinkel, C. I., T. A. Shaw, D. L. Hartmann, and D. W. Waugh, 2012: Does the Holton–Tan mechanism explain how the Quasi-Biennial Oscillation modulates the Arctic polar vortex? *J. Atmos. Sci.*, **69**, 1713–1733, <https://doi.org/10.1175/JAS-D-11-0209.1>.
- Garfinkel, C. I., S.-W. Son, K. Song, V. Aquila, and L. D. Oman, 2017: Stratospheric variability contributed to and sustained the recent hiatus in Eurasian winter warming. *Geophys. Res. Lett.*, **44**, 374–382, <https://doi.org/10.1002/2016GL072035>.
- Garfinkel, C. I., and Coauthors, 2021: Influence of the El Niño–Southern Oscillation on entry stratospheric water vapor in coupled chemistry–ocean CCM1 and CMIP6 models. *Atmospheric Chemistry and Physics*, **21**, 3725–3740, <https://doi.org/10.5194/acp-21-3725-2021>.
- Gilford, D. M., S. Solomon, and R. W. Portmann, 2016: Radiative impacts of the 2011 abrupt drops in water vapor and ozone in the tropical tropopause layer. *J. Climate*, **29**, 595–612, <https://doi.org/10.1175/JCLI-D-15-0167.1>.
- Giorgetta, M. A., L. Bengtsson, and K. Arpe, 1999: An investigation of QBO signals in the East Asian and Indian monsoon in GCM experiments. *Climate Dyn.*, **15**, 435–450, <https://doi.org/10.1007/s003820050292>.
- Gray, L. J., J. A. Anstey, Y. Kawatani, H. Lu, S. Osprey, and V. Schenzinger, 2018: Surface impacts of the Quasi Biennial Oscillation. *Atmospheric Chemistry and Physics*, **18**, 8227–8247, <https://doi.org/10.5194/acp-18-8227-2018>.



- Gregory, J. M., Andrews, T., Good, P., Mauritsen, T., and Forster, P. M., 2016: Small global-mean cooling due to volcanic radiative forcing. *Climate Dyn.*, **47**, 3979–3991, <https://doi.org/10.1007/s00382-016-3055-1>.
- Grise, K. M., S.-W. Son, G. J. P. Correa, and L. M. Polvani, 2014: The response of extratropical cyclones in the Southern Hemisphere to stratospheric ozone depletion in the 20th century. *Atmospheric Science Letters*, **15**, 29–36, <https://doi.org/10.1002/asl2.458>.
- Hall, A., and M. Visbeck, 2002: Synchronous variability in the Southern Hemisphere atmosphere, sea ice, and ocean resulting from the annular mode. *J. Climate*, **15**, 3043–3057, [https://doi.org/10.1175/1520-0442\(2002\)015<3043:SVITSH>2.0.CO;2](https://doi.org/10.1175/1520-0442(2002)015<3043:SVITSH>2.0.CO;2).
- Hardiman, S. C., N. Butchart, and N. Calvo, 2014: The morphology of the Brewer–Dobson circulation and its response to climate change in CMIP5 simulations. *Quart. J. Roy. Meteor. Soc.*, **140**, 1958–1965, <https://doi.org/10.1002/qj.2258>.
- Hartley, D. E., J. T. Villarín, R. X. Black, and C. A. Davis, 1998: A new perspective on the dynamical link between the stratosphere and troposphere. *Nature*, **391**, 471–474, <https://doi.org/10.1038/35112>.
- Haynes, P., P. Hitchcock, M. Hitchman, S. Yoden, H. Hendon, G. Kiladis, K. Kodera, and I. Simpson, 2021: The influence of the stratosphere on the tropical troposphere. *J. Meteor. Soc. Japan*, **99**, 803–845, <https://doi.org/10.2151/jmsj.2021-040>.
- Haynes, P. H., M. E. McIntyre, T. G. Shepherd, C. J. Marks, and K. P. Shine, 1991: On the “Downward Control” of Extratropical Diabatic circulations by eddy-induced mean zonal forces. *J. Atmos. Sci.*, **48**, 651–678, [https://doi.org/10.1175/1520-0469\(1991\)048<0651:OTCOED>2.0.CO;2](https://doi.org/10.1175/1520-0469(1991)048<0651:OTCOED>2.0.CO;2).
- Heggin, M. I., and T. G. Shepherd, 2009: Large climate-induced changes in ultraviolet index and stratosphere-to-troposphere ozone flux. *Nature Geoscience*, **2**, 687–691, <https://doi.org/10.1038/ngeo604>.
- Heggin, M. I., and Coauthors, 2014: Vertical structure of stratospheric water vapour trends derived from merged satellite data. *Nature Geoscience*, **7**, 768–776, <https://doi.org/10.1038/ngeo2236>.
- Held, I. M., M. Ting, and H. L. Wang, 2002: Northern winter stationary waves: Theory and modeling. *J. Climate*, **15**, 2125–2144, [https://doi.org/10.1175/1520-0442\(2002\)015<2125:NWSWTA>2.0.CO;2](https://doi.org/10.1175/1520-0442(2002)015<2125:NWSWTA>2.0.CO;2).
- Hitchcock, P., and I. R. Simpson, 2014: The downward influence of stratospheric sudden warmings. *J. Atmos. Sci.*, **71**, 3856–3876, <https://doi.org/10.1175/JAS-D-14-0012.1>.
- Hitchcock, P., and Coauthors, 2022: Stratospheric nudging and predictable surface impacts (SNAPSI): A protocol for investigating the role of stratospheric polar vortex disturbances in sub-seasonal to seasonal forecasts. *Geoscientific Model Development*, **15**, 5073–5092, <https://doi.org/10.5194/gmd-15-5073-2022>.
- Holton, J. R., and R. S. Lindzen, 1972: An updated theory for the quasi-biennial cycle of the tropical stratosphere. *J. Atmos. Sci.*, **29**, 1076–1080, [https://doi.org/10.1175/1520-0469\(1972\)029<1076:AUTFTQ>2.0.CO;2](https://doi.org/10.1175/1520-0469(1972)029<1076:AUTFTQ>2.0.CO;2).
- Holton, J. R., and H.-C. Tan, 1980: The influence of the equatorial Quasi-Biennial Oscillation on the global circulation at 50 mb. *J. Atmos. Sci.*, **37**, 2200–2208, [https://doi.org/10.1175/1520-0469\(1980\)037<2200:TIOTEQ>2.0.CO;2](https://doi.org/10.1175/1520-0469(1980)037<2200:TIOTEQ>2.0.CO;2).
- Holton, J. R., and H.-C. Tan, 1982: The Quasi-Biennial Oscillation in the Northern Hemisphere lower stratosphere. *J. Meteor. Soc. Japan*, **60**, 140–148, [https://doi.org/10.2151/jmsj1965.60.1\\_140](https://doi.org/10.2151/jmsj1965.60.1_140).
- Holton, J. R., and A. Gettelman, 2001: Horizontal transport and the dehydration of the stratosphere. *Geophys. Res. Lett.*, **28**, 2799–2802, <https://doi.org/10.1029/2001GL013148>.
- Hoskins, B. J., M. E. McIntyre, and A. W. Robertson, 1985: On the use and significance of isentropic potential vorticity maps. *Quart. J. Roy. Meteor. Soc.*, **111**, 877–946, <https://doi.org/10.1002/qj.49711147002>.
- Hu, D. Z., Z. Y. Guan, W. S. Tian, and R. C. Ren, 2018: Recent strengthening of the stratospheric Arctic vortex response to warming in the central North Pacific. *Nature Communications*, **9**, 1697, <https://doi.org/10.1038/s41467-018-04138-3>.
- Hu, D. Z., W. S. Tian, F. Xie, C. X. Wang, and J. K. Zhang, 2015: Impacts of stratospheric ozone depletion and recovery on wave propagation in the boreal winter stratosphere. *J. Geophys. Res.: Atmos.*, **120**, 8299–8317, <https://doi.org/10.1002/2014JD022855>.
- Hu, J. G., R. C. Ren, and H. M. Xu, 2014: Occurrence of winter stratospheric sudden warming events and the seasonal timing of spring stratospheric final warming. *J. Atmos. Sci.*, **71**, 2319–2334, <https://doi.org/10.1175/JAS-D-13-0349.1>.
- Hu, Y. H., W. S. Tian, J. K. Zhang, T. Wang, and M. Xu, 2022: Weakening of Antarctic stratospheric planetary wave activities in early austral spring since the early 2000s: A response to sea surface temperature trends. *Atmospheric Chemistry and Physics*, **22**, 1575–1600, <https://doi.org/10.5194/acp-22-1575-2022>.
- Hu, Y. Y., and K. K. Tung, 2003: Possible ozone-induced long-term changes in planetary wave activity in late winter. *J. Climate*, **16**, 3027–3038, [https://doi.org/10.1175/1520-0442\(2003\)016<3027:POLCIP>2.0.CO;2](https://doi.org/10.1175/1520-0442(2003)016<3027:POLCIP>2.0.CO;2).
- Huang, J. L., and W. S. Tian, 2019: Eurasian cold air outbreaks under different arctic stratospheric polar vortex strengths. *J. Atmos. Sci.*, **76**, 1245–1264, <https://doi.org/10.1175/JAS-D-18-0285.1>.
- Huang, J. L., P. Hitchcock, W. S. Tian, and J. Sillin, 2022: Stratospheric influence on the development of the 2018 late winter European cold air outbreak. *J. Geophys. Res.: Atmos.*, **127**, e2021JD035877, <https://doi.org/10.1029/2021JD035877>.
- Huang, J. L., P. Hitchcock, A. C. Maycock, C. M. McKenna, and W. S. Tian, 2021: Northern hemisphere cold air outbreaks are more likely to be severe during weak polar vortex conditions. *Communications Earth & Environment*, **2**, 147, <https://doi.org/10.1038/s43247-021-00215-6>.
- Huang, J. L., W. S. Tian, J. K. Zhang, Q. Huang, H. Y. Tian, and J. L. Luo, 2017: The connection between extreme stratospheric polar vortex events and tropospheric blockings. *Quart. J. Roy. Meteor. Soc.*, **143**, 1148–1164, <https://doi.org/10.1002/qj.3001>.
- Huang, J. L., W. S. Tian, L. J. Gray, J. K. Zhang, Y. Li, J. L. Luo, and H. Y. Tian, 2018: Preconditioning of Arctic stratospheric polar vortex shift events. *J. Climate*, **31**, 5417–5436, <https://doi.org/10.1175/JCLI-D-17-0695.1>.
- Huang, Y., Y. W. Wang, and H. Huang, 2020: Stratospheric water vapor feedback disclosed by a locking experiment. *Geophys. Res. Lett.*, **47**, e2020GL087987, <https://doi.org/10.1029/2020GL087987>.
- Huang, Y., M. H. Zhang, Y. Xia, Y. Y. Hu, and S.-W. Son, 2016: Is there a stratospheric radiative feedback in global warming simulations? *Climate Dyn.*, **46**, 177–186, <https://doi.org/10.1007/s00382-015-2577-2>.

- Huangfu, J. L., Y. L. Tang, T. J. Ma, W. Chen, and L. Wang, 2021: Influence of the QBO on tropical convection and its impact on tropical cyclone activity over the western North Pacific. *Climate Dyn.*, **57**, 657–669, <https://doi.org/10.1007/s00382-021-05731-x>.
- Iles, C. E., G. C. Hegerl, A. P. Schurer, and X. B. Zhang, 2013: The effect of volcanic eruptions on global precipitation. *J. Geophys. Res.: Atmos.*, **118**, 8770–8786, <https://doi.org/10.1002/jgrd.50678>.
- IPCC, 2001: Climate change 2001: The scientific basis. *Contribution of Working Group I to the Third Assessment Report of the Intergovernmental Panel on Climate Change*, J. T. Houghton, et al., Eds., Cambridge University Press, Cambridge, UK, and New York, USA.
- IPCC, 2014: Climate change 2014: Mitigation of climate change. *Contribution of Working Group III to the Fifth Assessment Report of the Intergovernmental Panel on Climate Change*, O. Edenhofer, et al., Eds., Cambridge University Press, Cambridge, UK, and New York, USA.
- IPCC, 2021: Climate change 2021: The physical science basis. *Contribution of Working Group I to the Sixth Assessment Report of the Intergovernmental Panel on Climate Change*, V. Masson-Delmotte, et al., Eds., Cambridge University Press, Cambridge, UK, and New York, USA.
- Ito, Y., and A. Matsuzaki, 2015: The action of water vapor on the stratospheric ozone chemistry. *Frontiers of Astronomy, Astrophysics and Cosmology*, **1**, 56–73.
- Ivanciu, I., K. Matthes, A. Biastoch, S. Wahl, and J. Harlaß, 2022: Twenty-first-century Southern Hemisphere impacts of ozone recovery and climate change from the stratosphere to the ocean. *Weather and Climate Dynamics*, **3**, 139–171, <https://doi.org/10.5194/wcd-3-139-2022>.
- Ivy, D. J., S. Solomon, N. Calvo, and D. W. J. Thompson, 2017: Observed connections of Arctic stratospheric ozone extremes to Northern Hemisphere surface climate. *Environmental Research Letters*, **12**, 024004, <https://doi.org/10.1088/1748-9326/aa57a4>.
- Joseph, R., and N. Zeng, 2011: Seasonally modulated tropical drought induced by volcanic aerosol. *J. Climate*, **24**, 2045–2060, <https://doi.org/10.1175/2009JCLI3170.1>.
- Kang, S. M., L. M. Polvani, J. C. Fyfe, and M. Sigmond, 2011: Impact of polar ozone depletion on subtropical precipitation. *Science*, **332**, 951–954, <https://doi.org/10.1126/science.1202131>.
- Karpechko, A. Y., and E. Manzini, 2012: Stratospheric influence on tropospheric climate change in the Northern Hemisphere. *J. Geophys. Res.: Atmos.*, **117**, D05133, <https://doi.org/10.1029/2011JD017036>.
- Karpechko, A. Y., P. Hitchcock, D. H. W. Peters, and A. Schneider, 2017: Predictability of downward propagation of major sudden stratospheric warmings. *Quart. J. Roy. Meteor. Soc.*, **143**, 1459–1470, <https://doi.org/10.1002/qj.3017>.
- Karpechko, A. Y., and Coauthors, 2022: Northern Hemisphere stratosphere-troposphere circulation change in CMIP6 models: 1. Inter-model spread and scenario sensitivity. *J. Geophys. Res.: Atmos.*, **127**, e2022JD036992, <https://doi.org/10.1029/2022JD036992>.
- Kawatani, Y., and K. Hamilton, 2013: Weakened stratospheric quasi-biennial oscillation driven by increased tropical mean upwelling. *Nature*, **497**, 478–481, <https://doi.org/10.1038/nature12140>.
- Keeble, J., and Coauthors, 2021: Evaluating stratospheric ozone and water vapour changes in CMIP6 models from 1850 to 2100. *Atmospheric Chemistry and Physics*, **21**, 5015–5061, <https://doi.org/10.5194/acp-21-5015-2021>.
- Kidston, J., A. A. Scaife, S. C. Hardiman, D. M. Mitchell, N. Butchart, M. P. Baldwin, and L. J. Gray, 2015: Stratospheric influence on tropospheric jet streams, storm tracks and surface weather. *Nature Geoscience*, **8**, 433–440, <https://doi.org/10.1038/ngeo2424>.
- Kilian, M., S. Brinkop, and P. Jöckel, 2020: Impact of the eruption of Mt Pinatubo on the chemical composition of the stratosphere. *Atmospheric Chemistry and Physics*, **20**, 11697–11715, <https://doi.org/10.5194/acp-20-11697-2020>.
- Kim, B.-M., S.-W. Son, S.-K. Min, J.-H. Jeong, S.-J. Kim, X. D. Zhang, T. Shim, and J.-H. Yoon, 2014: Weakening of the stratospheric polar vortex by Arctic sea-ice loss. *Nature Communications*, **5**, 4646, <https://doi.org/10.1038/ncomms5646>.
- Kim, J., S.-W. Son, E. P. Gerber, and H.-S. Park, 2017: Defining sudden stratospheric warming in climate models: Accounting for biases in model climatologies. *J. Climate*, **30**, 5529–5546, <https://doi.org/10.1175/JCLI-D-16-0465.1>.
- Kirk-Davidoff, D. B., E. J. Hintsa, J. G. Anderson, and D. W. Keith, 1999: The effect of climate change on ozone depletion through changes in stratospheric water vapour. *Nature*, **402**, 399–401, <https://doi.org/10.1038/46521>.
- Kolstad, E. W., T. Breiteig, and A. A. Scaife, 2010: The association between stratospheric weak polar vortex events and cold air outbreaks in the Northern Hemisphere. *Quart. J. Roy. Meteor. Soc.*, **136**, 886–893, <https://doi.org/10.1002/qj.620>.
- Konopka, P., M. C. Tao, F. Ploeger, D. F. Hurst, M. L. Santee, J. S. Wright, and M. Riese, 2022: Stratospheric moistening after 2000. *Geophys. Res. Lett.*, **49**, e2021GL097609, <https://doi.org/10.1029/2021GL097609>.
- Kremser, S., and Coauthors, 2016: Stratospheric aerosol—Observations, processes, and impact on climate. *Rev. Geophys.*, **54**, 278–335, <https://doi.org/10.1002/2015RG000511>.
- Kretschmer, M., D. Coumou, L. Agel, M. Barlow, E. Tziperman, and J. Cohen, 2018: More-persistent weak stratospheric polar vortex states linked to cold extremes. *Bull. Amer. Meteor. Soc.*, **99**, 49–60, <https://doi.org/10.1175/BAMS-D-16-0259.1>.
- Krüger, K., B. Naujokat, and K. Labitzke, 2005: The unusual mid-winter warming in the Southern Hemisphere stratosphere 2002: A comparison to Northern Hemisphere phenomena. *J. Atmos. Sci.*, **62**, 603–613, <https://doi.org/10.1175/JAS-3316.1>.
- Landrum, L. L., M. M. Holland, M. N. Raphael, and L. M. Polvani, 2017: Stratospheric ozone depletion: An unlikely driver of the regional trends in Antarctic sea ice in Austral Fall in the late twentieth century. *Geophys. Res. Lett.*, **44**, 11 062–11 070, <https://doi.org/10.1002/2017GL075618>.
- Larson, E. J. L., and R. W. Portmann, 2016: A temporal kernel method to compute effective radiative forcing in CMIP5 transient simulations. *J. Climate*, **29**, 1497–1509, <https://doi.org/10.1175/JCLI-D-15-0577.1>.
- Li, F., and P. Newman, 2020: Stratospheric water vapor feedback and its climate impacts in the coupled atmosphere–ocean Goddard Earth Observing System Chemistry–Climate Model. *Climate Dyn.*, **55**, 1585–1595, <https://doi.org/10.1007/s00382-020-05348-6>.
- Li, F., R. S. Stolarski, and P. A. Newman, 2009: Stratospheric ozone in the post-CFC era. *Atmospheric Chemistry and Physics*, **9**, 2207–2213, <https://doi.org/10.5194/acp-9-2207-2009>.



- 2009.
- Liang, Z. Q., J. Rao, D. Guo, and Q. Lu, 2022a: Simulation and projection of the sudden stratospheric warming events in different scenarios by CESM2-WACCM. *Climate Dyn.*, **59**, 3741–3761, <https://doi.org/10.1007/s00382-022-06293-2>.
- Liang, Z. Q., J. Rao, D. Guo, Q. Lu, and C. H. Shi, 2022b: Northern winter stratospheric polar vortex regimes and their possible influence on the extratropical troposphere. *Climate Dyn.*, <https://doi.org/10.1007/s00382-022-06494-9>.
- Lim, Y., S.-W. Son, A. G. Marshall, H. H. Hendon, and K.-H. Seo, 2019: Influence of the QBO on MJO prediction skill in the subseasonal-to-seasonal prediction models. *Climate Dyn.*, **53**, 1681–1695, <https://doi.org/10.1007/s00382-019-04719-y>.
- Limpasuvan, V., and D. L. Hartmann, 2000: Wave-maintained annular modes of climate variability. *J. Climate*, **13**, 4414–4429, [https://doi.org/10.1175/1520-0442\(2000\)013<4414:WMAMOC>2.0.CO;2](https://doi.org/10.1175/1520-0442(2000)013<4414:WMAMOC>2.0.CO;2).
- Lin, P., and Q. Fu, 2013: Changes in various branches of the Brewer–Dobson circulation from an ensemble of chemistry climate models. *J. Geophys. Res.: Atmos.*, **118**, 73–84, <https://doi.org/10.1029/2012JD018813>.
- Lindzen, R. S., and J. R. Holton, 1968: A theory of the Quasi-Biennial Oscillation. *J. Atmos. Sci.*, **25**, 1095–1107, [https://doi.org/10.1175/1520-0469\(1968\)025<1095:ATOTQB>2.0.CO;2](https://doi.org/10.1175/1520-0469(1968)025<1095:ATOTQB>2.0.CO;2).
- Liu, F., J. Chai, B. Wang, J. Liu, X. Zhang, and Z. Y. Wang, 2016: Global monsoon precipitation responses to large volcanic eruptions. *Scientific Reports*, **6**, 24331, <https://doi.org/10.1038/srep24331>.
- Liu, F., and Coauthors, 2022: Tropical volcanism enhanced the East Asian summer monsoon during the last millennium. *Nature Communications*, **13**, 3429, <https://doi.org/10.1038/s41467-022-31108-7>.
- Lu, H., M. P. Baldwin, L. J. Gray, and M. J. Jarvis, 2008: Decadal-scale changes in the effect of the QBO on the northern stratospheric polar vortex. *J. Geophys. Res.: Atmos.*, **113**, D10114, <https://doi.org/10.1029/2007JD009647>.
- Lu, H., T. J. Bracegirdle, T. Phillips, A. Bushell, and L. Gray, 2014: Mechanisms for the Holton–Tan relationship and its decadal variation. *J. Geophys. Res.: Atmos.*, **119**, 2811–2830, <https://doi.org/10.1002/2013JD021352>.
- Lu, Q., J. Rao, C. H. Shi, D. Guo, G. Q. Fu, J. Wang, and Z. Q. Liang, 2022: Possible influence of sudden stratospheric warmings on the atmospheric environment in the Beijing–Tianjin–Hebei region. *Atmospheric Chemistry and Physics*, **22**, 13 087–13 102, <https://doi.org/10.5194/acp-22-13087-2022>.
- Luo, J. L., W. S. Tian, Z. X. Pu, P. Q. Zhang, L. Shang, M. Zhang, and J. Hu, 2013: Characteristics of stratosphere–troposphere exchange during the Meiyu season. *J. Geophys. Res.: Atmos.*, **118**, 2058–2072, <https://doi.org/10.1029/2012JD018124>.
- Lynch, A., P. Uotila, and J. J. Cassano, 2006: Changes in synoptic weather patterns in the polar regions in the twentieth and twenty-first centuries, part 2: Antarctic. *International Journal of Climatology*, **26**, 1181–1199, <https://doi.org/10.1002/joc.1305>.
- Ma, T. J., W. Chen, J. L. Huangfu, L. Song, and Q. Y. Cai, 2021: The observed influence of the Quasi-Biennial Oscillation in the lower equatorial stratosphere on the East Asian winter monsoon during early boreal winter. *International Journal of Climatology*, **41**, 6254–6269, <https://doi.org/10.1002/joc.7192>.
- Ma, X., F. Xie, J. P. Li, X. L. Zheng, W. S. Tian, R. Q. Ding, C. Sun, and J. K. Zhang, 2019: Effects of Arctic stratospheric ozone changes on spring precipitation in the northwestern United States. *Atmospheric Chemistry and Physics*, **19**, 861–875, <https://doi.org/10.5194/acp-19-861-2019>.
- Madden, R. A., and P. R. Julian, 1972: Description of global-scale circulation cells in the tropics with a 40–50 day period. *J. Atmos. Sci.*, **29**, 1109–1123, [https://doi.org/10.1175/1520-0469\(1972\)029<1109:DOGSCC>2.0.CO;2](https://doi.org/10.1175/1520-0469(1972)029<1109:DOGSCC>2.0.CO;2).
- Mahfouf, J. F., D. Cariolle, J. F. Royer, J. F. Geleyn, and B. Timbal, 1994: Response of the Météo-France climate model to changes in CO<sub>2</sub> and sea surface temperature. *Climate Dyn.*, **9**, 345–362, <https://doi.org/10.1007/BF00223447>.
- Maleska, S., K. L. Smith, and J. Virgin, 2020: Impacts of stratospheric ozone extremes on arctic high cloud. *J. Climate*, **33**, 8869–8884, <https://doi.org/10.1175/JCLI-D-19-0867.1>.
- Man, W. M., T. J. Zhou, and J. H. Jungclaus, 2014: Effects of large volcanic eruptions on global summer climate and East Asian monsoon changes during the Last Millennium: Analysis of MPI-ESM simulations. *J. Climate*, **27**, 7394–7409, <https://doi.org/10.1175/JCLI-D-13-00739.1>.
- Marshall, A. G., H. H. Hendon, S.-W. Son, and Y. Lim, 2017: Impact of the quasi-biennial oscillation on predictability of the Madden–Julian oscillation. *Climate Dyn.*, **49**, 1365–1377, <https://doi.org/10.1007/s00382-016-3392-0>.
- Marshall, L. R., C. J. Smith, P. M. Forster, T. J. Aubry, T. Andrews, and A. Schmidt, 2020: Large variations in volcanic aerosol forcing efficiency due to eruption source parameters and rapid adjustments. *Geophys. Res. Lett.*, **47**, e2020GL090241, <https://doi.org/10.1029/2020GL090241>.
- Martin, Z., S.-W. Son, A. Butler, H. Hendon, H. Kim, A. Sobel, S. Yoden, and C. D. Zhang, 2021: The influence of the quasi-biennial oscillation on the Madden–Julian oscillation. *Nature Reviews Earth & Environment*, **2**, 477–489, <https://doi.org/10.1038/s43017-021-00173-9>.
- Matsuno, T., 1971: A dynamical model of the stratospheric sudden warming. *J. Atmos. Sci.*, **28**, 1479–1494, [https://doi.org/10.1175/1520-0469\(1971\)028<1479:ADMOTS>2.0.CO;2](https://doi.org/10.1175/1520-0469(1971)028<1479:ADMOTS>2.0.CO;2).
- Maycock, A. C., G. I. T. Masukwedza, P. Hitchcock, and I. R. Simpson, 2020: A regime perspective on the North Atlantic eddy-driven jet response to sudden stratospheric warmings. *J. Climate*, **33**, 3901–3917, <https://doi.org/10.1175/JCLI-D-19-0702.1>.
- Maycock, A. C., M. M. Joshi, K. P. Shine, S. M. Davis, and K. H. Rosenlof, 2014: The potential impact of changes in lower stratospheric water vapour on stratospheric temperatures over the past 30 years. *Quart. J. Roy. Meteor. Soc.*, **140**, 2176–2185, <https://doi.org/10.1002/qj.2287>.
- Maycock, A. C., and Coauthors, 2018: Revisiting the mystery of recent stratospheric temperature trends. *Geophys. Res. Lett.*, **45**, 9919–9933, <https://doi.org/10.1029/2018GL078035>.
- Min, S.-K., and S.-W. Son, 2013: Multimodel attribution of the Southern Hemisphere Hadley cell widening: Major role of ozone depletion. *J. Geophys. Res.: Atmos.*, **118**, 3007–3015, <https://doi.org/10.1002/jgrd.50232>.
- Mitchell, D. M., L. J. Gray, J. Anstey, M. P. Baldwin, and A. J. Charlton-Perez, 2013: The influence of stratospheric vortex displacements and splits on surface climate. *J. Climate*, **26**, 2668–2682, <https://doi.org/10.1175/JCLI-D-12-00030.1>.
- Muthers, S., F. Arfeuille, C. C. Raible, and E. Rozanov, 2015: The impacts of volcanic aerosol on stratospheric ozone and

- the Northern Hemisphere polar vortex: Separating radiative-dynamical changes from direct effects due to enhanced aerosol heterogeneous chemistry. *Atmospheric Chemistry and Physics*, **15**, 11 461–11 476, <https://doi.org/10.5194/acp-15-11461-2015>.
- Naoe, H., M. Deushi, K. Yoshida, and K. Shibata, 2017: Future changes in the Ozone Quasi-Biennial Oscillation with increasing GHGs and ozone recovery in CCMi simulations. *J. Climate*, **30**, 6977–6997, <https://doi.org/10.1175/JCLI-D-16-0464.1>.
- Nathan, T. R., and E. C. Cordero, 2007: An ozone-modified refractive index for vertically propagating planetary waves. *J. Geophys. Res.: Atmos.*, **112**, D02105, <https://doi.org/10.1029/2006JD007357>.
- Ndarana, T., D. W. Waugh, L. M. Polvani, G. J. P. Correa, and E. P. Gerber, 2012: Antarctic ozone depletion and trends in tropopause Rossby wave breaking. *Atmospheric Science Letters*, **13**, 164–168, <https://doi.org/10.1002/asl.384>.
- Neu, J. L., T. Flury, G. L. Manney, M. L. Santee, N. J. Livesey, and J. Worden, 2014: Tropospheric ozone variations governed by changes in stratospheric circulation. *Nature Geoscience*, **7**, 340–344, <https://doi.org/10.1038/ngeo2138>.
- Nie, J., and A. H. Sobel, 2015: Responses of tropical deep convection to the QBO: Cloud-resolving simulations. *J. Atmos. Sci.*, **72**, 3625–3638, <https://doi.org/10.1175/JAS-D-15-0035.1>.
- Nowack, P. J., N. L. Abraham, P. Braesicke, and J. A. Pyle, 2018: The impact of stratospheric ozone feedbacks on climate sensitivity estimates. *J. Geophys. Res.: Atmos.*, **123**, 4630–4641, <https://doi.org/10.1002/2017JD027943>.
- Nowack, P. J., N. Luke Abraham, A. C. Maycock, P. Braesicke, J. M. Gregory, M. M. Joshi, A. Osprey, and J. A. Pyle, 2015: A large ozone-circulation feedback and its implications for global warming assessments. *Nature Climate Change*, **5**, 41–45, <https://doi.org/10.1038/nclimate2451>.
- Oh, J., S. W. Son, J. Choi, E. P. Lim, C. Garfinkel, H. Hendon, Y. Kim, and H. S. Kang, 2022: Impact of stratospheric ozone on the subseasonal prediction in the southern hemisphere spring. *Progress in Earth and Planetary Science*, **9**, 25, <https://doi.org/10.1186/s40645-022-00485-4>.
- Osprey, S. M., N. Butchart, J. R. Knight, A. A. Scaife, K. Hamilton, J. A. Anstey, V. Schenzinger, and C. Zhang, 2016: An unexpected disruption of the atmospheric quasi-biennial oscillation. *Science*, **353**, 1424–1427, <https://doi.org/10.1126/science.aah4156>.
- Palmeiro, F. M., D. Barriopedro, R. García-Herrera, and N. Calvo, 2015: Comparing sudden stratospheric warming definitions in reanalysis data. *J. Climate*, **28**, 6823–6840, <https://doi.org/10.1175/JCLI-D-15-0004.1>.
- Parker, D. E., H. Wilson, P. D. Jones, J. R. Christy, and C. K. Folland, 1996: The impact of mount Pinatubo on world-wide temperatures. *International Journal of Climatology*, **16**, 487–497, [https://doi.org/10.1002/\(SICI\)1097-0088\(199605\)16:5<487::AID-JOC39>3.0.CO;2-J](https://doi.org/10.1002/(SICI)1097-0088(199605)16:5<487::AID-JOC39>3.0.CO;2-J).
- Perlwitz, J., and N. Harnik, 2003: Observational evidence of a stratospheric influence on the troposphere by planetary wave reflection. *J. Climate*, **16**, 3011–3026, [https://doi.org/10.1175/1520-0442\(2003\)016<3011:OEOASI>2.0.CO;2](https://doi.org/10.1175/1520-0442(2003)016<3011:OEOASI>2.0.CO;2).
- Polvani, L. M., A. Banerjee, and A. Schmidt, 2019: Northern Hemisphere continental winter warming following the 1991 Mt. Pinatubo eruption: Reconciling models and observations. *Atmospheric Chemistry and Physics*, **19**, 6351–6366, <https://doi.org/10.5194/acp-19-6351-2019>.
- Polvani, L. M., D. W. Waugh, G. J. P. Correa, and S.-W. Son, 2011: Stratospheric ozone depletion: The main driver of twentieth-century atmospheric circulation changes in the Southern Hemisphere. *J. Climate*, **24**, 795–812, <https://doi.org/10.1175/2010JCLI3772.1>.
- Quiroz, R. S., 1986: The association of stratospheric warmings with tropospheric blocking. *J. Geophys. Res.: Atmos.*, **91**, 5277–5285, <https://doi.org/10.1029/JD091iD04p05277>.
- Ramaswamy, V., Chanin, M.-L., Angell, J., Barnett, J., Gaffen, D., Gelman, M., et al., 2001: Stratospheric temperature trends: Observations and model simulations. *Reviews of Geophysics*, **39**, 71–122, <https://doi.org/10.1029/1999RG000065>.
- Randel, W. J., and Coauthors, 2009: An update of observed stratospheric temperature trends. *J. Geophys. Res.: Atmos.*, **114**, D02107, <https://doi.org/10.1029/2008JD010421>.
- Rao, J., and C. I. Garfinkel, 2020: Arctic ozone loss in March 2020 and its seasonal prediction in CFSv2: A comparative study with the 1997 and 2011 cases. *J. Geophys. Res.: Atmos.*, **125**, e2020JD033524, <https://doi.org/10.1029/2020JD033524>.
- Rao, J., and R. C. Ren, 2020: Modeling study of the destructive interference between the tropical Indian Ocean and eastern Pacific in their forcing in the southern winter extratropical stratosphere during ENSO. *Climate Dyn.*, **54**, 2249–2266, <https://doi.org/10.1007/s00382-019-05111-6>.
- Rao, J., and C. I. Garfinkel, 2021a: Projected changes of stratospheric final warmings in the Northern and Southern Hemispheres by CMIP5/6 models. *Climate Dyn.*, **56**, 3353–3371, <https://doi.org/10.1007/s00382-021-05647-6>.
- Rao, J., and C. I. Garfinkel, 2021b: The strong stratospheric polar vortex in March 2020 in sub-seasonal to seasonal models: Implications for empirical prediction of the low Arctic total ozone extreme. *J. Geophys. Res.: Atmos.*, **126**, e2020JD034190, <https://doi.org/10.1029/2020JD034190>.
- Rao, J., C. I. Garfinkel, and I. P. White, 2020a: Predicting the downward and surface influence of the February 2018 and January 2019 sudden stratospheric warming events in Subseasonal to Seasonal (S2S) models. *J. Geophys. Res.: Atmos.*, **125**, e2019JD031919, <https://doi.org/10.1029/2019JD031919>.
- Rao, J., C. I. Garfinkel, and I. P. White, 2020c: Projected strengthening of the extratropical surface impacts of the stratospheric Quasi-Biennial Oscillation. *Geophys. Res. Lett.*, **47**, e2020GL089149, <https://doi.org/10.1029/2020GL089149>.
- Rao, J., C. I. Garfinkel, H. S. Chen, and I. P. White, 2019: The 2019 new year stratospheric sudden warming and its real-time predictions in multiple S2S models. *J. Geophys. Res.: Atmos.*, **124**, 11 155–11 174, <https://doi.org/10.1029/2019JD030826>.
- Rao, J., C. I. Garfinkel, I. P. White, and C. Schwartz, 2020b: The Southern Hemisphere minor sudden stratospheric warming in September 2019 and its predictions in S2S models. *J. Geophys. Res.: Atmos.*, **125**, e2020JD032723, <https://doi.org/10.1029/2020JD032723>.
- Reed, R. J., W. J. Campbell, L. A. Rasmussen, and D. G. Rogers, 1961: Evidence of a downward-propagating, annual wind reversal in the equatorial stratosphere. *J. Geophys. Res.*, **66**, 813–818, <https://doi.org/10.1029/JZ066i003p00813>.
- Ren, R. C., Y. Yang, M. Cai, and J. Rao, 2015: Understanding the systematic air temperature biases in a coupled climate system model through a process-based decomposition method.

- Climate Dyn.*, **45**, 1801–1817, <https://doi.org/10.1007/s00382-014-2435-7>.
- Rind, D., R. Suozzo, N. K. Balachandran, and M. J. Prather, 1990: Climate change and the middle atmosphere. Part I: The doubled CO<sub>2</sub> climate. *J. Atmos. Sci.*, **47**, 475–494, [https://doi.org/10.1175/1520-0469\(1990\)047<0475:CCATMA>2.0.CO;2](https://doi.org/10.1175/1520-0469(1990)047<0475:CCATMA>2.0.CO;2).
- Robock, A., 2000: Volcanic eruptions and climate. *Rev. Geophys.*, **38**, 191–219, <https://doi.org/10.1029/1998RG000054>.
- Robock, A., and J. P. Mao, 1992: Winter warming from large volcanic eruptions. *Geophys. Res. Lett.*, **19**, 2405–2408, <https://doi.org/10.1029/92GL02627>.
- Robock, A., and J. P. Mao, 1995: The volcanic signal in surface temperature observations. *J. Climate*, **8**, 1086–1103, [https://doi.org/10.1175/1520-0442\(1995\)008<1086:TVSIST>2.0.CO;2](https://doi.org/10.1175/1520-0442(1995)008<1086:TVSIST>2.0.CO;2).
- Romanowsky, E., and Coauthors, 2019: The role of stratospheric ozone for Arctic-midlatitude linkages. *Scientific Reports*, **9**, 7962, <https://doi.org/10.1038/s41598-019-43823-1>.
- Rosenlof, K. H., 2003: How water enters the stratosphere. *Science*, **302**, 1691–1692, <https://doi.org/10.1126/science.1092703>.
- Rosenlof, K. H., 2018: Changes in water vapor and aerosols and their relation to stratospheric ozone. *Comptes Rendus Geoscience*, **350**, 376–383, <https://doi.org/10.1016/j.crte.2018.06.014>.
- Russell, A., G. Vaughan, and E. G. Norton, 2012: Large-scale potential vorticity anomalies and deep convection. *Quart. J. Roy. Meteor. Soc.*, **138**, 1627–1639, <https://doi.org/10.1002/qj.1875>.
- Ruti, P. M., V. Lucarini, A. Dell’Aquila, S. Calmanti, and A. Speranza, 2006: Does the subtropical jet catalyze the midlatitude atmospheric regimes? *Geophys. Res. Lett.*, **33**, L06814, <https://doi.org/10.1029/2005GL024620>.
- Sakaeda, N., J. Dias, and G. N. Kiladis, 2020: The unique characteristics and potential mechanisms of the MJO-QBO relationship. *J. Geophys. Res.: Atmos.*, **125**, e2020JD033196, <https://doi.org/10.1029/2020JD033196>.
- Scaife, A. A., and Coauthors, 2012: Climate change projections and stratosphere–troposphere interaction. *Climate Dyn.*, **38**, 2089–2097, <https://doi.org/10.1007/s00382-011-1080-7>.
- Scaife, A. A., and Coauthors, 2016: Seasonal winter forecasts and the stratosphere. *Atmospheric Science Letters*, **17**, 51–56, <https://doi.org/10.1002/asl.598>.
- Schirber, S., E. Manzini, T. Krismer, and M. Giorgetta, 2015: The quasi-biennial oscillation in a warmer climate: Sensitivity to different gravity wave parameterizations. *Climate Dyn.*, **45**, 825–836, <https://doi.org/10.1007/s00382-014-2314-2>.
- Schmidt, A., and Coauthors, 2018: Volcanic radiative forcing from 1979 to 2015. *J. Geophys. Res.: Atmos.*, **123**, 12 491–12 508, <https://doi.org/10.1029/2018JD028776>.
- Schoeberl, M. R., 1978: Stratospheric warmings: Observations and theory. *Rev. Geophys.*, **16**, 521–538, <https://doi.org/10.1029/RG016i004p00521>.
- Seviour, W. J. M., 2017: Weakening and shift of the Arctic stratospheric polar vortex: Internal variability or forced response? *Geophys. Res. Lett.*, **44**, 3365–3373, <https://doi.org/10.1002/2017GL073071>.
- Seviour, W. J. M., and Coauthors, 2019: The southern ocean sea surface temperature response to ozone depletion: A multi-model comparison. *J. Climate*, **32**, 5107–5121, <https://doi.org/10.1175/JCLI-D-19-0109.1>.
- Shepherd, T. G., 2008: Dynamics, stratospheric ozone, and climate change. *Atmosphere-Ocean*, **46**, 117–138, <https://doi.org/10.3137/ao.460106>.
- Shepherd, T. G., and C. McLandress, 2011: A robust mechanism for strengthening of the Brewer–Dobson circulation in response to climate change: Critical-layer control of subtropical wave breaking. *J. Atmos. Sci.*, **68**, 784–797, <https://doi.org/10.1175/2010JAS3608.1>.
- Sherwood, S. C., and A. E. Dessler, 2000: On the control of stratospheric humidity. *Geophys. Res. Lett.*, **27**, 2513–2516, <https://doi.org/10.1029/2000GL011438>.
- Sigmond, M., and J. C. Fyfe, 2010: Has the ozone hole contributed to increased Antarctic sea ice extent? *Geophys. Res. Lett.*, **37**, L18502, <https://doi.org/10.1029/2010GL044301>.
- Sigmond, M., J. F. Scinocca, V. V. Kharin, and T. G. Shepherd, 2013: Enhanced seasonal forecast skill following stratospheric sudden warmings. *Nature Geoscience*, **6**, 98–102, <https://doi.org/10.1038/ngeo1698>.
- Škerlak, B., M. Sprenger, S. Pfahl, E. Tyrlis, and H. Wernli, 2015: Tropopause folds in ERA-Interim: Global climatology and relation to extreme weather events. *J. Geophys. Res.: Atmos.*, **120**, 4860–4877, <https://doi.org/10.1002/2014JD022787>.
- Smith, K. L., and L. M. Polvani, 2014: The surface impacts of Arctic stratospheric ozone anomalies. *Environmental Research Letters*, **9**, 074015, <https://doi.org/10.1088/1748-9326/9/7/074015>.
- Solomon, A., and L. M. Polvani, 2016: Highly significant responses to anthropogenic forcings of the midlatitude jet in the Southern Hemisphere. *J. Climate*, **29**, 3463–3470, <https://doi.org/10.1175/JCLI-D-16-0034.1>.
- Solomon, A., L. M. Polvani, K. L. Smith, and R. P. Abernathy, 2015: The impact of ozone depleting substances on the circulation, temperature, and salinity of the Southern Ocean: An attribution study with CESM1(WACCM). *Geophys. Res. Lett.*, **42**, 5547–5555, <https://doi.org/10.1002/2015GL064744>.
- Solomon, S., K. H. Rosenlof, R. W. Portmann, J. S. Daniel, S. M. Davis, T. J. Sanford, and G.-K. Plattner, 2010: Contributions of stratospheric water vapor to decadal changes in the rate of global warming. *Science*, **327**, 1219–1223, <https://doi.org/10.1126/science.1182488>.
- Son, S.-W., N. F. Tandon, L. M. Polvani, and D. W. Waugh, 2009: Ozone hole and Southern Hemisphere climate change. *Geophys. Res. Lett.*, **36**, L15705, <https://doi.org/10.1029/2009GL038671>.
- Son, S.-W., Gerber, E. P., Perlwitz, J., Polvani, L. M., Gillett, N. P., Seo, K.-H., et al., 2010: Impact of stratospheric ozone on Southern Hemisphere circulation change: A multimodel assessment. *J. Geophys. Res.: Atmos.*, **115**, D3, <https://doi.org/10.1029/2010JD014271>.
- Son, S.-W., Y. Lim, C. Yoo, H. H. Hendon, and J. Kim, 2017: Stratospheric control of the Madden–Julian oscillation. *J. Climate*, **30**, 1909–1922, <https://doi.org/10.1175/JCLI-D-16-0620.1>.
- SPARC, 2022: SPARC Reanalysis Intercomparison Project (SRIP) Final Report. Masatomo Fujiwara, Gloria L. Manney, Lesley J. Gray, and Jonathon S. Wright (Eds.), SPARC Report No. 10, WCRP-6/2021, doi: 10.17874/800dee57d13, available online at [www.sparc-climate.org/publications/sparc-reports](http://www.sparc-climate.org/publications/sparc-reports). <https://doi.org/10.17874/800dee57d13,availableonlineatwww.sparc-climate.org/publications/sparc-reports>.
- Thompson, D. W. J., and S. Solomon, 2002: Interpretation of



- recent Southern Hemisphere climate change. *Science*, **296**, 895–899, <https://doi.org/10.1126/science.1069270>.
- Thompson, D. W. J., M. P. Baldwin, and J. M. Wallace, 2002: Stratospheric connection to Northern Hemisphere wintertime weather: Implications for prediction. *J. Climate*, **15**, 1421–1428, [https://doi.org/10.1175/1520-0442\(2002\)015<1421:SCTNHW>2.0.CO;2](https://doi.org/10.1175/1520-0442(2002)015<1421:SCTNHW>2.0.CO;2).
- Thompson, D. W. J., S. Solomon, P. J. Kushner, M. H. England, K. M. Grise, and D. J. Karoly, 2011: Signatures of the Antarctic ozone hole in Southern Hemisphere surface climate change. *Nature Geoscience*, **4**, 741–749, <https://doi.org/10.1038/ngeo1296>.
- Thompson, D. W. J., and Coauthors, 2012: The mystery of recent stratospheric temperature trends. *Nature*, **491**, 692–697, <https://doi.org/10.1038/nature11579>.
- Tian, W. S., and M. P. Chipperfield, 2005: A new coupled chemistry-climate model for the stratosphere: The importance of coupling for future O<sub>3</sub>-Climate predictions. *Quart. J. Roy. Meteor. Soc.*, **131**(605), 281–303, <https://doi.org/10.1256/qj.04.05>.
- Tian, W. S., and M. P. Chipperfield, 2006: Stratospheric water vapor trends in a coupled chemistry-climate model. *Geophys. Res. Lett.*, **33**, L06819, <https://doi.org/10.1029/2005GL024675>.
- Tian, W. S., M. P. Chipperfield, and D. R. Lü, 2009: Impact of increasing stratospheric water vapor on ozone depletion and temperature change. *Adv. Atmos. Sci.*, **26**, 423–437, <https://doi.org/10.1007/s00376-009-0423-3>.
- Tian, W. S., M. P. Chipperfield, L. J. Gray, and J. M. Zawodny, 2006: Quasi-biennial oscillation and tracer distributions in a coupled chemistry-climate model. *J. Geophys. Res.: Atmos.*, **111**, D20301, <https://doi.org/10.1029/2005JD006871>.
- Tilmes, S., and Coauthors, 2018: Effects of different stratospheric SO<sub>2</sub> injection altitudes on stratospheric chemistry and dynamics. *J. Geophys. Res.: Atmos.*, **123**, 4654–4673, <https://doi.org/10.1002/2017JD028146>.
- Trenberth, K. E., and A. G. Dai, 2007: Effects of Mount Pinatubo volcanic eruption on the hydrological cycle as an analog of geoengineering. *Geophys. Res. Lett.*, **34**, L15702, <https://doi.org/10.1029/2007GL030524>.
- Turner, J., and Coauthors, 2009: Non-annular atmospheric circulation change induced by stratospheric ozone depletion and its role in the recent increase of Antarctic sea ice extent. *Geophys. Res. Lett.*, **36**, L08502, <https://doi.org/10.1029/2009GL037524>.
- Vernier, J.-P., and Coauthors, 2011: Major influence of tropical volcanic eruptions on the stratospheric aerosol layer during the last decade. *Geophys. Res. Lett.*, **38**, L12807, <https://doi.org/10.1029/2011GL047563>.
- Vogel, B., T. Feck, and J.-U. Groö, 2011: Impact of stratospheric water vapor enhancements caused by CH<sub>4</sub> and H<sub>2</sub>O increase on polar ozone loss. *J. Geophys. Res.: Atmos.*, **116**, D05301, <https://doi.org/10.1029/2010JD014234>.
- von der Gathen, P., R. Kivi, I. Wohltmann, R. J. Salawitch, and M. Rex, 2021: Climate change favours large seasonal loss of Arctic ozone. *Nature Communications*, **12**, 3886, <https://doi.org/10.1038/s41467-021-24089-6>.
- Wallace, J. M., and V. E. Kousky, 1968: Observational evidence of kelvin waves in the tropical stratosphere. *J. Atmos. Sci.*, **25**, 900–907, [https://doi.org/10.1175/1520-0469\(1968\)025<0900:OEOKWI>2.0.CO;2](https://doi.org/10.1175/1520-0469(1968)025<0900:OEOKWI>2.0.CO;2).
- Wang, L., and W. Chen, 2010: Downward Arctic Oscillation signal associated with moderate weak stratospheric polar vortex and the cold December 2009. *Geophys. Res. Lett.*, **37**, L09707, <https://doi.org/10.1029/2010GL042659>.
- Wang, L., L. Wang, W. Chen, and J. L. Huangfu, 2021: Modulation of winter precipitation associated with tropical cyclone of the western North Pacific by the stratospheric Quasi-Biennial oscillation. *Environ. Res. Lett.*, **16**, 054004, <https://doi.org/10.1088/1748-9326/abf3dd>.
- Wang, T., W. S. Tian, J. K. Zhang, M. Xu, T. Lian, D. Z. Hu, and K. Qie, 2022: Surface ocean current variations in the North Pacific related to Arctic stratospheric ozone. *Climate Dyn.*, **59**, 3087–3111, <https://doi.org/10.1007/s00382-022-06271-8>.
- Wang, W., W. Tian, S. Dhomse, F. Xie, J. Shu, and J. Austin, 2014: Stratospheric ozone depletion from future nitrous oxide increases. *Atmospheric Chemistry and Physics*, **14**, 12 967–12 982, <https://doi.org/10.5194/acp-14-12967-2014>.
- Wang, Y. W., and Y. Huang, 2020: Stratospheric radiative feedback limited by the tropospheric influence in global warming. *Climate Dyn.*, **55**, 2343–2350, <https://doi.org/10.1007/s00382-020-05390-4>.
- Wang, T., H. L. Liu, and W. S. Tian, 2023: Simulation of the Seasonal Variation of Mesospheric Zonal Wind Reversal with Anisotropic Gravity Waves. ESS Open Archive. March 06, 2023, <https://doi.org/10.22541/essoar.167810265.51636031/v1>.
- Wernli, H., S. Dirren, M. A. Liniger, and M. Zillig, 2002: Dynamical aspects of the life cycle of the winter storm ‘Lothar’ (24–26 December 1999). *Quart. J. Roy. Meteor. Soc.*, **128**, 405–429, <https://doi.org/10.1256/003590002321042036>.
- Wittman, M. A. H., A. J. Charlton, and L. M. Polvani, 2007: The effect of lower stratospheric shear on baroclinic instability. *J. Atmos. Sci.*, **64**, 479–496, <https://doi.org/10.1175/JAS3828.1>.
- WMO, 2011: *Scientific Assessment of Ozone Depletion: 2010, Chapter 2 - Stratospheric Ozone and Surface Ultraviolet Radiation*. World Meteorological Organization, Geneva, Switzerland. Douglass, A., Fioletov, V., Godin-Beekmann, S., Müller, R., Stolarski, R. S., Webb, A., et al. [Available online from <https://orbi.uliege.be/handle/2268/163132>]
- WMO, United Nations Environment Programme (UNEP), National Oceanic and Atmospheric Administration (NOAA), National Aeronautics and Space Administration (NASA), European Commission. 2022: *Scientific Assessment of Ozone Depletion: 2022 - Executive Summary*. WMO, UNEP, NOAA, NASA, European Commission. [Available online from [https://library.wmo.int/index.php?lvl=notice\\_display&id=22164#.ZArmU-xBzAM](https://library.wmo.int/index.php?lvl=notice_display&id=22164#.ZArmU-xBzAM)]
- Xia, Y., Y. Huang, and Y. Y. Hu, 2018: On the climate impacts of upper tropospheric and lower stratospheric ozone. *J. Geophys. Res.: Atmos.*, **123**, 730–739, <https://doi.org/10.1002/2017JD027398>.
- Xia, Y., Y. Y. Hu, J. P. Liu, Y. Huang, F. Xie, and J. T. Lin, 2020: Stratospheric ozone-induced cloud radiative effects on Antarctic sea ice. *Adv. Atmos. Sci.*, **37**, 505–514, <https://doi.org/10.1007/s00376-019-8251-6>.
- Xie, F., J. K. Zhang, W. J. Sang, Y. Li, Y. L. Qi, C. Sun, Y. Li, and J. C. Shu, 2017: Delayed effect of Arctic stratospheric ozone on tropical rainfall. *Atmospheric Science Letters*, **18**, 409–416, <https://doi.org/10.1002/asl.783>.
- Xie, F., and Coauthors, 2016: A connection from Arctic stratospheric ozone to El Niño–Southern oscillation. *Environmental*

- Research Letters*, **11**, 124026, <https://doi.org/10.1088/1748-9326/11/12/124026>.
- Xie, F., and Coauthors, 2018: An advanced impact of Arctic stratospheric ozone changes on spring precipitation in China. *Climate Dyn.*, **51**, 4029–4041, <https://doi.org/10.1007/s00382-018-4402-1>.
- Xu, M., W. S. Tian, J. K. Zhang, J. A. Screen, J. L. Huang, K. Qie, and T. Wang, 2021: Distinct tropospheric and stratospheric mechanisms linking historical Barents-Kara sea-ice loss and late winter Eurasian temperature variability. *Geophys. Res. Lett.*, **48**, e2021GL095262, <https://doi.org/10.1029/2021GL095262>.
- Yang, L. S., Y. J. Gao, C. C. Gao, and F. Liu, 2022: Climate responses to Tambora-Size volcanic eruption and the impact of warming climate. *Geophys. Res. Lett.*, **49**, e2021GL097477, <https://doi.org/10.1029/2021GL097477>.
- Yoo, C., and S.-W. Son, 2016: Modulation of the boreal wintertime Madden-Julian oscillation by the stratospheric quasi-biennial oscillation. *Geophys. Res. Lett.*, **43**, 1392–1398, <https://doi.org/10.1002/2016GL067762>.
- Yu, P. F., D. M. Murphy, R. W. Portmann, O. B. Toon, K. D. Froyd, A. W. Rollins, R. S. Gao, and K. H. Rosenlof, 2016: Radiative forcing from anthropogenic sulfur and organic emissions reaching the stratosphere. *Geophys. Res. Lett.*, **43**, 9361–9367, <https://doi.org/10.1002/2016GL070153>.
- Yu, Y. Y., and R. C. Ren, 2019: Understanding the variation of stratosphere–troposphere coupling during stratospheric northern annular mode events from a mass circulation perspective. *Climate Dyn.*, **53**, 5141–5164, <https://doi.org/10.1007/s00382-019-04675-7>.
- Yu, Y. Y., R. C. Ren, J. G. Hu, and G. X. Wu, 2014: A mass budget analysis on the interannual variability of the polar surface pressure in the winter season. *J. Atmos. Sci.*, **71**, 3539–3553, <https://doi.org/10.1175/JAS-D-13-0365.1>.
- Yu, Y. Y., M. Cai, R. C. Ren, and H. M. van den Dool, 2015: Relationship between warm air mass transport into the upper polar atmosphere and cold air outbreaks in winter. *J. Atmos. Sci.*, **72**, 349–368, <https://doi.org/10.1175/JAS-D-14-0111.1>.
- Yu, Y. Y., M. Cai, C. H. Shi, and R. C. Ren, 2018: On the linkage among strong stratospheric mass circulation, stratospheric sudden warming, and cold weather events. *Mon. Wea. Rev.*, **146**, 2717–2739, <https://doi.org/10.1175/MWR-D-18-0110.1>.
- Yue, J., J. Russell III, Q. Gan, T. Wang, P. P. Rong, R. Garcia, and M. Mlynczak, 2019: Increasing water vapor in the stratosphere and mesosphere after 2002. *Geophys. Res. Lett.*, **46**, 13 452–13 460, <https://doi.org/10.1029/2019GL084973>.
- Zambri, B., S. Solomon, D. W. J. Thompson, and Q. Fu, 2021: Emergence of Southern Hemisphere stratospheric circulation changes in response to ozone recovery. *Nature Geoscience*, **14**, 638–644, <https://doi.org/10.1038/s41561-021-00803-3>.
- Zhang, C. D., 2005: Madden-Julian Oscillation. *Rev. Geophys.*, **43**, RG2003, <https://doi.org/10.1029/2004RG000158>.
- Zhang, J. K., W. S. Tian, M. P. Chipperfield, F. Xie, and J. L. Huang, 2016: Persistent shift of the Arctic polar vortex towards the Eurasian continent in recent decades. *Nature Climate Change*, **6**, 1094–1099, <https://doi.org/10.1038/nclimate3136>.
- Zhang, J. K., W. S. Tian, F. Xie, J. A. Pyle, J. Keeble, and T. Wang, 2020a: The influence of zonally asymmetric stratospheric ozone changes on the Arctic polar vortex shift. *J. Climate*, **33**, 4641–4658, <https://doi.org/10.1175/JCLI-D-19-0647.1>.
- Zhang, J. K., F. Xie, Z. C. Ma, C. Y. Zhang, M. Xu, T. Wang, and R. H. Zhang, 2019a: Seasonal evolution of the Quasi-Biennial Oscillation impact on the Northern Hemisphere polar vortex in winter. *J. Geophys. Res.: Atmos.*, **124**, 12 568–12 586, <https://doi.org/10.1029/2019JD030966>.
- Zhang, J. K., and Coauthors, 2018: Stratospheric ozone loss over the Eurasian continent induced by the polar vortex shift. *Nature Communications*, **9**, 206, <https://doi.org/10.1038/s41467-017-02565-2>.
- Zhang, J. K., and Coauthors, 2022: Responses of Arctic sea ice to stratospheric ozone depletion. *Science Bulletin*, **67**, 1182–1190, <https://doi.org/10.1016/j.scib.2022.03.015>.
- Zhang, R. H., W. S. Tian, and T. Wang, 2020b: Role of the quasi-biennial oscillation in the downward extension of stratospheric northern annular mode anomalies. *Climate Dyn.*, **55**, 595–612, <https://doi.org/10.1007/s00382-020-05285-4>.
- Zhang, R. H., W. S. Tian, J. K. Zhang, J. L. Huang, F. Xie, and M. Xu, 2019b: The corresponding tropospheric environments during downward-extending and nondownward-extending events of stratospheric northern annular mode anomalies. *J. Climate*, **32**, 1857–1873, <https://doi.org/10.1175/JCLI-D-18-0574.1>.
- Zhang, S. Y., and W. S. Tian, 2019: The effects of stratospheric meridional circulation on surface pressure and tropospheric meridional circulation. *Climate Dyn.*, **53**, 6961–6977, <https://doi.org/10.1007/s00382-019-04968-x>.
- Zhao, S. Y., J. K. Zhang, C. Y. Zhang, M. Xu, J. Keeble, Z. Wang, and X. F. Xia, 2022: Evaluating long-term variability of the Arctic stratospheric polar vortex simulated by CMIP6 models. *Remote Sensing*, **14**, 4701, <https://doi.org/10.3390/rs14194701>.
- Zuev, V. V., and E. Savelieva, 2019: The cause of the spring strengthening of the Antarctic polar vortex. *Dynamics of Atmospheres and Oceans*, **87**, 101097, <https://doi.org/10.1016/j.dynatmoce.2019.101097>.



• Review •

# A Review of Research on the Record-Breaking Precipitation Event in Henan Province, China, July 2021<sup>※</sup>

Qinghong ZHANG<sup>1,2</sup>, Rumeng LI<sup>1</sup>, Juanzhen SUN<sup>3</sup>, Feng LU<sup>4</sup>, Jun XU<sup>5</sup>, and Fan ZHANG<sup>2</sup>

<sup>1</sup>*Department of Atmospheric & Oceanic sciences, School of Physics, Peking University, Beijing 100871, China*

<sup>2</sup>*HIWeather International Coordination Office, Chinese Academy of Meteorological Sciences, Beijing 100081, China*

<sup>3</sup>*National Center for Atmospheric Science, Boulder, CO 80307, United States*

<sup>4</sup>*Innovation Center for Feng Yun Meteorological Satellite, National Satellite Meteorological Center (National Center for Space Weather), China Meteorological Administrations, Beijing 100049, China*

<sup>5</sup>*National Meteorological Center of China, Beijing 100081, China*

(Received 18 February 2023; revised 2 May 2023; accepted 9 May 2023)

## ABSTRACT

A record-breaking precipitation event, with a maximum 24-h (1-h) precipitation of 624 mm (201.9 mm) observed at Zhengzhou Weather Station, occurred in Henan Province, China, in July 2021. However, all global operational forecast models failed to predict the intensity and location of maximum precipitation for this event. The unexpected heavy rainfall caused 398 deaths and 120.06 billion RMB of economic losses. The high-societal-impact of this event has drawn much attention from the research community. This article provides a research review of the event from the perspectives of observations, analysis, dynamics, predictability, and the connection with climate warming and urbanization. Global reanalysis data show that there was an anomalous large-scale circulation pattern that resulted in abundant moisture supply to the region of interest. Three mesoscale systems (a mesoscale low pressure system, a barrier jet, and downslope gravity current) were found by recent high-resolution model simulation and data assimilation studies to have contributed to the local intensification of the rainstorm. Furthermore, observational analysis has suggested that an abrupt increase in graupel through microphysical processes after the sequential merging of three convective cells contributed to the record-breaking precipitation. Although these findings have aided in our understanding of the extreme rainfall event, preliminary analysis indicated that the practical predictability of the extreme rainfall for this event was rather low. The contrary influences of climate warming and urbanization on precipitation extremes as revealed by two studies could add further challenges to the predictability. We conclude that data sharing and collaboration between meteorological and hydrological researchers will be crucial in future research on high-impact weather events.

**Key words:** extreme precipitation, observation, dynamics, predictability, climate warming, urbanization

**Citation:** Zhang, Q. H., R. M. Li, J. Z. Sun, F. Lu, J. Xu, and F. Zhang, 2023: A review of research on the record-breaking precipitation event in Henan Province, China, July 2021. *Adv. Atmos. Sci.*, **40**(8), 1485–1500, <https://doi.org/10.1007/s00376-023-2360-y>.

## Article Highlights:

- Large-scale circulation may explain the occurrence of record-breaking precipitation during 17–21 July 2021 in Henan Province, China.
- The intensity and location of the maximum precipitation were associated with mesoscale weather systems.
- The predictability of this event was relatively low because of the complex multiscale interactive dynamics.
- Data sharing and collaboration between different research communities will be crucial in future research on high-impact weather events.

---

## 1. Introduction

High-impact weather events, such as severe local storms, tropical cyclones (TCs), and heat waves, have major effects on society and economic activity (Zhang et al., 2019). Climate warming is reported as the main driver of

---

<sup>※</sup> This paper is a contribution to the special issue on the National Report to the 28th IUGG General Assembly by CNC-IAMAS (2019–2022).

\* Corresponding authors: Qinghong ZHANG, Rumeng LI  
Emails: [qzhang@pku.edu.cn](mailto:qzhang@pku.edu.cn), [lirumeng@pku.edu.cn](mailto:lirumeng@pku.edu.cn)

the increase in frequency and intensity of high-impact weather events in most areas of the world, especially monsoon regions (IPCC, 2013; Wang et al., 2021). China has experienced rapid economic development and population growth in association with increasing urbanization over the past 30 years; therefore, the societal impacts related to high-impact weather events have also increased significantly. Although some progress has been made in our scientific understanding, monitoring and prediction of high-impact weather events, statistics on weather-related losses show that considerable challenges still exist in forecasting these events that often cause complex weather-related problems for society (Zhang et al., 2021a).

From 17 to 23 July 2021, Henan Province in China experienced a high-impact weather event with rainstorm magnitudes rarely experienced previously. According to a government report (<https://www.mem.gov.cn/gk/sgcc/tbzdsqdbcg/202201/P020220121639049697767.pdf>), the highest total rainfall during this event was 1122.6 mm, recorded at Hebi Science and Technology Innovation Center Weather Station (Cai et al., 2022), followed by 993.1 mm at Baizhai Weather Station in Xinmi City (Fig. 1). More than 20 national weather stations recorded record-breaking 24-h precipitation during the event (Xu et al., 2022b). A 24-h precipitation maximum of 624.0 mm was observed at Zhengzhou Weather Station from 0000 UTC 20 July to 0000 UTC 21 July 2021 (Yang et al., 2022), which was close to the average annual mean rainfall in Zhengzhou (640.8 mm) and

exceeded the largest amount ever recorded since the establishment of the station (189.4 mm in July 1978) by about 3.4 times (Cai et al., 2022). A maximum 1-h rainfall of 201.9 mm occurred at Zhengzhou Station from 1600 to 1700 local standard time, which broke the hourly precipitation record for mainland China.

However, the National Weather Center of the China Meteorological Administration (CMA) only forecasted a maximum 24-h precipitation of 150 mm on the morning of 20 July 2021. The ECMWF global operational forecast model predicted that the maximum daily precipitation (100–200 mm) would occur over the mountains 200 km northwest of Zhengzhou City. All of the THORPEX Interactive Grand Global Ensemble (TIGGE) models underestimated the area-averaged precipitation over Henan Province (Zhang et al., 2022) (Fig. 2). The area-averaged precipitation from observations was 74.5 mm, compared with an ensemble mean from the four best-performing operational models [Bureau of Meteorology (BoM), National Centre for Medium Range Weather Forecasting (NCMRWF), UK Meteorological Office (UKMO), and Korea Meteorological Agency (KMA)] of less than 55.0 mm. The mean maximum 24-h precipitation of the four models was 186.9 mm, which was far less than the observed amount of 505.5 mm (from 1200 LST 19 July to 1200 UTC 20 July; forecast initialization at 0000 UTC 19 July). The equitable threat score (ETS) under different rainfall intensities indicated limited forecasting ability for daily rainfall greater than 100.0 mm for all models (Figs. 2b–e). The CMA's global model was the second worst performing among the 12 operational models in terms of area-averaged precipitation forecasting (Zhang et al., 2022).

Similar to the global models, the CMA's regional mesoscale model (with 3-km horizontal grid spacing, hereafter referred to as CMA-MESO) underestimated the rainfall intensity, with a 24-h precipitation maximum (between 1200 UTC 19 July and 1200 UTC 20 July from a forecast initialized at 0000 UTC on 19 July) of 314.8 mm near the mountains (Fig. 3a), while the forecast initialized at 1200 UTC 19 July produced a better forecast in terms of the rainfall center and intensity (Figs. 3b and c). The maximum 24-h precipitation exceeded 400.0 mm within 20 km of Zhengzhou Station, although the precipitation peak hour in the forecast was a few hours earlier than observed. Unfortunately, the CMA-MESO forecast initialized at 1200 UTC 19 July was not considered in the final forecast issued on the morning of 20 July.

The unexpected precipitation led to urban waterlogging, debris flows, floods, and property damage in Henan Province, especially in Zhengzhou City (which has a population of 12.7 million). Floodwaters in 12 major rivers rose above the warning level. Eight floodwater storage and detention areas were opened across the province. The main urban areas were severely flooded on the afternoon of 20 July and the maximum water depth on the roads was nearly 2.6 m, resulting in more than half of the city's residential areas with underground spaces and important public facilities

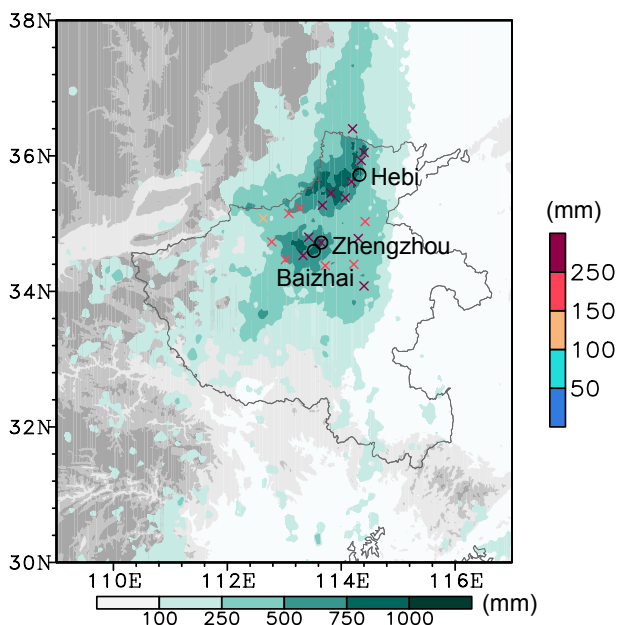


**Fig. 1.** Grid precipitation (shaded in green colors; units: mm) with a resolution of  $0.01^\circ$  from 0000 UTC 17 July to 0000 UTC 23 July 2021. Stations where the daily rainfall records from 1950–2021 were broken are denoted by a cross with a color corresponding to the key on the right-hand side of the figure. Gray shading denotes the terrain height (light gray: (100–500) m; medium gray: (500–1000) m; dark gray: above 1000 m). The dark line is the boundary of Henan Province.

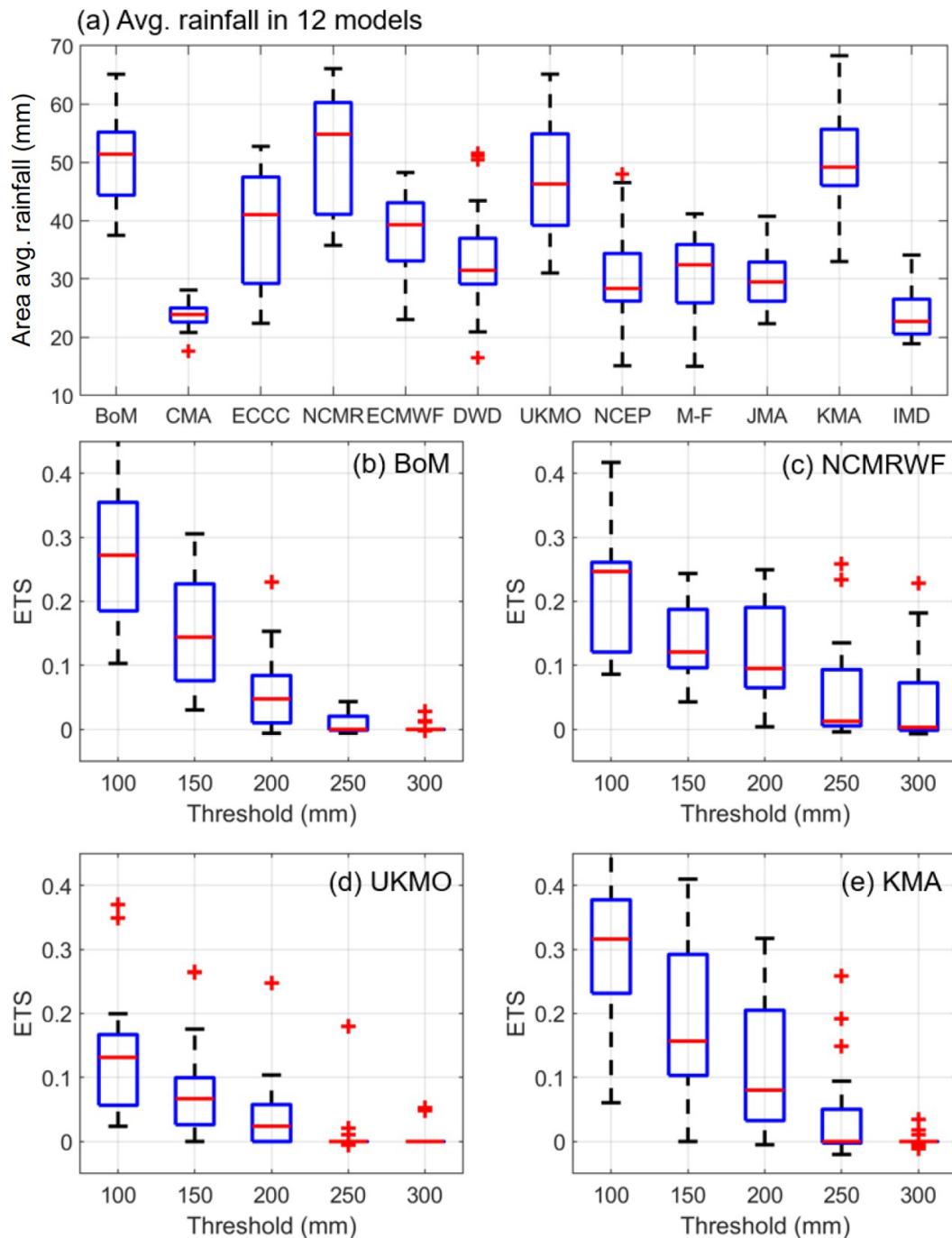


**Fig. 2.** Precipitation according to ensemble forecasts. (a) Boxplot of the area-averaged 24-h accumulated rainfall for ensemble members from 12 TIGGE models. NCMRWF is denoted by NCMR due to the limited space on the  $x$ -axis. (b–e) Boxplots of the ETSs for ensemble members from the (b) BoM, (c) NCMRWF, (d) UKMO, and (e) KMA models at various thresholds (range: 100–300 mm) over the study region. The whiskers extend to the most extreme data points not classified as outliers. Points were identified as outliers if they were larger than  $q_3 + 1.5(q_3 - q_1)$  or smaller than  $q_1 - 1.5(q_3 - q_1)$ , where  $q_1$  and  $q_3$  are the 25th and 75th percentiles, respectively [Reprinted from (Zhang et al., 2022), with permission from Springer Nature].

being flooded. A total of 398 people died or went missing, 14.8 million people were otherwise affected by the disaster, and the direct economic loss was 120.06 billion RMB, according to the government report (<https://www.mem.gov.cn/gk/sgcc/tbzdsdgcgbg/202201/P020220121639049697767.pdf>).

This record-breaking event received much attention from researchers in various scientific disciplines, such as atmospheric science, hydrology, and disaster management. The main purpose of the current paper is to provide a “meta-analysis” and review of recent studies on the event in the dis-

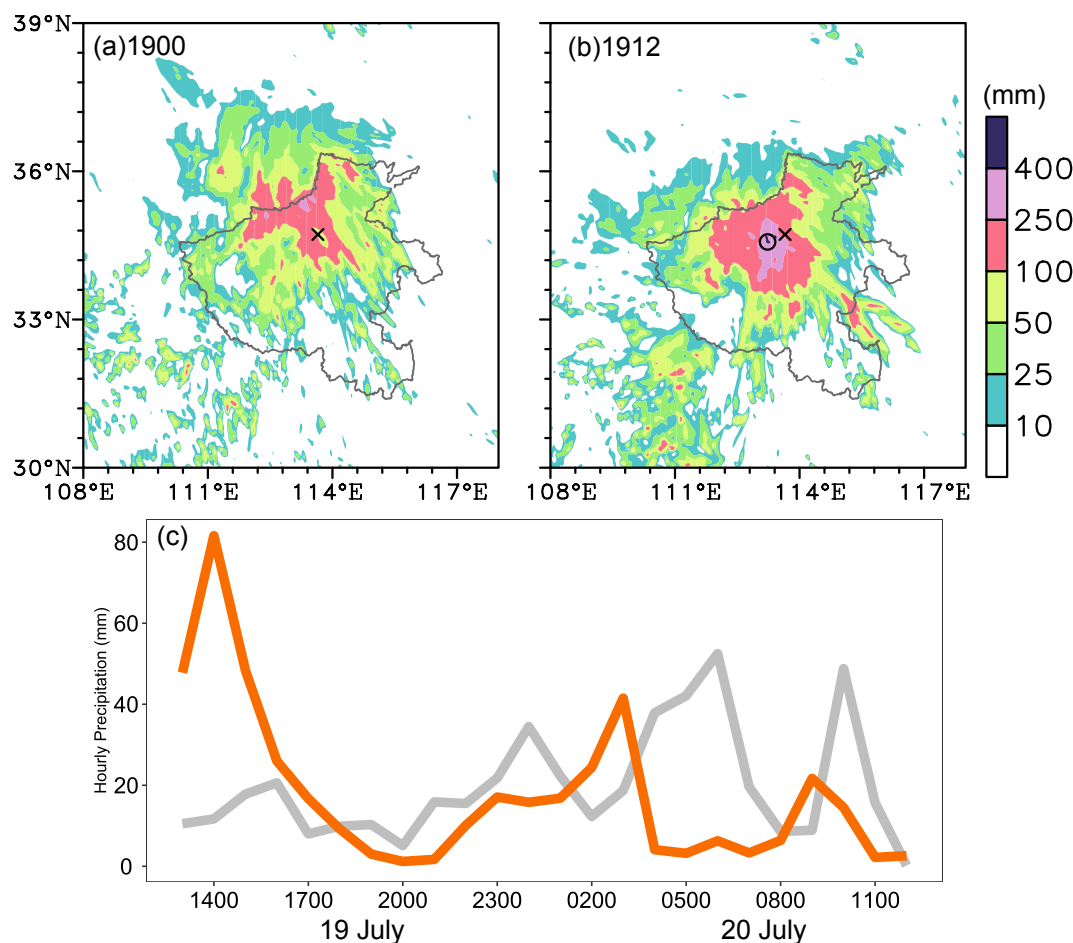


**Fig. 3.** (a) 24-h accumulated precipitation (shading) from 1200 UTC 19 July to 1200 UTC 20 July 2021 from the CMA-MESO forecast initialized at 0000 UTC 19 July. (b) As in (a) but for the forecast initialized at 1200 UTC. The cross in (a, b) represents the location of Zhengzhou City. The circle in (b) represents the grid point with the maximum forecasted 24-h precipitation. (c) Comparison of the hourly precipitation between the gridded observations (gray) at a grid point nearest to Zhengzhou and the forecasted maximum (orange) in the circle in (b).

cipline of atmosphere science. Section 2 introduces the large-scale circulation background of the event. The characteristics of the event as described by mesoscale observations and reanalysis data are summarized in section 3, and the dynamic processes and predictability are considered in section 4. The influences of climate warming and urbanization are discussed in sections 5 and 6, respectively. Finally, a summary and some further discussion are provided in section 7.

## 2. Large-scale circulation background

Several papers have described the large-scale circulation, anomalous atmospheric conditions, and local weather systems during 17–23 July using ERA5 data (Ran et al., 2021; Zhang et al., 2021b; Cai et al., 2022; Kong et al., 2022). In this section, we review the large-scale circulation background to the event as revealed by ERA5, and in the next section illustrate some mesoscale differences between ERA5 and a mesoscale reanalysis.

The large-scale circulations around Henan Province dis-

played a saddle-like pattern that formed on 12 July and persisted until 22 July (Cai et al., 2022; Kong et al., 2022; Chyi et al., 2023). The western Pacific subtropical high (WPSH) was located near the Japan Sea from 19 to 21 July 2021 (Fig. 4). Another continental subtropical high was located over North China. A trough in the midlatitudes and an inverted trough over South China were located between these two subtropical highs, and a binary TC system comprising TC In-Fa (2021; near the East Sea) and TC Cempaka (2021; near the South China Sea) was also a key factor (Fig. 4). The strong pressure gradient between TC In-Fa (2021) and the WPSH strengthened the easterly winds, which together with a southerly monsoon from the south of Henan brought abundant moisture inland (Fig. 4) (Kong et al., 2022; Wei et al., 2023). From 18 to 23 July 2021, TC In-Fa remained in the East China Sea, with a translation speed of  $6 \text{ km h}^{-1}$  (estimated using best-track data from the CMA), which was significantly slower than the global mean TC translation speed from 1951 to 2011 of  $17.5 \text{ km h}^{-1}$  (Chan, 2019; Yamaguchi et al., 2020). The stable saddle-like circulation



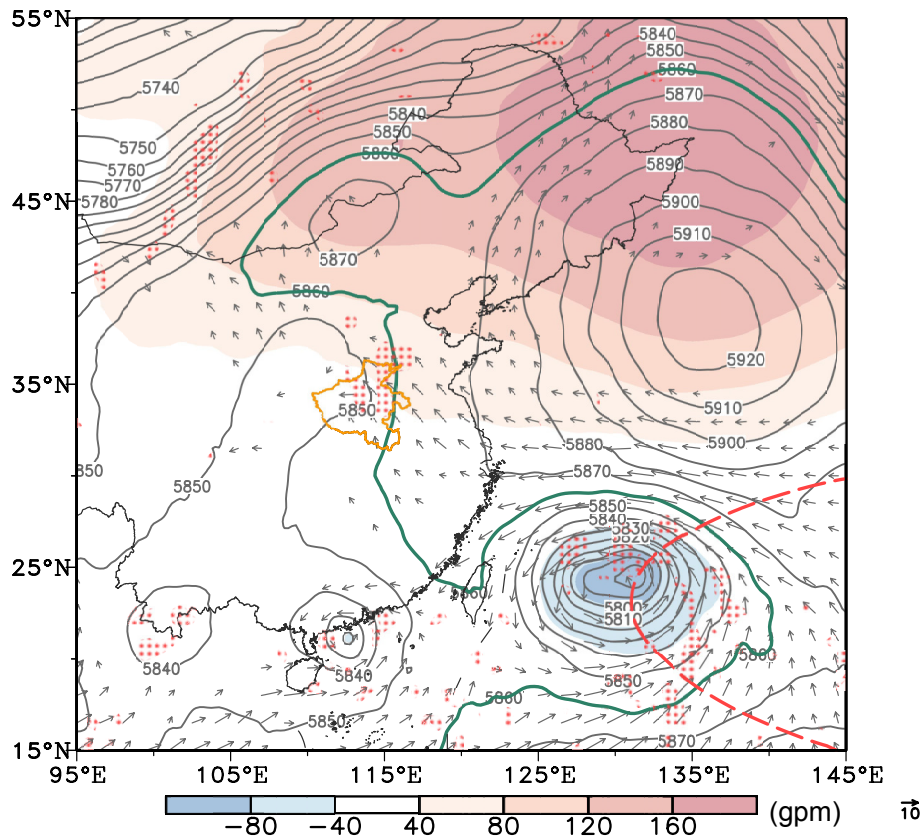


**Fig. 4.** Geopotential height (contours) and its anomalies (shaded; units: gpm) at 500 hPa from 19 to 21 July 2021. The green solid contour and red dashed contour denote the 5860 gpm contour in the three-day period and associated climatology in the period 1980–2021, respectively. The vectors correspond to the 925-hPa wind with a velocity  $> 4 \text{ m s}^{-1}$ . Red dots represent the 200-hPa divergence  $> 10^{-5} \text{ s}^{-1}$ . The orange line is the boundary of Henan Province.

pattern supported a stationary WPSH and the slow movement of TC In-Fa (2021), thereby favoring continuous moisture transport to inland areas (Kong et al., 2022; Chyi et al., 2023). An upper-level trough was located to the northwest of Henan Province at 200–300 hPa, which led to strong upper-level divergence. Such a circulation pattern is thought to be conducive to the formation of severe rainstorms (Cai et al., 2022; Kong et al., 2022; Xu et al., 2022a, b; Wei et al., 2023).

Compared with the mean circulation for July over the past 50 years, a significant anomaly in geopotential height was seen at 500 hPa in the period 19–21 July 2021, with the WPSH extending far to the north (to  $35^{\circ}$ – $40^{\circ}$ N) and a low occurring in association with a TC to the south. The WPSH ridgeline remained roughly  $15^{\circ}$  farther north than average (Fig. 4). The circulation anomalies were analyzed quantitatively using an obliquely rotated principal component scheme by Xu et al. (2022b). Based on the categorized daily atmospheric large-scale circulations over North China in the summers of 1979–2021 using the geopotential heights at 500 and 925 hPa in succession, they found that the circulation pattern during 19–21 July 2021 was previously observed in only 1.6% of all summer days in the past 43 years. However,

the anomalous large-scale circulation pattern could not completely explain the record-breaking event; other dynamic processes related to mesoscale convective storms may have been contributing factors.

### 3. Mesoscale observations and reanalysis

China has made major advances in terms of the development of comprehensive observation systems in recent years, by increasing the density of observations, hardware updates, innovative algorithms, and quality control, and by establishing new automatic detection systems such as the FY-4B satellite (replacing FY-4A) and raindrop spectrometers. The comprehensive observation systems provide valuable opportunity to mesoscale detection and analysis of high-impact weather events.

#### 3.1. Satellites

Satellite retrieval precipitation products have been shown to underestimate the intense rainfall significantly during this record-breaking event (Liu et al., 2022b). However, those products that integrate infrared and passive microwave data were better than those that only use infrared information, indicating the importance of microphysical pro-



cess in generating the extreme precipitation in this event. Nevertheless, the geostationary high-speed imager (GHI), which is a new instrument onboard the FY-4B satellite, demonstrated its monitoring ability during this event. GHI has 250-m grid spacing in the visible band and 2-km grid spacing in the thermal infrared band for a  $2000 \times 1800$  km region, and updates every 1 min (<https://space.oscar.wmo.int/instruments/view/ghi>). The target area can be changed every 30 min. Therefore, GHI provides accurate, reliable, and timely high-resolution data to meet emergency response requirements when high-impact weather occurs. As the record-breaking precipitation in Zhengzhou was not forecasted on 20 July, the GHI onboard FY-4B remained targeted on TC Cempaka and missed the Zhengzhou area (Fig. 5a). On the following day, FY-4B was turned to monitor Henan but the main area of precipitation had moved to the northern tip of Henan and the precipitation intensity became weaker (Fig. 5b).

Although FY-4B was not monitoring Zhengzhou on 20 July, assimilation of the clear-sky radiance data obtained by the advanced geostationary radiance imager onboard FY-4A was shown to improve the forecast of 24-h accumulated precipitation with an amount surpassing 500 mm, and the forecast of the precipitation location, using the regional mesoscale Weather Research and Forecasting (WRF) model (Xu et al., 2023). The assimilation updated the atmospheric temperature and humidity over the ocean, which in turn changed the vertical and horizontal wind fields over the ocean, leading to a narrower and stronger water vapor transport path to Zhengzhou in the lower troposphere. Conversely, in the control experiment, water vapor convergence and upward motion were more widely distributed, and thus the precipitation centers

were more diffuse. Using Geostationary Interferometric Infrared Sounder (GIIRS) water vapor channel data and CMA-MESO, Yin et al. (2022b) found the location error of maximum 24-h accumulated precipitation forecasts in GIIRS assimilation experiments decreased from 128.48 km in the control experiment to 28.97 km (Yin et al., 2022b). The effectiveness of satellite data assimilation was largely determined by the key dynamics that produced the record-breaking precipitation, which is discussed in the next section.

### 3.2. Surface-based observations

A  $650 \times 820$  km area near Henan Province has 24 Doppler weather radars, 3 wind profile radars, 351 national weather stations covering all variables (including raindrop spectrometers), and 6924 automatic weather stations (AWSs) covering four variables (temperature, wind, relative humidity and precipitation) (Fig. 6). The average distance between surface rain gauge stations in Zhengzhou Province has reached 100 m, which is one of the highest-resolution grid spacings in the world, and provides precise precipitation information for disaster prevention and model verification. The grid-averaged ERA5 and observed 24-h precipitation amounts were comparable during 19–21 July (24/29, 37/41, and 26/29 mm, respectively; Fig. 7). However, comparison of the observed 24-h precipitation and ERA5 data, both with  $0.25^\circ$  grid spacing, showed large differences in precipitation intensity and the center location of maximum precipitation. The ERA5 precipitation was at least 200 mm lower than the observed precipitation center during 19–21 July, indicating that the large-scale circulation alone cannot explain the record-breaking precipitation. However, ERA5 was used in several studies to

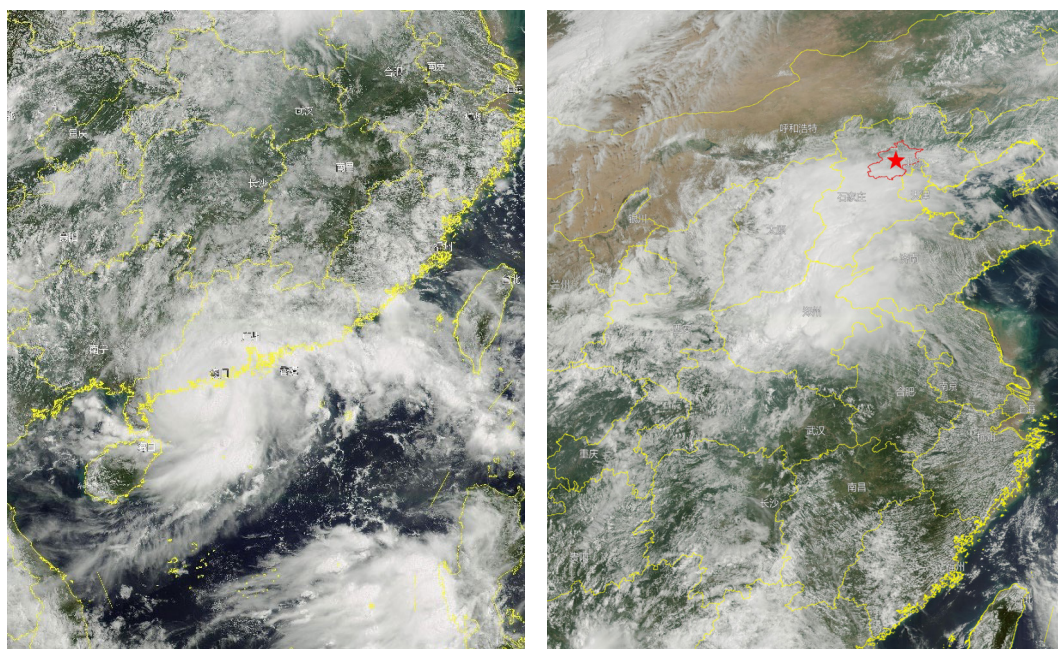


**Fig. 5.** Visible images from the FY-4B geostationary high-speed imager acquired at 0230 UTC 20 July 2021 (left) and 0230 UTC 21 July 2021 (right).

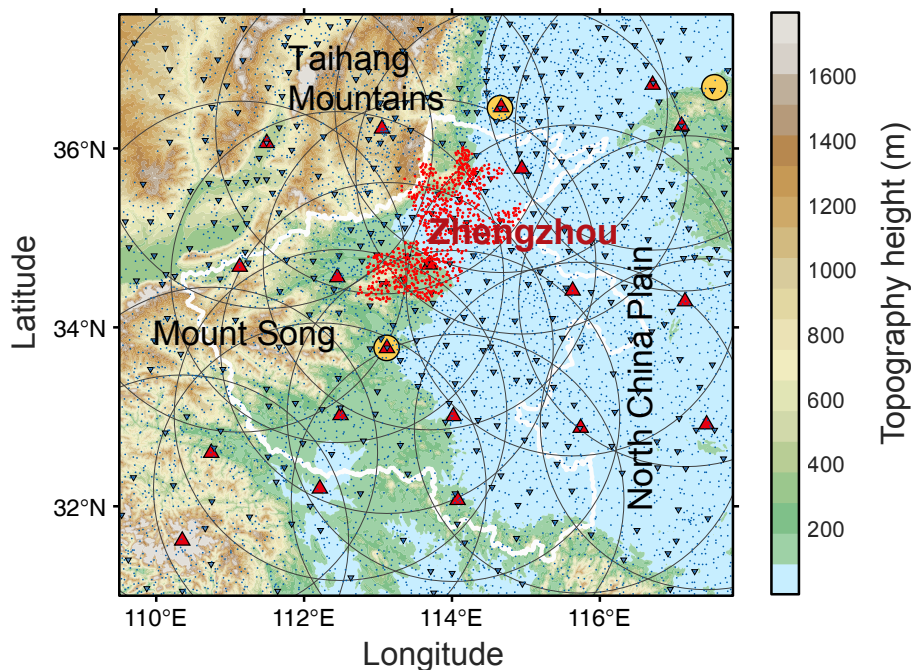


**Fig. 6.** Locations of surface-based observations from 24 doppler weather radars (red triangles), 3 wind profile radars (yellow circles), 351 raindrop spectrometers (blue triangles), and 6924 AWSs (small dots). The blue color represents stations belonging to the CMA and the red color represents those belonging to the Water Control Bureau. The white outline indicates Henan Province.

explain the observed mesoscale rainstorm and record-breaking precipitation (Fu et al., 2022; Kong et al., 2022).

### 3.3. Reanalysis at 2-km grid spacing with 6-min intervals

The availability of high-resolution radar data and high-density surface observations provided an opportunity to conduct a high-resolution reanalysis using the four-dimensional variational (4DVar) technique in the Variational Doppler Radar Assimilation System (VDRAS) (Sun and Crook, 1997). In a recent study, Sun et al. (2023) produced a rapid update analysis with a 6-min cycling interval and 2-km horizontal grid spacing. The 2-km reanalysis revealed the mesoscale factors responsible for the formation and development of the record-breaking precipitation that occurred in Zhengzhou on 20 July 2021. They found that the rainstorm was formed via the sequential merging of three convective cells (Fig. 8), which were initiated along the convergence bands in a meso-beta-scale low-pressure system (meso-low). The cells A and B in Fig. 8a initiated over the mountains southwest of Zhengzhou, while cell C initiated over the plains to the east. The first merging of cells A and B occurred at 0436 UTC near Mixian Station (Fig. 8c). The vertical motion intensified and extended to above the melting level after merging, associated with a tenfold increase in the number concentration for small (< 2 mm) and medium (2–4 mm) raindrops. The second merging occurred between merged cells AB and cell C near Zhengzhou Station around 0700 UTC 20 July (Fig. 8a), and this merged storm

remained at Zhengzhou for more than two hours and was responsible for the record-breaking hourly precipitation (Sun et al., 2023; Wei et al., 2023). The number and size of raindrops changed significantly after the second convection merging event (Fig. 8e). The number of small and medium raindrops increased by one to two orders after merging, and the high amount persisted for at least 1 h. Large raindrops also appeared. The convection merging event likely caused intense upward motion, which in turn accelerated the onset of new condensation and collision-coalescence processes (Chen et al., 2022). This implied an abrupt increase of graupel in the upper level after the merging of convection initiated over the mountains and plains, along with an increase in the number of small (< 2 mm) and medium (2–4 mm) raindrops (which accounted for nearly 90% of the rainfall at Zhengzhou Station between 0800–0900 UTC).

Comparison of the ERA5 and 2-km reanalysis data showed that there was little difference in the location and intensity of the meso-low between ERA5 and the 2-km reanalysis at 2200 UTC 19 July. However, the meso-low in ERA5 was 200 km farther to the north and with higher intensity than in the 2-km reanalysis at 0900 UTC 20 July, when the record-breaking hourly precipitation occurred (Fig. 9). This might explain the intensity and location errors in precipitation in the ERA5 analysis. The real-time ECMWF model also failed to accurately predict the location and intensity of the meso-low (Zhao et al., 2022). It is considered important to determine if the error in precipitation would be reduced if the meso-low was in the correct location.



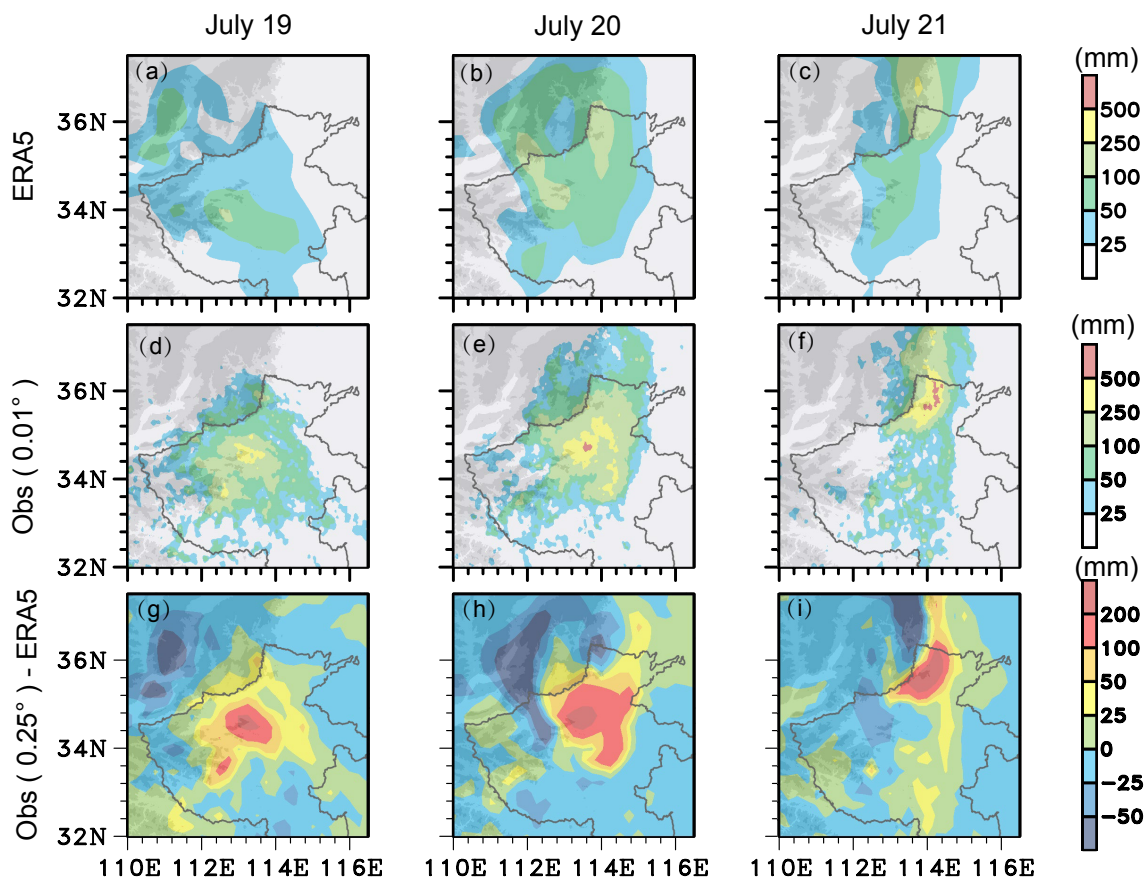


**Fig. 7.** (a–c) ERA5 daily precipitation, (d–f) observed gridded precipitation (color shaded; units: mm) with a horizontal resolution of  $0.01^\circ$ , and (g–i) difference in daily precipitation between the observed gridded precipitation with a horizontal resolution of  $0.25^\circ$  and the ERA5 daily precipitation from 19 to 21 July 2021. Gray shading denotes the terrain height (light gray: (100–500) m; medium gray: (500–1000) m; dark gray: above 1000 m). The dark line is the boundary of Henan Province. [Data from Fig. 10 in Xu et al. (2022b)], reproduced with permission from Springer Nature.

## 4. Dynamics and predictability

### 4.1. Dynamics

The mechanisms underlying the record-breaking precipitation have been the focus of several convection-permitting model simulation studies (Yin et al., 2022a; Sun et al., 2023; Wei et al., 2023). The first dynamical process was proposed by Yin et al. (2022a), who highlighted the significance of a mesoscale vortex encircled by arc-shaped updrafts. The arc-shaped convergence acted like a multidirectional lifting pump and transported precipitation from different areas into the same region. However, the maximum precipitation in their simulation was near the mountains west of Zhengzhou City, which is far away from the observed location. The merging of convective cells was not simulated in their study.

Wei et al. (2023) found that the record-breaking precipitation was caused by a quasi-stationary storm coming from east of Zhengzhou. Beside a low-level meso- $\beta$ -scale vortex [or meso-low as in Sun et al. (2023)] shown by Yin et al. 2022a, they found a barrier jet on the eastern slopes of the Taihang Mountains due to terrain blocking of the strong easterly synoptic low-level jet flow. The southerly winds associated

with the vortex achieved a similar intensity as the northerly flow originating from the barrier jet, resulting in the quasi-stationary storm in Zhengzhou City. This simulation was consistent in some respects with the 2-km reanalysis by Sun et al. (2023) based on observed radar and surface data and VDRAS 4DVar. The mesoscale reanalysis confirmed the roles of the mesoscale low-pressure system and the barrier jet along the Taihang Mountains. However, the reanalysis indicated that a downslope gravity current resulting from overnight mountain-top radiative cooling, and likely the evaporation of light rain over the Taihang Mountains too, was responsible for the northerly flow toward Zhengzhou. They also suggested that the barrier flow might not have played an important role without the interaction with this downslope gravity current.

Based on previous studies, we summarize the three mesoscale systems that played a critical role in the development of the rainstorm associated with the hourly record-breaking precipitation (Fig. 10). Among the three systems, the meso-low that developed from an inverted trough southwest of Zhengzhou was most important in terms of the formation and intensification of the rainstorm. Two terrain-influenced

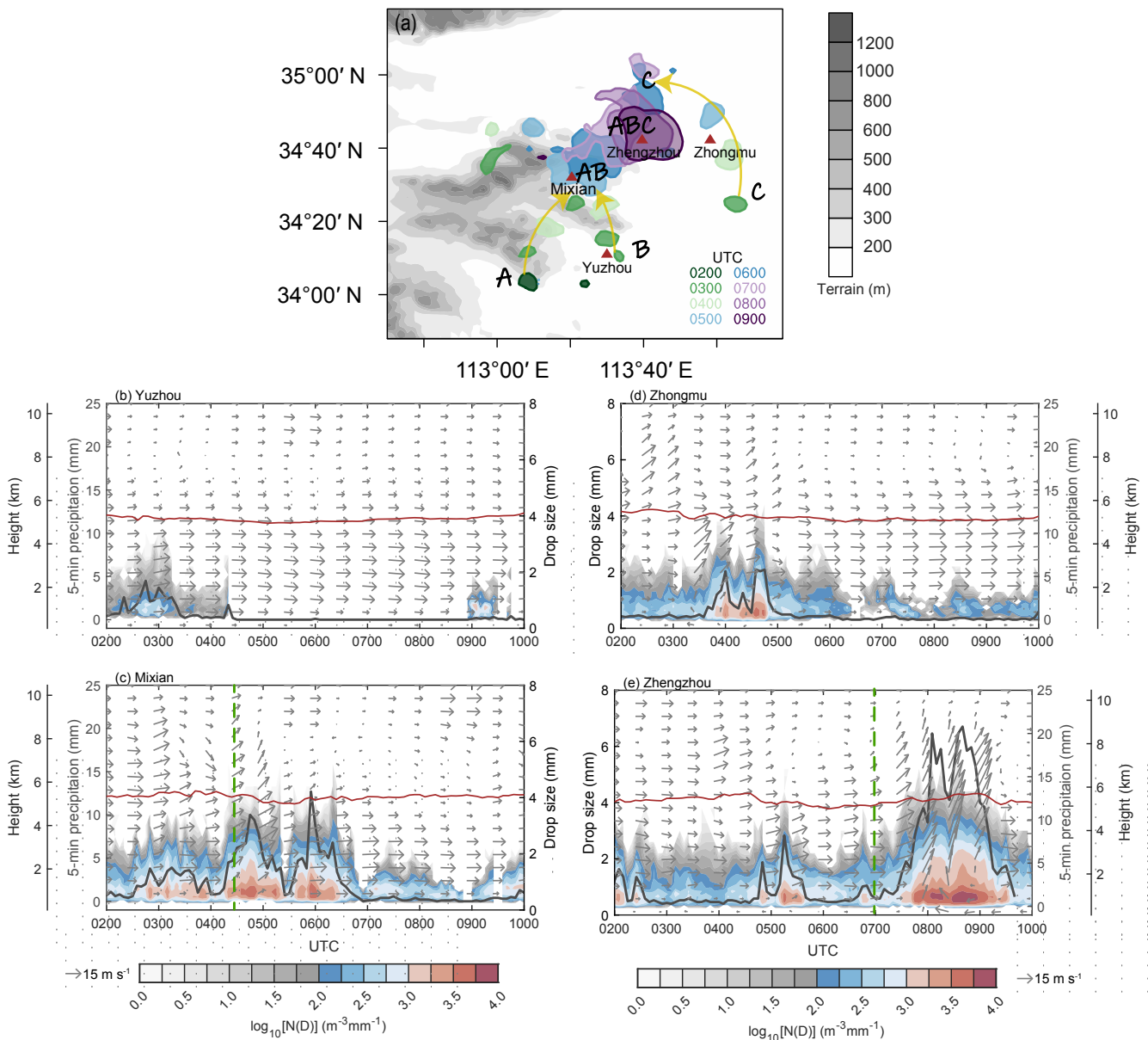


**Fig. 8.** (a) Storm swath generated by plotting mosaic reflectivity > 42 dBZ at 1-h intervals between 0200 and 0900 UTC. The four red triangles in represent the locations of stations. (b–e) Time series of the raindrop  $N(D)$  ( $m^{-3} mm^{-1}$ ) for Yuzhou, Mixian, Zhongmu, and Zhengzhou stations, respectively. The red lines indicate the evolution of the mean raindrop size. Black lines indicate the evolution of 5-min accumulated precipitation. The vectors represent the meridional and vertical components of the wind in the 2-km VDRAS reanalysis. The green dashed lines in (c, e) represent the convection merging times.

flows near the Taihang Mountains north of Zhengzhou, i.e., a barrier jet and downslope gravity current, contributed to the local intensification of the rainstorm and intense record-breaking hourly precipitation. These three mesoscale features synergistically enhanced the moisture transport to Zhengzhou in the north–south direction in the few hours prior to the occurrence of the extreme rainfall, in addition to the existing moisture transport by large-scale flow from the east.

In addition to dynamic processes, the precipitation efficiency was also analyzed by a WRF simulation (Yin et al., 2023). Water vapor flux convergence was the main factor

influencing the large-scale precipitation efficiency, while cloud-microphysical precipitation efficiency was dominated by the net consumption of water vapor by microphysical processes. Consumed water vapor mainly produced cloud water and ice-phase particles, which were subsequently converted to raindrops by the melting of graupel and the accretion of cloud water by rain water (Yin et al., 2023). The simulation suggested the importance of graupel melting, which agrees with the raindrop observations (Fig. 8).

#### 4.2. Predictability

The uncertainties and error growth in forecasting this high-impact rainfall event were analyzed at different spatial

and temporal scales, using forecasts from global to regional convection-permitting numerical models in Zhang et al. (2022). The forecasts from global operational models have been discussed in section 1 (Fig. 2). Here, we focus on regional synoptic and convection-permitting models.

Sensitive areas identified by a conditional nonlinear opti-

mal perturbation (CNOP) scheme using a coarse-grid-spacing regional model (horizontal grid spacing of 60 km and 21 terrain-following vertical levels), showed three areas of “total moist energy norm”. The first was in the mid and lower altitudes in the southeast of Henan Province, associated with the easterly low-level jet. The second peaked in the

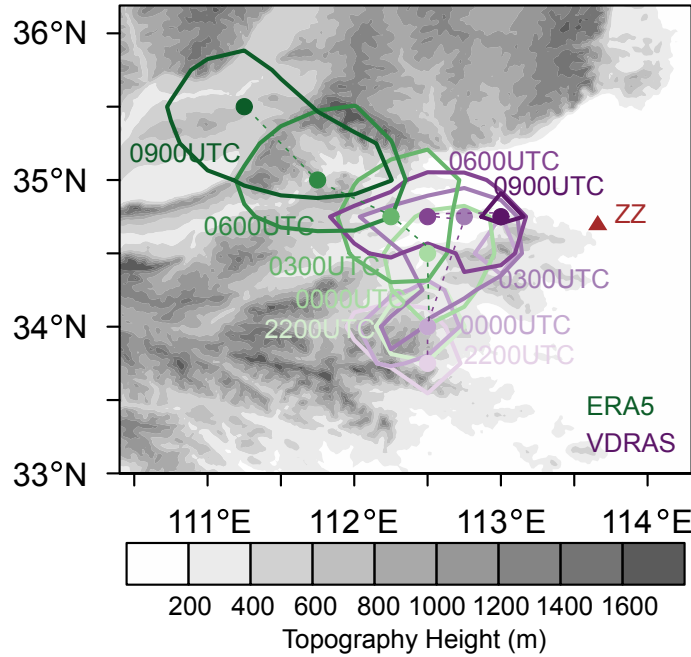


**Fig. 9.** Comparison of ERA5 (green lines and dots) and VDRAS (purple lines and dots) reanalysis data showing the evolution of the mesoscale low at 700 hPa (ERA5) and 3 km (VDRAS) from 2200 UTC 19 July to 0900 UTC 20 July, with 3-h intervals. The dots are the center locations of the meso-low represented by local maximums of relative vorticity. The contours are isolines of relative vorticity at  $2.8 \times 10^{-3} \text{ s}^{-1}$ . Zhengzhou Station is marked by a brown triangle.

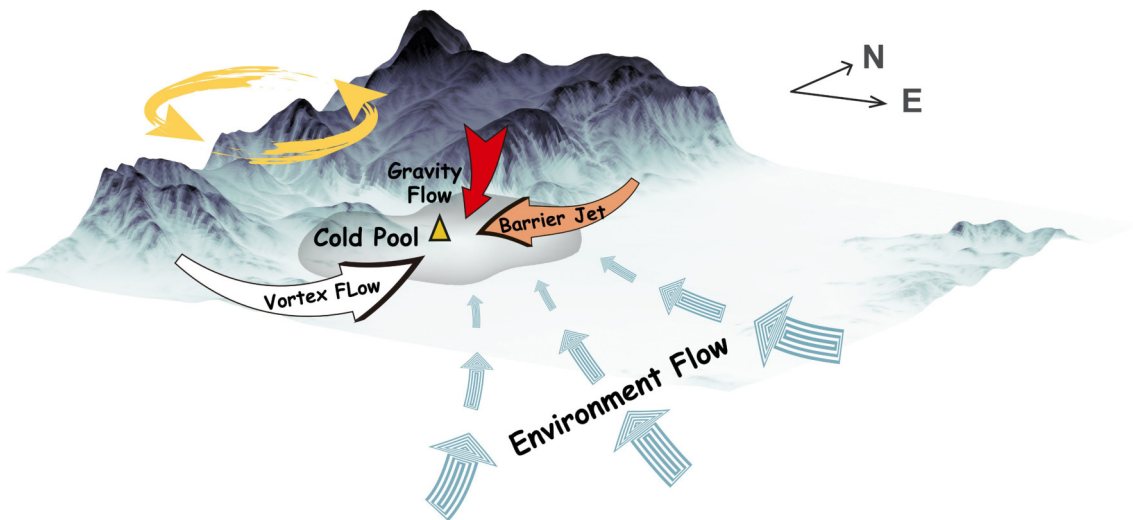


**Fig. 10.** Schematic of the multiscale dynamical processes responsible for the extreme hourly rainfall in Zhengzhou on 21 July 2021. The gold triangle is the location of Zhengzhou City. The turquoise, white, red, and brown arrows represent the environmental flow, the southwesterly flow from the meso-low, the downslope gravity flow originating from the top of the Taihang Mountains, and the barrier jet, respectively. The light yellow circular arrows indicate the midlevel circulation of the meso-low.



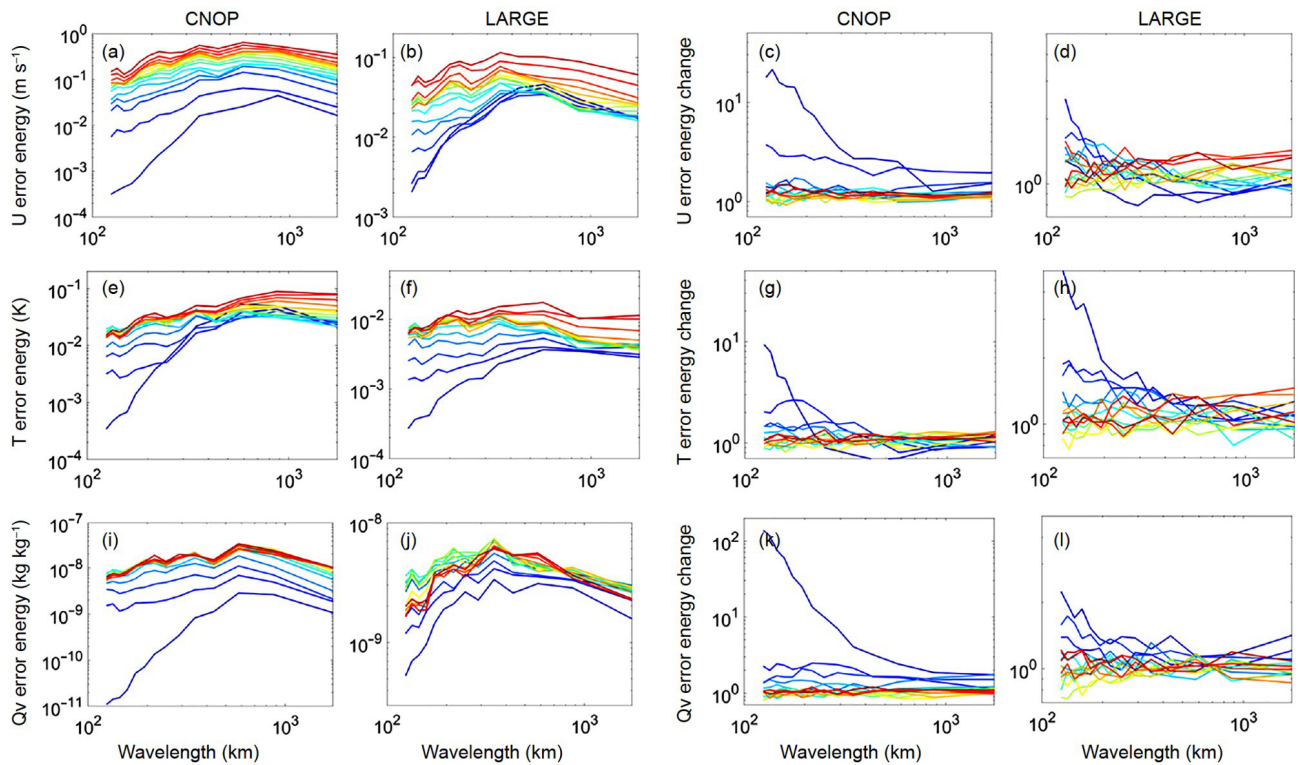


**Fig. 11.** Hourly power spectra (first and second columns) and growth of the power spectra (third and fourth columns) of the zonal ( $U$ ) wind perturbations (upper panels), Temperature ( $T$ ) perturbations (middle panels), and water vapor ( $Q_v$ ) perturbations (bottom panels) from 0600 UTC to 2100 UTC 19 July 2021 (first 15 h of the simulation), for the CNOP (first and third columns) and one of the best members in LARGE (second and fourth columns). Blue colors denote earlier times (shorter simulations) and red colors denote later times (longer simulations) [Reprinted from Fig. 13 in Zhang et al. (2022), with permission from Springer Nature].

mid and upper level, and centered at the mesoscale low and inverted trough at 500 hPa. The third area was in the northwest of Henan Province and was associated with a trough at 300 hPa. The second and third sensitive areas were likely influenced by the large-scale divergence from the mid to upper level, which favored upward motion (Zhang et al., 2021b; Cai et al., 2022), while the first area may have been associated with the moisture feeder band below 500 hPa (Zhang et al., 2022). These sensitive areas are associated with the anomalous circulation characteristics referred to in section 2. The importance of the easterly low-level jet was verified in the data assimilation research by Xu et al. (2023).

Practical and intrinsic predictability in the record-breaking rainfall in Zhengzhou were also analyzed in Zhang et al. (2022), using the convection-permitting WRF model with 40 ensembles whose initial uncertainties were from relatively large scales (LARGE). The initial conditions of the different ensemble members varied in terms of their representation of the upper-level ridge and trough, the mid-level low-pressure system over Henan Province, and the easterly low-level jet associated with the WPSH and TC In-Fa (2021). The general location of rainfall was easy to predict because rainfall regions were similar across all ensemble forecasts. However, the predictability of the extreme rainfall occurring during this event was intrinsically limited by the deterministic fore-

casting system, where there were large uncertainties in the 24-h precipitation amount in these forecasts, even with minute initial perturbations (Fig. 11). The authors demonstrated the inability of large-scale errors to grow unless the amplitude of small-scale errors increases sufficiently, because small-scale errors grow faster than large-scale ones.

In this event, the first echo formed at 0200 UTC on 20 July 2021, and then merged with two other convective systems, finally producing record-breaking precipitation at 0800–0900 UTC. Normally, it takes 6 h for mesoscale errors to grow to a large scale. Lower predictability is expected with longer durations of convection. This might be the reason that ECMWF gave the wrong location of the mesoscale low shown in Fig. 9.

The predictability of this extreme rainfall was also investigated by two 4-km convection-permitting ensemble forecast systems (CEFSs) based on the WRF model (Zhu et al., 2022). One was initialized from the NCEP Global Ensemble Forecast System (GEFS) (CEFS\_GEFS), and the other from time-lagged ERA5 data (CEFS\_ERA). The simulated rainfall centers in both CEFSs were located in the foothills of the Taihang Mountains, indicating that the heavy rainfall induced by orographic lift and blocking was predictable. Only a few ensemble members were able to simulate the hourly rainfall peak, which may shed light on the evolution and propagation of extreme rainfall. However, for the extreme 24-h rainfall

observed in Zhengzhou, most members had large positional errors within a few hundred kilometers, highlighting the limited intrinsic predictability of the location of city-scale extreme rainfall (Zhu et al., 2022). In this case, the position of the convergent region between the mesoscale low and easterly wind had a large uncertainty in the ensembles. This result agreed with that of Xu et al. (2022a), in which the intensity and structure of the easterly jet were the key factors for ensuring accurate precipitation forecasts.

## 5. Climate warming

The synoptic conditions during this extreme rainfall event in Henan were apparently highly unusual and most likely caused by chaotic atmospheric dynamics. However, given that the global mean temperature has increased by almost 1.0 K over the past century, there is also a need to consider how current global warming may have impacted this record-breaking event, and how future warming may generate similar synoptic-scale dynamics.

To estimate the effect of warming on the record-breaking precipitation, a narrative attribution approach was used based on simulations of the event with a small-domain, high-resolution cloud-resolving model (Qin et al., 2022). Warming was determined to have the potential to significantly intensify both regional-scale ( $7\% \text{ K}^{-1}$ – $9\% \text{ K}^{-1}$ ) and station-scale ( $10\% \text{ K}^{-1}$ – $14\% \text{ K}^{-1}$ ) precipitation extremes, depending on the convective organization. This resulted in shear-driven convective organization producing more precipitation extremes at both the regional and station scale than unorganized convection due to stronger diabatic heating feedback. The organized

convection in Qin et al. (2022) occurred along a squall line, in which there was a decrease of zonal wind from  $20 \text{ m s}^{-1}$  at the surface to  $0 \text{ m s}^{-1}$  at a height of 1 km. The simple shear was not the same as in the observations, in which convection merged under a convergent mesoscale low. The organized convection may not represent the actual situation in this case.

Climate warming could also impact large-scale daily circulations because uncertainty in climate projections are mainly due to large-scale circulations (Shepherd, 2014). Furthermore, extreme precipitation is frequently associated with convective storms (Dowdy and Catto, 2017; Yamaguchi et al., 2020; Ng et al., 2022), and large-scale circulation may create circumstances that favor convection (Liu et al., 2022a). From the 1980s to the 2010s, as the average TC track shifted to the north, the number of days with a similar circulation pattern to this event showed a significant increasing trend at the decadal scale (Xu et al., 2022b). Thus, the question of how the occurrence and intensity of extreme precipitation can be affected by climate warming remains to be addressed.

## 6. Urbanization

The effect of urbanization on the heavy rainfall that occurred over Zhengzhou on 20 July 2021 was analyzed using two ensemble WRF model simulations (each consisting of 11 members) with different land cover scenarios (Luo et al., 2023). The first included cities (CTRL), while the second replaced them with the most common nearby land type, i.e., mixed dryland/irrigated cropland and pasture (NURB)

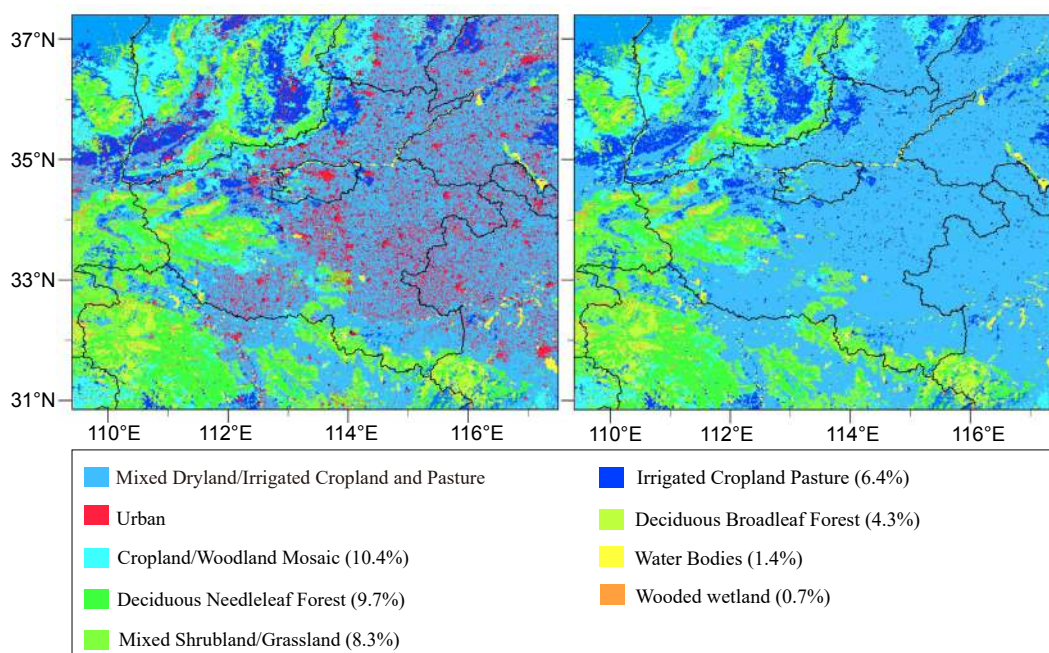


**Fig. 12.** Land-use/land type maps used in the CTRL (left) and NURB (right) experiments. Names and areal fractions (%) of the land cover/land-use types in CTRL are labeled at the bottom. [Adapted from Figs. 2b and c in (Luo et al., 2023), with permission from Springer Nature].

(Fig. 12).

The ensemble mean hourly accumulated rainfall over the Henan region was reduced by about 5% at the beginning of the simulation, and reached 30% after 20 h, which resulted in a 13% reduction in the 24-h accumulated rainfall in CTRL relative to NURB. The maximum hourly rainfall over Zhengzhou in CTRL was reduced by 15–70 mm in individual members compared with NURB runs. The reduction in rainfall was mainly due to the dryness caused by the limited evapotranspiration, combined with the wind stilling effect associated with the increased surface roughness in the urban areas upstream of Zhengzhou City. These effects resulted in a decrease in moisture inflow from the south and east to Henan Province, and a weakening of the convective updrafts. The continuous precipitation cloud over Zhengzhou City from 18 to 20 July greatly reduced the level of solar radiation, suggesting that the heat island effect of Zhengzhou was limited. This case study highlighted the importance of upstream urbanization over a broad upstream area, which was influenced by large-scale circulation. Flows from areas to the north, east, and south converged over Zhengzhou City, and the numerous towns and cities shown in Fig. 12b caused a reduction in precipitation in Henan Province.

## 7. Summary and implications

A record-breaking precipitation event that occurred during 17–21 July 2021 in Henan Province, China, had huge societal impacts. Now, after two years, it is important to examine whether our physical understanding can explain this extreme precipitation event; and if so, what action we can take to reduce the impacts of similar weather events in the future.

The anomalous nature of the large-scale circulation may explain the occurrence of this event from the viewpoint of moisture supply and large-scale dynamic lifting. However, the intensity and location of the maximum rainfall center were mainly associated with mesoscale weather systems. The extreme rainstorm that caused record-breaking hourly precipitation in Zhengzhou formed after two sequential convection merging processes, and remained over Zhengzhou City for more than two hours. The stationary position of this rainstorm can be attributed to the balance of three flows: a southerly flow to the east of the mesoscale low; a northeasterly flow due to the barrier jet caused by the synoptic southeasterly flow and steep mountains to the north of Zhengzhou; and a northwesterly downslope gravity flow due to the mountain-top radiative cooling and probably the evaporation of light rain over the Taihang Mountains.

The record-breaking precipitation was contributed by multiple-scale weather systems, and the mesoscale low might have been the key linkage in their multiple-scale interaction. While the location and structure of this mesoscale low was essential for the convection merging process, we have shown (Fig. 9) that in ERA5 this meso-low was ~200

km to the northwest compared with the mesoscale reanalysis based on the assimilation of radar and surface data. Inaccurate prediction of the meso-low could be one of the reasons why global operational weather prediction systems predicted the rainfall center to be over the mountains rather than the city of Zhengzhou. The genesis of the mesoscale low or vortex was also not clear, although several studies have suggested that heating of preexisting convection (Fu et al., 2022), the intensification of the large-scale easterly wind (Kong et al., 2022), or the downward invasion of moist potential vorticity from the middle and upper troposphere (Gou et al., 2023), might have been the key factors.

The complex multiscale interactive dynamics in this event may have resulted in the low predictability. Beside the errors in several sensitive areas (associated with the southeasterly wind, mesoscale low, and upstream trough near Henan Province), the prediction accuracy in terms of the precipitation was also limited owing to the rapid increase in mesoscale errors (Zhang et al., 2022). Nevertheless, data assimilation research using the satellite water vapor channel has provided hope for forecasting the location of heavy rainfall (Xu et al., 2023), although predicting the intensity remains a challenge.

Climate warming has the potential to significantly intensify regional-scale precipitation extremes (by 7%  $K^{-1}$ –9%  $K^{-1}$ ), as well as station-scale precipitation extremes (by 10%  $K^{-1}$ –14%  $K^{-1}$ , depending on the convective organization). This accords with similar research on other precipitation events. However, contribution of climate warming to an event does not mean that it caused it. Therefore, questions remain regarding the climate systems that influence circulation patterns, and how climate drivers respond to the warming climate.

Long-term increased rainfall has been observed over areas of rapid urbanization, and downwind, worldwide (Changnon, 1969; Kishtawal et al., 2010; Fu et al., 2019; Li et al., 2020). The increase has been attributed to urban thermal effects (Huff and Vogel, 1978), building barrier effects (Bornstein and Lin, 2000; Guo et al., 2006; Zhang et al., 2009; Miao et al., 2011), and urban anthropogenic aerosol emissions effects (Rosenfeld, 2000; Bell et al., 2009). High-impact rainfall usually has a longer lifespan and broader area of influence than local convection. Whether urbanization influences the extreme precipitation initiated by large-scale dynamic forcing is largely unknown. For this event, the local urbanization in Zhengzhou had a limited effect on the precipitation, while upstream urbanization resulted in a 13% reduction in the 24-h accumulated rainfall (Luo et al., 2023).

Research on this extreme precipitation event in Zhengzhou has contributed to improving our physical understanding of high-impact weather, partly owing to the application of high-resolution remote sensing and in-situ observations in several studies of this event. Since the goal of physical understanding is to improve the forecasting of future disasters and mitigate their impacts or prevent their occurrence, below we summarize several implications from this case



study in the context of improving our physical understanding and prediction of high-impact weather.

(1) Improving the application of high-resolution observations.

For this event in Zhengzhou, the large number of surface observations provided a realistic picture of the precipitation, surface temperature, humidity, and winds, while the radar observations provided detailed information on the clouds and three-dimensional structure of the atmosphere. ERA5 overestimated the intensity of the mesoscale low, with a location of ~200 km farther to the northwest than observed. Therefore, studies using ERA5 data may have overestimated the effects of topographic lift. There are large uncertainties in studies using ERA5 to explain convection, and high-resolution reanalysis data obtained by assimilation of high-resolution observations are needed for the study of high-impact precipitation events.

(2) Making data freely available to the research community and weather centers.

To the best of our knowledge, the surface observations from fewer than 1000 national surface stations are currently shared with the Global Telecommunication System, even though there are more than 60 000 AWSs and national observation stations in China. Furthermore, only users with a high priority level can download these data freely. This policy has restricted the development of weather-related science in China for many years. The weather observation system in China is one of the most extensive in the world, but weather-related research, especially high-impact weather research, is not fulfilling its potential partly due to limited data availability.

(3) Implementing real-time probability forecasts.

The deterministic predictability for high-impact weather events, like the Zhengzhou case, is limited. On the other hand, recent studies have shown that the predictability of extreme rainfall can be improved significantly by using a neighborhood “probability of precipitation” method in conjunction with an ensemble (Zhu et al., 2022).

(4) Developing impact-based forecasts.

The flooding of Henan Province caused by this event drew the attention of both the hydrology and meteorology research communities, and both have conducted extensive research with the same goal of disaster reduction. However, there have been few collaborative studies (e.g., impact-based studies with meteorological input). An extreme precipitation warning was issued before the Zhengzhou event, but the impact of the extreme precipitation (e.g., severe flooding) was not forecasted, and hence no relevant action was taken.

High-impact weather events have the potential to cause huge damage to society and are expected to be more frequent and intense due to climate warming. The annual mean surface temperature over continental China in 2021 was found to be 1.0°C above the average value for 1981–2010, which would make it the warmest year since 1961 (Zhou et al., 2022). Additionally, devastating high-impact weather events, such as

record-breaking precipitation, springtime droughts, cold snaps, thunderstorms, wildfires, and heat waves were reported by the CMA (2022). Research related to high-impact weather has improved in recent years; however, further improvements will be hindered without appropriate policies on data and the other issues outlined above.

**Acknowledgements.** This work was supported by the National Natural Science Foundation of China (Grant No. 42030607) and 2022 Open Research Program of the Chinese State Key Laboratory of Severe Weather.

## REFERENCES

- Bell, T. L., D. Rosenfeld, and K.-M. Kim, 2009: Weekly cycle of lightning: Evidence of storm invigoration by pollution. *Geophys. Res. Lett.*, **36**, L23805, <https://doi.org/10.1029/2009GL040915>.
- Bornstein, R., and Q. L. Lin, 2000: Urban heat islands and summertime convective thunderstorms in Atlanta: Three case studies. *Atmos. Environ.*, **34**, 507–516, [https://doi.org/10.1016/S1352-2310\(99\)00374-X](https://doi.org/10.1016/S1352-2310(99)00374-X).
- Cai, X. N., T. Chen, Y. Chen, J. L. Fu, and N. Hu, 2022: Dynamic impact of upper tropospheric cold low on persistent extreme rainstorm of Henan during 17–22 July 2021. *Meteorological Monthly*, **48**, 545–555, <https://doi.org/10.7519/j.issn.1000-0526.2022.021802>. (in Chinese with English abstract)
- Chan, K. T. F., 2019: Are global tropical cyclones moving slower in a warming climate? *Environmental Research Letters*, **14**, 104015, <https://doi.org/10.1088/1748-9326/ab4031>.
- Changnon, S. A., 1969: Recent studies of urban effects on precipitation in the United States. *Bull. Amer. Meteor. Soc.*, **50**, 411–421, <https://doi.org/10.1175/1520-0477-50.6.411>.
- Chen, G., and Coauthors, 2022: Variability of microphysical characteristics in the “21·7” Henan extremely heavy rainfall event. *Science China Earth Sciences*, **65**, 1861–1878, <https://doi.org/10.1007/s11430-022-9972-9>.
- Chyi, D., X. M. Wang, X. D. Yu, and J. H. Zhang, 2023: Analysis of the mechanisms for development and maintenance of synoptic-scale weather systems during the 19–21 July extreme heavy rainfall in Henan, China. *Acta Meteorologica Sinica*, **81**(1), 1–18, <https://doi.org/10.11676/qxxb2023.20220014>. (in Chinese with English abstract)
- Dowdy, A. J., and J. L. Catto, 2017: Extreme weather caused by concurrent cyclone, front and thunderstorm occurrences. *Scientific Reports*, **7**, 40359, <https://doi.org/10.1038/srep40359>.
- Fu, S. M., Y. C. Zhang, H. J. Wang, H. Tang, W. L. Li, and J. H. Sun, 2022: On the evolution of a long-lived mesoscale convective vortex that acted as a crucial condition for the extremely strong hourly precipitation in Zhengzhou. *J. Geophys. Res.: Atmos.*, **127**, e2021JD036233, <https://doi.org/10.1029/2021JD036233>.
- Fu, X. S., X.-Q. Yang, and X. G. Sun, 2019: Spatial and diurnal variations of summer hourly rainfall over three super city clusters in Eastern China and their possible link to the urbanization. *J. Geophys. Res.: Atmos.*, **124**, 5445–5462, <https://doi.org/10.1029/2019JD030474>.
- Gou, D. N., Y. M. Liu, G. X. Wu, T. T. Ma, X. Chen, and X. J. Lin, 2023: Potential vorticity analysis and fine forecast of extreme rainstorm event in Henan Province in July 2021. *Chinese Journal of Atmospheric Sciences*, **47**, 534–550, <https://doi.org/10.1029/2023JCLI100000>.

- [doi.org/10.3878/j.issn.1006-9895.2208.22029](https://doi.org/10.3878/j.issn.1006-9895.2208.22029). (in Chinese with English abstract)
- Guo, X. L., D. H. Fu, and J. Wang, 2006: Mesoscale convective precipitation system modified by urbanization in Beijing City. *Atmospheric Research*, **82**, 112–126, <https://doi.org/10.1016/j.atmosres.2005.12.007>.
- Huff, F. A., and J. L. Vogel, 1978: Urban, topographic and diurnal effects on rainfall in the St. Louis Region. *J. Appl. Meteorol.*, **17**, 565–577, [https://doi.org/10.1175/1520-0450\(1978\)017<0565:Utadeo>2.0.Co;2](https://doi.org/10.1175/1520-0450(1978)017<0565:Utadeo>2.0.Co;2).
- IPCC, 2013: Climate change 2013: The physical science basis. *Contribution of Working Group I to the Fifth Assessment Report of the Intergovernmental Panel on Climate Change*, T. F. Stocker, et al., Eds., Cambridge University Press, Cambridge, United Kingdom and New York, NY, USA.
- Kishtawal, C. M., D. Niyogi, M. Tewari, R. A. Pielke Sr., and J. M. Shepherd, 2010: Urbanization signature in the observed heavy rainfall climatology over India. *International Journal of Climatology*, **30**, 1908–1916, <https://doi.org/10.1002/joc.2044>.
- Kong, Q., J. L. Fu, Y. Chen, F. Zhang, and N. Hu, 2022: Evolution characteristics and formation analysis of mesoscale low-level jet and vortex in Henan Province during the July 2021 severe torrential rain. *Meteorological Monthly*, **48**(12), 1512–1524, <https://doi.org/10.7519/j.issn.1000-0526.2014.02.001>. (in Chinese with English abstract)
- Li, Y. F., and Coauthors, 2020: Strong intensification of hourly rainfall extremes by urbanization. *Geophys. Res. Lett.*, **47**, e2020GL088758, <https://doi.org/10.1029/2020GL088758>.
- Liu, H. S., X. G. Huang, J. F. Fei, C. Zhang, and X. P. Cheng, 2022a: Spatiotemporal features and associated synoptic patterns of extremely persistent heavy rainfall over China. *J. Geophys. Res.: Atmos.*, **127**, e2022JD036604, <https://doi.org/10.1029/2022JD036604>.
- Liu, S. N., J. Wang, and H. J. Wang, 2022b: Analysis of the monitoring ability of high-resolution satellites for the “21·7” heavy rain in Henan. *Acta Meteorologica Sinica*, **80**, 765–776, <https://doi.org/10.11676/qxxb2022.053>. (in Chinese with English abstract)
- Luo, Y. L., J. H. Zhang, M. Yu, X. D. Liang, R. D. Xia, Y. Y. Gao, X. Y. Gao, and J. F. Yin, 2023: On the influences of urbanization on the extreme rainfall over Zhengzhou on 20 July 2021: A convection-permitting ensemble modeling study. *Adv. Atmos. Sci.*, **40**, 393–409, <https://doi.org/10.1007/s00376-022-2048-8>.
- Miao, S. G., F. Chen, Q. C. Li, and S. Y. Fan, 2011: Impacts of urban processes and urbanization on summer precipitation: A case study of heavy rainfall in Beijing on 1 August 2006. *J. Appl. Meteorol. Climatol.*, **50**, 806–825, <https://doi.org/10.1175/2010jame2513.1>.
- Ng, C.-P., Q. H. Zhang, W. H. Li, and Z. W. Zhou, 2022: Contribution of thunderstorms to changes in hourly extreme precipitation over China from 1980 to 2011. *J. Climate*, **35**, 4485–4498, <https://doi.org/10.1175/JCLI-D-21-0701.1>.
- Qin, H., W. Yuan, J. Wang, Y. Chen, P. X. Dai, A. H. Sobel, Z. Y. Meng, and J. Nie, 2022: Climate change attribution of the 2021 Henan extreme precipitation: Impacts of convective organization. *Science China Earth Sciences*, **65**, 1837–1846, <https://doi.org/10.1007/s11430-022-9953-0>.
- Ran, L. K., and Coauthors, 2021: Observational analysis of the dynamic, thermal, and water vapor characteristics of the “7.20” extreme rainstorm event in Henan Province, 2021. *Chinese Journal of Atmospheric Sciences*, **45**, 1366–1383, <https://doi.org/10.3878/j.issn.1006-9895.2109.21160>. (in Chinese with English abstract)
- Rosenfeld, D., 2000: Suppression of rain and snow by urban and industrial air pollution. *Science*, **287**, 1793–1796, <https://doi.org/10.1126/science.287.5459.1793>.
- Shepherd, T. G., 2014: Atmospheric circulation as a source of uncertainty in climate change projections. *Nature Geoscience*, **7**, 703–708, <https://doi.org/10.1038/ngeo2253>.
- Sun, J., R. Li, Q. Zhang, S. Trier, Z. Ying, and J. Xu, 2023: Mesoscale factors contributing to the extreme rainstorm on 20 July 2021 in Zhengzhou, China as revealed by rapid update 4DVar analysis. *Mon. Wea. Rev.*, **151**, <https://doi.org/10.1175/MWR-D-22-0337.1>.
- Sun, J. Z., and N. A. Crook, 1997: Dynamical and microphysical retrieval from doppler radar observations using a cloud model and its adjoint. Part I: Model development and simulated data experiments. *J. Atmos. Sci.*, **54**, 1642–1661, [https://doi.org/10.1175/1520-0469\(1997\)054<1642:Dam-rfd>2.0.Co;2](https://doi.org/10.1175/1520-0469(1997)054<1642:Dam-rfd>2.0.Co;2).
- Wang, B., and Coauthors, 2021: Monsoons climate change assessment. *Bull. Amer. Meteor. Soc.*, **102**, E1–E19, <https://doi.org/10.1175/bams-d-19-0335.1>.
- Wei, P., and Coauthors, 2023: On the key dynamical processes supporting the 21.7 Zhengzhou record-breaking hourly rainfall in China. *Adv. Atmos. Sci.*, **40**, 337–349, <https://doi.org/10.1007/s00376-022-2061-y>.
- Xu, H. X., Y. H. Duan, Y. Li, and H. Wang, 2022a: Indirect effects of binary typhoons on an extreme rainfall event in Henan province, China from 19 to 21 July 2021: 2. Numerical study. *J. Geophys. Res.: Atmos.*, **127**, e2021JD036083, <https://doi.org/10.1029/2021JD036083>.
- Xu, J., R. M. Li, Q. H. Zhang, Y. Chen, X. D. Liang, and X. J. Gu, 2022b: Extreme large-scale atmospheric circulation associated with the “21·7” Henan flood. *Science China Earth Sciences*, **65**, 1847–1860, <https://doi.org/10.1007/s11430-022-9975-0>.
- Xu, L., W. Cheng, Z. R. Deng, J. J. Liu, B. Wang, B. Lu, S. D. Wang, and L. Dong, 2023: Assimilation of the FY-4A AGRI clear-sky radiance data in a regional numerical model and its impact on the forecast of the “21·7” Henan extremely persistent heavy rainfall. *Adv. Atmos. Sci.*, **40**, 920–936, <https://doi.org/10.1007/s00376-022-1380-3>.
- Yamaguchi, M., J. C. L. Chan, I.-J. Moon, K. Yoshida, and R. Mizuta, 2020: Global warming changes tropical cyclone translation speed. *Nature Communications*, **11**, 47, <https://doi.org/10.1038/s41467-019-13902-y>.
- Yang, H., W. Zhou, X. K. Wang, S. S. Li, J. Y. Wang, X. F. Wang, and B. Hu, 2022: Analysis on extremity and characteristics of the “21. 7” severe torrential rain in Henan province. *Meteorological Monthly*, **48**, 571–579, <https://doi.org/10.7519/j.issn.1000-0526.2021.111201>. (in Chinese with English abstract)
- Yin, J. F., H. D. Gu, X. D. Liang, M. Yu, J. S. Sun, Y. X. Xie, F. Li, and C. Wu, 2022a: A possible dynamic mechanism for rapid production of the extreme hourly rainfall in Zhengzhou city on 20 July 2021. *J. Meteor. Res.*, **36**, 6–25, <https://doi.org/10.1007/s13351-022-1166-7>.
- Yin, L., F. Ping, J. H. Mao, and S. G. Jin, 2023: Analysis on precipitation efficiency of the “21. 7” Henan extremely heavy rainfall event. *Adv. Atmos. Sci.*, **40**, 374–392, <https://doi.org/10.1007/s00376-022-2054-x>.



- Yin, R. Y., W. Han, H. Wang, and J. C. Wang, 2022b: Impacts of FY-4A GIIRS water vapor channels data assimilation on the forecast of “21·7” extreme rainstorm in Henan, China with CMA-MESO. *Remote Sensing*, **14**, 5710, <https://doi.org/10.3390/rs14225710>.
- Zhang, C. L., F. Chen, S. G. Miao, Q. C. Li, X. A. Xia, and C. Y. Xuan, 2009: Impacts of urban expansion and future green planting on summer precipitation in the Beijing metropolitan area. *J. Geophys. Res.: Atmos.*, **114**, D02116, <https://doi.org/10.1029/2008JD010328>.
- Zhang, Q. H., C.-P. Ng, K. Dai, J. Xu, J. Tang, J. Z. Sun, and M. Mu, 2021a: Lessons Learned from the Tragedy during the 100 km Ultramarathon Race in Baiyin, Gansu Province on 22 May 2021. *Adv. Atmos. Sci.*, **38**, 1803–1810, <https://doi.org/10.1007/s00376-021-1246-0>.
- Zhang, Q. H., and Coauthors, 2019: Increasing the value of weather-related warnings. *Science Bulletin*, **64**, 647–649, <https://doi.org/10.1016/j.scib.2019.04.003>.
- Zhang, X., H. Wang, X. M. Wang, L. Shen, D. Wang, and H. Li, 2021b: Analysis on characteristic and abnormality of atmospheric circulations of the July 2021 extreme precipitation in Henan. *Transactions of Atmospheric Sciences*, **44**, 672–687, <https://doi.org/10.13878/j.cnki.dqkxxb.20210907001>. (in Chinese with English abstract)
- Zhang, Y. J., H. Z. Yu, M. R. Zhang, Y. W. Yang, and Z. Y. Meng, 2022: Uncertainties and error growth in forecasting the record-breaking rainfall in Zhengzhou, Henan on 19–20 July 2021. *Science China Earth Sciences*, **65**, 1903–1920, <https://doi.org/10.1007/s11430-022-9991-4>.
- Zhao, P. J., Y. M. Hu, H. J. Kong, L. Y. Lü, and L. Xi, 2022: Reviewing the predictability of extraordinary rainstorm in Henan in July 2021 and the meteorological services for decision-making. *Meteorological and Environmental Sciences*, **45**, 38–51, <https://doi.org/10.16765/j.cnki.1673-7148.2022.02.005>. (in Chinese with English abstract)
- Zhou, T. J., and Coauthors, 2022: 2021: A Year of Unprecedented Climate Extremes in Eastern Asia, North America, and Europe. *Adv. Atmos. Sci.*, **39**, 1598–1607, <https://doi.org/10.1007/s00376-022-2063-9>.
- Zhu, K. F., C. Y. Zhang, M. Xue, and N. Yang, 2022: Predictability and skill of convection-permitting ensemble forecast systems in predicting the record-breaking “21·7” extreme rainfall event in Henan Province, China. *Science China Earth Sciences*, **65**, 1879–1902, <https://doi.org/10.1007/s11430-022-9961-7>.

## Recent Progress in Atmospheric Chemistry Research in China: Establishing a Theoretical Framework for the “Air Pollution Complex”<sup>※</sup>

Tong ZHU<sup>1</sup>, Mingjin TANG<sup>2</sup>, Meng GAO<sup>3</sup>, Xinhui BI<sup>2</sup>, Junji CAO<sup>4</sup>, Huizheng CHE<sup>5</sup>, Jianmin CHEN<sup>6</sup>, Aijun DING<sup>7</sup>, Pingqing FU<sup>8</sup>, Jian GAO<sup>9</sup>, Yang GAO<sup>10</sup>, Maofa GE<sup>11</sup>, Xinlei GE<sup>12</sup>, Zhiwei HAN<sup>4</sup>, Hong HE<sup>13</sup>, Ru-Jin HUANG<sup>14</sup>, Xin HUANG<sup>7</sup>, Hong LIAO<sup>12</sup>, Cheng LIU<sup>15</sup>, Huan LIU<sup>16</sup>, Jianguo LIU<sup>17</sup>, Shaw Chen LIU<sup>18</sup>, Keding LU<sup>1</sup>, Qingxin MA<sup>13</sup>, Wei NIE<sup>7</sup>, Min SHAO<sup>18</sup>, Yu SONG<sup>1</sup>, Yele SUN<sup>4</sup>, Xiao TANG<sup>4</sup>, Tao WANG<sup>19</sup>, Tijian WANG<sup>7</sup>, Weigang WANG<sup>11</sup>, Xuemei WANG<sup>18</sup>, Zifa WANG<sup>4</sup>, Yan YIN<sup>12</sup>, Qiang ZHANG<sup>16</sup>, Weijun ZHANG<sup>17</sup>, Yanlin ZHANG<sup>12</sup>, Yunhong ZHANG<sup>20</sup>, Yu ZHAO<sup>7</sup>, Mei ZHENG<sup>1</sup>, Bin ZHU<sup>12</sup>, and Jiang ZHU<sup>4</sup>

<sup>1</sup>*Peking University, Beijing 100871, China*

<sup>2</sup>*Guangzhou Institute of Geochemistry, Chinese Academy of Sciences, Guangzhou 510640, China*

<sup>3</sup>*Hong Kong Baptist University, Hong Kong SAR, China*

<sup>4</sup>*Institute of Atmospheric Physics, Chinese Academy of Sciences, Beijing 100029, China*

<sup>5</sup>*Chinese Academy of Meteorological Sciences, Beijing 100081, China*

<sup>6</sup>*Fudan University, Shanghai 200438, China*

<sup>7</sup>*Nanjing University, Nanjing 210023, China*

<sup>8</sup>*Tianjin University, Tianjin 300072, China*

<sup>9</sup>*Chinese Research Academy of Environmental Sciences, Beijing 100012, China*

<sup>10</sup>*Ocean University of China, Qingdao 266100, China*

<sup>11</sup>*Institute of Chemistry, Chinese Academy of Sciences, Beijing 100190, China*

<sup>12</sup>*Nanjing University of Information Science and Technology, Nanjing 210044, China*

<sup>13</sup>*Research Center for Eco-Environmental Sciences, Chinese Academy of Sciences, Beijing 100085, China*

<sup>14</sup>*Institute of Earth Environment, Chinese Academy of Sciences, Xi'an 710061, China*

<sup>15</sup>*University of Science and Technology of China, Hefei 230026, China*

<sup>16</sup>*Tsinghua University, Beijing 100084, China*

<sup>17</sup>*Anhui Institute of Optics and Fine Mechanics, Hefei Institutes of Physical Science, Chinese Academy of Sciences, Hefei 230031, China*

<sup>18</sup>*Jinan University, Guangzhou 510632, China*

<sup>19</sup>*Hong Kong Polytechnic University, Hong Kong SAR, China*

<sup>20</sup>*Beijing Institute of Technology, Beijing 100081, China*

(Received 12 December 2022; revised 6 March 2023; accepted 10 April 2023)

### ABSTRACT

Atmospheric chemistry research has been growing rapidly in China in the last 25 years since the concept of the “air pollution complex” was first proposed by Professor Xiaoyan TANG in 1997. For papers published in 2021 on air pollution (only papers included in the Web of Science Core Collection database were considered), more than 24 000 papers were authored or co-authored by scientists working in China. In this paper, we review a limited number of representative and significant studies on atmospheric chemistry in China in the last few years, including studies on (1) sources and emission inventories, (2) atmospheric chemical processes, (3) interactions of air pollution with meteorology, weather and climate, (4) interactions between the biosphere and atmosphere, and (5) data assimilation. The intention was not to provide a complete review of all progress made in the last few years, but rather to serve as a starting point for learning more about atmospheric chemistry research in China. The advances reviewed in this paper have enabled a theoretical framework for the

<sup>※</sup> This paper is a contribution to the special issue on the National Report to the 28th IUGG General Assembly by CNC-IAMAS (2019–2022).

\* Corresponding author: Tong ZHU  
Email: [tzhu@pku.edu.cn](mailto:tzhu@pku.edu.cn)

air pollution complex to be established, provided robust scientific support to highly successful air pollution control policies in China, and created great opportunities in education, training, and career development for many graduate students and young scientists. This paper further highlights that developing and low-income countries that are heavily affected by air pollution can benefit from these research advances, whilst at the same time acknowledging that many challenges and opportunities still remain in atmospheric chemistry research in China, to hopefully be addressed over the next few decades.

**Key words:** atmospheric chemistry, air pollution complex, theoretical framework, recent progress

**Citation:** Zhu, T., and Coauthors, 2023: Recent progress in atmospheric chemistry research in China: Establishing a theoretical framework for the “air pollution complex”. *Adv. Atmos. Sci.*, **40**(8), 1339–1361, <https://doi.org/10.1007/s00376-023-2379-0>.

**Article Highlights:**

- Very recent progress in atmospheric chemistry research in China is reviewed.
- Atmospheric chemistry research in China has grown rapidly in the last two decades.
- The “air pollution complex” has evolved from a concept to a theoretical framework.

---

## 1. Introduction

In 1997, Professor Xiaoyan TANG first proposed the “air pollution complex” concept (Zhu, 2018), building upon her scientific understanding of, and profound insights into, air pollution in China. She pointed out that, due to rapid economic and social developments, urban air pollution in China can be characterized by a combination of the “London Smoke” type (i.e., mainly caused by coal combustion) and the “Los Angeles” type (i.e., photochemical smog mainly caused by vehicle exhaust emissions). This concept reflects the fact that various environmental pollution problems that developed countries experienced in the last century (and perhaps even over a longer period) took place collectively and intensively in one to two decades in fast-developing regions in China. As a result, an air pollution complex, characterized by the co-existence of coal-smoke and photochemical-smog air pollution, appeared (and is still appearing) in many cities in China as a new type of air pollution, and one outstanding feature is its highly complicated formation mechanisms.

The air pollution complex concept opens a new perspective for air pollution control in China, and has been provoking intensive discussion and debates since it was proposed, thereby stimulating important advances in atmospheric chemistry research. A book chapter by Zhu (2005) summarized in brief the scientific understanding of this concept by 2005: rapid urbanization leads to emissions of large amounts of various pollutants into the air, and a myriad of pollutants with high concentrations co-exist in the atmosphere and interact with each other in a complicated manner. What we observe in air pollution complex includes an increase in the atmospheric oxidation capacity, a decrease in atmospheric visibility, and a spread of air quality deterioration over the regional scale. The underlying mechanisms include intricately intertwined sources and sinks of air pollutants, tightly coupled transformation processes of many pollutants, and synergistic or antagonistic effects among various pollutants with respect to their impacts on human and ecosystem health.

Zhu et al. (2011) emphasized that the central part of the air pollution complex concept is that the coexistence of high concentrations of primary and secondary gaseous and particulate pollutants provides a large amount of reactants for heterogeneous reactions. These reactions change the atmospheric oxidation capacity, as well as chemical compositions and physicochemical and optical properties of aerosol particles, thereby accelerating the formation of the air pollution complex.

In 2015, the National Natural Science Foundation of China funded a joint major research program entitled “Formation Mechanisms, Health Effects and Mitigation Strategies of the Air Pollution Complex in China” (Zhu, 2018). This joint research program has two programs, and the first program, entitled “Fundamental Researches on the Formation and Response Mechanism of the Air Pollution Complex in China” (hereafter referred to simply as “the research program”), is led by Tong ZHU and has a total budget of 240 million RMB (2016–23). This research program underscores that not only understanding formation mechanisms of air pollution complexes is a cutting-edge scientific challenge globally, but also its mitigation and control is one of the key national demands in China. It has two major goals: (1) to elucidate the chemical and physical processes critical to the formation of air pollution complexes, to reveal the formation mechanisms of air pollution complexes, and to construct an air pollution complex theoretical framework; and (2) to develop new theories and methodologies for the surveillance, source appointment and decision-making analysis of air pollution complexes, and to propose innovative ideas for controlling air pollution complexes in China.

Thanks to the support of this research program, an air pollution complex theoretical framework has recently been established, and it is of course subject to future development. The main concept of the air pollution complex is that interactions and feedbacks lead to nonlinear relationships between emissions and the level of air pollution (Fig. 1):

- (1) Interactions between gaseous molecules and clusters

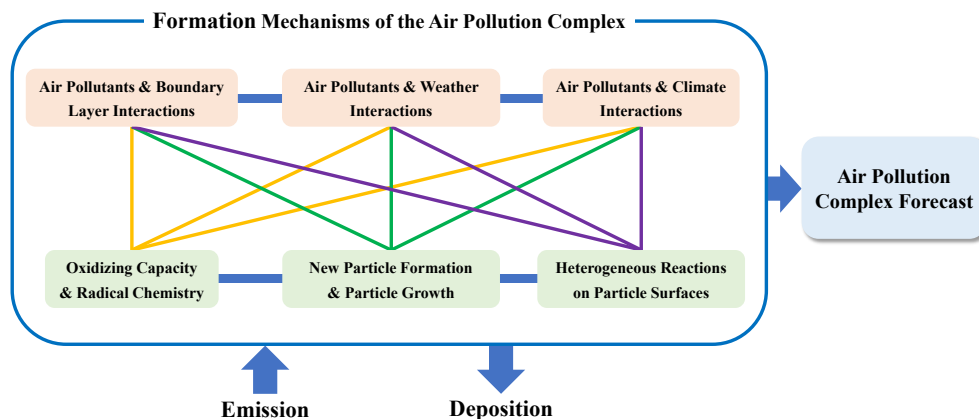


Fig. 1. Schematic showing the theoretical framework of the air pollution complex in China.

lead to the formation of new particles, and interactions and reactions of molecules and clusters on particle surfaces lead to the growth of particle sizes. These interaction processes not only result in the formation of secondary aerosols (such as sulfate, nitrate, and secondary organic aerosol), but also contribute to the atmospheric oxidation capacity as radicals and reactive oxygen species are formed via catalytic and photo-enhanced reactions.

(2) Interactions and feedbacks between physical properties and chemical components also play critical roles. Interactions between air pollutants and the planetary boundary layer (PBL) can reduce the boundary layer height, thereby suppressing the dispersion of air pollutants and subsequently enhancing the level of air pollution; and interactions between air pollution and weather as well as climate are larger in terms of spatial and temporal scales, such as the impacts on radiative forcing, cloud formation, and mesoscale and hemispheric circulations (e.g., impacts on monsoons).

The complicated, nonlinear and feedback nature of the air pollution complex can also be described mathematically:

$$\rho(t) = f\{E(t, P), P(t, \rho, C), C(t, E, \rho, P)\},$$

where  $\rho(t)$  represents concentrations of air pollutants at the time  $t$ ,  $E$  represents the emissions intensity, and  $P$  and  $C$  are the physical and chemical processes in the atmosphere.  $E$ , which is a function of anthropogenic activities and natural processes, is also influenced by  $P$ , such as meteorological factors. There is growing evidence to suggest that concentrations of air pollutants and heterogeneous reactions on the surfaces of aerosol particles have important impacts on  $P$ , such as boundary layer mixing and cloud formation. Finally, it is well established that  $C$  is a function of air pollutant concentrations and physical processes in the atmosphere.

Understanding these complicated interactions and feedbacks is essential to better simulate atmospheric physical and chemical processes that lead to the formation of an air pollution complex, to forecast air pollution with much lower uncertainties, and to support air pollution control measures and policies with robust science.

Under the support of this research program and many other funds, atmospheric chemistry research in China has been rapidly growing in various aspects in the last 10–20 years, as illustrated by the following evidence: In the Web of Science Core Collection database, we searched for papers published each year from 2010 to 2021 using the following two sets of keywords (on 31 October 2022): (1) topic: air pollution; address: China; (2) topic: atmospheric chemistry; address: China. As shown in Fig. 2, the number of papers on air pollution and atmospheric chemistry authored or co-authored by scientists working in China has been rapidly and steadily increasing each year in the last decade.

In total, 76 projects have been funded through the aforementioned research program led by Tong ZHU. In order to prepare this review article, the principle investigators of these projects were invited to summarize in brief between one and three important papers (not necessarily their own work) which, in their opinion, represent major progress in atmospheric chemistry research in China in the last two to three years. Their contributions were purely on a voluntary basis, and colleagues who contributed to this review were invited to be co-authors. Clearly, the purpose of this article is not to provide a comprehensive review of all the key progress in atmospheric chemistry research in China in the last few years; rather, it is intended to serve as a starting point for people who want to know more about recent atmospheric chemistry research in China. In this paper, we introduce recent progress in sources and emission inventories (section 2), atmospheric chemical processes (section 3), interactions of air pollution with meteorology, weather and climate (section 4), interactions between the biosphere and atmosphere (section 5), and data assimilation (section 6). In addition, a concise summary and future outlook is provided in section 7.

## 2. Sources and emission inventories

### 2.1. Emission inventories

Reliable emission inventories are vital for understanding the sources of air pollution and designing effective measures

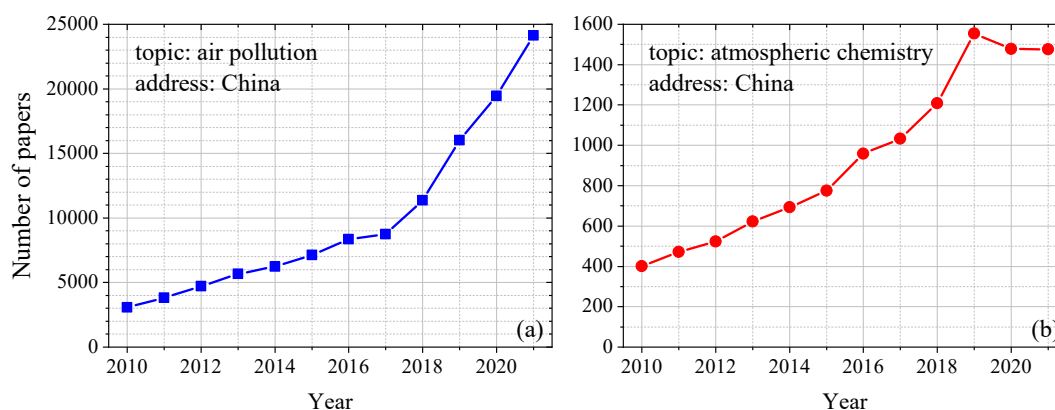


**Fig. 2.** Number of papers published each year from 2010 to 2021 in the Web of Science Core Collection database using two sets of keywords: (a) topic: air pollution; address: China; (b) topic: atmospheric chemistry; address: China.

for air pollution control. As reviewed recently (Li et al., 2017a), major anthropogenic sources in China include power plants, industry, residential areas, transportation, solvent use, and agriculture. Here, we review some very recent studies related to emission inventories in China, including transportation emissions (section 2.1.1), volatile organic compounds (VOCs; section 2.1.2), fugitive road dust (section 3.1.3), and methodological advances (section 2.1.4).

#### 2.1.1. Transportation emissions

Transportation emissions play an important role in the formation of urban air pollution, and ship emissions also contribute to air pollution in coastal cities and marine areas. However, it is highly challenging to estimate emissions from transportation, including ships, due to the complexity and inaccessibility of activity data. With the development of traffic “big data”, the technical methods for developing transportation emission inventories have been greatly improved. For truck emissions, Deng et al. (2020) developed a full-sample enumeration approach (TrackATruck), based on 19 billion trajectories, to achieve high-resolution estimation of emission inventories. Their model breaks through the limitations of traditional methods that rely on substitute parameters for spatial and temporal allocation, thus greatly improving the dynamic information density of emission inventories. For ship emissions, Wang et al. (2021e) updated their previous shipping emission inventory model to the second version (SEIM v2.0), which realizes the distinction of emissions from ocean-going, coastal and inland ships, as well as the evaluation of emission reduction benefits of policies.

Maritime transportation accounts for more than 80% of the global trade volume. However, both historical experience and future estimates show that it is rather difficult to achieve significant emission reduction effects by relying on globally collective technological and operational measures. To this end, Wang et al. (2021d) constructed a trade-linked shipping emissions model system (VoySEIM-GTEMS) based on global shipping big data and trade data, and quantitatively decomposed global high-resolution emissions into mil-

lions of trade flows, and revealed the heterogeneity of trade emissions efficiency among bilateral trading partners, commodities and shipping routes. An important innovation is that the vessel energy efficiency operational indicator was converted to the trade-emissions efficiency index by value, which enables understanding of the trade-related shipping emissions efficiency at the bilateral level. This model system enables the evaluation of emission reduction efforts from both technical advancement and international trade optimization viewpoints. Thus, it contributes to forming a new shipping emissions reduction framework based on international cooperation, in which contributions from ship owners, operators, and traders can be incorporated and synthetically assessed (Liu et al., 2021a).

#### 2.1.2. VOCs

Biogenic volatile organic compounds (BVOCs) play vital roles in  $O_3$  formation; however, BVOC emissions from urban green spaces have been largely ignored in traditional emission inventories, partly due to the coarse resolution of land cover data. Utilizing land cover data at a spatial resolution of 10 m, Ma et al. (2022) developed a high-resolution (1–27 km) BVOC emissions inventory from urban green spaces (U-BVOC) in China and found that U-BVOC emissions could account for a large fraction (~11%) of the total BVOC emissions in urban cores. It was further found that the addition of U-BVOC emissions could greatly reduce the underestimates of both  $O_3$  and its precursors (e.g., isoprene) in Beijing (Ma et al., 2019a; Gao et al., 2022e). This newly developed emissions inventory is publicly available, and continuous assessment is warranted to better understand its impact on air quality in megacities.

Comprehensive gridded emission inventories of semi-volatile/intermediate-volatility organic compounds (S/IVOCs) in China were established based on a parameterization method involving emission factors of primary organic aerosol (POA), emission ratios of S/IVOCs to POA, and domestic activity data (Wu et al., 2019, 2021a). It was found that S/IVOC emissions were mainly distributed in



highly industrialized and urbanized regions, with major contributions from industry and residential sectors (Wu et al., 2021a). The emission inventories of S/IVOCs were further coupled with improved degradation mechanisms and formation schemes of secondary organic aerosol (SOA) in the WRF-Chem model, resulting in a 20% improvement in the resolved fraction of observed SOA (Wu et al., 2019, 2021b). In addition, SOA formation was found to be highly sensitive to several factors, including consideration of SVOCs in the existing POA emissions, configuration of NO<sub>x</sub>-dependent SOA yields, uncertainties of S/IVOC emissions, and their reaction coefficients with OH radicals.

### 2.1.3. Fugitive road dust

Anthropogenic fugitive, combustion and industrial dust may contribute significantly to global and regional aerosol loadings, but the emission fluxes are not well understood. Chen et al. (2019b) constructed a high-resolution (500 × 500 m<sup>2</sup>) fugitive road dust PM<sub>2.5</sub> emissions inventory in Lanzhou (a major city in northwestern China) for the year of 2017. The fugitive road dust PM<sub>2.5</sub> emission rate, which was estimated to be 1141 ± 71 kg d<sup>-1</sup>, accounted for ~25% of the total PM<sub>2.5</sub> emission rate in urban Lanzhou (Chen et al., 2019b), and the premature mortality burden due to fugitive road dust PM<sub>2.5</sub> exposure in Lanzhou was estimated to be 234.5 deaths in 2017. A follow-up study (Xia et al., 2022b) suggested that surface radiative cooling induced by anthropogenic dust, estimated to be up to -15.9 ± 4.0 W m<sup>-2</sup> regionally, would cause a decrease in boundary layer height and thus deteriorate non-dust air pollution.

### 2.1.4. Methodological advances

Integration of new data from multiple sources has enabled spatial and temporal patterns of emissions to be characterized at finer scales. By using a point source database that includes around 100 000 individual emission facilities, Zheng et al. (2021) developed a new emissions inventory (MEIC-HR) in China with a horizontal resolution of ~1 km. The MEIC-HR dataset significantly improves the spatial representation of the bottom-up emissions inventory in China, with >84% of SO<sub>2</sub> emissions and >58% of NO<sub>x</sub> emissions presented by point sources. Using MEIC-HR can greatly reduce modeling biases of PM<sub>2.5</sub> concentrations at 4-km resolution (for example, normalized mean biases were reduced from 27% to 5%).

Zheng et al. (2020a) developed a novel approach to rapidly track dynamic emission changes with sectoral and spatial information by combining bottom-up emission estimates with satellite observations. The bottom-up emissions inventory approach with fast-track statistics was used to provide a preliminary estimate, while a satellite-based inverse modeling approach was developed to infer the 10-day moving average of NO<sub>x</sub> emissions, which was then combined with the bottom-up emissions map to constrain dynamic changes of emissions with sectors and grids. The newly developed approach was employed to track dynamic changes of NO<sub>x</sub> and CO<sub>2</sub> emissions during the COVID-19 lockdown in early 2020 in

China (Zheng et al., 2020a), demonstrating the promising prospect of understanding emission dynamics using satellite data.

## 2.2. Source appointment

In addition to emission inventories, source appointment based on ambient measurements is a major way to understand sources of air pollution. Zheng et al. (2020b) summarized characteristics of particulate matter pollution in China, and reviewed major methods used to elucidate sources of fine particles. A recent study (Yan et al., 2021) identified combustion to be major sources for brown carbon (BrC) and reactive oxygen species (represented by ·OH radicals) during winter in Beijing, and found that fossil fuel (especially coal) combustion was more important for BrC while biomass burning was more important for reactive oxygen species.

Advanced statistical methods, such as machine learning, have also been employed to understand sources and driving factors of air pollution in China. For example, a machine learning method (the Radom Forest model) was combined with positive matrix factorization to investigate PM<sub>2.5</sub> pollution in Tianjin between September 2017 and September 2018 (Zhang et al., 2022f), based on online measurements of gaseous and particulate species. It was suggested that source emissions and meteorological conditions contributed 67% and 33% to variations of PM<sub>2.5</sub> concentrations during the period examined (Zhang et al., 2022f). Furthermore, machine learning has also been used to understand O<sub>3</sub> and SOA formation (Wang et al., 2022b) and to elucidate formation pathways of sulfate aerosol (Gao et al., 2022a).

## 3. Atmospheric chemical processes

Our understanding of atmospheric chemical processes relevant to air pollution complexes in China has been substantially improved in the last few years. In this section, we introduce the recent advancements in instrument development (section 3.1), laboratory studies (section 3.2), field observation (section 3.3), and modeling studies (section 3.4).

### 3.1. Instrument development

Instrument development plays a critical role in advances in atmospheric chemistry. Atmospheric chemistry research in China has been relying heavily on instruments developed by, and imported from, other countries. Substantial efforts have been devoted to instrument development in China in the past one to two decades, and some recent advances are summarized herein.

#### 3.1.1. Trace gases

Amplitude-modulated multimode-diode-laser-based cavity-enhanced absorption spectroscopy, which has the advantages of high light injection efficiency and low cavity-mode noise, was developed to measure NO<sub>2</sub> at the wavelength of 406 nm (Zhou et al., 2022), and a detection limit of 8 pptv was achieved with a temporal resolution of 30 s. This technique provides a reliable, simple and self-calibrating

method for NO<sub>2</sub> measurement, and is especially suitable for long-term operation with minimal maintenance. Furthermore, a custom-built laser-induced fluorescence instrument (AIOFM-LIF) was developed to measure tropospheric OH and HO<sub>2</sub> radicals with high sensitivity (Zhang et al., 2022a); it was successfully deployed in several field campaigns, and good agreement with a well-characterized instrument was found (Yang et al., 2021a).

Total OH reactivity, which is equal to the reciprocal of the atmospheric lifetime of OH radicals, is an important parameter to assess atmospheric oxidation capacity. Wei et al. (2020) developed a novel instrument that combined laser-flash photolysis with a mid-infrared Faraday rotation spectrometer for direct measurement of total OH reactivity, and the 1 $\sigma$  detection precisions at a pressure of 50 mbar were determined to be  $4 \times 10^6$  molecule cm<sup>-3</sup> in 56 s for OH radicals and 0.09 s<sup>-1</sup> in 112 s for total OH reactivity. Based on magneto-optic effects of paramagnetic species, Faraday rotation spectrometry can effectively reduce spectral interferences caused by diamagnetic precursors, providing a new tool with high precision and high selectivity for OH radical chemistry research. The absorption path length has been further increased by implementing optical-feedback cavity-enhanced absorption spectroscopy technology (Yang et al., 2022b).

### 3.1.2. Aerosol particles

Several techniques were recently developed in China to investigate aerosol hygroscopicity, and aerosol hygroscopicity measurement techniques have also been reviewed (Tang et al., 2019a). For example, Zhou et al. (2020) developed a humidified cavity-enhanced albedometer for simultaneous measurement of RH-dependent light extinction, scattering, absorption, and single scattering albedo at 532 nm. It provided a new method for in-situ direct measurement of multiple optical hygroscopic parameters with a single instrument, and aerosol samples could be humidified from 10% to 90% relative humidity (RH) with a cycle time of 15–20 min. Furthermore, Pan et al. (2019) developed an instrument that can measure depolarization ratios of individual particles; it was employed to investigate morphological alteration of aerosol particles caused by heterogeneous chemistry (Pan et al., 2019), and it was found that irregularly shaped particles became more spherical as the mass fraction of water-soluble compositions (such as nitrate) increased up to 8% at high RH.

A series of aerosol liquid water content measurement techniques were developed, including an active RH-controlled dry-ambient aerosol size spectrometer (DAASS), a surface plasmon resonance microscopy (SPRM) imaging system, and a Fourier transform infrared spectroscopy (FTIR) method. The RH-controlled DAASS alternatively measures aerosol size distributions (i.e., 10–500 nm) under dry and ambient conditions, which are then used to quantify the additive volume of aerosol liquid water (Dai et al., 2022). The instrument also employs an active RH controlling scheme and is thus able to minimize the discrepancy between ambient

RH and the DAASS conditioning RH (i.e., below 1.5%), extending the application of DAASS to a wide RH range of 10%–90% (Dai et al., 2021b). The SPRM system provides insights into the hygroscopic growth of nano-sized single particles, by allowing imaging of 50-nm polystyrene standard particles with a temporal resolution of 10 ms (Kuai et al., 2020), and thus variations of aerosol water content and refractive index with RH can be derived accordingly. Moreover, hygroscopic growth of nano-sized particles is characterized by reconstructing absorption spectra of aerosol liquid water measured by FTIR, which can also provide information for phase transition dynamics at the molecular level (Wei et al., 2022).

Aerosol acidity impacts numerous physicochemical processes, but the determination of aerosol pH remains a significant challenge due to the non-conservative nature of H<sup>+</sup>. Cui et al. (2021) developed a direct pH measurement method that uses water as a general probe to detect H<sup>+</sup> in individual particles by micro-Raman spectroscopy. The spectra of hydrated ions were decomposed from the solution spectra as standard spectra by multivariate curve resolution analysis, and the concentration profiles of each ion were calculated. This study (Cui et al., 2021) demonstrated that utilizing water, the most common substance, as the spectroscopic probe to measure [H<sup>+</sup>], has the potential to measure the pH value of atmospheric particles.

Chen et al. (2022c) coupled an aerosol optical tweezer with stimulated Raman spectroscopy to investigate sulfate formation via heterogeneous uptake of SO<sub>2</sub> onto aerosol particles. This technique exploits the sensitive size-dependence of stimulated Raman scattering spectra of the droplet to achieve accurate measurement of droplet growth rates, which could be used to derive sulfate formation rates with the knowledge of sulfate hygroscopicity. The detection limit of the droplet radius and sulfate mass can reach 1 nm and  $1 \times 10^{-14}$  mol at 60% RH; in addition, this technique also facilitates long experimental times (hours to days) and well-controlled conditions.

Measuring chemical compositions of individual aerosol particles can provide direct evidence for their heterogeneous reactions and mixing states in the atmosphere. Wang et al. (2021b) used micro-Raman spectroscopy to measure chemical compositions of individual particles in aerosol samples collected in Beijing, and (NH<sub>4</sub>)<sub>2</sub>SO<sub>4</sub>, NH<sub>4</sub>NO<sub>3</sub>, minerals, carbonaceous materials and NaNO<sub>3</sub> were identified according to their characteristic Raman peaks; in addition, they also discussed formation mechanisms of Ca(NO<sub>3</sub>)<sub>2</sub> and CaSO<sub>4</sub> via heterogeneous aging of CaCO<sub>3</sub> particles based on their single particle analysis. This technique can directly identify functional groups and molecules in individual aerosol particles under normal ambient conditions (Wang et al., 2021b), rendering it a promising tool for studying coarse particles (>1  $\mu$ m).

Imidazoles are important photosensitizers in the troposphere, and can impact aerosol optical properties as BrC and have potential risks for human health. In order to measure

more imidazoles, Gao et al. (2021b) developed a screening workflow based on data-dependent acquisition auto MS/MS with a preferred targeted list containing 421 imidazoles, using ultra-performance liquid chromatography quadrupole time-of-flight mass spectrometry (UPLC-QTOF-MS). The method exhibited excellent performance and is able to identify a wide range of imidazoles in ambient aerosol particles with and without using standards.

A versatile aerosol concentration enrichment system (VACES) was developed for hourly measurements of components, ecotoxicity, and optical properties of atmospheric aerosols, significantly increasing detection limits and reducing measurement biases (Shang et al., 2021a), and it has been deployed in field measurements to investigate formation mechanisms of aerosol nitrite (Shang et al., 2021b) and BrC (Kang et al., 2022). For instance, the combination of VACES with ion chromatography and ecotoxicity assays can increase detection limits by one order of magnitude when compared to conventional methods; in addition, integration of VACES with optical instruments can reduce measurement biases by 85% and 47% for light absorption and scattering.

A new dust generation system, which can simulate natural dust emission processes well, was recently developed and verified (Wu et al., 2023). The abundance of water-soluble sulfate in soil-derived dust produced using this system showed good agreement with that found in ambient dust aerosols, supporting the existence of high levels of primary sulfate in dust aerosol emitted from the Taklamakan Desert (Wu et al., 2022). Using the newly developed dust generation system, Wu et al. (2022) further found that aerosol–soil fractionation in the saltation and sandblasting processes could increase water-soluble salts in dust aerosols relative to bulk soil, providing new geochemical constraints for understanding the origins of water-soluble ions in dust aerosol.

### 3.2. Laboratory studies

Under the highly complex air pollution conditions in China, strong homogenous nucleation and multiphase processes coexist, coupled with a strong atmospheric oxidation capacity and rapid growth of PM<sub>2.5</sub>. A concept of “haze chemistry” was proposed to reveal the complex air pollution (Chu et al., 2020), which is different from cloud chemistry in London smog and atmospheric photochemistry in Los Angeles photochemical smog. Beyond homogenous processes, gas–liquid–solid multiphase processes are a main issue in haze chemistry.

#### 3.2.1. Inorganic species

The NO–NO<sub>2</sub> cycle determines O<sub>3</sub> formation and can enhance heterogeneous and multiphase formation of sulfate, therefore playing a critical role in the tropospheric oxidation capacity. It was found that SO<sub>2</sub> can greatly promote heterogeneous transformation of NO into NO<sub>2</sub> and HONO on MgO particles under ambient conditions (Liu et al., 2020a). The active sites for adsorption and oxidation of NO were determined to be sulfate, where an intermediate complex, [SO<sub>4</sub>–

NO], was formed during adsorption. The decomposition of [SO<sub>4</sub>–NO] led to NO<sub>2</sub> formation accompanied by the change in sulfate configuration, and the formed NO<sub>2</sub> could further react with surface sulfite to generate HONO and sulfate (Ma et al., 2017), thus forming a positive feedback loop (Liu et al., 2020a).

Wang et al. (2021c) carried out environmental chamber experiments under near-ambient conditions and found that the Mn-catalyzed oxidation of SO<sub>2</sub> on aerosol surfaces is the dominant pathway for sulfate formation and may explain the missing source of sulfate aerosol. This conclusion was further supported by observation-constrained modeling work (Wang et al., 2022h), which suggested that Mn-catalyzed oxidation on aerosol surfaces could account for >90% of sulfate formation during haze events. For comparison, gas-phase oxidation contributed 3.1% ± 0.5% to sulfate formation due to low OH levels, and H<sub>2</sub>O<sub>2</sub> oxidation in aerosol water accounted for 4.2% ± 3.6% of sulfate formation because of rapid consumption of H<sub>2</sub>O<sub>2</sub>; contributions of O<sub>3</sub> and NO<sub>2</sub> oxidation and transition-metal-catalyzed reactions in aerosol water could be negligible owing to low aerosol water contents, low pH, and high ionic strength, while the contribution from in-cloud reactions was negligible due to the barrier caused by stable stratification during winter haze events. We note that several mechanisms have been proposed in the last few years to explain the rapid formation of sulfate aerosol (Cheng et al., 2016; Wang et al., 2016, 2020b; Liu et al., 2020b), and their actual importance is still under debate.

Chen et al. (2021b) investigated the thermodynamics and kinetics of chloride, nitrate and ammonium depletion in atmospheric aerosols. These depletion processes were generalized as a class of unique reactions in which strong acids (HCl and HNO<sub>3</sub>) and bases (NH<sub>3</sub>) are irreversibly displaced by weak acids (dicarboxylic acids) and bases (dicarboxylate salts), and these displacement reactions occur exclusively in multiphase aerosols with a large specific surface area that facilitates prompt degassing of volatile species. A subsequent study (Li et al., 2022b) utilized surface-enhanced Raman spectroscopy to measure pH evolution in aerosol microdroplets undergoing ammonium depletion and observed exponential decay of aerosol pH, indicating that a self-limiting feedback mechanism may govern the depletion process.

Tang et al. (2019b) investigated hygroscopic properties of mineral dust samples collected from different regions in northern China using a vapor sorption analyzer (Gu et al., 2017), and found that some mineral dust samples unexpectedly exhibited very high hygroscopicity, due to the presence of soluble ions (such as Cl<sup>−</sup>, SO<sub>4</sub><sup>2−</sup> and Na<sup>+</sup>). A follow-up study (Wang et al., 2022d) found that heterogeneous reactions of N<sub>2</sub>O<sub>5</sub> with mineral dust could form substantial amounts of ClNO<sub>2</sub>, and suggested that N<sub>2</sub>O<sub>5</sub> uptake onto saline mineral dust may be a previously unrecognized but potentially important source of tropospheric ClNO<sub>2</sub> in northern China.

Deliquescence and efflorescence RH (DRH and ERH) regulate the phase state and liquid water contents of aerosol



particles, and are thus of great interest in atmospheric science and many other fields. Peng et al. (2022a) developed for the first time a comprehensive database that included DRH and ERH values of 110 compounds reported by previous work, provided their preferred DRH and ERH values at 298 K, and identified current knowledge gaps in the deliquescence and efflorescence of atmospheric particles.

### 3.2.2. Soot particles

Heterogeneous processes can also lead to the formation of atmospheric radicals, contrary to the conventional view that aerosol particles are always a sink of atmospheric radicals and thereby reduce the atmospheric oxidation capacity. For example, a recent laboratory study (He et al., 2022a) found that the heterogeneous reaction of water and O<sub>2</sub> on carbonaceous surfaces could produce gas-phase OH radicals under irradiation, and thus revealed a new formation mechanism of gas-phase OH radicals.

Zhang et al. (2022c) found that diesel soot particles could promote heterogeneous conversion of SO<sub>2</sub> to H<sub>2</sub>SO<sub>4</sub> upon irradiation, and further proved that OH radical is the major reactive oxygen species promoting SO<sub>2</sub> oxidation. The photo-electrons from organic carbon react with O<sub>2</sub> to produce superoxide radicals ( $\cdot\text{O}_2^-$ ), which then combine with H<sup>+</sup> ions to form HO<sub>2</sub> and H<sub>2</sub>O<sub>2</sub>, and the photolysis of H<sub>2</sub>O<sub>2</sub> produces OH radical (Zhang et al., 2022c). This work provides new insights into H<sub>2</sub>SO<sub>4</sub> formation in the atmosphere and also has important implications for assessing health and climate effects of soot particles.

Zhu et al. (2020a) investigated changes in the physico-chemical properties and oxidative potential of soot under visible-light irradiation in an environmental chamber with or without O<sub>3</sub>. Visible light markedly promoted soot oxidation, leading to consumption of polycyclic aromatic hydrocarbons (PAHs), formation of oxygen-containing functional groups, and enhancement of oxidative potential. This study (Zhu et al., 2020a) also suggested that solar irradiation could trigger self-oxidation processes in soot, thereby affecting its atmospheric and health effects. Zhu et al. (2021b) further explored the microstructure, composition and photo-reactivity of soot, and found that the core component of soot to be more analogous to reduced graphene oxide rather than graphene. The generation of reactive oxygen species via electron transfer under visible light indicates that the reduced graphene oxide-like soot core can serve as a potential photocatalyst (Zhu et al., 2021b).

### 3.2.3. Organic aerosols

Using an indoor smog chamber, Yang et al. (2021b) examined the effects of SO<sub>2</sub> and NH<sub>3</sub> on photo-oxidation of 1,2,4-trimethylbenzene. In the presence of SO<sub>2</sub>, SOA yields were considerably enhanced due to acid-catalyzed heterogeneous reactions, and a large number of organosulfates were also identified; a similar positive correlation between NH<sub>3</sub> levels and SOA formation was also observed. A follow-up study (Yang et al., 2023) further examined the effects of SO<sub>2</sub> on ozonolysis of cyclooctene, and suggested that the

organosulfates produced through reactions of stabilized Criegee intermediates with SO<sub>2</sub> contributed remarkably to SOA formation and growth. Furthermore, SOA formation due to atmospheric oxidation of monocyclic aromatic hydrocarbons (Yang et al., 2022d) and anthropogenic effects on biogenic SOA formation (Xu et al., 2021b) have been reviewed recently.

Shen et al. (2022) found that >70% of highly oxygenated organic molecules (HOMs) unexpectedly formed from minor initial H abstraction channel (~10%) instead of the major OH addition channel in the OH oxidation of  $\alpha$ -pinene under both low NO (30–100 pptv) and high NO (~20 ppbv) conditions, and thus highlighted that minor reaction pathways can contribute significantly to SOA formation and growth. This work further identified the formation and arrangement of alkoxy radicals as a prerequisite for fast autoxidation and thus the formation of HOMs from  $\alpha$ -pinene OH oxidation (Shen et al., 2022). This new pathway of HOM formation, generally not considered in current chemical mechanisms, may also be important for OH oxidation of other monoterpenes and cyclic alkenes.

Li et al. (2022e) investigated the aqueous oxidation of eugenol, a typical aromatic compound, and found that the SOA yield could be larger than 100%; in addition, they suggested that aqueous products might be more light-absorptive and more toxic than the precursor (Li et al., 2022e), highlighting the impacts of aqueous SOA formation on air quality and climate. Wang et al. (2022j) investigated the aqueous-phase photolysis of methoxyphenols and nitrophenols in the presence of nitrate, and found that the nitration of methoxyphenols led to enhanced light absorption. It was also shown that organic chromophores, such as methoxyphenols, could in turn promote nitrite formation during nitrate photolysis, likely facilitated by solvated electrons (Wang et al., 2021f); the formed nitrite, either in the aqueous phase or partitioning to the gas phase as HONO, may perturb atmospheric chemistry by generating OH radicals upon photolysis.

## 3.3. Field observation

Recent progress in field measurements in China is introduced in this section, including trace gases (section 3.3.1), aerosol particles (section 3.3.2), and applications of isotopic techniques (section 3.3.3) and remote sensing (section 3.3.4).

### 3.3.1. Trace gases

OH radicals dominate daytime atmospheric oxidation processes in the troposphere. A number of field campaigns have been performed in various environments during the past several decades to explore atmospheric oxidation capacities and secondary pollution; however, few of these campaigns were conducted in cold seasons as OH was considered to play a minor role in winter. Three winter campaigns were carried out in Beijing to investigate OH radical chemistry, and revealed a strong atmospheric oxidation capacity that was about one to two times higher than that in European

and American urban areas (Tan et al., 2018; Lu et al., 2019; Ma et al., 2019b). The dominant primary source of OH radicals was HONO photolysis during wintertime in Beijing, but a large portion of primary sources were still missing. In addition, Wang et al. (2022c) carried out the first field observation of OH radicals in the Yangtze River Delta (YRD) region, and suggested that monoterpenes could significantly aggravate O<sub>3</sub> pollution in this region due to co-occurrence of high NO<sub>x</sub> and monoterpenes from anthropogenic activities.

HONO is a crucial precursor of OH radicals, but its formation mechanisms are still controversial. Multi-day measurements of HONO and related pollutants were performed at three heights (8, 120 and 240 m) for the first time in Beijing (Zhang et al., 2020c). HONO concentrations were found to be highest at 120 m, followed by those at 8 m and 240 m. Ground and aerosol surfaces played similar roles in NO<sub>2</sub> conversion at 8 m height during the whole measurement period, and NO<sub>2</sub> conversion on aerosol surfaces was the most important HONO source aloft during haze days. A strong missing HONO source was found in the urban aloft in the daytime, which was related with solar radiation and consumed OH (Zhang et al., 2020c), thereby suggesting a new formation pathway of HONO in the urban atmosphere.

Cl and Br atoms are potent oxidizers and can strongly influence the abundance of climate- and air quality-relevant trace gases. Previous research in polluted regions was mainly focused on ClNO<sub>2</sub> (and to a lesser extent, Cl<sub>2</sub>), and knowledge of other Cl and Br precursors is very limited. Significant amounts of daytime dihalogen gases were recently observed in China—up to 1 ppbv for Cl<sub>2</sub> and 10 pptv for Br<sub>2</sub> at a polluted coastal site in Hong Kong (Peng et al., 2022c; Xia et al., 2022a), and up to 60 pptv for BrCl at an inland rural site on the North China Plain (NCP; Peng et al., 2021), suggesting the presence of significant daytime sources. Laboratory experiments showed that photolysis of particulate nitrate under acidic conditions (pH < 3.0) could activate chloride and bromide, accounting for a large fraction of the observed daytime Cl<sub>2</sub> and Br<sub>2</sub> production in Hong Kong (Peng et al., 2022c; Xia et al., 2022a); in northern China, heavy rural household coal burning during winter and nitrate photolysis led to the elevated daytime BrCl (Peng et al., 2021). After photolysis, these dihalogens would produce Cl and Br atoms, thereby impacting VOC oxidation, O<sub>3</sub> production and haze formation (Li et al., 2021b; Peng et al., 2021; Xia et al., 2022a). It was further suggested that nitrate photolysis can also be a significant daytime Cl and Br source in other polluted regions.

The ability in characterizing atmospheric non-methane organic compounds has been significantly improved in recent years using multiple online mass spectrometry methods, and the number of organic compounds identified and quantified can reach >1000 (Wu et al., 2020a; Ye et al., 2021a). Concentrations of oxygenated organic compounds were higher than expected in the Pearl River Delta and NCP regions, comprising ~50% or higher of non-methane

organic compounds (Wu et al., 2020a; He et al., 2022b). The “missing” OH reactivity in urban regions was significantly reduced after considering these oxygenated species, the photolysis of which could be a large radical source and thus would affect O<sub>3</sub> formation (Wang et al., 2022i).

Wang et al. (2020a) revealed a significant contribution of biomass burning to reactive organic gases in eastern China during the harvest season, via field measurements of a near-complete speciation of reactive organic gases. A follow-up study (Gao et al., 2022d) further quantified the contribution of biomass burning to reactive organic gases, and underscored the importance of household biomass burning in addition to open biomass burning.

### 3.3.2. Aerosol particles

A 10-year-long (2011–20) measurement campaign of water-soluble inorganic ions in PM<sub>2.5</sub> was conducted in Beijing. Due to the implementation of strict air pollution control measures, significant decreases in PM<sub>2.5</sub> were observed in Beijing, with nitrate, sulfate and ammonium decreasing at 5.10%, 8.80% and 7.64% per year (Wang et al., 2022e), and emission reductions of gaseous precursors, especially SO<sub>2</sub>, made a large contribution to the reduced PM<sub>2.5</sub> mass concentrations in Beijing. PM<sub>2.5</sub> mass concentrations have also experienced a substantial decrease (−9.1% per year) in Nanjing since 2013, accompanied by a larger reduction in SO<sub>2</sub> (−16.7% per year) (Ding et al., 2019). In contrast, the nitrate fraction was significantly increased in the cold season (Ding et al., 2019), mainly due to the increased oxidization capacity and increased ammonia availability caused by substantial reductions in SO<sub>2</sub>.

The change in aerosol chemical compositions with rapidly declining emissions was also well demonstrated during the COVID-19 lockdown. Huang et al. (2021) combined in-situ measurements, satellite observations, and numerical simulations to analyze the nonlinear response of aerosol chemical compositions to emission reductions during the lockdown. A sharp drop in transportation emissions led to a substantial decrease in NO<sub>x</sub>, and the nonlinear response of O<sub>3</sub> to NO<sub>x</sub> increased the atmospheric oxidation capacity and subsequently accelerated the formation of secondary aerosols (Ren et al., 2021). Under unfavorable meteorological conditions, faster oxidation offset emission reductions and caused severe haze pollution in eastern China. As a result, a synchronous control of VOCs was proposed as an effective way to overcome deteriorating haze pollution due to NO<sub>x</sub> reduction.

Chen et al. (2020a) conducted the first vertical observation of precursors (e.g., N<sub>2</sub>O<sub>5</sub>, HONO and NO<sub>x</sub>) relevant for aerosol nitrate formation in urban Beijing. A conceptual model was meanwhile developed to understand the spatial and temporal distribution of nitrate formation mechanisms by combining vertical observations and measurements at two other ground sites in urban and suburban Beijing. They found that nitrate formation was mainly driven by OH oxidation in the daytime and by NO<sub>3</sub> oxidation at night during the wintertime in Beijing (Chen et al., 2020a).



The first comprehensive vertical measurements of fine particle composition were conducted on a 325 m tower in urban Beijing (Lei et al., 2021; Li et al., 2022f), using a PM<sub>2.5</sub> time-of-flight aerosol chemical speciation monitor, and it was found that there were significantly larger vertical gradients of aerosol species in winter than summer. In particular, vertical ratios of aqueous-phase to photochemical SOA in winter decreased significantly with height, indicating stronger aqueous-phase chemistry at ground level than the city aloft. Lei et al. (2021) observed large increases in the ratios of most aerosol species at 240 m compared to those at ground level in the early morning in winter, and thus highlighted the impacts of the residual layer on air pollution of the second day. Comparatively, Li et al. (2022f) suggested that aerosol liquid water played a more important role in aerosol formation in summer. Furthermore, it was suggested that the higher nitrate concentration in the city aloft than at ground level during daytime was mainly due to the enhanced gas-particle partitioning driven by aerosol water content and acidity.

Aqueous production of secondary aerosols is a vital but less studied contributor to aerosol pollution and haze events. Wang et al. (2020b) proposed a two-step aqueous-phase sulfate formation pathway based on field observations during winter in Beijing: under fog/cloud conditions, SO<sub>2</sub> can be rapidly oxidized by NO<sub>2</sub> to form sulfate and HONO/NO<sub>2</sub><sup>-</sup>, and HONO/NO<sub>2</sub><sup>-</sup> will further oxidize SO<sub>2</sub> to produce N<sub>2</sub>O at a pH of 5.5–7 (due to efficient uptake of ammonia). Moreover, aqueous oxidation of fossil-fuel POA was found to be a major source of SOA during winter in Beijing (Wang et al., 2021a), and ring-breaking oxidation of aromatic species in POA was proposed to be the dominant mechanism, leading to the formation of carbonyls and carboxylic acids.

Low-volatility organic vapors are crucial intermediates that connect VOC oxidation to SOA formation; however, measuring these intermediates poses a considerable challenge owing to their complex compositions and very low concentrations. Detailed measurements of these intermediates, named oxygenated organic molecules (OOMs), were conducted using a Chemical Ionization Atmospheric Pressure Interface Time of Flight Mass Spectrometer in eastern China starting in 2018 (Nie et al., 2022). More than 1500 OOMs were identified and assigned to their likely precursors, with anthropogenic aromatic and aliphatic compounds predominating in winter and non-negligible contributions from biogenic monoterpenes and isoprene found in summer (Liu et al., 2021b; Xu et al., 2021c). The condensation of these OOMs contributed significantly, if not dominantly, to SOA formation, and the unexpected increase in OOM concentrations from very clean to highly polluted environments suggests a positive feedback loop between OOM formation and pollution.

Field measurements (Huang et al., 2020a; Yuan et al., 2020) showed that major light-absorbing species, including methoxyphenols, nitrophenols, PAHs, and oxidized PAHs, could in total account for ~10% of light absorption by

organic aerosol. Yuan et al. (2020) further used these light-absorbing species, instead of non-light absorbing organic markers, as inputs in positive matrix factorization analysis to identify sources of light-absorbing organic aerosol in Xi'an. Solid fuel combustion was found to be the dominant source for light-absorbing organic aerosol in winter (~80%), while secondary formation became the main source in summer (~60%).

Wang et al. (2019) developed a black-carbon-tracer method coupled with a statistical approach to separate the light absorption of primary and secondary BrC. In the NCP region, primary emissions were found to contribute more to BrC light absorption than secondary processes, and biomass burning and coal combustion contributed to 60% and 35% of primary BrC absorption at 370 nm (Wang et al., 2019). In contrast, when compared to primary BrC, secondary BrC contributed more to aerosol light absorption in the Tibetan Plateau region (Zhu et al., 2021a).

Single particle analysis has been used in China to understand the formation and aging of aerosol particles. Zhang et al. (2019) performed in-situ measurements of the chemical composition of individual particles across the four seasons in Guangzhou, and observed enhanced aqueous formation of oxalate associated with Fe-containing particles. In addition, in-cloud processes have been found to be an important pathway for the formation of light-absorbing organic nitrogen compounds (Zhang et al., 2020b; Lian et al., 2021; Sun et al., 2021b), such as amines and imidazoles. Using size-resolved single-particle chemical compositions and mixing states, a method for evaluating particle aging was developed and used to investigate aerosol particles in Beijing (Chen et al., 2020b, c). It was suggested that regional transport dominated haze formation when PM<sub>2.5</sub> was < 100 μg m<sup>-3</sup>, while accumulation of local primary particles and secondary formation prevailed when PM<sub>2.5</sub> exceeded 100 μg m<sup>-3</sup>.

A quadrupole aerosol chemical speciation monitor and single-particle aerosol mass spectrometry were synchronously deployed to investigate the chemical composition and mixing state of aerosols over the East China Sea (Liu et al., 2020c, 2022d; Sun et al., 2021a). Monomethylamine, trimethylamine, and diethylamine were identified as the most abundant amines, accounting for 50%, 16%, and 29% of amine-containing particles, respectively. Elemental carbon-, K-, Mn-, and Fe-rich particles were abundant in monomethylamine-containing particles, and V-rich particles were abundant in trimethylamine-containing particles, indicating that monomethylamine and trimethylamine mainly originated from terrestrial and harbor anthropogenic sources. For comparison, both terrestrial anthropogenic and marine markers were observed in diethylamine-containing particles, suggesting multiple sources for diethylamine.

Marine aerosols are generally divided into sea spray aerosol (produced via wind–sea surface interaction) and secondary marine aerosol (formed via gas-to-particle formation), and the inability to distinguish between these two aerosol types greatly hinders accurate prediction of the

marine radiative balance. Xu et al. (2022b) developed a unique approach to identify sub-micron sea-spray aerosol by using size-resolved hygroscopicity measurements, and found that the number concentrations of sub-micron sea-spray aerosol have been significantly underestimated by traditional methods. In addition, combining field measurements with lab experiments, Huang et al. (2022) found that iodine-initiated heterogeneous chemistry can substantially accelerate particle growth, and this new mechanism may explain the fast growth of marine secondary aerosol.

Fe solubility is one of the major factors affecting health and biogeochemical effects of aerosol Fe. Individual particle analysis (Li et al., 2017b; Zhu et al., 2020b) has shown that nanosized iron oxides from anthropogenic sources can be internally mixed with secondary sulfate/nitrate particles in the atmosphere. Liu et al. (2022b) also found that Fe solubility was correlated positively with aerosol acidity and negatively with particle size (0.32–5.6  $\mu\text{m}$ ), as fine iron oxide particles had a longer residence time in the troposphere and larger surface for heterogeneous aging, when compared to coarse particles. Furthermore, Zhang et al. (2022b) observed higher Fe solubility in fine particles than coarse particles, and suggested that primary emissions and secondary formation of dissolved Fe played different roles for Fe solubility enhancement in fine and coarse particles. Very recently, Li et al. (2023) found that leaching solutions and contact time used to extract dissolved aerosol trace metals would greatly influence their measured solubilities, and these effects showed large variations for different trace metals. As a result, in order to increase data comparability, it is warranted to standardize aerosol trace metal solubility measurement protocols.

A series of rain and snow samples in China were examined at the molecular level using Fourier transform ion cyclotron resonance mass spectrometry (Chen et al., 2022a). The derivatives of BVOCs were found to be widely distributed along the Yangtze River Basin and contributed to rainwater dissolved organic matter, and variations in their molecular compositions were influenced by combinations of different climatic, geographical and anthropogenic activities (Chen et al., 2022a). Snow samples from four megacities in North China were analyzed to elucidate the potential “precursor–product” pairs of organic nitrogen substances at the molecular level, revealing that more than 50% of the snow CHON molecules may be related to oxidized and hydrolyzed processes of atmospheric organics (Su et al., 2021). Moreover, a new structural classification was provided for atmospheric organosulfur species using the modified oxygen and redefined aromaticity index, and typical sulfonates and anionic surfactants of anthropogenic origins could be easily distinguished using this method (Su et al., 2022a).

### 3.3.3. Application of isotopic techniques

Measurements of isotopic compositions provide a powerful tool and a new perspective to explore sources and chemical processes of aerosol particles, as demonstrated by a number of recent studies in China, a few examples of which are introduced below.

Fan et al. (2020) compared sulfur isotope fractionation produced in atmospheric sulfate formation via different oxidation processes in Beijing, and found that  $\text{SO}_2$  oxidized by  $\text{O}_2$  (catalyzed by transition metal ions) and by  $\text{NO}_2$  dominated aerosol sulfate formation in a wintertime haze episode. Fan et al. (2022) explored vertical distributions of nitrate formation pathways in Beijing by combining oxygen anomalies ( $\Delta^{17}\text{O}$ ) and a Bayesian model. It was found that hydrolysis of  $\text{NO}_2$  to HONO promoted nitrate production at 120 m height (Fan et al., 2022), and low RH at 260 m height inhibited  $\text{N}_2\text{O}_5$  hydrolysis in the residual layer on winter haze days. Zhang et al. (2022e) carried out 3 h-resolution isotope measurements in Nanjing and revealed that heterogeneous hydrolysis of  $\text{N}_2\text{O}_5$  played an important role in nitrate formation on haze days even during the daytime, while OH oxidation dominated nitrate formation in the clean atmosphere.

Compound-specific dual-carbon isotope ( $\delta^{13}\text{C}$ - $\Delta^{14}\text{C}$ ) analysis was developed to investigate sources and atmospheric chemical processes of organic aerosols (Xu et al., 2021a). A recent study (Xu et al., 2022a) employed this technique to track precursors and the formation of aerosol oxalate, an important component of aqueous SOA. It was found that precursors emitted by anthropogenic activities (e.g., fossil fuel combustion) contributed to >50% of aerosol oxalate (Xu et al., 2022a), in contrast to the traditional view that it originated mainly from biogenic precursors.

Non-conventional isotopic techniques have also been employed in atmospheric chemistry research in China. For example, Fe isotopic compositions have been measured for desert and fly ash samples (Li et al., 2022d) as well as airborne magnetic particulate matter collected in Beijing (Zuo et al., 2022).

### 3.3.4. Remote sensing

Satellite remote sensing from American and European space-borne spectrometers, such as the Tropospheric Monitoring Instrument (TROPOMI) and Ozone Monitoring Instrument (OMI), has been widely used to provide long-term and large-scale information on air pollutants. For instance, Chen et al. (2022b) retrieved kilometer-level glyoxal data from TROPOMI, which were used to identify anthropogenic VOC emission sources.

On the other hand, the poor spectral quality of the Environmental Trace Gases Monitoring Instrument (EMI)—the first Chinese satellite-based ultraviolet-visible spectrometer—makes retrieval of air pollutants difficult. In order to obtain reliable results from EMI, the following optimizations of remote sensing algorithms were conducted: (1) on-orbit wavelength calibration was set up to calculate daily instrumental spectral response functions and wavelength shifts to diminish the fitting residuals; (2) an adaptive iterative retrieval algorithm was developed to select the best retrieval setting with the minimum retrieval uncertainty; and (3) simulated irradiance (instead of measured irradiance) was used to eliminate cross-track stripes in the retrieval. Through these optimizations, global distributions of gaseous pollutants, such as  $\text{NO}_2$ ,  $\text{SO}_2$  and HCHO, were successfully retrieved from

EMI and used to locate high-emission spots (Zhang et al., 2020a; Xia et al., 2021; Su et al., 2022b). Furthermore, global air quality variations during the COVID-19 pandemic in early 2020 were evaluated from EMI observations, and the abrupt drop in NO<sub>2</sub> for many cities when effective measures were implemented to prevent the spread of the pandemic (Liu et al., 2022a) was successfully captured.

Le et al. (2020) analyzed TROPOMI NO<sub>2</sub> data and found substantial reductions in NO<sub>2</sub> levels over China during the COVID-19 lockdown period (23 January to 13 February); however, severe PM<sub>2.5</sub> pollution still occurred in northern China. Observational analysis and modeling work were combined to understand the causes of severe PM<sub>2.5</sub> pollution during that period (Le et al., 2020), suggested to include enhanced heterogeneous chemistry under high RH, stagnant meteorological conditions, and unaffected power plant and petrochemical industry emissions.

Ozonesonde data and TROPOMI NO<sub>2</sub> data were combined with WRF-Chem to investigate the effects of typical strong convection on the vertical redistribution of air pollutants in Nanjing (Zhang et al., 2022d). Ozonesonde observations showed higher O<sub>3</sub> and water vapor mixing ratios in the upper troposphere after convection, indicating that strong updrafts transported lower-level air masses into the upper troposphere. Ozone production in the upper troposphere was driven by chemistry (5–10 times the dynamic contribution) and reduced (–40%) by lightning NO<sub>x</sub> during the whole convection life cycle. In addition, a new high-resolution retrieval algorithm was developed and employed to estimate the lightning NO<sub>x</sub> production efficiency, which was determined to be 60 ± 33 mol NO<sub>x</sub> per flash (Zhang et al., 2022d).

Current assessments of aerosol radiative effects still contain large uncertainties, partly because aerosols with complex sources have different shapes, chemical compositions and optical properties. Following the deployment of nationwide ground-based observation networks and the development of satellite remote sensing technology, the knowledge base regarding aerosol chemical, optical and radiative properties over regional and global scales has been significantly improved in recent years. For example, using multi-year observations at 50 sites from the China Aerosol Remote Sensing Network, Che et al. (2019a) characterized the aerosol climatologies for representative remote, rural and urban areas in China, and suggested that coarse particles played a dominant role at rural sites near deserts while light-absorbing fine particles were dominant at most urban sites. Decadal-scale trends in total aerosol loading and aerosol optical depth (AOD) were examined for five aerosol components using multi-angle imaging spectroradiometer retrievals (Gui et al., 2022), and small-sized and spherical aerosols (composed of sulfate, organic matter and black carbon) were found to be the dominant aerosol types driving the interannual variability in land AOD during 2003–18. In addition to anthropogenic and natural emissions, the contribution of meteorological factors to interdecadal changes in regional AOD was

found to be non-negligible (Che et al., 2019b). Furthermore, a climatology of concentrations of different aerosol compositions was obtained (Li et al., 2022c) using the newly developed Generalized Retrieval of Atmosphere and Surface Properties component approach.

### 3.4. Modeling studies

Recently, the Chinese Earth System Science Numerical Simulator Facility (EarthLab) was successfully constructed, and an integrated air quality modeling system (IAQMS-street), which covers global, regional, urban, and street scales based on a two-way coupling technology, was developed as a key component of EarthLab (Chen et al., 2021a; Wang et al., 2022g). Modules of heterogeneous chemistry, size-resolved aerosol microphysical processes, and mixing states were developed for IAQMS-street to better simulate air pollution in China. Careful comparison with observations has revealed that IAQMS-street can reproduce global and regional aerosol mass and number concentrations reasonably well, and in particular the prediction accuracy of heavy pollution episodes has greatly improved. In addition, a high-resolution online global air quality source-receptor model (GNAQPMS-SM) with an uncertainty analysis tool was developed to effectively compute the contributions of various sources to ambient air pollutants (Ye et al., 2021b, 2023).

Model intercomparison using consistent model inputs is an extremely valuable approach to evaluating the performance of numerical models and understanding the magnitude and sources of model uncertainties. In the last two decades, scientists in China have been actively participating in model intercomparison studies (Han et al., 2008; Wang et al., 2008). Very recently, in the Model Inter-Comparison Study for Asia (MICS-Asia) phase III, scientists in China led model intercomparisons for NO<sub>2</sub>, CO and NH<sub>3</sub> (Kong et al., 2020), O<sub>3</sub> and relevant species (Li et al., 2019b), aerosol concentrations (Chen et al., 2019a), reactive nitrogen deposition (Ge et al., 2020), and aerosol radiative effects and feedbacks (Gao et al., 2020).

The heterogeneous uptake of HO<sub>2</sub> may be a significant sink of HO<sub>x</sub>, hence impacting the atmospheric oxidation capacity. A multiphase chemical kinetic box model, PKU-MARK, was developed to simulate heterogeneous reactions of HO<sub>2</sub> with aerosol particles based on a novel parameterization of  $\gamma(\text{HO}_2)$  (Song et al., 2020), and it was found to reproduce well the time series of  $\gamma(\text{HO}_2)$  reported by a summer field campaign at a rural site. A follow-up study (Song et al., 2022a) suggested that, although HO<sub>2</sub> uptake may not change the O<sub>3</sub> sensitivity regime classification in a single day, it could reduce net O<sub>3</sub> production rates by up to 6 ppbv h<sup>-1</sup> in the morning.

Surface O<sub>3</sub> concentrations steadily increased from 2013 to 2019 (Li et al., 2020b), but emission trends of NO<sub>x</sub> and VOCs alone cannot explain well the increase in O<sub>3</sub>. Based on surface observations and model simulations with GEOS-Chem, Li et al. (2019c) suggested that a decrease in PM<sub>2.5</sub> could increase summertime O<sub>3</sub> over the NCP, due to the role of PM<sub>2.5</sub> as a scavenger of HO<sub>2</sub> radicals that would other-



wise react with NO to produce O<sub>3</sub>. Such an O<sub>3</sub> “penalty” was further confirmed by observational evidence that O<sub>3</sub> production is suppressed under high PM<sub>2.5</sub> conditions (Li et al., 2021a). As O<sub>3</sub> pollution is less sensitive to NO<sub>x</sub> emission controls, the need to regulate VOC emissions was underscored (Li et al., 2019c).

Due to the abrupt drop in NO<sub>x</sub> emissions during the COVID-19 lockdown, the maximum daily 8-h average O<sub>3</sub> concentrations reached 60–70 ppbv in January 2020 when they were expected to be very low. Using GEOS-Chem simulations, Li et al. (2021a) found that fast O<sub>3</sub> production was driven by HO<sub>x</sub> radicals from the photolysis of formaldehyde, which was generated by VOC oxidation. It was further suggested that high O<sub>3</sub> occurrences could increase in terms of frequency and severity during winter and spring without continuous control to reduce VOC emissions.

An observation-based method was developed to investigate the sensitivity of O<sub>3</sub> formation to precursors during two persistent elevated O<sub>3</sub> episodes in Guangdong (Song et al., 2022b). Average OH concentrations between 0800 and 1300 (UTC+8), derived using this method, fell into a narrow range ( $2.5\text{--}5.5 \times 10^6 \text{ mol cm}^{-3}$ ) with a weak dependence on NO<sub>x</sub>, and agreed well with those observed at a rural site in the Pearl River Delta. This method was further used to evaluate O<sub>3</sub> production efficiencies,  $\varepsilon(\text{NO}_x)$  or  $\varepsilon(\text{VOC})$ , defined as the number of O<sub>3</sub> molecules produced per molecule of NO<sub>x</sub> (or VOC) consumed, and the average  $\varepsilon(\text{NO}_x)$  and  $\varepsilon(\text{VOC})$  were determined to be 3.0 and 2.1 ppbv/ppbv, respectively (Song et al., 2022b).

Gao et al. (2021a) combined online measurement data with 3D factor analysis to quantify the contributions of different pathways to secondary inorganic aerosol formation, and identified mixed NH<sub>4</sub>NO<sub>3</sub> and (NH<sub>4</sub>)<sub>2</sub>SO<sub>4</sub> aqueous processes as the most important pathway during heavy haze events. A solute-strength-dependent thermodynamic and kinetic model was developed and employed to investigate sulfate aerosol formation (Gao et al., 2022a), revealing that aqueous oxidation by H<sub>2</sub>O<sub>2</sub> was the dominant pathway for sulfate formation, and thus suggesting that target oxidant control could be an effective way to mitigate sulfate aerosol.

By integrating a chemical transport model, nationwide measurements, and a sophisticated ammonia emissions model, Liu et al. (2019) found that controlling ammonia emissions would significantly aggravate acid rain pollution, thus offsetting the benefit of reduced fine particle pollution. As a result, region-specific ammonia control strategies could provide a more rational and effective way to achieve co-benefits in protecting human and ecosystem health in China. They further proposed region-specific emission control strategies in the near future (Liu et al., 2019)—for instance, implementing a reduction in NH<sub>3</sub> emissions by 20%–30% in areas with scarce acid rain but heavy fine particle pollution (e.g., northern China), while giving higher priorities to SO<sub>2</sub> and NO<sub>x</sub> emission controls in current acid rain areas like southern China.

Zhu et al. (2022) investigated the spatiotemporal charac-

teristics of multi-pollutant air pollution over China and attributed the decline in multi-pollution to decreases in PM<sub>2.5</sub>–PM<sub>10</sub> and PM<sub>2.5</sub>–O<sub>3</sub> co-pollution days. In the YRD region, co-pollution days with a maximum daily 8-h average O<sub>3</sub> > 160 μg m<sup>-3</sup> and PM<sub>2.5</sub> > 75 μg m<sup>-3</sup> generally occurred under conditions of high RH, low wind speed, and high near-surface air temperature (Dai et al., 2021a). Dai et al. (2023) further found a decreased frequency in PM<sub>2.5</sub>–O<sub>3</sub> co-pollution days in the Beijing–Tianjin–Hebei (BTH) region during the warm season (April to October) in 2013–20, but increased proportions of PM<sub>2.5</sub>–O<sub>3</sub> co-pollution days in PM<sub>2.5</sub> pollution days, implying a strengthened relationship between O<sub>3</sub> and PM<sub>2.5</sub> under low-PM<sub>2.5</sub> conditions (Dai et al., 2023). Based on GEOS-Chem simulations, PM<sub>2.5</sub>–O<sub>3</sub> co-pollution days in the BTH region were found to be associated with high concentrations of OH and total oxidants, sulfur oxidation ratio and nitrogen oxidation ratio, with the sulfate concentration ranking top among all aerosol species (Dai et al., 2023).

#### 4. Interactions of air pollution with meteorology, weather and climate

PBL meteorology plays a vital role in air quality via modulating the diffusion and transformation of pollutants. Both multi-altitude measurements and atmospheric dynamic–chemistry coupled simulations indicate that turbulent motion shapes the vertical stratification of secondary pollution (Huang et al., 2020c). Enhanced nitrate and sulfate production in the upper PBL and residual layer may contribute substantially to near-surface haze pollution through vertical mixing, underscoring the importance of understanding air pollution in China from a vertical perspective. In turn, aerosols might affect PBL evolution by perturbing the radiative energy balance. Under highly polluted conditions, the attenuation and absorption of incident solar radiation by aerosols can heat the atmosphere and cool the surface, thereby strengthening the inversion layer and deteriorating near-surface air pollution (Wang et al., 2018). Such interactions between aerosols and the PBL could amplify regional haze pollution in eastern China (Huang et al., 2020b).

Besides emission and chemical reactions, the distribution and evolution of air pollutants are also modulated by meteorological conditions. In winter, cold fronts occur periodically and transport air pollutants quickly to downstream regions. Combining observations and tracer-tagged simulations, Kang et al. (2021) described 3D structures of PM<sub>2.5</sub> during a cold front over eastern China. It was suggested that the strong northwesterly transported aerosol particles from the highly polluted NCP to YRD and transported warm and polluted air mass to the free troposphere along the frontal surface over the YRD. In addition, the contributions of sources in the NCP region to PM<sub>2.5</sub> in the YRD region increased from ~15% to 30% during the cold front. Liu et al. (2022c) further found a seesaw pattern of interannual anomalies of PM<sub>2.5</sub> between the BTH and YRD regions, and suggested that the low (high) PM<sub>2.5</sub> difference between the BTH and YRD

regions was associated with a strong (weak) East Asian winter monsoon.

An online coupled regional climate–chemistry–aerosol model (RIEMS-Chem) was developed and applied with process analysis to investigate aerosol radiative feedback to haze formation and evolution in the BTH region (Li et al., 2020a). It was found that feedback-induced domain-averaged changes in PM<sub>2.5</sub> concentrations could reach 45.1 μg m<sup>-3</sup> (39%) during severe haze episodes (Li et al., 2020a). This feedback effect increases aerosol accumulation in the haze growth stage through weakening vertical diffusion, promoting chemical reactions and enhancing horizontal advection of upwind pollutants; plus, it also enhances removal rates in the dissipation stage, but the effect is weak in the persistence stage.

Gao et al. (2022c) characterized common features of the influence of the aerosol direct radiative effect on meteorology based on five severe PM<sub>2.5</sub> pollution events in winter during 2013–16. It was found that aerosols caused a significant decrease in radiative flux by 52.1–86.7 W m<sup>-2</sup>, a decrease in 2-m temperature by 0.28°C–0.97°C, and a decrease in PBL height by 23.1–58.5 m (Gao et al., 2022c). Aerosol–radiation interactions, including aerosol–photolysis interactions and aerosol–radiation feedback, can also affect near-surface O<sub>3</sub> during co-pollution days. Using WRF-Chem simulations, Yang et al. (2022a) investigated four PM<sub>2.5</sub>–O<sub>3</sub> co-pollution episodes that occurred in 2014–17 and found that aerosol–photolysis interactions dominated the reduction in daytime near-surface O<sub>3</sub> in North China by inhibiting the chemical production of O<sub>3</sub>.

Using WRF-Chem coupled with an urban canopy scheme, Wang et al. (2022a) found that local circulation regulated the spatial distribution of aerosols and led to diverse impacts of aerosol radiative effects in urban heat islands. It was further found that adopting cool roofs tends to aggravate PM<sub>2.5</sub> pollution mostly in lightly polluted regions, indicating that green roofs could be better choices given the current severity of air pollution in China (Wang et al., 2020b). These results may offer valuable information on cooperative management of heat islands and air pollution in China.

The anticyclonic anomalies over northeastern Asia associated with stagnant weather conditions, including weak near-surface winds, temperature inversion in the lower troposphere, low PBL height and high RH, are favorable for haze pollution in the NCP region (Li et al., 2019a). Using a weather classification technique, Li et al. (2022a) identified two conducive patterns with the most occurrences of severe PM<sub>2.5</sub> pollution (daily PM<sub>2.5</sub> >150 μg m<sup>-3</sup>), and then linked them to various climate factors. It was suggested that the East Atlantic–West Russia teleconnection pattern and the Victoria Mode of sea surface temperature anomalies, which are found to be the top two dominant climate drivers leading to conducive weather patterns in North China, can be used to predict the frequency of severe PM<sub>2.5</sub> pollution over North China in the winter (Li et al., 2022a).

Global warming is likely to bring more hot days, which

may increase the frequency of O<sub>3</sub> pollution days in regions with high anthropogenic emissions. Wang et al. (2022f) suggested that more than half of O<sub>3</sub> pollution days during 2014–19 in the NCP region occurred under high-temperature extremes when hot and stable atmospheric conditions enhanced O<sub>3</sub> chemical production. Using a Random Forest algorithm combined with GEOS-Chem and CMIP6 climate models, Gong et al. (2022) suggested that future risks of O<sub>3</sub> exceedance during hot days would significantly decrease in the 2030s under the SSP1-2.6 scenario, but increase until the 2050s under the SSP5-8.5 scenario.

Zhong et al. (2021) suggested that the 0.8% (10 yr)<sup>-1</sup> decrease in clouds in China from 1957 to 2005 was primarily caused by global warming, and the moisture–convection–latent-heat feedback cycle was the primary driver of the trends in clouds in China as well as globally. The decreasing trend of clouds in China has important implications for the atmospheric oxidation capacity (Zhong et al., 2021), because enhanced solar insolation as a result of less cloud cover will lead to higher concentrations of OH radicals and O<sub>3</sub>.

Rapid changes in emissions, such as the unexpected emission reductions during COVID-19 and the stringent emission controls in China since 2013, may affect weather and climate. By using Community Earth System Model version 2 (CESM2) simulations, Yang et al. (2022c) revealed that the dramatic reduction in aerosols during the COVID-19 epidemic in eastern China could have caused a positive sea level pressure anomaly over the northwestern Pacific Ocean, thereby strengthening moisture convergence and contributing to the record rainfall in June–July 2020 in eastern China. Gao et al. (2022b) further employed CESM2 to examine the rapid climate responses to emission reductions in aerosol and O<sub>3</sub> precursors over China in 2013–17, and suggested that the increase in O<sub>3</sub> and decrease in aerosols in the lower troposphere together resulted in an anomalous warming of 0.16°C ± 0.15°C in eastern China.

## 5. Interactions between the biosphere and atmosphere

The biosphere emits a number of trace gases (such as N<sub>2</sub>O, NO<sub>x</sub> and VOCs) into the atmosphere, affecting O<sub>3</sub> and secondary aerosol formation and thus further impacting the radiative balance and climate change. On the other hand, some atmospheric pollutants, such as O<sub>3</sub>, have direct adverse effects on various plants, the interaction of solar radiation with trace gases and aerosol particles can also impact photosynthesis, and dry and wet deposition is an important source of nutrients and toxic elements for many ecosystems.

Zhao et al. (2022) combined a generalized additive model and an air quality response surface model to analyze source–sink relationships of sulfur and nitrogen oxides using the ratios of deposition to emissions (D/E). Deposition of sulfate and nitrate was found to decline more slowly than



the emissions of their precursors ( $\text{SO}_2$  and  $\text{NO}_x$ ), attributed in part to increased precipitation (Zhao et al., 2022). Furthermore, enhanced transport of air pollution has also played an important role in the rising D/E values in four developed regions of China (Zhao et al., 2022), as has changing aerosol chemistry in the case of sulfur compounds.

Xie et al. (2019) developed a regional climate–chemistry–ecology coupled model (RegCM-Chem-YIBs) that includes a regional climate–chemistry model (RegCM-Chem) and a terrestrial vegetation model (YIBs), which is capable of exploring the interactions among  $\text{O}_3$ ,  $\text{CO}_2$  and  $\text{PM}_{2.5}$  by simulating interactions between the ecosystem and the atmosphere. Meteorological factors and pollutant concentrations from RegCM-Chem are used to drive YIBs every 6 min, and YIBs simulates physiological processes of vegetation and calculates land surface parameters. Using RegCM-Chem–YIBs, Xie et al. (2019) found that tropospheric  $\text{O}_3$  had a detrimental effect on plant carbon uptake and led to a greater accumulation of  $\text{CO}_2$  in the atmosphere, and that the terrestrial carbon sink in China was reduced by  $112.2 \pm 22.5 \text{ TgC yr}^{-1}$  due to  $\text{O}_3$  damage. A follow-up study (Xie et al., 2020) further suggested that atmospheric aerosols contribute to the terrestrial carbon cycle through diffuse radiation fertilization effects and hydrometeorological feedbacks, and that the current aerosol loading can increase the terrestrial carbon sink in China by  $60 \text{ TgC yr}^{-1}$ .

Methane is an important greenhouse gas that contributes significantly to global warming. Atmospheric OH oxidation is a major sink of methane and thus affects its lifetime and abundance. The methane growth rate in 2020, relative to 2019, was attributed to increased natural emissions and an increased atmospheric lifetime (Peng et al., 2022b). The latter was caused by a decrease in the tropospheric OH concentration by  $\sim 1.6\%$  when compared to 2019, mainly due to reduced anthropogenic  $\text{NO}_x$  emissions associated with the spread of COVID-19. This work provides an interesting example demonstrating that changes in emissions from the biosphere and atmospheric chemical processes both play important roles in determining the abundance of atmospheric species.

## 6. Data assimilation

Chemical data assimilation combines observations of atmospheric composition and chemical transport modeling to improve the accuracy of air quality forecasts, to generate chemical reanalysis datasets, and to constrain emission estimates or other uncertain parameters. Kong et al. (2021) released the first high-resolution Chinese air quality reanalysis dataset (CAQRA), which provides surface fields of  $\text{PM}_{2.5}$ ,  $\text{PM}_{10}$ ,  $\text{SO}_2$ ,  $\text{NO}_2$ , CO and  $\text{O}_3$  in China between 2013 and 2018 with high spatial (15 km) and temporal (1 h) resolutions. This dataset assimilates observations from more than 1000 surface air quality monitoring sites by using an ensemble Kalman filter and the Nested Air Quality Prediction Modeling System (NAQPMS); in addition, several algorithms have

been developed to address the challenges in chemical data assimilations, ensuring the high accuracy of CAQRA. This high accuracy and fine resolution of CAQRA facilitates assessment of long-term human and crop exposure to air pollution and other research related to air quality. A modified ensemble Kalman filter, which addresses filter divergence and enables reuse of costly ensemble simulations, was developed by Wu et al. (2020b) for emission inversions in order to make the process with high temporal and spatial resolutions more affordable. Based on this method, CO and  $\text{NO}_x$  emissions were inverted with a temporal resolution of one week and a spatial resolution of 5 km (Wu et al., 2020b).

Furthermore, under the support of this research program, a data center for China air pollution complexes has recently been developed and will be released for research community access in 2023.

## 7. Summary and outlook

The air pollution complex concept proposed in 1997 by Professor Xiaoyan TANG was based on the observation that coal combustion and vehicle exhaust emissions coexisted in major cities in China. This concept has led to a paradigm shift in our perspective on the formation mechanisms and control policies of air pollution, with emphasis on complexity, interactions, feedbacks, and nonlinearity of chemical and physical processes in the atmosphere. In the last 25 years, the air pollution complex has evolved from a concept to a comprehensive and sophisticated theoretical framework, thanks to active research on air pollution in China supported by the National Natural Science Foundation of China and many other funding agencies.

Due to the length limitation, we were only able to summarize in this paper a limited number of representative and significant studies in atmospheric chemistry in China in the last couple of years. These advances, together with those not covered in this paper, have enriched the theoretical framework of the air pollution complex and provided air pollution control policies in China with robust scientific support. For example, the work that revealed the important contribution of residential emissions to regional air quality (Liu et al., 2016) has eventually led to large-scale control of residential emissions in northern China via the replacement of domestic usage of coal and biofuels with natural gas and electricity. In addition, the finding that controlling ammonium emissions would mitigate aerosol pollution and nitrogen deposition but aggravate acid rain in some regions (Liu et al., 2019) has not only made policymakers realize the complexity of air pollution in China and empathize with region-specific multipollutant control strategies, but also stimulated ammonia control actions enforced by the ministries of Eco-Environment and Agriculture of China.

Joint efforts from all interested parties in China have led to huge success in air pollution control, and  $\text{PM}_{2.5}$  mass concentrations in many regions in China have been reduced at unprecedented rates in the last several years. In addition,

atmospheric research activities in China have also offered great opportunities in education, training, and career development for many graduate students and young scientists, who have been contributing to, and will undoubtedly make even larger contributions to, advancements in atmospheric chemistry. Although mainly based on research activities in China, the theoretical framework of the air pollution complex is also applicable to other countries and regions in the world. A great number of people in many developing and low-income countries are heavily affected by severe air pollution, and knowledge of the air pollution complex concept and lessons learned from air pollution control in China can help these countries improve their air quality and protect human and ecosystem health, similar to what has been happening in China.

Despite remarkable progress, many challenges remain. The National Ambient Air Quality Standards in China were modified in 2012 to set the annual average PM<sub>2.5</sub> level to be below 35 µg m<sup>-3</sup>, which is a threshold much higher than the value (5 µg m<sup>-3</sup>) recommended by the World Health Organization in 2021 (Xue et al., 2022). Meanwhile, the significant decrease in PM<sub>2.5</sub> mass concentrations during the last several years has been accompanied by a slow but steady increase in O<sub>3</sub> concentrations in many regions, posing a major challenge for air pollution control in China. Therefore, cost-effective co-control of PM<sub>2.5</sub> and O<sub>3</sub> in China requires further understanding in terms of air pollution complex formation mechanisms. Moreover, China has committed to reach carbon neutrality by 2060, and dramatic changes in atmospheric composition will occur accordingly in the next few decades in China during its journey toward this goal, providing not only a natural laboratory for domestic and international scientists to advance our knowledge in atmospheric chemistry, but also a challenge to coordinate carbon emissions reduction and air quality improvement to achieve the most benefits for human health. Further research is required to address the above-mentioned challenges.

## Author contributions

Tong ZHU conceived the idea behind this paper; Tong ZHU, Mingjin TANG and Meng GAO coordinated the preparation of the paper with contributions from all other authors; except Tong ZHU, Mingjin TANG and Meng GAO, all the other authors are listed alphabetically.

**Acknowledgements.** This work was funded by the National Natural Science Foundation of China (Grant No. 91844000). We would like to thank the IGAC (International Global Atmospheric Chemistry) China Working Group and China Young Scientist Working Group for their input.

**Open Access** This article is licensed under a Creative Commons Attribution 4.0 International License, which permits use, sharing, adaptation, distribution and reproduction in any medium or format, as long as you give appropriate credit to the original author(s) and

the source, provide a link to the Creative Commons licence, and indicate if changes were made. The images or other third party material in this article are included in the article's Creative Commons licence, unless indicated otherwise in a credit line to the material. If material is not included in the article's Creative Commons licence and your intended use is not permitted by statutory regulation or exceeds the permitted use, you will need to obtain permission directly from the copyright holder. To view a copy of this licence, visit <http://creativecommons.org/licenses/by/4.0/>.

## REFERENCES

- Che, H. Z., and Coauthors, 2019a: Large contribution of meteorological factors to inter-decadal changes in regional aerosol optical depth. *Atmospheric Chemistry and Physics*, **19**, 10 497–10 523, <https://doi.org/10.5194/acp-19-10497-2019>.
- Che, H. Z., and Coauthors, 2019b: Spatial distribution of aerosol microphysical and optical properties and direct radiative effect from the China Aerosol Remote Sensing Network. *Atmospheric Chemistry and Physics*, **19**, 11 843–11 864, <https://doi.org/10.5194/acp-19-11843-2019>.
- Chen, L., and Coauthors, 2019a: MICS-Asia III: Multi-model comparison and evaluation of aerosol over East Asia. *Atmospheric Chemistry and Physics*, **19**, 11 911–11 937, <https://doi.org/10.5194/acp-19-11911-2019>.
- Chen, S., and Coauthors, 2022a: Source and formation process impact the chemodiversity of rainwater dissolved organic matter along the Yangtze River Basin in summer. *Water Research*, **211**, 118024, <https://doi.org/10.1016/j.watres.2021.118024>.
- Chen, S. Y., and Coauthors, 2019b: Fugitive road dust PM<sub>2.5</sub> emissions and their potential health impacts. *Environ. Sci. Technol.*, **53**, 8455–8465, <https://doi.org/10.1021/acs.est.9b00666>.
- Chen, X. S., and Coauthors, 2021a: Global–regional nested simulation of particle number concentration by combing microphysical processes with an evolving organic aerosol module. *Atmospheric Chemistry and Physics*, **21**, 9343–9366, <https://doi.org/10.5194/acp-21-9343-2021>.
- Chen, X. R., and Coauthors, 2020a: Field determination of nitrate formation pathway in winter Beijing. *Environ. Sci. Technol.*, **54**, 9243–9253, <https://doi.org/10.1021/acs.est.0c00972>.
- Chen, Y., and Coauthors, 2020b: Simultaneous measurements of urban and rural particles in Beijing – Part 2: Case studies of haze events and regional transport. *Atmospheric Chemistry and Physics*, **20**, 9249–9263, <https://doi.org/10.5194/acp-20-9249-2020>.
- Chen, Y., and Coauthors, 2020c: Simultaneous measurements of urban and rural particles in Beijing – Part 1: Chemical composition and mixing state. *Atmospheric Chemistry and Physics*, **20**, 9231–9247, <https://doi.org/10.5194/acp-20-9231-2020>.
- Chen, Y. J., and Coauthors, 2022b: Kilometer-level glyoxal retrieval via satellite for anthropogenic volatile organic compound emission source and secondary organic aerosol formation identification. *Remote Sensing of Environment*, **270**, 112852, <https://doi.org/10.1016/j.rse.2021.112852>.
- Chen, Z., P. Liu, Y. Liu, and Y.-H. Zhang, 2021b: Strong acids or bases displaced by weak acids or bases in aerosols: Reactions driven by the continuous partitioning of volatile products into the gas phase. *Accounts of Chemical Research*, **54**, 3667–3678, <https://doi.org/10.1021/acs.accounts.1c00318>.

- Chen, Z., P. Liu, W. G. Wang, X. Cao, Y.-X. Liu, Y.-H. Zhang, and M. F. Ge, 2022c: Rapid sulfate formation via uncatalyzed autoxidation of sulfur dioxide in aerosol microdroplets. *Environ. Sci. Technol.*, **56**, 7637–7646, <https://doi.org/10.1021/acs.est.2c00112>.
- Cheng, Y. F., and Coauthors, 2016: Reactive nitrogen chemistry in aerosol water as a source of sulfate during haze events in China. *Science Advances*, **2**, e1601530, <https://doi.org/10.1126/sciadv.1601530>.
- Chu, B. W., Q. X. Ma, F. K. Duan, J. Z. Ma, J. K. Jiang, K. B. He, and H. He, 2020: Atmospheric “Haze Chemistry”: Concept and research prospects. *Progress in Chemistry*, **32**, 1–4, <https://doi.org/10.7536/PC191230>. (in Chinese with English abstract)
- Cui, X. Y., M. J. Tang, M. J. Wang, and T. Zhu, 2021: Water as a probe for pH measurement in individual particles using micro-Raman spectroscopy. *Analytica Chimica Acta*, **1186**, 339089, <https://doi.org/10.1016/j.aca.2021.339089>.
- Dai, H. B., J. Zhu, H. Liao, J. D. Li, M. X. Liang, Y. Yang, and X. Yue, 2021a: Co-occurrence of ozone and PM<sub>2.5</sub> pollution in the Yangtze River Delta over 2013–2019: Spatiotemporal distribution and meteorological conditions. *Atmospheric Research*, **249**, 105363, <https://doi.org/10.1016/j.atmosres.2020.105363>.
- Dai, H. B., and Coauthors, 2023: Composited analyses of the chemical and physical characteristics of co-polluted days by ozone and PM<sub>2.5</sub> over 2013–2020 in the Beijing–Tianjin–Hebei region. *Atmospheric Chemistry and Physics*, **23**, 23–39, <https://doi.org/10.5194/ACP-23-23-2023>.
- Dai, H. S., H. Q. Gui, J. S. Zhang, X. L. Wei, Z. B. Xie, J. J. Bian, D.-R. Chen, and J. G. Liu, 2021b: An active RH-controlled dry-ambient aerosol size spectrometer (DAASS) for the accurate measurement of ambient aerosol water content. *Journal of Aerosol Science*, **158**, 105831, <https://doi.org/10.1016/j.jaerosci.2021.105831>.
- Dai, H. S., and Coauthors, 2022: Characteristics of aerosol size distribution and liquid water content under ambient RH conditions in Beijing. *Atmos. Environ.*, **291**, 119397, <https://doi.org/10.1016/j.atmosenv.2022.119397>.
- Deng, F. Y., Z. F. Lv, L. J. Qi, X. T. Wang, M. S. Shi, and H. Liu, 2020: A big data approach to improving the vehicle emission inventory in China. *Nature Communications*, **11**, 2801, <https://doi.org/10.1038/s41467-020-16579-w>.
- Ding, A. J., and Coauthors, 2019: Significant reduction of PM<sub>2.5</sub> in eastern China due to regional-scale emission control: Evidence from SORPES in 2011–2018. *Atmospheric Chemistry and Physics*, **19**, 11 791–11 801, <https://doi.org/10.5194/acp-19-11791-2019>.
- Fan, M.-Y., and Coauthors, 2020: Roles of sulfur oxidation pathways in the variability in stable sulfur isotopic composition of sulfate aerosols at an urban site in Beijing, China. *Environmental Science & Technology Letters*, **7**, 883–888, <https://doi.org/10.1021/acs.estlett.0c00623>.
- Fan, M.-Y., and Coauthors, 2022: Important role of NO<sub>3</sub> radical to nitrate formation aloft in urban Beijing: Insights from triple oxygen isotopes measured at the tower. *Environ. Sci. Technol.*, **56**, 6870–6879, <https://doi.org/10.1021/acs.est.1c02843>.
- Gao, J., G. L. Shi, Z. C. Zhang, Y. T. Wei, X. Tian, Y. C. Feng, A. G. Russell, and A. Nenes, 2022a: Targeting atmospheric oxidants can better reduce sulfate aerosol in China: H<sub>2</sub>O<sub>2</sub> aqueous oxidation pathway dominates sulfate formation in haze. *Environ. Sci. Technol.*, **56**, 10 608–10 618, <https://doi.org/10.1021/acs.est.2c01739>.
- Gao, J., and Coauthors, 2021a: Impact of formation pathways on secondary inorganic aerosol during haze pollution in Beijing: Quantitative evidence from high-resolution observation and modeling. *Geophys. Res. Lett.*, **48**, e2021GL095623, <https://doi.org/10.1029/2021GL095623>.
- Gao, J. Y., and Coauthors, 2022b: Fast climate responses to emission reductions in aerosol and ozone precursors in China during 2013–2017. *Atmospheric Chemistry and Physics*, **22**, 7131–7142, <https://doi.org/10.5194/acp-22-7131-2022>.
- Gao, K., Y. D. Zhang, Y. Y. Liu, M. G. Yang, and T. Zhu, 2021b: Screening of imidazoles in atmospheric aerosol particles using a hybrid targeted and untargeted method based on ultra-performance liquid chromatography–quadrupole time-of-flight mass spectrometry. *Analytica Chimica Acta*, **1163**, 338516, <https://doi.org/10.1016/j.aca.2021.338516>.
- Gao, M., and Coauthors, 2020: Air quality and climate change, Topic 3 of the Model Inter-Comparison Study for Asia Phase III (MICS-Asia III) – Part 2: Aerosol radiative effects and aerosol feedbacks. *Atmospheric Chemistry and Physics*, **20**, 1147–1161, <https://doi.org/10.5194/acp-20-1147-2020>.
- Gao, Y., and Coauthors, 2022e: Impacts of biogenic emissions from urban landscapes on summer ozone and secondary organic aerosol formation in megacities. *Science of the Total Environment*, **814**, 152654, <https://doi.org/10.1016/j.scitotenv.2021.152654>.
- Gao, Y. C., H. Liao, H. S. Chen, B. Zhu, J. L. Hu, X. L. Ge, L. Chen, and J. D. Li, 2022c: Composite analysis of aerosol direct radiative effects on meteorology during wintertime severe haze events in the North China Plain. *J. Geophys. Res.: Atmos.*, **127**, e2022JD036902, <https://doi.org/10.1029/2022JD036902>.
- Gao, Y. Q., and Coauthors, 2022d: Unexpected high contribution of residential biomass burning to non-methane organic gases (NMOGs) in the Yangtze River Delta region of China. *J. Geophys. Res.: Atmos.*, **127**, e2021JD035050, <https://doi.org/10.1029/2021JD035050>.
- Ge, B., and Coauthors, 2020: Model Inter-Comparison Study for Asia (MICS-Asia) phase III: Multimodel comparison of reactive nitrogen deposition over China. *Atmospheric Chemistry and Physics*, **20**, 10 587–10 610, <https://doi.org/10.5194/acp-20-10587-2020>.
- Gong, C., Y. Wang, H. Liao, P. Y. Wang, J. B. Jin, and Z. W. Han, 2022: Future co-occurrences of hot days and ozone-polluted days over China under scenarios of shared socioeconomic pathways predicted through a machine-learning approach. *Earth's Future*, **10**, e2022EF002671, <https://doi.org/10.1029/2022EF002671>.
- Gu, W. J., and Coauthors, 2017: Investigation of water adsorption and hygroscopicity of atmospherically relevant particles using a commercial vapor sorption analyzer. *Atmospheric Measurement Techniques*, **10**, 3821–3832, <https://doi.org/10.5194/amt-10-3821-2017>.
- Gui, K., and Coauthors, 2022: The significant contribution of small-sized and spherical aerosol particles to the decreasing trend in total aerosol optical depth over land from 2003 to 2018. *Engineering*, **16**, 82–92, <https://doi.org/10.1016/j.eng.2021.05.017>.
- Han, Z., and Coauthors, 2008: MICS-Asia II: Model intercomparison and evaluation of ozone and relevant species. *Atmos. Environ.*, **42**, 3491–3509, <https://doi.org/10.1016/j.atmosenv.2008.05.017>.

- 2007.07.031.
- He, G. Z., and Coauthors, 2022a: Generation and release of OH radicals from the reaction of H<sub>2</sub>O with O<sub>2</sub> over soot. *Angewandte Chemie International Edition*, **61**, e202201638, <https://doi.org/10.1002/anie.202201638>.
- He, X. J., and Coauthors, 2022b: Volatile organic compounds in wintertime North China Plain: Insights from measurements of proton transfer reaction time-of-flight mass spectrometer (PTR-ToF-MS). *Journal of Environmental Sciences*, **114**, 98–114, <https://doi.org/10.1016/j.jes.2021.08.010>.
- Huang, R.-J., and Coauthors, 2020a: Water-insoluble organics dominate brown carbon in wintertime urban aerosol of China: Chemical characteristics and optical properties. *Environ. Sci. Technol.*, **54**, 7836–7847, <https://doi.org/10.1021/acs.est.0c01149>.
- Huang, R.-J., and Coauthors, 2022: Heterogeneous iodine-organic chemistry fast-tracks marine new particle formation. *Proceedings of the National Academy of Sciences of the United States of America*, **119**, e2201729119, <https://doi.org/10.1073/pnas.2201729119>.
- Huang, X., A. J. Ding, Z. L. Wang, K. Ding, J. Gao, F. H. Chai, and C. B. Fu, 2020b: Amplified transboundary transport of haze by aerosol–boundary layer interaction in China. *Nature Geoscience*, **13**, 428–434, <https://doi.org/10.1038/s41561-020-0583-4>.
- Huang, X., and Coauthors, 2020c: Chemical boundary layer and its impact on air pollution in northern China. *Environmental Science & Technology Letters*, **7**, 826–832, <https://doi.org/10.1021/acs.estlett.0c00755>.
- Huang, X., and Coauthors, 2021: Enhanced secondary pollution offset reduction of primary emissions during COVID-19 lockdown in China. *National Science Review*, **8**, nwaal37, <https://doi.org/10.1093/nsr/nwaa137>.
- Kang, H. H., and Coauthors, 2022: Accurate observation of black and brown carbon in atmospheric fine particles via a versatile aerosol concentration enrichment system (VACES). *Science of the Total Environment*, **837**, 155817, <https://doi.org/10.1016/j.scitotenv.2022.155817>.
- Kang, H. Q., and Coauthors, 2021: Three-dimensional distribution of PM<sub>2.5</sub> over the Yangtze River Delta as cold fronts moving through. *J. Geophys. Res.: Atmos.*, **126**, e2020JD034035, <https://doi.org/10.1029/2020JD034035>.
- Kong, L., and Coauthors, 2020: Evaluation and uncertainty investigation of the NO<sub>2</sub>, CO and NH<sub>3</sub> modeling over China under the framework of MICS-Asia III. *Atmospheric Chemistry and Physics*, **20**, 181–202, <https://doi.org/10.5194/acp-20-181-2020>.
- Kong, L., and Coauthors, 2021: A 6-year-long (2013–2018) high-resolution air quality reanalysis dataset in China based on the assimilation of surface observations from CNEMC. *Earth System Science Data*, **13**, 529–570, <https://doi.org/10.5194/essd-13-529-2021>.
- Kuai, Y., and Coauthors, 2020: Real-time measurement of the hygroscopic growth dynamics of single aerosol nanoparticles with bloch surface wave microscopy. *ACS Nano*, **14**, 9136–9144, <https://doi.org/10.1021/acsnano.0c04513>.
- Le, T. H., Y. Wang, L. Liu, J. N. Yang, Y. L. Yung, G. H. Li, and J. H. Seinfeld, 2020: Unexpected air pollution with marked emission reductions during the COVID-19 outbreak in China. *Science*, **369**, 702–706, <https://doi.org/10.1126/science.abb7431>.
- Lei, L., and Coauthors, 2021: Vertical distributions of primary and secondary aerosols in urban boundary layer: Insights into sources, chemistry, and interaction with meteorology. *Environ. Sci. Technol.*, **55**, 4542–4552, <https://doi.org/10.1021/acs.est.1c00479>.
- Li, J., and Coauthors, 2019b: Model evaluation and intercomparison of surface-level ozone and relevant species in East Asia in the context of MICS-Asia Phase III – Part 1: Overview. *Atmospheric Chemistry and Physics*, **19**, 12 993–13 015, <https://doi.org/10.5194/acp-19-12993-2019>.
- Li, J. D., H. Liao, J. L. Hu, and N. Li, 2019a: Severe particulate pollution days in China during 2013–2018 and the associated typical weather patterns in Beijing-Tianjin-Hebei and the Yangtze River Delta regions. *Environmental Pollution*, **248**, 74–81, <https://doi.org/10.1016/j.envpol.2019.01.124>.
- Li, J. D., and Coauthors, 2022a: Winter particulate pollution severity in North China driven by atmospheric teleconnections. *Nature Geoscience*, **15**, 349–355, <https://doi.org/10.1038/s41561-022-00933-2>.
- Li, J. W., Z. W. Han, Y. F. Wu, Z. Xiong, X. G. Xia, J. Li, L. Liang, and R. J. Zhang, 2020a: Aerosol radiative effects and feedbacks on boundary layer meteorology and PM<sub>2.5</sub> chemical components during winter haze events over the Beijing-Tianjin-Hebei region. *Atmospheric Chemistry and Physics*, **20**, 8659–8690, <https://doi.org/10.5194/acp-20-8659-2020>.
- Li, K., D. J. Jacob, L. Shen, X. Lu, I. De Smedt, and H. Liao, 2020b: Increases in surface ozone pollution in China from 2013 to 2019: Anthropogenic and meteorological influences. *Atmospheric Chemistry and Physics*, **20**, 11 423–11 433, <https://doi.org/10.5194/acp-20-11423-2020>.
- Li, K., and Coauthors, 2019c: A two-pollutant strategy for improving ozone and particulate air quality in China. *Nature Geoscience*, **12**, 906–910, <https://doi.org/10.1038/s41561-019-0464-x>.
- Li, K., and Coauthors, 2021a: Ozone pollution in the North China Plain spreading into the late-winter haze season. *Proceedings of the National Academy of Sciences of the United States of America*, **118**, e2015797118, <https://doi.org/10.1073/pnas.2015797118>.
- Li, L., and Coauthors, 2022c: Climatology of aerosol component concentrations derived from multi-angular polarimetric POLDER-3 observations using GRASP algorithm. *Earth System Science Data*, **14**, 3439–3469, <https://doi.org/10.5194/essd-14-3439-2022>.
- Li, L.-F., Z. Chen, P. Liu, and Y.-H. Zhang, 2022b: Direct measurement of pH evolution in aerosol microdroplets undergoing ammonium depletion: A surface-enhanced raman spectroscopy approach. *Environ. Sci. Technol.*, **56**, 6274–6281, <https://doi.org/10.1021/acs.est.1c08626>.
- Li, M., and Coauthors, 2017a: Anthropogenic emission inventories in China: A review. *National Science Review*, **4**, 834–866, <https://doi.org/10.1093/nsr/nwx150>.
- Li, Q. Y., and Coauthors, 2021b: Halogens enhance haze pollution in China. *Environ. Sci. Technol.*, **55**, 13 625–13 637, <https://doi.org/10.1021/acs.est.1c01949>.
- Li, R., and Coauthors, 2022d: Mass fractions, solubility, speciation and isotopic compositions of iron in coal and municipal waste fly ash. *Science of the Total Environment*, **838**, 155974, <https://doi.org/10.1016/j.scitotenv.2022.155974>.
- Li, R., and Coauthors, 2023: Evaluating the effects of contact time and leaching solution on measured solubilities of aerosol trace metals. *Applied Geochemistry*, **148**, 105551, <https://doi.org/10.1016/j.apgeochem.2022.105551>.



- Li, W. J., and Coauthors, 2017b: Air pollution–aerosol interactions produce more bioavailable iron for ocean ecosystems. *Science Advances*, **3**, e1601749, <https://doi.org/10.1126/sciadv.1601749>.
- Li, X. D., and Coauthors, 2022e: Optical and chemical properties and oxidative potential of aqueous-phase products from OH and <sup>3</sup>C\*-initiated photooxidation of eugenol. *Atmospheric Chemistry and Physics*, **22**, 7793–7814, <https://doi.org/10.5194/ACP-22-7793-2022>.
- Li, Y., and Coauthors, 2022f: Vertically resolved aerosol chemistry in the low boundary layer of Beijing in summer. *Environ. Sci. Technol.*, **56**, 9312–9324, <https://doi.org/10.1021/acs.est.2c02861>.
- Lian, X. F., and Coauthors, 2021: Evidence for the formation of imidazole from carbonyls and reduced nitrogen species at the individual particle level in the ambient atmosphere. *Environmental Science & Technology Letters*, **8**, 9–15, <https://doi.org/10.1021/acs.estlett.0c00722>.
- Liu, C., and Coauthors, 2020a: Efficient conversion of NO to NO<sub>2</sub> on SO<sub>2</sub>-aged MgO under atmospheric conditions. *Environ. Sci. Technol.*, **54**, 11 848–11 856, <https://doi.org/10.1021/acs.est.0c05071>.
- Liu, C., and Coauthors, 2022a: First Chinese ultraviolet–visible hyperspectral satellite instrument implicating global air quality during the COVID-19 pandemic in early 2020. *Light: Science & Applications*, **11**, 28, <https://doi.org/10.1038/S41377-022-00722-X>.
- Liu, H., S. Kaewunruen, W. N. K. Ahmad, A. Shamsuddin, G. K. Ayetor, J. Hansson, and T. Bräunl, 2021a: A net-zero future for freight. *One Earth*, **4**, 1517–1519, <https://doi.org/10.1016/j.oneear.2021.11.001>.
- Liu, J., and Coauthors, 2016: Air pollutant emissions from Chinese households: A major and underappreciated ambient pollution source. *Proceedings of the National Academy of Sciences of the United States of America*, **113**, 7756–7761, <https://doi.org/10.1073/pnas.1604537113>.
- Liu, L., and Coauthors, 2022b: Size-dependent aerosol iron solubility in an urban atmosphere. *NPJ Climate and Atmospheric Science*, **5**, 53, <https://doi.org/10.1038/s41612-022-00277-z>.
- Liu, M. X., and Coauthors, 2019: Ammonia emission control in China would mitigate haze pollution and nitrogen deposition, but worsen acid rain. *Proceedings of the National Academy of Sciences of the United States of America*, **116**, 7760–7765, <https://doi.org/10.1073/pnas.1814880116>.
- Liu, T. Y., S. L. Clegg, and J. P. D. Abbatt, 2020b: Fast oxidation of sulfur dioxide by hydrogen peroxide in deliquesced aerosol particles. *Proceedings of the National Academy of Sciences of the United States of America*, **117**, 1354–1359, <https://doi.org/10.1073/pnas.1916401117>.
- Liu, X. H., B. Zhu, T. Zhu, and H. Liao, 2022c: The seesaw pattern of PM<sub>2.5</sub> interannual anomalies between Beijing–Tianjin–Hebei and Yangtze River Delta across eastern China in winter. *Geophys. Res. Lett.*, **49**, e2021GL095878, <https://doi.org/10.1029/2021GL095878>.
- Liu, Y. L., and Coauthors, 2021b: Formation of condensable organic vapors from anthropogenic and biogenic volatile organic compounds (VOCs) is strongly perturbed by NO<sub>x</sub> in eastern China. *Atmospheric Chemistry and Physics*, **21**, 14 789–14 814, <https://doi.org/10.5194/acp-21-14789-2021>.
- Liu, Z., and Coauthors, 2020c: Size-resolved mixing states and sources of amine-containing particles in the East China Sea. *J. Geophys. Res.: Atmos*, **125**, e2020JD033162, <https://doi.org/10.1029/2020JD033162>.
- Liu, Z., and Coauthors, 2022d: Real-time single particle characterization of oxidized organic aerosols in the East China Sea. *npj Climate and Atmospheric Science*, **5**, 47, <https://doi.org/10.1038/s41612-022-00267-1>.
- Lu, K. D., and Coauthors, 2019: Fast photochemistry in wintertime haze: Consequences for pollution mitigation strategies. *Environ. Sci. Technol.*, **53**, 10 676–10 684, <https://doi.org/10.1021/acs.est.9b02422>.
- Ma, M. C., and Coauthors, 2019a: Substantial ozone enhancement over the North China Plain from increased biogenic emissions due to heat waves and land cover in summer 2017. *Atmospheric Chemistry and Physics*, **19**, 12 195–12 207, <https://doi.org/10.5194/acp-19-12195-2019>.
- Ma, M. C., and Coauthors, 2022: Development and assessment of a high-resolution biogenic emission inventory from urban green spaces in China. *Environ. Sci. Technol.*, **56**, 175–184, <https://doi.org/10.1021/acs.est.1c06170>.
- Ma, Q. X., T. Wang, C. Liu, H. He, Z. Wang, W. H. Wang, and Y. T. Liang, 2017: SO<sub>2</sub> initiates the efficient conversion of NO<sub>2</sub> to HONO on MgO surface. *Environ. Sci. Technol.*, **51**, 3767–3775, <https://doi.org/10.1021/acs.est.6b05724>.
- Ma, X. F., and Coauthors, 2019b: Winter photochemistry in Beijing: Observation and model simulation of OH and HO<sub>2</sub> radicals at an urban site. *Science of the Total Environment*, **685**, 85–95, <https://doi.org/10.1016/j.scitotenv.2019.05.329>.
- Nie, W., and Coauthors, 2022: Secondary organic aerosol formed by condensing anthropogenic vapours over China’s megacities. *Nature Geoscience*, **15**, 255–261, <https://doi.org/10.1038/s41561-022-00922-5>.
- Pan, X. L., and Coauthors, 2019: Synergistic effect of water-soluble species and relative humidity on morphological changes in aerosol particles in the Beijing megacity during severe pollution episodes. *Atmospheric Chemistry and Physics*, **19**, 219–232, <https://doi.org/10.5194/acp-19-219-2019>.
- Peng, C., L. X. D. Chen, and M. J. Tang, 2022a: A database for deliquescence and efflorescence relative humidities of compounds with atmospheric relevance. *Fundamental Research*, **2**, 578–587, <https://doi.org/10.1016/j.fmre.2021.11.021>.
- Peng, S. S., and Coauthors, 2022b: Wetland emission and atmospheric sink changes explain methane growth in 2020. *Nature*, **612**, 477–482, <https://doi.org/10.1038/s41586-022-05447-w>.
- Peng, X., and Coauthors, 2021: An unexpected large continental source of reactive bromine and chlorine with significant impact on wintertime air quality. *National Science Review*, **8**, nwaa304, <https://doi.org/10.1093/nsr/nwaa304>.
- Peng, X., and Coauthors, 2022c: Photodissociation of particulate nitrate as a source of daytime tropospheric Cl<sub>2</sub>. *Nature Communications*, **13**, 939, <https://doi.org/10.1038/s41467-022-28383-9>.
- Ren, C. H., and Coauthors, 2021: Nonlinear response of nitrate to NO<sub>x</sub> reduction in China during the COVID-19 pandemic. *Atmos. Environ.*, **264**, 118715, <https://doi.org/10.1016/j.atmosenv.2021.118715>.
- Shang, X. N., and Coauthors, 2021a: A semicontinuous study on the ecotoxicity of atmospheric particles using a versatile aerosol concentration enrichment system (VACES): Development and field characterization. *Atmospheric Measurement Techniques*, **14**, 1037–1045, <https://doi.org/10.5194/amt-14-1037-2021>.
- Shang, X. N., and Coauthors, 2021b: PM<sub>1.0</sub>-nitrite heterogeneous



- formation demonstrated via a modified versatile aerosol concentration enrichment system coupled with ion chromatography. *Environ. Sci. Technol.*, **55**, 9794–9804, <https://doi.org/10.1021/acs.est.1c02373>.
- Shen, H. R., L. Vereecken, S. Kang, I. Pullinen, H. Fuchs, D. F. Zhao, and T. F. Mentel, 2022: Unexpected significance of a minor reaction pathway in daytime formation of biogenic highly oxygenated organic compounds. *Science Advances*, **8**, eabp8702, <https://doi.org/10.1126/sciadv.abp8702>.
- Song, H., K. D. Lu, H. B. Dong, Z. F. Tan, S. Y. Chen, L. M. Zeng, and Y. H. Zhang, 2022a: Reduced aerosol uptake of hydroperoxyl radical may increase the sensitivity of ozone production to volatile organic compounds. *Environmental Science & Technology Letters*, **9**, 22–29, <https://doi.org/10.1021/acs.estlett.1c00893>.
- Song, H., and Coauthors, 2020: Influence of aerosol copper on HO<sub>2</sub> uptake: A novel parameterized equation. *Atmospheric Chemistry and Physics*, **20**, 15 835–15 850, <https://doi.org/10.5194/ACP-20-15835-2020>.
- Song, K. X., and Coauthors, 2022b: Observation-based analysis of ozone production sensitivity for two persistent ozone episodes in Guangdong, China. *Atmospheric Chemistry and Physics*, **22**, 8403–8416, <https://doi.org/10.5194/acp-22-8403-2022>.
- Su, S. H., and Coauthors, 2021: High molecular diversity of organic nitrogen in urban snow in North China. *Environ. Sci. Technol.*, **55**, 4344–4356, <https://doi.org/10.1021/acs.est.0c06851>.
- Su, S. H., and Coauthors, 2022a: A new structural classification scheme for dissolved organic sulfur in urban snow from North China. *Environmental Science & Technology Letters*, **9**, 366–374, <https://doi.org/10.1021/acs.estlett.2c00153>.
- Su, W. J., and Coauthors, 2022b: First global observation of tropospheric formaldehyde from Chinese GaoFen-5 satellite: Locating source of volatile organic compounds. *Environmental Pollution*, **297**, 118691, <https://doi.org/10.1016/j.envpol.2021.118691>.
- Sun, J. F., and Coauthors, 2021a: Secondary inorganic ions characteristics in PM<sub>2.5</sub> along offshore and coastal areas of the megacity Shanghai. *J. Geophys. Res.: Atmos*, **126**, e2021JD035139, <https://doi.org/10.1029/2021JD035139>.
- Sun, W., and Coauthors, 2021b: Measurement report: Molecular characteristics of cloud water in southern China and insights into aqueous-phase processes from Fourier transform ion cyclotron resonance mass spectrometry. *Atmospheric Chemistry and Physics*, **21**, 16 631–16 644, <https://doi.org/10.5194/acp-21-16631-2021>.
- Tan, Z. F., and Coauthors, 2018: Wintertime photochemistry in Beijing: Observations of RO<sub>x</sub> radical concentrations in the North China Plain during the BEST-ONE campaign. *Atmospheric Chemistry and Physics*, **18**, 12 391–12 411, <https://doi.org/10.5194/acp-18-12391-2018>.
- Tang, M. J., and Coauthors, 2019a: A review of experimental techniques for aerosol hygroscopicity studies. *Atmospheric Chemistry and Physics*, **19**, 12 631–12 686, <https://doi.org/10.5194/acp-19-12631-2019>.
- Tang, M. J., and Coauthors, 2019b: Hygroscopic properties of saline mineral dust from different regions in China: Geographical variations, compositional dependence, and atmospheric implications. *J. Geophys. Res.: Atmos*, **124**, 10 844–10 857, <https://doi.org/10.1029/2019JD031128>.
- Wang, F., G. R. Carmichael, J. Wang, B. Chen, B. Huang, Y. G. Li, Y. J. Yang, and M. Gao, 2022a: Circulation-regulated impacts of aerosol pollution on urban heat island in Beijing. *Atmospheric Chemistry and Physics*, **22**, 13 341–13 353, <https://doi.org/10.5194/acp-22-13341-2022>.
- Wang, F., and Coauthors, 2022b: Machine learning and theoretical analysis release the non-linear relationship among ozone, secondary organic aerosol and volatile organic compounds. *Journal of Environmental Sciences*, **114**, 75–84, <https://doi.org/10.1016/j.jes.2021.07.026>.
- Wang, G. H., and Coauthors, 2016: Persistent sulfate formation from London Fog to Chinese haze. *Proceedings of the National Academy of Sciences of the United States of America*, **113**, 13 630–13 635, <https://doi.org/10.1073/pnas.1616540113>.
- Wang, H. C., and Coauthors, 2022c: Anthropogenic monoterpenes aggravating ozone pollution. *National Science Review*, **9**, nwac103, <https://doi.org/10.1093/nsr/nwac103>.
- Wang, H. C., and Coauthors, 2022d: N<sub>2</sub>O<sub>5</sub> uptake onto saline mineral dust: A potential missing source of tropospheric ClNO<sub>2</sub> in inland China. *Atmospheric Chemistry and Physics*, **22**, 1845–1859, <https://doi.org/10.5194/ACP-22-1845-2022>.
- Wang, H. L., and Coauthors, 2020a: Atmospheric processing of nitrophenols and nitrocresols from biomass burning emissions. *J. Geophys. Res.: Atmos*, **125**, e2020JD033401, <https://doi.org/10.1029/2020JD033401>.
- Wang, J. F., and Coauthors, 2020b: Fast sulfate formation from oxidation of SO<sub>2</sub> by NO<sub>2</sub> and HONO observed in Beijing haze. *Nature Communications*, **11**, 2844, <https://doi.org/10.1038/s41467-020-16683-x>.
- Wang, J. F., and Coauthors, 2021a: Aqueous production of secondary organic aerosol from fossil-fuel emissions in winter Beijing haze. *Proceedings of the National Academy of Sciences of the United States of America*, **118**, e2022179118, <https://doi.org/10.1073/pnas.2022179118>.
- Wang, J. Q., J. Gao, F. Che, Y. L. Wang, P. C. Lin, and Y. C. Zhang, 2022e: Decade-long trends in chemical component properties of PM<sub>2.5</sub> in Beijing, China (2011–2020). *Science of the Total Environment*, **832**, 154664, <https://doi.org/10.1016/J.SCITOTENV.2022.154664>.
- Wang, M. J., N. Zheng, D. F. Zhao, J. Shang, and T. Zhu, 2021b: Using micro-Raman spectroscopy to investigate chemical composition, mixing states, and heterogeneous reactions of individual atmospheric particles. *Environ. Sci. Technol.*, **55**, 10 243–10 254, <https://doi.org/10.1021/acs.est.1c01242>.
- Wang, P. Y., and Coauthors, 2022f: North China Plain as a hot spot of ozone pollution exacerbated by extreme high temperatures. *Atmospheric Chemistry and Physics*, **22**, 4705–4719, <https://doi.org/10.5194/acp-22-4705-2022>.
- Wang, Q. Y., and Coauthors, 2019: Wintertime optical properties of primary and secondary brown carbon at a regional site in the North China plain. *Environ. Sci. Technol.*, **53**, 12 389–12 397, <https://doi.org/10.1021/acs.est.9b03406>.
- Wang, T., and Coauthors, 2022g: An integrated air quality modeling system coupling regional-urban and street models in Beijing. *Urban Climate*, **43**, 101143, <https://doi.org/10.1016/j.uclim.2022.101143>.
- Wang, T. T., and Coauthors, 2022h: Sulfate formation apportionment during winter haze events in North China. *Environ. Sci. Technol.*, **56**, 7771–7778, <https://doi.org/10.1021/acs.est.2c02533>.
- Wang, W. G., and Coauthors, 2021c: Sulfate formation is dominated by manganese-catalyzed oxidation of SO<sub>2</sub> on aerosol

- surfaces during haze events. *Nature Communications*, **12**, 1993, <https://doi.org/10.1038/s41467-021-22091-6>.
- Wang, W. J., and Coauthors, 2022i: Direct observations indicate photodegradable oxygenated volatile organic compounds (OVOCs) as larger contributors to radicals and ozone production in the atmosphere. *Atmospheric Chemistry and Physics*, **22**, 4117–4128, <https://doi.org/10.5194/acp-22-4117-2022>.
- Wang, X.-T., and Coauthors, 2021d: Trade-linked shipping CO<sub>2</sub> emissions. *Nature Climate Change*, **11**, 945–951, <https://doi.org/10.1038/s41558-021-01176-6>.
- Wang, X. T., and Coauthors, 2021e: Ship emissions around China under gradually promoted control policies from 2016 to 2019. *Atmospheric Chemistry and Physics*, **21**, 13 835–13 853, <https://doi.org/10.5194/acp-21-13835-2021>.
- Wang, Y. L., and Coauthors, 2021f: Enhanced nitrite production from the aqueous photolysis of nitrate in the presence of vanillic acid and implications for the roles of light-absorbing organics. *Environ. Sci. Technol.*, **55**, 15 694–15 704, <https://doi.org/10.1021/acs.est.1c04642>.
- Wang, Y. L., and Coauthors, 2022j: Decay kinetics and absorption changes of methoxyphenols and nitrophenols during nitrate-mediated aqueous photochemical oxidation at 254 and 313 nm. *ACS Earth and Space Chemistry*, **6**, 1115–1125, <https://doi.org/10.1021/acsearthspacechem.2c00021>.
- Wang, Z., and Coauthors, 2008: MICS-Asia II: Model inter-comparison and evaluation of acid deposition. *Atmos. Environ.*, **42**, 3528–3542, <https://doi.org/10.1016/j.atmosenv.2007.12.071>.
- Wang, Z. L., X. Huang, and A. J. Ding, 2018: Dome effect of black carbon and its key influencing factors: A one-dimensional modelling study. *Atmospheric Chemistry and Physics*, **18**, 2821–2834, <https://doi.org/10.5194/acp-18-2821-2018>.
- Wei, N. N., B. Fang, W. X. Zhao, C. H. Wang, N. N. Yang, W. J. Zhang, W. D. Chen, and C. Fittschen, 2020: Time-resolved laser-flash photolysis faraday rotation spectrometer: A new tool for total OH reactivity measurement and free radical kinetics research. *Analytical Chemistry*, **92**, 4334–4339, <https://doi.org/10.1021/acs.analchem.9b05117>.
- Wei, X. L., and Coauthors, 2022: Technical note: Real-time diagnosis of the hygroscopic growth micro-dynamics of nanoparticles with Fourier transform infrared spectroscopy. *Atmospheric Chemistry and Physics*, **22**, 3097–3109, <https://doi.org/10.5194/acp-22-3097-2022>.
- Wu, C. H., and Coauthors, 2020a: Measurement report: Important contributions of oxygenated compounds to emissions and chemistry of volatile organic compounds in urban air. *Atmospheric Chemistry and Physics*, **20**, 14 769–14 785, <https://doi.org/10.5194/acp-20-14769-2020>.
- Wu, F., N. Song, T. F. Hu, S. S. H. Ho, J. J. Cao, and D. Z. Zhang, 2023: Surrogate atmospheric dust particles generated from dune soils in laboratory: Comparison with field measurement. *Particuology*, **72**, 29–36, <https://doi.org/10.1016/j.partic.2022.02.007>.
- Wu, F., and Coauthors, 2022: Saltation–sandblasting processes driving enrichment of water-soluble salts in mineral dust. *Environmental Science & Technology Letters*, **9**, 921–928, <https://doi.org/10.1021/acs.estlett.2c00652>.
- Wu, H. J., X. Tang, Z. F. Wang, L. Wu, J. J. Li, W. Wang, W. Y. Yang, and J. Zhu, 2020b: High-spatiotemporal-resolution inverse estimation of CO and NO<sub>x</sub> emission reductions during emission control periods with a modified ensemble Kalman filter. *Atmos. Environ.*, **236**, 117631, <https://doi.org/10.1016/j.atmosenv.2020.117631>.
- Wu, L. Q., X. M. Wang, S. H. Lu, M. Shao, and Z. H. Ling, 2019: Emission inventory of semi-volatile and intermediate-volatility organic compounds and their effects on secondary organic aerosol over the Pearl River Delta region. *Atmospheric Chemistry and Physics*, **19**, 8141–8161, <https://doi.org/10.5194/acp-19-8141-2019>.
- Wu, L. Q., Z. H. Ling, H. Liu, M. Shao, S. H. Lu, L. L. Wu, and X. M. Wang, 2021a: A gridded emission inventory of semi-volatile and intermediate volatility organic compounds in China. *Science of the Total Environment*, **761**, 143295, <https://doi.org/10.1016/j.scitotenv.2020.143295>.
- Wu, L. Q., and Coauthors, 2021b: Roles of semivolatile/intermediate-volatility organic compounds on SOA formation over China during a pollution episode: Sensitivity analysis and implications for future studies. *J. Geophys. Res.: Atmos.*, **126**, e2020JD033999, <https://doi.org/10.1029/2020JD033999>.
- Xia, C. Z., C. Liu, Z. N. Cai, F. Zhao, W. J. Su, C. X. Zhang, and Y. Liu, 2021: First sulfur dioxide observations from the environmental trace gases monitoring instrument (EMI) onboard the GeoFen-5 satellite. *Science Bulletin*, **66**, 969–973, <https://doi.org/10.1016/j.scib.2021.01.018>.
- Xia, M., and Coauthors, 2022a: Pollution-Derived Br<sub>2</sub> boosts oxidation power of the coastal atmosphere. *Environ. Sci. Technol.*, **56**, 12 055–12 065, <https://doi.org/10.1021/acs.est.2c02434>.
- Xia, W. W., and Coauthors, 2022b: Double trouble of air pollution by anthropogenic dust. *Environ. Sci. Technol.*, **56**, 761–769, <https://doi.org/10.1021/acs.est.1c04779>.
- Xie, X. D., T. J. Wang, X. Yue, S. Li, B. L. Zhuang, and M. H. Wang, 2020: Effects of atmospheric aerosols on terrestrial carbon fluxes and CO<sub>2</sub> concentrations in China. *Atmospheric Research*, **237**, 104859, <https://doi.org/10.1016/j.atmosres.2020.104859>.
- Xie, X. D., T. J. Wang, X. Yue, S. Li, B. L. Zhuang, M. H. Wang, and X. Q. Yang, 2019: Numerical modeling of ozone damage to plants and its effects on atmospheric CO<sub>2</sub> in China. *Atmos. Environ.*, **217**, 116970, <https://doi.org/10.1016/j.atmosenv.2019.116970>.
- Xu, B. Q., and Coauthors, 2021a: Compound-specific radiocarbon analysis of low molecular weight dicarboxylic acids in ambient aerosols using preparative gas chromatography: Method development. *Environmental Science & Technology Letters*, **8**, 135–141, <https://doi.org/10.1021/acs.estlett.0c00887>.
- Xu, B. Q., and Coauthors, 2022a: Large contribution of fossil-derived components to aqueous secondary organic aerosols in China. *Nature Communications*, **13**, 5115, <https://doi.org/10.1038/s41467-022-32863-3>.
- Xu, L., L. Du, N. T. Tsona, and M. F. Ge, 2021b: Anthropogenic effects on biogenic secondary organic aerosol formation. *Adv. Atmos. Sci.*, **38**, 1053–1084, <https://doi.org/10.1007/s00376-020-0284-3>.
- Xu, W., J. Ovadnevaite, K. N. Fossom, C. S. Lin, R. J. Huang, D. Ceburnis, and C. O'Dowd, 2022b: Sea spray as an obscured source for marine cloud nuclei. *Nature Geoscience*, **15**, 282–286, <https://doi.org/10.1038/s41561-022-00917-2>.
- Xu, Z. N., and Coauthors, 2021c: Multifunctional products of isoprene oxidation in polluted atmosphere and their contribution to SOA. *Geophys. Res. Lett.*, **48**, e2020GL089276, <https://doi.org/10.1029/2020GL089276>.
- Xue, T., and Coauthors, 2022: New WHO global air quality guidelines help prevent premature deaths in China. *National Science Review*, **9**, nwac055, <https://doi.org/10.1093/nsr/nwac055>.

- Yan, C. Q., S. X. Ma, Q. F. He, X. Ding, Y. Cheng, M. Cui, X. M. Wang, and M. Zheng, 2021: Identification of PM<sub>2.5</sub> sources contributing to both Brown carbon and reactive oxygen species generation in winter in Beijing, China. *Atmos. Environ.*, **246**, 118069, <https://doi.org/10.1016/j.atmosenv.2020.118069>.
- Yang, H., L. Chen, H. Liao, J. Zhu, W. J. Wang, and X. Li, 2022a: Impacts of aerosol–photolysis interaction and aerosol–radiation feedback on surface-layer ozone in North China during multi-pollutant air pollution episodes. *Atmospheric Chemistry and Physics*, **22**, 4101–4116, <https://doi.org/10.5194/acp-22-4101-2022>.
- Yang, N. N., and Coauthors, 2022b: Optical-feedback cavity-enhanced absorption spectroscopy for OH radical detection at 2.8 μm using a DFB diode laser. *Optics Express*, **30**, 15 238–15 249, <https://doi.org/10.1364/OE.456648>.
- Yang, X. P., and Coauthors, 2021a: Observations and modeling of OH and HO<sub>2</sub> radicals in Chengdu, China in summer 2019. *Sci. Total Environ.*, **772**, 144829, <https://doi.org/10.1016/j.scitotenv.2020.144829>.
- Yang, Y., and Coauthors, 2022c: Abrupt emissions reductions during COVID-19 contributed to record summer rainfall in China. *Nature Communications*, **13**, 959, <https://doi.org/10.1038/s41467-022-28537-9>.
- Yang, Z. M., L. Du, Y. J. Li, and X. L. Ge, 2022d: Secondary organic aerosol formation from monocyclic aromatic hydrocarbons: Insights from laboratory studies. *Environmental Science: Processes & Impacts*, **24**, 351–379, <https://doi.org/10.1039/D1EM00409C>.
- Yang, Z. M., K. Li, N. T. Tsona, X. Luo, and L. Du, 2023: SO<sub>2</sub> enhances aerosol formation from anthropogenic volatile organic compound ozonolysis by producing sulfur-containing compounds. *Atmospheric Chemistry and Physics*, **23**, 417–430, <https://doi.org/10.5194/acp-23-417-2023>.
- Yang, Z. M., L. Xu, N. T. Tsona, J. L. Li, X. Luo, and L. Du, 2021b: SO<sub>2</sub> and NH<sub>3</sub> emissions enhance organosulfur compounds and fine particle formation from the photooxidation of a typical aromatic hydrocarbon. *Atmospheric Chemistry and Physics*, **21**, 7963–7981, <https://doi.org/10.5194/acp-21-7963-2021>.
- Ye, C. S., and Coauthors, 2021a: Chemical characterization of oxygenated organic compounds in the gas phase and particle phase using iodide CIMS with FIGAERO in urban air. *Atmospheric Chemistry and Physics*, **21**, 8455–8478, <https://doi.org/10.5194/acp-21-8455-2021>.
- Ye, Q., and Coauthors, 2021b: High-resolution modeling of the distribution of surface air pollutants and their intercontinental transport by a global tropospheric atmospheric chemistry source–receptor model (GNAQPMS-SM). *Geoscientific Model Development*, **14**, 7573–7604, <https://doi.org/10.5194/gmd-14-7573-2021>.
- Ye, Q., and Coauthors, 2023: Uncertainties in the simulated intercontinental transport of air pollutants in the springtime from emission and meteorological inputs. *Atmos. Environ.*, **293**, 119431, <https://doi.org/10.1016/j.atmosenv.2022.119431>.
- Yuan, W., and Coauthors, 2020: Characterization of the light-absorbing properties, chromophore composition and sources of brown carbon aerosol in Xi'an, northwestern China. *Atmospheric Chemistry and Physics*, **20**, 5129–5144, <https://doi.org/10.5194/acp-20-5129-2020>.
- Zhang, C. X., and Coauthors, 2020a: First observation of tropospheric nitrogen dioxide from the Environmental Trace Gases Monitoring Instrument onboard the GaoFen-5 satellite. *Light: Science & Applications*, **9**, 66, <https://doi.org/10.1038/s41377-020-0306-z>.
- Zhang, G. H., and Coauthors, 2019: Oxalate formation enhanced by Fe-containing particles and environmental implications. *Environ. Sci. Technol.*, **53**, 1269–1277, <https://doi.org/10.1021/acs.est.8b05280>.
- Zhang, G. H., and Coauthors, 2020b: High secondary formation of nitrogen-containing organics (NOCs) and its possible link to oxidized organics and ammonium. *Atmospheric Chemistry and Physics*, **20**, 1469–1481, <https://doi.org/10.5194/acp-20-1469-2020>.
- Zhang, G. X., and Coauthors, 2022a: Intercomparison of OH radical measurement in a complex atmosphere in Chengdu, China. *Science of the Total Environment*, **838**, 155924, <https://doi.org/10.1016/j.scitotenv.2022.155924>.
- Zhang, H. H., and Coauthors, 2022b: Abundance and fractional solubility of aerosol iron during winter at a coastal city in northern China: Similarities and contrasts between fine and coarse particles. *J. Geophys. Res.: Atmos.*, **127**, e2021JD036070, <https://doi.org/10.1029/2021JD036070>.
- Zhang, P., T. Z. Chen, Q. X. Ma, B. W. Chu, Y. H. Wang, Y. J. Mu, Y. B. Yu, and H. He, 2022c: Diesel soot photooxidation enhances the heterogeneous formation of H<sub>2</sub>SO<sub>4</sub>. *Nature Communications*, **13**, 5364, <https://doi.org/10.1038/s41467-022-33120-3>.
- Zhang, W. Q., and Coauthors, 2020c: Different HONO sources for three layers at the urban area of Beijing. *Environ. Sci. Technol.*, **54**, 12 870–12 880, <https://doi.org/10.1021/acs.est.0c02146>.
- Zhang, X., and Coauthors, 2022d: Influence of convection on the upper-tropospheric O<sub>3</sub> and NO<sub>x</sub> budget in southeastern China. *Atmospheric Chemistry and Physics*, **22**, 5925–5942, <https://doi.org/10.5194/acp-22-5925-2022>.
- Zhang, Y.-L., and Coauthors, 2022e: A diurnal story of Δ<sup>17</sup>O(NO<sub>3</sub><sup>-</sup>) in urban Nanjing and its implication for nitrate aerosol formation. *npj Climate and Atmospheric Science*, **5**, 50, <https://doi.org/10.1038/s41612-022-00273-3>.
- Zhang, Z. C., and Coauthors, 2022f: Machine learning combined with the PMF model reveal the synergistic effects of sources and meteorological factors on PM<sub>2.5</sub> pollution. *Environ. Res.*, **212**, 113322, <https://doi.org/10.1016/j.envres.2022.113322>.
- Zhao, Y., and Coauthors, 2022: Decline in bulk deposition of air pollutants in China lags behind reductions in emissions. *Nature Geoscience*, **15**, 190–195, <https://doi.org/10.1038/s41561-022-00899-1>.
- Zheng, B., and Coauthors, 2020a: Satellite-based estimates of decline and rebound in China's CO<sub>2</sub> emissions during COVID-19 pandemic. *Science Advances*, **6**, eabd4998, <https://doi.org/10.1126/sciadv.abd4998>.
- Zheng, B., and Coauthors, 2021: Mapping anthropogenic emissions in China at 1 km spatial resolution and its application in air quality modeling. *Science Bulletin*, **66**, 612–620, <https://doi.org/10.1016/j.scib.2020.12.008>.
- Zheng, M., C. Q. Yan, and T. Zhu, 2020b: Understanding sources of fine particulate matter in China. *Philosophical Transactions of the Royal Society A: Mathematical, Physical and Engineering Sciences*, **378**, 20190325, <https://doi.org/10.1098/rsta.2019.0325>.
- Zhong, X., S. C. Liu, R. Liu, X. L. Wang, J. J. Mo, and Y. Z. Li, 2021: Observed trends in clouds and precipitation (1983–2009): Implications for their cause(s). *Atmospheric*

- Chemistry and Physics*, **21**, 4899–4913, <https://doi.org/10.5194/acp-21-4899-2021>.
- Zhou, J. C., and Coauthors, 2020: Simultaneous measurements of the relative-humidity-dependent aerosol light extinction, scattering, absorption, and single-scattering albedo with a humidified cavity-enhanced albedometer. *Atmospheric Measurement Techniques*, **13**, 2623–2634, <https://doi.org/10.5194/amt-13-2623-2020>.
- Zhou, J. C., and Coauthors, 2022: Amplitude-modulated cavity-enhanced absorption spectroscopy with phase-sensitive detection: A new approach applied to the fast and sensitive detection of NO<sub>2</sub>. *Analytical Chemistry*, **94**, 3368–3375, <https://doi.org/10.1021/acs.analchem.1c05484>.
- Zhu, C.-S., Y. Qu, H. Huang, J. Chen, W.-T. Dai, R.-J. Huang, and J.-J. Cao, 2021a: Black carbon and secondary brown carbon, the dominant light absorption and direct radiative forcing contributors of the atmospheric aerosols over the Tibetan Plateau. *Geophys. Res. Lett.*, **48**, e2021GL092524, <https://doi.org/10.1029/2021GL092524>.
- Zhu, J., L. Chen, and H. Liao, 2022: Multi-pollutant air pollution and associated health risks in China from 2014 to 2020. *Atmos. Environ.*, **268**, 118829, <https://doi.org/10.1016/j.atmosenv.2021.118829>.
- Zhu, J. L., J. Shang, and T. Zhu, 2021b: A new understanding of the microstructure of soot particles: The reduced graphene oxide-like skeleton and its visible-light driven formation of reactive oxygen species. *Environmental Pollution*, **270**, 116079, <https://doi.org/10.1016/j.envpol.2020.116079>.
- Zhu, J. L., J. Shang, Y. Y. Chen, Y. Kuang, and T. Zhu, 2020a: Reactive oxygen species-related inside-to-outside oxidation of soot particles triggered by visible-light irradiation: Physicochemical property changes and oxidative potential enhancement. *Environ. Sci. Technol.*, **54**, 8558–8567, <https://doi.org/10.1021/acs.est.0c01150>.
- Zhu, T., 2005: Urban and regional air pollution complex. *Series in Advances in Chemistry: Advances in Environmental Chemistry*, S. G. Dai, Ed., Chemical Industry Press, Beijing, 544pp. (in Chinese)
- Zhu, T., 2018: Air pollution in China: Scientific challenges and policy implications. *National Science Review*, **4**, 800, <https://doi.org/10.1093/nsr/nwx151>.
- Zhu, T., J. Shang, and D. F. Zhao, 2011: The roles of heterogeneous chemical processes in the formation of an air pollution complex and gray haze. *Science China Chemistry*, **54**, 145–153, <https://doi.org/10.1007/s11426-010-4181-y>.
- Zhu, Y. H., and Coauthors, 2020b: Iron solubility in fine particles associated with secondary acidic aerosols in east China. *Environmental Pollution*, **264**, 114769, <https://doi.org/10.1016/j.envpol.2020.114769>.
- Zuo, P. J., and Coauthors, 2022: Stable iron isotopic signature reveals multiple sources of magnetic particulate matter in the 2021 Beijing sandstorms. *Environmental Science & Technology Letters*, **9**, 299–305, <https://doi.org/10.1021/acs.estlett.2c00144>.

**2020-2023**

**China National Report on Physical  
Sciences of the Oceans**

For

The 28th General Assembly of IUGG

Berlin Germany, 11-20 July 2023

Prepared by Chinese National Committee for

The International Union of Geodesy and Geophysics

**July 7<sup>th</sup>, 2023**



## **PREFACE**

This quadrennial report is the sixth report in the new millennium, which is one of the China National Reports (2020-2023), prepared by the Chinese National Committee for IAPSO for the 28<sup>th</sup> General Assembly of International Union of Geodesy and Geophysics to be held in Berlin, Germany, 11-20 July 2023. This report composes of 8 sections which reviewed the main work done and the major progress made in the research on Physical Oceanography in the South China Sea and the Tropical Indian Ocean, floating ice sheets, Climate and Earth System Model, decomposition of Multiscale Oceanic Motions, eddy-mean flow interaction in the Pacific low-latitude western boundary current region in China, organic carbon burial in the Western Pacific Margins, internal Solitary Waves Research, Seismic Oceanography Studies in China. It should be noted that this report only provides an overview of the subjects mentioned in the above, but it does show encouraging progress in physical sciences of the oceans in Mainland China over the past four years. It is pleasant to see the fact that some of papers in this report have been written by the younger scientists, which shows that the younger generation of marine scientists in China has grown up. I would like to take this opportunity, on behalf of the Chinese National Committee for IAPSO, to express my deep appreciation to all the authors for their contributions. Finally, the editing of this report was supported by several projects, e.g. 2019YFE0125000 of M.O.S.T. in China.

Xun GONG and Chunxin YUAN

Editor-in-Chief

Secretary-General, Chinese National Committee for IAPSO

## CONTENTS

### Preface

Progress of Physical Oceanography in the South China Sea and the Tropical Indian Ocean from 2018 to 2023 .....	4
Progress of research on floating ice sheets in China from 2020 to 2023 .....	19
Progress of Climate and Earth System Model in China from 2020 to 2023 .....	21
Progress of Dynamical Decomposition of Multiscale Oceanic Motions from 2020 to 2023.....	26
Progress of eddy-mean flow interaction in the Pacific low-latitude western boundary current region in China from 2020 to 2023 .....	30
Progress of Organic carbon burial in the Western Pacific Margins research in China from 2020 to 2023 .....	33
Progress of internal Solitary Waves Research in China from 2020 to 2023 .....	38
Progress of Seismic Oceanography Studies in China from 2020 to 2023.....	42

# **Progress of Physical Oceanography in the South China Sea and the Tropical Indian Ocean from 2018 to 2023**

*Dongxiao Wang*

School of Marine Sciences, Sun Yat-sen University, Zhuhai, China

The layered basin circulation is identified in geopotential level based on Stokes theorem (Gan et al., 2016) and density level (Zhu et al., 2017) that flows in ‘cyclonic-anticyclonic-cyclonic’ direction in upper-middle-deep layers of SCS (Zhu et al., 2019; Cai et al., 2020), and it is maintained mainly by the surface wind forcing and the exchanging current through the lateral straits, particularly the Luzon Strait (Gan et al. 2016; Cai and Gan, 2020, 2021; Cai et al., 2023). Several hotspots are identified mainly near Luzon strait, Mindoro strait, and basin slope (Gan et al., 2022). Those hotspots contribute majority of the vorticity and energy of each layer’s circulation, thus control the intensity and structure of layered circulation. The upper layer basin scale circulations show distinct interannual variability (Sun and Lan, 2021, 2022; Zu et al., 2019, 2020, Wang et al., 2020), with alternating ‘U’ or ‘O’ pattern in the southern SCS in winter (Zu et al., 2019a), and alternating enhanced ‘eastward’ or ‘northward’ branch in summer (Zu et al., 2020), these interannual variability are revealed to be mainly forced by the ENSO modulated monsoon wind and the Luzon Strait transport (Yang, et al., 2017; Wang et al., 2020). On decadal time scale, the abnormal winter monsoon and LST modulated by the joint effect of IOD and AMO lead to the ‘weak-strong-weak’ phase change of the SCS western boundary currents (Wang et al., 2023). During the transition from winter to summer monsoon, the baroclinicity of the SCSWBC is obvious, and the flow transition below the thermocline lags that above it (Xie et al., 2022). While for the month to month variability of the SCS western boundary currents, besides wind and LST, buoyancy effect also plays a role (Yan et al., 2019). All above studies provide more accurate and detailed observations, as well as comprehensive dynamical investigations for heat and salt analysis of SCS.

Both observation and numerical studies provide evidence for the existence of SCS abyssal cyclonic circulation, which is related to the Luzon Strait overflow (Zheng et al., 2022a; Zhou et al., 2020). The decadal weakening trend of abyssal circulation in SCS corresponds to the weakening Luzon Strait overflow (Zhu et al., 2022a, b). The deep circulation presents significant intraseasonal variability, mainly related to topographic Rossby waves and deep eddies (Wang et al., 2019, 2021; Zheng et al., 2021, 2022b; Shu et al., 2022). On the northern South China Sea (NSCS) continental slope, the TRWs contribute more than 40% of the total deep current variance and present significantly spatial distribution in the frequency and intensity, which are largely controlled by the mesoscale perturbations in the upper layer (Wang et al., 2021, 2019). In the deep sea basin of NSCS and to the west of Luzon Strait, Zheng et al. (2021, 2022b) observed the propagation of TRWs with a period of about 70 and 28 days, respectively. In Xisha Islands, Shu et al., (2022) pointed that both TRWs and deep eddies triggered by upper-layer perturbations through potential vorticity conservation can explain the deep-current variability. Based on numerical studies, Quan et al. (2021, 2022) suggested that the TRWs can gain energy from upper-layer perturbations through the vertical pressure work in NSCS. These studies show direct observations of SCS deep circulation, which improve our understanding about three-dimensional circulation of SCS.

Mesoscale eddies are an important component of dynamical oceanography across the range of scales (Sun et al., 2018; Qiu et al., 2019; Lian et al., 2019; Zu et al., 2019b; Chu et al., 2020). Mesoscale eddies exert great impact on the thermohaline structures in the northern SCS, which can induce maximum temperature anomalies from 22.58 to 2.28°C (Zhao, 2017). The mesoscale eddy-induced transports are an important process of the interior dynamics of SCS circulation, which feed back to the adjustment of large-scale circulation (Nan et al., 2011; Chen et al., 2012; Wang et al., 2015; Zhang et al., 2016; Sun et al., 2017, 2019) and induce active air–sea interaction (Sun et al., 2020, 2016). More and more eddies are evident in hydrographic datasets (Zhang et al., 2016) and satellite sea level anomaly data. Moorings, automatic unmanned vehicle and underwater gliders could reveal the three-dimensional structures of mesoscale eddies

(Shu et al., 2019; Qiu et al., 2020). Model output and satellite altimeter data indicate a mean number of  $32.9 \pm 2.4$  eddies each year with mean radius and lifetime of 132 km and 8.8 weeks, respectively (Chen et al., 2011). The NSCS shelf is an energetic region for eddy activity, and these mesoscale eddies are the main contributors to intraseasonal variability in the NSCS (Zhuang et al., 2010). Mesoscale eddies in the SCS can be generated by different mechanisms such as Kuroshio shedding topography gradients (Qiu et al., 2020), wind forcing and baroclinic gradients (Chen et al., 2012; Wang et al., 2006, 2020). Mesoscale eddies distort at continental slopes and cause cross-slope transport (Chen et al. 2012; Wang et al. 2018; Su et al. 2020; Qiu et al. 2022). Dong et al. (2022) and Yang et al. (2019) estimated the dissipation rate of mesoscale eddies in the SCS, indicating that sub-mesoscale motion and turbulent mixing are efficient paths for mesoscale kinetic energy loss. The studies of mesoscale eddies at different time scale (seasonal, intraseasonal) and various depths help to connect large-scale circulation energy changes more realistic.

In addition to large-scale circulation and mesoscale eddy, research on sub-mesoscale and small-scale has also progressed in recent years (Lin et al., 2020; Wang et al., 2022). The near-inertial energy excited by tropical cyclones can be penetrated the bottom boundary layer and contribute to deep mixing (Ma et al., 2022). And the tropical storm-generated near-inertial oscillations exhibited a slope-intensified feature regardless of its trajectories (Li et al., 2021). Sub-mesoscale processes around mesoscale eddies (Qiu et al., 2022; Tang et al., 2022) play an important role in downward energy cascade (Dong et al., 2022), and material transport (Chen et al., 2022). Sub-mesoscale front (Dong and Zhong, 2020) and sub-mesoscale eddies (Huang et al., 2023; Ni et al., 2021) have gained more and more attention. In small-scale waves, Zou et al. (2019) pointed out that the magnitude and angle of the wind stress changed by swell waves depend on the relative angle between the turbulent stress and swell direction. The turbulent structure of the marine atmospheric boundary Layer (Huang et al., 2021) and the marine Langmuir turbulence (Wang et al., 2022; Li et al., 2023) play an important role in the air-sea interactions. All above studies are closely connected to



mesoscale studies and even large-scale studies, which deepen our cognition on energy cascade.

With the development of observation technology, on the basis of the existing mesoscale hydrological and marine meteorological observation network in the South China Sea consisting of research vessels, satellites, buoys, mooring buoys and stations (Yang et al., 2015; Zeng et al., 2015), various unmanned vehicles such as autonomous underwater vehicle (AUV), underwater glider, wave glider, unmanned surface vessel (USV), and unmanned aerial vehicle (UAV) are used in a large number of applications and network observation tests (Shu et al., 2019; Qiu et al., 2020), as well as the promotion of the use of new instruments such as Moving Vessel Profiler (MVP), Vertical Microstructure turbulence Profiler (VMP), and Current-Pressure equipped Inverted Echo Sounder (CPIES) (Zhao et al., 2022; Zheng et al., 2022a; Zheng et al., 2022b). It not only promotes the research of large-scale processes in the South China Sea circulation, but also extends the research scale from mesoscale to sub-mesoscale and small-scale processes, provides applicable observation methods for the research of dynamic processes at different scales, and builds a three-dimensional observation network in the South China Sea with higher spatial and temporal resolution and more observation parameters.

Since March 2010, the South China Sea Institute of Oceanology (SCSIO) has established a hydrological and marine meteorological observation network over the tropical eastern Indian Ocean to enhance the understanding of the Indian Ocean air-sea interaction. There include 12 years Indian Ocean open cruise and along these cruise routes, consecutive oceanic and meteorological observations have been made, including CTD, GPS radiosonde, and automatic weather station. Furthermore, an enhanced observational system, consisting of six moorings, has also been conducted since 2015 to continue the suspended RAMA current observation (Zeng et al., 2022). The dynamic processes of the equatorial and near-equatorial Indian Ocean circulation systems show significant multi-scale variability associated with the Indian Monsoon. Based on these large-scale hydrological observations and numerical simulations of the

South China Sea Institute of Oceanology, eastern boundary wave bridge of tropical Indian Ocean have been reveal. On the equator, the wind-driven Kelvin and Rossby waves, and boundary-reflected Rossby waves significantly regulate the formation and evolution of the currents in the upper layer, the thermocline (EUC), and the middle layer (EIC), which effectively transport energy horizontally and vertically (Huang et al., 2018a, 2018b, 2018c, 2022a, 2023; Chen et al., 2019, 2020a). Off the equator, the currents are still modulated by the equatorial dynamics, as equatorial wave signals transmit energy there relying on the eastern boundary in the form of coastal Kelvin waves and off-equatorial reflected Rossby waves (Chen et al., 2018, 2020b, 2023; Huang et al., 2019, 2020, 2022b; Huang et al., 2021). The equatorial wind-driven dynamics are the main factor controlling the inter-annual variability of the thermocline in the eastern Indian Ocean upwelling. Under the support of the dynamic fulcrum of the eastern boundary, the eastern boundary wave bridge of tropical Indian Ocean is thus an energy belt, which links generation and variation of the circulation in the tropical Indian Ocean.

## Reference

- Cai, Z., J. Gan, Z. Liu, Rex Hui, J. Li, 2020: Progress on the formation dynamics of the layered circulation in the South China Sea, *Prog. Oceanogr.*, 181 (202) 102246.
- Cai, Z. and J. Gan, 2021: Dynamics of the layered circulation inferred from kinetic energy pathway in the South China Sea, *J. Phys. Oceanogr.*, 1671-1685, doi: 10.1175/JPO-D-20-0226.
- Cai, Z., D. Chen and J. Gan, 2023: Formation of the layered circulation in South China Sea with the mixing stimulated exchanging current through Luzon Strait. *J. Geophys. Res.*, 17673334, doi: 10.1029/2023JC019730.
- Chen, G. X., W. Han, X. Zhang, and coauthors, 2020a: Determination of tempo-spatial variability of the Indian Equatorial Intermediate Current, *J. Phys. Oceanogr.*, <https://doi.org/10.1175/JPO-D-20-0041.1>
- Chen, G. X., D. Wang, W. Han, M. Feng, and A. Gordon, 2020b: The extreme El Nino events

- suppressing the intraseasonal variability in the eastern tropical Indian Ocean, *J. Phys. Oceanogr.*, 50(8), 2359-2372.
- Chen, G. X., W. Han, X. Ma, Y. Li, T. Zhang, and D. Wang, 2023: Role of extreme Indian Ocean Dipole in regulating three-dimensional freshwater content in the Southeast Indian Ocean, *Geophys. Res. Lett.*, 50, e2022GL102290. <https://doi.org/10.1029/2022GL102290>
- Chen, G. X., W. Han, Y. Li, J. Yao, and D. Wang, 2019: Intraseasonal variability of the Equatorial Undercurrent in the Indian Ocean, *J. Phys. Oceanogr.*, 49, 85-101, doi: 10.1175/JPO-D-18-0151.1.
- Chen, G., Y. Hou, and X. Chu, 2011: Mesoscale eddies in the South China Sea: Mean properties, spatiotemporal variability, and impact on thermohaline structure. *J. Geophys. Res. Oceans*, **116**, <https://doi.org/10.1029/2010JC006716>.
- Chen, G. X., Y. Li, Q. Xie, and D. Wang, 2018: Origins of Eddy Kinetic Energy in the Bay of Bengal, *J. Geophys. Res. Oceans*, 123, doi: 10.1002/2017JC013455.
- , J. Gan, Q. Xie, X. Chu, D. Wang, and Y. Hou, 2012: Eddy heat and salt transports in the South China Sea and their seasonal modulations. *J. Geophys. Res. Oceans*, **117**, 5021, <https://doi.org/10.1029/2011JC007724>.
- Chen, Y., Q. P. Li, and J. Yu, 2022: Submesoscale variability of subsurface chlorophyll-a across eddy-driven fronts by glider observations. *Prog. Oceanogr.*, 209, 102905, <https://doi.org/10.1016/j.pocean.2022.102905>.
- Chow, C., J. Hu, L. Centurioni, and P. P. Niiler, 2008: Mesoscale Dongsha Cyclonic Eddy in the northern South China Sea by drifter and satellite observations. *J Geophys Res*, **113**, C04018.
- Chu, P. C., C. W. Fan, C. J. Lozano, and J. L. Kerling, 1998: An airborne expendable bathythermograph survey of the South China Sea, May 1995. *J Geophys Res*, **103**, 21 637-21 652, <https://doi.org/10.1029/98JC02096>.
- Chu, X., H. Xue, Y. Qi, G. Chen, Q. Mao, D. Wang, and F. Chai, 2014: An exceptional anticyclonic eddy in the South China Sea in 2010. *J. Geophys. Res. Oceans*, **119**, 881–897, <https://doi.org/10.1002/2013JC009314>.
- , G. Chen, and Y. Qi, 2020: Periodic Mesoscale Eddies in the South China Sea. *J. Geophys.*

- Res. Oceans*, **125**, <https://doi.org/10.1029/2019JC015139>.
- Dong, J., and Y. Zhong, 2020: Submesoscale fronts observed by satellites over the Northern South China Sea shelf. *Dyn. Atmos. Ocean.*, **91**, 101161, <https://doi.org/10.1016/j.dynatmoce.2020.101161>.
- , B. Fox-Kemper, Z. Jing, Q. Yang, J. Tian, and C. Dong, 2022: Turbulent Dissipation in the Surface Mixed Layer of an Anticyclonic Mesoscale Eddy in the South China Sea. *Geophys. Res. Lett.*, **49**, <https://doi.org/10.1029/2022GL100016>.
- Gan, J., Z. Liu and C. Hui, 2016: A three-layer alternating spinning circulation in the South China Sea, *J. Phys. Oceanogr.*, doi:10.1175/JPO-D-16-0044.
- Gan, J., Kung, H., Cai, Z., Liu, C. Hui, J. Li, 2022: Hotspots of the stokes rotating circulation in a large marginal sea. *Nat. Commun.* **13**, 2223. <https://doi.org/10.1038/s41467-022-29610-z>
- Huang, C., L. Zeng, D. Wang, Q. Wang, P. Wang, and T. Zu, 2023: Submesoscale eddies in eastern Guangdong identified using high-frequency radar observations. *Deep. Res. Part II Top. Stud. Oceanogr.*, **207**, 105220, <https://doi.org/10.1016/j.dsr2.2022.105220>.
- Huang, H. M., D. Wang, L. Yang, and K. Huang, 2021: Enhanced intraseasonal variability of the upper layers in the southern Bay of Bengal during the summer 2016, *J. Geophys. Res. Oceans*, **126**, e2021JC017459. <https://doi.org/10.1029/2021JC017459>
- Huang, J., Zou, Z., Zeng, Q., Li, P., Song, J., Wu, L., et al., 2021: The turbulent structure of the marine atmospheric boundary layer during and before a cold front. *J. Atmos. Sci.*, **78**, 863–875, <https://doi.org/10.1175/JAS-D-19-0314.1>.
- Huang, K., D. Wang, G. Chen, and coauthors, 2022a: Intensification and dynamics of the westward Equatorial Undercurrent during the summers of 1998 and 2016 in the Indian Ocean, *Geophys. Res. Lett.* **49**, e2022GL100168. <https://doi.org/10.1029/2022GL100168>.
- Huang, K., D. Wang, W. Han, M. Feng, G. Chen, W. Wang, J. Chen and J. Li, 2019: Semiannual Variability of Mid-depth Zonal Currents along 5°N in the Eastern Indian Ocean: Characteristics and Causes, *J. Phys. Oceanogr.*, **49**, 85-101, <https://doi.org/10.1175/JPO-D-19-0089.1>.
- Huang, K., D. Wang, W. Wang, J. Chen, L. Chen, and G. Chen, 2018b: Multi-scale variability

- of the tropical Indian Ocean circulation system revealed by recent observations, *SCIENCE CHINA Earth Sciences*, doi: 10.1007/s11430-017-9179-x.
- Huang, K., D. Wang, Y. Qiu, Y. Wu, K. Liu, B. Huang and D. Sui, 2023: Meridional-width variability of near-equatorial zonal currents along 80.5°E on seasonal to interannual timescales in the Indian Ocean, *J. Geophys. Res. Oceans*, 128, e2022JC019147. <https://doi.org/10.1029/2022JC019147>.
- Huang, K., M. McPhaden, D. Wang, W. Wang, Q. Xie, J. Chen, Y. Shu, Q. Wang, J. Li, and J. Yao, 2018c: Vertical propagation of mid-depth zonal currents associated with surface wind forcing in the equatorial Indian Ocean, *J. Geophys. Res. Oceans*, 123. <https://doi.org/10.1029/2018JC013977>.
- Huang, K., M. Feng, Y. Wu, and coauthors, 2022b: Leading-Mode Connections of Inter-annual Variability in Upper-Ocean Salinity in the Tropical Indian Ocean, *J. Phys. Oceanogr.*, 52(12): 3309-3329, <https://doi.org/10.1175/JPO-D-21-0267.1>.
- Huang, K., W. Han, D. Wang, W. Wang, Q. Xie, J. Chen, and G. Chen, 2018a: Features of the equatorial intermediate current associated with basin resonance in the Indian Ocean, *J. Phys. Oceanogr.*, 48, 1333-1347.
- Huang, K., D. Wang, M. Feng, and coauthors, 2020: Baroclinic characteristics and energetics of annual Rossby waves in the southern tropical Indian Ocean, *J. Phys. Oceanogr.*, 50 (9): 2591–2607, <http://doi.10.1175/JPO-D-19-0294.1>
- Li, G., C. Dong, J. Pan, A. T. Devlin, and D. Wang, 2023: Influence of the upper mixed layer depth on Langmuir turbulence characteristics. *J. Oceanol. Limnol.*, 41, 17–37, <https://doi.org/10.1007/s00343-022-1123-4>.
- Li, R., and Coauthors, 2021: Slope-Intensified Storm-Induced Near-Inertial Oscillations in the South China Sea. *J. Geophys. Res. Ocean.*, 126, 1–21, <https://doi.org/10.1029/2020JC016713>.
- Zeng, L., and Coauthors, 2021: A Decade of Eastern Tropical Indian Ocean Observation Network (TIOON). *Bull. Amer. Meteor. Soc.*, 102, E2034–E2052, <https://doi.org/10.1175/BAMS-D-19-0234.1>.
- Lian, Z., B. N. Sun, Z. X. Wei, Y. G. Wang, and X. Y. Wang, 2019: Comparison of eight



- detection algorithms for the quantification and characterization of mesoscale eddies in the South China Sea. *J Atmos Ocean. Technol*, **36**, 1361–1380, <https://doi.org/10.1175/JTECH-D-18-0201.1>.
- Lin, H., Z. Liu, J. Hu, D. Menemenlis, and Y. Huang, 2020: Characterizing meso- to submesoscale features in the South China Sea. *Prog. Oceanogr.*, 188, 102420, <https://doi.org/10.1016/j.pocean.2020.102420>.
- Ma, Y., D. Wang, Y. Shu, J. Chen, Y. He, and Q. Xie, 2022: Bottom-Reached Near-Inertial Waves Induced by the Tropical Cyclones, Conson and Mindulle, in the South China Sea. *J. Geophys. Res. Ocean.*, 127, 1–13, <https://doi.org/10.1029/2021JC018162>.
- Nan, F. Yu, 2022: Observation of Bottom-Trapped Topographic Rossby Waves to the West of the Luzon Strait, South China Sea. *J. Phys. Oceanogr.*, 52, 2853–2872, doi:10.1175/JPO-D-22-0065.1.
- Nan, F., Z. He, H. Zhou, and D. Wang, 2011: Three long-lived anticyclonic eddies in the northern South China Sea. *J. Geophys. Res. Oceans*, **116**, <https://doi.org/10.1029/2010JC006790>.
- Ni, Q., X. Zhai, C. Wilson, C. Chen, and D. Chen, 2021: Submesoscale Eddies in the South China Sea. *Geophys. Res. Lett.*, 48, 1–8, <https://doi.org/10.1029/2020GL091555>.
- Nof, D., Y. Jia, E. Chassignet, and A. Bozec, 2011: Fast Wind-Induced Migration of Leddies in the South China Sea. *J. Phys. Oceanogr.*, **41**, 1683–1693, <https://doi.org/10.1175/2011JPO4530.1>.
- Qiu, C., H. Mao, H. Liu, Q. Xie, J. Yu, D. Su, J. Ouyang, and S. Lian, 2019: Deformation of a Warm Eddy in the Northern South China Sea. *J. Geophys. Res. Oceans*, **124**, 5551–5564, <https://doi.org/10.1029/2019JC015288>.
- Qiu, C., Z. Yang, D. Wang, M. Feng, and J. Su, 2022: The Enhancement of Submesoscale Ageostrophic Motion on the Mesoscale Eddies in the South China Sea. *J. Geophys. Res. Ocean.*, 127, 1–12, <https://doi.org/10.1029/2022JC018736>.
- Quan, Q., Liu, Z., Sun, S., Cai, Z., Yang, Y., Jin, G., et al. , 2021: Influence of the Kuroshio Intrusion on Deep Flow Intraseasonal Variability in the Northern South China Sea. *J. Geophys. Res. Ocean.*, 126(7), 1–13. <https://doi.org/10.1029/2021jc017429>

- Quan, Q., Liu, Z., Yang, Y., Cai, Z., Zhang, H., & Liu, X., 2022: Characterization of intraseasonal fluctuations in the abyssal South China Sea: An insight into the energy pathway. *Prog. Oceanogr.*, 206, 102829. <https://doi.org/10.1016/j.pocean.2022.102829>
- , H. Liang, Y. Huang, H. Mao, J. Yu, D. Wang, and D. Su, 2020: Development of double cyclonic mesoscale eddies at around Xisha islands observed by a ‘Sea-Whale 2000’ autonomous underwater vehicle. *Appl. Ocean Res.*, **101**, 102270, <https://doi.org/10.1016/j.apor.2020.102270>.
- , Z. Yi, D. Su, Z. Wu, H. Liu, P. Lin, Y. he, and D. Wang, 2022: Cross-Slope Heat and Salt Transport Induced by Slope Intrusion Eddy’s Horizontal Asymmetry in the Northern South China Sea. *J. Geophys. Res. Oceans*, **127**, <https://doi.org/10.1029/2022JC018406>.
- Shu, Y., J. Chen, S. Li, Q. Wang, J. Yu, and D. Wang, 2019: Field-observation for an anticyclonic mesoscale eddy consisted of twelve gliders and sixty-two expendable probes in the northern South China Sea during summer 2017. *Sci. China Earth Sci.*, **62**, 451–458, <https://doi.org/10.1007/s11430-018-9239-0>.
- Shu, Y., Wang, J., Xue, H., Huang, R. X., Chen, J., Wang, D., et al, 2022: Deep-Current Intraseasonal Variability Interpreted as Topographic Rossby Waves and Deep Eddies in the Xisha Islands of the South China Sea. *J. Phys. Oceanogr.*, 52(7), 1415–1430. <https://doi.org/10.1175/JPO-D-21-0147.1>
- Su, D., P. Lin, H. Mao, J. Wu, H. Liu, Y. Cui, and C. Qiu, 2020: Features of Slope Intrusion Mesoscale Eddies in the Northern South China Sea. *J. Geophys. Res. Oceans*, **125**, e2019JC015349, <https://doi.org/10.1029/2019JC015349>.
- Sun, Y. Fang, B. Liu, and Tana, 2016: Coupling between SST and wind speed over mesoscale eddies in the South China Sea. *Ocean Dyn*, **66**, 1467–1474, <https://doi.org/10.1007/s10236-016-0993-4>.
- , ——, Y. Zu, B. Liu, Tana, and A. A. Samah, 2020: Seasonal characteristics of mesoscale coupling between the sea surface temperature and wind speed in the South China Sea. *J Clim.*, **33**, 625–638, <https://doi.org/10.1175/JCLI-D-19-0392.1>.
- Sun, Y., and J. Lan, 2021: Summertime eastward jet and its relationship with western boundary current in the South China Sea on the interannual scale, *Clim Dyn.*, 56, 935–947, doi:

10.1007/s00382-020-05511-z.

- Sun, Y., and J. Lan, 2022: Significant difference of the summertime eastward jet enhancement in the South China Sea during the El Niño developing summers of 1982 and 1997, *J. Geophys. Res.*, 127, e2022JC018687, doi: 10.1029/2022JC018687.
- Sun, W., C. Dong, R. Wang, Y. Liu, and K. Yu, 2017: Vertical structure anomalies of oceanic eddies in the Kuroshio Extension region: 3-D EDDY IN THE KUROSHIO EXTENSION REGION. *J. Geophys. Res. Oceans*, **122**, 1476–1496, <https://doi.org/10.1002/2016JC012226>.
- , ——, W. Tan, Y. Liu, Y. He, and J. Wang, 2018: Vertical Structure Anomalies of Oceanic Eddies and Eddy-Induced Transports in the South China Sea. *Remote Sens.*, **10**, 795, <https://doi.org/10.3390/rs10050795>.
- , ——, ——, and Y. He, 2019: Statistical Characteristics of Cyclonic Warm-Core Eddies and Anticyclonic Cold-Core Eddies in the North Pacific Based on Remote Sensing Data. *Remote Sens.*, **11**, 208, <https://doi.org/10.3390/rs11020208>.
- Tang, H., Shu, Y., Wang, D., Xie, Q., Zhang, Z., Li, J., et al. 2022: Submesoscale processes observed by high-frequency float in the western South China sea. *Deep Sea Res. Part I Oceanogr. Res. Pap.*, 103896, <https://doi.org/10.1016/j.dsr.2022.103896>.
- Wang, D., Qiu, C., Shu, Y., Wang, Q., Zu, T., Liang, C., et al. 2022: Progress in the Dynamic Process and Mechanisms of Multi-Scale Currents in the South China Sea. *Adv. Mar. Sci.*, **40**, <https://doi.org/10.12362/j.issn.1671-6647.20220602001>.
- , G. Li, L. Shen, and Y. Shu, 2022b: Influence of Coriolis Parameter Variation on Langmuir Turbulence in the Ocean Upper Mixed Layer with Large Eddy Simulation. *Adv. Atmos. Sci.*, **39**, 1487–1500, <https://doi.org/10.1007/s00376-021-1390-6>.
- Wang, G., J. Su, and P. C. Chu, 2003: Mesoscale eddies in the South China Sea observed with altimeter data. *Geophys Res Lett*, **30**, 2121, <https://doi.org/10.1029/2003GL018532>.
- Wang, G., D. Chen, and J. Su, 2006: Generation and life cycle of the dipole in the South China Sea summer circulation. *J Geophys Res*, **111**, <https://doi.org/10.1029/2005JC003314>.
- Wang, J., Shu, Y., Wang, D., Xie, Q., Wang, Q., Chen, J., et al, 2022: Observed Variability of Bottom-Trapped Topographic Rossby Waves Along the Slope of the Northern South China

- Sea. *J. Geophys. Res. Ocean.*, 126(12), 1–17. <https://doi.org/10.1029/2021JC017746>
- Wang, Q., L. Zeng, W. Zhou, Q. Xie, S. Cai, J. Yao, and D. Wang, 2015: Mesoscale eddies cases study at Xisha waters in the South China Sea in 2009/2010. *J. Geophys. Res. Oceans*, **120**, 517–532, <https://doi.org/10.1002/2014JC009814>.
- Wang, Q., Zeng, L., Shu, Y., Li, J., Chen, J. U., He, Y., et al, 2019: Energetic topographic rossby waves in the Northern South China sea. *J. Phys. Oceanogr.*, 49(10), 2697–2714. <https://doi.org/10.1175/JPO-D-18-0247.1>
- , ——, J. Li, J. Chen, Y. He, J. Yao, D. Wang, and W. Zhou, 2018: Observed Cross-Shelf Flow Induced by Mesoscale Eddies in the Northern South China Sea. *J. Phys. Oceanogr.*, **48**, 1609–1628, <https://doi.org/10.1175/JPO-D-17-0180.1>.
- Wang, Q., W. Cai, L. Zeng, D. Wang, 2018: Nonlinear meridional moisture advection and the ENSO-southern China rainfall teleconnection, *Geophys. Res. Lett.*, 45. 9, 4353-4360.
- Wang, Q., L. Zeng, Y. Shu, Q. Liu, T. Zu, J. Li, J. Chen, Y. He ,D. Wang, 2020a: Interannual variability of South China Sea winter circulation: response to Luzon Strait transport and El Niño wind, *Clim. Dyn.*, 54:1145–1159, doi: 10.1007/s00382-019-05050-2.
- Wang, Q., Y. Wang, J. Sui, W. Zhou, D. Li, 2021: Effects of weak and strong winter currents on the thermal state of the South China Sea, *J. Clim.*, 34(1):313-325, doi: 10.1175/JCLI-D-19-0790.1.
- Wang, Q., W. Zhong, S. Yang, J. Wang, L. Zeng, J. Chen, Y. He, 2022a: Southern China winter rainfall modulated by South China Sea warming, *Geophys.Res. Lett.*, doi: 10.1029/2021GL097181.
- Wang, Q., L. Zeng, J. Chen, Y. He, Q. Liu, D. Sui, and D. Wang, 2023: Phase shift of the winter South China Sea western boundary current over the past two decades and its drivers, *Geophys.Res. Lett.*, 50.
- Wang, Y., C. Li, and Q. Liu, 2020: Observation of an anti-cyclonic mesoscale eddy in the subtropical northwestern Pacific Ocean from altimetry and Argo profiling floats. *Acta Oceanol. Sin.*, **39**, 79–90, <https://doi.org/10.1007/s13131-020-1596-y>.
- Xie, Y., Q. Wang, L. Zeng, J. Chen, Y. He, 2022: Winter-summer transition in the southern South China Sea western boundary current, *J. Phys. Oceanogr.*, 52:917-927, doi:

10.1175/JPO-D-21-0282.1.

- Yan, Y., G. Wang, H. Xue, and F. Chai, 2019: Buoyancy effect on the winter South China Sea western boundary current. *J. Geophys. Res.*, 124, doi: 10.1029/2019JC015079.
- Yang, H., L. Wu, S. Sun, and Z. Chen, 2017: Selective Response of the South China Sea Circulation to Summer Monsoon. *J. Phys. Oceanogr.*, 47, 1555–1568, doi: 10.1175/JPO-D-16-0288.1.
- Yang, L., J. Huang, X. Wang, L. Zeng, R. Shi, Y. He, Q. Xie, S. Wang, R. Chen, J. Yuan, Q. Wang, J. Chen, T. Zu, Y. Li, D. Sui, S. Peng, and D. Wang, 2015: Toward a Mesoscale Hydrological and Marine Meteorological Observation Network in the South China Sea. *Bull. Amer. Meteor. Soc.*, 96, 1117–1135, doi:150204133247008. 10.1175/BAMS-D-14-00159.1.
- Yang, Q., M. Nikurashin, H. Sasaki, H. Sun, and J. Tian, 2019: Dissipation of mesoscale eddies and its contribution to mixing in the northern South China Sea. *Sci. Rep.*, 9, <https://doi.org/10.1038/s41598-018-36610-x>.
- Yang, Y., and Coauthors, 2016: The topography effect on the sudden deceleration of the mesoscale eddy propagation speed around the Dongsha Islands in northern South China Sea. *Aquat. Ecosyst. Health Manag.*, 19, 242–249, <https://doi.org/10.1080/14634988.2016.1215747>.
- Zeng, L. L., G. Chen, K. Huang, and coauthors, 2021: A Decade of Eastern Tropical Indian Ocean Observation Network (TIOON), BAMS, E2034–E2052.
- Zeng, L., Q. Wang, Q. Xie, P. Shi, and D. Wang, 2015: Hydrographic field investigations in the northern south china sea by open cruises during 2004–2013. *Science Bulletin*, 60(6), 607–615, doi:10.1007/s11434-015-0733-z.
- Zhang, Z., P. Li, L. Xu, C. Li, W. Zhao, J. Tian, and T. Qu, 2015: Subthermocline eddies observed by rapid-sampling Argo floats in the subtropical northwestern Pacific Ocean in Spring 2014. *Geophys. Res. Lett.*, 42, 6438–6445, <https://doi.org/10.1002/2015GL064601>.
- , J. Tian, B. Qiu, W. Zhao, P. Chang, D. Wu, and X. Wan, 2016: Observed 3D Structure, Generation, and Dissipation of Oceanic Mesoscale Eddies in the South China Sea. *Sci. Rep.*, 6, 24349, <https://doi.org/10.1038/srep24349>.



- , W. Zhao, B. Qiu, and J. Tian, 2017: Anticyclonic Eddy Sheddings from Kuroshio Loop and the Accompanying Cyclonic Eddy in the Northeastern South China Sea. *J. Phys. Oceanogr.*, **47**, 1243–1259, <https://doi.org/10.1175/JPO-D-16-0185.1>.
- Zhao, R., 2017: The impact of monsoon winds and mesoscale eddies on thermohaline structures and circulation patterns in the northern South China Sea. *Cont. Shelf Res.*,
- Zhao, R., X. Zhu, C. Zhang, H. Zheng, Z. Zhu, Q. Ren, Y. Liu, F. Nan, F. Yu, 2022: Summer anticyclonic eddies carrying Kuroshio waters observed by a large CPIES array west of the Luzon Strait. *J. Phys. Oceanogr.*, **53**, 341–359, doi:10.1175/JPO-D-22-0019.1.
- Zheng, H., Zhu, X.-H., Zhang, C., Zhao, R., Zhu, Z.-N., & Liu, Z.-J, 2021: Propagation of Topographic Rossby Waves in the Deep Basin of the South China Sea Based on Abyssal Current Observations. *J. Phys. Oceanogr.*, **51**, 2783–2791. <https://doi.org/10.1175/jpo-d-21-0051.1>
- Zheng, H., Zhu, X. H., Zhang, C., Zhao, R., Zhu, Z. N., Ren, Q., et al, 2022: Observation of Abyssal Circulation to the West of the Luzon Strait, South China Sea. *J. Phys. Oceanogr.*, **52**(9), 2091–2109. <https://doi.org/10.1175/JPO-D-21-0284.1>
- Zheng, H., Zhu, X.-H., Chen, J., Wang, M., Zhao, R., Zhang, C., et al, 2022: Observation of Bottom-Trapped Topographic Rossby Waves to the West of the Luzon Strait, South China Sea. *J. Phys. Oceanogr.*, **52**(11), 2853–2872. <https://doi.org/10.1175/jpo-d-22-0065.1>
- Zhou, M., Wang, G., Liu, W., & Chen, C, 2020: Variability of the observed deep western boundary current in the South China Sea. *J. Phys. Oceanogr.*, **50**(10), 2953–2963. <https://doi.org/10.1175/JPO-D-20-0013.1>
- Zhu, Y., J. Sun, Y. Wang, S. Li, T. Xu, Z. Wei, and T. Qu, 2019: Overview of the multi-layer circulation in the South China Sea. *Prog. Oceanogr.*, **175**: 171-182, <https://doi.org/10.1016/j.pocean.2019.04.001>.
- Zhu, Y., J. Sun, Y. Wang, Z. Wei, D. Yang, and T. Qu, 2017: Effect of potential vorticity flux on the circulation in the South China Sea. *J. Geophys. Res. Oceans*, **122**(8): 6454-6469, doi:10.1002/2016JC012375.
- Zhu, Y., Yao, J., Li, S., Xu, T., Huang, R. X., Nie, X., et al, 2022: Decadal Weakening of Abyssal South China Sea Circulation. *Geophys. Res. Lett.*, **49**(20), 1–9.

<https://doi.org/10.1029/2022GL100582>

Zhu, Y., Yao, J., Xu, T., Li, S., Wang, Y., & Wei, Z., 2022: Weakening Trend of Luzon Strait Overflow Transport in the Past Two Decades. *Geophys.Res. Lett.*, 49(7), 1–9.

<https://doi.org/10.1029/2021GL097395>

Zhuang, W., Y. Du, D. X. Wang, Q. Xie, and S. P. Xie, 2010: Pathways of mesoscale variability in the South China Sea. *Chin J Ocean. Limnol*, **28**, 1055–1067, <https://doi.org/10.1007/s00343-010-0035-x>.

Zou, Z., J. Song, P. Li, J. Huang, J. A. Zhang, Z. Wan, and S. Li, 2019: Effects of Swell Waves on Atmospheric Boundary Layer Turbulence: A Low Wind Field Study. *J. Geophys. Res. Ocean.*, 124, 5671–5685, <https://doi.org/10.1029/2019JC015153>.

Zu, T., D. Wang, C. Yan, I. Belkin, W. Zhuang, and J. Chen, 2013: Evolution of an anticyclonic eddy southwest of Taiwan. *Ocean Dyn.*, **63**, 519–531, <https://doi.org/10.1007/s10236-013-0612-6>.

Zu, T., H. Xue, D. Wang, B. Geng, L. Zeng, Q. Liu, J. Chen, Y. He, 2019a: Interannual variation of the South China Sea circulation during winter: Intensified in the southern basin, *Clim. Dyn.*, 52:1917 – 1933, doi: 10.1007/s00382-018-4230-3.

Zu, T., D. Wang, Q. Wang, M. Li, J. Wei, B. Geng, Y. He, J. Chen, 2020: A revisit of the interannual variation of the South China Sea upper layer circulation in summer: correlation between the eastward jet and northward branch, *Clim. Dyn.*, 54:457-471, doi: 10.1007/s00382-019-05007-5.

Zu, Y., S. Sun, W. Zhao, P. Li, B. Liu, Y. Fang, and A. A. Samah, 2019b: Seasonal characteristics and formation mechanism of the thermohaline structure of mesoscale eddy in the South China Sea. *Acta Oceanol. Sin.*, **38**, 29–38, <https://doi.org/10.1007/s13131-018-1222-4>.

# Progress of research on floating ice sheets in China from 2020 to 2023

*Zhan Wang*

Institute of Mechanics, Chinese Academy of Sciences, Beijing 100190, P. R. China

Waves generated by moving loads on floating ice sheets are called hydroelastic or flexural-gravity waves. Hydroelastic waves enjoy wide usage in marine transport in the polar region. 1950s Antarctic explorations started to rely heavily on aircraft landing on floating ice sheets, and resultant ice sheet deflection was studied. In 1958, James Wilson from the University of Michigan reported his experiments on sea ice in the bay at Hopedale, Labrador. He found that the response of the floating ice sheet to a moving load on it is sometimes surprising since localized, stable, significant responses were observed as the plane moved steadily on an ice cover with speed in a specific range. The linear theory shows that there exists a critical speed  $c_{min}$  due to competition between gravity and elastic bending. The critical speed occurs at a finite wavenumber where the group velocity equals the phase velocity. It follows physically that if a moving load is travelling with  $c_{min}$ , then energy will not be able to propagate relative to the load and will therefore accumulate. This phenomenon is very much like the vibrations of a fast train track which can be described by an external force moving on a beam resting on an elastic foundation (*i.e.*, Pasternak-type foundations).

Although the linear theory identifies the critical speed and provides some physical explanation, it fails to depict the actual wave phenomenon near resonance since it predicts unlimited wave amplitude growth owing to its non-dispersive nature. To explore the nonlinear dynamics, a unidirectional, weakly dispersive nonlinear model is proposed to describe the novel bifurcation arising from hydroelastic waves in deep water (Wang 2022). This model equation, including quadratic, cubic, and quartic nonlinearities, extends the famous Whitham equation. The newly developed model can capture essential features near the bifurcation point, rich with Stokes, solitary,

generalized solitary, and dark solitary waves. The nonlinear dynamic response to a fully localized constant-moving load near  $c_{min}$  was investigated thoroughly by Meng & Wang (2022b). The time-dependent solutions were compared with the data from the field measurements, and good agreement was achieved between the numerical results and experimental records. These results were also extended to the three-dimensional case, especially in the shallow water limit, and the near-resonance dynamics show the shedding of lumps, the three-dimensional counterpart of wavepacket solitary waves (Meng & Wang 2022a).

The problem also has extensions, for instance, to include mean flow and shear current to the system to understand the wave-current-structure interactions (Gao *et al.* 2019; Wang *et al.* 2020). New envelope equations for modulational instabilities were proposed, including the vorticity-NLS equation, second harmonic resonance, and long-short-wave interaction. In addition, particle trajectories and streamline structures were studied and analyzed carefully. The most striking phenomenon is the net vertical transport of particles beneath some hydroelastic solitary waves due to wave-current interactions. The streamline patterns alternate between net vertical transport and a closed orbit, forming a series of nested cat's-eye structures.

## References

- Tao Gao, Zhan Wang, Paul A. Milewski, 2019: Nonlinear hydroelastic waves on a linear shear current at finite depth[J]. *Journal of Fluid Mechanics*, 876: 55-86.
- Yanghan Meng, Zhan Wang, 2022a: Hydroelastic lumps in shallow water[J]. *Physica D*, 434: 133200.
- Yanghan Meng, Zhan Wang, 2022b: Dynamic response of a floating ice sheet to a localized moving load[J]. *Chinese Journal of Theoretical and Applied Mechanics*, 54(4): 864-873.
- Zhan Wang, 2022: A universal bifurcation mechanism arising from hydroelastic waves[J]. *Theoretical & Applied Mechanics Letters*, 12(1): 100315.
- Zhan Wang, Xin Guan, Jean-Marc Vanden-Broeck, 2020: Progressive flexural-gravity waves with constant vorticity[J]. *Journal of Fluid Mechanics*, 905: A12.

# **Progress of Climate and Earth System Model in China from 2020 to 2023**

*Ying Bao<sup>1,2</sup>, Zhenya Song<sup>1,2</sup>*

<sup>1</sup> First Institute of Oceanography, Key Laboratory of Marine Science and Numerical Modeling, Ministry of Natural Resources, Qingdao, 266061, China

<sup>2</sup> Shandong Key Laboratory of Marine Science and Numerical Modeling, Qingdao, 266061, China

The climate and earth system model is a product of multidisciplinary and multisphere interaction research and plays important role in climate research. Its developmental level has become an indicator to measure the scientific and technological strength of a country. In China, significant efforts have been made to promote the progress of climate and earth system models during the past years. In this short survey, we will express the recent achievements of climate and earth system models in China and provide several suggestions and trends for their development.

Recently, the sixth Assessment Report of Intergovernmental Panel on Climate Change (IPCC AR6) <sup>[1]</sup> has been officially published, with the directly support from simulations of the phase 6 Coupled Model Inter-comparison Project (CMIP6) models. There are 10 model versions from 7 institutes in China participating in the CMIP6. This is a significant increase compared to the 6 model versions from 4 institutes in the phase 5 of CMIP (CMIP5), which supported to IPCC AR5 <sup>[2]</sup>. It indicates that the climate model research and development in China is experiencing a rapid development stage. The models are mainly developed at the Chinese Academy of Sciences, ministries and universities. The 10 models versions participated in CMIP6 are including three model versions of FGOALS-f3 <sup>[3]</sup>, FGOALS-g3 <sup>[4]</sup> and CAS-ESM <sup>[5]</sup> from Institute of Atmospheric Physics, Chinese Academy of Sciences (IAP, CAS), BCC-CSM2<sup>[6]</sup> and BCC-ESM1 <sup>[7]</sup> from Beijing Climate Center, China Meteorological Administration (BCC, CMA), CAMS-CSM <sup>[8]</sup> from the Chinese Academy of Meteorological Sciences



(CAMs), FIO-ESM v2.0 <sup>[9]</sup> from the First Institute of Oceanography, Ministry of Natural Resources (FIO, MNR), CIESM <sup>[10]</sup> from Tsinghua University (THU), NESM v3 <sup>[11]</sup> from Nanjing University of Information Science & Technology (NUIST), and TaiESM <sup>[12]</sup> from the Research Center for Environmental changes (RCEC), Academia Sinica Taiwan, China. The BNU-ESM from Beijing Normal University (BNU) which participated in CMIP5 did not participate in CMIP6. However, CAS-ESM, CIESM, NESM and TaiESM are new models in CMIP6.

Since CMIP5, the climate system model has gradually evolved into the earth system model, incorporating the global carbon cycle processes by combining them with biogeochemical cycle processes of ocean and land ecosystem and even global vegetation dynamics in the land surface. The trend of climate model development is to involve more processes in the model system and to have finer resolution with advancements in high-performance computing. In comparison to CMIP5, each model team from China has made great efforts to develop their model by incorporation biogeochemical processes, new physical parameterization schemes, finer resolution, and so on <sup>[13]</sup>. BCC-CSM and FIO-ESM v2.0 are earth system models with global carbon cycles with the prognostic spatial CO<sub>2</sub> in the atmosphere for C4MIP (Coupled Climate-Carbon Cycle Model Inter-comparison Project) simulations of CMIP6 <sup>[6,14]</sup>. BCC-ESM includes prognostic aerosols and conducted AerChemMIP (Aerosols and Chemistry Model Inter-comparison Project) simulations of CMIP6 <sup>[7]</sup>. BCC-CSM, CAMS-CSM and FGOALS-f3 have high-resolution versions and participate the HighResMIP (High Resolution Model Inter-comparison Project) of CMIP6 <sup>[8,15,16]</sup>.

FIO-ESM v2.0 is the only CMIP6 models that employs an ocean surface wave model, and considers three wave-related parameterizations <sup>[9,17]</sup>. These parameterizations include the nonbreaking wave-induced mixing, which enhances the turbulence mixing in the upper ocean, the wave-induced Stokes drift, which affects the air-sea fluxes by influencing the air-sea relative wind speed, and the wave-induced sea spray, which affects the air-sea heat fluxes when the surface wave is broken and water droplets are emitted into the air. FIO-ESM v2.0 is also the first model to incorporate a

parameterization of sea surface temperature (SST) diurnal cycle and can simulate better SST diurnal variation [9, 17]. The nonbreaking wave-induced mixing and SST diurnal cycle also affect the global carbon cycle processes in the earth system [14]. The SST and ENSO simulation of FIO-ESM show much better improvement with its previous version in CMIP5, which indicates that the importance of impacts of small-scale physical processes on climate system [17].

For the future development of climate and earth system models in China, in-depth studies on small-scale physical processes such as ocean mixing, air-sea fluxes and cloud physical processes, as well as the development of parameterization schemes of these processes, are keys to improve the climate model performance. Additionally, future studies and incorporation of the ocean and land ecosystem model, biogeochemical model, atmospheric chemistry model and land ice are needed to develop the earth system model. As the resolution of international climate models increases rapidly, evolving the convection-resolving scale in atmosphere model and eddy-resolving scale in ocean model, high-resolution simulations should be development. Furthermore, high-performance computing technology is also necessary as the climate and earth system becoming more complex.

## Reference

- [1] IPCC, Climate Change 2021: the Physical Science Basis, Contribution of Working Group I to the Sixth Assessment Report of the Intergovernmental Panel on Climate Change [Masson-Delmotte, V., P. Zhai, A. Pirani, S.L. Connors, C. Péan, S. Berger, N. Caud, Y. Chen, L. Goldfarb, M.I. Gomis, M. Huang, K. Leitzell, E. Lonnoy, J.B.R. Matthews, T.K. Maycock, T. Waterfield, O. Yelekçi, R. Yu, and B. Zhou (eds.)]. Cambridge University Press, Cambridge, United Kingdom and New York, NY, USA, 2391 pp. doi:10.1017/9781009157896., 2021.
- [2] IPCC, Climate Change 2013: The Physical Science Basis. Contribution of Working Group I to the Fifth Assessment Report of the Intergovernmental Panel on Climate Change [Stocker, T.F., D. Qin, G.-K. Plattner, M. Tignor, S.K. Allen, J. Boschung, A.

- Nauels, Y. Xia, V. Bex and P.M. Midgley (eds.)]. Cambridge University Press, Cambridge, United Kingdom and NewYork, NY, USA, 1535 pp, 2013.
- [3] Bao, Q., X. F. Wu, J. X. Li, et al., Outlook for El Niño and the Indian Ocean Dipole in autumn–winter 2018–2019, *Chinese Sci. Bull.*, 63, 73–78, doi: 10.1360/N972018-00913, 2019.
- [4] Tang, Y. L., Y. Q. Yu, L. J. Li, et al., Introduction of FGOALS-g model and the experiment design in CMIP6, *Climate Change Res.*, 15, 551–557, doi: 10.12006/j.issn.1673-1719.2019.042, 2019. (in Chinese)
- [5] Zhang, H., M. Zhang, et al., CAS-ESM 2: Description and climate simulation performance of the Chinese Academy of Sciences (CAS) Earth System Model (ESM) version 2, *Journal of Advances in Modeling Earth Systems*, 12,e2020MS002210, <https://doi.org/10.1029/2020MS002210>, 2020.
- [6] Wu, T. W., Y. X. Lu, Y. J. Fang, et al., The Beijing Climate Center climate system model (BCC-CSM): The main progress from CMIP5 to CMIP6, *Geosci. Model Dev.*, 12, 1573–1600, doi: 10.5194/gmd-12-1573-2019, 2019.
- [7] Wu, T. W., F. Zhang, J. Zhang, et al., The Beijing Climate Center earth system model version 1 (BCC-ESM1): Model description and evaluation, *Geosci. Model Dev. Diss.* doi: 10.5194/gmd-2019-172, 2019
- [8] Rong, X. Y., J. Li, H. M. Chen, et al., Introduction of CAMS-CSM model and its participation in CMIP6, *Climate Change Res.*, 15, 540–544, doi: 10.12006/j.issn.1673-1719.2019.186, 2019 (in Chinese)
- [9] Song, Z. Y., Y. Bao, and F. L. Qiao, Introduction of FIOESM v2.0 and its participation plan in CMIP6 experiments, *Climate Change Res.*, 15, 558–565, doi: 10.12006/j.issn.1673-1719.2019.033, 2019. (in Chinese)
- [10] Lin, Y. L., X. M. Huang, Y. S. Liang, et al., The Community Integrated Earth System Model (CIESM) from Tsinghua University and its plan for CMIP6 experiments, *Climate Change Res.*, 15, 545–550, doi: 10.12006/j.issn.1673-1719.2019.166, 2019 (in Chinese)

- [11] Cao, J., L. B. Ma, J. Li, et al., Introduction of NUIST-ESM model and its CMIP6 activities, *Climate Change Res.*, 15, 566–570, doi: 10.12006/j.issn.1673-1719.2019.064, 2019. (in Chinese)
- [12] Lee, W.-L., Wang, Y.-C., Shiu, C.-J., et al., Taiwan Earth system model version 1: Description and evaluation of mean state, *Geosci. Model Dev.* 13 (9), 3887–3904.
- [13] Zhou, T. J., Z. M. Chen, L. W. Zou, et al., 2020: Development of Climate and Earth System Models in China: Past Achievements and New CMIP6 Results. *J. Meteor. Res.*, 34(1), 1-19, doi: 10.1007/s13351-020-9164-0, 2020.
- [14] Song Z Y, Bao Y, Qiao F L, Global carbon cycle of earth system model FIO-ESM. *Advances in Marine Science*, 40(4): 1-14, 2022 (in Chinese)
- [15] Xin, X. G., T. W. Wu, J. Zhang, et al., Introduction of BCC models and its participation in CMIP6, *Climate Change Res.*, 15, 533–539, doi: 10.12006/j.issn.1673-1719.2019.039, 2019 (in Chinese)
- [16] Bao, Q., Y. Liu, G. Wu, et al., CAS FGOALS-f3-H and CAS FGOALS-f3-L outputs for the high-resolution model intercomparison project simulation of CMIP6, *Atmospheric and Oceanic Science Letters*, 13:6, 576-581, DOI: 10.1080/16742834.2020.1814675, 2020.
- [17] Bao, Y., Song, Z., and Qiao, F, FIO-ESM version 2.0: Model description and evaluation, *Journal of Geophysical Research: Oceans*, 125, e2019JC016036. <https://doi.org/10.1029/2019JC016036>, 2020.

# **Progress of Dynamical Decomposition of Multiscale Oceanic Motions from 2020 to 2023**

*Zhiyu Liu, Chuanyin Wang, Hongyang Lin*

State Key Laboratory of Marine Environmental Science, and Department of Physical Oceanography, College of Ocean and Earth Sciences, Xiamen University, Xiamen, China

To date, large uncertainties remain in our quantitative understanding of the mechanical energy transfers in the world ocean characterized by multiscale and multi-regime motions. A robust decomposition of multiscale oceanic motions is crucial to exploring dynamics of various flow regimes and quantifying oceanic scale interactions and energy exchanges, but remains a great challenge in dynamical oceanography. Conventional approaches focus on time-scale or space-scale decomposition which usually achieves incomplete separation of different flow regimes. In this report, we concisely summarize how fundamental ocean dynamics can be used to develop simple approaches for disentangling various dynamical regimes. It is hoped that these dynamics-based decomposition approaches will help reveal the mechanisms of oceanic scale interactions and the associated energy transfers.

## **Disentangling six prototypical oceanic flow regimes <sup>[1]</sup>**

Dynamical characteristics of prototypical oceanic motions are utilized to decompose oceanic flows into six distinct regimes (i.e., large-scale circulations, barotropic tides, low-mode internal gravity waves, mesoscale flows, high-mode internal gravity waves and submesoscale flows). Specifically, large-scale currents and barotropic tides are isolated as flows with the largest horizontal scale and are further separated from each other through temporal filtering; mode-1 and mode-2 internal gravity waves, together termed as low-mode internal gravity waves, are extracted according to their dispersion relations to guarantee that the polarization relations are satisfied; mesoscale flows are recovered as the low-frequency flows with the horizontal scale larger than the first baroclinic deformation radius; high-mode internal gravity



waves (i.e., internal gravity waves excluding low-mode ones) and submesoscale flows are distinguished from each other based on the relative size of spectral magnitudes of the horizontal divergence and relative vorticity, without any a priori assumption that submesoscale flows (high-mode internal gravity waves) are non-divergent/weakly divergent (irrotational). The proposed approach satisfactorily yields dynamically-consistent decomposition over the global ocean and is particularly useful for diagnostic analysis of model outputs from realistic tide-resolving and submesoscale-admitting simulations such as the MITgcm LLC4320. For example, the energy transfers among prototypical regimes could be straightforwardly quantified.

### **Disentangling vortical and wavy motions of oceanic flows <sup>[2]</sup>**

The classic theory of vortical and wavy modes is extended with the introduction of a background flow. The extended theory is then utilized to devise a dynamical filter for disentangling the vortical and wavy motions of oceanic flows, based on relative magnitudes of the relative vorticity and the modified horizontal divergence in spectral space. Correspondingly, the governing equations of the vortical and wavy motions are rigorously derived from the primitive equations. This simple decomposition approach proves efficient over the global ocean and can be used particularly for disentangling vortical and wavy motions in model outputs from realistic tide-resolving and submesoscale-admitting simulations. Combined with conventional time-scale or space-scale decomposition (e.g., Fourier <sup>[3]</sup>, Leonard <sup>[4]</sup> or Liang filtering <sup>[5]</sup>), the proposed dynamical approach not only paves the way for parameterizing isopycnal mixing essentially caused by vortical motions and diapycnal mixing mainly induced by wavy motions, but also facilitates the exploration of multi-regime and multiscale interactions in the ocean. For example, submesoscale dynamics can be strictly defined and properly explored through spatially high-pass filtering the isolated vortical motions which will contribute to revealing the compelling mystery of coupling between submesoscale processes and internal gravity waves.

### **Disentangling vortical and wavy motions from snapshot satellite measurements <sup>[6]</sup>**

The fundamental fact that wavy motions do not carry potential vorticity is used to

decompose a pair of snapshot sea surface height and velocity into wavy and vortical components. This simple but efficient decomposition approach only requires that a single concurrent snapshot of sea surface height and velocity is available. Therefore, not only can this snapshot-style decomposition be applied for diagnosis of model outputs, but also it is useful for disentangling wavy and vortical motions observed by upcoming wide-swath satellite missions such as SWOT [7], Guanlan [8], WaCM [9], OSCOM [10]. For example, for the first time, internal gravity waves, including but not limited to internal tides, in the real ocean could be readily quantified in the near future.

## Reference

- [1] Wang C, Liu Z, Lin H. On dynamical decomposition of multiscale oceanic motions, *Journal of Advances in Modeling Earth Systems*, 15(3): e2022MS003556, 2023.
- [2] Wang C, Liu Z, Lin H. A simple approach for disentangling vortical and wavy motions of oceanic flows, *Journal of Physical Oceanography*, 53(5): 1237–1249, 2023.
- [3] Frisch, U. *Turbulence: The Legacy of A.N. Kolmogorov*, Cambridge University Press, 1995.
- [4] Aluie, H., M. Hecht, and G. K. Vallis. Mapping the energy cascade in the North Atlantic Ocean: The coarse-graining approach, *Journal of Physical Oceanography*, 48(2): 225–244, 2018.
- [5] Liang, X. S. Canonical transfer and multiscale energetics for primitive and quasigeostrophic atmospheres, *Journal of the Atmospheric Sciences*, 73(11): 4439–4468, 2016.
- [6] Wang C, Liu Z, Lin H., et al. Disentangling wavy and vortical oceanic motions in snapshots of sea surface height and velocity in anticipation of upcoming wide-swath satellite missions, under review in *Journal of Physical Oceanography*.
- [7] Morrow, R., Fu, L. L., Arduin, F., Benkiran, M., Chapron, B., Cosme, E., et al. Global observations of fine-scale ocean surface topography with the Surface Water and Ocean Topography (SWOT) Mission, *Frontiers in Marine Science*, 6: 232, 2019.

- [8] Chen, G., Tang, J., Zhao, C., Wu, S., Yu, F., Ma, C., et al. Concept design of the “Guanlan” science mission: China’s novel contribution to space oceanography, *Frontiers in Marine Science*, 6: 194, 2019.
- [9] Rodríguez, E., Bourassa, M., Chelton, D., Thomas Farrar, J., Long, D., Perkovic-Martin, D., & Samelson, R. The winds and currents mission concept, *Frontiers in Marine Science*, 6: 438, 2019.
- [10] Du, Y., Dong, X., Jiang, X., Zhang, Y., Zhu, D., Sun, Q., et al. Ocean surface current multiscale observation mission (OSCOM): Simultaneous measurement of ocean surface current, vector wind, and temperature, *Progress in Oceanography*, 193: 102531, 2021.

# **Progress of eddy-mean flow interaction in the Pacific low-latitude western boundary current region in China from 2020 to 2023**

*Linlin Zhang, Xiaomei Yan, Yuchao Hui, Fan Wang, Dunxin Hu*

Institute of Oceanology, Chinese Academy of Sciences, Qingdao 266071, P. R. China

During 2020-2023, Chinese scientists made significant progress in studying eddy-mean flow interactions in the Pacific low-latitude western boundary currents region based on mooring measurements, hydrographic observations and numerical model outputs. Particularly, they revealed the energetics of interaction between meso-scale eddies and the Kuroshio, elucidated the lens-like structures and dynamics of subthermocline eddies east of the Philippines. The major results are introduced as follows:

## **1. Interaction between the Kuroshio and meso-scale eddies**

Mooring measurements east of the Luzon Island confirm the strong interaction between meso-scale eddies and the Kuroshio (Ma et al., 2022). The energetics of the eddy-mean flow interactions along the Kuroshio are further investigated. It is shown that owing to the large horizontal and vertical shears of the Kuroshio, both barotropic and baroclinic instabilities cause intense energy conversions between eddies and the mean current (Yan et al. 2019). The eddy kinetic energy in different parts of the Kuroshio is found to exhibit distinct seasonal cycles, which are governed by various mechanisms (Yan et al. 2023). In addition, for the mesoscale eddies that are originated in the Subtropical Countercurrent region and impinge onto the Kuroshio east of the Taiwan Island, the energy pathways during their decay are revealed (Yan et al. 2022).

## **2. Lens-like structure and dynamics of subthermocline eddies east of the Philippines**

The region east of the Philippine coast is featured with abundant subthermocline eddies. This kind of eddies is different from the traditional surface-intensified eddies.

They generally center below the thermocline, playing crucial roles in the intraseasonal variation of the undercurrents and transport of subsurface waters (Hu et al., 2020).

Hydrographic transects along 8°N reveal lens-like vertical structures of two subthermocline eddies (Song et al. 2022). Both center at about 900m, with isopycnals above the eddy center doming upward and those below depressing downward. The temperature anomalies caused by the two eddies reach about 1°C at the centers. Dynamic and energy diagnosis analysis suggest that the subthermocline eddies are mainly generated locally through the instability progresses of mean flows (Wang et al. 2022). Differing from the traditional view that baroclinic instability dominates the generation of eddies, it is found that barotropic instability is essential in the eddies' generation, the contribution reaches up to 65% in the south part of the Philippine coast (Zhang et al. 2021).

The enhanced subthermocline eddy activities cause significantly high eddy kinetic energy (EKE) east of the Philippine coast between 5°-14°N. Separated by 10°N, the EKE in the northern and southern part displays opposite seasonal cycle. Furthermore, prominent interannual variation of subthermocline EKE is also detected, which seems related to the ENSO events and lags the Nino 3.4 index for about 1 year (Hui et al. 2022). Further instability analysis suggests that the barotropic instability associated with the background currents, such as North Equatorial Undercurrent, Mindanao Undercurrent and Halmahera Eddy, is responsible for the seasonal and interannual variations of subthermocline EKE (Zhang et al., 2021; Hui et al., 2022).

## References

- Hu D., F. Wang, J. Sprintall, L. Wu, S. Riser, S. Cravatte, A. Gordon, L. Zhang, D. Chen, H. Zhou, K. Ando, J. Wang, J. Lee, S. Hu, J. Wang, D. Zhang, J. Feng, L. Liu, C. Villanoy, C. Kaluwin, T. Qu, Y. Ma (2020). Review on observational studies of western tropical Pacific Ocean circulation and climate, *Journal of Oceanology and Limnology*, 38, 4, 906-929, doi:10.1007/s00343-020-0240-1.
- Hui, Y., Zhang, L., Wang, Z., Wang, F., & Hu, D. (2022). Interannual modulation of



- subthermocline eddy kinetic energy east of the Philippines. *Journal of Geophysical Research: Oceans*, 127(5), e2022JC018452. <https://doi.org/10.1029/2022JC018452>
- Ma, J., Hu, S., Hu, D., Villanoy, C., Wang, Q., Lu, X., & Yuan, X. (2022). Structure and variability of the Kuroshio and Luzon Undercurrent observed by a mooring array. *Journal of Geophysical Research: Oceans*, 127, e2021JC017754. <https://doi.org/10.1029/2021JC017754>
- Song, W. Q., Zhang, L. L., & Hu, D. X. (2022). Observed subsurface lens-like features east of the Philippines. *Deep Sea Research Part I*, 190, 103901, <https://doi.org/10.1016/j.dsr.2022.103901>
- Wang, Z., Zhang, L., Hui, Y., Wang, F., & Hu, D. (2022). Two flavors of intraseasonal variability and their dynamics in the North Equatorial Current/Undercurrent region. *Frontiers in Marine Science*, 9, 845575. <https://doi.org/10.3389/fmars.2022.845575>
- Yan, X. M., Kang, D. J., Curchitser, E. N., & Pang, C. G. (2019). Energetics of Eddy–Mean Flow Interactions along the Western Boundary Currents in the North Pacific. *Journal of Physical Oceanography*, 49(3), 789–810, <https://doi.org/10.1175/JPO-D-18-0201.1>
- Yan, X. M., Kang, D. J., Pang, C. G., Zhang, L. L., & Liu, H. W. (2022). Energetics Analysis of the Eddy–Kuroshio Interaction East of Taiwan. *Journal of Physical Oceanography*, 52(4), 647-664, <https://doi.org/10.1175/JPO-D-21-0198.1>
- Yan, X. M., Kang, D. J., Curchitser, E. N., Liu, X. H., Pang, C. G., & Zhang, L. L. (2023). Seasonal variability of eddy kinetic energy along the Kuroshio Current. *Journal of Physical Oceanography* (Accepted)
- Zhang, L. L., Hui, Y. C., Qu, T. D., & Hu, D. X. (2021). Seasonal variability of subthermocline eddy kinetic energy east of the Philippines. *Journal of Physical Oceanography*, 51(3), 685–699. <https://doi.org/10.1175/JPO-D-20-0101.1>

# **Progress of Organic carbon burial in the Western Pacific**

## **Margins research in China from 2020 to 2023**

*Limin Hu*<sup>1,2,3</sup>, *Xueshi Sun*<sup>1</sup>, *Peng Yao*<sup>4</sup>, *Yazhi Bai*<sup>2,3</sup>, *Yuying Zhang*<sup>1</sup>, *Xun Gong*<sup>5</sup>

<sup>1</sup> College of Marine Geosciences, Ocean University of China, Qingdao, China;

<sup>2</sup> Key Laboratory of Marine Geology and Metallogeny, First Institute of Oceanography, MNR, Qingdao, China

<sup>3</sup> Laboratory for Marine Geology, Laoshan Laboratory, Qingdao, China

<sup>4</sup> Key Laboratory of Marine Chemistry Theory and Technology, Ministry of Education, Ocean University of China, Qingdao, China

<sup>5</sup> Institute for Advanced Marine Research, China University of Geosciences, Guangzhou, China.

The past five years have witnessed vigorous efforts made by Chinese scholars to promote the progress of organic carbon burial from the low to the mid-high latitude Northwest Pacific. In this short survey, we will introduce the recent progress with emphases on the modern organic carbon (OC) burial records along these coastal margins of Western Pacific, the long-term records of OC burial and its implications from decadal-millennial to glacial scale. Several suggestions and trends of development are also addressed.

### **Latitudinal OC burial in the tropical and arctic coastal margins**

Recently, Chinese scholars have made a significant progress in marine sediment organic matter (SOM) within tropical and subarctic coastal margin of the western Pacific (the Gulf of Thailand (GoT) and the Bering Sea). In these tropical coastal margins, the seasonal reversal of monsoon climatology modulates precipitation, currents, river influx and a variety of biogeochemical processes, which accelerate the regional soil erosion and promote land-based OM burial<sup>[1]</sup>. In addition, the majority of the terrigenous SOM settles within the estuary in the upper GOT, while a selective dispersal of land-based SOM through long-distance transport toward the modern

depocenter in the lower GOT [2]. These researches reveal the important roles of source variability and the selective dispersal of land-based OM on the supply and accumulation of OC in the tropical coastal margin. While on the high-latitude shelf margin, since the late 1970s, a greater contribution of terrigenous OM was observed under recent warming scenario. The molecular indicator of IP<sub>25</sub> and the phytoplankton marker-IP<sub>25</sub> index (PIP<sub>25</sub>) reflected a decreased sea-ice cover after the late 1970s. There existed a synchronous variability of reduced sea-ice cover with the enhancement of phytoplankton productivity since the late 1970s, suggesting a coupled interaction of the sea-ice condition and marine OC production and burial in the Bering shelf with spatial heterogeneity [3].

### **Preservation and Fate of sediment OC within the East China Seas**

Climate change-triggered episodic and intensive flood events play a disproportionate role in the carbon cycle at land-ocean interfaces. Terrestrial POC delivered by the Yangtze River flood is dominated by C<sub>3</sub> plant detritus, followed by petrogenic OC, and soil. Hydrodynamic sorting of lithogenic particles exerts first-order control on POC by selecting particles with unique signatures. During estuarine mixing, when POC<sub>petro</sub> may be easily oxidized by microbial activity. In contrast, OC-phyllsilicates interactions exert a first-order control on the preservation of OC<sub>petro</sub> in marine sediments [4]. Our findings suggest that the importance of POC<sub>petro</sub> oxidation and loss in carbon cycling and budget assessments of estuaries may be underestimated [5]. In the other hand, the burial efficiencies of OC were mainly controlled by OC reactivity and sediment mixing dynamics. The selective decomposition of younger and more labile marine and terrestrial OC, which resulted in the accumulation of older and more recalcitrant OC in the Yangtze River sediment dispersal system, while in Yellow River sediment dispersal pathway, resulted in more recalcitrant terrestrial OC. The East China marginal sea (ECMS) is an important sink of both petrogenic and biospheric OC over a timescale of ~100 years. However, dam building in river basins has reduced sediment loads of the Yangtze and Yellow Rivers, which will continually decrease OC burial in the ECMS for decades to come [6].

## **Centennial to Millennial burial records of OC in the East China Seas**

Over the past decades, due to the construction of the Three Gorges Dam in 2003, the input of eroded material from the downstream and subaqueous delta of the Yangtze River increased, profoundly altering the local hydrodynamics and sedimentary redox levels, which in turn, could accelerate the degradation of sedimentary OC, preventing OC deposition and preservation <sup>[7]</sup>. The high-resolution sediment footprint of black carbon-materials reveal anthropogenic energy-consumption-based impacts around the Bohai over the past century <sup>[8]</sup>. While on the millennial-scale, we found that the climate change had a threshold effect on the fire regime, and dominated the char emissions in the Holocene. Anthropogenic forces have overwhelmed the natural causes of soot emissions in northern China since ~4 ka BP (Bronze Age). Soot/black-carbon (BC) signals depict the evolution of the ancient Chinese civilization <sup>[9]</sup>.

## **Glacial OC burial in the western Pacific**

The Northwest Pacific (NWP) spans subarctic and subtropical gyre, where long-term OC burial is highly sensitive to the global climate change, under the forcing of diverse ocean circulation systems and Asian monsoon systems in different spatial-temporal evolution patterns <sup>[10]</sup>. The distinct cyclicity of higher OC burial in glacial periods was observed in the Northern Kyushu Ridge <sup>[11]</sup>, which was coupled with the enhanced OC input from the Asian dust and Kuroshio Current, and the better OC preservation of reducing conditions from the complex ocean circulations. In the other hand, glacial OC burial in the NWP exhibits a distribution pattern of “higher in the north/lower in the south”. The OC burial peak in the subarctic gyre region during the last deglaciation may be related to the rich nutrients and primary productivity in the surface, which was mainly controlled by the weakened stratification and enhanced vertical mixing <sup>[12, 13]</sup>. Meanwhile high OC burial in the subtropical gyre region during the last glacial may be associated with increased dust input and relatively reducing bottom waters <sup>[11]</sup>.

## **References**

- [1] Wu Bin, Wu Xiaodan, Shi Xuefa, et al., Influences of tropical monsoon climatology on the delivery and dispersal of organic carbon over the Upper Gulf of Thailand. *Marine Geology*, **426**, doi:10.1016/j.margeo.2020.106209, 2020.
- [2] Bai Yazhi, Hu Limin, Wu Bin, et al., Impact of source variability and hydrodynamic forces on the distribution, transport, and burial of sedimentary organic matter in a tropical coastal margin: The Gulf of Thailand. *Journal of Geophysical Research: Biogeosciences*, **126**, doi:10.1029/2021JG006434, 2021.
- [3] Hu Limin, Liu Yanguang, Xiao Xiaotong, et al., Sedimentary records of bulk organic matter and lipid biomarkers in the Bering Sea: A centennial perspective of sea-ice variability and phytoplankton community. *Marine Geology*, **429**, doi:10.1016/j.margeo.2020.106308, 2020.
- [4] Sun Xueshi, Fan Dejiang, Hu Limin, et al., Oxidation of petrogenic organic carbon in a large river-dominated estuary, *Geochimica et Cosmochimica Acta*, **338**: 136-153, 2022.
- [5] Sun, Xxueshi, Fan Dejiang, Cheng Peng, et al., Source, transport and fate of terrestrial organic carbon from Yangtze River during a large flood event: Insights from multiple-isotopes ( $\delta^{13}\text{C}$ ,  $\delta^{15}\text{N}$ ,  $\Delta^{14}\text{C}$ ) and geochemical tracers. *Geochimica et Cosmochimica Acta*, **308**: 217-236, 2021.
- [6] Zhao Bin, Yao Peng, Li Dong, et al., Effects of river damming and delta erosion on organic carbon burial in the Changjiang Estuary and adjacent East China Sea inner shelf, *Science of The Total Environment*, 793, doi:10.1016/j.scitotenv.2021.148610, 2021
- [7] Sun, Xxueshi, Fan Dejiang, Liu Ming, et al., The fate of organic carbon burial in the river-dominated East China Sea: Evidence from sediment geochemical records of the last 70 years, *Organic Geochemistry*, **143**, doi:10.1016/j.orggeochem.2020.103999, 2020.
- [8] Chen Bin, Hu Limin, Liu Jihua, et al., High-resolution depositional records of lead isotopes and polycyclic aromatic hydrocarbons in the Bohai Sea, China: Implications for a sediment footprint of anthropogenic impact. *Marine Geology*, **432**: doi:10.1016/j.margeo.2020.106396, 2021.
- [9] Sun Xiang, Hu Limin, Hu Bangqi, et al., Remarkable signals of the ancient Chinese civilization since the Early Bronze Age in the marine environment, *Science of The Total Environment*, 804, doi:10.1016/j.scitotenv.2021.150209, 2022.



- [10] Li Z, Zhang Y, Torres M, et al., Neogene burial of organic carbon in the global ocean. *Nature*, **613**(7942): 90-95, 2023.
- [11] Zhang Yuying, Hu Limin, Wu Yonghua, et al., Glacial-Interglacial Variations in Organic Carbon Burial in the Northwest Pacific Ocean Over the Last 380 kyr and its Environmental Implications. *Frontiers in Earth Science*, **10**, doi: 10.3389/feart.2022.886120, 2022.
- [12] Liu Yanguang, Qiu Yue, Li Donging, et al., Abrupt fluctuations in North Pacific Intermediate Water modulated changes in deglacial atmospheric CO<sub>2</sub>. *Frontiers in Marine Science*, **9**, doi:10.3389/fmars.2022.945110, 2022.
- [13] Yao Zhengquan, Liu Yanguang, Shi Xuefa, et al., Paleoproductivity variations and implications in the subarctic northwestern Pacific since MIS 7: Geochemical evidence. *Global and Planetary Change*, **209**, doi:10.1016/j.gloplacha.2021.103730, 2022.

# Progress of internal Solitary Waves Research in China from 2020 to 2023

*Yuan Chunxin<sup>1</sup>, Gong Yankun<sup>2</sup>*

<sup>1</sup> School of Mathematical Sciences, Ocean University of China, Qingdao 266100, P. R. China

<sup>2</sup> State Key Laboratory of Tropical Oceanography, South China Sea Institute of Oceanology,  
Chinese Academy of Sciences, Guangzhou 510301, P. R. China

On the progress of internal solitary waves (ISWs) in the China Sea, massive works have been done and reviewed by Chinese scientists from 2020 to 2023. In this report, these efforts are summarized on the basis of four investigation approaches, namely, remote sensing images, in situ measurements, numerical simulations and theoretical models.

Two different kinds of remote sensing approaches were commonly applied to capture ISWs in the CS. The one is synthetic aperture radar (SAR). Jia et al. (2021) demonstrated the generation of shoreward ISWs on the continental shelf south of the Hainan Island in the South China Sea (SCS) might be originated from the Xisha Island. In addition to the SCS, Liu et al. (2022) revealed the evidence and characteristics of ISWs in the northern Yellow Sea via SAR. Moreover, according to Sentinel-1 SAR Imagery, a global internal wave dataset was proposed and verified to better detect ISWs (Tao et al., 2022). The other approach is MODIS sensors. Based on considerable numbers of MODIS images, Zhang et al. (2022) detected significant reflection phenomenon of ISWs near the continental shelf of the Dongsha Atoll in the norther SCS and quantitatively estimated the reflection coefficient (~60 %).

With the development of field instruments, in-situ observations gradually became one of the essential methods in understating ISWs. An extreme mode-1 ISW with peak horizontal velocity of 2.94 m/s and vertical velocity of 0.63 m/s was first observed in the vicinity of the Dongsha Atoll (Xu and Chen, 2021). Nearby, Xu et al. (2020) observed the interaction process of ISWs and an anti-cyclonic eddy and Wu et al. (2023)

indicated the asymmetric chlorophyll responses enhanced by ISWs. In addition to mode-1 ISWs, mode-2 ISWs with a re-appearance period of 24.9 h were also observed in the SCS (Chen et al., 2020), which were related to diurnal internal tides. Shoaling and convective breaking processes of ISWs were clearly observed at three mooring sites over the upper continental slope in the northern SCS (Chang et al., 2021; Chang, 2021). Apart from traditional moorings, some acoustic instruments were recently applied to investigate ISWs in the SCS, e.g., seismic data acquisition (Gong et al., 2021) and acoustic backscatter data (Feng et al., 2021).

It is evident that the capabilities of numerical simulations, in particular three-dimensional (3D) model, have been substantially improved in recent years. Based on a two-dimensional (2D) model, evolution and propagation processes of ISWs on the typical slope-shelf topography were numerically investigated with varying initial amplitude, seasonal stratification and topographic characteristics (Wang et al., 2020). From the perspective of a 3D model, numbers of non-hydrostatic high-resolution model with realistic initial and boundary conditions were developed over the past five years, including unstructured-grided FVCOM (Jin et al., 2021), ORCTM (Huang et al., 2023), and MITgcm (Gong et al., 2023). It worth mentioning that they all showed well performance in predicting wave properties of ISWs in the northern SCS. On the basis of numerical simulation, southern East China Sea was confirmed as a generation source of ISWs as well (Min et al., 2021).

To understand ocean dynamics, the theoretical models are very important and powerful tool, nevertheless, most of the theories are for 2D internal waves, such as the celebrated Korteweg–de Vries (KdV) equation and its numerous variants, the Benjamin–Ono (BO) equation, and the Miyata–Choi–Camassa (MCC) equation etc.. For 3D internal waves, the Kadomtsev–Petviashvili (KP) equation is usually used. However, two shortcomings - unidirectional propagation and anisotropy - limit its application in some general cases. To tackle these difficulties, Yuan et al. (2020) and Yuan and Wang (2023) derived an isotropic and bidirectional model, the modified Benney–Luke (mBL) equation. Comparisons between the MITgcm model confirm the

accuracy of the mBL equation over the classical KP equation.

## References:

- Chang, M. H. (2021). Marginal instability within internal solitary waves. *Geophysical Research Letters*, 48(9), e2021GL092616.
- Chang, M. H., Lien, R. C., Lamb, K. G., & Diamessis, P. J. (2021). Long-term observations of shoaling internal solitary waves in the northern South China Sea. *Journal of Geophysical Research: Oceans*, 126(10), e2020JC017129.
- Chen, L., Xiong, X., Zheng, Q., Yuan, Y., Yu, L., Guo, Y., ... & Hui, Z. (2020). Mooring observed mode-2 internal solitary waves in the northern South China Sea. *Acta Oceanologica Sinica*, 39, 44-51.
- Feng, Y., Tang, Q., Li, J., Sun, J., & Zhan, W. (2021). Internal solitary waves observed on the continental shelf in the northern south China Sea from acoustic backscatter data. *Frontiers in Marine Science*, 8, 734075.
- Gong, Y., Chen, X., Xu, J., Xie, J., Chen, Z., He, Y., & Cai, S. (2023). An internal solitary wave forecasting model in the northern South China Sea (ISWFM-NSCS). *Geoscientific Model Development*, 16(10), 2851-2871.
- Gong, Y., Song, H., Zhao, Z., Guan, Y., & Kuang, Y. (2021). On the vertical structure of internal solitary waves in the northeastern South China Sea. *Deep Sea Research Part I: Oceanographic Research Papers*, 173, 103550.
- Huang, H., Song, P., Qiu, S., Guo, J., & Chen, X. (2023). A nonhydrostatic oceanic regional model, ORCTM v1, for internal solitary wave simulation. *Geoscientific Model Development*, 16(1), 109-133.
- Jia, T., Liang, J., Li, Q., Sha, J., & Li, X. M. (2021). Generation of shoreward nonlinear internal waves south of the Hainan Island: Synthetic aperture radar observations and numerical simulations. *Journal of Geophysical Research: Oceans*, 126(6), e2021JC017334.
- Jin, G., Lai, Z., & Shang, X. (2021). Numerical study on the spatial and temporal characteristics of nonlinear internal wave energy in the Northern South China sea. *Deep Sea Research Part I: Oceanographic Research Papers*, 178, 103640.

- Liu, H., Yang, W., Wei, H., Jiang, C., Liu, C., & Zhao, L. (2022). On characteristics and mixing effects of internal solitary waves in the northern Yellow Sea as revealed by satellite and in situ observations. *Remote Sensing*, *14*(15), 3660.
- Min, W., Li, Q., Xu, Z., Wang, Y., Li, D., Zhang, P., ... & Yin, B. (2023). High-resolution, non-hydrostatic simulation of internal tides and solitary waves in the southern East China Sea. *Ocean Modelling*, *181*, 102141.
- Tao, M., Xu, C., Guo, L., Wang, X., & Xu, Y. (2022). An Internal Waves Data Set From Sentinel-1 Synthetic Aperture Radar Imagery and Preliminary Detection. *Earth and Space Science*, *9*(12), e2022EA002528.
- Wang, S., Meng, J., Li, Q., & Chen, X. (2020). Evolution of internal solitary waves on the slope-shelf topography in the northern South China Sea. *Ocean Dynamics*, *70*, 729-743.
- Wu, M., Xue, H., & Chai, F. (2023). Asymmetric chlorophyll responses enhanced by internal waves near the Dongsha Atoll in the South China Sea. *Journal of Oceanology and Limnology*, *41*(2), 418-426.
- Xu, A., & Chen, X. (2021). A strong internal solitary wave with extreme velocity captured northeast of Dong-Sha atoll in the northern South China Sea. *Journal of Marine Science and Engineering*, *9*(11), 1277.
- Xu, J., He, Y., Chen, Z., Zhan, H., Wu, Y., Xie, J., ... & Cai, S. (2020). Observations of different effects of an anti-cyclonic eddy on internal solitary waves in the South China Sea. *Progress in Oceanography*, *188*, 102422.
- Yuan, C., Wang, Z. & Chen, X. (2020) The derivation of an isotropic model for internal waves and its application to wave generation, *Ocean Modelling* *153*, 101663.
- Yuan, C. & Wang, Z. (2022) On diffraction and oblique interactions of horizontally two-dimensional internal solitary waves, *Journal of Fluid Mechanics* *936*, A20.
- Zhang, H., Meng, J., Sun, L., & Li, S. (2022). Observations of Reflected Internal Solitary Waves near the Continental Shelf of the Dongsha Atoll. *Journal of Marine Science and Engineering*, *10*(6), 763.



# Progress of Seismic Oceanography Studies in China from 2020 to 2023

*Lei Xing, Yuzhao Lin, Huaishan Liu*

Ocean University of China, Qingdao 266100, P. R. China

Between 2020 and 2023, Chinese scientists have made significant progress in using seismic data to study the ocean, and their research results are good evidence that seismic detection has become one of the new vital tools for studying the ocean. The research interests extend from the Pacific and Indian Oceans to the global oceans, and some of the research has received significant attention worldwide. Representative results are as follows.

## **1. Observation of fine-scale and unique water columns**

Since 2004, when Papia Nandi et al. (2004) used seismic data collected in the Norwegian Sea to accurately invert water boundaries and temperature gradients, demonstrating the effectiveness and high accuracy of seismic oceanography, many Chinese scholars have carried out various studies. A significant advantage of seismic oceanography is that it can achieve large-scale real-time observation of all scale water bodies in the ocean.

Accurate imaging of short-lived anticyclonic eddy in the northern Gulf of Alaska based on multichannel seismic data is achieved by Tang et al. (2020). This fine-scale observation confirmed the existence of a strongly tilted eddy. The high-resolution spatial diapycnal diffusivity reveals that the strongest turbulence for this asymmetric eddy occurs in the ambient water not far from the eddy, instead of the eddy center or the frontal zone. Meanwhile, the high spectrum level in the internal wave subrange of the frontal zone implies that the frontal zone rather than the eddy center is the internal wave excitation source under the mechanism of eddy decaying to internal waves. The result also suggest that the shortened life span of this eddy was in part the result of the irregular vortex structure that may reduce the structural stability, facilitate energy

conversion, and accelerate the eddy dissipation.

Zhang et al., (2022) combined multichannel seismic and ADCP data to accurately identify 23 mesoscale salt oblique vortices in the western Arctic Ocean Chukchi region, including 4 cyclone vortices and 19 anticyclonic vortices. Vortices' distribution and structural parameters were determined by seismic images, indicating that vortices were mainly distributed in areas with severe topographic changes, such as near seamounts and on both sides of the north wind ridge. Based on the seismic profile, combined with CTD data and synchronous XBT data, the upper and lower edges of the vortex are strongly reflected, corresponding to the strong temperature and sound velocity changes at the vortex edge. The interior of the vortex nucleus is almost blank or shows medium weak horizontal reflection, corresponding to the relatively uniform temperature structure or slow change of the temperature structure inside the vortex nucleus.

## **2. Inversion of water physical parameters**

In addition, seismic data can achieve high-resolution physical parameter inversion of the target medium, which is essential for ocean observation. Especially due to the characteristics of high-resolution and large-scale observation of multichannel seismic, it can accurately reflect various scales and parameters of the ocean.

Tang et al., (2021,2022) quantifies the diapycnal diffusivity of the sub-thermocline (300-1200 m depth) turbulence around Mariana Ridge based on the seismic image. The auto-tracked wavefields on seismic images can be used to derive the dissipation rate and diapycnal diffusivity based on the Batchelor model, which relates to the horizontal slope spectra. A strong agreement between the dissipation results between seismic observation and numerical simulation is found for the first time. Such an agreement confirms the suitability of the seismic method in turbulence quantification. It suggests the energy cascade from large-scale tides to small-scale turbulence via possible mechanisms of local direct tidal dissipation and near-local wave-wave. Fan et al., (2021) used seismic oceanographic methods to discover the first isolated wave complex in the second mode on the Pacific coast of Central America. By observing the change of the fine structure of the isolated complex in the second mode, it is found that the second

modal isolated wave located on the land slope reflects the inverting axial bifurcation, merging, and the depth of the center depth of the dense cline during the acquisition process of about 50s, which is speculated to be caused by the instability of the seawater layer here. Moreover, the propagation velocity of the internal solitary wave calculated by the KdV equation is the same as that of seismic oceanographic methods.

Gong et al., (2021) used seismic data to observe the vertical structure of internal waves. It was found that the shape of vertical structures is mainly determined by nonlinearity. A linear vertical structure function can describe a vertical structure with low nonlinearity. In contrast, an ISW with a high degree of nonlinearity conforms to a first-order nonlinear vertical structure function. The final analysis shows that nonlinearity dominates the vertical structure; Terrain, ISW amplitude, water depth, and background flow can all affect the vertical structure.

### **3. Observation of sub-seafloor structures and fluid-solid interface**

Furthermore, seismic is not only the detection of water columns but also the reflection information of subseafloor strata, which can carry out researches of the impact of seafloor structures on water columns and the exchange of materials at the fluid-solid interface.

Based on seismic and bathymetric data, Yin et al., (2021) describes a major shift in the NPSG paleo circulation. These data outline two contour sedimentary systems, one burial system formed in the late Miocene and the other formed in the late Miocene to the present. These two regions are separated by a major regional discontinuity representing a significant shift in the late Miocene (~6.5Ma) paleo circulation.

### **4. Time-lapse Observation**

It is noted that seismic detection originated from the detection of underground oil and gas reservoirs and has developed into a very mature industrial process. Zou et al., (2021) conducted a 6-month industrial oil and gas exploration of the ocean, especially water bodies, in the Gulf of Mexico, and obtained high-precision three-dimensional multichannel seismic survey data, resulting in a three-dimensional marine seismic image. The three-dimensional seismic image shows that the temporal variation in the

direction of the crossline direction is more pronounced than the temporal change in the straight line, resulting in a discontinuity of the crossline image. However, a series of 3D inline images can be seen as snapshots of water columns at different times, capturing temporal changes in thermohaline structures caused by ocean dynamics.

## 5. Overview

Finally, Song et al. (2021) published an overview summarizing the development of seismic oceanography over the past 20 years, which has received widespread attention from the industry.

## References

- Fan, W., Song, H., Yi, G., Sun, S., Zhang, K., Wu, D., Kuang, Y., & Yang, S. (2020). The shoaling mode-2 internal solitary waves in the Pacific coast of Central America investigated by marine seismic survey data. *Continental Shelf Research*, 212, 104318. <https://doi.org/10.1016/j.csr.2020.104318>
- Fan, W., Song, H., Zhang, K., Hsu, H., Yi, G., & Sun, S. (2020). Seismic oceanography study of internal solitary waves in the northeastern South China Sea Basin. *Chinese Journal of Geophysics- Chinese Edition*, 63, 2644-2657. <https://doi.org/10.6038/cjg2020N0358>
- Fan, W., Song, H., Yi, G., Zhang, K., & Sun, S. (2021). Seismic oceanography study of mode-2 internal solitary waves offshore Central America. *Chinese Journal of Geophysics- Chinese Edition*, 64, 195-208. <https://doi.org/10.6038/cjg2021O0071>
- Gong, Y., Song, H., Zhao, Z., Guan, Y., & Kuang, Y. (2021). On the vertical structure of internal solitary waves in the northeastern South China Sea. *Deep Sea Research Part I: Oceanographic Research Papers*, 173, 103550. <https://doi.org/https://doi.org/10.1016/j.dsr.2021.103550>
- Gunn, K. L., White, N., & Caulfield, C.-c. P. (2020). Time-Lapse Seismic Imaging of Oceanic Fronts and Transient Lenses Within South Atlantic Ocean. *Journal of Geophysical Research: Oceans*, 125(7), e2020JC016293. <https://doi.org/https://doi.org/10.1029/2020JC016293>
- Nandi, P., Holbrook, W. S., Pearse, S., Páramo, P., & Schmitt, R. W. (2004). Seismic reflection

- imaging of water mass boundaries in the Norwegian Sea. *Geophysical Research Letters*, 31(23). <https://doi.org/10.1029/2004GL021325>
- Song, H., Chen, J., Pinheiro, L. M., Ruddick, B., Fan, W., & Gong, Y., et al. (2021). Progress and prospects of seismic oceanography. *Deep Sea Research Part I: Oceanographic Research Papers*, 177, 103631
- Tang, Q., Gulick, S. P. S., Sun, J., Sun, L., & Jing, Z. (2020). Submesoscale Features and Turbulent Mixing of an Oblique Anticyclonic Eddy in the Gulf of Alaska Investigated by Marine Seismic Survey Data. *Journal of Geophysical Research: Oceans*, 125(1), e2019JC015393. <https://doi.org/10.1029/2019JC015393>
- Tang, Q., Jing, Z., Li, J., & Sun, J. (2022). Enhanced Diapycnal Mixing in the Deep Ocean Around the Island of Taiwan. *Journal of Geophysical Research: Oceans*, 127(5), e2021JC018034. <https://doi.org/10.1029/2021JC018034>
- Tang, Q., Jing, Z., Lin, J., & Sun, J. (2021). Diapycnal Mixing in the Subthermocline of the Mariana Ridge from High-Resolution Seismic Images. *Journal of Physical Oceanography*, 51(4), 1283-1300. <https://doi.org/10.1175/JPO-D-20-0120.1>
- Yang, S., Song, H., Coakley, B., Zhang, K., & Fan, W. (2022). A Mesoscale Eddy with Submesoscale Spiral Bands Observed From Seismic Reflection Sections in the Northwind Basin, Arctic Ocean. *Journal of Geophysical Research: Oceans*, 127(3), e2021JC017984. <https://doi.org/10.1029/2021JC017984>
- Yin, S., Hernández-Molina, F. J., Lin, L., Chen, J., Ding, W., & Li, J. (2021). Isolation of the South China Sea from the North Pacific Subtropical Gyre since the latest Miocene due to formation of the Luzon Strait. *Scientific Reports*, 11(1), 1562. <https://doi.org/10.1038/s41598-020-79941-4>
- Zhang, K., Song, H., Coakley, B., Yang, S., & Fan, W. (2022). Investigating Eddies from Coincident Seismic and Hydrographic Measurements in the Chukchi Borderlands, the Western Arctic Ocean. *Journal of Geophysical Research: Oceans*, 127(10), e2022JC018453. <https://doi.org/10.1029/2022JC018453>
- Zou, Z., Bakhtiari Rad, P., Macelloni, L., & Zhang, L. (2021). Temporal and spatial variations

in three-dimensional seismic oceanography. *Ocean Sci.*, 17(4), 1053-1066.  
<https://doi.org/10.5194/os-17-1053-2021>



**2019-2022**  
**China National Report on**  
**Seismology and Physics of Earth's Interior**

For

28<sup>th</sup> IUGG General Assembly  
Berlin, German, July 11-20, 2023

Prepared by Chinese National Committee  
For International Association of Seismology and Physics of  
Earth's Interior (CNC-IASPEI)

July 3, 2023

# Contents

Preface .....	3
1. China Seismic Experimental Site (CSES): A systems engineering perspective.....	4
1.1 Introduction .....	4
1.2 The scientific agenda.....	5
1.3 The system metaphor .....	7
1.4 System performance evaluation (SPE) and system design.....	9
1.5 Discussion with(out) conclusions .....	10
2. Introduction to China's Earthquake Emergency Response System .....	15
2.1 Introduction .....	15
2.2 Emergency Automated Response System (EARS) .....	16
2.3 Emergency duty system .....	23
2.4 Earthquake Emergency Work System .....	25
2.5 Discussion and conclusions .....	30
3. Crust and upper mantle structure of East Asia from ambient noise and earthquake surface wave tomography.....	35
3.1 Introduction .....	35
3.2 Data .....	38
3.3 Methods .....	39
3.4 Results .....	42
3.5 Discussion.....	51
3.6 Conclusions .....	55
4. Crustal velocity, density structure, and seismogenic environment in the southern segment of the North-South Seismic Belt, China .....	69
4.1 Introduction .....	70
4.2 Data and methods.....	72
4.3 Analysis of inversion uncertainty .....	77
4.4 Results and discussion.....	82
4.5 Conclusions .....	90

# Preface

This report presents the progress of research and development on seismology and the physics of Earth's interior during the past four years. It is to be submitted, on behalf of the Chinese National Committee for International Association of Seismology and Physics of Earth's Interior (CNC-IASPEI), to the IASPEI General Assembly at the 28<sup>th</sup> IUGG General Assembly to be held in Berlin, German, July 11-20, 2023.

The report includes the following contents:

1. China Seismic Experimental Site: A systems engineering perspective
2. China's Earthquake Emergency Response System
3. Crust and upper mantle structure of East Asia from seismic tomography
4. Crustal velocity, density structure in the North-South Seismic Belt, China

It is hoped that this national report would be of help Chinese scientists in exchanging the results and ideas in the research, development and application of seismology and physics of Earth's interior with scientists all over the world.

The contents of report are taken from the journal "Earthquake Science". Colleagues listed bellow made their contribution for this national report (in alphabetical order):

BAO Xuewei, GUO Lianghai, LI Li, LI Mengkui, LI Jiangtao, LIANG Jianhong, LIU Jie, SHI Hongbo, SONG Xiaodong, SUN Xun, XI Nan, YANG Jingqiong, WU Zhongliang, YANG Zhigao.

Prof. DING Zhifeng

President of CNC-IASPEI

# 1. China Seismic Experimental Site (CSES): A systems engineering perspective

Zhongliang Wu\*

(Institute of Earthquake Forecasting, China Earthquake Administration, Beijing 100036, China)

**Abstract:** China Seismic Experimental Site (CSES) deals with a long-term process of development of a multidisciplinary technical system. In the construction, maintenance, and upgrading of CSES, ideas of systems engineering play an important role. This article discusses several concepts which might be useful for CSES, including system metaphor, system performance evaluation, and system design.

## 1.1 Introduction

China Seismic Experimental Site (CSES), a continuation and extension of the West Yunnan Earthquake Prediction Experiment Site (1980-) and the Sichuan-Yunnan National Experimental Site for Earthquake Monitoring and Prediction (2014-2018), has raised much attention since its inauguration in 2018 (CSES, 2020a, b; Wu ZL, 2020a; Wu ZL et al., 2021). Comparing to the experimental sites or natural laboratories in other countries, for example, the Parkfield earthquake prediction experiment (Bakun and Lindh, 1985; Roeloffs and Langbein, 1994; Roeloffs, 2000), the Turkish dilatancy project (TDP, Evans et al., 1987), the Tokai earthquake prediction experiment (Mogi, 2004), and the Southern California Earthquake Center (SCEC), CSES emphasizes design and planning in its organization.

It has been recently proposed that seismic experimental site, a natural laboratory for interdisciplinary study on the predictability of earthquakes and reduction of earthquake disaster risk, can be regarded as<sup>1</sup> a ‘system of systems’ (Jordan, 2006, 2009, 2014). Meanwhile, systems engineering perspective plays an important role in the planning, deployment, functioning, maintenance, and upgrading of interdisciplinary systems related to Earth science, such as the system for monitoring and verifying a Comprehensive Test Ban Treaty (CTBT), characterized by multidisciplinary nature and needs for life-cycle management (Wu ZL and Richards, 2011). Such ideas may shed light on the design and planning of CSES.

---

\* [DOI] 10.29382/eqs-2021-0006

## 1.2 The scientific agenda

Prediction is one of the central agenda of CSES. The CSES system consists of the subsystems of long-to-intermediate term earthquake prediction, short-to-imminent term earthquake prediction, prediction of induced/triggered earthquakes, prediction of seismic strong ground motion, and prediction of seismic disasters and secondary disasters. The cutting-edge development of earthquake science and technology provides CSES with good opportunities to carry out field experiments for testing or falsifying scientific hypotheses related to the important scientific agenda such as stress transfer from large (plate boundary) to small (fault) scale, stress mediated fault interactions, evolution of fault resistance during seismic slip, structure and evolution of fault zones and fault systems, and causes and effects of transient deformations (using the language of SCEC). Articles in this special issue provides the hypothesis testing with case examples.

Figure 1.1 is a conceptual diagram of the scientific agenda of CSES. Logically different predictions are interconnected to each other, as shown by the red lines in the figure. At present time there are still difficulties in the connection between long-to-intermediate term earthquake prediction and short-to-imminent term earthquake prediction. As an alternative approach, through the earthquake scenario approach, prediction of strong ground motion can still be connected to long-to-intermediate term earthquake prediction and contribute to the reduction of earthquake disaster risk. The figure also shows an important concept represented by the words and boxes in blue, that is, to tackle the problem of earthquake prediction, especially short-to-imminent term earthquake prediction, a combination strategy is taken that combines field laboratory approach to carry out in-situ experiments, physical or in-house laboratory approach to carry out laboratory experiments, and numerical/digital laboratory approach to carry out numerical experiments for simulation and/or data mining. Besides, recent developments of data science and new technology provide CSES with new opportunities of scientific and technological breakthrough. The potential of the application of artificial intelligence (AI) techniques is especially noticeable.

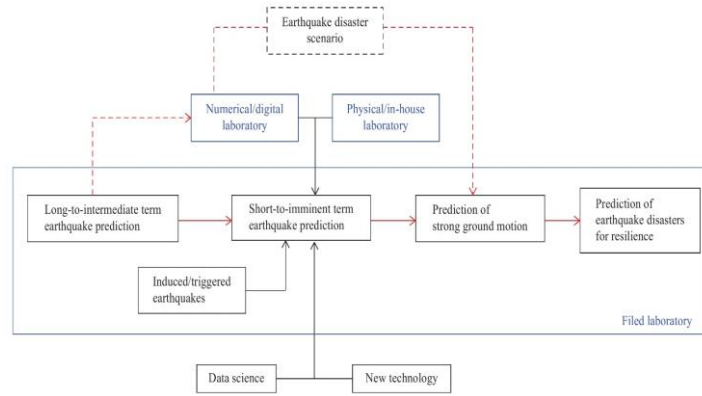


**Fig. 1.1 Conceptual system diagram of the scientific agenda of CSES**

### **1.2.1 Long-to-intermediate term earthquake prediction: the last mile**

Defining the physical basis of earthquake prediction is one of the dreams of earthquake science (Scholz et al., 1973). Up to now, for long-to-intermediate term earthquake prediction, such a dream has been reaching the ‘last mile’ of realization (Barbot et al., 2012; Kato and Ben-Zion, 2021; Working Group on Forecasting Researches on Earthquake Risk Regions and Disaster Loss of Chinese Mainland During 2016 – 2025, 2020). For CSES the scientific goal is the dual ‘last mile’, that the ‘last mile’ of tracking the stress transfer from the boundaries of the Indian plate and the Eurasian plate to a specific fault in Sichuan and Yunnan, and the ‘last mile’ of implementing the physics-based prediction of strong earthquakes. Similar to the SCEC approach (Field et al., 2014), one of the core products of CSES designed is the unified forecast of earthquake ruptures in Sichuan and Yunnan region, with the community models (of faults, velocity structure, rheology, and stress) as inputs. Remarkably, the experiment along the eastern boundary of the ‘Sichuan-Yunnan Diamond’, from the north to the south including the Xianshuihe, Anninghe, Zemuhe, Daliangshan, and Xiaojiang fault, considers the strike-slip faults in different stages of an earthquake cycle. This is similar to the strategy in astronomy in studying the lifecycle of stars, and makes CSES unique not only in geography but also in science.

### **1.2.2 Short-to-imminent term earthquake prediction: the first mile**

Short-to-imminent term earthquake prediction remains a difficult problem. Within the next decade it cannot be envisaged that CSES will be able to solve this problem. However, CSES may push the realization of the ‘first mile’ in this direction, that in CSES the potential precursors are to be considered not only by phenomenology but also by physics. When the word ‘physics’ is used here, it means physical concepts, physical models, and physical observations to constrain the models. It should be noted that traditional earthquake prediction experiment sites (such like the West Yunnan Earthquake Prediction Experiment Site) focused on the testing of earthquake precursors.



This direction will be continuing in CSES, while more physics will be introduced. One of the conditions for such a development is based on the new advancement of observations, in which the precision of monitoring the temporal variation dramatically enhanced (e.g., Niu FL et al., 2008; Chao K and Peng ZG, 2009; Audet, 2010). As a matter of fact, focusing on ‘targeted’ earthquakes by densely deployed observations with the reference of physical model/s is one of the distinguishing features of CSES different from the traditional approaches carried out in China Earthquake Administration (CEA) for the past decades.

### **1.2.3 Prediction of strong ground motion**

Even if short-to-imminent term earthquake prediction cannot be realized within a limited time, reduction of seismic disaster risk can still be promoted by CSES through the prediction of strong ground motion by earthquake rupture scenarios. In fact, a general understanding of time-dependent seismic hazard assessment may provide new horizon of earthquake prediction (Marzocchi, 2018; Wu ZL, 2020b). CSES also has the mission of implementing ‘the first mile’ to combine earthquake prediction with the prediction of strong ground motion.

The dual last mile of long-to-intermediate term earthquake prediction, the first mile of physics-based short-to-imminent term earthquake prediction, and the first mile of the combination of earthquake prediction with strong ground motion prediction define the Earthquake Prediction 2.0, kernel output of CSES.

## **1.3 The system metaphor**

System metaphor (Flood and Jackson, 1991) plays an important role in the ‘total systems intervention’. Flood and Jackson (1991) proposed several optional system metaphors, in which the most relevant options to CSES include: (1) machine metaphor, or closed system view; (2) organic metaphor, or open system view; and (3) neuro-cybernetic metaphor, or viable system view. Depending on the problems subject to discussion, system metaphor of CSES have different options. Or exactly speaking, CSES itself has different aspects to consider in its development. Figure 1.2 provides a descriptive picture of CSES. Comparing to the ‘standard/professional’ system representations in systems engineering, this is only a rough and preliminary representation. In the first order, the whole experimental site can be divided into two parts: the experimental system, and the supporting system. Within the field laboratory, observation network (including both permanent and temporary) produces data of different disciplines. Through the analysis by a combination of field laboratory, in-house laboratory, and numerical laboratory, data products are produced as the output of the system. Predictions play an essential role for the advice on the countermeasures for

resilience. Three kinds of system metaphors can all be used for CSES, albeit emphasizing different aspects, as marked approximately by the words in red.

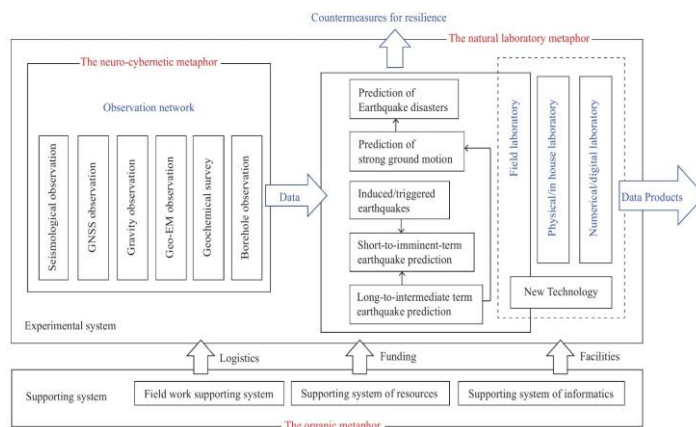


**Fig. 1.2 A descriptive picture of CSES**

### 1.3.1 The neuro-cybernetic metaphor

The first useful system metaphor is the neuro-cybernetic system, mainly corresponding to the observation network. Indeed CSES consists of distributed observations in different disciplines from different research institutions. All these distributed observations form the sensing system of CSES which is similar to a neuro-network. Different from other scientific infrastructures such as accelerators in high-energy physics or telescope in astronomy, the importance of a single observational site in CSES is expressed by a percolation-like process, that eliminating a single observational site may have little effect on the performance of the whole sensing system, but when the ratio of such eliminated sites increases to a critical point, the whole system will change completely.

### 1.3.2 The natural laboratory metaphor

The second useful system metaphor is a natural laboratory. Besides observation, laboratory experiments, theoretical modeling and numerical simulation, in-situ experiments have been playing an important role in earthquake science. In the history of seismology, some paradoxes, such as the heat flux paradox (e.g., Lachenbruch et al., 1995; Mora and Place, 1998), were recognized and resolved by field experiments, or exactly speaking, the combination of laboratory and field experiments. Strengthening the concept of natural laboratory is important at the present time in China, since in the recent decade, with the implementation of the national policy of innovation, more and more research teams ‘emerged’ in different universities in China. The configuration of Chinese research institutions of earthquake science is to some extent similar to that in America and Europe. This trend of development calls for a mechanism of data sharing (similar to IRIS) and research coordination similar to SCEC. An important

mission of CSES is to provide colleagues, both in China and abroad, with backbone (observational facilities), background (information for further studies), and baseline (for testing the variations with a shorter time scale). Such b<sup>3</sup> mission (i.e., backbone, background, and baseline) is the basic requirement for a natural laboratory.

### **1.3.3 The organic metaphor**

In the perspective of the sustainability of CSES, a useful system metaphor is an organic system. In a long time scale and broader range, CSES has to consider its ecology of scientific resources. In the planning of CSES for implementing its scientific goals, a wide range of scientific resources has to be taken into account, which includes but not limited to the National Natural Science Foundation of China (NSFC), the State Key R&D Project, the basic research funds of the national non-profit institutions, the funds for equipment and infrastructures, the funds for personnel and laboratory, and the local/industrial R&D resources, among others. All these resources form an ‘ecology’ which facilitates the development of CSES.

## **1.4 System performance evaluation (SPE) and system design**

Systems engineering focuses on how to design, integrate, and manage complex systems over their life cycles, utilizing systems thinking principles. The outcome of such efforts, an engineered system, can be defined as a combination of components that work in synergy to collectively perform a useful function. A holistic and interdisciplinary view plays the central role in systems engineering (e.g., Flood and Jackson, 1991).

As an analogue, construction and operation of CSES can get useful hint from neighboring fields such like the monitoring and verification system of a Comprehensive Test Ban Treaty (CTBT), which require an international observational system composed of observational stations, communication links from the stations to data center/s, and tools for the analysis of signals recorded for verification purposes. The evaluation and design of the monitoring and verification system from the perspective of systems engineering is one of the significant advances in recent years in this field.

In the perspective of systems engineering, evaluation is to assess the readiness and capability of a system, while design is to plan the road-map to ensure the expected readiness and capability. Design and evaluation of CSES as a system include three perspectives:

(1) Physical Perspective. Observation stations, data centers, supporting and maintenance centers, communication links, and system for the automatic data

processing, database, and data sharing devices.

(2) Functional Perspective. Data transmission, automatic data processing and interpretation, data analysis and data products, and routine evaluation of the state-of-health of the system.

(3) Operational Perspective. Design, implementation, management, utilization, evaluation, and upgrading of the whole system.

Somehow interesting is that the three system metaphors and the three perspectives have some correspondence, that the physical perspective corresponds to the neuro-cybernetic metaphor, the functional perspective corresponds to the natural laboratory metaphor, and the operational perspective corresponds to the organic metaphor.

It may be unnecessary for CSES to directly copy the concepts and tools of systems engineering. However, methodologies such as specification of the system and its components as well as the relationships among the components, specification of the functions of the system and decomposition of system functional requirements into component functional requirements, and development of measures of performance at system level and component level, respectively, provide a clear concept for the ‘evolution’ of CSES.

In the design of the observational system, geographic and seismic factors play an important role, since by its nature, CSES has the feature of ‘playing games’ (in the sense of game theory, see e.g., Wu ZL, 2014) with earthquakes. Humans were not successful in the past: earthquakes tend to occur in the ‘unexpected’ place or at the ‘unexpected’ time, such as the 1989 Loma Prieta earthquake in the period of the Parkfield experiment, and the 1996 Lijiang earthquake in the period of the western Yunnan earthquake prediction experiment. Dealing with such a ‘game’, a tactic solution is to treat ‘gray rhino’ (Wucker, 2016) firstly, and to consider ‘black swan’ secondly, that is, deployment of the experimental/observational/monitoring system put the seismic risky regions identified (Working Group on Forecasting Researches on Earthquake Risk Regions and Disaster Loss of Chinese Mainland During 2016 - 2025, 2020) as the first priority. Meanwhile, a strategic solution is to consider coordinated distributed experiments (CDEs, Fraser et al., 2013; Wu ZL et al., 2019) so that CSES has the capability to respond and contribute in case that earthquakes occur out of the spatial range of CSES.

## **1.5 Discussion with(out) conclusions**

Traditional systems engineering was applied only to physical systems, such as spacecraft. Since recent years, systems engineering has evolved to accommodate a much broader meaning especially when humans were seen as an essential component

of a system. It is evident that CSES is such a system in which not only scientific facilities but also research teams are important components. As defined by the systems engineering body of knowledge (SEBoK), there are three types of systems engineering (Checkland, 1999): (1) product systems engineering (PSE), the traditional systems engineering, focusing on the design of physical systems consisting of hardware and software; (2) enterprise systems engineering (ESE), pertaining to the view of enterprises, that is, organizations or combinations of organizations, as systems; and (3) service systems engineering (SSE), dealing with the engineering of service systems additionally. It seems that the systems engineering of CSES is a hybrid version of PSE, ESE and SSE.

CSES is located near the ‘eastern Himalayan syntaxis’, with a total area of 780,000 km<sup>2</sup> (approximately 4 times of southern California, and 2 times of Japan islands). CSES is a complex system that relies on the observation, experiment, modeling and simulation of different disciplines/fields, from geology, geodesy, geophysics, and geochemistry, to geodynamics, earthquake engineering, and disaster science. Not yet fully considered at the present time, earthquake preparation and occurrence could be related to factors other than those inside the solid Earth. For example, meteorological and hydrological factors might be part of the process. The underlying philosophy of CSES is that the solution to the problem of prediction, long-to-intermediate term earthquake prediction, short-to-imminent term earthquake prediction, prediction of induced/triggered earthquakes, prediction of strong ground motion, and prediction of earthquake disasters and secondary disasters, is not possible to implement solely by any of the particular disciplines, but the synergistic combination of all its elements. Reduction of earthquake disaster risk may need more disciplines from natural science to technology further to social sciences (but that is somehow out of the scope of CSES – in the language of system science, it may play the role of ‘environment’ ). This holistic view of CSES requires the design and planning of the observation, experiment, data analysis, and simulation for the whole system, rather than independently for each of its components.

Functioning and sustainability of CSES are determined by a variety of factors from science to technology further to management. Coordinating such a complex system needs ideas of systems engineering. Using the concept of CDEs in environmental science (Fraser et al., 2013; Wu ZL et al., 2019), consideration and discussion on the systems engineering of CSES may also be useful for other experimental sites in earthquake science. On the other hand, experiences and lessons of other natural laboratories may also be helpful for CSES.

Last but not the least, when dealing with the physics at a certain level from microscopic to macroscopic, some new phenomenology and new physics will emerge,

known as ‘emergence’ in physics (Licata and Sakaji, 2008). What kind of new understandings would be emerged from CSES at the system level is an important, yet unsolved problem which is worth consideration and discussion.

## References

- [1] Audet P (2010). Temporal variations in crustal scattering structure near Parkfield, California, using receiver functions. *Bull Seismol Soc Am* **100**(3): 1356 – 1362 .
- [2] Bakun WH, and Lindh AG (1985). The Parkfield, California, earthquake prediction experiment. *Science* **229**(4714): 619–624.
- [3] Barbot S, Lapusta N, and Avouac JP (2012). Under the hood of the earthquake machine: toward predictive modeling of the seismic cycle. *Science* **336**(6082): 707–710.
- [4] Chao K, and Peng ZG (2009). Temporal changes of seismic velocity and anisotropy in the shallow crust induced by the 1999 October 22 *M*6.4 Chia-Yi, Taiwan earthquake. *Geophys J Int* **179**(3): 1800 – 1816 .
- [5] Checkland P (1999). *Systems thinking, systems practice: includes 30-year retrospective*. John Wiley & Sons, New York
- [6] China Seismic Experimental Site (CSES) (2020a). *China Seismic Experimental Site: Scientific challenges*. China Standard Press, Beijing (in Chinese)
- [7] China Seismic Experimental Site (CSES) (2020b). *Annual data report of China Seismic Experimental Site (2019)*. Seismological Press, Beijing (in Chinese)
- [8] Evans R, Beamish D, Crampin S, and Üçer SB (1987). The Turkish dilatancy project (TDP3): multidisciplinary studies of a potential earthquake source region. *Geophys J Int.* **91**(2): 265–286.
- [9] Field EH, Arrowsmith RJ, Biasi GP, Bird P, Dawson TE, Felzer KR, Jackson DD, Johnson KM, Jordan TH, Madden C, Michael AJ, Milner KR, Page MT, Parsons T, Powers PM, Shaw BE, Thatcher WR, Weldon II RJ, and Zeng YH (2014). Uniform California earthquake rupture forecast, version 3(UCERF3) - the time-independent model. *Bull Seismol Soc Am* **104**(3): 1122 –1180 .
- [10] Flood RL, and Jackson MC (1991) *Creative problem solving: total systems intervention*. John Wiley & Sons, Chichester.
- [11] Fraser LH, Henry HAL, Carlyle CN, White SR, Beierkuhnlein C, Cahill JF Jr, Casper BB, Cleland E, Collins SL, Dukes JS, Knapp AK, Lind E, Long RJ, Luo YQ, Reich PB, Smith MD, Sternberg M, and Turkington R (2013). Coordinated distributed experiments: an emerging tool for testing global hypotheses in ecology and environmental science. *Front Ecol Environ* **11**(3): 147–155.



- [12] Jordan TH (2006). Earthquake system science in southern California. *Bull Earthq Res Inst Tokyo Univ* **81**(3/4): 211–219.
- [13] Jordan TH (2009). Earthquake system science: potential for seismic risk reduction. *Sci Iran* **16**(5): 351–366.
- [14] Jordan TH (2014). The prediction problems of earthquake system science. *Seismol Res Lett* **85**(4): 767–769.
- [15] Kato A, and Ben-Zion Y (2021) The generation of large earthquakes. *Nat Rev Earth Environ* **2** (1): 26-39
- [16] Lachenbruch AH, Sass JH, Clow GD, and Weldon R (1995). Heat flow at Cajon Pass, California, revisited. *J Geophys Res-Sol Ea* **100**(B2): 2005 – 2012 .
- [17] Licata I, and Sakaji A (eds.) (2008). *Physics of emergence and organization*. World Scientific, Singapore .
- [18] Marzocchi W (2018). Predictive seismology. *Seismol Res Lett* **89**(6): 1998 – 2000 .
- [19] Mogi K (2004). Two grave issues concerning the expected Tokai earthquake. *Earth Planets Space* **56**(8): li–lxvi.
- [20] Mora P, and Place D (1998). Numerical simulation of earthquake faults with gouge: toward a comprehensive explanation for the heat flow paradox. *J Geophys Res-Sol Ea* **103**(B9): 21067-21089.
- [21] Niu FL, Silver PG, Daley TM, Cheng X, and Majer EL (2008). Preseismic velocity changes observed from active source monitoring at the Parkfield SAFOD drill site. *Nature* **454**: 204–208.
- [22] Roeloffs E, and Langbein J (1994). The earthquake prediction experiment at Parkfield, California. *Rev Geophys* **32**(3): 315–336.
- [23] Roeloffs E (2000). The Parkfield, California earthquake experiment: an update in 2000. *Current Sci* **79**(9): 1226–1236.
- [24] Scholz CH, Sykes LR, and Aggarwal YP (1973). Earthquake prediction: a physical basis. *Science* **181**(4102): 803–810.
- [25] Working Group on Forecasting Researches on Earthquake Risk Regions and Disaster Loss of Chinese Mainland During 2016–2025 (2020). *Forecasting Researches on Earthquake Risk Regions and Disaster Loss of Chinese Mainland During 2016–2025*. SinoMaps Press, Beijing (in Chinese).
- [26] Wu ZL (2020a). Seismic experimental sites: challenges and opportunities. *J Geol Soc India* **95**(2): 113–116.
- [27] Wu ZL (2020b) Time-dependent seismic hazard assessment. In: *Encyclopedia of Solid Earth Geophysics*. Encyclopedia of Earth Sciences Series. Springer, Cham, Switzerland.

- [28] Wu ZL (2014) Chapter 25- Ethical issues in the decision-making for earthquake preparedness, prediction, and early warning: A discussion in the perspective of game theory. In: *Geoethics: ethical challenges and case studies in earth sciences*. Elsevier, Amsterdam: pp 313-321.
- [29] Wu ZL, Ding ZF, Zhang XD, Li L, Shao ZG, Li Y, Hu CF, and Che S (2021). China Seismic Experimental Site: retrospective and prospective. *Rev Geophys Planet Phys* **52**(2): 234–238 (in Chinese).
- [30] Wu ZL, and Richards PG (2011). Seismology, monitoring of CTBT. In: *Encyclopedia of solid earth geophysics*. Encyclopedia of earth sciences series. Springer, Dordrecht, pp 1340-1344.
- [31] Wu ZL, Zhang Y, and Li JW (2019). Coordinated distributed experiments (CDEs) applied to earthquake forecast test sites. In: *Earthquake and disaster risk: decade retrospective of the Wenchuan earthquake*. Higher Education Press and Springer Nature, Singapore, pp 107–115.
- [32] Wucker M (2016) *The gray rhino - how to recognize and act on the obvious dangers we ignore*. St Martin's Press, New York.

# 2. Introduction to China's Earthquake Emergency Response System

Jianhong Liang and Jie Liu\*

(China Earthquake Networks Center (CENC), Beijing 100045, China)

**Abstract:** Following the  $M_s6.4$  earthquake that occurred on May 21, 2021 in Yangbi, Yunnan, China, the earthquake emergency response system (EERS) responded immediately. The real-time software delivered many seismic parameters that provided a preliminary assessment of the earthquake. The 24-hour on-duty staff and scientific researchers revised these parameters and produced more detailed reports to understand the cause of the earthquake and the potential damage, which provided valuable information for emergency rescue operations and earthquake situation assessment. Emergency personnel were dispatched immediately to the earthquake site to observe the aftershocks, investigate the damage, and guide and assist in the relief efforts. This paper describes the EERS response to the Yangbi earthquake to demonstrate the characteristics of the system and discuss the potential for further improvement.

## 2.1 Introduction

At 21:48 on May 21, 2021 (Beijing time), an  $M_s6.4$  earthquake occurred in Yangbi county, Dali prefecture, Yunnan province; its epicenter was at  $25.67^\circ$  N,  $99.87^\circ$  E, with a focal depth of 8 km. As of May 22, 2021, approximately 20,265 households with 72,574 residents were affected, including 190 collapsed houses, three deaths, and 28 injuries (<https://jnews.xhby.net/v3/waparticles/10/FaEvUagnowxba2yA/1>). This earthquake occurred along the edge of the tectonically complex Sichuan-Yunnan rhombic block. Both longitudinal and transverse faults (Deng QD et al., 2003) cause frequent earthquakes in this region, such as the moderately strong Eryuan  $M_s5.5$  and  $M_s5.0$  earthquakes in 2013 and the Yunlong  $M_s5.0$  earthquake in 2016 (Figure 2.1). The north-by-northwest(NNW)-oriented Weixi-Weishan fault is located east of the epicenter. The Honghe fault runs parallel to it, on the eastern side of Cangshan. The Honghe fault is characterized by many transverse faults, some of which extend to the Weixi-Weishan fault.

---

\* [DOI] 10.29382/eqs-2021-0032

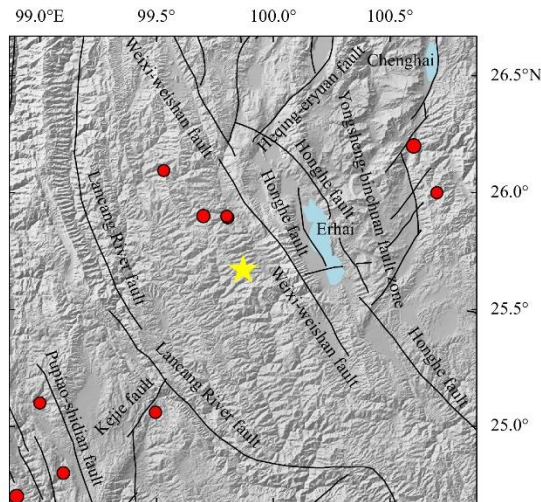


**Fig. 2. 1 The regional tectonic and seismic activities for the Yunnan Yangbi  $M_s6.4$  earthquake. The yellow star represents the epicenter of the earthquake, the black lines represent main faults, and the red dots represent earthquakes of magnitude 5 or greater since 2020**

Following the Yunnan Yangbi  $M_s6.4$  earthquake, China’s Earthquake Emergency Response System (EERS) quickly responded with the time, location, and magnitude, moment tensor solution, intensity distribution map, disaster assessment report, trend report, precise aftershock locations, regional tectonic map, crustal movement velocity background field, and other products for the earthquake. These products promptly provided the necessary data for trend determination, emergency rescue, and research. Meanwhile, emergency rescue operations were conducted quickly. In response to the earthquake disaster, the Ministry of Emergency Management immediately launched a three-level emergency response. The China Earthquake Administration (CEA) dispatched mobile monitoring teams to the earthquake site to facilitate the monitoring of the aftershocks and disaster investigations. In this paper, the relevant responses of the EERS during the Yunnan Yangbi  $M_s6.4$  earthquake are introduced in chronological order.

## 2.2 Emergency Automated Response System (EARS)

### 2.2.1 Earthquake monitoring system

China Earthquake Network consists of over 1,000 continuously operated stations that are primarily equipped with short-period, broadband, and very broadband flat velocity seismographs with a sampling rate of 100 Hz. Within the dense eastern area,

the stations are 30 – 60 km apart; in areas such as Xinjiang and the Tibetan Plateau, the distance is 100 – 200 km (Liu RF et al., 2008).





Following the 2008 Wenchuan  $M_s8.0$  earthquake, the CEA developed and deployed automatic rapid earthquake information report software and quasi-real-time moment tensor inversion software. These software tools reduced the time required to determine the time, location, and magnitude of the earthquake from tens of minutes to approximately 2 minutes, and the time required to produce the moment tensor solution from a few hours to 10 – 25 minutes.

The automatic rapid report software uses the short-term average/long-term average (STA/LTA) ratio of the seismic wave energy and the Akaike information criterion to determine the arrival time (Allen, 1982; Wang J et al., 2006), and utilizes a 3D grid search algorithm for event association and positioning. The magnitudes  $M_L$ ,  $M_W$ , and  $m_b$  are respectively calculated using the methods of Jin X et al. (2004), Tsuboi et al. (1995, 1999), and Saul and Bormann (2007), and the magnitude of an event is determined by combining the three scales. This software released the following Yangbi earthquake parameters to the public three minutes after the event: time (21:48:37), location ( $25.66^\circ$  N,  $99.86^\circ$  E), and magnitude (5.9). These deviated from the manually revised parameters by 1.8 km and 0.5 for the location and magnitude, respectively.

The quasi-real-time moment tensor inversion software can read real-time waveform data. Using the seismic parameters from the automatic rapid report software, the waveform window and filter frequency band of the event can be determined. Through the W-phase centroid moment tensor inversion algorithm (Kanamori and Rivera, 2008; Hayes et al., 2009; Duputel et al., 2011, 2012), the centroid moment tensor solution can be obtained as each station becomes available, continually updating the inversion moment tensor solution. It has been running in real time at the China Earthquake Networks Center (CENC) since 2014. For domestic earthquakes measuring  $M_W \geq 5.5$ , stable moment tensor solutions can usually be obtained within 15 minutes of their occurrence. These solutions can assist in identifying the type and movement of the fault where the earthquake occurred, and can serve as the basis for strong ground motion evaluation, finite fault inversion, and other emergency research. This software produced stable moment tensor solutions 9.6 minutes after the Yangbi earthquake. Following this, the Institute of Earthquake Forecasting (IEF) and the Institute of Geophysics (IGP) of the CEA received successive moment tensor solutions for various times, using time-domain inversion and Time Domain Moment Tensor Inversion (TDMT-INV) software (Dreger, 2003) and the “Cut and Paste” method and software (Zhu LP and Helmberger, 1996; Zhu LP and Ben-Zion, 2013), respectively. The Global Centroid Moment Tensor (GCMT) project also released moment tensor results (<https://www.globalcmt.org>). The focal mechanism solutions and moment magnitude scales of each institution are listed in Table 2.1. The results were largely consistent and suggested that the seismogenic

fault was a near-vertical strike-slip fault.

**Table 2.1:** Comparison of focal mechanism solutions and moment magnitudes released by various institutions

Contributor	Delay	$M_w$	Strike/Dip/Rake(°)	Mechanism	Kagan(°)
CENC	9.6 min	6.2	314/79/-172		21
IEF, CEA	~2 hours	6.3	136/84/-179		15
IGP, CEA	~3 hours	6.0	138/82/-161		14
GCMT	N/A	6.1	315/86/168		0

### 2.2.2 Earthquake early warning system

In 2018, the CEA launched the national intensity rapid report and early warning project to build more than 15,000 stations equipped with seismometers, strong motion accelerographs, and seismic intensity instruments, and establish the China Earthquake Early Warning Network. To date, most stations have been completed, greatly increasing station density, and are used in an early warning system demonstration in North China, the North-South Seismic Belt (NSSB), the southeast coast, and the center of the Tianshan mountains in Xinjiang. As shown in Figure 2.2, Sichuan and Yunnan, both of which are in the NSSB, have recently built approximately 2,200 stations. In these four demonstration areas, the earthquake early warning system has been tested, and their rapid intensity report and warning information will be made public in the second half of 2021.



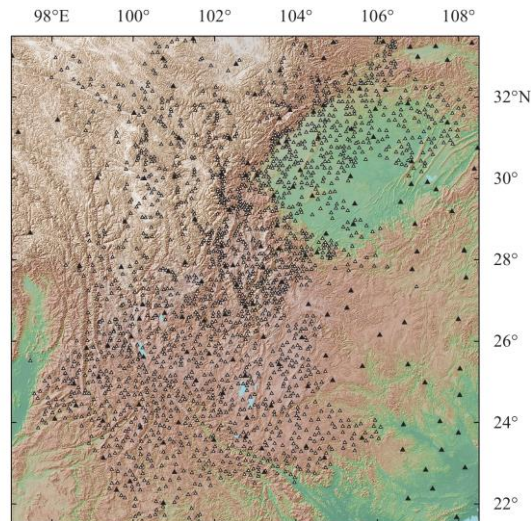


**Fig. 2.2** Station distribution for the China Earthquake Early Warning Network in the Sichuan-Yunnan area. The black triangles represent the stations of the China Earthquake Network, the empty triangles represent the stations of the China Earthquake Early Warning Network.

In the early warning system, the arrival time at a triggered station and information from an untriggered station (Horiuchi et al., 2005; Satriano et al., 2008) are used for real-time positioning, and the maximum displacement ( $P_d$ ) of the initial part of the P wave is used to calculate the magnitude (Wu YM and Zhao L, 2006; Kuyuk and Allen, 2013). Once the time, location, and magnitude of the earthquake are determined, warnings are immediately issued to the public through television, speakers, text messages, and mobile apps, and these parameters are continuously updated and published. For the Yangbi earthquake, these were measured 6 s after the event as follows: 21:48:35; 25.69° N, 99.89° E; and Magnitude 4.9. The first warning was sent to participating test users. The deviation from the manually revised parameters was 3.0 km and 1.5 for the location and magnitude, respectively. The parameters were updated 7 s after the earthquake, when the magnitude was updated to 5.4. During the next two minutes, 88 updates were made, including the magnitude of 5.8 at 49 s after the earthquake. The changes in the magnitude, magnitude deviation, and epicenter deviation in the 30 s following the earthquake are presented in Figure 2.3. The first reported magnitude was 1.5 lower, due to only two stations participating in the positioning and magnitude calculations, and only the last 2-3 s of the P waveform being available for magnitude calculation. The magnitude was measured as 4.5 at station L2203, with an epicentral distance of 11.0 km, and 5.4 at station L2204, with an epicentral distance of 14.0 km; the average was 4.9. As more stations and waveforms became available, the magnitude improved. Within 49 s, stations with greater epicentral distances were used to calculate the magnitude. The number of stations reached 45, and the magnitude was updated to 5.8. Despite the large magnitude deviation, the earthquake early warning system played a crucial role in alerting test participants and

assisting them in averting disaster.

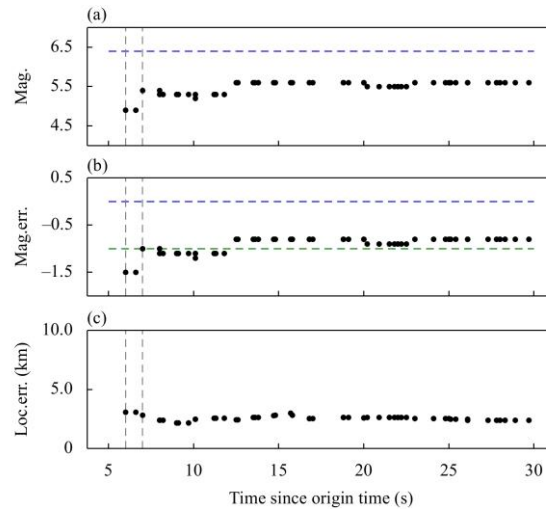


**Fig. 2.3** Variations in the magnitude (a), magnitude deviation (b), and epicenter deviation (c) of the earthquake early warning system over time. The blue dashed line in (a) represents the official rapid report magnitude of 6.4. The blue dashed line in (b) represents a magnitude deviation of 0.0, and the green dashed line represents a deviation of  $-1.0$ . The two gray dotted lines represent the time of 6 s and 7 s after the earthquake, respectively.

### 2.2.3 Earthquake disaster assessment system

Within 10 minutes of receiving the official earthquake rapid report information, the national basic geographical data, population economic data, historical earthquake damage data, remote sensing images, and other thematic data were used to rapidly produce an “Earthquake Disaster Rapid Assessment”. The earthquake impact field was predicted using an empirical seismic intensity attenuation model. The casualties were estimated based on a building vulnerability model, information regarding local building types, and expert experience. Information regarding the residential areas, population, economy, transportation, hospitals, and reservoirs in each intensity area was produced, as well as related images, including remote sensing images and maps of the epicenter location, historical earthquake disasters, active fault zones, earthquake impact range predictions, population distribution, distance between the epicenter and surrounding residences, and traffic near the epicenter. The estimated maximum intensity of the Yangbi earthquake was VIII (degree 8), and the total area with a seismic intensity above VI (degree 6) was approximately  $5577 \text{ km}^2$ , affecting approximately 7.46 million people. This area has an average population density of  $130 \text{ people/km}^2$ , and it covers 26 townships and 2,514 villages, as shown in Figure 2. 4.

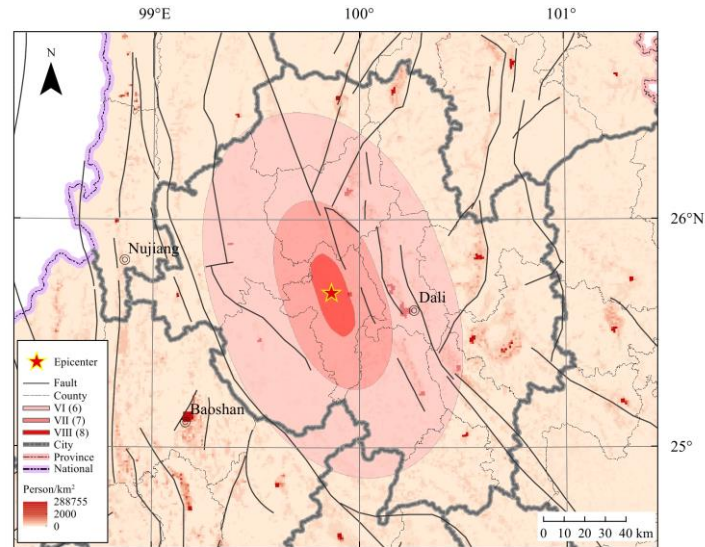


**Fig.2. 4 The rapidly estimated impact area of the Yangbi earthquake and the corresponding population distribution map.**

Additionally, the seismic intensity system triggered automatically upon receiving the rapid report information. Instrumental intensities were calculated using the peak ground acceleration (PGA) and peak ground velocity (PGV) measured by seismic stations at the earthquake site. Within 10 minutes following the earthquake, instrumental seismic intensity, PGA, and PGV distribution maps were produced. Data from more than 600 stations were collected and processed for this earthquake. Among them, the largest ground motion was recorded at the Yangbi Station, which is approximately 9 km from the epicenter; the instrumental intensity was approximately 8.2, the PGA was approximately 720 gal, and the PGV was approximately 30.5 cm/s, as shown in Figure 2.5.

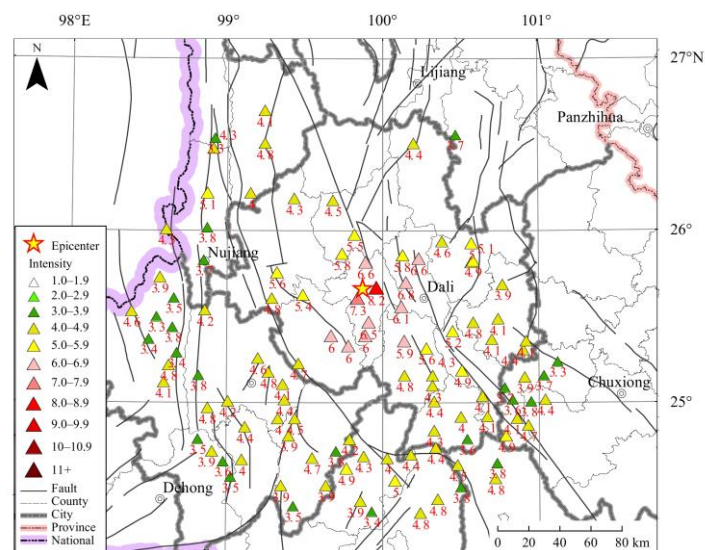


**Fig.2. 5 The map of instrumental seismic intensities around the Yangbi earthquake.**

## 2.2.4 Earthquake prediction system

Recently, earthquake prediction researchers at the CEA have systematically collected historical data on strong earthquakes in Chinese mainland to compile a relatively complete database, including catalogs of instrumental earthquakes since 1970, focal mechanism solutions of historical earthquakes, earthquake sequences since 1966, statistics on earthquake sequence types, and active tectonics in China. Based on this, Chinese mainland was divided into dozens of regions according to tectonic characteristics, and a system for rapid determination of post-earthquake trends was developed. This system can estimate the characteristics of new earthquake sequences and the maximum aftershock activity level based on historical earthquake sequence characteristics in the same area. A preliminary earthquake situation analysis report can also be generated automatically. Additionally, the conclusions can be revised through manual interventions, and the first opinions regarding the earthquake can be produced within 30 minutes. In the case of the Yangbi earthquake, the first special report was issued within 27 minutes of the event. The tectonic divisions and focal mechanisms around this earthquake, as well as the distribution of historical earthquake sequences, are illustrated in Figure 2.6.

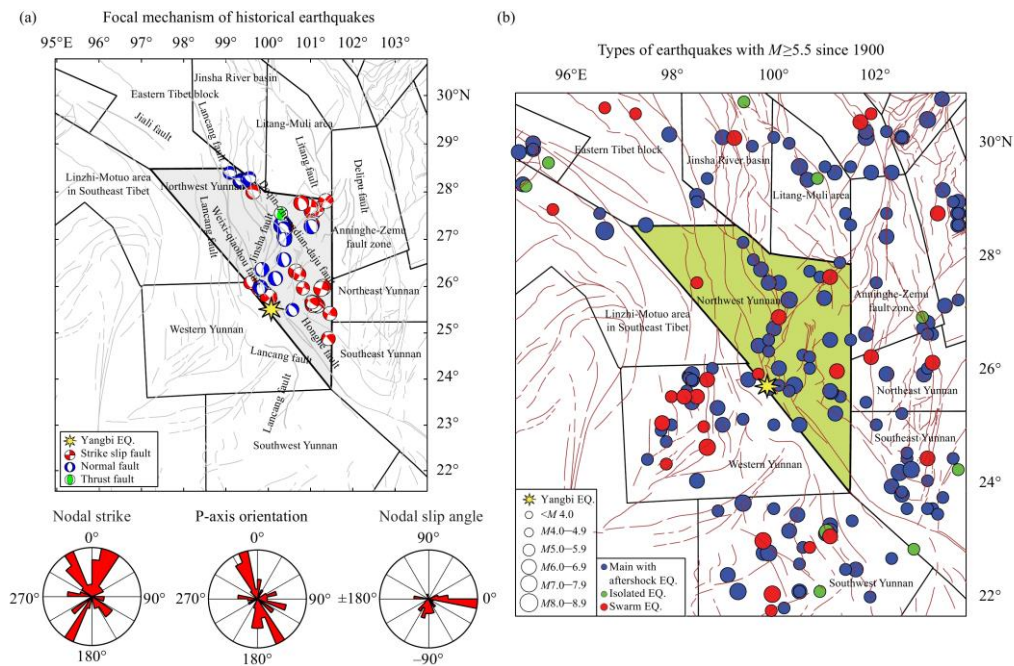


Fig. 2.6 The schematic diagram of the tectonic divisions and focal mechanisms around the Yangbi earthquake (a) and the distribution map of historical earthquake sequences (b).

## 2.3 Emergency duty system

### 2.3.1 Earthquake monitoring system

In the event of an earthquake, the real-time earthquake detection software uses the STA/LTA to detect the earthquake and alerts the 24-hour on-duty staff. On hearing the alarm, the staff immediately use the interactive analysis software (Song R et al., 2001) to read the automatic rapid report; visually adjust the arrival time of the P wave, S wave, and other phases; and employ a grid search to locate the earthquake and calculate the magnitude, thereby obtaining a revised and accurate time, location, and magnitude. Following the “Technical Management Regulations for Earthquake Rapid Reports (2015 Revised Edition)”, manual revisions for the Yunnan earthquake were completed within 20 minutes, and the final rapid report parameters were released 7.5 minutes after earthquake, as follows: 21:48:35; 25.67° N, 99.87° E; depth of 8.0 km; and Magnitude 6.4. These results were used in the CEA’s official rapid report and were released to the public and government through the national earthquake information sharing software, EQIM, text messages, and mobile phone apps. The interface for the visual interactive revision of the seismic parameters used by the staff is shown in Figure 2.7.

Upon receiving the official rapid report, other staff used the revised time, location, and magnitude and more complete waveform data to recalculate a more accurate moment tensor solution based on a more comprehensive understanding of the earthquake. For earthquakes with  $M_w \geq 6.5$ , the finite fault inversion method (Ji C et al., 2002; Zhang Y et al., 2014) is applied to invert the rupture process and determine the earthquake’s kinematic characteristics. Due to the relatively small magnitude in this case, the rupture process was not inverted. Approximately 30 minutes after the earthquake, the revised moment magnitude ( $M_w 6.0$ ) and focal mechanism solution (Nodal plane 1: 44° /77° /11° , Nodal plane 2: 312° /79° /167° ), which were nearly identical to the GCMT results, were released.



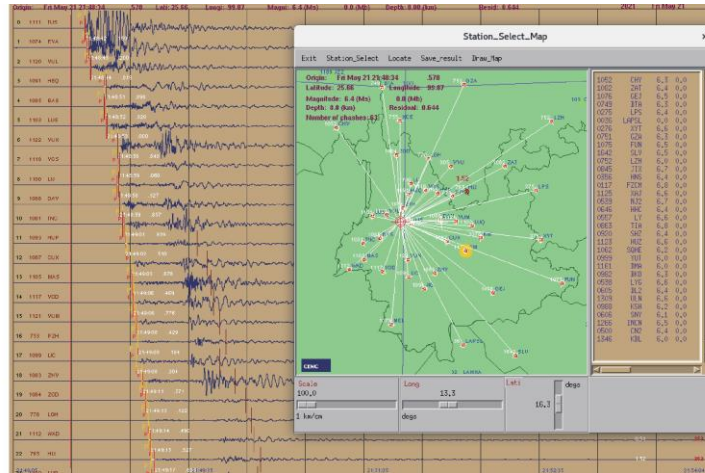
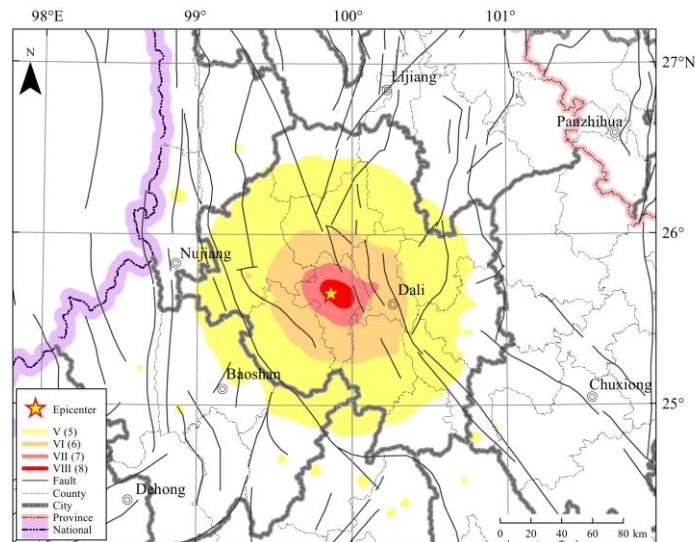


Fig. 2.7 Interface for visual interactive revision of seismic parameters.

### 2.3.2 Earthquake disaster assessment system

When official parameters were released, the seismic intensity rapid report system screened out abnormal waveforms and ground motions. Based on the directional effect of the near-field ground motions and the attenuation model for ground motion fault distance, the rupture fault direction and rupture mode of the earthquake were determined from the historical ground motion attenuation trends. An intensity attenuation model was developed using the motion data. Interpolation points were then supplemented based on the station distribution density, and their intensity was calculated using the measured intensity attenuation model. Finally, the Kriging interpolation method was used to calculate the estimated seismic intensity distribution, for which a map was produced within 30 minutes of the earthquake. The estimated maximum intensity of this earthquake was VIII (8 degrees). The area with an intensity of VI (6 degrees) and above was approximately 6780 km<sup>2</sup>, of which the intensity VIII (8 degrees) area was approximately 279 km<sup>2</sup>, the intensity VII (7 degrees) area was approximately 949 km<sup>2</sup>, and the intensity VI (6 degrees) area was approximately 5552 km<sup>2</sup>, as shown in Figure 2.8.





**Fig. 2.8** Estimated seismic intensity distribution map of the Yangbi earthquake.

### 2.3.3 Earthquake consultation system

The CENC, Yunnan Earthquake Agency, Sichuan Earthquake Agency, and IEF arranged a video conference consultation on the Yangbi earthquake to analyze and discuss the historical data, mainshock parameters, aftershock records, and emergency products (focal mechanism of the mainshock, intensity distribution, aftershock distribution, etc.). The seismogenic fault, rupture characteristics of the mainshock (unilateral or bilateral), and distribution of the aftershocks were thereby determined. The type of earthquake sequence and the recent level of aftershock activity were also assessed. Approximately two hours after the earthquake, they released the second post-earthquake trend report.

## 2.4 Earthquake Emergency Work System

Immediately after the Yangbi earthquake, the CEA initiated emergency response procedures and organized and scheduled the emergency response work. Under the unified deployment guidelines from the Earthquake Relief Headquarters of the State Council, the Ministry of Emergency Management and the CEA dispatched an on-site team, headed by the deputy director of the CEA, to guide and assist the local rescue and disaster relief efforts in Yunnan. The Yunnan Earthquake Agency also dispatched a team to the site over night. In collaboration with emergency personnel from the First Monitoring Center of the CEA, Sichuan Earthquake Agency, Institute of Engineering Mechanics of the CEA, and Earthquake Disaster Prevention Center of the CEA, a team was assembled to assist the local government in organizing emergency rescue operations and carry out on-site tasks, including mobile monitoring, earthquake situation monitoring, tracking, decision-making, disaster loss investigation, earthquake

intensity assessment, and scientific investigation.

### 2.4.1 Earthquake site work team

The CEA dispatched 57 members from the Yunnan Earthquake Agency and Sichuan Earthquake Agency to the earthquake site with emergency equipment to set up mobile stations and densify the seismic network. These stations monitored and analyzed the aftershocks, and were vital for monitoring smaller aftershocks and precise aftershock positioning. Data on large quantities of aftershocks helped determine the distribution and shape of the faults and trends in aftershock development. The distributions of the mobile stations and aftershocks are shown in Figure 2.9.

The on-site team that conducted earthquake damage investigation and intensity assessment overcame many difficulties, including long-distance travel, continuous aftershocks, and difficult road conditions. In a race against time, they investigated the disaster, assessed the earthquake damage scientifically and rigorously, and evaluated the intensity. On the evening of May 24, they drew an earthquake intensity map, as shown in Figure 2.10, which was released to the public the following day, after careful evaluation ([http://www.yndzj.gov.cn/yndzj/\\_300559/\\_300651/629959/index.html](http://www.yndzj.gov.cn/yndzj/_300559/_300651/629959/index.html)). The figure shows that the maximum intensity of this earthquake was VIII (8 degrees), and the area with an intensity of VI (6 degrees) and above was approximately 6,600 km<sup>2</sup> (including Erhai lake). The long axis of the isoseismal lines was NNW-oriented and measured 106 km, the short axis measured 76 km. The axes span six counties and cities in Dali prefecture. The area with an intensity of VIII (8 degrees) was approximately 170 km<sup>2</sup>, covering three townships, namely Cangshan West, Yangjiang, and Taiping township in Yangbi county. The timely release of this map provided a valuable reference and scientific basis for decisions and relief efforts in the affected areas, as well as for planning the recovery and reconstruction in the area.

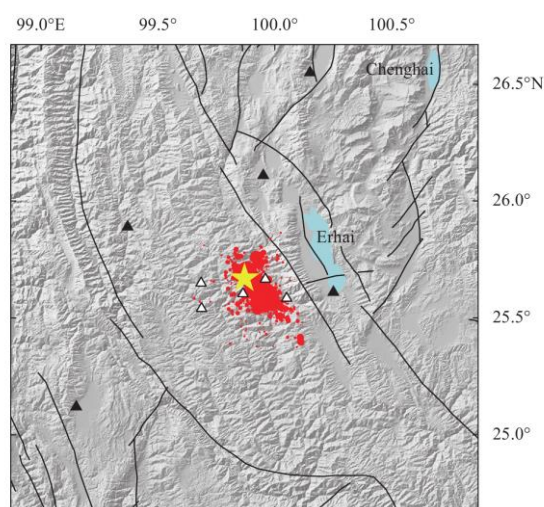


**Fig. 2.9** Distributions of mobile stations and aftershocks of the Yangbi earthquake. The black triangles represent the stations used to analyze the earthquake, the white triangles represent

the temporary mobile stations. The yellow star represents the main shock of magnitude 6.4, the red dots represent the aftershocks, and the black lines represent the faults.

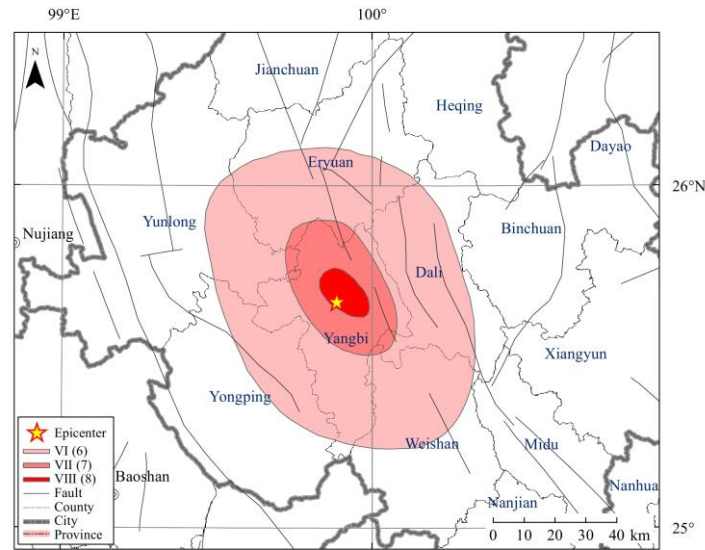


Fig.2. 10 Intensity map of the Yunnan Yangbi  $M_{5.4}$  earthquake.

## 2.4.2 Earthquake monitoring emergency products

After an earthquake, the staff on duty produce a catalog of the aftershocks. Simultaneously, earthquake emergency researchers immediately begin studying the earthquake to produce rupture processes, Coulomb stress changes, aftershock focal mechanism solutions, and other results. These products and results are promptly made available for earthquake prediction, emergency rescue, and disaster assessments.

Many aftershocks occurred in the aftermath of the Yangbi earthquake, making monitoring and analyzing them extremely difficult. To support the Yunnan Earthquake Agency, Jiangxi and Jianguo Earthquake Agency dispatched personnel to take part in continuous aftershock monitoring and analysis, and to update the aftershock catalog and observation report hourly. The completion of the mobile station densified network greatly improved monitoring capability. As of 15:00 on June 12, 2021, a total of 5,077 aftershocks had been located. The changes in aftershocks over time and their cumulative distribution are shown in Figure 2.11, the red vertical line represents the significant decrease in the magnitude of the aftershocks before and after station densification.

The aftershock catalog and observation report were used to determine the precise location of the earthquake sequence and to provide a detailed description of the fault distribution and morphology, as shown in Figure 2.12. The results further verified that the fault was nearly vertical and approximately 20 km long. These updates were used in the earthquake situation consultation.

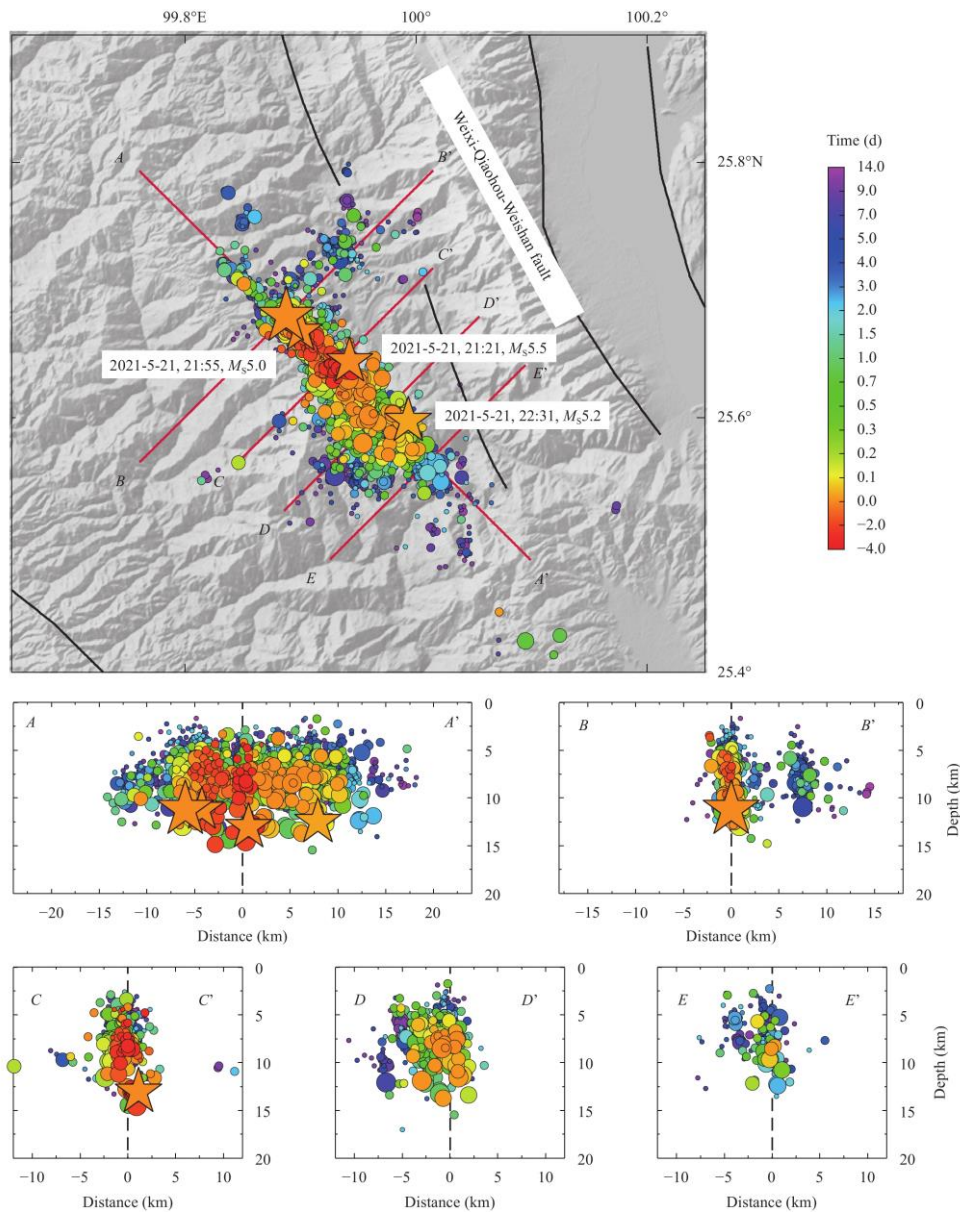


**Fig. 2.12** The precise location of the Yangbi earthquake sequence. The star indicates earthquakes with  $M_s \geq 5.0$ ,  $AA'$ ,  $BB'$ ,  $CC'$ ,  $DD'$  and  $EE'$  indicates the selected focal depth profile and its projection on the ground, the dashed black line represents the vertical reference line.

A rapid report process was implemented for aftershocks of magnitude 3.0 or higher in Yangbi, 31 were reported by the CENC during this period. Additionally, the CENC produced moment tensor solutions 20 minutes after any aftershock above 4.0. The focal mechanism solutions for some of these aftershocks are shown in Figure 2.13.

Approximately two hours after the earthquake, earthquake emergency research scientists analyzed the data and produced maps of the regional tectonics, Coulomb stress, and background velocity field of the regional crustal movement (Figure 2.14). These products were of crucial for understanding the cause of the earthquake and the development of subsequent aftershocks.

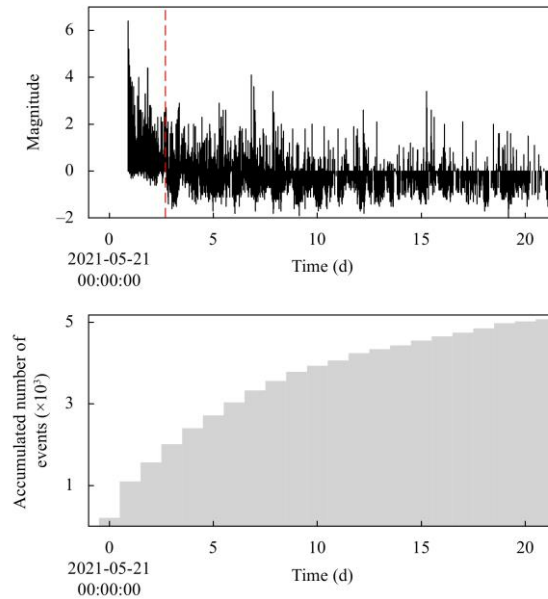


**Fig. 2.11** Variation in Yangbi aftershocks over time and their cumulative distribution. The red dotted line indicates the time when the station was built and began seismic monitoring.

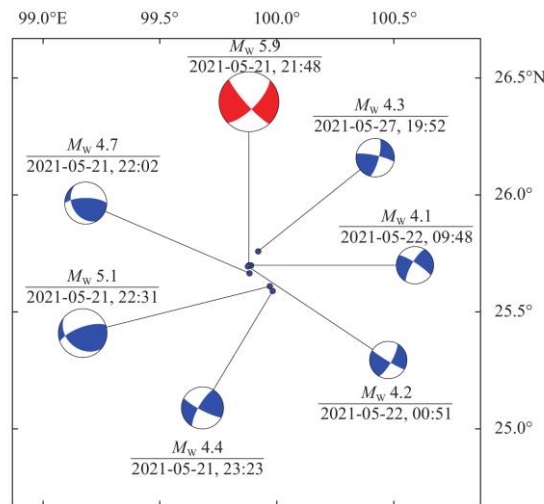


**Fig. 2.13** Focal mechanism solutions of main shock (red) and some aftershocks (blue).

### 2.4.3 Earthquake situation prediction

Approximately two hours after the emergency consultation meeting, provinces throughout the country arranged another video conference to discuss the impact of the earthquake on the rest of Chinese mainland and finalize the national opinion on the situation, which was reported on the same day as the earthquake.

Afterward, conferences were held twice a day based on the latest monitoring product results. In the morning, research and analysis of the earthquake sequence were conducted primarily using the most recent data. The resulting conclusions were used by the local government and earthquake site team to conduct relief work. In the afternoon, a national conference was held to research and analyze the national



earthquake situation based on the latest observation data. These were continued until the on-site team completed the intensity assessment and the earthquake sequence attenuated. Normally, the consultation process lasts one week or longer, before transitioning into weekly and monthly consultations.

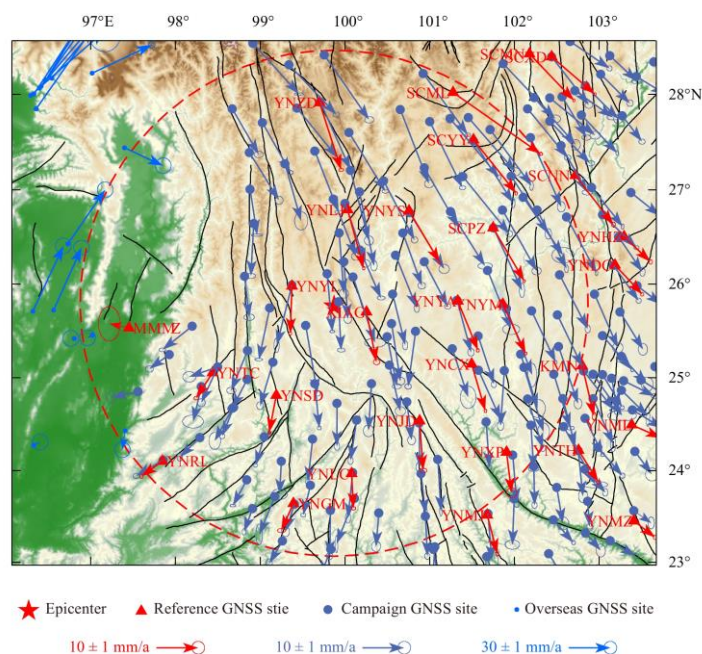


**Fig. 2.14 Background velocity field of the regional crustal movement. The blue circle refers to the error in velocity field processing and represents the accuracy of vector.**

If there is a sudden strong aftershock, consultations on the development of the earthquake sequence intensify again. In addition, during certain special events, such as the national college entrance examination beginning on June 7, shorter-term judgments of the earthquake sequence trend and national earthquake situation become necessary.

## 2.5 Discussion and conclusions

This paper has illustrated China's EERS and its responses after the Yangbi  $M_s6.4$  earthquake. Table 2.2 details the products produced by the EARS, emergency duty system, and earthquake emergency work system within the EERS. This system exhibits rapid responses, timely outputs, efficient organization, and significant effectiveness, which demonstrates the progress made in the field of emergency response driven by the continuous emphasis of the CEA on construction and investment for monitoring and forecasting.



**Table 2.2:** Earthquake information supplied by China’ s EERS at different times.

Elapsed time	Product	Output mode	Update status	Function or usage
6s	Time, location, and magnitude	Real-time automatic	Continuous updates	Releases to some test users through the early warning terminal and mobile app
3min	Time, location, and magnitude	Real-time automatic	No updates	Releases to the public through websites, text messages, mobile app, etc.
7.5min	Time, location, and magnitude	Manual revision	No updates	Releases to the public through websites, text messages, mobile app, etc.
10min	Centroid moment tensor solution	Quasi-real-time automatic	Continuous updates	Post-earthquake analysis of earthquake trends
15min	Intensity distribution map prediction	Quasi-real-time automatic	No updates	Rapid earthquake disaster assessment
27min	Preliminary earthquake consultation opinions	Automatic + Manual	No updates	Emergency rescue + Decision-making
~2h	Earthquake consultation opinions	Video conference	No updates	Emergency rescue + Decision-making
~1h	Intensity distribution map prediction	Manual	No updates	Emergency rescue + Decision-making
~1h	Disaster assessment report	Manual	No updates	Emergency rescue + Decision-making
~2h	Coulomb stress diagram	Manual	No updates	Post-earthquake analysis of earthquake trends
~2h	Regional tectonic map	Manual	No updates	Post-earthquake analysis of earthquake trends
~2h	Crustal movement background velocity field	Manual	No updates	Post-earthquake analysis of earthquake trends
~3d	Mobile station	Manual	No updates	Post-earthquake aftershock monitoring
~4d	Intensity map	Manual	No updates	Post-earthquake recovery and reconstruction
~4h	National earthquake situation	Video conference	No updates	Emergency rescue decision-making

	consultation			
Continuous	Aftershock analysis and positioning	Automatic + Manual	Continuous updates	Post-earthquake analysis of earthquake trends
Continuous	Aftershock focal mechanism solutions	Automatic + Manual	No updates	Post-earthquake analysis of earthquake trends

CEA has continuously invested in the development of real-time automatic earthquake processing technology since the Lushan earthquake in 2013. A series of software tools were developed for the EARS, allowing earthquake information to be produced with exceptional timeliness and released immediately. This prompt information spares valuable time for earthquake emergency responses and disaster rescue operations, which have yielded impressive results. The trial earthquake early warning system sent an alert to the participants 6s after the earthquake. Despite the magnitude being listed as more than 1.0 smaller, it still demonstrated an advancement in the real-time earthquake processing technology in China. Within the China Earthquake System, a well-organized duty system with a clear hierarchy of responsibilities and many personnel has been established. Everyone, from the leaders of the CEA to the directors of the provincial earthquake bureaus and directly affiliated centers, to the early warning, earthquake disaster assessment, earthquake prediction, and all other personnel, follows a 24-hour duty schedule to ensure timely and efficient responses and minimize losses. Following the Yangbi earthquake, the CEA immediately dispatched teams to assist with disaster relief, mobile station construction, and damage investigation. Several scientists involved in emergency research tasks also assisted. This support is critical for determining aftershock trends, discovering the cause of earthquakes, and carrying out recovery and reconstruction efforts.

However, the system still has several shortcomings that require further improvement. First, the data and resource sharing between emergency subsystems should be enhanced to ensure data consistency, timeliness, and accessibility; furthermore, coordination between subsystems must be established to improve response efficiency. Second, the entire EERS must become more automated and intelligent and should take advantage of technological advancements, such as artificial intelligence and big data, to rapidly produce a wider variety of products. Third, the earthquake parameters published by the EARS need to be more accurate. Specifically, the magnitude detected by the early warning system was considerably low in this case, which limited the effectiveness of the early warning. This calls for continuous improvement of the early warning system and the accuracy of the published parameters. Finally, strengthened partnerships with universities and research institutes for the development of earthquake systems would allow them to deploy the most innovative methods and technologies. Efforts should be made to enhance disaster assessment

accuracy and reveal the corresponding mechanisms, thereby enhancing the ability to respond to emergencies.

## References

- [1] Allen R (1982). Automatic phase pickers: their present use and future prospects. *Bull Seismol Soc Am* **72**(6B): S225–S242.
- [2] Deng QD, Zhang PZ, Ran YK, Yang XP, Min W, and Chen LC (2003). Active tectonics and earthquake activities in China. *Earth Sci Front* **10**(S1): 66–73 (in Chinese with English abstract).
- [3] Dreger DS (2003). TDMT\_INV: Time Domain Seismic Moment Tensor INVersion. *Int Handb Earth Eng Seismol*, Volume 81B, pp. 1627
- [4] Duputel Z, Rivera L, Kanamori H, Hayes GP, Hirshorn B, and Weinstein S (2011). Real-time W phase inversion during the 2011 off the Pacific coast of Tohoku earthquake. *Earth Planets Space* **63**(7): 535–539.
- [5] Duputel Z, Rivera L, Kanamori H, and Hayes G (2012). W phase source inversion for moderate to large earthquakes (1990–2010). *Geophys J Int* **189**(2): 1125 – 1147 .
- [6] Hayes GP, Rivera L, and Kanamori H (2009). Source inversion of the W-Phase: real-time implementation and extension to low magnitudes. *Seismol Res Lett* **80**(5): 817–822.
- [7] Horiuchi S, Negishi H, Abe K, Kamimura A, and Fujinawa Y (2005). An automatic processing system for broadcasting earthquake alarms. *Bull Seismol Soc Am* **95**(2): 708–718.
- [8] Hunter JD (2007). Matplotlib: a 2D graphics environment. *Comput Sci Eng* **9**(3): 90–95.
- [9] Ji C, Wald DJ, and Helmberger DV (2002). Source description of the 1999 Hector Mine, California, earthquake, Part I: wavelet domain inversion theory and resolution analysis. *Bull Seismol Soc Am* **92**(4): 1192 – 1207 .
- [10] Jin X, Ma Q, and Li SY (2004). Real-time simulation of ground displacement and acceleration using digital velocity record. *Earthq Eng Eng Vibrat* **24**(6): 9–14 (in Chinese with English abstract).
- [11] Kanamori H, and Rivera L (2008). Source inversion of W phase: speeding up seismic tsunami warning. *Geophys J Int* **175**(1): 222–238.
- [12] Kuyuk HS, and Allen RM (2013). A global approach to provide magnitude estimates for earthquake early warning alerts. *Geophys Res Lett* **40**(24): 6329 – 6333 .
- [13] Liu RF, Gao JC, Chen YT, Wu ZL, Huang ZB, Xu ZG, and Sun L (2008).

- Construction and development of digital seismograph networks in China. *Acta Seismol Sin* **30**(5): 533–539 (in Chinese with English abstract).
- [14] Satriano C, Lomax A, and Zollo A (2008). Real-time evolutionary earthquake location for seismic early warning. *Bull Seismol Soc Am* **98**(3): 1482 – 1494 .
- [15] Saul J, and Bormann P (2007). Rapid estimation of earthquake size using the broadband P-wave magnitude  $m_b$ . *Eos, Transactions, American Geophysical Union, AGU 2007 Fall Meeting* **88** (52): Suppl Abstract S53A–1035
- [16] Song R, Gu XH, Wang YL, Zhao Y, Wang B, and Xie XW (2001). The software system for real-time processing and large earthquake rapid determination of NCDSN. *Earthquake* **21**(4): 47–59 (in Chinese with English abstract).
- [17] Tsuboi S, Abe K, Takano K, and Yamanaka Y (1995). Rapid determination of  $M_W$  from broadband P waveforms. *Bull Seismol Soc Am* **85**(2): 606–613.
- [18] Tsuboi S, Whitmore PM, and Sokolowski TJ (1999). Application of  $M_{WP}$  to deep and teleseismic earthquakes. *Bull Seismol Soc Am* **89**(5): 1345 – 1351 .
- [19] Wang J, Chen JH, Liu QY, Li SC, and Guo B (2006). Automatic onset phase picking for portable seismic array observation. *Acta Seismol Sin* **19**(1): 44–53.
- [20] Wessel P, Luis JF, Uieda L, Scharroo R, Wobbe F, Smith WHF, and Tian D (2019). The generic mapping tools version 6. *Geochem Geophys Geosyst* **20**(11): 5556 – 5564 .
- [21] Wu YM, and Zhao L (2006). Magnitude estimation using the first three seconds P-wave amplitude in earthquake early warning. *Geophys Res Lett* **33**(16): L16312.
- [22] Zhang Y, Wang RJ, Zschau J, Chen YT, Parolai S, and Dahm T (2014). Automatic imaging of earthquake rupture processes by iterative deconvolution and stacking of high-rate GPS and strong motion seismograms. *J Geophys Res* **119**(7): 5633 –5650.
- [23] Zhu LP, and Helmberger DV (1996). Advancement in source estimation techniques using broadband regional seismograms. *Bull Seismol Soc Am* **86**(5): 1634 – 1641 .
- [24] Zhu LP, and Ben-Zion Y (2013). Parametrization of general seismic potency and moment tensors for source inversion of seismic waveform data. *Geophys J Int* **194**(2): 839–843.

# 3. Crust and upper mantle structure of East Asia from ambient noise and earthquake surface wave tomography

Mengkui Li<sup>1</sup> and Xiaodong Song<sup>2\*</sup>

(1. School of Geodesy and Geomatics, Wuhan University, Wuhan 430079, China

2. School of Earth and Space Sciences, Peking University, Beijing 100871, China)

**Abstract:** The complex tectonic background of East Asia makes it an ideal region for investigating the evolution of the continental lithosphere, for which high-resolution lithospheric structural models are essential. In this study, we measured Rayleigh-wave phase-velocity dispersion curves at periods of 10 – 120 s and group velocity dispersion curves at periods of 10 – 140 s using event records from more than 1,000 seismic stations in and around China. By jointly inverting new and previously published dispersion data from ambient noise and earthquakes, we developed a high-resolution shear-wave velocity model down to a depth of ~300 km beneath East Asia. Our model revealed heterogeneous lithospheric structures beneath East Asia, and allowed us to investigate the velocity structure of the entire lithosphere. We also derived crustal and lithospheric thickness models from the three-dimensional (3D) shear-wave model, revealing strong spatial heterogeneity and a general thinning trend of lithospheric thickness from west to east across the study region. Overall, our models reveal important lithospheric features beneath East Asia and provide a valuable baseline dataset for understanding continental-scale dynamics and evolution.

## 3.1 Introduction

Our study region consists of Chinese mainland and the eastern marginal seas in East Asia including the Japan Sea, Bohai Sea, Yellow Sea, East China Sea, Taiwan Strait, and South China Sea (Figure 3.1). This region has drawn much attention because of its various lithospheric styles and complex tectonic background (e.g., Zhu JS et al., 2002; Liang CT et al., 2004; Priestley et al., 2006; Li YH et al., 2013; Pandey et al., 2014; Bao XW et al., 2015; Chen M et al., 2017). For example, the ongoing deformation of this region has been mainly affected by the continental collision of the Indian and Eurasian Plates to the west (e.g., Tapponnier et al., 1986; Yin A and Harrison, 2000)

---

\* [DOI] 10.1016/j.eqs.2022.05.004

and the subduction of the oceanic Pacific and Philippine Plates to the east and southeast (e.g., Northrup et al., 1995; Lallemand et al., 2001; Schellart and Lister, 2005). The collision of the Indian and Eurasian Plates has created the highest, largest and most active area of the Tibetan Plateau (TP) in the west, and in eastern China, the subduction of the Pacific and Philippine Plates has caused the development and widespread extension of the western Pacific marginal basins and the Mesozoic basins (e.g., Ren JY et al., 2002). The subduction of the Pacific Plate has also induced widespread asthenosphere upwelling, large-scale volcanic eruptions, and strong tectonic activity in eastern China. Such complex tectonic processes have caused strong lithospheric heterogeneities in East Asia, making it an ideal region for investigating the evolution of the continental lithosphere. Importantly, detailed knowledge of the thickness and velocity structures of the lithosphere in East Asia is crucial for understanding continental-scale tectonics and geodynamic processes.

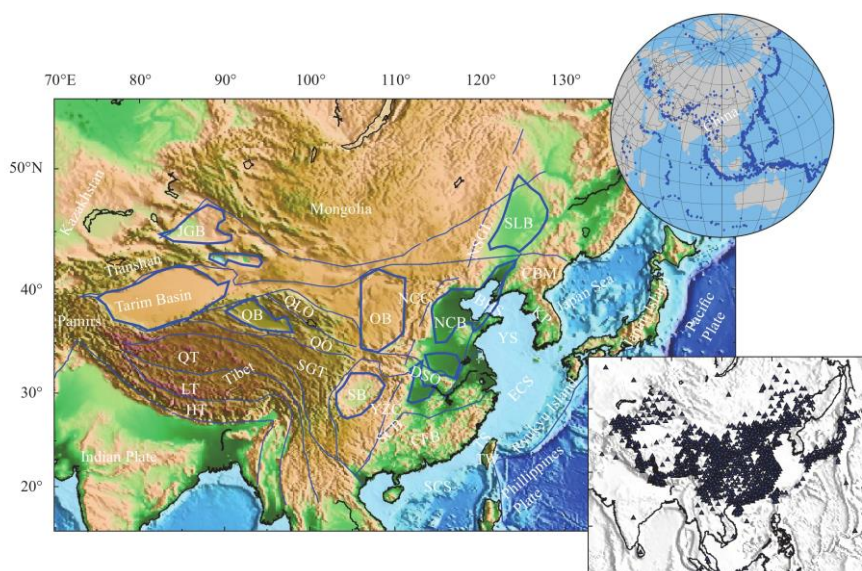


**Fig. 3.1** Topographic map of the study area showing the main tectonic units in the East Asia region, and the distributions of seismic stations (blue triangles) and earthquakes (blue dots). The thick blue lines represent the boundaries of geological units (from Liang CT et al., 2004, which is modified from the original map by Zhang ZM et al., 1984). The abbreviations are: Jungger Basin (JGB), Qaidam Basin (QB), Sichuan Basin (SB), Ordos Block (OB), Songliao Basin (SLB), North China Basin (NCB), Qiang-Tang Terrane (QT), Lhasa Terrane (LT), Himalaya Terrane (HT), Songpan-Garzê Terrane (SGT), Qilian Orogen (QLO), Qinling Orogen (QO), Dabie-Sulu Orogen (DSO), Changbai Mountain Range (CBM), Yangtze Craton (YZC), North China Craton (NCC), South China Block (SCB), Cathaysia Fold Belt (CFB), Taiwan Island (TW), Taiwan Strait (TS), North South Gravity Line (NSGL), Bohai Sea (BHS), Yellow Sea (YS), East China Sea (ECS), South China Sea (SCS).



Seismic tomography (including body and surface wave tomography) has been widely used to explore the lithospheric velocity structure beneath East Asia at different scales (e.g., Shapiro and Ritzwoller, 2002; Liang CT et al., 2004; Priestley et al., 2006; Zheng SH et al., 2008; Sun XL et al., 2010; Li YH et al., 2013; Xu Z et al., 2013; Huang ZC et al., 2014; Pandey et al., 2014; Bao XW et al., 2015; Shen WS et al., 2016; Chen M et al., 2017; Yang ZG and Song XD, 2019; Peng J et al., 2020). Continental-scale teleseismic body wave tomography provides three-dimensional (3D) P and S velocity images, which have revealed large-scale features in East Asia, including relatively low velocities in eastern China and high velocities underneath some basins. However, because of its steep ray path requirements, teleseismic body wave tomography typically has a low vertical resolution, which limits its detection of small-scale features. Xin HL et al. (2019) constructed a lithospheric velocity model for China continent using double-difference seismic travel time tomography, which was updated by incorporating surface wave dispersion data (Han SC et al., 2021). These authors report both  $v_p$  and  $v_s$  structures with a high resolution, especially in eastern China; however, the maximum depth of their model was approximately 150 km, providing structural information above the uppermost mantle only.

Surface wave tomography is an important tool for imaging lithospheric structures because of the depth sensitivity of surface waves with different frequencies. Many earthquake-based surface wave tomography studies at both continental and regional scales have been conducted in East Asia (e.g., Zhu JS et al., 2002; Li YH et al., 2013; Pandey et al., 2014). These studies reveal significant lateral variations in lithospheric structures in different geological units, yet the resolutions provided by these studies may be significantly influenced by the distribution of earthquakes and stations. The revolutionary ambient noise tomography (ANT) technique, which is based on the idea that Green's function between two receivers can be extracted from the cross-correlation of the diffuse field (noise interferometry) at the receivers, has been widely used to image the structure of the crust and uppermost mantle (e.g., Shapiro et al., 2005; Yao HJ et al., 2006; Zheng SH et al., 2008). Recent ANT studies at varying resolutions have also been conducted beneath East Asia, mainly in Chinese mainland and the eastern marginal seas (e.g., Zheng SH, 2008; Sun XL et al., 2010; Bao XW et al., 2015; Wang Q et al., 2017; Shen WS et al., 2016; Yang ZG and Song XD, 2019; Peng J et al., 2020). Most ANT studies have focused on Rayleigh waves; however, shear-wave models developed from the Love waves extracted from noise interferometry have also been proposed (e.g., Yang ZG and Song XD, 2019). Such studies have revealed the structure of the crust and upper mantle in greater detail. However, because ambient noise interferometry can only provide dispersion information over relatively short periods, ANT can only be applied to reveal the structure at relatively shallow depths (Bao XW et al., 2015; Peng J et al., 2020). One recent study (Zhang XZ et al., 2022)

systematically compared several seismic tomography models of the Chinese continental lithosphere and revealed large discrepancies in the existing velocity models both in absolute values and perturbation patterns. This indicates that there is a significant opportunity for improving the seismic models of this region.

Earthquake-based two-station (TS) analysis, which measures the dispersion curves from the empirical Green's functions extracted from the cross-correlation of the surface-wave chains generated by the same earthquake event, can provide dispersion information over longer periods (e.g., Yao HJ et al., 2006, 2008; Li YH et al., 2013; Chen HP et al., 2014; Wang WL et al., 2014). Compared with ANT, earthquake-based TS analysis can be applied to greater depths (e.g., Yao HJ et al., 2008; Li MK et al., 2018; Ojo et al., 2018). Thus, the joint analysis of dispersion data from both noise interferometry and earthquake-based cross-correlation (e.g., Xu Z et al., 2013; Bao XW et al., 2015) can increase path coverage and extend the period range, enabling the construction of lithospheric S-wave velocity models with higher lateral and vertical resolutions.

In this study, using event data from more than 1,000 seismic stations (Figure 3.1) from multiple national, global, permanent and temporary networks in and surrounding Chinese mainland (i.e., the China Earthquake Administration's CEArray; the Incorporated Research Institutions for Seismology Data Management Center's (IRIS DMS) Portable Array Seismic Studies of the Continental Lithosphere, PASSCAL; and the Global Seismographic Network, GSN), we systematically measured Rayleigh-wave phase-velocity dispersion curves at periods of 10 - 120 s and group velocity dispersion curves at periods of 10 - 140 s based on the earthquake-based TS method. We then combined the new dispersion measurements with three previously published datasets from Bao XW et al. (2015), Wang Q et al. (2017) and Ekström (2011) to construct a 3D lithospheric S-wave velocity model down to a depth of approximately 300 km in East Asia. The combined dataset provides a relatively uniform and perhaps the most complete surface wave data coverage of the study region. We show that our new model is generally consistent with previous models but with improved resolution, particularly at greater depths and in the marginal sea areas. Thus, our model can constraints the structure of the crust and upper mantle better, helping reveal the important lithospheric features of East Asia. Specifically, here we focus on variations in lithospheric thickness, the collision and interaction between the Indian and Eurasian Plates, and the delamination mechanism of Eastern China.

## 3.2 Data

We used waveform records from more than 1,000 seismic stations in East Asia to

derive high-quality Rayleigh-wave phases and group velocities based on the earthquake-based TS analysis method. Most of the stations are included within the dense China Regional Seismic Networks (CRSNs) (Zheng XF et al., 2010); the other stations included temporary deployments in the TP, the Tianshan region, and some other permanent stations within the Full Range Seismographic Network (F-NET) of Japan, South Korea, and Taiwan Islands, which are available from the IRIS DMC (Figure 3.1). Earthquake records from the CRSNs stations and the permanent stations in Japan and Taiwan covered the period from 2008 to 2011, which provided the largest contribution to our waveform dataset. The other stations were mostly temporary stations covering 2001 to 2010. The network codes and operation periods of the temporary stations are presented in Table 3.S1.

In addition to these newly measured dispersions, we also combined the following three datasets: (1) data from Bao XW et al. (2015) that across the Chinese continent, including Rayleigh-wave group and phase dispersion measurements derived from ambient noise correlations and earthquake group velocity measurements; (2) Rayleigh-wave group and phase dispersion measurements from Wang Q et al. (2017) for the marginal seas in East Asia derived from ambient noise correlations; and (3) Rayleigh-wave phase velocities between 130 and 250 s from Ekström (2011) during the inversions for the S-wave velocity structure. The addition of longer-period data helped constrain the S-wave velocity structure down to a depth of approximately 300 km, enabling us to investigate variations in lithospheric thickness beneath East Asia.

### 3.3 Methods

#### 3.3.1 Earthquake-based TS analysis

We used an earthquake-based TS analysis method (Yao HJ et al., 2006; 2008; Chen HP et al., 2014; Ojo et al., 2018) to measure the high-quality phase and group velocity between selected station pairs. Earthquake-based TS analysis requires that the target event and the two selected stations should be on a great circle; however, this is often challenging but ensured that the great circle paths between the earthquake and the two stations only have small offsets. We used the following two parameters to measure the offset: (1) the azimuthal difference,  $\alpha$ , of the earthquake to the two stations, and (2) the azimuthal difference,  $\beta$ , between the earthquake to the nearest station and the nearest station to the other station (Yao HJ et al., 2006; Figure 3.S1). The maximum permitted values were set to  $2^\circ$  and  $3^\circ$  for  $\alpha$  and  $\beta$ , respectively. For a given earthquake, a station pair that satisfied these criteria was selected, and the cross-correlation function (CCF) of the seismograms recorded by the two stations were calculated. The CCF can be considered as an approximation of the inter-station Green's function (Landisman

et al., 1969), which is used to extract the inter-station phase and group velocity. To ensure good excitation of the surface waves, only events with magnitudes  $>5.0$  and depths  $<100$  km were included. For each station pair, the distance between the event and either station was limited to  $30^\circ - 120^\circ$  to ensure good surface-wave waveforms. The distribution of selected events is shown in Figure 3.1.

### 3.3.2 Dispersion measurement and quality control

The dispersions were measured using the frequency-time analysis method (Ritzwoller and Levshin, 1998), which was integrated into the automatic frequency-time analysis (AFTAN) program. AFTAN is mainly used to analyze CCFs from ambient noise but can also be adapted to measure dispersion from event CCFs by setting the phase shift to  $\pi/4$  instead of  $-\pi/4$  (Chen HP et al., 2014). Here, we used AFTAN to measure Rayleigh-wave phase-velocity dispersions at periods of 10 – 120 s and group velocity dispersions at periods of 10 – 140 s. We then checked every dispersion curve by comparing it with the theoretical velocity derived from the GDM52 model (Ekström, 2011) to identify and reject poor dispersion measurements. Only the smooth part of the dispersion curve was retained. We also rejected dispersion curves that have less than 30 periods (Wang WL et al., 2014). Finally, for each selected station pair, all the dispersion curves derived from multiple earthquakes were averaged to provide the final dispersion measurement.

### 3.3.3 Strategy for combining dispersion measurements

Bao XW et al. (2015) measured phase dispersions from ambient noise correlations and group velocities from earthquakes across the Chinese continent. Wang Q et al. (2017) also measured the phase and group velocities from ambient noise correlations across marginal seas in East Asia. We combined our new dispersion measurements with these two dispersion datasets to construct Rayleigh-wave velocity maps. A comparison between the surface-wave velocities from the TS and noise interferometry at each overlapping period indicates a systematic bias, with the values from the TS generally greater than those from the noise interferometry (up to approximately 0.5%; Figures 3.S2 and 3.S3). This bias has also been observed in previous studies (e.g., Yao HJ et al., 2008; Ojo et al., 2018). Therefore, we followed the procedure of Yao HJ et al. (2008) and Li MK et al. (2018) to combine the dispersions from TS and noise interferometry. Briefly, for periods shorter than 20 s, we used the dispersions obtained from noise interferometry; for periods longer than 50 s, we used the dispersions from the TS analysis; and for periods between 20 and 50 s, we used the dispersions from the noise interferometry if the bias was  $<0.1$  km/s, otherwise, the dispersions from the TS analysis were used. The final dispersion dataset had a relatively denser path coverage and a wider period range. The final dispersion measurements were then used to

construct phase and group velocity maps for a set of periods on  $0.5^\circ \times 0.5^\circ$  grids using a linearized 2D inversion method (Bao XW et al., 2013; Xu Z et al., 2013). We used phase and group velocity images derived from the GDM52 model (Ekström, 2011) as the reference model to stabilize the inversion. Furthermore, for a certain period, by comparing the initial mean square travel time residual and the remaining uncounted residual, we rejected the paths with residual exceeded the unaccounted residual by three times or more. Subsequently, the velocity images were reinverted. The phase and group velocity maps produced after three iterations of this process were taken as the final velocity images.

### 3.3.4 Inversion for surface velocity map and S-wave velocity structure

The selected dispersion measurements were used to construct group and phase velocity maps at different periods using the linearized 2D inversion method of Xu Z et al. (2013), which is performed with a linearized inversion by minimizing the following quantity:

$$\min(\|\mathbf{A}\mathbf{m} - \mathbf{r}\|^2 + \lambda^2\mathbf{m}^2 + \phi^2\|\mathbf{L}\mathbf{m}\|^2) \quad (1)$$

where  $\mathbf{A}$  is the coefficient matrix;  $\mathbf{m}$  is the parameter vector; and  $\lambda$  and  $\phi$  are the damping and smoothing parameters, respectively. The smoothing operator  $\mathbf{L}$  is the Laplacian operator. We experimented with different pairs of  $\lambda$  and  $\phi$ , and selected those that best balanced the data misfit, model damping, and smoothness. Thus,  $\lambda = 10$  and  $\phi = 300$  were used in this study. Resolution tests (Figure 3.S4) showed that a  $1^\circ \times 1^\circ$  grid could be recovered in most parts of the study region at periods of 30, 60, and even 90 s; and a  $2^\circ \times 2^\circ$  grid could be recovered at periods  $>90$  s. Figures 3.S5 and 3.S6 show several representative phase and group velocity maps, respectively. Because we will mainly focus on the 3D shear-velocity model, detailed descriptions of the dispersion maps are not provided in the main text. Nevertheless, after constructing the phase and group velocity dispersion maps, we then extracted 10 - 120 s phase and 10 - 140 s group dispersion curves from our model as well as the 130 - 250 s phase dispersion curve from the GDM52 model (Ekström, 2011) at each grid point. We aimed to construct the shear-wave velocity structure of the crust and upper mantle (down to a depth of  $\sim 300$  km) to reveal the key features of the model. The long-period phase velocity dispersion proved much more sensitive to deeper structures than the group velocity. Therefore, we only used the long-period phase velocity dispersions from Ekström (2011). We merged the dispersion curves and inverted for 1-D shear-wave velocity profile at each grid point.

We jointly inverted the phase and group dispersion curves for each grid using a linearized iterative method (Herrmann and Ammon, 2004). The initial model was

modified from the global 1D reference model, AK135 (Kennett et al., 1995). Similar to Bao XW et al. (2015), we set the S-wave velocity in the top 100 km to a constant 4.5 km/s to avoid the assumption of a prefixed Moho interface. The deeper part of the initial model was obtained using the AK135 model. The layer thicknesses were 2 km in the top 10 km, 5 km at depths from 10 to 80 km, and 10 km below a depth of 80 km. Because surface wave dispersion curves are primarily sensitive to changes in S-wave velocity (although they also have some sensitivity to P-wave velocity and density; Julià et al., 2000; Bao XW et al., 2015), the S-wave velocity in the top 100 km was linked to the P-wave velocity using a Poisson's ratio of 0.25 and scaled to obtain density using the empirical relationship of Brocher (2005). Finally, we obtained a 3D crustal and upper-mantle S-wave velocity model for East Asia to a depth of approximately 300 km. The inversion results and data fitting at two selected grid-point pairs are shown in Figure 3.S7. Overall, the data from our dispersion maps and the GDM52 model matched the predicted dispersion matched well.

## 3.4 Results

We inverted the newly constructed surface-wave dispersion curve for each grid for the 1D S-wave velocity profile and then constructed a 3D S-wave velocity model beneath East Asia by assembling all the 1D velocity profiles. Based on the 3D model, we also constructed crustal and lithospheric thickness models. In this section, we first briefly describe the crustal thickness model (Section 4.1) and then focus on the 3D S-wave velocity model (Section 4.2) and the lithospheric thickness model (Section 4.3).

### 3.4.1 Crustal thickness

Dispersion data can effectively constrain the absolute S-wave velocities at different depths, even though they cannot constrain the depths of the velocity discontinuities (Julià et al., 2000). Xu Z et al. (2013) found that the average shear-wave velocity at the depth of the Moho as defined by the reference model CRUST 2.0 (Bassin et al., 2000) is almost constant at approximately 4.0 km/s, with a slight positive trend as a function of crustal thickness. Based on this, the depth of 4.0 km/s (the value can vary slightly) is a good estimate for the depth of the Moho. Although the method is simplistic, it has been successfully applied in previous studies to provide approximate estimations of crustal thickness (e.g., Bao et al., 2011, 2013, 2015; Wang Q et al., 2017).

Figure 3.2 shows the estimated crustal thickness beneath East Asia based on our models. There are significant lateral variations in thickness ranging from an extremely thin crust (<30 km) in eastern China and the marginal seas to intermediate thicknesses (~35 - 50 km) in Central China and the thickest crust (~70 - 80 km) in the TP region. The thickest crust beneath the TP reflects significant crustal thickening caused by the



Indo-Asian collision, while the thin crustal thickness in eastern China and the marginal seas reflects the strong influence of the Mesozoic extension tectonics caused by dramatic lithospheric thermo-tectonic reactivation (Ren JY et al., 2002). Several crustal thickness maps of the Chinese continent from historical deep seismic sounding profiles (e.g., Teng JW et al., 2013), teleseismic receiver functions (e.g., Li YH et al., 2014), and surface wave tomography analysis (e.g., Bao XW et al., 2015) have recently been provided. Our new map shows not only good consistency with these previously published models but also covers the marginal seas, providing a broader-scale map of crustal thickness variations in East Asia. A comparison with the crustal thickness map of the Chinese mainland (Figure 3.S8) shows good consistency between the two models. The largest discrepancy lies in the TP, where the distribution of seismic stations is extremely uneven. Importantly, our new map, based on dispersion inversion, provides a more uniform data coverage than that obtained from receiver function analysis.

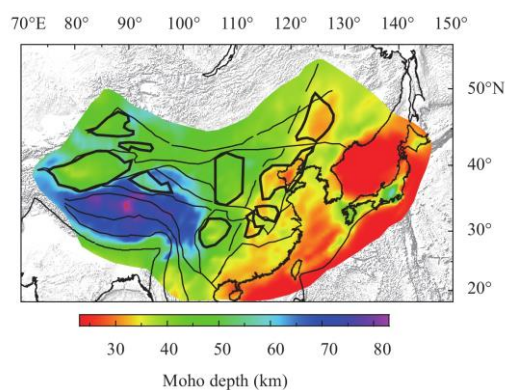


**Fig. 3.2 Map of crustal thickness of East Asia derived from our 3D shear-wave velocity model.**

Our new crustal thickness map also corresponds well with surface geology. For example, the North-South Gravity Lineament (NSGL) is well delineated by a sharp crustal thickness gradient that is compatible with the surface topography gradient. The coastline is also well identified by the crustal thickness transition zone in the sea-land interaction area. The Qilian orogeny in the northeastern TP is clearly identified by increased crustal thickness relative to its surrounding region. The margins of the TP are also well delineated by significant changes in crustal thickness associated with large elevation changes.

### **3.4.2 3D S-wave velocity model of East Asia**

We constructed a lithospheric S-wave velocity model from the Earth's surface to a depth of approximately 300 km, with some selected depth slices shown in Figures 3.3 and 3.4. As shown in Figure 3.3a, the velocity generally correlates well with surface geology and regional tectonics at a depth of 5 km. Large sedimentary basins in Chinese mainland (e.g., the Tarim Basin, Qaidam Basin, Sichuan Basin, North China Basin, and

Songliao Basin), the eastern marginal seas of East Asia, and the Japan Sea are dominated by low velocities. The Ordos Block shows relatively complex features in the western and central areas, and the Weihe Rift in the southeastern corner is dominated by low velocities. In comparison, the eastern part of this region is dominated by relatively high velocities suggesting stronger erosion in the eastern part of the Ordos Block. These features are consistent with those of previous studies on continental (Zheng SH et al., 2008; Sun XL et al., 2010; Xin HL et al., 2019; Xu Z et al., 2013; Bao XW et al., 2015; Shen WS et al., 2016) and regional scales (Bao XW et al., 2013; Guo Z and Chen YJ, 2017; Wei XZ et al., 2017). Low-velocity zones can also be identified in the northwestern part of the TP and the eastern Himalayan Syntaxis (EHS) region. In contrast, some mountain regions, such as the east Qinling orogen, Changbai Mountain Range, and Da Hinggan Ling, show high-velocity features.

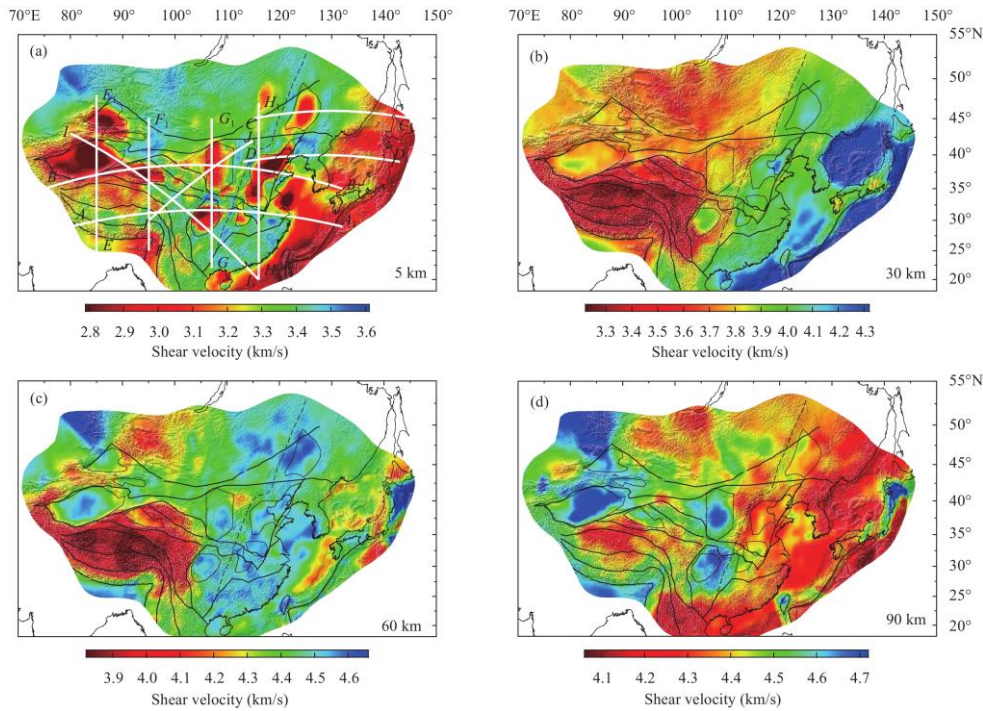


**Fig. 3.3** Shear-wave velocity maps at 5, 30, 60 and 90-km depths from this study. White lines in (a) represent the locations of the vertical cross-sections in Figures 3.5—3.7. The black lines represent the boundaries of geological units as shown in Figure 3.1.

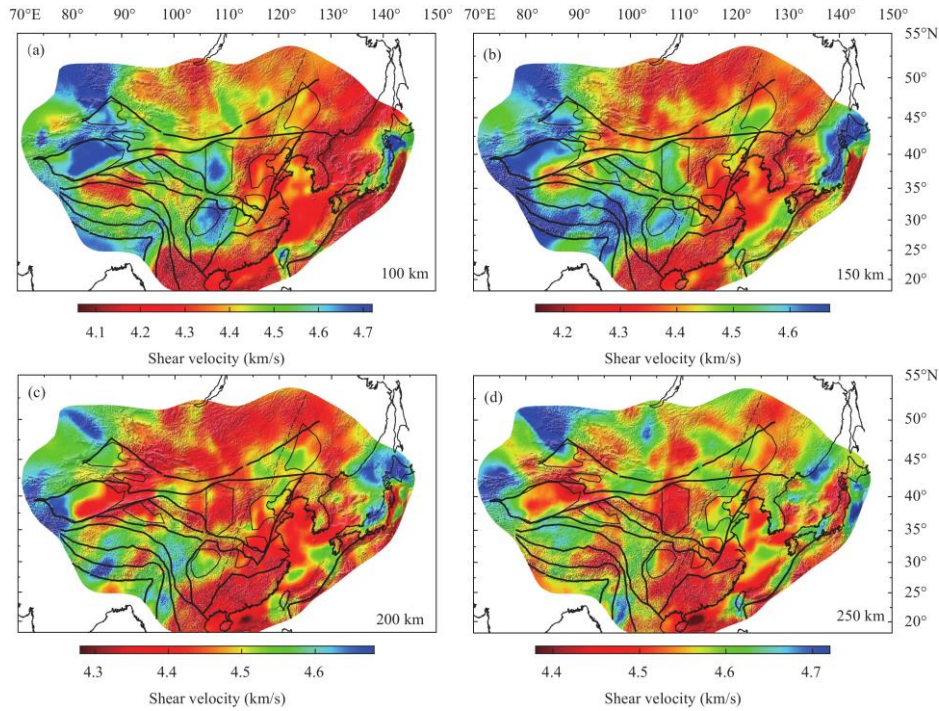


**Fig. 3.4 Shear-wave velocity maps at 100, 150, 200 and 250-km depths from this study. The black lines represent the boundaries of geological units as shown in Figure 3.1**

At a depth of 30 km (Figure 3.3b), the Japan Sea and the East and South China Seas reach the lower crust or uppermost mantle and exhibit high velocities. Western China, except for the Sichuan Basin, is dominated by low velocities, especially in the TP region and the northern part of Yunnan. The Sichuan Basin has a relatively higher velocity than the surrounding mountains. Northeastern China, the eastern part of north China, and southeastern China show intermediate velocities. In addition to the NSGL, there is a clear velocity contrast that correlates well with the sharp crustal thickness and surface topography gradient. In addition, the S-wave velocities in the Tarim Basin exhibit clear heterogeneity, with a small high-velocity zone in the southwestern part.

At a depth of 60 km (Figure 3.3c), most of the region reaches the uppermost mantle, except for the TP and the Pamirs and Tianshan regions, which remain at the depth of the lower crust. These regions are dominated by conspicuous low velocities. Some other regions, such as the surrounding regions of the Japan Sea and Ryukyu Island, are also clearly imaged as low-velocity zones. A prominent low-velocity anomaly is observed in the Datong volcanic region, which has also been identified in previous regional-scale surface and P-wave tomographic studies (Zhao DP et al., 2011; Chen HP et al., 2014), which may imply the upwelling of melt materials from the deeper mantle.

At depths of 90 and 100 km (Figures 3.3d and 3.4a), the S-wave velocity images show predominantly low velocities beneath most parts of the TP (especially the northern part), the Songpan-Garzê terrane, eastern China, the Korean Peninsula, and the marginal seas (including the Japan Sea). These low-velocity anomalies are broadly

consistent with global- and regional-scale tomographic studies (Shapiro and Ritzwoller, 2002; Friederich, 2003; Huang ZC et al., 2014; Huang JL and Zhao DP, 2006; Priestley et al., 2006; Feng M and An MJ, 2010; Wei W et al., 2012; Li YH et al., 2013; Bao XW et al., 2015; Li HY et al., 2018) but with higher resolutions. The prominent low velocities beneath the TP indicate significant deformation and high temperatures. Other predominant features at these depths are the high-velocity anomalies beneath the western part of the Yangtze Craton (including the Sichuan Basin), the Ordos Block, and the central and eastern parts of the Tarim Basin. The heterogeneities of the S-wave velocities inside these stable platforms imply different deformation states in these regions. High-velocity anomalies are also observed in the Taiwan Strait and the northern part of Japan Island.

At a depth of 150 km, the high-velocity anomalies beneath the Tarim Basin, the western part of the Yangtze Craton, and the Ordos Block extend to this depth, suggesting the existence of thick cratonic roots beneath these regions. The low-velocity anomalies in the TP are concentrated to the northwestern part, while most parts of the TP are dominated by high-velocity anomalies, such as the Songpan-Garzê Terrane in the east and other southwestern areas. A clear banded zone with a relatively low velocity is observed in the southern TP region, extending from the Indian Plate to the central TP with a NNE strike direction and extending to a depth of 200 km (Figure 3.4c) and even 250 km in some places (Figure 3.4d). This banded low-velocity zone correlates with the well-known Yadong-Gulu suture. The central and northern parts of Japan Island show a high-velocity anomaly that extends down to a depth of 200 km.

At depths of 200 km and below (Figures 3.4c – 3.4d), the high-velocity anomalies in the previously mentioned cratonic regions disappear, including the Sichuan Basin, Ordos Block, and Tarim Basin. The western part of the Tarim Basin shows a small-scale high-velocity anomaly from a depth of 150 to 200 km, which may imply the deep subduction of the Indian Plate to the cratonic root in the western Tarim Basin. It is worth noting that the low-velocity anomalies are concentrated in several banded zones located in the western and central parts of the TP, striking in a NNE direction from the Indian Plate to the northern and northwestern TP. These features may be related to slab tears of the subduction plates, as suggested by Li JT and Song XD (2018) based on P- and S-wave tomography. In general, eastern China and its marginal seas are dominated by widely distributed low velocities below a depth of 90 km (Figure 3.3d and Figure 3.4), which can be attributed to the intensive destruction of the lithosphere and the related upwelling asthenosphere.

Several representative cross-sections from the surface to a depth of approximately 300 km are presented in Figures 3.5-3.7. The locations of these cross-sections are shown in Figure 3.3a. These cross-sections have a number of common features. For example, the sedimentary basins and oceanic regions correlate with low-velocity



anomalies near the surface of all the profiles, and the boundaries between different geological units are well imaged at the lithospheric mantle depth, i.e., the boundaries between the sedimentary basins and surrounding mountainous regions are well imaged as relatively low-velocity anomalies.

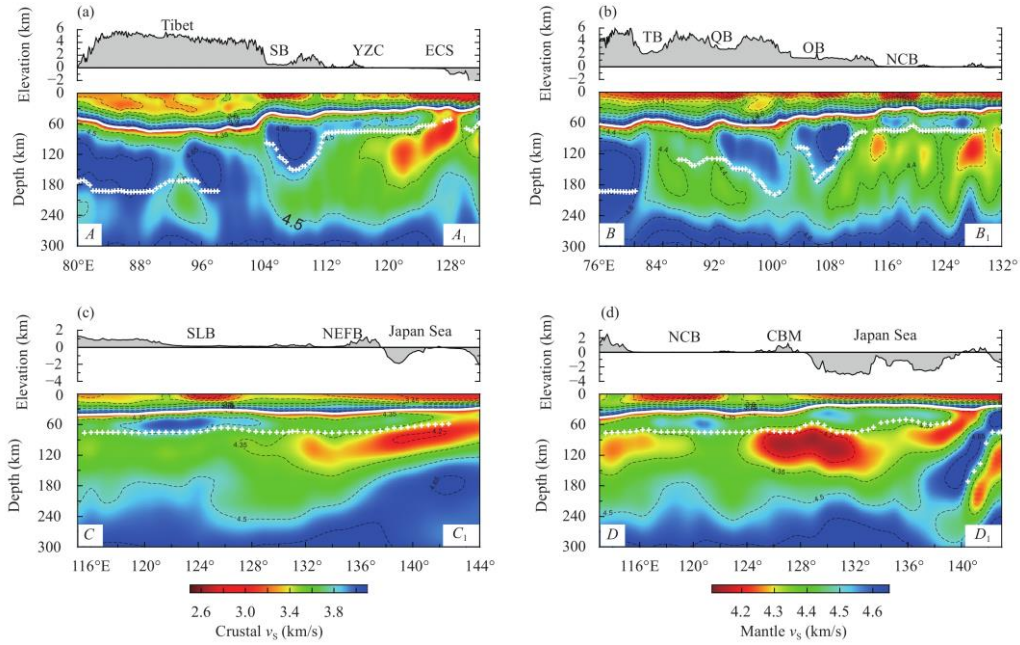


**Fig. 3.5** Four west-east trending cross-sections across of the shear-wave velocity model from this study. The locations of the profiles are denoted in Figure 3.3a. The white lines and white crosses denote the estimated Moho interfaces and LABs, respectively.

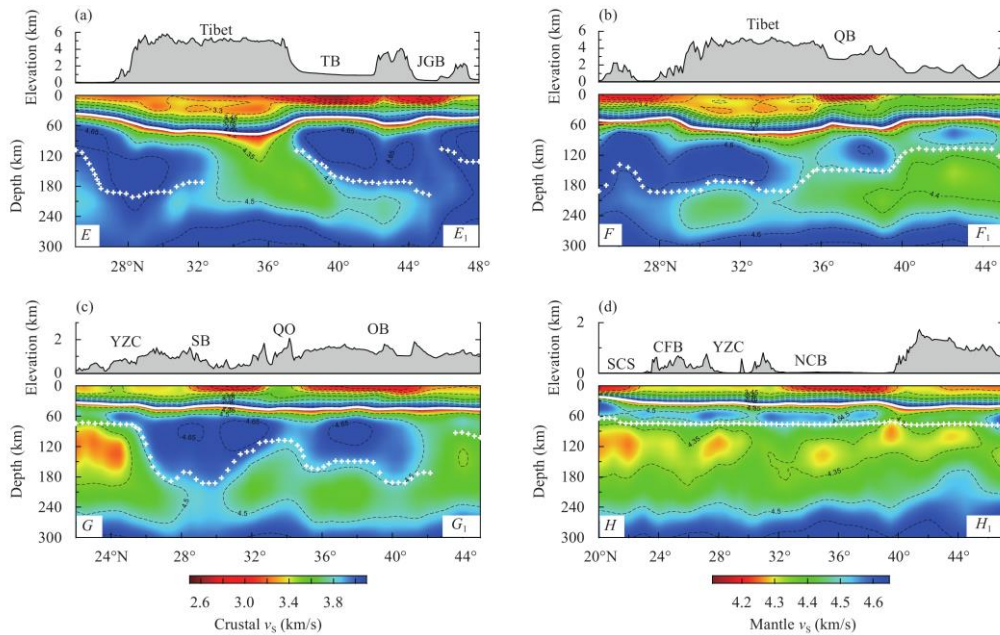


**Fig. 3.6** Same as Figure 3.5 but for four south-north trending cross-sections.

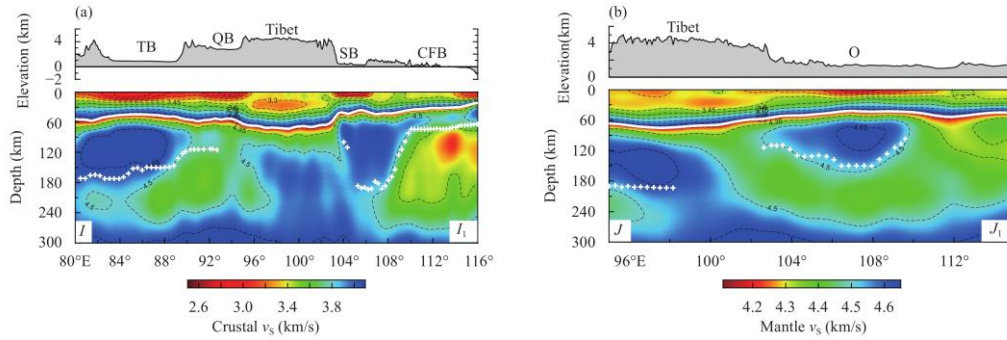


**Fig.3.7** Same as Figure 3.5 but for a northwest-southeast (a) and a southwest-northeast (b) trending cross-sections.

Figure 3.5 shows four west-east-trending cross-sections. The first two sections ( $A-A_1$  and  $B-B_1$  in Figures 3.5a and 3.5b, respectively) show a heterogeneous lithospheric mantle structure from west to east. Prominent high-velocity anomalies in the lithospheric mantle and a relatively clear lithosphere-asthenosphere boundary (LAB) are also observed beneath the sedimentary basins, especially those in central and western China, i.e., the Tarim Basin, Qaidam Basin, Ordos Block, and Sichuan Basin. Although the lithospheric mantle of the sedimentary basins in western and eastern China are all imaged as high-velocity anomalies, their velocity values show significant variation. The velocities of the basins in western China are higher than those in eastern China, suggesting changes in lithospheric strength from west to east. The second two sections ( $C-C_1$  and  $D-D_1$  in Figures 3.5c and 3.5d, respectively) cross the eastern part of the North China Craton (NCC) and northeastern China, respectively, and end in the oceanic regions. Subduction slab of the Pacific Plate to the Eurasian Plate is clearly seen as well as large low-velocity region beneath the Sea of Japan. Another important feature that can be observed from the four sections is the gradual thinning of the lithospheric thickness from west to east, which is consistent with the findings of Feng M and An MJ (2010).

Figure 3.6 shows four south-north-trending cross-sections. Sections  $E-E_1$  and  $F-F_1$  (Figures 3.6a and 3.6b) cross the western and eastern TP, respectively, while sections  $G-G_1$  and  $H-H_1$  (Figures 3.6c and 3.6d) cross central and eastern China, respectively. Sections  $E-E_1$  and  $F-F_1$  show that the underthrusting high-velocity Indian Plate approaches the central-to-northern part of the TP, at  $34^\circ$  N in the western TP and  $35^\circ$  N in the eastern TP. The subduction of the Indian Plate under the TP is associated with severe tectonic destruction. For example, the intrusion of weak materials from the TP to the lithosphere of the Tarim Basin under the extrusion force of the subduction slab also causes the destruction of the lithospheric base in the basin-mountain junction zone (see Section  $E-E_1$ , Figure 3.6a). In section  $F-F_1$  (Figure 3.6b), the lithospheric root of the Qaidam Basin is clearly imaged to have a high velocity; however, there is no



indication of southward continental subduction of the Asian Plate under the lithosphere of the TP, which is consistent with the results of seismic tomography and receiver function analyses (e.g., Liang XF et al., 2012; Shen XZ et al., 2017; Wei XZ et al., 2017).

Two other cross sections,  $I-I_1$  and  $J-J_1$ , are presented in Figure 3.7. Section Profile  $I-I_1$  (Figure 3.7a) starts from the northern boundary of the Tarim Basin and crosses the Tarim Basin, Qaidam Basin, TP, Sichuan Basin, Yangtze Craton, South China Block, and South China Sea. Section  $J-J_1$  (Figure 3.7b) starts from the southeastern corner of the TP and crosses the eastern TP, Qinling Orogen, and Ordos Block. Similar to sections  $A-A_1$  and  $B-B_1$  (Figure 3.5), these profiles show complex lithospheric mantle structures and significant differences between geological units, i.e., the velocity contrast between the basins and their surrounding regions. The lithospheric mantle is imaged as a high-velocity zone in the basins of these two sections, while the lithospheric roots are also easily recognizable.

### 3.4.3 Lithospheric thickness in East Asia

The lithosphere and asthenosphere are the most tectonically active parts of Earth's interior. A traditionally accepted broad definition of the asthenosphere based on seismic tomography is the low-velocity zone in the upper mantle. In many seismic studies, the high-velocity lid over the asthenosphere has often been equated to the lithosphere; however, the interface between the lithosphere and asthenosphere is often far from a distinct discontinuity, and the transition from the lithosphere to the asthenosphere is typically identified as the lithosphere-asthenosphere boundary (LAB). The distribution of the LAB (or lithospheric thickness) is important for understanding the deformation and dynamic processes in the Earth's deep interior. In this section, we focus on the implications of seismological studies for modeling lithospheric thickness, which we refer to as the seismic lithosphere, distinguishing it from the thermal lithosphere as inferred from temperature (e.g., An MJ and Shi YL, 2006).

The seismic lithospheric thickness (“lithospheric thickness” hereinafter) is more difficult to define using seismic velocity models (e.g., Li YH et al., 2013; Wang Q et al., 2017). In this study, we attempted to identify a proxy for the LAB by using the following strategies. Considering the relatively low velocity in the asthenosphere, we first discarded the 1D velocity profiles in which the velocity continuously increased with depth below the Moho interface. Several examples of discarded profiles are shown in Figure 3.S9. Second, for each remaining 1D velocity profile, we determined the maximum velocity,  $v_1$ , from the Moho to a depth of 200 km below, with the corresponding depth denoted as ‘ $H_1$ ’. We then identified the minimum velocity,  $v_2$ , from  $H_1$  to a depth of 150 km below, and recorded the corresponding depth as ‘ $H_2$ ’. The velocity difference (%),  $R$ , was then calculated as  $R = (v_1 - v_2) / v_1 \times 100\%$ , and the

1D velocity profiles with  $R$  values  $<2\%$  were discarded. Third, for each remaining velocity profile, we calculated the velocity gradient between  $H_1$  and  $H_2$ , and took the depth corresponding to the maximum negative gradient as a proxy for the LAB. Examples clearly showing the LAB are provided in Figure 3.S10. For comparison, we also show several 1D profiles with and without the LAB proxy in Figures 3.S11 and 3.S12, respectively.

By following these three steps, we obtained the lithospheric thickness map of East Asia from our S-wave velocity model (Figure 3.8). Although there are limitations in this approach, such as the measuring artifacts near the basin-mountain junction zones and subduction zones as well as the relatively arbitrary value of  $R$ , the LAB generally indicates the location of a rapid velocity decrease with depth in most parts of our study region (denoted by the white crosses in the cross-sections in Figures 3.5 – 3.7). As such, our approach is useful for examining the general variations in lithospheric thickness at a continental scale.

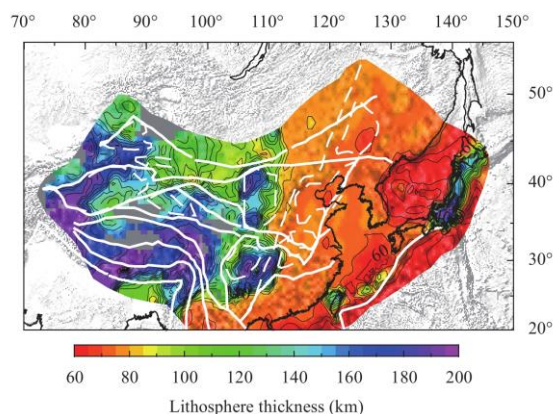


**Fig. 3.8** Map of lithosphere thickness derived from our 3D shear-wave velocity model. The white lines represent the boundaries of geological units as shown in Figure 3.1.

The lithospheric thickness map of East Asia derived from our velocity model is shown in Figure 3.8. We compare our map with the results of An MJ and Shi YL (2006), who first converted the 3D shear-wave velocity structure into a temperature structure and then extracted lithospheric thickness. Because of differences in our definitions of the LAB, the values inevitably differ slightly; however, the two maps are generally consistent in absolute values, perturbation patterns, and local features. For example, in both cases, lithospheric thinning is seen in eastern China, and a thick lithosphere is seen in the southern TP region and the Sichuan Basin (Figure 3.S13).

Based on these maps, lithospheric thickness shows significant lateral variation, ranging from extremely thin in the Japan Sea to its thickest in the western part of the Tarim Basin and the southeastern part of the Sichuan Basin. Except for the Yunnan region, western China (west to  $110^\circ$  E) has a thick lithosphere, while eastern China and its marginal seas (east to  $110^\circ$  E) show a relatively thinner lithosphere. Generally,

the lithosphere thins from west to east. Eastern and southwestern China have consistent lithospheric thicknesses, while central and western China show large variations. Notably, the boundary between eastern and southwestern China and western China is marked by a sharp change in lithospheric thickness. As shown in Figure 3.8, the western Yangtze Craton, the majority of the central and eastern TP, and the western Tarim Basin have a thick lithosphere (thicker than 180 km). Some other smaller regions, such as the northwestern and southwestern corners of the Ordos Block and the northern Qilian Orogen, also show a thick lithosphere. The eastern and southeastern Tarim Basin, Qaidam Basin, Qilian Orogen, east Qinling-Dabie Orogen, central and eastern Ordos Block, and the conjunction zone between the Sichuan Basin and TP show a relatively thin lithosphere.

In northern and eastern Tibet, the velocities increase continuously with depth below the Moho interface (Figure 3.S12); thus, we did not determine the LAB as previously described and the lithosphere in these regions may be thicker than the estimated thicknesses. The complex tectonic background in central and western China, including plate subduction and basin-mountain interactions, may contribute to the significant variations in lithospheric thickness. Crucially, despite some discrepancies in LAB values caused by different identification criteria and geophysical techniques, the general trend of our lithospheric thickness map is consistent with that presented in existing continental-scale (An MJ and Shi YL, 2006; Li YH et al., 2013) and regional-scale studies (Zhang XM et al., 2014; Wang Q et al., 2017).

### **3.5 Discussion**

We generated a 3D lithospheric S-wave velocity model for East Asia via the joint inversion of newly measured Rayleigh wave dispersion data from earthquake-based TS analysis, dispersion datasets from Bao XW et al. (2015) for Chinese mainland and Wang Q et al. (2017) for the marginal seas in East Asia, and the long-period dispersion map from Ekström (2011). This combined dataset broadened the period range of Rayleigh wave dispersion (periods from 10 to 140 s for group velocity and 10 to 250 s for phase velocity), allowing us to investigate the S-wave velocity structure in detail to a depth of approximately 300 km. Our new model has both high lateral and depth resolution; thus, we are able to reveal the key features of lithospheric thickness in East Asia, which are important for studying the geological evolution and tectonics of the region. In this section, after a brief comparison of our new model with some previously published continental-scale models, we focus on two important topics: (1) the lithospheric structure of eastern China and its marginal seas, and (2) subduction and collision interactions in the TP region.

### 3.5.1 Comparison with previous studies

Some continental-scale surface-wave tomographic studies of similar regions (e.g., Feng M and An MJ, 2010; Li YH et al., 2013; Pandey et al., 2014; Xin HL et al., 2019), and regional-scale tomographic studies for parts of our study region including Chinese mainland (e.g., Zheng SH et al., 2008; Sun XL et al., 2010; Xu Z et al., 2013; Bao XW et al., 2015; Shen WS et al., 2016), the TP and surrounding regions (e.g., Bao XW et al., 2013; Zhang XM et al., 2014; Wei XZ et al., 2017), and the region's marginal seas (e.g., Wang Q et al., 2017) have been performed. Here, we compare our model with some selected continental-scale tomographic models (e.g., Feng M and An MJ, 2010; Li YH et al., 2013; Pandey et al., 2014; Bao XW et al., 2015). The S-wave velocity models presented by Feng M and An MJ (2010), Li YH et al. (2013), and Pandey et al. (2014) cover a similar region and have a similar depth range to that of our new model; however, these studies used a few hundred stations and the lateral resolutions of their models are comparatively limited. Therefore, our model not only shows good agreement with these previous studies with respect to large-scale structures but also significantly improves the data resolution for some small-scale structures. For example, our model more clearly reveals lithospheric structures at basin-mountain junction zones as well as lithospheric roots beneath sedimentary basins, such as the Qaidam Basin and Ordos Block.

This work builds on two earlier studies from our research group on Chinese mainland (Bao XW et al., 2015) and the marginal seas in East Asia (Wang Q et al., 2017). By combining our newly measured dispersion data and the dispersion maps from Ekström (2011) with our group's previous two datasets, we have been able to (1) further increase the path coverage, and (2) extend the effective inversion depth to approximately 300 km. In comparison with the two models from Bao XW et al. (2015) and Wang Q et al. (2017), the effective depth of our new model reaches the asthenosphere, and even deeper parts, which allows us to investigate the features of the entire lithosphere in East Asia, including variations in lithospheric thickness.

### 3.5.2 Lithospheric thinning and destruction in east China and marginal seas

East China contains the North China Craton (NCC), South China Block (SCB), and Phanerozoic orogenic belts between the NCC and SCB (Zhao GC and Cawood, 2012). Figure 3.8 shows that eastern China and the marginal seas have a coherent lithospheric thickness, averaging ~80 km, with a clear thinning trend from west to east (see cross-sections  $A-A_1$  and  $B-B_1$  in Figures 3.5a and 3.5b). For the NCC, the lithosphere is still thick in its western part, such as the eastern part of the Ordos Block, and thins gradually to the eastern part. Similarly, for the SCB, the lithosphere is quite

thick in the Yangtze Craton (YZC) and becomes significantly thin in its eastern part and marginal seas (Figure 3.8). Thus, our results show that both the eastern NCC and SCB and their conjunction regions are characterized by lithospheric thinning. This is consistent with global and regional seismic tomographic studies (Feng M and An MJ, 2010; Bao XW et al., 2013, 2015; Li YH et al., 2013; Pandey et al., 2014; Wang Q et al., 2017) and receiver function studies (Chen L, 2009), which also report thinning and destruction of the lithosphere in east China and its marginal seas (e.g., Chen L et al., 2009; Zhu RX et al., 2012; Li YH et al., 2013; Pandey et al., 2014; Bao XW et al., 2015). Nevertheless, the mechanism of lithospheric keel destruction remains unclear (Zhu RX et al., 2012). Previous studies have proposed several tectonic processes that may be responsible for the thinning of the lithosphere in eastern China and its marginal seas including the far-field effect of the collision between the Indian and Eurasian Plates, mantle plume activity, and the westward subduction of the Pacific Plate under the Eurasian Plate [see Zhu RX et al. (2012) for a review]. Body-wave tomographic studies (e.g., Zhao L et al., 2012) have confirmed the existence of a deeply subducted slab from the Pacific Plate and its horizontal extension beneath east China, especially beneath Chinese mainland. The initial part of the subduction slab in the upper mantle, previously imaged as a high-velocity zone, is also observed in our model (see the eastern sides of cross-sections  $C-C_1$  and  $D-D_1$  in Figures 3.5c and 3.5d). The low-velocity anomalies observed at depths of  $\sim 80 - 180$  km depth beneath eastern China and its marginal seas are particularly notable (Figures 3.5 and 3.6d). Similar low-velocity zones have been observed in recent P-wave tomographic studies (e.g., Jiang GM et al., 2013; Zheng HW and Li TD, 2013) and surface-wave tomographic studies (e.g., Ouyang LB et al., 2014) carried out in the middle-lower Yangtze River based on the joint inversion of the receiver function and surface-wave dispersion in the SCB (Li HY et al., 2018). These low-velocity zones are interpreted as upwelling of the asthenosphere induced by the detached lithosphere, which could be related to the subduction of the Pacific Plate (Jiang GM et al., 2013; Ouyang LB et al., 2014). As shown in Figure 3.4, the velocities in these large low-velocity zones are significantly lower than those in the surrounding regions in the asthenosphere, and are possibly caused by the partial melting of the subduction slab or the detached lithosphere induced by the subduction slab.

Figure 3.6d shows the south-north trending velocity cross-section across east China, with distinct low-velocity zones in the asthenosphere that suggest the widespread existence of partial melting. Indeed, the upwelling of the melting materials likely causes a reducing velocity contrast between the high-velocity lithospheric mantle lid and the asthenosphere, and even the complete disappearance of the LAB, especially in oceanic regions (see the eastern part of cross-sections  $C-C_1$  and  $D-D_1$  in Figure 3.5). Complete intrusions of partial melting into the lithosphere are also observed in some

continental regions, i.e.,  $114^{\circ}$  E in section  $B-B_1$  (Figure 3.5b) showing the upwelling of melting materials near the NSGL. The upwelling of asthenospheric materials induced by the westward subduction of the Pacific Plate can erode the overlying lithospheric base, resulting in thinning of the lithosphere. Previous work has indicated that these regions have been strongly influenced by the tectonics of the circum-Pacific system (Ren JY et al., 2002). Therefore, the subduction of the Pacific Plate under the Eurasian Plate might be the main cause of the destruction of the lithosphere in eastern China and its marginal seas (Zhu RX et al., 2012).

### 3.5.3 Subduction and collision interactions in the TP region

The ongoing collision beginning  $\sim 50$  Ma ago between the Indian and Eurasian Plates created the TP as a highly deformed zone with thickened crust and elevated topography (Avouac and Tapponnier, 1993; Yin A and Harrison, 2000; Royden et al., 2008; Tapponnier et al., 2001). The complex tectonic evolution and deformation pattern here make it an ideal place to investigate the process of continental collision. Indeed, the subduction of the Indian Plate beneath the Eurasian Plate has played a key role in the tectonic evolution of Tibet. To better understand the formation and tectonic evolution of the TP, numerous geophysical studies based on different techniques have been proposed to investigate the Tibetan velocity structures (Kind et al., 2002; Tilmann et al., 2003; Liang CT and Song XD, 2006; Li C et al., 2008; Feng M and An MJ, 2010; Hung et al., 2010; Liang XF et al., 2012; Li YH et al., 2013; Pandey et al., 2014; Bao XW et al., 2015; Chen M et al., 2017; Li JT and Song XD, 2018). In this section, we discuss the deep velocity structures beneath the TP as revealed by our model alongside their possible tectonic implications.

Our new model reveals a strongly heterogeneous S-wave velocity structure at the lithospheric mantle depth beneath the TP (Figures 3.3 and 3.4). A distinctive feature is the presence of a large low-velocity zone in the northern and northeastern TP, ranging from  $\sim 90$  to 150 km. The scale of this zone decreases with depth, its extension covers the Qiangtang terrane and the entire Songpan-Garzê terrane at 90 and 100 km depths, respectively, and it is concentrated in the northwestern part of the TP at a depth of 150 km. A low-velocity feature at the lithospheric mantle depth has also been observed in many previously published seismic studies (Friederich, 2003; Huang JL and Zhao DP 2006; Priestley et al., 2006; Li C et al., 2008; Li YH et al., 2013; Bao XW et al., 2015). The spatial extension of this low-velocity zone corresponds well with the widespread Cenozoic magmatism in the northern part of the TP (Chung et al., 2005), suggesting that the hot and weak materials in the lithospheric mantle may be related to mantle upwelling induced by lithospheric delamination due to collision between the Indian and Eurasian Plates (Chung et al., 2005; Li YH et al., 2013; Bao XW et al., 2015). Furthermore, the large low-velocity zone beneath the TP may suggest lithospheric



delamination, as reported by some surface-wave tomographic studies (e.g., Li YH et al., 2013; Bao XW et al., 2015).

Another important issue in the TP region is the collision state of the Indian and Eurasian Plates, such as the northward extension of the subducted Indian lithosphere and the existence of south-verging subduction of the Asian Plate under the TP. Our model shows the subducting Indian slab in the southern part of the TP, which is imaged as having high velocities (Figures 3.6a and 3.6b) and is consistent with previous seismic studies (Tilmann et al., 2003; Li C et al., 2008; Feng M and An MJ, 2010; Hung et al., 2010; Li YH et al., 2013; Pandey et al., 2014; Bao XW et al., 2015). Sections  $E-E_1$  and  $F-F_1$  in Figures 3.6a and 3.6b indicate that the underthrusting of the Indian slab approaches the middle to north TP regions. Section  $E - E_1$  is located in the western part of the TP and shows that the Indian slab approaches  $\sim 34^\circ$  N and is then separated from the high-velocity Tarim cratonic keel by the low-velocity zone. Section  $F-F_1$ , on the other hand, is located in the eastern part of the TP region and shows that the Indian slab approaches  $\sim 34 - 35^\circ$  N and is then separated from the high-velocity Qaidam cratonic keel by a narrow low-velocity zone. Ceylan et al. (2012) observed high-velocity zones within Tibet and inferred that the northern limit of the Indian slab is up to  $\sim 34^\circ$  N. The research region examined by Ceylan et al. (2012) contains our  $F-F_1$  section, confirming the consistency of our results.

Inconsistent with some previous geophysical studies (e.g., Zhu JS et al., 2002; Priestley et al., 2006), our work shows that the Indian Plate does not subduct beneath the entire TP, and its northern limits vary from east to west. However, our results are consistent with more recent tomographic studies (Li C et al., 2008; Hung et al., 2010; Zhang H et al., 2012; Li YH et al., 2013), which also support the partial underthrusting of the Indian slab under the TP and the variable subduction northern limits of the Indian slab from west to east. Using high-resolution P- and S-wave tomography, one recent study showed that the subducted Indian mantle lithosphere has variable subduction angles and northern limits in different regions (Li JT and Song XD, 2018).

### **3.6 Conclusions**

We derived a 3D lithosphere S-wave velocity model for East Asia by combining newly obtained Rayleigh wave dispersions using the earthquake-based TS method, two previously published dispersion datasets (Bao XW et al., 2015; Wang Q et al., 2017), and the long-period dispersion maps derived by Ekström (2011). Our new model provides enhanced lateral and vertical resolutions compared with previous continental models, and provides a new valuable reference model for better understanding tectonics and geodynamic processes in East Asia.

Our new velocity model reveals heterogeneous lithospheric structures beneath East Asia. The enhanced effective depth (down to approximately 300 km) allows us to investigate the velocity structure features of the entire lithosphere, and we derive a lithospheric thickness map from the 3D velocity model. The lithospheric thickness map shows drastic variations from west to east. The boundary between eastern and southwestern China and western China is marked by a sharp change in lithospheric thickness, and East China and its marginal seas clearly indicate lithospheric thinning.

We observed widely distributed low-velocity zones in the asthenosphere above the sub-horizontal slab from the Pacific Plate beneath eastern China and its marginal seas, suggesting the ascent of hot partial melts derived from the subducted slab. Subduction of the Pacific Plate under the Eurasian Plate might be the main cause of the destruction of the lithosphere in eastern China and its marginal seas. We also observe a large low-velocity zone at a depth range of ~90 – 150 km beneath the northern and northwestern parts of the TP region indicative of lithospheric delamination. Furthermore, our model clearly images the subduction slab of the Indian Plate in the southern TP region. Here, high-velocity zones presumed to be the Indian slab are separated from the cratonic keels of the Tarim and Qaidam Basins by low-velocity zones, implying that the Indian Plate does not subduct beneath the entire TP. Finally, our results also provide evidence that the lateral extent of the Indian Slab varies from west to east.

## Data availability

The 3D S-wave velocity, crustal thickness, and lithospheric thickness models as well as the phase and group velocity maps at different periods described in this study are available at <https://www.equsci.org.cn/article/doi/10.1016/j.eqs.2022.05.004?pageType=en> in the Supplements.

**Table 3.S1:** List of network codes and corresponding operation period

Network Code	Operation period
XF	2002—2005
XE	2003—2004
XP	2005—2007
X4	2007—2009
YL	2001—2002
YA	2003—2004
Y2	2007—2010

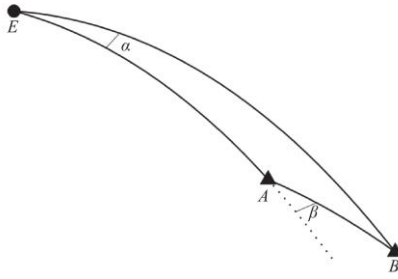


**Fig. 3.S1** Illustration of two deviation angles  $\alpha$  and  $\beta$  defined in the earthquake-based two-station (TS) method (Yao HJ et al., 2006). The parameters  $\alpha$  and  $\beta$  are defined as the azimuthal difference of the earthquake to the two stations, and the azimuthal difference between the earthquake to the nearest station and the nearest station to the other station, respectively.

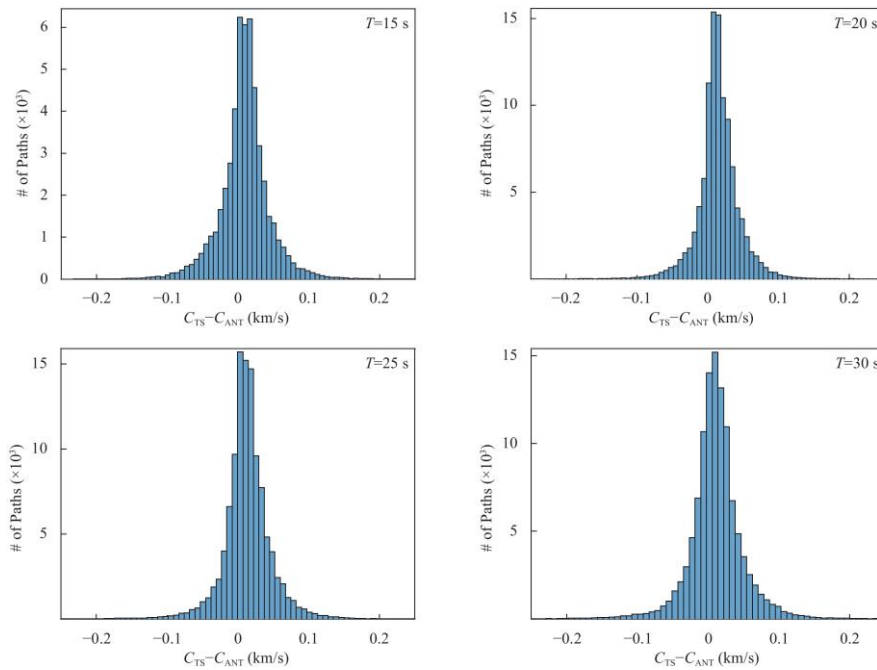


**Fig. 3.S2** Histogram of the Rayleigh wave phase velocity difference between the measurements from the earthquake-based TS method and the ANT at the overlapping 15, 20, 25, and 30 s, with the means of 0.013, 0.020, 0.022, and 0.020 km/s, respectively. Letter "T" represents period.

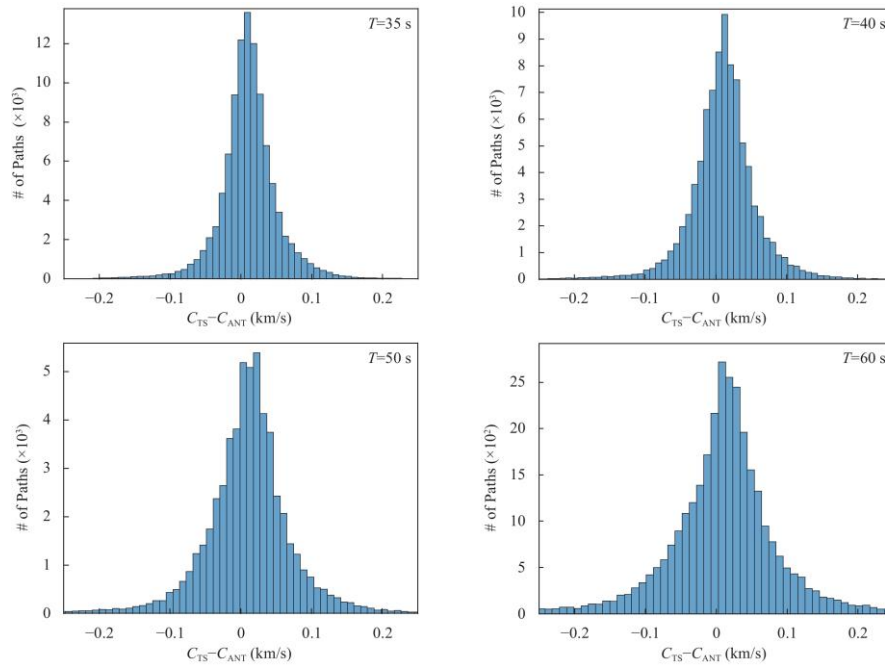


**Fig. 3.S3** Same as Figure S2 but for 35, 40, 50, and 60 s, with the means of 0.007, 0.007, 0.013, 0.014, respectively. Letter "T" represents period.

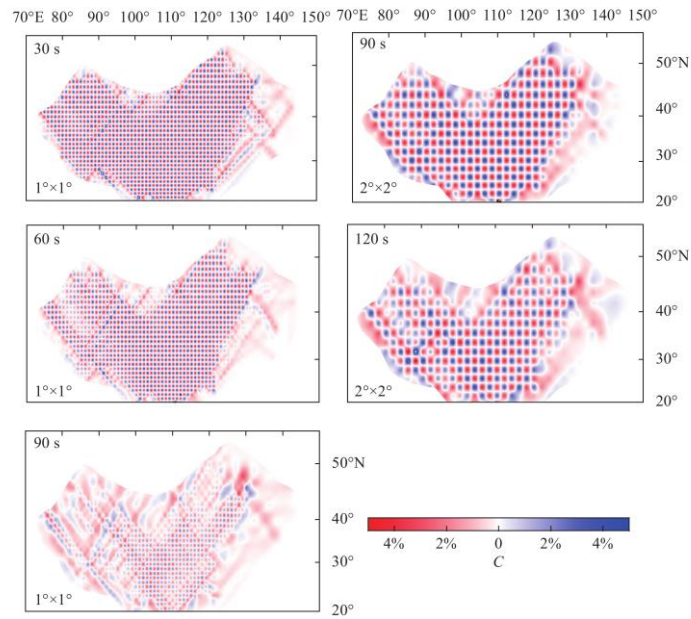


**Fig. 3.S4** Checkerboard tests at periods 30, 60, 90 and 120 s.

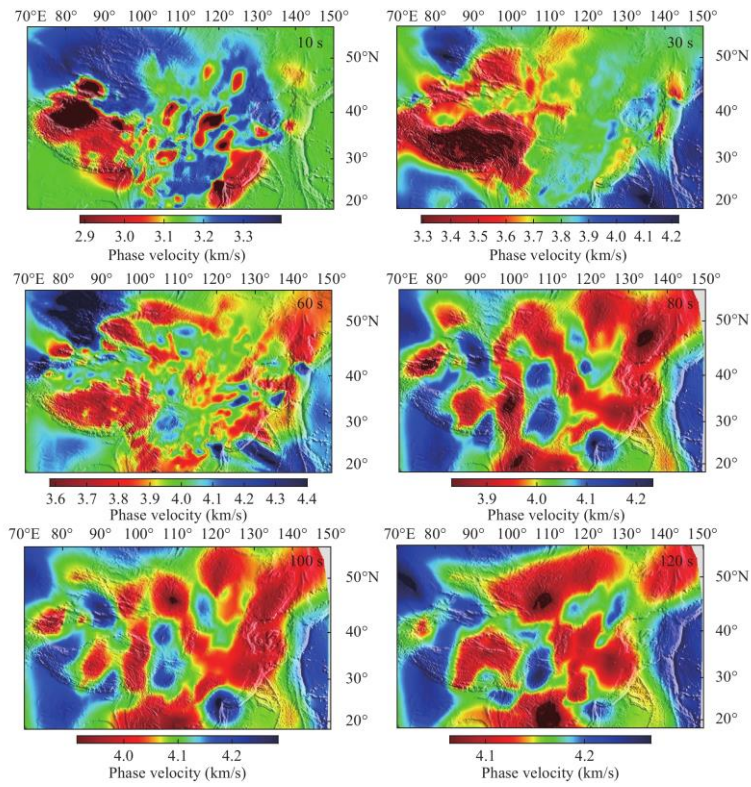


**Fig. 3.S5** Phase velocity dispersion maps at periods 10, 30, 60, 80, 100 and 120 s.

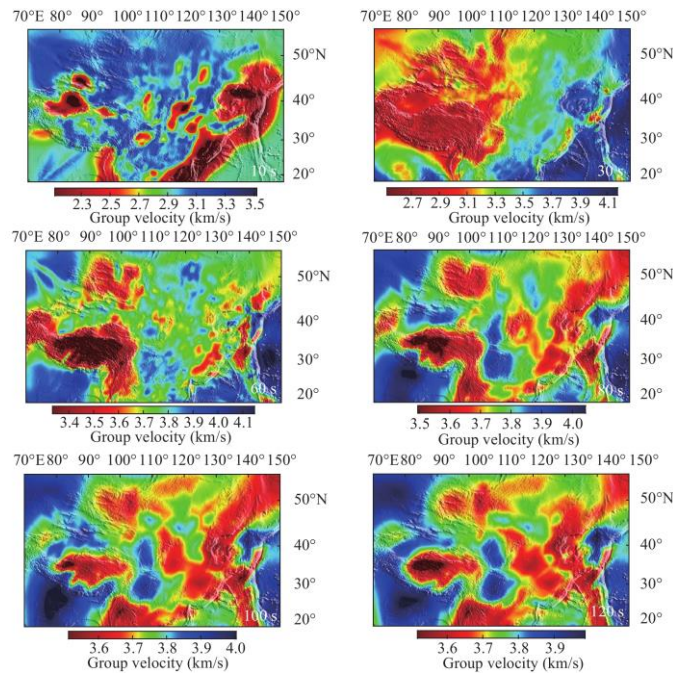


**Fig. 3.S6** Group velocity dispersion maps at periods 10, 30, 60, 80, 100 and 120 s.

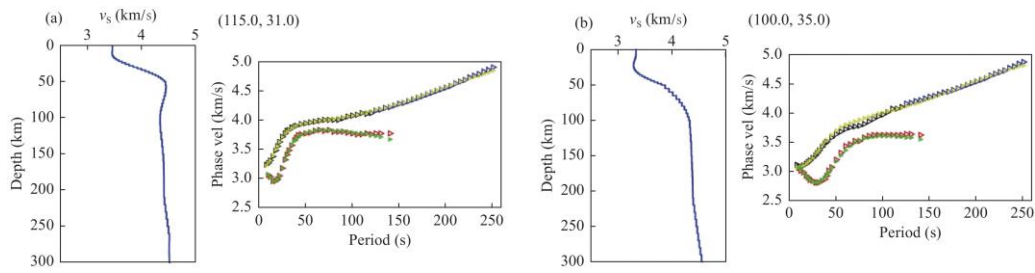


**Fig. 3.S7** Inversion results at grid points (115.0, 31.0) (a) and (100.0, 35.0) (b). The black and blue triangles represent phase dispersion that are extracted from our phase velocity dispersion maps and GDM52 model, respectively. The red triangles represent group dispersion that are extracted from our group velocity dispersion maps. The yellow and green triangles represent the predicted phase and group velocity dispersion, respectively.

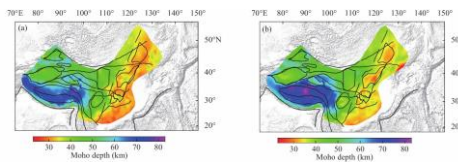


**Fig. 3.S8** Crustal thickness map of Chinese continent from this study (a) and Li YH et al. (2014) (b)

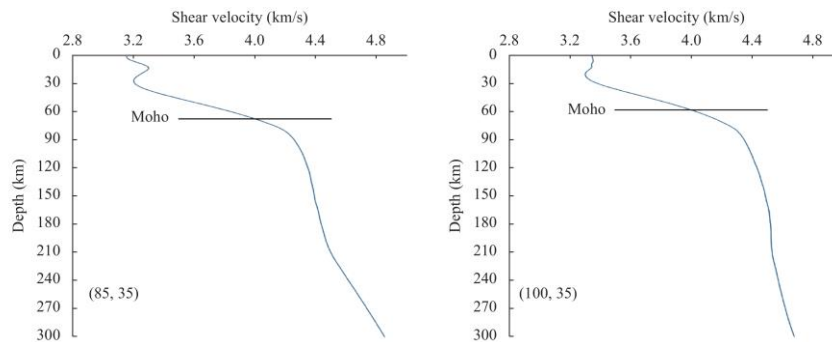


**Fig. 3.S9** Examples of 1-D velocity profiles having no negative velocity gradient at the depth below Moho interface.

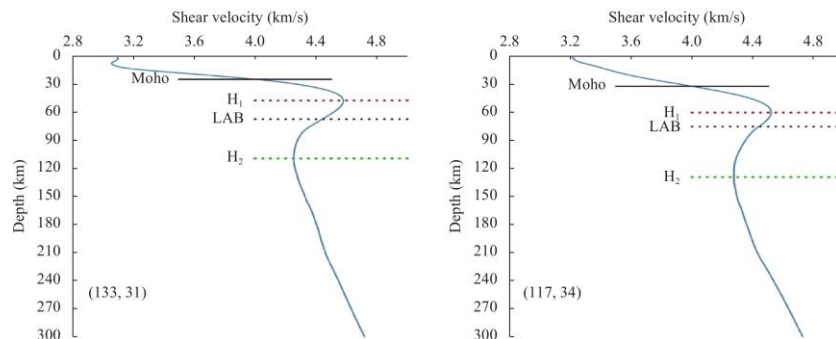


**Fig. 3.S10** Examples of 1-D velocity profiles having clear LAB.



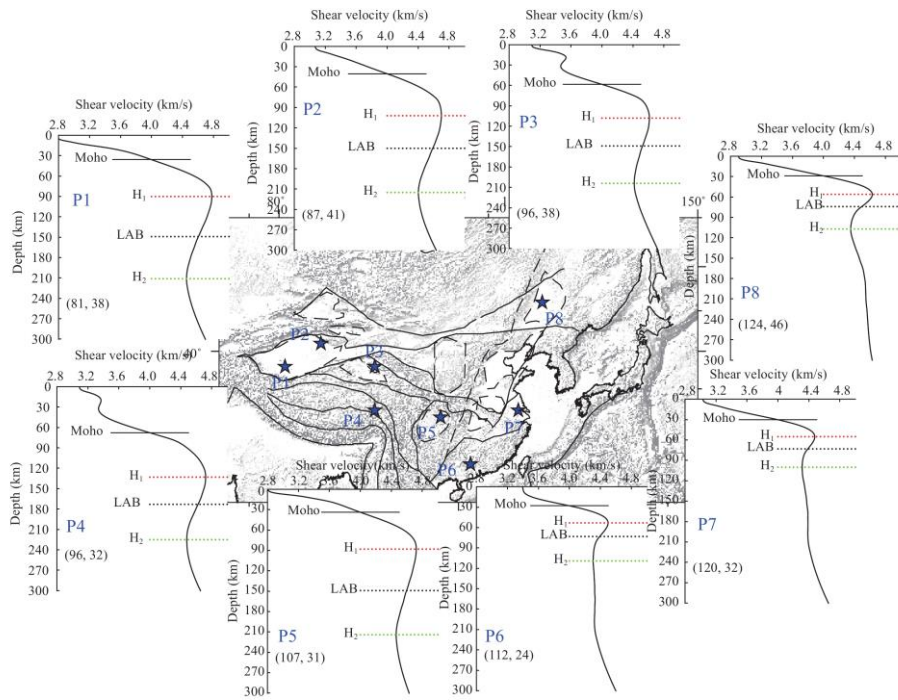


**Fig. 3.S11 Typical examples for 1-D velocity profiles having clear identified LAB.**

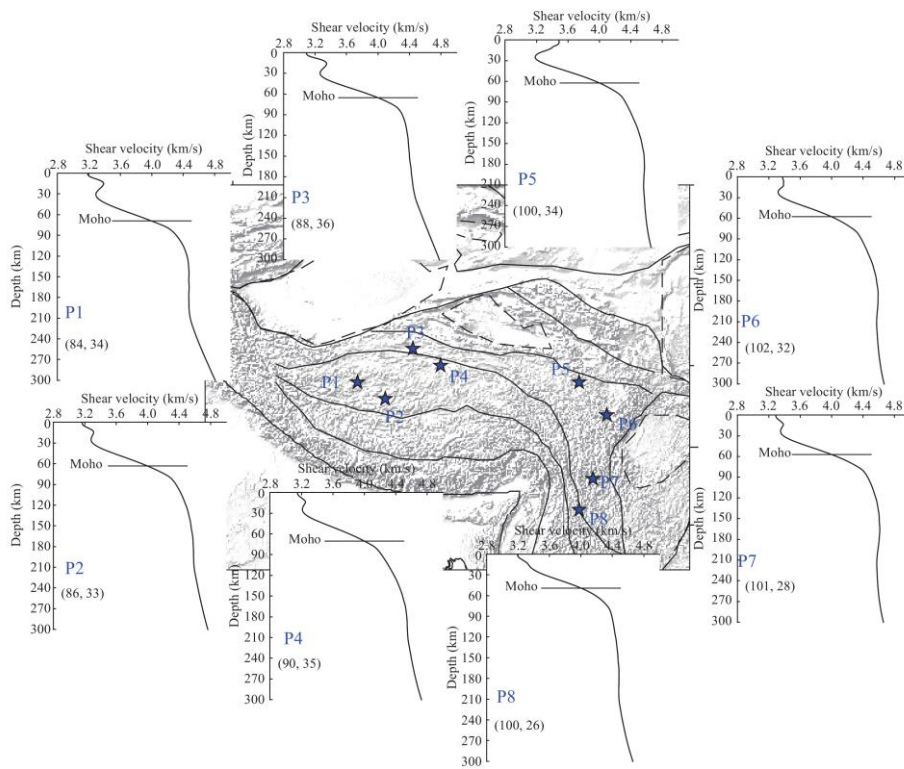


**Fig. 3.S12 Typical examples for 1-D velocity profiles having no proxy for LAB.**

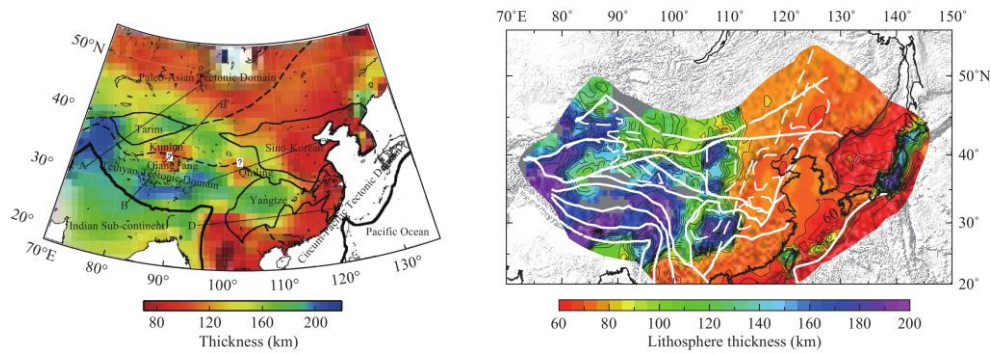


**Fig. 3.S13** Lithosphere thicknss from An and Shi (2006) (left panel) and this study (right panel).

## References

- [1] An MJ and Shi YL (2006). Lithospheric thickness of the Chinese continent. *Phys Earth Planet Inter* **159**: 257–266.
- [2] Avouac, JP and Tapponnier P (1993). Kinematic model of active deformation in central Asia. *Geophys. Res. Lett.* **20**(10): 895–898.
- [3] Bao XW, Xu MJ, Wang LS, Mi N, Yu DY, Li H (2011). Lithospheric structure of the Ordos block and its boundary areas inferred from Rayleigh wave dispersion. *Tectonophysics* **499**(1-4): 132–141.
- [4] Bao XW, Song XD, Xu MJ, Wang LS, Sun XX, Mi N, Yu DY, Li H (2013). Crust and upper mantle structure of the North China craton and the NE Tibetan Plateau and its tectonic implications. *Earth Planet Sci Lett* **369–370**: 129–137.
- [5] Bao XW, Song XD and Li JT (2015). High-resolution lithospheric structure beneath Mainland China from ambient noise and earthquake surface-wave tomography. *Earth Planet Sci Lett.* **417**: 132–141.
- [6] Bassin C, Laske G and Masters G (2000). The current limits of resolution for surface wave tomography in North America. *EOS Trans AGU* **81**: F897.
- [7] Brocher TM (2005). Empirical relations between elastic wave speeds and density in the Earth’s crust. *Bull Geol Soc Am* **95**(6): 2081–2092.
- [8] Ceylan S, Ni J, Chen YJ, Zhang Q, Tilmann F and Sandvol E (2012). Fragmented Indian plate and vertically coherent deformation beneath eastern Tibet. *J Geophys Res* **117**: B11303.
- [9] Chen HP, Zhu LB, Wang QD, Zhang P and Yang YH (2014). S-wave velocity structure of the North China from inversion of Rayleigh wave phase velocity. *J Asian Eath Sci* **88**: 178–191.
- [10]Chen L (2009). Lithospheric structure variations between the eastern and central

- North China Craton from S- and P-receiver function migration. *Phys Earth Planet Inter* **173**: 216–227.
- [11]Chen M, Niu FL, Tromp J, Lenardic A, Lee CT, Cao WR and Ribeiro J (2017). Lithospheric foundering and underthrusting imaged beneath Tibet. *Nat Commun* **8**: 2–11.
- [12]Chung SL, Chu MF, Zhang Y, Xie Y, Lo CH, Lee TY, Lan CY, Li X, Zhang Q and Wang Y (2005). Tibetan tectonic evolution inferred from spatial and temporal variations in post-collisional magmatism. *Earth-Sci. Rev.* (68): 173–196.
- [13]Ekström G (2011). A global model of Love and Rayleigh surface-wave dispersion and anisotropy, 25-250 s. *Geophys J Int* **187**: 1668–1686.
- [14]Feng M and An MJ (2010). Lithospheric structure of the Chinese mainland determined from joint inversion of regional and teleseismic Rayleigh-wave group velocities. *J Geophys Res* **115**: B06317.
- [15]Friederich W (2003). The S velocity structure of the East Asian mantle from inversion of shear and surface waveforms. *Geophys J Int* **153**: 88–102.
- [16]Guo Z and Chen YJ (2017). Mountain building at northeastern boundary of Tibetan Plateau and craton reworking at Ordos block from joint inversion of ambient noise tomography and receiver functions. *Earth Planet. Sci. Lett.* (463): 232–242.
- [17]Han SC, Zhang HJ, Xin HL, Shen WS and Yao HJ (2021). USTClitho2.0: Updated unified seismic tomography models for continental china lithosphere from joint inversion of body-wave arrival times and surface-wave dispersion data. *Seismol Res Lett* **93**(1): 201–215.
- [18]Herrmann RB and Ammon CJ (2004). Surface waves, receiver functions and crustal structure, in *Computer Programs in Seismology, Version 3.30*. Saint Louis University. Available at <http://www.eas.slu.edu/People/RBHerrmann/CPS330.html>
- [19]Huang JL and Zhao DP (2006). High-resolution mantle tomography of China and surrounding regions. *J Geophys Res* **111**: B09305.
- [20]Hung SH, Chen WP, Chiao LY and Tseng TL (2010). First multi-scale, finite-frequency tomography illuminates 3-D anatomy of the Tibetan Plateau. *Geophys Res Lett* **37**: L06304.
- [21]Huang ZC, Wang P, Zhao DP, Wang LS and Xu MJ (2014). Three-dimensional P wave azimuthal anisotropy in the lithosphere beneath China. *J Geophys Res: Solid Earth* **119**: 5686–5712.
- [22]Jiang GM, Zhang GB, Lü QT, Shi DN and Xu Y (2013). 3-D velocity model beneath the Middle-Lower Yangtze River and its implication to the deep geodynamics. *Tectonophysics* **606**: 36–47.

- [23] Julià J, Ammon CJ, Herrmann RB and Correig AM (2000). Joint inversion of receiver functions and surface wave dispersion observations. *Geophys J Int* **143**: 99–112.
- [24] Kennett BLN, Engdahl ER and Buland R (1995). Constraints on seismic velocities in the Earth from travel-times. *Geophys J Int* **122**: 108–124.
- [25] Kind R, Yuan XH, Saul J, Nelson D, Sobolev SV, Mechie J, Zhao WJ, Kosarev G, Ni J, Achauer U and Jiang M (2002). Seismic images of crust and upper mantle beneath Tibet: Evidence for Eurasian plate subduction. *Science* **298**: 1219–1221.
- [26] Lallemand S, Font Y, Bijwaard H and Kao H (2001). New insights on 3-D plates inter-action near Taiwan from tomography and tectonic implications. *Tectonophysics* **335**: 229–253.
- [27] Landisman M, Dziewonski A and Sato Y (1969). Recent improvements in the analysis of surface wave observations. *Geophys J Roy Astron Soc* **17**(4): 369–403.
- [28] Li C, van der Hilst, RD, Meltzer AS, Engdahl ER (2008). Subduction of the Indian lithosphere beneath the Tibetan Plateau and Burma. *Earth Planet Sci Lett* **274**: 157–168.
- [29] Li JT and Song XD (2018). Tearing of Indian mantle lithosphere from high-resolution seismic images and its implications for lithosphere coupling in southern Tibet. *Proc Natl Acad Sci USA* **115**(33): 8296–8300.
- [30] Li HY, Song XD, Lü QT, Yang XY, Deng YF, Ouyang LB, Li JP, Li XF and Jiang G (2018). Seismic imaging of lithosphere structure and upper mantle deformation beneath east-central China and their tectonic implications. *J Geophys Res* (123): 2856–2870.
- [31] Li MK, Zhang SX, Wu TF, Hua YJ and Zhang B (2018). Fine crustal and uppermost mantle S-wave velocity structure beneath the Tengchong volcanic area inferred from receiver function and surface-wave dispersion: constraints on magma chamber distribution. *B Volcanol* **80**: 25.
- [32] Li YH, Wu QJ, Pan JT, Zhang FX and Yu DX (2013). An upper-mantle S-wave velocity model for East Asia from Rayleigh wave tomography. *Earth Planet Sci Lett* **377–378**: 367–377.
- [33] Li YH, Gao MT and Wu QJ (2014). Crustal thickness map of the Chinese mainland from teleseismic receiver functions. *Tectonophysics* **611**: 51–60.
- [34] Liang CT, Song XD and Huang JL (2004). Tomographic inversion of Pn travel times in China. *J Geophys Res* **109**: B11304.
- [35] Liang CT and Song XD (2006). A low velocity belt beneath northern and eastern Tibetan plateau from Pn tomography. *Geophys Res Lett* **33**: L22306.
- [36] Liang XF, Sandvol E, Chen YJ, Hearn T, Ni J, Klemperer S, Shen Y and Tilmann

- F (2012). A complex Tibetan upper mantle: a fragmented Indian slab and no south-verging subduction of Eurasian lithosphere. *Earth Planet Sci Lett* **333–334**: 101–111.
- [37]Northrup CJ, Royden LH and Burchfiel BC (1995). Motion of the Pacific plate relative to Eurasia and its potential relation to Cenozoic extension along the eastern margin of Eurasia. *Geology* **23**(8): 719–722.
- [38]Ojo AO, Ni SD, Chen HP and Xie J (2018). Crust-mantle coupling mechanism in Cameroon, West Africa, revealed by 3D S-wave velocity and azimuthal anisotropy. *Phys Earth Planet Inter* **274**: 195–213.
- [39]Ouyang LB, Li HY, Lü QT, Yang YJ, Li XF, Jiang GM, Zhang GB, Shi DN, Zheng D, Sun SJ, Tan J and Zhou M (2014). Crustal and uppermost mantle velocity structure and its relationship with the formation of ore districts in the Middle-Lower Yangtze River region. *Earth Planet Sci Lett* **408**: 378–389.
- [40]Pandey S, Yuan XH, Debayle E, Priestley K, Kind R, Tilmann F and Li XQ (2014). A 3D shear-wave velocity model of the upper mantle beneath China and the surrounding areas. *Tectonophysics* **633**: 193–210.
- [41]Peng J, Huang JL, Liu ZK and Xing K (2020). Constraints on S-wave velocity structures of the lithosphere in mainland China from broadband ambient noise tomography. *Phys Earth Planet Inter* **299**: 106406.
- [42]Priestley K, Debayle E, McKenzie D and Pilidou S (2006). Upper mantle structure of eastern Asia from multimode surface waveform tomography. *J Geophys Res* **111**: B10304.
- [43]Ren JY, Tamaki K, Li ST and Zhang JX (2002). Late Mesozoic and Cenozoic rifting and its dynamic setting in Eastern China and adjacent areas. *Tectonophysics* **344**: 175–205.
- [44]Ritzwoller MH and Levshin AL (1998). Eurasian surface wave tomography: Group velocities. *J Geophys Res* **103**: 4839–4878.
- [45]Royden LH, Burchfiel BC and van der Hilst RD (2008). The geological evolution of the Tibetan plateau. *Science* **321**: 1054–1058.
- [46]Schellart WP and Lister GS (2005). The role of the East Asian active margin in widespread extensional and strike-slip deformation in East Asia. *J Geol Soc London* **162**: 959–972.
- [47]Shapiro NM, Campillo M, Stehly L and Ritzwoller MH (2005). High-resolution surface-wave tomography from ambient seismic noise. *Science* **307**: 1615–1618.
- [48]Shapiro NM and Ritzwoller MH (2002). Monte-Carlo inversion for a global shear-velocity model of the crust and upper mantle. *Geophys J Int* **151**: 88–105.
- [49]Shen WS, Ritzwoller MH, Kang D, Kim, YH, Lin FC, Ning JY, Wang WT, Zheng

- Y and Zhou LQ (2016). A seismic reference model for the crust and uppermost mantle beneath China from surface wave dispersion. *Geophys J Int* **206**: 954–979.
- [50] Shen XZ, Liu M, Gao Y, Wang WJ, Shi YT, An MJ, Zhang YS and Liu XZ (2017). Lithospheric structure across the northeastern margin of the Tibetan Plateau: Implications for the plateau's lateral growth. *Earth Planet Sci Lett* **459**: 80–92.
- [51] Sun XL, Song XD, Zheng SH, Yang YJ and Ritzwoller MH (2010). Three-dimensional shear wave velocity structure of the crust and upper mantle beneath China from ambient noise surface wave tomography. *Earthquake Sci* **23**: 449–463.
- [52] Tapponnier P, Peltzer G and Armijo R (1986). On the mechanics of the collision between India and Asia. *Geol Soc London Spec Publ* **19**: 113–157.
- [53] Tapponnier P, Xu ZQ, Roger F, Meyer B, Arnaud N, Wittlinger G and Yang JS (2001). Oblique stepwise rise and growth of the Tibet plateau. *Science* **294**(5547): 1671–1677.
- [54] Teng JW, Zhang ZJ, Zhang XK, Wang CY, Gao R, Yang BJ, Qiao YH and Deng YF (2013). Investigation of the Moho discontinuity beneath the Chinese mainland using deep seismic sounding profiles. *Tectonophysics* **609**: 202–216.
- [55] Tilmann F, Ni J, NDEPTH III Seismic (2003). Seismic Imaging of the Indian continental lithosphere. *Science* **300**: 1424–1427.
- [56] Wang Q, Song XD and Ren JY (2017). Ambient noise surface wave tomography of marginal seas in east Asia. *Earth Planet Phys* **1**: 13–25.
- [57] Wang WL, Wu JP, Fang LH, Lai GJ, Yang T and Cai Y (2014). S wave velocity structure in southwest China from surface wave tomography and receiver functions. *J Geophys Res: Solid Earth* **119**: 1061–1078.
- [58] Wei W, Xu JD, Zhao DP and Shi YL (2012). East Asia mantle tomography: New insight into plate subduction and intraplate volcanism. *J Asian Earth Sci* **60**: 88–103.
- [59] Wei XZ, Jiang MM, Liang XF, Chen L and Ai YS (2017). Limited southward underthrusting of the Asian lithosphere and material extrusion beneath the northeastern margin of Tibet, inferred from teleseismic Rayleigh wave tomography. *J Geophys Res* **122**: 7172–7189.
- [60] Wessel P, and Smith WHF (1998). New, improved version of the generic mapping tools released. *EOS Trans. AGU*
- [61] Xin HL, Zhang HJ, Kang M, He RZ, Gao L and Gao J (2019). High-resolution lithospheric velocity structure of continental china by double-difference seismic travel-time tomography. *Seismol Res Lett* **90**(1): 229–241.
- [62] Xu Z, Song XD and Zheng SH (2013). Shear velocity structure of crust and uppermost mantle in China from surface wave tomography using ambient noise



- and earthquake data. *Earth Sci* **26**: 267–281.
- [63] Yang ZG and Song XD (2019). Ambient noise Love wave tomography of China. *Earth Planet. Phys* **3**(3): 1–14.
- [64] Yao HJ, van der Hilst RD and De Hoop MV (2006). Surface-wave array tomography in SE Tibet from ambient seismic noise and two-station analysis – I. Phase velocity maps. *Geophys J Int* **166**(2): 732–744.
- [65] Yao HJ, Beghein C and van der Hilst RD (2008). Surface-wave array tomography in SE Tibet from ambient seismic noise and two-station analysis – II. Crustal and upper-mantle structure. *Geophys J Int* **173**: 205–219.
- [66] Yin A and Harrison M (2000). Geological evolution of the Himalayan–Tibetan orogen. *Annu Rev Earth Planet Sci* **28**: 211–280.
- [67] Zhang H, Zhao DP, Zhao JM and Xu Q (2012). Convergence of the Indian and Eurasian plates under eastern Tibet revealed by seismic tomography. *Geochem Geophys Geosyst* **13**: Q06W14.
- [68] Zhang XM, Teng JW, Sun RM, Romanelli F, Zhang ZJ and Panza G (2014). Structural model of the lithosphere-asthenosphere system beneath the Qinghai-Tibet Plateau and its adjacent areas. *Tectonophysics* **634**: 208–226.
- [69] Zhang XZ, Song XD, and Li JT (2022). A comparative study of seismic tomography models of the Chinese continental lithosphere. *Earthq Sci*, in press
- [70] Zhang ZM, Liou JG and Coleman RG (1984). An outline of the plate tectonics of China. *Geol Soc Am Bull* **95**: 295–312.
- [71] Zhao DP, Yu S and Ohtani E (2011). East Asia: Seismotectonics, magmatism and mantle dynamics. *J Asian Earth Sci* **40**(3): 689–709.
- [72] Zhao L, Allen RM, Zheng TY and Zhu RX (2012). High-resolution body wave tomography models of the upper mantle beneath eastern China and the adjacent areas. *Geochem Geophys Geosyst* **13**: Q06007.
- [73] Zhao GC and Cawood PA (2012). Precambrian geology of China. *Precambrian Res* **222–223**: 13–54.
- [74] Zheng HW and Li TD (2013). Deep structure of the middle and lower reaches of Yangtze River metallogenic belt from teleseismic P-wave tomography. *Prog Geophys* **28**(5): 2283–2293.
- [75] Zheng SH, Sun XL, Song XD, Yang YJ and Ritzwoller MH (2008). Surface wave tomography of China from ambient seismic noise correlation. *Geochem Geophys Geosyst* **9**: Q05020.
- [76] Zheng XF, Yao ZX, Liang JH and Zheng J (2010). The role played and opportunities provided by IGP DMC of China national seismic network in Wenchuan earthquake disaster relief and researches. *Bull Seismol Soc Am* **100**:

2886–2872.

[77]Zhu JS, Cao JM, Cai XL, Yan ZQ and Cao XL (2002). High-resolution surface wave tomography in East Asia and west Pacific marginal seas. *Chin J Geophys* **45**(5): 646– 664 (in Chinese with English abstract).

[78]Zhu RX, Xu YG, Zhu G, Zhang HF, Xia QK and Zheng TY (2012). Destruction of the North China Craton. *Sci China Earth Sci* **55**(10): 1565–1587.

# 4. Crustal velocity, density structure, and seismogenic environment in the southern segment of the North-South Seismic Belt, China

Xun Sun and Lianghai Guo\*

(School of Geophysics and Information Technology, China University of Geosciences, Beijing 100083, China)

**Abstract:** The southern segment of the North-South Seismic Belt in China is a critical region for earthquake preparedness and risk reduction efforts. However, limited by the low density of seismic stations and the use of single-parameter physical structural models, the deep tectonic features and seismogenic environment in this area remain controversial. Thus, a comprehensive analysis based on high-resolution crustal structures and multiple physical parameters is required. In this study, we applied the ambient noise tomography method to obtain the three-dimensional (3D) crustal S-wave velocity structure using continuous waveform data from 112 permanent stations and 350 densely distributed temporary stations in the southern segment of the North-South Seismic Belt. Then, we obtained the high-resolution 3D density structure through wavenumber-domain 3D gravity imaging constrained by the velocity structure. The low-velocity and low-density anomalies in the upper crust of the study area were mainly distributed in the Sichuan Basin and around Dali and Simao, while the high-velocity and high-density anomalies were primarily distributed in the Panxi region, corresponding to the surface geological features. Two prominent low-velocity and low-density anomalies were observed in the middle and lower crust: one to the west of the Songpan-Garzê block and Sichuan-Yunnan diamond-shaped block, and the other near the Anninghe-Xiaojiang fault. Combined with the spatial distribution of seismic events in the study area, we found that previous earthquakes predominantly occurred in the transition zones between high and low anomaly regions and in the low-velocity and low-density zones in the upper crust. In contrast, moderate-to-strong earthquakes mainly occurred within the transition zones between high and low anomaly regions and close to the high-velocity and high-density regions, often with low-velocity and low-

---

\* [DOI] 10.29382/eqs-2021-0052

density layers below their hypocenters. Fluids play a critical role in the seismogenic process by reducing fault strength and destabilizing the stress state, which may be a triggering factor for earthquakes in the study area. Additionally, the upwelling of molten materials from the mantle may lead to energy accumulation and stress concentration, providing an important seismogenic background for moderate-to-strong earthquakes in this area.

## 4.1 Introduction

The southern segment of the North-South Seismic Belt in China is located at the convergent boundary of the Eurasian and Indian plates. This region has long been influenced by the southeastward escape of crustal material from the interior of the Tibetan Plateau (Molnar and Tapponnier, 1975), where intense tectonic movement and frequent seismic activity occur. Numerous moderate-to-strong earthquakes have occurred in this region, such as the  $M_S7.0$  Lijiang earthquake in 1996,  $M_S7.2$  Gengma earthquake in 1998,  $M_S7.7$  Tonghai earthquake in 1970,  $M_S6.5$  Ludian and  $M_S6.6$  Jinggu earthquakes in 2014, and  $M_S6.4$  Yangbi earthquake in 2021, resulting in severe economic loss and some casualties. Therefore, investigating the crustal structures and seismogenic environment in this area is crucial to understand the deep tectonic activity and contribute to earthquake preparedness and risk reduction measures.

In recent years, several deep geophysical exploration programs have been undertaken in the southern segment of the North-South Seismic Belt. Using deep seismic reflection profiling, deep seismic sounding, broadband seismicity, magnetotelluric data, and gravity and magnetic data, scholars worldwide have conducted a considerable amount of research on the deep structures and tectonic features in this area, thus promoting our understanding of the seismogenic environment. The studies by surface wave and ambient noise tomography have revealed that low-velocity layers are widely distributed in the middle and lower crust in the southern segment of the North-South Seismic Belt (Yao HJ et al., 2010; Fu YV et al., 2017; Zhang ZQ et al., 2020; Liu Y et al., 2021). Additionally, strong earthquakes have predominantly occurred in the low-velocity zones in the crust or near the boundaries between high- and low-velocity regions (Huang ZX et al., 2013; Pan JT et al., 2015). The studies by body wave traveltime tomography have indicated that low-velocity zones are not widespread within the crust; instead, they are confined to specific regions by fault zones (Liu W et al., 2019; Qu C et al., 2020; Zhao Y et al., 2020). The earthquake hypocenters are mostly distributed within the transition zones between high- and low-velocity regions but slightly close to the side of high-velocity. (Wei W et al.,

2010; Li DH et al., 2018; Wang CY et al., 2003). The study by double-difference earthquake location revealed the existence of a low-velocity body 15 – 20 km below the hypocenter of the Yangbi earthquake, suggesting that earthquakes mainly occur in the transition zones between high- and low-velocity anomalies (Jia J et al., 2021). The seismic activity during the Yangbi earthquake sequence was in accord with the relatively low  $b$ -value in the northern segment of the Honghe fault, indicating potentially destructive earthquakes in the future (Zhang YY et al., 2022). The seismogenic fault of the Yangbi earthquake may be a relatively young branch fault of the Weixi-Weishan fault (Wang CZ et al., 2021), which agrees with the conclusion of Yang T et al. (2022). The two-dimensional (2D) crustal density structure obtained through gravity data inversion has shown noticeable differences between the north and south sides of the Honghe fault, which is speculated to be a causative factor of the difference in the earthquake frequency between the north and south sides (Shi L et al., 2015). The Moho is uplifted near Huaping-Panzhihua, where high-density bodies are present in the upper crust, which may block the southeastward escape of materials from the Tibetan Plateau and resist the lateral compression of the Himalayan east structural knot (Shen CY et al., 2015). Based on the inversion of the multi-scale density structure, Yang WC et al. (2015) observed three low-density belts in the middle and upper crust of West Yunnan, finding that most earthquakes of magnitude  $\geq 6$  occurred within these low-density anomalies or on their edges. Overall, previous studies have provided crustal and mantle structures for studying the geodynamic processes and seismogenic environment of strong earthquakes in the southern segment of the North-South Seismic Belt. Despite this progress, the tectonic features and seismogenic environment in this region remain unclear, limited by a low density of seismic stations and the use of single-parameter physical structural models. Therefore, high-resolution structures of multiple physical properties are required to comprehensively analyze the above problems.

In this study, we applied the ambient noise tomography method (Fang HJ et al., 2015; Fan XL and Chen QF, 2019) to obtain the crustal S-wave velocity structure in the southern segment of the North-South Seismic Belt. We used the continuous waveform data of 112 permanent stations, which were provided by the Data Management Center of China National Seismic Network, and the seismic array observations of 350 densely distributed temporary stations, which were provided by the “China Seismic Scientific Exploration Array – the southern segment of the North-South Seismic Belt.” The initial model was the community velocity model of the Sichuan-Yunnan region ( “SWChinaCVM-1.0” ) (Yao HJ, 2020; Liu Y et al., 2021). Further, the high-resolution crustal density structure of the study area was obtained using wavenumber-domain iterative approach for 3D gravity data imaging (Cui YT and Guo LH, 2019) constrained by the seismic velocity structure. Finally, we identified the

structural features in the study area based on the obtained velocity and density models, analyzed their correlations with seismic activities, and investigated the seismogenic background of moderate and strong earthquakes. The results of this study provide constraints for further research on tectonic movement and the seismogenic mechanisms in the study area.

## 4.2 Data and methods

### 4.2.1 Seismic and gravity data

The seismic data used in this study consisted of two parts: (1) continuous waveform data recorded by 112 permanent stations from January to December 2017, which were obtained from the Data Management Center of China National Seismic Network (Zheng XF et al., 2009; 2010) and (2) seismic array observations recorded by 350 densely distributed temporary stations from June 2011 to May 2013, which were provided by the “China Seismic Scientific Exploration Array - the southern segment of the North-South Seismic Belt” (ChinArray, 2006) (Figure 4.1a).

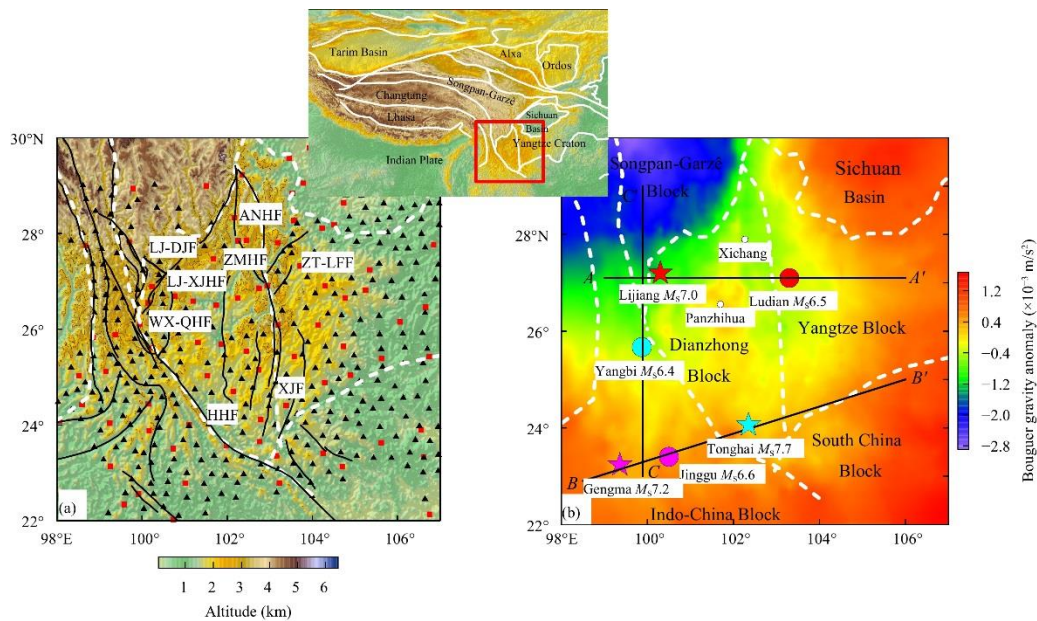


**Fig. 4.1** (a) Topography and station distribution in the study area. The white dashed lines indicate tectonic boundaries. The solid black lines denote the following faults, ANHF: Anninghe fault; LJ-DJF: Lijiang-Daju fault; LJ-XJHF: Lijiang-Xiaojinhe fault; WX-QHF: Weixi-Qiaohou fault; ZMHF: Zemuhe fault; ZT-LFF: Zhaotong-Lianfeng fault; XJF: Xiaojiang fault; and HHF: Honghe fault. The diamond-shaped block enclosed by the Zemuhe, Xiaojiang, and Honghe faults is called the Sichuan-Yunnan diamond-shaped block (Kan RJ et al., 1977). The red squares represent the permanent stations, and the black triangles represent the densely distributed temporary stations. (b) Regional Bouguer gravity anomaly map of the study area. The red,



purple, and cyan circles are the epicenters of the  $M_s6.5$  Ludian earthquake (2014),  $M_s6.6$  Jinggu earthquake (2014), and  $M_s6.4$  Yangbi earthquake (2021), respectively. The red, purple, and cyan pentagons are the epicenters of the  $M_s7.0$  Lijiang earthquake (1996),  $M_s7.2$  Gengma earthquake (1998), and  $M_s7.7$  Tonghai earthquake (1970), respectively. The solid black lines denote the locations of the vertical cross-sections in Figure 4.11. The small figure in the upper represents the location of the study area, and the red box denotes the study area.

The Bouguer gravity anomaly data for the study area were retrieved from the China Geological Survey (grid spacing of  $0.1^\circ \times 0.1^\circ$ ). The regional gravity anomalies were acquired by low-pass filtering to remove the high-frequency surface anomalies. As shown in Figure 1b, high gravity anomalies were observed in the northwest, whereas low gravity anomalies were observed in the southeast, southwest and northeast, with a variation of  $\sim 4.62 \times 10^{-3} \text{ m/s}^2$ . The block of the Tibetan Plateau in the northwest exhibited relatively low gravity anomalies, whereas the Sichuan Basin in the northeast and the Yunnan-Guizhou Plateau in the south displayed relatively high gravity anomalies. Panzhihua City and its surrounding areas in the central region exhibited locally high gravity anomalies.

#### 4.2.2 Ambient noise tomography

Ambient noise tomography is a recently developed method that, unlike traditional methods, does not rely on active seismic imaging and can determine high-resolution shallow velocity structures in areas of low seismic activity but with dense station coverage. With the increase in the number of permanent stations and the development of temporary seismic observations, ambient noise tomography has been widely applied and has achieved good results.

In this study, we extracted surface wave signals from the ambient noise following the methods described by Bensen et al. (2007) and Yang YJ et al. (2007). The steps can be briefly summarized as data preprocessing, calculation of the noise cross-correlation functions, extraction of surface wave dispersion curves, and surface wave tomography. The purpose of data preprocessing is to remove the effects of interfering signals, such as natural seismic signals and instrument faults. First, the data underwent resampling (1 Hz), de-meaning, de-trending, instrument response removal, and band-pass filtering (5 – 50 s). Subsequently, spectral whitening was applied to broaden the band of the ambient noise signal, and normalization was performed using the moving absolute average method. After completing data preprocessing, the daily cross-correlation functions between different station pairs were calculated and stacked in the time domain. Lin FC et al. (2007) has reported that the signal-to-noise ratio of symmetrical components is relatively high at all periods. Thus, we obtained the symmetrical components by adding the positive and negative lag components of the noise cross-

correlation functions inversely. Figures 4.2a and 4.2d present examples of the cross-correlation results between pairs of permanent stations and densely distributed temporary stations, respectively, where the surface wave signals can be clearly recognized.

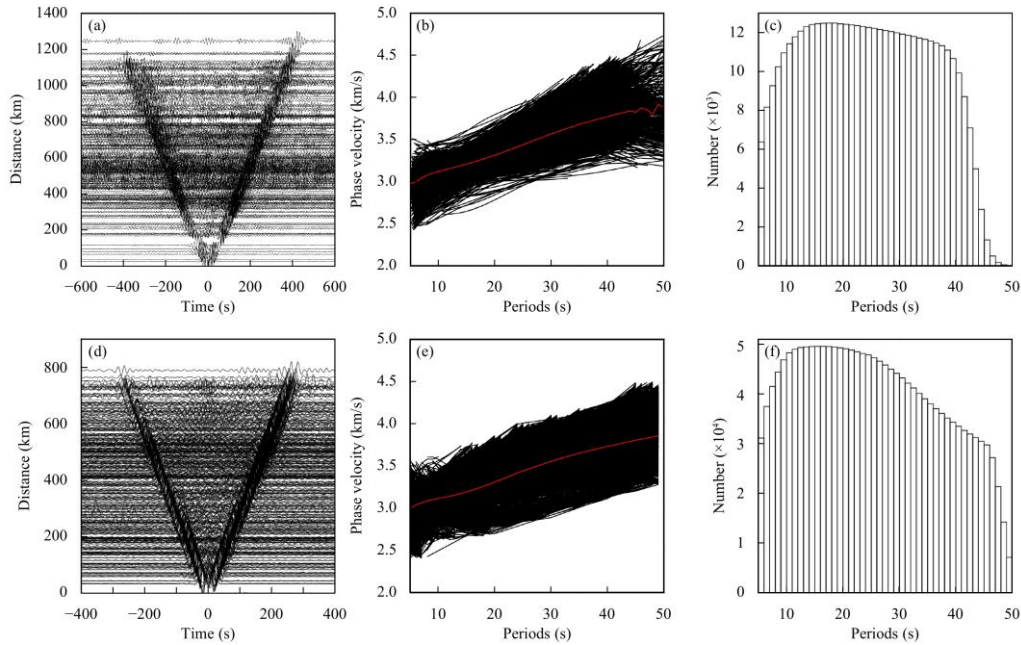


**Fig. 4.2 (a) Example of the cross-correlation results between permanent stations (showing data for station CQ-CHS); (b) phase-velocity dispersion curves for all pairs of permanent stations, with the average phase velocity delineated by the red line; (c) distribution of phase-velocity dispersion curves at different periods for permanent stations; (d) example of the cross-correlation results between densely distributed temporary stations (showing data for station XI-4501); (e) phase-velocity dispersion curves for all pairs of densely distributed temporary stations, with the average phase velocity delineated by the red line; (f) distribution of phase-velocity dispersion curves at different periods for densely distributed temporary stations.**

Second, we applied the time-frequency analysis method (Levshin and Ritzwoller, 2001) to extract the phase-velocity dispersion curves from the cross-correlation functions. To ensure the reliability of the dispersion data, we selected the noise cross-correlation functions with a signal-to-noise ratio  $>15$ . The station spacing had to be at least twice the wavelength to fulfill the assumption of far-field approximation of surface wave propagation. The phase-velocity dispersion curves for all pairs of permanent stations are shown in Figures 2b, while those of densely distributed temporary stations are presented in Figures 2e. The distributions of the number of phase-velocity dispersion curves at different periods are also shown Figures 4.2c and 4.2f. Figure 4.3 displays the path distribution of the permanent stations and densely distributed temporary stations at different periods and shows that all the dispersion curves are concentrated.

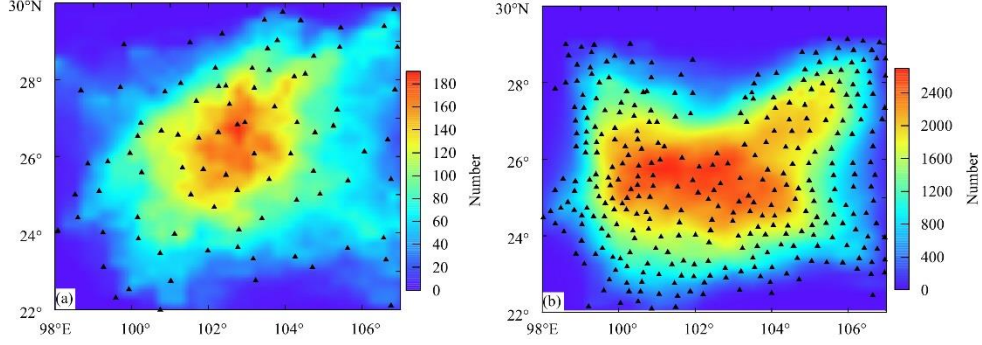


**Fig. 4.3 Path coverage density maps of the phase-velocity dispersion curves at a period of 30 s for permanent stations (a) and densely distributed temporary stations (b).**

Finally, we obtained the 3D crustal S-wave velocity structure based on the direct inversion of surface wave dispersion data (Fang HJ et al., 2015). As this method does not require the construction of 2D phase-velocity and group-velocity maps, the S-wave velocity structure can be obtained directly through inversion. Affected by the heterogeneity of subsurface structures, surface waves do not strictly propagate along the great-circle paths. This inversion method adopts a ray-tracing method (Rawlinson and Sambridge, 2005) to calculate the surface wave traveltime, which considers the non-great-circle propagation effects of surface waves with different periods due to complex structures and effectively improves the inversion accuracy. Because surface wave dispersion is more sensitive to the velocity of S-waves than that of P-waves, the velocity of P-waves and density are coupled with the velocity of S-waves using the following empirical formulae (Brocher, 2005) during the inversion process:

$$\alpha(z) = \sum_n \chi_n^{[\alpha]} \beta^n(z), \quad (1)$$

$$\rho(z) = \sum_n \chi_n^{[\rho]} \alpha^n(z), \quad (2)$$

where  $\alpha(z)$ ,  $\beta(z)$ , and  $\rho(z)$  are the compressional-wave velocity, shear-wave velocity, and density, respectively, and  $\chi_n^{[\alpha, \rho]}$  denotes the fitted polynomial coefficient.

To obtain a more reliable S-wave velocity structure, we first adopted the community velocity model of the Sichuan-Yunnan region, China, “SWChinaCVM-1.0” (Yao HJ, 2020; Liu Y et al., 2021), with a grid spacing of  $0.5^\circ \times 0.5^\circ$  in the horizontal direction, as the initial model. Then, we inverted the permanent station data to obtain a new crustal S-wave velocity structure, which was subsequently used as an updated initial model. The dispersion curve data of the densely distributed temporary stations were inverted with a finer grid spacing of  $0.25^\circ \times 0.25^\circ$  to obtain the final

crustal S-wave velocity structure for a depth range of 0 – 50 km. Based on several inversion experiments, we selected a weighting factor of 25 and a damping factor of 0.1.

### 4.2.3 Wavenumber-domain iterative approach for 3D gravity imaging

We used the wavenumber-domain iterative approach for 3D gravity imaging proposed by Cui YT and Guo LH (2019). This method introduces a priori information constraints and uses the iterative optimization algorithm for imaging, which is computationally efficient and convenient, and suitable for rapid 3D density imaging and evaluation based on large-scale gravity data.

Assuming that the observation surface is flat (0 m), the grid model consists of several stacked flat layers from top to bottom. The top and bottom depths of the  $j$ -th layer ( $z_j$ ) in the model are  $h_j$  and  $H_j$ , respectively, and  $\rho(\xi, \eta, z_j)$  is the two-dimensional density value of an arbitrary grid point  $(\xi, \eta)$  within this horizontal layer. Then, the gravity anomalies generated by this model on the observation surface can be calculated using the following frequency-domain forward modeling equation:

$$\Delta g(x, y, 0) = F_{2D}^{-1} \left\{ \sum_{j=1}^{n_z} \frac{2\pi G (e^{-kh_j} - e^{-kH_j})}{k} \cdot F_{2D}[\rho(\xi, \eta, z_j)] \right\}, \quad (3)$$

where  $G$  is the gravitational constant ( $6.67 \times 10^{-11} \text{ m}^3/\text{kg} \cdot \text{s}^2$ ),  $n_z$  is the number of layers in the  $Z$ -direction;  $k$  is the radial wavenumber in the 2D space, and  $F_{2D}$  and  $F_{2D}^{-1}$  represent the Fourier transform and inverse Fourier transform, respectively.

With a traditional deconvolution filter (Prietzhev, 2010), the imaged physical structures tend to be close to the observation surface in the depth direction. To improve the imaging accuracy, Cui YT and Guo LH (2019) incorporated a depth-scaling factor,  $\lambda$ , into the deconvolution filter to control its attenuation. For the  $j$ -th layer in the depth direction, the modified frequency-domain equation for imaging the gravity anomalies can be expressed as follows:

$$\rho(\xi, \eta, z_j) = F_{2D}^{-1} \left[ \frac{1}{2\pi G} \frac{(n+1)^{n+1}}{n!} k^{n+1} \left(\frac{z_j}{\lambda}\right)^n e^{-nk\left(\frac{z_j}{\lambda}\right)} F_{2D}[\Delta g(x, y, 0)] \right], \quad (4)$$

where  $\lambda$  is the depth-scaling factor (set to  $\geq 1$ ),  $n$  is the power of the vertical derivative (a positive integer), and  $n \in [1, 10]$ .

In this study, the process of the imaging method with a priori model constraints was as follows. First, the 3D S-wave velocity structure obtained through ambient noise tomography was transformed into a density model according to the empirical formula of Brocher (2005). The initial density model with a lateral grid spacing of  $10 \text{ km} \times$

10 km, a depth range of 0 – 50 km, and a step length of 2 km in the depth direction was constructed by linear interpolation. Then, frequency-domain gravity forward modeling was performed on the initial density model by using Equation (3) to obtain the theoretical gravity anomalies ( $\Delta g_i$ ). The deviations between the theoretical gravity anomalies  $\Delta g_i$  and the observed anomalies  $\Delta g_0$  and their root mean square (RMS) values were calculated. Subsequently, the deviations of the anomalies were applied in 3D imaging calculations using Equation (4) to obtain the density disturbances and update the 3D density model  $\rho_i$ . The model can be iterated following the above steps until one of the following two conditions is met: (1) the RMS reached the designed threshold or (2) the number of iterations reached the threshold. The second condition was chosen in this study, and the threshold for the number of iterations was set to 150.

### **4.3 Analysis of inversion uncertainty**

#### **4.3.1 Seismic imaging resolution test**

A resolution test examines the scale of velocity anomalies resolved from seismic data, reflecting the accuracy of seismic tomography. In this study, we conducted a checkerboard test to assess the resolving power of the inversion results by adding  $\pm 5\%$  velocity disturbances and 1% random traveltimes noise to the initial model, with the same grid spacing as in the actual inversion process.

Figure 4.4 displays the horizontal and vertical cross-sections of the checkerboard test results for the permanent stations (grid spacing of  $0.5^\circ \times 0.5^\circ$ ), and shows that the model was well recovered. Figure 4.5 presents the horizontal and vertical cross-sections of the checkerboard test results for the densely distributed temporary stations (grid spacing of  $0.25^\circ \times 0.25^\circ$ ), whereby anomalies of  $1^\circ \times 1^\circ$  can be identified.

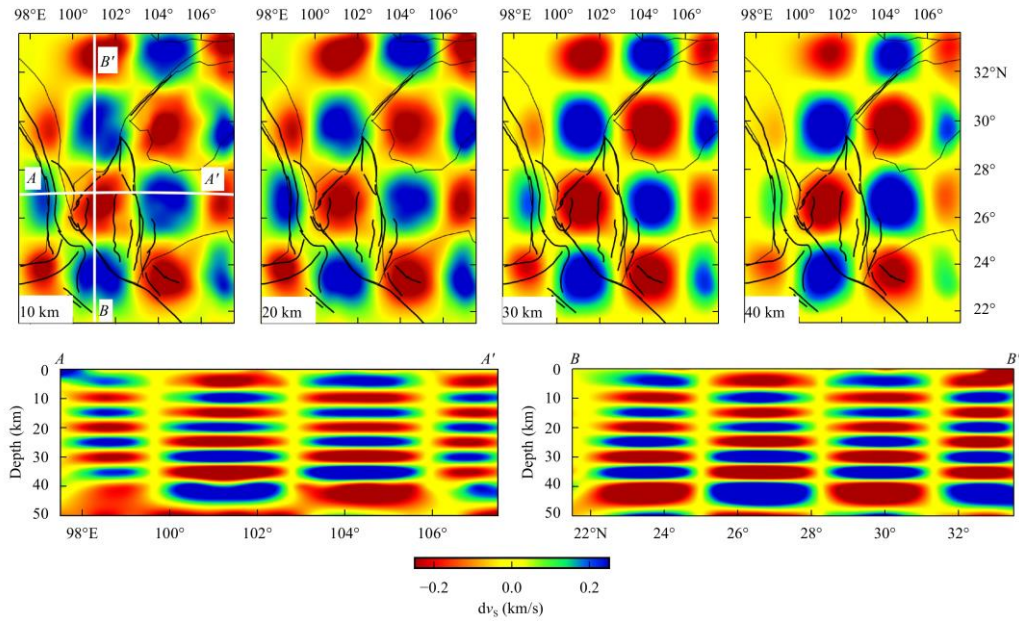


**Fig. 4.4** Checkerboard test results for the permanent stations of horizontal cross-sections at different depths and vertical cross-sections.

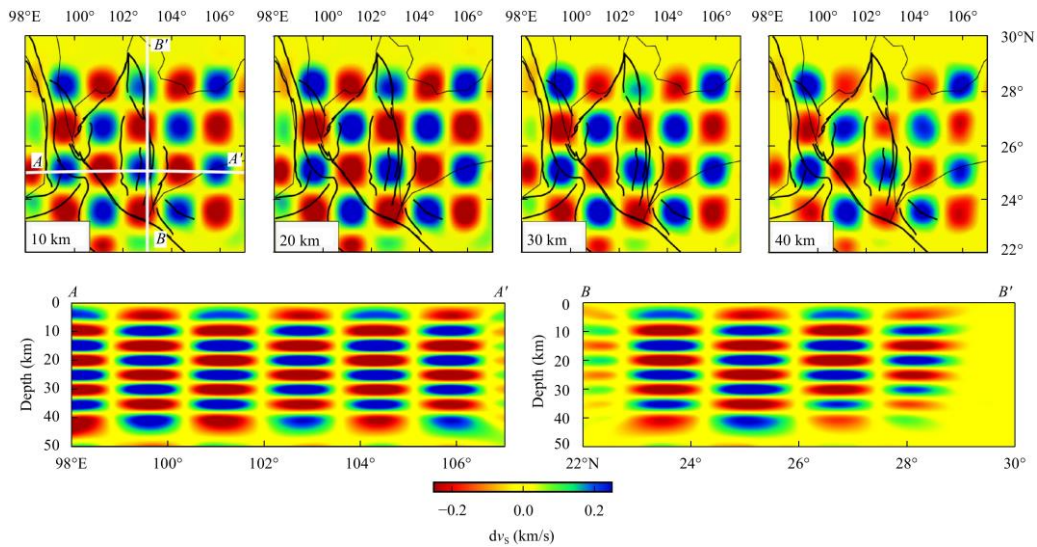


**Fig. 4.5** Checkerboard test results for the densely distributed temporary stations of horizontal cross-sections at different depths and vertical cross-sections.

### 4.3.2 Uncertainty analysis

Figures 4.6a and 4.6c plot the traveltimes deviations against the number of iterations for the permanent stations and densely distributed temporary stations, respectively. The deviations at the permanent stations decreased from 2.0 s before the inversion to  $\sim 0.5$  s after 10 iterations, whereas those at the densely distributed temporary stations decreased from 0.5 s to  $\sim 0.2$  s. Thus, both sets of deviations reduced and levelled out. Figures 6b and 6d display the histograms of the traveltimes deviation distributions before and after inversion for the permanent stations and densely distributed temporary stations, respectively. The two sets of traveltimes deviations were



closer to 0 after inversion, indicating that the inversion results are comparatively reliable.

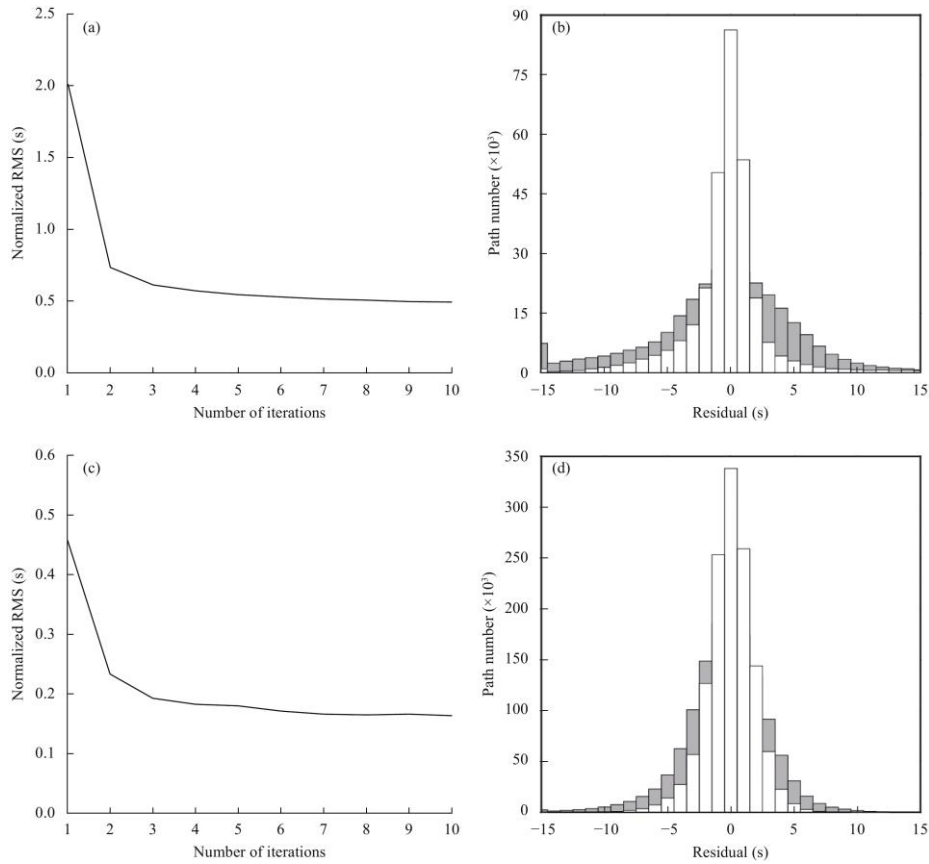


**Fig. 4.6 (a) Iterative convergence curves and (b) histogram of the deviation distribution before (solid grey boxes) and after (white boxes) inversion for the permanent stations. (c) Iterative convergence curves and (d) histogram of the deviation distribution before (solid grey boxes) and after (white boxes) inversion for the densely distributed temporary stations.**

Figure 4.7 plots the RMS of the gravity anomaly deviations against the number of iterations. The RMS declined rapidly with an initial increase in the number of iterations, leveled off, and reduced to approximately  $0.08 \times 10^{-5} \text{ m/s}^2$  after 150 iterations. The gravity anomaly values deviated by  $\pm 0.12 \times 10^{-5} \text{ m/s}^2$ , suggesting that the imaging results of this study are relatively reliable.

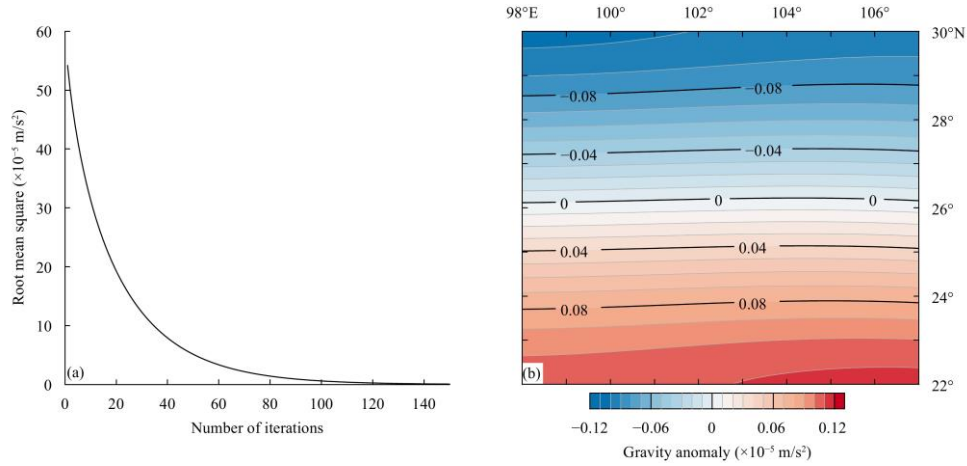


**Fig. 4.7 (a) Iterative convergence curve for the results of frequency-domain three-dimensional gravity data imaging, and (b) distribution map of the gravity anomaly deviations after inversion.**

### 4.3.3 Comparison between the results and the initial velocity model

Figure 4.8 compares the velocity structures of the inversion results in this study and the initial model in horizontal and vertical cross-sections. The results showed a basically consistent pattern with the initial model but with much more details. At a depth of 15 km, compared with the initial model, the revised distribution of low-velocity zones was more concentrated along the faults. The Panxi region exhibited a low-velocity anomaly, and relatively high-velocity regions were observed at the western and eastern borders of the Sichuan-Yunnan diamond-shaped block (Figures 4.8a and 4.8c). At a depth of 20 km, the revised range of the high-velocity zones in the Panxi region was smaller than that of the initial model, and the low-velocity zones on the east and west sides extended across the Honghe fault before intersecting in South Yunnan (Figures 4.8b and 4.8d). In the  $AA'$  cross-section (Figure 4.9c), high-velocity anomalies were observed to the north of the hypocenter of the  $M_s7.7$  Tonghai earthquake. In the  $BB'$  cross-section (Figure 4.9d), a prominent high-velocity-high-density region was observed 5 – 15 km below the Zhaotong-Lianfeng fault, and the low-velocity zones on the east and west sides were separated by the high-velocity Panxi region.

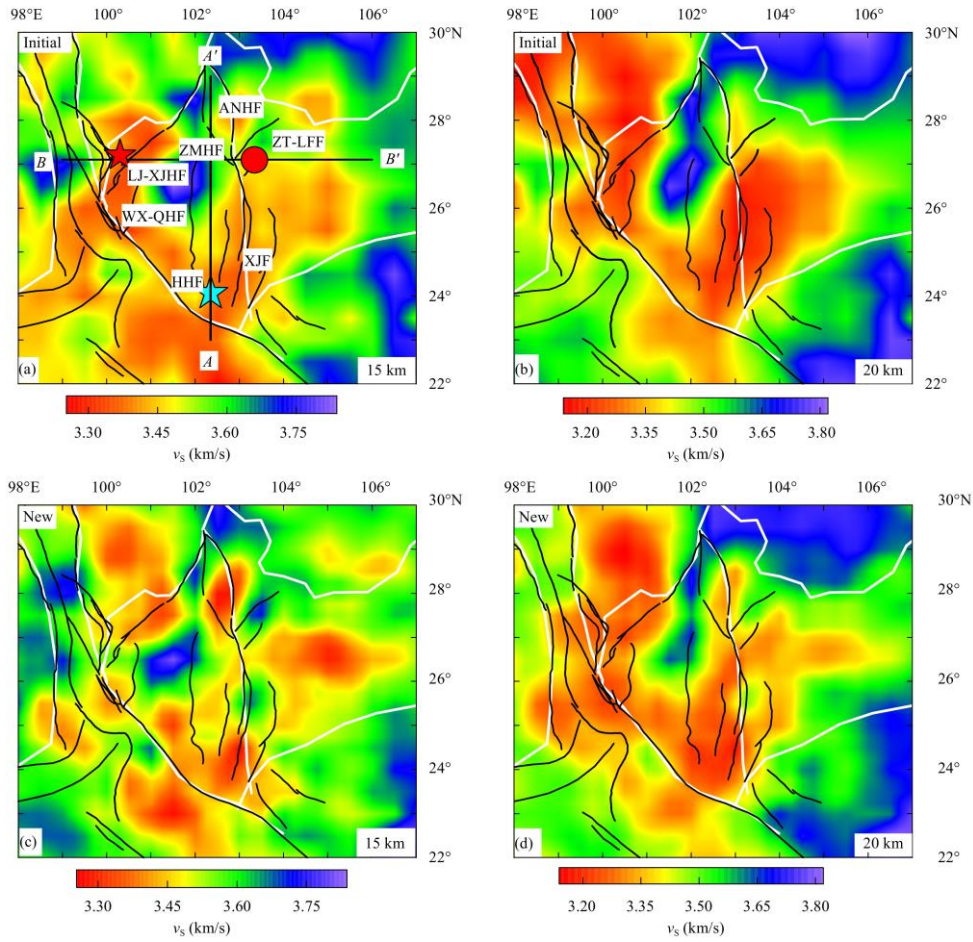


**Fig. 4.8** Comparison of the velocity structures determined in this study (“new”) and that based on the initial model at depths of (a, c) 15 km and (b, d) 20 km. The red circle, red pentagon, and cyan pentagon denote the hypocenters of the  $M_{s6.5}$  Ludian earthquake (2014),  $M_{s7.0}$  Lijiang earthquake (1996), and  $M_{s7.7}$  Tonghai earthquake (1970), respectively. ANHF: Anninghe fault; LJ-XJHF: Lijiang-Xiaojinhe fault; WX-QHF: Weixi-Qiaohou fault; ZMHF: Zemuhe fault; ZT-LFF: Zhaotong-Lianfeng fault; XJF: Xiaojiang fault; HHF: Honghe fault.

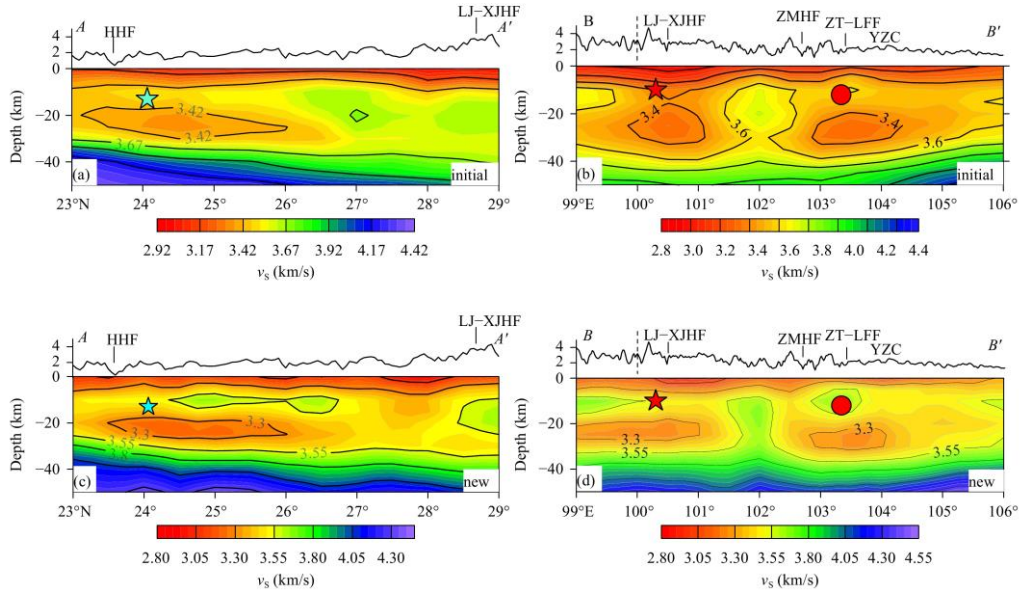


**Fig. 4.9** Velocity structures of the initial model (a, b) and that in this study (c, d) along the  $AA'$  and  $BB'$  cross-sections, respectively. The cyan pentagon, red circle, and red pentagon denote the hypocenters of the  $M_s7.7$  Tonghai earthquake (1970),  $M_s6.5$  Ludian earthquake (2014), and  $M_s7.0$  Lijiang earthquake (1996), respectively. LJ-XJHF: Lijiang-Xiaojinhe fault; ZMHF: Zemuhe fault; ZT-LFF: Zhaotong-Lianfeng fault; HHF: Honghe fault; YZC: Yangtze craton.

## 4.4 Results and discussion

### 4.4.1 Characteristics of the crustal S-wave velocity structure

In this study, we determined the crustal S-wave velocity structure at a depth of 0 – 50 km in the southern segment of the North-South Seismic Belt. Figure 4.10 displays the S-wave velocity structures at depths of 5, 10, 15, 20, 30, and 40 km.



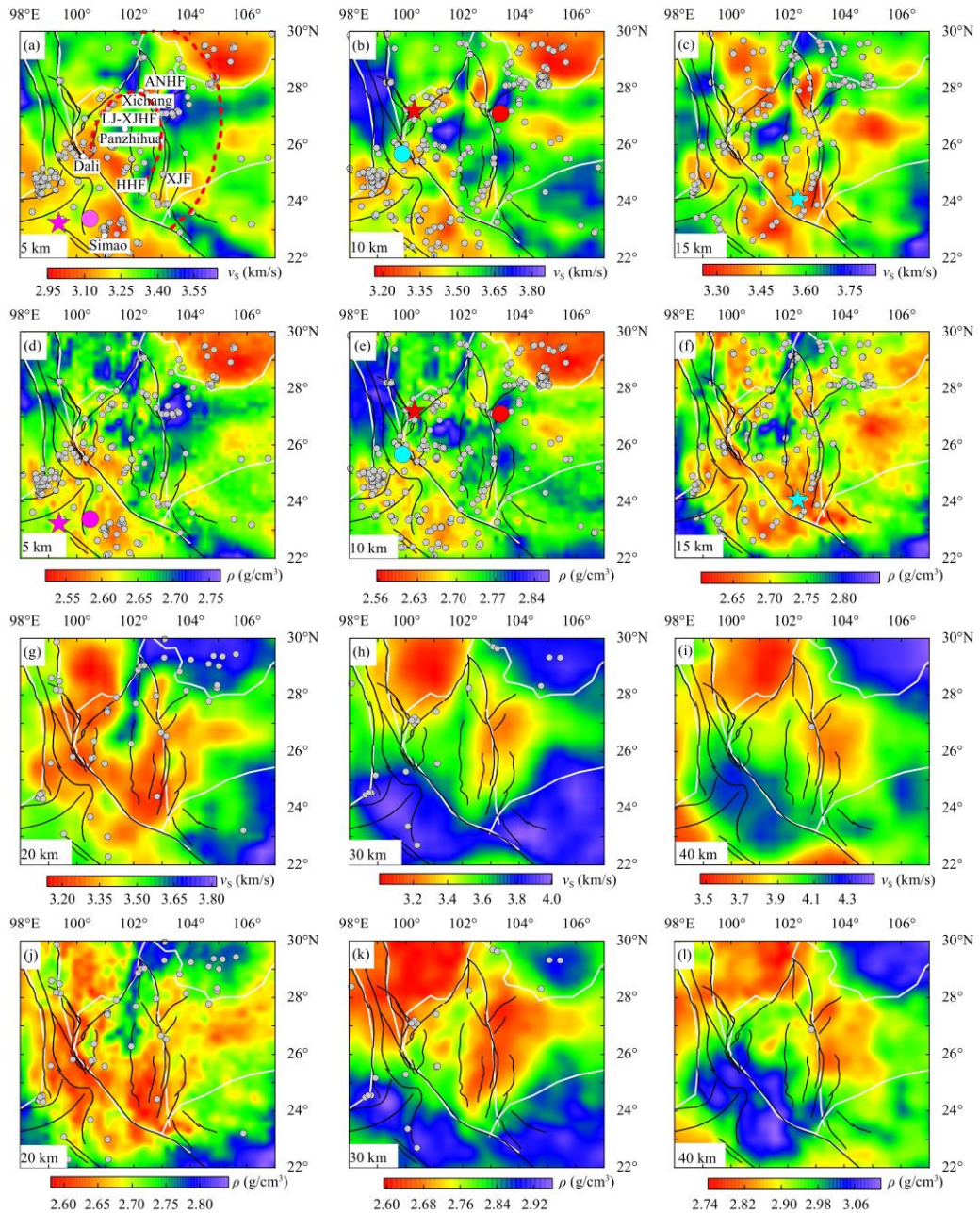


**Fig. 4.10** (a–c), (g–i) Horizontal cross-sections of the S-wave velocity structure at different depths. (d–f), (j–l) Horizontal cross-sections of the density structure at different depths.

The grey dots are the hypocenters of earthquakes with  $M_s > 3.5$  (data retrieved from <https://earthquake.usgs.gov/earthquakes/search/> and Yang T et al., 2022); the red, purple, and cyan circles are the hypocenters of the  $M_s$  6.5 Ludian earthquake (2014),  $M_s$  6.6 Jinggu earthquake (2014), and  $M_s$  6.4 Yangbi earthquake (2021), respectively; the red, purple, and cyan pentagons are the hypocenters of the  $M_s$  7.0 Lijiang earthquake (1996),  $M_s$  7.2 Gengma earthquake (1998), and  $M_s$  7.7 Tonghai earthquake (1970), respectively. The white solid lines are tectonic boundaries, and the solid black lines are faults; the red dashed lines indicate the boundary between the inner belt and the middle belt of the Emeishan large igneous rock province. ANHF: Anninghe fault; LJ-XJHF: Lijiang-Xiaojinhe fault; XJF: Xiaojiang fault; HHF: Honghe fault.

At a depth of 5 – 10 km, the velocity structure was significantly correlated with surface geological features. The low-velocity anomalies were observed to be mainly distributed in the Sichuan Basin and the Dali and Simao regions, where thick sedimentary layers were deposited (Xu Y et al., 2013; Pan JT et al., 2015). The high-velocity anomalies in the Panxi region increased with depth, consistent with the results of previous studies (Xu ZJ and Song XD, 2010; Wu JP et al., 2013). Some of the low-velocity anomalies in the study area spread along the faults (e.g., on the south sides of the Honghe and Xiaojiang faults). Combined with the distribution of seismic events, we found that previous earthquakes predominantly occurred within the low-velocity zones in the upper crust, which may be related to the presence of fluids in the fault zones.

Large-scale low-velocity anomalies were observed at a depth of 15 km in the study area, such as in the regions of the Songpan-Garzi block, Honghe fault, and the east and south sides of the Xiaojiang fault. Most earthquakes were distributed within these low-velocity anomalies, consistent with the results of Bao XW et al. (2015). However, high-velocity anomalies were observed in the Panxi region, possibly related to the intrusion of basic and ultramafic materials during the formation of the Emeishan large igneous province (Xu Y et al., 2013; Wu JP et al., 2013; Zhang ZQ et al., 2020). The Sichuan Basin exhibited overall high-velocity anomalies, indicating that the current depth has reached the crystalline basement of the basin.

Compared with the shallow crust pattern, the velocity structure at a depth of 20 km could be divided into more distinct blocks, indicating that the current depth has reached the middle and lower crust (Gao JY, 2016; Zhao Y et al., 2020). Two prominent low-velocity anomalies were observed in the study area: one distributed to the west of the Songpan-Garzi block and Sichuan-Yunnan diamond-shaped block, and the other near the Zemuhe and Xiaojiang faults. These results suggest that the western low-velocity zone is mainly affected by the extrusion of soft materials from the interior of the Tibetan Plateau to its southeastern margin, whereby these materials migrate southward after being blocked by the “hard” Sichuan Basin. The eastern low-velocity zone is also migrating southward under the influence of the regional stress field and the strike-slip motion of the adjacent Xiaojiang fault (Zhang ZQ et al., 2020); the two low-velocity zones have spread across the Honghe fault and intersected in the southern part of Yunnan. These low-velocity zones were also reported in previous research. For instance, Bao XW et al. (2015) and Li DH et al. (2018) found that the low-velocity zones lie across the Honghe fault, whereas Liu Y et al. (2021) and Zheng C et al. (2016) reported that they do not. Our findings indicate that the low-velocity zones on both sides are affected by the extrusion of materials from the Tibetan Plateau and the strike-slip fault movement and that they are migrating southward and have crossed the Honghe fault.



At a depth of 30 – 40 km, high-velocity anomalies were observed in the southern part of the study area, which is already situated at the top of the upper mantle. In contrast, low-velocity anomalies were observed in the northern area, which is within the range of the lower crust, agreeing with the results of Zhou LQ et al. (2012). In accord with its characteristics as a stable craton, the Sichuan Basin exhibited a significant high-velocity anomaly. The Honghe fault is a boundary line of the Sichuan-Yunnan diamond-shaped block, and the velocity structure on either side of the fault was found to differ considerably. The western side showed a high-velocity anomaly, while the eastern side exhibited a relatively low-velocity anomaly, indicating that the Moho is shallower on the west side than on the east side. These findings also reveal that the penetration depth of the Honghe fault has reached the top of the upper mantle.

Figure 4.11 presents three vertical cross-sections in the study area (refer to Figure 4.1b for their locations). All the cross-sections demonstrate widespread low-velocity layers in the middle and lower crust of the study area, such as those distributed beneath the Songpan-Garzê block, Lijiang-Xiaojinhe fault (LJ-XJHF), Zhaotong-Lianfeng fault (ZT-LFF), Xiaojiang fault (XJF), and Honghe fault (HHF). The depth of the low-velocity layer was found to differ between regions. According to the  $AA'$  cross-section, the two low-velocity layers underneath the Lijiang-Xiaojinhe fault and Yangtze craton block are located at a depth of  $\sim 15 - 30$  km and are separated by the high-velocity body in the Panxi region. In the  $BB'$  cross-section, the low-velocity layer beneath the Xiaojiang fault was found to be located at a depth of  $\sim 15 - 25$  km. In the  $CC'$  cross-section, the low-velocity layer beneath the Honghe fault extended to a depth of  $\sim 25$  km, and its depth increased further to  $\sim 30$  km in the north near the Songpan-Garzê block. The results indicate that seismic events are mainly distributed within the low-velocity zones and the transition zones between high- and low-velocity regions in the upper crust, often with underlying low-velocity and low-density layers. We speculate that the upwelling of deep materials also has a certain impact on the occurrence of moderate-to-strong earthquakes.

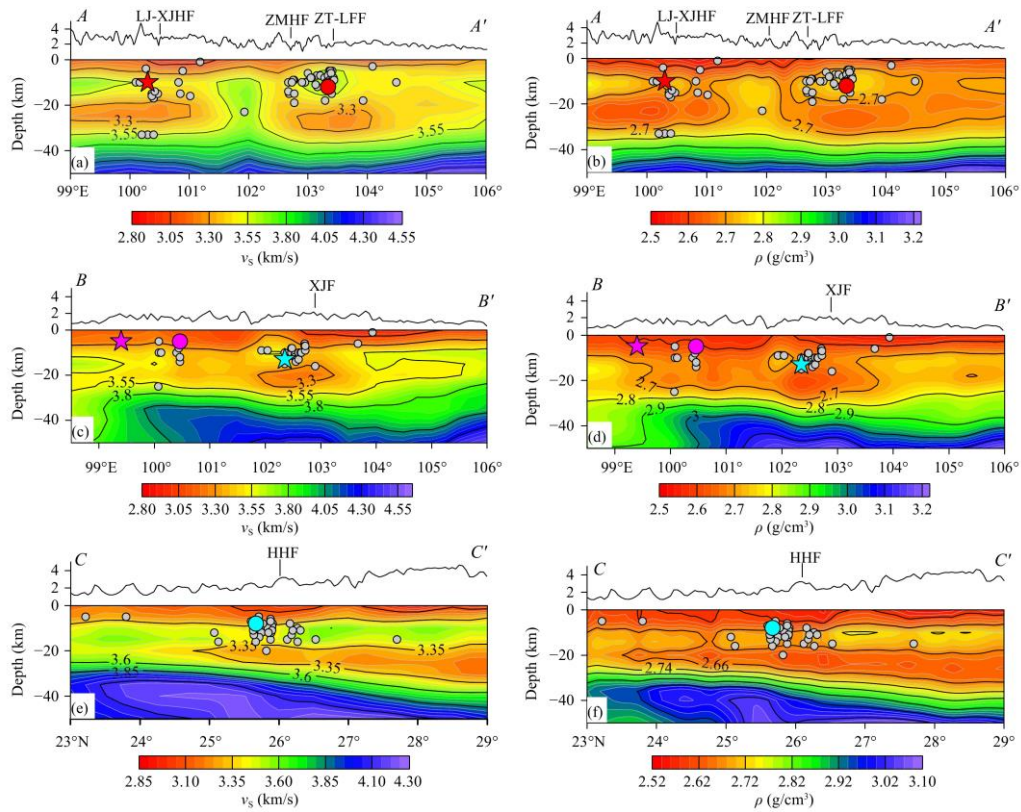


**Fig. 4.11** (a), (c) and (e) Vertical cross-sections of the S-wave velocity structure; (b), (d) and (f) vertical cross-sections of the density structure (see Figure 4.1b for their locations). The grey dots are the hypocenters of earthquakes with  $M_s > 3.5$ . The red, purple, and cyan circles are the hypocenters of the  $M_s 6.5$  Ludian earthquake (2014),  $M_s 6.6$  Jinggu earthquake (2014), and  $M_s 6.4$  Yangbi earthquake (2021), respectively; the red, purple, and cyan pentagons are the hypocenters of the  $M_s 7.0$  Lijiang earthquake in 1996,  $M_s 7.2$  Gengma earthquake (1998), and  $M_s 7.7$  Tonghai earthquake (1970), respectively. LJ-XJHF: Lijiang-Xiaojinhe fault; ZMHF: Zemuhe fault; ZT-LFF: Zhaotong-Lianfeng fault; XJF: Xiaojiang fault; HHF: Honghe fault.

## 4.2 Characteristics of the crustal density structure

In this study, we obtained the crustal density structure at a depth of 0 – 50 km in the southern segment of the North-South Seismic Belt. The density distributions at depths of 5, 10, 15, 20, 30, and 40 km are shown in Figure 4.10. The characteristics of the density structure were generally consistent with that of the S-wave velocity structure but were more detailed. At a depth of 5 – 10 km, low-density anomalies were mainly distributed in regions with relatively thick sedimentary layers (e.g., the Sichuan Basin and the Dali and Simao regions in Yunnan) or near the faults. Compared with the pattern of the velocity structure, the range of low-density anomalies near the faults was smaller. High-density anomalies (up to  $2.7 \text{ g/cm}^3$  in accord with the density range of basic rocks) were observed in and around the Panxi region and extended northward. The Panxi region is located in the inner and middle zones of the Emeishan large igneous province, where large quantities of Emeishan basalts are distributed (Xu T et al., 2015; Zhao Y et

al., 2020). Combined with the distribution of seismic events, the results implied that earthquakes mainly occur in the low-density zones and transition zones between low- and high-density regions. Similar to the pattern of the velocity structure, widespread low-velocity anomalies were observed at a depth of 15 km, distributed beneath the Songpan-Garzê block, Honghe fault, and Xiaojiang fault. The density anomalies in the Sichuan Basin exhibited lateral heterogeneity, with relatively high-density zones in the southwest and low-density anomalies in the southeast.

At a depth of 20 km, the low-density anomalies were interconnected and gradually expanded. For example, the low-density zone near the Songpan-Garzê block and Honghe fault in the west and the low-density zone near the Xiaojiang fault in the east were separated by the high-density Panxi region. The eastern zone had a density value of approximately  $2.65 \text{ g/cm}^3$ , suggesting that it is mainly comprised of felsic minerals, as reported in previous studies (Zhang ZQ et al., 2020). The formation of the low-density zone in the area of the Xiaojiang fault remains controversial. Zhang ZQ et al. (2020) speculated that the low-velocity region predominantly originates from the thickening and melting of the middle and lower crust. Bai DH et al. (2010) suggested that it may be a channel for the migration of crustal materials from the Tibetan Plateau. The Sichuan Basin exhibited a high-density anomaly that extended downward to the upper mantle, which may have a blocking effect on the eastward migration of materials from the Tibetan Plateau.

At a depth of 30 km, low-density anomalies were mainly observed in the region of the Songpan-Garzê block and on the eastern side of the Xiaojiang fault. The distribution range of these low-density anomalies exceeded that of the low-velocity anomalies. Similar to the findings of Zhao Y et al. (2020), high-density anomalies were observed in the southern part of the study area and in the Sichuan Basin. The Honghe fault is the southern boundary of the Sichuan-Yunnan diamond-shaped block. The density values on either side of the fault differ significantly, exhibiting prominent transition zone characteristics.

A low-density anomaly was observed in area of the Songpan-Garzê block at a depth of 40 km, where it reaches the lower crust. In contrast, a high-density anomaly was observed in the Sichuan Basin, which is situated at the top of the upper mantle. The three vertical cross-sections in Figure 4.11 reveal low-density layers that correspond well with the low-velocity layers, are often distributed beneath the earthquake hypocenters.

### **4.3 Relationship between moderate-to-strong earthquakes and crustal structures**

Owing to the long-term southeastward compression of the Indian Plate into the

Eurasian Plate, seismic events occur frequently in the southern segment of the North-South Seismic Zone. In this study, we projected the hypocenters of the Lijiang, Gengma, Tonghai, Ludian, Jinggu, and Yangbi earthquakes onto the horizontal and vertical cross-sections of the velocity and density structures to further explore the correlation between earthquakes and deep structures.

The  $M_S$  7.0 Lijiang earthquake occurred in 1996 on the Lijiang-Daju fault, the boundary between the Quaternary Lijiang faulted basin and Yulong-Haba Snow Mountains. As shown in Figures 4.10b and 10e, the hypocenter of the Lijiang earthquake was in the transition zone between high- and low-velocity anomalies but closer to the low-velocity region. Figures 4.11a and 11b display the vertical cross-sections passing through the hypocenter of the Lijiang earthquake, revealing an obvious low-velocity and low-density anomaly below it. Su YJ and Liu ZM (1997) and Xu T et al. (2015) also suggested the existence of an apparent low-velocity anomaly below the hypocenter of the Lijiang earthquake, which may have been formed by the material extruded southeastward from the Tibetan Plateau. The  $M_S$ 7.2 Gengma earthquake occurred in 1998 on the Lancang-Gengma fault, which belongs to the Sanjiang fold system. Figures 4.10 and 4.11 show that the hypocenter of the Gengma earthquake was located in the transition zone between high and low anomalies but slightly closer to the low anomaly region. We observed a low-velocity and low-density anomaly beneath this hypocenter, agreeing with the deep seismic sounding results of Wang SJ et al. (2015). This anomaly may be related to the upwelling of molten materials from the mantle. The  $M_S$  7.7 Tonghai earthquake occurred in 1970 at the structural intersection between the Honghe and Xiaojiang faults. Owing to the stress concentration related to the compression of the Sichuan-Yunnan diamond-shaped block, several strong earthquakes have occurred in this region, such as the  $M_S$ 7.0 Eshan earthquake in 1913. Figures 4.10c and 10f reveal that the Tonghai earthquake occurred within a low-velocity and low-density anomaly in the upper crust. Figures 4.11c and 4.11d display the vertical cross-sections passing through the hypocenter of the Tonghai earthquake, showing that the hypocenter was within a relatively high anomaly zone above the low-velocity and low-density anomaly. Xu Y et al. (2013) and Wu JP et al. (2013) reported a low-velocity anomaly in the southern segment of the Xiaojiang fault, corroborating with the results of the present study. The formation of this low-velocity anomaly might be related to fluid behavior. The action of fluids and the blocking effect of the low-velocity anomaly beneath the seismic hypocenter provide conditions for the occurrence of earthquakes.

The  $M_S$ 6.5 Ludian earthquake occurred in 2014 on the Zhaotong-Lianfeng fault to the east of the Xiaojiang fault, a region that has experienced frequent moderate earthquakes in recent years. The  $M_S$ 5.0 and  $M_S$ 5.1 Ludian earthquakes in 2003,  $M_S$ 5.6 Ludian earthquake in 2004, two  $M_S$ 5.1 Yanjin earthquakes in 2006, and  $M_S$ 5.7 and  $M_S$ 5.6 Yiliang earthquakes in 2012 all occurred within this area (Xu XW et al., 2014).

Figures 4.11a and 4.11b show the velocity and density structures along the  $AA'$  vertical cross-section, revealing that the hypocenter of the Ludian earthquake in 2014 was located within a high-velocity and high-density layer in the upper crust. The layer is approximately 15 km thick and experiences concentrated seismic events. An apparent low-velocity and low-density anomaly was observed at a depth of 20 km below this high-velocity and high-density layer. The low-velocity layer may be related to the partial melting of crustal materials or the presence of crustal fluids. This observation is consistent with the double-difference tomography results of Wang CZ et al. (2021). The aeromagnetic results of Li DH et al. (2019) also indicated that the crustal material above the hypocenter of the 2014 Ludian earthquake exhibited high magnetic intensities, while the material below it had low intensities. The significant physical-property differences between the materials above and below the focal depth are favorable for stress concentration. The presence of a high-velocity and high-density upper crustal layer together with a low-velocity and low-density middle lower crustal layer underneath may be a critical medium background for the development and occurrence of moderate-to-strong earthquakes in this region (Su YJ et al., 1999).

The  $M_s$ 6.6 Jinggu earthquake occurred in 2014 in the region between the Simao-Pu' er seismic zone to the east of the Lancangjiang fault and the Gengma-Lancang seismic zone to the west, but closer to the Simao-Pu' er seismic zone. Within 100 km of its epicenter, there have been 35 known earthquakes with magnitude  $\geq 5$  to date, including 22 events with magnitudes of 5.0 – 5.9, 10 events with magnitudes of 6.0 – 6.9, and 3 events with magnitudes of 7.0 – 7.9 (Li YH et al., 2014). Figures 4.11c and 4.11d present the velocity and density structures along the  $BB'$  vertical cross-section. These show that the hypocenter of the 2014 Jinggu earthquake was located in the transition zone between high and low anomaly regions but slightly closer to the low-value zone, with low-velocity and low-density layers widely distributed below it. The results of Li YH et al. (2014) indicated that the hypocenter of the Jinggu earthquake was within a low-velocity zone in the upper crust, without apparent low-velocity anomalies underneath it. The magnetotelluric sounding results of Cheng YZ et al. (2016) indicated that the Jinggu earthquake occurred on the interface between high- and low-resistivity layers in the crust. There are Quaternary basalts and craters in the Pu' er area (Guo SM et al., 1999), indicating historical volcanic activities. Geothermal data show relatively high terrestrial heat-flow values, and hot springs are widely distributed in this area (Tang HH et al., 2020). The formation of the low-velocity and low-density layers in this area might be driven by the upwelling of molten materials from the mantle. Faults are widely distributed in this area, and the low-velocity anomalies in the upper crust are related to water-bearing fluids in the crust (Li YH et al., 2014). Fluids can reduce the fault strength and destabilize the stress state, which may be the main reasons for the occurrence of the Jinggu earthquake and the frequent seismic events in the

nearby Simao-Pu' er seismic zone.

The  $M_s$  6.4 Yangbi earthquake occurred in 2021 in the southern segment of the Weixi-Qiaohou fault, and many earthquakes with small-to-medium magnitudes have occurred near this fault in recent years, such as the  $M_s$ 5.5 Eryuan earthquake in 2013 and the  $M_s$ 5.1 Yangbi earthquake in 2017. Figures 4.11e and 11f display the velocity and density distributions along the  $CC'$  vertical cross-section. The figure shows that the Yangbi earthquake occurred in the transition zone between the high and low anomalies of the upper crustal velocity and density structures. The magnetotelluric sounding results of Ye T et al. (2021) indicated that the Yangbi earthquake occurred in the transition zone between high- and low-resistivity regions, which is consistent with the results of the present study. Shi L et al. (2021) compared the difference between the theoretical isostatic Moho depth and the actual depth calculated with the receiver function to obtain the isostatic anomalies. Their results suggested that the hypocenter of the Yangbi earthquake was located in an isostatic anomaly gradient belt. Previous studies also indicated that earthquakes tend to occur in the transition zone between high- and low-velocity regions (Huang ZX et al., 2013; Li YH et al., 2014; Liu Y et al., 2021). Based on geothermal data, Tang HH et al. (2020) found that geothermal anomalies were prominent in this region, with a terrestrial heat-flow value of up to  $88 \text{ mW/m}^2$ . We speculate that the formation of this low-velocity and low-density body related to the upwelling of molten materials from the mantle. The hypocenter of the Yangbi earthquake was located beneath the NW-trending strike-slip fault (Weixi-Qiaohou fault) and was likely influenced by the upwelling of molten materials from the mantle and the intensive compression of materials escaping eastward from the Tibetan Plateau. The structure of a low-velocity and low-density layer overlain by a high-velocity and high-density layer is conducive to stress accumulation. The foreshocks and aftershocks of the Yangbi earthquake in 2021 were concentrated in the extensional stepovers of the NW-trending strike-slip fault. Such regions have low strength and are favorable for fluid flow (Lei XL et al., 2021), providing an environment for the occurrence of the Yangbi earthquake.

## 4.5 Conclusions

In this study, we applied the ambient noise tomography method to obtain the crustal S-wave velocity structure in the southern segment of the North-South Seismic Belt. Subsequently, we obtained the high-resolution crustal density structure through frequency-domain gravity imaging constrained by the velocity structure. Then we comprehensively analyze the crustal velocity and density structures and explore the seismogenic environment in the study area. The conclusions are as follows.



(1) In the study area, there are two significant low-velocity-low-density anomalies in the lower crust: one to the west of the Songpan-Garzê block and Sichuan-Yunnan diamond-shaped block, and the other near the Zemuhe and Xiaojiang faults. The low-velocity and low-density zone in the west is mainly affected by the extrusion of materials from the interior of the Tibetan Plateau to its southeastern margin. These materials migrate southward after being blocked by the “hard” Sichuan Basin. The low-velocity and low-density zone in the east may have been formed by the partial melting of crustal material. These two zones cross the Honghe fault and intersect in the southern part of Yunnan.

(2) Previous earthquakes in the study area mainly occurred within the low-velocity zones and the transition zones between high- and low-velocity regions in the upper crust, and low-velocity and low-density layers often existed beneath the hypocenters of moderate-to-strong earthquakes. The  $M_S$  7.0 Lijiang,  $M_S$  7.7 Tonghai, and  $M_S$  6.4 Yangbi earthquakes occurred in the transition zones between high and low anomalies in the upper crust, with significant low-velocity and low-density anomalies beneath their hypocenters. The  $M_S$  7.2 Gengma and  $M_S$  6.6 Jinggu earthquakes occurred in the transition zones between high and low anomalies in the upper crust, slightly closer to the low-value region, with widely distributed low-velocity and low-density anomalies beneath their hypocenters. The  $M_S$  6.6 Ludian earthquake occurred in the high-velocity and high-density upper crust, with apparent low-velocity and low-density anomalies below its hypocenter. Fluids play a critical role in the seismogenic process by reducing the fault strength and destabilizing the stress state, which may be a triggering factor for the earthquakes in the southern segment of the North-South Seismic Belt. Additionally, the upwelling of deep molten materials may lead to the accumulation of energy and concentration of stress, providing an important seismogenic background for moderate-to-strong earthquakes in this area.

## References

- [1] Bai DH, Unsworth MJ, Meju MA, Ma XB, Teng JW, Kong XR, Sun Y, Sun J, Wang LF, Jiang CS, Zhao CP, Xiao PF, and Liu M (2010). Crustal deformation of the eastern Tibetan plateau revealed by magnetotelluric imaging. *Nat Geosci* **3**(5): 358–362.
- [2] Bao XW, Sun XX, Xu MJ, Eaton DW, Song XD, Wang LS, Ding ZF, Mi N, Li H, Yu DY, Huang ZC, and Wang P (2015). Two crustal low-velocity channels beneath SE Tibet revealed by joint inversion of Rayleigh wave dispersion and receiver functions. *Earth Planet Sci Lett* **415**: 16–24.
- [3] Bensen GD, Ritzwoller MH, Barmin MP, Levshin AL, Lin F, Moschetti MP, Shapiro NM, and Yang Y (2007). Processing seismic ambient noise data to obtain

- reliable broad-band surface wave dispersion measurements. *Geophys J Int* **169**(3): 1239 – 1260 .
- [4] Brocher TM (2005). Empirical relations between elastic wavespeeds and density in the Earth's crust. *Bull Seismol Soc Am* **95**(6): 2081–2092
- [5] Cheng YZ, Tang J, Deng Y, and Dong ZY (2016). Electrical structure of upper crust in the source region of Jinggu Yunnan  $M_s$ 6.6 earthquake and the seismogenic environment. *Seismol Geol* **38**(2): 352–369 (in Chinese with English abstract).
- [6] ChinArray (2006). China Seismic Array Waveform Data. China Earthquake Administration. doi: 10.12001/ChinArray.Data
- [7] Cui YT, and Guo LH (2019). A wavenumber-domain iterative approach for rapid 3-D imaging of gravity anomalies and gradients. *IEEE Access* **7**: 34179 – 34188 .
- [8] Fan XL, and Chen QF (2019). Seismic constraints on the magmatic system beneath the Changbaishan volcano: Insight into its origin and regional tectonics. *J Geophys Res: Solid Earth* **124**(2): 2003 – 2024 .
- [9] Fang HJ, Yao HJ, Zhang HJ, Huang YC, and van der Hilst RD (2015). Direct inversion of surface wave dispersion for three-dimensional shallow crustal structure based on ray tracing: methodology and application. *Geophys J Int* **201**(3): 1251 –1263.
- [10] Fu YV, Gao Y, Li AB, Li L, and Chen AG (2017). Lithospheric structure of the southeastern margin of the Tibetan Plateau from Rayleigh wave tomography. *J Geophys Res: Solid Earth* **122**(6): 4631 – 4644 .
- [11] Gao JY (2016). Crustal velocity and density structure in the southeast Tibetan plateau by joint inversion of seismic data and gravity. Dissertation. Institute of Geophysics, China Earthquake Administration, Beijing, pp 43–55 (in Chinese with English abstract)
- [12] Guo SM, Wang Y, and Ji FJ (1999). Tectonic mechanism of moderate strong swarms in Yunnan's Simao Pu'er region. *J Seismol Res* **22**(2): 105–115 (in Chinese with English abstract).
- [13] Huang ZX, Li HY, and Xu Y (2013). Lithospheric S-wave velocity structure of the North-South Seismic Belt of China from surface wave tomography. *Chin J Geophys* **56**(4): 1121–1131 (in Chinese with English abstract).
- [14] Jia J, Wu QJ, and Wang FY (2021). Three-dimensional crustal P-wave velocity structure in the Yangbi and Eryuan earthquake regions, Yunnan, China. *Earthq Sci* **34**(4): 358–366.
- [15] Kan RJ, Zhang SL, Yan FT, and Yu LS (1977). Present tectonic stress field and its relation to the characteristics of recent tectonic activity in southwestern China.

- Chin J Geophys **20**(2): 96–109 (in Chinese with English abstract).
- [16]Lei XL Wang ZW, Ma SL, and He CR (2021). A preliminary study on the characteristics and mechanism of the May 2021  $M_s$ 6.4 Yangbi earthquake sequence, Yunnan, China. *Acta Seismol Sin* **43**(3): 261–286 (in Chinese with English abstract).
- [17]Levshin AL, and Ritzwoller MH (2001). Automated detection, extraction, and measurement of regional surface waves. *Pure Appl Geophys* **158**(8): 1531 – 1545 .
- [18]Li DH, Liao H, Ding ZF, Zhan Y, Wu PP, Xu XM, and Zheng C (2018). Joint inversion of the 3D P wave velocity structure of the crust and upper mantle under the southeastern margin of the Tibetan Plateau using regional earthquake and teleseismic data. *Acta Geol Sin-Engl Ed* **92**(1): 16–33.
- [19]Li DH, Ding ZF, Wu PP, Liang MJ, Wu P, Gu QP, and Kang QQ (2019). Deep structure of the Zhaotong and Lianfeng fault zones in the eastern segment of the Sichuan-Yunnan border and the 2014 Ludian  $M_s$ 6.5 earthquake. *Chin J Geophys* **62**(12): 4571– 4587 (in Chinese with English abstract).
- [20]Li YH, Xu XM, Zhang EH, and Gao JY (2014). Three-dimensional crust structure beneath SE Tibetan Plateau and its seismotectonic implications for the Ludian and Jinggu earthquakes. *Seismol Geol* **36**(4): 1204– 1216 (in Chinese with English abstract).
- [21]Lin FC, Ritzwoller MH, Townend J, Bannister S, and Savage MK (2007). Ambient noise Rayleigh wave tomography of New Zealand. *Geophys J Int* **170**(2): 649–666.
- [22]Liu W, Wu QJ, and Zhang FX (2019). Crustal structure of southeastern Tibetan Plateau inferred from double-difference tomography. *Acta Seismol Sin* **41**(2): 155– 168 (in Chinese with English abstract).
- [23]Liu Y, Yao HJ, Zhang HJ, and Fang HJ (2021). The community velocity model V. 1.0 of Southwest China, constructed from joint body- and surface-wave travel-time tomography. *Seismol Res Lett* **92**(5): 2972 – 2987 .
- [24]Molnar P, and Tapponnier P (1975). Cenozoic tectonics of Asia: effects of a continental collision: features of recent continental tectonics in Asia can be interpreted as results of the India-Eurasia collision. *Science* **189**(4201): 419–426.
- [25]Pan JT, Li YH, Wu QJ, and Ding ZF (2015). Phase velocity maps of Rayleigh waves in the southeast Tibetan plateau. *Chin J Geophys* **58**(11): 3993– 4006 (in Chinese with English abstract).
- [26]Prietzhev II (2010). Integrated interpretation technique of geophysical data for geological modeling. Dissertation. State University of Sergo Ordjonikidze, Moscow, pp 71–86

- [27] Qu C, Xu Y, Yang WC, Wang S, and Liu XY (2020). P-wave velocity imaging and lithosphere structure of the Tibetan plateau. *Chin J Geophys* **63**(3): 847–859 (in Chinese with English abstract).
- [28] Rawlinson N, and Sambridge M (2005). The fast marching method: An effective tool for tomographic imaging and tracking multiple phases in complex layered media. *Exploration Geophys* **36**: 341–350.
- [29] Shen CY, Yang GL, Tan HB, Xuan SB, Wu GJ, and Wang J (2015). Gravity anomalies and crustal density structure characteristics of profile Weixi-Guiyang. *Chin J Geophys* **58**(11): 3952–3964 (in Chinese with English abstract).
- [30] Shi L, Lou H, Wang QS, Lu HY, and Xu WM (2015). Gravity field characteristics and crust density structure in the Panxi region, China. *Chin J Geophys* **58**(7): 2402–2412 (in Chinese with English abstract).
- [31] Shi L, Li YH, and Zhang RQ (2021). The gravity isostatic characteristics of the epicenter and its surrounding regions of the Yangbi  $M_s6.4$ , Yunnan earthquake. *Seismol Ecol* **43**(5): 1140–1156 (in Chinese with English abstract).
- [32] Su YJ, and Liu ZM (1997). Discussion on the source environment and rupture process of the  $M7.0$  Lijiang earthquake. *J Seismol Res* **20**(1): 66–71 (in Chinese with English abstract).
- [33] Su YJ, Liu ZY, Cai MJ, Zhang JW, and Li ZH (1999). Deep medium environment of strong earthquakes occurrence in Yunnan region. *Acta Seismol Sin* **21**(3): 313–222 (in Chinese with English abstract).
- [34] Tang HH, Guo LH, and Fang Y (2020). Estimation of heat flow in southeastern margin of Tibetan Plateau and its analysis of the correlation with earthquake activity. *Chin J Geophys* **63**(3): 1056–1069 (in Chinese with English abstract).
- [35] Wang CY, Wu JP, Lou H, Zhou MD, and Bai ZM (2003). P-wave crustal velocity structure in western Sichuan and eastern Tibetan region. *Sci China: Earth Sci* **46**(2): 254–265.
- [36] Wang CZ, Wu JP, Liu YN, Yang T, Fan LP, and Liu J (2021). Three-dimensional P-wave velocity structure around the sources of Ludian and Qiaojia earthquakes. *Acta Seismol Sin* **43**(1): 1–12 (in Chinese with English abstract).
- [37] Wang SJ, Liu BJ, Zhang JS, Liu BF, Duan YL, Song XH, Deng XG, Ma CJ, and Zang YR (2015). Study on the velocity structure of the crust in Southwest Yunnan of the north-south seismic belt—Results from the Menghai-Gengma-Lushui deep seismic sounding profile. *Sci China: Earth Sci* **58**(12): 2175–2187.
- [38] Wei W, Sun RM, and Shi YL (2010). P-wave tomographic images beneath Southeastern Tibet: Investigating the mechanism of the 2008 Wenchuan earthquake. *Sci China: Earth Sci* **53**(9): 1252–1259.

- [39] Wessel P, and Smith WHF (1998). New, improved version of generic mapping tools released. *Eos, Trans Am Geophys Union* **79**(47): 579.
- [40] Wu JP, Yang T, Wang WL, Ming YH, and Zhang TZ (2013). Three dimensional P-wave velocity structure around Xiaojiang fault system and its tectonic implications. *Chin J Geophys* **56**(7): 2257– 2267 (in Chinese with English abstract).
- [41] Xu T, Zhang ZJ, Liu BF, Chen Y, Zhang MH, Tian XB, Xu YG, and Teng JW (2015). Crustal velocity structure in the Emeishan large igneous province and evidence of the Permian mantle plume activity. *Sci China: Earth Sci* **58**(7): 1133– 1147 .
- [42] Xu XW, Jiang GY, Yu GH, Wu XY, Zhang JG, and Li X (2014). Discussion on seismogenic fault of the Ludian  $M_s6.5$  earthquake and its tectonic attribution. *Chin J Geophys* **57**(9): 3060– 3068 (in Chinese with English abstract).
- [43] Xu Y, Yang XT, and Liu JH (2013). Tomographic study of crustal velocity structures in the Yunnan region southwest China. *Chin J Geophys* **56**(6): 1904– 1914 (in Chinese with English abstract).
- [44] Xu ZJ, and Song XD (2010). Joint inversion for crustal and Pn velocities and Moho depth in Eastern Margin of the Tibetan Plateau. *Tectonophysics* **491**(1-4): 185–193.
- [45] Yang T, Li BR, Fang LH, Su YJ, Zhong YS, Yang JQ, Qin M, and Xu YJ (2022). Relocation of the foreshocks and aftershocks of the 2021  $M_s6.4$  Yangbi earthquake sequence, Yunnan, China. *J Earth Sci*, doi: 10.1007/s12583-021-1527-7
- [46] Yang WC, Hou ZZ, and Yu CQ (2015). 3D crustal density structure of West Yunnan and its tectonic implications. *Chin J Geophys* **58**(11): 3902– 3916 (in Chinese with English abstract).
- [47] Yang YJ, Ritzwoller MH, Levshin AL, and Shapiro NM (2007). Ambient noise Rayleigh wave tomography across Europe. *Geophys J Int* **168**(1): 259–274.
- [48] Yao HJ, Van der Hilst RD, and Montagner JP (2010). Heterogeneity and anisotropy of the lithosphere of SE Tibet from surface wave array tomography. *J Geophys Res:Solid Earth* **115**(B12): B12307.
- [49] Yao HJ (2020). Building the community velocity model in the Sichuan-Yunnan region, China: Strategies and progresses. *Sci China: Earth Sci* **63**(9): 1425 – 1428 .
- [50] Ye T, Chen XB, Huang QH, and Cui TF (2021). Three-dimensional electrical resistivity structure in focal area of the 2021 Yangbi  $M_s6.4$  Earthquake and its implication for the seismogenic mechanism. *Chin J Geophys* **64**(7): 2267– 2277 (in Chinese with English abstract).
- [51] Zhang YY, An YR, Long F, Zhu GH, Qin M, Zhong YS, Xu Q, and Yang HF (2022).

- Short-term foreshock and aftershock patterns of the 2021  $M_S$  6.4 Yangbi earthquake sequence. *Seismol Res Lett* **93**(1): 21–32.
- [52] Zhang ZQ, Yao HJ, and Yang Y (2020). Shear wave velocity structure of the crust and upper mantle in Southeastern Tibet and its geodynamic implications. *Sci China Earth Sci* **63**(9): 1278– 1293 .
- [53] Zhao Y, Guo LH, Guo Z, Chen YJ, Shi L, and Li YH (2020). High resolution crustal model of SE Tibet from joint inversion of seismic P-wave travel-times and Bouguer gravity anomalies and its implication for the crustal channel flow. *Tectonophysics* **792**: 228580 .
- [54] Zheng C, Ding ZF, and Song XD (2016). Joint inversion of surface wave dispersion and receiver functions for crustal and uppermost mantle structure in Southeast Tibetan Plateau. *Chin J Geophys* **59**(9): 3223– 3236 (in Chinese with English abstract).
- [55] Zheng XF, Ouyang B, Zhang DN, Yao ZX, Liang JH, and Zheng J (2009). Technical system construction of Data Backup Centre for China Seismograph Network and the data support to researches on the Wenchuan earthquake. *Chin J Geophys* **52**(5): 1412– 1417 (in Chinese with English abstract).
- [56] Zheng XF, Yao ZX, Liang JH, and Zheng J (2010). The role played and opportunities provided by IGP DMC of China National Seismic Network in Wenchuan earthquake disaster relief and researches. *Bull Seismol Soc Am* **100**(5B): 2866 –2872.
- [57] Zhou LQ, Xie JY, Shen WS, Zheng Y, Yang YJ, Shi HX, and Ritzwoller MH (2012). The structure of the crust and uppermost mantle beneath South China from ambient noise and earthquake tomography. *Geophys J Int* **189**(3): 1565 –1583.



# **CHINA NATIONAL REPORT on Volcanology**

For

The 28th IUGG General Assembly

Berlin, Germany, July 11-20, 2023

Chinese Committee for IAVCEI (CNC-IAVCEI)

June, 2023

# Recent Advances in Volcanology Research in China

Zhengfu Guo<sup>1</sup> and Xiao-Long Huang<sup>2</sup>

1. Key Laboratory of Cenozoic Geology and Environment, Institute of Geology and Geophysics, Chinese Academy of Sciences, Beijing 10029, China
2. State Key Laboratory of Isotope Geochemistry, CAS Center for Excellence in Deep Earth Science, Guangzhou Institute of Geochemistry, Chinese Academy of Sciences, Guangzhou 510640, China (E-mail: xlhuang@gig.ac.cn)

## Abstract

Active volcano monitoring is important to reduce volcanic disasters. The Changbaishan volcano observatory station in Jilin Province of NE China has established an annual fund to improve research on the Changbaishan volcano monitoring. During the past years, CNC-IAVCEI has organized a national symposium on Volcanology and two subconferences (for the 4th and 5th Congress of China Geodesy and Geophysics) in China. The members of CNC-IAVCEI also edited a book entitled “Active Volcanoes of China” as Geological Society Special Publication 510 and two special issues on volcanology research in the journal.

**Key words:** Volcano monitoring, Changbaishan volcano observatory station, Active Volcanoes of China, Dynamics of magmatism.

## 1. Volcanologic research in China

The National Field Scientific Observation and Research Station of Changbaishan Volcano (the Changbaishan volcano observatory station) in Jilin Province is a special field station that was set up for monitoring the activity of the Changbaishan Volcano in China, understanding the genesis and activity history of the Changbaishan active volcano, and investigating the magma source and mantle structure of the Changbaishan volcano. Since 2020, the Changbaishan volcano station has established an annual fund to promote the development of the field station, to improve the research of Changbaishan volcano and to strengthen talent cultivation. On December 7, 2021, at

the first Annual Academic meeting of the National Field Scientific Observation and Research Station of the Institute of Geology of the China Earthquake Administration, Academician Liu Jiaqi was invited to give a report entitled "Playing the core link role of Volcanoes in the Earth Science System", systematically explaining the significance of volcanism in scientific research on the Earth system. Prof. Guo Zhengfu (chairman of CNC-IAVCEI) was invited to give a report entitled "Volcanic Gases and Volcanic Monitoring", which mainly covered the research progress of volcanic gases and monitoring.

Volcano monitoring is important for reducing volcanic disasters, effectively saving lives and property and protecting the economy. From December 8 to 11, 2020, the volcano monitoring stations of Changbaishan Volcano, Longgang Volcano, Tengchong Volcano, Wudalianchi Volcano, Jingpohu Volcano and Northern Hainan Volcano, together with the National Volcanic Platform Network Data Center, held a conference on annual volcano monitoring work. In the conference, they shared the main volcano monitoring data in China and exchanged new technologies and methods of volcano monitoring with the aim of promoting the monitoring of major volcanic activities in China and new volcanic monitoring technologies.

Volcanic stratigraphy and chronology are two important research directions in volcanology. To promote the intersections of volcanology and Quaternary Science, the member of the CNC-IAVCEI attended the annual meeting of the Committee of Stratigraphy and Chronology of China Quaternary Science Research Society and gave some reports to introduce the research progress of volcanic Stratigraphy and Chronology in East Asia.

## **2. Some important conferences on volcanology in China**

During the past years, CNC-IAVCEI organized a national symposium on Volcanology and two subconferences (for the 4th and 5th Congress of China Geodesy and Geophysics).

During the Boao Conference on Disaster Prevention and Reduction from February 12 to 15, 2023, the Subforum on Volcanic hazard Prevention, which is also

the 10th National Volcanic Academic Seminar, was convened by CNC-IAVCEI. The theme of the conference is "Continental volcanism and its environmental and hazard effects", focusing on the exchange of volcanic disaster in China and defense as well as the latest research results in the field of environmental resource effects of volcanic activities, etc. The conference exchanged the current research frontiers and advances in volcanic resources and disasters, volcanology, volcano monitoring, dating and many other fields and discussed the future development direction of volcanic research in China, the scientific utilization of volcanic resources, and the theoretical basis of disaster prevention.



**Subforum on Volcanic Disaster Prevention at the 2023 Boao Conference on  
Disaster Prevention and Reduction**

During the 5th Chinese Conference of Geodesy and Geophysics (CCGG), the CNC-IAVCEI organized the IAVCEI subconference that includes two themes, i.e., magmatic processes interacting with the geosphere (V01) and resource, environment and climate effects of volcanism (V02). Theme V01 focuses on the interaction between magmatism and the geosphere and mainly reports the latest research progress in plate subduction, formation and evolution of Big Mantle Wedge (BMW), magmatic activity and mineralization of mantle plumes and large igneous provinces, composition characteristics and material circulation mechanisms of the deep mantle. Theme V02 focuses on the resources, environment and climate effects of volcanic activities and is mainly conducted on the internal structure and material composition of volcanoes,

volcanic geology and hazards, eruption mechanism, monitoring, simulation and prediction of volcanic activities, and the latest achievements and progress in the field of volcanic research, volcanic detection and monitoring in China.

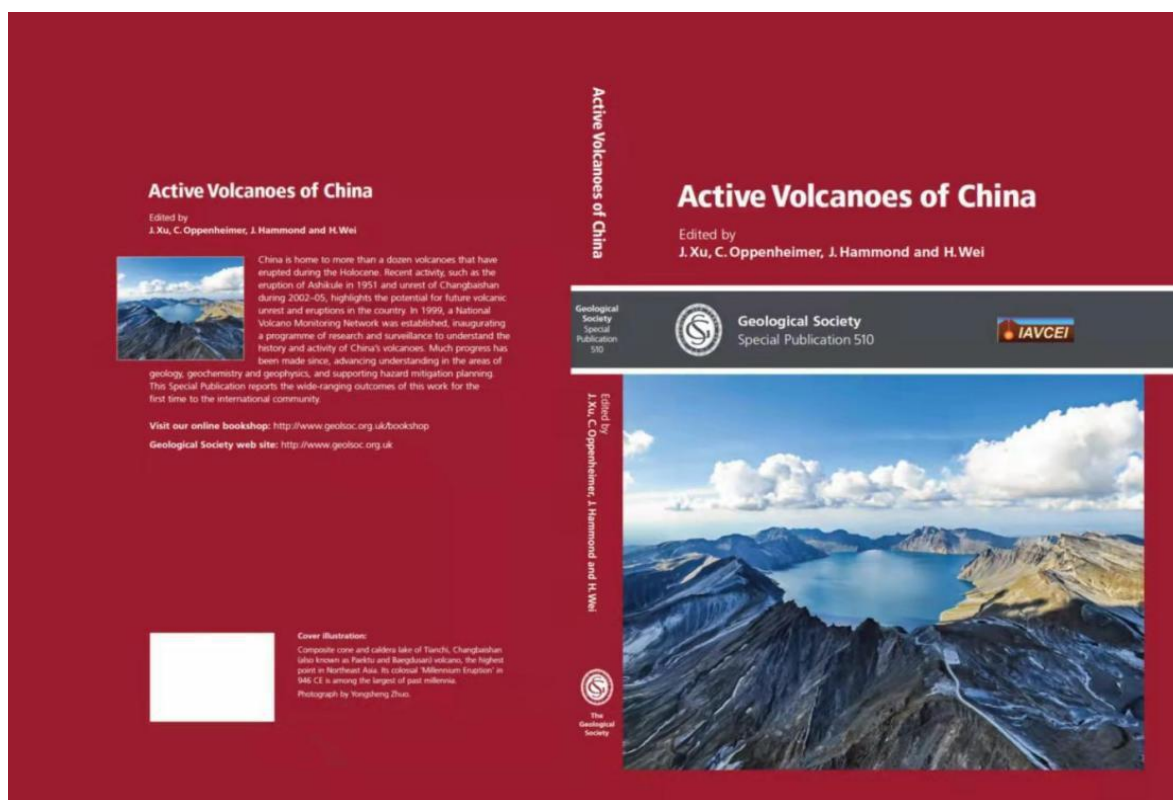


### **CNC-IAVCEI Subconference in the 5th CCGG Conference**

On July 17-18, 2021, the CNC-IAVCEI organized the IAVCEI subconference of the 4th CCGG at China University of Petroleum (East China). It includes three themes, i.e., magmatic processes interacting with the geosphere (V01); resources, environment and climate effects of volcanism (V02); and deep processes and mechanisms of magmatic activity (JS02). Theme V01 focuses on the interaction between magmatism and the geosphere and mainly reports the latest research progress on mantle plume activity, plate subduction, formation and evolution of Big Mantle Wedges (BMW), and deep material circulation. Theme V02 focuses on the resources, environment and climate effects of volcanic activities, conducted research on the internal structure and material composition of volcanoes, volcanic geology and hazards, eruption mechanism, monitoring, simulation and prediction of volcanic activities, and presented the latest achievements and progress in the field of volcanic research, volcanic detection and monitoring in China. Theme JS02 explores the process and mechanism of magmatic activity from geophysical exploration, geochemical tracing and petrogeochemical research. Members of the subcommittee actively participated in the meeting, exchanged the research frontiers and progress in volcanic and earthquake disasters, volcanology, monitoring and many other fields, and discussed the future development direction of volcanic research in China and the theoretical basis of disaster prevention.

### 3. Some special issues and books on volcanology research in China

China is home to more than a dozen volcanoes that erupted during the Holocene. Recent activity, such as the eruption of Ashikule in 1951 and the unrest of Changbaishan during 2002–2005, highlights the potential for future volcanic unrest and eruptions in the country. Prof. Jiandong Xu, as the first author, edited a book named “Active Volcanoes of China”, which collected 19 papers to introduce the volcanoes of China. In 1999, a National Volcano Monitoring Network was established, inaugurating a programme of research and surveillance to understand the history and activity of China’s volcanoes. Much progress has been made since, advancing understanding in the areas of geology, geochemistry and geophysics and supporting hazard mitigation planning. This Special Publication reports the wide-ranging outcomes of this work for the first time to the international community.



Geological Society Special Publication 510 “Active Volcanoes of China”



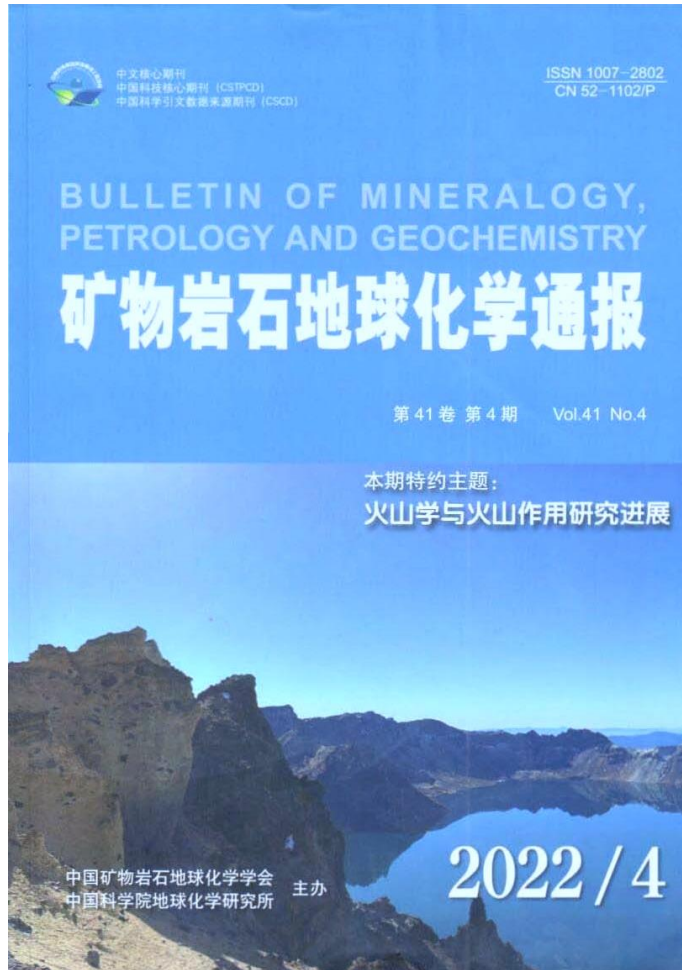
A special issue on volcanology research was published in the journal “Acta Petrologica Sinica” (Volume 36, Issue 7) in July 2020. This issue collected 20 papers on the resource, environment and climate effects of volcanic activity, magmatic processes interacting with the geosphere, or deep processes and mechanisms of magmatic activity.



**Special Issue on volcanology research published in the journal “Acta Petrologica Sinica” (Volume 36, Issue 7)**

A special issue on Advances in volcanology and volcanism was published in the journal “Bulletin of Mineralogy, Petrology and Geochemistry” (Volume 41, Issue 4) in April 2022. Volcanism is one of the important links between the Earth's internal processes and the evolution of the surface system. The characteristics of volcanic eruptions, volcanic effects, volcanic origins and dynamic mechanisms are all scientific issues that have attracted long-term attention. The Committee of Volcanology and Geochemistry of the Mineralogy, Petrology and Geochemistry Society of China invited some research teams engaged in the study of volcanology and volcanism in China to write articles. Chen X.Y. et al. (2022) initially constructed an integrated Holocene

volcanic ash stratigraphic framework in East Asia, demonstrating the application potential of volcanic ash chronology in the fine-correlation study of East Asian paleoclimate records. Li J.J. et al. (2022) summarized the classification, testing methods and main volatile compositions of melt inclusions in volcanic rocks and discussed the application prospect of melt inclusions in the study of the scale of volcanic CO<sub>2</sub> release. Lu J.X. et al. (2022) summarized the research progress of the paleoclimate and paleoenvironment of Maar Lake in China, showing the application significance of quantitative and ultrahigh resolution indicators. Wang L.Z. et al. (2022) studied the morphology of volcanic cones and the eruption process by using UAV photogrammetry technology, which is helpful for predicting the types and characteristics of volcanic eruptions and scientifically defending against volcanic disasters. Li X.M. et al. (2022) described the morphological distribution of calderas and the formation process of magma channels in rifts, providing a new model for understanding the genesis of terrestrial planetary grabens. Luo D. et al. (2022) reviewed the effects of cooling processes and chemical kinetics on basalt structure, mineral composition and thermodynamic parameter estimation, which are the key to a comprehensive understanding of magmatism and its deep processes. Ma Q. et al. (2022) comprehensively discussed the spatial and temporal distribution of Mesozoic volcanism in North China and the properties of volcanic rocks and magma origins under different spatiotemporal backgrounds, demonstrating that volcanism is an important link between deep dynamic processes and the evolution of superficial systems. In general, this special issue reflects the progress and achievements in recent years in the climatic and environmental effects of volcanic eruptions, the deep processes and shallow responses of volcanism, the dynamic processes and mechanisms of magmatism, and the application of new techniques for volcano monitoring.



**Special Issue on advances in volcanology and volcanism, published in “Bulletin of Mineralogy, Petrology and Geochemistry” (Volume 41, Issue 4)**

### **Acknowledgement**

We are grateful to Academician & Prof. Yigang Xu for his help and support.